13th International Conference on Clouds and Precipitation

Proceedings – Volume 1

Reno, Nevada USA

14–18 August 2000

International Cloud Physics Meetings

1954	I	4–6 October	Zurich, ETH
1956	II	January	London, Imperial College
1960		9–13 August	ATTI
1961	III	September	Canberra, Sydney
1965	IV	24 May–June 1	Tokyo, Sapporro
1968	V	26–30 August	Toronto
1972	VI	August	London, Royal Society
1976	VII	26–30 June	Boulder, Bur. St.
1980	VIII	15–19 July	Clermont Ferrand
1984	IX	21–28 August	Tallinn
1988	X	15–20 August	Bad Homburg
1992	XI		Montreal, McGill
1996	XII	19–23 August	Zurich, ETH
2000	XIII	14–18 August	Reno, DRI

Welcome to Reno – the Biggest Little City in the World!

As we welcome participants to the 13th International Conference on Clouds and Precipitation, we do so from a perspective that our subject is putting on our shoulders a responsibility to the scientific community which was not there before. More than ever, the enjoyment and interpretation of cloudscapes are taking second place to application of our knowledge in important political and technological decisions. Such decisions are based on an assessment of complex atmospheric processes including, for example, the influence of cloud particles on the global radiation budget or atmospheric chemical reactions.

Fundamental to this responsibility is assessing the reality—or otherwise—of how our technological society is influencing global climate through the generation and use of energy. This involves use of satellite remote sensors to attempt to retrieve cloud properties on a global scale, leading to insights into energy budgets related to radiation absorption and scatter, and latent heat transfer through different phase changes.

Meanwhile, more immediate problems include predicting likely precipitation rates, providing accurate warnings of severe storms, and assessing the impact of clouds on air quality. Solutions to these challenges require improved interpretations of radar signatures and more reasonable parameterizations within numerical weather and air quality forecast models. With all of these endeavors, from the use of remote sensing to improved modeling, there is a great danger that our drive for simplicity will lead to divergence from the reality we seek, and thus result in misleading information. Herein lies our responsibility.

We must advance the concept that algorithms for computing things work better if they are based on physical or chemical insight. This has been considered heretical in some circles and may have slowed advance in both understanding and representing certain problems. And there are areas where our understanding is still thin—the nature and role of mixing processes on a variety of scales, ice nucleation, the role of the surface layer on ice, and cloud electrification, to name a few.

Our perspective must encompass all approaches—observational, experimental, theoretical, and numerical. We seek to further our basic understanding as well as promote application to topics possibly well outside our immediate interests. Our goal for this meeting must be to further these objectives by successfully following the long tradition of scientific leadership set by the preceding International Conferences on Clouds and Precipitation.

John Hallett – Chair, Local Arrangements
George Isaac – Chair, Program Committee

June 2000

13th International Conference on Clouds and Precipitation
Reno Area, Nevada, USA
14-18 August 2000

Conference Organization

International Commission on Clouds and Precipitation

G.A. Isaac*, President	Canada	G. Vali*, Vice President	USA
B. Albrecht	USA	S. Bakan*	Germany
J.-L. Brenguier*	France	A. Blyth	USA
R. Bruintjes	USA	A. Chernikov	Russia
A. Flossman*	France	P.C.S. Devara*	India
D. Hegg*	USA	S. Fuzzi*	Italy
J. Joss	Switzerland	J. Jensen*	Australia
M. Murakami*	Japan	A. Korolev	Canada
C.M. Platt	Australia	Z. Levin*	Israel
R. Rosset	France	M. Nicolini*	Argentina
A.S. Stepanov	Russia	D. Starr*	USA
H. Sundqvist	Sweden	J. Stith*	USA
B. Wielicki	USA	G. Zhang*	P.R. China
M.K. Yau	Canada		

Honorary Members: Sir John Mason, UK and H. Pruppacher, Germany
Past Presidents: P. Jonas*, UK and P. Hobbs, USA

* Program Committee Members along with John Hallett of DRI. The Program Committee also wishes to express its appreciation to Elena Korolev and Natty Urquizo for their assistance.

Local Arrangements Committee

John Hallett, Chair, Desert Research Institute (DRI)
Peter Barber, DRI
James Hudson, DRI
Marcin Szumowski, DRI
Marilyn Allen, DRI
Margie Stuart, DRI
Morien Roberts, DRI
Roger Kreidberg, DRI
Olga Garro, DRI

Paper

Table of Contents for Papers

Page

Sessions 1 - 9.1, pages 1-660, are in Volume 1
Sessions 9.2 - 19, pages 661-1318 are in Volume 2

Session 1: INTRODUCTORY PAPERS

Session 2: AEROSOL MICROPHYSICS

Paper **Table of Contents for Papers** Page

Session 3: WARM CLOUD MICROPHYSICS

Session 13: CLOUD ELECTRICITY

Session 14: HAIL

List of Authors

COMPARISON OF CIRRUS CLOUD MODELS: A PROJECT OF THE GEWEX CLOUD SYSTEM STUDY (GCSS) WORKING GROUP ON CIRRUS CLOUD SYSTEMS

David O'C. Starr[1], Angela Benedetti[2], Matt Boehm[3], Philip R.A. Brown[4], Klaus M. Gierens[5], Eric Girard[6], Vincent Giraud[7], Christian Jakob[8], Eric Jensen[9], Vitaly Khvorostyanov[10], Martin Koehler[11], Andrew Lare[12], Ruei-Fong Lin[13], Ken-ichi Maruyama[14], Martin Montero[15], Wei-Kuo Tao[1], Yansen Wang[16], and Damian Wilson[17],

[1]Laboratory for Atmospheres, NASA Goddard Space Flight Center, Greenbelt, MD, 20771, USA
[2]Department of Atmospheric Sciences, Colorado State University, Fort Collins, CO, 80523, USA
[3]Department of Meteorology, Pennsylvannia State University, University Park, PA, 16802, USA
[4]Atmospheric Processes Research, U.K. Meteorological Office, Reading, Bracknell, RG12 2SZ, UK
[5]Institut fuer Physik der Atmosphere, DLR Oberpfaffenhofen, Wessling, D-82234, Germany
[6]CIRES, University of Colorado, Boulder, CO, 80309, USA
[7]Laboratoire d'Optique Atmosphere, Universite des Sciences et Technologies de Lille, Villeneuve d'Ascq Cedex, F-59655, France
[8]ECMWF, Reading, Berkshire, RG2 9AX, UK
[9]NASA Ames Research Center, Moffett Field, CA 94035, USA
[10]Department of Meteorology, University of Utah, Salt Lake City, UT, 84112, USA
[11]NOAA Geophysical Fluid Dynamics Laboratory, Princeton, NJ, 08542, USA
[12]SM&A Corp. at Code 913, NASA Goddard Space Flight Center, Greenbelt, MD, 20771, USA
[13]USRA at Code 913, NASA Goddard Space Flight Center, Greenbelt, MD, 20771, USA
[14]Frontier Research System for Global Change, NASDA Institute for Global Change Research, Tokyo, 105-679, Japan
[15]Department of Physics, Dalhousie University, Halifax, Nova Scotia, B3H 3J5, Canada
[16]JCET at Code 912, NASA Goddard Space Flight Center, Greenbelt, MD, 20771, USA
[17]Hadley Centre for Climate Prediction and Research, U.K. Meteorological Office, Reading, Bracknell, RG12 2SZ, UK

1. INTRODUCTION

The GEWEX Cloud System Study (GCSS, GEWEX is the Global Energy and Water Cycle Experiment) is a community activity aiming to promote development of improved cloud parameterizations for application in the large-scale general circulation models (GCMs) used for climate research and for numerical weather prediction (Browning et al., 1994). The GCSS strategy is founded upon the use of cloud-system models (CSMs). These are "process" models with sufficient spatial and temporal resolution to represent individual cloud elements, but spanning a wide range of space and time scales to enable statistical analysis of simulated cloud systems. GCSS also employs single-column versions of the parametric cloud models (SCMs) used in GCMs. GCSS has working groups on boundary-layer clouds, cirrus clouds, extratropical layer cloud systems, precipitating deep convective cloud systems, and polar clouds.

Corresponding author's address: David O'C. Starr, Code 913, NASA GSFC, Greenbelt, MD, 20771, USA; Email: David.O.Starr.1@gsfc.nasa.gov

Central to the GCSS strategy is the conduct of model comparison projects. These systematic comparisons document the performance of state-of-the-art models, detect problems with specific models, and identify fundamental issues resulting in significant inter-model differences, such as the approach to representing a specific process. Comparison to field observations, especially in a case study mode, is another cornerstone of the GCSS approach. The concept is that these activities will serve to markedly accelerate community-wide improvements in CSMs, as well as to provide better focus for planned field experiments in terms of key science issues related to the modeling of cloud systems. CSMs are quite well matched, in terms of scales and resolved physical processes, for such comparisons with observations. Moreover, when sufficient confidence is established in the models via validation versus field measurements, CSMs can serve as highly useful research platforms for the development of concepts and approaches to cloud parameterization because they do resolve the physical processes operating in cloud systems to a much greater extent than SCMs. While some processes must still be parameterized in CSMs, such

parameterizations are more focused, in terms of the represented physical process, and better correspond to the scales at which such processes actually operate.

2. IDEALIZED CIRRUS MODEL COMPARISON

The GCSS Working Group on Cirrus Cloud Systems (WG2) is conducting an Idealized Cirrus Model Comparison Project where cirrus cloud simulations by a variety of cloud models are compared for a series of idealized situations with relatively simple initial conditions and forcing. *Preliminary* results of this activity are reported herein. A second WG2 project, Cirrus Parcel Model Comparison, is reported in a companion paper in this volume (Lin et al., 2000). In the present project, results were submitted from 16 distinct models, including 3-dimensional large eddy simulation (LES) models, 2-dimensional cloud-resolving models (CRMs), and SCMs. The microphysical components of the models range from single-moment bulk (relative humidity) schemes to sophisticated size-resolved (bin) treatments where ice crystal growth is explicitly calculated. Radiative processes are also included in the physics package of each model and are similarly varied.

The baseline simulations include nighttime "warm" cirrus and "cold" cirrus cases where cloud top initially occurs at about –47°C and –66°C, respectively. The cloud is generated in an ice supersaturated layer about 1 km in depth (120% in 0.5 km layer) with a neutral ice pseudoadiabatic thermal stratification (Fig. 1).

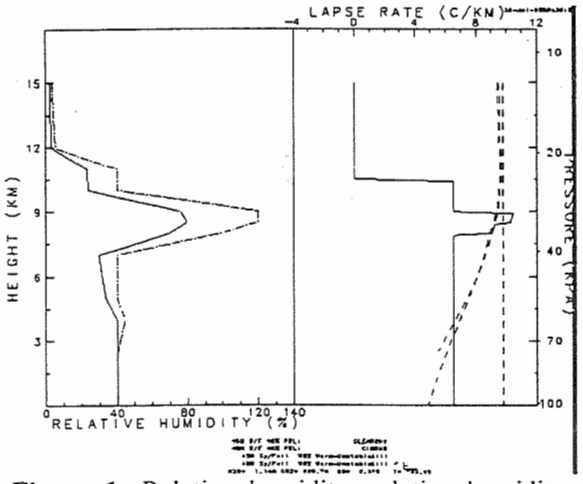

Figure 1: Relative humidity, relative humidity with respect to pure ice, and temperature lapse rate profiles for the "warm" cirrus case. Reference lapse rates corresponding to neutral stratification for ice pseudoadiabatic and dry adiabatic processes are also shown. Profile shape is similar for the "cold" cirrus case.

Away from cloud forming region, ambient conditions correspond to the Spring/Fall 45°N and Summer 30°N standards, where the tropopause occurs more than 1 km above the nominal cirrus layer in the "warm" and "cold" cirrus cases, i.e., at -56°C at 10.5 km and -75.5°C at 15.5 km, respectively.

Continuing cloud formation is forced via an imposed diabatic cooling representing a 3 cm s^{-1} uplift over a 4-hour time span followed by a 2-hour dissipation stage with no imposed "ascent" cooling. Variations of the baseline cases include no-radiation and stable-thermal-stratification cases.

The time-dependent behavior of the vertically-integrated and horizontally-averaged ice water path (IWP) are shown in Fig. 2 for the "warm" (lower panel) and "cold" (upper panel) cirrus comparisons (neutral stratification, infrared only). This is the grossest measure of model response to the prescribed conditions.

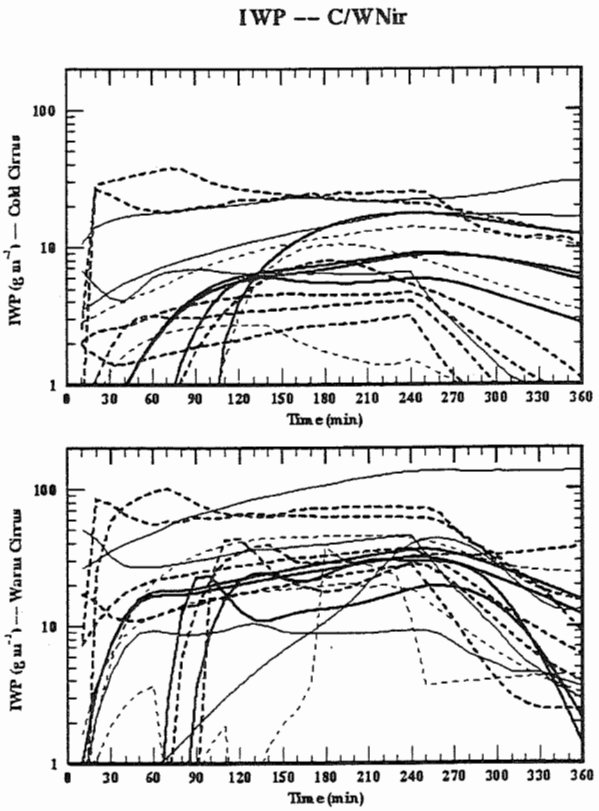

Figure 2: Time-dependent behavior of IWP (g m^{-2}) in simulations of "cold" (upper panel) and "warm" (lower panel) cirrus clouds with 16 cloud models -- see text for detailed description and explanation.

Results are shown for 16 models including 3 SCMs. Specific models are not identified here. Though somewhat arbitrary, the results are distinguished in terms of model heritage and design. Results from models built primarily to be cirrus models or with a strong cirrus heritage are shown by the heavy dashed or heavy solid lines. The heavy dashed lines denoted results from models with a bulk treatment of cloud microphysics

while the heavy solid lines indicate results from models with highly detailed bin treatments of cirrus cloud microphysical development. Thin dashed lines correspond to results from SCMs and the thin solid lines indicate models originally developed to treat deep convective cloud systems.

It is immediately obvious that a wide range of model response is found even in IWP (factor of 10). Focusing on the "cold" cirrus comparison, two significant groupings are evident. The bulk microphysics "cirrus heritage" models tend to behave in a similar manner. The "bin" models also group. The results from SCMs and models with a deep convection heritage yield results roughly spanning the range of the others. We will focus here on the cirrus heritage models.

Cloud formation is delayed in the bin models relative to the bulk models. All models employed an initial random field of weak thermal perturbations (0.02°C maximum). Thus, while the bulk models immediately respond to supersaturated conditions, the bin models wait until local conditions achieve sufficient relative humidity (up to 140% or more), via circulation, to trigger nucleation (Lin et al., 2000).

However, larger IWP is achieved in the bin models and is better maintained after the "ascent" forcing is turned off at 240 minutes. IWP is dissipated much more rapidly in the bulk models after this time. Even within these groups, differences amount to better than a factor of 2 at 240 minutes and are significantly greater at later times in the cold cirrus comparison. Results are more confused in the warm cirrus case where the overall spread is less (120-240 min.) and IWP declines precipitously after 240 minutes in most models. It should be noted that observations of "warm" cirrus have been much more plentiful than for cirrus at very cold temperatures and may be partly responsible for the greater convergence of results in the warm case.

Shown in Fig. 3 is a measure of circulation intensity within the cloud layers for the bulk and bin cirrus heritage models. Note that the simulations begin from a resting state. Focusing again on the cold cirrus case (top panel), two groups are again apparent. The models yielding the most dynamically energetic simulations of the cirrus heritage modles are the bin models. The bulk models produce significantly less intense circulation. Clearly, the two classes of models exhibit fundamentally different behavior for the cold cirrus case. As with IWP, the distinction is less clear for the warm cirrus case.

Another gross measure of model response is the location of cloud top and base. Shown in Fig. 4 are the locations of cloud top and cloud base, and the cloud thickness at 240 minutes in the cold cirrus simulations. These altitudes are determined by applying a suitable threshold to the horizontally-averaged ice water content profile where the same threshold is used for all the models. A range of more than 1 km is found in the

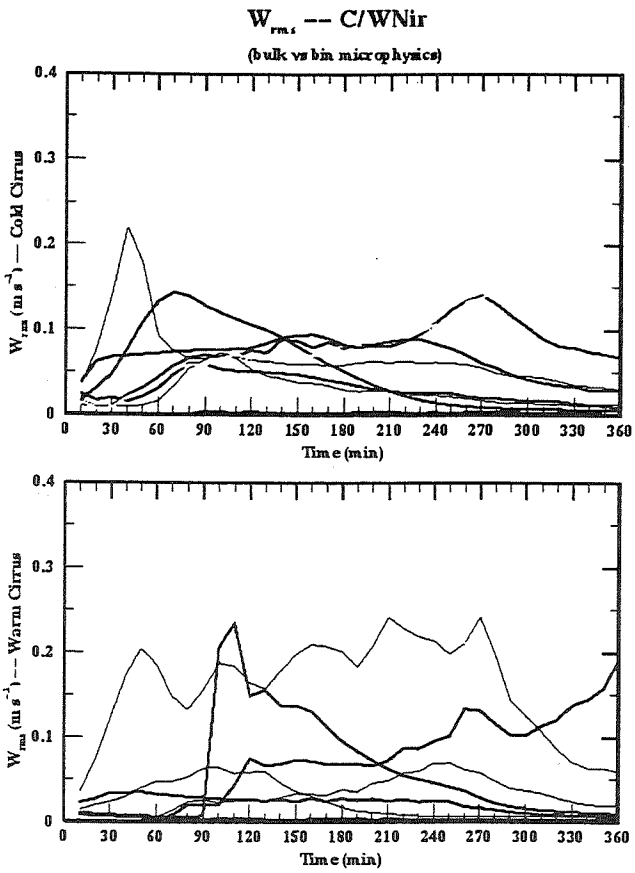

Figure 3: Time-dependent behavior of root mean square vertical velocity in the cloud forming region during simulations of cold (upper panel) and "warm" (lower panel) cirrus clouds by "cirrus heritage" models. See text for further explanation.

location of cloud top. Cloud base varies by more than 2 km among the models while cloud thickness ranges from 1.5 km to more than 4 km. This is a remarkable degree of inter-model difference.

To first order, these fundamental differences can be traced to differences in the size distribution of the ice crystal population represented in the two different classes of models. The bin models tend to have smaller, and consequently much more numerous, ice crystals while the bulk model are dominated by larger crystals, whether explicit or assumed. The primary effect of the differences in ice crystal size distribution is on the diagnosis of ice water fall speed. This was explicitly confirmed via calculations of an effective ice water fall speed integrated across the particle spectrum done within the bin models as part of this comparison project (not so easy a task). As noted by Starr and Cox (1985b), the ice water fallout process has a dominant effect on the vertical distribution of ice water and on the intensity of circulation within cirrus clouds. In the bin models, cloud top tends to grow upward while it is relatively static in

the bulk models. Correspondingly, the ice water content profiles are peaked more toward cloud top in the bin model simulations while the bulk models exhibit peak ice water content at a level below the middle of the cloud, much as seen in Starr and Cox (1985a). The downward extension of cloud base is enhanced in models with larger ice crystals.

As stated above, the relative agreement found in the warm cirrus case may be partly attributed to the availability of observations of "warm" cirrus clouds. Moreover, it should be noted that for homogeneous nucleation processes, disagreements among parcel models, from which the microphysical treatments in multi-dimensional bin models are derived, are significantly enhanced in the cold regime (Lin et al., 2000). The same ambient aerosol populations used in the WG2 Cirrus Parcel Model Comparison Project was also used here by the models requiring this information.

An additional set of experiments was performed in which the ice water fall speed was set to fixed values for all crystals, irregardless or size or habit. Values of 20 cm s^{-1} and 60 cm s^{-1} were used. The intent was to trick the bin models into behaving like the bulk models and vice versa, i.e., these values are roughly representative of the effective ice water fall speeds found in these model classes, respectively. The results largely confirmed the present interpretation. Tests of radiative impact (present versus no radiation simulations) revealed a consistent effect but not one that alters the present conclusion, i.e., relative to present simulation by each model, the no-radiation simulation produced similar relative changes.

3. CONCLUSIONS

While the present results may at first appear discouraging, they can also be seen to indicate that significant progress can be made in the very near future. The disagreements are substantial. Present observational capabilities, including recent advances in measurement of small ice crystal populations, should be able to adequately resolve the shape of the ice water content profile and the overall ice water path. The result that internal cloud dynamical intensity is highly correlated with ice crystal size distribution allows an additional confirming test that is within present measurement capability. Observations of bulk ice water fall speed are also now being derived from mm-wavelength Doppler radar. Further information about GCSS WG2 and its projects may be found at the GCSS WG2 webpage: http://eos913c.gsfc.nasa.gov/gcss_wg2/

REFERENCES

Browning, K. A., and collaborators, 1994: GEWEX Cloud System Study (GCSS) Science Plan. IGPO Publication Series No. 11, 62 pages and 3 appendices, World Climate Research Programme, Geneva.

Lin, R.-F., D.O'C. Starr, P.J. DeMott, R. Cotton, E. Jensen, and K. Sassen, 2000: Cirrus Parcel Model Comparison Project Phase 1. This volume.

Starr, D.O'C. and S.K. Cox, 1985a: Cirrus Clouds, Part I: A Cirrus Cloud Model. *J. Atmos. Sci.*, **42**, 2663-2681.

Starr, D.O'C., and S.K. Cox, 1985b: Cirrus Clouds, Part II: Numerical Experiments on the Formation and Maintenance of Cirrus. *J. Atmos. Sci.*, **42**, 2682-2694.

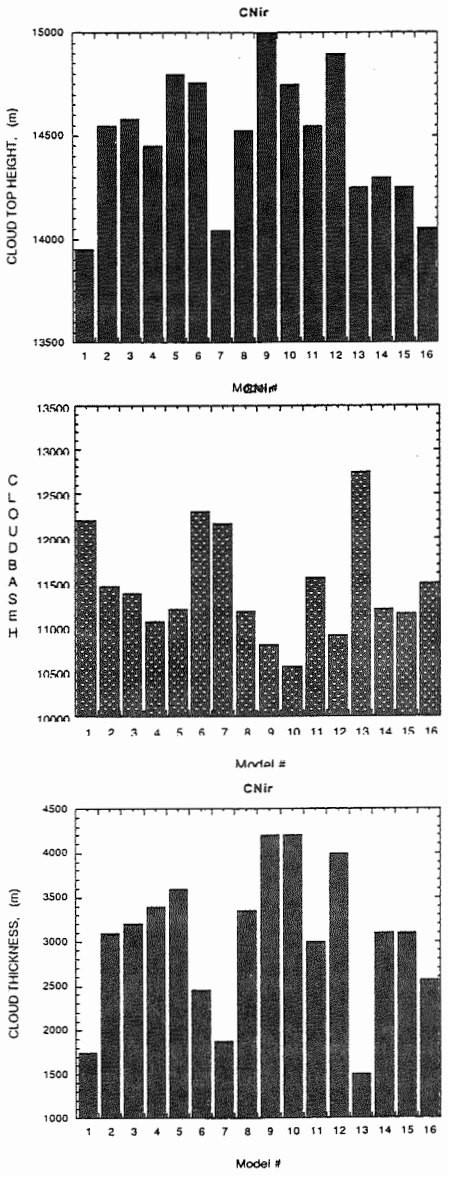

Figure 4: Distribution of cloud top (upper), cloud base (lower) locations, and corresponding cloud thickness for simulations of cold cirrus case. See text for discussion.

CLOUDSAT: AN EXPERIMENTAL STUDY OF THE GLOBAL PROPERTIES OF CLOUDS FROM SPACE

G. L. Stephens[1], D. G. Vane[2], R. T. Austin[1] and the CloudSat Science Team[3]

[1]Department of Atmospheric Science, Colorado State University, Ft. Collins, CO
[2]Jet Propulsion Laboratory, California Institute of Technology, Pasadena, CA
[3]See Acknowledgements for CloudSat Science Team List

1. INTRODUCTION

Large-scale cloud systems exert an enormous influence on our weather and climate. In addition to their key role in the atmospheric hydrological cycle, they dominate the energy budget of the planet through their effect on the Earth's solar and thermal radiation budgets. Clouds tend to cool the Earth by reflecting sunlight back to space and simultaneously warm the Earth by trapping thermal radiation emitted by the surface and lower atmosphere. By modulating the pole-to-equator variations of both solar insolation and radiation emitted to space, clouds provide a fundamental drive for the global circulations of the atmosphere and oceans.

The atmospheric circulation imposes a large-scale control on clouds in the sense that it governs where and when clouds form. The heating of the atmosphere and surface induced by clouds also affects the atmospheric circulation. The connection between clouds, radiative and latent heating and the atmospheric circulation establishes a complex feedback loop that is a major source of uncertainty in the predictions of climate change. The key to understanding this feedback lies in a deeper understanding than presently exists of the connections between cloudiness, heating and circulation. This understanding requires key information that is critical for understanding the connections between the processes illustrated in Fig. 1 but that cannot be obtained from current satellite measurement systems. This information includes:

- vertical profiles of cloud occurrence
- vertical profiles of cloud liquid water
- vertical profiles of cloud ice water content
- precipitation (solid and liquid) occurrence in relation to the above
- cloud optical properties (when radar data are combined with other sensor data).

CloudSat is a multi-satellite, multi-sensor experiment (e.g., Stephens et al., 2000) designed to provide this missing information. The mission's primary science goal is to furnish data needed to evaluate and improve the way clouds are parameterized in global models,thereby contributing to better predictions of clouds and thus to the poorly understood cloud-climate feedback problem. As highlighted above, the key missing data are the vertical profiles of cloud occurrence, cloud liquid water and ice contents and related cloud physical and radiative properties that are associated with these water contents. The CloudSat mission is a partnership between NASA/JPL, the Canadian Space Agency, Colorado State University, the US Air Force and the US Department of Energy. Ball Aerospace is building the spacecraft.

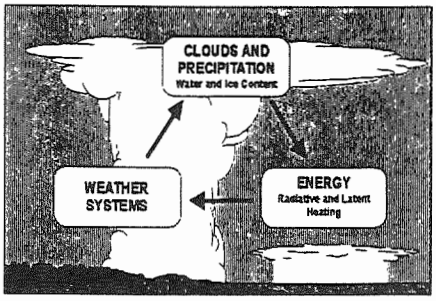

Fig 1. The main elements of cloud feedback emphasizing the connection between atmospheric circulation, cloud formation and radiative heating

2. MISSION GOALS AND CHARACTERISTICS

The CloudSat mission was selected in April 1999 under the NASA Earth System Science Pathfinder Program. Although the original CloudSat concept included the combination of lidar and radar (GEWEX, 1993), the estimated cost of this mission exceeded the maximum allowable under the ESSP program. The cost constraint imposed by ESSP led to two significant architectural decisions: the use of partners to provide funding for specific portions of the mission, reducing the net cost of the mission to NASA, and the use of formation flying with the another spacecraft to make near-simultaneous measurements from a combination of sensors on different spacecraft. CloudSat will be launched in 2003 along with a second ESSP mission selected as part of the same proposal cycle. This mission is the PICASSO-CENA lidar mission which will formation fly with CloudSat and EOS-PM (Aqua). In this way, CloudSat integrates the lidar measurements

Corresponding author's address: Graeme L. Stephens
Department of Atmospheric Science, Colorado State University, Ft. Collins, CO 80523-1371; Email: stephens@atmos.colostate.edu

of PICASSO-CENA and the observations from the suite of instruments flown on Aqua with the specific observations of the CloudSat payload, providing a rich source of information for studying clouds.

2.1 Mission Science Goals

The science goals of the mission are:

1. *Quantitatively evaluate the representation of clouds and cloud processes in global atmospheric circulation models, leading to improvements in both weather forecasting and climate prediction;*
2. *Quantitatively evaluate the relationship between the vertical profiles of cloud liquid water and ice content and cloud radiative properties, including the radiative heating by clouds;*
3. *Evaluate cloud information derived from other research and operational meteorological spacecraft; and*
4. *Improve our understanding of the indirect effect of aerosols on clouds by investigating the effect of aerosols on cloud formation.*

2.2 Payload

The primary CloudSat payload consists of a 94-GHz Cloud Profiling Radar (CPR) and a near-infrared Profiling A-Band Spectrometer/Visible Imager (PABSI). The measurements from these sensors are augmented by the dual wavelength lidar system of PICASSO-CENA and the various sensors of EOS Aqua, notably CERES, AIRS, AMSR and MODIS.

CPR: The CloudSat Cloud Profiling Radar provides calibrated radar reflectivity (*e.g.*, radar backscatter power), as a function of distance from the spacecraft. The CPR will provide a nominal minimum detectable reflectivity factor (hereafter MDS) of approximately -29 dBZ, a 70 dB dynamic range, and a calibration accuracy of 1.5 dB. The radar footprint is 1.4 km, which will be averaged over 0.3 seconds to produce an effective footprint of 4 km (along-track) by 1.4 km (cross-track). The normal mode of operation will yield 500 m vertical resolution between the surface and 25 km with a resolution of cloud boundaries at 250 m.

PABSI: The Profiling A-Band Spectrometer/Visible Imager measures sunlight reflected from the atmosphere and surface in the O_2 A-band rotational spectrum between 761.61 and 772.20 nm and records narrow-band images at 747.5 and 761.5 nm. The high-resolution spectrometer determines optical depth and cloud top pressure and can identify low cloud under higher cloud layers by making high spectral resolution (0.5 cm^{-1}) measurements in the oxygen A-band. This instrument thus complements the profiling radar by locating the vertical structure of that (small) percentage of clouds expected to be below the threshold of the CPR: thin cirrus and thin small-drop water clouds.

2.3 Mission Characteristics

The mission characteristics may be summarized as follows:

Management: The mission PI is the principal author of this abstract and is responsible for all aspects of the mission. The mission is managed for the PI by NASA's Jet Propulsion Laboratory.

Launch: The proposed launch date is March 2003. CloudSat and PICASSO-CENA are to be dual-manifested on the Delta 7240-10 launch vehicle.

Spacecraft: The spacecraft is designed around the Ball Aerospace RS2000 spacecraft bus used for both QuikScat and ICESat. Communications is accomplished via an S-band transceiver using a nearly omni-directional patch antenna.

Formation Flying: Formation flying enables CloudSat to track the orbit of PICASSO-CENA and EOS-PM in a very precise way. The radar and lidar footprints on the ground are estimated to directly overlap each other for a substantial fraction of all the orbits. In this way, the overlapped footprints of PICASSO-CENA create a coordinated and essentially simultaneous set of measurements with the CloudSat radar.

Orbit and Duration: The CloudSat orbit is dictated by the desire to formation fly with the EOS Aqua, which is a sun-synchronous, 705 km altitude orbit with an equator crossing time of 1:30 pm offering a full daylight (and nighttime) view of the Earth. The CloudSat mission was also designed with a two-year lifetime requirement to enable more than one seasonal cycle to be observed, although there is no technical reason that prohibits the mission lifetime extending beyond 2 years.

Ground Sector and Data Processing: The US Air Force Space Test Program is to provide ground operations and manage communications with the spacecraft. It is expected that the data will be downlinked up to about 10 times per day providing a data latency of about 2-4 hours. The Cooperative Institute for Research in the Atmosphere (CIRA) at Colorado State University (CSU) will handle data processing and archiving of the data for the duration of the mission. Some portion of the data will be processed and distributed to operational centers for use in near-real-time assimilation and cloud forecast evaluations. The archive of all data will be transferred to the NASA Langley DAAC at mission completion.

3. MEASUREMENT APPROACH AND ANTICIPATED PRODUCTS

Table 1 provides a summary of the level-2 products that will be derived from the measurements after launch

that are viewed as essential for meeting the goals of the missions. Further products are also expected from developing retrieval methods and from integration of other data with CloudSat. For example, all essential products except for one listed in Table 1 are derived from the CPR, the PABSI or the CPR-PABSI combination.

Products	Radar	PABSI	P-C Lidar
Cloud Geometrical Profiles (CGP)			
Radar-only CGP	✖		
PABSI-only CGP		✖	
Lidar/Radar/PABSI CGP	✖	✖	✖
Cloud Scenario Classification	✖	✖	✖
Cloud Ice Water Content (IWC)			
Radar-only IWC	✖		
PABSI/Radar IWC	✖	✖	
Cloud Liquid Water Content (LWC)			
Radar-only LWC	✖		
PABSI/Radar LWC	✖	✖	
Optical Depth			
PABSI-only Optical Depth		✖	
PABSI/Radar Optical Depth	✖	✖	
Fluxes and Heating Rates	✖	✖	✖
Precipitation Occurrence	✖	✖	
Particle Size Profiles (ice)	✖		✖
Particle Size Layer Mean (water)	✖	✖	
Layer-mean Drop Concentration	✖	✖	

Table 1. The required cloud level-2 products derived from CloudSat level –1 sensor data. Some experimental products are also included.

These products divide into four broad classes - cloud geometric profile information and cloud type classification derived from this information, cloud physics including ice and liquid water contents, cloud optical properties, and radiative fluxes and heating rates.

The measurement approach for deriving optical properties of clouds is discussed in Stephens and Heidinger (2000) and Heidinger and Stephens (2000). The algorithms developed for cloud physical properties are predicated on exploiting the different properties of active and passive observing systems. The benefits of combining these different measurement approaches into a single cloud observing system has been demonstrated over the past 20 years using measurements from both aircraft and ground based lidar, radar and radiometer systems.

Figure 2 provides results of a retrieval of cloud water using the CloudSat multisensor approach. The combination of radar reflectivity and cloud optical depth provide essentially independent information about cloud liquid water content and droplet size as illustrated in Fig. 2a showing theoretically calculated relationships between vertically integrated radar reflectivity (IZ), cloud optical depth τ, LWP and r_e, portrayed in the form of contours of LWP and r_e. The degree of independence of the IZ-τ information is indicated by the degree to which these contours lie in orthogonal directions to one another. Austin et al. (2000) describe how radar and optical information are optimally combined to retrieve cloud liquid water content (and particle size). An example of this retrieval using surface measurements is shown in Fig. 2b contrasted against LWP data retrieved from the ARM microwave radiometers. This agreement is also verified with recent aircraft data also reported by Austin et al.

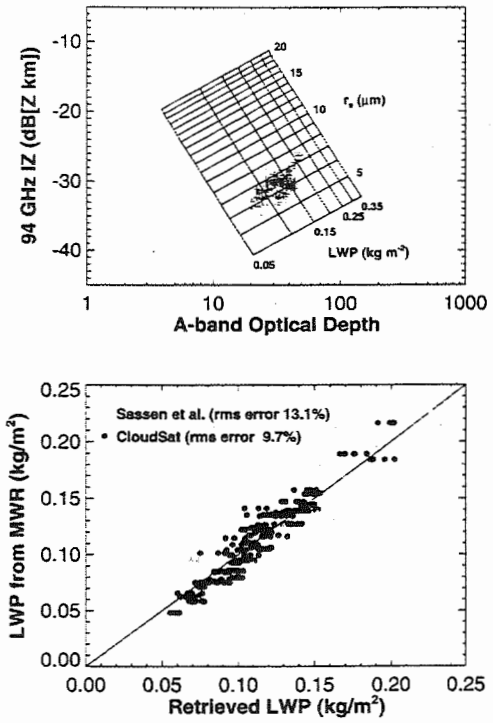

Fig. 2. An illustration of the CloudSat measurement approach as it applies to the measurement of cloud liquid water content. The relationship between radar reflectivity and cloud optical depth provides independent information about LWP and particle size. Observations of IZ and τ when placed together yield LWP and r_e. The LWP retrieved in this fashion using surface based radar and radiometer data collected at the ARM CART site yields LWP values that are within 10% of those determined independently from the ARM microwave radiometer (lower).

4. MEASUREMENT CHALLENGES

With the new retrieval methods that have been developed for analyses of cloud radar data and the new

information derived from these algorithms come a number of challenges and opportunities to expand on information that might be derived from combinations of space-borne radar measurements. Among these are:

- Detailed assessment of algorithm errors- involving direct validation of cloud information, end-to-end error analyses and understanding the ambiguities of the retrieval assumptions.
- Understanding the detection characteristics of the space-borne radar and the relation of these detection limits to cloud optical properties. For example Fig. 3 compares layer-averaged 94 GHz radar reflectivities for marine stratocumulus and cirrus clouds expressed as a function of cloud optical depth deduced from simultaneous aircraft measurements.
- Expanding on cloud information contained in the radar measurements. In particular, the rich information on precipitation contained in the CPR data needs to be further examined and retrieval schemes developed.
- Develop necessary techniques that integrate cloud radar data with other sensor information so as to optimize the information content provided by these additional data. For example, the combination of CPR with passive microwave radiances obtained from AMSR on EOS Aqua offers great potential in improving many cloud products, including precipitation.

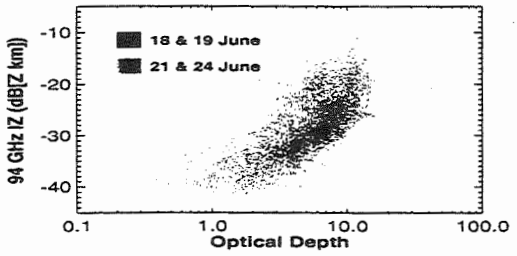

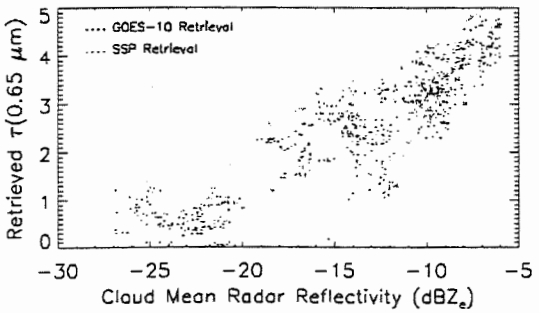

Fig. 3. The radar optical depth relationship derived from coincident measurements of marine stratocumulus, some with drizzle (Austin et al., 2000). The lower panel is the visible optical depth-radar reflectivity as derived from coincident data obtained for the cirrus cloud layer observed on April 30th.

5. SUMMARY

The CloudSat mission is expected to provide new knowledge about global cloudiness and will stimulate new areas of research on clouds including data assimilation, retrieval theory and cloud parameterization. The mission also provides an important opportunity to demonstrate active sensor technology for future scientific and tactical applications.

6. ACKNOWLEDGMENTS

We acknowledge the contributions of the entire CloudSat Science Team (T. P. Ackerman, H. Barker, D. Crisp, K. F. Evans, J. Fisher, D. Hudak, H. Kumagai, F. K. Li, Z. Li, G. G. Mace, S. Y. Matrosov, T. Nakajima, M. Quante, D. A. Randall, D. L. Reinke, W. B. Rossow, K. Sassan, J. D. Spinirne, R. E. Stewart, C. T. Swift, T. H. VonderHaar, S. J. Walter, and B. A. Wielicki. This research was performed under NASA Grants NCC5-288 and NAS5-99237.

7. REFERENCES

Austin, R.T, G.L. Stephens, Q. Min, S.D. Miller and S. Sekelsky, 2000: Retrieval of stratus cloud microphysical parameters from millimetric radar and visible optical depth. Submitted to *J. Appl. Met.*

GEWEX, 1993: Utility and feasibility of a cloud profiling radar. Report of the GEWEX Topical Meeting, IGPO, Pub. Series, No. 10.

Heidinger, A.J., and G. L. Stephens, 2000: Molecular Line Absorption in a Scattering Atmosphere. Part II: Application to Remote Sensing in the O_2 A Band. *J. Atmos. Sci.*, **57**, *1615-1634.*

Stephens, G. L., and A. Heidinger, 2000: Molecular Line Absorption in a Scattering Atmosphere. Part I: Theory. *J. Atmos. Sci.*, **57**, 1599-1614.

Stephens, G. L., D. G. Vane, and the CloudSat Science Team, 2000: A new dimension to space-based observations of clouds. Submitted to *Bull. Am. Meteorol. Soc.*

HARMONIZATION OF TERMOINOLOGY IN CLOUD PHYSICS

Ilia P. Mazin[1,2], George A. Isaac[3], and John Hallett[4]

[1]Central Aerological Observatory, Russia
[2]Computational Sciences and Informatics, CEOSR, George Mason University, Fairfax, USA.
[3] Meteorological Service of Canada, Toronto, Ontario, M3H 5T4, Canada
[4] Atmospheric Sciences Center, University of Nevada, USA

1. INTRODUCTION

Language is an important part of any collective activity. Terminology is an indispensable part of scientific language, which can promote the development of science, but can also slow down progress (like *phlogiston* in physics or *sublimation nuclei* in cloud physics)

Cloud physicists are now facing a terminology problem. Many terms are not defined clearly or precisely. Some terms have different meanings in various publications. Many of the commonly used terms are not included in well known (see Refs) meteorological glossaries, or definitions given in glossaries are not satisfactory and sometimes are not correct. We will try to show that ***the time has come for cloud physicists to harmonize their terminology.***

2. SITUATION WITH TERMINOLOGY IN CLOUD PHYSICS

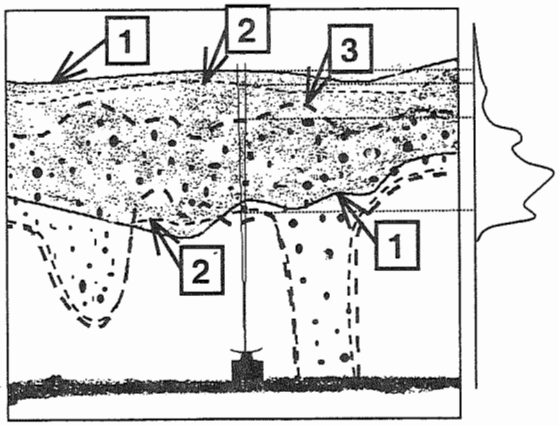

Fig. 1. Radar sounding a cloud and the corresponding reflectivity profile. 1: the visual cloud boundaries;2: the radar cloud boundaries; 3: the boundaries of large particle cloud.

Below, we will show some examples when terms are not defined clearly or precisely and are used to describe different objects. The very term *cloud* is one of the best examples. Mazin and Minervin (1993) emphasized that the contours of the each cloud are not the same for meteorologists, climatologists, radar observers, lidar observers, or observers on an aircraft. The difference is schematically shown in Fig.1. Statistics of the frequency of occurrence of clouds and their properties found by each of them will be also different. Thus, the statistics of frequency of occurrence of Ci clouds obtained by a lidar specialist will differ dramatically from those found in aircraft field experiments or based on radar observations. Fig.2 illustrates the statement. Here the "y" axis is the concentration of cloud droplets (N) and the "x" axis is the cloud droplet radius. If the point (r,N) (open circle) is lower than the line $Z=10^{-6}mm^6/m^3$ the cloud can not be seen by a radar observer. If it is lower than the line $\varepsilon=0.3\ km^{-1}$ (open triangle) the cloud can not be seen by lidar. The demarcation lines rises with the distance from clouds to the observer. If the point (open square) is lower the line LWC = $0.005\ g/m^3$ and the line $\varepsilon = 3\ km^{-1}$ the cloud will not be recorded by any of Nevzorov or King aircraft instruments (Korolev et al., 1998). Bold marks show that cloud can be recorded by using the proper instrument.

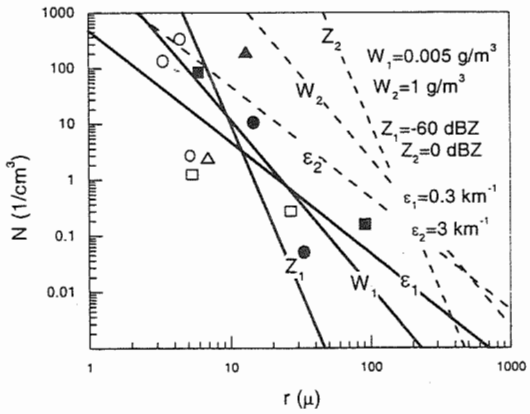

Fig. 2. Each line separates the cases when the clouds can be detected (to the right from a line) from those when it is not possible (see text).

Corresponding author's address: I.P. Mazin, CSI, CEOSR, George Mason University, Fairfax, VA 22030, USA

In order to be more precise, Hobbs and Rangno, (1998) suggested classifying clouds into 5 categories according to their microstructure. Another example is given by the terms *cloud droplets, drops, large drops* etc. The droplets in clouds (water and solution) have sizes from hundredths to thousands of microns. Their statistical parameters (concentration; mean, mode, median, and other specific radii) strongly depend on measuring intervals. Thus the question is, do we need to define precise intervals (for example, like it is done in Fig.3) to distinguish each class of droplets from the others?

All cloud physicists know the terms *CCN* (cloud condensation nuclei) and *CN.* But we cannot be sure that each of them will give the same answer

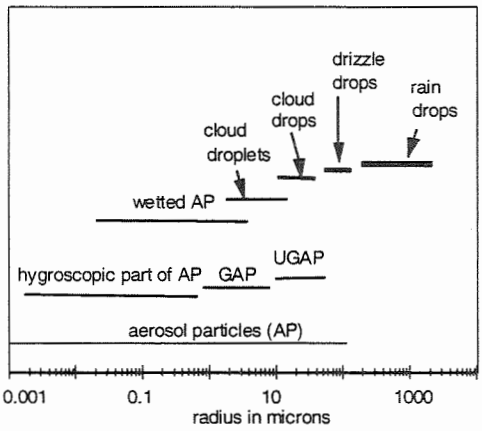

Fig 3. Cloud particle size intervals.

about which part of the *CN* forms the *CCN.* The question is, do we need to define *CCN* quantitatively?

Sometimes the same terms are used for different objects, like effective droplet radius in aircraft icing and in atmospheric radiation. In the first case it denotes the median volume radius, and in the second it is equal to the ratio of the average cube and the average square of the droplet radii.

There are many more terms that are worth being discussed and defined more precisely, like *cloud boundaries, cloud microstructure, stochastic condensation*, and others.

3. NEW TERMS

There are many relatively new but widely used terms that are not yet included in glossaries, which cause difficulties for readers like students, young researchers or our colleagues from the other branches of science. Here are some examples.

Homogeneous and *inhomogeneous mixing.* These terms were introduced by Baker et al.(1980). They help to improve our understanding and to better parameterize the role of turbulent mixing in the processes of droplet evaporation, condensation growth, and size distribution formation. It may be especially important and useful in describing the processes in *cloud boundary layers* (also a term that should be defined) (Paluch and Knight, 1984). *Phase relaxation time* (Mazin (1966), Mazin and Khrgian (1989)) reflects the rate of supersaturation relaxation to the equilibrium value. This notion helps us to better understand and to parameterize the processes of phase transformations in clouds . Connected with this notion is the term *phase scale of turbulence*, which helps to generalize some results of the theory of clear air turbulence onto the cloud medium. *Cloud phase indicator (CphI)* (Korolev (1998), Mazin (1998)) allows an investigator be more precise when speaking about cloud phase state. *CPhI* changes from 0 to 1 and describes quantitatively the relation between liquid droplet and ice particle contents in clouds. It also helps to better describe and to parameterize the processes of cloud glaciation and aircraft icing.

Today the term *CPhI* could be used efficiently in numerical modeling. Maybe later numerical models will help us to suggest the limits for cloud phase indicator values, to define liquid, mixed, and ice clouds more precisely.

4. PROBLEM OF AVERAGING

Processes in clouds are not reproducible, each experiment is unique and comparability of measurements performed in different clouds is a problem. This is even more evident for comparisons between experimental and numerical results.

Using the same terms (like average, averaging) to describe clouds and their structure is not sufficient to be sure that it means the same object or procedure. Gultepe and Isaac (1997, 1998) discuss how the average cloud properties changes with the averaging time interval used or the minimum threshold of the sensing instrument. An experimentalist averages the results of measurements and usually deals with the averaging like $\overline{F(X_1, X_2,...)}$, where F is a measured cloud parameter. F is a function of a number of variables, X_i, like time, coordinate, etc. In numerical modeling one often uses already averaged parameters as input values, thus the result of the simulations is like $F(\overline{X}_1, \overline{X}_2,...)$. Evidently, $\overline{F(X_1, X_2,...)} \neq F(\overline{X}_1, \overline{X}_2,...)$.

The next important point in averaging problem, not always clearly understandable from publications, is over what parameters the averaging

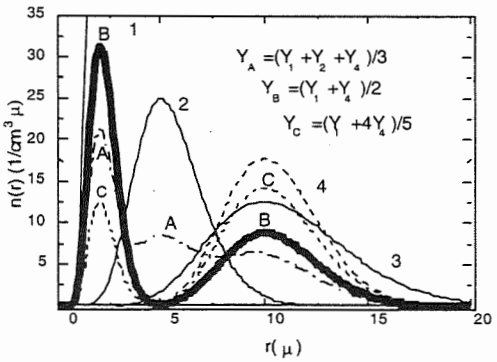

Fig.4. 1-4 are droplet size spectra for single samples. A-C are averaged spectra.

is performed. Very often it means averaging over all samplings. The sample selection criteria are also not always clear. This is especially important when averaging is made over a number of selected ensembles of the cloud population. Fig. 4 illustrates this point.

5. EMPIRICAL MODELS

An analogous problem arises when we try to analyze the empirical models that are widely used in cloud physics. Cloud thermodynamics and microstructure are good examples. To understand what kind of ensemble of clouds and samples was selected for averaging when constructing an empirical model is of great importance. Here is an example illustrating the point.

Imagine an empirical model of a woman constructed by a physician. He used the measurements of her legs, when she was 3 years old, the data for her upper body obtained when she was 30 years old and the data describing her head and hair when she was 80 years old. One can imagine how close to nature this model was. Such model will hardly satisfy anyone.

Let us return to cloud physics. What one can say about an empirical model of cumulus cloud that was constructed by the method described above? Imagine that the first pass through the cloud the researcher makes when the cloud was, let us say, 15 minutes old, the second when it was 25-30 minutes old, and the last when it was about 40 minutes old (Fig.5). Soon after that the cloud dies. Would this cloud physicist have any objections to the model he constructed basing on the collected data? Probably not. But we know that clouds are not isotropic and stationary objects. Thus, for proper interpretation of constructed models the process of any empirical modeling should be at least clearly described in each case.

Let us imagine that each pass through a Cu cloud gives a narrow unimodal droplet size distribution shown by the thin lines (curves 1-3), and dotted line (4). The modal values depend on the height *z* above cloud base and on cloud age. After averaging over several clouds and passes experimentalists A, B, and C have obtained the droplet size distribution labeled correspondingly. Three numerical modelers adjusted their non-averaged models to the respective averaged empirical data A-C. Which model describes the real cloud better? Which one, if any, can reproduce the intrinsic curves 1-4? Probably no further comments are needed in this situation.

Thus, it is evident that when averaged empirical results are presented, the procedure of selecting the ensemble of sampling over which the averaging is performed must be properly described. Otherwise numerical modelers do not have sufficient information to be able to compare numerical and empirical results.

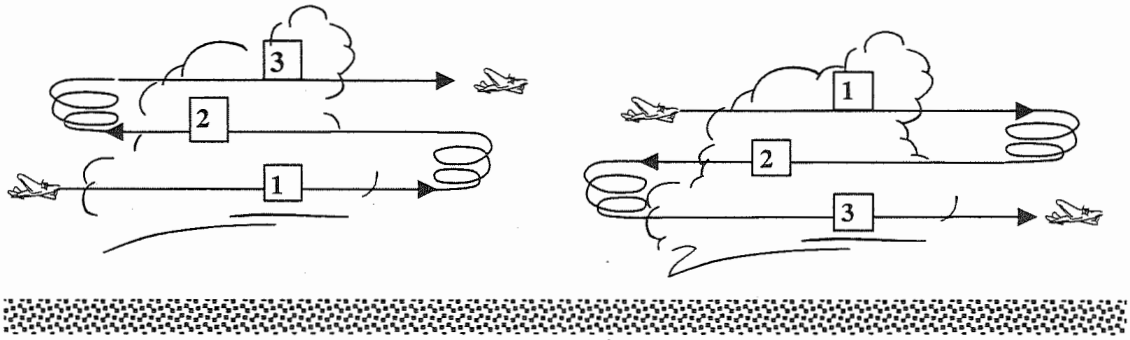

Fig. 5 . Scheme of aircraft Cu cloud sounding

6.CONCLUSIONS AND RECOMMENDATIONS

Terms and their definitions may be temporary, being specified with improving instruments and techniques of measurements or with better understanding. Some terms must remain vague and others can be better defined. However, it is essential that any term be properly described and its definition understood by the user.

We came to the following conclusions:

- **There is an urgent need to better define cloud physics terms and to publish these definitions for broad usage.**
- Where terms must remain vague, without quantifiable definitions, the authors should clearly describe what they mean.

We recommend the following to the International Commission on Clouds and Precipitation:

- To create a special Subcommittee or a Working Group (with WMO representatives) under the auspices of the International commission on Clouds and Precipitation for the purpose of preparing better cloud physics definitions.
- To charge the WG with preparing a report within two years in the working WMO languages. A list of terms to be included in this report should be distributed in the first year. It is desirable to include in such a list some terms from overlapping branches of sciences like atmospheric chemistry, electricity, turbulence, etc., and radar meteorology, climatology and others, as well as widely used abbreviations and notations. For this purpose, it will be necessary to include in the WG or consult representatives from some other Commissions of IAMAS. This report could be in the form of a new glossary, or a simple list of term definitions and some associated recommendations.
- To publish the report in all WMO working languages, as was done for the meteorological glossary. To ask the ICCP and WMO to support the publication and distribution among National Commissions on Cloud Physics and Precipitation, and among participants at the next (14th) International Conference on Clouds and Precipitation.

REFERENCES

GLOSSARIES:

Glossary of Meteorology 1959 Ed: R. E.Huschke: American Meteorological Society, Boston MAAMS.

AMS, 1996: Glossary of Weather and Climate, 271 pp.

Lewis, R.P.W., 1991: Meteorological Glossary, 6th ed HNSO, 335 pp..

WMO, 1992: International Meteorological Vocabulary, 2nd ed. WMO/OMM/BMO No.182 World Meteorological Organization, Geneva, 784 pp.

Baker M.B, Corbin R.G., and J. Latham, 1980: The influence of entrainment on the evalution of cloud droplet spectra:1. A model of inhomogeneous mixing. Quart. J. Roy. Met. Soc., 106, 581-598.

Gultepe, I., and G.A. Isaac, 1997: Relationship between liquid water content and temperature based on aircraft observations and its applicability to GCMs. J. Climate, 10, 446-452.

Gultepe, I., and G.A. Isaac, 1998: Scale effects on the relationship between cloud droplet and aerosol number concentrations: Observations and models. J. of Climate, 12, 1268-1279.

Hobbs P. & A. Rangno, 1998: Microstructures of low and middle-level clouds over the Beaufort Sea. Q.J.R.Meteorol.Soc. v.124, pp.2035-2071.

Korolev, A.V., 1998: About a definition of liquid, Mixed, and ice cloud. Proceedings of the FAA specialists' workshop on mixed-phase and glaciated icing conditions. Atlantic City, NJ,325-326.

Korolev, A. V., J. W. Strapp, G. A. Isaac, and A. N. Nevzorov, 1998: The Nevzorov airborne hot-wire LWC-TWC probe: principle of operation and performance characteristics. J. Atmos. Oceanic Technol. 15, pp.1495-1510.

Mazin, I.P., 1966: On temperature and humidity stratification in clouds. (In Russian). Trudy CAO, vyp.71, pp.3-15. See also "Effect of phase transition on formation of temperature and humidity stratification in clouds". Proc. Intern. Conf. on Cloud Physics. August. 26-30, 1968, Toronto, pp.132-137.

Mazin, I.P., 1998: Some remarks on mixing phase clouds related to aircraft icing. Proceedings of the FAA specialists' workshop on mixed-phase and glaciated icing conditions. Atlantic City, NJ,327-331.

Mazin and Khrgian, 1989: Clouds and Cloudy Atmosphere. Handbook. (in Russian). Leningrad, *Gidrometeoizdat*. 647p.Chep.8.3.3. Time of phase relaxation.319-322.

Mazin I.P. and V. E. Minervin, 1993: Regulation of terminology in cloud physics. *Russian Meteorology and Hydrology*, N 4, pp.1-8.

Paluch I.R. and C.A.Knight, 1984. Mixing and the evolution of cloud droplet size spectra in a vigorous continental cumulus. Jour. Atm. Sci.,v.41, 1801-1815.

LIDAR STUDY OF AEROSOLS IN MONSOON CLOUDS AND PRECIPITATION OVER PUNE, INDIA

P.C.S. Devara, P. Ernest Raj, G. Pandithurai, K.K. Dani and R.S. Maheskumar

Physical Meteorology and Aerology Division, Indian Institute of Tropical Meteorology, Pune 411 008, India

1. INTRODUCTION

Atmospheric aerosols play the most crucial role in cloud processes, and observations of aerosol characteristics prior to cloud formation and of the bulk cloud properties after formation would lead to better understanding of the influence of aerosols on clouds. Aerosol-cloud-precipitation cycle is the major mechanism responsible for the modification of aerosols in the troposphere, which influences the amount and distribution of precipitation. Moreover, aerosols and clouds are also important in air pollution as the latter control ventilation of pollutants that are generated at the Earth's surface. Their coverage is generally monitored and analyzed using satellite data, but sometimes their vertical profile becomes very important. Its derivation is difficult by satellite monitoring, but is easy by lidar monitoring. Moreover, aerosols and clouds are spatially and temporally varied in short period, so that a long-term continuous monitoring with a short repetition time is significant. The amount of solar radiation that reaches the Earth's surface depends on the amount of coverage, type of clouds, and as well as their physical and optical properties. In particular, the optical depth distribution of clouds, which is derivable from extinction coefficient, is found useful in modeling transport of radiation in the atmosphere (Pal et al., 1992). Therefore, besides the direct radiative effects of aerosols, and thereby the climate, it is important also to consider aerosols as a sub-system of clouds, because of strong interaction between aerosols and clouds (Twomey, 1977; Gultepe, 1995).

Lidars have been used in the past for cloud studies and have proven adequate in obtaining geometrical cloud parameters (Carswell et al., 1995) and also to retrieve optical cloud parameters (Young, 1995). Lidar measurements with excellent spatial and temporal resolution over extended time periods and in different geographical regions prove to provide an instantaneous picture of the optical properties of behaviour of clouds. Recently, the Experiment Cloud Lidar Pilot Study (ECLIPS) used worldwide lidar observations to gather statistics on cloud-base and cloud-top heights (WMO, 1988). The LITE program in which a lidar was flown on the space shuttle provided data on vertical profiles of clouds when viewed from above (McCormick et al., 1993). Moreover, it is well acknowledged that there is paucity of ground-based lidar data at low-latitude. Hence, extensive efforts from the international scientific community are being directed toward obtaining ground-based data from tropical sites.

An optical radar or lidar has been operational at the Indian Institute of Tropical Meteorology (IITM), Pune, India since 1985. The observations are specifically directed to the study of atmospheric aerosol characteristics with a view to establish a tropospheric aerosol climatology and to investigate its possible connection with concurrent meteorological parameters. In this paper, we present the results of the studies that have been carried out in this direction to examine the correspondence amongst the lidar-derived aerosol content (integration of altitude profile throughout the height range), meteorological parameters and south-west (SW) monsoon (June-September) activity over Pune during twelve successive SW monsoon seasons (1987-1998) including two contrasting seasons of 1987 and 1988. The lidar-observed cloud macro-physical parameters (base and ceiling heights, vertical thickness etc.) and their association with surface-generated aerosols and polarization characteristics at the experimental site are also discussed.

2. EXPERIMENTAL SITE CHARACTERISTICS

The lidar site is located at an elevation of about 573 m AMSL, approximately 100 km inland from the west coast, and is surrounded by some hillocks as high as 760 m AMSL (valley-like configuration). The transport and dispersion of aerosols, particularly in the lower levels of the

Corresponding author's address : P.C.S. Devara, Physical Meteorology and Aerology Division, Indian Institute of Tropical Meteorology, Dr. Homi Bhabha Road, NCL Post Office, Pune - 411008, India; E-Mail :devara@tropmet.ernet.in

atmosphere, are believed to be affected by the circulation processes that evolve because of this typical terrain. The major urban activity from the eastern side, and the mixture of water-soluble, dust-like and soot-like aerosols prevailing over the station also influence significantly on the aerosol loading at the lidar site. During the pre-monsoon (March-May) very hot weather prevails and cumulonimbus type cloud development takes place around late afternoon or evening. The airflow in the lower troposphere is predominantly westerly during the south-west (SW) monsoon season (June-September) which brings in a large influx of moist air from the Arabian Sea. The westerly flow weakens in the lower troposphere and the easterly flow sets in during post-monsoon (October-November). The continental air mass, rich in nuclei of continental origin, pass over the region during this season. Increase of dry polar continental air in the wake of low pressure systems (western disturbances) takes place during the winter season (December-February). Thus the meteorology at the experimental site varies markedly from continental (winter) to maritime (summer) environment.

3. LIDAR, OBSERVATIONS AND ANALYSIS

The IITM bistatic Argon-ion lidar (Devara and Raj, 1987; Devara et al., 1995) has been operational at Pune (18.5°N, 73.5°E, 559 m AMSL) since 1985. Its major goal is to study tropical atmospheric aerosol climatology and to investigate radiative effects and possible connection with concurrent meteorological parameters (Devara, 1997). Collocated with the lidar are multi-channel solar radiometers and spectroradiometer which also provide column-integrated aerosol optical depth and size distribution (Devara, 1998). More than 620 weekly-spaced vertical profiles of lower atmospheric aerosol number density have been collected during the 12-year period from October 1986 through September 1988. Apart from these routine measurements, almost an equal number of such profiles have been obtained during various special experiments, conducted from time to time, within the same period. Together these observations formed the database for the results presented here.

The scattered intensity profiles obtained with the Argon-ion laser light at wavelength of 0.5145 μm have been converted into aerosol number density profiles, involving particles of radius between 0.02 and 10 μm, by employing the inversion routine programs as detailed elsewhere (Devara et al., 1995). The aerosol number density profile obtained after every lidar experiment has been integrated up to an altitude of 1100 m to get aerosol columnar content in the atmospheric boundary layer over this station using the expression :

$$\sum_{i=50}^{1100}\left(\frac{C_i + C_{i+1}}{2}\right)\left(h_{i+1} - h_i\right) \qquad cm^{-2}$$

where C_i and C_{i+1} are concentration at the heights h_i and h_{i+1} respectively. The surface and altitude profile data of meteorological parameters at the experimental station during the above 12-year period of lidar observations also have been collected from the India Meteorological Department (IMD) which is almost 3 km east of the lidar site.

4. AEROSOL-CLOUD-PRECIPITATION RELATIONSHIP

Study of clouds is one of the important applications of lidar to meteorology. Aerosols of giant size (radius > 1 μm) act as cloud condensation nuclei (CCN) or ice nuclei (IN), and they play a pivotal role in cloud formation and time evolution (Twomey, 1977). Due to high density of nuclei and large optical cross-sections, lidar can better be applied for the study of clouds and their micro-physics (Zuev, 1982). In the presence of clouds, the received laser-scattered signal strength increases enormously, sometime by several orders of magnitude due to multiple scattering. Thus lidar is very useful for determining also the cloud macro-physical parameters. This phenomenon of multiple scattering in clouds has been receiving much attention in recent years in the development of space lidar. The capability of the lidar used in the present study for determining the cloud physical parameters such as base and ceiling heights and vertical thickness from the lidar signal strength profile observations obtained on two typical days during the SW monsoon season is shown in Figure 1 (a) and (b). The multiple cloud layers and different fine-scale atmospheric structures below the first cloud base from the ground as well as in between the cloud layers can be seen clearly. Interaction between the surface-generated aerosols and the structure of low and medium clouds can be an important interesting feature over urban environments. Furthermore, the fine structure of scattering in the air layer below the clouds can yield useful information on the properties of clouds forming over different geographical regions. Some of these aspects have been studied by comparing the lidar-measured aerosol number density distributions on

consecutive clear-sky and cloudy-sky days and pointed out the underlying mechanism "cloud scavenging". The results of the polarization lidar measurements during the above period also revealed that CCN in the lower altitude region are highly anisotropic and the depolarization ratio is quite different for raining and non-raining clouds.

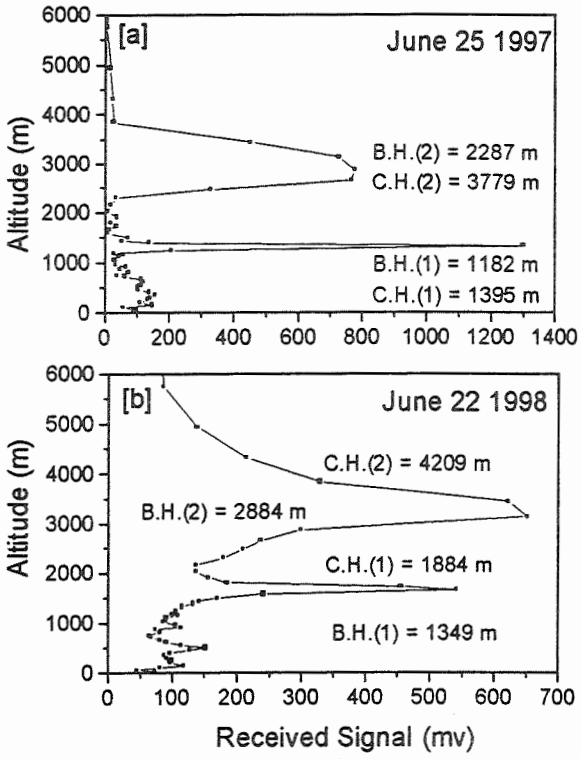

Figure 1 : Lidar-observed cloud macro-physical parameters on two typical SW monsoon days.

Most parts of India receive rainfall during the SW monsoon season. Hence, the relationship between boundary-layer aerosols and precipitation over Pune regions during the twelve successive SW monsoon seasons covering two contrasting monsoons have been examined utilizing the coincident, multi-year lidar aerosol and precipitation data for the period from 1987 to 1998. The aerosol columnar content or loading during different months of 1987 (weak monsoon year) and 1988 (active monsoon year) are depicted in Figure 2 (a) and (b) respectively. Since aerosols present in the air layers close to the ground contribute significantly to the total loading, the mean content in the air layer between 50 m and 200 m during different months are also shown in the figure. The SW season total rainfall during 1987 was 380 mm while during 1988 it was 885 mm. The mean aerosol content during 1987 was 129×10^6 cm^{-2} while during 1988 it was 179×10^6 cm^{-2}. Thus the results suggest a close correspondence between the SW monsoon activity and aerosol loading over Pune.

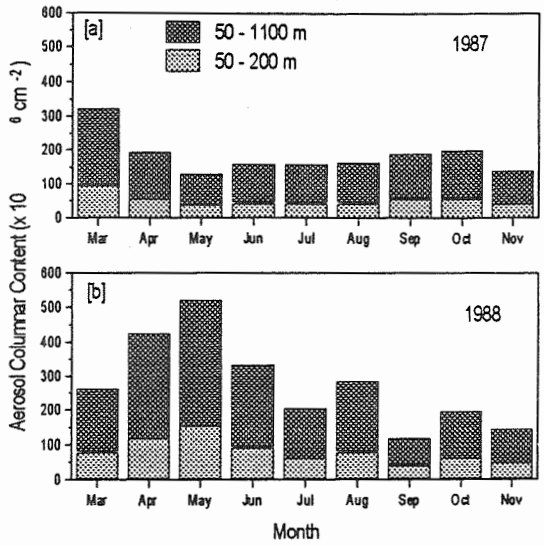

Figure 2 : Lidar-derived monthly mean aerosol columnar content during two contrasting SW monsoon seasons.

The above aerosol-precipitation relationship has also been examined further with long-term data recorded during the 12-year period. The decrease in aerosol columnar content from pre-monsoon (convection) to monsoon (rain washout) seasons is found to be about 40 per cent and showed a close agreement with the monsoon season total rainfall. This interesting feature has been studied (Figure 3) further by comparing the year-to-year change in aerosol loading (trend in per cent) and pre-monsoon minus monsoon aerosol columnar content, SW monsoon season rainfall and the maximum temperature that occurs every March. In the computation of year-to-year per cent change in the aerosol loading, the cumulative trend observed in the data for the first five years is considered as the initial long-term database and is updated every year by adding the lidar-derived aerosol columnar content data for that year. It is evident that all four parameters showed co-variation up to 1994 which is possible because increase in columnar content results in increase in trend and monsoon rainfall over this station. In addition, the negative correlation exhibited by the

percentage trend during 1995 and 1996 is considered to be due to non-uniform distribution of precipitation during those years. This station received rainfall of 618, 741 and 649 mm during SW monsoon season of 1996, 1997 and 1998 respectively. In 1997, the annual total precipitation

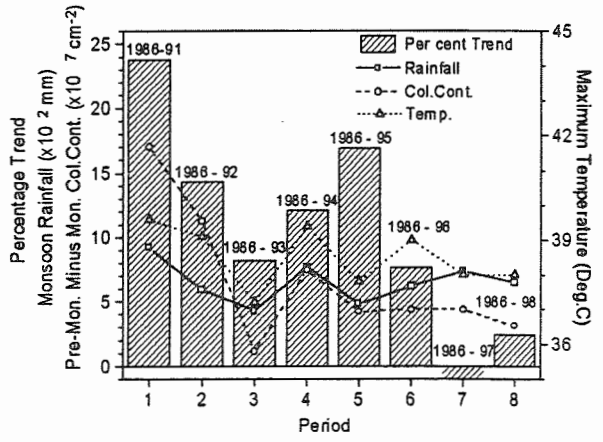

Figure 3 : Correspondence between aerosol columnar content, monsoon precipitation and temperature during 1987-1998.

intensity was more (1027 mm) as compared to that during 1997 (820 mm) and 1998 (813 mm). Since the precipitation distributed over the whole year, in 1997 the washout and rainout mechanisms might have acted very effectively on the aerosol loading over the station and altered the trend from positive to negative. The above correspondence between the aerosol columnar content and SW monsoon precipitation over Pune could be due to combined effect of the type of local aerosols and associated radiative forcing, and transport of marine air mass from Arabian Sea during the SW monsoon season. This feature, in some sense, suggests that change in pre-monsoon aerosol loading has strong bearing on ensuing SW monsoon precipitation. Such a relationship would be valuable to infer the behavior of monsoon from aerosol observations also.

Acknowledgements The authors are grateful to the Director, IITM for his keen interest in this study. The meteorological data support from the India Meteorological Department, Pune is acknowledged with thanks.

References

Carswell, A.I., A. Fong, S.R. Pal and I. Pribluda, 1995 : Lidar-derived distribution of cloud vertical location and extent. J. Appl. Meteor., 34, 107-120.

Devara, P.C.S., 1997 : Aerosols in meteorological studies. Ind. Aerosol Sci. Tech. Bull., 10, 45-46.

Devara, P.C.S., 1998 : Remote sensing of atmospheric aerosols from active and passive optical techniques. Int. J. Remote Sensing, 19, 3271-3288.

Devara, P.C.S. and P.E. Raj, 1987 : A bistatic lidar for aerosol studies. J. Inst. Electron. Telecommun. Eng. Tech. Rev., 4, 412-415.

Devara, P.C.S., P.E. Raj, S. Sharma and G. Pandithurai, 1995 : Real-time monitoring of atmospheric aerosols using a computer-controlled lidar. Atmos. Environ., 29, 2205-2215.

Gultepe, I., 1995 : Physical, radiative and dynamical processes within a nighttime marine stratus cloud. PAGEOPH, 144, 321-350.

McCormick, M.P., D.M. Winker, E.V. Browell, J.A. Coakley, C.S. Gardner, R.M. Hoff, G.S. Kent, S.H. Melfi, R.T. Menzies, C.M.R. Platt, D.A. Randall and J.A. Reagan, 1993 : Scientific investigations planned for the Lidar In-Space Technology Experiment (LITE), Bull. Am. Meteorol. Soc., 74, 205-214.

Pal, S.R., W. Steiinbrecht and A.I. Carswell, 1992 : Automated method for lidar determination of cloud-base height and vertical extent. Appl. Opt., 31, 1488-1494.

Twomey, S., 1977 : Atmospheric Aerosols, Elsevier, New York, 302 pp.

World Meteorological Organization (WMO), 1988 : Cloud-base Measurement Workshop. Report of the WCRP/CSIRO.

Young, S.A., 1995 : Analysis of lidar backscatter profiles in optically thin clouds. Appl. Opt., 34, 7019-7031.

Zuev, V.E., 1982 : Laser Beams in the Atmosphere, Plenum, New York, 504 pp.

CCN MEASUREMENTS DURING ACE-2 AND THEIR RELATIONSHIP WITH CLOUD MICROPHYSICAL PROPERTIES

P. Y. Chuang[1], D. R. Collins[2], H. H. Pawlowska[3], J. R. Snider[4], H. H. Jonsson[5], J. L. Brenguier[3], R. C. Flagan[6], and J. H. Seinfeld[6]

[1]National Center for Atmospheric Research, Boulder, CO, USA
[2]Texas A&M University, College Station, TX, USA
[3]Centre National de Recherches Météorologique, Toulouse, France
[4]University of Wyoming, Laramie, WY, USA
[5]Naval Postgraduate School, Monterey, CA, USA
[6]California Institute of Technology, Pasadena, CA, USA

1. INTRODUCTION

To better understand the indirect effect of aerosols on climate, the potential changes in cloud albedo, extent, and lifetime resulting from anthropogenic aerosols, the relationships among aerosols, cloud condensation nuclei (CCN), and cloud properties must be studied. During the Second Aerosol Characterization Experiment (ACE-2), the CIRPAS *Pelican* and Météo-France *Merlin*-IV flew coordinated missions as part of the CLOUDYCOLUMN sub-experiment. The *Pelican* measured below-cloud aerosol and CCN, while the *Merlin* performed a majority of measurements within cloud. Relationships among various measurements are derived, compared with model predictions, and discussed, with the goal of deriving new insight into some of the individual processes that link atmospheric aerosol and cloud properties.

2. INSTRUMENTATION

The *Pelican* ACE-2 payload included: the Caltech CCN instrument (Chuang et al., 2000) which during ACE-2 measured CCN at a fixed supersaturation of 0.1% at a frequency of one measurement approximately every 60 s; the Caltech Automated Classified Aerosol Detector (or ACAD) which measures the aerosol size distribution from 0.005 to 0.2 μm at a frequency of one distribution per 45 s using a radial differential mobility analyzer; a wing-mounted Particle Measuring Systems PCASP-100X optical particle counter measuring the aerosol size distribution from 0.1 to 3 μm; and supporting data measurements such as temperature, pressure, and relative humidity. The ACAD and PCASP data are combined to produce aerosol size distributions from 0.005 to 3 μm (Collins et al., 2000).

The *Merlin* ACE-2 payload included: the University of Wyoming CCN counter (similar to that described in Delene et al., 1998) which measured CCN concentration every 40 s for 4 different supersaturations (0.2, 0.4, 0.8 and 1.6%) for a CCN spectrum frequency of one every 160 s; the wing-mounted Météo-France Fast FSSP (Brenguier et al., 1998) for high frequency (1 Hz during this experiment) data acquisition of the droplet size distribution between 2 and 33 μm; liquid water content using a Gerber PVM 100 probe and a PMS King probe; and meteorological data.

To validate the Caltech CCN instrument performance we compared the instrument response against that of other CCN counters for a common aerosol sample. During ACE-2, there were a number of opportunities for such comparisons, mostly with the *Merlin* CCN instrument; during 4 periods the *Merlin* and *Pelican* were in close proximity for an extended time. There are also a number of longer periods over 6 flights for which both the *Merlin* and *Pelican* were sampling below cloud at about the same place and time. The ratio of *Merlin* to *Pelican* CCN concentration averaged over all flights is 1.15 ± 0.15 ($1\ \sigma$).

3. CCN CLOSURE

It is generally assumed that, if the number size distribution and chemical composition of an aerosol is perfectly known, then we can predict exactly the CCN spectrum. It is often further assumed that for determining the critical supersaturation of an aerosol particle, i.e., that supersaturation at which that particle activates, only two parameters are important: the number of moles of solution-phase species in the particle, and the volume of insoluble material present. This CCN model can be tested using CCN closure experiments, in which CCN concentration predicted using measured aerosol size distribution and chemical composition data, are compared with simultaneous CCN measurements. It is important to note that achieving such CCN closure implies that we understand the processes that govern CCN activation in the CCN instrument. It does not imply that we fully understand how CCN activate and grow in actual clouds, as there are several factors that may be relevant in real clouds that CCN instruments do not accurately reproduce at present, e.g. the kinetics of cloud droplet activation (Chuang et al., 1997), the presence of soluble gases (Laaksonen et al., 1998), and the time profile of supersaturation that an aerosol particle experiences, which is influenced by cloud dynamical processes such as entrainment, and by cloud microphysical factors such

Corresponding author's address: Patrick Y. Chuang, National Center for Atmospheric Research, P. O. Box 3000, Boulder, Colorado, 80307-3000, U.S.A.; E-Mail: chuang@ucar.edu

as the total CCN concentration. An inability to achieve closure could imply that the CCN concentration, aerosol size distribution, and/or chemical composition measurements require improvement for the purposes of closure experiments, or alternately that the traditional Köhler theory used to predict CCN concentration measurement data requires additional variables not previously considered in order to successfully achieve closure.

Pelican CCN and aerosol number size distribution measurements are used to evaluate the extent to which local CCN closure can be achieved during ACE-2. Size-resolved aerosol chemical composition data were not available at the same spatial and temporal resolution as the size distribution and CCN data. Instead, flight-averaged chemical profiles were estimated from a combination of ground-based filter measurements at Punta Del Hidalgo (PDH), Tenerife, and by making assumptions regarding the relative concentrations of the various components. A CCN spectrum was then computed based on these size/composition distributions. The predicted CCN concentration was then calculated by summing all CCN predicted to have critical supersaturation less than 0.1%.

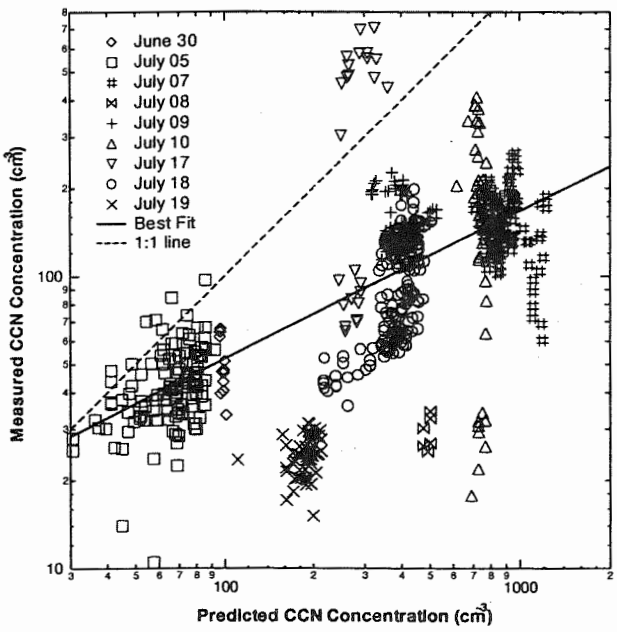

Figure 1: Local closure of CCN. Plot of measured and predicted number concentration of CCN at 0.1% supersaturation for cloudy (open symbols, e.g. X) and clear (closed symbols, e.g. O) conditions. The error bars for each measurement are not shown; the average relative standard deviation for the measured CCN data is 0.22. Error bars for the predicted CCN concentration are estimated to be at most 37% of the predicted value.

A total of 684 comparisons of measured and predicted CCN concentrations over 9 flights are shown in Figure 1. The data were taken in the boundary layer during constant altitude legs in both clear and cloudy conditions. While there is considerable scatter, a regression of all data (except data from July 08, 10, and 19, which are believed to be flawed) gives the relationship $N_{ccn} \sim N_{ccn,pred}^{0.51}$, with a 95% confidence interval for the exponent of 0.47 to 0.54, where N_{ccn} and $N_{ccn,pred}$ are measured and predicted CCN concentration at 0.1% supersaturation, respectively. Error estimates lead to the conclusion that the large variability observed in Figure 1 does not appear to originate only from random instrument error.

An analysis of the sensitivity of $N_{ccn,pred}$ to the assumed chemical composition profiles was conducted. Base case chemical composition profiles were obtained by adjusting the various amounts of sulfate, sea salt, OC, and EC until the integrated submicron mass matched the submicron composition profile measured at PDH for the same period. The amount of sea salt, OC, and EC were then varied by 50% from their base case values, which is a conservative estimate since the errors associated with the composition measurements are likely to be smaller. The typical error of $N_{ccn,pred}$ with respect to chemical composition is liberally estimated to be 37%. It appears, then, that even large changes in the chemical composition of the aerosol cannot explain fully the variability observed in Figure 1.

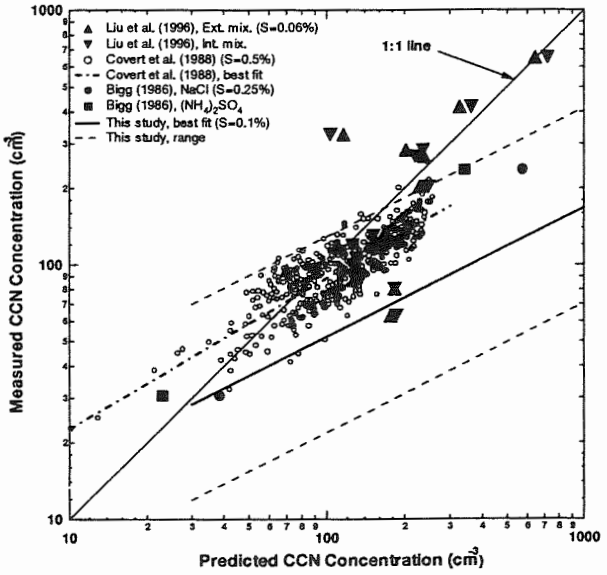

Figure 2: Results of previous closure experiments, along with those of the current study. The data from the present study are not plotted explicitly for presentation clarity.

Studies by Bigg (1986), Covert et al. (1998), and the present study (Figure 2) suggest that the relationship between measured and predicted N_{ccn} is sublinear, i.e. that the ratio of measured to predicted N_{ccn} decreases as measured N_{ccn} increases. Such a relationship does not correspond with proper CCN closure. The data from Covert et al. are particularly interesting. The slope of the best-fit curve for those data is very similar to that for the present study, although the curves are offset from one another. The present study also exhibits larger variability, but this may be a result of

the greater pollution levels associated with ACE-2 air masses. Whether this similarity is meaningful, and what that meaning may be, remains unclear.

A study by Liu et al. (1996) appears to achieve CCN closure, although even then, 3 of eleven cases show large deviations from a 1 to 1 relationship. Whether this discrepancy is a result of instrument malfunction, air mass characteristics, or other factors is unclear. The isothermal haze chamber Liu et al. used to measure CCN may explain their ability to achieve closure since CCN activation does not occur in such an instrument. Additional studies of CCN closure in a variety of conditions is required before this issue can be definitively settled.

The amount of insoluble material is often considered to be a free variable that is inferred from discrepancies between CCN measurements and predictions. In this study, the measured insoluble material is very small (less than 3% of the total submicron aerosol mass), and therefore cannot explain the lack of closure.

The presence of organic species in the aerosol in increasing amounts as aerosol concentrations increase is another possible explanation of such a sublinear relationship, since polluted air masses tend to contain greater quantities of organic compounds than clean air masses. It is known that organics can modify the traditional Köhler curve by altering the droplet surface tension, by exhibiting slightly soluble behavior (Shulman et al., 1996), and possibly by other mechanisms such as changes in the mass accommodation coefficient. Impeded droplet growth due to organic coatings has been hypothesized to explain observations of delayed droplet growth in static thermal diffusion CCN instruments (Bigg, 1986). Kinetic inhibition of CCN activation in CCN instruments due to the presence of organics could also further decrease measured N_{ccn} (Chuang et al., 1997), especially under polluted conditions. Such modifications to traditional Köhler theory would change the calculation of the CCN spectrum which would therefore alter predicted CCN concentrations. In the present study, however, the relative abundance of organic compounds is higher for clean air masses than for polluted ones (although polluted air masses have more total mass of OC). It is possible that these effects are caused only by those organic species formed from anthropogenic sources and not from naturally occurring ones, thereby causing the observed sublinear behavior. Without detailed organic speciation data in conjunction with the other measurements necessary for local closure, the effect of organics on CCN remains an open question.

4. CLOUD DROPLET NUMBER PREDICTION

Cloud properties depend on a number of variables, some microphysical and others of larger scale. Microphysical parameters include the CCN spectrum, which is related to the aerosol number size distribution and chemical composition, and larger scale variables include updraft velocity, cloud thickness, and turbulent mixing. The relationship between measured CCN concentration N_{ccn} and measured cloud droplet concentration N_{cd} will be discussed here. A consistent, quantitative relationship between these variables would prove to be extremely useful for parameterizations of cloud properties based on aerosol properties. If N_{ccn} is found not to be the only controlling variable for these cloud properties, it is useful to identify and quantify these other relevant variables.

Because the *Pelican* and *Merlin* did not fly at exactly the same position at exactly the same time, the CCN data and cloud microphysical data are compared by averaging constant altitude legs from each. Overall, the four flights for which complete data sets are available (07, 09, 16, and 19 July) can be separated into two categories: clean (16 and 19 July) and polluted (07 and 09 July). The N_{ccn} values encountered for both clean flights are approximately the same as can be seen from Figure 3. This is also true for the two polluted cases with the exception of a single *Merlin* observation (which is compared to two *Pelican* observations at different altitudes). As a result, almost all of the data are grouped closely together with respect to N_{ccn}. Unfortunately, this prevents any meaningful examination of the functional relationship between N_{ccn} and N_{cd}, since any two-parameter function can be fit to the data.

Figure 3 shows N_{cd} as a function of N_{ccn}. Overall, 33 observations were compiled from 103 minutes of in-cloud *Merlin* data and 13 hours of *Pelican* below cloud data. The horizontal bars in Figure 3 represent the standard deviation in N_{ccn} (which has a 60 s averaging time) for each observation period. The vertical bars represent the standard deviation in 30 s averaged N_{cd}.

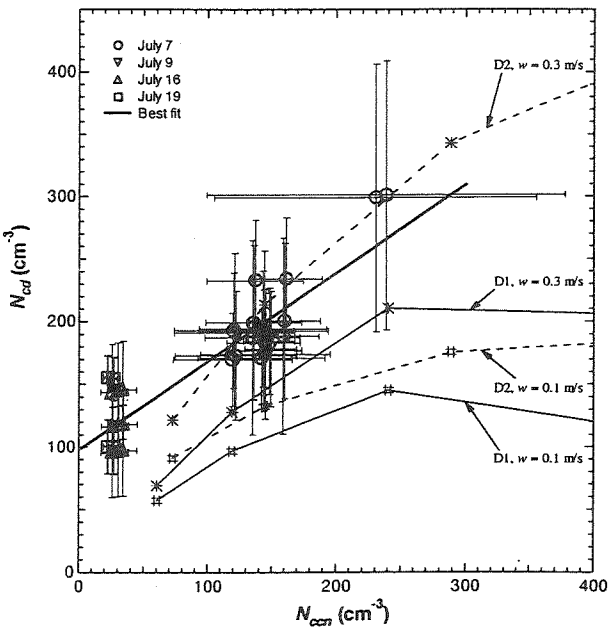

Figure 3: Cloud droplet number concentration N_{cd} as a function of below-cloud CCN concentration at 0.1% supersaturation for the four CLOUDYCOLUMN flights. Model predictions (* and #, solid and dotted lines) correspond to two updraft velocities (0.1 and 0.3 ms^{-1}) and two aerosol size/chemical composition distributions.

The horizontal and vertical bars represent the standard deviation in the observations over the averaging period for each datum.

One expects a sublinear relationship between N_{cd} and N_{ccn} because, for all variables held constant except the total number of CCN, an increase in N_{ccn} causes a suppression in the maximum supersaturation achieved in an air parcel that, in turn, should decrease the maximum critical supersaturation of the activated CCN. Therefore, the fraction of CCN that activate is reduced (for constant CCN spectrum) as the total number of CCN increases, resulting in a sublinear relationship between N_{cd} and N_{ccn}. Assuming a power law relationship, a regression of the data yields the best-fit relationship $N_{cd} \sim N_{ccn}^{0.31}$, with a 95% confidence interval for the exponent of 0.24 to 0.38.

This sublinear behavior agrees with adiabatic cloud parcel model predictions for two size distributions D1 and D2 (representative of clean and polluted conditions in the northeast Atlantic, respectively) and two updraft velocities (0.1 and 0.3 ms^{-1}), as seen in Figure 3. For both the predictions and measurements, the supersaturation at which N_{ccn} is determined is 0.1%, and N_{cd} is defined as those droplets greater than 2 μm diameter at cloud top. The predictions indicate that the slope of the relationship between N_{cd} and N_{ccn} is dependent on both updraft velocity and size distribution shape. The best fit curve for the ACE-2 measured data agrees fairly well with the predictions for a cloud with an updraft velocity of 0.3 ms^{-1}, a reasonable value for marine stratus clouds. The variability in the measured data is comparable to that caused by the different size distributions considered or reasonable variations (~0.1 ms^{-1}) in the updraft velocity. We conclude that, while there is a consistent, quantitative relationship between N_{cd} and N_{ccn}, the actual relationship depends on other factors such as updraft velocity and the shape of the aerosol size distribution. Therefore, an important conclusion is that knowledge of N_{ccn} is useful and likely necessary for predicting cloud properties, but it is not sufficient for doing so accurately.

5. CONCLUSIONS

Relationships among below-cloud aerosol properties and cloud microphysical properties are studied for clean and polluted marine stratiform clouds. Predicted and measured CCN concentrations were not in agreement, and exhibited large variability. This lack of CCN closure is consistent with most, but not all, previous studies. The measured relationship between N_{cd} and N_{ccn} is reasonable, and the results can be reproduced by 1-D adiabatic parcel model calculations. Along with below-cloud CCN concentration, updraft velocity and the shape of the aerosol size distribution (or CCN spectrum) are important controlling variables for cloud properties. Continued work, including improving instrumentation and measurements, in studying each link in the chain of processes that relate aerosols and clouds in different cloud-forming scenarios is needed to make further progress on the problem of indirect aerosol forcing of climate.

ACKNOWLEDGEMENTS

This research is a contribution to the International Global Atmospheric Chemistry (IGAC) Core Project of the International Geosphere-Biosphere Programme (IGBP) and is part of the IGAC Aerosol Characterization Experiments (ACE). Primary funding for this work has been provided by the National Science Foundation Grant ATM-9614105, and by the Office of Naval Research Grant N00014-91-0119.

REFERENCES

Bigg, E. K., 1986: Discrepancy between observation and prediction of concentrations of cloud condensation nuclei. *Atmos. Res.*, 20, 81-86.

Brenguier, J. L., T. Bourrianne, A. D. Coelho, J. Isbert, R. Peytavi, D. Trevarin and P. Weschler, 1998: Improvements of droplet size distribution measurements with the Fast-FSSP (Forward Scattering Spectrometer Probe). *J. Atmos. Ocean Technol.*, 15, 1077-1090.

Chuang, P. Y., R. J. Charlson and J. H. Seinfeld, 1997: Kinetic limitations on droplet formation in clouds. *Nature*, 390, 594-596.

Chuang, P. Y., A. Nenes, J. N. Smith, R. C. Flagan and J. H. Seinfeld, 2000: Design of a CCN instrument for airborne measurement. *J. Atmos. Ocean. Tech.*, in press.

Collins, D. R., H. H. Jonsson, J. H. Seinfeld, R. C. Flagan, et al., 2000: In-situ aerosol size distributions and CLEARCOLUMN radiative closure during ACE-2. *Tellus*, in press.

Covert, D. S., J. L. Gras, A. Wiedensohler, and F. Stratmann, 1998: Comparison of directly measured CCN with CCN modeled from the number-size distribution in the marine boundary layer during ACE-1 at Cape Grim, Tasmania. *J. Geophys. Res.*, 103, 16597-16608.

Delene, D. J., T. Deshler, P. Wechsler, and G. A. Vali, 1998: A balloon-borne cloud condensation nuclei counter. *J. Geophys. Res.*, 103, 8927-8934.

Laaksonen, A., P. Korhonen, M. Kulmala, and R. J. Charlson, 1998: Modification of the Köhler equation to include soluble trace gases and slightly soluble substances. *J. Atmos. Sci.*, 55, 853-862.

Liu, P. S. K., W. R. Leaitch, C. M. Banic, S. M. Li, D. Ngo and W. J. Megaw, 1996: Aerosol observations at Chebogue Point during the 1993 North Atlantic Regional Experiment: relationships among cloud condensation nuclei, size distribution, and chemistry. *J. Geophys. Res.*, 101, 28971-28990.

Shulman, M. L., M. C. Jacobson, R. J. Charlson, R. E. Synovec and T. E. Young, 1996: Dissolution behavior and surface tension effects of organic compounds in nucleating cloud droplets. *Geophys. Res. Lett.*, 23, 277-280.

LABORATORY STUDIES OF THE EFFICIENCY OF ORGANIC AEROSOLS AS CCN

D.A. Hegg[1], S. Gao[1], W. Hoppel[2], G. Frick[2], P. Caffrey[2], W.R. Leaitch[3], N. Shantz[3], J. Ambrusko[4] and T. Albrechcinski[4]

[1]Department of Atmospheric Sciences, University of Washington, Seattle, Washington, 98195-1640, USA
[2]Navel Research Laboratory, Washington, District of Columbia, 20375-5000, USA
[3]Meteorological Service of Canada, Downsview, Ontario, M3H 5T4, Canada
[4]Calspan UB Research Center, Buffalo, New York, 14225, USA

1. INTRODUCTION

Organic aerosols have long been known to constitute a portion of the atmospheric aerosol mass. However, recent studies have suggested that it is commonly a major and frequently the largest fraction of the submicron aerosol [cf., *Novakov et al.,* 1997]. Further, it has been shown that organics are a major component of the cloud condensation nucleus (CCN) reservoir in the atmosphere [*Novakov and Penner,* 1993; *Matsumoto et al.,* 1997]. Given this importance, it is natural to ask whether this organic component of the CCN differs in its mode of action or efficiency from that of the longer studied inorganic component. Some recent studies have in fact suggested this [*Shulman et al.,* 1996, 1997; *Facchini et al.,* 2000]. However, it is not yet entirely clear to what extent the above results are definitive. In contrast to the above studies, *Cruz and Pandis* [1997] found that a number of the organics found in atmospheric aerosols are equally as efficient as common inorganics in their action as CCN. Similarly, *Cruz and Pandis* [1998] found little impact of organic coatings, even for so hygrophobic a compound as DOP (dioctyl pthalate), on the mass transport of water to and from inorganic aerosol cores.

In light of these previous results, it seems worthwhile to examine further the CCN efficiency of selected organic species found in atmospheric aerosols, particularly in experimental scenarios more closely approximating cloud formation in the atmosphere than has hitherto been the case.

2. PLAN OF THE STUDY

2.1. The Calspan Chamber

The venue for the experiments reported here was the 600 m^3 expansion/smog chamber owned and operated by the Calspan Corporation near Buffalo New York. Details of the chamber construction, mode of operation and quality assurance tests are given in the recent chamber characterization report of *Hoppel et al.* [1999]. The key aspect of the chamber relevant to this study is the ability to form clouds by expansion. A roughly 40 mb expansion can be achieved in a period of about 3 minutes if necessary, corresponding to an updraft on the order of 1 ms^{-1}. However, the expansion is not adiabatic due to the heat flux from the chamber walls, which are at ambient temperature. Furthermore, the cloud lifetime is artificially truncated (by again over-pressurizing the chamber) to provide a definite, reproducible timescale for cloud processing calculations and is only a minute or two longer than the expansion period itself. Nevertheless, the very large size of the chamber and the consequent favorable volume to surface ratio and depth of the supersaturated zone result in clouds very similar microphysically to those observed in the atmosphere in the first few tens of meters above the lifting condensation level—where virtually all CCN activation takes place.

2.2. Instrumentation and Aerosol Generation

In addition to the conventional instrumentation associated with the chamber itself, there were three aerosol measuring instruments utilized in this analysis. The first of these was one of the well-known PMS Inc. laser-scattering spectrometers (CSASP) used to measure the cloud drop size distribution. The second was a somewhat less common differential mobility analyzer (DMA) used to measure the dry aerosol size distribution between 0.004 and 0.4 um radius [cf., *Hoppel et al.,* 1994]. Finally, to measure the CCN activation spectrum of the pre-cloud aerosol, a commercial static thermal diffusion chamber was employed operating at a set of sequential supersaturations (DH Associates, model 200).

For the analysis presented here, four different aerosol types were utilized. The first type, essentially utilized as a reference, was ammonium sulfate and was produced by nebulization of an aqueous solution with a Colison atomizer. Three different organic aerosols were then generated. The first of these was pinonic acid, a known product of the alpha-pinene-O_3 reaction and a known constituent of atmospheric aerosols, particularly in the canopies of boreal forests. This type was also generated with the Colison atomizer. The two remaining types were less well characterized but chosen to represent realistic organic aerosols in the atmosphere: the oxidation products of cyclohexene and alpha-pinene via ozonolysis. In both instances, the aerosols were formed by gas-phase reaction of the organic species with O_3 in the Calspan chamber prior to cloud formation. Also in both instances, it is quite conceivable that the actual

Corresponding author's address: Dean A. Hegg, University of Washington, Department of Atmospheric Sciences, Box 351640, Seattle, WA, 98195-1640, USA; E-Mail: deanhegg@atmos.washington.edu.

particle nucleation process involved trace amounts of SO_2 in the chamber even after the prefiltering used to remove pre-existing particles and gases [*Gao et al.*, 1999]. However, chemical analysis of the produced aerosol revealed no sulfate above the detection limit of the IC system utilized. Hence, we consider the aerosols to be essentially organic in nature.

3. RESULTS AND DISCUSSION

Several recent studies have suggested that organic CCN could act quite differently in conventional, water-based, CCN counters than do the highly soluble inorganics for which these counters were largely designed [cf., *Bigg*, 1986; *Chuang et al.*, 1997]. The assertion is that at least some organics, due to relative hygrophobicity and/or their lowering of water droplet surface tension, could alter either the growth rate or activation radius of the aerosol particles. Hence, both under and over estimates of the actual number of effective CCN (i.e., cloud drops formed) are possible. In the study of *Bigg* [1986], for example, the water-based counter employed could activate and thus measure only a small fraction of the organic particles whose size alone would have suggested effective CCN. To further explore this issue, CCN activation spectra measured by the DH CCN counter are compared with equivalent spectra derived from the DMA size distribution measurements under the assumption that the particles are completely soluble. Examples of such comparisons are given in Figures 1 and 2 for ammonium sulfate and pinonic acid, respectively. While it is somewhat disconcerting to note that, even for the soluble inorganic, there is a marked discrepancy between the counter and DMA spectra, the important point to note here is that the organic, which is only sparingly soluble, has a significantly larger discrepancy between measurement methods than does the inorganic, i.e., about a factor of 2 for the inorganic as compared to an order of magnitude for the organic. Taken as a whole, the four aerosols considered here reveal an interesting pattern discernable in the summary results shown in Table 1. The results indeed suggest a relationship between the solubility of the aerosol constituents and the CCN efficiency. In this regard, it is important to note that the aerosol produced by the oxidation of cyclohexene includes several soluble acids as major constituents (including the highly soluble glutaric acid). About 50% of the analyzed organic mass (measured by EGA) was found to be soluble (by IC analysis). In contrast, the aerosol products of the alpha-pinene oxidation revealed only a very small soluble acid component (~1%).

While certainly of interest, the above results are not clearly applicable to actual clouds. For example, if the discrepancy between the DMA and CCN counter results were a kinetic effect due, say, to slower condensational growth, it might induce an error in the counter measurements due to inappropriate time constants that would not necessarily be evident in actual cloud formation where quite different time constants could apply. To test this, we next turn to an examination of the cloud formation process in the Calspan chamber for the

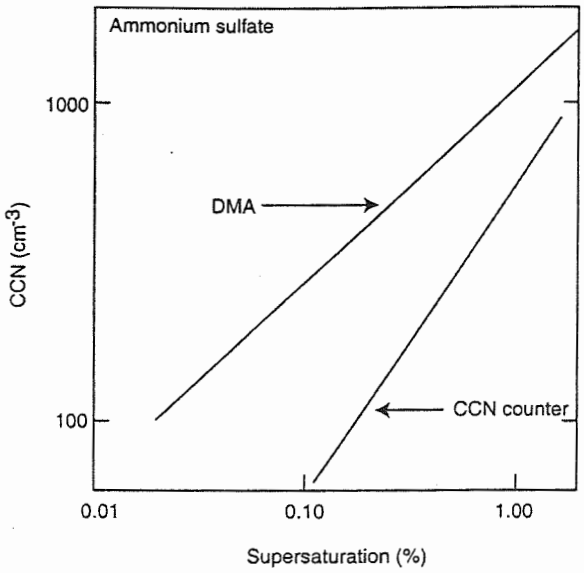

Figure 1. CCN activation spectrum based on the DMA size distribution and tan assumption of complete solubility, and on the directly measured CCN concentrations from the DH CCN counter. The aerosol composition was ammonium sulfate, generated on 11/13/98.

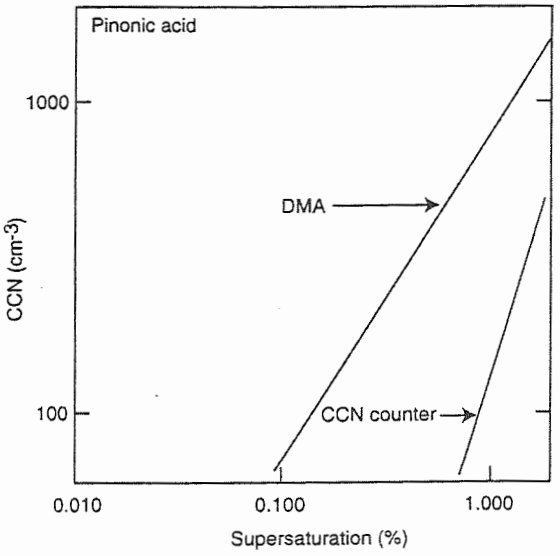

Figure 2. As in Figure 1 but for pinonic acid aerosol generated on 11/13/98.

Table 1. Fraction of DMA-Derived CCN Measured by the CCN Counter at a Supersaturation of 0.5%

Chemical Species	Date	CCN Fraction
$(NH_4)_2SO_4$	(11/13)	0.40
Pinonic acid	(11/13)	0.07
C_6 oxidation products	(10/16)	0.61
α-pinene oxidation products	(11/09)	0.04
$(NH_4)_2SO_4$	(10/8)	0.66

prototype organic and inorganic aerosols.

On November 13, clouds were formed in the chamber first on ammonium sulfate aerosol and then on aerosol formed from pinonic acid, both aerosols being generated by nebulization. There was clearly a difference between the rate of activation of the organic aerosol when compared to that of the inorganic. Plotted in Figure 3 are fractional activation of cloud drops (i.e., the ratio of cloud drop concentration at a given time after cloud formation divided by the maximum cloud drop concentration formed during the expansion) as a function of time since the commencement of cloud formation for both ammonium sulfate and pinonic acid aerosols. Two cloud runs for each of the aerosol types are shown to illustrate run to run variability due to sizing differences. The organic aerosols are activating more slowly than the inorganics, although the equivalent updrafts for the two types (as well as initial temperatures and so forth) are essentially the same (1.9-2.3 ms^{-1} in all cases). Nevertheless, it is conceivable that the irregularities in the size distributions between the ammonium sulfate and pinonic acid cases have at least something to do with the discrepancies observed. To test this phenomenology still further, we next turn to model/data intercomparison.

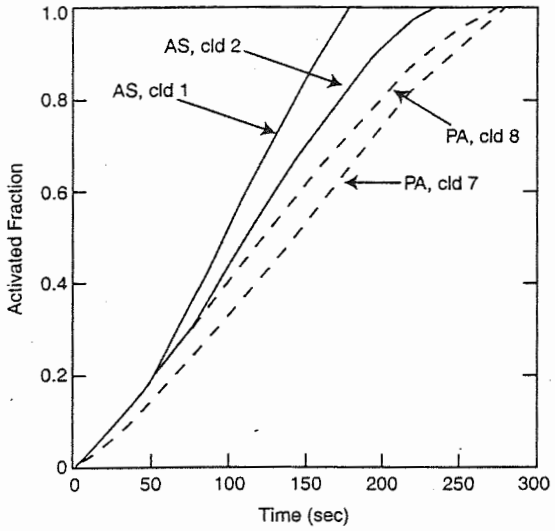

Figure 3. The fraction of CCN activated as a function of time (fraction activated at a given time normalized by the total number activated during the run) for four chamber runs on 11/13/98. AS refers to ammonium sulfate aerosol and PA to pinonic acid aerosol.

Using initial values for two cloud formation runs, one for ammonium sulfate and one for pinonic acid, an explicit microphysical, adiabatic parcel model [*Yuen et al.*, 1994] was utilized to predict the cloud drop number concentration in the chamber as a function of time. In addition to the updraft velocities, temperature, RH, pressure, etc., the model also requires a log normal aerosol size distribution of known composition to initialize. For the size distribution, the DMA data for each run were fitted to a log normal distribution function and the resultant parameters feed into the model. Not surprisingly given the similarity in initial conditions (even the size distributions had similar geometric standard deviations and modal radii though different total number concentrations by a factor of two), the cloud drop number concentrations as a function of time were essentially the same for each of the model runs. This is in contrast to the actual observed activation rates for the two different aerosols. A comparison of the observed with the modeled rates is given in Figure 4. The most immediately striking aspect of the figure is the large discrepancy between the modeled rate of activation and either of the observed rates. This is in large part due to the non-adiabatic nature of the expansion in the Calspan chamber (the measured rate of cooling in the chamber is only about 60% of the adiabatic value for both of the runs shown). However, this anomaly applies equally to the cloud formation on each of the aerosol types and there is still clearly a discrepancy between the organic and inorganic aerosols as to rate of cloud formation. Once again, this discrepancy is in the sense hypothesized in previous theoretical studies.

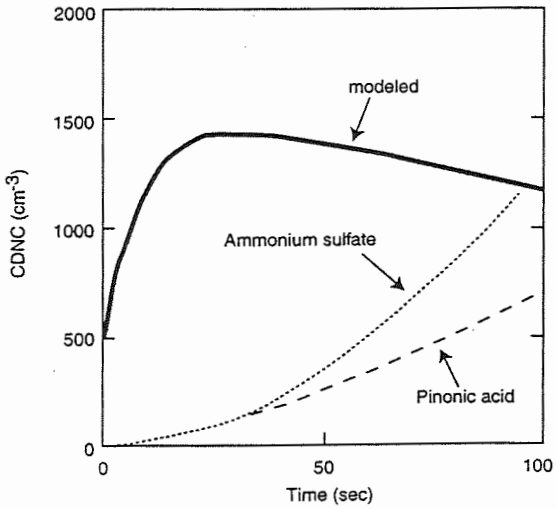

Figure 4. A comparison of the cloud drop number concentration (CDNC) as a function of time for both ammonium sulfate and pinonic acid aerosols. The graph shows observed curves for each aerosol together with the curve predicted by the model of *Yuen et al.* [1994] for the initial size distribution, temperature, updraft velocity, etc. for which the observations were made.

4. CONCLUSIONS

The results of this study support the contention that the presence of organic components in atmospheric aerosols, or at least of sparingly soluble or relatively hygrophobic organics, may significantly alter the CCN efficiency of the aerosol. This has been demonstrated for both activation in a conventional CCN counter and in clouds formed in the Calspan chamber, clouds reasonably similar to those which might be expected in

the actual atmosphere. Furthermore, these results were for relatively high updrafts such as are found in cumuliform clouds whereas theoretical predictions of anomalies due to organics indicate the discrepancy should be largest at low updrafts, on the order of 10's of cm s^{-1} [e.g., *Chuang et al.,* 1997]. On the other hand, the real significance of the results reported here is not yet entirely clear. Note, for example, that while the rate of activation of the organic CCN was apparently appreciably slower than that of the inorganic salt, eventually both the organic and inorganic aerosols fully activated in the sense that both closed with the model predicted values which were based on an assumed virtually complete solubility. Hence, for clouds of duration longer than a few minutes (by which we mean parcel residence times longer than a few minutes), it is not clear that there will be any marked discrepancy in the number of cloud drops produced due to an organic aerosol component. Furthermore, the limited data also suggest that factors such as updraft velocity and particle size can dominate composition as agents of CCN activation. Clearly more such studies as those reported here are in order, encompassing a broader range of initial conditions and more extensive list of aerosol types.

5. ACKNOWLEDGMENTS

The work reported here was supported by ONR grants N00014-97-1-1023 and N00014-97-1-0132, and by NSF grant ATM-9526402.

6. REFERENCES

Bigg, E. K., 1986: Discrepancies between condensation observation and prediction of concentrations of cloud nuclei. *Atmos. Res.,* **20,** 82-86.

Chuang, P. Y., R. J. Charlson, and J. H. Seinfeld, 1997: Kinetic limitations on the droplet formation in clouds. *Nature,* **390,** 594-596.

Cruz, C. N., and S. N. Pandis, 1997: A study of the ability of pure secondary organic aerosol to act as cloud condensation nuclei. *Atmos. Environ.,* **31,** 2205-2214.

Cruz, C. N., and S. N. Pandis, 1998: The effect of organic coatings on the cloud condensation nuclei activation of inorganic atmospheric aerosol. *J. Geophys. Res.,* **103,** 13,111-13,123.

Facchini, M. C., M. Mircea, S. Fuzzi, and R. J. Charlson, 2000: Organics depress surface tension of nucleating droplets and enhance albedo, *Nature,* In press.

Gao, S., D. Hegg, W. Hoppel, G. Frick, P. Caffrey, W. Sullivan, J. Ambrusko, T. Albrechcinski, C. Cantrell, W. Leaitch, and N. Shantz, 2000: Experi-mental and modeling studies of secondary organic aerosol formation and some applications to the marine boundary layer. *J. Geophys. Res.,* Submitted.

Hoppel, W., G. Frick, P. Caffrey, L. Pasternack, T. Albrechcinski, J. Ambrusko, W. Sullivan, D. Hegg, and S. Gao, 1999: *Report on the Characterization of Calspan's 600 m3 Chamber in Preparation for the NOPP Aerosol processes Experiments.* Naval Research Laboratory Report NRL/MR/6110-99-8370, April.

Matsumoto, K., H. Tanaka, I. Nagao, and Y. Ishizaka, 1997: Contribution of particulate sulfate and organic carbon to cloud condensation nuclei in the marine atmosphere. *Geophys. Res. Lett.,* **24,** 655-658.

Novakov, T., D. A. Hegg, and P. V. Hobbs, 1997: Airborne measurements of carbonaceous aerosols on the East Coast of the United States. *J. Geophys. Res.,* **102,** 30,023-30,030.

Novakov, T., and J. E. Penner, 1993: Large contribution of organic aerosols to cloud-condensation-nuclei concentration. *Nature,* **365,** 823-826.

Shulman, M. L., M. C. Jacobson, R. J. Charlson, R. E. Synovec, and T. E. Young, 1996: Dissolution behavior and surface tension effects of organic compounds in nucleating cloud droplets. *Geophys. Res. Lett.,* **23,** 277-280.

Shulman, M. L., R. J. Charlson, and E. J. Davis, 1997: The effects of atmospheric organics on aqueous droplet evaporation. *J. Aerosol Sci.,* **28,** 737-752.

Yuen, P.-F., D. A. Hegg, and T. V. Larson, 1994: The effects of in-cloud sulfate production on light-scattering properties of continental aerosol. *J. Appl. Meteor.,* **33,** 848-854.

AIRBORNE STUDIES OF ATMOSPHERIC ICE NUCLEI AND CLOUD ICE FORMATION IN MID-LATITUDE WINTER AND ARCTIC SPRING

D.C. Rogers[1], S.M. Kreidenweis, P.J. DeMott and K.G. Davidson

Colorado State University, Fort Collins, Colorado USA

1. INTRODUCTION

The initial formation of ice is a long-standing problem in cloud physics. To a significant extent, the formation of ice determines a cloud's microphysical and radiative properties, and for many mid-latitude clouds, ice is crucial for precipitation. Processes involved in the initial formation of ice are not well understood. There are a number of complicating factors; for example, ice can be produced through a variety of primary and secondary processes (Cooper 1991; Rasmussen 1995; Baker 1997).

Many field studies have been performed in the past with instrumented aircraft to examine ice formation, although simultaneous measurements of cloud microphysics and ice nuclei (IN) were usually not obtained. Attempts to correlate IN and ice crystal concentrations often had cloud observations from one location and time, aerosol samples at a different location and time, and processing of aerosol collections still later, at a laboratory. In some cases, IN measurements addressed temperature dependencies but did not include equally important variations in humidity.

This paper summarizes recent measurements of IN and cloud microphysical properties from instrumented aircraft in several field experiments in the U.S. Flights were made in winter lake-effect clouds (NCAR Electra), over the Arctic Ocean in springtime (NCAR C-130), and most recently, in wave clouds in the central Rocky Mountains (University of Wyoming King Air).

2. INSTRUMENTATION

Instruments for measuring IN, condensation nuclei (CN) and for collecting ambient particles were located inside the aircraft cabin and shared a common air inlet that was flushed at ~700-1000 L min^{-1}. Measurements of cloud condensation nuclei (CCN) were sometimes available also.

Real time measurements of IN were made with a continuous flow thermal gradient diffusion (CFD) chamber [Rogers et al. 2000]. This chamber is the annular space between two vertically oriented concentric cylinders that are coated with ice and held at different temperatures, thus creating a vapor supersaturation between them. The sample air is ~10% of the total flow and is sandwiched between two particle-free sheath flows. Ice crystals nucleate and grow to diameters of ~3 to 10 μm diameter in ~5 s residence time. At the outlet of the chamber, an optical particle counter (OPC) detects all particles larger than ~0.8 μm. Those particles larger than 3 μm are assumed to be the newly formed ice crystals and comprise the IN count. This technique detects deposition or condensation-freezing IN. Nucleation mechanisms that require times >~1 s are not detected (contact-freezing and immersion-freezing).

An inertial impactor immediately downstream of the OPC was used during selected time periods of 20-60 minutes duration to collect crystals (containing IN) on transmission electron microscope (TEM) grids. These were examined with single particle analysis and energy dispersive x-ray (EDX) microprobe techniques to determine the number, size, morphology and elemental composition of the nuclei (Kreidenweis 1998; Chen et al. 1998). The minimum particle size for EDX analysis is affected by detector sensitivity, atomic number and mixed composition of particles (Markowitz et al. 1986). The size limit is ~0.1 μm, which is within the range expected for IN particles (Rosinski et al 1987; Chen et al. 1998). Several hundred particles were usually collected.

Samples of all ambient aerosol particles (AP) >0.06 μm diameter were also collected onto TEM grids with a separate impactor. TEM analyses were done the same way as for IN particles. CN concentration was measured with a butanol type instrument (TSI-3076).

The CFD chamber exposes particles to one temperature (T) and one supersaturation, and these conditions can be adjusted. Over a period of time, ice nuclei measurements were made both above and below water saturation, with the maximum water supersaturation (SSw) typically about +5%, and the minimum typically -10%. The general strategy was to maintain constant (T, SSw) conditions during vertical profiles and when impactor samples were collected. Occasionally, samples were made at very high SSw (>10%) for a few minutes.

A wide range of sampling conditions was covered in these field experiments: temperatures -10 to -35°C and humidities from ice saturation to ~20% water supersaturation. Counts of IN were measured at 10 Hz

[1]Corresponding author's address: David C. Rogers, Colorado State University, Department of Atmospheric Science, Ft. Collins, CO 80523-1371;
Email: David.Rogers@ColoState.edu

and then averaged to 10 s to increase the number of non-zero values while preserving temporal resolution. Since the aircraft flew at ~100 m s^{-1}, the 10 s averages corresponded to ~1 km distance and ~0.17 L volume.

3. FIELD PROJECTS

3.1 Lake-ICE

Lake-effect clouds form as cold Arctic air masses move over Lake Michigan (Kristovich et al. 2000). Figure 1 shows aircraft data along the wind direction from the 13-Jan-98 case. Parcel time was calculated from the wind (11 m s^{-1}). The air was initially very cold (-20°C), dry and stably stratified. Steam fog and low level clouds formed rapidly over the relatively warm lake surface (+3°C). The boundary layer quickly became unstable and turbulent as the air advected across the lake. The convective transfer of heat, moisture and particles was very strong, with the boundary layer becoming steadily deeper downwind. By ~100 km, the convection organized into two-dimensional mesoscale cloud structures and snow showers.

The IN concentration was ~10-20 per liter at -22°C and 2 to 6% water supersaturation. Ice crystal concentrations were ~5-10 L^{-1}.(2D probe) and ~26 L^{-1} (260x probe). Ice crystals were detected near the upwind edge of the cloud, at the same location where the liquid cloud formed, suggesting that condensation-freezing was the major mechanism of ice formation in these clouds.

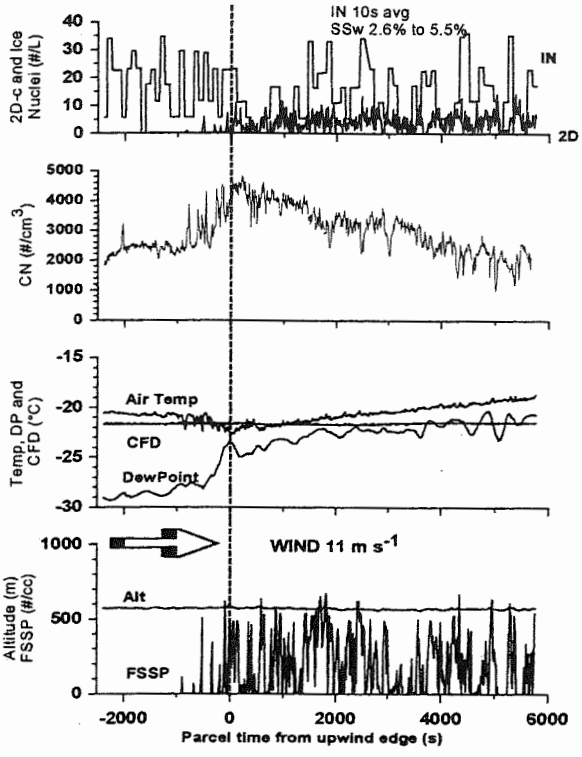

Fig. 1 Aircraft data, upwind pass 14:09-14:25UTC.

The concentration of all aerosol particles (CN) showed an abrupt transition where the aircraft crossed the top of the steadily growing boundary layer. This point was chosen to reference the travel time for air parcels in Figure 1. Downwind, CN decreased steadily due to scavenging and dilution. CN and cloud drop data (FSSP) show fine scale structure and rapid mixing within and near the top of the air mass.

3.2 NASA FIRE Arctic Cloud Experiment

Cloud microphysics and IN measurements were made during eight flights over the Arctic Ocean north of Alaska in May 1998 (Curry et al. 2000). These were part of projects, SHEBA (Surface Heat Budget of the Arctic) and NASA's FIRE-Arctic Cloud Experiment. The flights centered on an ice breaker vessel in the pack ice.

Cumulative probability distributions of IN and CN measurements for eight flights are shown in Figure 2 when the aircraft was within 100 km of the ice station. The IN measurements covered wide ranges of temperature and supersaturation, from -10 to -34°C and from ice saturation to ~20% SSw. Those measurements with SSw >5% are not included in Figure 2 because such large supersaturations are not representative of typical conditions in Arctic clouds.

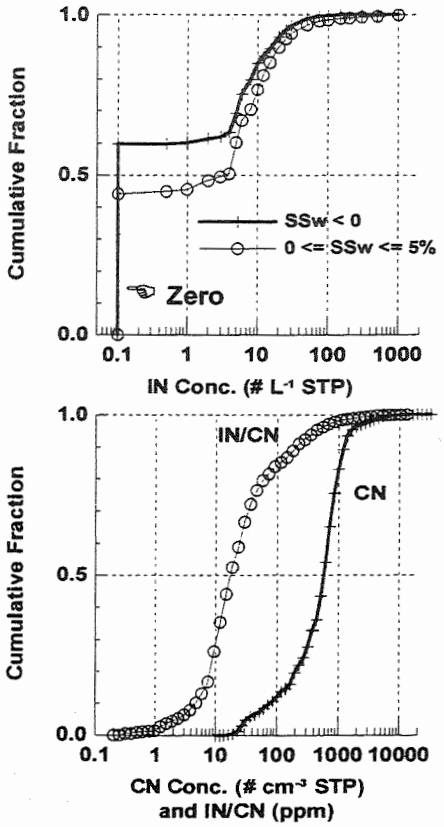

Fig. 2. Cumulative frequency distributions of 10 s average IN and CN conc. on Arctic flights in May 1998. For plotting convenience on log scale, zero IN conc. was plotted at 0.1. Total 41196 points.

A notable characteristic of the IN curves is that they are highly skewed. Concentrations of zero IN comprised ~60% of the 10 s measurements below water saturation, and ~45% of those above water saturation. On average, higher SSw was associated with greater IN concentrations, as expected. Nevertheless, some very high concentrations were measured below water saturation.

An unexpected and surprising observation was the rare occurrence of small regions of high IN concentrations (100's per liter) at low altitudes, near the surface of the ice pack. The small spatial extent over which high IN occurred suggests the source may be local or that higher IN might be confined within thin stable layers.

Aerosol particle concentrations were remarkably low; typical concentrations of CN (condensation nuclei) were ~100 cm^{-3} over extended regions. Median CN was ~600 cm^{-3}. CN values associated with extremely clean air (<100 cm^{-3}) occurred ~10% of the time. The fraction of all particles active as IN is the ratio of IN and CN concentrations. This ratio varied from zero to ~0.02, with a median ~20 ice nuclei per million CN.

3.3 Single Particle Analyses

Collections of all particles (AP) and IN from five Arctic flights have been analyzed, and the results are summarized in Table I. Generally, IN particles were a few tenths micrometer in size, and their shapes were non-spherical. Elements often detected in the IN samples included Si, S and some metals (Zn, Al, Fe). S and Na were more common for low altitude IN. Carbonaceous material may have been present in many IN particles with weak or no x-ray signatures, due to small mass or low atomic numbers (e.g., elemental or organic carbon). By comparison, a high proportion of the total particle samples (AP) contained primarily S, or Si and S. These results are in general agreement with Chen et al. (1998) who reported that the elemental compositions of IN are systematically different from the total ambient aerosol.

involved measuring the aerosol properties (IN, CN and CCN) upwind, within and downwind of the clouds and observing the formation of ice crystals and cloud droplets within the clouds. The principal advantages of studying ice formation in wave clouds are the relatively well defined vertical motions and simple air trajectories that are especially suitable for parcel analysis and modeling.

Data from a flight on March 17 are shown in Figure 3 for a 15-min period. The aircraft flew into the wind at 4.1-4.7 km altitude and crossed through five clouds in a wave train. The regular spacing is apparent for cloud drops (FSSP) and vertical wind. These clouds formed when the underlying (colder) air mass was forced above its lifting condensation level. Upon lifting, the strong vertical gradients in scalar quantities (temperature and CN) become strong horizontal gradients penetrated by the aircraft. Vertical shear across the air mass boundary was substantial: the aircraft measured horizontal winds of 260°/12 m s^{-1} in cloud and 240°/25 m s^{-1} between clouds.

IN were measured at –21 to –22°C and 4-6% SSw. IN concentrations (10 s average) ranged from 0 to 37 L^{-1}, with a mean of 15. Ice crystals were displaced slightly downwind of the water clouds. Crystal concentrations in cloud (-15 to –18°C) were 0-28 L^{-1}, as estimated from PMS 1-D (200x) and 2D-C probes. The efficiency with which these instruments detect small crystals decreases with particle size, hence some interpretation is necessary for using these data to estimate ice formation. The region of ice crystals was always displaced downstream (left in Fig. 3) of the region of cloud drops. This displacement may be due to nucleation processes and/or growth to detectable size.

4. CONCLUSIONS

These field studies have produced a wide variety of observations of ice and droplet formation in clouds. Measurements of the aerosol characteristics that are important for understanding and modeling these

TABLE I. Electron microscope analysis summary of IN and all particles (AP) from Arctic studies. Values are percent of particles containing indicated element (rounded to nearest whole percent). Altitude of collection **high** (700-3000m) or **low** (50-170m).

			shape																	
	#	dia.	Osphere																	no
ident	ptls.	(μm)	1other	Al	Ca	Cl	Co	Cr	Fe	K	Mg	Na	S	Sb	Si	Sn	Ti	V	Zn	x-ray
IN high	110	0.46	0.82	3	2	0	0	0	2	2	0	2	7	0	38	1	0	0	5	38
IN low	152	0.36	0.68	1	2	0	0	1	5	0	1	15	18	0	37	0	2	0	0	14
AP high	80	0.41	0.06	1	0	0	0	0	1	2	1	1	87	0	6	0	0	0	0	1
AP low	123	0.50	0.04	1	1	0	0	1	1	3	1	3	59	0	29	2	0	0	0	2

3.4 Wave Cloud Studies

Studies of ice formation in altocumulus standing lenticular wave clouds were conducted in Colorado and Wyoming during March 2000. The range of cloud temperatures was -10 to -37°C. Flight procedures

processes were also obtained, including ice nuclei and CCN. Future analyses are focussing on describing and modeling these processes, with the aim of testing whether measurements of ice nuclei can improve the capability of predicting the concentrations of ice particles that form in natural clouds.

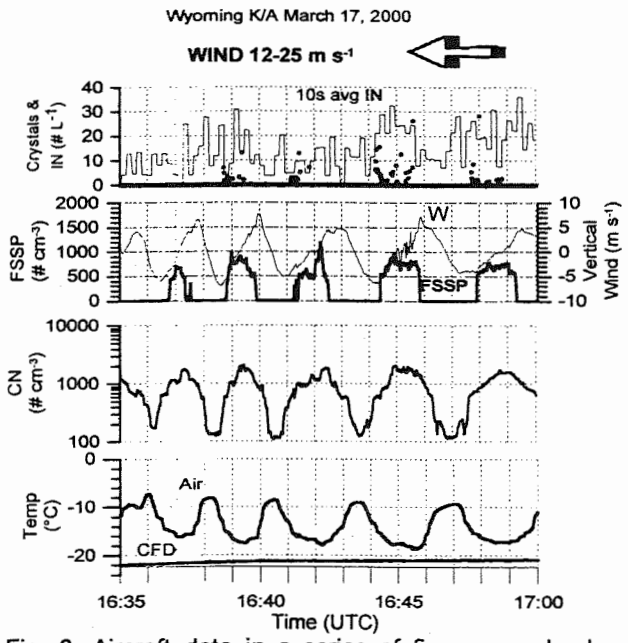

Fig. 3. Aircraft data in a series of five wave clouds. Crystal concentration (dots) from 1-D probe (PMS 200x). Concentrations are at ambient conditions.

ACKNOWLEDGEMENTS

This research was supported by NASA grant NAG-1-2063, and NSF grant ATM97-14177. Any opinions, findings, and conclusions or recommendations expressed in this material are those of the authors and do not necessarily reflect the views of the National Science Foundation. We acknowledge the technical support from the Research Aviation Facility at NCAR and the University of Wyoming for helping install the instruments and conducting the flights. We are grateful for the dedicated work of other FIRE – ACE and SHEBA investigators whose observations are helping our studies.

REFERENCES

Chen, Y., S.M. Kreidenweis, L.M. McInnes, D.C. Rogers and P.J. DeMott, 1998: Single particle analyses of ice nucleating particles in the upper troposphere and lower stratosphere, *Geophys. Res. Lett.*, 25, 1391-1394.

Cooper, W.A., 1991: Research in cloud and precipitation physics: Review of the U.S. theoretical and observational studies, 1987-1990. *Reviews of Geophysics*, Supplement, 69-79.

Curry, J.A., et al., 2000: FIRE Arctic Clouds Experiment, *Bull. Amer. Meteor. Soc.*, 81, 5-29.

Baker, M.B., 1997: Cloud microphysics and climate. *Science*, 276, 1072-1078.

Kreidenweis, J.M., Y. Chen, D.C. Rogers and P.J. DeMott, 1998: Isolating and identifying atmospheric ice-nucleating aerosols: A new technique, *Atmospheric Research*, 46, 263-278.

Kristovich, D.A.R., et al., 2000: The Lake-Induced Convection Experiment (Lake-ICE) and the Snowband Dynamics Project. *Bull. Amer. Meteor. Soc.*, in press.

Markowitz, A., B. Raeymaekers, R. Van Grieken and F. Adams, 1986: Analytical electron microscopy of single particles. in *Physical and Chemical Characterization of Individual Airborne Particles*, K.R. Spurny editor, John Wiley and Sons, NY, 173-197.

Rasmussen, R. M., 1995: A review of theoretical and observational studies in cloud and precipitation physics: 1991-1994. *Reviews of Geophysics*, Supplement, 795-809.

Rogers, D.C., P.J. DeMott, S.M. Kreidenweis, and Y. Chen, 2000: A continuous flow diffusion chamber for airborne measurements of ice nuclei. J. *Atmos. Ocean. Technol.* (in press).

Rosinski, J., P.L. Haagenson, C.T. Nagamoto and F. Parungo, 1987: Nature of ice-forming nuclei in marine air masses. *J. Aerosol Sci.*, 18, 291-309.

CLOUD CONDENSATION NUCLEI MEASUREMENT UNCERTAINTIES: IMPLICATIONS FOR CLOUD MODELS

J.R.Snider[1], W.Cantrell[2], G.Shaw[3], and D.Delene[4]

[1]University of Wyoming, Laramie, Wyoming
[2]Indiana University, Bloomington, Indiana
[3]University of Alaska, Fairbanks, Alaska
[4]University of Colorado, Boulder, Colorado

1 - INTRODUCTION

Cloud condensation nuclei (CCN) spectra can be either measured directly or predicted using Kohler theory initialized with aerosol physicochemical property (APP) data. APP (aerosol composition and size spectra), the CCN spectrum, cloud droplet number concentration (*CDNC*), and vertical velocity (w) at the base of a convective cloud updraft are linked by what is commonly called the droplet activation process. Using data sets obtained in cloud regions unaffected by entrainment and drizzle scavenging a comparison of predicted and observed droplet activation is possible. Assessments of the measurement uncertainties associated with APP, CCN, *CDNC*, and w are necessary for these closure studies. Here we summarize laboratory comparisons of CCN counter response to aerosols of known size and composition. Uncertainties associated with the CCN measurement are quantified. We also present field measurements from ACE-2 and examine the degree of closure between APP, CCN and *CDNC*.

2 - OVERVIEW

Cloud condensation nuclei (CCN) spectra are measured by exposing aerosol to a controlled supersaturation while monitoring droplet nucleation and growth. The measurement represents an assessment of the evolution of aerosols to cloud droplets in an environment which is not perturbed by the additional processes that influence droplet size and concentration within natural clouds (i.e., entrainment and drizzle scavenging). The measurement of the CCN is therefore one aspect of the current attempts to quantify aerosol/cloud interactions and to also parameterize them in cloud models. These ideas are summarized in Figure 1. The atmospheric fields of cloud droplet number concentration (*CDNC*), aerosol physicochemical properties (APP), and CCN are connected by two subprocesses. These are referred to as Kohler (I) and parcel (II) theory. Cloud model simulations often combine both subprocesses (I and II) and these can be validated independently by measuring the CCN spectra. These validation studies, or closure experiments, require assessments of the measurement uncertainties associated with the pertinent atmospheric fields. In this report we present uncertainties associated with three CCN instruments. We also examine the degree of closure between measurements of *CDNC*, CCN and w and between measurements of APP and CCN. Data sets used in these closure studies consist of CCN, from the University of Wyoming static diffusion chamber [4], vertical velocity and cloud microphysical data from the Meteo France Merlin [4], and measurements of submicrometric aerosol size distribution and composition from the Punto del Hidalgo site (PDH) [3].

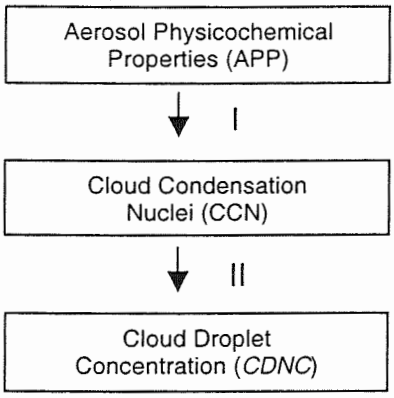

Figure 1 – APP (i.e., aerosol size and composition spectra) are related to CCN via Kohler theory (I). CCN are related to *CDNC* by parcel models (II), either analytic [6] or numerical.

3 - THE ALASKA COMPARISON

In November 1997 investigators from the University of Wyoming, the Desert Research Institute, and the University of Alaska met at the University of Alaska to intercompare CCN measurement systems [5]. We challenged two continuous flow and two static diffusion CCN measurement systems with quasi-monodisperse ammonium sulfate aerosols. We also measured the aerosol size distribution. This was transformed to a CCN activation spectrum via Kohler theory and the derived CCN spectrum was taken to be a reference. A total of seven tests were conducted, and within each of these CCN measurements at a range of applied supersaturation was obtained.

Corresponding author's address: Jefferson R. Snider, Department of Atmospheric Science, University of Wyoming, Laramie, WY. Email: jsnider@uwyo.edu

Results from three of the four instruments are summarized in Table 1, where the symbols WYO1, WYO2 and CCNR represent the Wyoming aircraft CCN instrument [4], the Wyoming balloon CCN [1], and the CCN Remover [2], respectively. The bias relative to the reference is characterized by mean values, *rerr*, that range between -38 and +19%, and its standard deviation, σ_{rerr}. In the case of the CCN instrument used in the closure studies presented below (WYO1), the results indicate that departures between the direct and derived CCN measurement should seldom exceed ± 50%. Also, data from the WYO1 is relatively unbiased.

WYO1			
n_{tot}	n_{test}	rerr, %	σ_{rerr}, %
255	5	2	45

WYO2			
n_{tot}	n_{test}	rerr, %	σ_{rerr}, %
73	3	-38	29

CCNR			
n_{tot}	n_{test}	rerr, %	σ_{rerr}, %
32	3	19	39

Table 1 - Results of the Alaska CCN comparison for applied supersaturations > 0.3%. n_{tot} is the total number of CCN measurements conducted, n_{test} is the number of tests involving that particular instrument, *rerr* is the relative average disparity, expressed as the average of the ratio of the departure between the CCN and reference concentrations divided by the reference concentration, and σ_{rerr} is the *rerr* standard deviation.

4 - CLOSURE BETWEEN *CDNC* AND CCN

The comparisons shown in Figure 2 are based on airborne measurements of *w*, CCN (from WYO1), and *CDNC* obtained by the Merlin during the ACE-2 Cloudy Column experiment. On the ordinate we present predicted values of *CDNC*. These were evaluated by inputting measurements of *w* and CCN into the Twomey equation [6]. The set of *w* values used in the calculation was sampled during straight- and level-flight traverses of the cloud layer. Data points plotted in Figure 2 are averages of the probability density functions (pdf) both for the observed *CDNC* (pdf(*CDNC*)) and *w* (pdf(w)), with the latter transformed to a pdf(*CDNC*) via the Twomey equation. This calculation is constrained to values of $w > 0$ and the constraint omits some of the cloud regions that have been affected by entrainment and drizzle formation. CCN measurements input into the calculation were not obtained simultaneous with the pdf(*CDNC*) and pdf(w), but were sampled within 60 km of the measurements of cloud microphysical properties. Details of this approach are discussed in reference 4. Figure 2 indicates a degree of closure that is consistent with experimental uncertainties associated with the WYO1 CCN measurement (i.e., a ± 50% relative error in concentration).

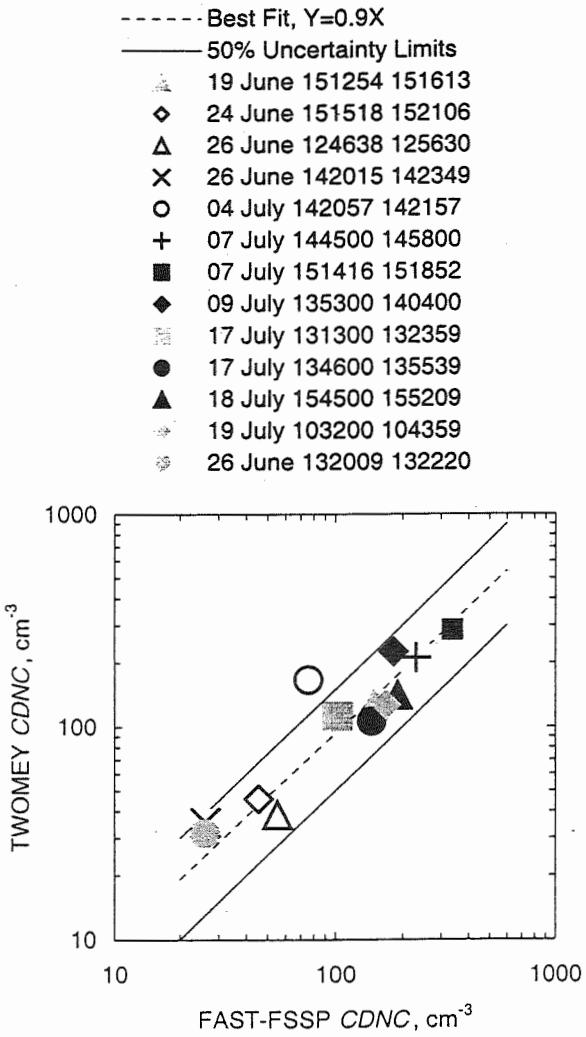

Figure 2 – A successful closure result based on ACE-2 (1997) field measurements. The compared values of *CDNC* correspond to measurements from the Meteo France Fast FSSP and calculations based on the Twomey equation initialized with measurements of *w* and CCN. The *CDNC* and *w* data were sampled during the straight- and level-flight cloud traverse intervals indicated in the caption. The standard error in the slope of the best-fit line (dashed) is ± 0.09.

5 - PREDICTING *CDNC* FROM CCN AND APP DATA

Here we present parameterizations of the *CDNC*/*w* relationship based on parcel model simulations. The parcel model was initialized with airborne WYO1 CCN measurements (from ACE-2) and with APP measurements obtained from the PDH monitoring site [3]. The size distribution measurements made at PDH (20 to 500 nm dry diameter) were averaged over the same time interval as the Merlin flights. The PDH is located on the north coast of Tenerife and is usually unaffected by local pollution sources. During ACE-2 the Merlin sampled both the marine boundary layer and stratocumulus approximately 100 km north of the PDH.

The *CDNC*/w parameterizations discussed here are fits of the form

$$CDNC = Aw^B \quad (1)$$

and are based on parcel model runs conducted at *w* equal to 0.05, 0.1, 0.2, 0.4, 0.8 and 1.6 m/s. Additional inputs include an assumed water mass accommodation coefficient (0.1) and an initial thermodynamic state. The latter was derived by extrapolating from the stratocumulus cloud base, observed by the Merlin, to 95% relative humidity along a dry adiabat.

The parameterizations are presented in Table 2. These are easily compared by considering the ratio of the "A" coefficients presented in the final column. Droplet concentration derived from the PDH data are seen to exceed those based on CCN. It is also evident that comparisons based on data collected in airmasses associated with non-seasalt sulfate concentrations larger than 1 $\mu g/m^3$ are associated with a larger *CDNC* bias. Finally, we note that non-seasalt sulfate is commonly used as an indicator of continental aerosol transported to the North Atlantic and that a threshold value of ~1 $\mu g/m^3$ is an indicator of continental influence. In light of the closure shown in the previous section, and because A_{PDH}/A_{CCN} is often larger than the probable error associated with the CCN measurement, we conclude that APP data may substantially overpredict *CDNC* relative to in-cloud observations of *CDNC*. The implication is that APP data may overpredict the extent of the stratocumulus albedo increase attributable to the anthropogenic aerosols.

6 - DISCUSSION AND CONCLUSIONS

We have presented uncertainties associated with CCN measurements obtained from three CCN instruments. For the CCN instrument used in ACE-2 (WYO1) these uncertainties are unbiased, but associated with a statistical error ($\pm$ 50%) that reflects a nonsystematic departure between the direct and derived CCN concentration measurements. The latter was obtained by inputting measurements of an ammonium sulfate aerosol spectrum into Kohler theory. Further, we show the results of a successful closure experiment which involves comparisons between measurements of *CDNC* and predicted values of *CDNC*. The latter was based on measurements of both CCN and *w*. In contrast, the Punto del Hidalgo (PDH) APP data was found to consistently overpredict *CDNC* relative to CCN, and the degree of this overprediction increased with increasing levels of continental pollution.

Several phenomena, both atmospheric and instrumental, may explain the implied disparity between the CCN and APP. First, since we are comparing data from two different measurement platforms (the Merlin and PDH) it is important to ascertain that there were no gradients in the measured fields. Second, since the WYO1 data is limited to applied supersaturation (*S*) values larger than 0.2% those measurements do not capture the slope of the activation spectrum at the low values of *S* that are important for droplet activation in stratocumulus. And finally, the process of selecting values of *CDNC* and *w*, with the intent of eliminating cloud regions affected by entrainment and drizzle scavenging, may unintentionally bias the closure result. Each of these issues must be addressed, and the accuracy and precision of all relevant measurement systems must be scrutinized before definite conclusions can be drawn from the field measurements

7 - REFERENCES

1. Delene, D., T.Deshler, P.Wechsler, and G.Vali, A balloon-borne cloud condensation nuclei counter, *J. Geophys. Res.*, 103, 8927-8934, 1998.
2. Ji, Q., G.E. Shaw, and W. Cantrell, A new instrument for measuring cloud condensation nuclei: Cloud condensation nucleus "remover", *J. Geophys. Res.*, 103, 28013-28019, 1998
3. Putaud, J.P., R.Van Dingenen, M.Mangoni, A.Virkkula, and F.Raes, Chemical mass closure and origin assessment of the submicron aerosol in the marine boundary layer and the free troposphere at Tenerife during ACE-2, *Tellus*, in press, 2000
4. Snider, J.R. and J.-L. Brenguier, Cloud condensation nuclei and cloud droplet measurements from ACE-2, in press *Tellus*, 2000
5. Snider, J.R., W.Cantrell, G.Shaw, J.Hudson, D.Delene, and S.S.Yum, Comparisons of four cloud condensation nucleus measurement systems, manuscript submitted to *J. Atmos. Oceanic Technol.*, 2000
6. Twomey, S., The nuclei of natural cloud formation. Part II: The supersaturation in natural clouds and the variation of cloud droplet concentration, *Geophy. Pura. Appl.*, 43, 243-249, 19

Date	Nss-Sulfate, $\mu g/m^3$	A_{PDH}	B_{PDH}	A_{CCN}	B_{CCN}	A_{PDH}/A_{CCN}
24-Jun	0.2	155	0.244	105	0.401	1.5
25-Jun	0.2	162	0.251	132	0.300	1.2
26-Jun	0.3	130	0.261	93	0.506	1.4
4-Jul	0.3	180	0.315	124	0.538	1.5
7-Jul	5.3	1130	0.550	467	0.451	2.4
9-Jul	2.8	557	0.348	332	0.271	1.7
17-Jul	1.6	476	0.411	254	0.465	1.9
18-Jul	3.1	669	0.466	285	0.542	2.3
19-Jul	1.4	567	0.374	220	0.324	2.6
21-Jul	0.7	246	0.217	146	0.429	1.7

Table 2 - $CDNC = Aw^B$ parameterizations based on the PDH Aerosol and CCN (WYO1) Inputs. The non-seasalt sulfate concentration data is from PDH [3]. The $CDNC=Aw^B$ parameterization is for w in meter per second and $CDNC$ in number per cubic centimeter.

ICE NUCLEATION IN OROGRAPHIC WAVE CLOUDS

Paul R. Field[1] , Richard J. Cotton[1] and Doug Johnson[1]

[1]Meteorological Research Flight, The Met. Office, UK.

1. INTRODUCTION

During October 1999 the Met. Office C-130 aircraft was involved in the INTACC (INTeraction between Aerosol and Cold Clouds) project, sampling gravity wave clouds that formed over the Scandinavian mountain range. A broad range of environmental conditions were encountered with vertical updrafts between 1 and 9 m s^{-1} and temperatures from −12°C to -40°C. To date, few wave cloud studies have surveyed this temperature range – most tending to observe clouds colder then -40°C that are dominated by the homogeneous freezing process. Ice was observed at all of these temperatures and this paper demonstrates that heterogeneous ice nucleation was responsible for the origin of the majority of the ice. A relationship between ice concentration and temperature is also presented indicating that ice concentrations and hence heterogeneous ice nuclei become relatively more prevalent at colder temperatures. Examination of aerosol concentrations suggest that the heterogeneous ice nuclei are larger than 0.1 μm in diameter.

2. NEW INSTRUMENTATION

This section contains a brief summary of some of the new instrumentation applied in INTACC to the study of wave clouds described in this paper.

(i) SID: the Small Ice Detector (Kaye et al. 1996)is a laser scattering device that can count, size and shape particles down to 2-3 μm. The probe uses six detectors arranged azimuthally at a forward scattering angle of 30°. By comparing the detector responses an 'asphericity' (*Af*) value can be obtained for each particle measured. Laboratory measurements have shown that 3 μm latex spheres have an *Af*<5. In practice a threshold of 6 appears to be better in the wave clouds studied. Therefore, an *Af*>6 indicates that the cloud particles are aspherical and assumed to be ice. The intensity of the scattered light can be used to estimate the particle size.

(ii) NEVZOROV PROBE: This bulk water probe consists of two probes that measure total condensed water and liquid water contents. The measurements from the probes diverge when ice is present so that the difference in total water and liquid water gives the ice water content (Korolev et al. 1998).

(iii) CLOUDSCOPE: essentially a video camera that views a 0.2 mm^2 window perpendicular to the direction of travel. This instrument provides a visual indication of the phase of a particle for sizes greater than 10 μm.

Corresponding author's address: Paul R. Field, Meteorological Research Flight, DERA, Y46, Farnborough GU14 0LX; E-Mail: prfield@meto.gov.uk

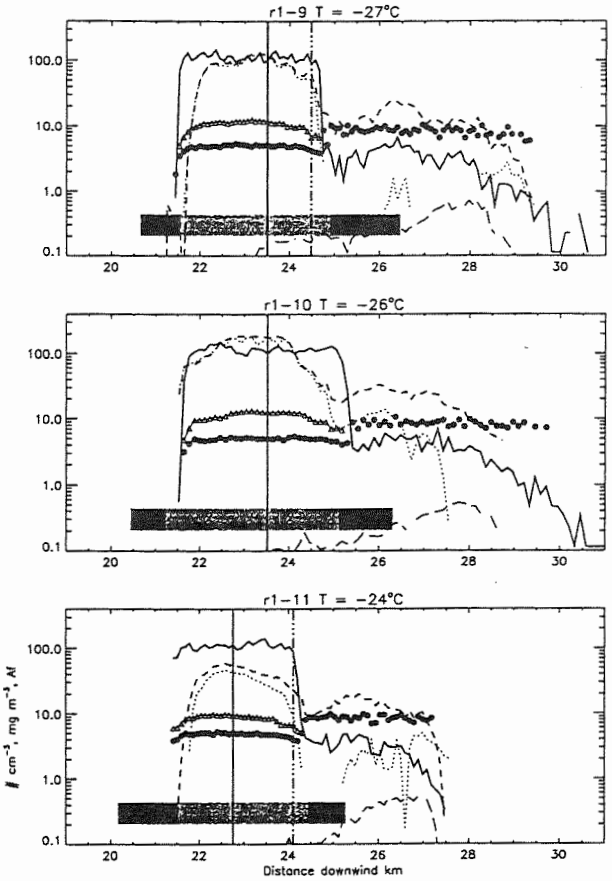

Figure 1. Three runs in wave cloud from flight A722. The solid line is the concentration from the SID probe (diameter > 3 μm) per cm^{-3}. The open triangles represent the volume weighted diameter of droplets from the SID probe in μm. The solid circles are the 1s mean asphericity values obtained from the SID probe (Af). The short dashed line is the total condensed water content measured with the Nevzorov probe (mg m^{-3}). The dotted line is the liquid water content obtained from the Nevzorov probe (mg m^{-3}). The vertical solid line marks the transition from updraft to down draft. The vertical dot-dash line marks the observed phase transition obtained from the cloudscope. The long dash line is the 2D-C concentration per cm^{-3} for particle larger than 25 μm in diameter. The grey shaded horizontal bar represents regions of supersaturation. The darker grey indicates ice supersaturation whereas the lighter grey indicates water supersaturation. The average temperature for the run is given at the top of each panel.

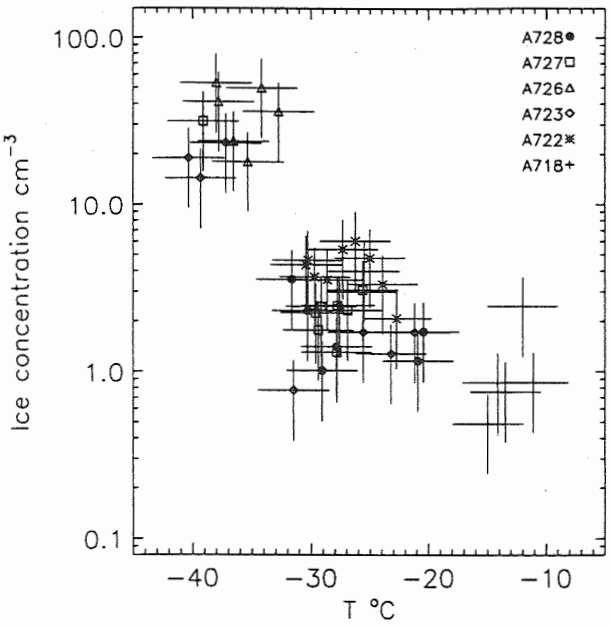

Figure 2. Ice concentrations (95th percentile) from 6 flights in orographic wave cloud versus ambient air temperature. The vertical bars represent a concentration uncertainty of 50%. The horizontal bars indicate that sampled particles may have originated at a different height in the cloud.

3. GRAVITY WAVE CASE STUDY

The wave clouds were sampled with straight and level runs parallel to the wind at different heights with cross-wind runs up- and down-wind of the cloud. The results shown in figure 1 are three runs from a flight that extensively sampled an isolated wave cloud over Scandinavia. The runs are arranged in height order and show observations from a number of aircraft mounted probes. The air is moving from left to right and experiences updrafts of up to 4 m s^{-1}. It can be seen that no cloud particles are produced until water saturation is encountered. When water saturation is reached there is a very sharp increase in cloud particle number concentration. The droplet diameter and Nevzorov water contents also show a rapid onset at the beginning of the water saturated region that is roughly symmetric about a maximum at the updraft-downdraft boundary. Near the downwind extent of the water saturated region several step changes take place that mark the change in the dominant phase of the cloud from liquid to ice: (i) the cloud particle concentration falls sharply; (ii) the Nevzorov total and liquid water contents fall and diverge; (iii) the SID asphericity measurement exhibits a step increase; (iv) on the downwind to upwind runs the cloudscope video imagery exhibits a phase change the high concentrations of supercooled droplets rime the cloudscope window on runs downwind so it is impossible to observed the onset of the ice phase on those runs). However, it should be noted that the presence of large (diameter > 25 μm) particles indicated by the 2D-C probe suggests that the ice particles were forming well before the step change suggesting that the latter half of the liquid dominated region contained some ice. The onset of water subsaturation in the presence of ice led to a rapid evaporation of the droplets revealing the ice population. Finally, as the particles leave the ice saturated region the SID concentration diminishes as the ice evaporates.

The main objective of figure 1 is to show that ice is not initiated until after droplets are formed and so the upwind concentrations of deposition ice nuclei must be low or absent. The temperatures at which these observations were made were much too warm for homogeneous freezing to be efficient which means that a heterogeneous nucleation process must have been acting. The possible candidates are 'condensation freezing' and 'contact nucleation', or some combination of these processes (see Prupacher and Klett 2nd editon p. 309 for definitions).

4. ICE AND AEROSOL CONCENTRATIONS

An initial attempt has been made to synthesise observations from a number of flights carried out in INTACC to provide a more comprehensive picture of the effect of heterogeneous ice nucleation as it varies with environmental conditions. The ice concentrations obtained from these wave cloud studies represent the combined result of heterogeneous freezing due to both the rapid cooling induced by the gravity wave and the age of the supercooled droplet at the environmental temperature. Because of this, if the ice concentration is used as a proxy for ice the nuclei (IN) concentration it will usually be an underestimate.

Figures 2, 3, and 4 show ice and aerosol concentration results from six INTACC flights. Figures 3 and 4 show a subset of values from only those runs that reached water saturation and temperatures warmer than -35°C. This was done to eliminate ice formed through homogeneous freezing but include ice that was formed after the formation of droplets. Because SID is a new probe a generous margin of error (±50%) has been placed on the sample volume until further intercomparisons can be made. The temperature at which the ice particles were observed was not necessarily the temperature at which they were formed. To account for the difference between a parcel streamline and the aircraft level an error of ±3°C was attributed to the measured temperature. The vertical and horizontal bars in the following three plots represent these uncertainties.

Figure 2 shows ice concentrations from the SID instrument versus temperature. With the exception of A727, most individual flights do not show a strong trend with temperature. However, taking all the flights together, a well defined trend of increasing ice concentrations with decreasing temperature is evident. The rate of change of concentration is approximately 2.5 orders of magnitude in 30°C. The points at temperatures colder than -35°C are probably affected or due to the homogeneous freezing process. The points at temperatures warmer than -35°C are due to

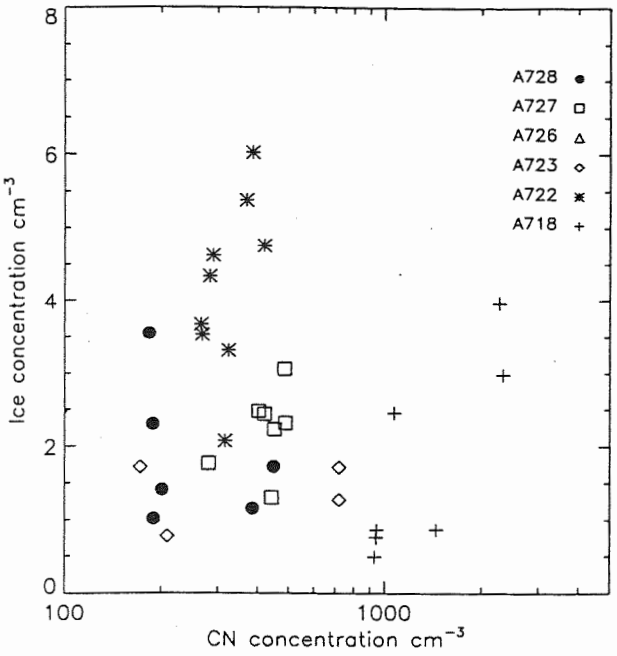

Figure 3. Ice concentrations (95th percentile) versus PCASP concentrations (aerosol diameter > 0.1 μm).

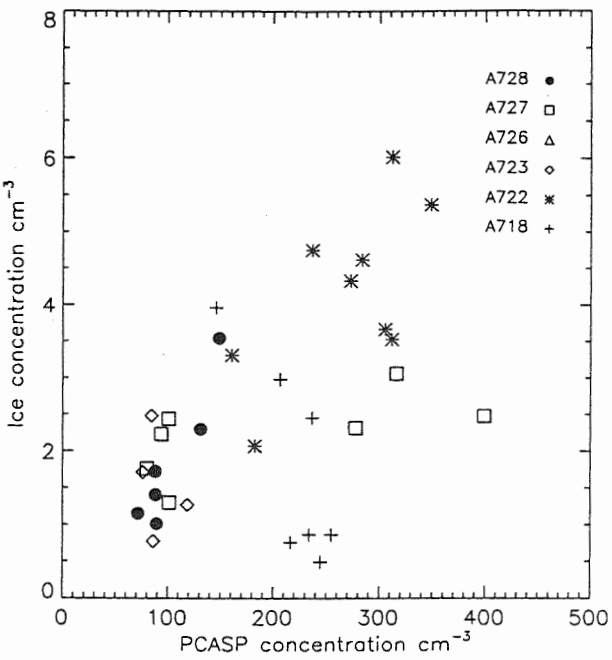

Figure 4. Ice concentrations (95th percentile) versus CN concentrations (aerosol diameter > 3 nm).

heterogeneous ice nucleation processes mentioned in the previous section. These ice concentrations appear to be quite high but the values between –35°C and -40°C are in agreement with theoretical estimates of 10-100 cm^{-3} presented by Heymsfield and Miloshevich (1993) for homogeneous freezing in wave clouds. The concentrations at temperatures warmer than -30°C are much greater than those obtained from the parameterisations of the numbers of contact nuclei such as Meyers et al. (1992) that gives ~0.04 cm^{-3} at -25°C, but agree better with the estimates of Young (1974a) : ~7 cm^{-3} at -18°C.

Figure 3 shows ice concentration versus the median concentration for out-of-cloud particles greater than 0.1 μm in diameter measured with a PMS Passive Cavity Aerosol Spectrometer Probe (PCASP), and figure 4 again shows ice concentration, but this time versus out-of-cloud aerosol in excess of 3 nm in diameter measured with a condensation nucleus (CN: TSI 3025) counter. The positive correlation between the ice concentration and the larger aerosols appears to better than the relation between ice concentration and aerosol of all sizes suggesting that the heterogeneous nuclei can be found amongst aerosol larger than 0.1 μm in size.

5. SUMMARY

In the wave clouds observed the dominant ice nucleation process was thought to have been a heterogeneous ice nucleation mechanism such as 'contact' and/or 'condensation freezing'. Deposition nucleation was thought to have little effect. Ice formation through heterogeneous nucleation was observed between –35°C and –15°C and produced ice concentrations of up to 6 cm^{-3}. The heterogeneous ice nuclei are probably a subset (~1%) of the larger aerosol population (diameters > 0.1 μm) with which the ice concentrations showed a good positive correlation.

6. ACKNOWLEDGEMENTS

The authors wish to thanks the staff of MRF and C-130 aircrew for their assistance and hard work. INTACC was partially funded by an EU research grant ENV4-CT97-0549.

REFERENCES

Heymsfield A. J. and Miloshevich L. M., 1993: Homogeneous ice nucleation and supercooled liquid water in orographic wave clouds. *J. Atmos. Sci.* **50** 2335-2353.

Kaye P. H., Hirst E., Saunders S., Johnson D. and Pickering M., 1996: An instrument for real-time classification of particle shape within clouds and aerosols. In Proceedings of: 12th International Conference on Clouds and Precipitation.

Korolev A.V., Strapp J. W. and Isaac G. A., 1998: The Nevzorov airborne hot-wire LWC-TWC probe: prinicple of operation and performance characteristics. *J. Atmos. Oceanic Technol.*, 15, 1495-1510.

Meyers M. P., DeMott P. J., and Cotton W. R., 1992: New primary ice nucleation parameterizations in an explicit cloud model. *J. App. Met.*, **31**, 708-721.

Pruppacher H. R. and Klett J. D., 1997: Microphysics of clouds and precipitation, 2nd Ed. Kluwer Academic Publishers.

Young K. C., 1974a: A numerical simulation of wintertime, orographic precipitation: part I. Description of model microphysics and numerical techniques. *J. Atmos. Sci.* **31**, 1735-1748.

FIRST FIELD RESULTS WITH A NOVEL CCN / KELVIN SPECTROMETER WITH INTRINSIC CALIBRATION

W. Holländer, W. Dunkhorst and H. Windt

Fraunhofer Institute of Toxicology and Aerosol Research
D-30625 Hannover, Germany
Email: hollaender@ita.fhg.de

1. INTRODUCTION

Assessing the anthropogenic impact on cloud nucleation is an important issue in the global change context. Normally, this impact is determined by simultaneously measuring cloud droplet spectra, total and interstitial aerosol Kelvin spectra and chemical aerosol composition accompanied by air trajectory calculations. This is exactly what is done in the current project 'Physical and chemical characterization of the interstitial aerosol' funded by the German Ministry of Research and Technology under grant # 07AF101/0. For this field project we developed a Kelvin spectrometer based on rapid expansion and constant angle Mie scattering (CAMS, Wagner, 1985) of the growing monodisperse droplets as well as their extinction. Performance characteristics of this Kelvin spectrometer and first results of the field experiment done at Mt. Brocken (1136 m a.s.l.) about 120 km southeast of Hannover will be presented here.

When supersaturation is set up slowly, large particles may start growing much earlier than smaller but still potentially activable ones. When vapor is depleted by many „early-growers", supersaturation may not reach the value necessary for growth of the small particles. This situation may be typical for the atmosphere but in order to prove it one needs an instrument which is capable of measuring true Kelvin spectra unaffected by concentration artefacts.

2. KELVIN SPECTROMETER CHARACTERISTICS

Since expansion type counters do not have this problem we decided to use a design as shown in Fig.1.

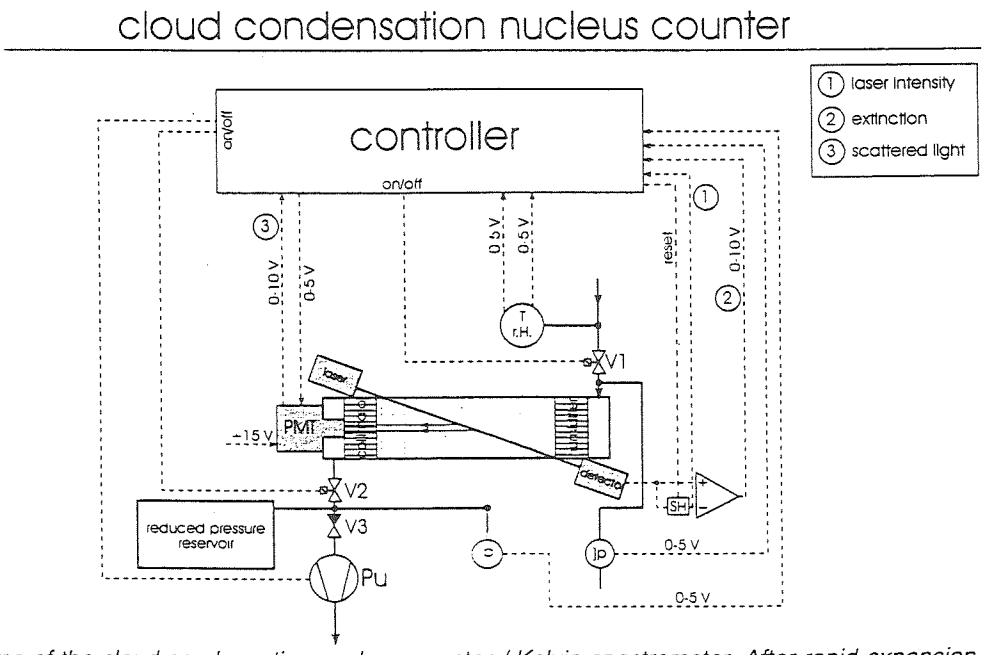

Fig.1: Scheme of the cloud condensation nucleus counter / Kelvin spectrometer. After rapid expansion within tens of milliseconds, particles nucleate and grow to a cloud of monodisperse droplets. Mie structures allow sizing at any time, and from extinction, the droplet concentration can be derived with good accuracy using Mie theory.

The experimental scattering intensity under a certain angle (30° in our case) $J_{30} = S_{30} \cdot \Delta\Omega \cdot N \cdot V$ is given by the product of Mie scattering intensity in that direction S_{30}, droplet concentration N, solid aperture angle $\Delta\Omega$ and an amplification factor V. The extinction coefficient $E = -\ln(T) = \beta \cdot DECS \cdot N \cdot L$ is according to

Lambert-Beer's law with the transmission T over length L, and the dimensionless extinction cross section $DECS = \alpha_{Mie}^2 \cdot Q_e$ with $\beta = \lambda_{light}^2/(4\pi)$, the Mie parameter $\alpha_{Mie} = d \cdot \pi / \lambda_{light}$, and the extinction efficiency Q_e. The experimental ratio E/J_{30} does not depend on the concentration and is proportional to the ratio $DECS/S_{30}$ obtained from theory, which uniquely characterizes droplet size.

Therefore, by comparing experimental E/J_{30} with theoretical $DECS/S_{30}$ values (e.g. Fig. 2) we obtain the size as a function of time which must fit growth theory as described e.g. in Wagner (1982).

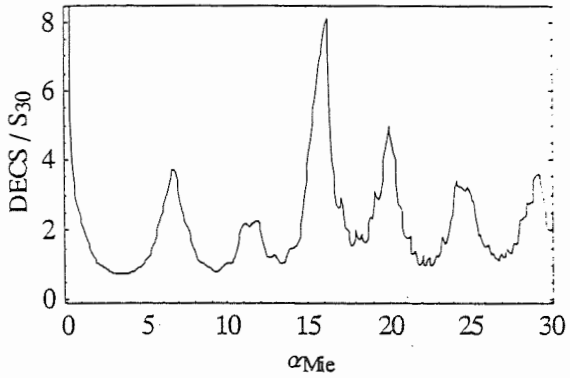

Fig.2: Calculated Mie - ratio of DECS and unpolarized scattering intensity under 30° S_{30} for water (n = 1.33 +I 10^{-3}).

Of course, the experiments provide measuring data as a function of time as shown in Fig. 3a-c.

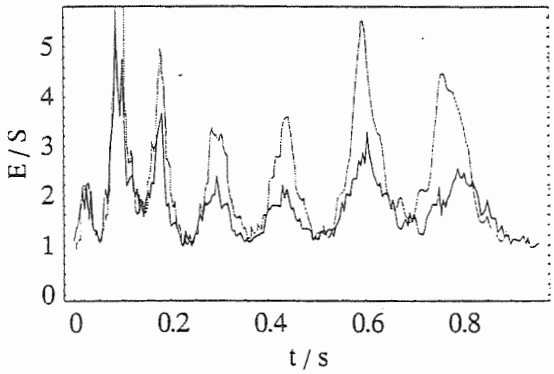

Fig:3a: Extinction scattering ratios: E/J_{30} (experimental, large amplitude, from Figs. 3b/c) and theoretical Mie-ratio $DECS/S_{30}$(black, from Fig.2 converted into time domain using growth theory). Zero time is here at $\alpha_{Mie} = 9.4$.

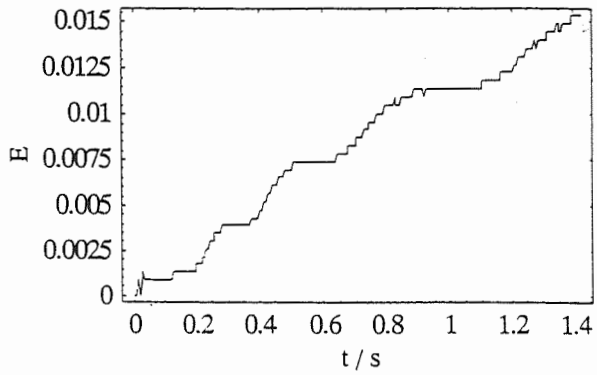

Fig. 3b: Example of an extinction coefficient vs. time.

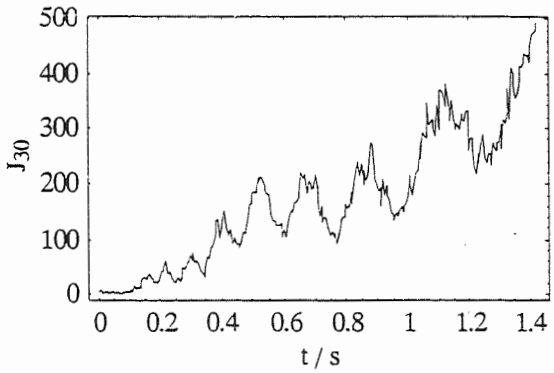

Fig. 3c: Example of a scattering signal vs. time.

Curves with good Mie structures as shown above in Figs. 3a-c typically occur at high supersaturations with low droplet concentrations. The variability of the experimental curves is rather large and not all signals are of this excellent quality so that finding the correct extrema is a nontrivial task requiring a fair amount of heuristics, the reason being not only noise but also the widely different growth time scales which depend on supersaturation and ambient temperature which is followed by the instrument.

The instrument inlet is a 5 μm cut-off impactor in order to make sure that interstitial aerosol is measured only. As saturator and optical collimator we use a cordierite car catalyst support with 1 mm honeycomb structure which carries water for about 3 days of continuous operation. The sampling rate of the transmission and scattering ADCs is 200 Hz and resolution is 12 Bits. Maximum droplet growth time is not limited by heat conduction from the walls (which would imply a time scale of significantly more than 10s) rather than by internal convection currents set up by small temperature gradients.

As a demonstration that extinction maxima are not suitable for high precision measurements of concentration, Fig.4 shows a variety of results. Clearly, exm (see capture) is not suitable for precision measurements.

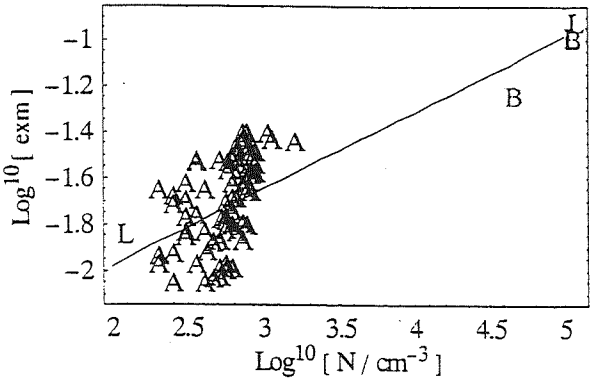

Fig. 4: Extinction coefficient maximum (exm) vs. droplet concentration for atmospheric (A) measurements (june 21 1999, see below), and from laboratory experiments with Latex particle suspension (L) and bi-distilled water (B). The solid line would be expected if the total amount of condensable water would be shared by N/cm^{-3} droplets.

Practically, concentrations can be measured between the detection limit (defined by scattering amplitude < 30 AND E<10^{-3}) of about 30 cm^{-3} and 150000 cm^{-3} at supersaturations > 1.5% (at room temperature). At smaller supersaturations especially at low temperatures, measuring signals are too small and/or required growth time is not available due to convection. The instrument is described in more detail elsewhere (Holländer et al., in preparation)

3. FIELD RESULTS

The next Fig. 5 shows that the instrument can determine the effective supersaturation in clouds. Activated particles will be scavenged and removed by the inlet while nonactivated ones will be unaffected. This is actually observed for particles with a critical supersaturation of about 2% in our example.

The instrument also provides information about the physicochemical properties of the CN by comparing actual growth speed with growth speed expected for nonsoluble particles.

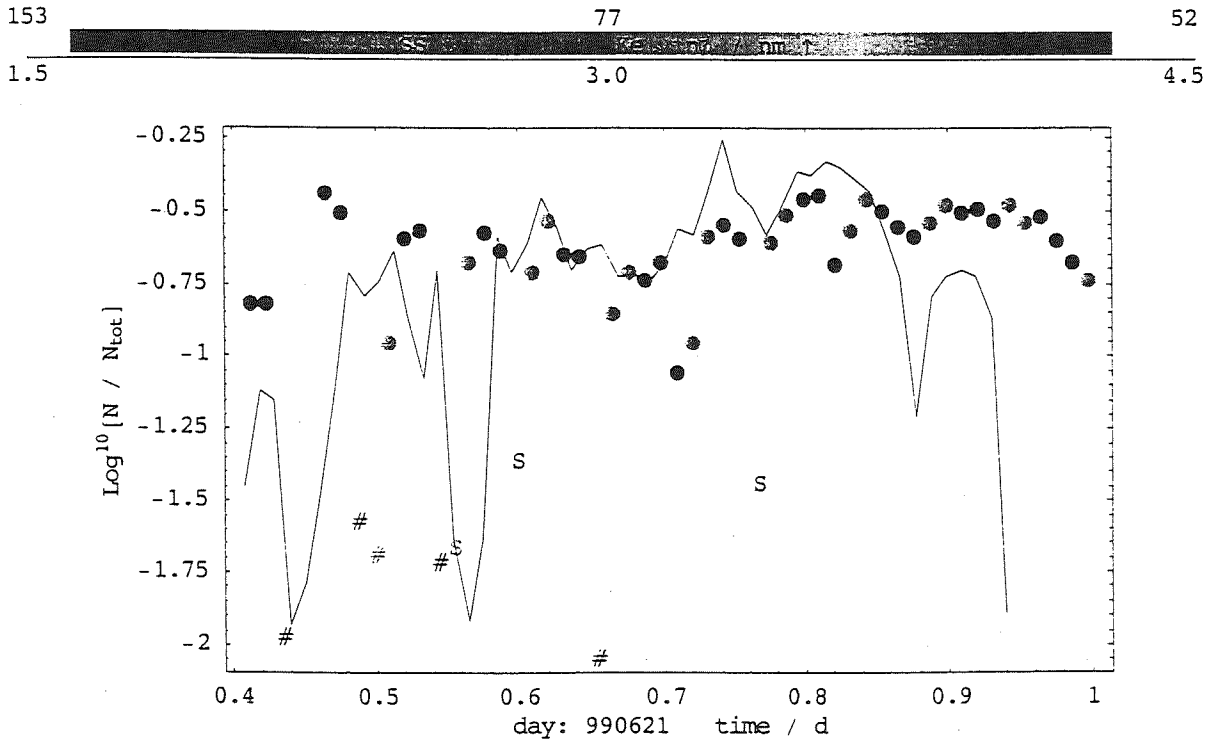

Fig. 5: During cloud events, the ratio N_{APS}/N_{tot} drops (solid line), where N_{APS} is the total concentration measured by the TSI APS3320, N_{tot} by TSI CNC3760. This also holds for particles with a critical supersaturation less than about 2% (mostly # and S data, see below) while those with still smaller Kelvin size remain at the previous relative concentration (most other points). S: weak signal without Mie structures; scattering amplitude used for concentration assessment only. #: below detection limit.

If the maximum growth speed of a droplet neglecting release of latent heat is called Φ_0, taking into account coupled heat and mass transport will slow it down to Φ_0 ψ_{th} with ψ_{th} < 1 for nonhygroscopic particles. ψ_{th} is a

factor strongly depending on temperature. Any soluble admixtures to the particle will result in an experimentally measured $\psi_{exp} > \psi_{th}$. We can introduce a normalized value $\psi_{norm} = \frac{\psi_{exp} - \psi_{th}}{1 - \psi_{th}}$ which characterizes the growth properties of the nuclei; it is shown in Fig. 6. for the above measurements indicating the presence of the whole property spectrum.

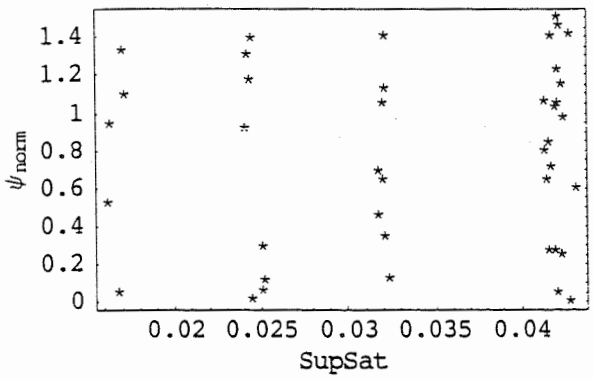

Fig. 6: ψ_{norm} for the above data plotted vs. supersaturation. The full property range is observed here with no dependence on supersaturation.

4. CONCLUSIONS

We have described a Kelvin spectrometer with the following characteristics:

- Supersaturation is achieved by rapid adiabatic expansion
- Droplet growth is monodisperse allowing application of Mie theory
- Actual droplet concentration is experimentally determined by scattering and extinction signals, providing intrinsic calibration
- Kelvin spectrum is measured sequentially using various supersaturations

We have also shown by first field results that the instrument is inherently capable of determining actual supersaturations in clouds by measuring objective Kelvin spectra of the cloud-processed interstitial aerosol and provide additional information on physicochemical nucleus properties.

5. REFERENCES

Holländer W., W. Dunkhorst & H. Windt; Design and characterization of an expansion type CCN: in preparation

Wagner, P. E., 1985; A Constant-Angle Mie Scattering Method (CAMS) for Investigation of Particle Formation Processes , J. Colloid Interface Sci. 105, 456.

Wagner P. E., 1982; Aerosol growth by condensation; pp 129 - 178 in: Topics in Current Physics - Aerosol Microphysics; Ed. W. H. Marlow; Springer

DETERMINATION OF THE VERTICAL DISTRIBUTION OF PRIMARY BIOLOGICAL AEROSOL PARTICLES

Sabine Matthias-Maser

[1] Institute for Atmospheric Physics, University of Mainz, D-55099 Mainz,

1. INTRODUCTION

Primary biological aerosol particles (PBAP) play an important role in the atmosphere; for instance they contribute to cloudforming processes. Meanwhile there exist a number of ground based measurements of their size distribution and composition (mean percentage of about 25% of the total aerosol, Matthias-Maser, 1998), but up to now less is known about their vertical distribution. Because of their physical characteristics (density, shape etc.) they are easily transported into higher altitudes. Therefore the information of their vertical profile is interesting.

During a study of feasibility, financed by the Federal Ministery of Education, Science, Research and Technology (BMBF) a new impaction system MOCIS (Mobile Cascade Impaction System) was developed. It allows the size fractionated sampling of atmospheric aerosol particles with radii larger 0.2 µm and is suitable for a single particle analysis to determine their biological components.

2. REQUIREMENTS

There were made several demands on the sampling system. Size fractionated sampling of particles larger 0.2 µm was desired which allows a possibility for single particle analysis afterwards. The whole system should work automatically in a compact, modular construction. It should be able to adapt the sampling time to real particle concentration, changing the sampling plates automatically. Constant cut-off's for all sampling conditions, e.g. volume flow control dependent on air density, was required. Desirable but not compelling was the possibility to adapt the instrument easily to different sampling platforms (i.e. for ground based or airborne mesurements).

Corresponding author's address: Sabine Matthias-Maser, Institute for Atmospheric Physics, University of Mainz, Becherweg 21, D-55099 Mainz, Germany;
E-Mail: matthias@mail.uni-mainz.de.

3. DESCRIPTION

The principle of the new instrument is based on the Two Stage Impaction System ZSI (Matthias-Maser und Jaenicke, 1994) used in several former projects on which comprehensive improvements necessary for the use aboard aircraft were performed. It is built modular and allows automatic, size fractionated sampling of particles with radius larger than 0.2 µm. It consists of four two-stage slit impactors (ZSI) with different cut-off's, and an automatic changing mechanism of the sampling plates. For the planned project they were combined in two modules each equipped with two ZSIs and the necessary periphery, i.e. vacuum system (PU), volume flow control unit (LFE) and optical particle counter (LPSC) (see Fig. 1, and 2). The control of automatic change of sampling plates, sampling time, and volume flow dependent on the real atmospheric conditions and on the real particle concentration is performed by a PC-based steering unit. The two modules can be integrated alternatively into an under wing pod (Fig. 3) of a research aircraft, or can easily be mounted on a wind vane for ground based measurements, while the PC is installed in the cabin of the aircraft respectively in a container.

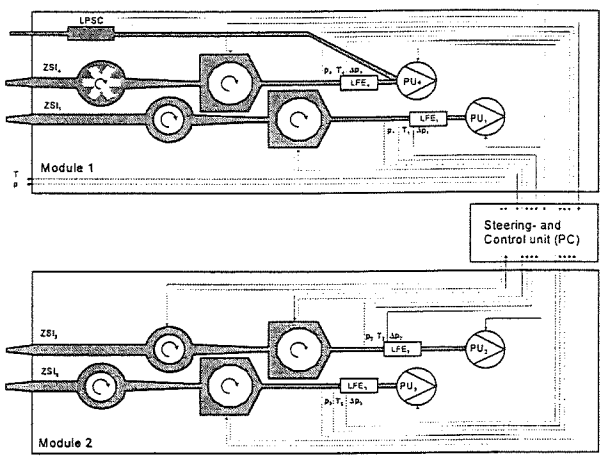

Fig. 1 Schematic concept of the two modules

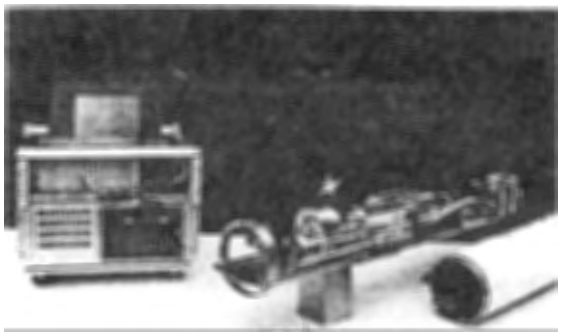

Fig. 2: Module with 2 ZSIs, PC-rack and under-wing pod.

Fig. 3: Research aircraft with under-wing pod.

Figs. 4 to 7 show some details of the ZSIs. The first stages of three of the 4 ZSIs consist of rotating cylinders which serve as pre-seperator.

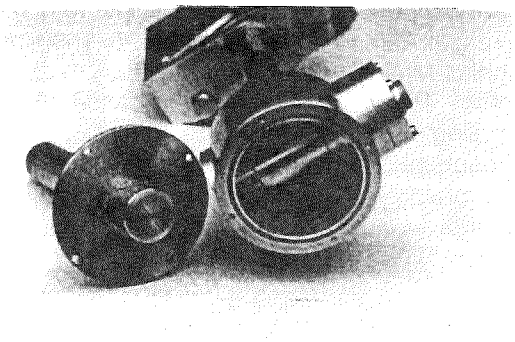

Fig. 4: 1.Stage: rotating cylinder.

The evaluated samples are mounted on a star-shaped sampling array (Fig. 5) respectively on four 12-edged- cylinders (Fig. 6). The single impaction stages consist of a changing mechanism which allows sampling on 12 resp. 6 different sampling plates during one cycle. For sampling glass slides or graphitic foils can be used for later single particle analysis.

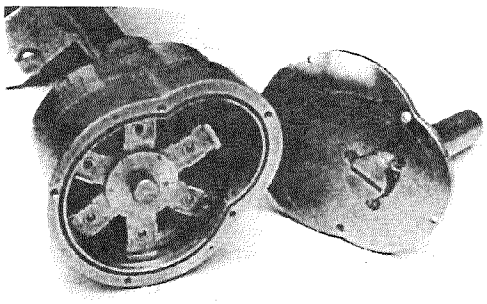

Fig. 5: 1.Stage: star-shaped sampling array with 6 arms.

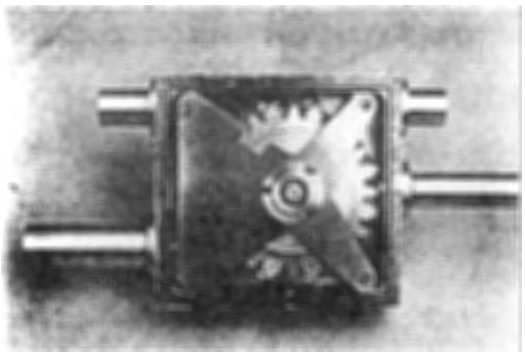

Fig. 6: 2.Stage: 12-edged cylinder.

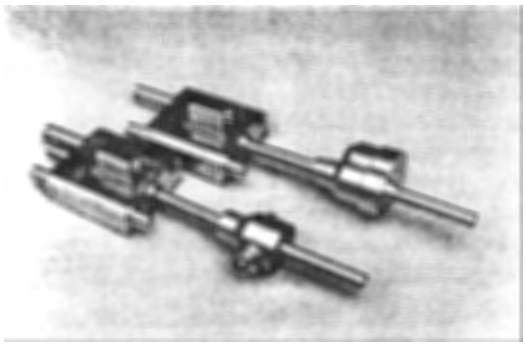

Fig. 7: Both stages combined in 2 ZSIs.

3.1 Steering of the Volume Flow

Stabilisation of cut-off's and isokinetic conditions requires control of the volume flow. This was realized by the measurement of the real conditions within the system. Here we use laminar-flow-elements (LFE), Δp-, T-, and p-sensors. With these the real volume flow is calculated and compared to pre-selected values. The controlling unit of the PC now adjusts the voltage of the pumps for the correct volume flow.

3.2 Steering of the Sampling Time

Single particle analysis requires an optimal particle density on the sampling substrates. Therefore the relation between the sampling time and the particle concentration of all stages was determined experimentally. At the beginning of each measurement the optical particles counter shows the real particle concentration. The real sampling times of all stages is now determined. The replacement of the impaction plates and steering of the pumps is controlled by PC.

3.3 Determination of PBAP

Different impaction plates are used for the different size classes. The particles with $r > 1.9\ \mu m$ are sampled on glas slides covered with coloured glycerine jelly (Matthias, 1987). This contains a protein dye and the protein containing biological particles are stained and can be distinguished from the non-dyed particles using a light microscope.

For the small particles ($0.2\ \mu m < r < 2\ \mu m$) graphitic foils are used which are examined after sampling in a scanning electron microscope (SEM) equipped with an energy dispersive x-ray spectrometer (EDX). Those biological particles show special morphology (spheres, rods, characteristic forms) together with a special elemental composition (P, S, K, Ca, sometimes Si, Cl) and some of them change their shape during EDX (shrinking) (Matthias-Maser and Jaenicke, 1994). The particles are counted and distinguished and the size distributions of non-biological and biological particles are determined.

3.4 Advantages of MOCIS

The advantage of the system is its compactness, the installation on the sampling platform can be carried out in a rather short time period. The measurement of max. 6 different sampling situations without manual replacement of sampling plates is possible. For the determination of vertical profiles this means size distributions in max. 6 different niveaus are available during one measurement. The sampling array can also be mounted with different impaction plates for the use of different evaluation methods for other components of the atmospheric particles.

4. EXPERIMENT

Using the small research aircraft (Fig. 3) field campaignes will be performed to measure vertical profiles above more and less densely populated regions. To see the seasonal differences (phenology) of PBAP we propose experiments during a time period in autumn and spring.

5. ACKNOWLEDGEMENTS

The author would like to acknowledge the BMBF for providing funding in frame of Aerosolförderungsschwerpunkt (AFS). The author wishes to thank enviscope and V. Dreiling for their support.

6. REFERENCES

Matthias, S.1987: Ein Beitrag zur biogenen Komponente des atmosphärischen Aerosols in Mainz *Masters Thesis* University of Mainz.

Matthias-Maser S., Jaenicke R.,1994: Examination of Atmospheric Bioaerosol Particles with Radii > 0.2 μm, J. Aerosol Science, 25 No. 8, 1605-1613.

Matthias-Maser S.,1998: Primary Biological Aerosol Particles: Their Significance, Sources, Sampling Methods and Size Distribution in the Atmosphere, Harrison R.M., Van Grieken R. (Eds) Atmospheric Particle , IUPAC Series , Volume 5, 349-368.

OBSERVATION OF BLACK CARBON (BC) AND CLOUD CONDENSATION NUCLEI (CCN) DURING THE CLOUDY PERIOD: CLIMATE IMPLICATIONS IN THE SOUTHEASTERN US

Shaocai Yu[1] and V.K. Saxena[2]

[1]Nicholas School of the Environment, Duke University, Durham, NC 27708, USA
[2]Department of Marine, Earth, and Atmospheric Sciences, North Carolina State University, Raleigh, NC 27695, USA

1. INTRODUCTION

It has been suggested that CCN potentially play an effective role in climate-regulation (i.e. counteracting the greenhouse warming due to CO_2 etc.) (Yu et al., 2000). A large number of studies have demonstrated the relationship between CCN concentration and cloud microphysics (Twomey and Wojciechowski, 1969; Saxena, 1996; DeFelice et al., 1997). Twomey and Wojciechowski (1969) showed that the observed difference in cloud droplet concentrations between maritime and continental air masses was determined to be caused by systematic differences in the concentrations of CCN between maritime and continental air masses. The purpose of this study is to present the extensive measurement of CCN and BC concentrations and analyze episodes of enhanced CCN concentrations near cloud boundaries at a regionally representative site in the southeastern US, namely, Mt. Mitchell.

2. EXPERIMENTAL SITE AND INSTUMENTATION

The research site is a mountain top station located on the peak of Mt. Gibbes (35.78 ^{0}N, 82.29 ^{0}W, 2006 m MSL), in the Blue Ridge Mountains of western North Carolina (see Bahrmann and Saxena, 1998). The measurements used in this study were obtained from May to August 1996, May to August 1997 and November 1997. The instruments include an ASRC passive cloud water collector, a Cal-Tech active cloud water collector and a PMS Forward Scattering Spectrometer Probe. The ion concentrations (Na^+, K^+, Ca^{2+}, Mg^{2+}, NH_4^+, Cu^{2+}, Zn^{2+}, Fe^{3+}, Al^{3+}, NO_3^-, Cl^-, SO_4^{2+}) in the cloud water were measured by Ion Chromatography (IC). All measurements of CCN activation spectrum reported in this paper were obtained with the CCN Spectrometer (Fukuta and Saxena, 1979). The concentrations of CCN (N, in cm^{-3}) active at a supersaturation S (in percent) can often be fitted to an expression of the form: $N=cS^k$, where N is the cumulative concentration of CCN active at or below a supersaturation S and c is the concentration of CCN active at 1% supersaturation, and k is dimensionless slope parameter. Since those particles with critical supersaturation greater than the supersaturation in the cloud (S_{eff}) will be incorporated into the cloud droplets and other with critical supersaturation less than S_{eff} will remain as particles, our in-cloud measurements represent interstitial CCN due to the fact that no cloud droplets were sampled during the CCN measurements. Real-time, continuous measurements of BC mass concentration were made by a commercial instrument named the Aethalometer (Hansen et al., 1996), manufactured by Magee Scientific.

Corresponding author's address: V.K. Saxena, Dept. of MEAS, N.C. State University, Raleigh, NC 27695; E-mail: saxena@eos.ncsu.edu

3. RESULTS AND DISCUSSION

3.1. General Trend of CCN and BC on Mt. Mitchell

Table 1 lists the concurrent measurement results of average monthly BC concentrations, CCN parameters for four different weather types (e. g. in-cloud, overcast, clear and rain). The average monthly CCN concentrations ranged from 152 to 937 cm^{-3}, 107 to 1006 cm^{-3}, 124 to 548 cm^{-3} and 66 to 326 cm^{-3} for incloud, overcast, clear and rain weather conditions respectively. The average monthly k values ranged from 0.60 to 0.89, 0.60 to 0.94, 0.53 to 1.09 and 0.38 to 0.76 for incloud, overcast, clear and rain weather conditions respectively. As can be seen, the CCN concentrations during the rain period were lower than those during other weather conditions. Hobbs et al. (1985) found that precipitation could reduce the concentration of larger (lower S_c) CCN. The average CCN concentrations during the cloud period had larger standard deviation and were often higher than those of other weather conditions, but not exclusively during these two summer field seasons. The dependence of CCN concentration on air mass history was investigated with the classification of air masses influencing the site as polluted, marine and continental. The average monthly BC concentrations ranged from 169 to 305 (245 ± 61) ng m^{-3}, 86 to 225 (155 ± 61) ng m^{-3} and 56 to 104 (79 ± 14) ng m^{-3} for polluted, continental and marine air masses, respectively. The average monthly CCN concentrations ranged from 261 to 1367 cm^{-3}, 63 to 377 cm^{-3} and 66 to 326 cm^{-3} for polluted, continental and marine air masses, respectively. The average monthly k values ranged from 0.57 to 1.09, 0.56 to 1.01 and 0.48 to 1.07 for polluted, continental and marine air masses, respectively. It is apparently that CCN and BC concentrations of polluted air mass were much higher than those of other air masses. Twomey

and Wojciechowski (1969) showed that CCN concentrations of maritime, unpolluted continental and polluted air masses were typically less than 200 cm^{-3}, between 200 and ~2000 cm^{-3} and above 2000 cm^{-3}, respectively. Obviously, the continental and marine classifications for our research site does not imply pure continental and marine air masses, but rather modified continental and marine air masses caused by additional influences from pollution sources over land.

Freshly emitted BC is hydrophobic and chemical inert in all atmospheric conditions. BC cannot act as CCN by itself. However, aerosol mechanism and in-cloud processes can render a BC particle hygroscopic in the atmosphere. Therefore, the change trend of BC may be used as a tracer of the change trend of anthropogenic aerosols in the atmosphere at our research site. The regression equations between the concurrent measurement data of BC and CCN active at 1% and 0.3% supersaturations for the data from June to August 1996 are as follows (sample number n=272):

$CCN(1\%)\ (cm^{-3})=180.3+2.13 \times BC\ (ng\ m^{-3})$ R=0.69
$CCN(0.3\%)\ (cm^{-3})=136.9+0.40 \times BC\ (ng\ m^{-3})$ R=0.52

where R is correlation coefficient. It is clear that correlation between BC and CCN at 1% supersaturation (small CCN) is more significant than that between BC and CCN at 0.3% supersaturation (large CCN). This seems reasonable because most of BC was present in the accumulation mode (0.1-1.0 μm) as shown by the studies of Pininick et al. (1993), and can only be activated to be CCN at high supersaturation. The positive correlation between BC and CCN indicates that a percentage of BC measured at the site might be in the form of an internal mixture and participate in the formation of CCN.

3.2. Case Studies of Episodes of Enhanced CCN Concentrations Near Cloud Boundaries

In the three cloud episodes of June 15-16 1997, June 20-22 1997, and June 22-23 1997, enhanced CCN concentrations were frequently observed. Figure 1 shows the example of temporal variations of the concurrent CCN and BC concentrations for the cloud episodes of June 15-16 1997. It was found that the CCN concentration increased dramatically during the cloud period in these three cloud episodes, and that high CCN concentrations were always accompanied by high BC concentration, and high total ion concentration in the cloud water. There is an apparent positive correlation between the CCN concentration and BC concentration for both cloud and non-cloud periods.

Since the CCN concentrations during the three cloud episodes exceeded 1500 cm^{-3} much higher than those during other cloud episodes, the cloud-mediated production mechanism of CCN should occur during these three cloud episodes. Here, we refer to the process that the CCN concentration increase unusually during the cloud period as the CCN burst or nucleation burst. The CCN burst lasted for about 23 hours from 8:30 AM June 15 to 7:30 June 16 1997 (Figure 1). The very high NH_4^+, NO_3^- and SO_4^{2+} concentrations in the cloud droplets and the very low pH (range from 2.66 to 3.56) of cloud water during the CCN burst periods indicate that the pollution was very high within the clouds in these three cases.

The typical CCN spectra were measured for air masses before cloud, within cloud and after cloud during the CCN burst for the cloud episode. It was found that the C and k values of CCN spectra during CCN burst period were higher than those before and after cloud. The C and k for 0.3 μm threshold were much high than those for 0.5 μm threshold. For example, the total CCN concentration is 2202 cm^{-3} for 0.3 μm threshold and is 508 cm^{-3} for 0.5 μm threshold at 3:00 AM of 21 June 1997. This indicates that there were a lot of small CCN instead of large CCN produced during the CCN burst because small CCN require high supersaturation and an increase in small CCN population will result in higher k values. Since the air masses within the clouds had been involved in widespread cloud processes before reached at the mountain site, the CCN spectra measured at our site represented those of the aged continental or marine air masses within the clouds. Therefore, the CCN burst processes might occur during the long-range transportation before reached at our site or occurred at our mountain site. This may be one of reasons that lead CCN parameters (C and k) to be very variable for the CCN burst episodes at our site.

3.3. Possible Particle Enhancement Mechanism Analysis

Since, by definition, CCN serve as the nuclei for the formation of cloud droplets, it is to be anticipated that air that has been involved in cloud information will have reduced CCN concentrations, e.g., the nuclei with the critical supersaturation S_c less than the supersaturation (S_{eff}) within the cloud will be found preferentially within the cloud droplets which are removed from the sample. However, the early work (Twomey and McMaster, 1955; Hegg et al., 1990; Saxena, 1996; Clarke et al., 1998) and our analysis in this study have demonstrated that enhanced CCN concentrations over the ambient levels are also found in the vicinity of clouds. Theoretical explanation and laboratory simulations about these CN (or CCN) enhancement mechanisms near and within the clouds so far have been few. It is assumed that in the non-precipitation clouds (stratus clouds), the photochemical reactions result in enhanced production of sulfuric acid gas (or maybe organic acids) that can lead to rapid homogeneous nucleation of new particles if the cloud event coincides with a relative maximum of OH. If the sulfuric acid gas was added to the existing CCN, no more CCN were produced. To find out whether the conditions were favorable for nucleation during our CCN enhancement periods, the following empirical equation was used to calculate the critical concentration C_{crit} ($\mu g\ m^{-3}$) of H_2SO_4 (g), required to achieve a nucleation rate of J=1 $cm^{-3}\ s^{-1}$ (Clarke et al., 1998) under the steady-state condition:

$$C_{crit}=0.16 \exp(0.1T-3.5RH-27.7)$$

where the temperature, T, is in Kelvin, and the relative humidity (RH) scale 0-1 is used. If the ambient $H_2SO_4(g)$ concentration exceed C_{crit}, the excess H_2SO_4 mass become available to form new particles by the homogeneous nucleation. Figures 1 show the change of $C_{crit}(H_2SO_4)$ during the nucleation burst period on the basis of the measured temperature and RH in the air parcel within the clouds. It is of interest to note that the $C_{crit}(H_2SO_4)$ during the CCN enhancement period was lower than other times. The low $C_{crit}(H_2SO_4)$ represents the favored regions for nucleation.

Since liquid water content (LWC) and cloud water ion concentrations were measured during the cloud period, the sulfate mass concentration per unit volume air can be derived using the equation from Lin and Saxena (1991) as:

$$(SO_4^{2-})_{airmass}=(SO_4^{2-})_{cloudwater}*LWC/\rho_w$$

where ρ_w is the density of liquid water. Note that the above equation assumes that the cloud water sulfate concentration is the same as that in the air masses. It was found that the sulfate concentrations in fine ambient aerosol phase at Mt. Mitchell were 2.94 $\pm$1.58 and 5.99 $\pm$0.04 g/m^3 for continental and polluted air masses respectively. By subtraction of these aerosol sulfate concentration from the total sulfate concentration in the air masses, the net sulfuric acid concentration in the air masses can be estimated. It was found that H_2SO_4 concentration (C_s) were in the range of 0.60 (0.15 ppbv) to 30.8 (7.6 ppbv) μg m^{-3}, and C_s/C_{crit} ratios range from 40 to 3226. Obviously, the sulfuric acid vapor concentrations were sufficient to achieve nucleation and nucleation burst during the three nucleation burst periods at the research site. Our observational results show that the ion (NH_4^+, NO_3^- and SO_4^{2+}) concentrations in the cloud water were also extremely high and pH was also very low (pH ranges from 2.67 to 3.37). This indirectly indicates that very active chemical reactions, which produce a lot of sulfuric acid, occurred within the clouds during the three nucleation burst periods.

4. CONCLUDING REMARKS

Our results provide additional support for the idea that clouds are not only a sink of CCN but also a source of CCN under special circumstances (Hegg et al., 1990; Saxena 1996; Clarke et al., 1998). As suggested by the observations of Clarke et al. (1998), nucleation can take place for $H_2SO_4(g)$ levels in the boundary layer that are nearly an order of magnitude less than required by classic nucleation theory. Our observations also indicate that many processes interact to determine the CCN concentrations on Mt. Mitchell.

5. ACKNOWLEDGMENTS

This research was supported by the NASA's Mission to Planet Earth (MTPE) under Contract No. NAS1-18944 from Langley Research Center, Hampton, VA and US EPA's STAR grant No. R-825248.

6. REFERENCES

Bahrmann, C.P., and Saxean, V.K., 1998: The influence of air mass history on black carbon concentrations in the southeastern US. *Journal of Geophysical Research*, 103, 23153-23161

Clarke, A.D., D. Davis, V.N. Kapustin, F. Eisele, G. Chen, I. Paluch, D. Lenschow, A.R. Bandy, D. Thornton, K. Moore, R.L. Mauldin, D. Tanner, M. Litchy, M.A. Carroll, J.Collins, and Albercook, G., 1998: Particle nucleation in the tropical boundary layer and its coupling to marine sufur sources,. *Science,* 282, 89-92.

DeFelice, T.P., Saxena, V.K., and Yu, Shaocai, 1991: On the measurement of cloud condensation nuclei at Palmer Station, Antarctica. *Atmospheric Environment,* **31**, 4039-4044.

Fukuta, N. and Saxena, V.K., 1979: A horizontal thermal gradient cloud condensation nucleus spectrometer. *Journal of Applied Meteorology,* **18**, 1352-1362.

Hansen, A.D.A., 1996: Magee Scientific Aethalometer user's guide, Magee Scientific Company, Berkeley, CA, 56 pp.

Hegg, D.H., Radke, L.F. and Hobbs, P.V., (1990) Particle production associated with marine cloud. *Journal of Geophysical Research.*, **95**, 917-926.

Hobbs, P.V., Bowdle, D.A. and Radke, L.F., 1985: Particles in the lower troposphere over the High Plains of the United States. Part II: cloud condensation nuclei. *J. Clim. Appl. Meteorol.*, **24**, 1344-1356.

Lin, N.H. and Saxena, V.K., 1991: In-cloud scavenging and deposition of sulfates and nitrates: case studies and parameterization. *Atmospheric Environment*, **25**, 2301-2320.

Pininick, R.G., Fernandez, G., Martinez-Andazola, E., Hinds, B.D., Hansen, A.D.A and Fuller, K., 1993: Aerosol in the arid southwestern United States: Measurements of mass loading, volatility, size distribution, absorption characteristics, black carbon content, and vertical structure to 7 km above sea level. *Journal of Geophysical Research.*, **98**, 2651-2666.

Saxena, V. K. 1996: Bursts of cloud condensation nuclei (CCN) by dissipating clouds at Palmer Station, Antarctica. *Geophysical Research Letters.,* **23**, 69-72.

Twomey, S., and McMaster, K.N., 1955: The production of condensation nuclei by crystallizing salt particles. *Tellus*, **7**, 458-461.

Twomey, S. and Wojciechowski, T.A., 1969: Observations of the geographical variations of cloud nuclei. Journal of Atmospheric Sciences, **26**, 684-690.

Yu, Shaocai, 2000: The role of organic acids in the formation of cloud condensation nuclei (CCN): a review. Atmos. Res., (in press).

Table 1. Average monthly BC mass concentrations (ng m^{-3}), CCN parameters (C and k) and sample number (n) for four types of different weather conditions. Average values and standard deviation

	incloud				overcast				clear				rain			
Month	BC	k	C(cm^{-3})	n	BC	k	C(cm^{-3})	n	BC	k	C(cm^{-3})	n	BC	k	C(cm^{-3})	n
Jun-96	179±167	0.89±0.33	440±325	54	208±82	0.94±0.36	397±148	20	262±101	1.09±0.30	773±313	28				
Jul-96	131±89	0.60±0.38	531±330	42	95±98	0.60±0.21	270±81	10	89±52	0.53±0.23	335±178	53	98±30	0.51±0.11	286±53	7
Aug-96	136±70	0.69±0.22	585±324	24	265±114	0.72±0.16	1006±102	8	118±45	0.75±0.23	427±225	31	53	0.38	244	1
Aver.-96	149±26	0.72±0.14	519±73	120	189±86	0.75±0.17	558±393	38	156±92	0.79±0.28	511±231	112	75±32	0.44±0.09	265±30	8
May-97	84±80	0.73±0.40	263±337	105	260±175	0.73±0.14	107±82	2	281±125	0.83±0.30	536±455	60	/	/	/	/
Jun-97	146±80	0.79±0.25	937±774	146	199±116	0.63±0.21	480±473	77	157±65	0.64±0.20	548±471	86	132±82	0.76±0.34	378±578	14
Jul-97	168±100	0.80±0.28	152±126	91	273±140	0.77±0.36	123±100	34	306±105	0.74±0.21	180±120	79	198±151	0.69±0.20	41±16	4
Aug-97	249±142	0.81±0.18	247±131	80	189±83	0.76±0.15	145±56	30	120±89	0.79±0.21	124±70	37	/	/	/	/
Aver.-97	162±68	0.78±0.04	400±361	422	230±42	0.72±0.06	213±178	143	216±91	0.75±0.08	347±225	262	165±46	0.72±0.05	210±238	18
Average	155±47	0.75±0.09	460±217	542	210±64	0.74±0.12	386±286	221	186±91	0.77±0.18	429±228	374	120±39	0.58±0.07	238±134	36
	incloud				snowing				clear,snow				rain			
Month	BC	k	C(cm^{-3})	n	BC	k	C(cm^{-3})	n	BC	k	C(cm^{-3})	n	BC	k	C(cm^{-3})	n
Nov-97	92±58	0.63±0.30	152±38	54	80±110	0.52±0.27	191±75	24	90±74	0.88±0.38	164±120	138	13±10	0.66±0.13	170±52	6

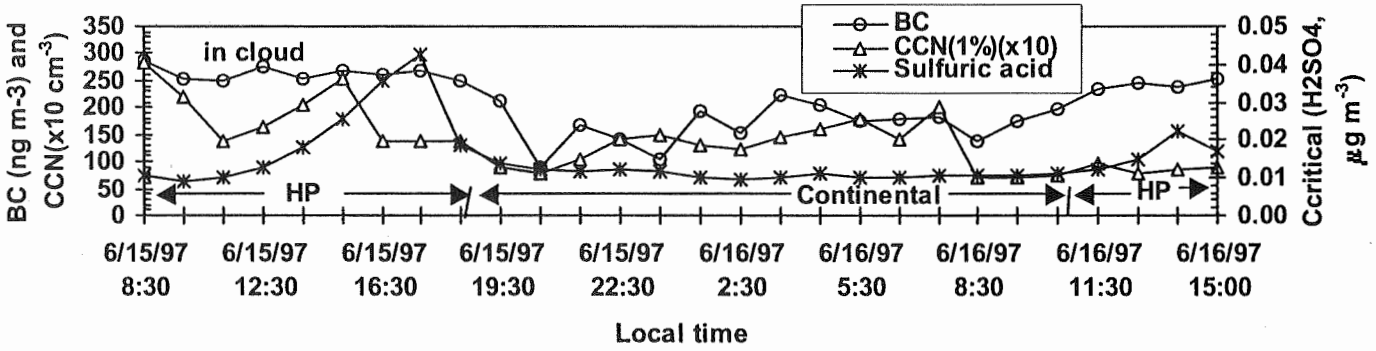

Figure 1. The temporal change of CCN, critical concentration of H_2SO_4, BC concentration and air mass types and weather conditions for CCN burst periods from 8:30 Am June 15 to 15:00 June 16 1997.

ON THE SOURCES AND COMPOSITION OF THE HAZE LAYER OVER THE DEAD SEA VALLEY

Hezi Gershon[1], Eliezer Ganor[2,1] and Zev Levin[1]
1 Department of Geophysics and Planetary Science, Tel-Aviv university, Tel-Aviv.
2 Ministry of the Environment, Sackler Medical School, Tel-Aviv University, Tel-Aviv.

Abstract

The formation, composition and life history of the haze layer that is often formed over the Dead Sea valley in Israel have been studied. The investigation consisted of airborne and ground measurements and theoretical calculations. The measurements were aimed at identifying the chemical composition of the particles and their size distributions. The theoretical studies were designed to better identify the sources of the haze aerosols. The results show that the particles are brought to the Dead Sea valley from distant sources such as the industrial regions near the Israeli Mediterranean coast and from a region to the south west of the Sea. In the morning hours the haze seems to consist of two layers having different compositions. The lower one mainly composed of sodium nitrate and sulfate particles. The upper one is composed of sulfate and mineral dust particles. These two layers get mixed together in the early afternoon as the convection increases. The haze itself disappears in the late afternoon as the Mediterranean sea breeze reaches the valley.

Introduction

The Dead Sea Valley is the lowest point on Earth (about – 415 m below sea level) and is of immense economic importance to both Israel and Jordan. From it various chemicals such as potash and magnesium are extracted by drying the water collected in solar ponds. Any reduction in the solar flux that reaches the surface leads to big economic losses to the local industries. One of the obstacles to the incoming solar radiation is the haze layer that is formed almost daily over this dry valley. This haze layer absorbs and reflects some of the incoming solar radiation (Stanhill, 1987, 1994), reduces the evaporation from the sea surface (Alpert et al., 1997) and impairs visibility.

Preliminary measurements of the aerosol composition made on the slopes of the Judean hills, near the sea shore and above the sea surface (Levin and Ganor, 1984) suggested that the dominant chemical element is sulfur. Since the sulfur is an indicator of industrial pollution and there is no known source nearby, it was suggested that these particles must be transported from distant sources, possibly from the Mediterranean coast some 80 km away.

In this paper we present some more recent results about the composition, size and concentrations of the particles in the haze, about the diurnal cycle of the haze layer and about the transport of the particles to the region. The results are based on measurements from an aircraft through the haze layer, from a ground station on the western slopes of the valley and from simulations using two numerical models.

Methods

The study consisted of both experimental and modeling components. The first was designed to provide a clue as to the particles composition and diurnal variation and the second was aimed at identifying the particles' sources.

1) Measurements of aerosol composition and size distribution were carried out from an instrumented airplane flying through the haze layer and from a ground station on the western slopes of the Dead Sea valley. The ground station was located at Mitzpe Dragot at a height of 400 m above the Dead Sea surface, where the haze layer is observed. In order to determine the vertical profile of the composition of the haze particles, their concentrations and the environmental temperature, a number of flights were performed in which particles were collected on filters as well as on electron microscope grids. The particle concentrations were obtained using a Rich Condensation Nuclei (CN) counter on board the plane.

Each flight consisted of a number of passes at different heights through the haze layer.

A study of the diurnal variations of the chemical and physical properties of the haze particles was carried out from a ground station at Metzukey Dragot during a three-day field campaign.

Bulk samples of collected aerosols from the plane and from the ground station were analyzed

by ion chromatograph in order to determine the soluble composition of the particles. A Scanning Electron Microscopy (SEM) with an Energy Dispersive Spectrometry (EDS) was used to identify the elemental composition of the particles and to determine the mass of the different elements in them using a calibration method previously obtained (Pardess et al., 1992).

2) We used the 3d mesoscale numerical model RAMS (Regional Atmospheric Modeling System) (Pielke et al. 1992) to identify the flow field over the eastern Mediterranean during a typical summer day in which a haze layer is observed. The calculated flow field was then used in the numerical model HYPACT (Hybrid Particle and Concentration Transport) (Utilaz, 1993) to determine the trajectories of particles from potential pollution sources emitting the same chemicals as those observed in the haze.

The 3d meso-scale RAMS simulations were performed using an IBM SP2, and the results were compared with observations. The numerical domain consisted of 144 X 104 X 35 grid points with 3.7 Km horizontal resolution and 30 m vertical resolution (stretched to 1000).

Results

a) Particle analysis

The airplane measurements during the mornings of 18/9/1998 and 29/4/99, suggested that a number of inversion layers existed. Fig. 1a shows that a small inversion appears at Mean Sea Level or at about 400 m above the surface of the Dead Sea (from here on this layer will be referred to as the lower layer). A large inversion (upper layer) appeared at about 300 m (MSL or 700 m above the Dead Sea) extending up to

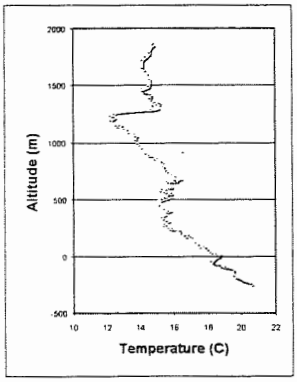

Figure 1a: A measured vertical temperature profile at the Dead Sea Valley (29 April, 99).

about 650 m MSL. A third inversion appeared higher up at about 1200 m MSL, above the haze layer and will not be discussed here.

Fig. 1b shows that the profile of the particle concentration during this time consisted of two main peaks around the height of the inversions. The lower layer appears as a distinct entity having peak particle concentration of close to 10^5 cm^{-3}. Although the upper layer appears to consist of two sub-layers, their composition appears to be very similar and will be considered here as one layer. The two peaks were not only identified by the their concentrations but mainly by their different chemical compositions.

Table 1 shows the average relative weight of the elements per particle at the two layers where the haze appeared.

Aver. relative [%] elemental mass per particle	Na	Mg	Al	Si	S	Ca
Upper layer	16.6	26.7	3.1	7.8	26.6	19.2
Lower layer	35.0	15.3	3.4	6.6	20.8	19.0

Table 1. The average relative elemental mass per particle.

The upper layer was dominated by small sulfur spheres and some silicon derivatives. The lower haze layer was dominated mainly by larger particles, many of which were sodium nitrate. The identification of these latter particles was established using the spot reaction technique of Mamane and Pueschel (1980). By coating the collected sample with Nitron, the nitrate ions

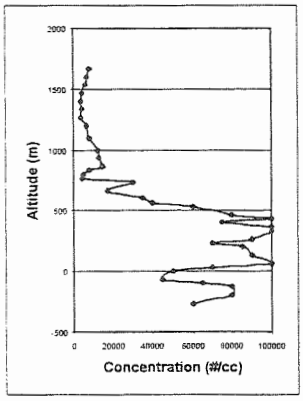

Figure 1b: Vertical profile of particle concentrations (#-cm^{-3}) (29 April, 99).

react with the reagent, forming particles with finger-like structure. These can be easily identified with a SEM. Using this technique we noticed that the particles containing sodium in the lower layer were mostly associated with nitrate (sodium nitrate). The sodium containing particles found in the upper layer were more aggregates without clear association with nitrate.

Further insight into the differences between the two layers can be seen in Fig 2 and 3. In Fig. 2 the average elemental mass (g) per particle is shown. In the upper layer the main elements have lower mass per particle than in the lower layer. Fig. 3 shows that the average elemental mass per particle volume (g-cm^{-3}) is larger in the upper layer. These two figures suggest that the particles in the upper layer were smaller and more numerous.

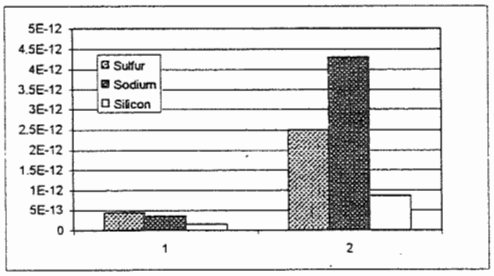

Figure 2: Average elemental mass per particle (g). 1 represents the upper and 2 the lower layer, respectively.

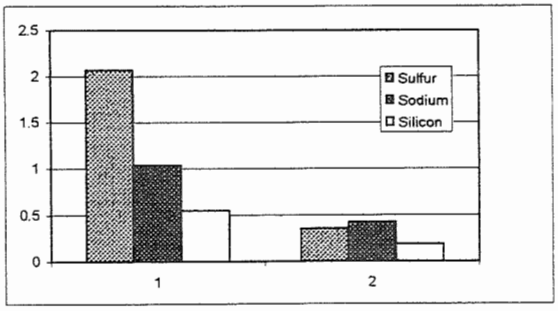

Figure 3: Elemental mass per particle volume (g-cm^{-3}). 1 represents the upper and 2 the lower layer, respectively.

Airborne measurements carried out during the early and late afternoon revealed that the two separate layers, that were seen in the morning, were combined in the afternoon, into one homogeneous layer of similar chemical composition.

The differences between the chemical composition of the upper and lower haze layers suggested that the sources of the two are different. A search for these sources was undertaken. The Dead Sea Works Co., at the southern end of the Sea, was ruled out as a potential source for the sodium nitrate because they do not emit this compound. On the other hand, a more distant source of sodium nitrate was identified in the Rotem industrial area located south west of the Dead Sea. Numerical simulations of the airflow confirmed the possibility that particles emitted from this source during the night could reach the Dead Sea Valley at lower levels. The particles remain there and are lifted with the early morning convection. They remain separated from the particles that are transported at higher levels from the west (mostly sulfate containing particles). As was pointed out above, as the day progresses, convection and mixing take place forming one homogeneous layer extending from near the surface to about 600 m.

Our three-day field campaign took place (Oct. 31 to Nov. 2, 1999) on the hills to the west of the Dead Sea. The site was located at the same elevation as the lower haze layer (~400 m above the Dead Sea). The results of the elemental analysis of individual particles showed that at night the particles were mainly composed of small clay minerals and large pollution particles, mainly sodium nitrate. The total concentrations as measured with a CN counter were relatively low (up about 20000 #/cc). During the day, and especially as the day progressed, particle concentrations increased, reaching their peak values around noon and remaining so until the afternoon when the northerly wind began. During this time the concentration of the sodium nitrate that dominated the pollution at night, decreased markedly and sulfate-containing particles dominated the spectrum.

b) Model simulations

The results of the numerical simulations mimic well the development of the Mediterranean sea breeze and its arrival in the Dead Sea valley. It also simulated well the available climatic observations (Bitan, 1974, 1977) of the local lake circulation in the valley above the Dead Sea itself. The simulations with the HYPACT model, in which parcels were transported from different locations in Israel, suggest that polluted particles from the

Mediterranean coast are transported eastward during the morning hours. Some of these particles manage to pass over the Judean hills and reach the Dead Sea valley. In addition, at night, land-lake breeze in the valley and catabatic down-slope winds along the hills to the west of the Dead Sea seem to bring pollution particles from the populated areas at the top of the Judean hills (e.g. Jerusalem and its surroundings). Because of the low inversion at night near the Dead Sea surface, these particles must remain close to the surface. As the sun rises, these low-lying particles create the lower haze layer observed in the morning hours. As the day goes on, the local heating of the lake develops small-scale convection causing the particles to rise to higher levels and the haze to extend from 400 to 600 m above the Dead Sea. The wind due to the Mediterranean Sea breeze reaches the Dead Sea valley in the afternoon, becoming northerly due to the topography (aligned north to south).

Summary

Although this study is still in progress, it already provided a reasonable explanation about the sources of the particles and their composition. The plan is to use the measured composition of the particles to model the growth of the dry aerosols to haze size droplets. These results will then be used to calculate the effects of the haze on the transmission of solar radiation and to compare them with observations.

Acknowledgments: This research was supported by a BSF grant # 96-00044/2

References

Alpert P., Shafir H. and Issahary D. 1997: Recent changes in the climate at the Dead Sea- A preliminary study. *Climate Change* **37** 513-537.

Bitan A., 1974: The wind regime in the north-west section of the Dead-Sea. *Arch. Met. Geophys. Biokl. Ser.* B **22** 313-335.

Bitan A., 1977: The influence of the special shape of the Dead Sea and its environment on the local wind system. *Arch. Met. Geophys. Biokl. Ser.* B **24** 283-301.

Levin Z. and E. Ganor, 1984: Measurements of aerosol size spectra and chemical composition in the Dead-Sea rift valley. Atmospheric aerosols and nucleation in Lecture note in physics 309, Spring-Verlag p 229-232.

Mamane Y. and Pureschel R.F., 1980: A method for the detection of individual nitrate particles. Atmospheric Envir. **14** 629-639.

Pardess D., Levin Z. and Ganor E., 1992: A new method for measuring the mass of sulfur in single aerosol particle. *Atmos. Environ.* **26A** 675-580.

Pielke R.A., W.R. Cotton, R.L. Walko, C.J. Tremback, W.A. Lyons, L.D. Grasso, M.E., Nicholls, M.D. Moran, D.A. Wesley, T.J. Lee and J.H. Copeland, 1992: A comprehensive meteorological modeling system -RAMS. *Meteorol. Atmos. Phys.* **49** 69-91.

Stanhill G. 1987: The radiation climate of the Dead-Sea. *J. of Climatol.* 7 247-265.

Stanhill G., 1994: Change in the rate of evaporation from the Dead-Sea.*Int. J. of Climatol.* **14** 465-471.

Uliasz M. 1993: The atmospheric mesoscale dispersion modeling system (MDMS), J. Appl. Meteor. 32, 139-149.

LARGE-EDDY SIMULATIONS OF ENTRAINMENT OF CLOUD CONDENSATION NUCLEI INTO THE ARCTIC BOUNDARY LAYER: 18 MAY 1998 FIRE/SHEBA CASE STUDY

Hongli Jiang[1], Graham Feingold[2], William R. Cotton[1], and Peter G. Duynkerke[3]

[1]Department of Atmospheric Science, Colorado State University Fort Collins, Colorado

[2]Cooperative Institute for Research in the Atmosphere
Colorado State University/NOAA, Environmental Technology Laboratory Boulder, Colorado

[3]Institute for Marine and Atmospheric Research Utrecht (IMAU)
Utrecht University, Utrecht, The Netherlands

April 6, 2000

1 INTRODUCTION

During the SHEBA/FIRE spring IOP (May 18, 1998) a high concentration of cloud nuclei in the air above the cloud was observed to over-lie a fairly clean boundary layer.

To understand how the microphysical and dynamical structure and radiation properties of Arctic stratus are modified by the entrainment of "polluted" air at cloud top in the arctic environment, we have performed a number of numerical simulations in a three-dimensional/LES framework with liquid-phase, bin-resolving microphysics (Feingold *et al.*, 1996). The key issue to be addressed is how long it takes for differences in cloud dynamics and microphysics to develop in response to variations in CCN concentrations due to entrainment, and how this process affects the Arctic cloud evolution.

2 MODEL DESCRIPTION

The Regional Atmospheric Modeling System (RAMS) is set up as a non-hydrostatic LES model combined with an explicit microphysics model. The explicit bin-resolving microphysics model is an accurate moment-conserving scheme, described in detail in Tzivion *et al.* (1989). The predicted variables include the three velocity components (u, v, w), the Exner function (π), the ice-liquid water potential temperature (θ_{il}), and total water mixing ratio r_t on a vertically stretched Arakawa C-grid (Walko *et al.*, 1995). A two-stream radiative transfer model that is interactive with the detailed bin-model hydrometeor size-spectra is utilized for this study (Harrington *et al.*, 1999).

[1]Corresponding author address: Hongli Jiang, Department of Atmospheric Science,Colorado State University, Ft. Collins, CO 80523,
e-mail: jiang@atmos.colostate.edu

3 EXPERIMENT DESIGN

In the control run, the initial CCN concentration is set to 30 cm $^{-3}$ (hereafter referred to as N30). In the sensitivity run, the initial CCN profile is derived from the actual CCN data collected on May 18, 1998 during FIRE-III by J. Hudson (hereafter referred to as N250). The CCN sounding exhibited concentrations ranging from 30 cm^{-3} below cloud base to a peak of 250 cm^{-3} at the inversion, lowering to 160 cm^{-3} at 700 m. A 5-h long simulation is performed for both runs.

The 3-D simulation has a domain of 45×45×55 grid points with a 50 m grid spacing in the horizontal and 25 m grid spacing in the vertical. The time step is 2s.

The lateral boundary conditions are cyclic. The boundary condition at the model top corresponds to a rigid lid, with a Rayleigh friction absorbing layer. The bottom boundary is specified to be consistent with surface conditions observed during FIRE/SHEBA, with a specified surface temperature of 266 K.

4 SIMULATION RESULTS

Figure 1 shows selected time-sequences from both runs. The local height of the inversion is determined by linearly interpolating grid values of total water mixing ratio r_t to 1.8 g kg^{-1}, which gives the corresponding interpolated inversion height in a column. The inversion height, z_i, (Figure 1a) is then defined as the horizontal average of these inversion height values. z_i shows a steady increase with time for both runs except that z_i is higher in the N250 run, suggesting stronger mixing at the inversion. Liquid water path, LWP (Figure 1b) is very similar for much of the simulation in both runs except for the last hour when LWP is about 10% higher in the N250 run. The reduction in LWP for N30 is associated with the increase in the surface drizzle flux (Figure 1c). Note that this reduction in LWP occurs despite the fact that the drizzle flux is approximately constant (Figure 1c), so that the response appears to be due to the integrated amount of drizzle rather than the increase in the drizzle rate (see also Feingold *et al.*, 1999).

Figure 2 shows the layer averages of CCN concentration (N_{ccn}) and drop concentration (N_d) at different simulation times for the N250 run, and N_d at 5 h for the N30 run. N_{ccn} is quickly doubled from the initial value in the cloud layer, while it stays low below cloud at 2 h. Note that the maximum N_{ccn} in the cloud layer never exceeds 60 cm^{-3} over the last 3 hrs of the simulation; instead higher values brought in by entrainment and turbulent mixing at the cloud top are continuously mixed throughout the entire boundary layer. Consequently, the CCN concentration is fairly well-mixed throughout the boundary layer by the end of simulation. Note that the constant N_{ccn} value of 30 cm^{-3} used for the N30 run is drawn for reference (solid vertical line). The maximum N_d is on the order of 55 – 60 cm^{-3} for the N250 run, while N_d is about 30 cm^{-3} for the N30 run. It can be seen that cloud top grows with time, in agreement with Figure 1a.

Snapshots of the layer-averaged effective radius r_e, drizzle rate, liquid water content LWC, and vertical velocity variance $< w'w' >$ at 5 h for both runs are shown in Figure 3.

The layer averaged effective radius r_e, defined as the ratio between the third and second moments of the drop distribution (Figure 3a), provides evidence that N250 produces smaller cloud drops than N30. With less drops competing for the available water vapor in the N30 run, drops grow to sizes considerably larger and fall to the subcloud layer, where r_e is significantly higher for N30 than for N250. Note that the values of r_e become progressively less meaningful as the moments tend to zero at heights below 50–100 m.

In the N250 run the drizzle rate (Figure 3b) has a maximum of 2.2 mm day^{-1}, mainly in the cloud layer with almost no drizzle reaching the surface. In the N30 run, however, the maximum is barely two thirds of that of N250 in the cloud layer, but approximately 16% of the maximum reaches the ground. The lower drizzle rates within the cloud are a result of depletion of cloud water through more drizzle reaching ground.

The differences between the LWC (Figure 3c) for N30 and N250 are characteristic of the differences between drizzling and non-drizzling clouds (e.g., Stevens *et al.*, 1998); In N250, LWC is about 21% higher in the layer near cloud top and lower near cloud base and in the subcloud layer compared with the N30 run. Drizzle effectively redistributes the liquid water downward with some losses occurring in N30 through sedimentation to the surface.

The dynamical response is significant at this time of the simulation, as expressed by higher $< w'w' >$ for the N250 run (Figure 3d).

The impact of the entrainment of CCN into the cloud on the cloud optical properties is evaluated in Figure 4. Optical depth (in the visible) is defined as

$$\tau \approx \int_{z_b}^{z_t} \int_0^{\infty} 2\pi r^2 n(r,z) dr dz, \qquad (1)$$

where $n(r)$ defines the drop spectrum with respect to radius r, z_b is cloud base, z_t is cloud top, and an asymptotic value of 2 has been assumed for the extinction efficiency (e.g., Platnick and Twomey, 1994). Albedo is calculated using the simple relationship between cloud albedo A and optical depth given by Bohren (1987).

$$A \approx \frac{(1-g)\tau}{2+(1-g)\tau} \qquad (2)$$

where g is the scattering asymmetry factor (Twomey, 1991). At small τ, A is approximately linearly dependent on τ and therefore A is positively correlated with τ. Both A (Figure 4a) and τ (Figure 4b) increase steadily from the beginning of the simulation. According to Twomey (1974), τ scales with $N_d^{1/3}$ for clouds of similar r_l. Figure 2b indicates that N_d(N250)/N_d(N30) $\approx$ 60/30 = 2, so that their optical depth ratio should scale by $2^{1/3}$=1.26. Figure 4b indicates that at 200 min, before N30 LWP has begun to lose significant water τ(N250)/τ(N30) $\approx$ 9.5/7.5=1.27 so that there is excellent agreement

with this simple scaling law when the runs have similar LWP. Notice that the differences between the two runs grows larger with time. In the case of N250, A is roughly 7% higher at 120 min and is about 12% higher at 300 min of simulation, while τ is 14% higher at 120 min and 33% higher at 300 min. This is related to the depletion in liquid water in N30 which reduces both τ and A.

The entrainment rate w_e is computed as the average $dz_i/dt - w_{sub}$ over the last 3 h of the simulation period. The imposed w_{sub} is about -0.25 cm s^{-1} at the inversion. The estimation of w_e is also provided with observational data based on the jump model (De Roode and Duynkerke, 1997), $w_e = \overline{(w'r_t')_{z_i}}/\Delta r_t$, where Δr_t is the jump of the mean total water across the cloud top and $\overline{(w'r_t')_{z_i}}$ is the total water entrainment flux right beneath the inversion height. As shown in Table 1, the model results (3 h average) are slightly larger, but compare reasonably well with the observation.

5 SUMMARY

The simulation with the observed CCN profile (high CCN) shows that the increase in CCN concentration resulting from entrainment results in a higher droplet concentration, smaller drop sizes, more liquid water retained in the cloud layer, and less drizzle reaching the surface.

The cloud optical properties respond to the change in CCN concentration from the beginning of the simulations with higher values of cloud albedo A and cloud optical depth τ.

The differences between the high CCN run and the low CCN run show characteristics of the differences between drizzling and non-drizzling clouds (e.g. Steven *et al.*, 1998), namely that drizzle redistributes heat and vapor in the vertical in a manner that stabilizes the boundary layer.

This work underscores the fact that knowledge of boundary layer deepening is critical to prediction of cloud optical properties. This is true both from the thermodynamic point of view where the properties of the entrained air affect bulk cloud features such as LWP; as well as from the microscale point of view where aerosol gradients across the top of the boundary layer can alter microphysical processes, and in turn, cloud optical properties. This issue is even more critical for mixed phase clouds given the sensitivity of such clouds to even small concentrations (order 1 l^{-1}) of ice forming nuclei (Jiang *et al.*, 1999).

6 ACKNOWLEDGMENTS

This research was supported by grants from the NASA/FIRE III (NAG-1-2045). G. Feingold was partially supported by a NOAA Office of Global Programs Grant. P.G. Duynkerke was supported for the participation in the SHEBA experiment by the Netherlands Geosciences Foundation (GOA) with financial aid (GRANT 750.295.03) from the Netherlands Organization for Scientific Research (NWO).

7 REFERENCE

Bohren, C.F., 1987: Multiple scattering of light and some of its observable consequences. *Am. J. Phys.*, **55**, 524-533.

De Roode, S.R. and P.G. Duynkerke, 1997: Observed Lagrangian transition of stratocumulus into cumulus during ASTEX: mean state and turbulence structure. *J. Atmos. Sci.*, **54**, 2157-2173.

Feingold, G., B. Stevens, W. R. Cotton, and A. S. Frisch, 1996: On the relationship between drop in-cloud residence time and drizzle production in stratocumulus clouds. *J. Atmos. Sci.*, **53**, 1108-1122.

Feingold, G., W.R. Cotton, S. M. Kreidenweis, and J. T. Davis, 1999: Impact of giant cloud condensation nuclei on drizzle formation in marine stratocumulus: Implications for cloud radiative properties. *J. Atmos. Sci.*, **56**, 4100-4117.

Harrington, J.Y., T. Reisin, W.R. Cotton, and S. M. Kreidenweis, 1999: Cloud Resolving Simulations of Arctic Stratus. Part II: Transition-Season Clouds. *Atmos. Res.*, **51**, 45-75.

Jiang, H., W.R. Cotton, J.O. Pinto, J.A. Curry, and M.J. Weissbluth, Cloud Resolving Simulations of Mixed-Phase Arctic Stratus Observed During BASE: Sensitivity to Concentration of Ice Crystals and Large-Scale Heat and Moisture Advection. *J. Atmos. Sci.*, in press, 2000.

Platnick, S., and S. Twomey, 1994: Determining the susceptibility of cloud albedo to changes in droplet concentration with the advance very high resolution radiometer. *J. Appl. Meteorol.*, **33**, 334-347.

Stevens, B., W.R. Cotton, G. Feingold, and C-H Moeng, 1998: Large-eddy simulations of

strongly precipitating, shallow, stratocumulus-topped boundary layers. *J. Atmos. Sci.*, **55**, 3616-3638.

Tzivion, S., G. Feingold, and Z. Levin, 1989: The evolution of raindrop spectra. Part II: Collisional collection/breakup and evaporation in a rain shaft. *J. Atmos. Sci.*, **46**, 3312-3327.

Twomey, S., 1974: Pollution and planetary albedo. *Atmos. Environ.*, **8**, 1251-1265.

Twomey, S., 1991: Aerosols, clouds and radiation. *Atmos. Environ.*, **Part A, 25**, 2435-2442.

Walko, R.L., W.R. Cotton, M.P. Meyers, J.Y. Harrington, 1995: New RAMS cloud microphysics parameterization Part I: the single-moment scheme. *Atmos. Res.*, **38**, 29-62.

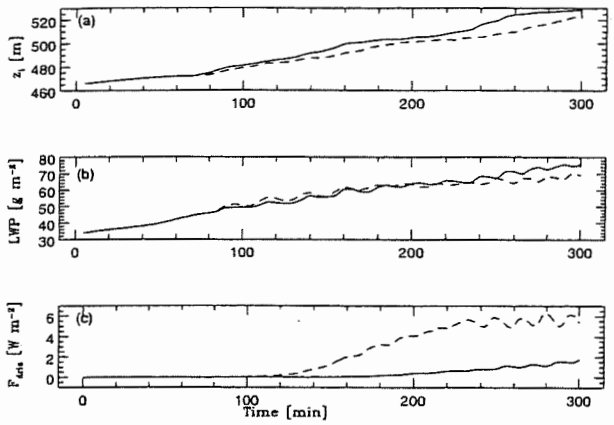

Figure 1: The temporal evolution of (a) inversion height, (b)LWP, (c)surface drizzle flux for both runs. The solid line denotes the N250 run and the dashed line denotes the N30 run.

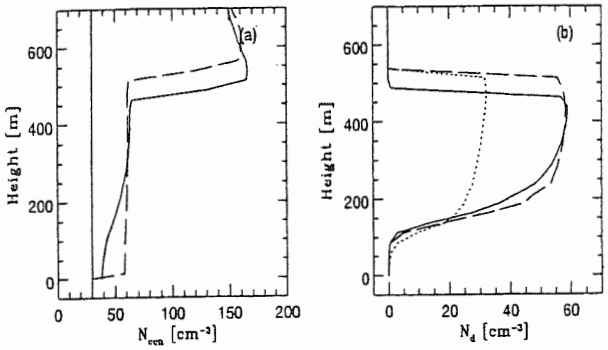

Figure 2: Layer-averaged profiles of (a) potential number of CCN that could be activated N_{ccn}, (b) drop number concentration N_d at 2 and 5 h of simulation for N250 . The solid line denotes values at 2 h, and the long-dashed line denotes values at 5 h. The dotted line denotes N_d at 5 h for N30.

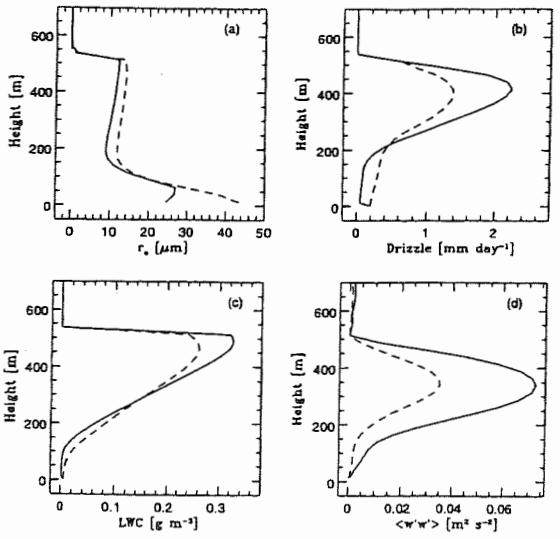

Figure 3: Layer-averaged vertical profiles of (a) effective radius r_e, (b) drizzle rate, (c) LWC, (d) vertical velocity variance at 5 h for both N250 and N30. Line types are the same as indicated in Fig. 1.

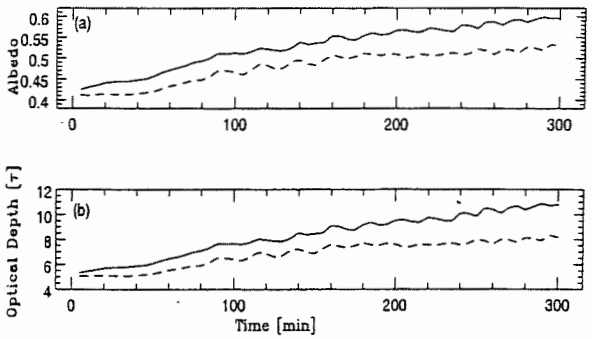

Figure 4: Time evolution of (a) cloud albedo, (b) cloud optical depth τ with line types as indicated in Fig. 1.

Table 1. Entrainment rates for model runs and observation.

	N30	N250	OBS
dz_i/dt $[cms^{-1}]$	0.364	0.388	
w_{sub} $[cms^{-1}]$	-0.25	-0.25	
$w_e = dz_i/dt - w_{sub}$ $[cms^{-1}]$	0.614	0.638	
$w_e = -\overline{(w'r_t')}_{z_i}/\Delta r_t$	Δr_t=-0.35 $[gkg^{-1}]$	$\overline{(w'r_t')}_{z_i}$=2. * 10^{-3} $[gkg^{-1}ms^{-1}]$	0.57 $[cms^{-1}]$

SIZE DEPENDENT COMPOSITION OF AEROSOL PARTICLES AND CCN SPECTRUM

M. Mircea*, M.C. Facchini, S. Decesari and S. Fuzzi

Istituto di Scienze dell'Atmosfera e dell'Oceano – CNR, I-40129, Bologna, Italy

1. INTRODUCTION

The microstructure of cloud controls the formation of precipitation and the cloud albedo. The variability of cloud microstructure in the same thermodynamic conditions can be explained by systematic differences in the cloud condensation nuclei (CCN) number concentrations (Squires, 1958a,b).

The CCN represent the fraction of aerosol upon which cloud droplets form. CCN are also called activated aerosol particles and the activation depends strongly on their physical and chemical properties (Hänel, 1981). Taking into account the gradual dissolution of the organic aerosol components (Shulman et al., 1992), dissolution of gases (Kulmala et al., 1997) and lowering of surface tension due to organic surface active compounds (Facchini et al., 1999) in the activation process, substantial variations in CCN number concentration were obtained.

The above studies have all considered bulk aerosol chemical composition. In this paper we use experimental size-segregated chemical composition of the aerosol particles to study its effect on CCN number concentrations.

The CCN number concentration represents the number of activated aerosol particles, those aerosol particle having a critical supersaturation lower than the air mass supersaturation. The critical supersaturation of an aerosol particle is computed using a modified Köhler theory. Numerical computations have been performed in order to study the influence of the size dependent chemical composition of aerosol particles and of associated changes in the surface tension of cloud droplets.

*Permanent affiliation: National Institute of Meteorology and Hydrology, Bucharest, Romania

Corresponding author address: M. Mircea, ISAO-CNR,Via Gobetti 101, Bologna, Itlay;
E-Mail: m.mircea@isao.bo.cnr.it.

2. CHEMICAL COMPOSITION OF AEROSOL PARTICLES

An aerosol sampling program was carried out at a location within the city of Bologna, Italy, during winter, using a five-stage Berner cascade impactor.The impactor collects particles with ambient diameter in the following ranges: #1: 0.05-0.14 μm; #2: 0.14-0.42 μm; #3: 0.42-1.2 μm; #4: 1.2-3.5 μm; #5: 3.5-10 μm). The particles were collected on tedlar foils, which were then extracted in water and analysed for organic and inorganic species.

In Fig. 1 the average percent chemical composition of the inorganic species and of some main classes of organic compounds is shown. As the particle size increases, the inorganic fraction increases from 48 to 60% of the aerosol mass, whereas the water soluble organic carbon (WSOC) concentration decreases.

WSOC concentration is modelled as a mixture of mono and dicarboxylic acids of low molecular mass (MA) and polyacidic compounds of higher molecular mass (MMC) (Decesari et al., 2000). INS represent the insoluble part of aerosol.

3. CCN SUPERSATURATION SPECTRA — THEORY

The CCN number concentration depends on both size and composition of the particles for a given aerosol population and on ambient supersaturation. The cumulative number concentration of CCN at a given supersaturation, s, and chemical composition is calculated as:

$$CCN(s) = \int_{r_s}^{\infty} n(r)dr \qquad (1)$$

where $n(r)$ is the number distribution of the aerosol population and r_S is the activation radius for the supersaturation s. The activation radius was determined according to the Köhler theory.

The Köhler theory (1936) describes the equilibrium growth of aerosol particles by water vapour condensation as a function of their size, chemical composition and physical and chemical properties of the cloud droplet solutions.

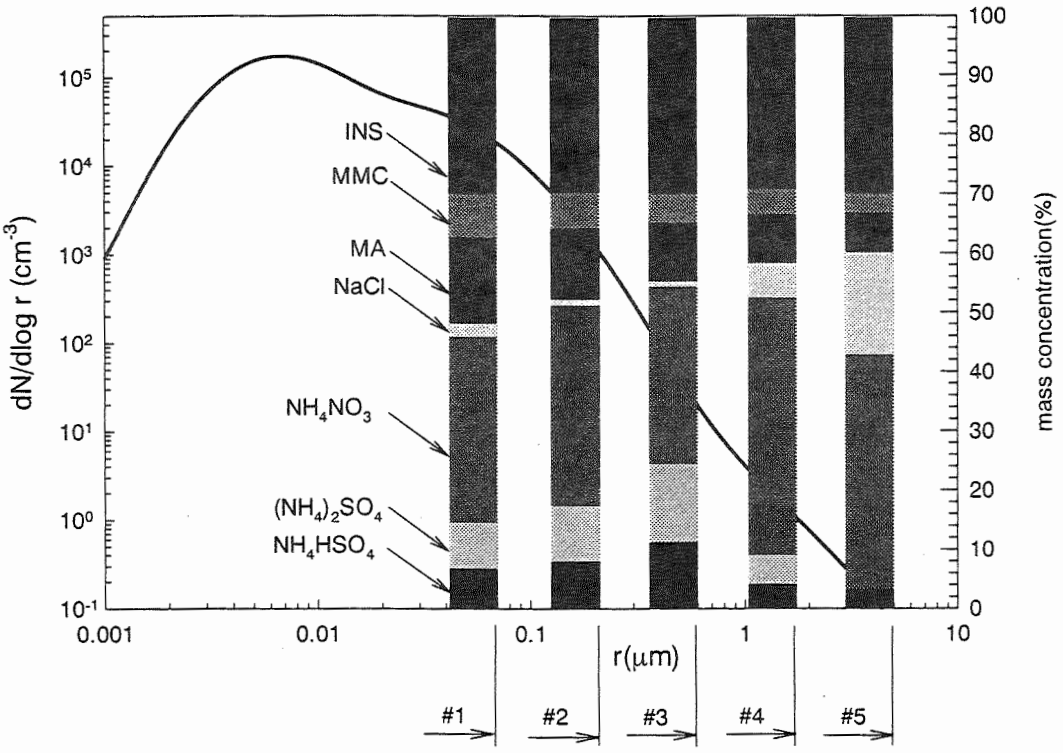

Figure 1. Number size distribution (solid line) for urban aerosol after Jaenicke (1993) and size-segregated chemical composition (stack bars) derived from impactor measurements. The size ranges of the impactor stages are marked under the x-axis.

The equation is composed of two terms: the *Kelvin term*, which accounts for the increase of the water vapor pressure due to the curvature of the droplet surface, and the *Raoult term*, which considers the lowering of the equilibrium vapor pressure with increasing solute concentration.

In order to evaluate the influence of droplet solution surface tension and of organic compounds on the growth of aerosol particles, we used a modified form of the Köhler equation:

$$s \cong 1 + \frac{2\sigma_s M_w}{RT\rho_w r} - \frac{3M_w \phi_s}{4\pi\rho_s (r^3 - r_N^3)} \left[\sum_{i=1}^{n} \frac{\nu_i m_i}{M_i} + \sum_{j=1}^{n} \frac{\nu_j m_j}{M_j} \right] \quad (2)$$

where s is the air saturation, M_w and ρ_w are molecular mass and density of water, σ_s the droplet solution surface tension, ρ_s the droplet solution density, R the gas constant, T temperature, r the droplet radius, r_N the radius of the insoluble aerosol residue and ϕ_s is the osmotic coefficient of the aqueous solution; ν_i, m_i, M_i and ν_j, m_j, M_j are the number of dissociated ions, soluble mass and molecular mass, respectively, of inorganic and organic components of aerosol particles. The above equation contains a modified *Raoult term* similar to that of Shulman et al. (1996), but also taking into account an insoluble aerosol core. The lack of information about the activity of such complex solutions and the fact that vapour pressure is proportionally depressed with the amount of dissolved material suggest that the effects of the organic and inorganic species can be considered additive.

The activation radius represents the numerical solution of the equation:

$$\frac{ds}{dr} = 0 \quad (3)$$

The number distribution of the aerosol population is considered as the sum of three superimposed log-normal functions (Jaenicke, 1993):

$$n(\log r) = \sum_{i=1}^{n} \frac{N_i}{\sqrt{2\pi}\log\sigma_i} \exp\left(-\frac{(\log r - \log \bar{r})^2}{2\log^2 \sigma_i} \right) \quad (4)$$

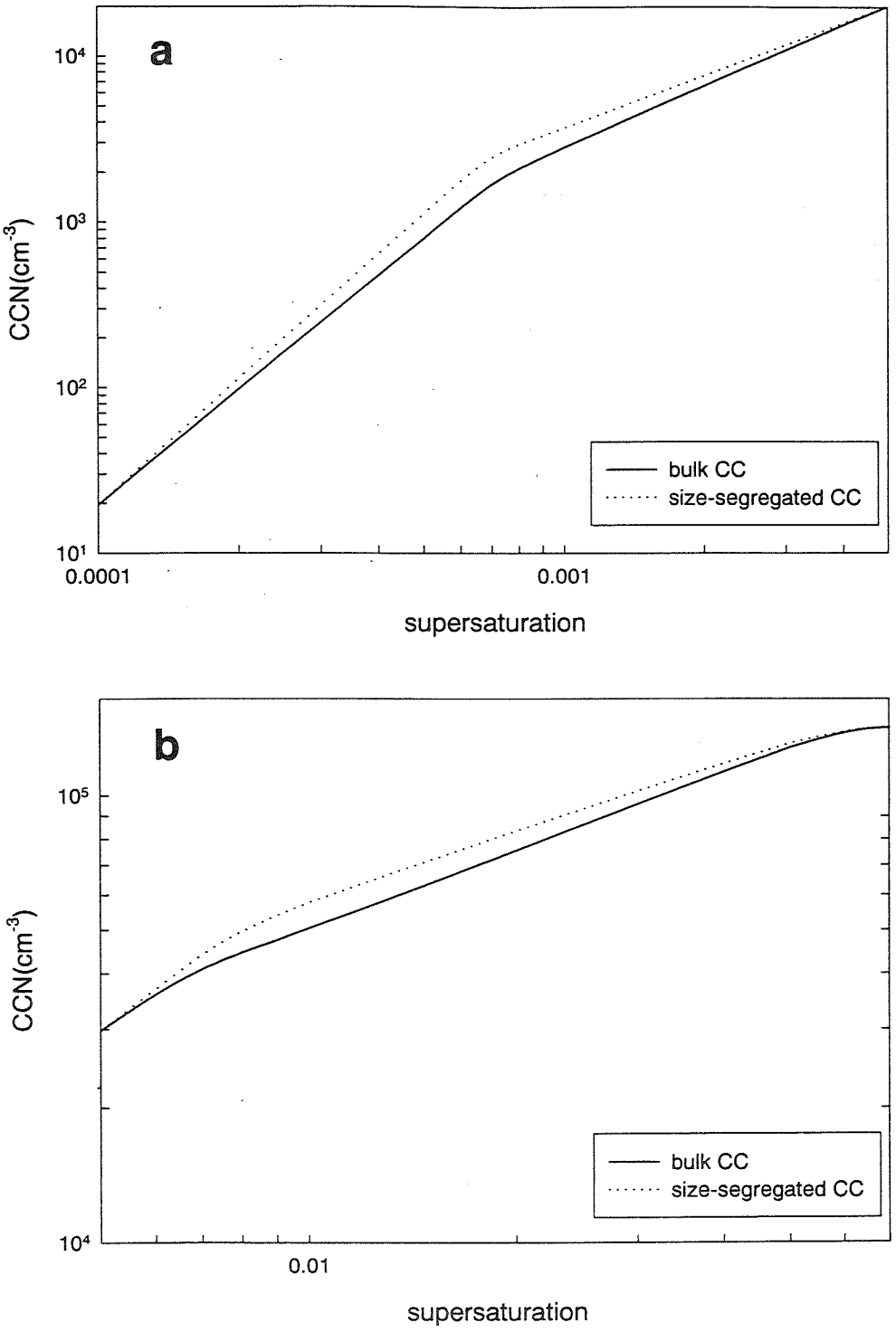

Figure 2. The CCN number concentration as a function of ambient supersaturation. Bulk chemical composition is drawn by solid line and size-segregated chemical composition by dotted line. Fig 2a represents the case of constant surface tension and Fig. 2b the case of variable surface tension.

where r is dry aerosol diameter, N_i is the aerosol particle number concentration, $\bar{r}_i$ is the geometric mean diameter and σ_i is the geometric standard deviation of the i^{th} log-normal mode.

The CCN number concentration is computed using the equations 1 ÷ 4.

4. RESULTS AND DISCUSSION

The number size distribution for urban aerosol (Jaenicke, 1993) and the size-segregated chemical composition are shown in Fig. 1. We have also considered the measured bulk chemical composition as: 10.4% NH_4HSO_4, 12.2% $(NH_4)_2SO_4$, 30.7% NH_4NO_3, 0.8% NaCl, 10.6% MA and 5.4% MMC.

The surface tension decrease due to the presence of WSOC was also taken into account as in Facchini et al. (1999).

In Fig. 2a and b the CCN supersaturation spectra are shown for two cases: constant surface tension (Fig. 2a) and variable surface tension (Fig. 2b).

All simulations were made using 74 bins for representing the aerosol spectra.

It can be seen that, in both figures the size-segregated chemical composition of the aerosol results in higher CCN number concentration for the same air mass supersaturation, as compared to the case of bulk chemical compostion.

An increase in CCN number concentrations up to 40% can be observed due to the size-segregated chemical composition when the surface tension is considered constant, but only up to 15% for variable surface tension. The increase in CCN occurs in different supersaturation ranges; both are comprised in the range of critical supersaturation of submicron aerosol particles.

The differences between the CCN supersaturation spectra computed here are of the same order of magnitude as those between measured and computed CCN supersaturation spectra in Fitzgerald (1973).

Further, the shape of the curves for the whole supersaturation range does not obey the power law function, usually used in cloud models, as also shown by Von der Emde and Wacker (1993).

5. CONCLUSIONS

Considering the size-segregated aerosol chemical composition in a detailed microphysical formulation of the nucleation process, significant changes in CCN number concentration were obtained with respect to the case of the bulk aerosol chemical composition. The CCN number concentration increases also if the surface tension is considered to vary with the WSOC concentration.

The differences between the computed CCN supersaturation spectra show that an accurate description for the chemical composition of submicron aerosol particles can explain the differences evidenced in the past between measured and computed CCN supersaturation spectra.

6. ACKNOWLEDGEMENTS

The present work was financed by the European Commission (EUROZEP Project ENV4-CT98-0785). Mihaela Mircea was supported by the "ICTP Programme for Training and Research in Italian Laboratories", Trieste, Italy.

7. REFERENCES

Decesari, S., M.C. Facchini, S. Fuzzi and E. Tagliavini, 2000: Characterization of water soluble organic compounds in atmospheric aerosol: a new approach. *J. Geophys. Res.*, **105**, 1481-1489.

Facchini, M.C., M. Mircea, S. Fuzzi and R. J. Charlson, 1999: Cloud albedo enhancement by surface-active organic solutes in growing droplets, *Nature*, **401**, 257-259.

Fitzgerald, J. W., 1973: Dependence of the supersaturation spectrum of CCN on aerosol size distribution and composition, *J. Atmos. Sci.*, **30**, 628-634.

Hänel, G., 1981: Influences of physical and chemical properties of atmospheric particles on the activation process in fogs and clouds, *Contr. Atmos. Phys.*, **54**, 159-172.

Köhler, H., 1936: The nucleus in the growth of hygroscopic droplets. *Trans. Faraday Soc.* **32**, 1152-1161.

Kulmala, M., A.. Laaksonen and R.J. Charlson, 1997: Clouds without supersaturation. *Nature*, **388**, 336-337.

Shulman, M.L., M.C. Jacobson, R.J. Charlson, R.E. Synovec and T.E. Young, 1996: Dissolution behavior and surface tension effects of organic compounds in nucleating cloud droplets. *Geophys. Res. Letters*, **23**, 277-280.

Squires, P., 1958a: The microstructure and colloidal stability of warm clouds. Part I: The relation between structure and stability, *Tellus*, 10, 256-261.

Squires, P., 1958b: The microstructure and colloidal stability of warm clouds. Part II: The causes of the variations in microstructure, *Tellus*, 10, 267-271.

Von der Emde, K. and U. Wacker, 1993: Comments on the relationship between aerosol spectra equilibrium drop size spectra and CCN spectra, *Contr. Atmos. Phys.*, **66**, 157-162.

Scavenging of aerosol by growing ice crystals obtained with control of electrical conditions

G.Santachiara[1], F.Prodi[1,2] and N.Buzzoni[1]

[1]Institute ISAO-CNR, Clouds and Precipitations Group, Bologna, Italy
[2]Department of Physics, University of Ferrara, Italy

1. INTRODUCTION

Atmospheric clouds and precipitation play a fundamental role in the removal of atmospheric aerosol via the following mechanisms: nucleation, inertial impaction and interception, diffusiophoresis, thermophoresis, convective Brownian diffusion, and electric effects caused by electrostatic charges on drops or crystals and aerosol particles, and by the presence of external electric fields. Field studies suggest that not only cloud and rain drops, but also snow crystals contribute to the removal of atmospheric aerosol particles (AP). Several field and laboratory studies have been carried out to determine the efficiency with which AP are scavenged by snow crystals below clouds (Graedel and Franey, 1975; Magono et al., 1974).

Murakami et al.(1981), by measuring not only the number and size of AP on snow crystals, but also the concentration and size distribution of aerosol in the air, obtained lower collection efficiency than those measured by Magono et al. (1974), and Graedel and Franey (1975). The collection efficiency increased with the increasing aerosol size from 0.2 to 5 μm, and ranged from $1x10^{-3}$ to $6x10^{-2}$.

As regards laboratory experiments, scavenging by snow flakes or by individual snow crystals have been studied. Aerosol scavenging by smaller ice crystals (35-150 μm diameter), falling through air at a saturation of about 70% with respect to ice, was investigated by Bell and Saunders (1995). The scavenging efficiency for 4 to 6 μm aerosol particles was in the range 0.9-0.2. Only relatively few investigations of aerosol scavenging by ice crystals growing in the presence of supercooled droplets, which is related to in-cloud scavenging, have been reported (Prodi and Oraltay, 1991; Song and Lamb,1994).

Theoretical studies of the ice crystal scavenging phenomenon have been carried out. Satisfactory agreement between the available experimental data and theoretical results has not been reached for a number of reasons, e.g. the difference in crystal size and shape between experimental and theoretical studies, the latter considering only small ice crystals with highly simplified shapes. To determine the relative importance of the main in-cloud scavenging mechanisms (Brownian diffusion and phoretic forces), Prodi (1976) performed experiments with growing ice crystals in the presence of NaCl and carnauba wax aerosol. NaCl aerosol particles were scavenged by growing crystals , but for carnauba wax (c.w) the results were not conclusive. In addition the problem of a possible electric charge on crystals and aerosol were not considered.

In order to estimate the rates of submicron aerosol scavenging by ice crystals in supercooled droplets as a function of particle diameter, crystal size, inorganic salts in the crystal and electricity, we performed laboratory experiments with Milli-Q water and an aqueous solution of inorganic salts.

Corresponding authors address: F.Prodi, Institute ISAO-CNR, Bologna,Italy.
E-Mail: f.prodi@isao.bo.cnr.it

2. EXPERIMENTAL

The experimental facility consists of a plexiglass cylinder, placed in a cold room. It was operated at atmospheric pressure and constant temperature (T≅-14°C). Liquid water clouds of Milli-Q water or 10^{-4} N solutions of ammonium sulphate were produced using an ultrasonic nebulizer. The liquid water content (LWC) of the cloud in the column was about 2 g m^{-3}. Droplets and aerosol were injected in the upper part of the column. The nucleation of the ice crystals was initiated by adiabatic expansion of moist compressed air using an air pistol , or by a brief insertion in the column of a metal rod previously cooled in liquid nitrogen. Crystals grew, in the absence of riming, at the expense of water vapour from evaporating supercooled droplets and fell to the bottom of the column. The hexagonal plate ice crystals were collected on microscope slides, previously covered with a thin layer of 2% formvar solution in chloroform and examined at the SEM. The temperature and relative humidity in the aerosol chamber were measured during the test by a dew point hygrometer. The air was found to be saturated with respect to the water.

2.1 Aerosol generation

The c.w. particles used in the experiments were produced using a condensation aerosol generator for solid particles implemented by V. Prodi (1972). The aerosol can be charged, since nuclei for condensation of c.w. are produced by the atomization of a water solution of NaCl and the charge is at least partially

preserved while particles grow. To obtain only uncharged aerosol, we used a parallel plate spectrometer. Charged aerosol is deposited on the plates, leaving the uncharged aerosol to reach the outlet.

2.2 Ice crystal charge measurements

The electric nature of the ice crystal plates was investigated using an induction ring, connected to an oscilloscope. It is capable of sensing the passage of charged drops or ice crystals in excess of 1.6×10^{-13} C, i.e. 1.6×10^{2} fC.

To estimate the sign of the charge on ice crystals we used an electric detection device , which consists of six 0.2 mm diameter wires, mounted horizontally in parallel 6 mm apart. The wires were charged one after the other positively and negatively. The voltages applied to the wires were +/- 310 V.

2.3 Crystal aggregation

Three parameters were evaluated to test the existence of an electric multipole in growing ice crystal. The firsts R_1, is the percentage of T-shaped junctions (crystals joined with the growing edge of one attached to the center of the plane on the other, and the c-axes normal to each other) with respect to single crystals. This parameter should highlight the influence of multipoles on aggregation. The second quantity , R_2, is the ratio of T-shaped junctions to the total junctions observed. Finally, R_3 is the ratio between aggregate number and single crystal number. Aggregate is defined as a cluster of 3 to 6 crystals.

2.4 Scavenging efficiency

The scavenging efficiency E(r) of aerosol particles on an individual snow crystal is determined by :
$E(r) = n_s(r) / n_0(r)$, where r : radius of AP; $n_s(r)$: number of AP of radius r collected by a snow crystal while falling through the chamber; $n_0(r)$ is the number of aerosol of radius r swept out by a crystal while falling. As in our experiments the crystals grow during the fall, we suppose that the crystal growth is linear , so that the volume swept out is a cone, with base radius equal to the final crystal radius. The concentration of aerosol in the scavenging experiments was in the range 2.8×10^{4}-5.0×10^{4} cm^{-3}.

3. RESULTS

3.1 Ice crystal charge detection

To evaluate if the ice crystals obtained in the chamber had a net charge or were uncharged, with or without an electric multipole, we made measurements with the induction ring, an electric detection device with wires, as well as by means of crystal aggregation.

Measurements with the induction ring did not reveal a net charge, either for crystals obtained from distilled water or from 10^{-4} N solution of ammonium sulphate. Thus, we can conclude from these measurements that crystals have either no charge, or a charge below the value of 1.6×10^{2} fC (the detection limit of our device).

Using the device with wires, we observed that the crystals obtained from solution are preferentially captured from positively charged wires, while those obtained from distilled water are preferentially not captured. In addition, replicas of ice crystals were examined at optical microscopy to evaluate crystal aggregation. Experiments involving 10^{-4} N concentrations of $(NH_4)_2 SO_4$ in supercooled cloud water gave similar values of parameters R_1 and R_2 (about 0.05 and 0.2, respectively), compared with those performed with Milli-Q water, while Finnegan and Pitter (1988) obtained different R_1 values for deionized and dilute solutions , i.e. 0.15 and 0.48, respectively. According to Smith-Johansen (1969), we assume that T agglomerates depend on hydrodynamic processes , and not electrical mechanisms. The R_3 parameter, i.e. the ratio between aggregate number and single crystal , is higher for dilute solutions (≅0.17) with respect to Milli-Q runs (≅0.09). These results and those obtained from runs with the wire device should confirm the existence of an electric multipole present in crystals obtained from ammonium sulphate solution, according to Finnegan and Pitter (1988).

3.2 Aerosol scavenging measurements

In Figs. 1 and 2 scavenging efficiencies are plotted as a function of the aerosol radius. The radius range is approximately from 0.1 to 0.5 μm for aerosol, and from 10 to 70 μm for crystal diameters. Each point represent at least 10 ice crystals. Scavenging efficiency E vs. aerosol radius is higher for crystals obtained from dilute solution of ammonium sulphate, with respect to those obtained from deionazed water, and presents a minimum at about 0.3 μm. As regards E vs. crystal diameter, we observe that E is higher for crystals

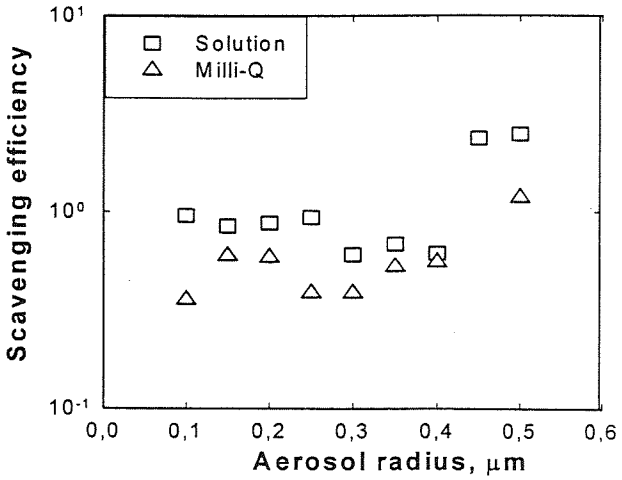

Fig.1. Scavenging efficiency as a function of not neutralized aerosol radius

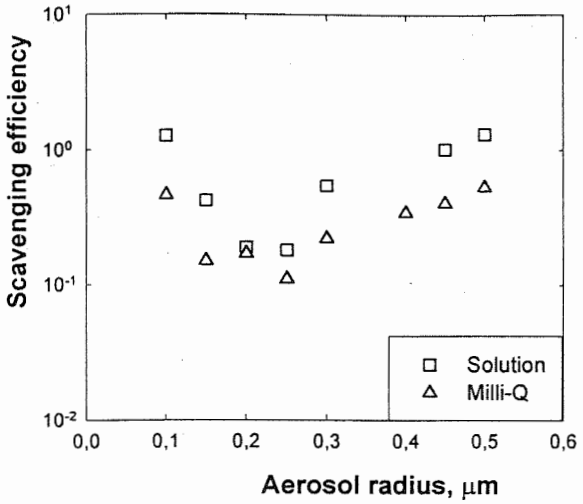

Fig.2. Scavenging efficiency as a function of neutralized aerosol radius

obtained from the dilute solution , and decreases with increasing crystal size. The same trend is observed for neutral aerosol (Figs.3 and 4). Runs with partially charged aerosol give higher efficiency than those with totally uncharged aerosol.

DISCUSSION

Comparison of our results with previous data is difficult because, as is commonly the case in field or laboratory studies, the considered ice crystals were usually greater than 1 mm, AP often had diameter > 0.5 μm and phoretic forces were not always considered.

Generally showing high scavenging efficiency, our results evidence the importance of the first stage of crystal growth in cloud scavenging, and are in better agreement with results of Magono et al. (1974), Bell and Saunders (1995), Graedel and Franey(1975), than with those of Murakami et al.(1981).

By estrapolating the data of Sauter and Wang (1989), who studied the scavenging of AP of mean radius 0.75 μm by natural snow crystals with small charges (10^{-4} esu or less), we can observe that they fall between our results obtained with ammonium sulphate solutions and distilled water (Fig.4).

In Fig.4 we show for comparison the scavenging efficiency measured by Song and Lamb (1994) for 86 μm diameter crystals.

In the range of aerosol and crystal diameters we considered, an important role is carried out by diffusio and thermophoretic forces, since Brownian and inertial forces are negligible.

Following Martin et al. (1980) , for the case of ice crystals growing or evaporating, the thermophoretic force on an aerosol particle dominates the diffusiophoretic force if r ≤2 μm. Therefore if air is saturated with respect to water, i.e. $(RH)_i$ >100%, the efficiency with which an ice crystal collects aerosol particles should be less than in ice saturated or ice subsaturated air.

Conversely, our results showing high efficiency scavenging during crystal growth, indicates that the net phoretic force arising from thermophoresis and diffusiophoresis increases scavenging. For example, by extrapolating our data until $D_{crystal}$=101μm, in the absence of salts and with uncharged aerosol with r=0.2 μm, we obtain E= $5x10^{-2}$, while Martin et al. (1980, Fig.12) gives about $1.3x10^{-3}$.

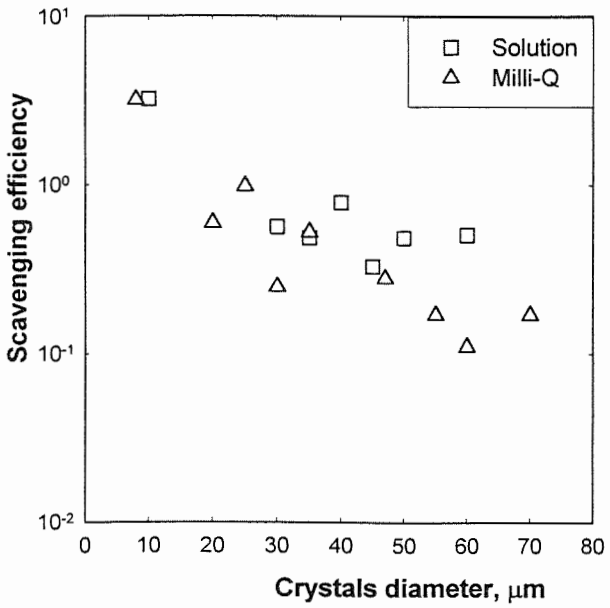

Fig.3. Scavenging efficiency for not neutralized aerosol as a function of crystal diameter

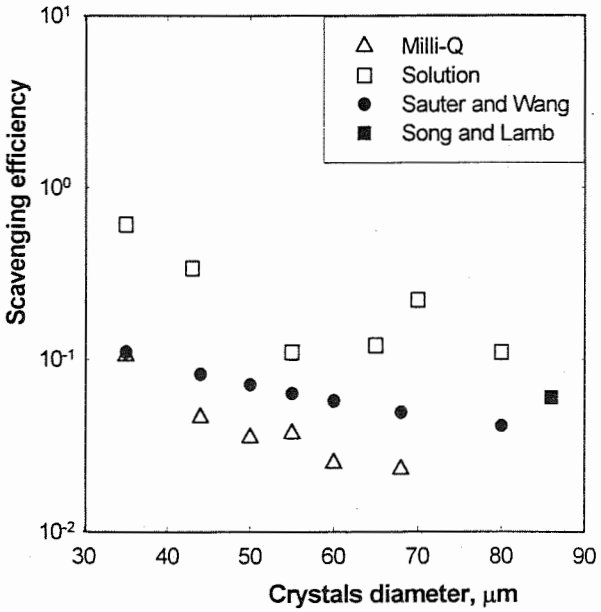

Fig.4. Scavenging efficiency of neutralized aerosol as a function of crystal diameter

It is important to note that the theoretical model considers a steady-state situation, i.e. a condition in which vapour and temperature gradient are constant. In reality, the growth of crystals in the presence of supercooled droplets is not a steady-state phenomenon. The coesistence of supercooled cloud droplets in the vicinity of the ice crystal makes the growth rate larger with respect to the theory of diffusional ice crystal growth, in which an ice crystal is placed in an infinite supersatured atmosphere.

Therefore, we agree with Vittori and Prodi (1967) that the dust-free space around supercooled cloud droplets approaching an ice crystal should increase the concentration of aerosol particles in the vicinity of the ice crystal, thereby increasing its capture efficiency. All aerosol particles which is in the space between the crystal and the droplet during the transient "flushes" of water vapour toward the crystal surface are expected to experience exceptionally strong diffusiophoretic (Stefan flow) forces toward the crystal and only weak thermophoretic forces away from it. This conclusion disagrees with Song and Lamb(1994), who affirm that supercooled cloud droplets do not enhance scavenging.

The higher scavenging efficiency of crystal grown from droplet of 10^{-4} N $(NH_4)_2 SO_4$, (as opposed to Milli-Q droplets) for both uncharged and partially charged aerosol, can be explained by supposing the development on an electric multipole during growth (Finnegan and Pitter,1988). The results obtained with the wire device, where the crystals are preferentially captured from positively charged wires, seem to confirm that, during growth, the ammonium ion tends to be retained in the ice while the sulphate ion mainly remains in the liquid-like layer on the crystal surface.

Zhang and Pitter (1991) presented a theoretical model which allows the computation of the efficiency with which aerosol particles are collected by simple ice crystals. Their results indicate that the presence of electric multipoles in ice crystals significantly affects the capture of aerosol particles, particularly in the aerosol range of $0.1 \leq r \leq 1.0$ μm, namely in the Greenfield Gap, and that the smaller the size of the ice crystal plates, the stronger the action of the electric multipole. Thus, aerosol scavenging efficiency by snow crystals depends on the chemical species present in the crystals, as well as the crystal growth status.

5. REFERENCES

Bell, D.A. and C.P.R. Saunders, 1995: An experimental study of aerosol scavenging by hexagonal plate ice crystals. *Atmos.Res.*, **38**, 9-19.

Finnegan, W.G. and R.L.Pitter, 1988: A postulate of electric multipoles in growing ice crystals: their role in the formation of ice crystal aggregates. *Atmos.Res.*, **22**, 235-250.

Graedel, T.E. and J.P.Franey, 1975: Field measurements of submicron aerosol washout by snow. *Geoph.Res.Letters*, **2**, 325-328.

Magono, C., T.Endoh, T.Harimaya and S.Kubota, 1974: A measurements of scavenging effect of falling snow crystals on the aerosol concentration. *J. Meteor.Soc.Japan*, **52**, 407-416.

Martin, J.J., P.K.Wang and H.R.Pruppacher, 1980: A theoretical determination of the efficiency with which aerosol particles are collected by simple crystal plates. *J.Atmos.Sci.*, **37**, 1628-1638.

Murakami, M., C.Hiramatsu and C.Magono, 1981: Observation of aerosol scavenging by falling snow crystals at two sites of different heights. *J.Meteor. Soc.Japan*, **59**, 763-771.

Prodi, F., 1976: Scavenging of aerosol particles by growing ice crystals. *Preprints Intern.Conf. Cloud Phys.*, Boulder, Colorado, *Am. Met. Soc.*, 70-75.

Prodi, F. and R.Oraltay, 1991: Scavenging of aerosol particles by growing and evaporating ice crystal: Assessing the role of competitive processes. *Proc. Fifth Intern.Conf.Precip.Atmos-Surf. Exchange processes.*, Richland, Washington, 15-19 July 1991, 75-86.

Prodi, V., 1972: A condensation aerosol generator for solid monodisperse particles. In: Assessment of airborne particles (Edited by TT. Mercer, P.E. Morrow and W.Stober), 169-181.

Sauter, D.P. and P.W.Wang, 1989: An experimental study of the scavenging of aerosol particles by natural snow crystals. *J.Atmos.Sci.*, **46**, 1650-1655.

Smith-Johannsen, R.I., 1969: Ice crystal agglomeration: T Formation. *J.Atmos.Sci.*, **26**, 532-534.

Song, N. and D.Lamb, 1994: Experimental investigations of ice supercooled clouds. Part II: Scavenging of an insoluble aerosol. *J.Atmos.Sci.*, **51**, 104-116.

Vittori, O.A. and V.Prodi, 1967: Scavenging of atmospheric particles by ice crystals. *J.Atmos.Sci.*, **24**, 533-538.

Zhang, R. and R.L.Pitter, 1991: A numerical simulation of the aerosol scavenging rate by simple ice crystals. *J. Geoph.Res.*, **96**, 22491-22500.

CCN AND CLOUD DROPLET MEASUREMENTS IN NORTHERN MEXICO

Daniel W. Breed, Roelof T. Bruintjes, and Vidal Salazar M.

Research Applications Program, National Center for Atmospheric Research, Boulder, CO 80307 USA

1. INTRODUCTION

1.1 Background

In response to severe drought conditions in the early 1990's, representatives from the state of Coahuila and local industry asked researchers at NCAR to develop a scientific program to evaluate the viability of increasing rainfall through cloud seeding techniques. The Program for the Augmentation of Rainfall in Coahuila (PARC) was proposed by NCAR as a four-year program consisting of a randomized seeding experiment, physical studies, and collaboration and training of Mexican scientists and students (*i.e.*, technology transfer). A detailed description of the history and physics behind PARC can be found in Bruintjes *et al.* (1998a). The initial results, which showed increases in radar-derived rainfall from individual storms, were very encouraging, and as a result, officials from the state of Durango also asked for an assessment for their region in northern Mexico. Hence, the Durango Rainfall Induction Program (DRIP) was developed and begun in the summer of 1999.

Although the primary emphasis in both projects is to develop, conduct, and evaluate cloud seeding experiments, based in large part on the work and results in South Africa (Mather *et al.*, 1997), physical studies are also being carried out to assess weather conditions and cloud characteristics in Coahuila and Durango. Initial results describing the cloud condensation nuclei (CCN) and cloud droplet measurements are presented here, with comments on data reduction problems that are still being investigated and may impact any final results.

1.2 Regions of Study

Coahuila is a northern state of Mexico bordering central Texas, with mountain ridges of the Sierra Madre Oriental dominating the central and western regions of the state. Precipitation falls primarily in the convective season between April and October with a strong gradient from eastern slope communities (*e.g.*, Muzquiz at 560 mm) to central mountain towns (*e.g.*, Cuatro Cienegas at 190 mm). Data were collected during PARC over three summers: 1996 (July-October), 1997 (July-September), and 1998 (June-August). The base of operations was located at the international airport in Monclova (actually in its sister city Frontera) at an elevation of 565 m and at about 27° N latitude.

Durango lies between southwestern Coahuila and the coastal state of Sinaloa. Western Durango is primarily forested over the Sierra Madre Occidental mountains, while semi-arid conditions are typical of the eastern and northeastern regions. Like Coahuila, convective rainfall from June through October dominates the precipitation climatology, although the peak rainfall period is shifted about one month later in Durango. The field portion of DRIP occurred in 1999 (late July through late October), with operations based out of the international airport near the city of Durango (1890 m elevation, 24° N latitude). Most of the flights were concentrated in north central Durango (near the radar) at about 25.5° N.

Corresponding author's address: Daniel W. Breed, NCAR/RAP, P.O. Box 3000, Boulder, CO 80307-3000, USA; Email: breed@ucar.edu

2. INSTRUMENTATION AND DATA REDUCTION

The aircraft that was used for these studies is a Piper Cheyenne (PA-31T) twin-engine turboprop airplane, equipped with instruments for measuring state parameters (pressure, temperature, dewpoint), aircraft parameters (airspeed, heading, rate of climb, GPS position, etc.), and cloud microphysical parameters (liquid water content, CCN, aerosol spectra, droplet spectra, cloud particle spectra). Some of the research flights were designed primarily to collect CCN data and near-base cloud droplet data. However, much of the data were collected at periods of opportunity during conduct of the randomized hygroscopic seeding experiments.

2.1 CCN Measurements

Airborne measurements of CCN were made using a University of Wyoming CCNC-100. This instrument automates the operation of a thermal-gradient diffusion chamber, counting droplets formed in the chamber via light scattering onto a photodetector. A description of the instrument and its calibration is described in de Oliveria and Vali (1995). Actually, two models of the CCNC-100 were used; one borrowed from AES-Canada in 1997 (S/N 103), and one borrowed in 1998 and 1999 from Weather Modification Inc. (S/N 107).

Although the two counters are essentially the same, their outputs (photodetector "signal" voltage) are related to CCN concentrations differently. S/N 103 was calibrated by comparison with the output of a TSI 3025 UCPC instrument using mono-dispersed nuclei of known composition. The calibration data appear quite linear, resulting in a relationship of the form: CCN = 223.2*V+17.1, where V is "peak" signal voltage and CCN is TSI concentration (assumed to be CCN concentration). The calibration of S/N 107 utilizes the results of de Oliveira and Vali (1995) and later work at Wyoming, which accounted for the fact that the signal voltage (*e.g.,* light scattered) is dependent on droplet size as well as concentration. Calibration data were collected using a laboratory aerosol generator and a video "frame grabber" system to capture and count the droplets formed in the chamber cloud at different supersaturations. The resulting relationship, which has a dependence on supersaturation, as applied to S/N 107 is: CCN = (3.64+2.39/SS)*V/SV, where SS is supersaturation in percentage, V is "peak" signal voltage, and SV is the video sample volume (0.0707 cm^{-3}). If the two models' signal voltages are similar (which is not necessarily true), then the equation with the SS dependence, when data are fit to the Twomey relationship ($N = CS^k$), results in a "flatter" curve (smaller k) and a smaller C. At 1% SS, the ratio of concentrations between the two equations is 2.62.

Operation of the CCNC-100 differed between years in that data were taken at various SS values. In 1997, a CCN spectrum was derived from samples nominally processed at 0.3, 0.5, 0.7, and 1.0 %SS. One cycle took 3-4 min to complete, and multiple cycles were used to derive a spectrum if they occurred in sequence under similar conditions (*i.e.,* same flight level). In 1998, samples were taken at slightly different supersaturations; 0.3, 0.5, 0.85 and 1.15 %SS. Also, two samples were obtained at each SS value before changing to the next value, resulting in a longer cycle time of 5.5-6 min. In 1999, the SS values were changed to 0.15, 0.4, 0.6, and 0.95 %SS, with one sample obtained at each value per cycle (about 3.5 min). Results at 0.15% SS were often suspect and needed careful examination for data quality. In retrospect, even though we wanted to better define CCN values at low supersaturations, the instrument is near its limit at this SS and should be operated at a slightly higher minimum SS level.

2.2 FSSP and the SPP Modification

The same PMS FSSP was used all four seasons, the so-called NCAR "short probe" (S/N 277-0676-06). In late 1998, a new signal-processing package was installed that enhanced the capabilities of the FSSP (DMT's SPP modification). Deadtime losses were eliminated, negating the need to make activity corrections, channel characteristics (number and size thresholds) became programmable, and the acquisition rate was increased to 10 Hz (about 10 m of flight path). However, the data output was also changed which has required software modifications in our data reduction programs that have not yet been completed. Therefore, only a limited amount of data has been examined for 1999 (DRIP) and no droplet concentrations are presented here.

Some uncertainties remain in the processing of FSSP data from PARC. First, difficulties in keeping the optics consistently clean affected sizing and possibly droplet counting. There was no obvious degradation in parameters such as *total strobes* and *gated strobes*, but fluctuations within natural variability would be masked. Second, as one of the house-keeping parameters, the FSSP output *fast resets*, while the airborne data system was setup to record the more common parameter *activity*. Corrections in the data reduction software were made and verified as being reasonable using ratios of the various counting parameters (such as *depth of field ratio - DOF* and *velocity acceptance ratio – VAR*). When uncertainties arose (primarily in 1996 data), then constant values of *DOF* and/or *VAR* were used in the calculations that determine the activity correction to the measured concentrations. Therefore, periods exist in which the FSSP droplet concentrations are not well known, but they are readily identifiable and used sparingly in characterizing conditions in PARC.

3. RESULTS

Although the primary utility of the aircraft was as a seeding platform, a typical flight was planned to take advantage of opportunities to record a number of microphysical parameters. After takeoff, the aircraft climbed high enough to allow the pilot to assess the types of clouds or storms in the area. While climbing, CCN measurements were usually made, and at the high altitude, if clouds were nearby, cloud droplet spectra would be obtained. After the completion of operations related to the randomized seeding experiment, samples of cloud droplet distributions were generally made just above cloud base and CCN would be measured in the vicinity, below cloud base. An example of the near cloud base sampling is shown in the time-series plots of Figure 3.1, from a flight on 21 July 1998. The top panel shows altitude, the middle panel shows temperature and mixing ratio, and the bottom panel shows cloud droplet concentration and CCN signal voltage. A climb to above cloud base for a penetration occurred at about 19:37:30, and the FSSP concentration peaked in the sampled cloud at about 500 cm^{-3}. The CCNC-100 started cycling after 19:42, and the double samples at each SS is obvious. These are the type of flights and data that were examined for CCN spectra and cloud droplet concentrations.

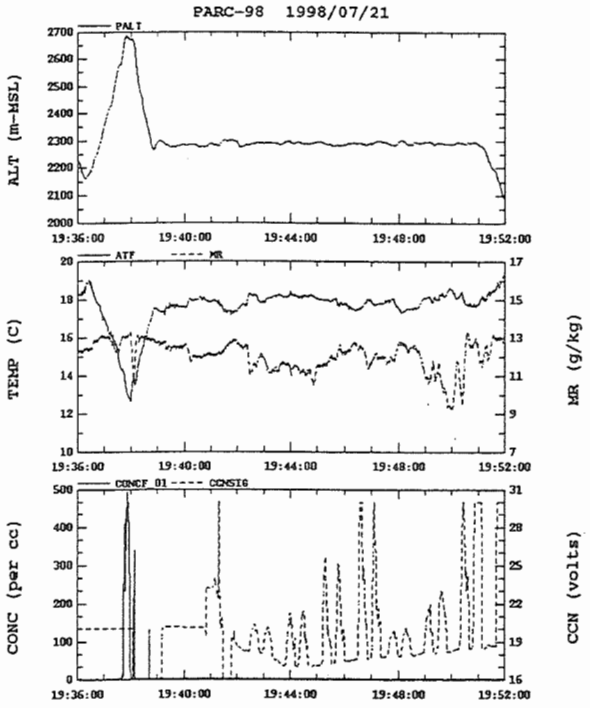

Figure 3.1 Time-series data for 16 min period from 1998/07/21. Top panel shows altitude in m-MSL, middle panel shows temperature (solid) and mixing ratio (dashed), and bottom panel shows FSSP concentrations (solid) and CCN signal voltage (dashed).

3.1 CCN Spectra

CCN spectra (represented as $N = cS^k$) are summarized in Table 3.1 for several days from the three years when a CCNC-100 was operated. A general difference between 1997 and 1998 is clear and likely related to the calibration differences. The ratio of the parameter *c* between the two CCNC-100 models is 2.73, which is close to the value derived from the calibration difference (2.62). Even though the calibration issue discounts comparisons between years with different CCNC-100 models, variations within each year and between 1998 and 1999 should be valid.

The five spectra of 1997 clearly reflect continental conditions, even with the calibration uncertainty. The continental conditions continue to dominate the spectra derived in 1998. Smoke from an unusual episode of Mexican forest fires in April-May of 1998 lingered into June, and appears to influence the four June spectra. However, a few days in July and August have similar spectra (high *c* values). The six samples from Durango (1999) also show continental conditions, but with a hint of slightly lower *c* values. The average *c* in 1999 is 497 compared with 671 in 1998 (Coahuila). Again, the difference is not clear, because the ranges of *c* and *k* overlap and there are limited samples to compare. One general feature of the CCN spectra in Table 2.1 is the lack of high variability, only about a factor of 2 in *c* and slightly more in *k*.

In 1997, more CCN sampling was done during climbs above the atmospheric boundary layer (ABL). A preliminary figure of CCN concentrations versus altitude, presented in Bruintjes *et al.* (1998b), clearly shows a drop in concentrations above the ABL. Therefore, another complicating factor in analyzing CCN spectra is the possibility of sampling mixed air parcels when near the top of the ABL (slightly below cloud base). Other parameters, such as mixing ratio or θ, assist in evaluating such conditions.

Table 3.1 CCN Spectra Parameters (from $N = cS^k$)

Date (yymmdd)	C	k
970725	1565	1.166
970726	1561	1.329
970805	2188	1.260
	1981	0.791
970815	1863	0.961
980610	905	0.387
	1054	0.434
980611	679	0.901
980617	919	0.816
980704	379	0.357
	579	0.450
980715	471	0.866
980721	869	0.744
980809	553	0.575
980814	960	0.639
980822	423	0.536
	463	0.619
	643	0.681
980831	494	1.029
990817	481	0.547
990819	852	0.639
990828	388	1.415
	361	0.760
990913	428	0.391
	472	0.585

3.2 Cloud Droplet Concentrations

In general, the cloud droplet concentrations measured during PARC reflect the continental characteristics of the CCN spectra. A table of the concentrations with auxiliary parameters is not yet completed, so the results are only summarized here. In 1996, the range of FSSP concentrations tended to be lower than in 1997 and 1998, probably due to the necessity of using theoretical constants for much of the data reduction. Twenty-seven samples near cloud-base ranged in concentrations from 210 to 450 cm^{-3}. Fewer cloud-base samples have been examined from 1997, but they were typically over 500 cm^{-3} (about 400-900 cm^{-3}). About a dozen cloud-

base penetrations have been compiled from 1998, and they are similar to the 1997 results.

4. CONCLUSIONS

Observations of microphysical conditions in convective clouds over northern Mexico have been made as part of the evaluation of two projects aimed at precipitation enhancement via hygroscopic seeding. CCN spectra and cloud droplet concentrations near cloud-base are characteristic of continental conditions and are generally similar to conditions found the South African study (Mather *et al.*, 1997), which served as the model for the Mexican experiments. The lack of variability (within the uncertainty of the measurements) suggests that the potential for hygroscopic seeding effects is relatively insensitive to the natural microphysical conditions. However, the variability of conditions is not well established for Durango. A more systematic analysis of both the CCN and FSSP measurements as well as investigations using other data sources, such as the aerosol measurements from the PMS ASASP and PCASP instruments flown in 1997-1999, is needed to verify these results.

5. REFERENCES

Bruintjes, R.T., D.W. Breed, M.J. Dixon, B.G. Brown, and V. Salazar, 1998a: Program for the Augmentation of Rainfall in Coahuila (PARC): Overview and preliminary results. *14th Conf. on Weather Modification,* Everett, WA, AMS, 600-603.

Bruintjes, R.T., D.W. Breed, V. Salazar, and H. Ramirez Rodriquez, 1998b: Microphysical characteristics of convective clouds in northern Mexico. *Preprints, Conf. Cloud Physics,* Everett, WA, AMS, J36-J39.

Mather, G.K., D.E. Terblanche, F.E. Steffens, and L. Fletcher, 1997: Results of the South African cloud seeding experiments using hygroscopic flares. *J. Appl. Meteor.*, **36**, 1433-1447.

de Oliveira, J.C.P. and G. Vali, 1995: Calibration of a photoelectric cloud condensation nucleus counter. *Atmos. Research*, **38**, 237-248.

OBSERVATIONS OF THERMALS IN CUMULUS CLOUDS

Alan M. Blyth*, Sonia G. Lasher-Trapp‡, and William A. Cooper§

* New Mexico Tech, Socorro, NM 87801
‡ Texas A&M University and NCAR†
§ National Center for Atmospheric Research†
Boulder, CO 80307

1 INTRODUCTION

The classic thermal circulation, which was determined in early laboratory experiments, is an updraught that diverges at the top, converges at the rear with downdraughts at the edges. One of the most detailed descriptions of air motions in cumulus clouds was given by Warner (1970) who illustrated the structure of the updraught at three levels in the cloud. He found that at cloud top there was a strongly turbulent region with organized overturning motions; at mid-levels there was a laminar-like updraught often paralleled with the liquid water content; and at cloud base there was a disorganized structure not necessarily related to the cloud boundaries. He did not find evidence of motion on a cloud scale resembling that in the laboratory thermal. McPherson and Isaac (1977) examined the details of the turbulence processes near the top of cloud. In doing so they presented a series of wind vectors representing the air motions about 250 m below the cloud top which indicate a pattern similar to that observed in the classic laboratory thermals. They further reported that downdraughts were more common than updraughts near cloud top occurring mostly within the edges of the cloud.

There have been several reports of the presence of adiabatic cores in cumulus clouds, even near cloud top (e.g. Jensen et al. 1985). Blyth et al. (1988) suggested that cumulus clouds are built of one or more thermals that contain an approximately adiabatic core for much their vertical ascent. In this picture, entrainment occurs through the ascending top and mixtures of cloud and entrained air descend around the edge. Some mixed air circulates around towards the centre of the thermal and the remainder goes into the turbulent wake. Support for this picture was provided by the measurements of Stith (1992) who found traces near the middle of the cloud of the SF_6 that had been released near cloud top.

Many penetrations of small cumulus clouds were made at a variety of altitudes during the Small Cumulus Microphysics Study (SCMS) held near Cape Canaveral, Florida in the summer of 1995. We present wind patterns determined from these measurements. We will also present measurements made in New Mexico cumulus congestus clouds during the summer of 1987 with the NCAR King Air. Most of the penetrations of these clouds were within 500 m or so of cloud top.

The results presented in this abstract are preliminary.

2 RESULTS

2.1 Evidence for thermal circulation

Figures 1 and 2 illustrate examples from New Mexico and Florida respectively of downdraughts surrounding the updraught. The penetrations were close to cloud top in New Mexico, but at a variety of altitudes below cloud top in SCMS.

Several features can be seen from the figures.

- Many of the examples from Florida and New Mexico show a relatively simple "classic" picture of divergence from the updraught into the downdraughts.
- It is evident in the cases shown with higher frequency data that there is usually considerable turbulence superimposed on the large-scale "overturning" motions. The vertical wind trace in Fig. 1b, for example, indicates that several scales of motion are present.
- Examination of the divergence in conjunction with the vertical wind and liquid water con-

* *Corresponding author address*: Alan M. Blyth, Dept. of Physics, New Mexico Tech, Socorro, NM 87801; e-mail: blyth@kestrel.nmt.edu

†NCAR is supported by the National Science Foundation

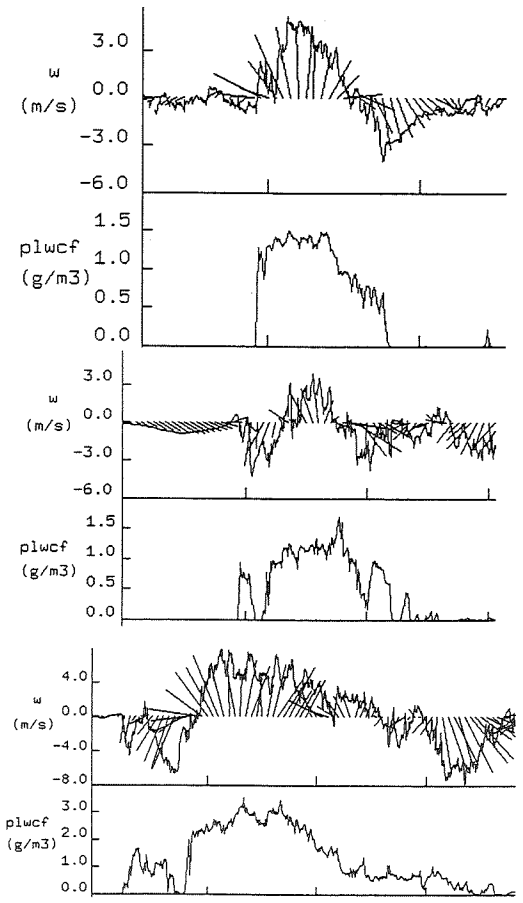

Figure 1: *Three penetrations made near cloud top in New Mexico clouds on 9, 10, and 12 August 1987 from top to bottom respectively. The individual figures show: vertical wind (top) and liquid water content measured with the FSSP (bottom). The average horizontal wind has been subtracted. The wind vectors are constructed from the vertical wind and the component of the horizontal wind along the flight track. The horizontal axes are time with tick marks indicating 10 s increments corresponding to about 1 km distance.*

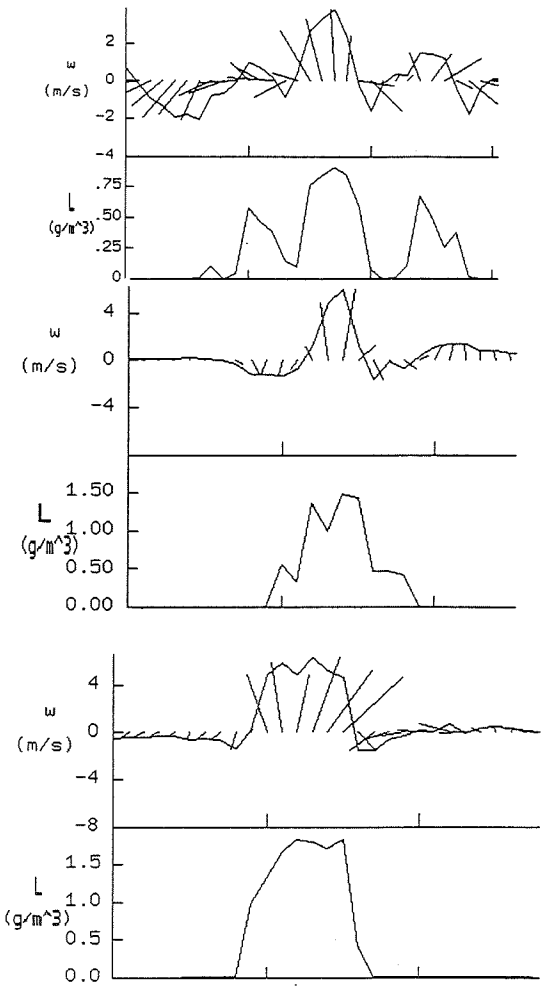

Figure 2: *As Fig. 1 but for three penetrations made in Florida clouds during SCMS on 11 August, 24 July and 28 July 1995 from top to bottom respectively.*

tent indicates that several thermal elements exist beside each other. This is a very common feature.

- Fig. 1c shows that the liquid water content and the updraught speed decreases gradually downshear. The downdraught is somewhat stronger on the downshear side.

2.2 Properties of Thermals

More than ninety adiabatic (or close to adiabatic) regions were observed by the NCAR C-130 aircraft. The majority of these were near cloud base, but a significant number were observed at higher altitudes, including near cloud top. There was no tendency for these cores to be found near the centre of thermals, as defined by the wind patterns.

Figure 3 shows 1 Hz data from all the penetrations made during SCMS. The preliminary results indicate:

- the majority of updraughts are smaller than 1 km;
- there is no tendency for the size of the most of the updraughts to change with height, although the largest updraughts are at the highest altitudes;
- relatively few regions were encountered with $L/L_A > 0.8$ (as measured by the FSSP), but the normalised width of such regions did not decrease with height;
- the maximum value at any level of the peak vertical wind speed measured in any single updraught increased with altitude, from about 3 m s^{-1} at 500 m MSL to 11-12 m s^{-1} at 2.5 km MSL;
- there is a slight tendency for the maximum value of L/L_A encountered in any single updraught to decrease with altitude.

More detailed analysis is continuing.

2.3 Thermals and Cloud Microphysics

Thermals play a significant role in the development and movement of the particles in the cloud. Ludlam (1952) presented a picture of how it is likely to work with two particles initially close together in the cloud. Both were carried upwards in a new thermal, but the slightly larger one sedimented into the core region while the other one was carried along in the very top of the thermal. It is likely that the smaller particle would be caught in a downdraught and transported back down into the cloud. In this way, downdraughts can play a significant role in the glaciation of the cloud. We have seen, particularly in Fig. 1 that strong downdraughts often exist at the edges of the updraught. Figure 4 shows an example of this process occurring in the New Mexico clouds. This picture of updraughts being ice-free and the downdraughts containing ice, was commonly observed in the NM clouds. It is likely, however, that the updraughts do contain ice particles that were too small to be detected by the 2DC probe (Ovchinnikov et al. 2000). Similar transport is likely to be important in the warm rain process.

Acknowledgements This work was supported in part by the National Science Foundation under grant no. ATM-9420333. Part of the research was performed while on sabbatical leave at the Department of Pure and Applied Physics, UMIST and the Department of Meteorology, University of Edinburgh.

3 REFERENCES

Blyth, A. M., W. A. Cooper, and J. B. Jensen, 1988: A study of the source of entrained air in Montana cumuli. *J. Atmos. Sci.*, **45**, 3944 - 3964.

Jensen, J. B., P.H. Austin, M.B. Baker and A.M. Blyth, 1985: Turbulent mixing, spectral evolution and dynamics in a warm cumulus cloud. *J. Atmos. Sci.*, **42**, 173 - 192.

Ludlam, F. H., 1952: The production of showers by the growth of ice particles. *Quart. J. Roy. Meteorol. Soc.*, **78**, 543 - 553.

McPherson, J. I., and G. A. Isaac, 1977: Turbulent characteristics of some Canadian cumulus clouds. *J. Appl. Meteorology*, **16**, 81-90.

Stith, J. L., 1992: Observations of cloud-top entrainment in cumuli. *J. Atmos. Sci.*, **49**, 1334-1347.

Warner, J., 1970: The microstructure of cumulus clouds: Part III. The nature of the updraft. *J. Atmos. Sci.*, **27**, 682-688.

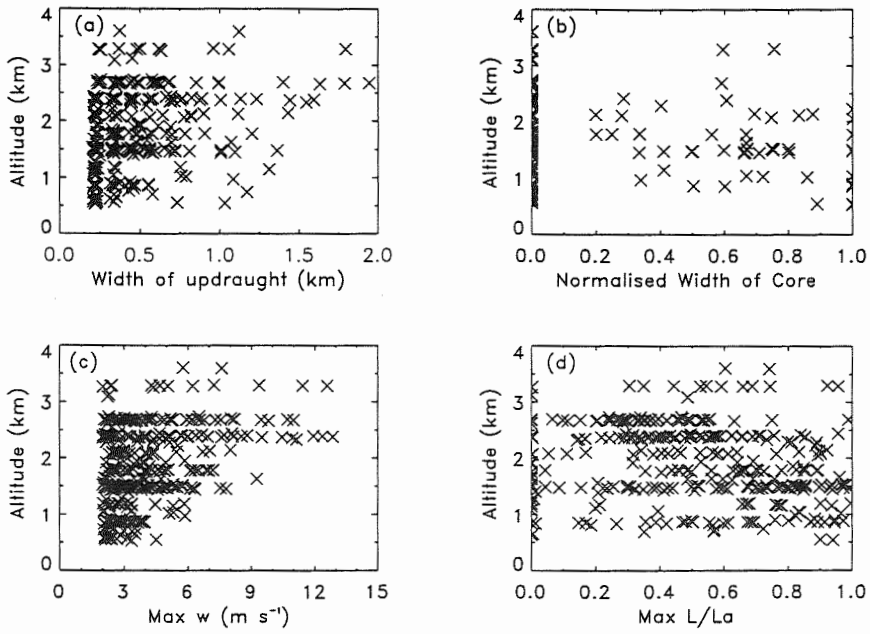

Figure 3: *1 Hz data from all cloud penetrations made in SCMS. The following are plotted versus altitude: (a) Width of cloud regions with $w > 2$ m s^{-1}; (b) Width of regions with $L/L_A > 0.8$ within the updraughts; (c) Maximum updraught speed measured in a single updraught; and (d) Maximum value of L/L_A.*

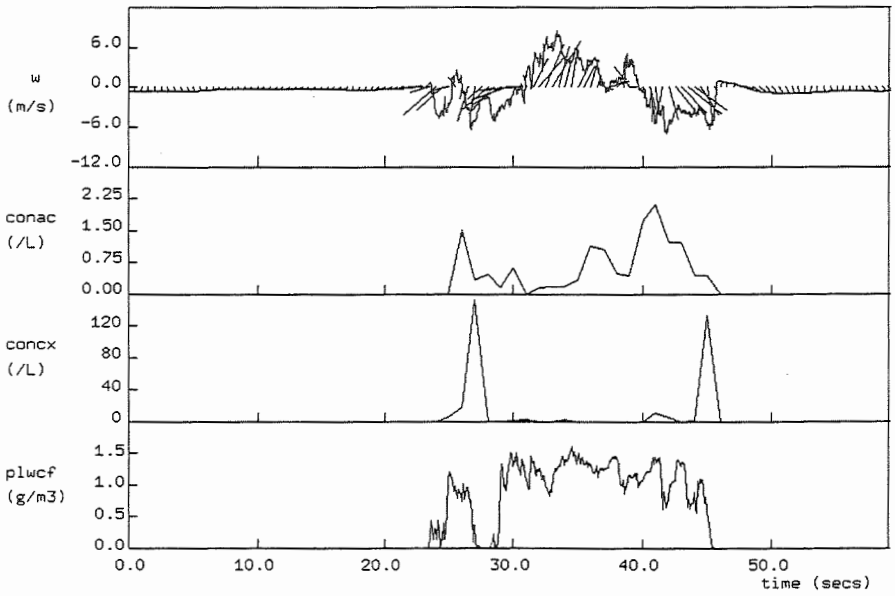

Figure 4: *Penetration made near cloud top on 19 August, 1987. The top trace is the vertical wind and wind vectors as in Fig. 1. The next three traces are, respectively, concentration from the 2DC, concentration from the 1D and liquid water content from the FSSP.*

CONTINENTAL/MARITIME DRIZZLE CONTRASTS IN STRATUS AND CUMULI

James G. Hudson and Seong Soo Yum

Desert Research Institute, Reno, Nevada

1. INTRODUCTION

Contrasts between continental and maritime cloud droplet concentrations discovered by Squires (1956) were attributed to differences in cloud condensation nuclei (CCN) concentrations (Squires 1958). This causes the Twomey Effect (Twomey 1977). The second Twomey Effect links CCN to precipitation (Albrecht 1989; Hudson 1993). We present extensive cloud microphysics measurements that support both Twomey Effects.

2. DESCRIPTION OF EXPERIMENT

NCAR research flights during the Atlantic Stratocumulus Transition Experiment (ASTEX) in June 1992 near the Azores islands and the Small Cumulus Microphysics Study (SCMS) in July and August 1995 in eastern Florida provide the data. ASTEX provided boundary layer stratus or stratocumulus while SCMS involved small developing cumulus clouds during mid to late morning at altitudes between 950 and 700 mb.

CCN were measured with the DRI airborne instantaneous CCN spectrometer (Hudson 1989) and condensation nuclei (CN) were measured with a TSI 3010 counter. Cloud droplets (2 to 50 μm diameter) were measured with a PMS FSSP (Knollenberg 1981). Larger drops (drizzle; 50 to 620 μm diameter) were measured with a PMS 260X probe (Knollenberg 1981).

3. AIR MASS DESIGNATION

During both ASTEX (Hudson and Xie 1999) and SCMS (Hudson and Yum 2000) wind direction, CN, and CCN concentrations (N_{CN} and N_{CCN}) revealed continental/maritime air. Table 1 summarizes these contrasts in N_{CN}, N_{CCN}(1%), cloud droplet concentrations (N_c), cloud droplet mean diameter (MD; only those between 2 and 50 μm), and liquid water contents of both cloud water (L_c; diameter 2-50 μm), and drizzle (L_d; diameter 50-620 μm).

Corresponding authors address: James G. Hudson, DRI-DAS, 2215 Raggio Pkwy, Reno, NV 89512-1095, USA, Email: hudson@dri.edu

	Stratus (ASTEX)				Cumuli(SCMS)	
	thick		thin			
	cont	mar	cont	mar	cont	mar
N_{CN} (cm^{-3})	1374	434	1374	434	3586	1228
N_{CCN}(cm^{-3})	878	217	878	217	1411	359
N_c(cm^{-3})	209	60	135	82	312	150
MD(μm)	10	14	8	12	11	15
L_c(g dm^{-3})	180	160	70	110	490	540
L_d(g dm^{-3})	54	108	2	23	2	29

Table 1. Averages of boundary layer total particle concentrations (N_{CN}), CCN concentrations (N_{CCN}, at 1% S), and cloud microphysical parameters for the two projects with the ASTEX cloud data divided according to cloud thickness (> or < 45 mb). The latter are averages over all altitudes of the averages of each flight for continental and maritime air masses. N_c is the average cloud droplet concentration (2-50 μm diameter) (minimum threshold 1 cm^{-3}) and MD is the mean diameter of the cloud droplets. L_c is the liquid water content of the cloud droplets (2-50 μm diameter) and L_d is the liquid water content of the drizzle drops (50-620 μm diameter). For convenience L_c and L_d are in grams decimeter $^{-3}$.

4. RESULTS

Higher N_c (row 3, Table 1) found in continental clouds, which were produced by higher N_{CCN} (Hudson and Xie 1999–ASTEX; Hudson and Yum 2000–SCMS)(row 2, Table 1), produced smaller MD (row 4, Table 1) because there was little difference in L_c between continental and maritime clouds (row 5, Table 1). But unlike N_c, MD depends on distance above cloud base (Fig. 1). Thus the greater thickness of the cumuli than the stratus produced larger droplets and greater L_c in SCMS than ASTEX (row 5, Table 1).

The last row of Table 1 displays the great continental/maritime contrast in drizzle. Figs. 2 and 3 show how drizzle also depends on cloud thickness (stratus) and height above cloud base (cumulus).

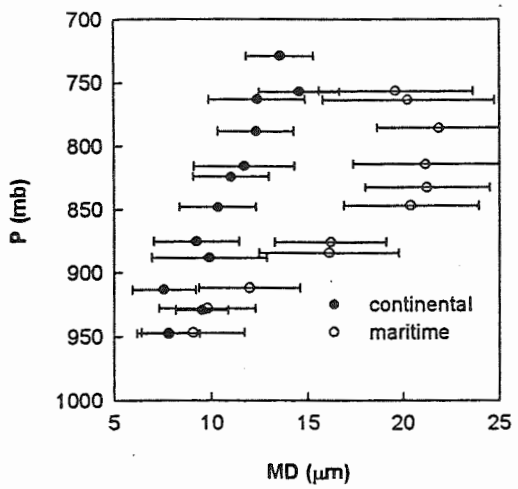

Fig. 1. Vertical distribution of averages and standard deviations of cloud droplet mean diameter (MD) at various altitudes. This represents all of the in-cloud data divided according to the continental and maritime flights for SCMS.

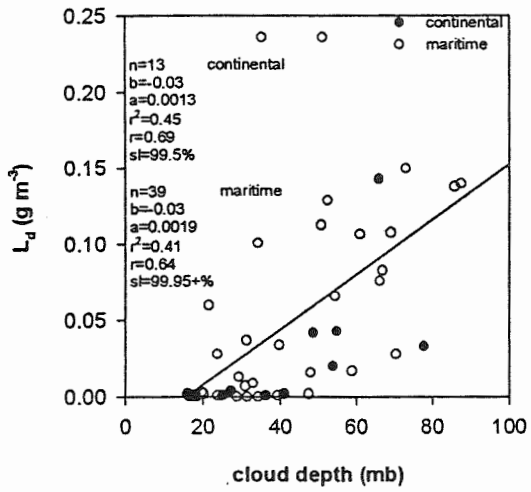

Fig. 2. Drizzle liquid water content measured during vertical soundings during ASTEX as a function of cloud thickness in mb for continental and maritime air masses. Linear regressions are also shown.

This is also seen by comparing the thin and thick columns in Table 1. Larger amounts of drizzle in thicker stratus (though thinner than the cumuli) are probably due to longer lifetimes of stratus. This is also probably the reason that there is less continental/maritime drizzle contrast for the thicker stratus. Once these long lasting clouds are thick enough they will drizzle regardless of droplet concentration. However the thinner stratus show a continental/ maritime contrast that is similar to cumuli. Fig. 3

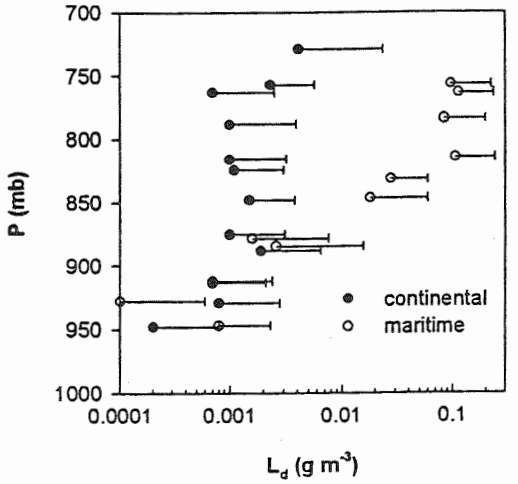

Fig. 3. As Fig. 1 for drizzle liquid water, L_d.

shows that the maritime/continental contrast in the short-lived cumuli is two orders of magnitude near cloud top! Fig. 4 also shows that at high altitudes there were an order of magnitude more large (diameter 30-50 μm) cloud droplets in maritime that is commensurate with the drizzle contrast.

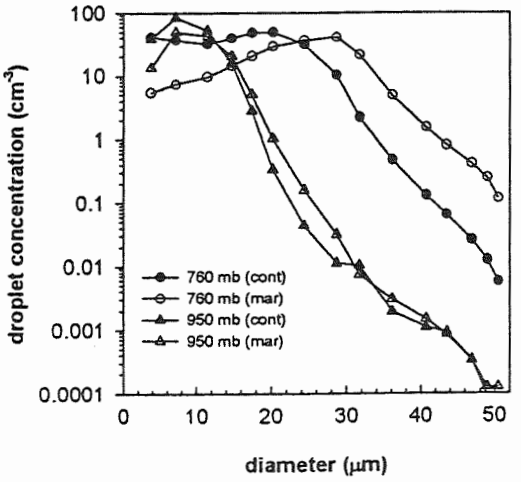

Fig. 4. Composite averages of cloud droplet spectra in continental and maritime clouds at low (950 mb) and high (760 mb) altitudes for SCMS.

Fig. 5 shows that larger MD appear to be a necessary condition for drizzle that was often achieved in maritime clouds but almost never achieved in continental clouds except perhaps the thick stratus. Fig. 5 (especially b and c) suggest a threshold MD for drizzle (Hudson and Svensson; 1995; Gerber 1996; Hudson and Yum 1997).

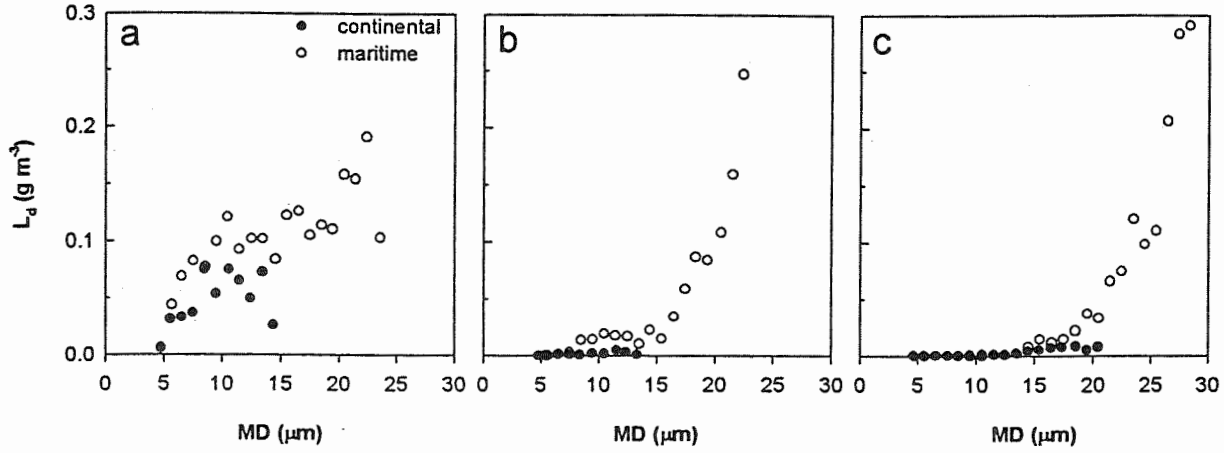

Fig. 5. Drizzle liquid water content versus mean diameter of cloud droplets within parcels for 1 μm wide bins. (a) is for thick stratus in ASTEX; (b) is for thin stratus in ASTEX; and (c) is for small cumuli in SCMS.

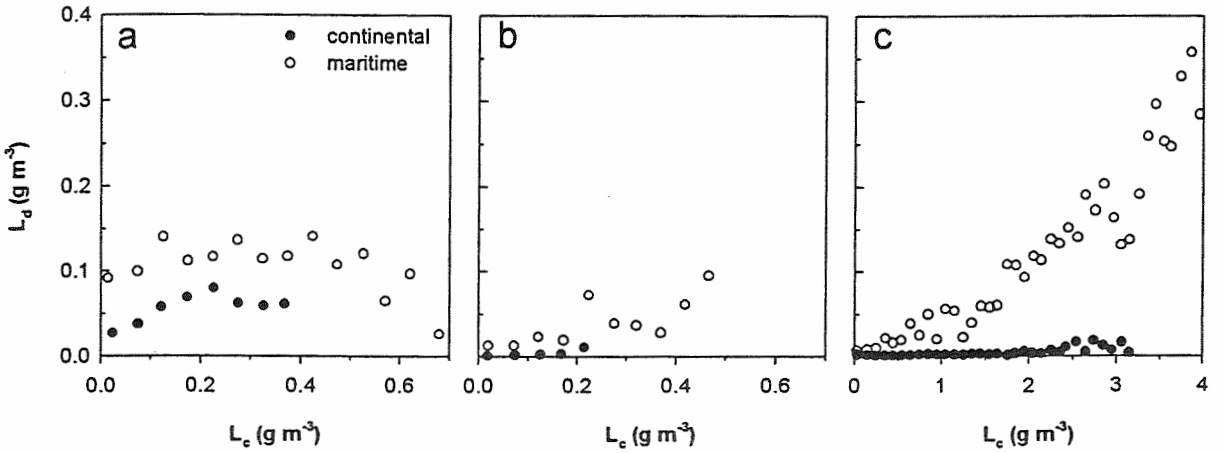

Fig. 6. *As Fig. 5 but for cloud droplet liquid water content.*

Fig. 6 shows that greater amounts of L_c also seemed to promote drizzle, especially for maritime clouds. However, unlike MD there was no L_c threshold for drizzle. The continental/maritime drizzle contrast for similar L_c, the apparent connections between N_{CCN} and N_c (Hudson and Yum 2000), N_c and MD (Table 1 and Fig. 1), large droplets and drizzle (Fig.4), and N_c and L_d (Table 1 and Figs. 2 and 3), along with the apparent droplet size threshold for drizzle (Fig. 5) support the concept that CCN concentrations affect drizzle. This is the basis of the second Twomey Effect.

5. DISCUSSION AND CONCLUSIONS

The continental CCN spectra in the two projects are similar (Fig. 7), but they are not as high as urban concentrations (e.g., Frisbie and Hudson 1993; Hudson 1991). SCMS maritime spectra are higher than most maritime spectra (e.g., Fig. 7) because of anthropogenic influence. Thus, the observed microphysical differences are more significant since the CCN differences were less than extreme. Satellite remote sensing measurements by Rosenfeld and Lensky (1998) show similar trends in warm rain for continental/polluted clouds compared to maritime clouds.

Fig. 4 shows continental/maritime cloud droplet spectral similarities at low altitudes. Droplet concentrations larger than 30 μm diameter are an upper bound of giant nuclei concentrations because giant nuclei should be this large even below cloud. These concentrations–10^{-2} cm^{-3}--could affect drizzle (Feingold et al. 1999). However, there is apparently no continental/maritime contrast of giant nuclei. In the upper layers of these maritime clouds the

concentrations of droplets greater than 40 μm diameter (large enough to collect droplets; Klett and Davis 1973), exceed 1 cm^{-3}, which is far above postulated giant nuclei concentrations. More than a factor of 10 greater drizzle for maritime (thin stratus or cumuli) for all altitudes (last row, Table 1) is comparable to the factor of 40 greater drizzle liquid water path predicted by Feingold et al. (1999) for clouds with similar N_c contrasts when the influence of giant nuclei was excluded . When they included the effects of giant nuclei the predicted drizzle contrast was only a factor of 2. Moreover, they predicted that giant nuclei would have less effect on drizzle for maritime clouds. Therefore it seems that average cloud microphysical properties including droplet concentration (N_c), droplet mean diameter (MD), and drizzle (L_d) are generated by CCN concentrations (N_{CCN}).

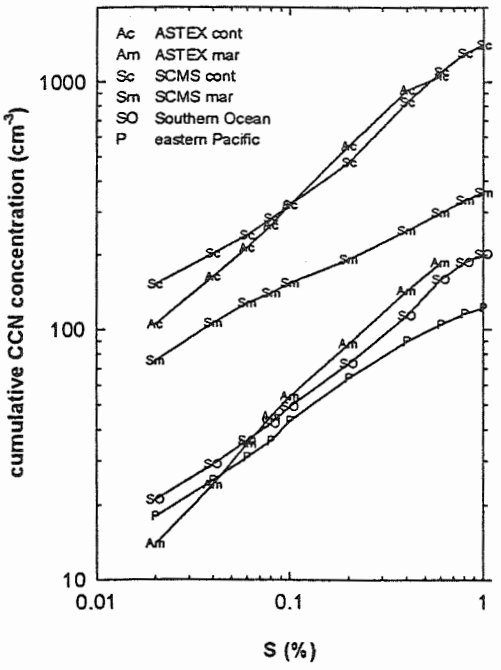

Fig. 7. Average and standard deviations of boundary layer cumulative CCN spectra for ASTEX and SCMS and two other maritime projects (Hudson et al. 1998; Hudson and Xie 1999).

6. ACKNOWLEDGMENTS.

This research was supported by NASA Grants NAG-1-1845 and NAG-1-2183; NSF Grant ATM-9422170; and by NOAA-NASA Grant NA67RJ0146. The NCAR RAF is greatly appreciated for the aircraft and flights.

7. REFERENCES

Albrecht, B.A., 1989: Aerosols, cloud microphysics and fractional cloudiness, *Science*, **245**, 1227-1230 .

Feingold, G, W.R. Cotton, S.M. Kreidenweis, and J.T Davis, 1999: The impact of giant cloud condensation nuclei on drizzle formation in stratocumulus: Implications for cloud radiative properties. *J. Atmos. Sci.*, **56**, 4100-4117.

Frisbie, P.R., and J.G. Hudson, 1993: Urban cloud condensation nuclei spectral flux, *J. Appl. Meteorol.*, **32**, 666-676.

Gerber, H., 1996: Microphysics of marine stratocumulus clouds with two drizzle modes. *J. Atmos. Sci.*, **53**, 1649-1662.

Hudson, J.G., 1989: An instantaneous CCN spectrometer. *J. Atmos. & Ocean. Techn.*, **6**, 1055-1065.

Hudson, J.G., 1991: Observations of anthropogenic CCN. *Atmos. Environ.*, **25A**, 11, 2449-2455.

Hudson, J.G., 1993: Cloud condensation nuclei, *J. Applied Meteor.*, **32**, 596-607.

Hudson, J.G., and H. Li, 1995: Microphysical contrasts in Atlantic stratus. *J. Atmos. Sci.*, **52**, 3031-3040.

Hudson, J.G., and G. Svensson, 1995: Cloud microphysical relationships in California marine stratus. *J. Appl. Meteorol.*, **34**, 2655-2666.

Hudson, J.G., Y. Xie, 1999: Vertical distributions of cloud condensation nuclei spectra over the summertime northeast Pacific and Atlantic Oceans. *J. Geophys. Res.*, **104**, 30219.

Hudson, J.G., Y. Xie, and S.S. Yum, 1998: Vertical distributions of cloud condensation nuclei spectra over the summertime Southern Ocean, *J. Geophys. Res.*, **103**, 16609-16624.

Hudson, J.G., and S.S. Yum, 1997: Droplet spectral broadening in marine stratus, *J. Atmos. Sci.* **54**, 2642-2654.

Hudson, J.G., and S.S. Yum, 2000: Maritime/continental drizzle contrast in small cumuli, submitted to *J. Atmos. Sci* Klett, J.D., and D.H. Davis, 1973: Theoretical collision efficiencies of cloud droplets at small Reynolds numbers. *J. Atmos. Sci.*, **30**, 107-117.

Knollenberg, R.G., 1981: Techniques for probing cloud microstructure. *Clouds: Their Formation, Optical Properties and Effects.* P.V. Hobbs and A. Deepak, eds., Academic Press, 494 pp.

Rosenfeld, D., and I.M. Lensky, 1999: Spaceborne sensed insights into precipitation formation processes in continental and maritime clouds. *Bull. Amer. Met. Soc.*, **79**, 2457-2476.

Squires, P., 1956: The microstructure of cumuli in maritime and continental air. *Tellus*, **8**, 443-444.

Squires, P., 1958: The microstructure and colloidal stability of warm clouds, Part II - The causes of the variations in microstructure, *Tellus*, **10**, 262-271.

Twomey, S., 1977: The influence of pollution on the shortwave albedo of clouds. *J. Atmos. Sci.*, **34**, 1149-1152.

Yum, S.S., J.G. Hudson, and Y. Xie, 1998: Comparisons of cloud microphysics with cloud condensation nuclei spectra over the summertime Southern Ocean. *J. Geophys. Res.*, **103**, 16625-16636.

CLOUD MICROPHYSICAL RELATIONSHIPS IN WARM CLOUDS

Seong S. Yum and James G. Hudson

Desert Research Institute, Reno, Nevada 89512, USA

1. INTRODUCTION

Precipitation initiation in warm clouds has been a subject of intense study and debate for several decades. The problem is that it takes longer to start precipitation after cloud is formed in theoretical calculations than for observation. The challenging task of explaining discrepancies between theory and observations has focused on short time initial droplet collection: i.e., giant nuclei (Johnson 1982), homogeneous mixing (Mason and Jonas 1974), inhomogeneous mixing (Baker et al. 1980), entity mixing (Telford and Chai 1980), or turbulent internal mixing (Cooper 1989; Hudson and Svensson 1995).

To check the validity of these theories, Yum (1998) examined relationships among cloud microphysical parameters for extensive data sets from four field projects. The most interesting finding was that correlations between cloud droplet (diameter < 50 μm) number concentration (N_c) and cloud droplet mean diameter (MD) were mostly positive for individual cloud segments, contrary to adiabatic calculations (Hudson and Yum 1997) and two external mixing theories--inhomogeneous mixing (Baker et al. 1980) and entity mixing (Telford and Chai 1980). The positive correlation between N_c and MD was rather consistent with homogeneous mixing (Mason and Jonas 1974) or Broadwell and Breidenthal (1982) mixing after final homogenization. Hence, these results seemed to suggest that entrainment did not promote enhanced droplet growth.

Results of the extensive data sets analyzed by Yum (1998) are convincing though not completely definitive. Here we add data from two other field projects. Relationships between cloud microphysical parameters for each project are are compared.

2. MEASUREMENTS

Data are from experiments carried out over the north eastern Pacific (FIRE1), the north eastern Atlantic (ASTEX), the Southern Ocean in three projects, SOCEX1 and 2 and ACE1, and the east coast of Florida (SCMS), Cloud types were predominantly stratocumulus during the first five projects. During SCMS almost all clouds were small cumuli.

Cloud droplets were measured with a Particle Measurement Systems (PMS) forward scattering spectrometer probe (FSSP; 3.5-50 μm, Knollenberg 1981). Drizzle drops (diameter > 50 μm) were measured with a PMS 260X probe(Knollenberg 1981; 50-640 μm).

Corresponding author's address: Seong Soo Yum, Desert Research Institute, 2215 Raggio Parkway, Reno, NV 89512, USA; e-mail: seongsoo@dri.edu

3. RESULTS

3.1 Scale dependence

Correlations between N_c and MD depend on the analysis scale (Fig. 1). The correlation coefficient, $\gamma[N_c\text{-MD}]$, was most negative when based on all 1 Hz data for a project. It is more positive for smaller scales, i.e., single flights and individual penetrations. A fairly good negative γ in ASTEX seems to be due to air mass changes (Hudson and Xie 1999). Continental clouds have higher N_c and smaller MD while maritime clouds have lower N_c and larger MD, thus they create a negative correlation when combined. Air mass changes were also observed during SCMS (Hudson and Yum, 2000) but the combination of these two air masses produced no such correlation. The distinctive differences between the two air masses seemed to act simply to erase the good positive correlations between N_c and MD shown for individual flights or penetrations. In fact the average γ of this cumulus project is the highest among the six projects analyzed here.

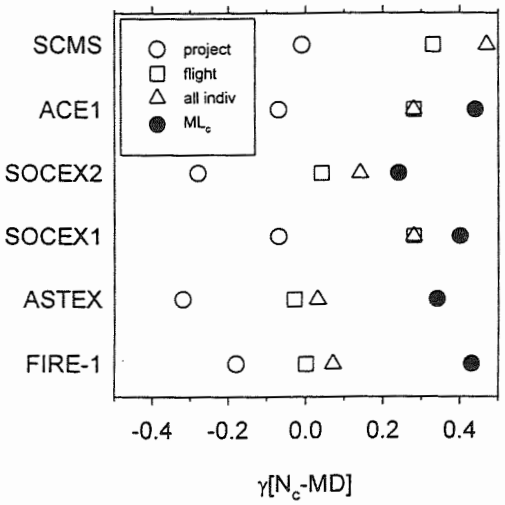

Fig. 1. Comparisons of $\gamma[N_c\text{-MD}]$ calculated for different scales: project, flight, individual and monotonic cloud liquid water content (L_c) sounding (ML_c) averages.

Table 1 . Averages of cloud microphysical parameters for the ML_c and NL_c soundings from the five stratocumulus projects (SOCEX-1, SOCEX-2 and ACE-1 are from Yum (1998)). The numbers after ± are standard deviations. Linear regressions are averages for individual soundings. The slope, a, of the linear regression of [σ_c vs. MD] is also shown in row 10. In row 12, the number of soundings with negative γ is shown in parentheses. In the last row, the regressions are for the ML_c and NL_c soundings combined. For example, the number of data points for FIRE-1 is 59 (15+44).

project	FIRE-1		ASTEX		SOCEX-1		SOCEX-2		ACE-1	
sounding type	ML_c	NL_c	ML_c	NL_c	ML_c	NL_c	ML_c	NL_c	ML_c	NL_c
no. of soundings	15	45	18	75	10	76	7	58	10	64
no. of data for a sounding	112	69	96	74	71	50	48	62	50	44
N_c (cm^{-3})	50±31	40±26	110±56	99±100	48±30	25±28	102±60	76±68	98±65	53±49
MD (μm)	15.4±3.7	14.7±4.2	13.1±4.6	11.5±4.5	16.2±5.7	17.7±5.8	12.4±4.6	14.0±5.4	13.4±4.6	15.5±5.8
L_c ($g\ m^{-3}$)	0.13±0.09	0.10±0.10	0.21±0.15	0.11±0.11	0.17±0.15	0.12±0.14	0.16±.16	0.15±0.14	0.19±0.16	0.17±0.21
σ_c (μm)	4.2±1.6	5.3±2.8	4.6±1.4	5.4±2.5	5.1±1.6	7.0±2.3	3.7±1.3	5.0±1.8	3.5±1.0	4.4±1.5
L_d ($g\ m^{-3}$)	0.04±0.06	0.07±0.09	0.05±0.06	0.08±0.16	0.03±0.16	0.12±0.26	0.01±0.01	0.06±0.08	0.01±0.03	0.05±0.15
W ($cm\ s^{-1}$)	48±70	54±57	-1±44	2±40	-58±109	-46±115	79±121	101±146	14±58	20±54
a [σ_c-MD]	0.156	0.205	0.191	0.399	0.165	0.147	0.125	0.097	0.029	0.060
γ [σ_c-MD]	0.40	0.27	0.59	0.64	0.67	0.34	0.51	0.25	0.11	0.19
γ [N_c-MD]	0.43 (0)	0.06 (18)	0.34 (1)	0.01 (32)	0.40 (0)	0.24 (20)	0.24 (2)	0.12 (21)	0.44 (0)	0.22 (11)
γ [L_d-MD]	-0.06	-0.01	0.07	0.07	0.07	0.08	0.15	0.11	0.05	0.06
γ[L_d-σ_c]	0.20	0.13	0.03	0.04	0.14	0.00	-001	-0.02	0.08	0.06
γ{γ [N_c-MD] vs. a [σ_c-MD]}	-0.38		-0.58		-0.34		-0.32		-0.43	

3.2 Monotonic vs. Non-monotonic LWC profiles

Since cloud droplet liquid water content, L_c, increases monotonically with height in adiabatic clouds, the clouds with monotonically increasing L_c profiles (ML_c) may be at least closer to adiabatic than those with non-monotonic L_c profiles (NL_c) (Hudson and Yum 1997). Hence the comparison of ML_c with NL_c clouds could be interpreted as the comparison of near adiabatic clouds with less adiabatic clouds. Table 1 compares averages for all 1 Hz data of the ML_c and NL_c soundings for the five stratocumulus projects. Also shown in Table 1 are the average linear regressions for individual soundings. SCMS could not be included because those clouds are too small for soundings. ML_c clouds have higher N_c, larger L_c and narrower droplet spectra (as expressed by standard deviation of diameter, σ_c) than NL_c clouds for all projects. This supports the idea that ML_c clouds are more adiabatic. NL_c clouds have more drizzle liquid water content, L_d, than ML_c clouds. The difference in L_d is more severe when MD is also larger for NL_c as in SOCEX1, SOCEX2 and ACE1.

Another important difference between ML_c and NL_c clouds in Table 1 is that the slope, a, of the linear regression between σ_c and MD is considerably lower in ML_c clouds for all projects except SOCEX2. Furthermore, the average γ[N_c-MD] is more positive in ML_c than NL_c soundings. In three projects, FIRE1, SOCEX1, and ACE1, the average γ[N_c-MD] for ML_c soundings is no less than 0.4 and no sounding has a negative γ[N_c-MD]. In fact, among the 60 ML_c soundings from all five projects, only three have negative γ[N_c vs. MD]. As shown in Fig. 1, the turnaround of γ[N_c vs. MD] from project scale to ML_c sounding averages is significant. In all five stratocumulus projects this difference is at least 0.47.

3.3 γ[N_c-MD] vs. a[σ_c-MD]

Higher γ[N_c-MD] and lower a[σ_c-MD] for ML_c soundings compared to NL_c soundings predict a negative correlation between these parameters (last row, Table 1). Fig. 2 shows that the combination of horizontal cloud penetrations and soundings shows even higher correlations for each of the five stratocumulus projects. Lack of correlation for SCMS (Fig. 2f) seems to be unique to cumulus clouds. ASTEX has the highest percentage of negative γ[N_c- MD] but even this was only 42% of the penetrations. This percentage was only 16% for ACE1 and less than 5% for SCMS. The slope, a, of the [σ_c-MD] linear regression is negative for many individual penetrations in all projects except ASTEX. It is notable that these negative and small positive values of a[σ_c-MD] seem to be associated with more positive values of γ[N_c-MD] in all stratocumulus projects. That is, the correlation between N_c and MD is more toward negative for the flights with greater spectral broadening.

3.4 Cumulus clouds

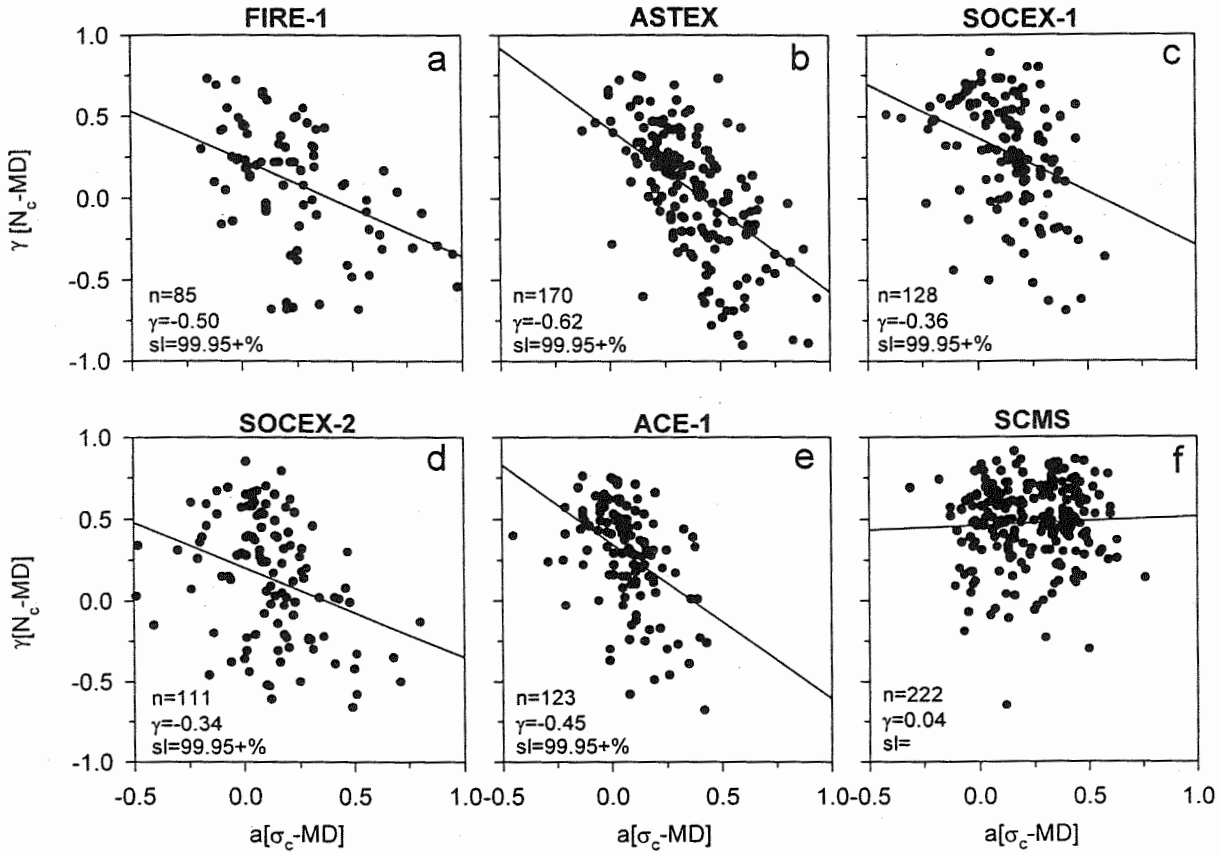

Fig. 2. Scatter plots of $\gamma[N_c\text{-}MD]$ vs. $a[\sigma_c\text{-}MD]$ for all individual penetrations (soundings and horizontal penetrations combined) in each of the six projects. Here sl is the significance level.

Figs. 1 and 2 show that cumulus clouds observed during SCMS have very different characteristics from stratocumulus. The reason for the highest positive $\gamma[N_c\text{-}MD]$ for SCMS may be due to the large variations of vertical velocity, W. Downdrafts were equally as strong as updrafts. Updraft core regions may have been able to maintain adiabatic values of N_c while complete evaporation of small droplets in downdraft regions may have reduced N_c, and those droplets that survived should have reduced sizes. This would lead to positive correlations between N_c and MD. A good example is shown in Fig. 3. The peaks in N_c are well matched with MD and W, which tends to be negative at cloud edges where N_c is low. The $\gamma[N_c\text{-}MD]$ and $[N_c\text{-}W]$ for this cloud segment were 0.67 and 0.66(sl=99.95+%) for the 43 data points, respectively.

Another important feature to be noticed in this plot is that N_c does not smoothly decrease from the center of the cloud to the edges, i.e., minor peaks are observed near the edges. This seems to provide evidence of the irregular nature of the mixing (Broadwell and Breidenthal 1982). Compare the four droplet spectra displayed at the bottom of Fig. 3. The second spectra from the left has a peak at channel 2, while the third, which is closer to the cloud edge but has more than a factor of four higher N_c, has its peak at channel 4. If mixing had proceeded gradually and homogeneously from the cloud edges to the center, smooth decreases of N_c from the centers to the edges would have been observed. This may indicate that somehow entrainment was more severe and homogenization of the mixed volume was more mature in the sample region of the second spectrum, which was further inside the cloud, than the third spectrum. The peak channels of the first (updraft core) and the third spectra being the same is similar to studies in continental cumuli (e.g., Paluch and Knight, 1984; 1986). Unlike those observations, however, the shift of the peak channel toward smaller sizes at low concentrations seems to be more prevalent in Florida cumuli as the solid positive correlation between N_c and MD for most of the SCMS flights implies.

4. SUMMARY

For 839 cloud penetrations the correlations between cloud droplet concentrations and mean diameters were negative in only 198 cases (24%). Clouds with monotonic L_c profiles, which had the least spectral broadening, tended to have positive correlations. Cumulus clouds almost always showed good positive correlations regardless of spectral broadening. The positive correlations between cloud droplet concentrations and mean diameters seemed to

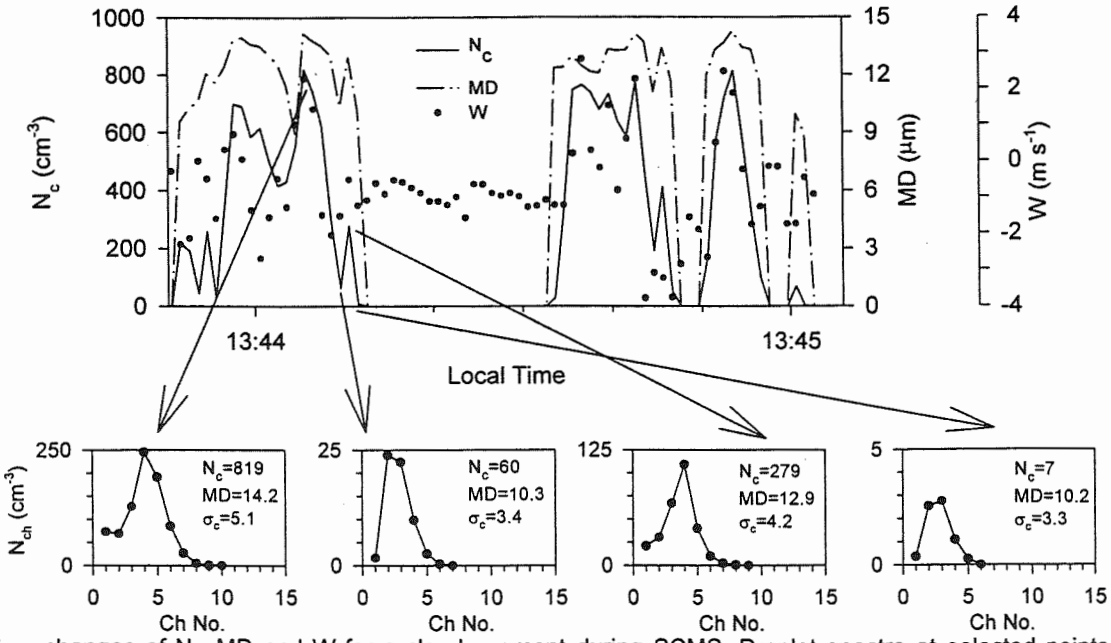

Fig. 3. Time changes of N_c, MD and W for a cloud segment during SCMS. Droplet spectra at selected points are shown at the bottom.

be caused by homogeneous mixing or Broadwell and Breidenthal (1982) mixing. Mixing in this way does not promote growth of large droplets. The droplet concentration in well-mixed parcels would have been diluted, but "superadiabatic" droplet growth in these diluted parcels seemed not to have occurred. Otherwise, negative correlations between cloud droplet concentration and meand diameter would have been more prevalent.

ACKNOWLEDGEMENTS

This research is supported by NASA Grant No. NAG-1-1845 and NAG-1-1113, NSF Grant No. ATM-9419263 and ATM-9422170, and NASA Grant No. NAGW-3753.

REFERENCES

Baker, M. B., R. G. Corbin, and J. Latham, 1980: The influence of entrainment on the evolution of cloud droplet spectra: I. A model of inhomogeneous mixing. *Quart. J. Roy. Meteor. Soc.*, 106, 581-598.

Broadwell, J. E., and R. E. Breidenthal, 1982: A simple model of mixing and chemical reaction in a turbulent shear layer. *J. Fluid Mech.*, 125, 397-410.

Cooper, W. A., 1989: Effects of variable droplet growth histories on droplet size distributions. Part I: Theory. *J. Atmos. Sci.*, 46, 1301-1311.

Hudson, J. G., and G. Svensson, 1995: Cloud microphysical relationships in California marine stratus. *J. Appl. Meteor.*, 34, 2655-2666.

Hudson, J. G., and S. S. Yum, 1997: Droplet spectral broadening in marine stratus. *J. Atmos. Sci.*, 54, 2642-2642.

Hudson, J. G., and S. S. Yum, 2000: Continental /maritime drizzle contrasts in small cumuli. *J. Atmos. Sci.*, in review.

Hudson, J. G. and Y. Xie, 1999: Vertical distributions of cloud condensation nuclei spectra over the summertime northeast Pacific and Atlantic Oceans. *J. Geophys. Res.*, 104,30219-39229.

Johnson D. B., 1982: The role of giant and ultragiant aerosol particles in warm rain initiation. *J. Atmos. Sci.*, 39, 448-460.

Knight, C. A., and L. J. Miller, 1998: Early radar echoes from small, warm cumulus: Bragg and hydrometeor scattering. *J. Atmos. Sci.*, 55, 2974-2992.

Knollenberg, R. G., 1981: Techniques for probing cloud microstructure. *Clouds, Their Formation, Optical Properties, and Effects*, P. V. Hobbs and A. Deepak, Eds., Academic Press, 495 pp.

Mason, B. J., and P. R. Jonas, 1974: The evolution of droplet spectra and large droplets by condensation in cumulus clouds. *Quart. J. Roy. Meteor. Soc.*, 100, 23-38.

Paluch, I. R., and C. A. Knight, 1984: Mixing and the evolution of cloud droplet size spectra in a vigorous continental cumulus. *J. Atmos. Sci.*, 41, 1801-1815.

Paluch, I. R., and C. A. Knight, 1986: Does mixing promote cloud droplet growth? *J. Atmos. Sci.*, 43, 1994-1998.

Telford, J. W., and S. K. Chai, 1980: A new aspect of condensation theory. *Pure. Appl. Geophys.*, 118, 720-742.

Yum, S. S., 1998: Cloud droplet spectral broadening in warm clouds-an observational and model study. Ph. D dissertation, University of Nevada, Reno, 191pp.

UPDRAFTS, DOWNDRAFTS AND TURBULENCE IN FAIR-WEATHER CUMULI — A RADAR PERSPECTIVE

Bruce Albrecht* and Pavlos Kollias

MPO/RSMAS University of Miami
4600 Rickenbacker Causeway
Miami, FL 33176

1. INTRODUCTION

Our current understanding of the vertical structure of updrafts and downdrafts in fair weather cumuli and the relationship of the drafts to entrainment processes has been inferred from aircraft observations obtained using repeated, but limited penetrations of the clouds (see review by Blyth, 1993). But since shallow cumuli evolve with time and their lifetime is relatively short, any explicit description of the vertical structure of these features from aircraft observations is limited.

In this paper we use observations made with a surface-based, upward-facing 94 GHz Doppler radar to examine the vertical structure of updrafts and downdrafts in fair weather cumuli. These structures are compared with the structures inferred from aircraft observations and the conceptual models that have evolved from these models.

2. OBSERVATIONS

A single-antenna Doppler radar operating at 94 GHz in an upward facing configuration was used to study small cumuli that passed overhead. Reflectivity measurements were based on the integration of 10,000 samples yielding a minimum detectable signal of –45 dBZ_e at 1 km. The vertical resolution for this case is 30 m and with an antenna beamwidth of 0.24°, the radar horizontal resolution is about 8 m at 2 km. For a 1-second dwell time and a cloud motion of 10 ms^{-1}, the "effective" beam cross section is approximately doubled. Doppler spectra are provided by a real time FFT algorithm. In the applications described in this paper, a 1 s signal sampling is followed by 3.5 s FFT processing so that a new vertical profile is obtained every 4.5 s. The 512-point FFT used in this study gives a velocity resolution of 3.2 cms^{-1}. Doppler spectra provide mean vertical velocities as well as detailed spectral shapes that can be used to infer small-scale vertical velocity shear, illuminate cloud microphysical processes, and estimate turbulence dissipation rates. Observations were also made from a 915 MHz wind profiler. The technical and operational characteristics of the radars used for this study are summarized in Kollias et al., (2000).

The observations shown in this paper are from small cumuli sampled on January 29, 1999 from Virginia Key, located about 10 km from downtown Miami. These clouds were associated with a classic trade-wind boundary layer structure with a capping inversion at 1700 m with $\Delta\theta \approx 6$ K , $\Delta q \approx -8$ g/kg, and $\Delta\theta_e \approx$ -15 K across the inversion.

3. RESULTS

Observations from small cumuli that passed over the site provide a detailed description of the cloud structure. The 94 GHz radar reflectivity mapping for one of the clouds sampled on this day is shown in Figure 1.

*Corresponding author address: Bruce Albrecht, Rosenstiel School of Marine and Atmospheric Science, Division of Meteorology and Physical Oceanography 4600 Rickenbacker Causeway of Miami, Florida 33149-1098.

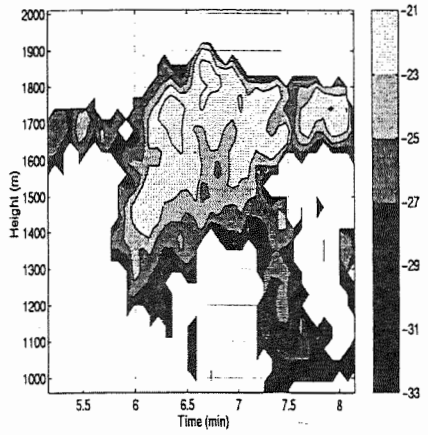

Fig. 1. 94 GHz reflectivities (contours are dBZs). Height resolution is 30 m and time resolution is 4.5 s.

The downwind side of this cloud and the cloud top area are regions of high reflectivities, reaching values of –18 dBZ. The cloud boundaries are defined by reflectivities as low as –31 dBZ. There is evidence of detrained cloud matter at the inversion associated with a relatively flat cloud top extending upwind. The cloud top observed before the main core reaches the observing site is about 150 m below that associated with the core. Since the mean horizontal wind speed in the cloud layer is about 9 ms^{-1}, the horizontal extent of the cloud is estimated to be about 1 km compared with a vertical extent of about 700 m.

The vertical velocities shown in Fig. 2 illustrate the draft structures in the cloud. A well-defined updraft core with a maximum velocity of 6.0 ms^{-1} is clearly evident. This updraft core coincides with the areas of highest radar reflectivities. The strong updraft core, which penetrates about 150 m into the inversion, is associated with an increase of the radar reflectivity with altitude that is consistent with adiabatic ascent. There is no evidence for penetrative downdrafts within the updraft core. There is, however, substantial vertical velocity variability within the detrained air observed upwind of the strong updraft.

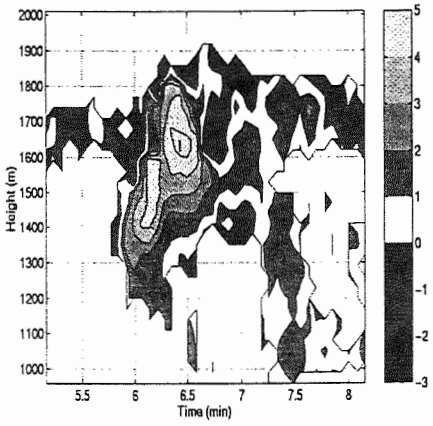

Fig. 2. Vertical velocities (contours are ms^{-1}). Updraft (indicated by I) and downdrafts (indicated by II and III) are considered in detail in subsequent analysis.

Two types of downdraft structures are identified in the cumuli sampled. One originates from near cloud top on the approaching (downwind) side of the cloud, the other penetrates through the cloudy air that detrains on the retreating (upwind) upper boundary of the cloud. In the downdraft on the downwind cloud edge, radar reflectivities are low, indicating that mixing may deplete the liquid water content. Inside the penetrative downdraft in the trailing detrainment area, however, the reflectivities are relatively high. Since the equivalent potential temperature jump across the capping inversion ($\Delta\theta_{e)}$ is approximately -15 K, mixing of the dry air above the inversion into penetrating cloud masses could result in saturated mixtures that are negatively buoyant relative to unmixed cloudy air.

To further illustrate the nature of the drafts in the cloud studied, in Fig. 3 we show representative examples of Doppler spectra from three different areas of the cloud as identified in Fig. 2.

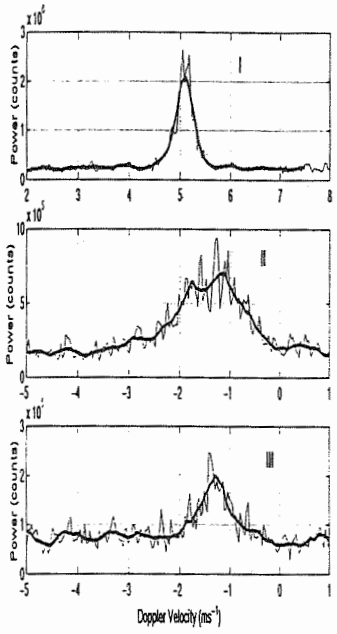

Fig. 3. Doppler spectra from different locations within the cloud. Lower case roman numerals correspond to locations indicated in Fig. 2. Heavy lines indicated smoothed spectra.

Within the updraft (Region I) the spectrum is relatively narrow and has symmetrical features that are consistent with broadening by turbulence only. Narrow Doppler spectra observed within the updraft indicate that turbulence is suppressed in this area, which is consistent with limited mixing into the core of the updraft. A broader and more skewed spectrum (Fig. 3b) is observed in the downdraft area (Region II) on the upwind side of the cloud. The skewness of the spectrum at higher fall velocities and the relatively high reflectivity observed in this region are consistent with the presence of larger droplets. Although there is also broadening of the Doppler spectrum (Region III) in the downdraft observed on the downwind boundary of the cloud, the Gaussian shape of the spectrum in this region is consistent with broadening due to turbulence and shear rather than the presence of larger droplets (Babb et al., 1999). The relatively low reflectivity in this region further indicates the lack of large droplets. In general, 94 GHz Doppler spectra and enhanced Bragg scattering at 915 MHz are observed in the regions of strong shear at the updraft-downdraft interfaces and where the cloud penetrates into the inversion layer. Evidence for the presence of big-drop production was only observed in the region of detrained cloud on the trailing side of the cloud.

4. DISCUSSION

The high temporal and spatial mapping of the in-cloud structure revealed coherent vertical structures. The updrafts remain unmixed as they penetrate about 150 m into the capping inversion layer where detrainment is evident by a relatively flat cloud top extending upwind. Minima in the 94 GHz Doppler spectral width and the 915 MHz Bragg scattering returns indicate that turbulent fluctuations in the updraft are minimal compared with other parts of the cloud.

The observations clearly indicate the presence of downward moving parcels that originate from the cloud top and extend in some cases almost to cloud base. At the upwind side there is evidence of downdrafts penetrating through detraining, dynamically inactive parts of the cloud matter. These downdrafts have horizontal dimensions of about 150 m, penetrate about 200 m into the cloud, with maximum vertical velocities of about -3 ms^{-1}. Detailed analysis of the Doppler spectrum width at the in-cloud boundaries between up and downdrafts revealed the existence of sharp discontinuities of the vertical velocity in the horizontal, supporting the concept of shallow cumuli as an ensemble of many cloud parcels. Furthermore, the updraft core in one of the clouds analyzed has a structure that is consistent with the idea that cumulus clouds comprise several successive bubbles that emerge from the sub-cloud layer. These results are consistent with airborne cloud radar observations of shallow cumuli described by French et al. (2000).

The observations provided in this manuscript help put many previous aircraft observations in perspective. Vertical velocities obtained as a function of time at a fixed height (1.7 km) through the core of the cloud indicates spatial structure that is strikingly similar to those obtained from some aircraft penetrations. A direct comparison of the cloud radar observations of vertical velocities at a fixed level with velocities measured from an aircraft

penetration is shown in Fig. 4. Although we have stretched the spatial scale associated with the radar observations by about 40%, the magnitude and relative location of the updraft and downdraft structures are nearly identical.

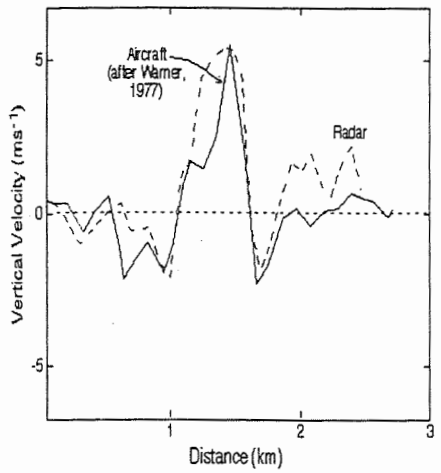

Fig. 4. Comparison of vertical velocity measurements at one level. Solid line corresponds to aircraft observations (Warner, 1977;) and dashed line to radar observations. The length scale of the radar observations was stretched by 40 % to facilitate the comparison.

Regions of higher vertical velocity variability observed with the radar were observed in the detraining air masses of the clouds. This also appears to be a region in the cloud where cloud-top entrainment processes are most active. Aircraft observations indicating high vertical velocity variability in updrafts may in some cases be sampling clouds that are easily defined visibly, but are in areas that are in a latter part of the cloud evolution. Warner (1977) discusses the difficulties in determining which part of the life cycle of a cloud is being sampled during aircraft penetrations. The results shown here indicate that the active updraft region occupies a relatively small part of the cloud. Thus even penetrating the adiabatic core of an active cumulus complex may not be assured by flying through the visible cloud.

5. CONCLUSIONS

This study illustrates the potential of cloud radars for studying small cumuli. Since the lifetime of the clouds is small, it is difficult to make aircraft penetrations at multiple levels. In addition to providing reflectivities and mean Doppler motions in the clouds, mm-wavelength radars can provide full Doppler spectra that can be used to obtain critical information on physical processes and their interaction with updraft and downdraft structures. Furthermore, the radar has great potential for studying the early precipitation stages of deeper cumulus clouds and, when used on a mobile platform (e.g. French et al., 2000) for studying the structure of fair weather cumuli through their entire life cycle. When used in a scanning mode, the radar has the potential for providing more on the three dimensional structure of the clouds. Currently, however, the retrievals from the radar cannot provide the microphysical detail that in available from *in situ* aircraft observations. A partial solution to this difficulty is to use a cloud radar on an instrumented aircraft (French et. al., 2000) or on a helicopter.

6. ACKNOWLEDGMENTS

This research was supported by the National Science Foundation under grant ATM9730119.

7. REFERENCES

Babb, D., J. Verlinde and B. A. Albrecht, 1999. Retrieval of cloud microphysical parameters from 94-GHz radar doppler power spectra. *J. Atmos. Oceanic Tech.*, **16**, 489-503.

Blyth, A. M., 1993. Entrainment in cumulus clouds. *J. Appl. Meteor.*, **32**, 626-641.

French, J. R., G. Vali and R. D. Kelly, 1999. Evolution of small cumulus clouds in Florida: Observations of pulsating growth. In press, *Atmos. Res.*, 30 pp.

Kollias, P., B. A. Albrecht, R. Lhermitte, and A. Savtchenko 2000: Radar Observations of Updrafts, Downdrafts, and Turbulence in Fair Weather Cumuli. *J. Atmos. Sci.* (submitted)

Warner, J., 1977. Time variation of updraft and water content in small cumulus clouds. *J. Atmos. Sci.*, **34**, 1306-1312.

ANALYTIC REPRESENTATION OF FRAGMENT DISTRIBUTIONS RESULTING FROM FILAMENT BREAKUP

Philip S. Brown, Jr. and Kimberly J. Edelman

Trinity College, Hartford, Connecticut

1. INTRODUCTION

Modeling of drop coalescence and breakup requires proper formulation of a governing equation that incorporates analytic expressions to describe the coalescence efficiency and the distribution of drop fragments resulting from breakup. Fragment distribution functions used in current models are based on those developed by Low and List (1982 a,b) (henceforth, LLa,b). Adjustments to those formulas were proposed by Brown (1997) for the purpose of ensuring that the fragment distribution functions would conserve mass. Those modifications were restricted to cases in which the mass of the large colliding drop greatly exceeds that of the small colliding drop.

As in the earlier work, attention here is focused on filament breakup, one of the three types of breakup identified by LLa,b in laboratory experiments. In filament breakup, very small satellite drops are formed from water mass originally contained in two colliding drops, each of which maintains its identity after collision. To describe the three-peaked fragment distribution resulting from filament breakup, LLb used a log-normal distribution to represent the satellite drops, and two normal distributions to represent the small- and large-drop remnants.

The aim of this research is to extend the earlier mass-conservation analysis of Brown (1997) to include a wider range of colliding drop-size pairs and to determine the implications of mass conservation on the form of the small-drop-remnant distribution. The earlier analysis pointed up the fact that if the mass of the large colliding drop greatly exceeds the combined mass of the small colliding drop and the satellite drops, the fractional change in the large-drop mass due to collision is insignificant. In terms of the fragment number distribution, the normal distribution representing the large-drop remnant then must have variance that is much smaller than that indicated in the fragment-distribution histogram of LLa that includes unavoidable, excess variance due to small departures of the colliding-drop diameters from their nominal values.

The analysis of Brown (1997) did not account for any adjustment of the small-drop-remnant distribution to eliminate variance attributable to differences between the colliding-drop diameters and their nominal values. In this work an assumption, based on physical considerations, is made with regard to the water mass transfer between the small and large colliding drops. This assumption, together with the mass-conservation constraint, allows estimation of the collision-produced variance in both the large- and small-drop-remnant distributions, provided a suitable, skewed distribution function is used to represent the small-drop remnant.

Corresponding author's address:
Philip S. Brown, Jr., Mathematics Department
Trinity College, Hartford, CT 06106 USA
E-Mail: philip.brown.1@mail.trincoll.edu

2.0 DISTRIBUTION OF THE SMALL-DROP REMNANT

Fig. 1 shows a least squares fit (solid curve) of a histogram (dashed curve) from the data of LLa for

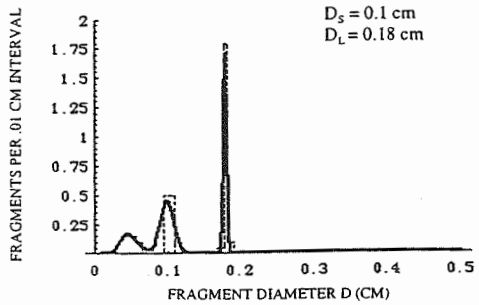

Fig. 1. Fragment distribution histogram (dashed curve) from results of LLa for colliding drops of diameters 0.18 cm and 0.10 cm. Smooth curve represents approximating function obtained by least squares fit of histogram values.

filament breakup when the large-colliding-drop diameter D_L is equal to 0.18 cm and the small-colliding-drop diameter D_S is 0.10 cm. When the independent variable is taken to be drop diameter D, use of a normal distribution centered about D_S to represent the small-drop remnant carries certain implications. The fact that the fragment number is assumed to be distributed symmetrically about D_S implies that the mass of the remnant, on average, is greater than that of the original drop. In the notation of LLb, the small-drop remnant is represented by the distribution

$$P_{f,2}(D) = H_{f,2}\exp\left[-\frac{1}{2}\left(\frac{D - D_S}{\sigma_{f,2}}\right)^2\right], \quad D_0 \le D \le D_C \quad (1)$$

where $H_{f,2}$ is the height of the peak, $\sigma_{f,2}$ is the standard deviation, D_0 (=.01 cm) is the smallest drop diameter resolved in the experiments, and D_C [= $(D_L^3 + D_S^3)^{1/3}$] is the diameter of the largest drop that can result from the collision. The fact that for filament breakup, a single remnant of each colliding drop is observed leads to the relation

$$\int_{-\infty}^{\infty} P_{f,2}(D)dD \approx \int_{D_0}^{D_C} P_{f,2}(D)dD = 1. \quad (2)$$

If ρ_w is the density of liquid water and M_S the mass of a spherical drop of diameter D_S, use of (2) leads to the result that the mass m_S of the small-drop remnant satisfies the relation

$$m_S \approx \int_{-\infty}^{\infty} \frac{\pi}{6}\rho_w D^3 P_{f,2}(D)dD = M_S + \frac{\sqrt{2\pi}}{24}\rho_w D_S \sigma^2. \quad (3)$$

It is seen from (3) that, on average, the mass of the remnant exceeds that of the original drop. The mass increase would have to be the result of mass transfer from the large drop to the small.

Filament breakup is characterized by a collision followed by temporary coalescence, at which stage the small and large drop become connected by a filament of water that then disintegrates into a number of small satellite drops. If σ denotes surface tension, then according to Whelpdale and List (1971), the pressures in the interiors of the small and large drops are $4\sigma D_S^{-1}$ and $4\sigma D_L^{-1}$, respectively. When the two drops are connected, the higher pressure in the interior of the small drop then would tend to induce water mass transfer from the small drop to the large, causing a decrease in the mass of the small drop rather than an increase. In the analytic representation of the fragment distribution for the small-drop remnant, then, it is more appropriate to use a form that allows for such a mass decrease.

The log-normal distribution is a single-peaked distribution that is skewed to the right. Depending on the parameters used, the skewness can be small, in which case the log-normal distribution looks very similar to the normal distribution. In this work, a slightly skewed, log-normal distribution with modal diameter D_S is reflected about D_S to represent the small-drop-remnant distribution. Thus, $P_{f,2}$ is modified to

$$\tilde{P}_{f,2}(D) = \frac{\tilde{H}_{f,2}}{(2D_S - D)}\exp\left[-\frac{1}{2}\left(\frac{\ln(2D_S - D) - \tilde{\mu}_{f,2}}{\tilde{\sigma}_{f,2}}\right)^2\right] \quad (4)$$

when $D_0 \le D \le 2D_S - D_0 \equiv D_{Max}$, and is zero elsewhere. Here, $\tilde{H}_{f,2}$ is a measure of the height, $\sigma_{f,2}$ is a measure of the spread, and $\tilde{\mu}_{f,2}$ is the natural logarithm of the median of the distribution before reflection. As constructed, the log-normal distribution is similar in shape to the normal distribution suggested by LLb but skewed slightly to the left to allow the average mass of the small-drop remnant to be less than that of the original drop in compliance with the mass-transfer principle implied by Whelpdale and List.

Fig. 2 shows three log-normal distributions reflected about $D=D_S$, each with modal diameter of 0.1 cm and with integral equal to unity. The

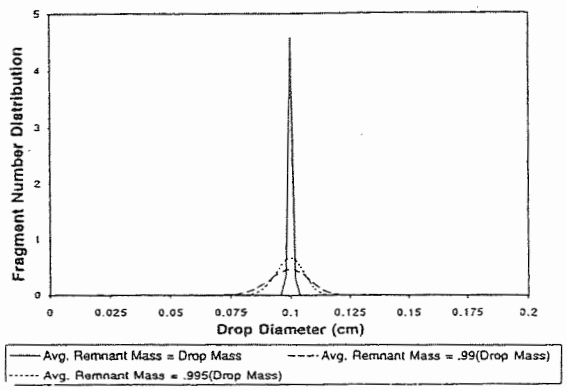

Fig. 2. Log-normal distributions, each reflected about modal diameter D_S = 0.10 cm and each with integral equal to unity. Distributions contain 100% (solid curve), 99.5% (short-dashed curve), and 99% (long-dashed curve) of mass of spherical drop 0.10 cm in diameter.

fragment distribution represented by the solid curve has mass equal to the mass of a spherical drop of diameter 0.1 cm. The drop distribution shown by the short-dashed curve has 99.5% of the mass of the 0.1-cm drop, while that shown by the long-dashed curve has 99%. Thus, only a small loss of drop mass greatly increases the variance of the distribution of the small-drop remnant. Visual comparison with the small-drop remnant distribution shown in Fig. 1 suggests that normally, very little mass of the small colliding drop is lost in the breakup event. Otherwise, the variance of the distribution centered about D_S would have to be considerably larger than that indicated by the histogram of LLa. (Recall that the variance in the histogram data includes not only the variance due to collision but also variance due to departure of the original drop diameter from the nominal value of D_S.)

3.0 DISTRIBUTION OF THE LARGE-DROP REMNANT

To represent the distribution of the large-drop remnant, LLb assumed a normal distribution with mean D_L for drop diameters up to D_C, above which value the fragment number was set to zero, since drops of diameter greater than D_C cannot be created from the mass available in the colliding drops. Then according to LLb, the fragment number distribution $P_{f,1}(D)$ for the large-drop remnant has the form

$$P_{f,1}(D) = H_{f,1}\exp\left[-\frac{1}{2}\left(\frac{D - D_L}{\sigma_{f,1}}\right)^2\right], \quad D_0 \le D \le D_C. \quad (5)$$

The cutoff value D_C for the large-drop remnant distribution can occur well within one standard deviation of the mean in the formulation of LLb when the diameter of the larger colliding drop greatly exceeds that of the smaller.

Three parameters determine the large-drop remnant distribution: the height of the peak $H_{f,1}$, the mean D_L, and the standard deviation $\sigma_{f,1}$. Two of the three parameters are determined by the specification of D_L and by the requirement that the integral of $P_{f,1}(D)$ be equal to unity. A third requirement might be the imposition of a least squares error requirement on $H_{f,1}$, which gives a fit such as that shown in Fig. 1, or the imposition of mass conservation, which gives a similar type of fit but often with a dramatic reduction in the standard deviation of $P_{f,1}(D)$ (especially for those cases in which the large-drop mass greatly exceeds that of the small drop [Brown, 1997]). Use of the mass-conservation constraint in place of a least squares fit of the data is justified only in those cases in which the large-drop and its remnant contain nearly all of the mass of the system, so that the mass-conservation requirement, in effect, fully determines the third parameter of the normal distribution.

The assumption now is made that during temporary coalescence any mass lost by the smaller colliding drop is transferred to the larger drop, which is assumed to include the water mass contained in the connecting filament. The satellite drops then are produced by the large colliding drop whose mass has been slightly increased by the transfer of water from the small drop. A temporary coalescence event then may ultimately result in just mass transfer to the large drop (partial coalescence), just satellite production, or both. In the limiting cases, a filament-producing event can result in either mass transfer from the small drop to the large drop without satellite production, or satellite production from the large drop without any mass transfer from the small drop. For these types of events, a mass-transfer relation can be included in the data-fitting procedure along with the overall mass-conservation constraint to determine an upper bound on the variances of the large- and small-drop-remnant distributions and, at the same time, avoid the uncertainties associated with the variance in the histogram data describing the colliding-drop-remnant distributions determined from experiments. For the cases under consideration, any mass lost by the small-drop will be transferred to the large drop and will be counted in that part of the large-drop-remnant distribution lying to the right of D_L. Accordingly, a mass-transfer condition that can be used for the fitting procedure in place of, say, a least squares requirement on $\tilde{H}_{f,2}$, would take the form

$$M_S - \int_{D_0}^{D_{Max}} \left(\frac{\pi}{6}\right) \rho_w D^3 \tilde{P}_{f,2}(D)dD =$$

$$\int_{D_L}^{D_C} \left(\frac{\pi}{6}\right) \rho_w D^3 P_{f,1}(D)dD - \left(\frac{\int_{D_L}^{D_C} P_{f,1}(D)dD}{\int_{D_0}^{D_C} P_{f,1}(D)dD}\right) M_L. \quad (6)$$

The right-hand side of (6) represents the

difference between the mass of the large-drop-remnants with diameter greater than D_L and the original mass of those large colliding drops that have grown as a result of mass transfer from the small colliding drop. For the other limiting case, the large drop that has lost some of its mass in the production of satellite drops will be counted in that part of $P_{f,1}(D)$ lying to the left of D_L. The satellite mass can be determined directly from the least squares fit of the data of LLa,b. The mass content of the large-drop remnants that have decreased in size then will necessarily equal the satellite mass if the mass-conservation constraint

$$\int_{D_0}^{D_C} P_{f,1}(D)dD + \int_{D_0}^{D_{Max}} \tilde{P}_{f,2}(D)dD + \int_{D_0}^{D_C} P_{f,3}(D)dD = M_S + M_L \quad (7)$$

is imposed.

Use of the relations (6) and (7) leads to narrow distributions describing the small- and large-drop remnants. If mass transfer and satellite production both occur in a filament-producing collision, as would be assumed to be the usual case, the large-drop-remnant distribution would be narrowed further, as any increase in the large-drop diameter due to mass transfer from the small drop would be offset by loss of mass due to satellite production. Thus, use of (6) with (7) yields a normal distribution $P_{f,1}(D)$ with the largest possible standard deviation.

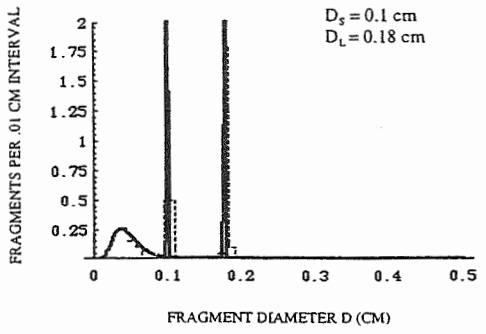

Fig. 3. As for Fig.1 but fit obtained using mass constraints (6) and (7) rather than least squares requirements on the heights of the small- and large-drop-remnant distributions.

Fig. 3 shows a fragment distribution function for colliding drops of diameters 0.18 and 0.10 cm. The fit is obtained by application of the mass-transfer relations above and a least squares fit of the histogram data of LLa for the satellite drops formed by collision. Comparison with Fig. 1 shows the narrowing of the distributions of the small- and large-drop remnants. Application of the relations to other cases involving other drop-sizes shows similar narrowing of the drop-remnant distributions. The results suggest that for filament breakup, delta functions would provide useful approximations to the small- and large-drop-remnant distributions. The next step in this research is to determine the effects of such modified fragment distribution functions on the evolution of the raindrop size distribution.

6. ACKNOWLEDGMENTS

This work was supported by the Division of Atmospheric Science of the National Science Foundation under Grant ATM-9812085.

7. REFERENCES

Brown, P. S., Jr., 1997: Mass conservation considerations in analytic representation of raindrop fragment distributions. *J. Atmos. Sci.*, **54**, 1675-1687.

Low, T. B., and R. List, 1982a: Collision, coalescence, and breakup of raindrops. Part I: Experimentally established coalescence efficiencies and fragment size distributions in breakup. *J. Atmos. Sci.*, **39**, 1591-1606.

_____, and _____, 1982b: Collision, coalescence, and breakup of raindrops. Part II: Parameterization of fragment size distributions. *J. Atmos. Sci.*, **39**, 1607-1618.

Whelpdale, D. M., and _____, 1971: The coalescence process in raindrop growth. *J. Geophys. Res.*, **76**, 2836-2856.

RESULTS OF CU INHOMOGENETIES STUDIES WITH THE HELP OF AIRCRAFT-LABORATORY

A.A.Sinkevich, J.A.Dovgaljuk, U.P.Ponomarev, V.D.Stepanenko

Cloud Physics Department, A.I.Voeikov Main Geophysical Observatory, Karbyshev str.7, St.Petersburg, 194021,Russia

1.INTRODUCTION

Cloud inhomogeneties are of great importance because they influence over cloud microphysics and hence cloud development. Different scales of cloud characteristics fluctuations were registered earlier - from short scale (cm and m) up to rather great scale - from hundreds of meters to kilometers (see Ackerman (1967), Brenguier (1993), Burtsev et al. (1992), Boicov et al.(1995), Drachyova et al.(1988), Sinkevich (1984), Vulfson et al. (1973), Zaicev and Ledohovich (1970), Rodi (1987). Role of these inhomogeneties in cloud development is not completely clear. Here we present some results of Cu inhomogeneties investigations which were obtained with the help of aircraft-laboratory; Begalishvily et al. (1993). Inhomogeneties with horizontal scale greater than 100 m were studied.

2.RESULTS OF EXPERIMENTS

2.1 Temperature fluctuations

Temperature fluctuations were studied with the help of IR radiometer operating in absorption water band centered at 6.3 mkm, Sinkevich (1981). Radiation was measured from horizontal path. The device provide possibility to exclude errors due to drops interaction with temperature probe and hence one correctly obtain data on temperature fluctuations.

20 aircraft flights were analyzed. Cu cong up to 4 km heights were studied. L- fluctuation length and T' - fluctuation amplitude were analyzed. L - is cloud length where fluctuation amplitude does not change sign. 427 fluctuations have been analyzed.

Corresponding authors address: Andrei A.Sinkevich, Cloud Physics Department, A.I.Voeikov Main Geophysical Observatory, Karbyshev str.7, St.Petersburg, 194021,Russia, E-Mail: sinkev@main.mgo.rssi.ru

2.1.1 Developing clouds

Averaged number of temperature fluctuations depends on height above cloud base (h) and minimum is observed at h=2-3 km. There is 3.8 fluctuations at this height. Averaged L and T' have here their maximums (L=0.43 km, T'=0.86 °C). Maximum repetition of L is observed within the range 0.1-0.5 km (more than 79% in dependence from height above cloud base). There is no clear dependency of T' from height above cloud base. Usually T' is within the limits 0.2 - 1.3 °C.

2.1.2 Dissipating clouds

Averaged number of temperature fluctuations does not depend on height above cloud base and is equal to 4.8. L is less than for developing clouds and is equal to 0.2-0.3 km. T' is also less here than for developing clouds. Maximum repetition is within the range 0.1-0.8°C.

2.2 Temperature fluctuations and drops concentration fluctuations

Simultaneous measurements of temperature fluctuations and relative drops concentration have been carried out. Location of subsequent maximums and minimums within cloud were analyzed. High correlation factor (0.96) was obtained for location of temperature and relative drops concentration maximums and minimums. 96 maximums and minimums were analyzed. Results of analyze show that there is temperature increase within regions where drop concentration increase and consequent decrease within the regions with smaller drops concentration.

2.3 Vertical length of temperature fluctuations

It is not a simple task to obtain information concerning vertical dimensions of cloud inhomogeneties. Some information is usually available by radar measurements, especially

Doppler radar measurements but radar data interpretation is also a problem. We have carried several experiments when 2 IR radiometers were operating simultaneously. One of them was measuring radiation from horizontal path and the other from nadir. Data analyze have shown that both devices have similar output signals within clouds. Radiation measured by devices is formed within the trace of nearly 50 m, so one can state that temperature fluctuations have vertical dimensions greater than 50-100 m.

2.4. In-cloud temperature structure

It is important for cloud modelling to obtain some dependency between in-cloud temperature from distance from cloud boundaries. To study such dependency we have chosen 20 clouds of nearly the same heights (2-3 km) where traverse path was divided into 10 parts in dependence from distance from cloud boundary (1 and 10 cloud parts are nearby parts to cloud boundaries, 5 and 6 - central cloud parts). Relative ratios T'i/T'm were analyzed (T'- difference between in-cloud and out-cloud temperatures, i-chosen cloud part, T'm - maximum T'i for chosen traverse). Though one can guess that there have to be some increase of ratio T'i/T'm in cloud central parts it was not discovered. The averaged T'i/T'm was within the limits 0.3-0.5 in most cases. Repetition of different values of this relation does not have expressed maximum or minimum and was usually the same for all cloud parts.

2.5. Temperature gradients

Temperature gradients is very important characteristic especially for different applied fields of science (radio waves propagation). Data on temperature gradients was analyzed for rather small Cu clouds (with heights 2-3 km). Temperature gradients in 20 clouds were analyzed. Data on |grad T| was obtained. Its value does not exceed 2.5 °C/100m. Averaged value was equal to 0.61, median - 0.5, mode - 0.3 °C/100 m. Maximum repetition was within the limits 0.2-1.0 °C /100 m - 83%.

2.6. Vertical flows velocity fluctuations

Vertical flows velocities fluctuations v' were investigated during one flight with the help of ultrasonic probe. Small Cu clouds were studied. Cloud base was at the height 1.0 km and cloud top reached 3 km. More than 200 fluctuations have been analyzed. v' varied from -5 up to 5 m/s. Maximum v' repetition was within the range 0.5 - 2 m/s for clouds in developing and mature living stage. Maximum v' repetition for clouds in dissipating stage were within the range -2 - 0.5 m/s.

2.7 Relative humidity fluctuations

Accurate measurements of relative humidity f in Cu clouds is a great problem. We have used dew point hygrometer to measure relative humidity. Small Cu clouds were studied. Measurements were carried out in 31 Cu. To exclude systematic errors differences between maximum relative humidity and minimum values (for each cloud) were analyzed. We guess that maximum measured f value in cloud is equal to 100%. Results have shown that this difference in 45 % of cases is greater than 5%, it is within the range of 10-20% - in 16% of cases.

2.8. Vertical flows, electrical field strength and temperature fluctuations

Simultaneous investigations of vertical flows, electrical field strength and temperature fluctuations were carried out. Cu cong transforming into Cb inc was studied. Aircraft had carried out 9 traverses through the cloud. 5-7 updrafts were registered in cloud with horizontal dimension 50-300 m. Updraft velocity reached 18 m/s and downdraft - -15 m/s. Measurements of electric field strength were carried out simultaneously. Correlation between vertical air velocity and electrical field strength E is small (this result was expected because E is integral characteristic but v' is local value) but there is E increase in downdrafts. It can be the result of charges separation due to precipitation which is observed there. High correlation is between vertical flows velocity and temperature fluctuations. Correlation factor for the discussed case was equal to 0.87. One can state that there is temperature increase in updrafts and temperature decrease in downdrafts. Just the same dependency was obtained for case of small Cu clouds measured with the same apparatus. Results have shown that for the same T,' v' for small Cu are 4 times less than v' for greater Cu clouds. So, though there is good correlation between T' and v' for chosen cloud (or cloud field) these dependency is very approximate in general.

3.Acknowledgements

Investigations were supported by Rosgidromet and RFBI.

4.References

Ackerman B.,1967: The nature of meteorological fluctuations in clouds. J.Appl.Met. v6, N1, p.61-71.

Begalishvily N.A. et al., 1993: Aircraft laboratory Yak-40. Meteorology and Hydrology, 4, 102-108.

Brenguier J.L.,1993: Observation of cloud microstructure at centimeter scale. J. Appl. Meteor.,32,783-793.

Burtsev I.I. et al., 1992: The investigation of convective clouds electrical structure dynamics. Proceedings 9 International Conference on Atmospheric Electricity, Leningrad, 189-192.

Boicov P.P., et al, 1995: Studies of lidar radiation extinction in clouds. VNIGMI MCD, dep.N1181, gm 95, 103-112.

Drachyova V.P., et al, 1988: Investigation of non-homogeneity of convective clouds, Leningrad, Gidrometeoizdat, Trudy MGO, 518, 145-150 .

Sinkevich A.A., 1981: To the analysis of IR-radiometer operation in measuring temperature of cloudless and cloud atmosphere. Trudy MGO, 439, 93-102.

Sinkevich A.A., 1984: Investigation of thermal characteristics of Cu cong using IR radiometer. Meteorology and Hydrology, 1, 40-46.

Rodi A., 1978: Small scale variability of the cloud droplet spectrum in cumulus clouds. Preprints Conference on Cloud Physics and Atmospheric Electricity. Washington, 88-91.

Vulfson N.I.,Laktionov A.G.,Skacky V.I., 1973: Cu structure at different stage of development. FAO, v.9, N5, 500-509.

Zaicev V.A. and Ledohovich A.A. 1970: Devices to investigate fogs and clouds and to measure humidity. Leningrad, Gidrometeoizdat, 256 p.

COMPARISON OF THEORY AND OBSERVATIONS OF BROADENING OF CLOUD DROPLET SIZE DISTRIBUTIONS IN WARM CUMULI

Sonia G. Lasher-Trapp[1,2] and William A. Cooper[2]

[1]Texas A&M University, College Station, TX, USA
[2]NCAR (ASP/MMM), Boulder, Colorado, USA

1. INTRODUCTION

As the search continues for the origin of large cloud drops capable of initiating coalescence in short-lived clouds like warm cumuli, a related issue is the apparent discrepancy between the narrowness of cloud droplet size distributions calculated using classic condensation theory and that of observed distributions. Parcel models that start with realistic CCN distributions and include the classic condensation theory are unable to produce broad size distributions, in the absence of entrainment and mixing. Compounding the problem, the observed size distributions are often artificially broadened by instrumental effects (see for e.g. Cooper 1988 and Baumgardner and Spowart 1990) which explain many of the differences between the modeled and observed size distributions.

Two different studies have addressed the discrepancy as real, and have given predictions of broadening that could occur within unmixed cores. Srivastava (1989) has suggested that the inadequacies of the present macroscopic theory of condensation, namely, the neglect of the spatial inhomogeneities in the droplet number and the effect of vertical velocity variations on supersaturation, can cause broadening of the size distribution. He has proposed a microscopic theory of condensation where the supersaturation is calculated at the droplet scale. Cooper (1989) has suggested that variations in vertical velocity at cloud base yield variations in supersaturation, which in turn cause variations in the number of droplets activated at cloud base, depending on the CCN distribution. Above the activation region, mixing of the parcels activated in different updrafts near cloud base then can broaden the size distribution.

Numerous studies have looked at the spatial distribution of droplets and their possible effect on broadening of the cloud droplet size distribution. Shaw et. al. (1998), using a Rankine vortex model, have suggested that spatial inhomogeneities of droplets (termed "preferential concentration") arising from vortex tubes within the cloud can lead to broadening of the cloud droplet size distribution caused by the resulting supersaturation variations. Vaillancourt (1998) has used direct numerical simulation (DNS) to calculate the distribution of the microscopic supersaturation perturbation over tens of thousands of droplets; he has found that sedimenting droplets grown in a turbulent field have much less size variation than they would have in the non-turbulent field considered by Srivastava (1989).

Chaumat and Brenguier (1998) have compared the observed spatial inhomogeneities of the droplets to the modeled spatial distributions of Vaillancourt and Shaw. The observed statistics are more in agreement with those of Vaillancourt's model, which has shown that the droplet spatial inhomogeneities have very short lifetimes (and thus contribute very little to broadening of the cloud droplet size distribution), rather than those of Shaw, where the inhomogeneities persist longer and have a broadening effect.

In the present study, the dispersion ($\frac{\sigma_d}{\bar{d}}$ or $\frac{\sigma_r}{\bar{r}}$) of cloud droplet size distributions from unmixed cloud regions observed during the Small Cumulus Microphysics Study are evaluated for several different clouds on two different days. These values are compared to modeled size distributions, using the adiabatic condensation parcel model of Cooper et al. (1997), initialized with the observed CCN distribution and cloud base properties. The differences in the modeled and observed size distributions arising from artificial instrumental broadening are addressed. The broadening predictions of Cooper (1989) and Srivastava (1989) are also evaluated with the available observations, to investigate if either prediction reconciles the observed and modeled size distribution dispersions after the instrumental broadening has been considered.

2. SELECTION OF UNMIXED CORES AND CLOUD DROPLET SIZE DISTRIBUTIONS

Unmixed regions of cloud penetrations are selected for study. A region is categorized as unmixed based on the maximum values and variances of (i) the 10 Hz FSSP (manufactured by Particle Measuring Systems, Boulder, CO) total cloud droplet number concentration, (ii) the 1000 Hz PVM-100A (Gerber 1994) liquid water content, (iii) the 25 Hz aircraft true air speed (only the variance) and (iv) the 25 Hz aircraft-measured vertical velocity. To be classified as an unmixed region, the maxima have to be

Corres. author's address: Sonia Lasher-Trapp, NCAR/MMM, P.O. Box 3000, Boulder, CO 80307-3000; E-mail: slasher@ucar.edu

reasonably colocated, and the variances have to be low. An example of an unmixed region is shown in Fig. 1.

Within the unmixed region of the cloud penetration, the FSSP cloud droplet size distribution over 1 s intervals is used to calculate the dispersion. (The dispersion is used here to evaluate the width of the size distribution, because the broadening predictions evaluated later are in terms of the dispersion). The size distributions have been partially corrected for dead-time effects (Baumgardner 1983) but have not been corrected for optical coincidences. (These corrections are addressed in the next section).

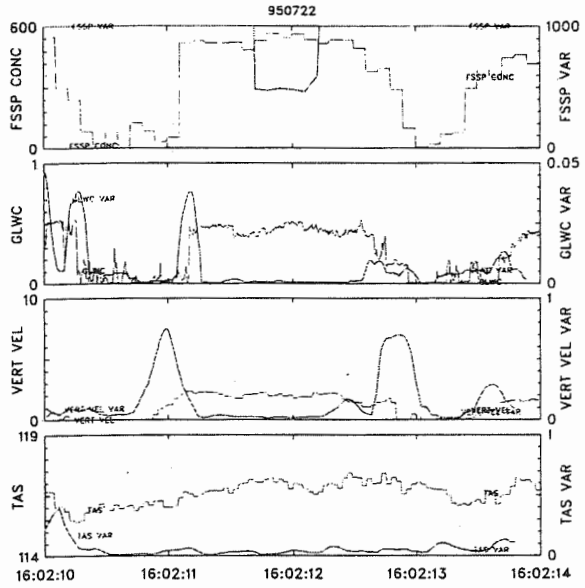

Fig. 1 Example of an unmixed region within a cloud penetration. Variables are, from top down, FSSP total concentration, cm^{-3} (left) and 1 s variance (right), PVM-100A liquid water content, g m^{-3} (left) and 0.2 s variance (right), vertical velocity, m s^{-1} (left) and 0.4 s variance (right), aircraft true air speed, m s^{-1} (left) and 0.4 s variance (right). Colocated maxima and low variances suggest the region between ~160211 and 160212.5 is unmixed.

3. MODELED SIZE DISTRIBUTIONS

To compare with the observed size distributions, the condensation parcel model of Cooper et al. (1997) is run. The model is initialized with the observed CCN distribution (C and k values), cloud base pressure and temperature and the environmental sounding. Entrainment and mixing are not considered. The parcel is given an initial 2 m s^{-1} vertical velocity, which then evolves with the buoyancy in the sounding. (An exception is the modeled size distributions very near cloud base; there the observed mean vertical velocity as measured by the aircraft is used). The C value from the CCN distribution is tuned, as well as the maximum height the model is run, to match the observed total droplet concentration and liquid water content of each observed size distribution.

The modeled size distributions are much narrower than those observed. To estimate the artificial broadening in the observed size distributions caused by optical coincidences, the modeled size distributions are run through the algorithm of Cooper (1988) and a newer algorithm to account for the effect of coincidences on the velocity acceptance test used in the FSSP data processing. The effect of coincidences increases the dispersion of the modeled size distribution. By calculating the additional variance in the modeled size distribution caused by coincidence effects, and subtracting this variance from the variance in the observed size distribution, an estimate of the true dispersion of the observed size distribution is made. The results are presented in Table 1.

4. BROADENING PREDICTIONS OF COOPER (1989) AND SRIVASTAVA (1989)

Three different predictions of broadening that could possibly widen the modeled size distributions are evaluated. Cooper (1989) has predicted that the amount of broadening near cloud base may be given by

$$\frac{\sigma_r}{\bar{r}} = \frac{k\sigma_w}{(4+2k)\bar{w}}, \qquad (1)$$

where k is the slope of the CCN distribution, σ_w is the vertical velocity standard deviation and $\bar{w}$ is the mean vertical velocity, all at cloud base. Table 1 contains the dispersion predictions from (1), where the mean vertical velocity and standard deviation are evaluated over 1 s. These values are the contribution to the overall dispersion, in addition to that calculated with the classic condensation theory which assumes a constant updraft speed. These predictions of broadening are quite small and do not fully explain the difference between the observed and modeled size distributions.

Srivastava (1989) has provided two predictions of broadening that can be evaluated with the observations higher up in the cloud, in unmixed regions. The first accounts for the effect of vertical velocity variations on a spatially inhomogeneous drop distribution, and is given by

$$\frac{\sigma_r}{\bar{r}} \approx \left[1 - 12\left(\frac{v}{\langle v\rangle_\infty}\right)^{2/3} l^{1/3}\right]\frac{\sigma_w}{\langle w\rangle_\infty}, \qquad (2)$$

where v is the volume occupied by a drop, $\langle v\rangle_\infty$ is the average volume occupied by a drop, l is the cloud liquid water content expressed as a volume fraction, σ_w is the standard deviation of the vertical velocity and $\langle w\rangle_\infty$ is the average vertical velocity. Observations of these variables on the droplet scale (for which (2) was derived) are unknown, but Srivastava asserts that evaluations over larger scales should show a similar effect. Thus $\langle v\rangle_\infty$, $\langle w\rangle_\infty$ and σ_w are evaluated over 1 s, and v is evaluated over

0.1s. As shown in Table 1, these values are always larger than (1), sometimes by an order of magnitude. The second prediction addresses broadening arising from both spatial inhomogeneities and size variations of the drops:

$$\frac{\sigma_r}{\bar{r}} \approx \frac{144}{2} l^{2/3} \Gamma\left(\frac{1}{3}\right)\left[\left(\frac{r}{\langle r\rangle_\infty} - \frac{1}{3}\right)^2 + \frac{1}{3}\right], \qquad (3)$$

where r is the 0.1 s average droplet radius and $\langle r\rangle_\infty$ is the 1 s average droplet radius. The derivation of (3) assumes a Poisson spatial distribution of drops. As shown in Table 1, these values are sometimes much smaller than those for (2), and are comparable to those evaluated using (1).

5. DISCUSSION

Observed and modeled cloud droplet size distributions at different heights, on two different days, have been compared. The modeled size distributions have dispersions an order of magnitude less than the observed size distributions. However, subtracting estimations of coincidence effects decreases the observed size distributions significantly.

For the 11 Aug cases, the difference in the dispersions of the modeled and observed (coincidence-corrected) size distributions is small, sometimes less than 0.1. These small differences might be explained by additional effects of coincidence or other instrumental broadening beyond that estimated. Thus, from the 11 Aug cases, it is not clear that any discrepancy between the modeled and observed size distributions is real.

The cases on 22 July show a different picture, however. Here the effect of the coincidence corrections is less important, and thus larger differences in the modeled and observed dispersions remain. For these cases, some additional source of broadening seems indicated. It appears possible that the differences in the modeled and observed dispersions for the 22 July case could be reconciled with the broadening predictions (2) and (3).

These preliminary results suggest further investigation of both coincidence effects and the microscopic theory of condensation is needed. Additional evaluations of Srivastava's predictions with observations are needed to support the microscopic theory; this should be possible using the SCMS data set.

Table 1. Calculated dispersion for observed (OBS), observed with estimated corrections for effects of coincidence (OBS-C), and modeled (MODEL) cloud droplet size distributions, for 22 July (J) and 11 Aug (A), difference in dispersions of OBS-C and MODEL (DIFF), predicted dispersions given by eqns (1), (2) and (3), and total predicted dispersion (TOTAL). Heights (HT) of observed size distributions are above cloud base.

TIME	HT (M)	OBS	OBS-C	MODEL	DIFF	(1)	(2)	(3)	TOTAL
J152002-04	1080	0.24-0.29	0.20-0.25	0.02	0.18-0.23	0.01-0.02	0.05-0.06	0.06-0.07	0.12-0.15
J160211-12.5	120	0.28-0.30	0.27-0.28	0.05	0.22-0.23	0.01-0.02	0.07-0.08	0.03-0.04	0.11-0.14
J163629-22	1060	0.25-0.27	0.20-0.22	0.02	0.18-0.20	0.01-0.02	0.07-0.09	0.06	0.14-0.17
A140256-57.5	80	0.22-0.26	0.09-0.17	0.01	0.08-0.16	0.02-0.03	0.15-0.30	0.03	0.20-0.36
A140540-45	80	0.25-0.29	0.16-0.24	0.01	0.15-0.23	0.02-0.03	0.08-0.31	0.02-0.03	0.12-0.37
A141949-51	400	0.20-0.22	0.15-0.18	0.02	0.13-0.16	0.02-0.03	0.17-0.21	0.08-0.09	0.27-0.33
A143650-54	385	0.20-0.22	0.13-0.17	0.02	0.1-0.15	0.02-0.03	0.10-0.15	0.05	0.17-0.23

6. ACKNOWLEDGMENTS

This research was supported in part from the NSF grant ATM-9707301 and the NCAR Advanced Study Program. All of the participants of the SCMS are thanked for their data collection efforts.

7. REFERENCES

Baumgardner, D., 1983: An analysis and comparison of five water droplet measuring instruments. *J. Appl. Meteor.*, **22**, 891-910.

_____, and M. Spowart, 1990: Evaluation of the forward scattering spectrometer probe. Part III: Time response and laser inhomogeneity limitations. *J. Atmos. Ocean. Tech.*, **7**, 666-672.

Brenguier, J. L., T. Bourrianne, A. A. Coelho, J. Isbert, R. Peytavi, D. Trevarin and P. Wechsler, 1998: Improvements of the droplet size distribution measurements with the Fast-FSSP. *J. Atmos. Ocean. Tech.*, **15**, 1077-1090.

Chaumat, L. and J. L. Brenguier, 1998: Droplet spectra broadening and concentration inhomogeneities. *Proceedings AMS Conf. on Cloud Physics*, 514-517.

Cooper, W. A., 1988: Effects of coincidence on measurements with a forward scattering spectrometer probe. *J. Atmos. Ocean. Tech.*, **5**, 823-832.

_____, 1989: Effects of variable droplet growth histories on droplet size distributions. Part I: Theory. *J. Atmos. Sci.*, **46**, 1301-1311.

_____, R. F. Bruintjes and G. K. Mather, 1997: Calculations pertaining to hygroscopic seeding with flares. *J. Appl. Meteor.*, **36**, 1449-1469.

Gerber, H., B. G. Arends and A. S. Ackerman, 1994: New microphysics sensor for aircraft use. *Atmos. Res.*, **31**, 235-252.

Shaw, R. A., W. C. Reade. L. R. Collins and J. Verlinde, 1998: Preferential concentration of cloud droplets by turbulence: Effects on the early evolution of cumulus cloud droplet spectra. *J. Atmos. Sci.*, **55**, 1965-1976.

Srivastava, R. C., 1989: Growth of cloud drops by condensation: A criticism of currently accepted theory and a new approach. *J. Atmos. Sci.*, **46**, 869-887.

Vaillancourt, P. A., 1998: Microscopic approach to cloud droplet growth by condensation. Ph.D. dissertation, Mc Gill University, Montral, Quebec, 154pp.

DROPLET SPECTRUM BROADENING: EFFECT OF IN-CLOUD NUCLEATION AND DROPLET COLLISIONS

Alexander Khain and Mark Pinsky

Department of Atmospheric Sciences, The Hebrew University of Jerusalem, Israel

1. INTRODUCTION

The width of droplet size spectra determines the precipitation formation, development of cloud ice, as well as radiative properties of clouds. Dues to this significance the processes of droplet size spectrum formation have attracted the attention of investigators for a long time. The history of these investigations is quite dramatic. The diffusion growth equation predicts a faster growth of smaller droplets, as well as a narrowing of the initial droplet size distribution with the height.

At the same time, in-situ observations (Warner, 1969; Brenguier, 1998) show wide spectra and a broadening of the spectra with the height in cumulus clouds, including the undiluted cores. Droplet size spectra regularly observed in cumulus clouds at distances of a few hundred meters above cloud base contain along with larger droplets of 10-15 μm in radius, also smaller 1 - 8 μm - radii droplets. These spectra are often bi-modal, with the maxima centered at about 5-7 μm and 10-12 μm . The existence of small droplets at so high levels is so mysterious, as the existence droplets with radii exceeding upper theoretical limit.

Another mystery problem is relatively rapid formation of raindrops (typically for 15-20 min): the classical theory based on the collision efficiencies and kernels calculated for calm air conditions demands several hours for formation of droplets with radii as large as 300 μm . Here we show that droplet size spectrum broadening in convective clouds at the stage of condensation growth is caused by in-cloud nucleation. The related droplet spectrum broadening makes droplet collisions possible. Realistic time of raindrop formation is shown to be the result of turbulence effects accelerating drop collisions.

2. CONCEPT OF THE DROPLET SPECTRUM BROADENING

Particles in supersaturated air can be separated into non-activated aerosol particles (AP) and droplets. The higher supersaturation is, the more AP are activiated and the higher the concentration of droplets is. When AP enter a cloud, some of them experience activation in the vicinity of the cloud base and grow as cloud droplets. The rest of AP rise within cloud updrafts together with cloud droplets. These APs serve as a potential reservoir of new droplets. If supersaturation in a rising cloud parcel exceeds the values of supersaturation in the parcel during its preceding ascent, a new portion of APs will be activated and new droplets will be nucleated. (Pruppacher and Klett, 1997). The mechanisms controlling the values of supersaturation in a rising liquid-phase cloud parcel can be expressed by the equation for saturation S (Pruppacher and Klett, 1997):

$$\frac{dS}{dt} = A_1 W - A_2 \frac{dq_L}{dt} , \qquad (1)$$

where W is the updraft speed, q_L is the molar mixing ratio of liquid water in the air, and the coefficients A_1 and A_2 depend on various thermodynamic parameters (temperature, latent heat of vaporization, air viscosity, etc).

In the vicinity of the cloud base the first term is much larger than the second one because of the lack of droplets, and S in the cloud parcel rapidly increases with height. Nucleated droplets absorb water vapor, tending to decrease S. As a result S attains its local maximum at 10-20 m above the cloud base. Thus, the problem of in-cloud nucleation of new droplets is reduced to the following question: under what conditions can the supersaturation within a rising cloud parcel exceed the maximum it reaches at the cloud base? It seems to be paradoxical that the crucial effect of the increase in vertical velocity with height has on the droplet size distribution, which follows from eq.(1), has not been well recognized. In most theoretical studies W is assumed to be constant (Rogers and Yau, 1987). The supersatiration in cloud parcel rising with a constant speed attains its maximum at about ten meters above the cloud base and then monotonically decreases with height, the whole droplet nucleation is concentrated in the vicinity of the cloud base. As a result, a monodisperse, narrow size spectrum is formed.

When realistic vertical profiles of updraft speed are taken into account, supersaturation in a rising cloud parcel can exceed the maximum at the cloud base, and thus in-cloud nucleation and the droplet size spectrum broadening takes place.

Formation of a wide droplet spectrum allows droplets to collide with the formation of large droplets of superadiabatic size and sequent raindrops.

3. MICROPHYSICAL MODEL

A low spatial resolution, small number of mass bins for the size spectrum reproduction, necessity to distribute intermediate drop masses between bins of a regular mass grid at each time step leads to an artificial non-controlled spectrum broadening in state-of the art cloud models.

We designed a microphysical model which contains no artificial broadening at any stages of droplet spectrum evolution. We use a cloud parcel model as a dynamic part of the model. The equation system includes the

*Corresponding author address: Prof. Alexander P. Khain, Institute of the Earth Science, The Hebrew University of Jerusalem, Givat Ram, Jerusalem 91904, Israel, Khain@vms.huji.ac.il

equation for diffusion growth, as well as the equations for supersaturation, temperature and updraft speed of a rising cloud parcel (Pruppacher and Klett, 1997). To describe the size distribution of non-activated AP and droplets we use 2000 mass bins corresponsing to particle radii 0.05μm to 2000 μm. In our calculations of the diffusion growth we do not differentiate atmospheric particles between aerosols and droplets. To eliminate any artificial broadening, we do not use any regular mass grid: particles (aerosols and droplets) grow according to the diffusion growth equation, so that new set of drop masses is formed at each sequent time step. Utilization of large number of bins allows us to conduct droplet activation smoothly avoiding sharp jumps in drop concentration.

We use an accurate method proposed by Bott (1998) to solve kinetic stochastic equation for collisions. Drop collisions are calculated using variable drop mass grid formed by diffusion. The growth of the collision kernels with height found by Pinsky et al. (2000a) was taken into account.

To take into account effects of turbulence the collision kernels were increased by factors depending on sizes of colliding droplets. The factors were chosen basing on the evaluations made by Pinsky et al (1999, 2000b) for turbulence intensities of 100-200 $m^2 s^{-3}$ typical of early cumulus clouds. The collision kernels were increased by factor of 5; 2; 1.5; 1.3 and 1.2 for droplet pairs containing droplets with radii smaller than 10 μm, for droplet pairs with radii 10 μm -20 μm, 20 μm -30 μm and 30-40μm, and for pairs containing small raindrops (r <250 μm) and small cloud droplets (r< 3 μm), respectively. For other drop pairs the collision kernel was increased by 15%.

The aerosol size distribution is taken as suggested by Respondek et al (1995). We do not include droplets with radii exceeding 4 μm at the cloud base. Cloud base level is equal to 0.75 km.

4. RESULTS

We have conducted simulations of a droplet size spectrum development up to the level of 4 km above the cloud base. **Figure 1a,b** shows vertical profiles of vertical velocity and supersaturation, respectively, for cloud parcels with updraft speeds at the cloud base W_0 of 3 ms^{-1} and 0.25 ms^{-1}. We believe that vertical velocities at cloud base of cumulus clouds fall within this range. **Figure 1c** shows vertical profiles of droplet concentration. In supplemental simulations analogous profiles were calculated for intermediate values of W_0, as well as for height independent vertical velocities assumed to be equal to those at the colud base. The analysis of the results shows that: a) For W =const the supersaturation decreases monotonically with height above the local maximum of supersaturation in the vicinity of the cloud base. This behavior accords to the classical results (Rogers and Yau, 1989); b) in case the vertical velocity acceleration is taken into account and W_0 is below about 1-1.5 ms^{-1}, supersaturation in a cloud updraft can exceed the local maximum at the cloud base. Within the layer, where supersaturation increases with height being higher than the local maximum at the cloud base (shaded zone in Figure 1b), in-cloud nucleation and the formation of a bimodal droplet size distribution takes place and leads to the droplet spectrum broadening. At $W_0 > 1.5 ms^{-1}$ supersaturation within the cloud does not exceed the local maximum at the cloud base; c) analysis allows one to divide vertical

Figure 1 a) Vertical profiles of updraft speed, b) supersaturation, and c) droplet concentration for cloud parcels with vertical velocities at the cloud base W_0 of 3 ms^{-1} and 0.25 ms^{-1}.

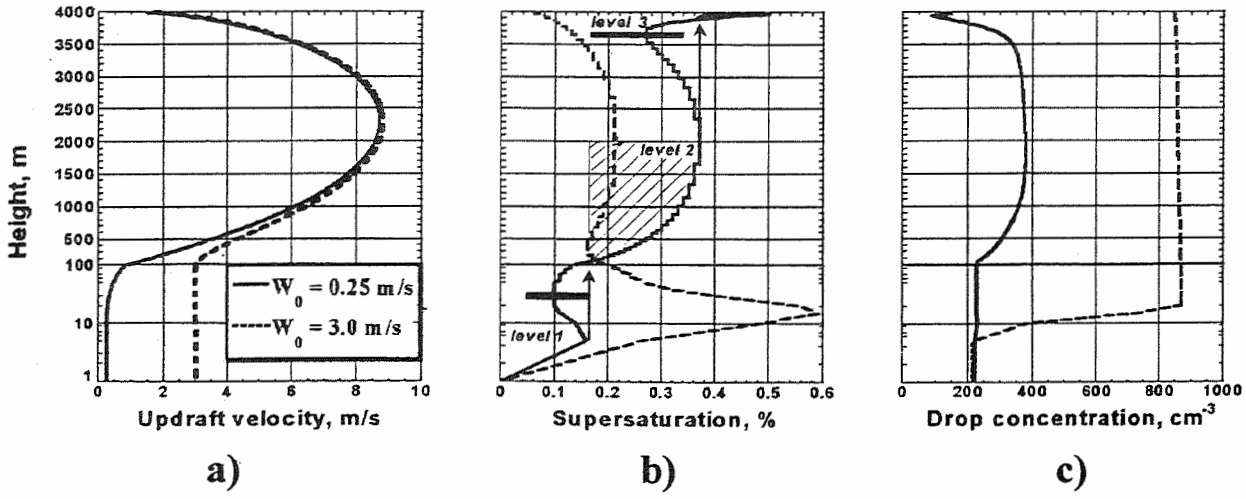

profiles of supersaturation into three layers clearly seen in case of low W_o and significant buoancy within the cloud layer (fig. 1b). The lowest 10-100 m depth layer is characterized by the local maximum of supersaturation in the vicinity of the cloud base. The magnitude of the maximum increases with the increase in W_o. Droplets formed in this layer will be of the maximum size in the droplet size distribution. The second layer is characterized by an increase in supersaturation due to the boyancy-induced acceletation of the updraft (stage of diffusional droplet growth). The in-cloud nucleation leads to the formation of the second peak in the droplet size distribution. Thus, the bi-modal spectrum arises. When the acceleration of the updraft speed slows down, the supersaturation begins to decrease with height. As a result, the second maximum in the supersaturation profile arises.

Beginning of efficient droplet collisions can be seen by a decrease in the droplet concentration above 2000 m. The latter leads to the formation of the third layer of supersaturation growth. The increase in supersaturation can lead to a new nucleation at heights as large as a few kilometers above the cloud base. These droplets form the third peak of the smallest droplets with sizes as low as 1-3 μm. This peak was observed in detailed measurements by Alkezweeny (1995) within the layer 4-8 km above the cloud base. The existence of the third peak can be considered as an indication of a strong collision rate at this level. It is clear that the exsistence/absence of one or another peak depends on the value of vertical velocity at the cloud base and its acceleration above.

Figure 2a,b show droplet size spectra at different height levels in cases W_o = 3 ms^{-1} and 0.25 ms^{-1}, respectively. High updraft speed at the cloud base leads to the droplet concentration of 850 cm^{-3} and no raindrop formation up to 4000 m above the cloud base. In contrast, low updraft speed at the cloud base leads to raindrop formation above 3500 m. In **Figure 3a,b** size spectra formed in case of no turbulence effects are presented. Comparison of Figures 2 and 3 indicates that turbulence increases the width of the droplet size distribution, but while in case W_o = 3 ms^{-1} this increase turned out to be not sufficient for triggering of collisions, it accelerates significantly raindrop formation in case of W_o = 0.25 ms^{-1}. Note that the major effect of turbulence is observed for clouds with droplet concentration of 300-500 cm^{-3}. While raindrops do not form in case of no turbulence, they rapidly form above 3 km layer with the

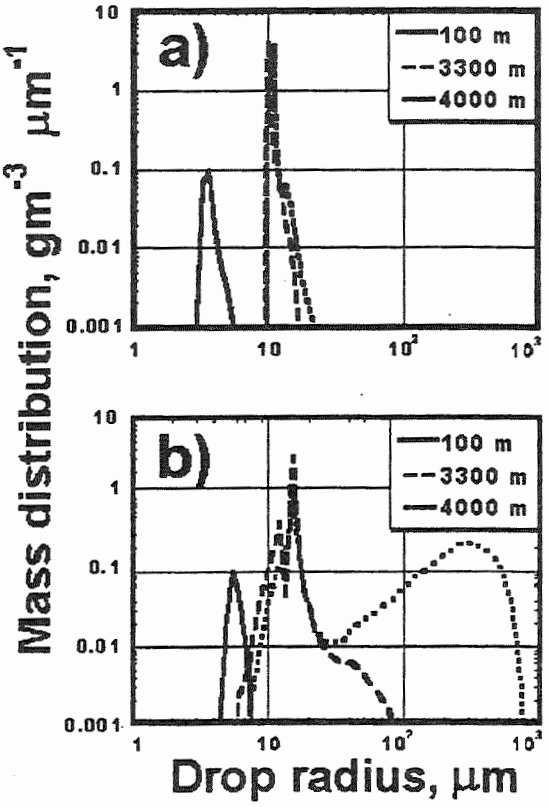

Figure 2. Droplet size spectra at different heights in cases (a) W_o = 3 ms^{-1} and (b) 0.25 ms^{-1}.

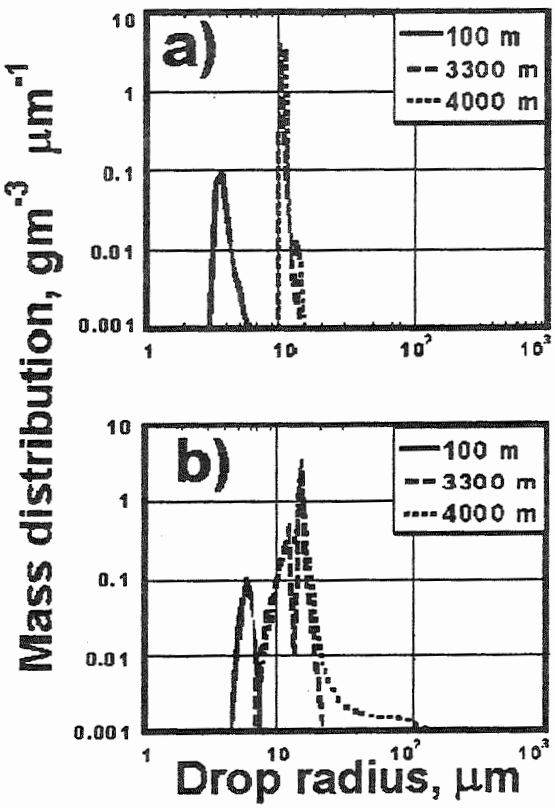

Figure 3. The same as in Figure 2, but with no turbulence effects.

turbulent effects included. This effect is illustrated in **Figure 4**, where the fraction of raindrop content (drops with radii exceeding 50 μm) in the total liquid water content is plotted both for non-turbulent and turbulent cases.

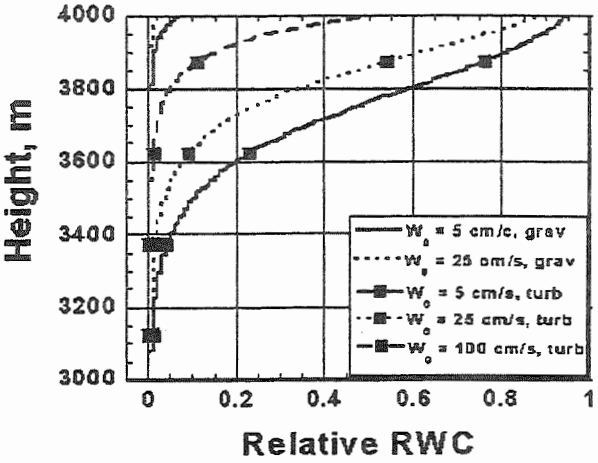

Figure 4. Fraction of rain content (drops with radii exceeding 50 μm) in the total liquid water content in non-turbulent and turbulent cases.

5. CONCLUSIONS

A precise microphysical model with no artificial broadening of droplet size spectrum is developed and used for investigation of the problem of the droplet spectrum formation. It is shown that two natural mechanisms contribute to formation of droplet size specrta: a) In-cloud This effect is especially pronounced for clouds with drop concentration of 300-500 cm^{-3}. In case the droplet concentration exceeds about 800 cm^{-3}, the broadening of droplet spectrum induced by turbulence is not enough to nucleation leading to formation of droplets with sizes below adiabatic value; b) the formation of droplets with size exceeding adiabatic value by collisions.

Turbulence accelerates significantly raindrop formation. This effect is especially pronounced for clouds with droplet concentration of 300-500 cm^{-3}. In case the droplet concentration exceeds about 850 cm^{-3}, the broadening of droplet spectrum induced by turbulence is not enough to trigger droplet collisions. For clouds with low droplet concentration (below 150 cm^{-3}) raindrops are formed for 20 min in non-turbulent case. In this case turbulence accelerates raindrop formation by 20-40 %.

The formation of wide and bi-modal droplet size spectra, the dependence of their occurence on thermodynamic conditions (see Segal et al, 2000 for more detail), raindrop formation during 15-20 min., etc., have found their explanation.

The results presented in the study are of significant importance for understanding the difference in formation of continental and maritime clouds. It is usually thought that the main factor determining one or the other cloud type is the shape of aerosol spectrum (Rosenfeld, 1999; Khain et al, 1999). It is known (Zipser and LeMone, 1980) that thermal instability of the tropical atmosphere is lower than in the extratropical latitudes or over continents, so that the mean updraft speeds in cumulus clouds over tropical oceans are lower than those typical of continental clouds. This means that stability conditions over the tropical oceans favor the formation of maritime clouds with a wide droplet spectrum and low droplet concentration, while stability conditions over the continents favor the formation of continental type clouds with higher droplet concentrations, narrower size distributions and significant ice phase contributions, even under the same assumed aerosol properties.

Acknowledgements. This study was partially supported by the Israel Science Foundation administrated by the Israel Academy of Sciences and Humanities (grants 572/97, 143/99) and the Germany-Israel Science Foundation (grant 0407-008.08/95).

References

Bott, A., 1998: A flux method for numerical solution of stochastic collection equation, *J.Atmos.Sci.*, 55, 2284-2293

Brenguier, J.-L., 1998: Droplet spectra broadening in cumulus clouds: review of advances in observations and numerical simulations. Proceed. of AMS Cloud Conference, Everett, Aug 17-22.

Alkezweeny, A.J., 1995: Field observations of in-cloud nucleation and the modification of atmospheric aerosol size distribution after cloud evaporation. *J. Appl. Meteor.*, 34, 2649-2654.

Khain, A., A. Pokrovsky, and I. Sednev (1999) Effects of cloud-aerosol interaction on cloud microphysics, precipitation formation and size distribution of atmospheric aerosol particles: numerical experiments with a spectral microphysics cloud model. *Atmos. Res.* 52, 195-220.

Pinsky, M., A. Khain, and M. Shapiro (1999) Collisions of small drops in a turbulent flow. Pt.1 : Collision efficiency: problem formulation and preliminary results. *J. Atmos. Sci.* , 56, 2585-2600.

Pinsky, M., A. Khain, and M. Shapiro and A. Pokrovsky, 2000a: Collision efficiency of drops in a wide range of Reynolds numbers: Effects of pressure on spectrum evolution. J. Atmos. Sci. (in press).

Pinsky, M., A. Khain , and M. Shapiro, 2000b: Stochastic effects of cloud droplet hydrodynamic interaction in a turbulent flow. *Atmospheric Research (in press).*

Politovich, M. K., 1993: A study of the broadening of droplet size distribution in cumuli. *J. Atmos. Sci.*, **50**, 2230-2244.

Pruppacher, H. R., and J. D. Klett, *Microphysics of clouds and precipitation*, Oxford Press, 950 p. (1997).

Respondek, P. S., A. I. Flossman, R. R. Alheit, and H. R. Pruppacher, 1995: A theoretical study of the wet removal of atmospheric pollutants. Part V: The uptake, redistribution, and deposition of $(NH_4)_2SO_4$ by a convective cloud containing ice. *J. Atmos. Sci.*, **52**, 2121-2132.

Rogers, R. R., and M.K. Yau, *A short course of cloud physics.* Pregamon, Oxford, 293 pp. (1989).

Rosenfeld, D.*Geophysical Research Letters.* 26 , No. 20 , 3105 (1999)

Segal, Y. , A.P. Khain, and M. Pinsky, 2000:The influence of thermodynamic conditions in the boundary and cloud layers on the droplet spectrum formation in cumulus clouds (this issue).

Warner, J., 1969: The microstructure of cumulus cloud. Part 1: general features of the droplet spectrum. *J. Atmos. Sci.*, **26**, 1049-1059.

Zipser, E.J. and M. A. LeMone, 1980:Cumulonimbus vertical velocity events in GATE. Part 2: Synthesis and model core structure. J. Atmos. Sci., 37, 2458-2469.

Turbulent nature of fine structure of cloud droplet concentration as seen from the Fast-FSSP measurements

M. Pinsky[1], A. Khain[1] and J.-L. Brenguier[2]

[1]Institute of the Earth Science, The Hebrew University of Jerusalem, 91904, Israel
[2]METEO-FRANCE(CNRM/GMEI) 42 Av. G. Coriolis, 31057, Toulouse Cedex 01, France

1. INTRODUCTION

According to the theory (e.g. Pinsky et al., 1999), droplet inertia can lead to the formation of centimeter-scale drop concentration fluctuations due to centrifugal forces resulting in the deviation of droplet tracks from surrounding air. The drop flux, therefore, turns out to be divergent in a non-divergent air flow. Some laboratory (Fessler et al. 1994) studies, as well as DNS (Wang and Maxey, 1993) support the theoretical predictions as concerns to the formation of small-scale concentration fluctuations of inertial particles a turbulent flow.

The small-scale fluctuations of droplet concentration can play important role in microphysical cloud processes (condensation and collisions). That is why the detection of such fluctuations and estimation of their parameters in clouds is an important problem. There no consensus concerning the existence of such drop concentration inhomogeneity in cumulus clouds (Grabowski and Vaillancourt, 1999).

Pinsky et al (1998, 2000) designed a precise statistical method allowing one to reveal such fluctuations in series of drop arrival times in-situ measured using the Fast Forward Scattering Spectrometer Probe (FFSSP) (Brenguier et al, 1998). This method was used for analysis of a single case, in which significant (30% on the mean value) centimeter-scale droplet concentration fluctuations were found. In this paper we use the method for analysis of series of droplet arrival times measured by FFSSP during aircraft flights in 79 cumulus clouds. The aim of the study is to evaluate the dependence of parameters of centimeter-scale drop concentration fluctuations on intensity of turbulence and drop size and compare the results to those following from the theory.

2. THEORETICAL BACKGROUND

The divergence of cloud droplet flux responsible for formation of drop concentration fluctuations is determined as (Maxey, 1987; Pinsky et al, 1999):

$$\mathrm{Div}\, V = -\frac{V_t}{g}\frac{\partial u_i}{\partial x_j}\frac{\partial u_j}{\partial x_i}, \qquad (1)$$

where V_t is the terminal fall velocity of droplets in cal air, u_i are the velocity components of a turbulent air flow.

The drop flux divergence attains its maximum centimeter-scales. Its value depends on the turbulen dissipation rate ε , and drop radius r_d as (Pinsky et 1999):

$$\sigma_D = \langle D^2 \rangle^{1/2} = \frac{1}{9}\frac{\varepsilon\,\rho_w}{\nu^2 \rho_a} r_d^2, \qquad (2)$$

where ν is the air kinematic viscosity, ρ_a and ρ_w a the densities of air and water. It is natural to assume th droplet concentration inhomogeneities caused by tl droplet inertia will also take place at these centimet scales. Dominating of spatial scale of about centimeter related to the increase in turbulent velocity shears down smaller scales in the inertial range until the viscosity effec become significant.

The formation of droplet concentrati inhomogeneities at larger scales is caused by oth mechanisms, for instance, fluctuations of vertical veloci at the cloud base (Cooper, 1989), entrainment of drop free air parcels with sizes from a few meters to several te of meters at the cloud periphery (Grabowski, 199 Korolev and Mazin, 1993), etc. These drop concentrati fluctuations are related to turbulent fluctuations of veloci which energy increases with the size of turbulent vortice Thus, one can expect that the amplitude of these drop concentration fluctuations increases with an increase in tl spatial scale, in accord with the energetic spectra turbulent velocities.

We expect, therefore, that the centimeter-scale dr concentration fluctuations are well separated fro fluctuations on larger scales.

3. METHOD OF ANALYSIS

In the analysis, the series of droplet arrival tim obtained using the FFSSP is regarded to as a generaliz

* Corresponding author address: Dr. Mark Pinsky, The Institute of Earth Sciences, The Hebrew University of Jerusalem, Givat Ram, Jerusalem, Israel. Email: mark@atmsg3.es.huji.ac.il

Poisson process with parameters changing with space. In accordance to the ideas of scale separation of drop concentration inhomogeneities, droplet concentration in a cloud along the aircraft track is represented as the sum of three components: average droplet concentration in a cloud; large-scale fluctuations of droplet concentrations described by the Fourier series, and a small-scale non-coherent fraction of concentration fluctuation characterized by the energy spectrum and the correlation function. Method of the analysis is discussed by Pinsky et al. (1998, 2000) in detail. Method allows one to estimate spectra and correlation functions of small-scale drop concentration fluctuations, as well as to estimate profiles of large-scale concentration fluctuations along an aircraft track.

The ability of the method to estimate the amplitude and spatial characteristics of small-scale droplet concentration fluctuations, as well as to calculate profile of large-scale concentration fluctuations is carefully tested using model simulated series of droplet arrival times. An example of the testing is presented in Figure 1.

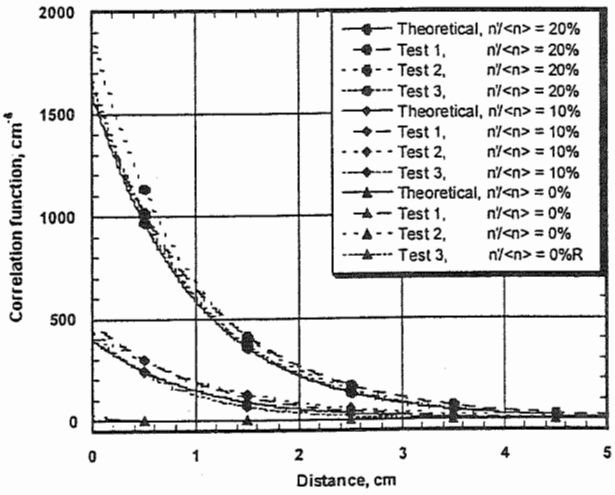

Figure 1. Exponential approximations of the estimated correlation functions obtained in proceeding test series of drop arrival times for small-scale droplet concentration fluctuations with root-mean-square amplitudes of 0%, 10% and 20% of the mean droplet concentration for different types of large-scale droplet concentration fluctuations. Small-scale fluctuations have the same correlation lengths (1 cm) and different amplitudes (0%, 20% and 40% of the mean value of drop concentration). Theoretical correlation functions are presented for sake of comparison (solid lines).

Errors in the restoring amplitudes and correlation scales of droplet concentration fluctuations do not exceed 10% in most tests.

In addition to parameters of drop concentration fluctuations, we conduct estimations of droplet size distributions and turbulent dissipation rate. We estimat the drop size distribution and its parameters using observ data of the same FFSSP. Energy dissipation rate w estimated using profiles of vertical air velocity along clo traverse. Using the values of vertical velocity fluctuatior we calculated transverse structure functions of the turbule velocities. The structure function is proportional $\varepsilon^{2/3} r^{2/3}$, where r is the spatial scale. An example of t estimated structure function is presented in Figure 2. T method of the determination of ε is illustrated in t Figure.

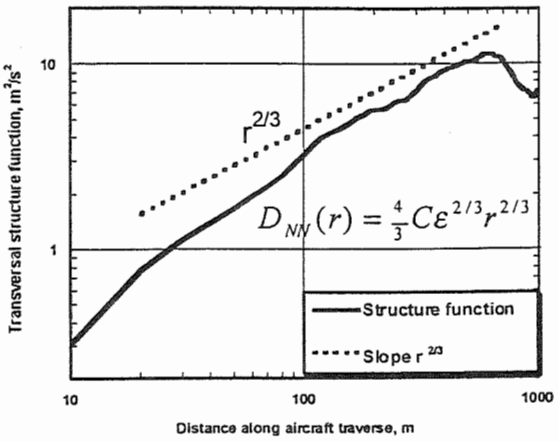

Figure 2. An example of the estimated structure function

4. RESULTS

We analyze in-situ observed data obtained during the flig on 22.12.97, 15.09-16.34. The aircraft crossed 79 cumul clouds at different height levels from 700 m to 2770 Drop concentration in these clouds varies from 20 cm^{-3} 450 cm^{-3}, the mean drop radius varies from 6 μm to μm. The estimated kinetic dissipation energy ranges fro 0.5 $cm^2 s^{-3}$ to 370 $cm^2 s^{-3}$.

We analyze clouds which the dissipation rate exceeded $cm^2 s^{-3}$. In addition, only sections covered by ascendi air were chosen. This way we tried to use mo homogeneous data set and to eliminate possible influen of processes at the cloud top. As a result, 64 travers among 79 were selected.

Figure 3 shows the amplitude of small-scale dr concentration fluctuations as a function of the droplet fl velocity divergence calculated according to (2). One c see a pronounced increase in the amplitude of centimet scale fluctuations with the divergence. The amplitude these fluctuations is of a few percents for the divergence 10^{-3} s^{-1}, and attains values as large as 30% at t

divergence of 2 s^{-1}. High values of divergence correspond as a rule to large values of $\mathcal{E}$ of 200-400 $cm^2 s^{-3}$. The correlation coefficient (0.8) is rather high for such type of measurements, taking into account significant inevitable errors in the determination of $\mathcal{E}$. Analysis allows us to determine a regression dependence, shown in the Figure. This dependence is of power type one.

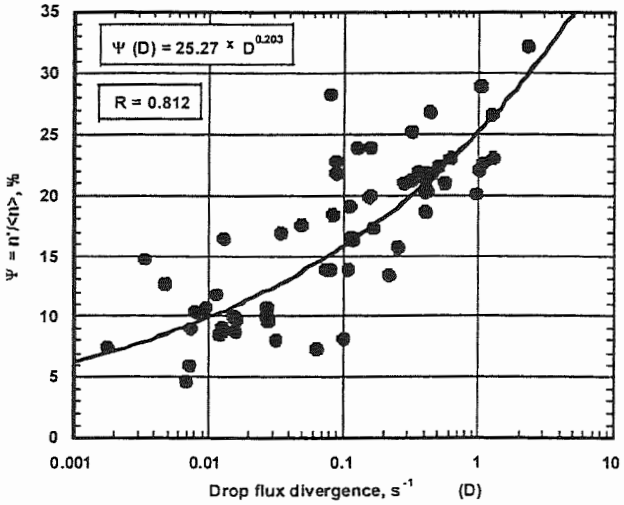

Figure 3. Amplitude of small-scale drop concentration fluctuations as a function of the droplet velocity flux divergence (2).

This dependence will be useful for further parameterization of the fine microstructure of clouds. This result clearly indicates that the centimeter-scale droplet concentration fluctuations are caused by the turbulent-inertia mechanism.

Figure 4 shows a scattering diagram of spatial scales of small-scale drop concentration fluctuations on droplet flux divergence. Expected decrease in the scales with the increase of the divergence can be seen. This fact can be attributed as an additional evidence of turbulent-inertia nature of the mechanism leading to formation of small-scale concentration fluctuations.

Figure 5 illustrates the ability of the method proposed to calculate the profile of large-scale drop concentration fluctuations. The profile obtained by Pawlowska and Brenguier (1997) using an optimal estimator is presented for comparison. A good agreement of results is clearly seen.

When analyzing in-situ measurements, we obtained an interesting result related to large-scale drop concentration inhomogeneities with wavelengths exceeding 3 m. We calculated spectra of these drop concentration fluctuations spectra of these fluctuations

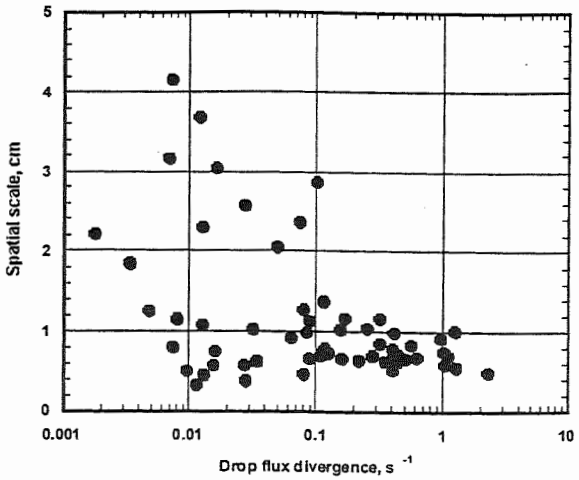

Figure 4. Scattering diagram of spatial scales of small-scale drop concentration fluctuations on droplet flux divergence.

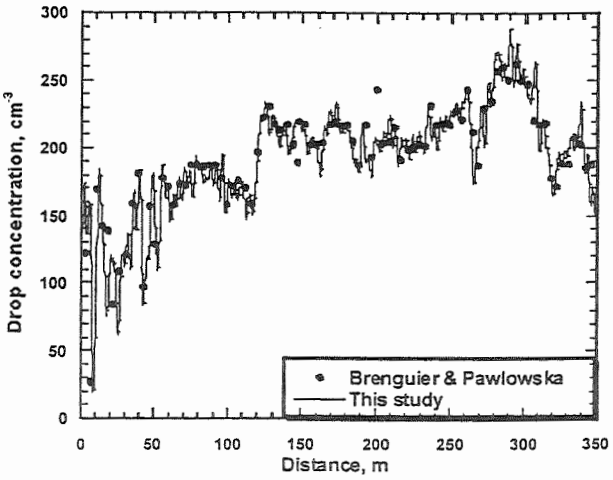

Figure 5. Profile of large-scale drop concentration fluctuations calculated using the method suggested in this study versus the profile restored using an optimal estimator developed by Pawlowska and Brenguier (1997).

for each of 79 clouds. All spectra obtained indicate a pronounced decrease (a power law) in the energy with the increase of spatial scale. Figure 6 indicates the powers (slopes) of the spectra. One can see that the slopes range from about –1 to –1.6, with mean value of –1.3. This result seems to reflect some physical mechanisms and can be useful for parameterization aims.

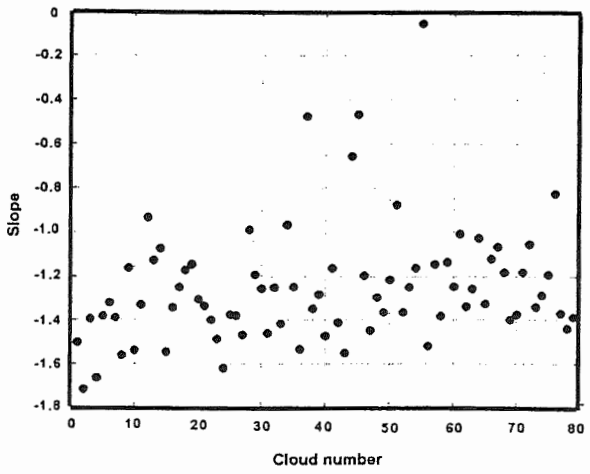

Figure 6. Powers (slopes) of spectra of large-scale drop concentration fluctuations for 64 clouds. The slopes concentrate around –5/3.

6. CONCLUSIONS

The results of statistical analysis of drop concentration fluctuations measured in situ by the FFSSP in cumulus clouds indicate:

1. There exist centimeter-scale drop concentration fluctuations with amplitudes of 5-30% of mean droplet concentration.
2. It is shown that the centimeter-scale fluctuations are caused by the inertia of droplets moving within a turbulent flow (in accord with the theoretical results). For the first time we show turbulence effects on droplet motion in real clouds. They lead to the formation of fine structure of drop concentration field (inch clouds).
3. A parameterization expression is obtained that relates the amplitude of these fluctuations with the intensity of turbulence and drop size.
4. Now the problem, what could be the effects of the concentration inhomogeneties on microphysical processes in clouds arises.

Acknowledgements

This study was partially supported by the Germany-Israel Science Foundation (grant 0407-008.08/95) and the Israel Science Foundation administrated by the Israel Academy of Sciences and Humanities (grant 572/97).

5. References

Brenguier, J.-L. , T. Bourianne, A. Coelho, J.Isbert, R. Peytavi, D. Trevarin and P.Wechsler, 1998: Improvements of droplet size distribution measurements with the Fast FSSP. *J. Atmos. and Oceanic Technology,* 15, 1077-1090.

Cooper, W.A., 1989: Effects of variable droplet growth histories on droplet size distributions. Part 1: Theory. *J. Atmos. Sci.*, 46, 1301-1311.

Fessler, J.R., J.D. Kulick and J.K. Eaton 1994, Preferential concentration of heavy particles in a turbulent channel flow. *Phys. of Fluids, 6, 3742-3749.*

Grabowski, W.W., 1993: Cumulus entrainment, fine-scale mixing, and buoyancy reversal. *Quart. J. Roy. Met. Soc.*, 119, 935-956.

Grabowski W.W, and P. Vaillancourt, 1999: Comments on the "Preferential concentration of cloud droplets by turbulence: effects on the early evolution of cumulus cloud droplet spectra", *J Atmos. Sci.*, 56, 1433-1436.

Korolev, A.V., and I.P. Mazin, 1993: Zones of increased and decreased droplet concentration in stratiform clouds. *J. Appl. Meteor.*, 32, 760-773.

Maxey, M.R., 1987: The gravitational settling of aerosol particles in homogeneous turbulence and random flow fields. *J. Fluid. Mech.*, 174, 441-465.

Pinsky, M., J-L. Brenguier, and A. Khain (1998) A fine structure of cloud drops concentration as seen from the Fast FSSP measurements. Conference on Cloud Physics, 17-21 Aug. Everett, Washington, 522-525.

Pinsky, M., A. Khain, and Z. Levin, 1999: The role of the inertia of cloud drops in the evolution of the drop size spectra during drop growth by diffusion. *Quart. J. Roy. Meteor. Soc.* ,125, 553-581.

Pinsky, M., J-L. Brenguier, and A. Khain, 2000: Fine structure of cloud droplet concentration as seen from the Fast-FSSP measurements: method of analysis and preliminary results *J. Appl. Meteor.* (in revision).

Wang, L-P., and M.R. Maxey, 1993: Settling velocity and concentration distribution of heavy particles in homogeneous isotropic turbulence. *J. Fluid Mech.*, 256, 27-68.

LABORATORY AND THEORETICAL STUDIES OF THE COLLISION EFFICIENCIES OF CLOUD DROPLETS AND SMALL RAIN DROPS

O. Vohl[1], S. Mitra[1], S. Wurzler[3], H.R. Pruppacher[1], M. Pinsky[2], and A. P. Khain[2]
[1]Johannes Gutenberg-University, Institute of Atmospheric Physics, Mainz, Germany
[2]Institute of Earth Science, The Hebrew University of Jerusalem, Jerusalem, 91904, Israel
[3]Institute for Tropospheric Research, Leipzig, Germany

1. INTRODUCTION

The collision efficiency of droplets in clouds is the main factor controlling the drop collision rate and rain formation. Determination of the collision efficiencies is a complicated hydrodynamic problem requiring calculations of mutual drop motion at small separation distances, when the flow induced by any one of the moving droplets influence the track of the other one in the drop pair. In the past, most studies dedicated to the determination of the collision efficiencies have been carried out using different numerical solution methods which were further supplemented by laboratory measurements (see Pruppacher and Klett, 1997). One characteristic feature of the theoretical calculations was that each study was concerned with a specific comparably narrow size range of colliding drops. In most of these studies dealing with interactions of small droplets fluid inertia was assumed negligible, which led to the Stokes equations used in the analyses. As a consequence, this approach can only be applied to cases of practically zero Reynolds numbers Re (see Lin and Lee, 1975 for more detail). The effect of inertia was taken into account by Klett and Davis (1973) using an analytical model based on modified Oseen's equations. They calculated the collision efficiencies of droplets with radii below 70 μm (Re$\leq$ 5). For larger collector drops (Re upto 100), the induced velocity field was calculated numerically (e.g., Shafir and Gal Chen, 1971; Lin and Lee, 1975; Beard and Grover, 1974; Schlamp et al. 1976). Even though the computed collision efficiencies agree qualitatively with each other as far as their trend with drop size is concerned, the individual values differed in certain size ranges quite significantly. The discrepancies and lack of reliable data exist particularly for collisions between small cloud droplets and other small drops as well as between small cloud droplets and raindrops. As a result, present tables widely used in numerical cloud models lack reliability.

Corresponding Author's addresses:

S. Mitra, Johannes Gutenberg-University, Institute of Atmospheric Physics, D-55099 Mainz, Germany;

E-mail: mitra@mail.uni-mainz.de

A.P. Khain, Institute of Earth Science, The Hebrew University of Jerusalem, Jerusalem, 91904, Israel;

E-mail: khain@vms.huji.ac.il

In order to remedy the situation, we conducted, during past years, laboratory experiments on the continuous growth of small rain drops freely floating within a cloud of small droplets using the vertical wind tunnel at the University of Mainz. The experiments were carried out under controlled environmental conditions.

At the same time a method to calculate the collision efficiencies for drop-drop collisions for a wide range of Reynolds numbers was developed at the Hebrew University of Jerusalem. The collision efficiencies calculated theoretically were used to evaluate the continuous growth equation applied to the growth of drops under laboratory conditions.

2. LABORATORY EXPERIMENTS

The experiment, designed to measure the rate of continuous growth of a collector drop produced by collisions with small droplets in a cloud, was carried out in the Vertical wind tunnel at Mainz. Before starting a new experiment the ambient conditions of the tunnel air were stabilised by running the tunnel for several hours. A single collector drop was then injected into the updraft of the tunnel set at a speed matching the terminal velocity of the drop thereby capturing the drop within the observation section of the tunnel in a free floating condition. The tunnel air contained a cloud of smaller droplets having a size distribution centered around 4μm radius and of known liquid water content. The droplet cloud was produced by a battery of sprayers where the sprayers were successively switched on as the tunnel speed increased during droplet growth in order to keep the liquid water content of the droplet cloud as stable as possible.

The rate of growth of the collector drop was determined from the change in terminal velocity while it was kept continuously suspended in the observation section during its growth. The tunnel velocities were converted into equivalent drop radii using the relation given by Beard (1976). The total liquid water content was determined from the actual temperature and the dewpoint of the tunnel air after the cloud of small droplets were completely evaporated within the heated inlet tube of the dewpoint meter. The droplet size spectrum was determined using a light scattering size spectrometer (CSASPE from Particle Measuring Systems). The residual turbulence in the tunnel was

found to lie below 0.5% for the whole range of tunnel speeds.

3. CALCULATION OF COLLISION EFFICIENCIES

To calculate the collision efficiencies, we have used the superposition method (Pruppacher and Klett, 1997), according to which each sphere is assumed to move in a flow field induced by its counterpart moving alone. This method has been successfully used by many investigators for a wide range of droplet Reynolds numbers.

Neglecting electrical effects, a drop about to collide with another one experiences three main forces: gravity, buoyancy and the drag force. The drag force can be represented as a sum of the drag force arising in a calm air while the drop is falling with its terminal velocity and the force arising due to the influence of the velocity field induced by its counterpart. The equation of motion can be written as (Pruppacher and Klett, 1997):

$$\frac{d\vec{V}}{dt} = g\left(1-\frac{\rho_a}{\rho_w}\right) - \frac{3}{8}\frac{\rho_a}{\rho_w}\frac{1}{r}C_D(Re)\left|\vec{V}-\vec{U^*}\right|\left(\vec{V}-\vec{U^*}\right) \quad \ldots (1)$$

where $\vec{V}$ is the vector of drop velocity, $\vec{U^*}$ is the velocity induced by the counterpart drop in the center of the current drop, ρ_a and ρ_w are densities of air and water, respectively. $C_D(Re)$ is the drag coefficient dependent on the Reynolds number

$$Re = \frac{2\,r\,\rho_a}{\eta}\left|\vec{V}-\vec{U^*}\right|$$

where η is the air viscosity and r is the drop radius. When the separation distance between the droplets is so large that the hydrodynamic interaction is negligible each drop falls with its terminal fall velocity V_t.

We calculated terminal fall velocities, according to Beard (1976). To compute the velocity fields induced by moving droplets we utilised the method of matching of two analytical solutions: Stokes solution valid for small droplets (Re<0.4) and Hamielec and Johnson's (1962) solution valid for drops with drop Reynolds numbers up to Re=100, which corresponds to drop radii equal to about 300 μm.

The equations of drop motion were then solved using the fifth-order Runge-Kutta method with automatic precision control and automatic choice of the integration time step (Press et al., 1992). In all cases, however, the time step was limited by one half of the characteristic adaptation time of the smaller droplet in a drop pair: $\Delta t < \frac{1}{2}\tau_{small} = \frac{1}{2}\frac{V_{t\,small}}{g}$. Droplets were separated initially by 20-40 radii of the largest drop in a drop pair. Initial velocities were assumed to be equal to the drop terminal fall velocities. The grazing tracks were found by changing the location of the smaller droplet in the horizontal direction. Relative errors of the calculation of collision efficiencies did not exceed 0.4% for E =1 and 4% for E= 0.01. Our computations have been summarized in form of a large number of tables which include also detailed values for the collision efficiency between small drops. An example is presented in Figure 1.

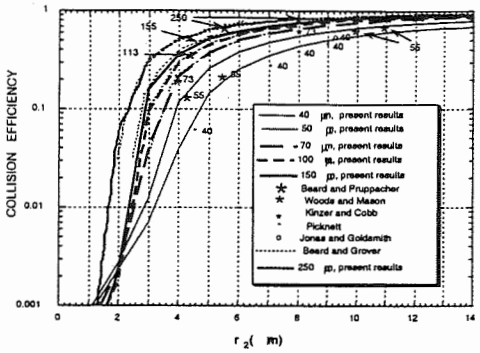

Figure 1. Comprison of our collision efficiencies with other theoretical computations and observed data.

4. RESULTS

Using the calculated collision efficiencies, and assuming coalescence efficiency to be equal to unity, the drop growth under laminar conditions was computed using the continuous growth equation (Pruppacher and Klett 1997) and compared to the laboratory measurements involving a single collector drop growing within a cloud of small droplets, a situation, for which the continuous growth equation is applicable. Figure 2 presents the results of the calculations of the two such growth experiments. One can see a good agreement between the measurements and the calculations.

5. CONCLUSIONS

Two conclusions can be drawn from our study:

a) Measrements of the growth rate of a single drop by collision with small drops carried out in a wind tunnel provide a useful tool to test theoretical collision efficiencies via the continuous drop growth equation involving drops for which it can be assumed that the coalescence efficiency is unity.

b) The agreement between our experiment and the newly computed collision efficiencies provide us, at present, with a large set of tables which include efficiencies in the range in which we previously lacked reliable values.

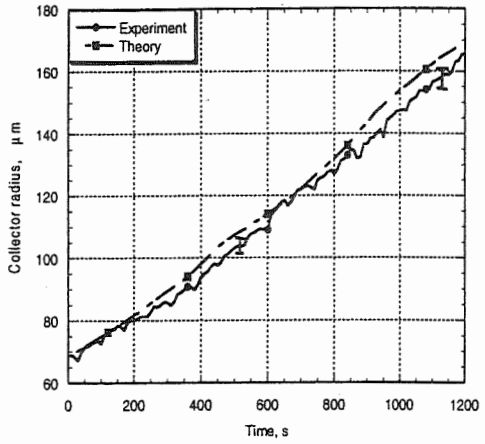

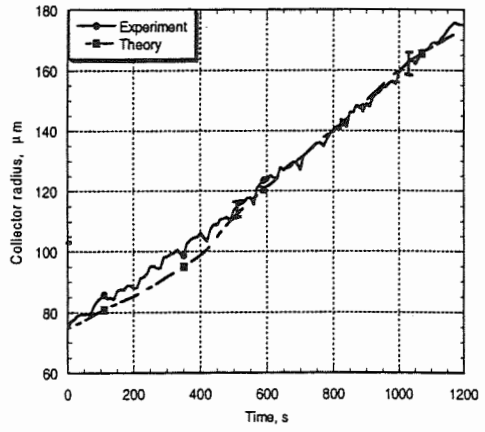

Figure 2. Two examples of increase of drop size with time as obtained from laboratory measurements and continuous growth calculations using theoretical values of the collision efficiencies.

ACKNOWLEDGEMENTS

This study was partially supported by the German-Israeli Science Foundation (grant 0407-008.08/95), by the Israeli Science Foundation administrated by the Israeli Academy of Sciences and Humanities (grant 572/97) and the Israeli Ministry of Science (grant 84291-96).

REFERENCES

Beard, K.V., 1976: Terminal velocity and shape of cloud and precipitation drops aloft. *J. Atmos. Sci.* **33**, 852-864.

Beard K.V., and S.N. Grover, 1974: Numerical collision efficiencies for small raindrops colliding with micron size particles. *J. Atmos. Sci.*, **31**, 543-550.

Beard, K.V., and H.R.Pruppacher, 1971: A wind tunnel investigation of collection kernels for small water drops in air. *Quart. J. Roy. Meteor.Soc.*, **97**,242-248

Hamielec, A.E., and A. I. Johnson, 1962: Viscous flow around fluid spheres at intermediate Reynolds numbers. *The Canadian Journal of Chemical Engineering*, **April**, 41-45.

Jonas, P.R., and P. Goldsmith, 1972: The collision efficiencies of small droplets falling through a sheared air flow. *J. Fluid Mech.*, **52**, 593-608.

Kinzer, G.D., and W.E. Cobb, 1958: Laboratory measurements and analysis of the growth and collection efficiency of cloud droplets. *J. Meteor.*, **15**, 138-148.

Klett, J.D. and M.H. Davis, 1973: Theoretical collision efficiencies of cloud droplets at small Reynolds numbers. *J. Atmos. Sci.*, **30**, 107-117.

Lin, C.L. and S.C. Lee, 1975: Collision efficiency of water drops in the atmosphere. *J. Atmos. Sci.*, **32**, 1412-1418.

Picknett, R.G., 1960: Collection efficiencies for water drops in air. *Int. J. air Pollution*, **3**, 160-167.

Press, W.H., S.A. Tenkolsky, W.T. Vetterling and B.P. Flannery, 1992: *Numerical Receipes in FORTRAN*, Cambridge Univ. Press, 963 pp.

Pruppacher H.R., and J.D. Klett, 1997: *Microphysics of Clouds and Precipitation.* 2d ed. Kluwer Academic 954 pp.

Shafrir, U. and T. Gal-Chen, 1971: A numerical study of collision efficiencies and coalescence parameters for droplet pairs with radii up tp 300 microns. *J. Atmos. Sci.*, **28**, 741-751.

Schlamp, R.J. Grover S.N., Pruppacher H.R. and Hamielec, A.E., 1976: A electric charges and vertical external fields on the collision efficiency of cloud drops. *J. Atmos. Sci.*, **33**, 1747-1755.

Woods, J.D., and B.J. Mason, 1964; The experimental determination of collection efficiencies of small drops in air, *Ibid.*, **90**, 373-381.

STRUCTURE OF SMALL CUMULUS CLOUDS

H. Gerber

Gerber Scientific Inc., Reston, VA 20190, U.S.A

1. INTRODUCTION

The Small Cumulus Microphysics Study (SCMS) held in Florida in 1995 provided an opportunity to deploy in a new way a Particulate Volume Monitor (PVM; Gerber et al. 1994) on the NCAR C-130 aircraft. Measurements of liquid water content (LWC) were made at 1000 Hz, and of effective radius (r_e) were made at 250 Hz. This gave a horizontal resolution of 10 cm for LWC for an aircraft speed of 100 m/s. This resolution is several orders of magnitude greater than usually used, thus providing a look of unprecedented clarity at the structure of the small cumulus clouds (Cu) found during SCMS.

The following outlines the results of studies that take advantage of this new look at Cu. The quantitative variability of LWC is determined as a function of the data sampling rate. The vertical dependence of LWC is found. The presence of adiabatic liquid water content (LWCa) is quantified in terms of parcel width and the probability as a function of height above Cu base. These findings are compared to the popular notion of "adiabatic cores", which are thought to exist in some Cu at heights up to 1 km or 2 km above cloud base, and with widths of hundreds of m. Spectral analysis is done on the high-frequency LWC measurements, and is compared to thoughts on droplet inhomogeneities caused by gradients at mixing interfaces and by inertial effects. The dominant type of mixing following entrainment is described.

2. DATA CHARACTERISTICS

The output of the PVM on the C-130 was recorded by the aircraft's data system. The scaling constants for LWC and r_e channels, and the droplet size response of the PVM are given in (Gerber, et al 1994). High-frequency PVM data were made available by NCAR for 11 of the SCMS flights listed in Table 1, which includes estimates of the height, pressure, and temperature of the lifting condensation level (LCL). The LCL was established with an uncertainty of about +/- 50 m by combining forward-looking video views of the Cu from the aircraft with downward calculations of LWC profiles from LWC measurements made about 100 m above cloud base and in updrafts. The mean cloud-base temperature for each flight varies over a small range for the 11 flights making it possible to reference all flights to the same cloud base, which is given by the parameters for flight 12 in Table 1. The resulting data base consists of 602 Cu traversed at various levels by the C-130, a total incloud distance of about 350 km, and 3.5 x 10^6 individual LWC measurements.

Gerber Scientific Inc., 1643 Bentana Way, Reston, VA 20190, U.S.A. E-Mail: gerber.gsi@erols.com

Table 1 *- Mean cloud-base conditions for flights of the NCAR C-130 during SCMS.*

Flt.	Date	Pressure (mb)	Temp. (C)	Ht.above surface (m)
4	7/22/95	955	23.8	490
5	7/24/95	924	23.0	747
6	7/26/95	958	23.0	465
8	7/28/95	953	23.4	580
11	8/4/95	957	23.0	474
12	8/5/95	960	23.2	450
13	8/6/95	958	22.9	457
14	8/7/95	948	22.3	411
16	8/10/95	959	23.0	458
17	8/11/95	960	23.2	444
19	8/13/95	966	23.5	399

3. SPATIAL VARIABILITY OF LWC

The variability of LWC in SCMS Cu depends on the rate at which LWC is measured. Figure 1 shows 1000-Hz and 1-Hz mean LWC data for a pass through a small Cu 885 m above cloud base. The high-resolution data show the typical complexity found in the Cu, while the 1-Hz data lose much of the detail. The 1000-Hz data show small portions of the Cu near time = 2.5 s where LWC approaches within 5% of the predicted LWCa. The low rate LWC data do not see this peak. This illustrates that 1-Hz LWC data is unreliable for identifying cloud parcels with LWCa. The average ratio for all Cu of the maximum LWC 1000-Hz data to the maximum LWC 1-Hz data found in each cloud is 1.41.

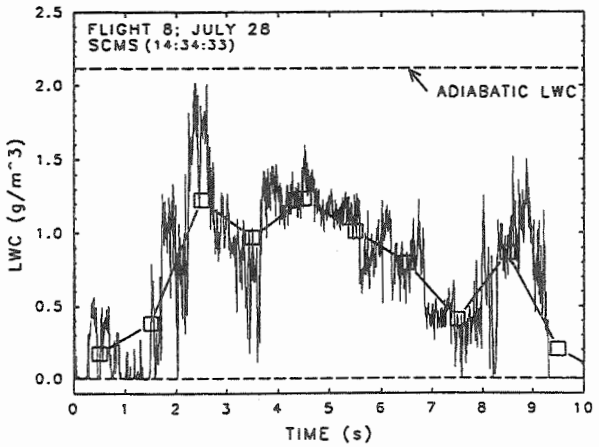

Fig. 1 *- Comparison of 1000-Hz and 1-Hz LWC data (squares) measured by the PVM in a SCMS cumulus cloud.*

Figure 2 shows the vertical variability of the average LWC measured in each of the 602 Cu. The data follow the trend of the average LWC measured for Cu by Warner (1955). Also shown are LWC measurements at

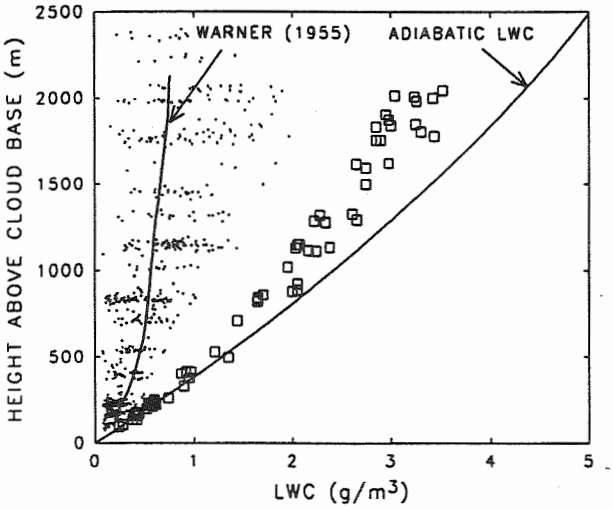

Fig. 2 - LWC in 10% of the Cu with the largest values of 1-kHz LWC (squares), and mean LWC (dots) in all Cu as a function of height above cloud base.

1000 Hz in 10% of the Cu with largest values of LWC at given height intervals above cloud base. The good agreement of the largest values of LWC with the calculated adiabatic profle, at least up to a height of about 1000 m, suggests that the PVM measurements are physically meaningful, because measured LWC should not exceed the adiabatic value, yet should be equivalent to LWCa in portions of the Cu, especially near cloud base.

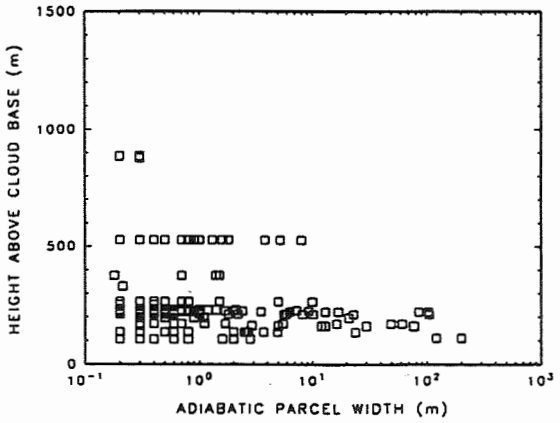

Fig. 3 - Adiabatic LWC parcels found in all Cu as a function of parcel width and height above cloud base.

The good agreement in Fig. 2 permits us to search the data base for the presence of cloud parcels with LWCa. Figure 3 shows the width of all the adiabatic parcels that were found as a function of height above cloud base; the criterion used for the presence of adiabatic water was that measured LWC was within +/-10% of predicted LWCa. The maximum width of the adiabatic parcels near cloud base is on the order of 100 m, smaller than 8 m at 500 m, and no more than 30-cm wide at 900 m. All Cu data and the data in Fig. 3 are used to calculate the probability of finding LWCa as a function of height. The results, given in Fig. 4, show a rapid decrease in the probability as height increases, with none above a limit of 900 m. This limit shows good agreement with the laboratory work of Johari (1992), where a bubble of buoyant fluid rises in a tank to a level above which all of the fluid is mixed with at least some ambient fluid in the tank.

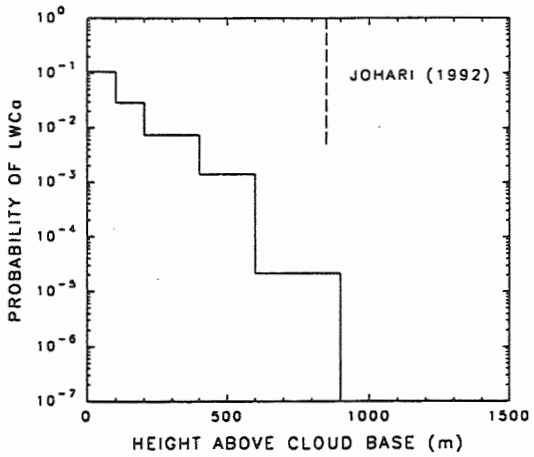

Fig. 4 - Probability of finding adiabatic LWC as a function of height above cloud base.

The results shown in Figs. 2 - 4 are inconsistent with the concept of "adiabatic cores", where some much wider and higher cloud parcels are thought to contain LWCa. The SCMS Cu entrain ambient air more effectively than expected, resulting in low probabilities and small parcels of LWCa except near cloud base. We conclude that the present concept of "adiabatic cores" is questionable, and does not apply to small Cu.

This conclusion carries the burden of showing that the previous publications that have claimed the presence of "adiabatic cores" are in error. A review of pertinent publications (Cooper 1978; Heymsfield et al. 1978; Paluch 1979; Boatman and Auer 1983; Jensen 1985; Jensen et al 1985; Raga et al. 1990; Cooper et al. 1996; Knight and Miller 1998; Lawson and Blyth 1998; Brenguier 1998; Brenguier and Chaumat 1999) finds potential problems with their claims of having observed "adiabatic cores". These problems include one or more of the following: use of 1-Hz or other low-rate LWC data,

use of indirect methods to infer LWC, use of overestimates in cloud-base height, and the inability to measure accurately LWC or incloud temperature.

These results suggest that the Cu are less buoyant than expected, and raise the possibility that the unexplained residual droplet spectral broadening (e.g.,see Chaumat and Brenguier 1999; Vaillancourt and Yau 2000) is a result of the interaction between LWC gradients in the cloud caused by entrainment and vertical mixing as described by Cooper (1989).

4. SMALL-SCALE VARIABILITY

The 10-cm and larger resolution of the PVM LWC measurements during SCMS show that droplet-free voids in Cu are rare except near cloud boundaries. The data do show, however, that the variability of LWC at scales smaller than several meters is often larger than expected for clouds with fully developed turbulence (Davis et al. 1999; Gerber et al. 2000). This is evident from the spectral analysis of the LWC data, where the spectral density (or variance) of the data is determined as a function of frequency (or scale of the cloud parcels). Figure 5 shows examples of such analyses for three Cu. At scales smaller than about 2 m - 5 m, the LWC

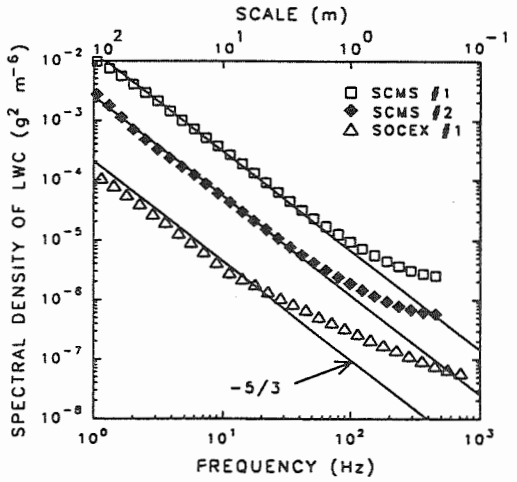

Fig. 5 - Power spectra of LWC in three cumulus clouds as a function of scale and frequency.

variance starts to exceed that predicted by the -5/3 scaling law. Similar results were seen earlier by Rodi et al. (1992) using droplet-concentration measurements. The explanation of the enhanced variability at small scales in some Cu is likely tied to the entrainment and mixing processes, which others (Baker 1992; Brenguier 1993) have suggested cause sharp droplet gradients at scales smaller than several cm. Droplet inertial effects (Pinsky and Khain 1997; Shaw et al. 1998) might be another reason for such small gradients. The time evolution of turbulence in the Cu may broaden sharp droplet gradients and result in the effects shown in Fig. 5.

5. ENTRAINMENT AND MIXING

The value of LWC depends on droplet size and concentration. By looking at the two dependencies separately it is possible to infer the prevalent mixing process in warm Cu with insignificant coalescence and precipitation. Austin et al. (1985) showed that the large droplet concentration was closely related to LWC. Paluch (1986) found that at a given level the droplet size at the peak of the size spectrum for such Cu remained nearly constant, while droplet concentration changed over a

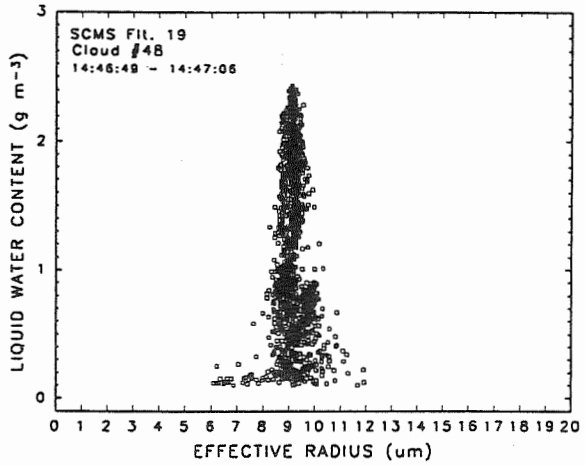

Fig. 6 - Liquid water content as a function of the effective radius of cloud droplets in one Cu pass.

large range. A similar result (Blyth and Latham 1991) in Cu showed nearly constant r_e values and large changes in LWC at a resolution of 10 m. These findings suggest that mixing following entrainment is of the inhomogeneous type. We repeated the analysis of Blyth and Latham (1991) of r_e vs LWC using the PVM data at a resolution of 40 cm. Figure 6 gives results for one pass through a SCMS Cu, which shows again the near independence of r_e on LWC.

We can estimate the quantitative dependence of LWC on droplet size and concentration (N) in the following manner (Gerber et al. 2000). If we assume that $LWC \propto N r_e^3$, the PVM measurements can be used to estimate this dependence for each factor that makes up the expression for LWC; N is given by the PVM measurement consisting of $LWC\ r_e^{-3}$. Figure 7 compares r_e^3 and N calculated in this manner for one Cu, and shows again that changes in LWC are dominated by changes in the droplet concentration rather than changes in size of the droplets that contribute most to LWC and r_e. We conclude that the mixing at 40-cm resolution in the cloud is also primarily inhomogeneous, where the Cu are diluted by total evaporation of cloud parcels following entrainment. The droplets activated near cloud base and grown to the largest sizes by condensation appear to dominate LWC as well as the value of r_e at any given level of the Cu.

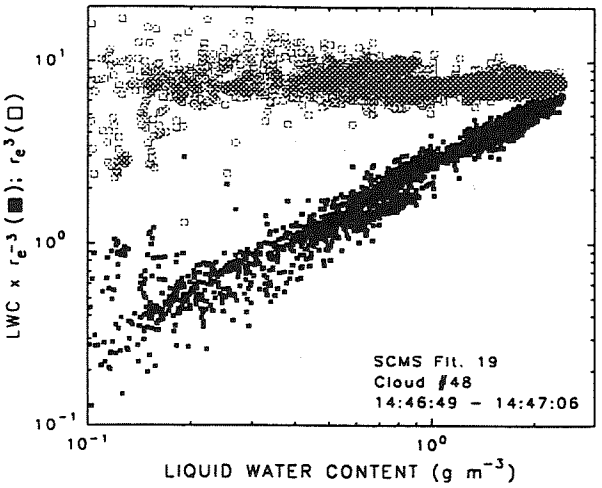

Fig. 7 - Relative change in the droplet concentration given by LWC/ r_e^3, and r_e^3 as a function of LWC in one Cu pass.

6. ACKNOWLEDGMENT

This work was supported by NSF (ATM-9521073).

7. REFERENCES

Austin, P.H., M.B. Baker, A.M. Blyth, and J.B. Jensen, 1985: Small-scale variability in warm continental cumulus clouds. *J. Atmos. Sci.*, **42**, 1123-1138.

Baker, B.A., 1992: Turbulent entrainment and mixing in clouds: a new observational approach. *J. Atmos. Sci.*,**49**, 387-404.

Blyth, A.M., and J. Latham, 1991: A climatological parameterization for cumulus clouds. *J. Atmos. Sci.*, **48**, 2367-2371.

Boatman, J.F., and A.H. Auer, Jr., 1983: The role of cloud top entrainment in cumulus clouds. *J. Atmos. Sci.*, **40**, 1517-1534.

Brenguier, J.-L., 1993: Observation of cloud microstructure at the centimeter scale. *J. Appl. Meteor.*, **32**, 783-793.

Brenguier, J.-L., 1998: Droplet spectra broadening in cumulus clouds: Review of advances in observations and numerical simulations. *Preprints, Conference on Cloud Physics*, American Met. Soc., 17-21 Aug., Everett, WA, pp. 510-513.

Brenguier, J.-L., and L. Chaumat, 1999: Droplet spectra broadening in cumulus clouds. Part I: Broadening in adiabatic cores. *J. Atmos. Sci.*, submitted.

Chaumat, L., and J.-L. Brenguier, 1999: Droplet spectra broadening in cumulus clouds. Part II: Effects of droplet concentration inhomogeneities. *J. Atmos. Sci.*, submitted.

Cooper, W.A., 1978: *Rept. No. AS 119*, Dept. of Atmos. Sci., U. of Wyoming, Laramie, WY.

Cooper, W.A., 1989: Effects of variable growth histories on droplet size distributions.Part I: Theory. *J. Atmos. Sci.*, **46**, 1301-1311.

Cooper, W.A., C.A. Knight, and J.L. Brenguier, 1996: Observed vs calculated rates of growth by coalescence. *Proceedings 12th Int. Conf. on Clouds and Precip.*, 19-23 Aug., Zurich, Switzerland, 53-56.

Davis, A.B., A. Marshak, H. Gerber, and W. Wiscombe, 1999: Horizontal structure of marine boundary-layer clouds from cm to Km scales. *J. Geophys. Res.*, **104**, 6123-6144.

Gerber, H., B.G. Arends, and A.S. Ackerman, 1994: New microphysics sensor for aircraft use. *Atmos. Res.*, **31**, 235-252.

Gerber, H., J.B. Jensen, A.B. Davis, A. Marshak, and W.J. Wiscombe, 2000: Spectral density of cloud liquid water content at high frequencies. *J. Atmos. Sci.*, submitted.

Heymsfield, A.J., P.N. Johnson, and J.E. Dye, 1978: Observations of moist adiabatic ascent in Northeast Colorado cumulus clouds. *J. Atmos. Sci.*, **35**, 1689-1703.

Jensen, J.B., 1985: Turbulent mixing, droplet spectral evolution and dynamics of warm cumulus clouds. *Ph.D Thesis*, University of Washington.

Jensen, J.B., P.H. Austin, M.B. Baker, and A.M. Blyth, 1985: Turbulent mixing, spectral evolution and dynamics in a warm cumulus cloud. *J. Atmos. Sci.*, **42**, 173-192.

Johari, H., 1992: Mixing in thermals with and without buoyancy reversal. *J. Atmos. Sci.*, **49**, 1412-1426.

Knight, C.A., and L. J. Miller, 1998: Early radar echoes from small, warm cumulus: Bragg and hydrometeor scattering. *J. Atmos. Sci.*, **55**, 2974-2992.

Lawson, R.P., and A.M. Blyth, 1998: A comparison of optical measurements of liquid water content and drop size distribution in adiabatic regions of Florida cumuli. *Atm. Res.*, **47-48**, 671-690.

Paluch, I.R., 1979: The entrainment mechanism in Colorado cumuli. *J. Atmos. Sci.*, **36**, 2467-2478.

Paluch, I.R., 1986: Mixing and cloud droplet size spectrum: Generalizations from CCOPE data. *J. Atmos. Sci.*, **43**, 1984-1993.

Pinsky, M.B., and A.P. Khain, 1997: Formation of inhomogeneity in drop concentration induced by drop inertia and their contribution to drop spectrum broadening. *Quart. J. Roy. Meteor. Soc.*, **123**, 165-186.

Raga, G.B., J.B. Jensen, and M.B. Baker, 1990: Characteristics of cumulus band clouds off the Coast of Hawaii. *J. Atmos. Sci.*, **47**, 338-355.

Rodi, A.R., J.-L. Brenguier, and J.P. Chalon, 1992: Case study of cumulus microstructure with the new FFSSP. *Preprints 11th Int. Conf. on Clouds and Precip.*, Montreal, Canada, Elsevier Sci. Pub. 169-172.

Shaw, R.A., W.C. Reade, L.R. Collins, and J. Verlinde, 1998: Preferential concentration of cloud droplets by turbulence: effects on the early evolution of cumulus cloud droplet spectra.*J. Atmos. Sci.*, **55**, 1965-1976.

Vaillancourt, P.A., and M.K. Yau, 2000: Review of particle-turbulence interactions and consequences for cloud physics. Bull. Am. Meteor. Soc., **81**, 285-298.

Warner, J., 1955: The water content of cumuliform cloud. *Tellus*, **7**, 449-457.

SMALL-SCALE PROPERTIES OF CLOUDS: SUMMARY OF RECENT RESULTS FROM AIRCRAFT MEASUREMENTS, LABORATORY EXPERIMENTS AND NUMERICAL MODELING

Szymon P. Malinowski, Krzysztof E. Haman, Mirosław Andrejczuk, Piotr Banat and Adam Jaczewski

Institute of Geophysics, Warsaw University, PL-02-093, Warsaw, Poland

1. INTRODUCTION

Despite intensive developement of cloud physics the small-scale (below one meter) thermodynamical and dynamical structure of clouds seems to be virtually not explored. The new generation of aircraft instrumentation, like PSM (Baumgardner et. al., 1993) FFSSP (Brenguier, 1993) and digital holographic camera (e.g. Lawson et al., 1998) airborne particulate volume monitor (PVM-100A, e.g. Davis et.al., 1999) provide us data about microphysical properties of clouds at small scales, but this knowledge is not supported by adequate information on the environment of cloud particles. In fact, measurements of the small-scale turbulent velocities in clouds have never been performed and there exist few preliminary data sets with raw data on structure of the temperature field (Haman and Malinowski 1998); detailed information on small-scale humidity fluctuations is not available.

Thus, in order to explain, verify or understand interaction between microphysics, dynamics and thermodynamics far going assumptions concerning small-scale dynamical and thermodynamical structure of clouds have to be made. Usually it is assumed (explicitly or implicitly, i.e. without mentioning it) that cloud turbulence is generated in large scales (about 100m or more); below exists a well-developed inertial range of turbulent eddies with turbulent velocities described by some statistical distribution estimated on a basis of laboratory investigations, DNS, or speculative theoretical approach. Turbulence is assumed to be isotropic and stationary, and usually temperature and humidity fields (if taken into account) are treated as passive diffusing scalars except evaporation/condensation. Examples of this approach are recent works by Shaw et al. (1998) or Pinski and Khain (1997), who studied various aspects of rain formation. Obtained results are obviously dependent on these assumptions. In this paper we would like to discuss physical backgrounds of these assumptions with use of recent results following from laboratory experiments, numerical simulations and in-cloud measurements.

Corresponding author address: Szymon P. Malinowski, Warsaw University, Institute of Geophysics, ul. Pasteura7, 02-093 Warsaw, Poland, E-Mail: malina@fuw.edu.pl

Most of the results summarized below is biased by the author's interest in the entrainment and turbulent mixing process, so they cannot be representative for the unmixed core of clouds. Certain results about droplet spatial distribution within the turbulent cloud core can be found in another papers presented in this volume (Jaczewski and Malinowski 2000, Bajer et al., 2000).

2. SMALL SCALE CLOUD-CLEAR AIR MIXING IN THE LABORATORY EXPERIMENT.

Fig.1. An example image from the cloud chamber.

In our laboratory mixing of cloud with clear air takes place in a chamber of dimensions 1.8m*1m*1m. A volume of saturated air containing cloud droplets (∅ 7-25μm), generated by an ultrasonic droplet generator in the small chamber above, enters the main chamber and undergoes mixing with unsaturated air. The process is illuminated by a 1.2mm wide sheet of laser light, oriented vertically or horizontally. Light, Mie-scattered by droplets, is observed at a 90° angle by

means of photo (Fig.1) and video cameras, digitized and processed. A more detailed description of the experiment is given in Malinowski et. al. (1998).

Within last five years thousands of images were collected and analyzed. In images collected until 1999 no individual droplets could be observed, however cloudy and clear air filaments were easy to determine (Fig.1). Geometrical properties of the interface separating these filaments, twisted and convoluted by turbulence, were investigated. The adopted analysis techniques as well as some results are presented in Malinowski and Jaczewski (1999) and Banat and Malinowski (1999, 2000).

Main findings may be briefly presented in a few statements. In the examined data there is a strong evidence of anisotropy of filamented small-scale structures created by mixing of cloud with clear air. This anisotropy, with the vertical direction privilledged is revealed by four experimental facts:

- For range of scales $2 \cdot 10^{-2}$-$2 \cdot 10^{-1}$ m scaling exponents of the cloud - clear air interface are direction dependent. In horizontal directions box-counting scaling exponents are equal $D_x = D_y \approx 0.718 \pm 0.003$ and these differ from the scaling exponent in the vertical, $Dz \approx 0.684 \pm 0.002$. This scaling breaks down at about 2 cm.
- In scales below 2 cm there is no scaling with fractional exponents (scaling exponents are close to 1 in all dimensions), however structure elements of the cloud-clear air interface are in average longer in vertical than in horizontal by factor about 1.6.
- The average horizontal component of intensity gradient at the cloud-clear interface (which is after r some averaging monotonically related to droplet concentration and/or liquid water content gradient) is greater than the vertical one suggesting more dilution in vertical than in horizontal;
- The absolute value of the vertical component of intensity gradient at the interface is larger for the case of cloud filament above a clear air filament, than for reverrse.

Above findings clearly show that in small scales in clouds we observe mixing patterns different from patterns representative for passive scalars under the action of isotropic turbulence. There are several physical mechanisms which in principle could lead to this effect. One of them is droplet sedimentation, which in scales close to dissipation range, where turbulent velocites are low, cannot be neglected. The dependence of the intensity gradient on the orientation means that the "thickness" of the cloud - clear air interface is also to certain extend governed by droplet sedimentation, which constitutes anisotropic transport mechanism of liquid water across the interface. We may then speculate that this mechanism influences thermodynamics at small scales and by evaporative cooling and subsequent buoyancy production may influence small-scale dynamics. In order to verify this hypothesis a series of numerical simulations have been performed.

3. SMALL SCALE CLOUD-CLEAR AIR MIXING IN NUMERICAL SIMULATIONS.

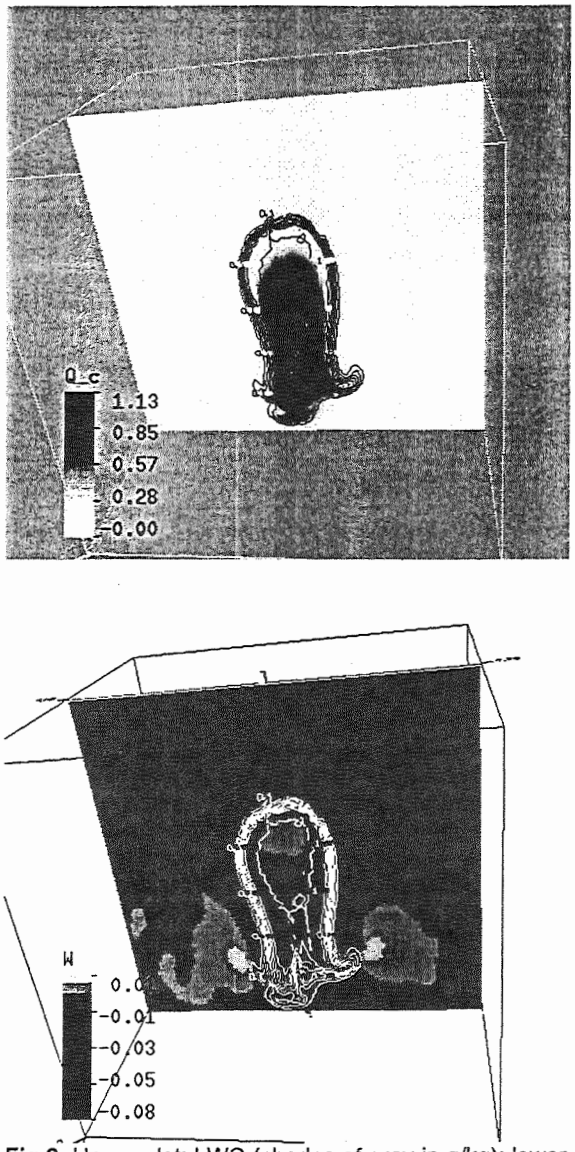

Fig.2. Upper plot: LWC (shades of gray in g/kg); lower plot: vertical velocity (shades, m/s); both plots: passive scalar (conc. isolines); on the central vertical cross-section after 11s of simulations. Partial separation of LWC and passive scalar due to droplets sedimentation is clearly visible.The maximum negative velocity is located in the bottom part of the cloudy blob.

Description of the numerical experiment is given in Andrejczuk et. al. (2000) in this volume. Here we notice, that a series of 2-D and 3-D simulations representing certain aspects of the cloud chamber experiment were performed. Equations of dynamics and thermodynamics were numerically solved with 1cm resolution. The detailed parameterization of microphysics accounting for 16 classes of droplet sizes sedimenting with terminal velocity appriopriate for each class was introduced. In Fig.2 an example result of simulations is presented. The initial condition in this particular experiment was as follows: a spherical cloudy bubble (saturated and containing liquid water) of zero buoyancy was placed in the middle of the computational domain (with periodic boundary conditions); environment was not saturated and initially there was no motion in the chamber. In order to distinguish between the mass motion of air and transport mechanisms for water (diffusion in gaseous phase and sedimentation of the liquid phase) the passive scalar was added to "mark" the initial bubble. After 11 s of simulations motions within the whole domain developed. The most negative buoyancy due to evaporative cooling appeared in the bottom part of the blob (see Fig.2) and was created by droplet sedimentation. The downward motion in this area resulted in early stages of turbulence, which, by formation of the filamented structure enhanced mixing and evaporation of next droplets. Control runs, where droplet sedimentation was not accounted for and droplet evaporation was possible only due to diffusion of the water vapour, did not lead to this series of events and ended with completely different dynamical patterns.

Presented results show that at least part of the small-scale cloud turbulence has its source in small-scales and is governed by droplet sedimentation and evaporation at the cloud-clear air interface. This gives a strong support to the hypothesis presented in section 2.

4. TEMPERATURE FLUCTUATIONS IN CLOUDS AT SMALL SCALES

Data from the cloud chamber seem to have their counterparts in observations of small scale features of temperature field in clouds and their vicinity observed by means of ultrafast aircraft thermometers UFT (Haman et al., 2000). These instruments with time constant of an order 10^{-4} s permit resolving spatial features down to about 2 cm. Measurements performed on various types of aircraft in Stratocumulus and small Cumulus clouds, warm and supercooled, show, that rapid jumps of temperature, up to few kelvins, over distance of few centimeters, sometimes in intermittent series, are often encountered in mixing regions of clouds (Fig. 3). This seems to confirm that mixing with environmental air during entrainment is a complex, multiscale process in which even small scale elements are not instantly erased by diffusional homogenization or sedimentation of droplets. This means in turn that dynamics of these parts of clouds should be modeled rather along the lines suggested by Haman and Pawlowska (1995) than under assumption of instantaneous homogenization. It also supports ideas of Korolev and Isaac (1998) that small-scale regions of strong supersaturation can be expected in mixing regions of clouds. However, homogenization processes may become essential for structures less than 2-3 cm thick. Such thin transition layers between cloud regions of different temperature were not observed, which may be partly attributed to the effects of inertia of UFT and filters in the recording system, but results from the cloud chamber presented in Section 2 suggest that 2 - 3cm may be as well a typical scale for fast smoothing by smallest scale mixing, droplet sedimentation and diffusion.

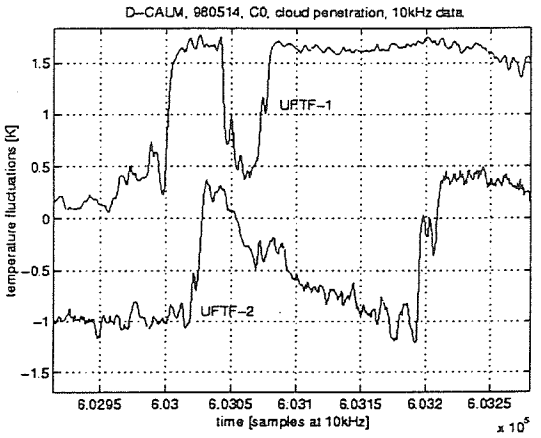

Fig.3 An example temperature fluctuations in cloud recorded by two UFT sensors 70 cm apart. Distance between grids corresponds to 35 cm, records are artificially separated in vertical for clarity.

It is interesting that at wavelengths below about 1 meter corresponding temperature power spectra often show an increase of spectral density with respect to power laws (usually close to typical -5/3 law) dominating for longer waves (Fig.4). This increase seems to be related mostly to the saturation deficit in clear air undergoing mixing with cloud. Though power spectrum of temperature fluctuations need not to be related directly to that of kinetic energy, some change of dynamic regime at these short wavelengths is evident. One may speculate, that strong local baroclinicity at sharp temperature jumps may be an additional source of small-scale turbulence in clouds. The latter may draw its energy not only from inertial, downscale transport of TKE from larger scales, but also from temperature gradients (and indirectly from evaporation of droplets) within thin transition layers at the folded and entangled cloud - clear air interface.

Thus in clouds neither temperature nor humidity or liquid water content can be treated as a passive scalar at scales below few meters.

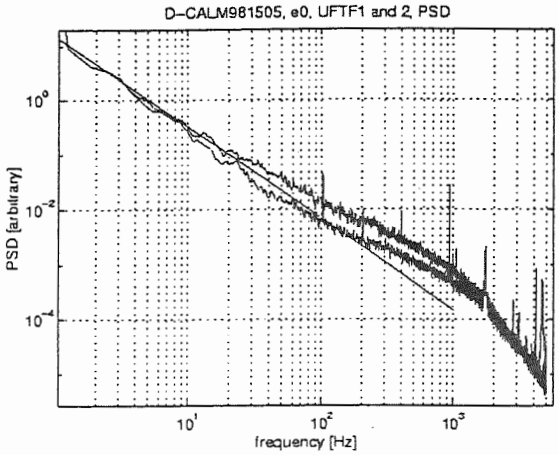

Fig.4. Power spectra of temperature records from cloud penetrations taken at 70m/s flightspeed (frequency 100Hz corresponds to 70cm wavelength, -5/3 slope is plotted for reference).

Replacing speculations by evidence would require simultaneous combined measurements of additional dynamic and thermodynamic parameters, with resolution corresponding to that of UFT. Unfortunately there was no opportunity to perform such complex (and presumably costly) measurements in past. However, considering evident importance of the smallest scale processes for larger scale cloud dynamics and cloud particles evolution, organizing such research in future may be worth of effort.

5. SUMMARY AND CONCLUSIONS.

Combined results of laboratory experiments, numerical simulations and airborne measurements suggest existence of small scale (down to about 2 cm or slightly less) intensive inhomogeneities of thermodynamic fields in clouds, particularly in regions of mixing with outer, clear air. Droplet sedimentation, revealed by anisotropy of mixing patterns at these scales seems to be an important transport mechanism influencing thermodynamics and dynamics through buoyancy effects dependent on mixing and evaporation. Presence of small scale, sharp gradients of temperature (and presumably humidity and supersaturation as well), forms an additional mechanism of turbulent kinetic energy generation. One may also speculate that these effects create conditions for strongly differentiated evolution of droplets by evaporation/condensation process, resulting in fast broadening of droplet spectra in clouds.

6. Acknowledgements

This research was supported by the grants of the Polish State Committee of Scientific Research (KBN) nos. 6 P04D 009 08 and 6 P04D 002 12. Computations were performed due to the computational grant from the Interdisciplinary Center for Mathematical and Computational Modeling, Warsaw University.

7. References

Bajer, K., S.P. Malinowski and K. Markowicz 2000: Influence of a small-scale turbulence structure on the concentration of cloud droplets. *In this volume.*

Banat, P and S.P. Malinowski, 1999: Properties Of The Turbulent Cloud-Clear Interface Observed in The Laboratory Experiment. *Phys. Chem. Earth B*, **6**, 741-745.

Banat, P and S.P. Malinowski, 2000: Nature of anisotropy in clouds in small scales, *in this volume.*

Baumgardner, D., K. Weaver and B. Baker, 1993: A technique for the measurement of cloud structure on centimeter scales. *J. Atmos. Ocean. Technol.*, **10**, 557-563.

Brenguier, J.L., 1993: Observation of cloud structure at the centimeter scale. *J. Appl. Meteorol.*, **32**, 783-793, 1993

Davis A.B., A. Marshak, H. Gerber H, W.J. Wiscombe, 1999: Horizontal structure of marine boundary layer clouds from centimeter to kilometer scales, *J. Geophys. Res.-Atmos.* **104**: (D6) 6123-6144.

Haman, K. E. and S.P. Malinowski, 1995: Temperature measurements in clouds on a centimetre scale - preliminary results. *Atmos. Res.*, **41** 161-175.

Haman, K. E. and H. Pawlowska, 1995: On the dynamics of non-active parts of convective clouds. *J. Atmos. Sci.*, **52**, 519-531.

Haman. K. E., S.P. Malinowski, A.M. Makulski, B.D. Struś, R. Busen, A. Stefko and H. Siebert, 2000: A Family of Ultrafast Aircraft Thermometers for Warm and Supercooled Clouds and Various types of Aircraft. *In this volume.*

Korolev, A. V and G. A. Isaac, 1998: Drop growth due to high supersaturation caused by isobaric mixing. *Conference on cloud physics, 17-21 August 1998, Preprints,* Everett, Washington, USA, American Meteorological Society, 542-545.

Jaczewski, A. and S. P. Malinowski, 2000: Investigations of droplet clustering on small scales in laboratory cloud-clear air mixing. *in this volume.*

Lawson, R.P., A.V. Korolev, S.G.Cober, T. Huang, J.W. Strapp, G.A. Isaac, 1998: Improved measurements of the drop size distribution of a freezing drizzle event, *Atmos. Res.* **48**: 181-191,

Malinowski, S.P., I. Zawadzki and P. Banat, 1998: Laboratory observations of cloud clear air mixing in small scales. *J. Atmos. Oceanic Technol.*, **15**, 1060-1065.

Malinowski S.P. and A. Jaczewski, 1999: Laboratory Investigation of The Droplet Concentration At The Cloud-Clear Air Interface, *Phys. and Chem. Earth B*, **5**, 477-480.

Pinski, M.B. and A.P. Khain, 1997: Turbulence effects on the collision kernel.I: Formation of velocity deviations of drops falling within a turbulent three-dimensional flow. *Q. J. R. Meteorol. Soc.*, **123**, 1517-1542.

Shaw, R.A., W.C. Reade, L.R. Collins and J. Verlinde, 1998: Preferential Concentration of Cloud Droplets by Turbulence: Effects on the Early Evolution of Cumulus Cloud Droplet Spectra., *J. Atmos. Sci.*, **55**, 1965-1976.

INVESTIGATING THE SMALL-SCALE STRUCTURE OF CLOUDS USING THE δ-CORRELATED CLOSURE: EFFECT OF CONDENSATION/EVAPORATION AND PARTICLE INERTIA

Christopher A. Jeffery*

University of British Columbia, Vancouver, Canada

1 INTRODUCTION

In a recent paper, Shaw et al. (1998) present a mechanism for the broadening of cloud droplet spectra during condensational growth: cloud droplets accumulate in regions of high strain and low vorticity in a turbulent flow due to inertia—a phenomena known as "preferential concentration". They further suggest that a non-uniform droplet field implies a non-uniform supersaturation field which leads to a broader distribution of droplet growth rates. In a short comment Grabowski and Vaillancourt (1999) question a number of Shaw et al. (1998)'s assumptions. In particular Grabowski and Vaillancourt (1999) suggest that the Stokes number (St)—the ratio between the particle response time due to its inertia and the turbulence timescale—is too small for significant preferential concentration to occur. They estimate that for typical atmospheric conditions St $\approx$ 0.07, whereas laboratory experiments demonstrate that significant preferential concentration occurs for St $= \mathcal{O}(1)$.

Adding fuel to this debate, Davis et al. (1999) present horizontal spectra $\phi(k_x)$ of cloud liquid water content (q_l), measured at an unprecedented resolution of 4 cm during the winter Southern Ocean Cloud Experiment (SOCEX), that exhibit anomalously large variability at small-scales. The scalar spectrum from the ensemble-average of the flight segments is shown in Figure 1 ($\Box$), along with the normal inertial-convective and viscous-convective regimes (–). What is particularly intriguing about these new observations are the implications for the scalar dissipation rate χ; with the new scale break, χ in the viscous-convective regime is a factor of 20 larger than the inertial-convective χ, suggesting that a source of scalar variance is present on scales of tens of centimeters. Marshak et al. (1998) suggest that the strong variability shown in Figure 1 on scales of 4 cm to 4 m is consistent with Shaw et al. (1998)'s discussion of strong preferential concentration. On the other hand, Mazin (1999) proposes that the non-inertial-convective scaling is caused by the temporal relaxation of the supersaturation to its steady-state value.

In this extended abstract I summarize recent investigations of the effect of both particle inertia (Jeffery, 2000b) and condensation/evaporation (Jeffery, 2000a) on the small-scale variability of cloud droplets. Both of these studies exploit the availability of an exact closure of the advection-diffusion equation for large particles at small scales discussed in Section 2. In Section 3 I derive an analytic expression for the scalar spectrum of inertial particles valid in the small St regime (St < 0.4), and in Section 4 a model of anomalous small-scale variability in condensation clouds is presented. Section 5 is reserved for conclusions.

2 δ-correlated closure

Numerical and theoretical studies [see (Jeffery, 2000b) and references therein] have shown that the δ-correlated closure is an exact closure for the advection-diffusion equation in the small-scale, large Prandtl number limit. The δ-correlated model derives its name from the temporal properties of the velocity field which are assumed to rapidly decorrelate. The key simplification afforded by the δ-correlated model is that the non-Markovian statistics of tracer trajectories arriving at $(t, \boldsymbol{x})$ from neighbouring points $\boldsymbol{x} + \Delta\boldsymbol{x}$ and from past times $t - \Delta t$ become Markovian, Eulerian statistics at $(t, \boldsymbol{x})$ (Jeffery, 2000b). As a result, each of the tracer particles in such a flow undergoes an effective Brownian motion and the first and second order moments of the passive scalar field (ignoring any source terms) obey diffusion equations. The diffusion equation for the second-order correlation function $\Phi(\boldsymbol{r})$ assuming an incompressible velocity field is (Jeffery, 2000b)

$$\frac{\partial \Phi}{\partial t} = 2D\nabla^2\Phi - 2[D_{mn}(0) - D_{mn}(\boldsymbol{r})]\frac{\partial^2 \Phi}{\partial x_m \partial y_n} + I, \tag{1}$$

where I is the contribution from any source terms, $\boldsymbol{r} = \boldsymbol{y} - \boldsymbol{x}$, $D_{mn}(\boldsymbol{r}) = \langle \tau u_m(0) u_n(\boldsymbol{r}) \rangle$, D is the

* *Corresponding author address:* Christopher Jeffery, Atmospheric Science Programme, Department of Geography, University of British Columbia, Vancouver,B.C., V6T 1Z2, Canada; email: cjeff@geog.ubc.ca

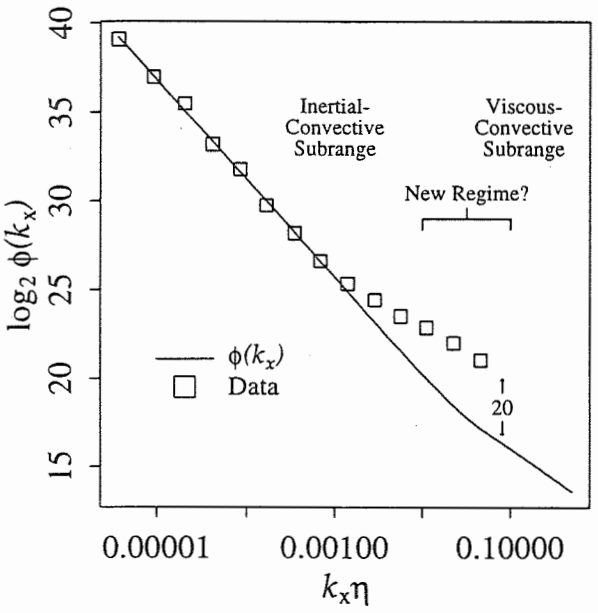

Figure 1: Ensemble-averaged 1D scalar spectrum for cloud q_l data measured during the SOCEX field program and first presented in (Marshak et al., 1998). A typical atmospheric value of 0.76 mm is assumed for the Kolmogorov length η. Also shown is the usual 1D inertial-convective/viscous-convective scaling. The observed spectrum is a factor of 20 greater than the normal spectrum in the viscous-convective regime.

molecular diffusivity and τ is a time constant. Using viscous-regime velocity correlation coefficients, (1) becomes (Jeffery, 2000a)

$$\frac{\partial \Phi}{\partial t} = 2D\nabla^2\Phi + \frac{|\gamma|}{3}\left[2r^2\delta_{mn} - r_m r_n\right]\frac{\partial^2 \Phi}{\partial r_m \partial r_n} + I, \quad (2)$$

where γ is a constant. Eq. (2) may be Fourier transformed to give

$$\frac{\partial \Psi}{\partial t} = -2Dk^2\Psi + \frac{|\gamma|}{3}\left[k^2\frac{\partial^2 \Psi}{\partial k^2} + 4k\frac{\partial \Psi}{\partial k}\right] + I, \quad (3)$$

where Ψ is the spectral density. Eq. (3) was first derived by Kraichnan (1968) who solved (3) with k greater than the Batchelor wave-number and found k^{-1} scaling. Eqs. (2) and (3) are the starting points for the work presented in (Jeffery, 2000b) and (Jeffery, 2000a).

3 Effect of particle inertia

In (Jeffery, 2000b) the effect of particle inertia on the viscous-convective subrange is investigated. The study builds on the work of Elperin et al. (1996) who use the δ-correlated model to assess the effect of particle inertia on spatial statistics and find a mechanism for intermittency in particle concentrations. They later present a solution for the correlation function of inertial particles at small scales (Elperin et al., 1998), i.e. the solution of a modified Eq. (2) that includes particle inertia. However, the results of (Elperin et al., 1996) and (Elperin et al., 1998) were not extended to spectral space and therefore the scales at which preferential concentration occurs were not ascertained. The interested reader is referred to (Jeffery, 2000b) for details concerning the derivation of Ψ for inertial particles. Here, the final result only is presented.

The spectral density Ψ of inertial particles is (Jeffery, 2000b)

$$\Psi = \begin{cases} C_1 k^\mu K_\nu(\lambda k) & k \geq k_m \\ C_3 \mathrm{Re}\left\{\xi^{-a}\,{}_2F_1(a,b,c;\xi^{-1})\right\} & k < k_m \end{cases} \quad (4)$$

where ${}_2F_1$ is a hypergeometric function, K_ν is a modified Bessel function, $\xi = (1 - ik/A)/2$, $C_3 = \Gamma(\nu)(2A)^{-a}(\lambda/2)^{-\nu}/[2\cos(a\pi/2)]C_1$, k_m is computed numerically from the intersection of the two functions, λ is a diffusive length scale proportional to the Batchelor length, and the constants C_1, ν, μ, A, a, b and c are defined in (Jeffery, 2000b). All of the constants in Eq. (4) are functions of St.

The scalar spectrum E, computed numerically using Eq. (4) and the inertial-convective range spectrum, is shown in Figure 2 along with the change in scalar dissipation rate $\chi_{vc}(k)/\chi_{ic}$. The suppression of the scalar spectrum in the viscous-convective regime at larger scales and the clumping of inertial particles are clearly visible. Beginning at $\sigma \approx 0.007$ a peak at $k_p \approx 0.1\eta^{-1}$ indicative of clumping is visible in the spectrum and becomes more pronounced as σ increases. Here σ is a parameter that represents the degree of particle inertia and is related to St according to

$$\frac{\sigma}{1+\sigma} = \frac{4}{15}\mathrm{St}^2. \quad (5)$$

The figure demonstrates that clumping does not occur until $\sigma > 0.007$ (St > 0.15). This finding supports the contention of Grabowski and Vaillancourt (1999) that cloud droplets are too small for significant preferential concentration to occur.

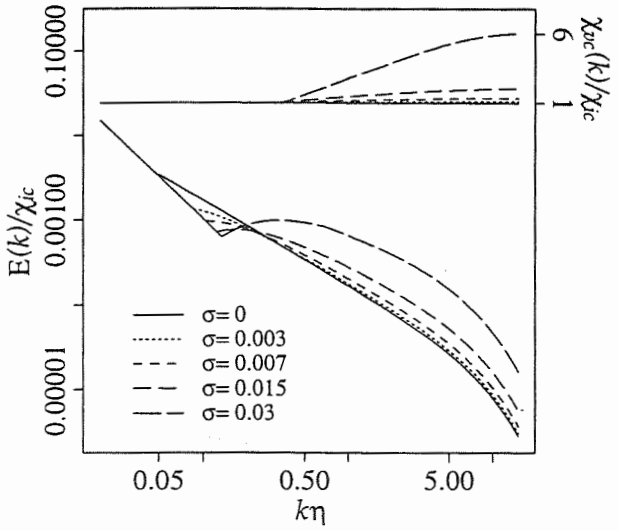

Figure 2: The scalar spectrum computed at various σ [Eq. (5)] using Eq. (4) and the corresponding increase in scalar dissipation rate.

4 Effect of condensation and evaporation

In (Jeffery, 2000a) the study of the effect of condensation/evaporation on the viscous-convective subrange begins with the following stochastic equation for the cloud liquid water content q_l:

$$\frac{\partial q_l}{\partial t} + \boldsymbol{u}' \cdot \nabla q_l = D\Delta q_l + \frac{w'}{z} q_l \qquad (6)$$

where z is the height above cloud base and D is the molecular diffusivity. Ignoring molecular diffusion and assuming stationarity and horizontal homogeneity gives $\langle w' q_l' \rangle \sim z$ which agrees well with observational and numerical data. The source term $w' q_l / z$ is a mean-field approximation that decouples q_l from the vapour and temperature fields. It is consistent with Lagrangian parcel models of diffusional growth of water drops in clouds where $\partial q_l / \partial t \sim (q_l/a) da/dt \sim q_l/t \sim w q_l / z$, and where a is the radius of the drop. The derivation of the source term is discussed in (Jeffery, 2000a) in more detail.

In (Jeffery, 2000a) I propose that the increased small-scale variability shown in Figure 1 is caused by the effect of condensation and evaporation on the viscous-convective subrange. Condensation and evaporation is modeled stochastically via the last term on the rhs of Eq. (6) where for small scales, $r \ll z$, z is treated as a constant parameter. The closure of Eq. (6) using the δ-correlated model is considerably more complicated than the corresponding closure for inertial particles (Section 3) because fluctuations of q_l are non-homogeneous ($|q_l'|$ increases with increasing z) and axisymmetric. As a result the the spectral density is axisymmetric and complex.

Derivation of the spectral density Ψ proceeds as follows. First, the axisymmetric equivalent of Eq. (3) is derived:

$$\begin{aligned} \frac{\partial \Psi}{\partial t} &= -2Dk^2\Psi + \frac{|\gamma|}{3} T(\Psi), \\ T(\Psi) &= k^2 \frac{\partial^2 \Psi}{\partial k^2} + 4k \frac{\partial \Psi}{\partial k} + \frac{2\cos\theta}{\sin\theta} \frac{\partial \Psi}{\partial \theta} + 2 \frac{\partial^2 \Psi}{\partial \theta^2}. \end{aligned}$$

The solution can be written as a infinite series of Legendre polynomials in $\mu = \cos\theta$:

$$\Psi(k,\mu) = \sum_{j=0}^{\infty} c_j k^{-3/2} K_{\nu(j)}(\lambda k) P_j(\mu)$$

where $\nu(j) = [9 + 8j(j+1)]^{1/2}/2$, and where the Fourier space symmetry relation $\Psi(\boldsymbol{k}) = \Psi^*(-\boldsymbol{k})$ restricts the c_j's such that for even j, $\mathrm{Re}\{c_j\} \in \mathbb{R}_+$ and $\mathrm{Im}\{c_j\} = 0$, whereas for odd j, $\mathrm{Re}\{c_j\} = 0$. Expansion of the scalar spectrum in terms of Legendre polynomials was first suggested by Herring (1974) who derived an equation for Ψ in axisymmetric turbulence using Kraichnan's direct interaction approximation (DIA).

The next step, described in Section V of (Jeffery, 2000a), is to add the source term. After some work the resulting equation for the scalar spectrum is

$$E(k) = \frac{\chi}{|\gamma|} k^{-1} [1 + \lambda k] \exp(-\lambda k) - \frac{\chi}{|\gamma|} \frac{\zeta}{3} \lambda^{-2} k^{-3}. \qquad (7)$$

where ζ is a Kolmogorov-like constant that represents the magnitude of the non-homogeneous (imaginary) component of the spectral density. The 1D horizontal spectrum defined by $\phi(k_x) = \int_{k_x}^{\infty} k^{-1} dk\ E(k)$ is shown in Figure 3 along with the experimental data from (Davis et al., 1999). Also shown is a "production subrange" where the scalar dissipation rate increases with increasing k. The good agreement between the modeled and observed spectra for $k \geq 0.02\eta^{-1}$ is not fortuitous—the unknown constant ζ was chosen to produce a close correspondence between the two spectra in this region. Figure 3 reveals that the effect of condensation and evaporation as modelled by Eq. (6) can explain the anomalous scaling found by Davis et al. (1999).

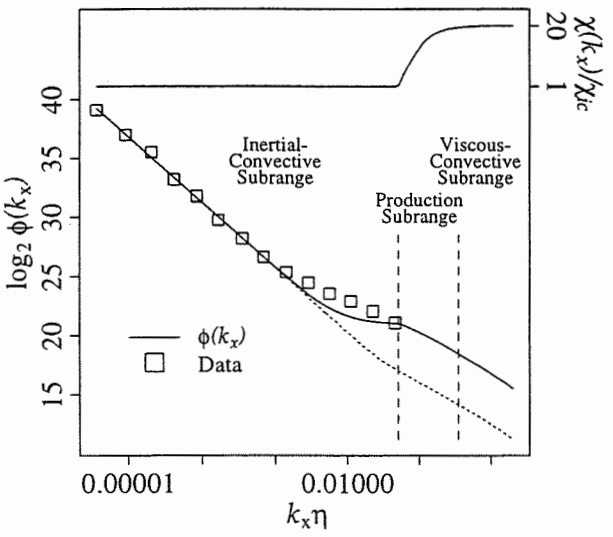

Figure 3: Comparison of the ensemble-averaged 1D q_l scalar spectrum measured during SOCEX (Davis et al., 1999) and the present model Eq. (7). A production subrange where $\chi(k_x)$ increases with increasing k (solid line), and normal viscous-convective scaling (dashed line) are also shown.

5 Summary

The small-scale variability of cloud liquid water is investigated using the δ-correlated closure. The spectral density of inertial particles in isotropic, homogeneous turbulence is derived in the small Stokes number regime (St < 0.4). In the scale range 13-60 η a peak in the spectrum is observed when the ratio of the energies in the compressible and the incompressible components of the particle's velocity is greater than 0.007 (St > 0.15). The peak is a manifestation of preferential concentration—the accumulation of inertial particles in regions of high strain and low vorticity. The effect of preferential concentration for Stokes numbers typical of cloud droplets, St ≈ 0.07, is not significant as discussed in (Grabowski and Vaillancourt, 1999) and contrary to the hypothesis of Shaw et al. (1998).

The effect of condensation and evaporation on the spectral density is also investigated using a simple mean-field model that reproduces the non-homogeneous vertical structure of liquid water fluctuations observed in atmospheric clouds. Expressions for the scalar density are derived and used to reproduce the spectral behaviour of new atmospheric measurements that exhibit anomalous scaling of cloud liquid water in the near inertial-convective regime. The model assumes a significant imaginary (non-homogeneous) component to the spectrum that is indicative of a strong vertical coherence in clouds. The strongly non-homogeneous (anisotropic) character of the predicted scalar spectrum is in stark contrast with atmospheric models of inertial-convective regime cloud inhomogeneity that are used in radiative transfer calculations and that are typically isotropic.

References

Davis, A., A. Marshak, H. Gerber and W. J. Wiscombe, 1999: Horizontal structure of marine boundary-layer clouds from cm to km scales. *J. Geophys. Res.*, **104**(D6), 6123–6144.

Elperin, T., N. Kleeorin and I. Rogachevskii, 1996: Self-excitation of fluctuations of inertial particle concentration in turbulent fluid flow. *Phys. Rev. Lett.*, **77**(27), 5373–5376.

Elperin, T., N. Kleeorin and I. Rogachevskii, 1998: Anomalous scalings for fluctuations of inertial particles concentration and large-scale dynamics. *Phys. Rev. E.*, **58**(3), 3113–3124.

Grabowski, W. W. and P. Vaillancourt, 1999: Comments on "Preferential concentration of cloud droplets by turbulence". *J. Atmos. Sci.*, **56**, 1433.

Herring, J. R., 1974: Approach of axisymmetric turbulence to isotropy. *Phys. Fluids*, **17**(5), 859–872.

Jeffery, C. A., 2000a: Effect of condensation and evaporation on the viscous-convective subrange. *Phys. Fluids*, Submitted.

Jeffery, C. A., 2000b: Effect of particle inertia on the viscous-convective subrange. *Phys. Rev. E*, **61**(6).

Kraichnan, R. H., 1968: Small-scale structure of a scalar field convected by turbulence. *Phys. Fluids*, **11**(5), 945–953.

Marshak, A., A. Davis, W. Wiscombe and R. Cahalan, 1998: Radiative effects of sub-mean free path liquid water variability observed in clouds. *J. Geophys. Res.*, **103**(D16), 19,557–19,567.

Mazin, I., 1999: The effect of condensation and evaporation on turbulence in clouds. *Atmos. Res.*, **51**, 171–174.

Shaw, R. A., W. C. Reade, L. R. Collins and J. Verlinde, 1998: Preferential concentration of cloud droplets by turbulence. *J. Atmos. Sci.*, **55**, 1965.

TIME-SCALE ANALYSIS ON THE INTERACTIONS BETWEEN TURBULENCE, DIFFUSION, SEDIMENTATION AND CONDENSATIONAL GROWTH OF CLOUD DROPLETS

Tzung-may Fu, Min-Hui Lo, and Jen-Ping Chen

Department of Atmospheric Sciences, National Taiwan University, Taipei, Taiwan, 106, R.O.C.

1. INTRODUCTION

The evolution of cloud drop size distributions (DSD's) has been extensively studied both experimentally and theoretically. Theoretical calculations show that DSD's produced by condensation in a closed parcel under adiabatic expansion are normally very narrow. Yet in-cloud observations conducted by Warner (1969a,b) and others have shown broad, bimodal DSD's prior to the onset of significant coalescence. This feature of the DSD's is a crucial factor to the development of precipitation in warm clouds.

Many hypotheses have been raised to explain the broadening of DSD's without involving collision-coalescence or sedimentation-sorting processes. Among them, entrainment-mixing induced broadening is one of the most popular school of thought. The classical approach to the mixing process assumes that the cloud and the entrained air are instantaneously and uniformly mixed (e.g., Warner 1970). That is to say, the mixing process is much faster than the condensational growth of cloud droplets. All droplets within the cloud are exposed to homogeneous conditions. Despite the simplicity of this model, the resulting DSD's greatly differ from those of Warner's observations.

A strictly inhomogeneous approach brought forward by Baker et al. (1980) assumes that the mixing process is much slower than the condensational growth of clouds droplets. In other words, the entrained air will affect only a small part of the cloud at a given level. Results from their study show better resemblance to the observation, although the actual mixing mechanism is not specified. Later, Baker and Latham (1982) proposed a diffusive model to represent the turbulent mixing of dry and cloudy air. However, the idea that turbulent mixing should take place as a single blob of dry air diffusing continuously still gives rise to much concern.

Disagreements still exist about whether the entrainment-mixing occurs as a homogeneous or inhomogeneous process. Some of the difficulties in resolving this problem stem from the ambiguities about the diverse time scales of various processes involved.

In this paper we provide a detailed examination on the time scales between four different processes: (1) condensational growth of cloud droplets; (2) molecular diffusion between the entrained dry air and the surrounding cloud; (3) turbulent break-up of the entrained air into the cloud; and (4) the sedimentation of cloud droplets into entrained air. We further propose an conceptual model by which entrainment-mixing takes place.

Corresponding author's address: Dr. Jen-Ping Chen, Department of Atmospheric Sciences, National Taiwan University, Taipei, Taiwan, 106, R. O. C.;
E-Mail: jpchen@water.as.ntu.edu.tw

2. TIME SCALE ANALYSIS

2.1 Condensational growth of cloud droplets

We follow Baker et al. (1980) by setting S (%) as the undersaturation, D_v (m^2 s^{-1}) the molecular diffusion coefficient of water vapor, and a (~5 μm) the length associated with the condensation coefficient (Fukuta and Walter 1970). The time scale τ_r of the evaporation of a cloud droplet of radius r (μm) in an undersaturated environment can be written as:

$$\tau_r \sim 6\times10^{-6}\left[(r+a)^2 - a^2\right]\Big/ D_v S . \qquad (1)$$

Therefore, smaller droplets will have a shorter response time to undersaturation.

The time scale τ_r is useful in evaluating the effect of various processes on the DSD. In general, if a physical process takes place much slower than the condensational growth of cloud droplets, the DSD's will remain unaffected by that process. On the other hand, if the physical process is extremely fast, it will impose a homogeneous effect on the surrounding cloud.

2.2 Molecular diffusion of air

Take λ_E as the dimension of a piece of entrained dry air. Note that we refrain from using the term "blobs of dry air," as is common in literature. Indeed, the chunks of dry air may take on various shapes. The time scale τ_d of molecular diffusion between the entrained piece and the surrounding environment can be written as:

$$\tau_d \sim \lambda_E^{\,2}/D , \qquad (2)$$

where D (m^2 s^{-1}) is the molecular diffusion coefficient of air, and is of the same order to D_v. Figure 1 shows the value of (τ_d / τ_r) as a function of cloud droplet radius and the dimension of dry air filament.

The critical dimension λ^*_{dr}, at which the ratio (τ_d / τ_r)=1, can be derived from (1) and (2) as:

$$\lambda^*_{dr} \sim \left\{6\times10^{-6}\left[(r+a)^2 - a^2\right]\Big/ S\right\}^{1/2} . \qquad (3)$$

For large (low curvature) pieces of dry air, the molecular diffusion is extremely slow, and is confined to the interface between the blob and the surrounding cloud. Below the critical dimension λ^*_{dr}, diffusion becomes more efficient, and tends to have a homogeneous effect on

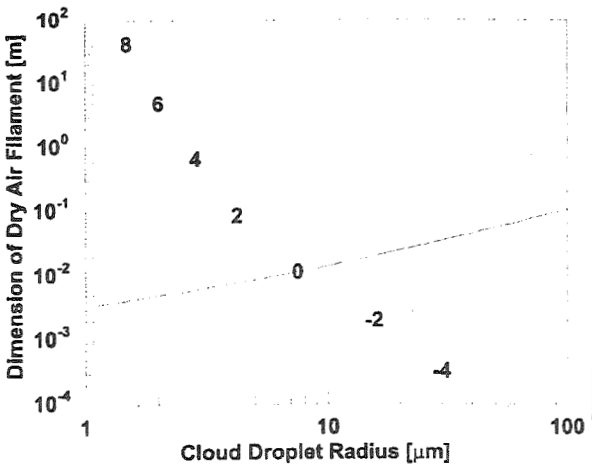

Figure 1. The time scale ratio (τ_d / τ_r) as a function of cloud droplet radius and the dimension of dry air filament. The contours are the $\log_{10}$ values of (τ_d / τ_r). Undersaturation S is set to 10%.

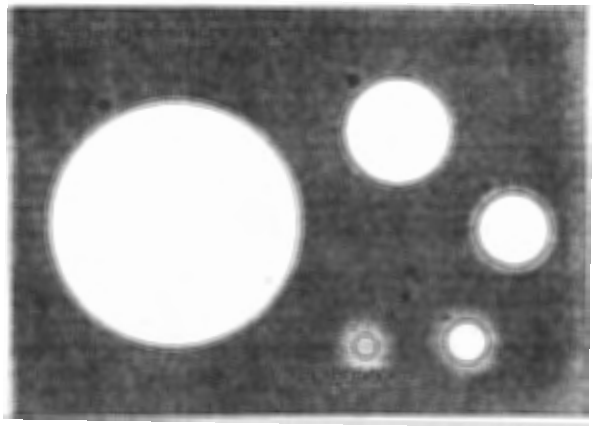

Figure 2. Conceptual illustration of water vapor diffusion. For large pieces of dry air, molecular diffusion is negligible. For smaller filaments of dry air, diffusion is more efficient, and the range of influence is extended further into the cloud.

the surrounding cloud (Fig. 2). Consider cloud droplets positioned at a same distance from the interface. Those droplets near a smaller piece of dry air will experience more evaporation. Note also that smaller cloud droplets are more vulnerable to undersaturation.

2.3 Turbulent break-up of the entrained air

Again, consider a piece of entrained air of the size λ_E. We may determine from dimensional grounds, similar to Baker et al. (1980), the decaying time scale τ_t as it mixes with the surrounding cloud:

$$\tau_t \sim c_1\left(\lambda_E^2/\varepsilon\right)^{1/3}, \qquad (4)$$

where ε is the rate of dissipation of turbulent energy within the cloud, with a typical value of 10^{-3} (m^2 s^{-3}). The constant c_1 (~0.06) is specific to the mixing mechanism.

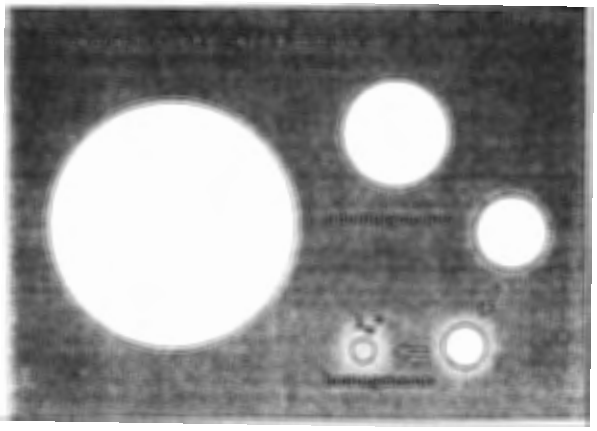

Figure 3. The conceptual illustration of the interaction between turbulent break-up and diffusion. Turbulence accelerates the diffusion process by breaking pieces of dry air into smaller filaments.

Under normal atmospheric conditions, turbulent break-up is much faster than molecular diffusion. However, we must keep in mind that the 'ultimate' mixing process occurs by molecular diffusion. What does this mean? Recall in Fig. 2, we see that for large pieces of dry air, diffusion is extremely slow. Only those droplets very near the interfaces are affected. As dry air breaks down to smaller components, diffusion becomes more efficient, and the range of influence is extended to a greater distance. Below the critical dimension λ_{dr}^*, the dry air will impose a homogeneous effect on the surrounding cloud. In other words, the overall molecular diffusion is greatly accelerated by turbulent break-up (Fig. 3).

2.4 Sedimentation of cloud droplets

While diffusion is slow for large filaments of dry air, exchange of water vapor can still be achieved through sedimentation of cloud droplets. Picture a cloud droplet of radius r falling at its natural terminal velocity u_∞, penetrating a piece of dry air of thickness λ_E. The time taken, τ_s, is:

$$\tau_s \sim \lambda_E / u_\infty . \qquad (5)$$

Figure 4 illustrates the ratio (τ_s / τ_r) for various droplet radius and dry air thickness. The cloud droplets will experience different degrees of evaporation, and thus altering the DSD's.

Three scenarios should be considered: (a) (τ_r / τ_s) << 1, (b) (τ_s / τ_r) ~ 1, and (c) (τ_r / τ_s) >> 1, as illustrated in Fig. 5. If droplets are too small, or that the dry air is too thick (i.e. (τ_r / τ_s) << 1), then the water vapor exchange is limit to the vicinity of the interface between the dry air and cloud (Fig. 5a). On the other extreme, if cloud droplets are big, or that the dry air is too shallow (i.e. (τ_r / τ_s) >> 1), then evaporation is minimal because droplets fall through rather quickly (Fig. 5c). Both scenarios contribute very little in eliminating the inhomogeneity between cloud and dry air. In scenario (b), however, if

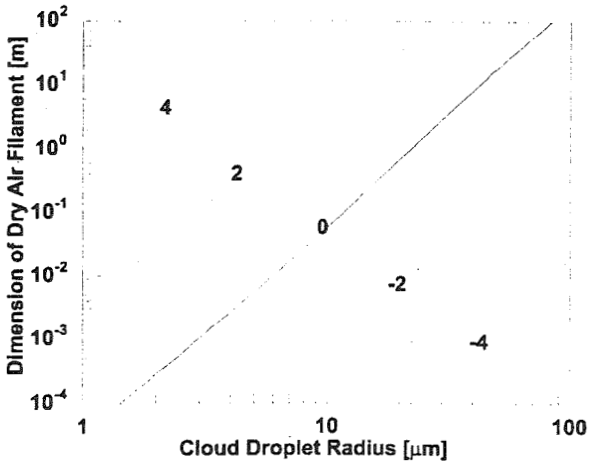

Figure 4. The time scale ratio (τ_r / τ_s) as a function of cloud droplet radius and the dimension of dry air filament. The contours are the $\log_{10}$ values of (τ_r / τ_s). Undersaturation S is set to 10%. The solid line indicates the critical dimension, as a function of cloud droplet radius, at which (τ_r / τ_s) ~ 1.

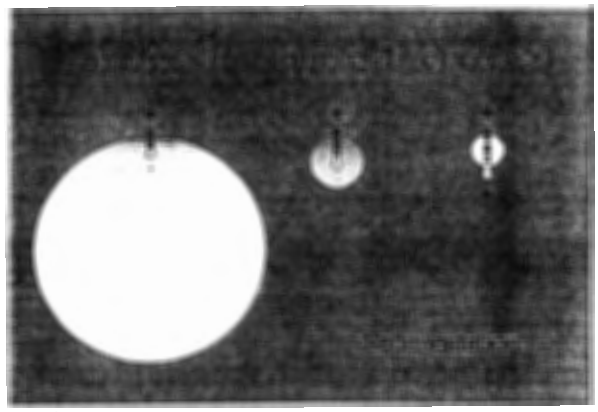

Figure 5. Conceptual illustration of the effect of cloud droplet sedimentation. (a) (τ_r / τ_s) << 1: Exchange of water vapor is confined to the vicinity of the interface. (b) (τ_r / τ_s) ~ 1: The dry air is effectively moistened as cloud droplets evaporate in its interior. (c) (τ_r / τ_s) >> 1: The cloud droplets fall too fast, evaporation is minimal.

(τ_s / τ_r) ~ 1, the evaporating droplets will bring a flux of water vapor to the interior of the dry air, moistening the dry air as they fall through (Fig. 5b). Thinking from a different point of view, the cloud droplets are actually creating more 'interfaces' between the cloud and the dry air, so as to accelerate the molecular diffusion of water vapor. The critical size λ_{rs}^*, at which (τ_s / τ_r) ~ 1, is a function of droplet radius:

$$\lambda_{sr}^* \sim u_\infty(r) \cdot \tau_r \,. \qquad (6)$$

For pieces of dry air of the same size, smaller droplets are more likely to evaporate. Note that if we take into account the motion of the dry air filaments, the inertia of cloud droplets will impose a secondary effect.

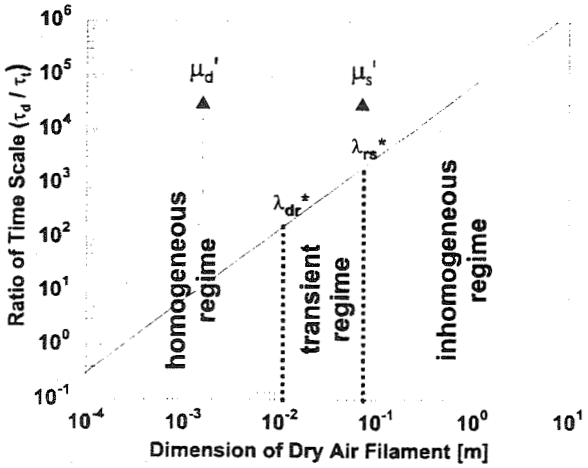

Figure 6. Illustration of the conceptual model. Here the undersaturation S *is set to* 10%, and the droplet radius r=10μm. Turbulence breaks the dry air into smaller components. Two critical dimensions, λ_{rs}^* and λ_{dr}^*, mark the three different regimes in which cloud droplets are affected by very different physical processes. See Section 3 for details.

3. THE CONCEPTUAL MODEL

Based on time-scale analysis in Section 2, we propose a conceptual model by which entrainment-mixing takes place. See Fig. 6 for illustration.

Initially, pieces of dry air are entrained into the cloud at a certain rate μ. They then break up into smaller and smaller components. We follow Kolmogorov (1941) by hypothesizing that the turbulence is steady. In other words, pieces of dry air of various dimensions exist and maintain a steady distribution on their sizes. Therefore the cloud, on the whole, is inhomogeneous.

Homogeneous mixing comes from two different sources. On the one hand, diffusion becomes efficient at the critical dimension λ_{dr}^*. Below this point, the dry air is homogeneously mixed with its surrounding cloud. Under the steady state assumption, this is as if a steady flux of dry air μ_d', is homogeneously blended into the cloud. On the other hand, near the critical size λ_{rs}^*, the pieces of dry air are efficiently moistened by droplet sedimentation. This exchange of water vapor can also be considered as a flux of dry air μ_s', mixing homogeneously with the cloud.

We stress that the critical sizes, λ_{rs}^* and λ_{dr}^*, are highly sensitive to cloud droplet radius. Therefore, a differential modification of DSD's is evident.

Pieces of dry air much larger than λ_{rs}^* are highly inhomogeneous, and all droplets falling into are evaporated. The average DSD's near these regions are likely to resemble that proposed by Baker et al. (1980). That is, a reduction in the number concentration of cloud droplets of all radii, while the general shape of the DSD's remains unchanged.

In the transient regime where the dimension of dry air filament is between λ_{rs}^* and λ_{dr}^*, neither diffusion nor

droplet sedimentation is efficient. The cloud droplets are roughly unaffected, until turbulence breaks the dry air into smaller component and diffusion takes over.

4. DISCUSSION

In the model presented here, the cloud on the whole is inhomogeneous. Pieces of dry air go through different regimes as they break into smaller and smaller components. At any instant, a flux of dry air ($\mu_d'+\mu_s'$) is homogeneously mixed with the cloud, changing the thermodynamic conditions within the cloud at that given level. On the other hand, large pieces of freshly entrained dry air remain almost intact and unmixed. They change the DSD's only through droplet sedimentation.

Observation aircraft will inevitably collect some portion of the cloud and the unmixed dry air as it samples in the cloud. Liu (1993) showed that the Marshall-Palmer distribution observed in raindrops can be produced by averaging over a large sample of gamma-distributed raindrops. Similarly, we suspect that the bimodal feature of cloud droplets as seen in observations may be a statistical result of the inhomogeneous components. Numerical studies are currently undertaken to test the new model.

Other physical processes may be considered to complete the picture. For example, on the microscopic scale, phoretic forces may have a secondary effect on the drift of droplets toward the dry air. On larger scales, Telford (1975) suggested that fluctuation in the vertical velocity inside a cloud might significantly broaden the DSD. In any case, a detailed time-scale analysis such as the present study will be useful in clarifying the relative importance of various processes.

5. REFERENCE

Baker, M. B., R. G. Corbin, and J. Latham, 1980: The influence of entrainment on the evolution of cloud droplet spectra: I. A model of inhomogeneous mixing. *Quart. J. R. Met. Soc.*, **106**, 581-598.

------, and J. Latham, 1982: A diffusive model of the turbulent mixing of dry and cloudy air. *Quart. J. R. Met. Soc.*, **108**, 871-898.

Fukuta, N., and L. A. Walter, 1970: Kinetics of hydrometeor growth from a vapour-spherical model. *J. Atmos. Sci.*, **27**, 1160-1172.

Landahl, M. T., and Mollo-Christensen, E., 1992: *Turbulence and Random Processes in Fluid Mechanics*, 2nd ed. Cambridge University Press, 168 pp.

Liu, Y., 1993: Statistical theory of the Marshall-Palmer distribution of raindrops. *Atmospheric Environment*, **27A**, No. 1, 15-19.

Kolmogorov, A. N., 1941: The local structure of turbulence in incompressible viscous fluid for very large Reynolds numbers. *Dokl. Akad. Nauk* SSSR **30**, 299-303.

Taylor, G. I., 1935: Statistical theory of turbulence, I-III. *Proc. Roy. Soc.*, **A151**, No. 874, 421-464.

Telford, J. W., 1975: Turbulence, entrainment, and mixing in cloud dynamics. *Pure Appl. Geophys.*, **113**, 1067-1084.

Warner, J., 1969a: The microstructure of cunulus cloud. Part I. General features of the droplet spectrum. *J. Atmos. Sci.*, **26**, 1272-1282.

------, J., 1969b: The microstructure of cumulus clouds. Pt. II. The effect on droplet size distribution of the cloud nucleus spectrum and updraft velocity. *J. Atmos. Sci.*, **26**, 1272-1282.

------, J., 1970: On steady-state one-dimensional models of cumulus convection. *J. Atmos. Sci.*, **27**, 1035-1040.

THE EFFECTS OF TURBULENCE ON THE GROWTH OF DROPLETS BY CONDENSATION OF WATER VAPOR IN CLOUDS

J. A. Martins [1], F. C. Almeida [2], N. J. Ferreira [2]

[1] *Centro Federal de Educação Tecnológica do Paraná, C. Procópio, PR, Brazil*
[2] *Instituto Nacional de Pesquisas Espaciais, S. J. Campos, SP, Brazil*

1. INTRODUCTION

The problem of how cloud particles (water droplets or ice crystals) grow has called the attention of the meteorologists for decades. The current accepted theory of the growth of cloud droplets by condensation of water vapor inside warm clouds is attributed to Howell (1949). According to this theory, the growth rate of cloud particles by condensation or deposition in a supersaturated environment decreases with the increasing radius of the particles. This implies that even if the initial size distribution is wide, the subsequent growth of these particles will narrow the distribution. However, for the precipitation process, it is necessary that the growth of cloud droplets by condensation results in a distribution capable of inducing the growth by collection.

Assuming that some degree of turbulence is present in clouds, it is important to consider its effects in the evolution of a droplet distribution. The main problem is to determine how the turbulence present in the initial stages of a cloud can affect the evolution of the droplet distribution. This complex problem was treated by Almeida (1976, 1979) in his theory on the effects of turbulence in the collisional growth of cloud droplets. Almeida's results indicate that turbulence tends to increase the collision efficiency for small droplets. Almeida's work represents a significant progress in the attempt to develop a growth theory capable of explaining the stochastic nature of the precipitation process. However, his studies do not approach the possible effects of turbulence in the growth phase by condensation. In this work, the presence of turbulence in updraft motions in real clouds is assumed as a factor that could be responsible for the broadening observed in the size distribution of cloud droplets, as a result of the growth process by condensation.

2. GROWTH OF CLOUD DROPLETS

The diffusion of water vapor and heat, in addition to the effects of curvature, solubility and the dependence of the saturation pressure with the temperature are the mechanisms directly involved in the condensation of water vapor in clouds. These mechanisms constitute the basis of the development of the accepted theory about the growth of cloud droplets by condensation, called here the theory of continuous growth. Following this theory the growth equation (Srivastava, 1989) can be written as:

$$r\frac{dr}{dt} = a(s - s_{eq}),$$

where r is the droplet radius, s is the supersaturation and a and s_{eq} are functions of the temperature, pressure, chemical composition and droplets radius. Curves for the equilibrium supersaturation in the droplet surface as a function of the radius and the mass of the solute inside droplets, known as Kohler curves, are shown in Fig. 1 with typical values for the troposphere.

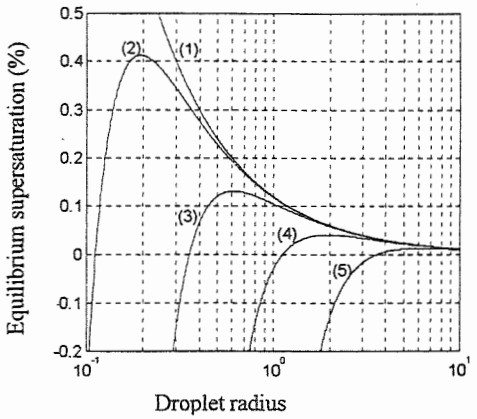

Fig. 1 Variation of the droplet equilibrium supersaturation with the droplet radius, as a function of NaCl in solution at 0 °C. The values of the solute masses are 0 kg (1), 10^{-19} kg (2), 10^{-18}kg (3), 10^{-17}kg (4), and 10^{-16}kg (5).

Fig. 1 shows that both terms, curvature and solute, decrease in importance as the droplet radius increases. Due to this dependence, these effects are usually neglected when the droplets reach sizes larger than a few micrometers. The present work involves fundamentally the effects of turbulence during nucleation of the droplets. In this context it will be shown that these terms (curvature and solute) in a turbulent environment should not be neglected, as they induce a different behavior to the growth problem as compared to na assumed constant supersaturation environment.

3. CONCEPTUAL MODEL

3.1. Fluctuating Supersaturation Field

Essentially the solute mass and the radius of the particle characterize the equilibrium supersaturation. It defines the minimum amount of water vapor necessary to activate the nucleus. This activation is possible only if the environment

Corresponding author's address: Jorge A. Martins,
Centro Federal de Educação Tecnológica do Paraná,
86300-000 Cornelio Procópio, Paraná, Brazil,
jmartins@onda.com.br

supersaturation is larger than the equilibrium supersaturation. In a turbulent environment the field of supersaturation in which the droplet grows, will be characterized as a fluctuating field in time. From this, two important questions can be formulated:

a) If supersaturation is fluctuating (around an average value), will the evolution of the droplet size distribution be the same as in the case of a constant supersaturation?
b) Does a field of fluctuating supersaturation (turbulent environment) cause broadening or narrowing in the droplet distribution?

3.2. Model Description

Regarding the answers for the previous questions, some aspects could be inferred from Fig. 2, which depicts a small sample of the supersaturation field in which the droplets grow. For this example, as shown in Fig. 2., the instantaneous supersaturation s is fluctuating in time and can be represented by:

$$s = \bar{S} + s'$$

where $\bar{S}$ is the average supersaturation and s' is the departure from average.

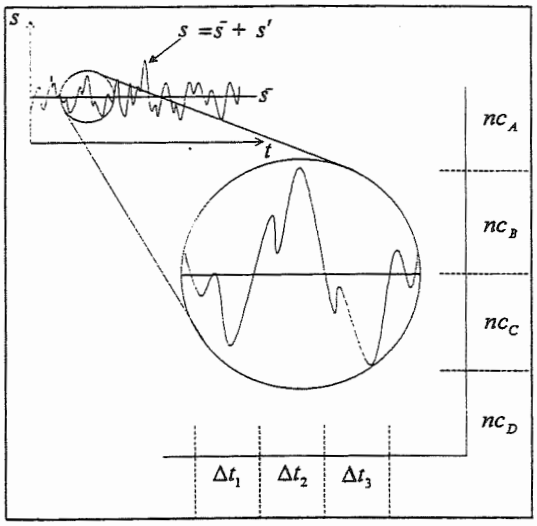

Fig. 2. Outline of a small sample of supersaturation inside clouds. The straight line shows the average supersaturation, while the curve represents the instantaneous supersaturation.

To understand the importance of turbulence in the nucleation of droplets, let us consider four nuclei classes in the distribution, or: nc_A, nc_B, nc_C and nc_D . These classes were chosen taking into account the value of the maximum equilibrium supersaturation for each class (critical value). It is observed that, in agreement with the currently accepted theory (growth at constant supersaturation), just the nucleus belonging to classes nc_C and nc_D will play a role in the resulting droplet distribution. In this case, the environment supersaturation considered constant and taking to be represented by $\bar{S}$ is always above the critical value. As for the nuclei belonging to classes nc_A and nc_B , having critical values above the assumed 'constant supersaturation' $\bar{S}$, they will not be activated. A different behavior will be noticed for each nuclei class. The nuclei belonging to the class nc_A have critical value above the characteristic value of the environment supersaturation and they will never be activated. These nuclei will not take part in the droplet distribution during its evolution. On the other hand, nuclei belonging to the classes nc_B and nc_C are submitted to environment supersaturations that, in certain intervals of time, assume values above the nuclei classes critical values. These nuclei have the probability of being activated and thus becoming part of the distribution. This probability is larger for nuclei belonging to class nc_C than those belonging to class nc_B. Finally, the nuclei belonging to class nc_D will always be activated as they present equilibrium supersaturations below the value of the turbulent environment supersaturation.

From the previous considerations, the current accepted model of cloud droplets growth by condensation could be understood as a 'continuous model of growth'. In this context, all the nuclei, with equilibrium supersaturations below the average environment supersaturation value (considered constant), grow at a given rate, and the other ones remain nonactivated. However, this model does not explain the probability of nucleus activation, whose critical value is above the average one. Also, it does not explain the probability of nonactivation of those nuclei having critical values below the environment supersaturation average value. In other words, the real atmosphere is turbulent and the environment supersaturation is not constant in the vicinity of the droplets. For this reason, the probabilistic features of droplet activation should be considered.

3.3. Determinant Factors

There are two main important factors for the nucleation of droplets in a turbulent environment The first one is the time scale involved with the supersaturation fluctuations in a turbulent atmosphere. The importance of the supersaturation is due to its high correlation with the field of vertical velocity (Bartlett and Jonas, 1972). Positive fluctuations in the vertical velocity (positive means updraft) imply negative fluctuations in the temperature (adiabatic expansion). On the other hand, negative fluctuations in the temperature are associated with negative fluctuations in the saturation pressure (Clausius-Clapeyron equation) or positive fluctuations in the environment supersaturation. From the nucleus activation, the growth rate is dependent on the droplet radius and consequently variable in time. To remain activated, a nucleus belonging to class nc_B demands that the time scale Δt_2 be large enough to lead it to a value of equilibrium supersaturation (s_{eq}) typical of the class nc_D. In Fig. 2 the time scale Δt_2 corresponds to positive fluctuation in the supersaturation field and nc_D is a class of nuclei characterized by nuclei permanently activated. Negative fluctuations in the supersaturation field are observed in the time scales Δt_1 and Δt_3 (Fig. 2).

The second important factor related to the turbulent effects in nuclei activation is related to the amount of extra nuclei that would be activated by the fluctuating supersaturation field. If the amount of extra nuclei is not representative, the changes in the size distribution are not significant and the effects of the turbulence in the activation phase can be neglected. A

synthesis of the distribution of nuclei measured in several parts of the world is found in Twomey and Wojciechowski (1969), where the total number of activated nuclei N_{nc}, as function of the supersaturation s can be given approximately by the expression:

$$N_{nc} = Cs^{K}$$

where the constant values C and K depend on the nature and the distribution of the nuclei. From the above equation the number of condensation nuclei activated in a cloud is proportional to the supersaturation. This fact can be interpreted as a progressive activation in the direction of the smallest nuclei.

4. DISCUSSION

4.1. Turbulence Simulation Model

There are a few models of turbulence simulation inside clouds available. The models of Jonas and Bartlett (1972) and Almeida (1979a) are examples of models where the turbulence simulation lead to a spectrum of turbulent kinetic energy that follows a -5/3 power law. As our purpose is to investigate the trends of the turbulence supersaturation field as affecting the initial process of precipitation formation, the simpler model of Jonas and Bartlett (1972) will be used. Supersaturation is taken as a linear function of the vertical velocity.

4.2. Effects of Turbulence

4.2.1. Extra Nuclei Activation

The main consequence of a turbulent atmosphere in the growth of droplets was discussed previously and it is related to the droplet activation. It was argued that an environment with a fluctuating supersaturation field (Fig. 3.a) will result in a 'extra quota' of activated nuclei than it would happen in a constant supersaturation environment ($S = \overline{S}$). Thus, occurring the nucleation, the equilibrium supersaturation evolves rapidly to a pattern of inverse proportionality with the radius (Fig. 1). This indicates that the probability of nonactivation of the droplets tends to zero rapidly, since the environment stays supersaturated.

Fig. 3.b shows a sample of an event in which a NaCl nucleus with mass of 10^{-19} kg is submitted to a given supersaturation field (the maximum value for the equilibrium supersaturation of this nucleus is approximately equal 0,42%). Curve I of this figure shows a supersaturation field fluctuating in time with an average value equal to 0,35%. Curve II shows a supersaturation field with constant value equal to 0,35% (theory of continuous growth). It is observed that if the supersaturation field of 0,35% is fluctuating, the droplets can be activated (curved I of Fig. 3.b) and if this field is considered constant in time, the activation does not occur (curve II of the same figure). This feature answers the first question formulated in our conceptual model (item 3.1). In other words, when the supersaturation is fluctuating around an average value, additional droplets become part of the distribution. Thus the evolution of the droplet size distribution will be not the same as in the case of continuous growth.

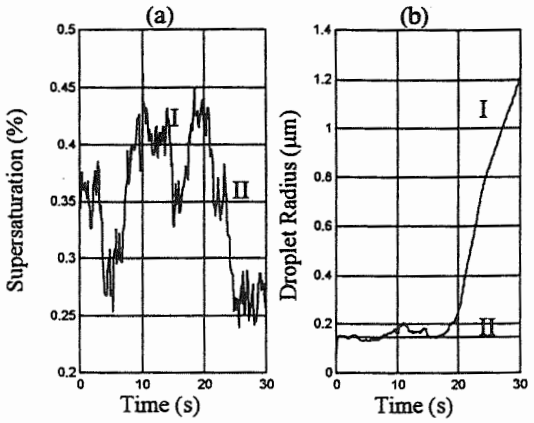

Fig. 3. Supersaturation field and time evolution of the droplet radius for an event involving droplets activation with an average value below the critical value.

4.2.2. Dispersion

There are two other important aspects related to the dispersion of a droplet distribution. When the supersaturation is constant (theory of continuous growth), only one final value exists for an initial droplet radius. However, if the supersaturation value is fluctuating in time, even if the average value is equal to the constant value, the final droplet radius can be smaller, equal or larger than the corresponding radius for constant supersaturation. It is observed that when droplets are activated in any of the situations (constant supersaturation or fluctuating supersaturation in time), the growth history will be different for each event. The nucleus activation can be immediate and the final droplet radius is slightly above the value obtained at constant supersaturation in one instance. If the activation does not occur immediately, the final droplet radius will be smaller than at constant supersaturation. After analyzing a series of events, we observe that when a droplet grows in a turbulent environment, there is not a single unique value for the final radius. Instead, it is observed a distribution of probabilities for the final radius of each droplet.

To illustrate the probabilistic nature associated with the expected value for the droplet radius in a fluctuating supersaturation environment, the behavior for the final radius of a droplet submitted to one hundred different events in a fluctuating supersaturation field with an average value of 0,45% is shown in Fig. 4. A nucleus of NaCl (10^{-19} kg) was used for this example. The number of realized events is limited and therefore does not represent realistic features of a droplet distribution. However, the results shown in Fig. 4 indicate that there is a tendency for the growth of droplets in a fluctuating supersaturation to reach values which can be either larger or smaller than the ones it would reach if growing in a constant supersaturation (nom turbulent) environment.

Another important aspect that contributes to the dispersion in the droplet distribution can be observed in Fig. 5 where the final radius is related to the solute radius that originates the droplet. In this illustration the curve that defines the limit between the nucleus activation and nonactivation is displaced to the left. Curve I shows the limit of activation at constant supersaturation and curves II and III show the limit at

fluctuating supersaturation (the rates of energy dissipation are about 10^2 cm^2s^{-3} and 10^3 cm^2s^{-3} for curves II and III respectively). According to these results, a small nucleus not activated at constant supersaturation, could be part of the droplet distribution in a fluctuating supersaturation environment, leading to a broadening in the distribution. This occurs because during the evolution of the distribution it is possible that some 'extra quota' of nuclei become part of the droplet distribution for different instances of the process.

(Fig. 4) (Fig. 5)

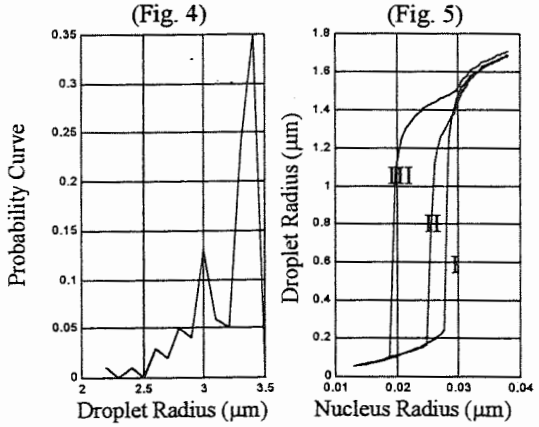

Fig. 4. Probability curve corresponding to one hundred events for a droplet, with a NaCl nuclei of 10^{-19} kg, growing for 30s in of supersaturation field with an average value of 0,45%.
Fig. 5. Curves of variation of the final droplet radius as a function of the initial radius for a NaCl nucleus with masses in the interval of 10^{-20} kg and 10^{-18} kg obtained from supersaturation fields with average values of 0,30%.

5. CONCLUSIONS

The current theory of growth of cloud droplets by condensation leads to a narrowing tendency in the evolution of the droplet distribution. However, the equation that describes the growth of the droplets considers the supersaturation in the vicinity of the droplets as constant, during each stage of the growth process. Also, usually the model calculations do not take into account the solute and curvature terms. These models generally start from distributions with radius typically in the range of a few micrometers where these terms can be neglected.

In the present work where the activation of nuclei in a fluctuating supersaturation environment is considered the effects due to the presence of the solute and curvature are preserved, and shown to be responsible for the differences observed in the growth rates. In analyzing a series of fluctuating supersaturation fields a preliminary conclusion has been drawn.

A nucleus growing in an environment at constant supersaturation reaches a single unique value for the final radius. However, if this nucleus grows in a fluctuating (turbulent) supersaturation environment, the resulting growth shows a distribution of probabilities for the final radius. Also, the nuclei class growing in a fluctuating supersaturation field implies the presence of an 'extra quota' of nuclei present in the distribution These results suggest that turbulence acting on the supersaturation field in which the droplet grows tends to broaden the droplet distribution.

Further research is necessary in the treatment of the effects of turbulence in the growth of droplets by condensation. We think that the next important step is the development of a theory taking into account the probabilistic behavior as illustrated in the present study. To develop a stochastic approach for the condensation growth process, as it was done for the existing stochastic collection growth theory. This new approach should replace the so-called continuos condensation growth as used today.

5. REFERENCES

Almeida, F. C., 1976: The collisional problem of cloud droplets moving in a turbulent environment - Part I: A method of solution. *J. Atmos. Sci.*, **33**, 1571-1578.

___, 1979a: The collisional problem of cloud droplets moving in a turbulent environment - Part II: Turbulent Collision Efficiencies. *J. Atmos. Sci.*, **36**, 1564-1576.

___ , 1979b: The effects of small-scale turbulent motions on the growth of a cloud droplet spectrum. *J. Atmos. Sci.*, **36**, 1557-1563.

Bartlett, J. T., and Jonas, P. R., 1972: On the dispersion of the sizes of droplets growing by condensation in turbulent clouds. *Quart. J. Roy. Meteor. Soc.*, **98**, 150-164.

Howell, W. E., 1949: The growth of cloud drops in uniformly cooled air. *J. Meteor.*, **6**, 134-149.

Jonas, P. R., and Bartlett, J. T., 1972: The numerical simulation of particle motion in a homogeneous field of turbulence. *J. Comp. Physics*, **9**, 290-302.

Srivastava, R., C., 1989: Growth of cloud drops by condensation: A criticism of currently accepted theory and a new approach. *J. Atmos. Sci.*, **46**, 869-887.

Twomey, S., Wojciechowski, T. A., 1969: Observations of the geographical variation of the cloud nuclei. *J. Atmos. Sci.*, **26**, 684-688.

EXPERIMENTAL INVESTIGATION OF THE PROCESSES OF FORMATION AND EVOLUTION OF NATURAL AND ARTIFICIAL FOGS MICROSTRUCTURE

N. P. Romanov

SPA "Typhoon" Institute of Experimental Meteorology, Obninsk, Russia

1. Introduction

A great body of information on fog microstructure has been obtained during aircraft flights. The data obtained concern the upper boundary of the fogs already formed. For studying fogs characteristics near the ground an experimental site was organized in the country place 27 km away from Obninsk. Such a location makes it possible, on the one hand, to perform the studies removed from large populated areas without expensive expeditions. On the other hand, hourly measurements of meteorological parameters made at the High Meteorological Mast in Obninsk allow to assess the meteorological conditions at the height of 300 m. To measure the microstructural parameters a version of a ground-based photoelectric cloud drop sizes counter (PECDSC) was used. The device makes continuous measurements of drop spectra with the drop radii more than 0.3 μm with the results stored in PC files. The observations were performed in the summer-autumn period from August to November up to stable frosts. During the whole observation period it was possible to study three developing fogs. Two of them were formed after sunrise, the third one was formed in the evening at a short clearing and dissipated when a cloud bank appeared. Due to uncertainties in natural fogs appearance forecasting their detailed studies presents great difficulties. Therefore studies of artificial fogs appearance and evolution were simultaneously carried out in the Big Aerosol Chamber of the Institute of Experimental Meteorology.

2. Microstructure of a morning radiation fog

The experimental results on the drop size distribution function f(r) of the fog formed in an hour and a half after sunrise on September 20, 1997 due to dew evaporation during the fog initiation, evolution and dissipation are given in Fig. 1. The air temperature at the height of 2 m changed from 0^0C at the moment of the fog initiation up to 7^0C at the end of the fog life-time.

From the figure it is seen that at the moment of the fog initiation a narrow drop spectrum appears with an effective drop radius of about 1 μm. Then it was observed that the effective radius began to grow gradually and became stable

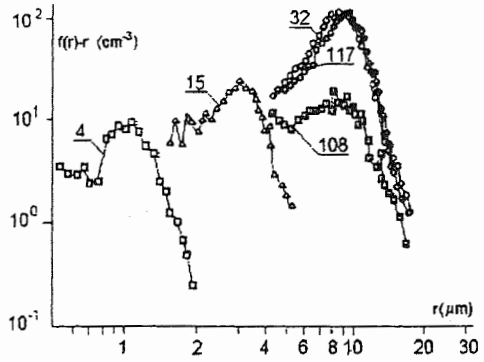

Figure 1. Evolution of morning fog microstructure. The curve numbers correspond to time (in minutes) when measurements were begun.

at the next stages within the range of 10 – 15 μm. The drop concentration underwent great fluctuations within the range of 40 – 150 cm^{-3} but a spectrum relative dispersion at all the stages remained practically constant and equal to about 0.3. The process of fog dissipation proceeded as a fast decrease of drop concentration at the effective radius conserved. A similar pattern was observed in other two radiation fogs (one evening and one morning fogs) studied. From this one can conclude that the scheme of the fog microstructure evolution described is typical of most of radiation fogs. The analysis of the meteorological situation supports the known statement [Mason, 1987] that the process of radiation fogs formation is greatly effected by the competition between the processes of moisture sink onto the ground at its cooling and vapor supersaturation due to air cooling.

Corresponding author's address: Nickolay P. Romanov, SPA "Typhoon" Institute of Experimental Meteorology, 82 Lenin Avenue, Obninsk, Kaluga Region, 249020, Russia;
E-Mail: post@typhoon.obninsk.org;
personal E-Mail: vernik@obninsk.ru

3. Description and characteristics of the fog chamber

To study the peculiarities of cloud and fog microstructure formation the Institute of Experimental Meteorology has the Big Aerosol Chamber (fog chamber). It has the form of a cylinder with the diameter of 15 m and the height of 16 m. The basic method of cloud media simulation in the chamber is air cooling at a decrease of excessive pressure made by the compressor. When considering natural processes one should first of all consider air heat exchange between the chamber and its walls because the chamber walls and metallic structures in it integral heat capacity is by about an order and a half more than the integral heat capacity of the air in the chamber. At studies of heat exchange processes it has been stated that the convective heat transfer coefficient is proportional to the temperature difference of the air and the chamber wall to the 1/3 power during a pressure decrease and to the zero power at a constant pressure with the proportionality factor depending only on fog humidity. In the latter case at constant fog liquid water content the process of creation of the equilibrium temperature between the air and the wall is of an exponential character with the time constant τ. Its value for our chamber without a fog is τ = 10 minutes. Practically all the temperature difference in air and lateral chamber walls is concentrated within the layer of 5 cm. In the rest of the range the temperature horizontal distribution is homogeneous and the vertical one is inverse. The heat exchange parameters obtained give a possibility to model the thermodynamic processes of fogs and clouds formation and evolution. During pumping the air temperature exceeds the walls temperature by 3 – 4 degrees. Therefore by adjustment of initial humidity and of the moment of a pressure decrease the process can be realized when a 100% relative humidity is attained at the air temperature equal to the walls temperature. In this case the processes of heat exchange between the air and the walls do not take place and thus the initial stage of condensation under the air adiabatic ascent is modeled. Similarly the situation can be created when during the expansion at the air temperature equal to that of the walls the fog formed will already have a sufficient liquid water content. When the expansion process is terminated we simulate a stable fog or stratified cloudiness. The air aerosol composition in the chamber differs slightly from that of the ambient air as the chamber before the experiments is kept under a free exchange with the ambient air. A possible income of additional aerosol as a result of evaporation of water pipe drops created by the compressor is prevented by a Petryanov filter installed in the outlet pipe.

4. Conditions for obtaining and experimental results on artificial fogs

During the experiments on artificial fogs measured were the temperatures in the chamber center at three heights, the wall temperature (by the sensor placed outside the chamber) and the temperature of water covering the chamber floor. For measuring the fog parameters in the chamber center at a height of about 2 m a meter of the attenuation coefficient α at the wavelength of 0.63 μm, the photoelectric cloud drop counter PECDSC and an aspiration meter of relative humidity ε were installed. The data of all the measurements were registered with the aid of two PC. Steady – state relative humidity of air and chamber wall temperatures measured were used in a numerical model of the behavior of thermodynamic parameters, relative humidity and thermodynamic liquid water content during a decrease of the pressure. The calculation is necessitated by the time constant of the relative humidity aspiration meter of an order of a minute that does not give the real humidity values at the rate of their variations used. Calculated values of the attenuation and of fog liquid water content W found on the base of the spectra were compared with the measured coefficient α and with the calculations of liquid water content obtained with the use of the thermodynamic relationships. The agreement in the values compared was a basis of awareness in the correctness of the drop spectra measurements. The given paper presents the experimental results of the year 2000 in cyclonic conditions. Figs. 2 – 4 are an illustration of the experimentally obtained smoothed logarithmic drop size distribution function. Curves numbers in these figures correspond to time in seconds from the beginnings of the processes. Fig. 2 gives a sequence of spectra measured at the air adiabatic expansion. The rate of the temperature decrease in this experiment was 0.008 deg/s that corresponded to the rate of air ascent of about 0.8 m/s. The time of one spectrum measurement was 3 s.

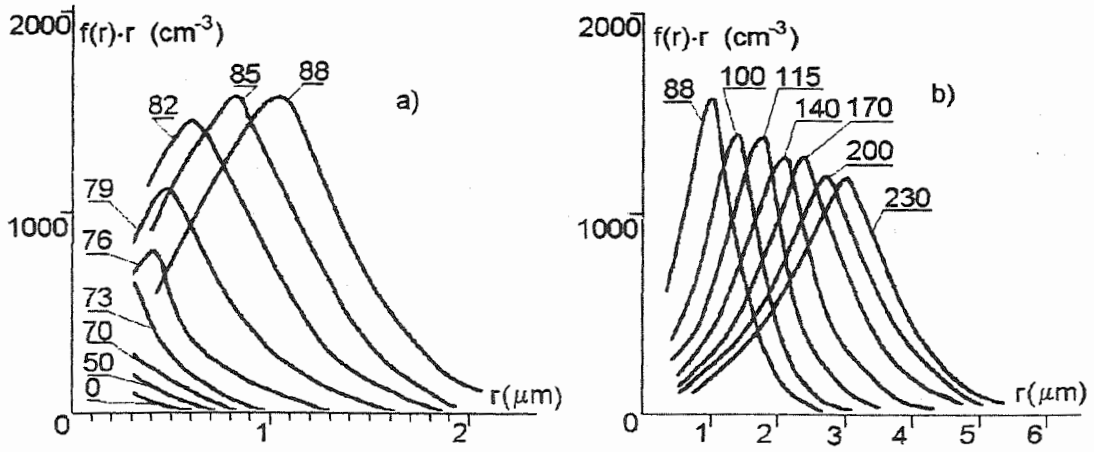

Figure 2. Fog microstructure formation under air adiabatic expansion with an equivalent growth rate of 0.8 m/s.

The initial air relative humidity for this case was ε = 97-98%, air temperature was 22^{0}C, and the temperature of the walls was –21^{0}C. The initial excessive pressure was 250 hPa. Background aerosol concentration with the equivalent radius r ≥ 0.3 μm was about 10 cm^{-3}. Fig. 2a gives a sequence of spectra measured at the initial stage of the fog formation. From this figure it is seen that from the 76th second a fast growth of drop concentration and sizes occurs and during 6-9 seconds a narrow single-modal spectrum with the effective radius of 0.8 – 1μm is formed. Note that the real spectra should be given in this figure as narrower ones because during 3 seconds of a spectrum formation it changes considerably. At the 85 – 88th seconds maximum drop concentration is attained. Its value reduced to normal conditions is equal to 1500 cm^{-3}. From the thermodynamic calculation it follows that a 100% humidity was attained at the 50 – 70th seconds. As it is seen from Fig.2a at these time moments the measured spectra differ slightly from the background ones. The microstructure evolution at the next time moments is shown in Fig. 2b from which a gradual drop size growth is seen. Their concentration decreases. A relative spectrum dispersion also decreases, at first reaches the value of 0.3 and remains practically constant at this level.

The study of the microstructure evolution processes at other rates of temperature variation was carried out in the range of ascent equivalent rates V from 0.2 to 4 m/s. It appeared that at small rates at the initial moment fog formation occurs in separate regions. It shows itself in the interchange of drop spectra with the background ones. The spectra formed are single-modal with the effective radius of the order of 1 μm. Such a situation can be explained by temperature fluctuations and heterogeneities that in the chamber were of the order of 0.1 degree. A further evolution of the spectrum is similar to that described above but the drop concentration at the rate V = 0.2 m/s was considerably lower and was within the limits of 500 – 600 cm^{-3}. At higher rates of the temperature decrease the processes of microstructure formation are similar to those shown in Fig. 2 at an increased drop concentration. The dependence of maximum drop concentration within the rates range studied was almost proportional to $\sqrt{V}$.

The studies of the microstructure evolution processes at a constant temperature has shown that in the course of time drop concentration decreases at the effective sizes and spectrum relative width conserved. The same is also observed at a low temperature increase that is illustrated by Fig. 3. For the time period shown the air temperature increased by 0.25 degrees, the drop concentration decreased by more than the order of the magnitude and the location of the spectrum maximum practically did not change. The results presented are almost adequately explained by the effect of the surface curvature on the pressure of saturated vapors.

Of interest is a behavior of fog microstructure at a sharp change of the temperature decrease rate. This case is illustrated by the data of Fig. 4 where the rate of the temperature decrease of 0.001 deg/sec grew to 0.025 deg/sec. It is seen that a fine–droplet mode was formed

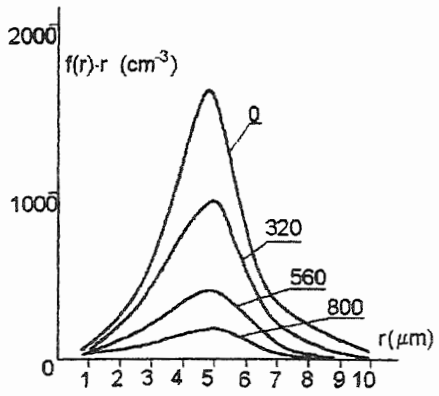

Figure 3. Fog microstructure evolution at a temperature increase by 0.25 degrees.

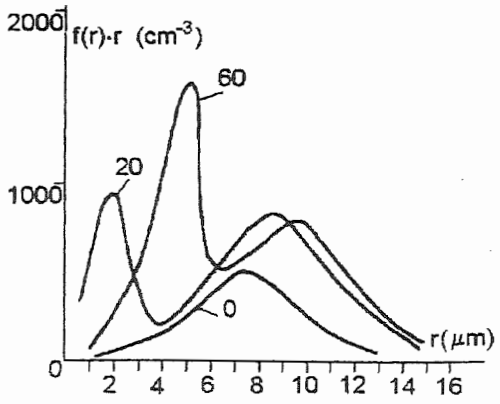

Figure 4. Fog microstructure behavior at an increase of the temperature decrease rate

and the resultant spectrum became a bimodal one. A similar mechanism may be responsible for the formation of bimodal or wide spectra observed by the author at the fog upper boundary [Romanov, 1990].

5. Discussion of results

From the data presented above it follows that in the conditions studied a drop spectrum is formed on condensation nuclei with the radius of dry nuclei of no more than 0.2 μm. Therefore in the spectrum formed even at the first moment with the drop radii of about 1 μm the water mass is by almost two orders more than that of the dry nuclei and the effect of the nuclei hygroscopicity may be neglected. In this case integration of the equation for drop mass growth [Sedunov, 1972] over the distribution function results in the following relationship for the fog liquid water content W:

$$\frac{dW}{dt} = H(T,p)\cdot C\cdot\left(\bar{r}\delta - B\right) \qquad (1)$$

Here the values of C, $\bar{r}$ and δ are the drop concentration, mean radius and vapor supersaturation. The parameter H governing the process of the condensation growth of a drop ensemble depends on the temperature T and on the ratio of pressure p to the normal pressure p_0. For the temperature range T from 0 to 30°C it can be approximated by the following relationship:

$$H\left(\frac{г}{см\cdot сек}\right) = \left(0.8 + 0.04T(^{\circ}C)\right)\cdot 10^{-5}\cdot p_0/p \qquad (2)$$

The value B considering the effect of the surface curvature on the vapors pressure weakly depends on the temperature and for water drops in the above-mentioned temperature range varies only within the limits of $(1.2\text{-}1.0)\cdot 10^{-7}$ cm.

For the case in Fig. 2 the rate of liquid water content growth during the period from 73 to 85 seconds found from the spectra measured is constant and equal to $0.75 \cdot 10^{-2}$ g/m^{3}s. From equation (1) with the measured values of C and $\bar{r}$ at this rate we obtain that δ during this period is approximately equal to 0,45%. The processes of the formation of the fogs studied in natural conditions and in the chamber are similar. Therefore one can assume that for the formation of natural fogs in conditions without contamination a supersaturation of the order of 0.5% is needed. This situation is likely to prevent the fogs formation as the process of dew formation ensuring the sink of excessive moisture from air may proceed at humidities less than 100%.

References

Mason J. 1982; The physics of radiation fog. J. Meteorol. Soc. Jap., 60, 486-499.

Romanov N.P. 1990; Some fog characteristics in the center of the European territory of the USSR in October of 1987. Meteorologiya i gidrologiya; 4, 63-68.

Sedunov Yu.S. Physics of liquid droplet phase formation in the atmosphere. 1972, Hydrometeoizdat, Leningrad, 208 pp.

ENHANCED COLLISION RATES IN TURBULENT CLOUDS: THE INFLUENCE OF INTERMITTENCY

Raymond A. Shaw

Department of Physics, Michigan Technological University, Houghton, Michigan, USA

1. INTRODUCTION

The process of collision and coalescence of cloud droplets is a key link in the chain of events leading to precipitation formation in clouds. Arguably, it also is one of the most poorly understood, especially in the presence of turbulence. The influence of turbulence on the collision–coalescence process has been the focus of a large amount of research and the results have been reviewed in the literature (e.g., Pinsky and Khain 1997). It still is not clear whether turbulence can accelerate significantly the collision rate of small droplets in the early stages of cloud formation.

The purpose of this paper is to identify a mechanism for enhancing the collision rate and, therefore, the collision kernel for cloud droplets in a turbulent flow. The fundamental idea behind the mechanism is that atmospheric turbulence usually has an exceedingly large Reynolds number and is, therefore, characterized by intermittent bursts of energy dissipation. That such intermittency might be important in the context of the collision–coalescence process has been suggested before. For example, Rogers and Yau (1989, pgs. 146-147) make the following statement:

> An important property of turbulence that has not yet been considered in calculations of droplet collisions is its intermittent character. This intermittence manifests itself by abrupt inhomogeneities in the velocity field, with strong energy dissipation in some regions and very little in others. Because the effects of turbulence on droplet collisions are likely to be highly nonlinear, a turbulence field consisting of a few patches of intense turbulence surrounded by regions of weak turbulence may have a more significant influence on droplet growth than a field of homogeneous turbulence having the same average intensity.

This concept was explored by Tennekes and Woods (1973) but a dearth of information on the 3-dimensional structures responsible for the observed intermittency limited their ability to generalize the results. More recent laboratory measurements and numerical studies have shed light on these structures, identifying them as intense, small-scale vortices within the turbulent flow (e.g., Belin et al. 1997; see Shaw 2000 for a list of relevant references). Studies of these vortex tubes show that they scale with Reynolds number in the following way: radii scale with the dissipation or Kolmogorov scale, and peak azimuthal velocities scale with the large eddy velocity.

The mechanism proposed here is that vortex tubes in atmospheric turbulence are sufficiently intense so as to strongly accelerate cloud droplets residing within a vortex. A scale analysis in Sec. 2 suggests that these accelerations are expected to be an order of magnitude larger than that due to gravity and, therefore, greatly enhance the collision kernel. Measurements from the atmospheric boundary layer, presented in Sec. 3, confirm the existence of these intense accelerations and support the scaling factors used in the initial estimates.

2. COLLISION RATE ENHANCEMENTS

A key variable in models of continuous or stochastic collection is the collision kernel, here defined as the product of the total droplet cross section, the difference in droplet velocity, and the droplet collision efficiency,

$$\kappa(r_1, r_2) = \pi (r_1 + r_2)^2 (v_1 - v_2) E(r_1, r_2).$$

For small cloud droplets the differential velocity can be written as

$$v_1 - v_2 = \frac{2\rho_l}{9\mu}\left(r_1^2 - r_2^2\right) a,$$

where μ is the dynamic viscosity of air, ρ_l is the density of water, and a is the acceleration experienced by the droplets. Traditionally, a is taken to be equal to the gravitational acceleration g. If, however, a pair of droplets in a turbulent flow is contained within a vortex, the acceleration due to the vortex must be considered. When the Stokes drag law is valid the radial acceleration of the droplets may be written as

Corresponding author's address: Raymond A. Shaw, Dept. of Physics, Michigan Tech, 1400 Townsend Dr., Houghton, MI 49931 USA; E-Mail: rashaw@mtu.edu

$$a_r = \frac{u_v^2}{r_v},$$

where u_v is the azimuthal velocity of the vortex and r_v is the radius of the vortex (Shaw 2000). To consider the influence of this turbulence-induced acceleration it is convenient to write the ratio of the vortex collision kernel to the gravitational collision kernel:

$$\frac{\kappa_v}{\kappa_g} = \frac{u_v^2}{r_v g}\frac{E_v}{E_g}.$$

Here, E_v and E_g are the collision efficiencies for the differential velocity expected for a strong vortex and for gravity, respectively. It should be noted that this ratio is independent of droplet size, insofar as the underlying assumptions for Stokes flow are valid. As discussed previously, for an intense vortex tube in a turbulent flow, the vortex velocity scale is of the same order as the large eddy velocity scale and the vortex radius lies between the Kolmogorov and Taylor microscales. Representative numbers for a turbulent, convective cloud are 1 m s^{-1} and 0.01 m, resulting in $a_r/a_g \approx 10$. For an intense vortex such as this, it is expected that the vortex collision efficiency will be enhanced relative to the traditional value representing gravitational accelerations alone (e.g., Pinsky et al. 1999). This implies that the ratio of collision kernels will be greater than 10. In order to simplify the problem, however, the two efficiencies will be assumed to be equal so that, for the specific example under consideration,

$$\frac{\kappa_v}{\kappa_g} \approx 10.$$

This order of magnitude increase in collision kernel is a localized phenomenon, occurring in vortex tubes that occupy some fraction of the total volume of the cloud. It remains to be seen whether this will increase significantly the growth of precipitation embryos early in the lifetime of a cloud.

3. ESTIMATES FROM ATMOSPHERIC TURBULENCE MEASUREMENTS

In order to make estimates of the possible influence of turbulence on the collision rate of cloud droplets it is necessary to consider velocity fluctuations, or accelerations, at scales relevant to cloud microphysical processes. To this end, results of a preliminary analysis of turbulence velocity data obtained from the atmospheric boundary layer are presented. The data were obtained during the FLAT campaign near Carpenter, Wyoming, USA using a hotwire probe; details of the experiment have been published previously (Oncley 1992). The hotwire measurements provide horizontal velocities and velocity gradients at approximately 1-mm resolution thereby allowing the full energy cascade to be explored down to dissipative scales. As is characteristic of atmospheric turbulence (Wyngaard 1992), the probability distribution function of velocity gradients (or energy dissipation) has exponential tails, meaning that the probability of encountering a "burst" of energy dissipation is much higher than expected from a Gaussian function. For example, the fourth moment, or kurtosis, of a Gaussian is 3 and of a sample of the FLAT velocity derivative time series is greater than 10. This level of intermittency cannot be attained in numerical simulations of turbulence or in typical laboratory turbulence, making the use of atmospheric data crucial in considering the influence of intermittent events on the cloud droplet collision rate.

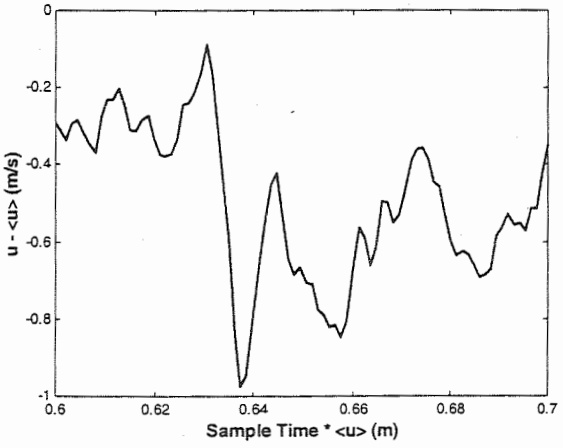

Figure 1. Hotwire velocity measurements from the atmospheric boundary layer illustrating an intermittent energy dissipation event.

Figure 1 illustrates the intense accelerations that are possible in atmospheric turbulence. This piece of the data set is representative of the sharp velocity gradients encountered in atmospheric turbulence. Specifically, this plot shows a velocity difference of 0.9 m s^{-1} over a distance of 0.01 m. It represents a local violation of Kolmogorov-41 scaling in the sense that a velocity change of the same order as the large eddy (rms) velocity exists on a spatial scale close to the Kolmogorov (dissipation) scale. For the full data series considered here, the rms velocity fluctuation is 0.7 m s^{-1} and the Kolmogorov scale is less than 1 mm. Although a 1-dimensional time series cannot be used to uniquely identify 3-dimensional structures, such as vortex tubes, it can be used in

combination with physically-based arguments to provide plausible estimates of parameters such as vortex amplitude and radius (e.g., Fuehrer and Friehe 1999). Indeed, the dissipation event shown in Fig. 1 qualitatively matches the velocity signature expected for the cross section of a vortex. The complete series of intermittent events is reminiscent of the model of intense vortex tubes superimposed on Gaussian turbulence that has been supported by previous laboratory measurements (e.g., Belin et al. 1997).

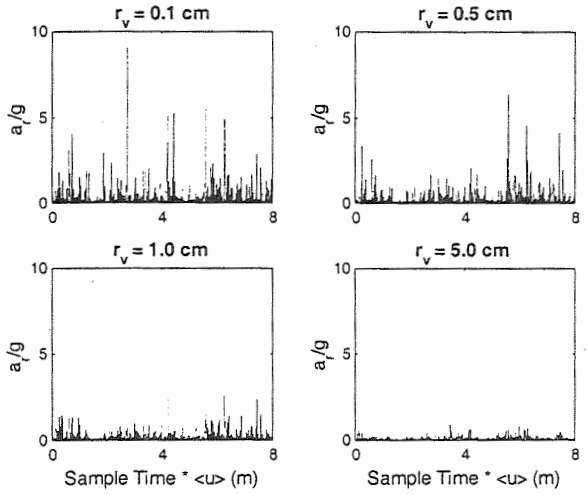

Figure 2. Estimates of radial acceleration relative to gravity for 4 vortex scales. The plots are derived from hotwire velocity measurements from the atmospheric boundary layer.

Assuming that intermittent dissipation events can be modeled as vortex tubes, estimates of the radial acceleration of a cloud droplet in a vortex can be made using the hotwire data. The results of such a calculation are shown in Fig. 2 where a_r is calculated for 4 different values of r_v. As expected, at scales less than several centimeters cloud droplets can experience accelerations much larger than that due to gravity. These accelerations are expected to increase for larger rms velocities. Above radius scales of approximately 5 cm the turbulence induced accelerations are of the same order or less than acceleration due to gravity and, therefore, are not expected to enhance droplet collision rates. Finally, turbulence measurements independent of the specific vortex model used here confirm that, even for the relatively low Reynolds numbers attainable in the laboratory, large accelerations are encountered (Hill and Thoroddsen 1997).

4. CONCLUSIONS

In order to evaluate this mechanism it will be necessary to consider more carefully the interaction of droplets with strong vortices and to continue to explore the structure of small-scale atmospheric turbulence. A crucial aspect of the problem is the possible enhancement of collision efficiency due to the increased relative velocity of droplets. Finally, the enhanced collision kernel must be included within the framework of a full model of stochastic collection in order to obtain realistic estimates of the impact of vortex accelerations on precipitation formation.

Acknowledgements: I thank Steve Oncley, NCAR, for providing the hotwire data, and Alex Kostinski for helpful discussions. This work was supported by the NCAR Advanced Study Program and the National Science Foundation (ATM-9984294).

5. REFERENCES

Belin, F., J. Maurer, P. Tabeling, and H. Williame, 1997: Velocity gradient distributions in fully developed turbulence: An experimental study. *Phys. Fluids*, **9**, 3843-3850.

Fuehrer, P. L., and C. A. Friehe, 1999: A physically-based turbulent velocity time series decomposition. *Bound.-Layer Meteor.*, **90**, 241-295.

Hill, R. J., and S. T. Thoroddsen, 1997: Experimental evaluation of acceleration correlations for locally isotropic turbulence. *Phys. Rev. E*, **55**, 1600-1606.

Oncley, S., 1992: TKE dissipation measurements during the FLAT experiment. Proc. 10th Symp. on Turbulence and Diffusion, AMS, Boston, 165-166.

Pinsky, M. B., and A. P. Khain, 1997: Turbulence effects on droplet growth and size distribution in clouds—A review. *J. Aerosol Sci.*, **28**, 1177-1214.

Pinsky, M., A. Khain, and M. Shapiro, 1999: Collision of small drops in a turbulent flow. Part I: Collision efficiency. Problem formation and preliminary results. *J. Atmos. Sci.*, 56, 2585-2600.

Rogers, R. R., and M. K. Yau, 1989: *A Short Course in Cloud Physics*. Pergamon Press, 293 pp.

Shaw, R. A., 2000: Supersaturation intermittency in turbulent clouds. *J. Atmos. Sci.*, **57**, in press.

Tennekes, H., and J. D. Woods, 1973: Coalescence in a weakly turbulent cloud. *Quart. J. Roy. Meteor. Soc.*, **99**, 758-763.

Wyngaard, J. C., 1992: Atmospheric turbulence. *Ann. Rev. Fluid Mech.*, **24**, 205-233.

ON THE SPATIAL DISTRIBUTION OF CLOUD PARTICLES

A.B. Kostinski[1] and A.R. Jameson[2]

[1]Physics Department, Michigan Technological University, Houghton, MI
[2]RJH Scientific, Inc., Alexandria, VA

These brief remarks are intended as a supplement to (Kostinski and Jameson 2000) where data analysis and mathematical details can be found. We adopt a stationary random process point of view on the problem of spatial distribution of cloud droplets suspended in turbulent air.

From the point of view of stochastic processes, fluid turbulence is not just any random process but one with pronounced vorticity. However, vorticity implies spatial correlations in the random velocity field. This is well known. Note, for example, that the classic studies of Taylor, Batchelor, and Kolmogorov viewed homogeneous and isotropic turbulence this way, that is, along with the assumptions of statistical homogeneity and isotropy, velocity correlation or structure functions were used to represent stochastic structures in these random fields. The main point here is: presence of physical inhomogeneities (structure functions) is not in conflict with the statistical homogeneity and isotropy of the random field.

What happens to particles suspended in such a velocity field? Obviously, there is an extensive literature on the subject. One scenario is to imagine a localized source and subsequent dispersion. An initially homogeneous "blob" of droplets released in this velocity field will be twisted and distorted by a succession of turbulent eddies as time progresses. However, spatial correlations persist. The resultant "structures" must be viewed stochastically. Then the random field of concentration can also be regarded as statistically homogeneous but correlated (e.g., see Wilson 95). One might, therefore, expect fluctuations in particle count to be in excess of that implied by the Poisson distribution because of intermittent local variations in the mean concentrations, i.e. because of spatial correlations.

Another scenario is to imagine that the particles are sprinkled completely uniformly and with no spatial correlations (according to Poisson law) in this velocity field throughout the volume of interest. Even in the passive tracer case, it is not clear to us that random advection preserves Poissonian distribution (recall that numerical simulations of homogeneous turbulence employ periodic boundary conditions in a closed domain). Furthermore, several recent studies have shown that particle inertia causes clustering to occur as well (e.g., Shaw et al 1998).

Hence, it appears that the intermittent mixing and random advection by atmospheric turbulence lead to patchiness of clouds on the scales of most counting experiments. This patchiness, in turn, is associated with spatial correlations between droplet counts corresponding to non-overlapping volumes. Such correlations represent departures from the statistical independence assumption and, therefore, lead to deviations from the Poisson process. Local concentration distributions are often exponential (Hozzler and Siggia 1994). Quantitatively, this yields quadratic (rather than linear as in the Poissonian case) dependence of the number density variance on the mean local concentration.

Furthermore, homogeneous uncorrelated clouds yield Poissonian distribution of the number of collisions experienced by a droplet per unit time (just like in the ideal gas of molecules). The time between droplet collisions is then exponentially distributed. Super-Poissonian variance, on the other hand, broadens the collision distribution. This

Corresponding Author: A.B. Kostinski, Department of Physics, MTU, Houghton, MI 49931. E-mail: kostinsk@mtu.edu

puts "lucky" drops moving through patches of locally high droplet concentration and experiencing several times the average number of collisions early in their development, in a position to grow relatively rapidly. Furthermore, pockets of high concentration in clouds may involve particle separation distances on the same order their hydrodynamic "sphere of influence" so that the idea of dilute suspension behind the stochastic coalescence approach may become invalid. The quadratic fluctuations in the number of collisions can greatly accelerate growth of such "lucky" droplets and help explain the vexing problem of the size distribution broadening.

Acknowledgments: This work was supported by NSF grant ATM95-12685, ATM-9419523 and ATM-9708657.

REFERENCES

Hozler, M., and E.D. Siggia, 1994: Turbulent mixing of a passive scalar, *Phys. Fluids A*, **6**, 1820-1828.

Kostinski, A. B., and A.R. Jameson, 2000: On the spatial distribution of cloud particles. *J. Atmos. Sci.*, **57**, 901-915.

Shaw, R.A., W.C. Reade, L.R. Collins and J. Verlinde, 1998: Preferential concentration of cloud droplets by turbulence: Effects on the early evolution of cumulus cloud droplet spectra. *J. Atmos. Sci.*, **55**, 1965-1976.

Wilson, D. J., 1995: *Concentration Fluctuations and Averaging Time in Vapor Clouds.* American Inst. of Chem. Eng., 181 pp.

INVESTIGATIONS OF DROPLET CLUSTERING ON SMALL SCALES IN A LABORATORY CLOUD-CLEAR AIR MIXING

Adam Jaczewski and Szymon P. Malinowski

Institute of Geophysics, Warsaw University, Warsaw, 02-093 Warsaw, Poland

1. INTRODUCTION

In order to understand process of rain formation as well as radiative transport through clouds, knowledge on spatial distrubution of cloud particles is required. There is a certain experimental evidence, that in some regions cloud droplets are distributed in space randomly (e.g. Malinowski et al., 1994) or even more precisely in accordance with more or less sophisticated Poissonian-type statistics (Kozikowska et al., 1984, Brenguier, 1993, Pawlowska et. al., 1997). On the other hand many cloud physicists reported non-Poissonian deviations or patchy structure of clouds on many length scales. Paluch and Baumgardner, 1989 and Baker, 1992 observed that phenomenon in convective cumulus clouds even down to scales of several centimeters. Uhlig et al, 1998, basing on holographic in-situ measurments in stratiform clouds, found significant deviations between spatial droplet distribution and theoretical random distrbutions. Davis et al., 1999, noticed that spatial droplet distributions do not always follow a uniform Poisson law at scales of a few centimeters and multifractal properties of the large structure of the clouds. Jameson et al.,1998, suggested that on scales of several centimeters to several meters, droplet clustering associated with deviations from a Poisson distribution may occur in turbulent environments of convective clouds. Finally, Bajer et al. (2000) have shown an important role of vortical structures in small-scale turbulence on droplet spatial distribution.

Generally, deviations from random distribution, named sometimes "preferrential concentration" (Shaw et. al., 1998) are atributed either to inertia forces due to in-cloud turbulence, or to entrainment and mixing of the cloudy air with the environmental air. Recent results concerning patchiness due to cloud-clear air mixing are summarized in Malinowski et. al. (2000), here some experimental results concerning preferential concentration problem will be presented.

Complete in-situ investigations of small scales of cloud-clear air mixing are hardly possible due to lack of aircraft instrumentation able to resolve very small scales of dynamical and thermodynamical fields. Aircraft microphysical measurements, very sophisticated and complex (see Baumgardner et. al., 1993, Brenguier, 1993) suffer from the shape of the sampling volume, which results in small statistics of counted droplets in thermodynamically uniform cloud volumes. Authors propose another experimental approach to the problem: laboratory model of a cloud. In the following preliminary results from observations of the cloud droplet distribution on the two-dimensional vertical cuts through an atrificial cloud will be presented.

Corresponding authors address: Adam Jaczewski, Warsaw University, Institute of Geophysics, ul. Pasteura 7, 02-093 Warsaw, Poland, e-mail: ajacz@gwizd.igf.fuw.edu.pl

2. LABORATORY EXPERIMENT

In the laboratory we observe cloud properties in a chamber of dimensions $1.8\times1\times1m^3$. A volume of saturated air containing cloud droplets (of diameter 7-25μm), generated by an ultrasonic droplet generator in the small chamber above and then enters the main chambe. The process is illuminated by a 1.2mm wide sheet of argon laser (green and blue) light obtained with cylindrical optics. Light, Mie-scattered by droplets, is observed at a 90° angle by a photo camera. Recorded images are processed, digitized and analyzed.

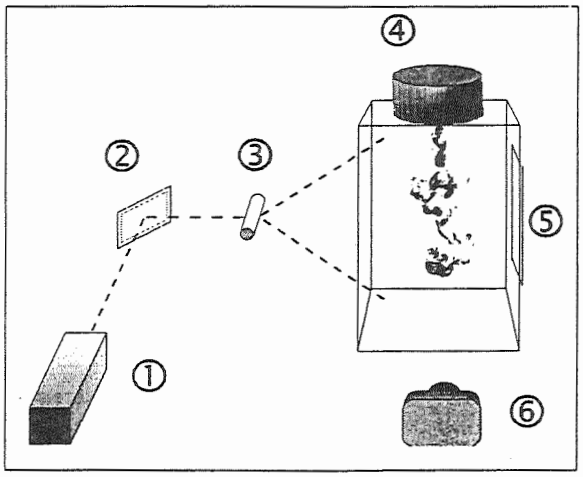

Fig.1. The experimental setup.
1) An argon laser (P=3.5W, blue and green light in six wavelenths), 2) a mirror, 3) a cylindrical lens, 4) a small chamber with the droplet generator inside, 5) a main chamber with a mirror, 6) a photographic camera (panchromatic film, 3200 ASA, 135mm lens).

For the purpose of the present study significant modifications with respect to the setup described in

Malinowski et al., (1998) have been introduced. The illuminating laser was substantially modified, which increased power of the light beam up to 3.5W. An additional mirror was added in order to incerase amount of light in the sheet. This, together with change of the camera optics (telephoto 135mm lens) allowed for distinguishing between individual droplets on the images. The photographic media used was Kodak T-MAX P3200 panchromatic film forced during processing to 6400ASA sensitivity only, which significantly reduced the grain size with respect to prior experiments. Obtained negative films were digitized with 1950dpi resolution in 256 greyscale and processed.

To record a sharp image of moving droplets the shutter speed had to be matched to droplet velocites. Thus the aperture and observation distance were set to minimum allowable by optics and light intensity to maximum. Experience showed that the best results were obtained for relatively slow, spontaneous mixing of cloud with clear air (no dynamical forcing of the clody plume) and shutter speed of 1/125s or 1/250s. To exclude mixing with the environmental unsaturated air, inflow of cloudy air the cloud chamber lasted few minutes until the whole volume of the main chamber was saturated and filled with droplets. Then inflow was switched off and there was no more forcing of turbulence. Turbulent velocities decreased and droplets' images could be taken. We believe that such conditions can be treated as representative for the inner, unmixed volumes of clouds.

3. PRINCIPLES OF CORELATIONAL ANALYSIS

In this study dependence of droplet concentration on length scale is investigated. It means, that for every droplet the number of neighbours inside the ball of radius r centered on that droplet N(r) is computed and averaged. In order to avoid influence of image edges in the average <N(r)> only droplets not closer than r to the edge are accounted for. The average droplet concentration C(r) is then defined as:

$$C(r)=<N(r)>/V(r) \qquad (1)$$

where V(r) is the volume of the ball of radius r embedded in Euclidian space of dimension E (in our case of planar images E=2 and ball is a circle). When C(r) fulfills:

$$C(r) \sim r^{D-E} \qquad (2)$$

in certain range of scales, then D is an estimate of the correlational dimension in this range of scales.

Test aimed at verification if the observed droplet spacing fulfills (2) consists of calculating C(r) and plotting it as function of r in log-log coordinates. When points form a straight line on this plot for certain range of r's, then for this range slope of this line is equal to D-E. If D-E<0 then droplets are distributed in space in self-similar manner, not filling the space like random distributed droplets.

4. DATA ANALYSIS

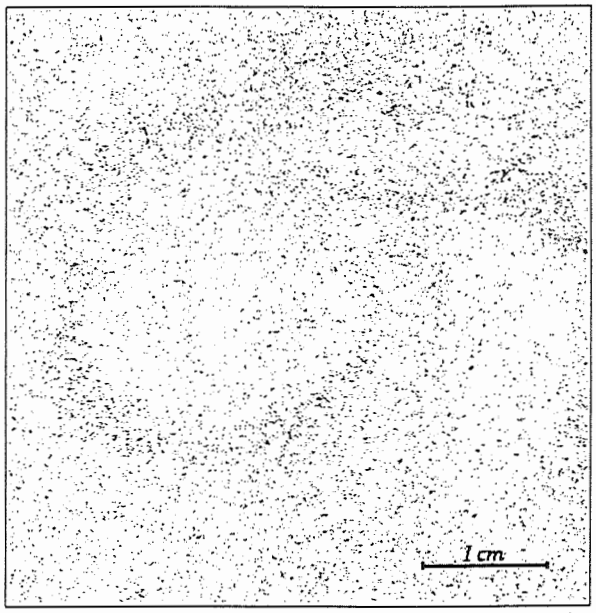

Fig.2. A typical segment of an image from the experiment.

Analyzed images are vertical cross-sections from the cloud chamber, a typical example is given in Fig.2. Visual inspection of the image reveals a weak pattern, such a patterns were typical for this experiment Correlational analysis, described in section 3, was performed for 3 independent images collected at exposure lasting 1/250s. After digitization each image consisted of 2500 by 1800 square pixels of side corresponding to 86μm in physical space.

In first step droplets were detected on the scans. The adopted algorithm selected pixels brighter than four nearest neighbours in principal directions of the image (Fig.3, Fig.4). In the next step number of droplets N(r) inside the circle of radius r centered in each droplet was computed. Radius length was bounded from below by pixel spacing and from above by the distance of the central droplet to the nearest edge of the image. Then the averaging on all droplets was performed and average concentrations in 2-D euclidian space of the image with corresponding standard deviations were calculated for each radius. Results of these calculations are plotted in log-log coordinates.

In Fig. 5 curve C(r) for one of the images together with standard deviations for each r are plotted. For the reference, an average concentration C is plotted as a horizontal line. At small scales (below 2mm) C(r)

increases according to the fact that within even the smallest circle there is one drop at the centre. At larger scales wery weak constant decrease of concentration with the increase of the radius is obviously present.

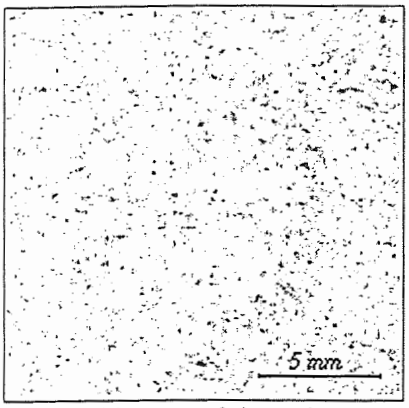

Fig.3. A central fragment of above picture.

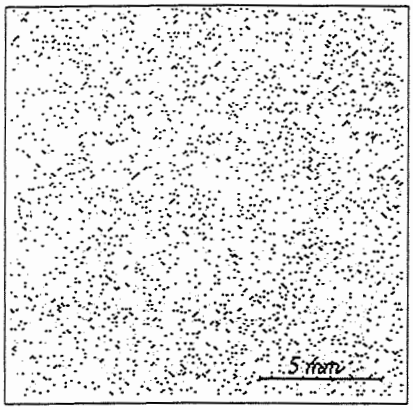

Fig.4. Detected droplets for the above image.

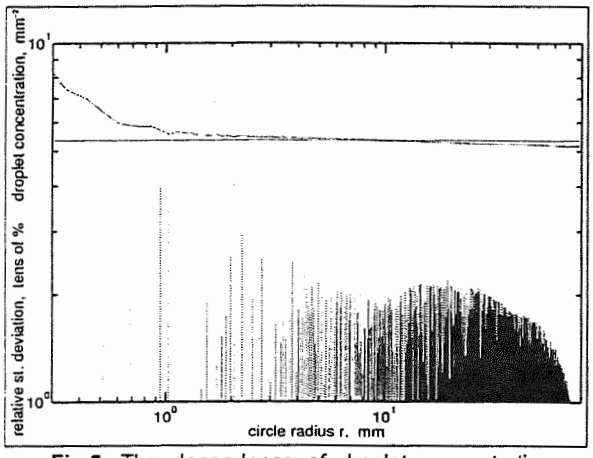

Fig.5. The dependence of droplet concentration on circle radius for example image (log-log plot). Horizontal line shows average concentration. The bars below diagram signify relative standard deviations of droplet concentration in tens of percent.

In Fig. 6 function C(r) is plotted in log-log coordinates for all three investigated images in the range of scales from 1 mm to 80 mm. Plot of C(r) for randomly distributed points is given for reference. The difference between the random and observed distribution is obvious: in large scales random approaches the average while observed drops below the average. "Sawtooths" visible at small scales in the observed distribution are effects of digitization and pixel size.

It seems, that for a certain range of scales linear fit to the experimental data is justifed. The best fits are obtained for the range of scales scales from 2mm to 4cm. These fits, corresponding to D-E in eq. (2), together with the average concentrations are summarized in Table 1.

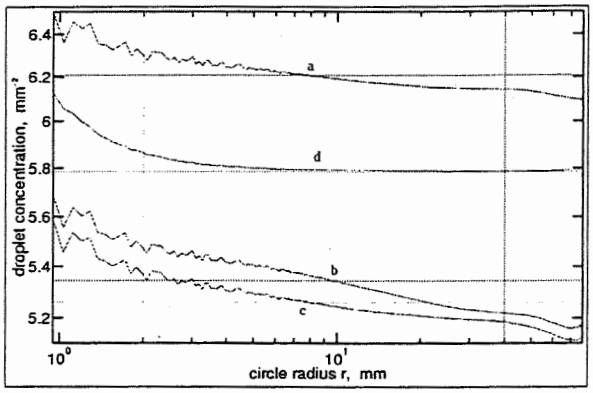

Fig.6. The dependence of droplet concentration on circle radius C(r) for the analyzed images (plots a, b, c) and for random distrbution of points (plot d) in loglog coordinates. Horizontal lines show average concentration, vertical lines show limits of considered scales (2-40mm).

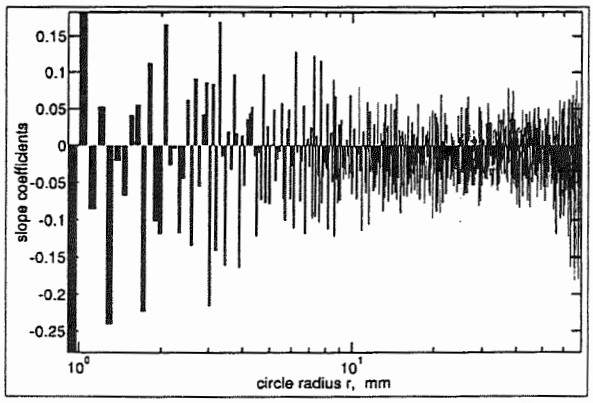

Fig.7. The dependence of local slope on circle radius for b-plot (see Fig.6) - semi-log scale.

In order to verify applicability of linear fitting (which could be questionable e.g. in case of constant weak curvature of C(r) in log-log coordinates), local slopes of C(r) (defined as $[C(r+\delta r)-C(r)]/\delta r$ for each r) were plotted in Fig.7 for the range of scales as in Fig.6. It is evident that within 2mm and 40mm there is no

curvature of C(r), however at scales above 40mm downward change of slope is noticeable. Unfortunately, field of view and resolution of imaging facility in use does not give a chance to investigate larger scales and verify if there is another scaling range above 40mm.

Tab.1. Average droplet concentrations and slope coefficients (D-E) in range of scales 2mm-4cm for three analyzed images.

image	C(r), average droplet concentration, mm^{-2}	D-E, slope for $2mm < r < 40mm$
a	6.21	-0.009 ± 0.007
b	5.34	-0.017 ± 0.007
c	5.26	-0.012 ± 0.006
mean		**-0.013 ± 0.004**

Fig. 5 informs, that standard deviations of droplet concentration reach 20% of C(r). Despite this variability Tab.1 shows that slopes are negative within the error limits. The mean slope for all three images equals -0.013 with standard deviation 0.004. This indicates existence of weak droplet clustering in the investigated range of scales.

5. SUMMARY AND CONCLUSIONS

Correlational analysis of the droplet distribution in images from the cloud chamber indicates weak droplet clustering on scales from 2mm to 4cm. This corresponds well to the visual inspection of the laser-sheet cut in the cloud chamber: some patterns, definitely not random, rather in spiral or ring shapes are usually present (Fig.1). Thus, in turbulent environment within the chamber, formation of patches and filaments due to droplet inertia and sedimentation takes place. Whether these patterns correspond more to the description proposed by Shaw et al., 1998 or Bajer et al., 2000 is still a question.

On the other hand the observed clustering is wery weak and statistically significant results are obtained due to huge statistics only: in each image about 200000 of droplets were detected.

The observed clustering is within the smallest dynamical scales of turbulence at which dissipation of TKE is important. It is interesting, if at scales above 4 cm clustering is also present and how strong is it. Analysis of droplet spacing on scales larger than few tens of cm is not possible in the cloud chamber, this would require in-situ observations.

Results presented here are very preliminary. More experimental data should be analyzed to obtain better statistics and confirm the existence of droplet clustering at small scales in clouds.

6. References

Bajer, K., S.P. Malinowski and K. Markowicz 2000: *Influence of a small-scale turbulence structure on the concentration of cloud droplets. In this volume.*

Baker, B. A., 1992: *Turbulent entrainment and mixing in clouds: A new observational approach. J. Atmos. Sci.*, **49**, 387-404.

Baumgardner, D., K. Weaver and B. Baker, 1993: *A technique for the measurement of cloud structure on centimeter scales. J. Atmos. Ocean. Technol.*, **10**, 557-563.

Brenguier, J.L., 1993: Observation of cloud structure at the centimeter scale. *J. Appl. Meteorol.*, **32**, 783-793, 1993

Davis, A. B., A. Marshak, H. Gerber and W. J. Wiscombe, 1999: *Horizontal structure of marine boundary layer clouds from centimeter to kilometer scales. J. Geophys. Res.*, **104**, 6123-6144.

Falconer, K., 1990: *Fractal Geometry: Mathematical Foundations and Applications.* John Wiley & Sons

Feder, J.,1988: *Fractals.* Plenum press.

Jameson, A. R., A. B. Kostinski and R. A. Black, 1998: *The texture of clouds. J. Geophys. Res.*, **103**, 6211-6219.

Kostinski, A. B. and A. R. Jameson, 2000: *On the spatial distribution of cloud properties. J. Atmos. Sci.*, **57**, 901-915.

Kozikowska, A., K. Haman and J. Supronowicz, 1984: *Preliminary results of an investigation of the spatial distrbution of fog droplets by a holographic method. Q. J. R. Meteorol. Soc.*, **110**, 65-73.

Malinowski, S. P., M. Y. Leclerc and D.I G. Baumgardner, 1994: *Fractal analysis of the high resolution FSSP data. J. Atmos. Sci.* **51**, 397-413.

Malinowski, S. P. and A. Jaczewski, 1999: *Laboratory investigation of the droplet concentration at the cloud-clear air interface. Phys. Chem. Earth*, **24**, 477-480.

Paluch I. R. and Baumgardner D. G., 1989: *Entrainment and fine-scale mixing in a continental convective clouds. J. Atmos. Sc.*, **46**, 261-278.

Pawłowska, H., J. L. Brenguier and G. Salut, 1997: Optimal nonlinear estimation for cloud particle measurements. *J. Atmos. Ocean. Technol.* **14**, 88-104

Shaw, R. A., C. R. Walter, R. C. Lance and V. Johannes, 1998: *Preferential concentration of cloud droplets by turbulence: Effects on the early evolution of cumulus cloud droplet spectra. J. Atmos. Sci.*, **55**, 1965-1976.

Uhlig, E. M., S. Borrmann and R. Jaenicke, 1998: *Holographic in-situ measurments of the spatial distribution in stratiform clouds. Tellus B*, **50**, 377-387.

Formation of small-scale droplet concentration inhomogeneity in a turbulent flow as seen from experiments with an isotropic turbulence model.

B. Grits, M. Pinsky, and A. Khain

Institute of Earth Science, The Hebrew University of Jerusalem, Givat Ram, Jerusalem, 91904, Israel.

1.Introduction.

Inertial drops tend to deviate from streamlines of surrounding air. The mechanism of the formation of the relative velocity between drops different in a turbulent flow consists in their inertial response to the accelerations and shears of the flow (Pinsky and Khain, 1997). As a result, the flux of droplet velocity is divergent in a non-divergent flow. According to Pinsky *et al.* (1999) there is a pronounced maximum for drop velocity flux divergence at the centimeter scale. The nonzero divergence leads to the formation of an inhomogeneous field of drop concentration within clouds. Because the processes of droplet size distribution formation are different in the cases of a homogeneous and inhomogeneous drop concentration field, the determination of the parameters of small-scale fluctuations is potentially very important for cloud microphysics, particularly in relation to the problem of droplet size distribution broadening.

The fine structure of a particle concentration moving within a turbulent flow was found by Wang and Maxey (1993) in DNS. At the same time, there is no consensus concerning the existence of fine cloud structure (Grabowski and Vaillancourt, 1999).

In this paper we investigate the statistical characteristics of a droplet concentration field by simulation of inertial drop motion in a turbulent flow.

2. Description of the simulation experiment.

We solve the equation of drop motion in a turbulent flow for 50000 droplets of similar size. The background air velocity field was simulated using a 2-dimensional model of a homogeneous isotropic turbulent flow (Pinsky and Khain, 1995). The velocity components of the flow are modeled as the sum of a large number of harmonics, corresponding to different wave numbers and different directions. These harmonics are non-correlated with each other. In order to simulate the time dependence of the turbulent velocity, we allow the amplitude of each harmonic to vary with time.

The characteristic time scale is different for harmonics of different wavelengths. The evolution of each velocity harmonic with time is simulated by means of an autoregression sequence of the first order (Hamilton, 1994).

The resulting velocity field averaged over large numbers of realizations is statistically stationary, homogeneous and isotropic, and obeys the continuity equation. Small-scale droplet concentration fluctuations are caused by turbulent vortices with scales below several centimeters (they form maximal values of shears and accelerations). Larger vortices mainly advect these vortices and the droplet concentration field. That is why we exclude vortices with scales exceeding 5 cm from consideration. As a result, we use 21 wave numbers (scales ranging from 6 mm up to 5 cm; thus the external turbulent scale is equal to 5 cm) and 60 directions. Thus this model describes the inertial regime and the transition to viscous ranges (less than 1 cm). The dissipation rate in all of our simulations is 0.01 m^2s^{-3}.

We use a Gaussian form of the initial spatial distribution of droplets. The initial diameter of the droplet spot (4 σ) containing 50.000 droplets is set equal to 20 cm. The spot enlarges with time due to turbulent diffusion, but maintains the Gaussian profile (Monin and Yaglom, 1975, p.562). The drops motion is governed by inertia and the drag force (Pinsky and Khain, 1997). As a first step we neglect the effects of drop sedimentation. We performed simulations for 10 μm, 15 μm and 20 μm radii droplets. To reveal the role of droplet inertia, we conducted analogous calculations for non-inertial particles (passive scalar).

Boris Grits, The Department of the Atmospheric Sciences, The Hebrew University of Jerusalem, Givat Ram, Jerusalem, Israel.
Tel: (02) – 658 – 58 – 24;
Email: boris@atmsg3.es.huji.ac.il

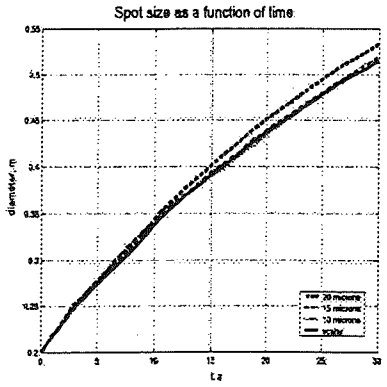

Fig. 1 The spot diameter as a function of time.

Figure 1 shows an increase of the spot diameter with time for these four cases. The dependence of the droplet spot size on time does not follow the $t^{1/2}$ law since its size is comparable with the external turbulent scale used (Monin and Yaglom, 1975, p. 543). Note that the spot consisting of 20 μm droplets enlarges more rapidly.

We calculate fluctuations of number of droplets in a certain surrounding volume of moving droplets. This fully Lagrangian approach is as follows. We randomly choose 1000 droplets within the droplet spot. Then each droplet is surrounded by a set of concentric circles of different radii. We follow each of these droplets, calculating time variations of drop amount within each circle. The diameters of the circles range from 4 mm to 5.2 cm with a 4 mm increment, thus forming spatial scales. The circles move with the moving drop locating in their center. **Figure 2** shows one such droplet with its circles in the spot of droplets. This droplet is moving along the arrow.

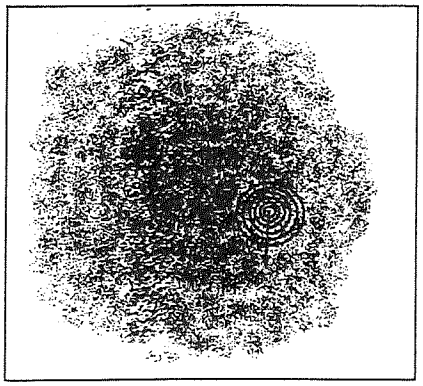

Fig. 2 An example of a set of circles for one droplet in the field of droplets.

Note that mean droplet concentration decreases from the center of the spot to its periphery. We investigate the deviations of drop concentration from the mean value. For each circle of diameter d, we calculate a deviation of the number of particles, N_d, from

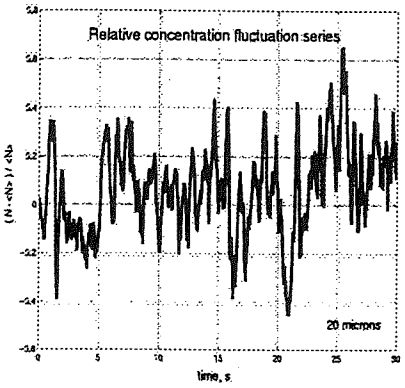

Fig. 3 $\Psi_d(r,t)$ realization for the circle with diameter 1 cm of 20 μm drops.

the mean value calculated from a Gaussian distribution, $\langle N \rangle_d$, as a function of time (the time step is equal to 0.01 sec). In order to compensate the diffusive expansion of the spot, we divide this deviation by the mean value, $\langle N \rangle_d$ to calculate :

$$\Psi_d(\mathbf{r},t) = (N_d(\mathbf{r},t) - \langle N \rangle_d(r,t) / \langle N \rangle_d (r,t) ,$$

where r is the distance from the spot center. Thus, we characterize relative drop concentration fluctuations by the value $\Psi_d(r)$, which we regarde as a homogeneous and stationary variable (in a statistical sense).

Figure 3 shows an example of a Ψ_d realization for the circle with radius 1 cm. One can see that fluctuations of Ψ_d are approximately statistically stationary. Ψ_d includes both the fluctuations due to drops inertia and the natural Poisson fluctuations, which are due to finite number of particles and exist even in a homogeneous case.

3. Statistical processing

The retrieval of inertia induced drop concentration fluctuations is a complicated problem, because of significant natural Poisson noise. Moreover, the drops-to-scalar fluctuations ratio ("signal-to-noise" ratio) decreases as drops radius decreases and becomes less than 1 for drops radius less than 15 μm. Therefore one should apply powerful statistical methods for detection of the useful signal. Besides that we need to know the statistical characteristics of the passive scalar signal. We solve this problem by : a) using a large statistical ensemble (1000 drops); b) using effective parametric spectral estimations.

The direct FFT method gives very irregular power spectrum estimation, even after averaging over a large number of particles.

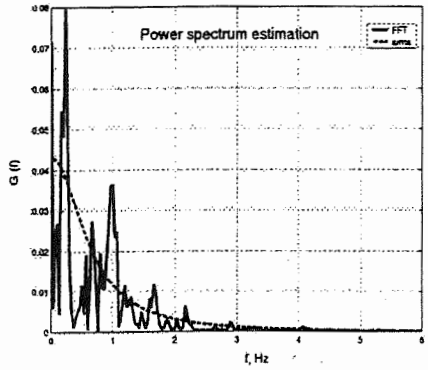

Fig. 4 Power spectrum, calculated using FFT and ARMA methods for the realization, depicted in Fig. 2.

Figure 4 presents an example of the power spectrum obtained from the single realization plotted on the Figure 3. In order to obtain a smooth power spectrum, we use the so-called ARMA (moving average autoregression) method. In this method the signal is analyzed by analogy with ARMA stochastic process (Hamilton, 1994). The power spectrum is a function of these ARMA coefficients, which in turn may be found from the time series. We use the 10-th order of the autoregression and the 3rd order of the moving average (see example on Figure 4).

In order to investigate inertia-induced effects, we subtract the passive scalar power spectra from the drop spectra. This is possible, since the scalar and inertial parts of the fluctuations are non-correlated.

4. Results

The power spectrum of inertia-induced droplet concentration fluctuations within a circle of diameter d, $G_d(f)$, is determined by scales greater then d, since scales less than d are averaged to zero within it. Therefore, the difference between the spectra of the neighboring circles roughly describes the contribution of scales, ranging from the diameter of the smaller circle to that of the larger one.

Thus, the time spectrum of droplet concentration fluctuations $G_k(f)$ of a certain spatial scale k is equal to:

$$G_k(f) = (G_{d1}(f) - G_{d2}(f)) / (k_1 - k_2),$$

where k_1 and k_2 are wave numbers of the smaller d_1 and larger d_2 diameters, respectively, and k the mean of k_1 and k_2.

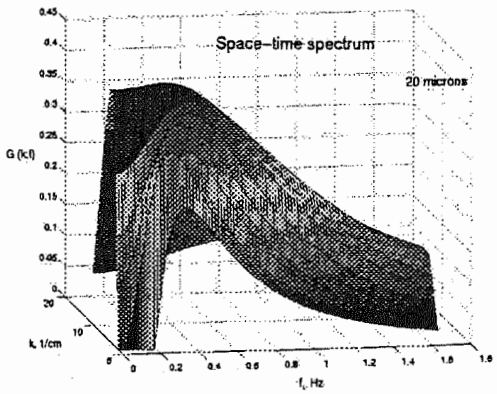

Fig. 5a. The spatial-time spectrum G(k,f) for 20 μm drops.

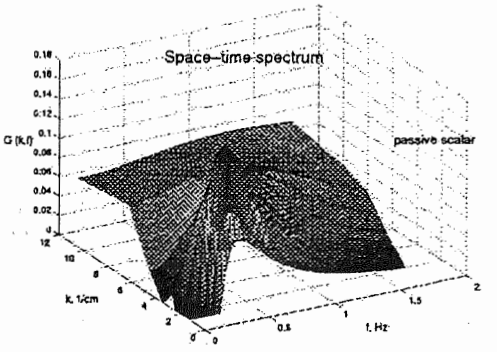

Fig. 5b. The spatial-time spectrum G(k,f) for non-inertial drops (passive scalar).

The set of such time spectra for all spatialscales forms the full spatial-time spectrum G(k,f). **Figures 5 a,b** shows the spectrum for 20 μm-radii droplets and for non-inertial droplets (passive scalar), respectively. The volume below the spectrum surface is the total energy of drop concentration fluctuations. The amplitudes of the relative concentration fluctuations for droplets of radius 10 μm, 15 μm, 20 μm are 5.5, 15.8 and 26.5 %, respectively.

Comparison of the spectra for inertial and non-inertial droplets indicates that a) in both cases there are pronounced maxima in the frequency cross-section at small wave numbers. While the spectrum of non-inertial particles does not contain any significant maximum at large wave numbers, there is a pronounced maximum for inertial particles. This maximum is located at spatial scales of about 1 cm. Thus, the characteristic spatial

scale of drop concentration fluctuations is similar to that of the velocity flux divergence (see the Introduction). The same maximum is seen in the spectrum for droplets of 15 μm radius

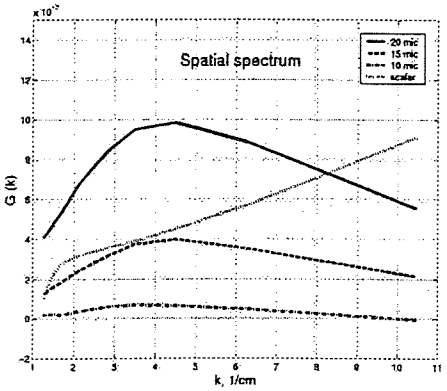

Fig. 6 The space spectrum, G(k), for 10 μm, 15 μm, 20 μm and scalar particles.

Figure 6 shows the dependence of fluctuations power on wave number (the spatial spectrum). Each point of the spectrum is the integral of the spatial-time spectrum cross-section with respect to the frequency for the corresponding wave number.

We see that the droplets of the radii analyzed show a peak near 1 cm amplitude, which increases with the droplet radius. While the amplitude of the fluctuations clearly depends on drops radius, the spatial structure of droplet concentration does not reveal any dependence on the drop radius for droplets of the size considered in the study. The spectrum for non-inertial particles increases with k, since the effect of natural Poisson fluctuations increases toward small scales. There is also a clear cutoff near 5 cm related to the external turbulent scale used.

5. Conclusions.

For the first time a fully Lagrangian approach is used to investigate of drop concentration fluctuations. This investigation shows that :

a) Drop inertia does lead to the droplet concentration fluctuations.
b) The spatial spectrum for the drops of 10 μm, 15 μm and 20 μm radii was calculated and the maximum located at about 1 cm was revealed.
c) The characteristic spatial scale of inertia-induced drop concentration fluctuations is similar to that of the velocity flux divergence.
d) We calculated the full spatial-time spectrum of the drop concentration fluctuations.

A special study is required to investigate characteristic time scales of the drop concentration fluctuations. The effect of droplet sedimentation is the subject of future investigations as well.

Acknowledgements.

This study was partially supported by the Germany-Israel Science Foundation (grant 0407-008.08/95) and the Israel Science Foundation administrated by the Israel Academy Sciences and Humanities (grant 572/97).

6. References

Brenguier J.L., 1993: Observations of cloud microstructure at the centimeter scale. *J. Appl. Met.*, **32**, 783-793.

Grabowski W.W., and Vaillancourt P., 1999: Comments on the "Preferential concentration of cloud droplets by turbulence : effects on the early evolution of cumulus cloud droplet spectra", *J. Atmos. Sci.*, **56**, pp. 1433-1436.

Hamilton J. D., 1994: Time series analysis, Princeton University Press, Princeton, New-Jersy, 799 pp.

Monin A.S., and Yaglom A.M., 1975: Statistical Fluid Mechanics : Mechanics of Turbulence. Vol. 2., MIT Press, 874 pp.

Pinsky M.B., and Khain A.P., 1995: A model of a homogeneous isotropic turbulent flow and its application for the simulation of cloud drop tracks. *Geoph. Astroph. Fluid Dynamics*, **81**, 33-55.

Pinsky M.B., Khain A.P., and Levin Z., 1999: Droplet spectrum formation in clouds by condensational growth in a turbulent medium. *Q. J. R. Met. Soc.*, **125**, pp. 553-581.

Pinsky M.B., and Khain A.P., 1997: Turbulence effects on droplet growth and size distribution in clouds – a review. *J. Aerosol. Sci.*, **28**, 7, 1177-1214.

Wang L.-P., and Maxey M.R., 1993: Settling velocity and concentration distribution of heavy particles in homogeneous isotropic turbulence. *J. Fluid Mech.*, **256**, 27-68.

THE EFFECT OF IN-CLOUD UPDRAUGHT VELOCITY VARIANCE ON SPECTRAL BROADENING IN STRATOCUMULUS CLOUDS

S. L. Irons[1], R. Wood[2] and P. R. Jonas[1]

[1] Department of Physics, UMIST, Manchester, UK
[2] Meteorological Research Flight, The Met. Office, Farnborough, Hants, UK

1. INTRODUCTION

Modeling studies of the effect of fluctuations in updraught velocity on droplet spectra do not show appreciable broadening (Bartlett and Jonas, 1972) due to the direct relationship between the updraught and the supersaturation in the cloud. It is therefore hypothesized that mixing between individual parcels that have experienced different updraught trajectories (Cooper, 1989) may be more important than turbulent fluctuations within an updraught.

In this study, a Lagrangian model is used to investigate droplet nucleation in air ascending at varying constant updraught velocity. The mixing of these parcels according to a probability distribution function (PDF) of measured in-cloud updraught velocities will be carried out to produce an average droplet distribution. This may then be compared with the distribution arising from a run at the mean velocity of the PDF to establish the possible effect of mixing on droplet spectral evolution.

2. DATA RETRIEVAL

The data used in this study were measured by the UK Met. Office C130 aircraft during a field study of stratocumulus cloud over the South West approaches of the UK during December 1998. Back trajectories reveal that the air was a continental flow from the Southeast, having passed over most of Northern Mainland Europe. Ambient aerosol and droplet distributions were recorded over several horizontal runs above and below cloud base. Standard meteorological parameters and turbulence data were also retrieved.

3. DATA EXTRACTION

A PDF of vertical velocity was constructed from the data (Figure 1) by selecting eddies from the data which obeyed the following coherence criterion,

$$\tau_{LIFT} \leq \tau_{MIX}$$

where τ_{LIFT} is the time taken for a parcel of air rising at an updraught (w), within the eddy, to lift to a reference height, h above cloud base, where the activation process is assumed to be complete.

$$\tau_{LIFT} = h / w$$

τ_{MIX} is the time taken for the parcel to lose its identity due to mixing with the surrounding air and is related to the dissipation of turbulent kinetic energy, ϵ and the scale length, L.

$$\tau_{MIX} = \left(L^2/\varepsilon\right)^{1/3}$$

The PDF is calculated from a Weibull distribution using only the positive fluctuations in vertical velocity.

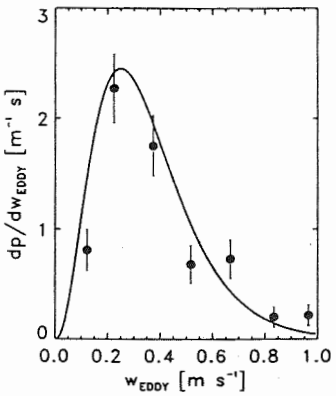

Figure 1. PDF of positive vertical velocity fluctuations

4. MICROPHYSICAL MODEL

The model used in this study is a simple parcel with an explicit microphysical droplet growth scheme. The closed parcel (i. e. There is no entrainment and the total mass of water is conserved) rises with a constant prescribed updraught. Droplets grow and evaporate according to the well-documented Köhler theory (Pruppacher and Klett, 1978) including kinetic considerations (Fukuta and Walter, 1970). The model is initiated using a lognormal fit to a dry aerosol spectrum derived from an average ambient particle distribution below cloud base. The composition of the particles was not measured during the experiment, therefore for the purposes of these simulations the aerosol was assumed to be composed of ammonium sulfate.

5. RESULTS AND DISCUSSION

Figure 2 represents the variation in spread, mean droplet radius (r_m) and activated droplet concentration (N_d) as a function of updraught velocity in the cloud. Spread is defined here as the standard deviation of the distribution (σ). The increase in N_d with increasing updraught is due to the occurrence of larger peak supersaturations in the cloud.

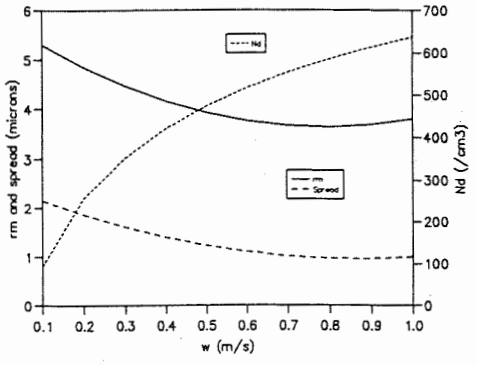

Figure 2. Varation of spread, mean droplet radius and activated droplet concentration with parcel updraught velocity (100m above cloud base).

A decrease in r_m is also seen, which corresponds to the increase in N_d. The decrease in σ with updraught is thought to be because high updraught velocities result in greater supersaturation changes with time. Since droplet growth rate is proportional to supersaturation but inversely proportional the droplet radius, small droplets will grow more quickly in updraughts of high velocity, resulting in more efficient narrowing of the droplet spectrum.

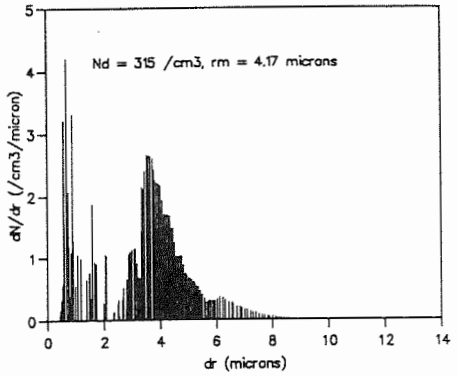

Figure 3. Average droplet distribution.

Individual simulated droplet spectra logged at 100m above cloud base in the model runs may be combined together with weighting given by the PDF shown in figure 2. This produces an average spectrum (figure 3) which may be compared with the spectrum arising from a run at the mean updraught of the cloud (figure 4), which for this case study is 0.4 m/s.

The average spectrum is seen to have a greater spread (σ~1.5μm) than the spectrum from the mean velocity run (σ~1.3μm). Thus, the effect of mixing between parcels according to a PDF of measured in-cloud velocity fluctuations for this case study is to broaden the spectrum compared to a droplet distribution which develops at the mean updraught in the cloud. The observed average droplet spectrum 100m above cloud base has a dispersion (σ/r_m) of 0.403 which is greater than the dispersion of the average theoretical spectrum of 0.360. However, the total droplet concentration in the average spectrum (N_d = 315 cm^{-3}) compares well with the number of droplets in the observed spectrum (N_d = 300 cm^{-3}).

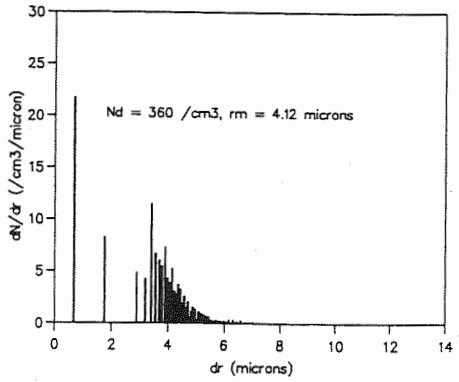

Figure 4. Droplet distribution at the mean updraught of 0.4 m/s.

The spectra shown here do not show the presence of droplets larger than 14μm in radius. However, very small numbers of droplets with radii up to 26μm are present in both the average spectrum (0.23 cm^{-3}) and the spectrum produced at mean updraught velocity (0.20 cm^{-3}). In contrast the observed droplet spectrum has far fewer large droplets, with only 0.04 cm^{-3} having a radius greater than 14μm. Note that a slightly greater number of large droplets are present in the average case, and may be sufficient to initiate the coalescence process, though this has not been investigated at this stage.

In summary, these results confirm the hypothesis that interactions between parcels of air rising with differing vertical velocities are more important than turbulent fluctuations within an updraught.

ACKNOWLEDGEMENTS

This work was funded by the UK Natural Environment Research Council (NERC).

REFERENCES

Bartlett, J. T. and P. R. Jonas, 1972: On the dispersion of the sizes of droplets growing by condensation in turbulent clouds. Q. J. R. Met. Soc., **98**, 150-164.

Cooper, W. A., 1989: Effects of variable growth histories on droplet size distributions. J. Atmos. Sci., **46**, 1301 – 1311.

Fukuta, N. and L. A. Walter, 1970: Kinetics of hydrometer growth from a vapour spherical model. J. Atmos. Sci., **27**, 1160 - 1172

Pruppacher, H. R. and J. D. Klett, 1978: Microphysics of clouds and precipitation. D. Reidel Publishing Company.

EFFECTS OF ENTRAINMENT AND MIXING ON DROPLET SPECTRA BROADENING

F. Burnet and J. L. Brenguier

Météo-France, CNRM-GMEI (France)

1. INTRODUCTION

During the convective ascent of a cloud cell, environmental dry air is engulfed by entraining eddies, thus resulting in dilution and evaporation of the cloud droplets. The size of the turbulent eddies is a critical parameter that determines the droplet response to the mixing process. At the interface between dry and cloudy air the droplets are totally evaporated until the entrained air approaches saturation, while adjacent droplets are not affected. During this process, referred to as inhomogeneous mixing (Baker et al. 1980), the total droplet number concentration (CDNC) is reduced by dilution, but the shape of the droplet spectrum remains unchanged. Progressively the scale of the entrained eddies decreases as they become more homogeneously mixed with cloudy air and their water vapour content increases. At this point, droplets can be partially evaporated, resulting in a shift of the droplet spectra towards smaller diameters. This is referred to as homogeneous mixing. There is also a possibility of secondary cloud condensation nuclei (CCN) activation in an ascending parcel if the updraft velocity is sufficient and if the liquid water content, more precisely the droplet integral radius (Cooper, 1989), has been significantly reduced. Secondary activation is reflected in the spectra by a small droplet mode.

Droplet evaporation following mixing and CCN secondary activation are responsible for a broadening of the droplet spectra towards small values of the diameter. The scale and time evolutions of these processes can hardly be documented because the turbulence cannot be directly measured with an aircraft at the sub-meter scale. Indirect information can however be obtained from the examination of the droplet spatial distribution because the response time of the droplets to unsaturated air is shorter than the life time of the turbulent structures down to a scale of a few centimetres (Baker et al. 1980).

2. THE DATA SET

The cloud samples analysed here were collected with the Météo-France Merlin-IV instrumented aircraft (M-IV) during the SCMS-1995 experiment, with the Fast-FSSP. This probe is an improved version of the standard PMS FSSP-100, and it provides information on each single droplet detection: droplet size, pulse duration and inter-arrival time between detections (Brenguier et al. 1998).

Corresponding author's address: F. Burnet
Météo-France, CNRM/GMEI, 42 av. Coriolis,
31057 Toulouse Cedex 01, FRANCE.
Email : burnet@cnrm.meteo.fr

Pulse duration and inter-arrival time are measured with a resolution of 1/16 of microsecond, that is a distance of *6 μm* along the aircraft track. They are used to derive the series of droplet arrivals in the probe's detection beam, that can be further processed for statistical analysis of the droplet spatial distribution.

The selected case study is a cloud cell sampled on 10 August 1995. The M-IV started the sampling at cloud top (15:26:48 UTC at 2170 m) and made 5 penetrations, following the ascending cell up to 2420 m (15:32:55 UTC), before it collapsed during the 6th penetration at 2340 m (15:34:07 UTC). Fig. 1 shows the time series of altitude for the 6 cloud penetrations. The sounding on this day shows a water vapour deficit in the environment of *4 g.Kg^{-1}* (*13 g.Kg^{-1}* inside the cloud and *9 g.Kg^{-1}* in the environment, that is a relative humidity of *70 %*).

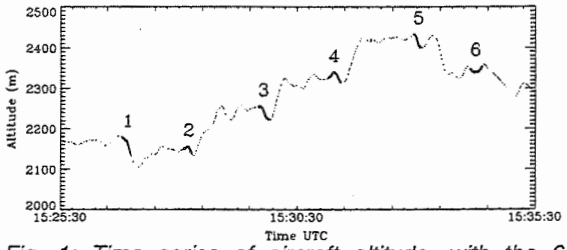

Fig. 1: Time series of aircraft altitude, with the 6 sampled cloud sections.

3. THE FISHING TEST

Droplet counting with a single particle counter is a random process and the arrivals of homogeneously distributed particles in the probe follow the Poisson statistics. The deviation from this idealized model can be measured by the variance of the counts. A cloud sample is thus divided into n sub-samples of length L, the number of counts N in each sub-sample is extracted from the measured series of counts, and its mean value $\overline{N}$ over the whole cloud sample is calculated. The deviation from Poisson, at the length scale L, can be measured by: $VR(L)=\sigma^2(N)/\overline{N}-1$

The Fishing test (Baker, 1992) is derived from the above formula after normalisation by the *VR* standard deviation: $FT(L)=VR(L)/\sqrt{2/(n-1)}$. If the droplets are randomly and homogeneously distributed in the cloud sample, $-3<FT(L)<+3$ with *99.7 %* chance.

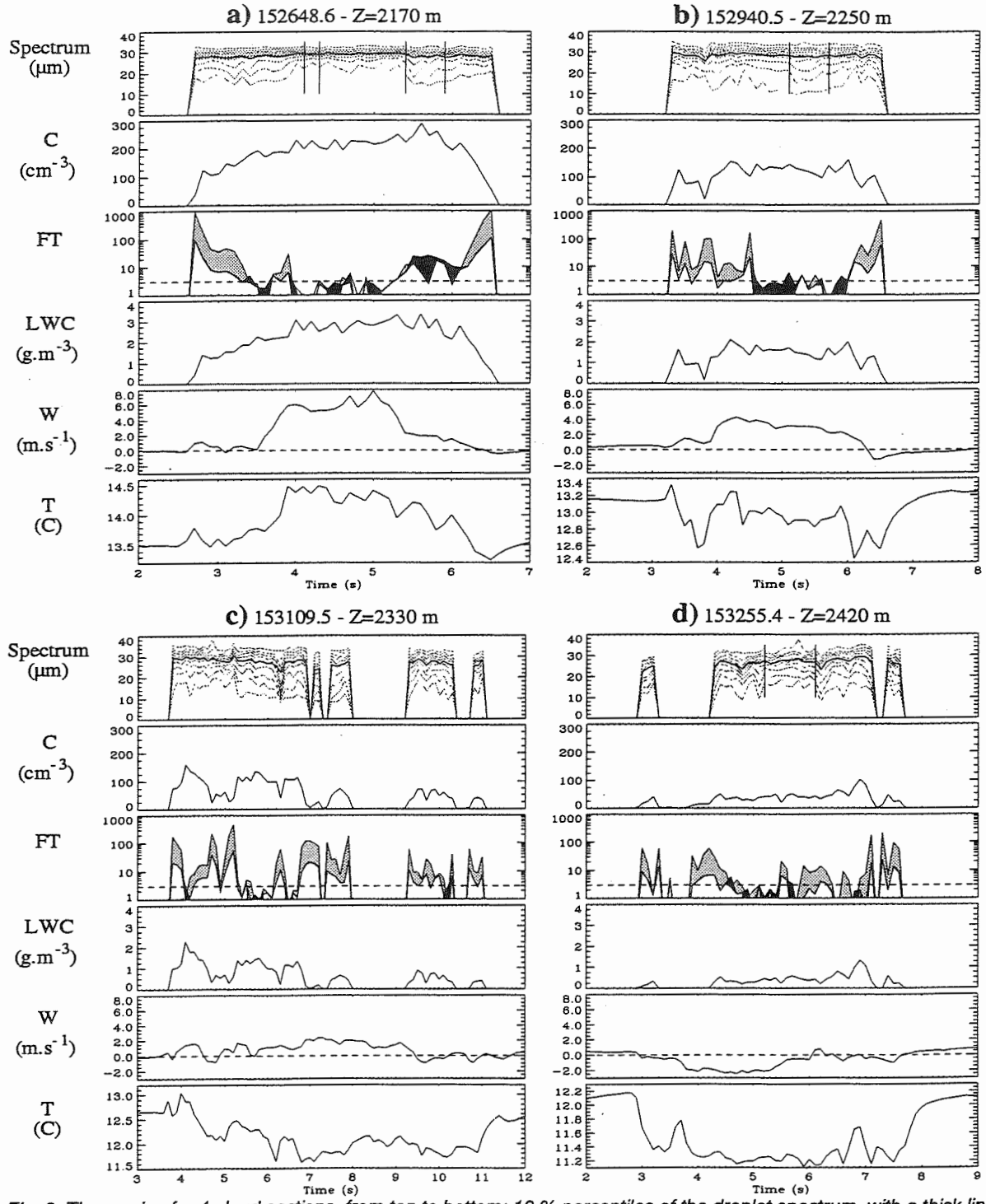

Fig. 2: Time series for 4 cloud sections, from top to bottom: 10 % percentiles of the droplet spectrum, with a thick line for the mean volume diameter; droplet concentration C; FT(1) and FT(0.01); LWC; vertical velocity w; and temperature T. The time origin of each section is indicated on top of each graph, with the mean altitude of the penetration. Vertical bars designate sub-sections for calculation of the droplet spectra.

The Fishing test is applied here to *10 Hz* samples (*10 m*) and it is calculated at two length scales: *1 m FT(1),* and *1 cm FT(0.01)*. The *FT* values provide information about the level of heterogeneity in the droplet spatial distribution. As pointed out by Baker (1992), when large scale heterogeneities are present they also affect the *FT* values at smaller scale. Therefore, when large values of *FT(1)* and *FT(0.01)* are observed, that does not imply that a high level of heterogeneity exists at the cm scale. However when *FT(0.01) > FT(1)*, it actually reflects heterogeneities at the cm scale.

4. RESULTS

Figure 2 shows 4 cloud traverses at *2170 m* (a), *2250 m* (b), *2330 m* (c), and *2420 m* (d), referred to as 1, 3, 4 and 5 in Fig. 1 respectively. Each section is characterized by the time series of, from top to bottom, the spectrum *10 %* percentiles (the thick line represents the mean volume diameter), the droplet concentration *(C)* , *F(1)* and *F(0.01)* (the interval between the two lines is filled with grey when *F(1) > F(0.01),* and filled with black otherwise), the liquid water content *(LWC)*, the vertical air velocity (*w*), and the air temperature (*T*). The 4 traverses illustrate the time evolution of the convective cell.

At 15:26:48 (a) the cell is ascending rapidly (up to *8 m.s^{-1}*), with an internal temperature warmer than the environment by almost *1*°C. Both CDNC and LWC time series exhibit a bowl shape, with large values at the centre, *C=220 cm^{-3}* and *LWC=2.8 g.m^{-3}* (the adiabatic LWC at that level is *3.41 g.m^{-3}*). The Fishing test shows a remarkable feature, with high values on both sides and values lower than the homogeneity threshold (*FT=3*) at the centre. Its shape looks like the complementary of the CDNC and LWC time series. The large *FT* values on the sides are also associated to lower values of vertical velocity and temperature values colder than the environment. In particular, the region of downdraft and coldest temperature, on the right hand side of the figure, extends farther than the cloud boundary. These observations suggest that mixing is active on the sides, with complete droplet evaporation on the right hand side, and production of a cold downdraft. This is reflected in the droplet spectrum by an increase in the proportion of small droplets (the *10* and *20 %* percentiles are smaller than in the centre).

Fig. 3 shows droplet spectra selected as designated by vertical bars in Fig. 2. The two first spectra are extracted from the first traverse. Spectrum (a) originates from the centre of the cell, in the most homogeneous region according to the *FT* values. The spectrum is remarkably narrow, with a mode at *29 μm* and the concentration density drops rapidly on both sides of the mode.

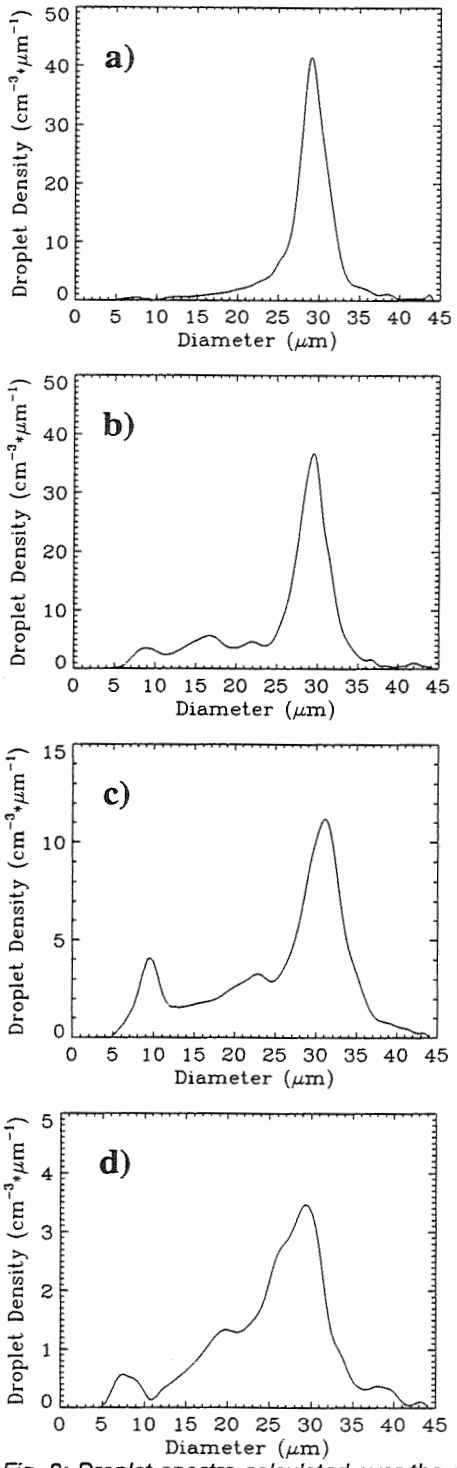

Fig. 3: Droplet spectra calculated over the cloud sub-sections designated by vertical bars in Fig. 2: 15:26:52.7 over 300 ms; 15:26:54.0 over 500 ms; 15:29:45.6 over 600 ms; 15:33:00.6 over 900 ms.

In contrast spectrum (b) is issued from a specific region where *FT(1)<FT(0.01)*. CDNC is larger than in the centre (peak value at *300 cm^{-3}*) and LWC is as large as in the centre. The spectrum percentiles reveal a larger proportion of small droplets and the vertical velocity and temperature are lower than in the centre. Spectrum (b) shows that the increased value of CDNC is due to the presence of small droplets, while the density at the mode is almost as high as in the centre. These features are typical of homogeneous mixing at the small scale, with some partially evaporated droplets mixed with droplets whose diameter is close to the adiabatic value (the mode at *29 μm*).

At 15:29:40.5 (b), *80 m* above the first penetration, the temperature in the cell is almost everywhere colder than in the environment, though this latter (*13.15 °C*) has only decreased by *0.35 °C*. This observation implies that evaporative cooling is intense. The vertical velocity is lower than *4 $m.s^{-1}$*, and *FT* values larger than *100* are observed close to the centre of the cell, though a homogeneous section of more than *150 m* is still present at the centre. Spectrum (c) in Fig. 3, calculated over this homogeneous section, reveals that the main mode is still significant at *31 μm*, but with a density 4 times lower than in spectra (a) and (b). One can also notice the presence of a second peak that corresponds to either partially evaporated or newly activated droplets.

At 15:31:09.5 (c), (*2330 m*), the temperature is now much colder than in the environment (*12.6 °C*), with values as small as *11.6 °C*. The vertical velocity is still positive but lower than 2 $m.s^{-1}$. CDNC and LWC are less than half of their adiabatic values and the Fishing test shows large *FT* values all over the section.

Finally at 15:32:55.4 (d), (*2420 m*), both the vertical velocity and the temperature difference with the environment are negative, CDNC and LWC are lower than *100 cm^{-3}*, and *1 $g.m^{-3}$*, respectively. The *FT(1)* values lower than in the previous sections, suggest that large scale turbulence is no longer supported by the convective motion. It is however remarkable that the main droplet mode in Fig. 3-d is still well pronounced at *30 μm*. This is close to the adiabatic mean volume diameter at that level which is equal to *32 μm* for a CDNC value of *220 cm^{-3}*, as in the first undiluted section (the adiabatic LWC at that level is *3.84 $g.m^{-3}$*).

The last cloud penetration, not shown here, was made at 15:34:07.4 *(2340 m)*, while the cloud turret was collapsing. Only isolated cloud fragments were traversed, with *FT* values between *10* and *100* all over the section and CDNC values lower than *50 cm^{-3}*. However the mean volume diameter was still as high as *25 μm* in most of these fragments.

5. CONCLUSION

The case study presented here is part of a larger investigation of the onset of precipitation in cumulus clouds. On 10 August 1995, three cloud cells were successively sampled with the M-IV, over time periods of *8, 5* and *15 min*, respectively. The three cells had similar time evolutions, though the first two collapsed before any precipitation was produced, while the third one reached a level of *2770 m* and produced heavy precipitation. Cell A presented here is representative of the two following cells, at least for the period preceding the precipitation phase in cell C.

The observations described in the paper aim at demonstrating that the Fishing test is a powerful tool to document the intensity and scales of turbulence during the mixing process. They show that large scale eddies (larger than *1 m*) are initiated at the cloud boundaries and progressively penetrate the cell, while some droplets are evaporated. Further inside the cell, heterogeneities of the droplet spatial distribution are characterized by smaller scales, down to a *cm*. These features of the turbulent mixing are correlated with variations of the vertical velocity, temperature, CDNC, LWC, and the proportion of small droplets in the spectra. However, it is remarkable that the main droplet mode corresponding to the air ascending from the cloud base, is generally well pronounced and that the mean volume diameter is almost not affected by mixing.

5. ACKNOWLEDGMENTS

The authors acknowledge the support of Météo-France and INSU, under grant D13570. The SCMS experiment was supported by NCAR/MMM+ATD.

6. REFERENCES

Baker, M. B., R. G. Corbin, and J. Latham, 1980: The influence of entrainment on the evolution of cloud droplet spectra: I. A model of inhomogeneous mixing. *Quart. J. Meteor. Soc.*, **106**, 581-598.

Baker, B., 1992: Turbulent entrainment and mixing in clouds: a new observationnal approach. *J. Atmos. Sci.*, **49**, 387-404.

Brenguier, J.L., T. Bourrianne, A. Coelho, J. Isbert, R. Peytavi, D. Trevarin, and P. Wechsler, 1998: Improvements of the droplet size distribution measurements with the Fast FSSP, *J. Atmos. Oceanic Technol.*, **15**, 1077-1090.

Cooper, A., 1989: Effects of variable droplet growth histories on droplet size distributions. *J. Atmos. Sci.*, **46**, 1301-1311.

NATURE OF ANISOTROPY IN CLOUDS IN SMALL SCALES

P. Banat, S. P. Malinowski

[1]Warsaw University, Institute of Geophysics, PL-02-093 Warsaw, Poland

1. INTRODUCTION

Many papers about using fractal and multifractal formalism to describe turbulent flows and turbulent mixing have appeared (Sreenivasan, 1991). Attempts to apply a similar approach in order to study fractal properties of clouds have also been undertaken. In (Lovejoy, 1982), the fractal dimension of clouds has been estimated from satellite and radar images. Estimates based on satellite images (Cahalan and Joseph, 1989), gave a different result from (Lovejoy, 1982). In (Malinowski and Zawadzki, 1993) and (Malinowski et al., 1994) the aircraft data from cloud penetrations were used in order to investigate the fractal dimension of the cloud-clear air interface. Most of these efforts, however, assumed the passive nature of the cloud in a turbulent environment and the isotropy of turbulence in clouds. The first assumption is not fulfilled. Cloud droplets evaporate and liquid water content cannot be treated as a passive dust or dye. Additionally, the evaporative cooling and the following production of negative buoyancy is an important mixing mechanism (see e.g. Grabowski, 1995). Thus, due to the privileged vertical direction, the assumption of isotropy is questionable at least.

In the paper we investigate only geometrical properties of images of turbulent mixing because the experimental technique adopted can't give relation between the intensity of a scattered light and the droplet concentration unless we assume a droplet size spectrum. The method used for anisotropy analysis (a modified box-counting) has been previously tested on various kinds of sets, both self-similar and not.

The paper is organized in the following way: in the next section a short description of the experimental setup and data is given and preliminary results from box counting are discussed, then an extended method of box counting allowing for simple detection of anisotropy is introduced, and finally the results of the data processing and their interpretation in terms of dimensional analysis are presented.

2. THE EXPERIMENTAL DATA

The details of the experiment can be found in (Malinowski et al., 1998), here only a brief description is given. Using a planar sheet of a laser light (λ=0.488 μm, thickness 1.2 mm) we observed cross-sections through cloud (a slightly negatively buoyant plume of saturated air and water droplets $\varnothing \approx 14$ μm) mixing with clear unsaturated air in the laboratory cloud chamber. Light, scattered on cloud droplets at 90° angle, was photographed or recorded by CCD video camera. The maximum resolution of photographs varied but was always better than 1536x1024 pixels, with minimum pixel size corresponding to about 1.5×10^{-4} m. The maximum resolution of the images from the CCD camera was 600x400 pixels, with the pixel size controlled by the zoom of the lens. Thus, although the individual image from the CCD camera covered a smaller range of scales than the photography, the statistics of images recorded at various magnifications allowed us to avoid this limitation. For further analysis 36 photos and 573 images recorded by CCD camera were chosen. Data was collected in 20 series, each of them at given physical conditions in the chamber, lighting conditions and magnification. Both horizontal and vertical sections through mixing volumes were analyzed. In Fig.1 examples of vertical and horizontal cuts from the chamber are presented. An interface between cloudy and clear air filaments (CCAI: Cloud Clear Air Interface) was defined at a certain threshold of brightness in the recorded image. Scaling properties of CCAI were analyzed by means of standard and modified box counting methods.

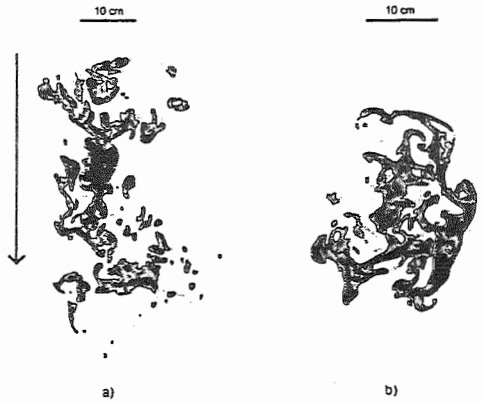

Fig.1 Examples of numerically enhanced images obtained in the experiment. Darker regions correspond to higher droplet concentration, the black line shows an arbitrarily determined boundary between the cloud and clear air. **a** - vertical cut (y=const.), **b** - horizontal cut (z=const.).

Preliminary results obtained from the first data series of 11 photos (Malinowski et al., 1998) (vertical

Corresponding author's address: P. Banat, Institute of Geophysics UW, Pasteura 7, PL.-02-093 Warsaw, Poland; E-mail: banat@fuw.edu.pl

cross-sections only) indicate a change of the box dimension from about 1 in the range of scales from 1×10^{-3} m to 2×10^{-2} m, to about 7/5 in scales 2×10^{-2} - 1.5×10^{-1} m for a wide range of brightness thresholds. The effects of this result on the surface of the cloud-clear air interface was discussed in (Banat and Malinowski, 1999).

The more detailed analysis performed for the purpose of the present study on one-dimensional sections of the images questions the applicability of the standard box counting approach. For the non-trivial scaling region, i.e. for boxes exceeding 2×10^{-2} m, there is a substantial and persistent difference in scaling exponents for horizontal and vertical sections. In 14 data sets appropriate for this kind of the analysis (8 sets consisting of vertical xz cross-sections and 6 sets of horizontal xy cross-sections through the mixing volume) the average of D_x/D_z over all suitable 8 sets is 1.1±0.01, while the average of D_x/D_y over 6 sets equals 1.0±0.01 (see Fig. 2).

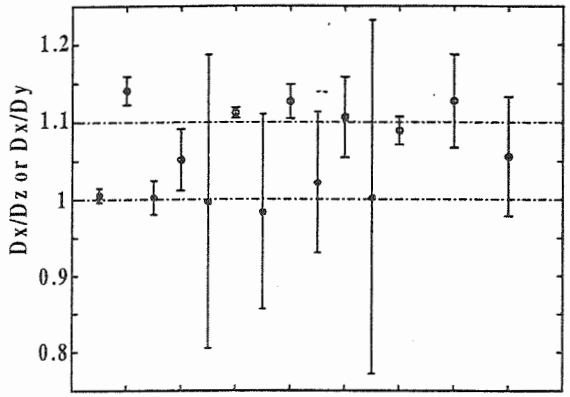

Fig. 2 Each point represents a ratio of scaling exponents (box counting dimensions) in principal directions estimated from a series of images obtained in constant conditions. Stars represent horizontal cross-sections (D_x/D_y), circles represent vertical cross-sections (D_x/D_z). While for horizontal cross-sections the scaling exponents in both directions, Dx and Dy, are the same within the experimental error, for vertical cross-sections the D_x's are substantially greater than the D_z's for each data series.

Here D_x and D_y denote scaling exponents (box counting dimension) in horizontal directions and D_z in the vertical. This anisotropy suggests self affinity rather than the self similarity of the CCAI and indicates, that the CCAI behaves in a different manner from the isoconcentration surface of passive scalars investigated by (Prasad and Sreenivasan, 1990).

3. MODIFIED BOX-COUNTING AND ANISOTROPY

It is known (see e.g. Meakin, 1998) that for self-affine sets the value of the fractal dimension depends essentially on the estimate. In particular, to know the dimension of a cut is not enough to determine the dimension of a whole set. On the other hand there are some self-affine sets for which a certain value of dimension may be prescribed based on known dimensions of cuts. An example is a Cartesian product of three Cantor sets with different scaling exponents D_x, D_y, D_z in three principal directions. (Mandrelbrot, 1983) argues that in this particular case of the self-affinity fractal dimension of such a set is equal to $D_x+D_y+D_z$.

Now, forgetting for a while about the above example, we will define a function $box_S(x,y,z)$, given for a specified set S in the Cartesian coordinate system (x, y horizontal, z vertical):

$$box_S(x,y,z) \overset{def}{=} \text{Number of boxes of sides x, y and z, needed to cover the set S} \quad (3.1)$$

In the case x=y=z, a function $box_S(x,y,z)$ can be used to estimate the box-counting dimension D_{xyz}:

$$\log\left(box_S(x,x,x)\right) \approx -D_{xyz}\cdot\log(x)+const. \quad (3.2)$$

In analogy $box_S(x,y=x,z=const.)$ may be used to estimate the box counting dimension D_{xy} on a horizontal cut through the set at a height z. Vertical and one-dimensional cuts may be investigated in a similar manner. Thus, by examining the function $box_S(x,y,z)$ one may test whether the set S scales with the rule of additive codimesions like isotropic fractals, or like a product of independent Cantor sets in Mandelbrot's example, or in the another way.

For the special case of Mandelbrot's example with dimensions D_x, D_y, D_z in three principal directions:

$$box_S(x,y,z) \propto x^{-D_x}\cdot y^{-D_y}\cdot z^{-D_z}, \quad (3.3)$$

and the scaling exponents D_x, D_y and D_z may be estimated by fitting a plane on a logarithmic plot of function $box_S(x,y,z=const)$ (horizontal cross-section) and $box_S(x,y=const.,z)$ (vertical cross-section). Moreover, if at least of one of D_k ($k\in\{x,y,z\}$) differs from the others, then we may talk about the existence of a specific kind of anisotropy. For an isotropic set S the parameters D_k are equal and $D=3D_x$. In case of a preferred direction z, and isotropy in x, y plane we have $D_x=D_y\neq D_z$.

For another special case of a set S isotropic in the x-z plane the following should occur:

$$box_S(x,y=const.,z)-box_S(z,y=const.,x)=0 \quad (3.4)$$

In this case of affinity $z=\lambda x$, the value of λ may be calculated by finding the minimum of the expression:

$$box_S(x,y=const.,\lambda\cdot x)-box_S(\lambda\cdot x,y=const.,x) \quad (3.5)$$

The above examples show that analysis of the function $box_S(x,y,z)$ may give a lot of information about the geometrical properties of the set S. An additional advantage is that computation of *box* is simple and efficient, thus may be used for a large amount of data.

The method described above, as well as the standard box counting procedure, have been adopted to analyze all collected series of images. Due to the observed break in scaling, scaling exponents were estimated for large scales (>$2 \cdot 10^{-2}$ [m]) and small scales (<$2 \cdot 10^{-2}$ [m]) separately. For each data series a range of brightness thresholds with nearly constant scaling exponents was found and mean values of D-s over the range were calculated.

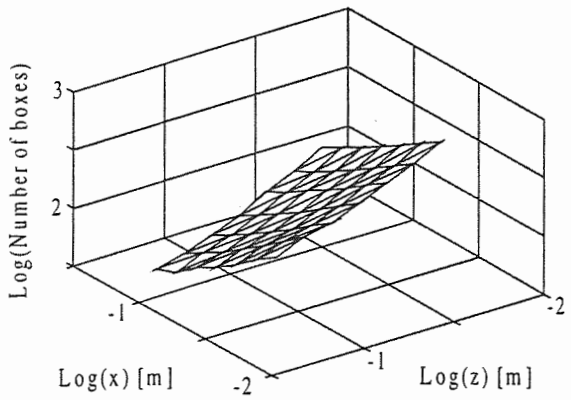

Fig. 3 An example of the function box(x,z) for one series of six images from CCD camera for scales above 1 cm. Scaling exponents (D_x and D_y or D_x and D_z) are estimated assuming (3.3) by fitting a plane to the surface shown.

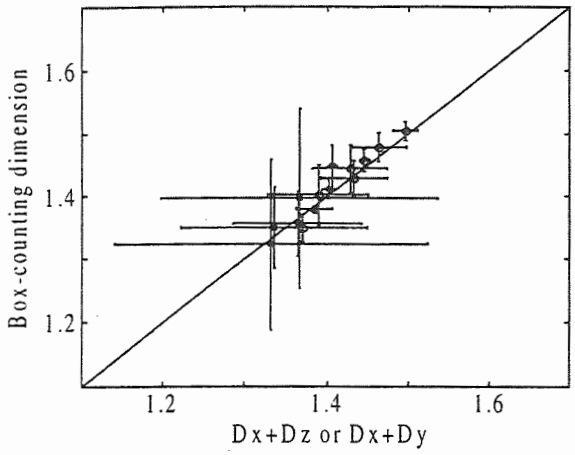

Fig. 4 Comparison of scaling exponents obtained by the box counting dimension in 2-D space and the extended box counting dimension assuming (3.3) for horizontal (stars) and vertical (circles) cross-sections.

In Fig. 3 an example of a surface obtained by an extended box counting method is presented. Scaling exponents estimated from extended box counting with the use of (3.3) and standard box counting for each data series are compared in Fig. 4. The results are in agreement within error limits (with one exception), which reflect differences in fitting the straight line (standard box counting) and plane (extended box counting) to the experimental data. Despite some scatter in values of scaling exponents the data indicates that in the observed images for each series (3.3) is better fulfilled than the assumptions of isotropy and the codimension rule

Finally results for all series were averaged for each scaling region. The results may be summarized as follows:

a) For large scales (>$2 \cdot 10^{-2}$ [m]) relations $box_S(x,y) \propto x^{-D_x} \cdot y^{-D_y}$ and $box_S(x,z) \propto x^{-D_x} \cdot z^{-D_z}$ are well fulfilled (correlation better than 0.99 in each case). In horizontal cuts $D_x = D_y \approx 0.718 \pm 0.003$ and these differ from the scaling exponent in the vertical, $Dz \approx 0.684 \pm 0.002$.

This allows us to estimate the effective box-counting dimension in a 3-D space, assuming that (3.3) is fulfilled: $D_{xyz}=D_z+2D_x \propto 2.12 \pm 0.01$$.

b) For small scales (3.3) is not applicable. The box counting dimension in two-dimensional cuts is close to 1 (more precisely, it is equal 1.10 ± 0.06). There is no self-affinity, however, in these scales λ =const. Estimating from (3.5) the value of λ we get $\lambda=1.6 \pm 0.1$. This means that in scales below 2 cm there is no fractality, however CCAI is anisotropic elongated in the vertical by a factor of 1.6. Assuming an additive codimension rule the effective box-counting dimension in a 3-D space should be $D'_{xyz} = 1.10+1 \propto 2.1 \pm 0.06$ in this case.

4. DIMENSIONAL ANALYSIS

In this section we wish to answer the following question: whether the dimensional analysis may explain why the self-affinity occurs in scales larger than 2 cm? We do not wonder particularly that the self-affinity does not occur in scales smaller than 2 cm because maximum dissipation scale is of the order of 1 cm (Malinowski, Grabowski 1997).

Imagine two particles of air separated by small distance (we assume that this distance is within the inertial range). Applying the dimensional analysis (identically as for Kolmogorov-Obuchov law, see e.g. Landau and Lifszyc, 1994) we obtain that distance separating particles changes in time as:

$$\frac{d\lambda}{dt} \propto (\varepsilon\lambda)^{\frac{1}{3}} \qquad (4.1)$$

where λ is a distance between air particles and ε is a dissipation energy. If we want to apply the latter formula for water droplets instead of air particles we have to modify factor ε. Therefore, this factor should depend on droplet size, since the small droplets move almost exactly like air particles but larger do not.(Pruppacher and Klett, 1978). So, relative distances of small droplets should change in time in different way than distances between large droplets or various droplets. This phenomenon results in differential sedimentation. Notice that $d\lambda/dt$ grows with λ (4.1). Since small droplets fall in air slower than the large ones distances between droplets in a vertical plane are larger than distances in a horizontal plane. Also relative velocities of droplets diverging in these

planes are different. Large droplets separate faster from smaller ones in vertical than in horizontal plane and simultaneously they should form „thicker" filamentation of cloud structure in that direction (i.e. in direction of region occupied both by large and small droplets). On the other hand, a „thicker" filamentation in vertical plane should respond $D_z < D_x$ – and this is what we observe.

5. CONCLUSIONS

In some range of scales (> 2 cm) CCAI are characterized by some specific kind of self-affinity, the same as exists for a Cartesian product of sets with different dimensions. Scaling exponents in the horizontal and vertical differ systematically for each data series by a factor 1.1; on average D_x and D_z differ slightly. So we may say that CCAI are anisotropic in a sense of dimension. Consequently, the additive codimension rule cannot be applied. If it were applied for horizontal cross-sections, we would obtain $D_{xyz}=D_{zx}+1 \approx 2.4$and this result is substantially different from that obtained, $D_{xyz} \approx 2.12$. That means that using the additive codimension rule without checking whether the set is isotropic or not may lead to serious errors.

For small scales (< 2 cm) CCAI is also anisotropic but in a different way. Simply CCAI is a set of patterns elongated in the vertical by a factor of 1.6 ± 0.1 with respect to the horizontal.

The results presented indicate that patterns resulting from turbulent mixing of cloud with clear air on small scales different significantly from those observed in passive scalars. While the latter seem to be isotropic, anisotropy with a preferred vertical direction is a key feature of in-cloud turbulent mixing. This may indicate that small-scale turbulence in clouds results not only from energy transfer of turbulent kinetic energy from large scales but also from production due to evaporative cooling on small scales directly at the cloud-clear air interface. Some support for this hypothesis can be found in recent results by [15] and [16], who show that in-cloud spectra of liquid water content and temperature on scales less then a few meters deflect from Kolmogorov spectra towards higher energies.

The break in scaling at about 2 cm may result either from the approaching dissipation range (the Kolmogorov scale for the laboratory experiment is about 2.5 mm) or from the effect of droplet sedimentation or, finally, from the non-continuity of the field of droplet concentration at small scales. Whichever is the reason, geometrical anisotropy on small scales suggests the importance of either buoyancy effects in these scales or droplet sedimentation in the Stokes regime. Thus accounting for anisotropy is important for proper description of cloud-clear air turbulent mixing.

6. ACKNOWLEDGMENTS

This research was sponsored by grant No. 6 P.04D 002 12 and No. 6 P04D 048 11 of the Polish Committee for Scientific Research.

7. REFERENCES

Banat, P. and S. P. Malinowski, 1999: Properties of the turbulent cloud-clear air interface observed in the laboratory experiment, *Phys. Chem. Earth (B)*, **24**, 741-745.

Cahalan, R. F. and J. H. Joseph, 1998: Fractal statistics of cloud fields, *Mon. Wea. Rev.* **117**, 261-272.

Davis, A. B., A. Marshak, H. Gerber and W. J. Wiscombe, 1999: Horizontal structure of marine boundary layer clouds from centimeter to kilometer scales, *JGR-Atmospheres*, **104:(D6)**, 6123-6144.

Falconer, K., 1990: Fractal Geometry, *John Willey &.Sons*.

Grabowski, W. W., 1995: Entrainment and mixing in buoyancy reversing convection with applications to cloud-top entrainment instability, *Q. J. Roy. Meteorol. Soc.*, **121**, 231-253.

Landau, L. D. and E. M. Lifszyc, 1994: Hydrodynamika, *Wydawnictwo Naukowe PWN.*

Lovejoy, S. 1982: Area-perimeter relation for rain and clouds areas, *Science*, **216**, 185-187.

Malinowski, S. P. and I. Zawadzki, 1993: On the surface of clouds, *J. Atmos. Sci.*, **50**, 5-13.

Malinowski, S. P., M. Y. Leclerc and D. Baumgardner, 1994: Fractal analysis of high resolution cloud droplet measurments, *J. Atmos. Sci.*, **52**, 397-413.

Malinowski, S. P. and W. W. Grabowski, 1997: Local increase in concentration of cloud droplets and water content resulting from turbulent mixing, *J. Tech. Phys.*, **38**, 2, 397-406.

Malinowski, S. P., I. Zawadzki and P. Banat, 1998: Laboratory observations of cloud-clear air mixing in small scales, *J. Atmos. Oceanic Technol.*, **15**, 1060-1065.

Malinowski, S. P. and A. Jaczewski, 1999: Laboratory investigation of droplet concentration at the cloud-clear air interface, *Phys. Chem. Earth (B)*, **24**, 477-480.

Malinowski, S. P. et al., 2000: Small-scale properties of clouds: summary of recent results from aircraft measurements, laboratory experiments and numerical modeling, *in this volume*.

Mandrelbrot, B. B., 1983: The fractal geometry of nature. *Freeman New York*, p.365.

Meakin, P., 1998: Fractals, scaling and growth far from equilibrium. *Cambridge University Press*, pp. 119-121.

Prasad, R. R. and K. R., Sreenivasan, 1990: The measurment and interpretation of fractal dimensions of surfaces in turbulent flows, *Phys. Fluids*, **A 2**, 792-807.

Pruppacher, H. R. and J. D. Klett, 1978: Microphysics of clouds and precipitation, *D. Riedel*.

Sreenivasan, K. R., 1991: Fractals and multifractals in fluid turbulence, *Ann. Rev. Fluid Mech.*, **23**, 539-600.

NUMERICAL INVESTIGATION OF TURBULENT MIXING OF CLOUDS WITH CLEAR AIR IN SMALL SCALES: INTERACTIONS OF TURBULENCE AND MICROPHYSICS.

Mirosław Andrejczuk[1], Wojciech W. Grabowski[2], Szymon P. Malinowski[1] and Piotr Smolarkiewicz[2]

[1]Warsaw University, Institute of Geophysics, PL-02-093 Warsaw, Poland
[2]National Center for Atmospheric Research, Boulder Colorado, USA.

1. INTRODUCTION

A series of computational experiments aimed at investigation of small scale turbulent mixing of cloud with clear air has been performed with the EULAG numerical model. The goal of these simulations was to investigate small-scale interactions between microphysics, dynamics and thermodynamics during process of turbulent mixing of cloud with clear air and to verify some experimental findings from the cloud chamber described in Malinowski and Banat (1999) and Jaczewski and Malinowski (1999) concerning importance of droplet sedimentation. The grid size choice - 1cm and 0.5cm- was a compromise between parameterized microphysics and willing to resolve dissipation scales of turbulence.

In usually adopted for dynamics/thermodynamics study of cloud behavior the bulk microphysical parametrization is used. Cloud is assumed to be saturated; supersaturation required for growth of cloud droplets is not accounted for. Sedimentation of cloud droplets is also neglected. These assumptions are valid for simulations with spatial resolution not better than few meters. Report from 2D simulations with 2m resolution (Grabowski 1989) shows, that replacing bulk microphysics with detailed microphysics does not change dynamics of the cloud.

On the other hand, experimental results by Banat and Malinowski (1999) and Malinowski and Jaczewski (1999) as well as numerical simulations by Malinowski and Grabowski (1997) suggest that when turbulent mixing in small scales (comparable to Kolmogorov scale) is investigated, sedimentation of the cloud droplets may be an important factor influencing the dynamics and microphysics of the cloud. Shaw et al. (1998) argues, that also supersaturation in these scales. Thus, for the purpose of present study special parameterization of microphysics with sixteen classes of droplets, accounting for the sedimentation velocity in each class, has been developed.

Corresponding author's address: M. Andrejczuk, Institute of Geophysics UW, ul. Pasteura 7, 02-093 Warszawa, Poland. E-mail: mireka@gwizd.igf.fuw.edu.pl

2. THE MODEL

2a. Bulk microphysics

The model used in this simulations is nonhydrostatic anelastic model described by Smolarkiewicz (1996). with moist thermodynamics Grabowski and Smolarkiewicz (1996). The governing equation applaied in this simulations can be written as follows:

$$\frac{D\,v}{D\,t} = -\nabla\pi + kB + \mu\Delta\, v$$

$$\nabla\, v = 0$$

$$\frac{D\,\theta}{D\,t} = \frac{L\,\theta_e}{c_p\,T_e}\,C_d + \mu\Delta\,\theta$$

$$\frac{D\,q_v}{D\,t} = -C_d$$

$$\frac{D\,q_c}{D\,t} = C_d \qquad (*)$$

Where **v** denotes velocity vector, π pressure perturbation with respect to a hydrostaticaly balanced environment profile normalized by the density, **k** is vertical unit vector, $\varepsilon = R_v/R_d - 1$; L, c_p - latent heat of condensation and specific heat of constant pressure and index "e" denotes environmental undisturbed value. **B** is buoyancy defined as :

$$B = g\left(\frac{\theta - \theta_e}{\theta_0} + \varepsilon(q_v - q_{ve}) - q_c\right)$$

where g - acceleration of gravity; θ - potential temperature; q_v, q_c water vapor and cloud water mixing ratio; θ_e- environmental temperature profile.

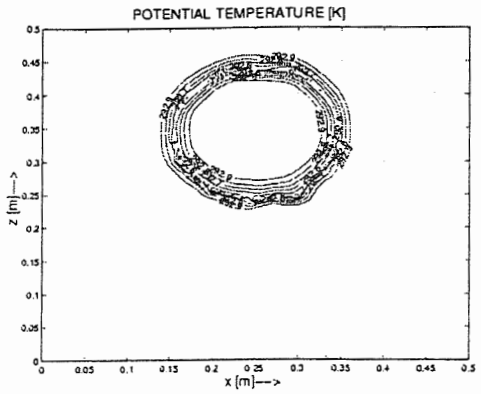

Fig. 1 Potential temperature at time 2.4 s, 7.2 s, 12 s for bulk microphysical parameterization. Central vertical cross section.

Fig. 2 Potential temperature at time 2.4 s, 7.2 s, 12 s for detail microphysical parameterization. Central vertical cross section.

2b Detailed microphysics

In the detailed microphysical model (closely following Grabowski (1989)) equation (*) is replaced by the conservation equation for the number density function

$$\frac{Df(x,r,t)}{Dt} = \frac{\partial \eta}{\partial t} - \frac{\partial}{\partial r}\left(f(x,r,t)\frac{dr}{dt} \right)$$

f(x,r,t) where f(x,r,t)dr is the concentration of droplets of radius between t and r+dr at a given point x in space and at given time t. The equation is:

Here $D/Dt=\partial/\partial t + (v-v_t(r_i))\nabla$, $v_t(r_i)$ is sedimentation velocity for the droplets of the radius r_i; dr/dt describe changes of the number density function due to diffusional growth of cloud droplets dr/dt=AS/r where $A=10^{-10}$ m^2/s, $S = q_v/q_{vs}-1$ – supersaturation, and $\partial\eta/\partial t$ is the nucleation rate. For the detailed condensation model

$$C_d = \sum_i f_i \frac{dm_i}{dt}$$

with finite number of size bins the condensation rate is given by:

In the simulation presented here we used 16 clases of droplets (of radiuses in range from 0.78 to 24 μm). Sedimentation velocity is prescribed for each class according to Stokes law: Cr^2 , where C gives 1 cm/sec for 10 μm droplet.

3. SIMULATIONS

In presented here first group of numerical simulations a spherical bubble, "thermal" of cloud (saturated air with cloud droplets) of zero buoyancy with respect to the environment was investigated. The thermal and the environment were initially at rest and the only mechanism leading to development of motion was evaporative cooling of droplets. The environmental air had 90 percent relative humidity and was in neutral equilibrium (constant potential temperature). Cyclic horizontal and vertical boundary conditions were specified. The domain was 0.5 m x 0.5 m x 0.5 m with 0.005 m resolution. The time step used in simulations was 1.2^{-2}s. Figs 1 and 2 show evolution of the potential temperature at time 2.4s 7.2s 12s, for the bulk microphysical model (fig 1) and for detailed microphysical model (fig 2). In case of detailed mirophysics sedimentation of the droplets effects in most of the cooling and production of the negative buoyancy. This occurs in the early stage of instability development in the sheet bellow the cloud volume, contrary to the bulk case where weak evaporation and cooling appears around the cloud.

4. CONCLUSIONS

The results show, that droplet sedimentation is an important mechanism influencing smallest scales of turbulent mixing of clouds with clear air. At these scales a significant amount of turbulent energy is produced from evaporation, thus turbulence differs from the usually assumed inertial one (resulting from TKE transport downscale). This finding can be important for the theories of statistical coalescence as well as understanding and parameterization of subgrid processes in cloud models.

5. ACKNOWLEDGMENTS:

This research was supported by grant No. 6P04D00212 of the Polish Committee for Scientific Research. Computations were performed at the Interdisciplinary Center for Mathematical and Computational Modeling of Warsaw University.

6. REFERENCES

Banat, P and S.P. Malinowski, 1999: Propertirs of the turbulent cloud-clear air interface observed in the laboratory experiment. *Phys. Chem. Earth (B),* **24**, 741-745

Grabowski, W. W., 1989: Numerical experiments on the dynamics of the cloud-environment interface: Small cumulus in a shear free environment. J. Atmos. Sci., 49, 3513-5341.

Grabowski, W.W., and P.K. Smolarkiewicz, 1996: Two-time-level semi-Lagrangian modelling of precipitating clouds. Mon. Wea. Rev., 124,487-497.

Malinowski, S.P. and W.W. Grabowski, 1997: Local increase in concentration of cloud droplets and water content resulting from turbulent mixing. *J. Tech Phys.*, **38**, 397-406.

Malinowski, S.P. and A. Jaczewski, 1999: Laboratory investigation of droplet concentration at the cloud-clear interface. *Phys. Chem. Earth,* **24**, 477-480.

Shaw, R.C., W.C. Reade L.R. Collins and J. Verlinde, 1998: Preferential concentration of cloud droplets by turbulence: effects of the early evolution of cumulus droplet spectra. *J. Atmos. Sci., **55**,* 1965-1976.

Smolarkiewicz, P.K., and L.G. Margolin, 1997: On forward -in-time differencing for fluids: An Eulerian / semi-Lagrangian nonhydrostatic model for stratified flows. Atmos.-Ocean, 35, 127-152

PREFERENTIAL CONCENTRATION AND GROWTH OF CLOUD DROPLETS

Paul A. Vaillancourt*, Man K. Yau
McGill University, Montréal, Québec,Canada
Wojciech W. Grabowski
NCAR, Boulder, Colorado, USA

1. INTRODUCTION

The broad size distributions observed in clouds suggests that the droplets do not all have the same Lagrangian integral of supersaturation. Observations have shown that even in quasi-adiabatic cloud regions the size distributions are broader than expected (Brenguier and Chaumat 2000). These observations suggest that broadening mechanisms other than mixing may exist.

Srivastava (1989) suggested one possible mechanism. He hypothesized that both the random spatial distribution of droplets and the variations in the vertical air velocity could cause non-negligible deviation of the supersaturation experienced by individual droplets (*microscopic* supersaturation) from the supersaturation calculated for cloud parcels containing a large number of droplets (*macroscopic* supersaturation). Furthermore, because of their finite inertia, cloud doplets moving in a turbulent fluid may not be randomly distributed but rather preferentially concentrated in regions of low vorticity. The impact of this phenomenon on cloud droplet growth has only recently been taken into consideration (Shaw et al. 1998, Grabowski and Vaillancourt 1999, Pinsky et al. 1999, Vaillancourt and Yau 2000).

The focus of this work is to provide answers to the two following questions:
i) Can preferential concentration occur in conditions typical of cloud droplets in cumulus clouds?
ii) Can non-uniformity in the spatial distribution of droplets and/or variable vertical velocity in a turbulent medium contribute to the broadening of the droplet size distributions?

2. APPROACH

Since it is extremely difficult to resolve this question analytically or from observations, a numerical model is used. The strategy and model used is presented in Vaillancourt et al. (2000). A brief summary is now presented. We simultaneously solve two sets of equations. The *macroscopic* equations and the *microscopic* equations. The former correspond to a simple Lagrangian parcel experiment in which all droplets are exposed to the same supersaturation. The latter explicitly solves for the growth and trajectory of each droplet as a function of the conditions in their individual ambient environments. The grid size is chosen to be small enough such that only a fraction of the grid cells contain one or more droplet but big enough such that the grid values are representative of conditions at a distance greater than a few tens of droplet radius. The grid size must also be small enough to resolve the turbulent flow down to the Kolmogorov length scale. A grid size of $\approx 1mm$ is necessary to satisfy those conditions.

A set of six prognostic variables are solved for in the *microscopic* approach, i.e vorticity, temperature, water vapor mixing ratio, droplet size, droplet velocity and droplet position. The *macroscopic* results are obtained from a simplified set of equations. In this approach, the whole domain is one grid cell. Therefore, advection and molecular diffusion is not considered. The forcing for the droplet growth is provided by the imposition of a uniform constant updraft of $2.5ms^{-1}$ on the entire domain.

The turbulent flow field in the *microscopic* approach is obtained from a direct numerical simulation (DNS) using the pseudo-spectral technique as implemented in Bartello et al. (1994). The flow is forced at the large scales to ensure that it is stationary in the sense that the total kinetic energy varies about a constant value. Time stepping is done using the leapfrog scheme while the diffusive terms are integrated exactly. Periodical boundary conditions are used for all variables as well as for the moving droplets.

*Corresponding author address: Paul Vaillancourt, Meteorological Service of Canada, Dorval, Quebec, Canada, H9P 1J3, e-mail: paul.vaillancourt@ec.gc.ca

	flowA	*flowB*	*flowC*
$\Delta t(s)$	$5. \times 10^{-3}$	$2. \times 10^{-3}$	$8. \times 10^{-4}$
$u_0(cms^{-1})$	3.1	6.7	15.2
$\epsilon(cm^2s^{-3})$	1.9	14.	161.
$l_0(cm)$	3.1	2.9	2.5
$\tau_0(s)$	1.8	.72	.29
R_λ	12.	21.	34.

Table 1: Descriptive parameters of the three flows

3. RESULTS

We first briefly describe the three turbulent flow configurations used in all experiments, we then present the results of the experiments on preferential concentration. Finally, we present the results on the impact of the *microscopic* approach on the development of the size spectra and its sensitivity to the inertia effect and to sedimentation of the droplets.

All simulations were done using 80^3 grid points and a grid size of $.125cm$. The volume is $10 \times 10 \times 10cm^3$ and the total number of droplets followed is 50000 (at $50cm^{-3}$).

3.1 Turbulent flows

We specified three values for the initial mean kinetic energy per unit mass to obtain three well resolved realizations of statistically stationary, 3D homogeneous and isotropic turbulence. The eddy dissipation rates obtained for the three flow configurations are within the range of those measured in clouds. To obtain statistical stationarity , we integrated the turbulence model over $\approx$ 20 large eddy turnover times(τ_0) before time zero for the experiments with droplets.

The characteristic parameters for the three flow configurations are listed in Table 1. All quantities, except the time step, are time averages over a minimum time of $20\tau_0$. The entries in the table, from top to bottom, are the time step, the root mean square velocity, the eddy dissipation rate, the integral scale, the large eddy turnover time, and the Taylor based Reynolds number. As can be seen in the table, the eddy dissipation rate is almost two orders of magnitude higher in *flowC* than in *flowA*.

Despite the small R_λ, the flows exhibit complex and intermittent behavior. Some indication of this is found from the kurtosis of the frequency distribution of components of the vorticity. The time average increases from .5 to 3. from *flowA* to *flowC*. The increasing deviation from a Gaussian distribution (zero kurtosis) is a signature of the presence of coherent vortices.

3.2 Preferential concentration

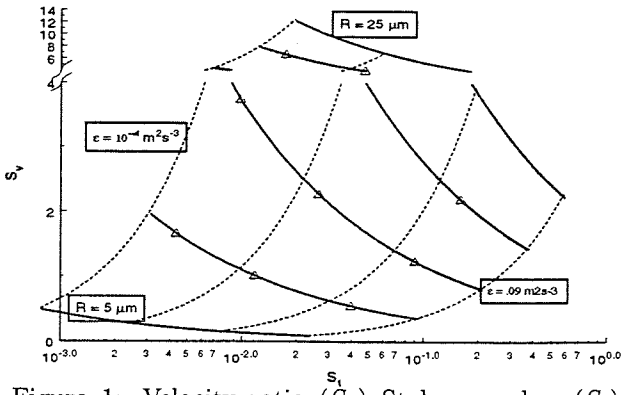

Figure 1: Velocity ratio (S_v)–Stokes number (S_t) diagram for cloud droplets for appropriate range of eddy dissipation rates. The dashed lines are for constant ϵ ($10^{-4}, 10^{-3}, 10^{-2}$, and $.09m^2s^{-3}$) and radii varying from 5 to 25 μm, while the solid lines are for constant radii (5,10,15,20, and 25 μm).

Preferential concentration of particles occurs in dilute particle-laden turbulent flows when particle time constants are of the same order as turbulence time scales. Two non-dimensional numbers are useful as predictors of the significance of preferential concentration (cf. Vaillancourt and Yau 2000). The first one is the Stokes number. This number is the ratio of the particle response time , τ_P, and the Kolmogorov time scale, τ_η: St $= \tau_P/\tau_\eta$. It is expected that maximum clustering results when $S_t \approx 1$. Particles with $S_t \gg 1$ react very slowly to the changes in the flow while particles with $S_t \ll 1$ behave like a tracer.

The relative importance of sedimentation in reducing the time of interaction between a droplet and an eddy with size equals the Kolmogorov length scale can be estimated from the ratio of the droplet terminal velocity v_t and the Kolmogorov velocity scale v_η: $S_v = v_t/v_\eta$. If $S_v \gg 1$ then the droplets and the eddies will have no time to interact. If $S_v \ll 1$, sedimentation can be neglected.

Fig. 1 presents a summary of $S_v - S_t$ values for typical cloud droplets evolving in turbulence with eddy dissipation rates observed in cumulus clouds. As can be seen, $S_v \sim 1$ which implies that sedimentation of cloud droplets is not negligible. The Stokes number spans about three orders of magnitude, approaching 1 only for the larger droplets in moderate to high turbulence.

To quantify preferential concentration, we calculate the clustering index: $C = \widehat{V(n)}/V(n) - 1$, where $\widehat{V(n)}$ is the measured variance of the number density and $V(n)$ is the Poisson variance given

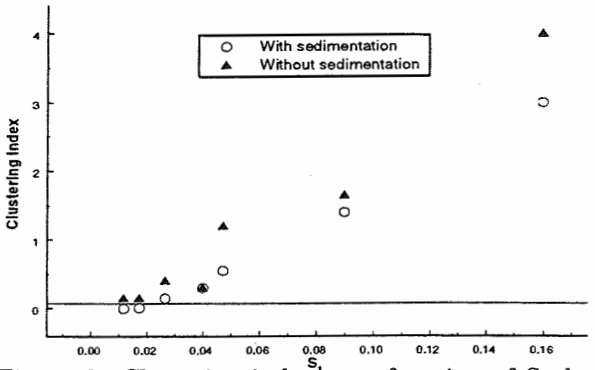

Figure 2: Clustering index as a function of Stokes number at a sampling length scale of 1cm. Horizontal reference line shows level of statistical significance.

the mean concentration. It is calculated for several sampling volumes. Clustering is diagnosed if, for any sampling length scale, the ratio significantly departs from $\pm\sqrt{2/N}$, the expected standard deviation of the statistical error related to the finite number of sampling volumes (N).

To examine the effects of inertia and sedimentation on the spatial distribution of non-condensing droplets, the equation of motion , with or without the sedimentation term, is time advanced for all droplets in conjunction with the flow equation . We performed a series of experiments with $10, 15$ or $20\mu m$ sedimenting or non-sedimenting droplets in the three flows. This represents a total of 18 experiments. The triangles in Fig. 1 denote the $S_v - S_t$ values for these experiments.

Fig. 2 shows the clustering index at one sampling length scale (1 cm) for the experiments in which some preferential concentration was observed. It can be seen that: i) In the absence of sedimentation C increases as a function of increasing S_t. ii) The smallest S_t at which statistically significant clustering is found is $\approx .02$. iii) Sedimentation reduces C

3.3 Condensational growth and evolution of spectra

We now present the results of the experiments including the condensational growth of the droplets. The experiments performed are described in Table 2. These experiments have a duration of $10s$. A few selected $200s$ experiments were made and led to the same conclusions. The initial size distribution in all runs is monodispersed with droplets of $15\mu m$ radius. Inertial effect is neglected ($\tau_P \equiv 0$) in the runs involving *flowA* because at that Stokes number (see Fig. 1) the spatial distribution was found to be ran-

name	flow	inertia	sedimentation
A	*A*	no	yes
B	*A*	no	no
C(F)	*B(C)*	yes	yes
D(G)	*B(C)*	yes	no
E(H)	*B(C)*	no	yes

Table 2: Experiments with condensational growth.

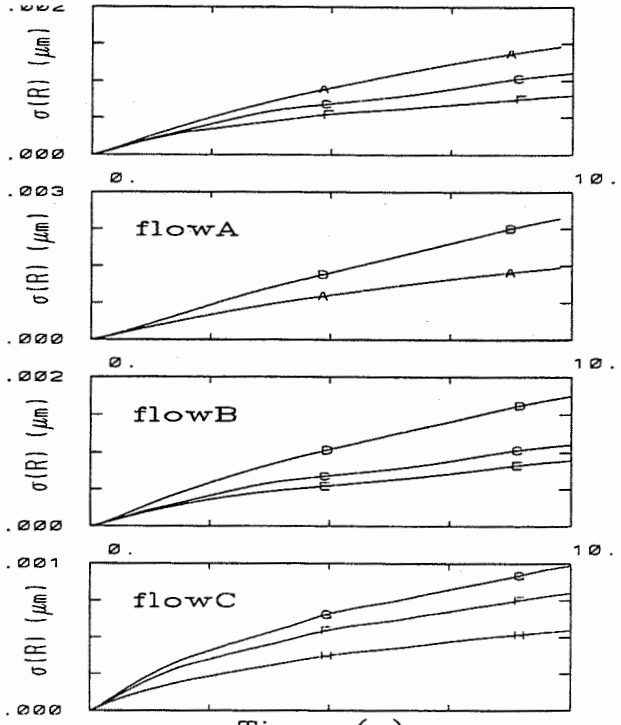

Figure 3: Temporal evolution of the standard deviation of the size distribution for all experiments in Table 2 . Note the different scales for the different panels.

dom. For the experiments with inertia, the initial flow field and spatial distribution of the droplets are obtained from a run with non-condensing droplets.

Fig. 3 shows the temporal evolution of the standard deviation of the size distribution, $\sigma(R)$ for the experiments described in Table 2. Comparing the curves A, C and F in the top panel, we see clearly that $\sigma(R)$ decreases as ϵ increases. The other panels depict the results of sensitivity experiments in the three flow configurations. Obviously, neglecting sedimentation has a significant positive impact on spectral broadening (compare curves B to A, D to C and G to F). Furthermore, the inertia induced clustering also contributes positively to broadening (compare curves C to E and F to H).

We now compare these results to two reference experiments and to some observations. In Vaillancourt et al. (2000), we used a similar but simplified

approach to examine non-sedimenting randomly distributed droplets growing in an environment without turbulence. These unrealistic experiments showed some significant broadening potential. Fig. 4 shows the temporal evolution of $\sigma(R)$ for the two reference experiments, R1 (curve 1) and R2 (curve 2), as well as for A extended to $200s$. The initial size distribution in all these experiments is the same. In $R2$ the spatial distribution of the droplets is random while in $R1$ clustering is present (initial spatial distribution produced by G). Clearly, for a frozen configuration of droplets, clustering has an important broadening effect. However, $\sigma(R)$ is much smaller in A at all times. It is clear that even weak turbulence significantly decreases the broadening potential of the *microscopic* approach that is found in experiments with no turbulence and no sedimentation.

These results can be understood as a function of two effects. First, the presence of turbulence (and sedimentation) significantly decreases the dispersion of the instantaneous distribution of supersaturation (not shown). This decrease is related to the fact that regions void of droplets and regions of high droplet concentration, where significant perturbations in the scalar fields can develop, will exist only for a short time when turbulence and sedimentation modifies the droplet configuration. Furthermore, the decrease of the broadening as a function of increasing ϵ of the flow (despite an increase in clustering) can be directly related to a decrease in the decorrelation time (not shown) of the Lagrangian supersaturation perturbation as a function of increasing ϵ.

The results in Fig. 4 can be quantitatively compared to the observations of Brenguier and Chaumat (2000). By comparing the narrowest spectra found at several altitudes in the same cumulus clouds they found that the dispersion of the distribution of the degree of growth was greater or equal to $\approx 20\%$. The degree of growth is a factor proportional to the Lagrangian time integral of the supersaturation. The broadening of the spectra is directly related to the variance in the degree of growth experienced by the droplet population. This minimum dispersion inferred from their measurements is much larger than the maximum dispersion we found under the most favorable conditions of no flow and no sedimentation (4.36% in $R1$ compared to $< .5\%$ in experiment A).

4. CONCLUSION

We found that some clustering is possible in conditions typical of cloud droplets. In the absence of sedimentation, the quantitative significance of clustering can be directly related to S_t. Sedimentation

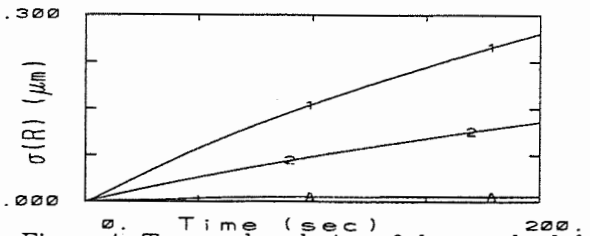

Figure 4: Temporal evolution of the standard deviation of the size distribution for A extended to $200s$ and both reference experiments

tends to decrease clustering. We found that turbulence severely decreases the broadening of the size distribution (despite clustering) compared to experiments performed in the absence of turbulence. Furthermore, the broadening found in the most favorable experiments was significantly smaller than the observed broadening in adiabatic cloud cores of cumulus clouds.

5. REFERENCES

Bartello, P., O. Metais, and M. Lesieur, 1994: Coherent structures in rotating three–dimensional turbulence. *J. Fluid Mech.*, **273**,1–29.

Brenguier, J.-L., and L. Chaumat, 2000: Droplet spectra broadening in cumulus clouds. Part I: Broadening in adiabatic cores. *J. Atmos. Sci.*, submitted.

Grabowski, W. W., and P. A. Vaillancourt, 1999: Comments on "Preferential concentration of cloud droplets by turbulence: effects on the early evolution of cumulus cloud droplet spectra". *J. Atmos. Sci.*, **56**, 1433–1436.

Pinsky, M. B., A. P. Khain, and Z. Levin, 1999: The role of inertia of cloud droplets in the evolution of the spectra during drop growth by diffusion. *Quart. J. Roy. Meteor. Soc.* , **125**, 553–581.

Shaw, R. A.,W. C. Reade, L. R. Collins, and J. Verlinde, 1998: Preferential concentration of clouds droplets by turbulence: effects on early evolution of cumulus cloud droplet spectra. *J. Atmos. Sci.*, **55**, 1965–1976.

Srivastava, R. C., 1989: Growth of cloud droplets by condensation: A criticism of currently accepted theory and a new approach. *J. Atmos. Sci.*, **46**, 869–887.

Vaillancourt, P. A., and M. K. Yau, 2000: Review of particle-turbulence interactions and consequences for cloud physics. *Bull. Amer. Meteor. Soc.*, **81**, 285–298.

Vaillancourt, P. A., M. K. Yau, and W.W. Grabowski 2000: Microscopic approach to cloud droplet growth by condensation. Part I: Model description and results without turbulence. *J. Atmos. Sci.*, submitted.

INFLUENCE OF THE SMALL-SCALE TURBULENCE STRUCTURE ON THE CONCENTRATION OF CLOUD DROPLETS

Konrad Bajer*, Szymon P. Malinowski, Krzysztof Markowicz

Institute of Geophysics, Warsaw University, PL-02-093, Warszawa, Poland

1. INTRODUCTION

The simple adiabatic parcel model of the condensational growth of cloud droplets fails to explain the creation of droplets large enough to initiate rain on the observed time-scale. Shaw et al. (1998, see also Grabowski & Vaillancourt 1999) put forward a mechanism of accelerated condensation induced by small-scale non-uniformities in the concentration of droplets.

A pocket of lower concentration would have higher level of supersaturation and therefore droplets in such a pocket should grow faster. In their model local concentration deficits are caused by the small-scale vortices, believed to form spontaneously at the dissipative scales of developed turbulence. They considered the purely two-dimensional process of centrifugal expulsion from the vicinity of a vortex patch of droplets dragged around by the Stokes's force. Here we consider a different effect related to the small-scale vortical structures in turbulence.

There is still much uncertainty about the mechanisms of the formation of such structures but all candidates considered involve vortex stretching. The individual filaments can emerge due to the concentration and enhancment of the background vorticity or they can form when a stretched vortex sheet either breaks up or rolls up from its ends (Jimenez 1999). We show that the combined effects of gravity and of the irrotational component of the flow responsible for vortex stretching are more relevant for the "growth gap" problem for two reasons. Firstly, they accelerate condensational growth by creating pockets of concentration deficit on a faster time-scale than the purely centrifugal evacuation and, secondly, they induce high relative velocities of the droplets thus signifficantly increasing the probability of the formation of large droplets by coalescense.

*Corresponding author's address: Konrad Bajer, Warsaw University, Institute of Geophysics, ul. Pasteura 7, 02-093 Warszawa, Poland; e-mail: kbajer@fuw.edu.pl

2. STRETCHED VORTICES

We are interested in the effect of the small-scale turbulence on the motion of a droplet inside the unmixed volume in the cloud interior. The characteristic structures in the smallest scales of turbulence have been identified both in direct numerical simulations (Vincent & Meneguzzi 1984) and in laboratory experiments (Douady *et al.* 1991) and it is reasonable to assume that similar structures should form in clouds. They take the form of the long slender vortex filaments. The estimates of their cross-sectional size are not quite definite and range from the Taylor microscale down to the Kolmogorov dissipation scale.

Let us consider a cloud droplet having radius R, mass m and velocity $\mathbf{V}$. We assume the droplet to be small enough to retain its spherical shape and its velocity to be small enough for the drag force to be well approximated by the Stokes formula. The equation of motion is

$$m\frac{d\mathbf{V}}{dt} = -6\pi R\mu(\mathbf{V}-\mathbf{u}) + m\mathbf{g}, \qquad (1)$$

where μ is the viscosity of the air, $\mathbf{g}$ is gravitational acceleration and $\mathbf{u}$ is a the air flow field in the cloud which for the sake of this problem we assume to be prescribed, i.e. unaffected by the droplets. Although droplets are passively carried by the air they are not passive tracers, as the trajectories they trace out are different from the paths of the fluid elements.

Let (r,θ,z) be polar co-ordinates with the Oz direction along the vortex axis inclined at an angle ϕ from the vertical. In this frame of reference the gravity force takes the form

$$\mathbf{g} = g\sin\phi\cos\theta\hat{\mathbf{e}}_r - g\sin\phi\sin\theta\hat{\mathbf{e}}_\theta - g\cos\phi\hat{\mathbf{e}}_z. \qquad (2)$$

The velocity field $\mathbf{u}$ is a sum of the flow due to the uniform irrotational straining flow, and the flow due to an axisymetric vortex having azimuthal velocity $u(r)$,

$$\mathbf{u} = -\tfrac{1}{2}\alpha r\hat{\mathbf{e}}_r + \alpha z\hat{\mathbf{e}}_z + u(r)\hat{\mathbf{e}}_\theta. \qquad (3)$$

The equation (1) takes the form

$$\tau_d \left(\frac{dV_r}{dt} - \frac{V_\theta^2}{r} \right) = - \left(V_r + \tfrac{1}{2}\alpha r \right) + V_g \sin\phi\cos\theta, \quad (4)$$

$$\tau_d \left(\frac{dV_\theta}{dt} + \frac{V_\theta V_r}{r} \right) = - \left(V_\theta - u(r) \right) - V_g \sin\phi\sin\theta, \quad (5)$$

$$\tau_d \frac{dV_z}{dt} = - \left(V_z - \alpha z \right) - V_g \cos\phi, \quad (6)$$

where $\tau_d = m/(6\pi R\mu)$ is the characteristic time of the droplet response to the changes in fluid velocity and $V_g = g\tau_d$ is the terminal velocity of the gravitational settling.

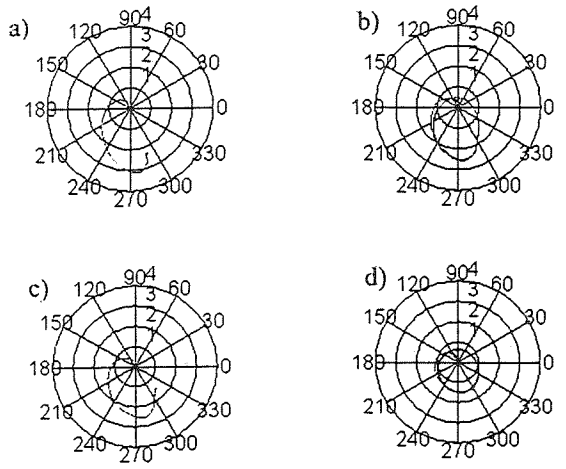

Figure 1: The trajectories of droplets with L_1/L_2^2 equal a) 0.8; b) 1.004; c) 1; d) 2.

In the following we will consider a model vortex with total circulation Γ and gaussian distribution of vorticity. The azimuthal velociy $u(r)$ is given by

$$u(r) = \frac{\Gamma}{2\pi r}\left(1 - \mathrm{e}^{-(r/2\delta)^2}\right), \quad \delta = N\sqrt{\nu/\alpha}. \quad (7)$$

Here the dimensionless number N is the ratio of the vortex radius δ and the radius of the familiar Burgers vortex, an exact steady solution of the Navier-Stokes equation likely to be a good model of the small-scale coherent structures in turbulence.

Little is known about the small-scale structure of cloud turbulence. The resolution of the *in situ* pressure measurements is too low to identify individual vortices, so we have to make assumptions based on the results of numerical simulations and laboratory experiments. The typical radius of the smallest vortices is usually assumed to be of the order of either Kolmogorov scale or Taylor microscale, so in an active cloud we take $1\,\mathrm{mm} \lesssim \delta \lesssim 10\,\mathrm{mm}$. However, such extrapolation from the regime of much lower Reynolds number and much higher turbulence intensity still awaits experimental verification. The vortices are products of competition between viscous diffusion and amplification of vorticity by stretching. We can infer the rate of strain (α) from the radius of the vortex, $\alpha = \nu(\delta/N)^{-2}$, where $N \sim 1$ assuming the vortex is close to its equilibrium Burgers-like state.

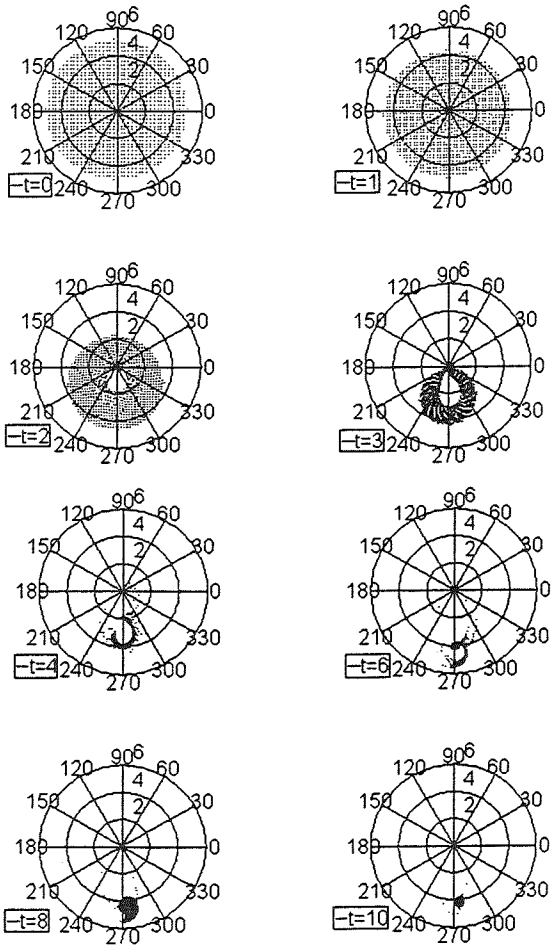

Figure 2: Temporal evolution of the distribution of identical droplets near a horizontal vortex with axial stretching.

In this paper we focus on the motion of droplets whose distance from the vortex axis is bigger than the vortex radius. The flow in this outer region is that of a *line vortex* which corresponds to the limit $\delta \to 0$, $u(r) = \Gamma/(2\pi r)$. We

take $\phi = \pi/2$, as the key effect we are concerned with is the interplay of gravity and axial stretching and that is most pronounced when the vortex is horizontal.

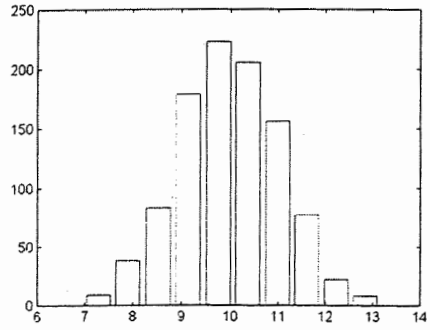

Figure 3: Initial droplet spectrum. Number of droplets (vertical axis) versus their diameter in μm (horizontal axis).

In the Stokes regime (1) droplets of radius R adapt their speed to that of ambient flow on the time-scale

$$\tau_d = (2\rho_w R^2)/(9\mu), \tag{8}$$

where ρ_w is the density of water and μ is the viscosity of air and the corresponding length scale is equal

$$S = \sqrt{\Gamma \tau_d / 2\pi}. \tag{9}$$

The motion along the vortex axis separates and in dimensionless units equations (4-5) governing the motion in the vertical plane take form

$$\ddot{r} - r\dot{\theta}^2 = -\tfrac{1}{2}L_1 r - \dot{r} - L_2 \sin\theta, \tag{10}$$

$$2\dot{r}\dot{\theta} + r\ddot{\theta} = r^{-1} - r\dot{\theta} - L_2 \cos\theta, \tag{11}$$

where

$$L_1 = \alpha\tau_d, \quad L_2 = g\tau_d^2(2\pi/\Gamma\tau_d)^{1/2} \tag{12}$$

are two non-dimensional numbers characterising the droplet.

3. DROPLET TRAJECTORIES

Equations (10-11) have one stable fixed point when $L_1 < L_2^2$ and one limit cycle otherwise. Small droplets tend to the limit cycle and keep circulating around the vortex axis. Large droplets move towards the fixed point (figure 1).

The fixed point of the two-dimensional motion is not an equilibrium position where droplets could rest. Due to stretching they continue to accelerate along the vortex axis according to (6).

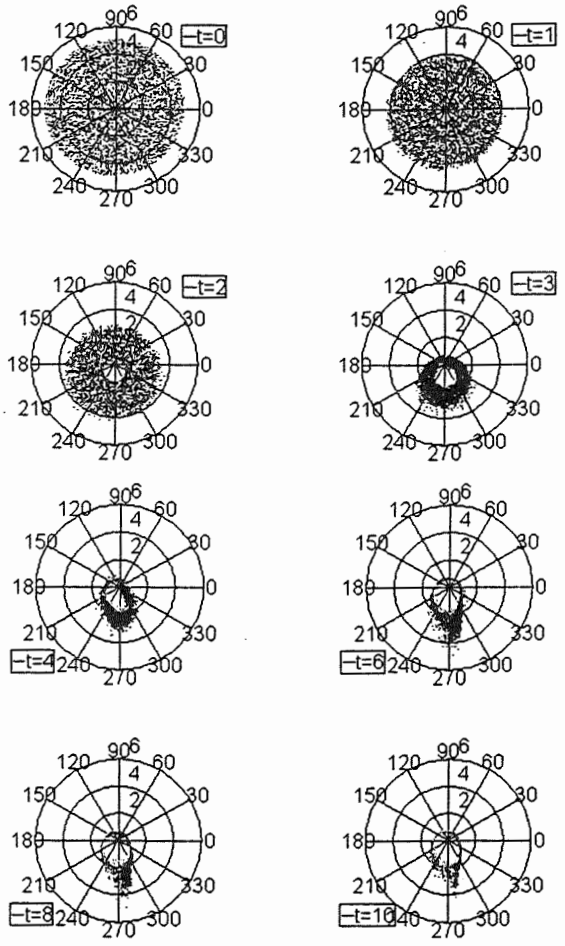

Figure 4: Temporal evolution of the distribution of droplets with gaussian spectrum near a horizontal vortex with axial stretching.

At the stable fixed point the dominant balance is between gravity and the Stokes drag associated with the straining flow towards the axis, $-\frac{1}{2}r\hat{\mathbf{e}}_r$. The larger the droplet the farther the fixed point is from the axis. In reality the radial inflow does not increase indefinitely with r and it will have a maximum at some distance from the axis where the linear strain approximation breaks down. The droplets that are big enough will then, not suprisingly, escape from the influence of the stretched vortex and continue to fall under gravity reaching their terminal velocity $g\tau_d$.

4. EVOLUTION OF AN ENSEMBLE OF DROPLETS

We solved equations (10-11) numerically for 1000 droplets which where stationary at $t = 0$.

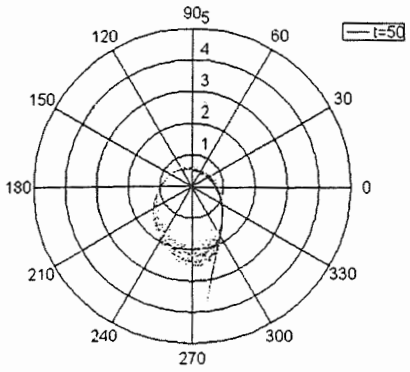

Figure 5: Distribution of droplets with gaussian spectrum after 2.5 turnover times of the vortex. Initial distribution was spatially uniform.

Figure 2 shows the evolution of the ensemble of identical droplets which at $t = 0$ were uniformly distributed in the disc $r < 5$.

The condition L_1/L_2^2 is satisfied, so all droplets eventually end up in the fixed point. Large area around the vortex is quickly cleared off droplets. Interestingly there is a noticeable number of droplets 'lagging behind'. They remain scattered near the axis, e.g. at $t = 4$, and take much longer to reach the fixed point. This may be due to the fact that near the axis there is a second (unstable) fixed point where the dominant balance is between gravity and the Stokes drag associated with the azimuthal flow of the vortex. Droplets starting from the immediate vicinity of that fixed point are initially slow and take much longer to reach the stable fixed point.

We have also computed the motion of an ensemble of 1000 droplets of various radii. Figure 4 shows the time sequence for the initial spectrum given in figure 3. Droplets of diferent sizes are spatially separated. Heavier droplets tend to the fixed point while lighter ones follow the limit cycle. The final distribution is shown in figure 5. Statistically it does not change as time progresses.

5. CONCLUSIONS

Small-scale structures of the atmospheric turbulence can have signifficant influence on the spatial distribution of cloud droplets. The mechanism proposed earlier (Shaw *et al.* 1998) relied on the centrifugal ejection. This process can be efficient only in the region where the Stokes number $St \sim 1$ while, as was pointed out by Grabowski and Vaillancourt (1999), for vortices and droplets considered by Shaw *et al.* the effect can hardly be expected to show as $St \ll 1$ everywhere in the flow.

The details of the small-scale atmospheric vortices are not known. Little is known about the geometry and the flow in those important basic structues. However, we may reasonably assume that typically they are axially stretched, like Burgers vortex, their idealised model. We have shown that this axial stretching, if present, would have signifficant effect on cloud droplets, more signifficant than centrifugal rejection. Near a stretched vortex droplets uniformly distributed over a three-dimensional region will rapidly gather in a one-dimensional region (heavier droplets) or in a two-dimensional region (lighter droplets) leaving an empty space around the vortex. This is much faster process that centrifugal ejection of a Stokes particle.

To what extent the *spatial* density of droplets increases depends on the details of the strain field, especially on the dynamics of the vortex 'ends'. Creating a void in one place a stretched vortex is likely to create a region of increased density elswhere. This in itself increases the probability of droplet collisions and subsequent coallescence. This effect is greatly enhanced by high relative droplet velocities due to the 'beam' of droplets accelerating along the vortex axis.

ACKNOWLEDGMENTS

This research was supported by the State Committee for Scientific Research (KBN) grant no. 2 P03B 135 17.

REFERENCES

DOUADY, S., Y. COUDER, M.E. BRACHET, 1991: Direct observation of the intermittency of intense vorticity filaments in turbulence. *Phys. Rev. Lett.* **67**, 983–986.

GRABOWSKI, W., P. VAILLANCOURT, 1998: Comments on "Preferential Concentration of Cloud Droplets by Turbulence: Effects of the Early Evolution of Cumulus Cloud Droplet Spectra". *J. Atmo. Sci.* **56**, 2127–2130.

JIMENEZ, J. 1998: Small scale intermittency in turbulence. *Eur. J. Mech./B - Fluids*, **17**, 405–419.

SHAW, R.C., W.C. READE, L.R. COLLINS & J. VERLINDE, 1998: Preferential Concentration of Cloud Droplets by Turbulence: Effects on the Early Evolution of Cumulus Cloud Droplet Spectra. *J. Atmo. Sci.* **55**, 1965–1976.

VINCENT, A., M. MENEGUZZI, 1991: The spatial structure and statistical properties of homogeneous turbulence. *J. Fluid Mech.* **225**, 1–25.

Collection Efficiencies for Detailed Microphysical Models

Harry T. Ochs III and Kenneth V. Beard

Illinois State Water Survey, 2204 Griffith Drive, Champaign, IL 61820 and
Department of Atmospheric Sciences, University of Illinois Urbana-Champaign

1. INTRODUCTION

The purpose of this paper is to present the methodology used to develop a comprehensive set of collection efficiencies for drop sizes from cloud droplets through millimeter raindrops. The efficiencies are primarily based on data from our experiments obtained for laboratory conditions of temperature and pressure. The assumptions used to extrapolate across data void regions are discussed and are used to highlight the need for additional data to accurately complete the description of collision efficiencies. This paper reports the first stages of an update and expansion of the data reported in Beard and Ochs (1984).

2. COLLECTION EFFICIENCIES

The data for accretion and formulas used to calculate coalescence and collection efficiencies are given in Beard and Ochs (1984). The formulas used to calculate coalescence efficiencies for small precipitation drops (the self-collection process) are found in Beard and Ochs (1985). A significant obstacle to a unified set of collection efficiencies that cover the entire range of drop sizes relevant to processes in clouds is that the results of the formulas describing accretion and self-collection do not merge. Figure 1 shows the geometric collection efficiencies for accretion and self-collection for a 200 μm collector drop as a function of size ratio, p=R/r. In Fig. 1 the efficiencies from the formulas are plotted from p = 0.0 to 0.95. Clearly neither of these formulas apply for the full range of size ratio. The self-collection formula applies to larger values of size ratio while the accretion formula applies to smaller values. There appears to be no obvious way to create a transition between the two curves at intermediate size ratios. Given the existing gap in size ratio between our experiments for accretion and self-collection, there is no data to guide the process of creating a transition.

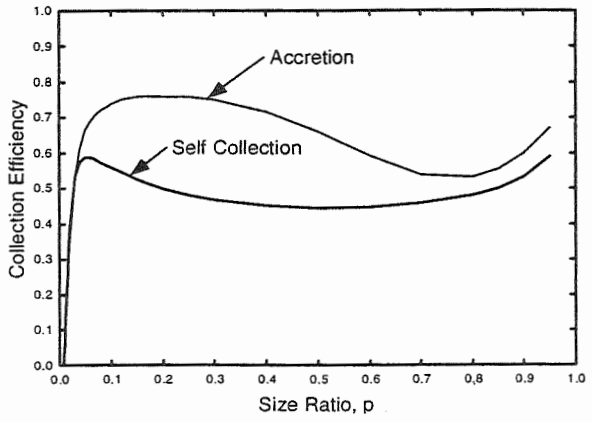

Figure 1. Collection Efficiencies for Accretion and Self-Collection for a 200 μm Collector Drop

Corresponding author: Harry Ochs, Illinois State Water Survey, 2204 Griffith Dr., Champaign, Illinois 61820, USA; E-Mail: h-ochs@uiuc.edu

In our accretion experiments we measured collection efficiencies directly while in our self-collection experiments we measured coalescence efficiencies and deduced collection efficiencies by multiplying the coalescence efficiencies by published collision efficiencies deduced from superposition calculations. A complete set of linear collection efficiencies is plotted in Fig. 2.

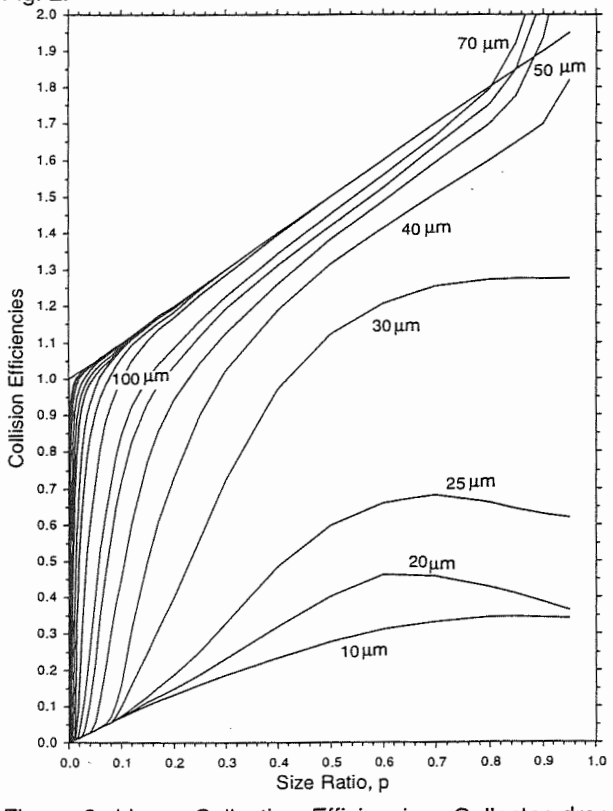

Figure 2. Linear Collection Efficiencies. Collector drop radii are shown.

As a first attempt at developing a unified set of collection efficiencies for laboratory conditions of temperature and pressure we decided to merge together the coalescence efficiencies determined from

the formulas given in Beard and Ochs (1984) and Beard and Ochs (1985). The collection efficiencies were then computed by multiplying the resulting unified coalescence efficiencies by the collision efficiency data used to plot Fig. 1. Figure 3 shows the coalescence efficiencies for a 200 μm collector drop. In order to blend the two curves in Fig. 3 together a simple method of developing a straight line between the curves was employed. The gap in our laboratory data occurs at small to medium size ratios and, thus, we desired a method that would place the transition lines at about the proper size ratios. In addition, the transition between the two curves should not be abrupt. Figure 4 shows a transition line for a 200 μm collector drop that meets these criteria. The transition line was determined by following the accretion coalescence efficiency from small size ratios to the point where the coalescence efficiency = 0.5 and then constructing a straight line to the self-collection curve at the point where the self-collection = 0.6. This scheme was used for each collector drop where it was possible to apply the algorithm. The collision efficiency data was then used to develop the set of collection efficiency data shown in Fig. 5. These efficiencies represent a first cut in the development of a consistent data set that spans the entire range of drop sizes required by numerical models of precipitation initiation and evolution.

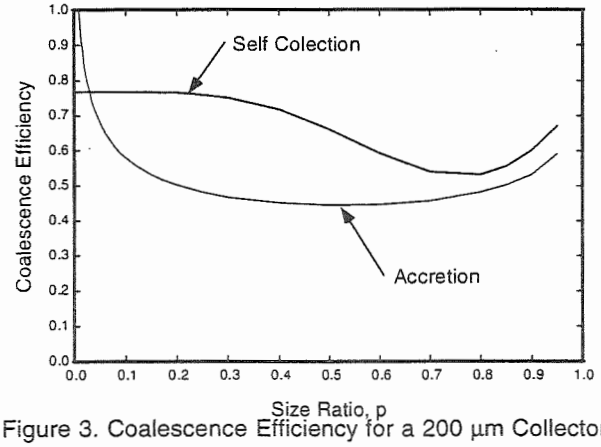

Figure 3. Coalescence Efficiency for a 200 μm Collector Drop.

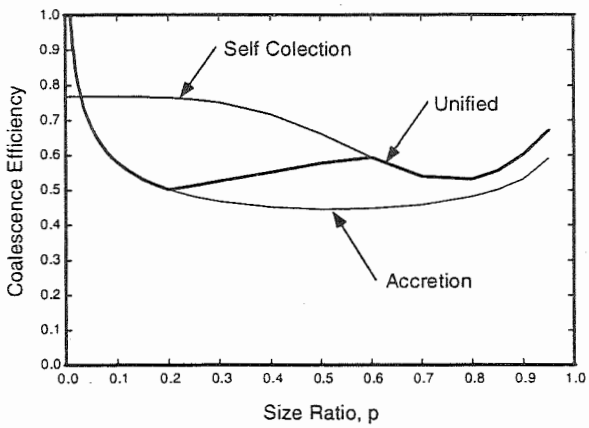

Figure 4. Unified Coalescence Efficiency for a 200 μm Collector Drop.

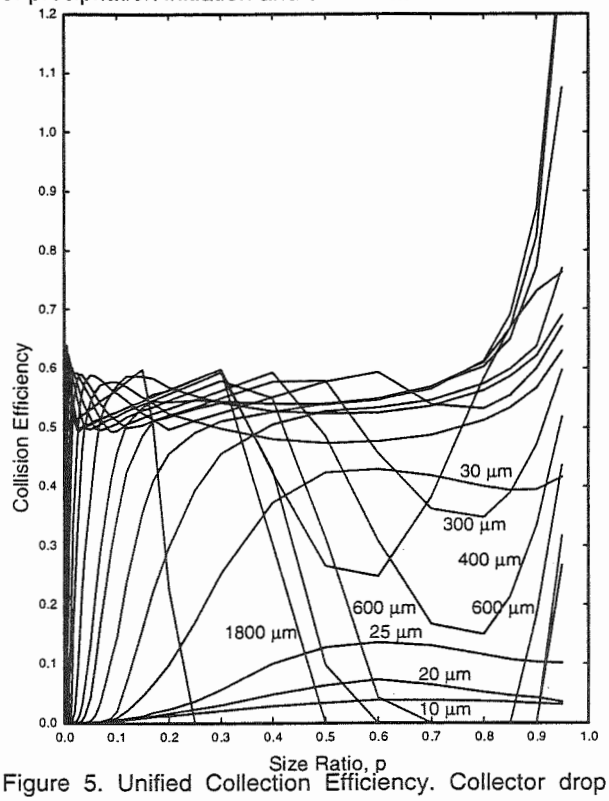

Figure 5. Unified Collection Efficiency. Collector drop radii are shown.

3. FUTURE RESEARCH

A revision of this data set is underway with the aim of using the envelope of the laboratory measured data for accretion and self-collection as a guide to choose the starting and ending points for the linear line joining the accretion and self-collection coalescence efficiency lines for each collector drop size. This data set will not include satellite production during temporary coalescence or breakup which should be added for a complete description of the results of drop collisions. When a final complete data set has been developed it will be tested using a parcel model of condensation and collection.

Acknowledgements. This research was supported by the National Science Foundation under grant NSFATM 9421735.

4. REFFERENCES

Beard, K. V., and H. T. Ochs, 1984: Collection and coalescence efficiencies for accretion. *J. Geoph. Res.*, **89**, 7165-7169.

Beard, K. V., and H. T. Ochs, 1995: Collisions between small precipitation drops. Part II: Coalescence efficiency formulas for charged and uncharged drops. *J. Atmos. Sci.*, **52**, 3977-3996.

INFLUENCE OF THE CONDENSATION AND ACCOMMODATION COEFFICIENTS ON THE DROPLET SIZE DISTRIBUTION IN WARM CLOUDS

J.B.V. Leal Jr., J.A.K. Freire, A.A. Coelho, M.P. Almeida and V.N. Freire

Departamento de Física, Universidade Federal do Ceará, Fortaleza, Ceará, CEP 60455-760, Brazil

1. INTRODUCTION

The initial stage of droplet growth by condensation, that constitutes the beginning of warm clouds development, can be described by several equivalent theoretical formulations (Barret and Clement, 1988). All of these formulations, however, still do not explain one important feature in cloud microphysics: the calculated cloud droplet size distribution tend to be very narrow, in contrast to airbone measurements. There are many mechanisms which are candidates to explain this spectral broadening. They can be divided into two main groups: one related to dynamical processes like mixing or entrainment (Paluch and Knight, 1986; Bower and Choularton, 1988; Paluch and Baumgardner, 1989); the second tries to explain the broadening in terms of some characteristic features of the condensation process, like variability in the CCN composition (Fitzgerald, 1974; Hindman et al., 1977; Takeda and Kuba, 1982; Ghan et al., 1998), supersaturation fluctuations experienced by individual droplets (Srivastava, 1989; Korolev, 1995), which could be caused by turbulence (Manton, 1979; Cooper, 1989; Jensen and Baker, 1989; Shaw et al., 1998), modification on the formulation of the Köhler equation (Laaksonen et al., 1998) or the variability in the condensation coefficient, which will be discussed in this work. A variation of the condensation coefficient (hereafter denoted within the text as β) and the accommodation coefficient (hereafter denoted as α) exerts an important influence in the condensation process in clouds, as argued by Fukuta and Walter (1970), Fitzgerald (1972) and Roth (1989). The former is defined as the probability that a vapor molecule enters the liquid phase when it strikes the interface (Pruppacher and Klett, 1978), while the latter is defined as the probability of the vapor molecule comes into thermal equilibrium with the droplet after one collision (Kennard, 1983).

Existing experimental measurements of β for water vapor on liquid water vary over two orders of magnitude, from near unity to about 0.01. Pruppacher and Klett (1978) have tabulated several experimental values ranging from 0.035 to about unity. Using a thermal diffusion chamber, Chodes et al. (1974) found an average value of 0.033 with a standard deviation of 0.005. Mozurkewich (1986) indicated with theoretical arguments that β for pure water should be near unit. Using a cloud simulation chamber, Hagen et al. (1989) obtained a coefficient decreasing from a value near unity to about 0.01 as the chamber experimented in-cloud conditions. The controversy around the precise value of the condensation coefficient still exists nowadays and its value has not been yet accurately determined, according to these authors' knowledge. There are two sources of experimental errors identified in the literature: uncertainty on the measurement of the droplet surface temperature; and the presence of contaminants. Concerning α, its value is unit in most of the studies beginning with Alty and Mackay (1935). Consequently, there is an unjustified consensus of choosing a value of unity for α and establishing a one-to-one relationship between both coefficients.

In this study, numerical simulations are performed in order to evaluate the implications of the uncertainty of the values of β and α on the condensational growth characteristics of warm clouds. An isolated cloud parcel model is used to calculate the droplet size evolution and the supersaturation field. It will be shown that an absolute variation of β modifies remarkably the droplet spectra evolution. On the other hand, the influence of the variation of α will be shown to be small.

Corresponding author's address: João Bosco V. Leal Jr. Universidade Federal do Ceará, Campus do Pici, Caixa Postal 6030, Fortaleza, CE, CEP 60455-760, Brazil.
E-Mail: bosco@fisica.ufc.br.

2. MODEL DESCRIPTION

The model is based on a nonentraining air parcel, e.g., a parcel with no mass, heat and momentum exchange with its environment, ascending with uniform updraft velocity, including surface tension forces and dissolved salts effects (Freire and Brenguier, 1995). Cloud droplets are formed by condensation upon a previously specified population of spherical cloud condensation nuclei. There is no sedimentation of cloud droplets and the parcel ascent is a moist-adiabatic process.

The model is based on a set of four linear differential equations: one for the growth rate of the spherical droplets as a function of the ambient supersaturation, other describing the rate of change of the ambient supersaturation, a third one describing the rate of change of the temperature and another one to describe the rate of change of the pressure. The numerical solution for this set of coupled differential equations was obtained using a fourth-order Runge-Kutta method (Press et al., 1996).

3. SIMULATION DESIGN

For all the simulations, the updraft velocity was assumed to be constant and equal to 1.0 $m \cdot s^{-1}$. The chosen value for the vertical velocity was not intended to

reproduce actual profiles, but to give a rough idea for in-cloud situations. The initial values for the temperature and the pressure in the parcel are respectively 281.45 K and 800 hPa. The initial droplet radii distribution is calculated as CCN in equilibrium at a humidity of 0.99. The type of CCN used in the simulations was the sea salt (NaCl), with minimum (maximum) radius of 0.01 μm (10.0 μm) and density of 10^3 cm^{-3} (10^{-4} cm^{-3}). The cumulative CCN distribution consists of 60 size classes of equal width, forming a straight line on a logarithmic scale graph.

Once significant changes in the values for α ($1.0 \leftrightarrow 0.01$) do not produce significant modification neither on the droplet size distribution nor the droplet radius evolution, its value is fixed constant, equal to 1.0 for all the model runs. On the other hand, four different cases of varying β are considered:

- Case I: there is no dependence of β with any variable and its value is fixed constant, equal to 0.01, corresponding to the minimum tabulated measurement found in the literature.
- Case II: there is also no dependence of β with any variable and its value is fixed constant, equal to 0.1, an intermediate value.
- Case III: there is no dependence of β with any variable and its value is fixed constant, equal to 1.0, corresponding to the maximum found in the literature.
- Case IV: the value of β is a function of the droplet radius. The function is obtained from the simplest interpolation of the measured values obtained by Hagen et al. (1989) in a cloud simulation chamber experiencing in-cloud conditions, as depicted in Fig. 1.

4. RESULTS

It is shown in Fig. 2 the droplet radius time evolution for droplets formed on five different CCN size classes. It could be observed that variations in β of one order of magnitude ($1.0 \leftrightarrow 0.1$) does not exert a great influence in the droplet growth rate, whereas variations of two orders of magnitude ($1.0 \leftrightarrow 0.01$) modify remarkably the droplet radius evolution. This variation also delays the instant of activation of the nuclei, as shown in Fig. 3, allowing more nucleus classes to be activated, which can be confirmed also by the increase of the maximum supersaturation. In case I, the maximum supersaturation reached a value of 1.536% at t=35 s. In case II, it reached 0,729% at t=18 s and in case III, it reached only 0.577% at t=15 s. For the case IV, the maximum supersaturation was equal to 0.634% at t=16 s. The variable value for β does not seem to produce a different result, showing that it is not important whether it is considered fixed or variable.

The shape of the droplet radius distribution is also affected by the value of β. It is shown in Fig. 4 that the spectrum obtained for β=1.0, corresponding to the case III, just after activation time, t_c, are very similar to the one obtained for β=0.1, corresponding to the case II, and the one obtained for β variable, corresponding to the case IV. They are all different from the one obtained

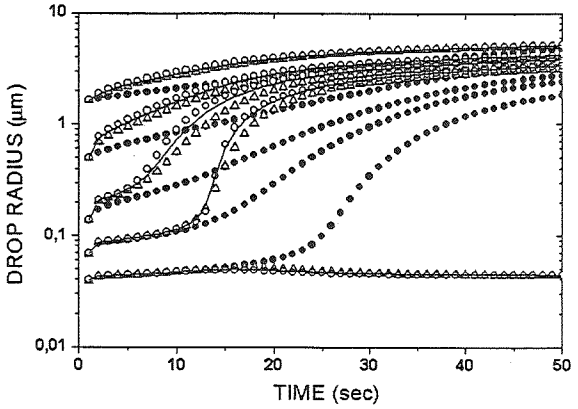

Figure 2: Droplet radius time evolution. The solid circle graph expresses the case I. The open up-triangle graph is the case II. The open circle is the case III and the solid line represents the case IV.

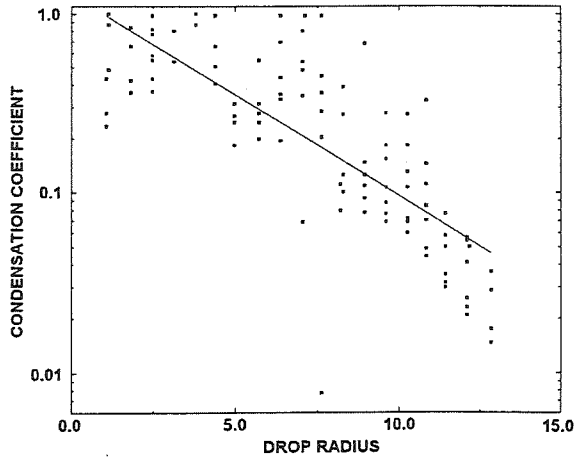

Figure 1: Condensation coefficient as a function of the droplet radius (μm). The function is obtained from an interpolation (line) of the measured values (dots), as given in Hagen et al. (1989).

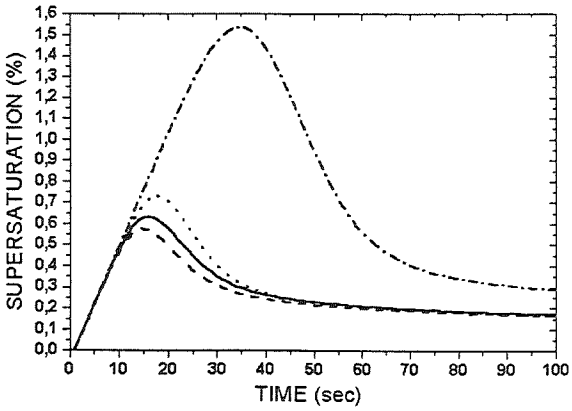

Figure 3: Supersaturation time evolution for all the simulation cases: the dash-dot line expresses the case I, the dot line is the case II, the dashed line is the case III and the solid line represents the case IV.

for β=0.01, corresponding to the case I, that differs remarkably from the others because it presents a higher concentration of smaller droplets around 1.6 μm. The time of droplet activation is the time in which the parcel attains its maximum supersaturation. It is important to emphasize that the droplet activation time is not necessarily the same for all the simulation cases. After 200 s, the spectrum obtained for the case IV remained similar to the one obtained for the case III, which is still similar to the one obtained for the case II. They still differ from the spectrum obtained for the case I. The parameter used to measure the spread of the distribution was the dispersion coefficient, defined as the ratio of the standard deviation of the distribution to the mean droplet radius.

Table 1 presents the values for the standard deviation, mean radius and dispersion coefficient for the droplet size distributions in each simulation case, corresponding to distinct values of β, at time $t=t_c$ and t=200 s. After activation, the dispersion coefficient for the case I is almost twice the one for the case III, which is approximately equal to the one for the case IV, showing that a variation in two orders of magnitude in β also modifies the shape of the distribution, also confirming that lower values of β produce a broader droplet size distribution. At time t=200 s, the dispersion coefficient for the case I accentuated its difference in relation to the one obtained for the cases III and IV and now presents an isolated value, distant even from the one obtained for the case II. The values obtained for the standard deviation, for the mean radius and for the dispersion coefficient at t=200 s are very similar to those obtained by Takeda and Kuba (1982), in their study of the CCN effect on the cloud droplet size distribution, adopting the same initial conditions and a value of β=0.036 in a closed air parcel model.

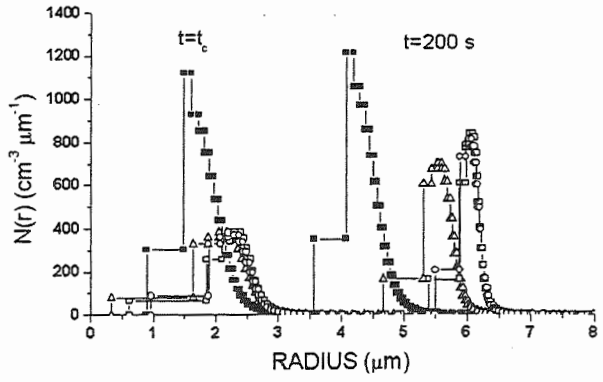

Figure 4: Droplet size distributions for all the simulation cases in two distinct times. The solid square graph expresses the case I. The open up-triangle graph is the case II. The open square graph is the case III. The case IV is represented by the open circle graph.

Time	β	Std. Dev.	Mean Rad.	Dispersion
$t=t_c$	case I	0.35236	1.6451	0.21419
	case II	0.36748	2.0830	0.17642
	case III	0.27296	2.2692	0.12029
	case IV	0.28763	2.2237	0.12935
t=200s	case I	0.30541	4.2321	0.07217
	case II	0.20590	5.5403	0.03716
	case III	0.12827	6.0563	0.02118
	case IV	0.13669	6.0401	0.02263

Table 1: Mean radius, standard deviation and dispersion coefficient for the droplet size distributions for each simulation case at two distinct times.

5. CONCLUDING REMARKS

The variation of the condensation coefficient can modify remarkably the droplet radius evolution, the shape and time evolution of the droplet size distribution. The usage of a variable value of β did not produce any remarkable modification over the previous results. The observed spectral broadening for small values of β indicates that it can reproduce better the airbone measured droplet size distribution.

All those results show the importance of the condensation coefficient in explaining the broadening of the droplet size distribution. According to these results, new experimental measurements are necessary to obtain improved values of the coefficients, which could help on the elucidation of their effective role on actual cloud droplet size distributions. In this sense, molecular dynamics simulations or even newer techniques, like indirect measurements through optical devices, can contribute significantly for its estimation.

6. ACKNOWLEDGEMENTS

One of the authors, J. B. V. Leal Junior, would like to acknowledge the graduate fellowship he receives from the Science Funding Agency of the Ceará State in Brazil (FUNCAP) for the development of this research. The authors would like to acknowledge the partial financial support received from FUNCAP, Conselho Nacional de Desenvolvimento Científico e Tecnológico (CNPq), and the Ministry of Planning through FINEP.

REFERENCES

Alty, Y., and C. A. Mackay, 1935: The accommodation coefficient and the evaporation coefficient of water. *Proc. Roy. Soc. London Ser. A*, **149**, 104–106.

Barret, J. C., and C. F. Clement, 1988: Growth rates for liquid drops. *J. Aerosol Sci.*, **19**, 233–242.

Bower, K. N., and T. W. Choularton, 1988: The effects of entrainment on the growth of droplets in continental cumulus clouds. *Quart. J. Roy. Meteor. Soc.*, **114**, 1411–1434.

Chodes, N., J. Warner, and A. Gagin, 1974: A determination of the condensation coefficient of water from the growth rate of small droplets. *J. Atmos. Sci.*, **31**, 1351–1357.

Cooper, W. A., 1989: Effects of variable droplet growth histories on droplet size distributions. Part I: Theory. *J. Atmos. Sci.*, **46**, 1301–1311.

Fitzgerald, J. W., 1972: *A Study of the Initial Phase of Cloud Droplet Growth by Condensation: Comparison between Theory and Observation.* Tech. Rep. No. 44., Dept. of Geophysical Sciences, The University of Chicago.

——, 1974: Effect of aerosol composition on cloud droplet size distribution: A numerical study. *J. Atmos. Sci.*, **31**, 1358–1367.

Freire, V. N., and J.-L. Brenguier, 1995: The influence of CCN spectra and updraft velocities on the validity of the b^2 parameterization of the condensation process. *Atmos. Res.*, **35**, 189–199.

Fukuta, N., and L. A. Walter, 1970: Kinetics of hydrometeor growth from a vapor-spherical model. *J. Atmos. Sci.*, **27**, 1160–1172.

Ghan, S. J., G. Guzman, and H. Abdul-Razzak, 1998: Competition between sea salt and sulfate particles as cloud condensation nuclei. *J. Atmos. Sci.*, **55**, 3340–3347.

Hagen, D. E., J. Schmitt, M. Trueblood, J. Carsten, D. R. White, and D. J. Alofs, 1989: Condensation coefficient measurement for water in the UMR cloud simulation chamber. *J. Atmos. Sci.*, **46**, 803–816.

Hindman II, E. E., P. V. Hobbs, and L. F. Radke, 1977: Cloud condensation nucleus size distributions and their effects on cloud droplet size distributions. *J. Atmos. Sci.*, **34**, 951–956.

Jensen, J. B., and M. B. Baker, 1989: A simple model of droplet spectral evolution during turbulent mixing. *J. Atmos. Sci.*, **46**, 2812–2829.

Kennard, E. H., 1983: *Kinetic Theory of Gases.* McGraw-Hill, pp. 312–315.

Korolev, A. V., 1995: The influence of supersaturation fluctuations on droplet size spectra formation. *J. Atmos. Sci.*, **52**, 3620–3634.

Laaksonen, A., P., Korhonen, M. Kulmala, and R. J. Charlson, 1998: Modification of the Köhler equation to include trace gases and slightly soluble substances. *J. Atmos. Sci.*, **55**, 853–862.

Manton, M. J., 1979: On the broadening of a droplet distribution by turbulence near cloud base. *Quart. J. Roy. Meteor. Soc.*, **105**, 899—914.

Mozurkewich, M., 1986: Aerosol growth and the condensation coefficient for water: A review. *Aerosol Sci. Technol.*, **5**, 223–236.

Paluch, I. R., and C. A. Knight, 1986: Does mixing promote cloud droplet growth? *J. Atmos. Sci.*, **43**, 1994–1998.

——, and D. Baumgardner, 1989: Entrainment and fine-scale mixing in a continental convective cloud. *J. Atmos. Sci.*, **46**, 261–278.

Press, W. H., S. A. Teukolsky, W. T. Vetterling, and B. P. Flannery, 1996: *Numerical Recipes in Fortran 77: The Art of Scientific Computing.* 2nd ed. Cambridge University Press, **1**, pp. 704–716.

Pruppacher, H. R., and J. D. Klett, 1978: *Microphysics of Clouds and Precipitation.* D. Reidel.

Rooth, C., 1989: On a special aspect of the condensation process and its importance in the treatment of cloud particle growth. *Tellus*, **9**, 372–377.

Shaw, R. A., W. C. Reade, L. R. Collins, and J. Verlinde, 1998: Preferential concentration of cloud droplets by turbulence by turbulence: Effects on the early evolution of cumulus cloud droplet spectra. *J. Atmos. Sci.*, **55**, 1965–1976.

Srivastava, R. C., 1989: Growth of cloud drops by condensation: A criticism of currently accepted theory and a new approach. *J. Atmos. Sci.*, **46**, 869–887.

Takeda, T., and N. Kuba, 1982: Numerical study of the effect of CCN on the size distribution of cloud droplets. Part I. Cloud droplets in the stage of condensational growth. *J. Meteor. Soc. Japan*, **60**, 978–992.

MONTE CARLO SIMULATION OF CLOUD DROP GROWTH BY CONDENSATION AND COALESCENCE

Qing Xia and Ramesh Srivastava

Department of Geophysical Sciences,
The University of Chicago, Chicago, IL 60637, USA

1. INTRODUCTION

The process of condensation is essentially continuous and deterministic because it involves the diffusion of water molecules in the vapor phase to the liquid drop. The collection process involves collision and coalescence of water drops. This process is essentially discrete and stochastic because of the random distribution of water drops. Previous research has considered the stochastic nature of the collection process in calculating growth by collection alone. In this paper, we develop a new method to simulate the random nature of the coalescence process in our calculations of growth by condensation and coalescence using a Monte Carlo method. The consideration of condensation and coalescence occurring simultaneously brings in new factors which will be discussed in this paper. We will use our method to address the following questions which are fundamental to the "warm rain" process: (1) what does drop growth process look like during transition range, i.e. the range of drop sizes where both condensation and coalescence are important? (2) what is the critical variance for initiating the coalescence rain process given the mean and concentration of the initial drop size distribution? and (3) we shall compare the results of our calculations with observations from the Small Cumulus Microphysics Study, SCMS.

2. NEW APPROACH

2.1 Gillespie's Method for the Stochastic Collection Equation

Melzak (1953) used a continuous distribution of drop sizes and the following known as the Stochastic Collection Equation:

$$\frac{\partial n(m,t)}{\partial t} = \frac{1}{2}\int_0^m n(m',t)n(m-m',t) K(m',m-m')dm' - n(m,t) \times \int_0^\infty n(m',t)K(m,m')dm' \quad (1)$$

to describe collection involving all pairs of drops. Here $n(m,t)$ is drop concentration such that $n(m,t)\Delta m$ is the concentration of drops in the drop mass interval m to $m+\Delta m$ at time t, and K is the collection kernel which is defined later. Given the initial locations of drops in space, in principle, it is possible to follow the trajectory of each drop and allow a collection event to occur whenever a pair of drops approach to within the region of influence where collection is possible. This so-called ballistic aggregation is computationally prohibitive, even impossible for cloud physics purposes. The computational difficulty and the uncertainties inherent in determining drop trajectories make a purely probabilistic approach to the problem attractive. This approach was discussed by Gillespie (1975).

Consider N drops, numbered 1.2...N contained in volume V. Gillespie defined a function $p(t,j,k)d\tau$ as follows: $p(t,j,k)d\tau$= probability at time t that the next coalescence will occur in the time interval $(t+\tau, t+\tau+d\tau)$ and will be the coalescence of droplets j and k. This probability is the product of the probabilities p_0 and $p_{jk}d\tau$, with p_0= probability of no collision in the time interval $(t,t+\tau)$, and $p_{jk}d\tau$= probability of one collision in the next time interval $d\tau$ between drops j and k. It is found that the probability of no collision

Corresponding author address: Qing Xia, 5734 South Ellis Ave, Chicago, IL 60637; E-Mail: xia@cirrus.uchicago.edu

between any two drops in the time interval is:

$$p_0 = c_0 \exp(-c_0 \tau) d\tau \qquad (2)$$

where

$$c_0 = \sum_{j=1}^{N-1} \sum_{k=j-1}^{N} K_{jk} / V ,$$

$$K_{jk} = \pi (r_j + r_k)^2 \mid W_j - W_k \mid E(r_j, r_k),$$

$E(r_j, r_k)$ = collection efficiency,

and

W_j = terminal fall speed of drops.

Gillespie prescribed the following three-step recipe for simulation of the stochastic collection process: Step1, find the time τ_1 to the first collision between two drops. This is calculated from a random number r_1, uniformly distributed over the interval $(0,1)$, according to:

$$\tau_1 = -\frac{1}{c_0} \ln(r_1) \qquad (3)$$

Steps 2, and 3 are used to specify the indexes of the drops undergoing collection. Details for calculating steps 2 and 3 may be found in Gillespie (1975). Gillespie claimed that 3 to 10 realizations are sufficient to yield a reliable average concentration. As emphasized by Gillespie, the above results and simulation method are valid only if the collection kernel K_{jk} remains constant between successive collection events. After each collection event, the K_{jk} changes because of changes in drop sizes.

2.2 Simulation of Growth by Condensation and Stochastic Collection

While a considerable amount of work has been done on the stochastic collection process based on Gillespie's method, no work has been reported on the stochastic collection process when condensation is also occurring. As the drops grow continuously by condensation, the collection kernel changes continuously between collision events and, therefore, Gillespie's method is not valid for this case.

In the following, we develop a method for simulating the stochastic condensation-collection process and report preliminary results from the simulations. First we extend the Gillespie method to the condensation-collection process. This involves consideration of time variation of the K_{jk}. As the sizes of the drops increase by condensation, the function K_{jk} increases rapidly because of increase in drop radius and collection efficiency. This is shown in figure 1, where we have plotted the mean time to collision $1 / c_0$, as a function of time.

We again consider the function $p(t, j, k)$ as defined above and evaluate the probability as the product of the two

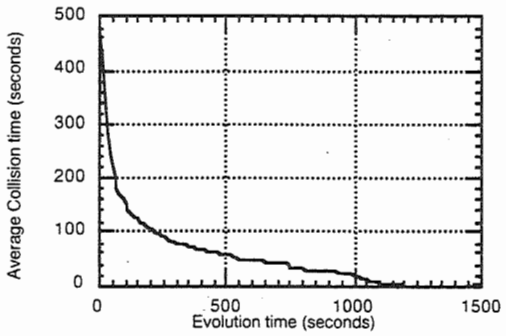

Figure 1: Average collision time projected in condensation-coalescence process. Initial distribution is a gamma function with liquid water $0.1\,g/m^3$, variance=1.0, updraft is $2\,m/s$.

probabilities p_0 and $p_{jk} d\tau$. To evaluate p_0, in this case, we subdivide $(t, t+\tau)$ in m small subintervals Δt. In each subinterval, The probability of no collision is $\exp(-c_0(t)\Delta t)$ where we have explicitly indicated that c_0 is a function of time t. The probability of no collision in the interval $(t, t+\tau)$ is then

$$\exp(-c_0(t)\Delta t) \times \exp(-c_0(t+\Delta t)\Delta t) \times \ldots \exp(-c_0(t+m\Delta t)\Delta t) \qquad (4)$$

In the limit of Δt tending to zero, the above expression becomes: $\exp(-\int_t^{t+\tau} C_0(t')dt')$. We use a random number r_1 uniformly distributed over $(0,1)$ to specify this probability by:

$$\ln(1 / r_1) = \int_t^{t+\tau} C_0(t')dt' \qquad (5)$$

The next collision time τ is then obtained through numerical solution of (5). The determination of collision pair indexes follows Gillespie's method.

3. APPLICATIONS

3.1 Drop Growth Features in Transition Range

We first use the above Monte Carlo method to determine the role of condensation and coalescence in early warm rain stages. We use one typical case to show how droplets grow from around 0.05 μm in radius to 50 μm or slightly more in radius. Calculations start with a power-law CCN spectrum of $n = CS^k$ with $C = 300 / cm^3$, $k = 0.7$. It is found that during the first 100 seconds, no coalescence occurs, and the largest droplet reaches 12.8 μm. After 180 seconds, it is seen in figure 2 that coalescence occurs between drops of very nearly the same size at the peak of the spectrum. At 1000 seconds, condensation has moved the peak of the size distribution to near 16 μm, while the largest drop is still less than 22 μm in radius. Condensation is already driving most drops to nearly the same size. Stochastic coalescence between two drops near the peak of the size distribution can produce a drop of radius about 20 μm. In this sense they are statistically fortunate drops. It turns out that all those fortunate droplets will have opportunity to grow through coalescence into a so-called coalescence mode (figure 3), and eventually these drops behave like a collector in a continuous collection model. Before this, collision was favored between drops of nearly equal size near the peak of the spectrum (figures 2, 3). After the appearance of this second peak, collision is favored between drops of the second peak and the main peak. So initially coalescence generates a collection mode and then drops in that mode begin to rapidly collect drops in the condensation mode as those drops grow bigger and their distribution narrows by condensation. In short, considering condensation and coalescence, the growth process displays the following characteristics: (1) coalescence first produces a coalescence mode by collisions between drops of nearly equal size in the condensation mode, (2) continued condensation narrows the condensation mode and translates it to bigger sizes and (3) subsequently coalescence between drops in the collection and condensation modes is favored.

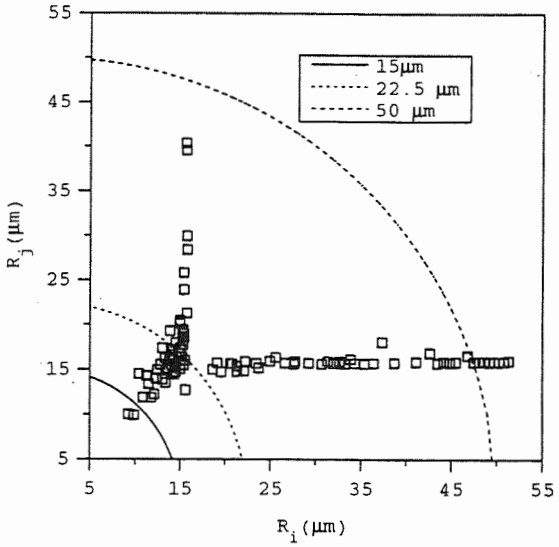

Figure 2: History of size of drops in collision pairs in one Monte Carlo run, with C=300 / cm^3, k=0.7, and updraft velocity of 2 m / s.

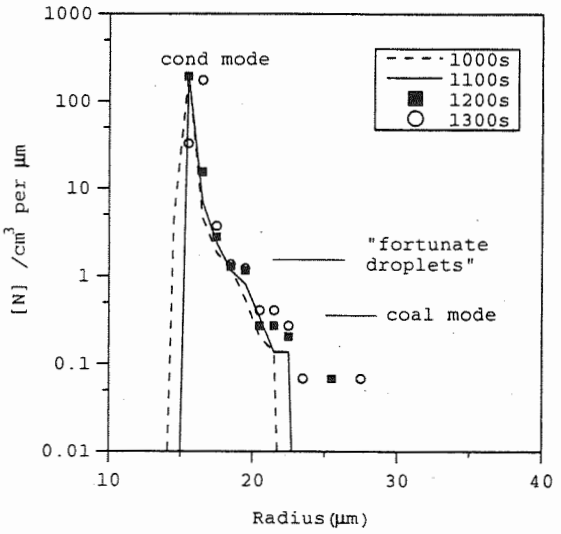

Figure 3: Droplet spectrum in one Monte Carlo run (same initial CCN spectrum as figure 2). Fast moving big size tail (1300 seconds) is triggered by collisions between collector and main peak (condensation mode). Coalescence mode (at 21 μm) is slightly increased at the same time.

3.2 Critical Variance of Initial Droplet Spectrum for Rain Initiation

Another important problem is: for a given mean droplet size and liquid water content, what is the critical variance of an initial size distribution for successful rain initiation. This critical variance is defined as the lowest initial variance such that rain initiation is still possible during the typical lifetime of warm rain clouds. We could not use Eulerian scheme to study this problem, as that scheme tends to have diffusion problem when handling very narrow droplet spectrum.

We performed a number of calculations with initial gamma distribution of liquid water content $0.1g/m^3$ but a higher concentration, $300/cm^3$. An updraft of $2m/s$ and cloud base temperature of $10^{\circ}C$ and pressure of $800mb$ was used. We found that if the initial variance is less than 1.0 (relative variance in radius less than 0.5), 90% of the cases did not produce rain. Observed clouds generally have smaller variance; therefore, we may conclude that in such clouds, rain is unlikely.

3.3 Comparison with SCMS DATA

Cloud pass data for SCMS experiment of Aug. 11, 1995 are used. Detailed description of data is given in Lawson et. al. (1996). Assuming average updraft velocity of $1m/s$, we located four adiabatic cores that could have resulted from the same parcel. They are at approximately $300m$, $600m$ and $1800m$ above the lowest flight pass level ($946mb$). At $946mb$, droplet spectrum spans the range from $1.5\ \mu m$ to $12.5\ \mu m$ in radius; at $1800m$ above that height, the biggest droplet is about $25\ \mu m$ in radius; so this makes a good candidate for studying droplet growth in the transition range. Temperature at $946mb$ level was $23^{\circ}C$, and updraft velocity was taken as $1m/s$.

The Monte Carlo runs (figure 4) generally follow the observed droplet spectrum, yet get lower concentrations in big size tail. This means, combined condensation and coalescence can not fully explain the observed droplet spectra at big size.

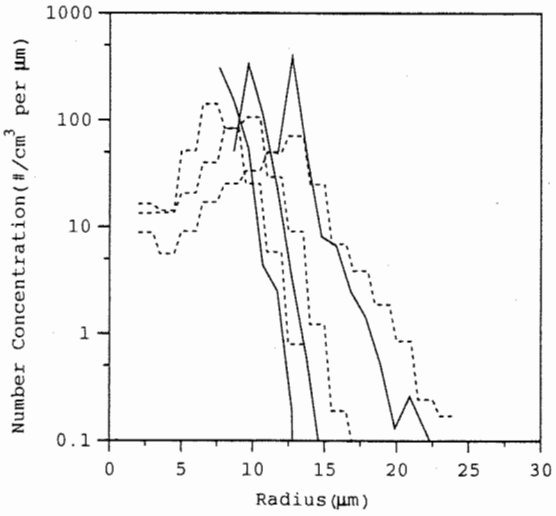

Figure 4: Droplet spectrum calculated (Solid) vs observed (dashed) on Aug. 11, 1995, at 300m, 600m, and 1800m above the lowest penetration level (946mb).

4. ACKNOWLEDGMENT

Access to SCMS data was made possible by W.A. Cooper and Charles A. Knight of NCAR. This research was supported by the National Science Foundation under grants ATM9407074 and ATM9978186.

5. REFERENCES

Gillespie, D.T., 1975: An exact method for numerically simulating the stochastic coalescence process in a cloud, *J. Atmos. Sci*, **32**, 1977-1989.

Lawson, R.P., Leigh J. Angus, Tizhi Huang, Kim A. Weaver, 1996: New Airborne measurement in adiabatic cores during very early coalescence development in Florida cumuli. *12th International Conference on Clouds and Precipitation Proceedings*, **1**. pp 1-4.

Melzak, A.Z., and W. Hitschfeld, 1953: A mathematical treatment of random coalescence. Stormy Weather Group Report, MW-11, 28pp.

The influence of thermodynamic conditions in the boundary and cloud layers on the droplet spectrum formation in cumulus clouds

Yaron Segal, Alexander Khain, and Mark Pinsky

Institute of the Earth Science, The Hebrew University of Jerusalem, Givat Ram, Jerusalem, 91904, Israel

1. INTRODUCTION

Mechanisms of the droplet size spectrum formation in clouds remain largely unclear. Warner (1969) found that the average fraction of samples having a bimodal distribution in cumulus clouds increases with thermal instability in the cloud layer. In case of relatively stable stratification ($d\Theta/dz>6.5$C/km) in the cloud layer, no bimodal drop size spectra were observed. No interpretation of these observations, as well as of the mechanisms of bimodal spectra formation has been suggested.

The formation of continental versus maritime types of clouds is usually attributed to the differing properties of aerosol particles (AP) over the sea and continents. At the same time the possible effect of differential thermodynamic conditions on cloud microphysics is often ignored altogether. An increase in the precipitation rate accompanying an increase in the boundary layer humidity is often interpreted in just "quantitative" sense, as a result of an increase in the amount of water vapor entering a cloud through the cloud base and available for condensation.

However, one can expect intuitively that an increase in subcloud layer humidity, say, from 80% to 90%, and a corresponding 10% increase the humidity flux from below should lead to an increase in precipitation more than by 10%. A non-linear response of precipitation amount to humidity changes can be expected.

The present paper is dedicated to revealing the physical mechanisms, through which thermodynamic conditions influence the formation and shape of droplet size spectra.

2. HOW THERMODYNAMICAL PARAMETERS INFLUENCE DROPLET SIZE SPECTRA

It is well known that updraft speed at the cloud base determines the maximum supersaturation and droplet concentration in the vicinity of cloud base (e.g, Warner, 1969). Note that the maximum in supersaturation leads to activation of only a certain fraction of aerosol particles (AP), so that ascending cloud parcels contain both nucleated water droplets and non-activated AP at height levels above cloud base. It seems to be paradoxical that the effect of an acceleration of vertical velocity by buoyancy on the droplet concentration and droplet size distribution is not well recognized. In most studies dedicated to the investigation of the cloud droplet spectrum formation, the vertical velocity of an ascending cloud parcel is assumed to be height independent (Rogers and Yau, 1989). Note that an increase in the vertical velocity with height can lead to the growth of supersaturation, so that the supersaturation can exceed the cloud base maximum at some height. In this case, a corresponding fraction of AP will be activated and new droplets will be nucleated at this height. Khain and Pinsky (2000) discussed the mechanism of in-cloud nucleation in more detail. Nucleation of new droplets at distances as large as a few hundred meters above cloud base leads to a) the droplet spectrum broadening through the formation of smaller droplets and b) the formation of bimodal droplet size spectra.

Whether wide bimodal spectra will form or not depends on the conditions under which supersaturation within a cloud can exceed the supersaturation maximum at cloud base. In-cloud nucleation and the formation of bimodal spectra should be observed more often in cases where updraft speed at the cloud base is low (the local maximum of supersaturation is small) and the instability within a cloud layer is high.

Low vertical velocities at cloud base can be expected when the subcloud layer is relatively stable and when the cloud base is located at small heights above the surface. We expect, therefore, that an increase in the subcloud layer humidity leading to a decrease of the cloud base height favors the formation of wide bimodal droplet spectra. If the cloud layer is unstable enough, the buoyancy-induced acceleration of the vertical velocity will lead to a growth of supersaturation that may exceed the local maximum at the cloud base.

We verify the validity of these assumptions by simulations of droplet size spectrum in an ascending air parcel under different thermodynamical conditions.

3. MODEL DESCRIPTION

Corresponding author address: Yaron Segal, Department of Atmospheric Sciences, The Hebrew University of Jerusalem, Jerusalem 91904, Israel. E-mail: mai@vms.huji.ac.il

We conduct the calculations using an air parcel model ascending from the underlying surface up to three kilometers height due to buoyancy. The equation system includes the equation for diffusional growth (Rogers and Yau, 1989):

$$r\frac{dr}{dt}=\frac{S-\left(1-\frac{b}{r^3-r_s^3}\right)e^{\frac{a}{r}}}{F_d+F_k}$$

where r is cloud droplet radius, S is saturation, r_s is the radius of the nucleus, F_d represent the thermodynamic term, F_k is associated with vapor diffusion, and a and b are the so called curvature and solution terms, respectively. The same equation is used for simulating the growth of AP and of droplets.

Temperature within an air parcel is calculated by (Kornfeld, 1970):

$$\frac{dT}{dt}=\frac{-(M_a+M_v)\left(g+\frac{du}{dt}\right)\mu-L\frac{dM_v}{dt}}{(M_a+M_v)Cp+s^*M_w}$$

where M_a, M_v, and M_w, are the masses per unit volume of air, water vapor and water, respectively, g is gravity, u is vertical velocity, L is the latent heat, C_p is heat capacity under constant pressure, and s is the fraction of heat released by condensation which increases droplet temperature.

The water mass conservation equation is:

$$-\frac{dM_v}{dt}=\frac{dM_w}{dt}=\sum_i N_i\frac{dm_i}{dt}$$

where N_i is the number of droplet in each category, and dm_i is the change of mass in each category.

The updraft speed of a rising of the parcel is described as:.

$$\frac{d^2Z}{dt^2}=\frac{du}{dt}=\frac{g}{1+\gamma}\left(\frac{T-T'}{T'}-\frac{M_w}{M_a}\right)-\mu u^2$$

where T is parcel temperature, T' is the ambient air temperature, μ is the entrainment parameter, and γ=0.5.

To describe the size distribution of non-activated AP and droplets we use 600 radii bins, with radius increment ranging exponentially from 0.01μm up to 0.5μm. In our calculations of diffusional growth we use variable-bin size, where each droplet category corresponds to a curtain nucleus (NaCl) radius, giving droplet formation size.

Background temperature and humidity vertical profiles in the control experiment are chosen to be the same as measured at day 261 of GATE Brad and Houze (1989). In both sets of experiments the temperature gradient in the lowest 1-km layer is assumed to be close to dry adiabatic. In the second set of experiments the lapse rate within the cloud layer varies around the observed value, while all other parameters remain unchanged.

The results of two sets of experiments are analyzed. In the first set, the humidity in the lowest 1-km layer varies around the observed value, 80%, from 65% to 95%. In the second set, relative humidity in the vicinity of the surface layer is set to 80%, and the in-cloud temperature gradient is modified from +1.5C/km to –4.0C/km to simulate in-cloud instability.

The aerosol size distribution in the vicinity of the surface matches the maritime distribution suggested by (Yin and Levin, 2000), with only the first two modes (MR0). The distribution of CCN chosen provides 300cm^{-3} of droplets at a supersaturation of 1%. In all experiments cloud parcels rise from the surface forced by small temperature anomaly of 0.04C. This anomaly leads to the formation of a vertical velocity of 1.0 m/s at the cloud base in the control run.

In the microphysical part of the model we do not use the assumption of water vapor equilibrium. With that we allow all nuclei to grow as much as they can in the ambient humidity. In this respect, we do not calculate a "critical radius" for droplet generation. In our simulation, the largest CCN that reaches the cloud base is smaller than 4μm.

Within every time step, the amount of water that is exchanged between the ambient air and droplets, regardless if it condensed or evaporated from the droplets, is calculated and is subtracted (or added) from the overall amount of water in the air parcel. To allow precise calculation of diffusion growth of small AP, the time step chosen is as small is as $5.0\cdot10^{-6}$sec. The dynamical time step is $1.0\cdot10^{-3}$sec. At the end of each time step, all the physical properties of the air parcel are calculated and used during the next time frame.

4. RESULTS

Set 1: Effect of humidity in the boundary layer

Figure 1a,b shows profiles of (a) vertical velocity and (b) supersaturation in experiments with different humidities in the boundary layer. An increase in humidity leads to a lowering of the cloud base level, a decrease in the vertical velocity at the cloud base, and a corresponding decrease in the magnitude of supersaturation. Areas where values of superstauration within rising parcels allow for in-cloud nucleation are shaded. One can see that the increase in the boundary layer humidity in the experiment leads to a lowering the height level where in-cloud nucleation starts. In the case of 70% humidity, supersaturation remains less than the maximum at the cloud base indicating no in-cloud nucleation.

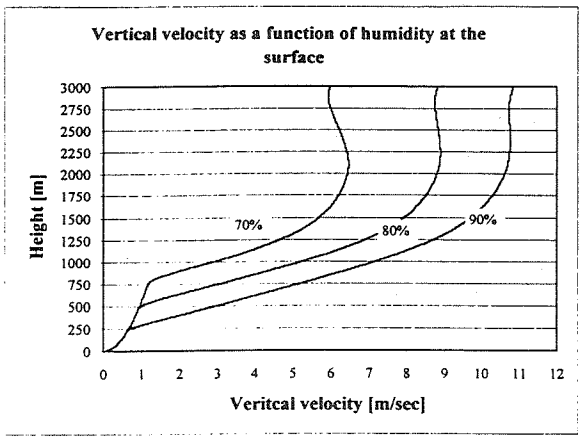

Figure 1a. Vertical velocity formed under different magnitudes of initial air humidity. The higher the humidity value, the lower the cloud base and the lower the vertical velocity at cloud base.

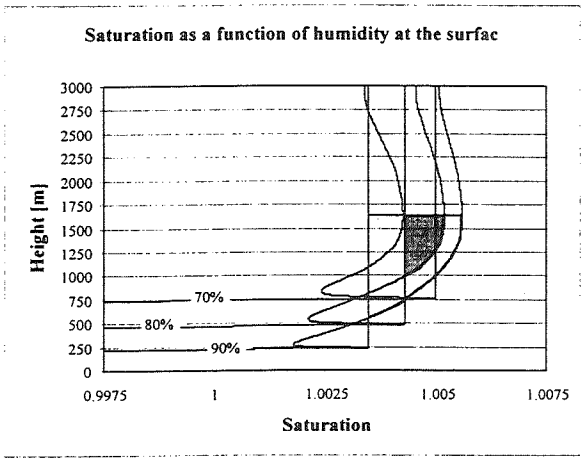

Figure 1b. Vertical profiles of supersaturation under different humidities at the surface. The areas where in cloud nucleation occurs are shaded. In the case of 70% surface humidity, the saturation value does not exceed the peak value at the cloud base and no bimodal droplet distribution forms. In the case of 80% and 90% surface humidity - in-cloud nucleation is efficient.

Figure 2 shows the droplet size spectra formed at 1.5 km above the surface in experiments with 70%, 80% (control run) and 90% relative humidity in the vicinity of the surface layer. The spectra is wide and bimodal in the case of 90% and 80% surface humidity and is narrow and single-modal in the case of 70% surface humidity. While the first two spectra are typical maritime ones, the last spectrum is typical of continental clouds. We see, therefore, that an increase in boundary layer humidity increases droplet spectrum width, thereby accelerating rain formation.

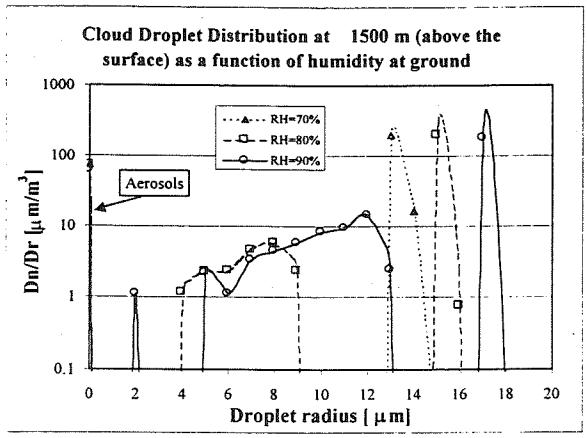

Figure 2. In-cloud droplet spectra for parcels with different humidities at the surface layer. We can see a wide bimodal spectra in the case of the 90% surface humidity, and a mono-modal droplet distribution in the case of the 70% surface humidity.

Set 2. The effect of the cloud layer instability

Figure 3 shows vertical profiles of supersaturation when the lapse rate of temperature changes above the cloud base (500m). One can see that an increase in the cloud layer stability leads to an increase in the height of the level where in-cloud nucleation starts (a bimodal spectrum forms).

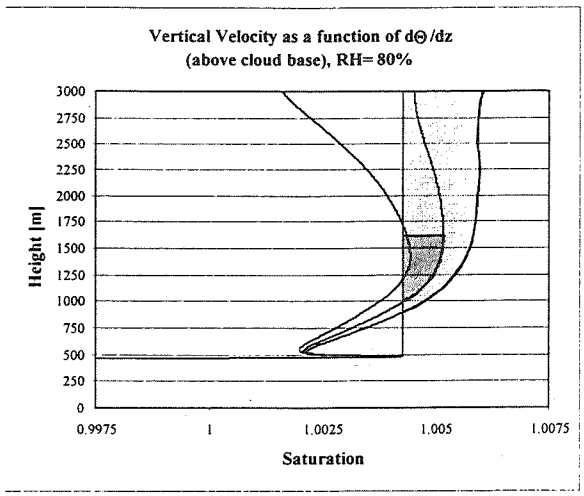

Figure 3. Vertical profile of supersaturation under different temperature gradients within cloud layers. The most stable temperature gradient (left curve) shows that saturation does not exceed the cloud base saturation peak and no bimodal spectra develops. However, in the other cases saturation does exceed the cloud base peak and bimodal spectra forms. In the more unstable case (right curve), in-cloud nucleation continues because the saturation keeps rising with height. In the control case (middle curve), the layer of in-cloud nucleation extends from 1000m to about 1600m.

When the difference in potential temperature gradient exceeds +1.5C/km (with respect to the potential temperature gradient in the control run, which is close to the moist adiabatic lapse rate), no in-cloud nucleation and no bimodal spectrum form. From this, we conclude that: a) the fraction of bimodal spectra in samples should increase with height, b) at a given level above the cloud base, bimodal spectra occurrence should decrease with the stability of the cloud layer.

To evaluate the rate of "bimodality" of droplet size spectra we introduce the parameter "mode concentration ratio". This parameter is equal to the ratio of cloud droplets in the second mode (generated by in cloud nucleation) to the number of droplets in the first mode (generated by the saturation peak at cloud base). In the case where no bimodal spectrum is generated, the ratio is zero.

Figure 4 indicates the "modal concentration ratio" for $d\Theta/dz$ ranging from +1.5C/km to –4C/km (with respect to the control temperature lapse rate) at different heights above cloud base. We can see that as predicted, the modal concentration ratio increases with height, and with an increase in instability. Comparison of Fig 4 with the results of Warner (1969) shows a good qualitative agreement, indicating the validity of the physical mechanism suggested for explanation of the bimodal droplet size spectra.

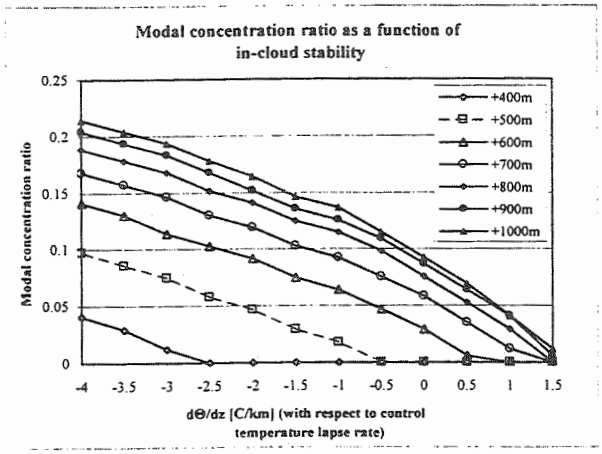

Figure 4. Modal concentration ratio formed for temperature gradients ranging from +1.5C/km to –4C/km in respect to the control temperature lapse rate, as a function of height above cloud base. Vertical velocity at cloud is about 1m/sec .

5. DISCUSSION AND CONCLUSIONS

We show that the width and shape of droplet size spectra crucially depend on thermodynamical conditions determining the vertical velocity at the cloud base and the velocity acceleration above it. Increases in the rate of subcloud and cloud layer instability, as well as a decrease in subcloud layer humidity, favor the formation of narrow monomodal droplet size spectra, typical of continental clouds. An increase in stability and humidity leads to the formation of wide bimodal spectra typical of maritime clouds.

These results have important applications. Since boundary layer instability influences cloud droplet distribution formation, clouds developing at different times of day can have different droplet size spectra and different time evolution of precipitation. This effect should be taken into account when cloud seeding experiments are conducted

Another important application is associated with the fact that majority of measurements of precipitation over the oceans are made over islands, the surface temperatures of which usually exceed the SST. This means that clouds over islands can be "more continental" than those arising over the sea, and their macrostructure possibly differs from that of clouds over the open sea. Thus, the question arises to what extent these measurements are applicable to clouds arising over the open sea.

Thus, the type of clouds and their precipitation potential are determined not only by aerosol particle concentration and size distribution, but also by thermodynamic conditions under which cloud development takes place. Effects of aerosols on precipitation should be considered, therefore, on the background of significant natural fluctuations caused by variations of meteorological conditions.

6. Acknowledgements

This study was supported by the Israel Science Foundation Administration and by the Israel Academy of Sciences and Humanities (grants 572/97, 143/99)

7. References

1. Brad S. F. and Houze R. A. 1989: One-dimensional time-dependent modeling of GATA cumulonimbus convection. *J. Atmos. Sci. 46*, 330-352.
2. Khain and Pinsky, 2000: Droplet spectrum broadening: effect of in-cloud nucleation and droplet collisions. (This issue).
3. Kornfeld P. 1970: Numerical solution for condensation of atmospheric vapor on soluble and insoluble nuclei. *J. Atmos. Sci. 27*, 256-263.
4. Pruppacher and Klett, 1997: *Microphysics of Clouds and Precipitation*. D. Reidel, Publishing Company.
5. Rogers R. R. and Yau M. K. 1989: *A Short Course in Cloud Physics*. Pergamon Press.
6. Warner, J. 1969: The Microstructure of Cloud. Part I. Genera Features of the Droplet Spectrum. *J. Atm. Sci. 26*, 1049-1059.
7. Yin Y. Levin Z. Reisin T. G and Tzivion S. 2000: The effect of giant cloud condensation nuclei on the development of precipitation in convective clouds – A numerical study. *Atmospheric Research*, in press.

A NEW ACCURATE AND EFFICIENT MULTI-SPECTRAL MOMENTS METHOD FOR SOLVING THE KINETIC COLLECTION EQUATION

Shalva Tzivion[1] , Tamir G. Reisin[2] and Zev Levin[1*]

[1] Department of Geophysics and Planetary Sciences, Tel Aviv University, Tel Aviv, Israel
[2]Soreq Nuclear Research Center, Yavne, Israel

1. INTRODUCTION

The numerical method used for solving the Kinetic Collection Equation (KCE) considerably influences the accuracy of numerical simulations (e.g. cloud and precipitation development). In the present work some modifications of the formulation of the Spectral Multi Moment Method (SMMM) (Tzivion et al., 1987, 1999) are presented. This modified method provides accurate results while maintaining a small number of bins, thus making it more efficient. The new method is based on a different formulation of the approximation of the distribution function in the spectral bins and a more accurate relationship between spectral moments in a bin (Tzivion et al., 2000).

The new method is applied to 36 bins and the results are compared with those obtained with the original algorithm for 36, 72 and 108 bins and with the "reference" solution obtained for 144 bins (Tzivion et al., 1999). Three kernels were used, Golovin's (1963) for which an analytical solution exists and the hydrodynamical kernel with two different sets of collection efficiencies.

2. METHOD DESCRIPTION

For the numerical solution of the KCE (for details see Tzivion et al., 1999), the particle spectrum is divided into discrete bins as follows:

$$m_{k+1} = pm_k, \qquad p = \text{const} > 1$$

where k is the bin number and m_k and m_{k+1} are the lower and upper boundaries of the kth bin, respectively. The width of the bin is represented by the parameter p.

From the KCE a set of equations is obtained for the Jth moment of the distribution function $M_k^J(t)$ at bin k, defined as:

$$M_k^J(t) = \int_{m_k}^{m_{k+1}} m^J f_k(m,t)dm \qquad (1)$$

where $f_k(m,t)dm$ is the number of particles with masses between m and $m+dm$ in bin k per unit volume at time t. When J=0,1 and 2 one obtains the physical moments of number concentration – $N_k(t)$, mass concentration – $M_k(t)$ and radar reflectivity – $Z_k(t)$, respectively. Fractional moments can be defined as well, e.g. $J = 1/2$ named here $S_k(t)$.

Following the procedure shown in Tzivion et al. (1987, 1999) a set of coupled integro–differential equations can be obtained with respect to the first two physical moments in each bin – $N_k(t)$ and $M_k(t)$. These equations contain some inner integrals over incomplete bins. In these cases it is necessary to approximate the distribution function, namely, expressions of the type $m^J f_k(m,t)$ for $J = 0, 1$ and 2. The approximation is in the form:

$$m^J f_k(m,t) = \frac{m_k^J}{(p-1)}\Psi_{J,k}(t)\left(p - \frac{m}{m_k}\right) + \frac{m_{k+1}^J}{(p-1)}\Phi_{J,k}(t)\left(\frac{m}{m_k} - 1\right) \qquad (2)$$

With this approximation, the positiviness of $m^J f_k(m,t)$ is guaranteed if $\Psi_{J,k}(t)$ and $\Phi_{J,k}(t)$ are positive. By introducing (2) into (1) one can solve for $\Psi_{J,k}(t)$ and $\Phi_{J,k}(t)$ as a function of two moments. In the original algorithm (Tzivion et al., 1987) the approximations were always based only on the first two moments (namely, $J = 0, 1$) and the functions $\Psi_{J,k}(t)$ and $\Phi_{J,k}(t)$ were the same for any J. In contrast, in the present new algorithm the two moments used in the approximation are not always the same but the selection depends on the moment one wants to evaluate; the subscript J in Ψ and Φ represents the moment that is being approximated. Note that the functions $\Psi_{J,k}(t)$ and $\Phi_{J,k}(t)$ are actually the values of the distribution function at the beginning and at the end of the bin, namely $f_k(m_k,t)$ and $f_k(m_{k+1},t)$, respectively. Following this approach, the approximation of $f_k(m,t)$ is done using the moments $J = 0$ and $1/2$, $mf_k(m,t)$ uses the moments $J = 1/2$ and 1 and $m^2 f_k(m,t)$ the moments $J = 1$ and 2. After replacing Eq. (2) into Eq. (1) expressions for $\Psi_{0,k}, \Psi_{1,k}, \Psi_{2,k}, \Phi_{0,k}, \Phi_{1,k}, \Phi_{2,k}$ can be obtained.

After introducing the approximation of the distribution function $m^J f_k(m,t)$ into the integro–differential equations, moments of higher order appear (2,3 and 4; $Z_k(t)$, $M_k^{(3)}(t)$ and $M_k^{(4)}(t)$, respectively). In Tzivion et al. (1987) these moments were calculated by the first two moments - $N_k(t)$ and $M_k(t)$ using a nondimensional

* *Corresponding author address:* Prof. Zev Levin, Department of Geophysics and Planetary Sciences, Tel Aviv University, Tel Aviv 69978, Israel; e-mail: zev@hail.tau.ac.il

parameter - ξ, that depends only on the bin width p:

$$M_k^J(t) = \xi_p^{J(J-1)/2} \frac{M_k^J(t)}{N_k^{J-1}(t)} \quad (3)$$

provided $m_k \leq \frac{M_k(t)}{N_k(t)} \leq m_{k+1}$.

Tzivion et al. (1987) showed that ξ_p is within the range:

$$1 \leq \xi_p \leq \frac{(p+1)^2}{4p} \quad (4)$$

For practical uses it was suggested to replace ξ_p in (3) by $\bar{\xi}_p$ as given by:

$$\bar{\xi}_p = 0.5[(\xi_p)_{min} + (\xi_p)_{max})]x \quad (5)$$

For $p = 2$ the range of variation of ξ is between 1 and 17/16, namely 6.25%. Therefore, when calculating the higher moments using Eq. (3), ξ introduces an inaccuracy that varies between 6.25% for the second moment ($Z_k(t)$) up to 44% for the fourth moment ($M_k^{(4)}(t)$).

In order to reduce these inaccuracies, higher moments are calculated using a modified expression for the relationship between consecutive moments (Eq. (3)):

$$M_k^J(t) = \xi_{J,p} \left[\frac{M_k(t)}{N_k(t)}\right]^{J-1} M_k(t) \quad (6)$$

here, the nondimensional parameter ξ is also determined by the sought moment. Following a similar approach used to calculate ξ in Tzivion et al. (1987, 1988), expressions for $\bar{\xi}$ for $J = 1/2$, 2, 3, 4 and $p = 2$ can be found. This new formulation significantly reduces the inaccuracies in ξ. For example, for the fourth moment the inaccuracy is now only 5.2%, in comparison to 44% using the former formulation. Fig. 1 shows the variations of ξ as a function of the normalized average mass ($(M_k/N_k)/m_k$) in the bin for different values of J.

Using these expressions for $\bar{\xi}_J$, the set of couple equations can be expressed as a function of the two first moments only ($N_k(t)$ and $M_k(t)$) and the set of equations is thus closed.

3. RESULTS

Numerical simulations of cloud drop growth by collection were conducted for three different kernels: Golovin (1963), for which an analytic solution exists, and the hydrodynamical kernel with collection efficiencies by Long (1974) and Hall (1980). The initial cloud drop mass distribution function was represented by an exponential function with a total number concentration of 300 particles cm^{-3} and a total mass of 1,2 and 3 g m^{-3}. In all the cases the minimum radius - r_1 was 1.5625 μm and the maximum r_{max} was 6400 μm. Simulations with the new algorithm were conducted for $p = 2$ (36 bins). In all the numerical experiments, total mass was perfectly conserved.

Fig. 2 represents the mass distribution function after 20 and 40 min of simulation using Golovin's kernel. The total mass in this case is 1 g m^{-3}. In this case the numerical results are compared with the analytical solution. Results obtained with 144 ($p = 1/4$), 108 ($p = 1/3$), 72 ($p = 1/2$) and 36 bins ($p = 2$) using the original approximation are also shown. Note that the horizontal axis is linear, in order to visually maximize the differences. Since the results for diameters smaller than 0.2 mm were identical they are not displayed. It is clearly seen in the plot that up to 0.65 mm the numerical results obtained with the new algorithm are similar to the analytical solution. For larger diameters the new results are still better than those obtained with 108 bins and very close to those obtained with 144 bins.

Numerical simulations were also conducted for two hydrodynamical kernels for which no analytical solution exists. Figs. 3, 4 and 5 display the mass concentration distributions obtained using Long's kernel for a total mass concentration of 1, 2 and 3 g m^{-3}, respectively.

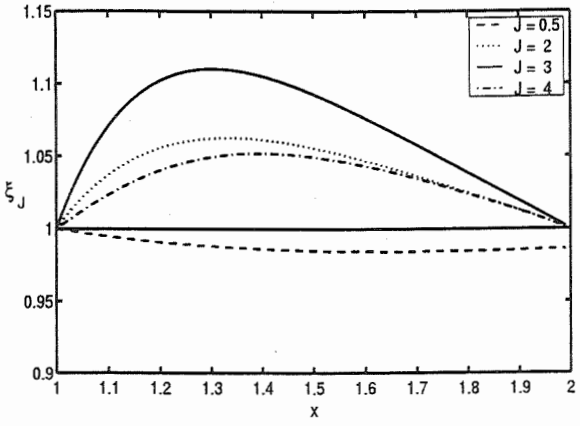

Figure 1: The nondimensional parameter ξ as a function of the normalized average mass (x) in the bin for different values of J.

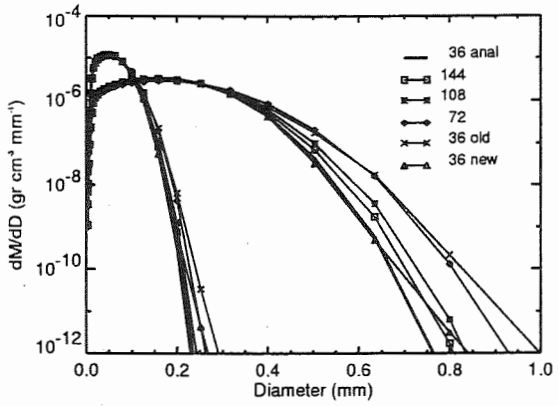

Figure 2: Mass concentration distribution for Golovin's kernel after 20 and 40 min of simulation. The total mass is 1 g m^{-3}.

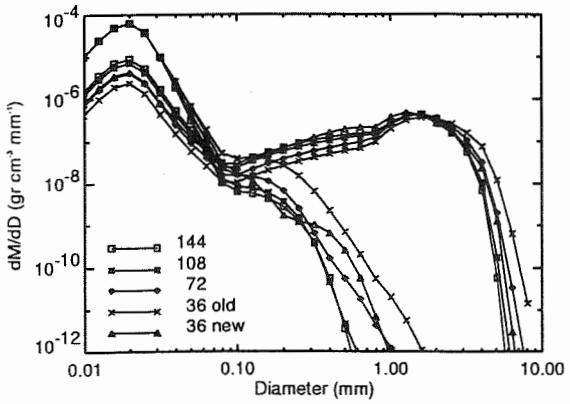

Figure 3: Mass concentration distribution for Long's hydrodynamical kernel after 20 and 40 min of simulation. The total mass is 1 g m^{-3}.

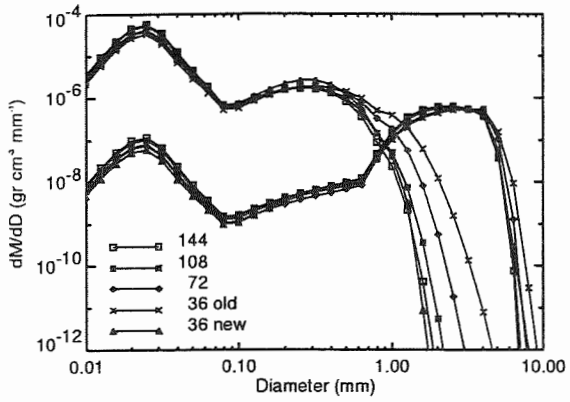

Figure 4: Mass concentration distribution for Long's hydrodynamical kernel after 10 and 20 min of simulation. The total mass is 2 g m^{-3}.

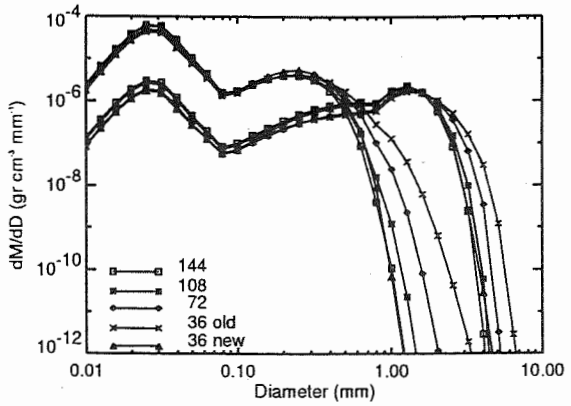

Figure 5: Mass concentration distribution for Long's hydrodynamical kernel after 5 and 8 min of simulation. The total mass is 3 g m^{-3}.

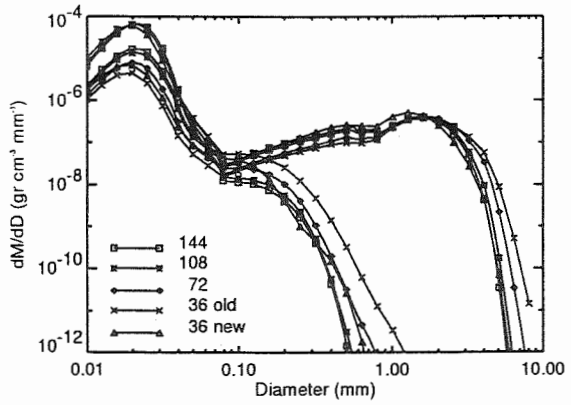

Figure 6: Mass concentration distribution for Hall's hydrodynamical kernel after 20 and 40 min of simulation. The total mass is 1 g m^{-3}.

Results obtained for Hall's kernel are shown in Figs. 6, 7 and 8, respectively. For a total mass of 1 g m^{-3} the results are shown after 20 and 30 min of simulation, for 2 g m^{-3} after 10 and 20 min of simulation and for 3 g m^{-3} after 5 and 8 min of simulation. In all these cases, the results are compared with those obtained with 144 bins, considered as 'reference'. As clearly seen in the plots, for both kernels the numerical results with the new algorithm are significantly closer to the reference than the original one. The results are even better than those obtained with 108 bins.

In order to quantitatively evaluate the accuracy of the results obtained with the different formulations the mass concentration accumulated in 14 bins (containing 99.9 % of the total mass) was evaluated. The 14 bins correspond to those defined by the 36 bins division. The evaluation consisted in calculating the average and standard deviation of the ratios between the mass at one of the 14 bins for one of the formulations and the mass predicted by the "reference" solution. Namely,

$$\frac{1}{14}\sum_{k=k^*}^{k^*+14}\frac{M_k^{(\#)}}{M_k^{(144)}} \qquad (7)$$

where $M_k^{(\#)}$ represent the mass at bin k for one of the formulations (36 bins new, 72 or 108). The evaluation was conducted for the numerical experiment using Long's kernel, a total mass concentration of 2 g m^{-3} and after 20 min of simulation. The results thus calculated show that the new formulation with 36 bins differed from the "reference" solution (144 bins) by 4.5 % with a standard deviation of 3.2 %. The new formulation was even more accurate than the 108 bins model which differed from the "reference" solution by 10.8 % on the average with a

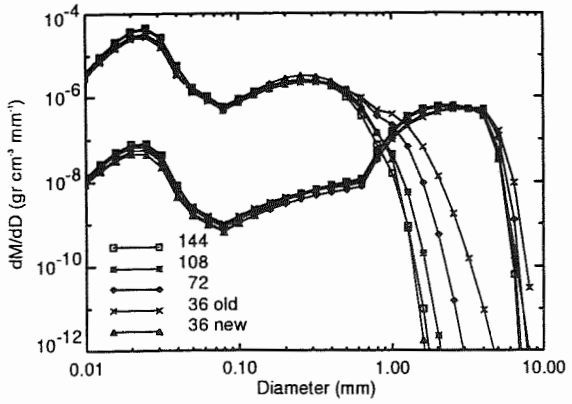

Figure 7: Mass concentration distribution for Hall's hydrodynamical kernel after 10 and 20 min of simulation. The total mass is 2 g m^{-3}.

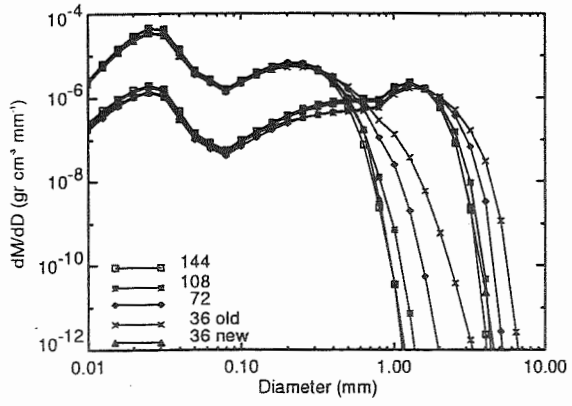

Figure 8: Mass concentration distribution for Hall's hydrodynamical kernel after 5 and 8 min of simulation. The total mass is 3 g m^{-3}.

standard deviation of 8.3 %. According to these results one can claim that the new formulation performs similarly to the 108 bins model but required significantly less computation time, by a factor of 25.When compared to the 72 bins case the new method is much more accurate and requires about five times less computation time.

4. CONCLUSIONS

A new formulation of the approximation of the distribution function used in the Spectral Multi–Moments Method was developed and implemented in the numerical solution of the kinetic collection equation. In the new approximation there is a correspondance between the moment one wants to evaluate and the moments used in the approximation. This new method provides an accurate and efficient numerical solution of the KCE, appropriate for use in dynamical cloud models. The results show a significant improvement in the accuracy of the calculations while maintainig a low number of bins and high computation efficiency, independently of the initial distribution and kernel used. Compared to the original SMMM the computation time in the present method can be reduced by more than one order of magnitude while maintaining similar accuracy

Acknowledgments:

Special thanks are due to Mrs. Zipi Rosen and Mrs. Sara Rehavi for their help with the programming and the testing of the code. Part of this work was conducted under a grant from the German–Israeli Foundation (GIF) under contract I–544–156.08/97.

REFERENCES

Golovin, A. M., 1963: The solution of the coagulation equation for cloud droplets in a rising air current. *Izv. Zkad. Nauk. SSSR Ser. Geofiz.*, **5**, 783–791.

Hall, W.D., 1980: A detailed microphysical model within a two-dimensional dynamic framework: Model description and preliminary results. *J. Atmos. Sci.*, **37**, 2486–2507.

Long, A. B., 1974: Solutions to the droplet coalescence equation for polynomial kernels. *J. Atmos. Sci.*, **11**, 1040–1057.

Tzivion, S., G. Feingold, and Z. Levin,1987: An efficient numerical solution of the stochastic collection equation. *J. Atmos. Sci.*, **44**, 3139–3149.

Tzivion, S., G. Feingold, and Z. Levin, 1989: The evolution of raindrop spectra. Part II: Collisional collection/breakup and evaporation in a rainshaft. *J. Atmos. Sci.*, **46**, 3312-3327.

Tzivion, S., T.G. Reisin, and Z. Levin, 1999: A reference numerical solution of the kinetic collection equation (KCE) for evaluating the accuracy of other numerical methods. *J. of Comput. Phys.*, **148**, 527–544.

Tzivion, S., T.G. Reisin, and Z. Levin, 2000: A new formulation of the method of moments for calculating the Kinetic Collection Equation: more accuracy with less bins. Submitted to the *J. of Comput. Phys.*

MEASUREMENTS OF THE RESPONSE OF HOT-WIRE LWC AND TWC PROBES TO LARGE DROPLET CLOUDS

J. Walter Strapp[1], J. Oldenburg[2], R. Ide[2], Z. Vukovic[1], S. Bacic[1] and L. Lilie[3]

[1] Meteorological Service of Canada, Downsview, Ont. Canada
[2] NASA Glenn Research Center, Cleveland, OH
[3] Science Engineering Assoc., Willington, CT

1. INTRODUCTION

Recent research has focused on the effects of supercooled large droplets on airframe icing, and regulation agencies have discussed the possibility of widening aircraft certification requirements to consider large droplet icing. This had led to increased interest in the characterization large droplets in winter clouds, and a number of field programs have been conducted to establish a database of such events. This in turn has led to renewed interest in the response of aircraft microphysical probes to large droplets.

A three-week wet wind tunnel investigation was conducted at the NASA Glenn Icing Research Tunnel (IRT) in the fall of 1998, to study the response of airborne cloud instrumentation to large droplet conditions. The IRT produces quite repeatable conditions up to a median volume diameter (MVD) of ~50 μm, but has also been calibrated for a number of specific points between nominally 50 and 270 μm. A number of common particle spectrometers and liquid water probes, and several new prototype probes were tested (Table 1). Approximately 50 test points for each instrument (over 900 2.5 minute runs total) were accomplished at 67 and 100 ms^{-1}, ranging from nominally 14-270 μm in MVD, and 0.2-1.4 gm^{-3} in liquid water content (LWC). In this article, we describe the calibration procedures, and will then focus on results of hot-wire testing. Other articles (Wendisch et al. , Twohy et al., both this issue) describe results for the Gerber Scientific PVM-100 and NCAR Counter Flow Virtual Impactor testing.

2. TUNNEL CALIBRATION

The strategy used for instrument calibrations was to calibrate the tunnel once for LWC and MVD using accepted instrumentation, and then rely on the high repeatability of the tunnel to ensure that conditions during instrument runs were adequately similar to those during the calibration. A PMS King probe was mounted during all tests to estimate the tunnel LWC repeatability, and examination of repeats (up to 30 per spray condition) revealed a LWC dispersion (120 second avg.) of the order of 4%. The NASA icing blade reference LWC was also measured during the tests. LWC is deduced from the amount of ice accreted on the blade during a measured period of time. The results of these measurements were approximately the same as earlier blade measurements that had been used to establish the official LWC calibration of the tunnel. The absolute accuracy of the icing cylinder (used by the National Research Council) and the icing blade reference LWC methods has been estimated by Stallabrass(1978), who implied from his error analysis that rotating cylinder and blade LWC estimates should be accurate to within a few percent. Rotating icing cylinder measurements were also made during these tests, and comparisons to the NASA icing blade will be reported elsewhere. NASA estimates that the overall accuracy considering the repeatability of the tunnel is of the order of ± 10% for LWC.

Hot-wires	Particle Spectrometers	Others
PMS King	PMS FSSP (3-45, 5-95 μm)	Gerber PVM-100
Johnson-Williams	PDPA (2-120 μm)	Rosemount ice detector
Nevzorov LWC/TWC	PDPA (80-2000 μm)	SPEC CDS
Prototype Nevzorov LWC/TWC, King-type electronics	PMS 2DC (25-800 μm)	NCAR counter-flow virtual impactor
Prototype Johnson-Williams constant T wire	PMS 2D2C (25-800 μm)	NASA Icing Blade
	PMS 2DC grey (15-960 μm)	NRC Icing Cylinder
	PMS 2DC grey (25-1600 μm)	
	PMS 1D230X (15-450 μm)	
	PMS 1D260X (10-600 μm)	
	PMS 1DP (50-1500 μm)	
	PMS 2DP (200-6400 μm)	
	SPEC CPI (2.3 –2000 μm)	

Table 1: Summary of instrumentation tested at the NASA IRT

The calibration of the tunnel for MVD is more complicated, and non-trivial. NASA has calibrated the tunnel MVD for each condition using PMS FSSP, OAP-230X, and 1D-P probes, and adopts these results as their official calibration. We refer to these values herein as the "standard" tunnel MVDs. During these tests we also ran calibrations with a number of combinations of small droplet (e.g. FSSP, PDPA) and large droplet probes (e.g.

Corresponding Author: J.W. Strapp, Meteorological Service of Canada, 4905 Dufferin St., Downsview, ON, Canada M3H 5T4

PMS OAP probes), and encountered a number of difficult discrepancies leading to values differing significantly from standard values. The droplet concentrations in the tunnel are very high, leading to FSSP activity values often in the 60-90% range. These conditions lead to coincidence-oversizing (Cooper 1988), and the often-observed behaviour of tunnel FSSP LWC values exceeding the fairly accurate tunnel reference values by factors of 2 or more. Although the NASA standard calibration was performed with fewer spray nozzles to create lower concentrations, it is suspected that even these results are not immune to this problem. Furthermore, there were significant differences in the measurement of the large droplet part of the spectrum by the various PMS OAP probes. Four probes were found to measure quite similarly, and three others were found to measure significantly more developed spectra. The MVD of the tunnel was deduced by combining parts of the size spectrum from the various probes to form a composite spectrum. For example, one composite spectrum was formed by combining the FSSP (5-95 μm), the PMS 2D-C (75-600 μm), and the 2DP (>600 μm). A second composite spectrum was formed by substituting the PDPA data for the FSSP data above. The PDPA seemed to have some advantages over the FSSP. First, it is not sensitive to coincidence errors. Second, unlike the FSSP, the PDPA LWC was found to be very linear with tunnel LWC at low MVDs. A scale factor error was interpreted as a correctable sample volume error, and PDPA concentrations were scaled up a factor of 1.6 accordingly. The third composite spectrum was the standard tunnel calibration with the NASA FSSP, OAP-230X, and 1DP probes. Due to the differences observed during intercomparisons of these same probes, it was not surprising to observe a significant change in the MVD depending on which combination of probes was used. A comparison of first and second type composite spectrum MVD to the tunnel standard MVD is given in Figure 1. Note that there is a large difference in MVD, with the NASA nominal MVDs the largest, the FSSP+2DC+2DP the lowest, and the PDPA+2DC+2DP in between. The range of measured MVDs at tunnel standard 20, 70, 120, and 270 μm MVD are 17.1-23.5 μm, , 27-70 μm, 57-120μm, and 127-270 μm respectively, a notably poor comparison. Full composite spectra were derived for all points at 67 ms^{-1}. Pending completion of analysis of the 100 ms^{-1} spectra, we have assumed that the MVD is unchanged with tunnel velocity, and applied 67 ms^{-1} MVDs to points at 100 ms^{-1} with equal nozzle water and air pressure.

Figure 1: Comparison of MVD estimates to tunnel standard

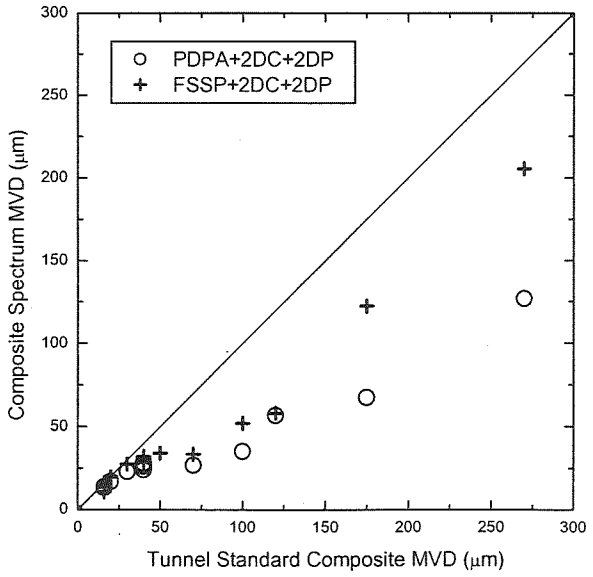

The most accurate MVD remains a topic of discussion among the participants in this study. For the purpose of the articles presented in this conference, we have adopted the MVD values calculated with the PDPA+2DC+2DP probes, on the basis that these composite spectra provide integrated LWCs that are closest to the relatively accurate tunnel reference LWCs, and the large particle part of the spectrum is representative of the majority of OAP probes tested during this experiment. Further measurements with a Fast FSSP are planned in 2000 to cast further light on this problem, although it is expected that MVD will remain a difficult measurement, especially in an environment like an icing tunnel.

3. HOT-WIRE LWC PROBE RESULTS

Table 1 reveals that several standard hot-wire probes were tested in the NASA IRT, as well as two new prototype variations of existing probes. Probably the most commonly used these days on research aircraft is the PMS King probe, a constant-temperature hot-wire probe (King et al. 1978). A standard Johnson-Williams (JW) probe was also tested during these tests, along with a new prototype device using the standard JW sensor head operated with constant-wire-temperature electronics like the King probe. Also tested were a standard Nevzorov LWC and total water content (ice+liquid; TWC) instrument (Korolev et al. 1998), and a new prototype instrument using the standard Nevzorov sensor vane, but modified electronics very similar to the King probe. All results hereafter have been calculated with standard procedures, and cylindrical hot-wires have been corrected for collection efficiencies using data from Finstad et al. (1988). The largest correction is for the Nevzorov TWC, estimated from experimental data of Korolev et al. (1998) as a function of effective diameter. Figure 2 displays the response of the standard Johnson-Williams and Nevzorov LWC and TWC probes to three LWCs at low MVD (11-16 μm measured) and 67 ms^{-1}. The small number of sampled LWCs reflects the lack of time available to complete all runs, due to the need for frequent de-icing of the Nevzorov probe

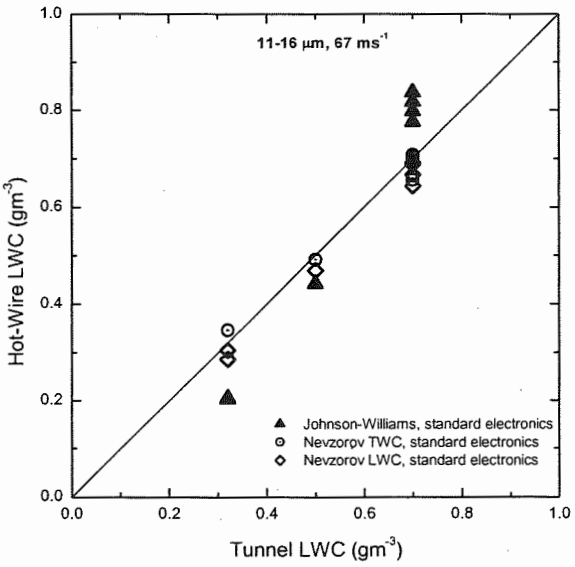

Figure 2: Response of the standard Johnson-Williams and standard Nevzorov LWC/TWC probes at low MVD.

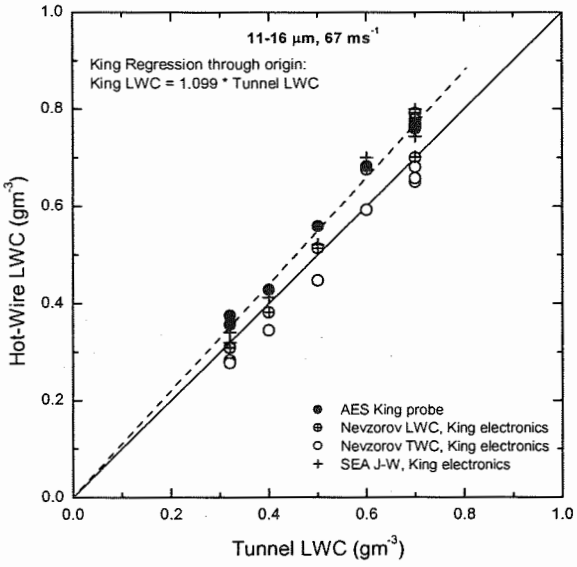

Figure 3: Response of the PMS King, prototype Nevzorov LWC/TWC, and prototype Johnson-Williams probes at low MVD.

vane. This icing caused a small uncertainty in the Nevzorov baseline, but was not a severe problem. Note that the Johnson-Williams probe under-reads at low LWC, and over-reads at the highest LWC point, implying a non-linearity to the response. On the surface, these limited results appear to be poorer than those reported by Strapp and Schemenauer(1982) for the JW, where very linear response was most often observed. The Nevzorov LWC and TWC probes agree within 10% of tunnel LWCs, and are quite linear.

Figure 3 displays the response of the PMS King probe, the prototype Nevzorov LWC and TWC probes using King-type electronics, and the prototype JW probe also using constant wire-temperature electronics, to low MVD sprays at 67 ms^{-1}. .These probes have been grouped together because due to their similar calculations and electronics, they represent the best illustration of differences due primarily to sensor wire geometry. The probes are all linear with respect to tunnel standard LWC, and span a difference of ~+/- 10% of the tunnel standard. This level of error is to be expected due to uncertainties in power gains, sample area, and collision efficiency (especially for the Nevzorov TWC). Figure 4 shows the response of the same 4 probes to a significantly higher MVD (29-32 μm). Note that there is an indication of diminished response of the 3 LWC probes, especially the JW probe. Figure 5 displays the response of the same 4 probes to roughly constant LWC (0.7-1.0 gm^{-3}), but increasing MVD. In order to take into account the small gain differences observed in the probes in Figure 3, each probe response has received a small adjustment to force the LWC at the lowest MVD to equal the fraction of tunnel LWC expected without a collision efficiency correction. Note that the fraction of LWC measured by the 3 LWC probes decreases with increasing MVD. For the PMS King probe, the response drops below 70% by ~50 μm MVD, and is ~45% at 200 μm MVD. These results are similar to those reported by Biter et al. (1987), also plotted in Figure 5 for comparison. The cause of the reduced response is likely incomplete evaporation due to re-entrainment of drops from the wire, as postulated by Biter et al. (1987). The results for the Nevzorov LWC probe are quite similar to those of the King probe, albeit with a somewhat slower rolloff. The similarity is not unexpected, due to the nearly equal length and diameter of the two systems' sensor wires. The JW probe, with the

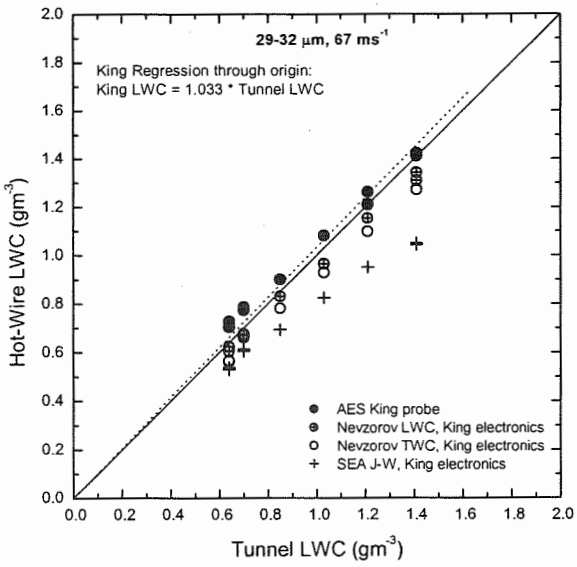

Figure 4: As in Figure 3, but for an intermediate MVD of 29-32 μm

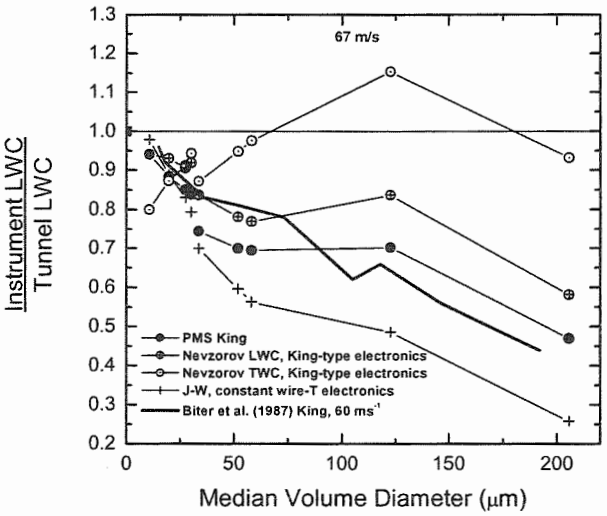

Figure 5: Fraction of tunnel LWC measured by hot wire as a function of MVD. Past data by Biter et al. (1987) for the PMS King probe at 60 ms^{-1} (mass balance tests) are also shown.

smallest diameter wire, has the most rapid rolloff with MVD, dropping to ~70% by ~30 μm MVD, and ~25% by 200 μm MVD. Note that the dropoff is non-linear with MVD, as best illustrated by the JW probe. The results for the Nevzorov TWC are quite different. The TWC probe has a conical sample area facing into the airstream, which one would intuitively expect to trap LWC and resist re-entrainment. Indeed, Figure 5 illustrates that the response of the TWC probe is much more constant. Due to its much large diameter, it tends to under-read at low MVDs, and then is roughly constant above ~60 μm. LWC estimated from the TWC probe agrees within ± 20% of tunnel standard LWC across the entire range of MVDs.

4. SUMMARY AND CONCLUSIONS

A very large data set of LWC comparisons of 23 instruments, over a wide variety of MVDs at 67 and 100 ms^{-1}, has been collected in the NASA IRT. The overall tunnel reference LWC accuracy was estimated to be of the order of ± 10%. MVD was found to be a difficult measurement, requiring the superimposition of spectra from up to three different particle spectrometers. Due to observed fundamental differences in the response of probes that covered similar size ranges, MVD calculated from various combinations of particles spectrometers yielded significantly different values. In fact, based on the differences observed from relatively standard instrumentation, it is clear that a significant bias could exist throughout the community in MVD estimates. The composite spectra adopted for the 3 articles in this conference were based on a combination of probes that provided the best comparison of integrated LWC to tunnel LWC, and used large particles spectra from probes that agreed with the majority of the probes tested. However, more work is required to establish the absolute accuracy of these MVD estimates.

Several hot-wire LWC probes with different wire diameters and sensor shapes were tested to determine the response to large droplet LWC. Most hot-wire probe response was found to roll off with increasing MVD. The PMS King probe and the Nevzorov LWC probes, both with cylindrical sensor wires of ~2 mm diameter, were found to measure ~50% of the LWC at an MVD of 200 μm, very similar to the results reported by Biter et al. (1987) for the King probe. The Johnson-Williams probe, with its 0.6 mm wire diameter, rolled off more rapidly to ~25% response at 200 μm. The Nevzorov TWC probe was found to agree within ± 20% of tunnel reference LWC across the entire tested range of ~11-205 μm MVD. The Nevzorov TWC is therefore considered the most accurate hot-wire estimate of LWC in large droplet conditions in water-only clouds.

5. ACKNOWLEDGEMENTS

This study was supported by the NASA Glenn Research Center Icing Branch, the Meteorological Service of Canada, the FAA Technical Center and Transport Canada. Particle spectrometer calibrations were overseen by the GKSS, Germany. PDPA data were supplied by CIRA, Italy.

6. REFERENCES

Biter, C.J., J.E. Dye, D. Huffman, and W.D. King, 1987: The drop-size response of the CSIRO liquid water probe. *J. Atmos. Oceanic Technol.*, **4**, 359-367.

Cooper, W.A.,1988: Effects of coincidence on measurements with A Forward Scattering Spectrometer Probe. *J. Atmos. Oceanic Technol.*, **5**, 823-832.

Finstad, K.J., E.P. Lozowski, and E.M. Gates, 1988: Computational investigation of water droplet trajectories. *J. Atmos. Oceanic Technol.*, **5**, 150-170.

King, W.D., D.A. Parkin, and R.J. Handsworth, 1978: A Hot Wire Liquid Water Device Having Fully Calculable Response Characteristics. *J. Appl. Meteor.*, **17**, 1809-1813.

Korolev, A.V., J.W. Strapp, G.A. Isaac and A.N. Nevzorov, 1998: The Nevzorov Airborne Hot-wire LWC-TWC Probe: Principle of operation and performance characteristics. *J. Atmos. Oceanic Technol.*, **15**, 6,1495-1510.

Stallabrass, J.R., 1978: An appraisal of the single rotating cylinder method of liquid water content measurement. *Report LTR-LT-92*, 26 pp., National Research Council Canada.

Strapp, J.W., and R.S. Schemenauer, 1982 : Calibrations of Johnson-Williams liquid water content meters in a high speed icing tunnel. *J. Appl. Meteor*, **21**, 98-108.

Twohy, C., J.W. Strapp, and J.R. Oldenburg, 2000: Performance of a Counterflow Virtual Impactor in the NASA Icing Research Tunnel. Preprints, 13th Intl. Commission on Clouds and Precipitation, Reno, Nevada (this issue).

Wendisch, M., T. Garrett, P.V. Hobbs, and J.W. Strapp, 2000: PVM-100A performance tests in the NASA and NRC wind tunnels. Preprints, 13th Intl. Commission on Clouds and Precipitation, Reno, Nevada (this issue).

The Nozzle-Counter — A New Device for Counting CN and CCN in the Atmosphere

R. Jaenicke[1], J. Yang[2] and V. Dreiling[3]

[1]Institut für Physik der Atmosphäre, University of Mainz, D-55099 Mainz, Germany
[2]Department of Atmospheric and Oceanic Sciences, McGill University, Montreal H3A 2K6, Canada
[3]Deutsches Zentrum für Luft- und Raumfahrt e.V., Oberpfaffenhofen, Germany

KEYWORDS: Atmospheric Aerosol, Condensation Nuclei, Cloud Condensation Nuclei, CNC, CCN

1. INTRODUCTION*

Condensation nucleus counters (CNC) today enjoy frequent use because of their wide applications in studying atmospheric aerosols, cloud physics, and environmental air pollution. One principle of a CNC is creating a temperature decrease for producing a supersaturation in an expansion vessel, which causes water vapor heterogeneously to condense on particles. These particles, in spite of variations in the sizes of the original nuclei, then grow into larger water droplets of rather uniform size. Their number can be counted by inspection and photography, or by detection with electronic devices through their scattering of a detectable amount of light.

Since the first CNC constructed by Aitken (1891), numerous CNCs with various designs have been developed. The cooling in CNC, which is necessary for creating supersaturation, has been achieved by mechanical volume expansion (Aitken 1891), pressure expansion (Nolan and Pollak 1946), and later thermal diffusion (Sinclair 1975; Agarwal and Sem 1980). Since only the thermal diffusion method provides a continuous flow, it was adopted in today's commercial CNCs. Organic substances like ethanol, glycol and butanol instead of water must be used in these commercial counters as condensation fluids in aerosol measurements. Water cannot be used in the same way. Water would condense at the inner wall of the instrument. However, doubts arise whether the particles in these organic vapors are activated in the same way as in water vapor, and whether the measured number of the atmospheric nuclei can stand for the "absolute" nuclei number in the natural atmosphere. Furthermore, the sampled air in those thermal cooling saturation tubes is not cooled isentropically and simultaneously in the whole volume, which can result in an uneven saturation distribution in the tubes.

The necessary temperature drop for a continuous flow water CNC can be achieved by nozzle expansion, which opens an alternative for creating a new kind of "Nozzle-CNC".

2. NOZZLE EXPANSION

Air can undergo adiabatic and continuous expansion in nozzles. Homogeneous nucleation can take place in supersonic nozzles with high Mach numbers because of the abrupt temperature decrease. Fukuta et al. (1976) once studied the ice nucleation on pre-existing condensation nuclei (CN) in the Laval nozzle.

From the expansion in the nozzles, airflows are accelerated. The cooling of air molecules in the nozzle is mainly due to the energy conversion from static thermal energy to increased dynamical one, which can be expressed as

$$H=h+0.5\,U^2$$

where U is velocity of airflow and H is the total enthalpy, given in terms of the static enthalpy h. Because of the temperature drop, saturation of water vapor in the air increases although the water vapor density decreases at the same time.

As the surrounding gas is moving with respect to the particles, the mass exchange rate of water vapor between particle surfaces and gas medium is increased because of a "forced" convection. Therefore aerosol particles can have a rapid condensational growth rate in the nozzle by the condensation of water vapor if the flow is water-saturated. Recent studies have shown the rapid growth of particles also in subsonic nozzle flows (Mallina et al., 1997; Yang et al., 1998). This could be a base for designing a CNC operating for continuous measurements.

3. EXPERIMENTS

Figure 1 is the schematic diagram of the new experimental CNC with the nozzle to create a temperature decrease. Aerosol firstly passes through a regulator by which its flow rate will be controlled and measured. This sample aerosol flow is mixed and diluted with clean air. The clean air is provided from the filtration of ambient air by a filter. In order to get water saturated air, the ambient air is slightly heated

* Corresponding author's: R. Jaenicke, Institut für Physik der Atmosphäre, University of Mainz, D-55099 Mainz, Germany; E-mail: jaenicke@mail.uni-mainz.de

and humidified in a water pool with a fixed temperatures of 40 centigrade. The water surface is large enough so that the air has ample of time becoming saturated. The aerosol and the clean saturated air mix with each other at the entry of the nozzle. There the temperature and pressure can be measured and the saturation can be calculated. The capillary condensation nozzle has an internal diameter of 1.0 mm with a length of 12 cm to 30 cm depending on the flow rate. The aerosol flow was carefully measured by "bubble flowmeter" that can precisely measure flow rates of 1 cm^3/min, and was "diluted" with water saturated clean air before entering into the nozzle.

The adiabatic expansion causes the initiation of the condensation of water vapor on aerosol particles that are larger than the critical size $\dot{r}$. By adjusting the total flow rate as well as the dilution ratio of aerosol in this total flow, the anticipated super-saturation for condensation nuclei (CN) and cloud condensation nuclei (CCN) in the nozzle could be obtained. The grown particles with radius larger than 0.35 μm are counted by laser-pulse counting. An electrical signal processor and a counting recorder are connected to this detecting device for recording the output signals in this experiment. Pressure, temperature and flow rate are also measured at the end of the nozzle.

The optical detecting system processes the mode of single particle counting, by which the optical system produces one signal when a particle passes through the sensing volume. So the number of signals per second reflects the number of particles in the volume of aerosol sample through the nozzle per second. If more than one particle passes through the sensing volume at the same time, the coincidence effect should be considered (Jaenicke 1972).

Experimental data were recorded after 30 min running of the instruments. It ensures that the flow field in the nozzle can reach the state of heat balance, that is the balance of heat conduction between the nozzle wall and the flow inside, so that the flow field, especially the saturation in the nozzle keeps stable.

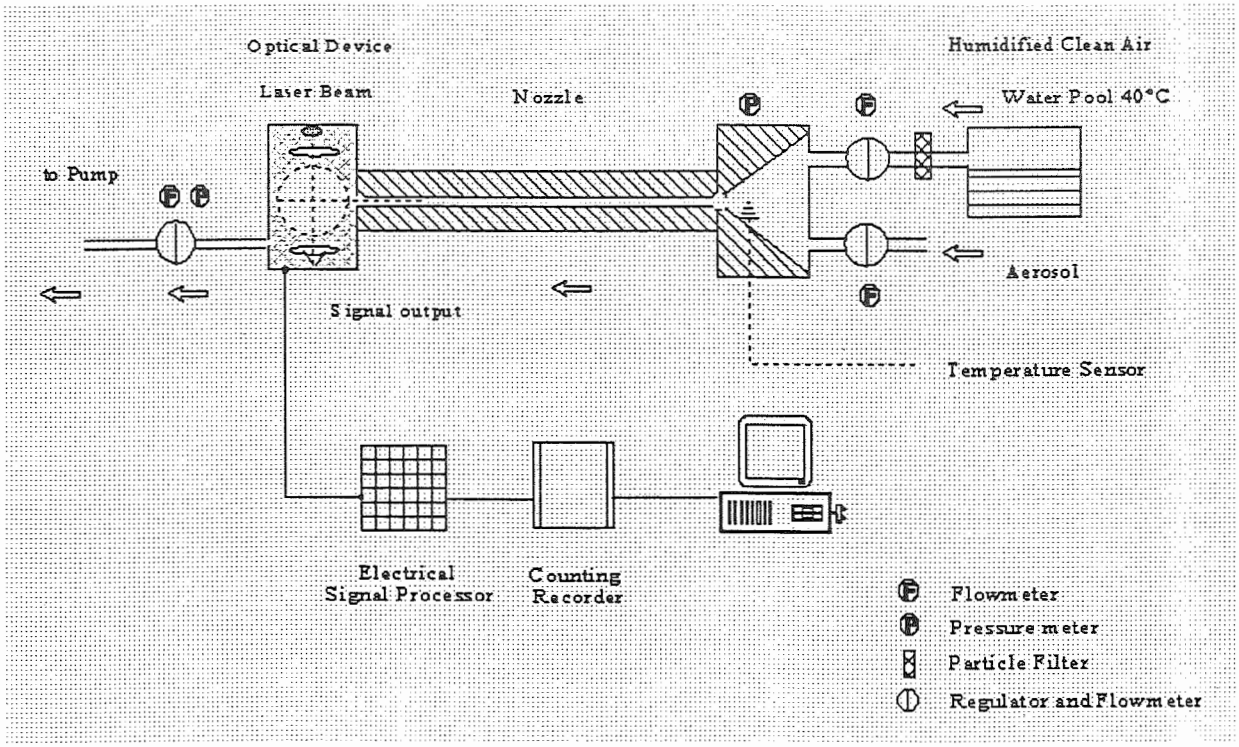

Fig. 1 Schematic diagram of the Nozzle-CNC

4. RESULTS AND ANALYSES

Various saturations in the nozzle can be obtained by adjusting the total flow rate as well as the mixing ratio of the aerosol flow diluted with clean air. Because of the decrease of density of water vapor in the nozzle, the final saturation reached in the nozzle can't be very large, with values usually smaller than 2.0. This value of saturation is however significant for CN and cloud condensation nuclei (CCN).

Fig. 2 shows the change of measured nuclei concentration with the saturation by this Nozzle-CNC in a measuring example. Calibrations against counting errors of the instrument including the coincidence and the influence of flow rate were con-

sidered. The result indicates that there exists an exponential relation between the measured nucleus number concentration N and saturation S in the nozzle:

$$N = CS^{\alpha}$$

where α and C are constants. This relation is similar to the one given by Twomey (1963, 1969) and Pruppacher (1997).

The variation of the saturation in the nozzle gives a possibility of extending the counting region, from measuring hygroscopic nuclei (HN) with S smaller than 1.0, to CCN and to CN. The minimum detectable size of this Nozzle-CNC is estimated to be 0.04 μm.

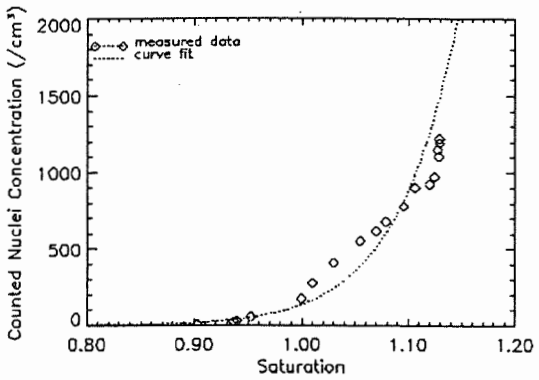

Fig. 2 Measured condensation nuclei number concentration vs the saturation in the nozzle

Although the inner size of the nozzle is rather small, the diffusion loss of particles is found to be within only 2% because of the short residence time of the particles in the nozzle.

5. CONCLUSIONS

An idea of constructing a new Nozzle-Counter was put forward by using a nozzle to produce cooling. The nozzle cooling has several benefits as the cooling is adiabatic and simultaneous. The saturation produced is very suitable for atmospheric CN and CCN counting. Because of the adjustability of the saturation, this nozzle CNC extends the measuring range for the nuclei in the atmosphere, which is helpful understanding basic behaviors of these nuclei in the formation of cloud droplets and their indirect climate effects.

In comparison with other CNCs, this Nozzle-CNC has several obvious advantages such as no condensation delay, as particles larger than the critical size grow simultaneously, low diffusion losses of particles, little water condensation at the inner wall of the instrument, as the temperature in the nozzle flow is lower than that at the wall, and adjustable saturation - therefore the wide counting region, as well as no calibration compared to non-water condensation substances.

REFERENCES

Agarwal, J. K., and Sem, G. J. (1980) Continuous flow single-particle-counting condensation nucleus counter. *J. Aerosol Sci.* **11**, 343.

Aitken, J. (1891) On a simple pocket dust counter. *Proc. Roy. Soc.* **18**, London.

Fukuta, N. and Paik, Y. (1976) A supersonic expansion method of ice nuclei generation for weather modification. *J. Appl. Meteor.* **15**, 996-1003.

Jaenicke, R. (1972) The optical particle counter: cross-sensitivity and coincidence. *J. Aerosol Sci.* **3**, 95-111.

Mallina, R. V., Wexler, A. S. and Johnston, M. V. (1997) Particle growth in high-speed particle beam inlets. *J. Aerosol Sci.* **28**, 2, 223-238.

Nolan, P. J., and Pollak, L. W. (1946) The calibration of a photoelectric nucleus counter. *Proc. Royal Irish Acad.* 51A, 9-31.

Pruppacher, H. R. and Klett, J. D. (1997) *Microphysics of Clouds and Precipitation*. Second Revised and Enlarged Edition, pp. 167-190. Kluwer Academic Publishers.

Sinclair, D., and Hoopes, G. S. (1975) A continuous flow condensation nucleus counter. *J. Aerosol Sci.* **6**, 1-7.

Twomey, S. (1963) Measurements of natural cloud nuclei. *J. Rech. Atmos.* **1**, 101-104.

Twomey, S. and Wojciechowski, T. (1969) Observations of the geographical variation of cloud nuclei. *J. Atmos. Sci.* **26**, 684-688.

Yang, J. L., Jaenicke, R., Dreiling, V., and Peter, Th. (1998) Rapid condensational growth of aerosol particle in air stream — numerical simulation. *J. Aerosol Sci.* **30**, S793-794.

CONCEPT AND DESIGN OF A NEW AIRSHIP-BORNE CLOUD TURBULENCE MEASUREMENT SYSTEM

H. Siebert and U. Teichmann

Institute for Tropospheric Research, Permoserstraße 15, 04318 Leipzig, Germany

1 INTRODUCTION

Cloud-top entrainment is an important process influencing cloud microphysical properties and hence their radiative properties. Turbulent mixing of cloud-free air into the cloud is supposed to take place on very small scales which requires accurate measurements of dynamical, thermodynamical and cloud microphysical properties.
The intention of this work is the design and concept of a ballon-borne platform which can fill the gap between tower and aircraft measurements to heights of up to 2000 m.

2 PLATFORM DESIGN

The platform is designed for turbulence measurements (3D-wind vector, humidity and temperature) as well as liquid water content (LWC) and particle number concentrations inside, above and below stratiform clouds. The complete system is about 3.50 m long and the payload is about 110 kg all inclusive.

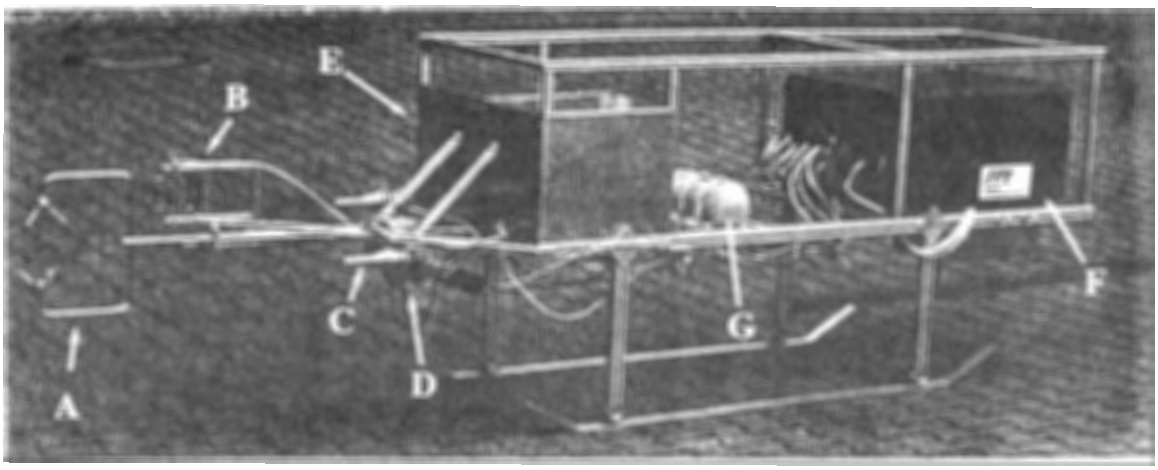

Figure 1: Airship-borne Cloud Turbulence Measurement System (see text for details)

2.1 TURBULENT WIND MEASUREMENTS

The 3D-wind vector is measured with an ultrasonic anemometer/thermometer ("sonic") with a sampling frequency of 100 Hz. Feasibility of turbulent wind measurements within clouds using sonics has been demonstrated by Siebert and Teichmann (2000). The sensor head is placed in the front of the system (cf. Fig. 1-A) to keep the influence (flow distortions) of the boxes (cf. Fig.1-E) negligible. Fig. 2 shows power spectra of each velocity component measured in a closed laboratory room under very calm wind conditions. The

Corresponding author's address: Holger Siebert,
Institute for Tropospheric Research, Germany
Permoser Straße 15, 04318 Leipzig
siebert@tropos.de

spectral noise floor of the system can be estimated from Fig. 2 to $S_u^{(n)} \approx 10^{-5}\,m^2\,s^{-2}\,Hz^{-1}$. This corresponds to a standard deviation due to uncorrelated noise of $\sigma^{(n)} = (S_u^{(n)}\, f_{Ny})^{1/2} \approx 20\,mm\,s^{-1}$ for each velocity component. With a criterium suggested by Muschinski et al. (2000) this leeds to a resolveable energy dissipation rate of $\epsilon \approx 10^{-5}$ to $10^{-4} m^2\,s^{-3}$ which is the lower limit for stratiform clouds (e.g. Pruppacher and Klett (1997)).

A built-in inclinometer gives the roll and pitch angles of the system with a time resolution of 0.1 s which allows corrections for the influence of the platform motion.

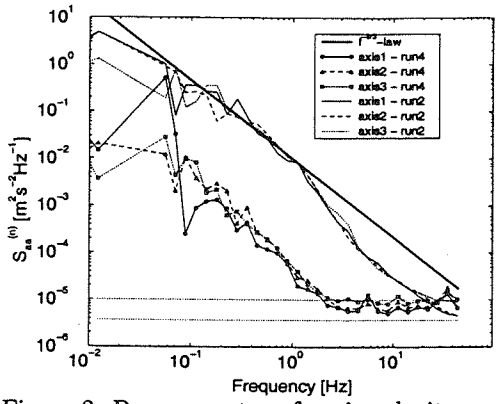

Figure 2: Power spectra of sonic velocity components measured in a closed laboratory .

2.2 FAST IN-CLOUD TEMPERATURE MEASUREMENTS

Fast temperature fluctuations are resolved with a newly designed "Ultrafast Thermometer" (UFT-B). This sensor is based on a 2.5 μm thin platin-coated tungsten wire of 5 mm length (cf. Fig 1-B) and is also situated near the front of the system. Short bursts of compressed dry air (cf. bottle Fig. 1-G) protect the wire from cloud drop impaction (Haman et al. (2000)). The short time constant of about 10^{-4} s allows the sensor to recover very fast from these bursts. Two intermittently working sensors ensure continuous measurements.

An additional highly precise Pt-100 (ROSEMOUNT) with a time constant of about 1 s serves as calibration standard (cf. Fig. 1-C).

2.3 TWC, LWC, AND AEROSOL MEASUREMENTS

A heated inlet will evaporate all cloud drops before entering a group of microphysical sensors. The inlet consist of 1m stainless steel tube with an inner diameter of 4 mm and a tube wall heated to about 120° C. The air is sucked through this tube with about 4 $m\,s^{-1}$. Therefore the velocity translates to a resistance time of 0.25 s which is enough to heat the air homogeneously after about 40 cm and evaporate all drops.

The first sensor behind the heated inlet consists of a Lyman-α hygrometer with a sampling frequency of 100 Hz for measuring the total amount of water vapour content (TWC) in the system. For calibration of the Lyman-α a capacitive humidity sensor (HUMICAP by VAISALA) is integrated. The last stage is a CPC for measuring the particle number concentration in the range of 10 to 800 nm.
A Particulated Volume Monitor (PVM) (cf. Fig.1-D) measures the LWC in the clouds with time resolution of 0.01 s. From these data the water vapour density can be estimated as the difference of the LWC and the TWC (measured with the Lyman-α). All three sensors are protected in a box in the front of the platform (cf. Fig. 1-E).

2.4 DATA ACQUISITION SYSTEM AND POWER SUPPLY

All data are sampled with a real-time data acquisation system and transmitted via telemetry link to a ground station which allows monitoring during the experiment. The complete system is powered by a 200 W battery-pack. Power management, data acquisition and telemetry transmitter are located together in a water and electromagnetically protected box (cf. Fig. 1-F). The height above ground is derived from a barometer (VAISALA) with a resolution of 1 Pa and an absolute accuracy of about 10 Pa. This leeds to a height resolution of $\approx$ 10 cm.

3 OUTLOOK

First test and calibration flights are carried out at a coastal site in Northern Germany in April 2000 using a tethered-balloon system of the German army. After successful tests a GPS and INS-based navigation system will be included to allow wind measurements also under moving airships/blimps.

4 ACKNOWLEDGEMENTS

We thank the members of the electronical and mechanical workshop of our institute for their essential assistance designing the platform and sensor equipment. We are also grateful to the Bundeswehr for the cooperation with their tethered-balloon system.

5 REFERENCES

Haman, K., S. Malinowski, B. Stru, R. Busen, A. Stefko, and H. Siebert: 2000, 'A family of ultrafast aircraft thermometers for warm and supercooled clouds and various types of aircraft'. In: *13 th International Conference on Clouds and Precipitation.* Reno, USA.

Muschinski, A., R. Frehlich, M. Jensen, R. Hugo, A. Hoff, F. Eaton, and B. Balsley: 2000, 'Fine-scale measurements of turbulence in the lower troposphere: An intercomparison between a kite- and balloon-borne and a helicopter-borne measurement system'. submitted to *Boundary-Layer Meteorol.*

Pruppacher, H. and J. Klett: 1997, *Microphysics of clouds and precipitation.* Kluwer Academic Publishers.

Siebert, H. and U. Teichmann: 2000, 'The behaviour of an ultrasonic under cloudy conditions'. *Boundary-Layer Meteorol.* **94**, 165–169.

ANALYSIS OF THE FSSP PERFORMANCE FOR MEASUREMENT OF SMALL CRYSTAL SPECTRA IN CIRRUS

W. Patrick Arnott*, David Mitchell, Carl Schmitt, David Kingsmill, and Dorothea Ivanova
Desert Research Institute, Division of Atmospheric Sciences, Reno NV 89512

Michael R. Poellot
Dept . of Atmospheric Sciences, Univ. North Dakota, Grand Forks, ND

[1]1. INTRODUCTION

Heymsfield and Platt report close match of 1-DC spectra with fssp data in the overlapping size bins (Heymsfield et al., '84). Gardiner and Hallet report that the fssp strongly overcounts crystal concentration in clouds with high concentrations of large ice crystals along with small crystals (Gardiner et al., '85). Twohy shows good agreement of ice mass content in wave cloud between the CVI and fssp probes (Twohy et al., '97). Gayet shows cases of both good and poor overlap of fssp and 2DC size spectra, depending on the concentration of large ice crystals in the 2DC data. Gayet suggests acceptance of fssp data as valid when overlap with 2DC data is adequate. Impactor data (Arnott et al., '94), (Miloschevich et al., '97) (replicator, cloudscope, vips, etc) can in principle provide size spectra, though collection efficiency and overlap issues combined with the labor intensive nature of data reduction make this approach less attractive. However, there is a need for characterization of the small crystal content (D < 50 μm) for lidar-radiometer applications (Platt et al., '98), cloud mass content, and cloud radiative properties estimation (Fu et al., '93). The CPI probe is now becoming a common instrument for cirrus crystal imagery and quantification (Lawson et al., '98) and may turn out to be a good instrument for the job. However, the issue of small crystal content in cirrus is still unsettled in our opinion.

Small ice crystal concentrations in cirrus are difficult to measure due to particle non- sphericity, size, and to the dynamic range that must be spanned, both in time and in particle dimension. Their contributions to the cirrus ice mass, radiative properties, and cloud life cycle and regeneration downstream can be assessed through accurate in-situ measurements. These contributions vary widely with latitude, season, altitude, and cloud generation mechanism. The forward scattering spectrometer probe (fssp) provides a possible solution to the measurement dilemma, and analysis of this potential continues in our laboratory and in others throughout the world. Our approach is multi-fold and includes the following elements. First, supposing that only small particles are present, what influence does particle non-sphericity have on obtained size spectra? This issue is most critical in young contrail cirrus, for example. Second, supposing that the fssp spectra overlaps adequately with other probe data such as the PMS 2DC electrooptical probe, or the DRI cloudscope, is this a sufficient condition to trust the fssp data in the non-overlapping size bins? Third, when the fssp spectra does not overlap adequately with other probe data, how can we quantify the reasons for the poor overlap, and which probe(s) do you trust? We present progress on our approaches to these issues, and will include laboratory measurements along with field data from Department of Energy Atmospheric Radiation Measurement Program and the Tropical Rainfall Measuring Mission (TRMM), a joint mission between the NASA and the National Space Development Agency (NASDA) of Japan.

[2]2. LABORATORY MEASUREMENTS

The lab component was a setup similar to that used in our previous efforts (Arnott et al., '95: (Schmitt et al., '99). The growth chamber and cloud chambers were both cooled to -20°C. Later, the temperature of the growth chamber was adjusted to grow different habits of ice crystals (columns and plates). An ultrasonic nebulizer was positioned to deliver water drops into the top of the growth chamber. A cloud seeder was placed two meters from the top of the growth chamber. The seeder consisted of a looped spring that was passed through liquid nitrogen, then into the chamber. The cloud chamber was a 1m x 1m x 1.2m interior diameter freezer. A laboratory cloudscope was used to sample the ice crystals. A microscope objective and a compact video camera were used to image crystals. The collection surface was an optical bar of saphirre heated at the sides with a nichrome wire to sublimate ice crystals. The collection surface of the new cloudscope is 1 mm wide, and the incoming air velocity is 3 m/s. An aspirated fssp was colocated with the cloudscope to provide water drop equivalent sizing of the ice crystals. It should be noted that the lab arrangement produced only small ice crystals – no influence from larger crystals.

[1]* *Corresponding author address:* W. Patrick Arnott, Desert Research Institute, 2215 Raggio Parkway, Reno, NV 89512; email: pat@dri.edu.

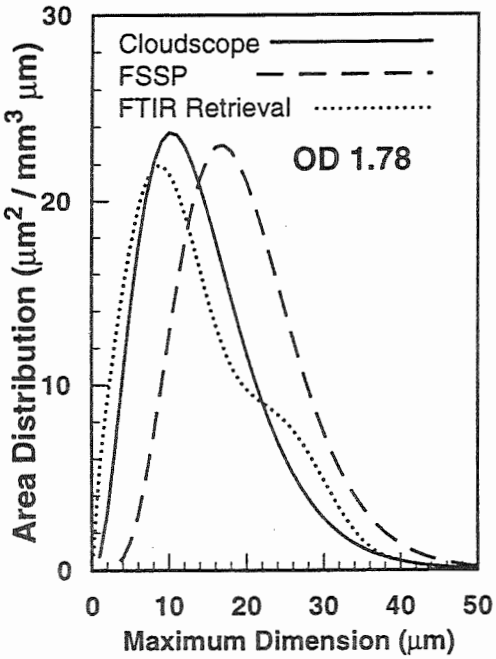

Figure 1. Smoothed area distributions obtained from the indicated probes. The optical depth at 685 nm was 1.78.

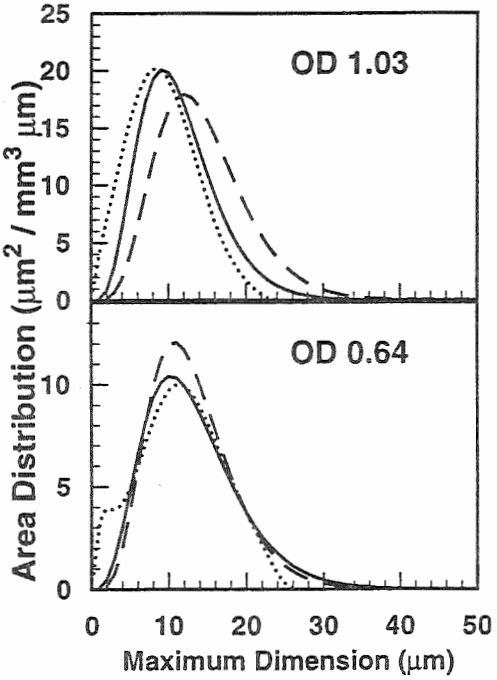

Figure 2. Same as figure 1, though for lower optical depths.

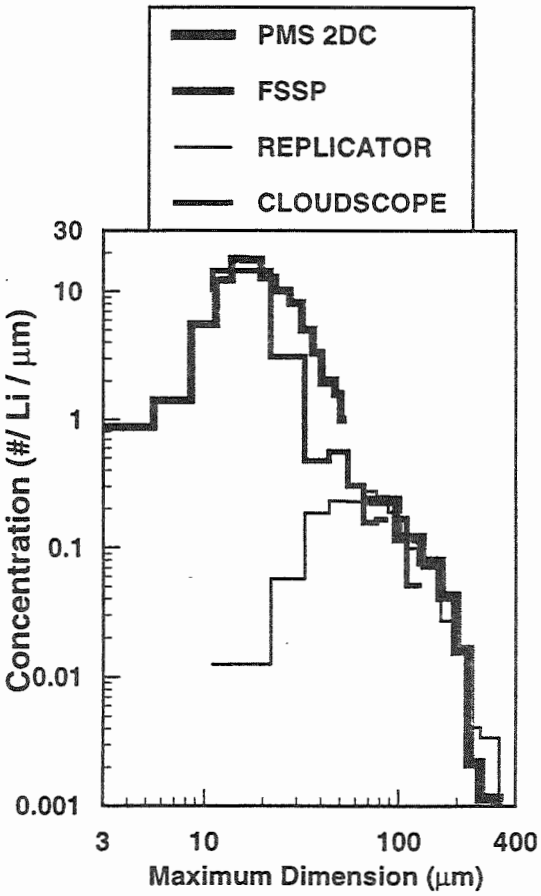

Figure 3. Size spectra from 26 September 97, DOE ARM IOP, Hurricane Nora Outflow, 19:09:15 - 19:11:00 UTC, -48.3 C to -50.3 C, 11.95 km to 12.18 km, T.A.S. = 118.5 m/s.

Figures 1 and 2 display the smoothed area distributions obtained from the cloudscope, fssp, and from retrieival of FTIR spectral extinction measurements (Arnott et al., '96) using the modified Mie method for computing synthetic IR spectra for ice crystals (Schmitt et al., '99). Area distributions were compared because this is the primary influence on cloud radiation, and because the FTIR retrieval is rather insensitive to the contributions of particles smaller than a few microns. The results indicated that the three methods agreed well when the laboratory cloud's visible optical depth was below a rough cut-off value of 1.25. This optical depth value corresponded to particle concentrations of greater than 2000 particles per cc. Measurements were performed with particle concentrations as low as 400/cc with good agreement between the cloudscope and FSSP. There is a trend for the fssp to slightly oversize particles (afterall, it is calibrated for water refractive index and spheres).

3. CIRRUS OBSERVATIONS AT THE SGP

An intensive operational period at the DOE Southern Great Plains (SGP) site yielded an interesting cirrus display associated with remnants of hurricane Nora (http://www.dri.edu/Projects/replica/DOE.ARM/doearm97iop/09_26_97case/09_26_97case.html). The data displayed in Figure 3 was obtained from this case study.

Figure 3 shows fssp, cloudscope, replicator, and PMS 2dc ice crystal size spectra. Below 250 μm, the main crystal habits were plates (70%) and columns; above this, the main habit was polycrystalline plate entities. The cloudscope data was analyzed using the entire-in method. More details can be obtained at http://www.dri.edu/Projects/replica/cloudscope/. A number of observations can be made about Fig. 3. First, the cloudscope and fssp spectra are in reasonable agreement, though the fssp suggests larger numbers of particles near 50 μm than the cloudscope. The cloudscope spectra merges smoothly with the 2DC and replicator spectra for sizes beyond 50 μm. The replicator spectra exhibits a roll-off for particle dimensions below 50 μm, as a likely consequence of collection efficiency problems. This cloud was thin enough that cloudscope data did not suffer appreciably from crystal overlap.

The Nora cirrus presented here does not have significant concentrations of large ice crystals (D > 500 μm), in contrast to much of the data from the TRMM project. The preliminary analysis of TRMM data indicates decent overlap of fssp and 2DC spectra when the concentration of large crystals is low enough. This assessment is in accord with the Gayet analysis.

The roll-off of replicator spectra in Fig. 3 is somewhat in contrast to the results discussed in (Arnott et al., '94). The earlier spectra was analyzed using a motion picture projector, while those in Fig. 3 were obtained from high resolution video microscopy and digital image analysis (Turner, '96). The smallest size bin in the older work was 25 μm. It is conceivable that the instrument was operated differently during the acquisition of the data, especially concerning the flow of dry air out the sample inlet that is used to dry the formvar. However, collection efficiency calculations are suggestive of a roll-off similar to that observed. Finally, the conclusions of the earlier paper are likely valid, given that we often see spectra like that of Fig. 3 in cirrus. The cloudscope data provides useful qualitative imagery in rarefied cirrus (cirrus with mostly small crystals); it can confirm the presence of small crystals.

Acknowledgements. DOE-ARM support is acknowledged for the laboratory and field work at the SGP, and NASA provided support for the TRMM work and development of the cloudscope data analysis algorithm.

4. REFERENCES

Arnott, W. P., Y. Y. Dong, and J. Hallett, 1995: Extinction efficiency in the infrared (2-18μm) of laboratory ice clouds: observations of scattering minima in the Christiansen bands of ice. *Appl. Opt.*, **34**, 541-551.

Arnott, W. P., Y. Dong, J. Hallett, and M. R. Poellot, 1994: Role of small ice crystals in radiative properties of cirrus: A case study, FIRE II, November 22, 1991. *J. Geophys. Res.*, **99**, 1371-1381.

Arnott, W. P., C. Schmitt, Y. Liu, and J. Hallett, 1996: Droplet size spectra and water vapor concentration of laboratory water clouds: Inversion of FTIR (500-5000 cm^{-1}) optical depth measurement.

Fu, Q. and K. N. Liou, 1993: Parameterization of the radiative properties of cirrus clouds. *J. Atmos. Sci.*, **50**, 2008-2025.

Gardiner, B. A. and J. Hallett, 1985: Degradation of in-cloud forward scattering spectrometer probe measurements n the presence of ice particles. *J. Atmos. Ocean. Tech.*, **2**, 171-180.

Heymsfield, A. J. and C. M. R. Platt, 1984: A parameterization of the particle size spectrum of ice clouds in terms of the ambient temperature and ice water content. *J. Atmos. Sci.*, **41**, 846-855.

Lawson, R. P., A. J. Heymsfield, S. M. Aulenbach, and T. L. Jensen, 1998: Shapes, sizes, and light scattering properties of ice crystals in cirrus and a persistent contrail during SUCCESS. *Geophys. Res. Lett.*, **25**, 1331-1334.

Miloschevich, L. M. and A. J. Heymsfield, 1997: A balloon-borne continuous cloud particle replicator for measuring vertical profiles of cloud microphysical properties: Instrument design, performance, and collection efficiency analsis. *J. Atmos. Ocean. Tech.*, **14**, 753-768.

Platt, C. M. R., S. A. Young, P. J. Manson, G. R. Patterson, S. C. Marsden, R. T. Austin, and J. H. Churnside, 1998: The Optical Properties of Equatorial Cirrus from Observations in the ARM Pilot Radiation Observation Experiment. *J. Atmos. Sci.*, **55**, 1977-1996.

Schmitt, C. G. and W. P. Arnott, 1999: Infrared emission (500 - 2000 1/cm) of laboratory ice clouds. *Journal of Quantitative Spectroscopy and Radiative Transfer*, **63**, 701-725.

Turner, M., 1996: Digital image analysis of replicator ice crystal data for detection of small particles in cirrus clouds, Atmospheric Sciences, University of Nevada, 114.

Twohy, C. H., A. J. Schanot, and W. A. Cooper, 1997: Measurement of Condensed Water Content in Liquid and Ice Clouds Using an Airborne Counterflow Virtual Impactor. *J. Atmos. Ocean. Tech.*, **14**, 197-202.

PVM-100A performance tests in the NASA and NRC wind tunnels

M. Wendisch[1], T. Garrett[2], P. V. Hobbs[2], and J. W. Strapp[3]

[1]Institute for Tropospheric Research, Leipzig, 04318, Germany
[2]Department of Atmospheric Sciences, University of Washington, Seattle, Washington, 98195-1640, USA
[3]Meteorological Service of Canada, Toronto, Ontario, M3H 5T4, Canada

1. INTRODUCTION

The PVM (Particle Volume Monitor, manufactured by Gerber Scientific, Inc., Reston, Virginia, USA) is widely used to measure cloud *LWC* (Liquid Water Content) and cloud droplet effective radius. Cloudy air within the PVM sample volume is illuminated by a laser diode. Light forward-scattered by the droplets passes through spatial filters to produce a signal proportional to *LWC* and cloud droplet effective radius (Gerber 1991, Gerber et al. 1994). The performance of the airborne version of this instrument (PVM-100A) with regard to *LWC* measurements for varying values of *LWC* and *MVD* (Median Volume Diameter) was tested in two independent experiments conducted in the NASA (Cleveland, Ohio, USA) and NRC (Canadian National Research, Ottawa, Canada) wind tunnels. Both tunnels use accepted standard techniques (icing blade in the NASA tunnel and rotating icing cylinder in the NRC tunnel) for their *LWC* calibration. Furthermore, the tunnels provide liquid (in some cases frozen) sprays with repeatable *MVD*. The experiments included testing of other *LWC* probes (mainly hot wire instruments) and several state-of-the-art droplet size-resolving instruments. Other results for the NASA tests are reported by Strapp et al. (this issue) and Twohy and Strapp (this issue). PVM-100A *LWC* measurements obtained in both experiments are compared in order to obtain a consistent picture of the sensitivity of the PVM-100A *LWC* measurements to droplet size.

The NASA tests took place in September/October 1998. Altogether, about 150 runs with different spray conditions in warm (zero degrees Celsius) and cold (-6 degrees Celsius) environments and varying air speeds (67 and 100 m s^{-1}) were carried out with the NCAR PVM-100A (serial no. 013) during three days of measurements. The tunnel *LWC* varied between 0.23 and 1.41 g m^{-3}. Composite droplet size distributions in the tunnel were derived using PDPA (Phase Doppler Particle Analyzer, Bachalo 1980) and OAP (Optical Array Probe, type 2DC and 2DP, Knollenberg, 1981) measurements.

The NRC PVM-100A data were collected in April 1999 (tunnel speed 100 m s^{-1}) with the University of Washington (UW) PVM-100A (serial no. 003). Compared to the NASA tunnel, the NRC facility provides the opportunity to test the PVM-100A for a wider range of *LWC* values than in the NASA tunnel. Icing cylinder measurements of *LWC* varied between 0.08 and 2.1 g m^{-3} during the NRC tests. Droplet size distributions were measured using a Malvern laser-diffraction spectrometer probe (Swithenbank et al. 1977).

From the resulting size distribution measurements in the NASA (PDPA + OAP/2DC + OAP/2DP) and NRC (Malvern) wind tunnels, *MVD* values were calculated for each of the tunnel settings.

Corresponding author's address: Manfred Wendisch, Institute for Tropospheric Research, Leipzig, Permoser-str. 15, 04318, Germany; E-Mail: wendisch@tropos.de.

2. PVM-100A *LWC* MEASUREMENTS AT FIXED *MVD*

In Figure 1 measurements of *LWC* from the PVM-100A are compared with the respective wind tunnel calibration values of *LWC*, for fixed values of *MVD*.

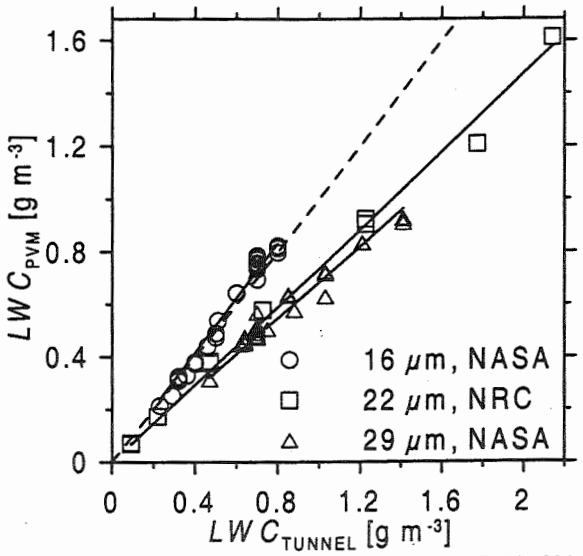

Figure 1: *LWC* measurements obtained from the PVM-100A (LWC_{PVM}) as a function of tunnel *LWC* (LWC_{TUNNEL}) for the three fixed *MVD* values 16, 22 and 29 μm in the NASA and NRC wind tunnels. The 1:1 line is indicated by the dashed curve.

The response of the PVM-100A is nearly linear for the range of *LWC* measured in the NASA and NRC wind tunnels. The PVM-100A is an optical probe, therefore no air speed dependence was observed in either the NASA or NRC data set. Further, no temperature dependence was observed in the NASA tunnel. In the NASA tunnel,

for an *MVD* of 16 μm, the NCAR PVM-100A is in excellent agreement with the icing blade standard. However, for an *MVD* of 29 μm, measurements of *LWC* from the PVM-100A are significantly lower than the standard. In the NRC wind tunnel, for an *MVD* of 22 μm, the response of the UW PVM-100A lies between the 16 μm and 22 μm response curve measured in the NASA wind tunnel.

3. PVM SENSITIVITY FOR VARYING DROPLET SIZE

3.1 Measured PVM sensitivity

The measured sensitivity function of the PVM-100A to *LWC*, as a function of *MVD*, is given by:

$$S_{PVM}(MVD) = \left.\frac{\partial(LWC)_{PVM}}{\partial(LWC)_{TUNNEL}}\right|_{MVD} \cong \left.\frac{LWC_{PVM}}{LWC_{TUNNEL}}\right|_{MVD} \quad (1).$$

In Figure 2 measured values of S_{PVM} are plotted against *MVD*, using results obtained in the NASA and NRC wind tunnels.

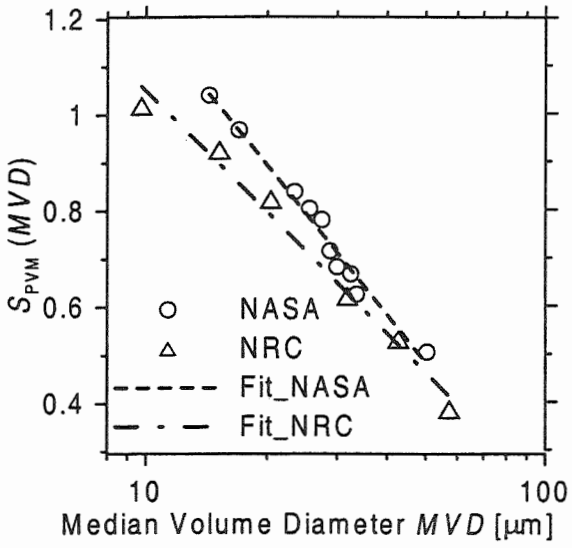

Figure 2: Measured sensitivity function of the PVM-100A (Eq. 1) for the NASA and NRC experiments. The dashed and dashed-dotted lines are logarithmic fits to the data.

The measured sensitivity of the PVM-100A to droplet *MVD* decreases logarithmically in both the NASA and NRC data sets. The measurements show that for *MVD* ≈ 50 μm the measured sensitivity of the PVM-100A decreases to ≈ 50%. The measured sensitivity of the UW PVM-100A to values of *MVD* < 30 μm appears to be significantly lower than for the NCAR PVM-100A. For larger values of *MVD* the response of the two probes converges. It is unclear whether the differences are due to differences between the PVM-100A probes themselves or differences between the techniques used to measure *MVD* in the NASA and NRC wind tunnels.

3.2 Calculated PVM sensitivity

The fraction of *LWC* the PVM-100A senses at droplet diameter *D* is the droplet size response function, $R_{PVM}(D)$. The measured sensitivity function, $S_{PVM}(MVD)$, described in section 3.1 may be reproduced from the measured droplet size distribution, $\frac{d(LWC)}{dD}$, if $R_{PVM}(D)$ is accurately known:

$$S_{PVM}(MVD) = \frac{\int \frac{d(LWC)}{dD}(D')\, R_{PVM}(D')\, dD'}{\int \frac{d(LWC)}{dD}(D')\, dD'} \quad (2).$$

The values of $R_{PVM}(D)$ used here are shown in Figure 3.

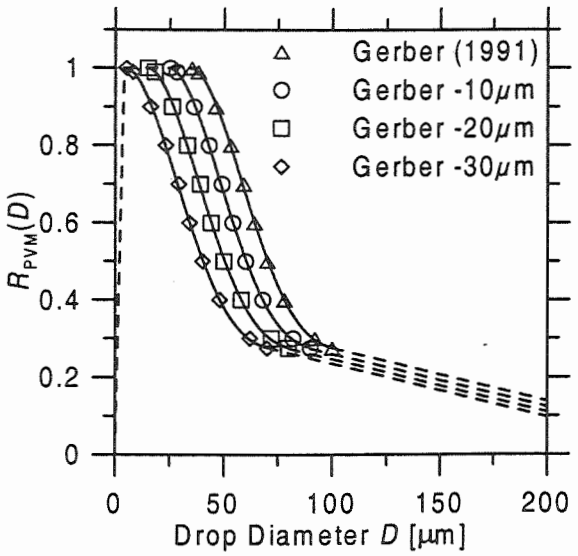

Figure 3: PVM-100A response functions $R_{PVM}(D)$ used in Eq. 2. The open triangles represent the published data and are adopted from figure 4 by Gerber (1991). The other three types of symbols are obtained by shifting the Gerber (1991) data along the diameter axis by -10, -20, and -30 μm. The solid lines represent fourth order polynomial fits to the data. The dashed lines represent linear extrapolations to $R_{PVM}(D{=}300\mu m) = 0$. For $D{>}300\mu m$ PVM response is set to be zero.

Four response functions and a range of values of wind tunnel *MVD* are used to examine the sensitivity of the PVM-100A to droplet size. The first is the published response curve of the ground-based PVM-100 (Gerber, 1991). In addition, three hypothetical PVM-100A response functions are obtained by shifting the Gerber (1991) response curve along the diameter axis by –10, -20, and –30 μm.

From Eq. 2, the sensitivity function of the PVM-100A may be calculated for each value of $R_{PVM}(D)$ and the range of values of *MVD* measured in the NASA and NRC wind tunnels. The results are presented in Figures 4a and 4b. The measured sensitivity of the PVM-100A,

from section 3.1, is included for comparison. Assuming measurements of the droplet size distribution in the wind tunnels are perfectly accurate, and the correct response function is used, the calculated values of $S_{PVM}(MVD)$ should agree with the measured values of $S_{PVM}(MVD)$.

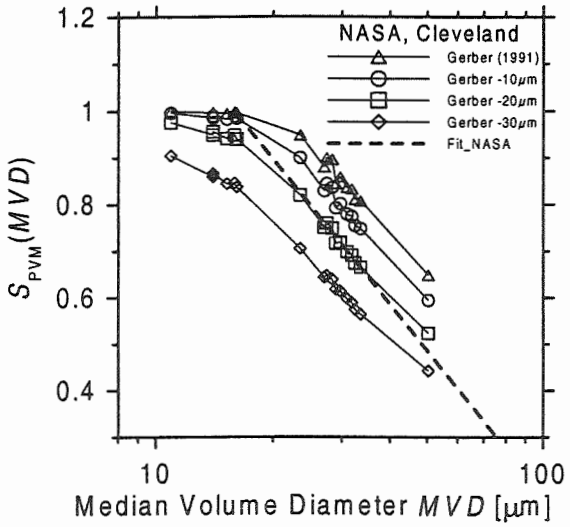

Figure 4a: Calculated sensitivity functions of the NCAR PVM-100A used in the NASA wind tunnel. The measured sensitivity function of the NCAR PVM-100A is shown by the dashed line.

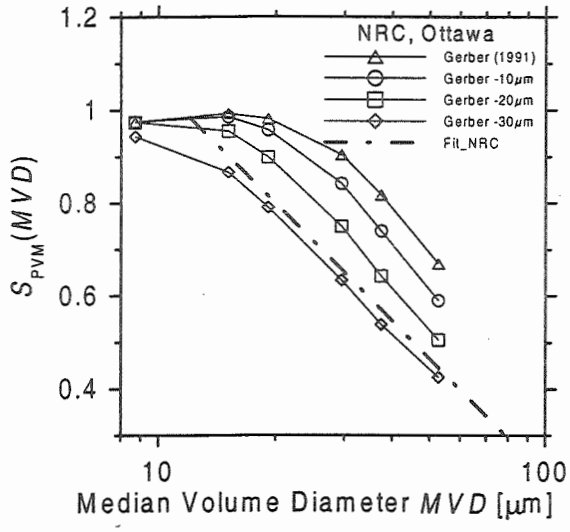

Figure 4b: Calculated sensitivity functions of the UW PVM-100A used in the NRC wind tunnel. The measured sensitivity function of the UW PVM-100A is shown by the dashed-dotted line.

The Gerber (1991) response function significantly overestimates the measured sensitivity of the PVM-100A for $MVD > 17$ μm in the NASA wind tunnel, and for $MVD > 12$ μm in the NRC wind tunnel. The difference between the calculated and measured PVM sensitivity function is smaller for the hypothetical response functions where it is assumed that the response of the PVM-100A to large droplets is less than that proposed by Gerber (1991).

For the NCAR PVM-100A tested in the NASA wind tunnel, the agreement between the calculated and measured $S_{PVM}(MVD)$ is best if the Gerber-20μm response curve is used (Figure 4a). This suggests that, whereas the tail in the response of the Gerber (1991) response function begins at 40 μm, the true response function of the PVM-100A tails off beginning between 20 and 30 μm. Uncertainties remain regarding the accuracy of the MVD measurements in the NASA wind tunnel. However using FSSP-100 (also obtained in the NASA wind tunnel) rather than PDPA data to derive MVD from the composite size distributions yields similar conclusions regarding the value of $R_{PVM}(D)$.

For the UW PVM-100A tested in the NRC wind tunnel a good fit between the calculated and measured $S_{PVM}(MVD)$ is obtained for the Gerber–30μm response function (Figure 4b). However, for $MVD < 15$ μm better agreement is obtained if the Gerber-20μm response function is used. Therefore the estimated value of $R_{PVM}(D)$ for the UW PVM-100A begins to drop off for droplet sizes greater than about $D = 20$ μm, and falls off more sharply for larger droplet sizes.

4. CONCLUSION AND OUTLOOK

The response function of the PVM-100A has been derived using independent measurements conducted in the NASA and NRC wind tunnels. The sensitivity of the PVM-100A to large droplets has been suggested by Gerber (1991) to tail off starting for droplet sizes >40 μm diameter. However, measurements obtained in the NASA and NRC wind tunnels suggest the true tail in the response of the PVM-100A to large droplets begins between 20 and 30 μm diameter.

There remain some uncertainties in the droplet size distribution measurements obtained in the NASA and NRC wind tunnels. Further measurements are planned to determine the shape of the droplet size distributions in the wind tunnels more accurately. As soon as these data are available it should be possible to precisely retrieve the PVM-100A response function $R_{PVM}(D)$ by inverting the following integral equation using standard numerical techniques:

$$\frac{LWC_{PVM}}{LWC_{TUNNEL}} = \frac{\int \frac{d(LWC)}{dD}(D')\, R_{PVM}(D')\, dD'}{\int \frac{d(LWC)}{dD}(D')\, dD'} \quad (3).$$

5. ACKNOWLEDGEMENTS

The authors wish to thank Zlatko Vukovic for preparing the NASA composite droplet size distributions, and Luigi Imperato for help with PDPA data. Furthermore, the generous sponsorship of tunnel time from NASA and NASA Grant NAG-1-079 to the University of Washington are acknowledged. IFT was supported by Grant Kan ENV70.

6. REFERENCES

Bachalo, W. D., 1980: A method for measuring the size and velocity of spheres by dual beam scatter interferometry. *Appl. Opt.*, **19**, 363-370.

Gerber, H., 1991: Direct measurement of suspended particulate volume concentration and far-infrared extinction coefficient with a laser-diffraction instrument. *Appl. Opt.*, **30**, 4824-4831.

Gerber, H., B. G. Arends, and A. S. Ackerman, 1994: New microphysics sensor for aircraft use. *Atmos. Res.*, **31**, 235-252.

Knollenberg, R. G., 1981: Techniques for probing cloud microstructure. P. V. Hobbs and A. Deepak, Ed., *Clouds, Their Formation, Optical Properties and Effects*, Academic Press, 15-92.

Strapp, J. W., J. Oldenburg, R. F. Ide, S. Bacic, L. Lilie, and Z. Vukovic, 2000: Measurements of the response of hot wire *LWC* and *TWC* probes to large droplet clouds. this issue.

Swithenbank, J., J. M. Beer, D. S. Taylor, D. Abbot, and G. C. McCreath, 1977: A laser diagnostic technique for the measurement of droplet and particle size distribution. *Progress in Astronautics and Aeronautics*, **53**, 421-447.

Twohy, C. H., and W. J. Strapp, 2000: Performance of a counterflow virtual impactor in the NASA Icing Research Tunnel. this issue.

THE CLOUD, AEROSOL AND PRECIPITATION SPECTROMETER (CAPS) A NEW INSTRUMENT FOR CLOUD INVESTIGATIONS

D. Baumgardner[1,2], H. Jonsson[3], W. Dawson[1], D. O'Connor[1] and R. Newton[1]

[1]Droplet Measurement Technologies, Boulder, CO 80308, USA
[2]Universidad Nacional Autónoma de México, Mexico City, Mexico
[3]Naval Post Graduate School, Monterey, CA , USA

1. INTRODUCTION

The PMS FSSP-100 and 2D OAP (Knollenberg, 1981), along with the hot-wire liquid water probe (King et al., 1978), have been the principal instruments for characterizing cloud particle properties for more than 20 years. The measurement techniques are well characterized and extensive research on measurement uncertainties has established the principal operating limitations for these three measurement techniques. With the introduction in 1999 of the Droplet Measurement Technologies (DMT) cloud, aerosol and precipitation spectrometer (CAPS), an improvement has been made on these measurement techniques. The remainder of this abstract highlights these improvements and presents a representative set of data that demonstrates this instrument's capabilities.

2. DESCRIPTION OF THE CAPS

The CAPS consists of five sensors: the aerosol and cloud droplet spectrometer (CAS: 0.35 – 50 μm), the cloud imaging probe (CIP: 25 – 1550 μm), the liquid water detector (0.01 – 3 gm^{-3}), the air speed sensor, and temperature probe.

The CAS measurement technique is similar to the FSSP-100, i.e. collection of forward-scattered light (5° – 14°) from single particles passing through a focused laser beam. The sample volume, however, is defined with a pinhole aperture, similar to the slit aperture used in the FSSP-300 (Baumgardner et al, 1992). The CAS has an additional set of optics and detector that measures back scattered light (5° – 14°). A comparison of the forward and back-scattered signals provides an estimate of aerosol refractive index, similar to the NCAR MASP (Baumgardner et al., 1996). A additional advantage of the two scattering signals is in determining particle asphericity. These two aspects of the forward and backscatter signals are discussed in the following section. Figure 1 is a schematic showing the optical configuration of the CAS.

The CIP measures particle images with the same technique as the PMS 2D OAP, i.e. capturing the shadow of particles that pass through a focused laser. The principle difference comes from improvements in signal processing, as discussed in the next section.

The DMT hot-wire liquid water sensor uses the technique described by King et al. (1978), but has a different geometry than the other commercially available sensor from PMS Inc.

Rounding out the CAPS is the pitot tube for measuring airspeed and a thermistor to measure ambient temperature. Figure 2 is a photograph showing the exterior of the CAPS. The CAPS fits into a standard PMS canister.

3. SPECIAL FEATURES AND IMPROVEMENTS

The CAPS covers the size range and capabilities of the PMS FSSP-300, FSSP-100, 2D-C, and hot-wire liquid water sensor, all in a single package. Co-located measurements reduce power and space and, more importantly, provide a continuous size distribution from the same region of the cloud.

The extended range of the CAS provides a continuous spectrum of particle sizes that covers much of the accumulation mode aerosols and up to small drizzle-sized drops in clouds. This is an important feature when studying cloud/aerosol interactions and looking at deliquesced aerosols prior to droplet activation near cloud base.

The simultaneous measurement of forward and back-scattered light from the same particle can be used to determine refractive index of aerosol particles, or asphericity of cloud particles. Figure 3 shows how the forward to back scatter ratio is a function of refractive index and Fig. 4 shows how this ratio changes for particles with different aspect ratios.

Corresponding author's address: Darrel Baumgardner, Droplet Measurement Technologies, 2400 Central, Suite A, P.O. Box 20293,Boulder, CO 80308, USA; e-mail: darrel@servidor.unam.mx.

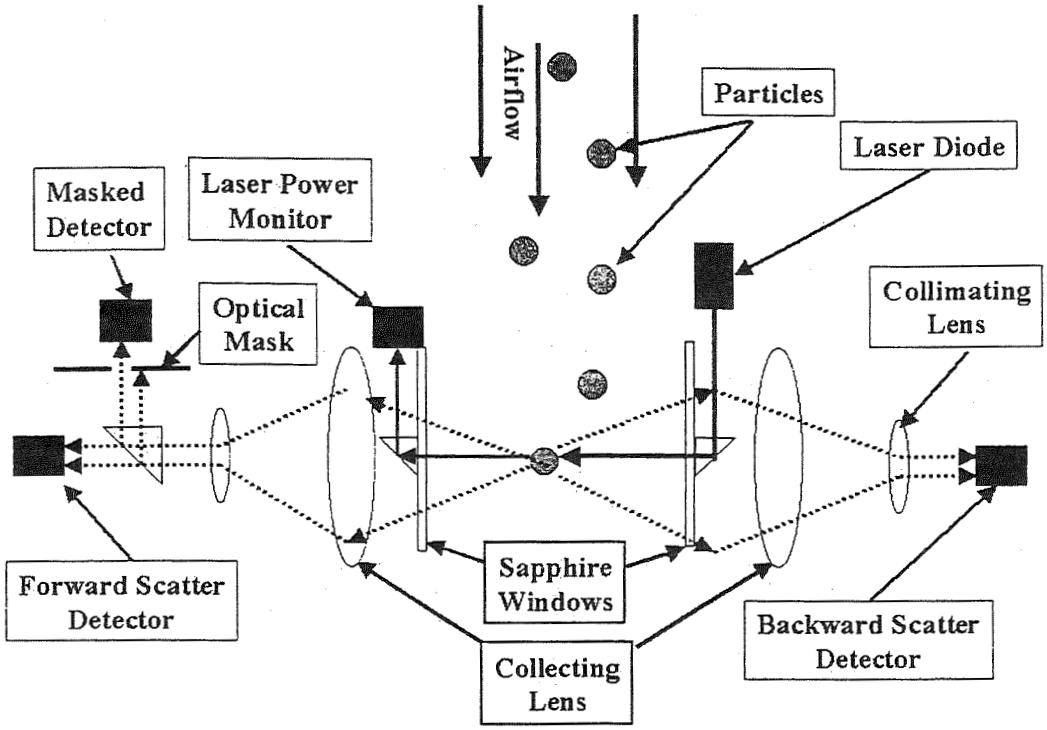

Forward/Backscatter Sensor Optical Path Diagram

Figure 1

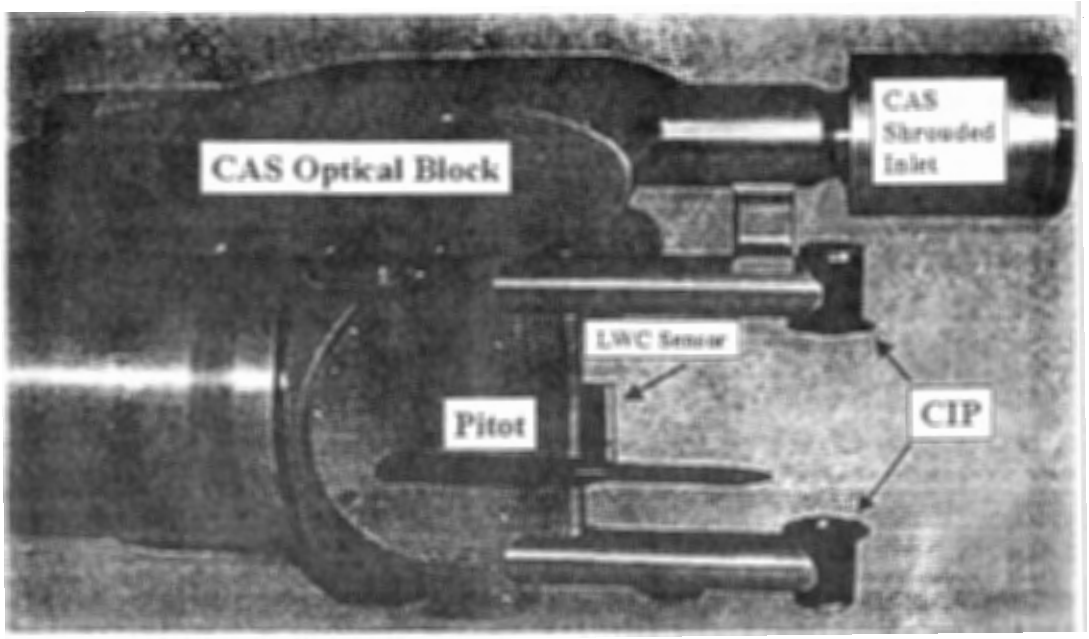

Figure 2
Exterior view of the CAPS showing principal sensors

This is particularly important for indicating whether small cloud particles are water or ice.

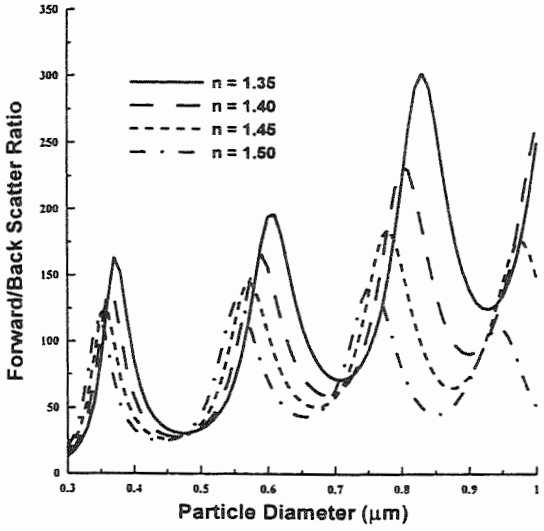

Figure 3 The forward to back scatter ratio is a sensitive indicator of refractive index, n.

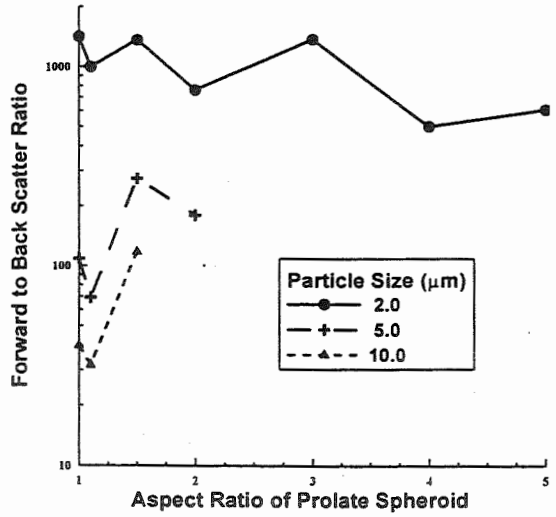

Figure 4 The forward to back scatter ratio is also a sensitive indicator of asphericity.

Many of the advantages of the CAPS are found in the signal processing. Previously, FSSP measurements needed corrections for under-sizing at air speeds greater than 100 ms^{-1} due to electronic time response limitations. The CAS does not require this correction due to its faster time response of 0.1 μs. The FSSPs also had significant counting losses when concentrations exceeded about 500 cm^{-3} as a result of electronic deadtime (Baumgardner et al., 1985). The CAS has no deadtime losses until particle This latter capability will be rates exceed 140K s^{-1}.

Two additional features extend the capabilities of the probe for self-calibration and for evaluating the fine scale structure of aerosols and cloud particle fields. The CAS has 40, user programmable size channels whereas the FSSP-100 had 15 fixed threshold channels. The programmable channels allow specific sections of the Mie scattering curve to be either bracketed or selected. In the latter case, the selection of more channels in the multi-valued size range of the Mie scattering curve provides a self calibration as described by Brengiuer et al (1998). Shifts in where the peaks and valleys fall in the measurements, within the multi-valued size region, will indicate changes in the instrument due to optical misalignment, dirty optics, or electronic gain changes. The second feature implemented in the CAS is the arrival time frequency distribution calculated for every time period. The frequency distribution of time intervals between particles is an independent measure of concentration (Brengiuer et al, 1994) and also provides a measure of small-scale inhomogeneities (Paluch and Baumgardner, 1989).

The principal improvements of the CIP are added stability against vibration, increased response time, and decreased deadtime. The 2 Mw HeNe laser of the PMS OAPs has been replaced with a 35 Mw diode laser. The additional intensity allows the beam to be expanded over the diode array and eliminates the false triggering of the probe that was often a problem with the OAPs when vibration caused movement of the beam across the array. The CIP also has a 64-diode array for an expanded size range. The PMS 2Ds had a 5 MHz limitation for clocking the image information into the buffers. This limited the air speed to size resolution ratio of these instruments, i.e. for 25 μm resolution 2D-Cs, the maximum airspeed was 125 ms^{-1} ($125/25x10^{-6}$ = 5 MHz) . Particle images were truncated at higher speeds. The CIP can clock images into its buffer at 8 MHz, which increases this limit to 200 ms^{-1} at 25 μm resolution. Conversely, for slower airspeeds, the size resolution can be increased to detect smaller particles, but requires custom optics to get to 10 μm resolution.

2D OAPs have a particle rate limitation imposed the amount of time required to download a particle buffer to the data system. The "overload" period, i.e. the amount of time the 2D was not taking data when it finished downloading a buffer, is a function of concentration and image size. This problem has not been eliminated, but has been minimized by increasing the number of images stored in a buffer by almost a factor of ten using data compression.

The other improvement has been the time tagging of individual particles. Each particle's time in the storage buffer is now an actual time of day in hours, minutes, seconds and milliseconds. This eliminates the decoding problem that was associated with PMS 2Ds where particle times were deduced from a "time word" that actually was just the number of clock pulse occurring since the previous particle. These clock pulses depended upon the air speed and introduced uncertainties in the timing. Each particle in the CIP buffer can be quickly decoded from a header in the buffer. This also is an improvement from the PMS 2D that used synchronization words that could not always be easily identified and particles were often missed.

The communication between the CAPS and data system is a combination of RS-232 and a high-speed serial line. The size distribution from the CAS and CIP and the analog data from the LWC sensor, pitot and temperature probes is encoded serially and sent at a baud rate of 56,000 via an RS-232 or RS-422 serial communications port on a PC. Image data from the CAPS is high-speed RS-422, sent to a commercial, ISA serial interface card in the PC at 4 Mb s^{-1}.

4. MEASUREMENT EXAMPLE

The CAPS was first used operationally during measurements of marine stratus off the coast of California, approximately 150 Km from the Big Sur. The instrument was mounted on the Twin Otter operated by the Center for Interdisciplinary Remotely-Piloted Aircraft Studies (CIRPAS). An FSSP-100, with the DMT SPP-100 upgrade, was also installed on this aircraft. Figure 5 shows the average spectra measured by the CAS, FSSP and CIP during a cloud pass through a shallow stratus deck with drizzle on July 16, 1999.

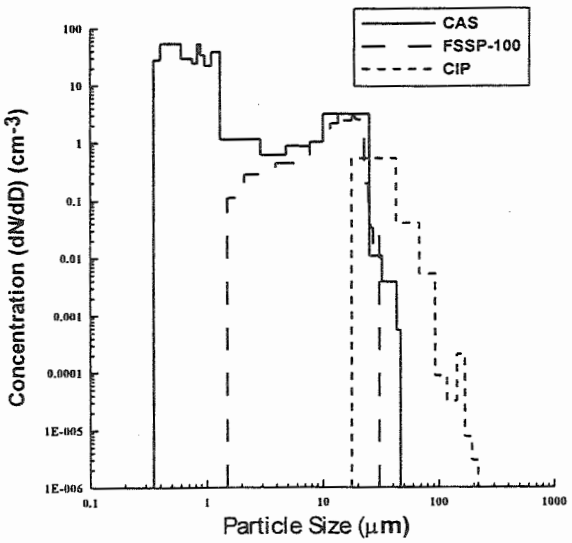

Figure 5

5. ACKNOWLEDGEMENTS

The authors wold like to thank Robert Bluth of the Naval Postgraduate School for his help with this development, funded under the ONR SBIR program, contact # N00014-97-C-0295

6. REFERENCES

Baumgardner, D., W. Strapp and J. E. Dye, 1985: Evaluation of the Forward Scattering Spectrometer Probe. Part II: Corrections for coincidence and dead-time losses. *J. Atmos. Oceanic. Technol.*, **2**, 626-632.

Baumgardner, D., J.E. Dye, R.G. Knollenberg, and B.W. Gandrud,1992: Interpretation of measurements made by the FSSP-300X during the Airborne Arctic Stratospheric Expedition, *J. Geophys. Res., 97*, 8035-8046.

Baumgardner, D., J.E. Dye, B. Gandrud, K. Barr, K. Kelly, K.R. Chan, 1996: Refractive indices of aerosols in the upper troposphere and lower stratosphere, *Geophys. Res. Lett*, 23, 749-752.

Brenguier, J.L., D. Baumgardner, B. Baker, 1994: A review and discussion of processing algorithms for FSSP concentration measurements, *J. Atmos. Ocean. Tech.*,11, 1409-1414.

Brenguier, J. L., et al., 1998: Improvements of droplet size measurements with the fast-FSSP (Forward Scattering Spectrometer Probe), *J. Atmos. Ocean. Tech.*,15, 1077-1090.

King, W.D., D.A. Parkin, and R.J. Handsworth, A hot wire water device having fully calculable response characteristics, *J. Appl. Meteor.*, 17, 1809-1813, 1978.

Knollenberg, R.G., Techniques for probing cloud microstructure, In *Clouds, Their Formation, Optical Properties and Effects*, P.V. Hobbs and A. Deepak, Eds., Academic Press, New York, 1981, pp. 15-92.

Paluch, I. R., and D. G. Baumgardner, 1989: Entrainment and fine-scale mixing in continental convective clouds. *J. Atmos. Sci.*, **46**, 261-278.

AIRCRAFT CONDENSATIONAL HYGROMETER

M.Yu. Mezrin, E.V. Starokoltsev
Central Aerological Observatory, Moscow Region, Russia

1. INTRODUCTION

The aircraft condensation hygrometer (ACH) is designed to measure air humidity (dew-/frost-point temperature) on board an aircraft. This instrument had been developed at CAO, with principal investigator M. Yu. Mezrin, and was employed in several research projects such as Arctic Haze (1994), BASE (Beaufort and Arctic Storm Experiment), Canada, 1994; APE (Airborne Polar Experiment), Finland, 1997; APE-THESEO (Third European Stratospheric Experiment on Ozone), the Indian Ocean, Seychelles, 1999; etc.

This instrument was operated on board the Russian research aircraft IL-18, the Canadian research aircraft Convair-580, and the Russian stratospheric aircraft M-55 "Geophysika". When on board IL-18 and Convair, it was complemented by an ultra-violet hygrometer permitting also the collection of data on turbulent humidity pulsations /Mezrin, 1997; Strunin, 1997/.

2. OBJECTIVES

On board M-55, ACH was to perform in an automated regime (without operator) under severe climatic conditions (up to a 20-km level or higher). The control box installed in a compartment without hermetic sealing was also exposed to these conditions. More stringent noise-protection requirements were to be met. Apart from that, It was necessary to expand the range of the parameter measurements. It is understood that frost-point temperature in stratospheric air could be -80^0C and lower.

All this demanded considerable upgrading of the instrument.

3. DESIGN

ACH includes a fairing, a control box, and connecting cables (Fig. 1). The fairing houses a sensor, an analogue-to-digital converter (ADC), and a processor.

The control box consists of a power source and an automated data acquisition system. ACH electric circuitry is composed of elements tolerant of low temperature and pressure. The processor and ADC, however, can be affected by such conditions, which necessitated their thermal stabilization. The control box provides thermal stabilization control.

Corresponding author's address: Mezrin M. Yu., Central Aerological Observatory, 3, Pervomayskaya St., Dolgoprudny, Moscow Region, 141700, Russia
E-Mail: mezrin@glasnet.ru

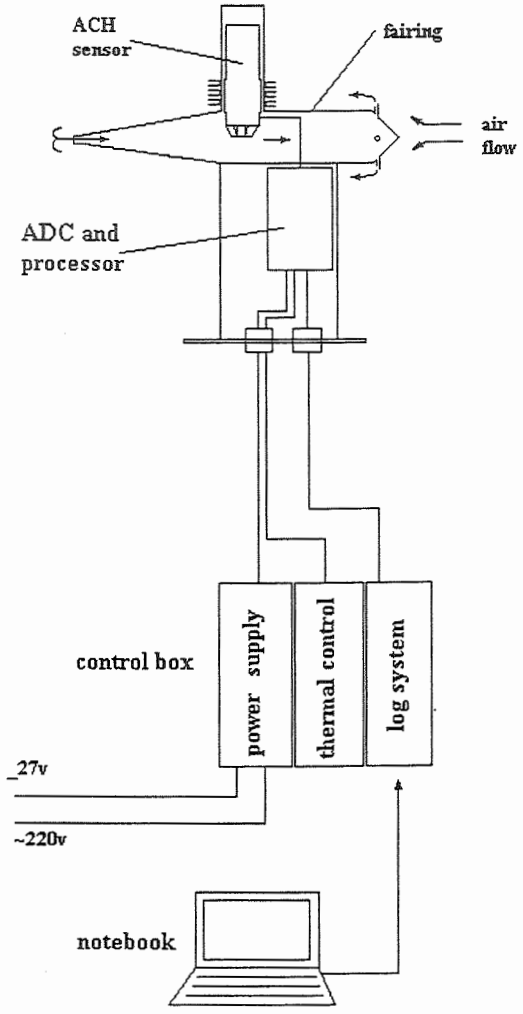

Fig.1 ACH design

ADC measurements are handled by the processor and passed to the automated log system using sequential code RS232. The data storage capacity is 2 Mb. The data collected in the flight is read out by computer on the ground.

On the aircraft M-55 "Geophysika", the fairing was mounted below the right wing so that it was in an undisturbed flow. The sensor's working space is aired in a natural way due to the difference of air pressure along the fairing surface. The control box is in the central part of the fuselage.

4. ADVANCED MEASUREMENT PRINCIPLE

It is commonly known that condensation hygrometer performance is based on the principle of maintaining phase equilibrium between condensate on a cooled mirror and water vapor of the ambient air. This equilibrium is maintained through a sophisticated feedback between condensate optical detector and refrigerator control, involving processes of heat exchange, the growth of droplets or crystals, and radiation scattering on them. The mirror surface temperature is a measure of dew- or frost-point. Condensate phase estimation using an optical detector helps to avoid errors caused by the difference between these two quantities, which may reach 2^0C at a -20^0C dew-point temperature /Mezrin, 1997/. This measurement procedure holds within a temperature range from 0 to - 50^0C.

The authors succeeded in measuring, with a fairly good accuracy, frost-point temperature of about –60^0C and somewhat lower (APE, 1997).

However, a further drop in temperature and, consequently, a fast lowering of absolute air humidity, would cause the rate of condensate growth or drying to decrease proportionally. All this results in a longer lag of the instrument. With the lag exceeding10 min., aircraft measurements lose their scientific meaning.

Efforts to solve this problem through accelerating ventilation of the sensor's working space or increasing the feedback response would lead to excitation of the measurement process.

A model to simulate the instrument's operation was constructed using advanced software. This model enabled investigation of the feedback parameters, aimed at larger measurement range and faster operation. A significant increase (100-fold) in the gain of feedback signals to the refrigerator control at temperatures diminishing from -20 to -60^0C
has proved successful. As absolute humidity and hence condensate growth rate rapidly diminish following drop in temperature, this solution does not lead to excitation.

Based on experimental evidence, the temperature measurement range has been extended to –85^0C and still lower values, with a 200-300 s. time constant.

The technical realization of this idea has been made possible by significantly increasing the photodetector temperature stability and preventing its accidental exposure to sunlight. Due to the large gain coefficient, even minor changes in the optical signal intensity affect the instrument performance, especially at low temperatures.

5. MEASUREMENT ACCURACY

The measurement errors include those of the hygrometer itself and those due to the disturbance of the air to be analyzed on its entering the working space inside the fairing.

As the hygrometer was to be operated at low temperatures, its thermometer measuring the mirror's temperature was re-calibrated using an operational standard (ferrum-rhodium resistance thermometer) in a wider range of temperatures from +20^0C to -100^0C. The deviation from the previous calibration of 1995 was not more than 0.3^0C.

A direct comparison using a standard dynamic moist air generator ("Iney") within a temperature range from +20^0C to -40^0C yielded a discrepancy of not more than 0.5^0C /Mezrin, 1997/.

Errors due to airflow disturbance investigated on board an IL-18 aircraft /Mezrin, 1992/ did not exceed –0.2^0C in clear-sky conditions and +2.8 % in clouds (which corresponds to +0.5 ÷ +0.3^0C).

The analysis of the measurements in terms of common sense shows their consistency. Thus, in situ measurements in cirrus clouds reveal the correspondence of humidity to saturation with respect to ice (frost-point is close to air temperature). Super-saturation with respect to ice is observed but accidentally and just for a short span of time, while that with respect to water is never detected (based on APE-THESEO data). In clear sky, frost point can be 10 – 20^{0}C below air temperature (hence a 10 – 20^{0}C frost-point deficit). Occasionally, dry aerosol clouds with a 10^{0}C frost-point deficit could be observed.

6. SOME EXPERIMENTAL RESULTS

The experiment that yielded the results concerned (APE-THESEO) was conducted in the vicinity of Seychelles (04^{0}40' S, 55^{0}31'E) during February-March, 1999. This experiment included a series of research flights aimed at exploring atmospheric structure in the equatorial tropical zone. It employed a high-altitude aircraft M-55 (provided by Myasishchev Design Bureau, Russia) equipped, besides navigational instrumentation, with instruments to measure temperature, water vapor content, ozone and some other gaseous and aerosol minor species, the optical density of the atmosphere, etc. The clouds were also sounded with a zenith lidar mounted on board the aircraft "Falcon", which followed M-55 at a lower level.

It is now worth while considering some results of the flight on March 6, 1999. The flight pattern is presented in Fig. 2. This graph includes the flight altitude curve provided by the aircraft data acquisition system (UCSE), the position of cirrus clouds determined with the lidar on board "Falcon" that operated at an altitude of about 15 km, and the position of a convective cloud from a concurrent satellite-borne picture. Latitude is plotted over the x-axis, longitude being practically invariable. Cirrus clouds are seen to be limited by the tropopause from above at approximately 18-km. Above the tropopause, light cirrus clouds with the lower limit at about 20 km can be discerned. Note that during this experiment, no convective clouds crossing the tropopause (hot towers) were observed, and hence the cirrus clouds detected may be assigned to the traces of moisture previously transported to the tropopause and higher above.

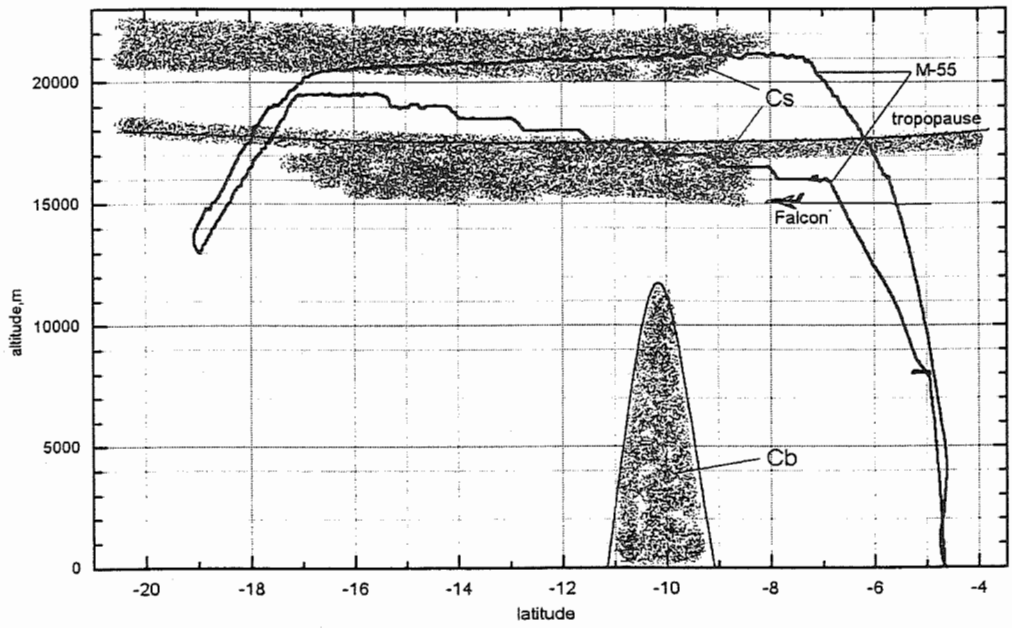

Fig.2 Flight pattern, 06.03.99

The other graph (Fig. 3) shows the same flight altitude as well as temperature (UCSE) and ACH frost-point values, versus time (UTC). The measurements in the zone of clouds is shown as gray background.

It is clearly seen that in the zone of clouds the frost point is close to air temperature (saturation with respect to ice) as was also the case during the clime across and above the tropopause (03:45).

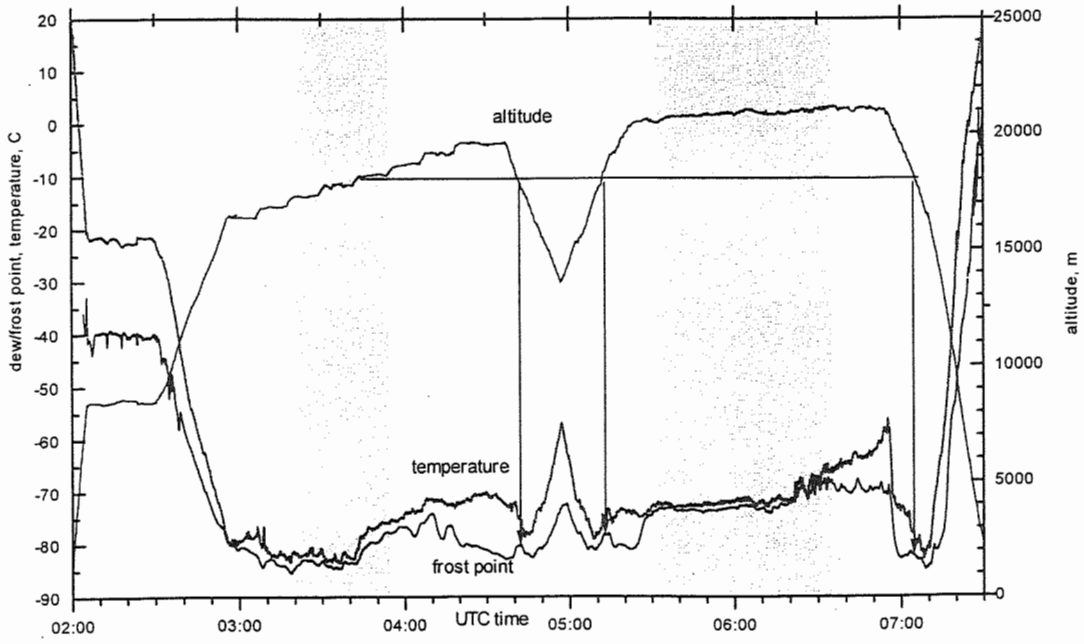

Fig.3 Flight altitude, temperature, ACH frost point versus UTC time, 06.03.99

In crossing the tropopause (minimum temperature) there is a rise in air humidity (shown by arrows). Here the aircraft is seen to cross a layer of light cirrus clouds in the tropopause (see Fig. 1). It is of interest that during the aircraft "dive" this layer (04:41 and 05:15) was somewhat above the temperature minimum. The humidity minimum (the hydropause)18^{0}S of the equator is a bit higher (-81^{0}C frost point) than when at 10^{0}S and 6^{0}S (-85^{0}C frost point).

In the zone above the convective cloud (03:30, 06:25), a disturbance of the temperature and humidity fields can be seen (in conditions of saturation with respect to ice).

7. CONCLUSIONS

The ACH experimental humidity values compared with the data on temperature and cloud distribution testify to ACH practicability at temperatures as low as –85^{0}C.

The measurement data obtained seem to give evidence of the existence in the stratosphere of zones with saturation with respect to ice and frost point of about –70^{0}C (mixing ratio of about 40 ppm). In the tropopause, however, minimum frost-point values can be close to -85 ^{0}C (about 3 ppm).

It should be noted that the above conclusions are confirmed by measurements in other flights under the same project that will be discussed elsewhere.

8. ACKNOWLEDGEMENTS

The authors extend their thanks to the scientists and technical personnel that took part in the project APE-THESEO for the organization of the campaign and possibility of using the data collected by many researchers involved. In particular, the authors are thankful to the MDB (Myasishchev Design Bureau) personnel for the data provided by the aircraft UCSE system and the science team of the aircraft "Falcon" (DLR) for their making the lidar data available, and especially to the daring Russian pilots that hoisted the scientific tools above the clouds.

8. REFERENCES

Mezrin, M.Yu., 1997. Humidity measurements from aircraft. J. Atmospheric Research, 44, 53-59.

Strunin, M.A., et al., 1997. Meteorological potential for contamination of arctic troposphere: Boundary layer structure and turbulent diffusion characteristics. J. Atmospheric Research, 44, 37-51.

Mezrin, M.Yu., 1992. An analysis of the airborne disturbances of humidity. Proceedings, CAO, 180. Hydrometizdat, Moscow (in Russian).

PERFORMANCE OF A COUNTERFLOW VIRTUAL IMPACTOR IN THE NASA ICING RESEARCH TUNNEL

C. H. Twohy[1], J. W. Strapp[2] and J. R. Oldenburg[3]

[1]Oregon State University, Corvallis, Oregon, USA
[2]Meteorological Service of Canada, Toronto, Ontario, Canada
[3]NASA Glenn Research Center, Cleveland, OH, USA

1. INTRODUCTION

In September and October of 1998, an assessment of cloud physics instrumentation was conducted at NASA's Icing Research Tunnel (IRT) in Cleveland, Ohio. The performance of most cloud microphysical probes currently used for research was evaluated under a wide variety of conditions. Results from 1 October measurements of liquid water content using a counterflow virtual impactor (CVI) are summarized here.

Tests were conducted for airspeeds of 67 m s^{-1} and 100 m s^{-1}, for liquid water contents of 0.23 to 1.4 g m^{-3}, and for droplet median volume diameters (MVDs) of about 10 to 240 microns. An overview of the tests and instrument results is presented by Strapp et al. (this issue) and a summary of the performance of the Particle Volume Monitor (PVM) is given by Wendisch et al. (this issue).

The IRT is calibrated and characterized in terms of liquid water content with accepted reference techniques (icing blade and rotating icing cylinder). Droplet distributions generated for specific conditions within the tunnel are very repeatable from run to run. However, as discussed by Strapp et al. (this issue), the standard values of tunnel MVD are subject to large bias errors.

2. CVI DESCRIPTION AND PROPERTIES

The CVI (Ogren et al., 1985, Noone et al., 1988; Twohy et al., 1997) has been utilized both in the air and on the ground in studies of aerosol/cloud interactions, cloud physics, and climate. At the CVI inlet tip, cloud droplets or ice crystals larger than a certain aerodynamic diameter are separated from the interstitial aerosol and water vapor and impacted into dry nitrogen gas. This separation is possible via a counterflow stream of nitrogen out the CVI tip, which only larger (cloud) particles are able to penetrate. The water vapor and non-volatile residual nuclei remaining after droplet evaporation are measured downstream of the inlet with selected instruments. These may include a Lyman-alpha or similar hygrometer, a condensation nucleus counter, an optical particle counter, or particle filters for chemical analyses. Because droplets or crystals in a large sampling volume are impacted into a relatively small sample stream, concentrations within the CVI are significantly enhanced. This permits detection of ambient ice water contents as low as 1 mg m^{-3} in cirrus clouds (e.g., Ström and Heintzenberg, 1994). Ice water contents measured by the CVI and PVM in orographic wave clouds with predominantly small ice crystals have shown excellent agreement (Gerber et al., 1998).

A CVI designed at the National Center for Atmospheric Research (NCAR) and flown on their Lockheed Electra aircraft was tested in the IRT. A standard Lyman-alpha hygrometer was used downstream of the inlet as the sensor for water content, and a TSI 3760 condensation nucleus counter was used to measure particle number. For the Lyman-alpha, the baseline value obtained before the droplet spray was introduced into the tunnel was subtracted from the liquid water content (LWC) signal with the spray on. LWCs presented here are corrected for the enhancement factor within the CVI and are 60s averages.

The impaction characteristics of the CVI are determined by inlet geometry, airspeed, and ambient conditions. For most airborne CVIs, the minimum size of unit-density particle sampled with 50% efficiency ("cut size") is about 5 to 10 microns in diameter. For the conditions of the IRT tests, the minimum CVI cut size was 7.5 microns and 9 microns diameter, respectively, for airspeeds of 100 and 67 m s^{-1}. One of the unique characteristics of the CVI is that the cut size can be increased by increasing the counterflow rate,

Corresponding author's address: Cynthia H. Twohy, Oceanography Admin 104, College of Oceanography and Atmospheric Sciences, Oregon State University, Corvallis, OR 97331-5503, USA; Email: twohy@oce.orst.edu.

thereby rejecting droplets in a broader size range. For most of the tunnel runs, the CVI cut size was increased to about 20 microns in diameter for a short period near the beginning of the run. By subtracting the LWC measured at the large cut size from the LWC measured at the small cut size, the amount of water present in the smaller drop size range was determined.

Uncertainty in the CVI liquid water content is induced by flow and geometry considerations in calculating the enhancement factor within the CVI (+/-8%), by calibration, offset and hysteresis factors related to the Lyman-alpha hygrometer (+/-5%, +/-9% and +/-5%, respectively), and by variation in tunnel conditions throughout the sampling period (+/-5%). Combination of the above errors by the root-sum-squared (RSS) method leads to an overall uncertainty in CVI LWC for these tests of +/-15% .

3. CVI PERFORMANCE

3.1 Liquid Water Content as f(size)

A series of 54 tunnel runs at various LWCs were made at a range of MVDs and two different airspeeds. The ratio of CVI LWC to the tunnel reference LWC as a function of MVD is presented in Fig. 1. Error bars reflect the uncertainty in CVI LWC of 15%.

Figure 1.

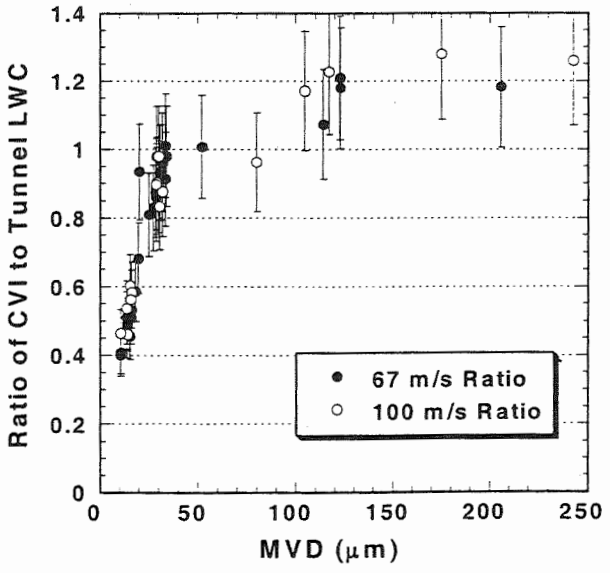

For Fig. 1 and elsewhere in this paper, MVDs are presented as calculated from a composite PDPA (Phase Doppler Particle Analyzer), 2D-C and 2D-P distribution, discussed by Strapp et al. (this issue). "Standard" tunnel MVDs are generally larger and are determined primarily by the FSSP-100 probe for small MVDs. Large number concentrations of very small droplets are generated for these runs (for our tests, generally greater than 1000 cm^{-3} uncorrected concentration). For these conditions, sizing errors related to particle coincidence in the FSSP are large and undefined, resulting in overestimation of tunnel MVD. This conclusion was also reached by Wendisch et al. (this issue) and Strapp et al. (this issue). As a result, we use MVDs derived from PDPA+2DC+2DP composite spectra, which when integrated to obtain LWC, agree better with the reference LWC values. Uncertainty in the PDPA-derived MVDs is estimated here to be about 25%.

For the smallest MVD tested (10.7 μm), the CVI LWC is 40-50% of the tunnel reference values. The 50% cut size of the CVI is calculated to be 9.0 microns at 67 m s^{-1} and 7.5 microns diameter at 100 m s^{-1}. Since uncertainty in the CVI cut size is estimated at about 1 μm, the PDPA-derived MVD and CVI cut size are consistent within the uncertainty of both values. Note that MVDs, even if accurate, are substantially larger than arithmetic mean diameters; for example, an MVD of 16 μm corresponds to an arithmetic mean diameter of only 5 μm for a lognormal distribution with a geometric standard deviation of 2.0 (e.g., Reist, 1993). Thus, at the smaller tunnel MVDs, droplets are smaller (and number concentrations are higher) than those in most natural clouds.

For MVDs between about 28 and 100 μm, agreement between the CVI and tunnel reference LWC is within the 15% estimated uncertainty for CVI LWC. Slightly greater departures occur for drops larger than 100 μm, where the tunnel LWCs are most uncertain (R. Ide, NASA, personal communication). Uncertainty in the tunnel reference LWC of about 10% (Strapp et al., this issue) can explain most of the remaining variation between CVI and tunnel LWCs. The maximum deviation (28%) at 175 μm MVD is for the same tunnel spray conditions (but a different airspeed) as the outlying point at 123 μm in Fig. 5 of Strapp et al. (this issue). This suggests that the tunnel uncertainty may be larger than 10% for this particular set of conditions.

Response to a range of different LWCs was assessed for droplet distributions with MVDs of about 30 μm, where CVI cut size effects should be negligible. Results are shown in Fig 2. For nearly all points, the CVI LWC matches the tunnel LWC within the CVI measurement uncertainty, and no systematic dependence on LWC or airspeed is apparent.

Figure 2.

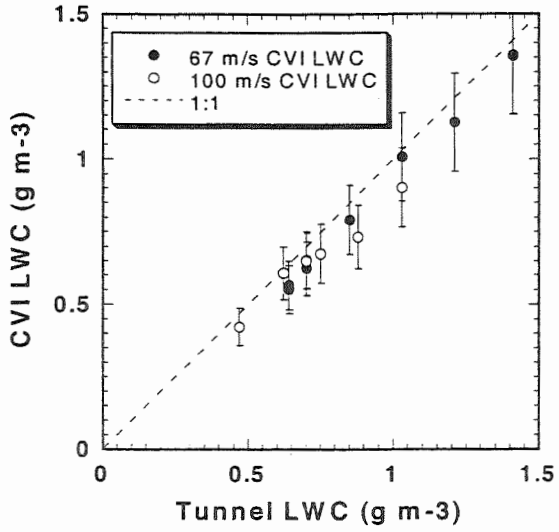

3.2 Effect of Shroud

A few 100 m s^{-1} tunnel conditions were run with and without a flow straightening shroud around the CVI inlet. The shroud was originally designed to be isokinetic on the NASA DC-8 aircraft at transonic airspeeds (approximately 225 m s^{-1} and Mach > 0.8). At lower airspeeds, computational fluid dynamical (CFD) modeling predicts airflow within the shroud to be superisokinetic by about 20% (Twohy, 1998). Small droplets should respond to these airspeed changes, thus increasing the effective sampling volume impinging on the CVI tip. A comparison of CVI LWCs with and without the shroud as a function of MVD is shown in Fig. 3.

Figure 3.

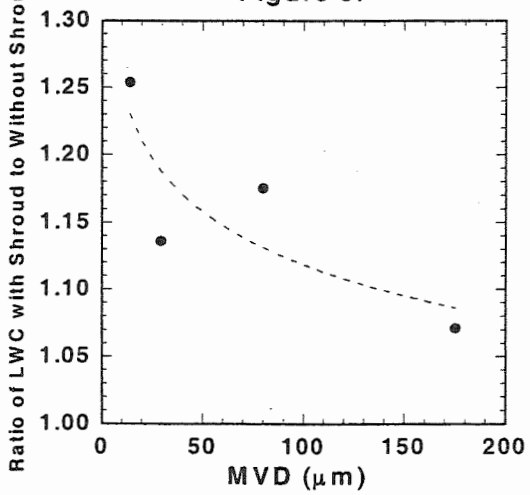

LWC values are 15 to 25% higher with the shroud than without for small droplet sizes, approximately as expected based on the CFD results. Thus, for clouds without an appreciable drizzle or large ice crystal mode, a 20% correction factor may be applied when sampling with the shroud at low airspeeds.

3.3 Cut Size Experiments

As discussed earlier, very high concentrations of small drops are produced in the IRT, which cause large uncertainties in derived MVDs. During most runs, the CVI cut size was increased to about 20 μm for a short time to assess the relative percentage of liquid water contained in small and large drops. The results of these comparisons are shown in Fig. 4 for the 100 m s^{-1} runs. The liquid water content in drops between 7.5 μm (the minimum cut size) and 20 μm was determined by subtracting the >20 μm value from the >7.5 μm value, and the ratio of small drop LWC to total LWC was calculated. Fig. 4 indicates that for small MVDs, almost all the water is present in drops smaller than 20 μm. At 21.7 μm MVD, the ratio is about 50%, indicating that the CVI ratios and PDPA-derived MVDs are consistent. For the largest MVDs, about 20% of the total water is still contained within small droplets, which is an unexpected result.

Figure 4.

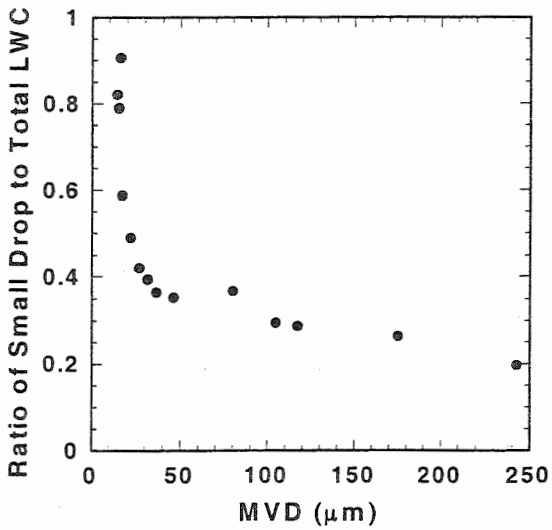

4. SUMMARY AND CONCLUSIONS

The NASA Icing Research Tunnel provides a valuable venue for testing instrument response to a range of droplet distributions and conditions. For droplet distributions with median volume diameters larger than 28 μm, liquid water content measured by the CVI agreed with tunnel values within the uncertainty of the measurements (15% for the CVI LWC and 10% for the tunnel LWC), with the exception of one outlying point. For a range of LWCs at 30 μm MVD, the relationship was near 1:1, and no systematic dependence of CVI results on LWC or airspeed was observed.

At the smallest MVDs, CVI LWCs were lower than tunnel reference values, indicating a substantial fraction of water was below the CVI cut size of 7.5 to 9 μm. A CVI efficiency of 40-50% for LWC occurred at a tunnel MVD of 10.7 μm, in reasonable agreement given the uncertainty in both CVI cut size and tunnel MVD. The relative proportion of liquid water in small and larger droplets was assessed by increasing the CVI cut size to 20 μm; this experiment also confirmed the validity of the 21.7 μm MVD test point.

A few tunnel runs were repeated with a flow straightening shroud around the CVI inlet. The shroud was designed to be isokinetic at higher (transonic) airspeeds, but is predicted to be subisokinetic by about 20% at lower airspeeds. Corresponding increases in CVI LWCs of about 20% were observed for small droplet runs, as expected from modeling results.

5. ACKNOWLEDGEMENTS

We wish to acknowledge the donation of wind tunnel time by NASA and the professional assistance of Dr. Bob Ide and the staff of the NASA IRT. The Federal Aviation Administration, Transport Canada, and the Research Aviation Facility of the National Center for Atmospheric Research provided joint support for travel and analysis.

6. REFERENCES

Gerber, H., Twohy, C.H, Gandrud, B., Heymsfield, A.J., McFarquhar, G.M., DeMott, P.J. and D. C. Rogers, Measurements of wave-cloud microphysical properties with two new aircraft probes, Geophys. Res. Lett., 25, 1117-1120, 1998.

Noone, K.J., Ogren, J.A., Heintzenberg, J., Charlson, R.J. and D.S. Covert, Design and calibration of a counterflow virtual impactor for sampling of atmospheric fog and cloud droplets, Aer. Sci. Technol., 8, 235-244, 1988.

Ogren, J.A., Heintzenberg, J. and R.J. Charlson, In-situ sampling of clouds with a droplet to aerosol converter, Geophys. Res. Lett., 12, 121-124, 1985.

Reist, P.C., Aerosol Science and Technology, New York, Mc-Graw Hill, 2nd Ed., 379 pp., 1993.

Strapp, J.W., Oldenburg, J., Ide, R., Vukovic, Z., Bacic, S. and L. Lilie, Measurements of the response of hot wire LWC and TWC probes to large droplet clouds, Preprints, 13th International Commission of Clouds and Precipitation, Reno, Nevada, 14-18 August 2000 (this issue).

Ström, J. and J. Heintzenberg, Water vapor, condensed water, and crystal concentration in orographically influenced cirrus clouds, J. Atmos. Sci., 51, 2368-2383, 1994.

Twohy, C.H. and D. Rogers, Airflow and water drop trajectories at instrument sampling points around the Beechcraft King Air and Lockheed Electra, J. Atmos. Oceanic Technol., 10, 566-578, 1993.

Twohy, C.H., Schanot, A.J. and W.A. Cooper, Measurement of condensed water content in liquid and ice clouds using an airborne counterflow virtual impactor, J. Atmos. Oceanic Technol., 14, 197-202, 1997.

Twohy, C.H., Model calculations and wind tunnel testing of an isokinetic shroud for high-speed sampling, Aer. Sci. and Technol., 28, 261-280, 1998.

Wendisch, M., Garrett, T., Hobbs, P.V. and J.W. Strapp, PVM-100A performance tests in the NASA and NRC wind tunnels, Preprints, 13th International Commission of Clouds and Precipitation, Reno, Nevada, 14-18 August 2000 (this issue).

MEASUREMENTS OF RAINDROP AXIS RATIO USING AIRCRAFT 2DP PROBES

Jasbir S. Naul and Kenneth V. Beard

Department of Atmospheric Sciences, University of Illinois at Urbana-Champaign

1. INTRODUCTION

Although general agreement has been found between numerical force balance models of the equilibrium shape of raindrops and observations of drops in wind tunnels (e.g., see Beard and Chuang 1989), axis ratios can differ from the equilibrium shape because of oscillations. Laboratory measurements reveal that water drops falling in still air oscillate continually in response to vortex shedding for drop sizes d_0 > 1 mm (equivalent volume diameter), e.g., see Andsager et al. (1999). Field studies at the ground have also documented that small-to-large raindrops of d_0 = 1-4 mm continually oscillate, in the absence of significant collisions, turbulence and wind shear (Tokay and Beard 1996). The subject of the present study is to evaluate the effect of aircraft-disturbed airflow on raindrop shape ahead of wingtip-mounted PMS 2DP probes.

2. DATA

In our previous studies (Xu 1995, Beard et al., 1999), we have analyzed raindrop shapes from aircraft data obtained during the 1991 Convection and Precipitation/Electrification Experiment (CaPE). Raindrop images were recorded using PMS 2DP diode array probes on King Air cloud physics aircraft operated by NCAR and University of Wyoming. The optical axes were horizontal to acquire raindrop profiles as typically presented to radar. The 2DP data analyses were limited to temperatures warmer than 15°C to avoid the potential influence of unmelted ice cores on raindrop shape.

The 2DP images were smoothed using Fourier and moment methods to minimize systematic errors and improve estimates of the principal axes and image orientation (Chandrasekar et al. 1988). Simulations of 2DP images based on equilibrium raindrop shapes (Beard and Chuang 1987) showed that the axes, axis ratios and equivalent volume diameters were reproduced with good accuracy for $d_0 \geq 2$ mm.

3. RESULTS

From the analysis of 8 King Air flights during July 1991, we found that the image canting angles of 20 - 45 degrees were nearly twice as large as expected from the apparent canting created by an elliptical raindrop falling through the 2DP probe array (see Fig. 1). We also found a horizontal asymmetry in the average images for all raindrop sizes in the form of a triangular distortion (see Fig 2). These results are not unexpected because of distortion found in 2DP images for larger aircraft. For example, Black and Hallett (1986) noted "the elongation and canting in the raindrop images in comparison to the graupel images" of similar sizes obtained in a hurricane.

The aircraft-induced flow ahead of the PMS 2DP sampling location on the King Air was evaluated by Xu (1995) using a wing airflow model (King 1986). In level flight at 90 m/s, the major disturbance is a wing-induced upwash of 3.0, 4.5 and 6.5 m/s at 1.0, 0.5 and 0.0 m ahead of the 2DP sampling point. The induced horizontal air motions in the direction of the aircraft are 0.5, 1.5 and 3.5 m/s at the same locations. The corresponding orthogonal disturbances are 0.4, 0.7 and 2.0 m/s in the outboard direction.

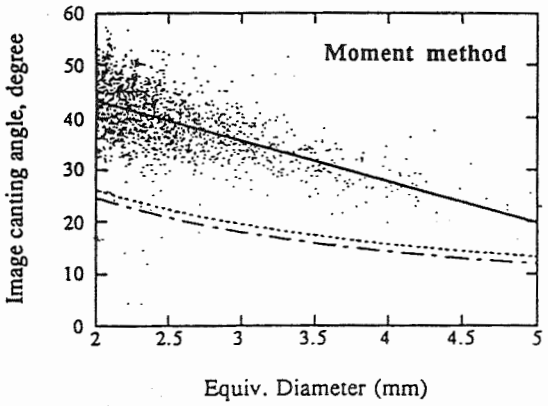

Fig 1. Scatter plot and regression line for the 2DP image canting angles as a function of d_0. The expected canting angle is shown by dotted & dash-dot curves.

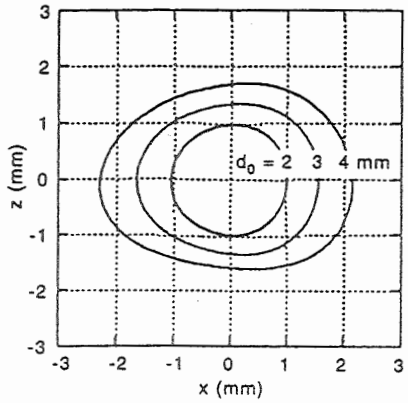

Fig. 2. Average raindrop shapes for d_0 = 2, 3 and 4 mm.

Although these velocity disturbances are an appreciable fraction of raindrop terminal speeds, there is not nearly enough time for raindrops to adjust their speed; their velocity response time is about 1 sec, whereas the aircraft transit time for one meter is only 11 ms. Thus, raindrops within 1 meter of the 2DP sampling point experience a significant fraction of the

Corresponding author: Ken Beard, Atmospheric Sciences, UIUC, 105 S Gregory St, Urbana, IL 61801
Email: k-beard@uiuc.edu

increased airflow which has a magnitude of 3-8 m/s and is directed upward, ahead and outboard at 12-32° from vertical.

The effect of this disturbance on raindrop shape will depend on the time that it takes for a raindrop to distort. One estimate is the response time for an oblate distortion: τ = 2.1, 3.8 and 5.8 ms for d_0 = 2, 3, and 4 mm (Beard 1983). During these periods, an aircraft moving at 90 m/s will have traveled 0.18, 0.34 and 0.52 m, respectively. It therefore appears likely that there is sufficient time for a raindrop to distort in response to the tilted airflow disturbance ahead of the King Air wing.

Raindrop shape was revaluated because of potential image canting caused by the airflow disturbance. Thus, the canting from the vertical motion of a raindrop was removed before the axis ratio was calculated from a fitted ellipse using the moment method. As shown in Fig. 3 the resultant axis ratio are lower than the equilibrium axis ratios by 0.13, 0.12 and 0.09 for d_0 = 2, 3, and 4 mm. The axis ratios are also considerably lower than those of Chandrasekar et al. (1988) from the ratio of maximum vertical scan to horizontal extension.

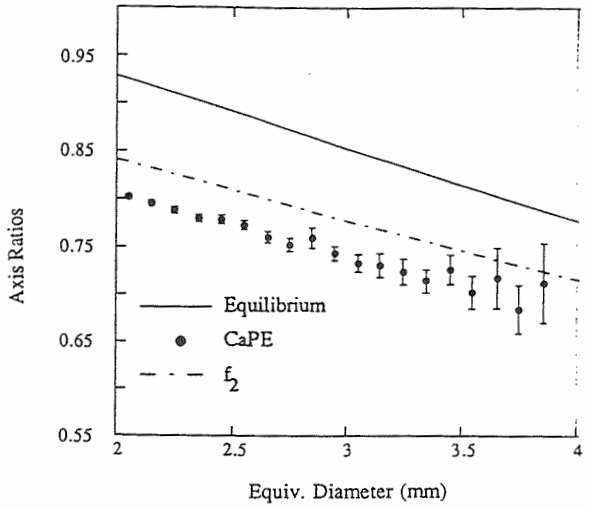

Fig. 3 Geometric mean axis ratios and 95% confidence intervals for airflow-distorted raindrops in comparison to theoretical equilibrium axis ratio (solid line). The dash-dot line is the oblate response to the wing airflow disturbance using the harmonic oscillator model of Chandrasekar et al. (1988).

Raindrop distortion was also estimated using the forced harmonic oscillator model of Chandrasekar et al. (1988) for the fundamental (oblate) mode. The axis ratios were lower than the equilibrium by about 0.09, 0.08 and 0.07 for d_0 = 2, 3, and 4 mm (Fig. 3). Incorporation of the first harmonic in this model decreased the axis ratio further by 0.02-0.03.

The amount of raindrop distortion was also estimated from the instantaneous axis ratio in the accelerated airflow ahead of the wing (Beard 1977). The instantaneous axis ratios were lower than the equilibrium axis ratios by 0.12, 0.11 and 0.10 for d_0 = 2, 3, and 4 mm at 0.75-1.00 m at 0.13-0.38 m and 1.4-4.2 ms ahead of the 2DP sampling location. These instantaneous axis ratios are in good agreement with the Fig. 3 analysis of the image data: axis ratios 0.13-0.09 below equilibrium for d_0 = 2-4 mm.

If raindrops are significantly distorted by the airflow ahead of a 2DP probe, then what useful information can be obtained from the images? Clearly, it is not a trivial task to separate the aircraft distortion of raindrops from the undisturbed shape. Yet, we may still be able to use the scatter in axis ratio to infer the magnitude of raindrop oscillation amplitudes. In the present analysis, the distribution of axis ratio shows a spread of ±5% for less than about 70% of the raindrops of a particular size. If this variation is applied to *equilibrium axis ratios* for d_0 = 2 mm and 3 mm drops, the variation in axis ratios would be 0.89-0.97 and 0.81-0.89.

In our presentation, we will show results from new analyses of axis ratios, canting angles and shape asymmetry for the same 2DP data set used by Bringi et al. (1998). In addition, we will describe ways to improve the measurement of raindrop axis ratios in their natural environment.

Acknowledgments The research reported here is based on work supported by the National Science Foundation under Grants ATM 91-21698 and ATM 95-05298. Any opinions, findings and conclusions or recommendations expressed in this material are those of the authors and do not necessarily reflect the views of the National Science Foundation.

3. REFERENCES

Beard K.V., 1983: Reorientation of hydrometeor in aircraft accelerated airflow. J. Climate Appl. Meteor., 22, 1961-1963.

Beard, K. V., and C. Chuang, 1987: A new model for the equilibrium shape of raindrops. *J. Atmos. Sci.*, **44**, 1509–1524.

Beard, K. V., X. Xu, H. T. Ochs and J. S. Naul, 1999: Raindrop axis ratios from aircraft 2DP measurements in CaPE for application to dual-polarization radar measurements, Preprints 29th Intern. Conf. Radar Meteor., AMS, 297-300.

Black, R. A., and J. Hallett, 1986: Observations of the distribution of ice in hurricanes. *J. Atmos. Sci.*, **43**, 802-822.

Bringi, V. N., V. Chandrasekar and R. Xiao, 1998: Raindrop axis ratios and size distributions of Florida rainshafts: An assessment of multiparameter radar algorithms. *IEEE Trans. Geosci. Remote Sens.*, **36**, 703-715.

Chandrasekar, V., W. A. Cooper and V. N. Bringi, 1988: Axis ratios and oscillations of raindrops. *J. Atmos. Sci.*, **45**, 1323–1333.

King, W. D., 1986: Air flow and particle trajectories around aircraft fuselages. IV: Orientation of Ice Crystals. *J. Atmos. Oceanic Technol.*, **3**, 433-440.

Tokay, A. and K. V. Beard, 1996: A Field Study of Raindrop Oscillations. Part 1: Observations of size spectra and evaluation of oscillation causes. *J. Appl. Meteor.*, **5**, 1671–1687.

Zu, X., 1995: Analyses of Aircraft Measurements of Raindrop Shape in CaPE, M.S. Thesis, Dept. of Atmospheric Sciences, University of Illinois, 117 pp.

MEASUREMENT OF THE ASYMMETRY PARAMETER OF CLOUD PARTICLES

H. Gerber
Gerber Scientific Inc., Reston, VA 20190, U.S.A.

Y. Takano
UCLA, Department of Atmospheric Sciences, Los Angeles, CA 90095, U.S.A.

Timothy J. Garrett and Peter V. Hobbs
Department of Atmospheric Science, U. of Washington, Seattle, WA 89195, U.S.A.

I. INTRODUCTION

The asymmetry parameter, g, of cloud particles such as drops and ice crystals plays an important role in radiative transfer calculations, because it is used to parameterize the scattered-light phase function. The value of g for ice crystals has been estimated almost exclusively from calculations using model ice crystals, or inferred from light scattered by ice clouds. Actual in-situ measurements of g have been scarce.

This paper describes a new experimental method for measuring g directly and continuously in clouds, and presents results from measurements made from the U. of Washington research aircraft during the Arctic SHEBA/FIRE field study in 1998 (Gerber et al. 2000; Garrett et al. 2000). This method utilizes the integrating-nephelometer principle, where four channels of integrated light scattered by the particles are combined for a measure of g, as well as for a measure of the particles' volume-scattering and backscatter coefficient. Correc- tions are made to account for the scattered light diffracted at small scattering angles. This permits measurements of g for particles as large as several 1000 um in diameter.

The following measurements made in Arctic clouds are described: Calculated PDFs of g are given for a cloud consisting of water and ice. The average value of g for the water cloud is close to the value expected from Mie calculations, and the overall average (0.824) is slightly less than the water-cloud value, given the contribution from ice cloudswhich were a small percentage of the clouds sampled with the aircraft. A glaciated cloud containing primarily large bullet rosettes gave an average value of 0.737, which compares well with a model of crystals consisting of bullet aggregates, but is smaller than the value of g recently attributed to ice clouds.

Gerber Scientific Inc., 1643 Bentana Way, Reston, VA 20190, U.S.A. E-Mail: gerber.gsi@erols.com

2. METHOD

The asymmetry parameter is defined by Twomey (1977) as

$$g = \frac{\int_{-1}^{1} \cos\theta \, (i_1 + i_2) \, n(r) \, dr \, d\cos\theta}{\int_{-1}^{1} (i_1 + i_2) \, n(r) \, dr \, d\cos\theta} \qquad (1)$$

where θ is the scattering angle with respect to the optical axis of the incident light, i_1 and i_2 are the scattering intensity functions, r the particle radius, and n(r) the size distribution of the particles.

The denominator of Eq. (1) is closely related to the scattering coefficient σ_s of the particles, and the numerator is similar, but weighted by the cos of the scattering angle.

It is shown by Gerber et al.(2000) that Eq. (1) can be approximated by

$$g = \frac{(F+B)\,f + (\cos F - \cos B)\,(1-f)}{F+B} \qquad (2)$$

where F is forward scattered light, B is backscattered light, cosF is cos-weighted forward scattered light, cosB is cos-weighted backscattered light, and f is the fraction of the total scattered light that is diffracted.

Given that the diffracted light is concentrated at near-forward scattering angles for large particles, permits an estimate to be made of the value of f (≈ 0.5) and of the total scattered light from measurements of the scattered light (F, B, cosF, cosB) over a range of scattering angles (10^o - 175^o) which is practical from an instrumentation standpoint. These estimates contain some error, because the diffracted light extends to some degree over all scattering angles. A sensitivity test using phase functions for typical droplet spectra and ice crystal sizes and habits, shows that the estimate of f is sufficiently accurate so that meaningful measurements of g can be made for particles ranging in size from a few to several thousand microns in diameter.

The parameters shown in Eq. (2) can also be combined to measure the scattering coefficient or extinction coefficient, σ_e, of non-absorbing particles

$$\sigma_s = \sigma_e = C\frac{F+B}{1-f} \qquad (3)$$

where C is a scaling constant, and to measure the hemispheric backscatter ratio b_r given by

$$b_r = \frac{B(1-f)}{(F+B)} \qquad (4)$$

3. INSTRUMENTATION

The instrument for measuring g is based on suggestions by Heintzenberg and Charlson (1996) and Gerber (1996) that the integrating-nephelometer principle could be applied. The resulting device, named CIN (cloud integrating nephelometer), combines four integrating nephelometers to make the four measurements of the integrated scattered-light quantities required by Eq. (2). The schematic sketch of the CIN in Fig. 1 shows that four light diffusers with Lambertian response are placed parallel to a laser beam that scatters light from the particles. Two of the diffusers use in addition "cos masks" that weight the scattered light by the cos of the scattering angle. Photomultipliers behind the diffusers quantify the scattered light. This nephelometer arrangement is one of the types first discussed by Beutell and Brewer (1949).

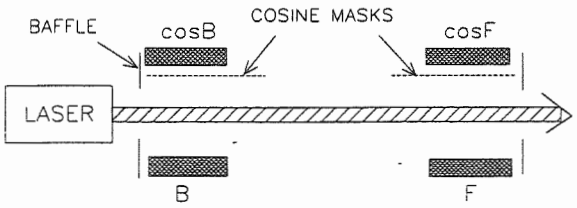

Fig. 1 - Schematic of CIN. Particles irradiated by the laser beam scatter light into four circular diffusers (seen edge on) behind which are located photomultipliers. The two diffusers on the right measure forward scattered light, F; and those on the left measure backscattered light, B. The top two diffusers use in addition masks that weight the scattered light by the cosine of the scattering angle.

Each pair of diffusers/photomultipliers are mounted in a wing-shaped arm, each of which resembles half of a strut with an ellipitical cross section that is split parallel to its long axis to form each wing. The diffusers are mounted on the inside flat surface of the wings which are placed parallel to each other and 3.5-cm apart. For aircraft measurements the CIN is mounted so that the long dimension of the wings are perpendicular to the wind direction and the flat surfaces are parallel to the wind direction, which minimizes deviation of the streamlines through the 3.5-cm gap.

The volume of atmosphere irradiated by the laser beam and seen by the sensors is about 30 cm^3, which gives a volume sampling rate of 300 liters s^{-1} at an aircraft speed of 100 ms^{-1}. The measurements are independent of air speed; and the laser has a wavelength of 635 nm.

4. MEASUREMENTS

We present here two examples of CIN measurements for a water cloud and glaciated cloud traversed by the U. of Washington CV-580 research aircraft during the FIRE/ SHEBA Arctic study. A detailed analysis of the CIN measurements made during that study is presented by Garrett et al. elsewhere in this volume.

Figure 2 shows values of σ_e and g measured during horizontal flight in a stratus cloud located near the Barrow ARM site. The average value of g of 0.835 is close to the value predicted by Mie theory for a cloud with droplets with a measured effective radius of about 6.0 μm, suggesting that the CIN was operating as intended.

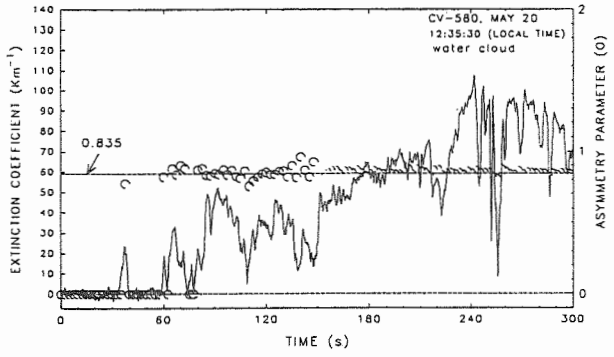

Fig. 2 - The optical extinction coefficient and asymmetry parameter measured by the CIN on the University of Washington CV-580 aircraft during horizontal flight through a water cloud near the ARM site in Barrow Alaska.

Figure 3 shows values of σ_e and g measured by the CIN during flight through a glaciated cloud at a temperature of -42 C. This cloud contained mostly bullet rosettes with sizes averaging about 150 μm in diameter. The values of g shown in Fig. 3 are substantially smaller than the value of g measured in the water cloud.

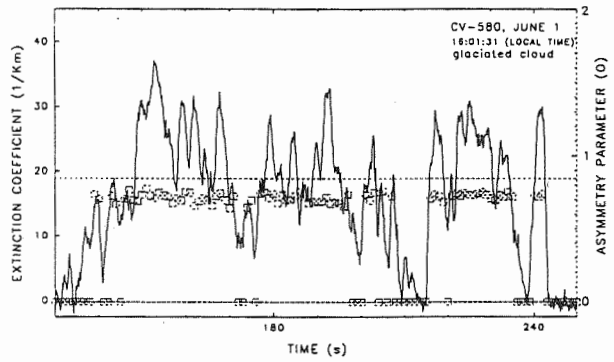

Fig. 3 - Measurements of the optical extinction coefficient and the asymmetry parameter measured with the CIN in a glaciated cloud containing large bullet rosettes.

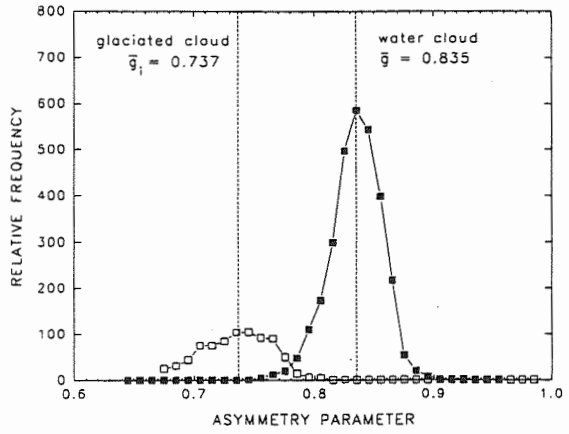

Fig. 4 - PDF (probability distribution function) of the asymmetry parameter g measured in the water cloud (Fig. 2) and the ice cloud (Fig. 3). Average value of g is given for each distribution.

The PDFs for the values of g for the water and ice cloud are shown in Fig. 4. The average value of g = 0.737 for the ice cloud inclues a correction of 0.02 for "δ light transmission" (Takano and Liou, 1989) through the ice crystals. This transmission occurs through paralel facets of the crystals without imperfections. The correction is based on model calculations, and has an unconfirmed applicability to actual atmospheric ice crystals.

The values of g ranging from the uncorrected 0.707 to the "corrected" 0.737 for the rosettes in this ice cloud are smaller than the values of g estimated for ice clouds in some recent work (e.g., Francis 1995; Mitchell et al. 1996; Macke et al. 1998), but agree better with earlier work where values of g on the order of 0.700 were measured indirectly (e.g., Wielicki et al. 1990; Stephens et al. 1990.)

5. CONCLUSIONS

We have demonstrated that it is possible to measure from an aircraft the single-scattering properties consisting of the asymmetry parameter, extinction coefficient, and backscatter coefficient in water and ice clouds using an integrating-nephelometer approach. This is made possible by applying a correction for the light scattered by the droplets and ice crystals in the near-forward direction where light diffraction dominates, and where it is impractical to make scattered-light measurements. The angular scattering range of 10° to 175° used in the CIN is practical from a measurement standpoint, and permits measurement with acceptable accuracy of the single-scattering properties independent of particle shape and size over a range of a several thousand μm in diameter. These results can also be applied to polar nephelometers (e.g., see Gayet et al 1997).

The measurement of relatively small values of g in the ice clouds decribed here should not be considered representative of all ice clouds, because g will vary with crystal size and habit. The measurements do show, however, that earlier estimates of g with similar small values are feasible. Determining representative values of g in typical ice clouds requires more CIN measurements done in conjunction with imaging probes.

ACKNOWLEDGMENTS

Jack Russel (deceased) and Don Spurgeon of the University of Washington are thanked for their work on installing and maintaining the CIN on the CV-580 aircraft. This work was supported by NASA grants NAS1-20506 and NAS1-96020 to Gerber Scientific Inc.; NSF Grant ATM97-96277 to the University of California, Los Angeles; NASA grant NAG-1-2079, NSF grant OPP-9808163, and grant PF904717 from FRONTIER/IARC to the University of Washington.

REFERENCES

Beutell R.G.. and A.W. Brewer, 1949: Instruments for the measurement of the visual range. *J. Sci. Instrum.*, **26,** 357-359.

Francis, P.N., 1995: Some aircraft observations of the scattering properties of ice crystals. *J. Atmos. Sci.*, **52**, 1142-1154.

Garrett, T.J., P.V. Hobbs, and H. Gerber, 2000: Shortwave, single-scattering properties of Arctic ice clouds. *J. Geophys. Res.,* submitted.

Gerber, H., 1996: Measurement of the asymmetry parameter and optical extinction coefficient of ice crystals and water droplets. *Final Report*, NAS1-20506. NASA Langley Research Center, Hampton, VA 23681, 23pp.

Gerber, H., Y. Takano, T.J. Garrett, and P.V. Hobbs, 2000: Nephelometer measurements of the asymmetry parameter, volume extinction coefficient and backscatter ratio in Arctic clouds. *J. Atmos. Sci.*, in print.

Heintzenberg, J., and R.J. Charlson, 1996: Design and application of the integrating nephelometer: A review. *J. Atmos. Oceanic Technol.*, **13**, 987-1000.

Macke, A., P.N. Francis, G.M. McFarquhar, and S. Kinne, 1998: The role of ice particle shapes and size distributions in the single scattering properties of cirrus clouds. *J. Atmos. Sci.*, **55**, 2874-2883.

Mitchell, D.L., A. Macke, and Y. Liu, 1996: Modeling cirrus clouds. Part II: treatment of radiative properties. *J. Atmos. Sci.*, **53**, 2968-2988.

Stephens, G.L., S.-C. Tsay, P.W. Stackhouse, and P.J. Flatau, 1990: The relevance of microphysical and radiative properties of cirrus clouds to climate feedback. *J. Atmos. Sci.*, **47**, 1742-1753.

Takano, Y., and K.N. Liou, 1989: Solar radiative transfer in cirrus clouds. Part I: Single-scattering and optical properties of hexagonal ice crystals. *J. Atmos. Sci.*, **46**, 3-18.

Twomey, S., 1977: *Atmospheric Aerosols.* Elsevier Publishing, 302 pp.

Wielicki, B.A., J.T. Suttles, A.J. Heymsfield, R.M. Welch, J.D. Spinhirne, M.-L.C. Wu, D. Starr, L. Parker, and R.F. Arduini, 1990: The 27-28 October 1986 FIRE IFO cirrus case study: Comparison of radiative transfer theory with observations by satellite and aircraft. *Mon. Wea. Rev.*, **118**, 2356-2376.

A NUMERICAL SIMULATION OF THE FSSP DEPTH OF FIELD

A.A. Coelho, J.C.C Silva,, R.V. de Souza, J.B. V. Leal Jr., and G.A. Farias

Department of Physics, Ceará's Federal University, Fortaleza, Brazil

1. INTRODUCTION

A numerical model that simulates the Forward Scattering Spectrometer Probe (FSSP) functioning was used to simulate the depth of field validation criterion of this probe.

The cloud droplet concentration is a very important parameter for the research in cloud physics. Most of the *in situ* cloud droplet concentration measurements are derived from droplet countings carried out by airborne mounted FSSPs. However, one of the main sources of error in the estimation of the droplet concentration in clouds is due to the sampling volume uncertainty (Brenguier *et al.*, 1994). The sampling volume is defined by the product of the selection beam cross section area, the aircraft speed and the time sampling period. The selection beam cross section is the surface in the beam where the laser intensity is stronger. It is referred as the FSSP Depth of Field (DOF) surface. The DOF area is measured in laboratory by moving a scattering medium back and forth along the FSSP laser beam. This value is applied to derive the cloud droplet concentration regardless the size of the counted droplets. However, in 1984, Dye and Baumgardner showed from an experimental result that the DOF area can vary as a function of water droplet diameter (see fig. 8 of Dye and Baumgardner, 1984). Therefore, the real cloud droplet size distributions can be different from those derived by the FSSP. The present work shows preliminary results of simulations of the FSSP DOF selection criterion of the first FSSP version - the FSSP-100 - and the most recent one - the Fast FSSP.

2. THE FSSP DOF

The general aspects of the DOF selection criterion in the FSSP-100 are similar to the Fast FSSP one - both of them use a beam splitting prism in order to deviate scattered light onto a central masked photodetector and later make a voltage comparison.

Figure 1 illustrates schematically the optical path and components in FSSP. One portion of the scattered light entering the splitting prism illuminates a photodetector that, after amplification, generates a voltage directly proportional to the light intensity according to the preset probe calibration. Such a voltage, or signal, is posteriorly converted to a particle size using a 15

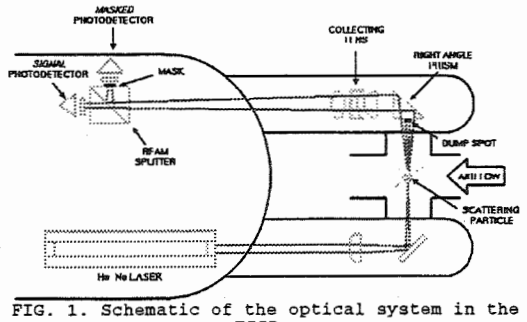

FIG. 1. Schematic of the optical system in the FSSP.

channel pulse height analyzer in the FSSP-100 or an analog to digital conversion module in the Fast FSSP. This photodetector is referred to as the *Signal* detector.The other portion of the light falls on another photodetector that is partially masked by a dump spot in the FSSP-100, and a narrow slit, in the Fast FSSP. This is the above mentioned masked photodetector and it is referred to as the *Annulus* detector in the FSSP-100 and the *slit* detector in the Fast FSSP. In both of these two spectrometers the masked photodetector voltage is more amplified than the *Signal* one and the DOF region in the beam could be drawn by comparing *Signal* and masked photodetector voltages.

The focused image of the scattering particle upon the masked photodetector plane takes a form of a "ring of light" due to the FSSP optical aperture - the scattered light is collected only in a certain range of scattered angles. When the particle passes through the middle of the sampling tube (the focal plane of the laser beam), the lighted ring becomes very small, almost a point of light. The further the particle is from the focal plane, the larger the ring becomes upon the photodetector plane. Because the *Signal* and the masked photodetectors are symmetrically located with reference to the splitting prism, the particle image is focused upon the *Signal* photodetector plane in the same way as just described above.

2.1 The FSSP-100 DOF

As mentioned above, the DOF selection in the FSSP-100 is obtained by placing a dump spot in the center of the masked photodetector - the *Annulus* detector. When a scattering particle passes through the focal plane of the laser beam, its image is focused upon the dump spot and the *Annulus* voltage is quite attenuated. On the other hand, if such a particle passes

Corresponding author's address: Afrânio de A. Coelho, Departamento de Física, Universidade Federal do Ceará, Campus do Pici, C.P.: 6030, Fortaleza-CE, 60125-150, Brazil; e-mail: coelho@fisica.ufc.br.

far from the focal plane, the focused image becomes larger than the dump spot and only a small portion of light reach the detector. Because the *Annulus* gain is greater than the *Signal* gain, when a particle is outside the DOF its *Annulus* amplitude is bigger than the *Signal* one. Thus, a particle is selected within the DOF whenever its *Annulus* amplitude is smaller than the *Signal* one. It should be noted that, because the laser beam diameter is much smaller then the dump spot, a particle could be DOF validated within the focal plane even if it passes through the edges of the beam.

2.2 The Fast FSSP DOF

In the FAST FSSP, the DOF selection is obtained by placing a narrow slit (0.4 mm width), oriented parallel to the droplet trajectory in the beam. If a particle crosses the beam at a distance far from the middle of the focal plane only a small fraction of the scattered light passes through the slit before detection by the *Slit* detector. On the other hand, if the particle crosses the beam at the focal plane and across the beam center, all the scattered light can cross the slit before reaching the detector. However, if the particle crosses the focal plane through the edges of the beam, its image is focused on the side of the slit and cannot reach the detector. As in the FSSP, the masked detector gain is greater than the *Signal* one, so that when a particle is outside the DOF its *Slit* amplitude is smaller than the *Signal* one. Thus, the DOF selection criterion in the Fast FSSP is the inverse of the FSSP-100: a particle is selected within the DOF whenever its *Slit* amplitude is greater than the *Signal* one. This optical-electronic criterion defines the DOF as a narrow region in the beam, around the beam axis and at the middle of the sampling tube. Differently from the FSSP-100, it allows the rejection of particles passing through the edges of the beam without an electronic average of its *transit times* - the FSSP-100 Velocity Acceptance Criterion (VAC).

3. THE NUMERICAL MODEL

The model simulates as precise as possible the optical and electronic characteristics of the FSSP and its response to cloud droplets. It has been developed in the *Centre National de Récherches Météorologiques* (CNRM) of Météo-France, Toulouse (Coelho, 1996) for providing the calculation of the transfer matrix - whose elements are the conditional probabilities for a droplet of a certain size to be counted in given classes of *Signal* amplitude and *transit time* - of the Fast FSSP. This matrix allows the size distribution correction from inhomogeneities in the laser beam and ambiguities in the Mie scattering curve (Brenguier *et al.*, 1998). Because the model provides the amount of scattered light reaching the *Signal* and masked (*Slit* or *Annulus*) detectors, it can determine the DOF region defined by a FSSP based on its optical-electronic settings: laser beam geometry and intensity profile, FSSP response, size and position of the optical devices, and gain amplification ratio between the two detectors. Although this work sets fixed values for some parameters, all of these settings can vary from one probe to another. Except for the mask, these settings are the same for Fast FSSP and FSSP-100 simulations. Below, the fixed settings adopted in the model are described.

3.1 The Laser Beam

The wavelength of the laser beam is equal to 0.6328 μm and its diameter is 0.2 mm. The geometric references in this study are established in a rectangular coordinates system: the *x*-axis has the direction of the beam axis; the *y*-axis is oriented along particles trajectories and the *z*-axis is in the vertical direction; the origin of the coordinates is located at the intersection of the focal plane with the beam axis; the distances are given in millimeters (mm).

The laser intensity profile is determined analytically by a parametrization of the measured intensity profile of the CNRM's Fast FSSP multimode laser (§3.1, Coelho, 1996). According to this parametrization, the laser intensity in the *x*-direction is uniform in a region of 6 mm length around the focal plane and decreases otherwise. In *y* and *z*-directions, the laser intensity decreases from the beam axis to the edges. The parametrized laser intensity profile is symmetrical with respect to the beam axis and the focal plane.

3.2 The Optical Devices Configuration

Table 1 furnishes the fixed distances (in mm) used in the model among a particle located at the focal plane and the right angle prism, the collecting lens and the photodetectors (diodes). Table 2 provides the nominal dimensions (in mm) of the dump spot - the central mask in the FSSP-100, the slit - the central mask in the Fast FSSP, the collecting lens and the sensitive surface of the photodetectors.

Device	*prism*	*lens*	*diodes*
Distance	37	72	307

Table 1: The distances of some optical devices to the focal plane of the FSSP laser beam.

Device	*lens*	*diodes*	*dump spot*	*slit*
Size	29	2.6	1.0	0.4

Table 2: Some FSSP optical devices dimensions.

3.3 The FSSP Response

The photodetectors, after amplification, transform linearly the falling light intensity upon its sensitive surfaces into voltage. The scattered light falling upon

the photodetectors come into a narrow solid angle defined by the dimensions of the FSSP sampling aperture, the dump spot attached to the right angle prism (see Fig.1), the collecting lens aperture, the size and geometric form of the mask, the photodetectors diameter and the particle position in the laser beam. The intensity of the radiation scattered in a certain direction by a particle of a certain diameter and for a given incident light intensity is calculated in the model by using Barber's code (Barber and Hill, 1990). Therefore, the total light intensity reaching the photodetectors for a scattering particle of a certain diameter, at a given beam position and for a given incident light intensity is calculated by integrating the scattered radiation intensity over the respective sampling solid angle. The image construction of a single scattered beam by using the thin lens formula allows to establish whether the beam passes into the sampling solid angle or not.

The calibration of the FSSP consists in finding the linear equation relating the *Signal* photodetector input light intensity and its respective output voltage. Because the scattered light intensity depends on the particle diameter, the calibration allows to attribute a certain diameter range to a certain class number of particle size - 1 to 15 in the FSSP-100 and 1 to 255 in the Fast FSSP. The model simulates the light intensity-voltage conversion according to the FSSP calibration presented in Wendisch *et al.*, 1996.

According to the parametrized laser intensity profile, the maximum of the light scattered intensity occur whenever a particle reaches the middle of the beam trajectory line. Therefore, the photodetectors amplitudes are determined by the calibration equation when applied to the total detected intensity coming from the scattering radiation of particles located at the *y=0* beam plane.

4. THE DOF SIMULATION

The model simulates the DOF selection criterion of the FSSP by comparing the *Signal* amplitude to the *masked* amplitude produced by a spherical particle of a certain diameter when it passes through a given (x_i,z_i) trajectory position. The x and z-axis are divided into N small cells characterized by a (x_i,z_i) trajectory position with $1 \leq i \leq N$. The DOF boundary is defined by the trajectory positions where the *Signal* amplitude is equal to the *masked* amplitude. The DOF area is calculated by the sum of the area of the cells where the DOF selection criterion is valid. Because the FSSP-100 DOF criterion is the opposite of the Fast FSSP and the mask form also changes from one to another, the simulations of each probe are carried out separately. The preliminary results obtained by the first simulations applied to cloud droplets are presented below.

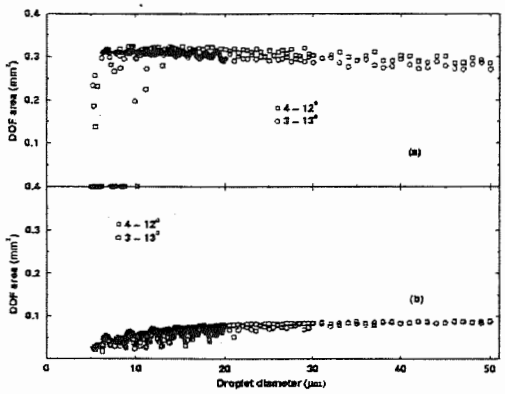

Fig. 1: The FSSP DOF area as a function of the water droplet diamter: (a) for the FSSP-100;(b) for the Fast FSSP.

The figures 2a and 2b show the FSSP-100 and the Fast FSSP DOF area as a function of the droplet diameter, respectively. In these figures, the circle scattered points represent simulations of a probe with sampling aperture defined by a scattering angle range between 3 and 13° when the particle is located at the center of the beam coordinates - note that in this case only the sampling window diameter, the diameter of the first dump spot and the lens aperture defines the collecting solid angle; the square scattered points for collecting scattering angles between 4 and 12°. In all of these simulations, the amplification ratio between *the masked* voltage M and the *signal* voltage S is $M/S = 2$.

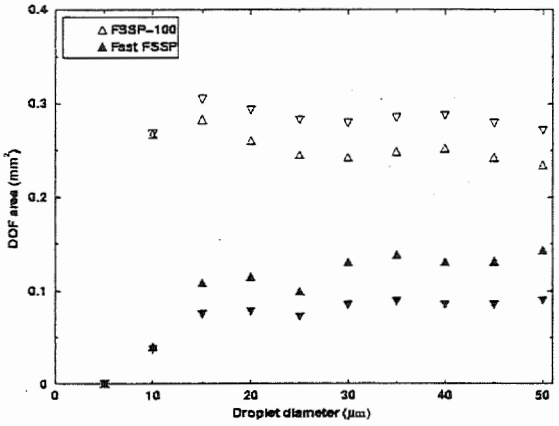

Fig. 3: The FSSP DOF area for different values of *Masked/Signal* amplification ratio

The figure 3 shows the FSSP-100 and the Fast FSSP DOF area as a function of the droplet diameter for two different M/S amplification ratios. The filled triangle scattered points represent simulations of the Fast FSSP and the open ones of the FSSP-100. The triangle down scattered points - filled or not - represent the simulations with $M/S = 2$ and the triangle up ones represent simulations with $M/S = 2.5$.

The figure 4 shows the FSSP-100 and the Fast FSSP DOF area as a function of the droplet diameter for different values of the mask size. As in the fig. 3, the filled triangle scattered points represent simulations of the Fast FSSP and the open ones represent simulations of the FSSP-100. The triangle down scattered points - filled or not - represent simulations with the mask size 20% smaller than the nominal value (see table 2) and the triangle up with 20% bigger than

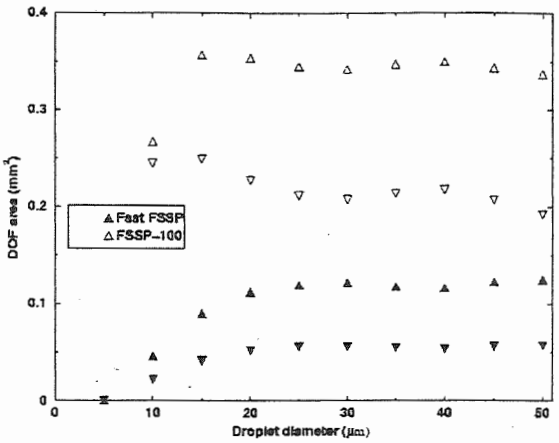

Fig. 4: The FSSP DOF area for different values of the mask size

the nominal value. In all of these simulations, the *M/S* amplification ratio is the same and equal to 2. Also, the collecting angle range is the same, between 3 and 13°.

5. DISCUSSION

The variation of the collected radiation intensity with the scattering particle diameter cause also the FSSP DOF area to vary with the droplet diameter. As can be seen from fig. 2, the DOF area in both of the simulated FSSPs varies along a certain droplet diameter range, mainly for small droplets - smaller than 15 μm. Furthermore, the FSSP DOF area for big droplets - greater than 30 μm - are larger than for small droplets while the FSSP-100 presents a slight decreasing tendency, as observed by Dye and Baumgardner, 1984. Because of the DOF area variations, the probe can even never DOF validate some small droplet so that the DOF area vanishes. For example, according to the calibration adopted in the model, the Fast FSSP could never DOF validate droplets with diameters about 10 μm. On the other hand, the amplitude of the DOF area variations in the Fast FSSP does not decrease by closing the sampling aperture.

As it should be expected (Knollenberg, 1976), the FSSP-100 DOF area for a certain particle diameter decreases if the *M/S* ratio increases, as can be seen from fig. 3. On the contrary, the Fast FSSP DOF area for a certain particle diameter increases if the *M/S* ratio increases. This difference is due to the inverse electronic DOF criterion between the two probes: around the focal plane, the *Annulus* amplitude approaches the *Signal* amplitude as the *Annulus* amplitude increases while the *Slit* amplitude becomes higher than the *Signal* amplitude as the *Slit* amplitude increases. However, the DOF area almost does not change for very small droplets because the *Signal* and *Masked* voltages are too weak to producing a significant amplitude variation. For example, the DOF area for a 10 μm droplet diameter in both of the probes is almost the same whatever the *M/S* changes, as can be seen from figure 3.

The FSSP DOF area can be very sensitive to the size variations of the mask (see fig. 4). The Fast FSSP DOF is more sensitive than the FSSP-100 because the Fast FSSP DOF area for a certain particle diameter is smaller than the respective FSSP-100 DOF area. However, the sensitivity of both of the probes to mask size changes is quite attenuated for droplets as small as 10 μm of diameter.

6. CONCLUSIONS

The simulations of the FSSP-100 DOF agree with the previous experimental work. Both the FSSP-100 and the Fast FSSP present a strong variation in the DOF area for small droplets and these variations can not be reduced by opening or closing the sampling aperture and increasing or decreasing the *Masked* to *Signal* amplification ratio. However, the FSSP becomes more sensitive for small droplets only if the size mask increases. Because of the strong variations of DOF area for small droplets, the droplet size distribution derived from the FSSP would underestimate the real concentration of small droplets. Further analysis will be carried out to simulate the droplet size distribution distortions caused by the FSSP. Furthermore, the authors will attempt to develop a numerical algorithm in order to correct these distortions.

REFERENCES

Barber, P. W., and S. C. Hill, 1990: *Light Scattering by Particles: Computational Methods.* World Scientific Publishing, 261pp.

Brenguier, J. L., T. Bourrianne, A. de A. Coelho, J. Isbert, R. Peytavi, D. Trevarin, and P. Weschler, 1998: Improvements of droplets size distribution measurements with the fast FSSP. *J. Atmos. Oceanic. Technol.*, **15**, 1077-1090.

Coelho, A., 1996: Mesure aéroportée de la distribution dimensionnelle des gouttelettes d'eau en nuage. Ph. D. thesis, No. 2246, University of Toulouse, 151pp.

Dye, J. E., and D. Baumgardner, 1984: Evaluation of the forward scattering spectrometer probe. Part I: electronic and optical studies. *J. Atmos. Oceanic Technol.*, **1**, 329-344.

Knollenberg, R. G., Three new instruments for cloud physics measurements: the 2-D spectrometer, the forward scattering spectrometer probe, and the active scattering aerosol spectrometer, *Am. Meteorological Society,* International Conf.

Wendisch, M., A. Keil, and A. V. Korolev, 1996: FSSP characterization with monodisperse water droplets, *J. Atmos. Oceanic. Technol.*, **13**, 1152-1165.

A TETHERED BALLOON CLOUD MICROPHYSICS SOUNDER

R.D. Borys,

Desert Research Institute, Reno, NV, 89512, U.S.A.

1. INTRODUCTION

As part of the Surface Heat Budget of the Arctic project (SHEBA) an instrument package was developed to be to be flown from a tethered balloon at the SHEBA ice camp to obtain routine measurements of cloud microphysical parameters from the lower 2 km of the arctic atmosphere in the absence of an aircraft. This instrument was developed from the basis gained from a prior development project (Wetzel et al., 1996). It was decided that a package that could be launched from a tethered balloon would provide the measurements required without the expense of multiple free-launched packages. Instruments of the latter type have been developed in the past (Adriani, Gobbi, Viterbini, and Ugazio; 1993; Murakami and Matsuo, 1990; Muakami, Matsuo, Nakayama and Tanaka; 1987; Magono and Tazawa, 1966). They operated autonomously and provided one sounding through the clouds.

2. INSTRUMENT DESCRIPTION

The instrument, hereafter called a Cloud Videometer (CV) is designed to be remotely controllable, operate over long periods of time at specific altitudes or to provide a sounding of cloud microphysical properties. Other instruments can be interfaced to the CV providing multiple parameter soundings. The altitude over which measurements can be made is limited by the balloon system available. The system designed for the SHEBA program included a hot tether/winch (built by SPEC, Inc.) which can power the instrument for an indefinite period of time. Power dissipation along the tether permits operation in icing conditions. The power up, data down tether with two conductors is larger than the normal Kevlar tether resulting in additional drag and weight which limits the maximum altitude of operation to 1 km with a 9 m^3 balloon. The CV is also designed to operate on battery power. This limits the duration of operation but allows greater heights to be achieved. This also permits the instrument to be flown form any airborne platform capable of providing sufficient power.

The CV operates in two modes. One to measure cloud droplets in the 2 - 50 micron diameter

TABLE 1
CLOUD DROPLET AND ICE PARTICLE VIDEOMETER SPECIFICATIONS

Description: Inertial impaction of cloud droplets and ice particles with microvideography and subsequent PC-based image analysis of size and number concentration.

Impactors:

CDV: Jet dia.- 0.8 mm, Jet velocity - 25 ms^{-1}, Min det. drop size- 2 μm dia.; Max drop size- approx. 50 μm dia., Coll. eff.. 100% at 2 μm dia.

IPV: Jet dia.- 6.1 mm, Jet velocity - 2.7 ms^{-1}, Min det. part. size - 50 μm dia., Max part. size approx. 1 mm, Coll. eff. 100% at 50 μm dia. water sphere equivalent.

Power: Rechargeable Li-ion batteries/power tether: 12VDC

Weight: CDV and IPV 3.5 kg, CNC module 1.5 kg

Dimension: 13 cm dia. X 130 cm length w/o CNC

Operation: 1.25 hrs w/batteries, unlimited w/power tether.

Data Rate: For 100 cm^{-3} cloud droplets 10 s/ spectra, for 1/l ice particle 1 hr/spectra.

Controls: Remote RF modem control of film drive speed, video focus, illumination, heated inlet temp., sample pump flow, alternate heat (power tether only).

Frequencies: Spread spectrum RF modem: 902-928 MHz w/30 km range, Video: 1687.0 MHz w/8 km range.

Other data: Two pressure and two temperature channels to monitor flow rates and ambient temp. and press.

Operation: Icing condition capable, variable flowrate for isokinetic control, add-on capability of CNC or other instrumentation.

Measured cloud parameters: Ice particle and cloud droplet size and concentration, cloud liquid and ice water content, droplet average, mode and effective radius, layer optical depth, interstitial aerosol concentration, ice particle habit.

Author address: Randolph D. Borys, Storm Peak Laboratory , Desert Research Institute, P. O. Box 770799, Steamboat Springs, CO 80477; email: borys@dri.edu.

range called a Cloud Droplet Videometer (CDV) and the other to measure ice particles in the range 50 - 1000 microns called an Ice Particle Videometer (IPV). During SHEBA the CV flew with a TSI Model 8020 CN counter allowing measurements of the aerosol concentration in the 0.02 to 1.0 micron size range and a 4-Pi radiometer (designed by K. Stamnes) to measure solar actinic flux The CV specifications are listed in Table 1.

The physical layout of the CV is shown in figures 1 and 2. These pictures are of the CV without

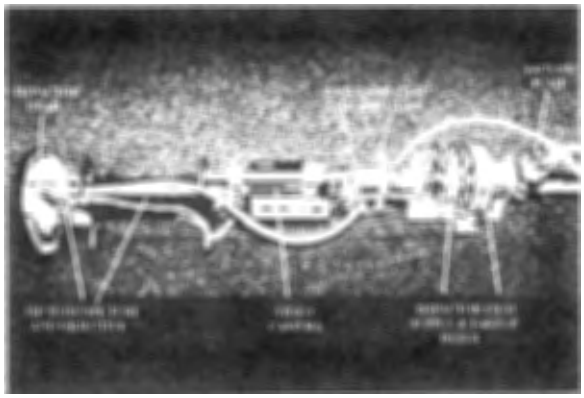

Figure 1. The forward measurement section of the CV showing the impactor head, microscope, video camera, film drive mechanisms and vacuum pump.

its protective case which consists of rigid 1.25 cm thick foam pipe insulation. This provides impact protection and also insulation for operations in cold conditions. Battery life was extended by placing chemical hand-warmer packets on the battery pack prior to flight when ambient temperatures dropped below -20° C.

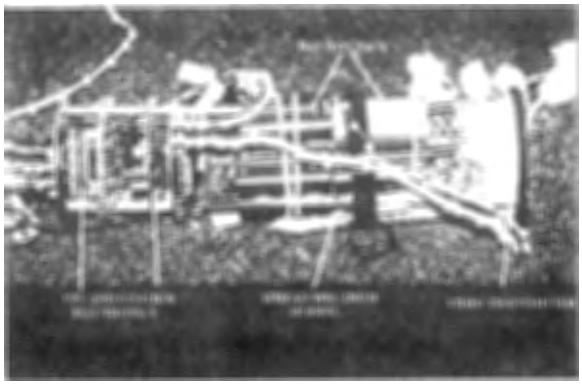

Figure 2. The rear section of the CV showing the CPU boards, placement of the spread-spectrum modem and battery pack with the video transmitter mounted to the back end cap. The white plastic connectors interfaced with the auxiliary equipment including the CNC, 4-Pi radiometer and heaters.

3. MEASUREMENTS

Figures 3, 4 and 5 are examples of droplet images acquired with the CV during SHEBA. Figure 6 is an example of an ice particle image. These images are then analyzed using PC-base image analysis software to count and size the droplets. Ice particles are analyzed manually for habit, size and concentration.

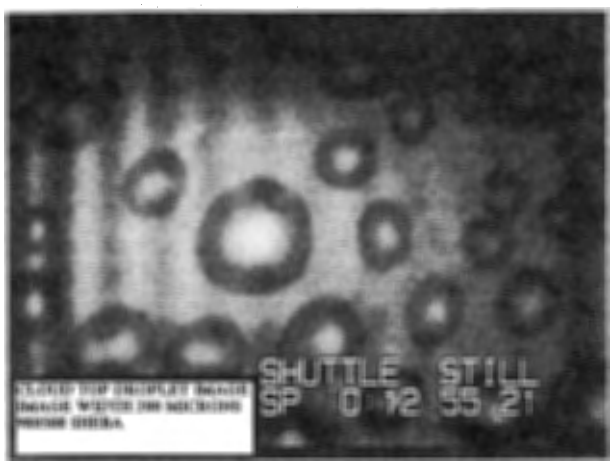

Figure 3. Images of cloud droplets at cloud top in arctic stratus.

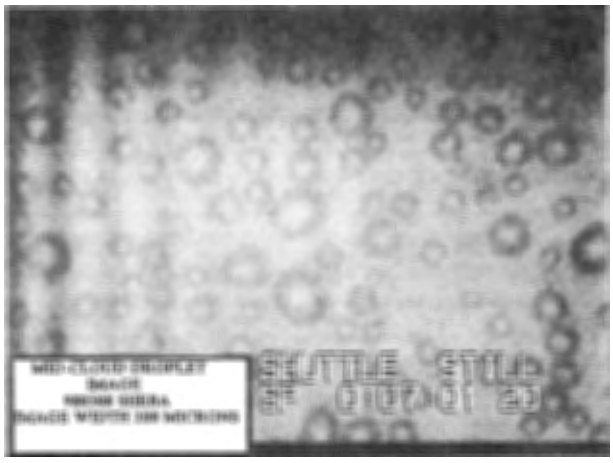

Figure 4. Images of cloud droplets at mid-cloud in arctic stratus.

In this set of images the growth of droplet size with altitude in the cloud is evident. The ice particle in Figure 6 was collected at cloud base from an arctic stratus cloud.

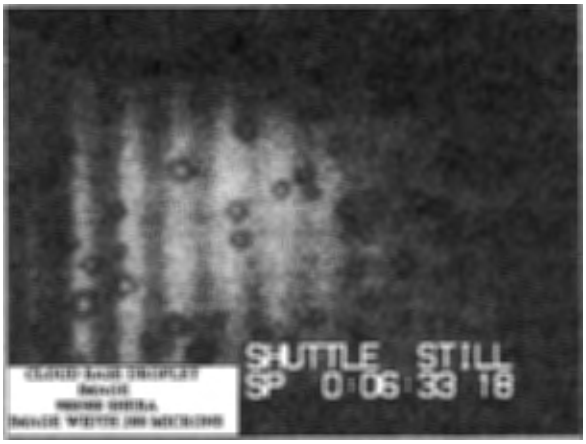

Figure 5. Images of cloud droplets at cloud base in arctic stratus.

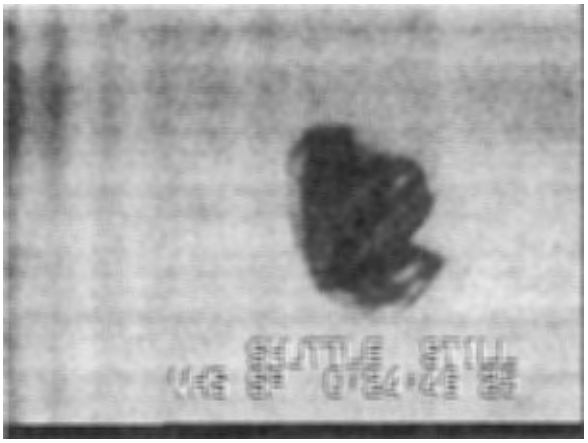

Figure 6. Image of an ice particle collected at cloud base in arctic stratus. Image width 450 μm.

4. ANALYSIS

Figures 7 and 8 are droplet spectra derived from the CV data collected on SHEBA. These data have not been corrected for size and should be considered preliminary.

Figures 9 and 10 are CN soundings obtained during SHEBA during overcast and clear conditions. Figure 9 is a sounding obtained on a clear day showing different aerosol concentrations above and below the inversion where winds were southerly and easterly respectively. Figure 10 shows very clean conditions below cloud base at 300 m. Above cloud base CN concentrations drop to zero suggesting all the particles functioned as CCN.

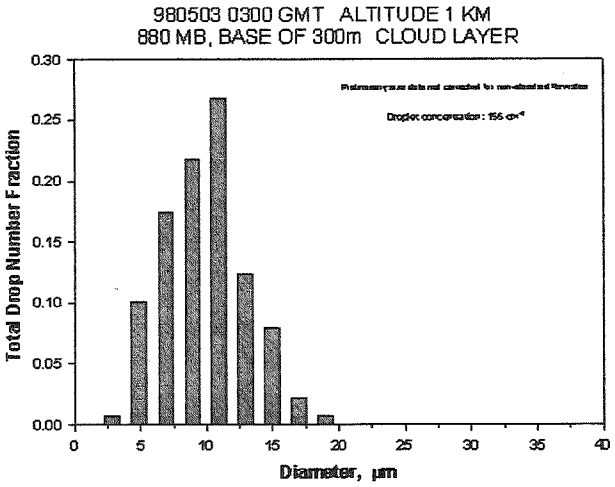

Figure 7. Droplet spectra at cloud base in arctic stratus.

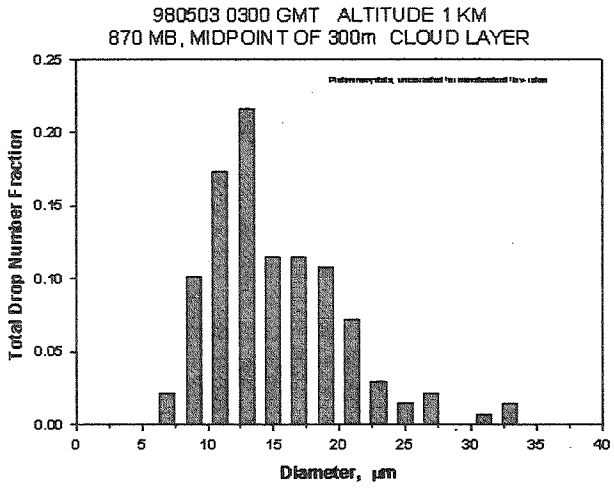

Figure 8. Droplet spectra from mid level of 300m deep arctic stratus.

5. CONCLUSION

A tethered balloon cloud microphysics and aerosol sounder, a Cloud Videometer (CV), is described and preliminary data from the instrument presented. Operating in two modes, the CV can measure cloud particles from 2 μm to 1 mm diameter. The CV can operate on battery or with a powered tether to altitudes exceeding 2 km. Additional control and power ports allow the CV to be interfaced with other instruments. Coupled with a meteorological sounding package, the CV can provide a wealth of information about the state of the lowest levels of the atmosphere as well as the microstructure of fogs and low clouds.

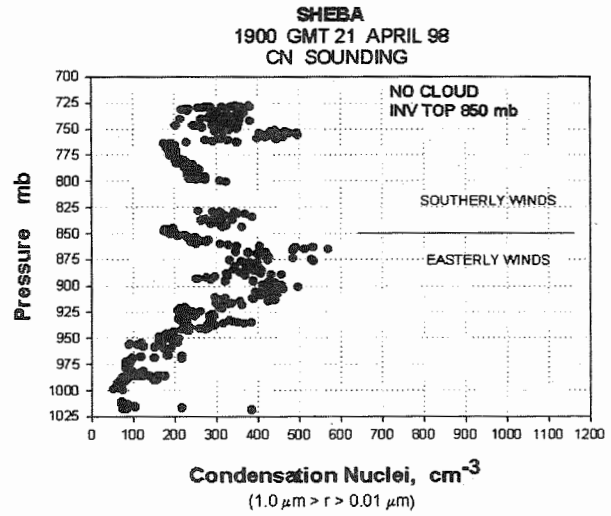

Figure 9. CN sounding through the surface inversion showing a maximum in aerosol concentration at the top of the surface inversion.

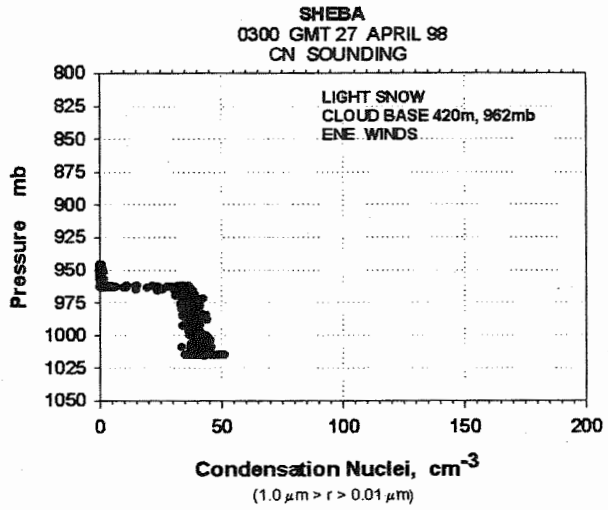

Figure 10. CN sounding through cloud base indicating all aerosol function as a CCN.

6. ACKNOWLEDGMENTS

This work was supported by the Office of Polar Programs, National Science Foundation Grant 9703565. The author wishes to acknowledge Dan Wermers for the design and fabrication of the electronics package, Rick Purcell for the design and fabrication of the mechanical components and Morien Roberts for the software design. The author also appreciates the support of Dr. Peter Barber during the building phase and the crew of the C.C.G.S. *Des Groseilliers* without whose efforts the deployment of the equipment during SHEBA would not have been possible.

7. REFERENCES

Adriani, A., G.P. Gobbi, M. Viterbini, and S. Ugazio, 1993: Combined system for observations of trop[ospheric and stratospheric thin clouds. *J. Atmos. Ocean. Tech.*, **10**, 34-44.

Magono, C. and S. Tazawa, 1966: Design of a "snow crystal sonde". *J. Atmos. Sci.*, **23**, 618-625.

Muakami, M., T. Matsuo, T. Nakayama and T. Tanaka, 1987: Development of cloud particle video sonde. *J. Meteor. Soc. Japan*, **65**, 803-809.

Murakami, M. and T. Matsuo, 1990: Development of the hydrometeor videosonde. *J. Atmos. Ocean. Tech.*, **7**, 613-620.

Wetzel, M.A., R.D. Borys and L. Xu, 1996: Satellite microphysical retrievals for land-based fog with validation by balloon profiling. J. Appl. Meteorol., **35**, 810-829.

A FAMILY OF ULTRAFAST AIRCRAFT THERMOMETERS FOR WARM AND SUPERCOOLED CLOUDS AND VARIOUS TYPES OF AIRCRAFT

K. E. Haman[1], S. P. Malinowski[1], A. Makulski[1], B. D. Struś[1], R. Busen[2], A. Stefko[3] and H. Siebert[4]

[1]Warsaw University, Institute of Geophysics, PL-02-093 Warsaw, Poland
[2]DLR Oberpfaffenhofen, Institute of Atmospheric Physics, D-82234 Wessling, Germany
[3]Faculty of Power and Aeronautical Engineering, Warsaw University of Technology, PL-00-663, Poland
[4]Institute for Tropospheric Research, D-04303 Leipzig, Germany

1. INTRODUCTION

In recent years a number of cloud physicists paid attention to small-scale inhomogeneities in clouds, recognizing that they may play a crucial role in many fundamental microphysical and dynamical processes. Knowledge of the fine scale structure of dynamical and thermodynamical parameters in clouds (particularly in the convective ones) is fundamental for understanding the dynamics of entrainment and mixing processes. In turn, the latter control a good deal of both microphysics and bulk dynamics of these clouds. Particularly important questions refer to the time and space scales of the inhomogeneities created by early stages of mixing as well as to the speed and nature of their evolution towards full homogenization of the cloudy air. Small scale inhomogeneities of temperature and humidity may result in high local supersaturations creating conditions for formation of a large droplet "tail" of the spectrum and subsequent speeding up the coalescence process.

Unfortunately the fine scale processes - scales of order 10^{1} - 10^{-3}m - are extremely difficult to investigate. Resolution of remote sensing instruments is much too poor for this purpose and that of the *in situ* techniques is in most cases also not good enough. In the case of temperature the indications of typical immersion airborne thermometers are strongly contaminated by the influence of their supports and housings and their effective time constants are usually of the order 10^{-1}s or more. For typical airspeeds of research aircraft this permits a spatial resolution of the order 10 - 100m; radiometric instruments are faster, but their measurements are averaged over relatively big volumes and thus their spatial resolution is not much better.

In efforts to overcome these limitations the authors of the present paper developed a new airborne immersion thermometer in which the sensor is protected against impact of cloud droplets by means of a thin rod, which has negligible thermal influence on the measured temperature. It was named UFT (for ultrafast thermometer) and described in detail in the paper by Haman and al. (1997). The time constant of its sensing elements is of an order 10^{-4}s (what permits spatial resolution going down to centimeters - fairly close to Kolmogorov scale). Some preliminary results of measurements made with use of this instrument can be found in the papers by Haman and Malinowski (1996a,b). Unfortunately aerodynamic disturbances behind the anti-droplet rod induced adiabatic fluctuations of temperature, which at airspeeds exceeding 40 ms^{-1} became intolerably strong. This limited the applicability of this instrument to slow aircraft or gliders; on faster aircraft some filtering of the record became necessary what resulted in considerable loss of spatial resolution

Efforts aimed at overcoming this limitation brought to development of a bigger family of ultrafast thermometers based on similar principle but adapted for use on various platforms and in various conditions. In order to introduce certain logical rule in naming various members of this family we decided to refer to this early instrument as UFT-S (S for slow), reserving the acronym UFT for the whole family.

In the present paper four new members of this family are presented on the background of the „old" UFT-S. These are: UFT-F (F for fast), its variety UFT-D (D for deiced), UFT-B (B for balloon) and UFT-St (St for stratosphere). UFT-F was designed for use on faster aircraft at airspeeds 50 to 100m/s or perhaps more. In order to reduce the aerodynamic noise the anti-droplet rod was redesigned and endowed with a suction system effectively damping excessive aerodynamic disturbances. UFT-D was designed for use in supercooled clouds, in response certain theoretical considerations (Korolev and Isaac 1998) suggesting that very small scale inhomogeneities in supercooled, low level clouds may be essential for creating dangerous icing conditions. UFT-D works on similar principle like UFT-F, but has different mechanical design which permits all its icing-sensitive parts to be electrically heated.

Intention of extending UFT family to use in very slow airflow on such platforms like airships or tethered balloons led to construction of UFT-B. Protective rod could be here only of secondary importance. Instead, the sensing wire is being periodically cleaned from collected droplets with short bursts of compressed air.

Interest in small scale structures in stratospheric turbulence resulting mainly from breaking of gravity waves gave impulse to design the UFT-St. In UFT-St the sensing wire is protected only during climbing through troposphere. In stratosphere which is clean and free of droplets and crystals the protective cover is deflected, exposing the sensing wire directly to the airflow.

In the following more details on the construction and exploitation of UFT instruments are presented.

Corresponding author's address: K. E. Haman, Institute of Geophysics UW, Pasteura 7, PL-02-093 Warsaw, Poland; E-mail: khaman@fuw.edu.pl

2. CONSTRUCTION OF UFT INSTRUMENTS

2.1 UFT-S

The basic design of key mechanical components of the UFT-S thermometric unit is shown in Fig.1.

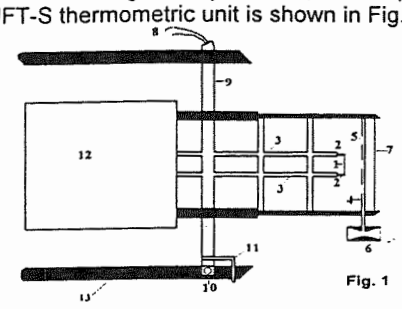

Fig. 1

Fig. 1. Schematic view of UFT-S. See text for details.

The device consists of a light, well-balanced pivoting frame with an attached wind vane. The front part of the frame is a thin, suitably shaped rod, which acts as an anti-droplet shield and mechanical protection for the sensing element - an ultra-fine thermoresistive wire. The vane fixes the position of the shielding rod upwind with respect to the local instantaneous flow. The sensing element (1) is a thermoresistive, platinum coated (9% platinum) tungsten wire, 2.5μm thick and 5mm long. In a room temperature its resistance is about 50 ohms, depending on individual manufacturing and mounting differences. Wire ends are soldered to a 0.3mm Teflon-insulated copper supports (2), hidden in 0.8mm stainless-steel tubs (3). The sensing wire is located 6.5mm behind the rod (4) which protects it against wetting by cloud droplets as well as from destruction by other objects like insects, sand grains, etc.). The rod is made of a 1.1mm thick, stainless-steel tube deformed to a hollow, triangular cross-section with back wall 1.3mm wide. Two or three holes (5) in the back wall of the rod permit removal of water collecting behind the rod; it can be sucked out by means of a small Venturi nozzle (6) attached to the rod. The protective effects of the rod are additionally enhanced by a 0.25mm thick nylon thread (7) located 3mm ahead of the rod. Two copper connectors (8) connect the supports electrically to a three-wire extension line. They are made of soft, flexible litz wires so that the frame can rotate freely around the stainless-steel shaft (9) on a ball-point bearing (10), directed against the wind by vane (12). The bearings of the rotatable frame are placed at the ends of a stiff, fork-like support (13), located in an aerodynamically undisturbed place on the aircraft (preferably on a boom), with the shaft of wind vane directed vertically.

The three-wire extension line connects the sensor with the electronics box so that the sensing wire becomes a branch of a typical Wheatstone bridge. The outgoing signal is amplified and filtered with a low-pass filter adjusted to the characteristics of the recording unit in use.

Laboratory and in-flight tests described more detaily in Haman et al (1997) have shown that the effective sensitivity of this instrument is limited mostly by adiabatic temperature fluctuations in the eddies in the aerodynamic wake of the anti-droplet rod. The direct thermal influence of the rod is small - not more than about 3% of temperature difference between the rod and the sensor - but the wake effects increase with the airspeed - at 100m/s their amplitude becomes greater than 1K. At airspeeds 30 - 40 m/s these disturbances are smaller than ±0.1K, what looks acceptable. Example of measurements made at such low speeds from a powered glider is shown in Fig.2.

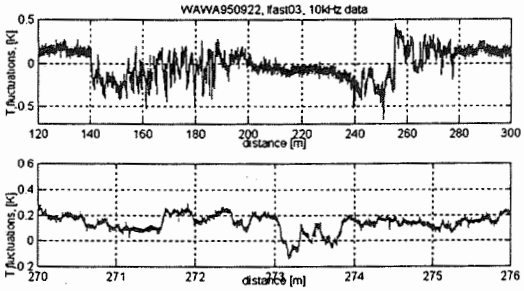

Fig. 2. Fragment of record taken with UFT-S at 30 m/s.

2.2 UFT-F

The UFT-F sensor presents a version of UFT redesigned in order to eliminate the excessive thermal "noise" created by aerodynamic fluctuations in the wake of the protective rod. The main idea was to reshape the rod into an airfoil-like device and apply suction to its boundary layer in order to suppress the eddies which were suspected to be the main source of the problem.

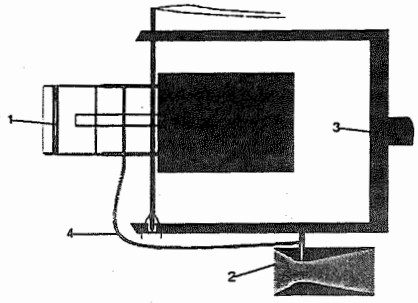

Fig. 3. Schematic view of UFT-F. See text for details.

Fig. 3 shows schematically the general view of the recent design of UFT-F. In order to suppress the eddies behind the protective rod, its surface layer is sucked off by means of two slots 0.3x12mm (1) located just behind the camber of the rod's profile; the slots also collect and remove water swept by the rod within clouds. A big Venturi nozzle (2) with 32mm inlet diameter, fixed to the supporting fork (3) and connected with the sensor's frame by means of a thin, elastic silicone tube (4), creates suction sufficiently

effective for operating these relatively big slots. The frame itself is made of a hermetically sealed stainless steel tubes and serves as a pneumatic connector between the rod and the Venturi nozzle.

In Fig. 4 the record taken with UFT-F while passing through a small convective cloud at speed 160knots (80m/s) is shown. Notice that the noise level doesn't exceed 0.1K.

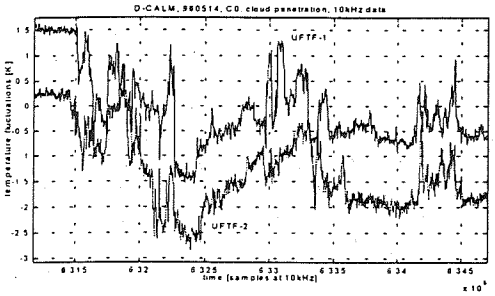

Fig. 4. Fragment of record taken at 80 m/s with two UFT-F sensors located 70cm apart from each other; UFTF-2 shifted down 1°C. Distance between grids is 4m.

2.3 UFT-D

UFT-D is a mutation of UFT-F designed for investigation of icing processes in supercooled clouds. While main idea of functioning remained unchanged a heating system had to be added to prevent accumulation of ice on sensitive parts of the instrument. This forced entire change of design of its mechanical structure. Fig. 5 shows the schematic view of this construction.

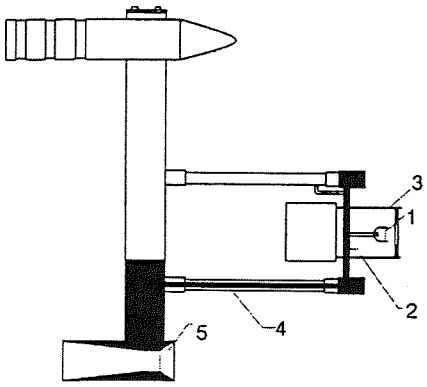

Fig. 5. Schematic view of UFT-D. See text for details.

The main mechanical difference with respect to UFT-F is that while in the latter the frame and vane form an integrated system with the support of the sensing wire, in UFT-D the sensing wire support in form of a small fork (1) is removable. While in the UFT-F in case of damage of the wire, the whole unit including the frame and vane has to be replaced, in UFT-D only the fork with the wire is exchanged. This permitted designing a relatively simple system of electric heating the icing-sensitive parts (marked black on Fig. 5): the shaft with its bearing system (2), the frame with protective rod (3), the water removal channel (4) with the big Venturi nozzle (5) and the small fork with sensing wire (1) as well. The shaft in this design is made of a hollow fiberglass pipe which serves as a duct for air-sucking and water-removal system. It is plated with 0.2 mm thick stainless steel, which forms a complex design and serves as an electric heater. In contrary to one point-ball bearing in UFT-F, the shaft turns on two well sealed ball bearings, which nests filled with silicone grease are also electrically heated. The frame with protective rod is made of one 1.8mm thick stainless steel tube and is electrically heated by current flowing directly through it. Venturi nozzle (which is particularly sensitive to icing) is embedded in heated glycol bath which is also electrically heated. The heating system is supplied from aircraft 28VDC network. Its total resistance should be adjusted to provide current sufficient for heating the protective rod and the shaft above the melting point for expected flying conditions. Usually it is about 7 - 10A. Example of a record from one of flights with UFT-D is presented in Fig.6.

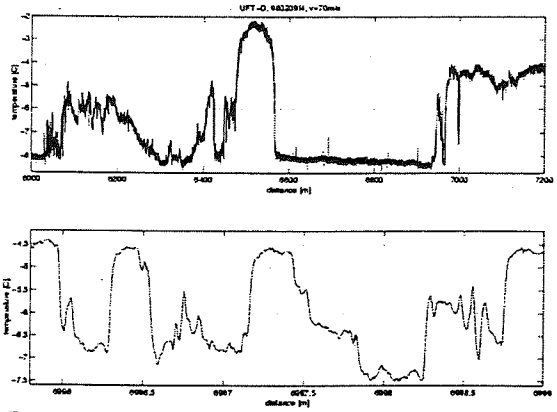

Fig. 6. Fragment of record taken with UFT-D at 100 m/s in icing conditions.

More details on UFT-F and UFT-D can be found in Haman et al. (2000).

2.4 UFT-B

UFT-B is a variety of UFT which is supposed to work on an airship or tethered balloon in warm clouds and weak airflow. In such conditions neither the rod from UFT-S nor UFT-F can be effective against impact of cloud droplets. However, it was found in laboratory experiments that in airflow faster than 20m/s no droplets can stick to the 2.5 μm wire. The UFT-B sensor (schematically shown in Fig. 7, looking from the direction of prevailing airflow or wind) takes advantage of this fact. Its sensing wire (1) is fixed 10mm in front of a flat nozzle (2) through which each second a short blow of dry, compressed air cleans the wire of few droplets which in this time may stick to it. The blow of speed over 50m/s lasts about 20ms and creates a cloud of disturbed air, which in about 0.2s is displaced behind the sensor by a cross-wind even as weak as 1m/s. During this 0.2s indications of the

sensor may be false. In order to have continuos measurements a second sensor (3) , with nozzle fixed in direction opposite to the first one and working intermittently with it, is installed. Both sensors are mounted together on a rotatable frame (4) with vane (perpendicular to the plane of Fig. 7 and not visible on it) which keeps them properly oriented with respect to the wind.

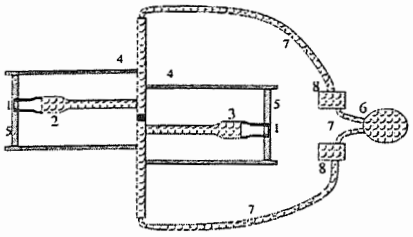

Fig. 7. Schematic view of UFT-B (not in scale). See text for details.

Additionally both sensors are protected by rods (5), identical as in UFT-S. They may be effective as mechanical protection against impact of insects, or even cloud droplets if the wind is sufficiently strong or the airship moves with sufficient speed. The compressed air for cleaning the wire is stored in small high pressure bottle (6) and directed to the nozzles through plastic pipes (7) and electronically controlled valves (8).

2.5 UFT-St

UFT-St (schematically shown in Fig. 8) was designed for measurements in the stratosphere, where wetting of the sensor nor impact of any hard objects is not to be expected, but where aerodynamic noise from the protecting rod may mask weak variations of temperature which are there the main point of interest.

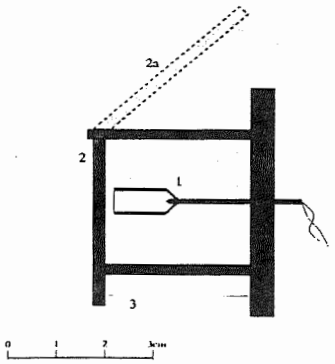

Fig.8. Schematic view of UFT-St. See text for details.

Thus the UFT-St uses the same type of sensor as UFT-D in form of a small fork, (1) protected mechanically against destruction during climbing by a hollow cover (2). The cover is spring loaded and kept in place by a thin wire (3) which is electrically burnt after reaching the operational level. In that moment the cover deflects (2a) and exposes the sensing wire directly to the airflow. The sensor may become destroyed during return, but it was found that replacing it for each flight is a more practical solution than developing a separate mechanism protecting the sensor during the descent. UFT-St is mounted on the aircraft in the support of UFT-F, but has no vane nor rotatable shaft, which are not necessary in this case.

3. CONCLUDING REMARKS

Until now, UFT sensor was used for investigation of small scale structure of clouds with powered glider Ogar in vicinity of Warsaw, with 1kHz and 10kHz recording, and on Meteo-France Merlin IV aircraft in the Small Cumulus Microphysics Study in Florida in August 1995 (with samplig rate reduced to 250Hz for aerodynamic noise elimination). UFT-F was tested in a number of flights through small Cumuli on Do-228 aircraft belonging to DLR Oberpfaffenhofen (10kHz sampling). UFT-D was flown on Canadian Convair 580 in 3rd Canadian Freezing Drizzle Experiment in January-February 1998 as well as Alliance Icing Research Study in winter 1999/2000. Results from these flights look interesting and are subject of further studies to be published elsewhere. UFT-B and UFT-St are to be used in close future in study of boundary layer clouds (UFT-B) and stratospheric turbulence (UFT-St).

4. AKNOWLEDGMENTS

The authors are due much to assistance of numerous colleagues who for the lack of space cannot be presented by names. Apart from the authors mother institutions, help from CNRM (France), NCAR (USA) and AES (Canada) should be acknowledged. The research was also supported by Grant 6 P04D 009 08 of the Polish Committee for Scientific Research.

5. REFERENCES

Haman, K. E., and S. P. Malinowski, 1996a: Temperature measurements in clouds on a centimeter scale - preliminary results. *Atmos. Res.*, **41**, 161-175.

Haman, K. E., and S. P. Malinowski, 1996b: Structure of a temperature field in small Cumuli on a centimeter scale. *12 th Int. Conf. on Clouds and Precipitation, Zurich, Switzerland, ICCP - IAMAS,* 510-513.

Haman, K. E., A. Makulski, S. P. Malinowski, and R. Busen, 1997: A new ultrafast thermometer for aiborne measurements in clouds. *J. Atmos. Oceanic Technol.*, **14**, 217-227

Haman, K. E., S. P. Malinowski, B. D. Struś, R. Busen, A. Stefko, 2000: Two New Types of Ultrafast Aircraft Thermometer, *J. Atmos. Oceanic Technol.* (in press)

Korolev, A. V and G. A. Isaac, 1998: Drop growth due to high supersaturation caused by isobaric mixing. *Conference on cloud physics, 17-21 August 1998, Preprints,* Everett, Washington, USA, American Meteorological Society, 542-545.

COMPARISON OF FAST FSSP, PVM AND KING PROBE MICROPHYSICAL MEASUREMENTS DURING ACE 2

S. Schmidt[1], M. Wendisch[1], J.-L. Brenguier[2]

[1]Institute for Tropospheric Research (IFT), Leipzig, 04318, Germany
[2]National Center of Meteorological Research (CNRM), Toulouse, 31057, France

1. INTRODUCTION

Widely used instruments for in-situ measurements of cloud microphysical properties are the King Probe, the Particle Volume Monitor (PVM), and the Forward Scattering Spectrometer Probe (FSSP). The King Probe (King et al., 1978) is a hot-wire instrument that measures the liquid water content (*LWC*), which is proportional to the heat of vaporization of impinging cloud drops. The PVM (Gerber 1991, Gerber et al. 1994) detects the light scattered by a drop population illuminated by a laser beam, which is related to *LWC* and the effective drop radius R_{eff}. The FSSP (Dye and Baumgardner, 1984) is a single particle counter for measuring drop size distributions. Problems of this probe are related to its long electronic dead time and coincidence-events (more than one droplet simultaneously in the sampling volume) which entail an underestimation of the droplet concentration and of the *LWC* (Brenguier and Amodei, 1989). To reduce these effects, a modified version, the so-called Fast FSSP, was developed at CNRM (Brenguier et al., 1998). Digital electronics almost eliminates dead time losses, and a modified optics reduces the sampling volume, thereby diminishing coincidence. Storing the series of size, pulse duration, particle interarrival time and a flag for the droplet position with respect to the depth of field (DOF flag) of *every* droplet provides a fine spatial resolution for airborne measurements down to the centimeter scale. Using a nonlinear optimal estimation technique permits low concentration measurements (Pawlowska et al., 1997). The high size resolution (256 adjustable channels) allows a self-calibration of the probe (Brenguier et al., 1998).

In 1997 during ACE 2 (Aerosol Characterization Experiment), for the first time two Fast FSSPs (owned by CNRM and IFT), a King Probe and a PVM were flown in parallel on one aircraft (French Merlin). For these instruments, drop size distributions, effective drop radius, drop concentration, and *LWC* measurements are compared.

2. SIZE DISTRIBUTIONS

Figures 1a and 1b show size distributions (1a: monomodal, 1b: bimodal) measured with the two Fast FSSPs (hereafter referred as Fast FSSP 1 and Fast FSSP 2) using different accumulation times. The spikes in the distributions are partly due to inhomogeneities of the Mie response curve. These become visible only with the high size resolution of the Fast FSSPs. They are superimposed by the statistical counting process which gives a high noise at low droplet rates. The agreement

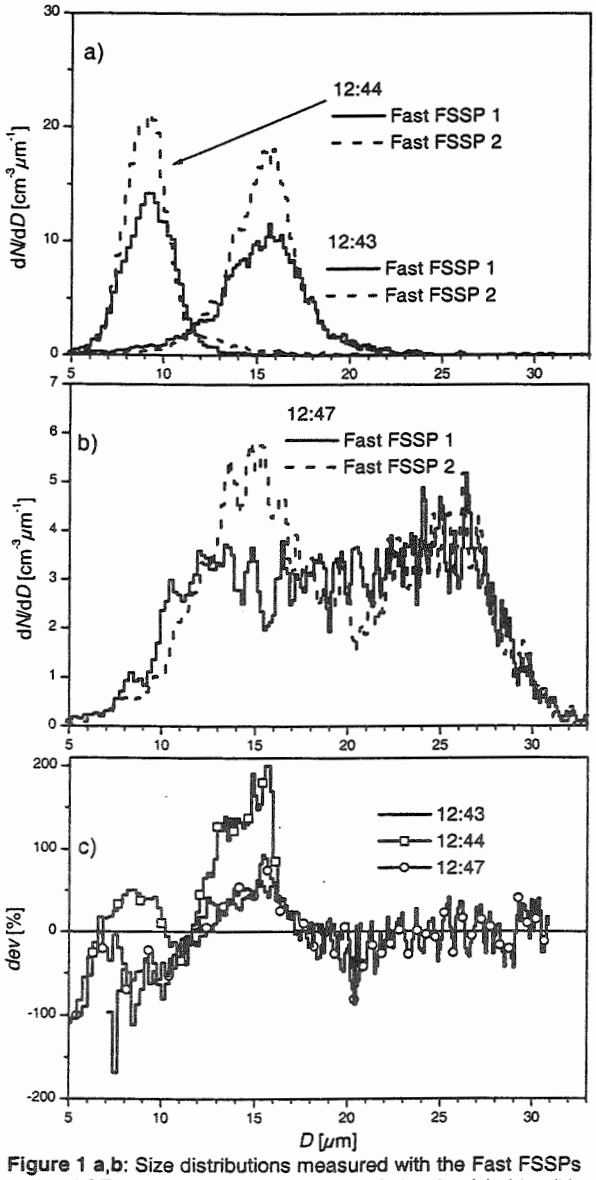

Figure 1 a,b: Size distributions measured with the Fast FSSPs during ACE 2 on June 26, 1997; accumulation 2 s (a), 20 s (b), **c:** relative deviation of size distribution levels in percent

of the two probes with regard to the drop size measurement is very good (distance between the peaks of the distribution about 0.5 μm). However, there are considerable size-dependent discrepancies between the *levels*

Corresponding author's address: Sebastian Schmidt, Institute for Tropospheric Research, Leipzig, Permoserstr. 15, 04318 Leipzig, Germany; E-Mail: schmidt@tropos.de

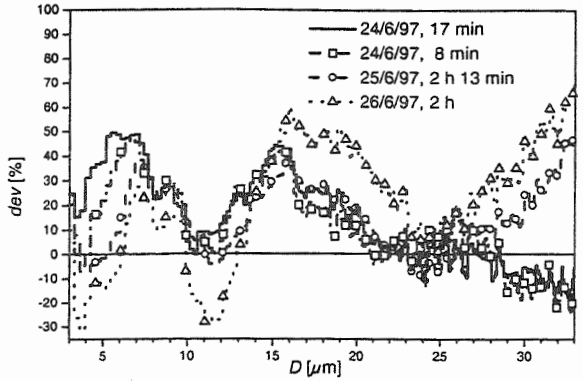

Figure 2: Relative deviation of size distributions accumulated for long times for three different days

of the distributions. This is quantified in Figure 1c, where the deviations

$$dev(D) = 2\frac{[dN/dD(D)]_2 - [dN/dD(D)]_1}{[dN/dD(D)]_2 + [dN/dD(D)]_1} \times 100\%$$

between Fast FSSP 1 and Fast FSSP 2 are plotted. Especially for $D<17$ μm the relative differences between both Fast FSSPs are significant.

In order to make sure that the deviations in Figure 1c are no statistical fluctuations, the distributions of three subsequent flights were accumulated over long time intervals. The deviations of the two Fast FSSPs for these periods are shown in Figure 2. The effects of over- or underestimation of the drop concentration in the respective size regions are quite persistent throughout the flights considered.

A possible reason for these discrepancies could be a size-dependent sampling volume. For the commercial FSSP, Dye and Baumgardner (1984) have found that it increases for small sizes. For the Fast FSSP with *reduced* sample volume there is a more complicated dependence. It is different for the two examined probes and depends on their specific opto-electronic configuration.

3. EFFECTIVE DROP RADIUS, CONCENTRATION AND LWC COMPARISON

In Figure 3a, 4a and 5a, vertical profile measurements of R_{eff}, total drop concentration C and LWC for a flight on June 24, 1997, are plotted. Figures 3b, 4b and 5b relate the data to a reference (Fast FSSP 2).

Figure 3a shows the profile of R_{eff}. There is a nearly perfect correspondence for R_{eff} measured by the two Fast FSSPs which proves the high sizing accuracy of the two instruments. The PVM, however, measures lower effective drop radii, especially for low drop concentrations (cf. Figure 4). The correlation of this difference between Fast FSSP and PVM derived R_{eff} with the

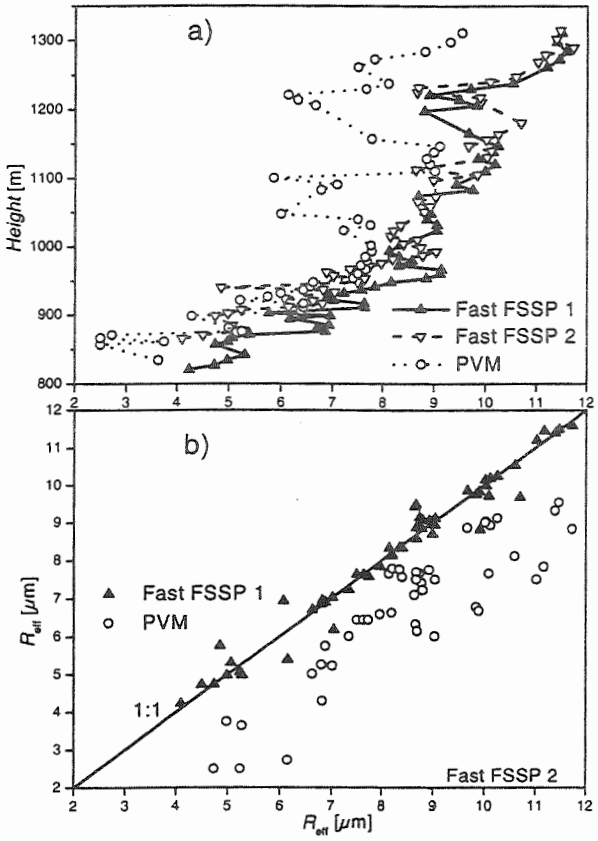

Figure 3: Effective radius - **a:** profile; **b:** vs. Fast FSSP 2

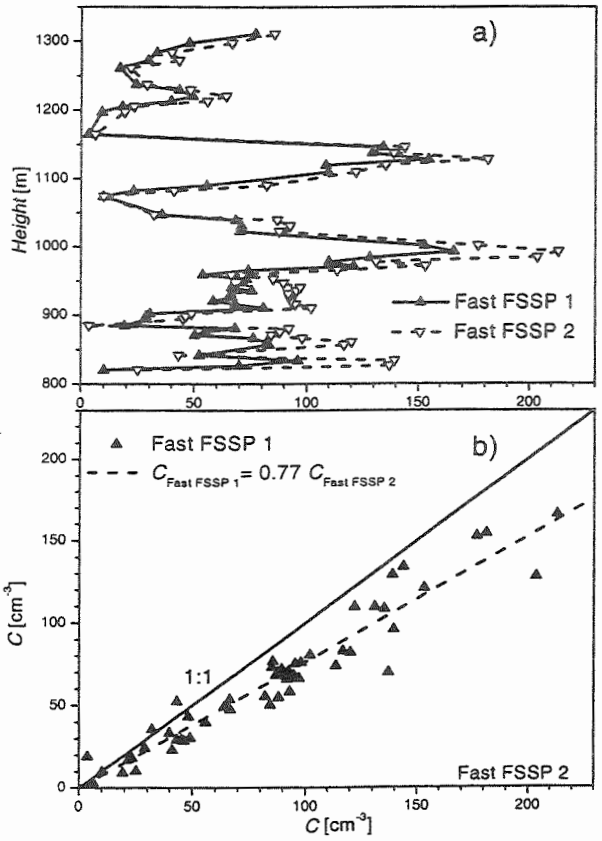

Figure 4: Total drop concentration - **a:** profile; **b:** vs. Fast FSSP 2

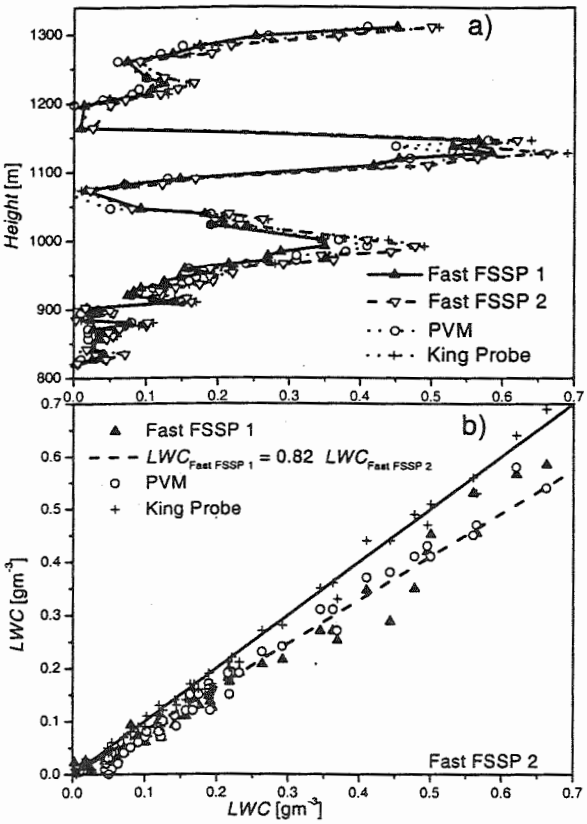

Figure 5: Liquid water content - a: profile; b: vs. Fast FSSP 2

drop concentration is not explicitly shown here.

In Figure 4, total drop concentration measurements are presented. As for the size distributions, there are differences between the two Fast FSSPs for the total drop concentration as well. On average, Fast FSSP 1 measures a 23 % lower drop concentration compared to Fast FSSP 2. This affects the *LWC* derived from the size distribution, which is shown in Figure 5. The *LWC* values correspond quite well for all instruments. The data from the King Probe rather agree with the data from Fast FSSP 2, whereas the PVM measurements correspond with Fast FSSP 1. Fast FSSP 1 measures about 18 % less than Fast FSSP 2 which can be explained by the difference in the concentration values.

4. DISCUSSION AND OUTLOOK

It has been shown that there is an excellent agreement of the drop size measurement between the two Fast FSSPs running in parallel during ACE 2. This is due to the refined size resolution, providing significantly improved calibration compared to the commercial FSSP.

However, there were considerable size-dependent deviations of drop concentration measurements. They arise from the enhanced sensitivity of the reduced sample volume to optical and electronic parameters which possibly results in a size-dependent sample volume. Consequently, the *LWC* is also linearly biased.

One way to exclude this error source for concentration is to measure the sampling volume for a large number of drop diameters (this is usually done for only one size). This problem with the variable sample volume is inherent to all single particle counters. An improved technique for defining the sample volume more precisely and independently of the drop diameter has to be considered.

Presently, a new data acquisition system which can detect coincidences is under development at IFT. This will allow to enlarge the sample volume in order to decrease its sensitivity towards the discussed parameters.

5. ACKNOLEDGEMENTS

We would like to thank Thierry Bourrianne who calibrated and kept up the Fast FSSPs during ACE 2. Stephan Günnel is presently developing the new data acquisition system at IFT. Jost Heintzenberg has continuously supported this work.

REFERENCES

Brenguier, J. L., and L. Amodei, 1989: Coincidence and dead-time corrections for particle counters. Part I: A general mathematical formalism. . *J. Atmos. Oceanic Technol.*, **6**, 575-584.

Brenguier, J. L., T. Bourrianne, A. Coelho, J. Isbert, R. Peytavi, D. Trevarin and P. Wechsler, 1998: Improvements of droplet size distribution measurements with the Fast-FSSP. *J. Atmos. Oceanic Technol.*, **15**, 1077-1090.

Dye, E., and D. Baumgardner, 1984: Evaluation of the Forward Scattering Spectrometer Probe. Part I: Electronic and optical studies. *J. Atmos. Oceanic Technol.*, **10**, 329-344.

Gerber, H. E., 1991: Direct measurement of suspended particulate volume concentration and far-infrared extinction coefficient with a laser-diffraction instrument. *Appl. Opt.*, **30**, 4824-4831.

Gerber, H. E., B. G. Arends and A. Ackermann, 1994: New microphysics sensor for aircraft use. *Atmos. Res.*, **31**, 235-252.

King, W. D., D. A. Parkin and R. J. Handsworth, 1978: A hot-wire liquid water device having fully calculable response characteristics. *J. Appl. Meteor.*, **17**, 1809-1813.

Pawlowska, H., J. L. Brenguier and G. Salut, 1997: Optimal nonlinear estimation for cloud particle measurements. . *J. Atmos. Oceanic Technol.*, **14**, 88-104.

DEVELOPMENT OF AN AXIAL FLOW CYCLONE FOR THE COLLECTION OF CLOUDWATER FROM AN AIRCRAFT PLATFORM

Derek Straub[1], Jeffrey L. Collett, Jr.[1], Darrel Baumgardner[2], and Richard Friesen[2]

[1]Colorado State University, Department of Atmospheric Science, Fort Collins, CO 80523, USA
[2]National Center for Atmospheric Research*, Research Aviation Facility,
P.O. Box 3000, Boulder, CO 80307, USA

1. INTRODUCTION

The presence of clouds in the atmosphere can dramatically alter the concentration and chemical composition of atmospheric aerosols and trace gases. Soluble trace gases can be absorbed into cloud drops, while aerosols can serve as cloud condensation nuclei (CCN) or be incorporated through other scavenging processes. After these species are incorporated, aqueous phase processes occurring in the cloud drops provide a significant pathway for gas to particle conversion, oxidation and neutralization. The evaporation of cloud drops, after chemical reaction or aggregation of multiple scavenged aerosols, can result in the production of new aerosol particles with altered size and chemical composition. Alternatively, cloud drops can be removed from the atmosphere through precipitation scavenging or sedimentation.

In order to investigate these processes, numerous ground-based collection devices have been developed in the past to provide cloudwater samples for chemical analysis (e.g. Munger et al., 1989; Demoz et al., 1996; Collett et al., 1993, 1995; Straub and Collett, 2000). These devices have typically relied on inertial impaction for sample collection, with a number having fairly well characterized 50% cut diameters and efficiency curves.

In comparison to ground-based collectors, fewer devices exist for aircraft-based cloud drop collection. Mohnen slotted-rod collectors (Winters et al., 1979), or modified versions of Mohnen slotted-rod collectors (Huebert et al., 1988) have been used most frequently for aircraft-based cloud sampling. Other aircraft-based cloudwater collection devices employing inertial impaction are the Isokinetic Cloud Water Probing System (ICPS) collector (Maser et al., 1994) and a device described by Khemani et al. (1987). Finally, Scott (1978) designed and built a centrifuge that relied on freestream airflow interaction with angled vanes for rotation and Walters et al. (1983) developed a fixed-vane centrifugal cloudwater separator.

Evaluation of the efficiency and collection characteristics of these aircraft-based devices has generally been quite limited, or nonexistent in some cases, which can lead to inaccurate conclusions regarding the chemical makeup of the sampled cloud. In addition, the aircraft-based collection systems that have been developed in the past have typically been designed for a particular aircraft application and often require manual operation for deployment and sample storage. This has limited previous collectors to use on specific aircraft and to flights that can accommodate the necessary space and personnel requirements.

2. COLLECTOR DEVELOPMENT

In an effort to alleviate the shortcomings of previous aircraft-based collectors, a new, well-characterized aircraft-based cloudwater collection system is under development. The design will improve upon previous aircraft-based collectors by offering a portable, automated collection system that is capable of obtaining multiple, consistent, well-characterized cloudwater samples.

2.1 Collector Design

To provide efficient separation of cloud drops from the ambient airstream, an axial flow cyclone design was selected for the new collection system. This design has the ability to process relatively large quantities of air in a compact space. The collector design (see Figure 1) consists of a 6 cm diameter duct containing fixed, curved vanes. As the incoming air encounters these stationary vanes, the flow is redirected to produce a rotational flow field about the duct centerline. Centrifugal force resulting from the rotational flow acts to remove cloud drops to the duct wall, where they accumulate and are removed through a

*The National Center for Atmospheric Research is sponsored by the National Science Foundation

Corresponding author's address: Derek Straub, Colorado State University, Department of Atmospheric Science, Fort Collins, CO 80523, USA; E-Mail: straub@lamar.colostate.edu

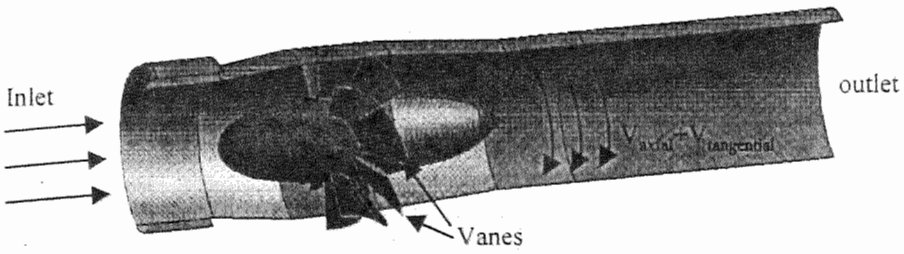

Figure 1. Cut-away view of the axial-flow cyclone cloudwater collector. Eight stationary, curved vanes produce a rotational flow field about the duct centerline. Inlet diameter is 6.0 cm.

circumferential extraction slot. The eight fixed vanes are mounted on a 3.0 cm diameter aerodynamically shaped center body. The design of the vane geometry followed the procedure described by Horlock (1966) for the optimal design of axial flow turbine blades. The vane outlet angle of 65° with respect to the duct centerline was selected to provide a compromise between pressure drop and the ability to extract cloudwater from the duct walls (Walters et al., 1983).

The cloudwater collection system has been designed for eventual use on the NCAR/NSF EC-130Q aircraft, but will be easily portable to other research aircraft through the use of standard mounting and electronic interfaces. The axial flow cyclone collector and the sample storage system will both be contained in a modified Particle Measurement Systems (PMS) canister. This will enable the collector to be placed on any research aircraft that currently supports PMS probe installation. In order to retain multiple cloudwater samples per flight during field campaigns, an automated multiple sample storage system that is integrated with the EC-130Q's on-board control system will be developed.

2.2 Collector Evaluation

Numerical fluid flow modeling was used as a design and analysis tool throughout the collector development process. An analysis of the axial flow collector design was conducted using the finite volume based Computational Fluid Dynamics (CFD) software package, FLUENT (Fluent, Inc., Lebanon, NH). CFD modeling has been applied successfully to a range of multiphase flows (e.g. Chen and Ahmadi, 1997; McFarland et al., 1997; Laucks and Twohy, 1998; Jurcik and Wang, 1995). Straub and Collett (1999, 2000) applied FLUENT's multiphase capabilities in the analysis of two ground-based multi-stage cascade inertial cloud drop impactors with good results.

The interior region of the axial flow collector was modeled to investigate the interaction of the airflow with the vane assembly. Regions upstream of the inlet and downstream of the outlet were also included in the flow domain to allow free stream boundary conditions to be imposed. For the initial modeling effort, free stream conditions typical of research aircraft flights were selected (115 m/s velocity, standard atmosphere at 3000 m elevation). The numerical analysis provided predictions of air flow patterns in and around the collector, the flow rate and pressure drop through the collector, and profiles of temperature and pressure in the interior of the collector.

Continuous phase (air) turbulence was accounted for in the numerical modeling through Reynolds averaging of the governing equations (Fluent, 1996) followed by closure of the turbulent equation set with a Reynolds Stress Model (RSM). Non-equilibrium wall functions (Fluent, 1996) were used to empirically derive flow properties in wall adjacent cells without explicitly solving for viscous effects that are present close to wall surfaces.

Following fabrication of the initial collector hardware, wind tunnel tests will be conducted to assess the actual performance of the collector under well-controlled conditions. This experimental work will provide feedback for verification of the numerical modeling effort. Comparisons between the experimental test results and the numerical predictions are planned.

3. RESULTS AND DISCUSSION

Results from the numerical modeling indicate that the vanes do impart a significant tangential velocity component in the flow field that results in rotation about the duct centerline (see Figure 2). The continuous phase flow solution served as the basis for the investigation of cloud drop motion through the collector. Drops from 0.5 to 50 μm in diameter were released into the continuous phase flow field and tracked until they exited the domain or were captured on surfaces of the collector. Centrifugal force in the rotational flow field caused larger drops to quickly migrate towards the duct wall downstream of the vanes. Smaller drops remained with the flow for a longer duration and impacted the duct wall farther downstream (see Figure 3). The majority of drops smaller than 1 μm in diameter passed through the collector entirely.

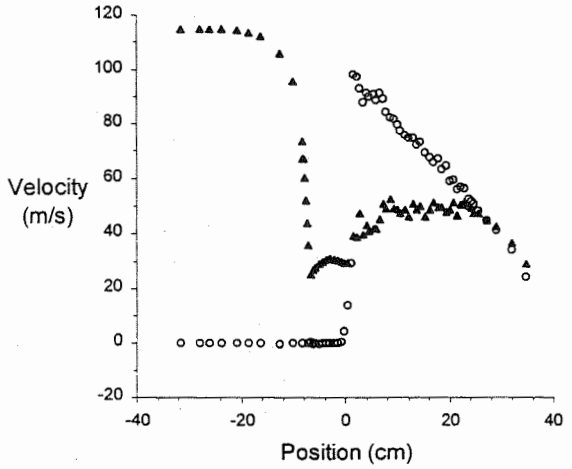

Figure 2. Axial (solid triangles) and tangential (open circles) components of velocity as a function of position through the axial-flow cloudwater collector. The inlet is located at –7.0 cm, the vanes at 0 cm, and the exit at 20.0 cm. The axial component of velocity is reduced at the collector inlet due to partial stagnation conditions. The tangential component is negligible before increasing to 100 m/s immediately after the vanes. The tangential velocity then decays through the remainder of the duct.

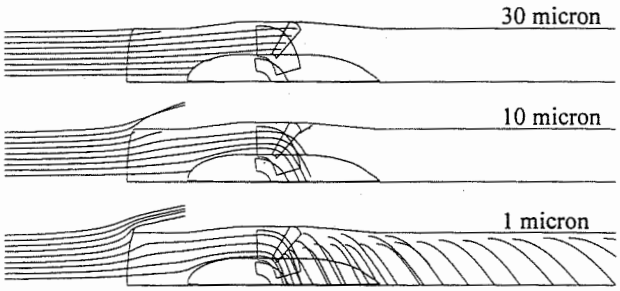

Figure 3. Sample CFD trajectory simulations for 30, 10, and 1 micron drops. The flow domains shown are 90° sections of the axial-flow cyclone duct.

This information proved useful for placing the extraction port, which partially determines the collector's 50% cut diameter and collection efficiency curve. Drops deposited on the duct wall upstream of the extraction port will be available for removal and storage, while drops deposited on the duct wall downstream of the extraction port will remain uncollected. The objective of the axial-flow cyclone cloudwater collector is to obtain samples containing cloud drops representing the entire drop distribution. Based on the numerical trajectory predictions, the extraction slot for the collector was therefore located 3.0 cm downstream of the vanes to provide a 50% cut diameter of approximately 5 μm. This ensures collection of the majority of cloud drop sizes while excluding interstitial aerosol particles and most unactivated haze particles.

By examining the fates of the cloud drops released into the continuous phase domain during the numerical trajectory simulations, the collection efficiency of the axial flow cyclone was evaluated. The collection efficiency as a function of drop size is illustrated in Figure 4. Based on this numerically derived efficiency curve, when sampling a cloud with a liquid water content of 0.3 g/m^3 at an aircraft speed of 115 m/s, the collection rate would be approximately 4.7 g/min. This collection rate should provide sufficient sample volume for chemical analysis, while maintaining adequate time and spatial resolution.

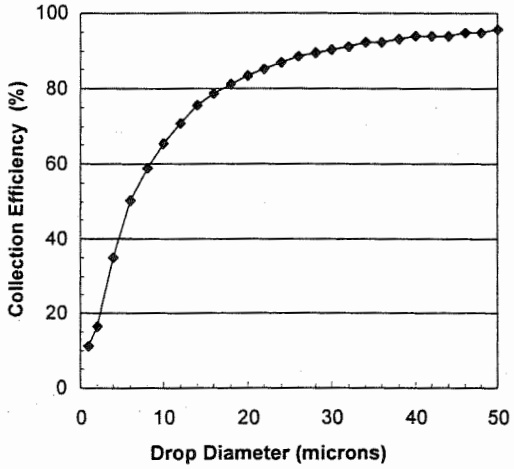

Figure 4. Total collection efficiency as a function of drop size for the axial-flow cyclone collector.

The numerical trajectory simulations have also allowed the investigation of drop shatter in the axial-flow cyclone. The trajectory simulations indicated that a fraction of the drops entering the inlet of the collector posses enough inertia to impact on the surfaces of the stationary vanes instead of remaining with the airflow. If these impacts occur with high enough velocities, drop shattering and secondary droplet formation could result. In the axial-flow collector, the partial stagnation that occurs at the collector inlet reduces the velocity of the drops significantly before they reach the interior vane surfaces. Using impact velocities predicted from the numerical trajectory modeling and the analysis of Cossali et al. (1997), it was found that for drops less than approximately 40 microns in diameter, no splashing should occur in the axial-flow collector. For larger drops, shattering may take place. However, for most typical cloud drop size distributions, the majority of cloud drops are expected to be at sizes smaller than 40 μm, minimizing the occurrence of drop

shattering. In the event that larger drops are encountered, the findings of Mundo et al. (1995) suggest that the majority of secondary drops resulting from shattering should be of sufficient size (10 to 20% of the primary drop diameter) that they will be collected in the rotational flow field downstream of the vanes.

4. COLLECTOR DEPLOYMENT

NCAR's Asian Pacific Regional Aerosol Characterization Experiment (ACE-Asia) and the Megacity Impact on Regional and Global Environment – Mexico City (MIRAGE-Mexico) mission are being explored as two possibilities for collector deployment. Both of these campaigns have substantial cloud/aerosol interaction components that have similar objectives: to study in detail the effects of cloud processing on aerosol particles and the influence of aerosol physical and chemical properties on cloud formation. Both projects would benefit from airborne cloudwater collection and chemical analysis that would help elucidate the local role of cloud processing of aerosols and trace gases.

Specifically, the capacity of the sampled clouds for rapid aqueous phase oxidation of sulfur dioxide to sulfate by various potentially important oxidation pathways will be examined. Rate laws will be taken from the literature to calculate sulfate production rates for S(IV) oxidation by hydrogen peroxide, ozone and oxygen catalyzed by trace metals. The cloudwater pH, and concentrations of aqueous S(IV), trace metal catalysts and hydrogen peroxide will be measured. Cloudwater concentrations of major ions (nitrate, sulfate, chloride, ammonium, sodium, potassium, calcium, and magnesium) and total organic carbon (TOC) will also be measured. Cloud scavenging efficiencies of these species may be determined during periods where appropriate aerosol and gas phase measurements are available.

ACKNOWLEDGEMENTS

We would like to thank A. Cooper and the Advanced Study Program (ASP) for providing financial support for this work.

REFERENCES

Chen, Q., and Ahmadi, G., 1997: Deposition of particles in a turbulent pipe flow. *J. Aerosol Sci.*, **28**,789-796.

Collett, J. L. Jr., Oberholzer, B., and Staehelin, J., 1993: Cloud chemistry at Mt. Rigi Switzerland: Dependence on drop size and relationship to precipitation chemistry. *Atmos. Environ.*, **27A**,33-42.

Collett, J. L. Jr., Iovinelli, R., and Demoz, B., 1995: A three-stage cloud impactor for size-resolved measurements of cloud drop Chemistry. *Atmos. Environ.*, **29**,1145-1154.

Cossali, G. E., Coghe, A., and Marengo, M. ,1997: The impact of a single drop on a wetted solid surface. *Experiments in Fluids.*, **22**,463-472.

Demoz, B.B., Collett, J. L. Jr., and Daube, B. C. Jr., 1996: On the Caltech active strand cloudwater collectors. *Atmos. Res.*, **41**,47-62.

Fluent Incorporated, 1996: *FLUENT User's Guide, Release 4.4.* Lebanon, N.H., Vol. 1-4.

Horlock, J., 1966: Axial Flow Turbines, Fluid Mechanics and Thermodynamics. Butterworth, London.

Huebert, B. J., Vanbramer, S., Tschudy, K. L., 1988: Liquid cloudwater collection using modified Mohnen slotted rods. *J. Atmos. Chem.*, **6**,251-263.

Jurcik, B., and Wang, H. C., 1995: On the shape of impactor efficiency curves. *J. Aerosol Sci.*, **26**,1139-1147.

Khemani, L. T., Momin, G. A., Naik, M. S., Prakasa Rao, P. S., Safai, P. D., and Murty, A. S. R., 1987: Influence of alkaline particulates on pH of cloud and rain water in India. *Atmos. Environ.*, **21**,1137-1145.

Laucks, M. L., and Twohy, C. H., 1998: Size-dependent collection efficiency of an airborne Counterflow Virtual Impactor. *Aerosol Sci. Technol.*, **28**,40-61.

Maser, R., Franke, H., Preiss, M., and Jaeschke, W., 1994: Methods provided and applied in a research aircraft for the study of cloud physics and chemistry. *Beitr. Phys. Atmos.*, **67**,321-334.

McFarland, A. R., Gong, H., Muyshondt, A., Wente, W. A., and Anand, N. K., 1997: Aerosol deposition in bends with turbulent flow. *Environ. Sci. Technol.*, **31**,3371-3377.

Mundo, CHR., Sommerfield, M., and Tropea, C., 1995: Droplet-wall collisions: experimental studies of the deformation and breakup process. *Int. J. Multiphase Flow.*, **21**,151-173.

Munger, J. W., Collett, J. L. Jr., Daube, B. Jr., and Hoffmann, M. R., 1989: Chemical composition of coastal stratus clouds: Dependence on droplet size and distance from the coast. *Atmos. Environ.*, **23**,2305-2320.

Scott, W. D., 1978: The pH of cloud water and the production of sulfate. *Atmos. Environ.*, **12**,917-921.

Straub, D. J., and Collett, J. L. Jr. , 2000: Numerical and experimental performance evaluation of the 3-stage FROSTY supercooled cloud collector. *Aerosol Sci. Tech.*, in press.

Straub, D. J., and Collett, J. L. Jr., 1999: Numerical and experimental performance evaluation of two multi-stage cloud collectors. Department of Atmospheric Science Report No. 676. Colorado State University, Fort Collins, CO.

Winters, W., Hogan, A., Mohnen, V., and Barnard, S., 1979: ASRC airborne cloud water collection system. ASRC-SUNYA Publication 728, Albany, NY.

Walters, P. T., Moore, M. J., and Webb, A. H., 1983: A separator for obtaining samples of cloud water in aircraft. *Atmos. Environ.*, **17**,1083-1091.

SCATTERING CALCULATIONS AND OUTLINE SPECIFICATIONS FOR A GROUND-BASED CLOUD PROFILING RADAR

Norbert Witternigg[1] and Walter L. Randeu[2]

[1] JOANNEUM RESEARCH Forschungsgesellschaft mbH, Graz, Austria
[2] Technical University Graz, Austria

1. INTRODUCTION

Space-borne cloud radars are limited in their spatial resolution and penetration depth, especially what concerns clouds with precipitation and melting region. This is due to the rather high frequencies and large observation ranges used. A complete picture of these volumes, however, would be necessary for a better understanding of the tropospheric water and energy household processes that govern the Earth's radiation budget.

Ground-based cloud radars provide supplementary ground truth data of cloud macro and micro structures while excessive attenuation by structures in and below clouds can be avoided. The purpose of our study was to determine estimates of scattering and propagation parameters to be expected in real world scenarii and from that generate outline specifications for the design of such a radar.

2. SCATTERING CALCULATIONS

2.1 Approach

The simulation of radar returns in realistic cloud scenarii is one important step before the parameter specification of a cloud profiling radar. Scattering calculations for cloud particle distributions are already available from the literature. Most promising results are obtained when combined remote sensors are applied, e.g., see Matrosov (1998). However, there are still not many studies focussing on the scattering properties of ice crystals at mm-wave frequencies and above. Calculations are often limited to only one or two frequencies and a small range of cloud particle types investigated.

We analyzed 6 frequencies (5.6, 14, 24, 35, 78 and 94 GHz) according to available slots in the ITU frequency plan. Our scattering calculations were aimed at sensitivity considerations, power budget and frequency selection for a cloud radar. Trying to cover the range of the most common ice and water clouds, a literature study was performed on the micro and macro physical characteristics of four major cloud types (high clouds, middle layer clouds, low clouds and clouds with precipitation). Size distributions given by the different authors were often particle spectra from airborne cloud measurements with PMS probes (Particle Measuring Systems, one or two dimensional), optical array probes and others. We digitized the number of particles per size class directly and did not convert into parameters of a gamma size distribution. This approach allowed also to treat special cases like bimodal distributions (e.g., as expected in a cloud with developing precipitation).

2.2 Cloud Particles

Cloud water droplets have a size range from below 0.5 up to about 100 microns and can practically all be treated as Rayleigh scatterers, even at the highest investigated frequency of 94 GHz. Larger droplets are usually considered raindrops. The refractive index of water (Ray, 1972) has been calculated according to each assumed medium temperature.

Ice crystals in clouds have a size range from a few microns up to a few millimetres. Their basic shape is hexagonal prismatic. For the purpose of scattering calculations some of these particles can well be approximated by simple geometrical bodies (columns, needles, plates, etc.). The method chosen for our calculation was the approximation by oblate and prolate spheroids with varying size and axial ratio. Other particle forms as sector like, stellar, dendritic, fern like, hollow and others were not treated in this study.

We also made the simplifying assumption of pure ice consistence of all solid particles and calculated the refractive index of ice for a fixed temperature of -10 °C after Warren (1984). While the density of the plates is assumed to remain around 0.9 g/cm³, there may be a size dependent density reduction for the columns of ice, which we neglected in our calculation (for columns with an actual density of 0.7 g/cm³ this would result in an overestimation of reflectivity and absorption by about 45 % after Aydin and Tang, 1997).

2.3 Rayleigh Scatterers

Scattering calculations were done for cloud water droplets and cloud ice particles. All small cloud particles can be treated as Rayleigh scatterers if the wavelength of the incident field both inside and outside of the particle is large compared to the particle size. The second necessary condition for Rayleigh scattering is a small retardation of the incident field within the particle. Scattering cross sections for water droplets (spheres) and small ice particles (spheroids) have therefore been calculated after Van de Hulst (1981). Cloud particle spectra have been modelled by polydisperse distributions of water droplets or spheroidal ice particles with empirical size/diameter relations. These relations have been taken from Auer and Veal (1970). Similar relations were found by Hobbs (1974).

Corresponding author's address: Norbert Witternigg
JOANNEUM RESEARCH, IAS, Schießstadtg. 14b,
A-8010 Graz, Austria

2.4 Mie Type Scatterers

Scattering cross sections of ice particles with larger size parameter have been calculated using the Fredholm Integral method. Needles and plates among the ice particles have been simulated by highly eccentric spheroids (the total range of axial ratios was 0.025 to 80, where prolate particles like needles and columns have an axial ratio <1, plates have an axial ratio >1).

We verified the single-particle results from the Fredholm Integral method (FIM) against two other calculations (Point Matching and T-Matrix). Between them the Fredholm Integral was the only method that maintained convergence for the complete range of axial ratios and sizes that we envisaged. The fact that highly distorted, even non-homogeneous scatterers can be calculated with moderate processing effort seems to be the main advantage of the FIM. Other methods allow to model complex particle shapes (e.g., the FDTD method, Tang 1995), their use requires increasing processing time for the modelling of fine particle details, however.

We calculated the scattering characteristics of single spheroids of ice at different incidence and canting angles. We investigated the transition to Mie type scattering in dependence of the size parameter and due to increasing axial ratio of the spheroids. The results showed the expected deviation from Rayleigh scattering beginning with size parameters (of equivolumetric spheres) greater than approximately 0.1. For different orientations the elongation in beam direction was the most important parameter.

2.5 Scatter Tables for Ice Particles

Scatter tables were used to hold the single particle scatter results needed for the calculation of cloud distributions. The following parameters were used (Table 1):

- Particles of pure ice at T= -10 °C
- Frequencies: 5.6 / 14 / 24 / 35 / 78 and 94 GHz
- Refractive index fixed for each frequency
- Equivol. sphere radii: 0.05 - 0.59 mm (11 steps)
- Axial ratios: 0.025 - 80 (25 steps)
- Incidence angles: 0°, 22.5°, 45°, 67.5°, 90°
- Canting angles: 0° - 180° (16 steps)

Table 1: Scatter Table Parameters

Forward and backward scattering amplitudes were calculated, random orientation of the particles was simulated by averaging the results over the sets of incidence and canting angles.

Fig. 1 shows an example of backscatter cross sections of two randomly oriented spheroidal ice particles with equivolumetric radii of 0.1 mm and 0.58 mm. Cross sections were normalized to that of a Rayleigh scattering equivolumetric sphere in order to identify the transition to Mie type scattering. The frequency dependence and the influence of the axial ratio can be seen in the

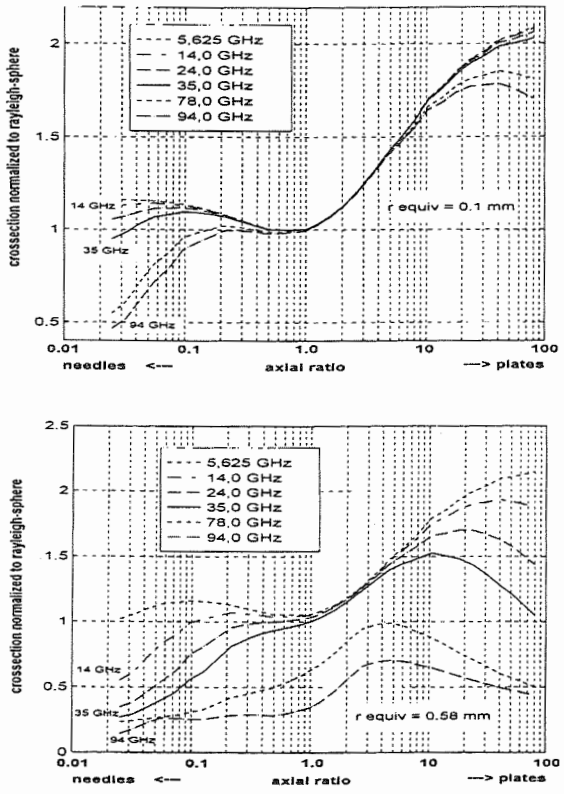

Fig. 1: Backscatter cross section normalized to Rayleigh scattering sphere r_ equv = 0.1 and 0.58 mm

figure. For the smaller particle all frequencies up to 35 GHz show Rayleigh (top curve, all axial ratios) or Near-Rayleigh characteristics. The enhancement of up to a factor 2 for the plates is due to geometrical reasons. For the larger particle and higher frequencies the normalized cross section is more and more reduced due to Mie type scattering.

3. SIMULATION OF CLOUD PARTICLE DISTRIBUTIONS

The radar parameters reflectivity, effective reflectivity, specific attenuation and linear depolarization ratio were calculated for 14 digitized spectra out of four major cloud types. Although the particle spectra were assumed to be typical for each cloud type, they have nevertheless to be considered examples, as the attenuation values are always connected to the liquid (or frozen) water content of the clouds, reflectivity values are strongly influenced by the development of larger particle sizes, e.g., during the development of precipitation. Lower values of depolarisation are expected in case of mixtures of air and ice.

3.1 High Clouds

Reflectivities of 4 different cirrus cloud samples were calculated with approx. -16 dBZe to +9 dBZe

effective reflectivity. Their ice water contents (IWC) varied between 0.006 and 0.26 g/m³ ('warm' Ci 0.006 , Ci unc 0.19, Ci spi 0.26 and Cs: 0.21 g/m³).

Thin cirrus clouds appear at the highest altitudes of the troposphere reaching up to the stratosphere. Their average ice water content is in the order of 0.001 to 0.01 g/m³. One spectrum of a cold and thin cirrus cloud resulted in a very low reflectivity of about -39 dBZe with an ice water content of 0.0004 g/m³.

The specific attenuation was very low for all ice clouds and was found for the cirrus samples to be below 0.005 dB/km for 35 Ghz and below 0.11 dB/km for 94 GHz. The linear depolarisation ratios of the randomly oriented particles were calculated within approx. -16 dB to -18 dB. The results for the high clouds are shown in Fig 2.

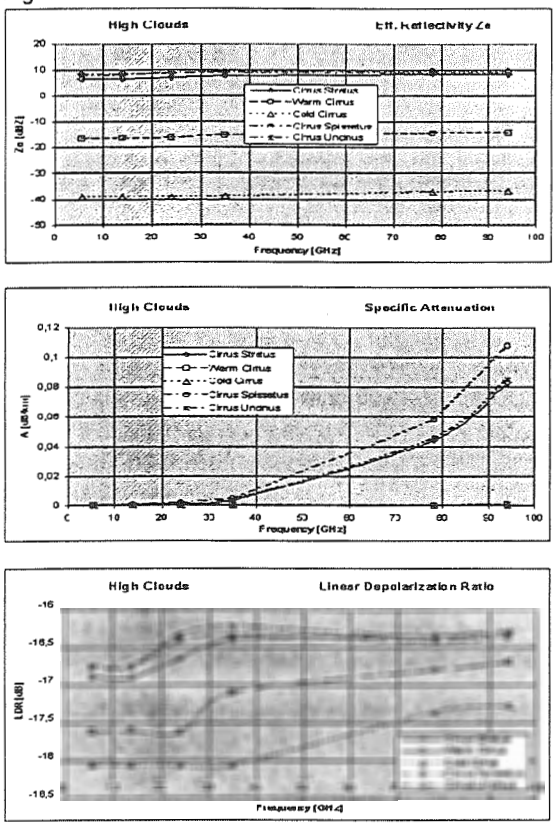

Fig. 2: Calculated Eff. Reflectivity, Specific Attenuation and Linear Depolarisation for 5 cirrus clouds

3.2 Middle Layer Clouds

Particles of middle layer clouds may consist of water droplets, ice particles or, in the case of mixed clouds, both phases. The micro physical properties of middle layer ice clouds are similar to cirrus clouds with generating cells. Indeed, the calculated radar parameters of these clouds showed similar results as the ones obtained for cirrus clouds.

Middle layer water clouds typically are thin altocumuli consisting of small droplets with a narrow particle spectrum. Reflectivities of these clouds may be low. The sample spectrum of a non-ice-producing altocumulus cloud resulted in a reflectivity of about -39 dBZ. Due to the low liquid water content of these clouds the specific attenuation is low.

3.3 Low Clouds

At temperatures above 0 °C low clouds are usually entirely composed of water droplets. Mean droplet size distributions are affected by the origin of the cloud (sea or continent). We have calculated the radar parameters for the sample particle distributions of two continental cumulus and one maritime stratocumulus cloud.

Reflectivities were between -28 dBZ and -33 dBZ. The specific attenuations showed the expected dependence on the liquid water content, calculated LWC from the sample particle distributions was within the typical range for these clouds (0.05 - 0.24 g/m³). Higher liquid water contents can be expected for stratus clouds (stratus: max 1 g/m³). Measured reflectivities in stratus will strongly depend on the development of larger droplets within the cloud.

3.4 Clouds with Precipitation

'Clouds with Precipitation' are not really a separate cloud type but belong to all three previously listed groups. The liquid water content in the non precipitating region is normally higher than within the precipitating one. More expressed, however, is the shift of the spectrum towards larger particle sizes. This can lead to an enormous increase in reflectivity. In one stratocumulus sample the calculated reflectivity was -37 dBZ in the non-precipitating part and +4.7 dBZ in the precipitating part of the cloud.

Attenuation due to precipitation was low or moderate up to 14 GHz. At and above 24 GHz rain attenuation may become excessive.

4. RADAR CONCEPTUAL DESIGN

14 GHz was therefore chosen as the preferred frequency, allowing the recognition of high clouds (as seen from the ground) even in precipitation situations. This frequency would also be suited to acquire information on the transition from cloud to precipitation and the micro structure of melting layers. For an optional dual-frequency design, intended to exploit the Mie-Rayleigh scattering differences, 35 GHz was selected as the second frequency, paying attention to an economic realisation and the fact that this frequency still allows to detect thin high clouds at -40 dBZe and 13 km height even during slight precipitation (1 mm/h).

The radar type was chosen to be pulsed to prevent from receiver saturation by TX-RX leakage and close-range ground clutter experienced in FM-CW systems. In order to resolve even the highest and thinnest clouds,

additional signal processing gain must be included. There are, in principle, two well known approaches to achieve such a gain: The use of wide-band pulse modulation and compression or the use of coherent integration. The use of coherent integration as a method for SNR-improvement is, compared to pulse compression, is rather simple. A conventional pulsed Doppler radar samples a number of N pulses in the time domain, and converts to the frequency domain by standard method FFT. For an infinitely narrow echo spectrum (i.e., all signal power contained in only one spectral line), the SNR-gain of a N-point FFT is 10 log(N) dB. In practice, depending on the echoe's spectral width, the achievable signal gain is about 3 to 5 dB lower. Some additional reduction must be taken into account due to target coherency time limits, and, in the case of a scanning system, the change of echo volume during time series sampling. Apart from the usefulness of a Doppler radar for SNR-improvement, it also delivers important information on the observed target, i.e., its velocity and turbulence characteristics and estimates about drop size spectra and precipitation types below the clouds (mean fall speed and fall speed distribution).

Further recommendations are the provision of cross polar echo reception (receiver only), to measure LDR and correlation co- vs. cross polar (both of value in the particle type and arrangement estimation, ice-water discrimination and clutter identification) and limited antenna beam scanning (say 20 degrees off-zenith). This allows the scanning over footprint areas of space borne cloud and/or rain radars (i.e., footprint diameter >1 km above 1.5 km altitude) as well as the acquisition of cloud and precipitation macro structure information.

As a result the following instrument characteristics for a receiver-coherent Doppler radar have been recommended (Table 2):

Transmitter:	
Peak Power:	75 kW (14) , 20 kW (35 GHz)
Spatial Resolution:	50 - 200 m (std. 100), 0.6 deg
Antenna diameter:	2.5 m (14), 1 m (35 GHz)
Doppler Resolution:	115 - 173 km/h
Receiver:	
(triple channel log Z, lin I&Q per frequ.)	
Dynamic range:	115 dB
Sensitivity:	-45 dBZ @ 10 km altitude
Polarisation:	dual linear (option)

Table 2: Key Technical Data of the Cloud Radar

5. CONCLUSION

We calculated scattering properties of water and ice clouds using model particles and real-measured particle spectra. Needles and plates were simulated by spheroids with high eccentricities using the Fredholm Integral method. Mie type scattering for cloud ice particles can be expected for frequencies of 35 GHz and above. The observed variation of radar reflectivity with frequency was below 4 dB for all samples and frequencies investigated. The frequency dependence of specific attenuation could be exploited with the combination of a Rayleigh scattering frequency and one of the higher frequencies. Paying attention to attenuation by precipitation below the clouds, 14 GHz has been suggested as the preferred frequency and 35 GHz as an optional second frequency for a ground-based receiver-coherent Doppler cloud radar.

6. ACKNOWLEDGEMENTS

The work of the original study was performed within Work Order 6 of ESTEC Contract 9949/92/NL/PB(SC). P. Cavazzini, F. Prodi, W. Schmid and E. Barthazy did the literature study in the frame of this contract.

The Fredholm Integral Method (FIM) Holt package was originally implemented by Prof. A. Holt of Essex University (UK). Prof. Holt made it available to ESA and to the Radar OPEX group. He agreed to put the package in the public domain. A description of the method can be found in Holt (1980) and Baptista (1974).

The adaptation of the FIM Holt package and programming for the scattering tables was done by M. Leitner.

7. REFERENCES

Auer, A.H. and D.L. Veal, 1970: The dimension oficecrystals in natural clouds, J. Atm. Trop. Sci., 27, 919-926.

Aydin K. and C. Tang, 1997: Relationships between IWC and Polarimetric Radar Measurands at 94 and 200 GHz for Hexagonal Columns and Plates, J. Atm. Ocean. Technol.,14, 1055 -1063

Baptista Poiares, J.P.V. (ed.), 1994: Reference Book on Radar (Volume 4), Second Workshop of the OLYMPUS Propagation Experimenters, Nov 8-10, Noordwijk, NL, ESA WPP-083.

Hobbs P.V., S. Chang and J.D. Locatelli, 1974: The Di mensions and Aggregation of Ice Crystals in Natural Clouds, J. Geoph. Res., 79(15), 2199-2206.

Holt A.R., N. 1980: The Fredholm integral equation method and comparison with the T-Matrix Approach, in *Acoustic, Electromagnetic and Elastic Wave Scattering: Focus on the T-Matrix Approach,* V.K. and V.V. Varadan (eds.),Pergamon Press, N. Y.

Matrosov S.Y., A.J. Heymsfield et al., 1998: Comparisons of Ice Cloud Parameters Obtained by Combined Remote Sensor Retrievals and Direct Methods, J. Atm. Ocean. Technol.,15, 184 - 196

Ray P.S., 1972: Broadband complex refractive indices of ice and water, Applied Optics, 11(8), 1836-1844.

Tang C, K. Aydin, 1995: Scattering from Ice Crystals at 94 and 220 GHz Millimeter Wave Frequencies, IEEE Trans. Geosci. Remote Sensing, 35(1), 140-146

Van de Hulst H.C., 1981: Light scattering by small particles, Dover Publications, New York

Warren S.G., 1984: Optical constants of ice from the ultraviolet to the microwave, Applied Optics, 23(8), 1206-1225.

SYNERGY IN ICE CLOUDS BETWEEN AIRBORNE NADIR POINTING RADAR AND LIDAR

Claire Tinel and Jacques Testud

IPSL - Centre d' études des Environnements Terrestre et Planétaires, Vélizy, France

1. INTRODUCTION

A prototype airborne Radar-Lidar (RALI) system was flown during the CLARE (Cloud and Radiation Experiment) field project (in October 1998, near Chilbolton, UK). The RALI system currently under development at IPSL will consist of 95 GHz cloud radar and a dual wavelength (0.5 and 10 μm) backscattering lidar on the same airborne platform. The test version consisted of the Service d'Aéronomie LEANDRE-1 lidar and the University of Wyoming cloud radar (Kestrel). These instruments were mounted on the IGN Fokker-27 aircraft (ARAT). The LEANDRE lidar had a fixed nadir looking beam, while Kestrel had a nadir beam and a beam 40 degrees forward of nadir.

The LEANDRE lidar is a 0.5 micron backscattering lidar with a 0.2 degree beamwidth, 10 ns pulse, 15 m range resolution (direct detection), and a 10 Hz repetition cycle. The Wyoming cloud radar is a 95 GHz Doppler radar. Kestrel beams both had a 0.7 degree beamwidth and 30 or 60 m range resolution. A 50 ns transmit/receiver switch network allowed pairs of pulses to be sent alternately to each antenna. Reflectivity and Doppler velocity were recorded for each beam.

During the CLARE campaign the UK Meteorological Office C-130 made some in-situ measurements with 2DP, 2DC and FSSP probes in ice clouds at various altitudes. It flew simultaneously along the same legs as the ARAT, in clouds sampled essential by RALI. These measurements are since they allow checking the validity of our results for the analyzed CLARE data.

First, power laws between integrated and microphysical parameters from an Inverse Model are given. Then, a method that combines radar reflectivity and lidar backscattering coefficient to infer properties of the particle size distribution is described. Finally the results of the analysis applied to CLARE data are given.

2. INVERSE MODEL FOR RADAR AND LIDAR RETRIEVAL

Thanks to the proportionality of integrated parameters defining the response of remote sensing instruments (radar reflectivity Z_e, radar specific attenuation K, lidar backscattering coefficient β_a, lidar extinction coefficient α) and microphysical parameters interesting to evaluate cloud radiative properties (ice water content IWC and effective radius r_e of particles) to the moments of particle size distribution (PSD), relationships between those parameters are established.

We will use hereafter the formulation of the normalized PSD by Dou et al. (1999) and Testud et al. (2000a and 2000b) :

$$N(D) = N_0^* F(D/D_m) \quad (1)$$

where N_0^* parameter is the normalization parameter along concentration axis, D_m the normalization parameter alond diameter axis and F(X) is the "normalized PSD" describing the "intrisic" shape of the PSD (noting $X=D/D_m$)

The relationships between the different parameters are :

$$K = a\left[N_0^*\right]^{1-b} Z_e^{\ b} \quad (2)$$

$$\alpha = c\left[N_0^*\right]^{1-d} K^d \quad (3)$$

$$IWC = p\left[N_0^*\right]^{1-q} K^q \quad (4)$$

The normalization model considered in the retrieval for the CLARE data is the following, corresponding to Fig.1 for the relationship between K and Z_e :

$$K = 2.7758.10^{-5}\, N_0^{*\,0.3288}\, Z_e^{\ 0.6712}$$
$$\alpha = 0.1485\, N_0^{*\,0.3056}\, K^{0.6944} \quad (5)$$
$$IWC = 6.994.10^{-2}\, N_0^{*\,0.2149}\, K^{0.7851}$$

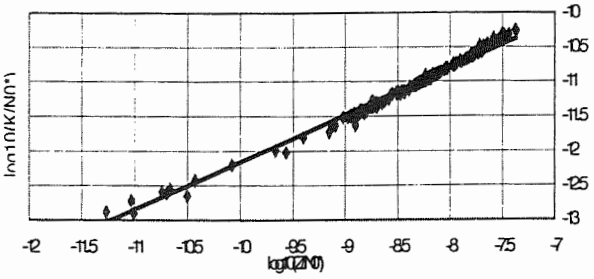

Fig. 1: The K/N_0^* versus Z_e/N_0^* relationship for the CLARE microphysical data set and for a 95 GHz radar

3. SYNERGETIC ALGORITHM FOR RADAR AND LIDAR

In this section we present the mathematical formulation of a synergetic algorithm for radar and lidar. In a set of data, zones, where both measurements of radar and lidar are available, and where there is only one type of particles will be selected for the analyzis. This method is formulated for ice clouds.

Corresponding author's address: Claire Tinel, Centre d'études des Environnements Terrestre et Planétaires,10-12, avenue de l'Europe, 78140 Vélizy, France;
E-Mail: claire.tinel@cetp.ipsl.fr

3.1 Radar measurements

The radar does not measure the true reflectivity Z_e, but an attenuated reflectivity Z_a subject to the two-way path attenuation because of the attenuation at 95GHz. Z_a and Z_e are related through :

$$Z_a = Z_e.10^{0.2\int_0^r K(s)ds} \quad (6)$$

where K [dB.km^{-1}] is the specific attenuation.

As we assumed in the precedent section K and Z_e can be related with a power law.

Under this assumption, Hitschfeld and Bordan (1954) gave the exact solution of the inversion of the solution expressed as :

$$Z_e(r) = \frac{Z_a(r)}{(1 + aN_0^{*1-b} I(r,r_0))^{\frac{1}{b}}} \quad (7)$$

where $I(r,r_0) = 0.46b\int_r^{r_0} Z_a^{\ b}(s)ds$

This solution is numerically instable as recognized by the authors. One of the reasons of this instability is the impossibility to set a fixed relationship between K and Z_e because of the natural variability of the N_0^* parameter.

The equation (7) may be written with respect to the attenuation in the following manner (Testud and al., 2000c):

$$K(r) = \frac{K(r_0)Z_a^{\ b}(r)}{Z_a^{\ b}(r_0) + 0.46b\int_r^{r_0} Z_a^{\ b}(s)ds} \quad (8)$$

where r_0 is the reference bound ($r<r_0$). We will see later how this boundary is determined.

The interests of this formulation are the elimination of the very fluctuating N_0^* parameter and the providing of an expression of a K profile not subject to the radar calibration.

3.2 Lidar measurements

Similarly the lidar does not measure the true backscattering coefficient β_e, but an apparent backscattering coefficient β_a which is related to β_e through :

$$\beta_a = \beta_e \exp[-2\alpha(s)ds] \quad [km^{-1}.sr^{-1}] \quad (9)$$

where α [km^{-1}] is the extinction coefficient.

The assumption of a linear law between α et β_e is made : $\alpha = f.\beta_e$ (10)

The problem posed by the inversion of (9) is the same as the one posed by the inversion of (6). Klett et al. (1954) gave the exact solution of this inversion:

$$\beta_e(r) = \frac{\beta_a(r)}{1 + 2f\int_0^r \beta_a(s)ds} \quad (11)$$

As the equation (7), this expression of the true backscattering coefficient is numerically instable because of the uncertainty of the lidar calibration and of the f coefficient.

The Klett solution may be written as an expression of the attenuation coefficient :

$$\alpha(r) = \frac{\alpha(r_0)\beta_a(r)}{\beta_a(r_0) + 2\alpha(r_0)\int_r^{r_0} \beta_a(s)ds} \quad (12)$$

The interest of this expression is the independence from the linear coefficient f and from the lidar calibration.

3.3 A combined lidar and radar algorithm

The equations (8) et (12) depend respectively from $K(r_0)$ and $\alpha(r_0)$. To determinate those two entities the following integral constraint is used:

$$\int_{r_1}^{r_0}\alpha(s)ds = c\left[N_0^*\right]^{1-d}\int_{r_1}^{r_0}K^d(s)ds \quad (13)$$

This constraint expresses the consistency of K(r) and α(r) profiles with the power-law obtained by the Inverse Model:

- r_0 is the reference bound where the lidar signal is available.
- r_1 is the reference bound and the maximal height where both measurements lidar and radar are available.

We assume that the type of particles is the same along the beam, and that the N_0^* and f parameters are constant along the path. Replacing K(r) from (8) and α(r) from (12) in the equation (13), an implicit equation in $\alpha(r_0)$ is obtained which can be written as:

$$\alpha(r_0) = \frac{\beta_a(r_0)}{2\int_r^{r_0}\beta_a(s)ds}(\exp(2\alpha(r_0)J(r_1,r_0)) - 1) \quad (14)$$

where

$$J(r_1,r_0) = \int_{r_0}^{r_1}\left(\frac{Z_a^{\ b}(r)}{Z_a^{\ b}(r_0) + \left(\frac{\alpha(r_0)}{cN_0^{*1-d}}\right)^{1/d} I(r_1,r_0)}\right)^d dr$$

$\alpha(r_0)$ can be determined by resolving (14). Then the K and α profiles between r_1 and r_0 may be derived and subsequently IWC and r_e, through. The difficulty to overcome is related to the presence of the N_0^* parameter in equations (13) et (14). The way to get around is to start with a first guess of N_0^*, and finally to determine a value of $\alpha(r_0)$ and $K(r_0)$, then to derive an improved estimate of N_0^* as in Testud et al. (2000c) through:

$$N_0^* = \left[\frac{1}{a}\frac{K(r_0)}{Z_a(r_0) + K(r_0)I(r_1,r_0)}\right]^{\frac{1}{1-b}} \quad (15)$$

where $I(r,r_0) = 0.46b\int_r^{r_0} Z_a^{\ b}(s)ds$.

This new estimate may be used in (14) to restart the process and to determine a new $\alpha(r_0)$. The results in generally converge in 10 to 15 iterations.

An estimation of the linear coefficient f can be deduced by:

$$f = \frac{\beta_a(r_0)}{\alpha(r_0)} + 2\int_{r_1}^{r_0}\beta_a(s)ds \quad (16)$$

4. APPLICATION OF THE SYNERGETIC ALGORITHM TO CLARE DATA

The synergy between radar and lidar is particularly efficient when probing an ice cloud since the penetration of the radar and the lidar in this type of cloud is comparable. The subsequent data analysis is focused on a particular leg (20 October 1998 from 14:41 to 14:48 UTC) where the ARAT was flying at 4.8 km altitude and the C130 was flying at 5.5 km altitude along the same leg. The altitude of the freezing level was around 1.8 km. Thanks to a good coordination between the two aircrafts, a very satisfactory coincidence in space and time of the ground tracks of the two aircrafts was met on this leg.

Between longitudes -1.7 et -2°W and above 3 km altitude, both instruments (nadir looking) really see the same cloud and the synergetic algorithm can be efficiently performed.

Fig.2 shows an example of retrieved profiles of Z_e, α, IWC and r_e at -1.8°W.

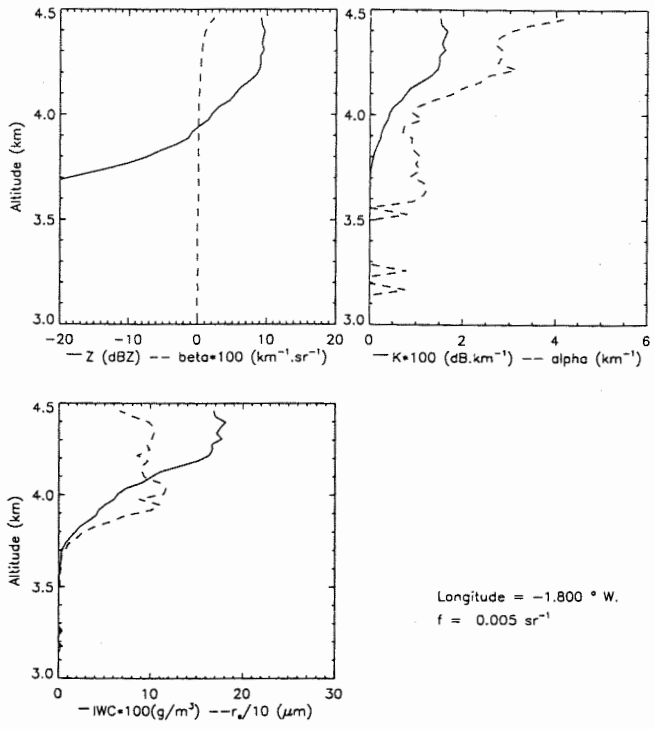

Fig. 2: Illustration of the profiles of Z_e and β_e [in (a)], K and α [in (b)], IWC and r_e [in (c)] retrieved by the synergetic algorithm (longitude along aircraft track: -1.8°W)

Fig.3 displays the along track evolution of the parameters retrieved by the synergetic algorithm [Z_e, α, IWC, r_e and N_0] at the highest altitude observable with the cloud radar and lidar: 4.48 km latitude. Fig. 6 also shows the along track evolution of IWC, r_e and N_0 deduced from the C130 microphysical probes at 5.5 km altitude. The agreement between the radar/lidar retrieval and the microphysical probes is rather good between longitudes -1.65°W and -1.84°W, particularly for α and IWC. Beyond -1.84° longitude the synergetic algorithm diverges because of the insufficiency of the lidar penetration. So we calculated the f coefficient and β_e, then we used the f_{mean} between -1.65°W and -1.84°W to calculate the α profile with this mean and the restituted backscattering coefficient where it diverges. We found f_{mean} = 0.086 with a standard deviation equal to 0.025. Then the IWC and r_e profiles may be obtained.

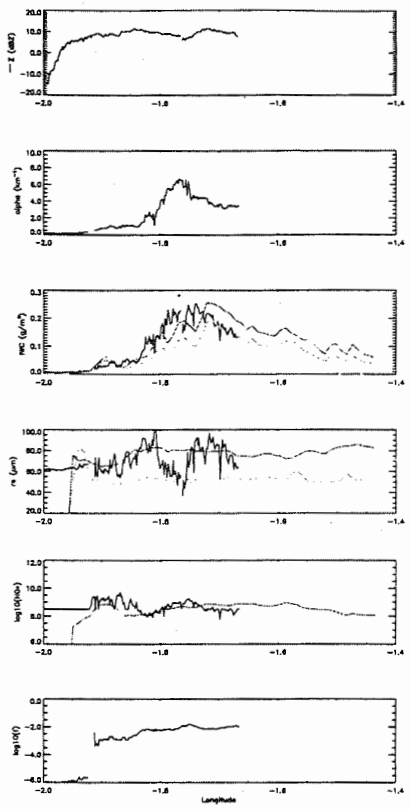

***Fig.3**: Along track evolution at 4.48 km altitude of the various parameters retrieved from the synergetic algorithm. From top to bottom: radar reflectivity Z_e, extinction coefficient α, ice water content IWC, effective radius r_e, PSD parameter N_0^*, linear coefficient f. The IWC, r_e and N_0^* are compared with estimates derived from the C130 microphysical data at 4.6 km altitude.*
For each comparison, the tick line represents the parameters retrieved from the synergetic algorithm, and the thin lines represent the values derived from the C130 microphysical data.

5. CONCLUSION

From these first tests with from the CLARE data set, the potential of the cloud radar and lidar combination on the same platform seems very promising. Further analysis should be directed to investigate the segmentation of the analysis in the conditions were different types of cloud are met along the beam.

References

Dou X., J. Testud, P. Amayenc and R. Black, 1999: The parameterization of rain for a weather radar, Earth and Planetary Sciences, **328**, 577-582

Hischfeld, W., and J. Bordan, 1954: Errors inherent in the radar measurements of rainfall at attenuating wavelengths. J. Meteor., **11**,58-67.

Klett J.D., 1981: Stable Analytical Inversion Solution for Processing Lidar returns, Applied Optics, **20**, 2, 211-220.

Testud J., S. Oury, R. A. Black, P. Amayenc and X. Dou, 2000a: The concept of "normalized" distribution to describe raindrop spectra: a tool for cloud physics and cloud remote sensing, submitted to Jour. Of Atmosph. Scienc.

Testud J., C. Tinel, A. Guyot and K. Caillault, 2000b: Cloud parameter retrieval from combined remote sensing observations, The First International Workshop on Spaceborne Cloud Profiling Radar.

Testud J. , E. Le Bouar, E. Obligis and M. Ali Mehenni, 2000c: The rain profiling algorithm applied to polarimetric weather radar, Jour. Of Atmosph. And Oceanic Technol., **17**, N0 3, 332-356.

Evaluation of a Slant-Linear Polarization State for Distinguishing Among Drizzle Drops and Regular and Irregular Ice Particles

Roger F. Reinking[1], Sergey Y. Matrosov[2], Robert A. Kropfli[1], and Bruce W. Bartram[1]

[1]National Oceanic and Atmospheric Administration, Environmental Technology Laboratory, Boulder, Colorado 80303 USA
[2]Cooperative Institute for Research in Environmental Sciences, University of Colorado, and NOAA Environmental Technology Laboratory, Boulder Colorado 80303 USA

1. INTRODUCTION

This work shows that millimeter-wavelength dual-polarization radar can be used to identify hydrometeors in clouds and precipitation, and that selection of the polarization state is important. The radar polarization parameter used for this purpose is the depolarization ratio, DR, a parameter influenced by hydrometeor type if the right polarization state is used. DR, the simplest of polarization parameters, is the logarithmic ratio of received power in the cross-polarized channel to that in the co-polarized channel. Hydrometeors will backscatter a depolarized microwave signal according to their aspect ratio (shape), settling orientation, bulk density, and the polarization state of transmitted radiation. The first three factors are determined by cloud properties, but the fourth, the transmitted polarization state, can be engineered. Various polarization states transmitted with our 8.6-mm wavelength radar, NOAA/K (Kropfli et al. 1995), are being tested for a capability to identify the ice particles in glaciated or mixed-phase clouds and to distinguish clouds of supercooled, drizzle-sized droplets from clouds of various ice particles. Identification of these ~50-500 μm-diameter droplets is of interest because they present a significant aircraft icing hazard when supercooled (Politovich 1989, Ashendon and Marwitz 1997). Effective identification of the differing ice particles is important as well, because some types will themselves create hazards to aircraft, e.g., graupel, and because ice particles of differing growth characteristics, through vapor consumption and riming, can influence liquid water content.

The transmitted polarization state can be selected from a continuum of possible elliptical polarizations, where linear and circular define the limits. So what polarization states will provide the greatest separation by particle type? We have tested several polarization states through the use of a rotatable phase-retarding plate on the RF transmission and reception path for NOAA/K. Matrosov (1991) has examined the use of pure horizontal polarization, achievable with our radar by means of a 0° or 180° phase shift, (ellipticity $\epsilon = 0$) and circular polarization (90° or 270° phase shift, $\epsilon = 1$) for the purpose of identifying various hydrometeors. These calculations demonstrate the high sensitivity of horizontal depolarization ratio to variations in ice crystal orientation, measured as the standard deviation of the canting angle, σ_θ, compared to that for a circularly polarized signal. Because of this, horizontal polarization is not appropriate for particle identification because the linear depolarization ratio, LDR, is as dependent on orientation angle as on particle shape. For these pure polarization states, the full dynamic range in DR between 0 dB and the cross-talk limit of the radar is fully utilized. However, polarizations transmitted as either pure horizontal or circular produce unacceptably weak returns in the cross-polarized channel, especially in low-reflectivity clouds where distinguishing drizzle from all forms of ice will most likely be required.

Practically, it is difficult to achieve pure horizontal or circular polarization and so our first attempt produced an elliptical state (80° phase shift, $\epsilon = 0.832$). It was found theoretically and experimentally that, for this first phase retarding plate, the ability to detect low-reflectivity clouds in the cross-polarized channel was very good, but the dynamic range of observable DR values was restricted to the extent that differentiating drizzle from some ice types (e.g., columns or graupel) was difficult (Reinking et al. 1997 a,b).

To overcome this problem, a slant-linear polarization state, which is not commonly used, was explored since it results in DR being much more dependent on particle shape than on σ_θ, in contrast to horizontal polarization. Also, it produces greater cross-polar signal strength than horizontal polarization and greater useful dynamic range of DR values. Again, pure slant-linear polarization was not achieved. The slightly elliptical, 45°-slant polarization state produced by our second plate reduced the dynamic range of DR somewhat, but not to the extent of the more elliptical polarization previously tested. Advantageously, it increased the cross-polar return power and thus the distance over which such measurements can be made (because of the increased cross-polar return).

To test this 45°-slant, quasi-linear polarization state (177.4° phase shift, $\epsilon = 0.023$) for its ability to identify hydrometeors the NOAAK radar was operated at the Mt. Washington Icing Sensors Project (MWISP) in New Hampshire in April 1999 (Ryerson et al. 2000). The radar site was mid-way up the west slope of the mountain. Supporting in-situ data were gathered at the Mount Washington Observatory (MWO) at the summit, and at the radar site. Theory and results are presented.

Corresponding author's address: Dr. Roger F. Reinking, NOAA/ETL/ET6, 325 Broadway, Boulder CO 80303 USA; E-mail: rreinking@etl.noaa.gov.

2. SCATTERING CALCULATIONS

The NOAA/K radar measures DR as a function of antenna elevation, χ, from constant-azimuth, variable-elevation RHI scans. The scattering calculations presented here generate DR signatures of drizzle droplets and various ice crystals, as a function of χ, for the 45°-slant quasi-linear polarization. We define the depolarization ratio for this hybrid state as SLDR*-45 = DR (177.4°, 22.5°), where 22.4° is the rotation from horizontal of the radar's phase-retarding plate that induces a 177.4° phase shift. [the standard horizontal linear depolarization ratio would be LDR = DR (180°,0°)]. The details of radar hardware and operation for obtaining these measurements are explained by Reinking et.al. (1997a). The median crystal sizes and the bulk densities used in the calculations are representative of experimental values recorded in the literature. The standard Magono and Lee classification of crystals is used. Dimensions affect shape, and the columnar crystals are separated according as the length/diameter ratio, L/D. Plots of calculated SLDR*-45 as a function of χ are presented in Figs. 1a and 1b for σ_θ = 3° and σ_θ = 15°, respectively.

The 45° tilt of the transmitted signal polarization plane enhances the cross-polarized signal level because it excites dipole moments along both principle axes of the scattering hydrometeors. (Horizontal polarization excites only the horizontal dipole moment unless particles flutter as they fall, in which case DR is more a function of σ_θ than particle shape.) The cross-polar signal strength is further enhanced when going from pure slant-linear 45° to the slightly elliptical SLDR*-45 measurement, but this is done at a cost of some reduced contrast (DR difference) between different particle types. Once the (dwell-time-dependent) minimum detectable polarization difference needed to distinguish ice from water droplets is determined, the ellipticity needed to generate this minimum difference between spherical droplets and low-DR ice particles can then be determined exactly through appropriate scattering calculations.

For planar crystals, calculated SLDR*-45 is strongly dependent on χ, whereas the signature for columns is nearly constant as shown in both Figs. 1a and 1b. The SLDR*-45 signatures for the planar and columnar crystals are *all* well-separated, by 2-20 dB, from that of spheres at low elevation angles (χ < 70°), whereas horizontally-polarized LDR signatures of columnar and planar crystals (not shown) approach the those of spheres at low and high χ, respectively. Our calculations show that the use of the 45° slant polarization will increase (over horizontal polarization) the separation of the signatures of all basic regular crystals from the drizzle signature by 5-15 dB at most elevation angles.

The effect of σ_θ must be considered. SLDR*-45 values for σ_θ = 3° and σ_θ = 15° are compared in Figs. 1a and 1b. The weak dependence on σ_θ for this polarization state is unlike the signatures in LDR (not shown). SLDR*-45 shows minor sensitivity to changes in σ_θ (< 2dB for the 12° change in σ_θ at χ < 70°, for example), whereas has variations as large as ~8 dB for the 12° change in σ_θ at any χ. Therefore, measurement of SLDR*-45 is expected to be much more dependent on shape and less on orientation than what one would expect for LDR.

3. RESULTS

The clouds during MWISP contained a full range of ice particle types as well as warm and supercooled drizzle sized-droplets. A corresponding range of depolarization ratio data was acquired with the K_a-band radar. The depolarization signatures of ice particle types were verified with many *in situ* measurements, including photographs of crystals collected on black velvet at the radar site, PMS 2DGC probe and Cloud Particle Imager (CPI) samples at the summit, a few PMS 2DC samples from a research

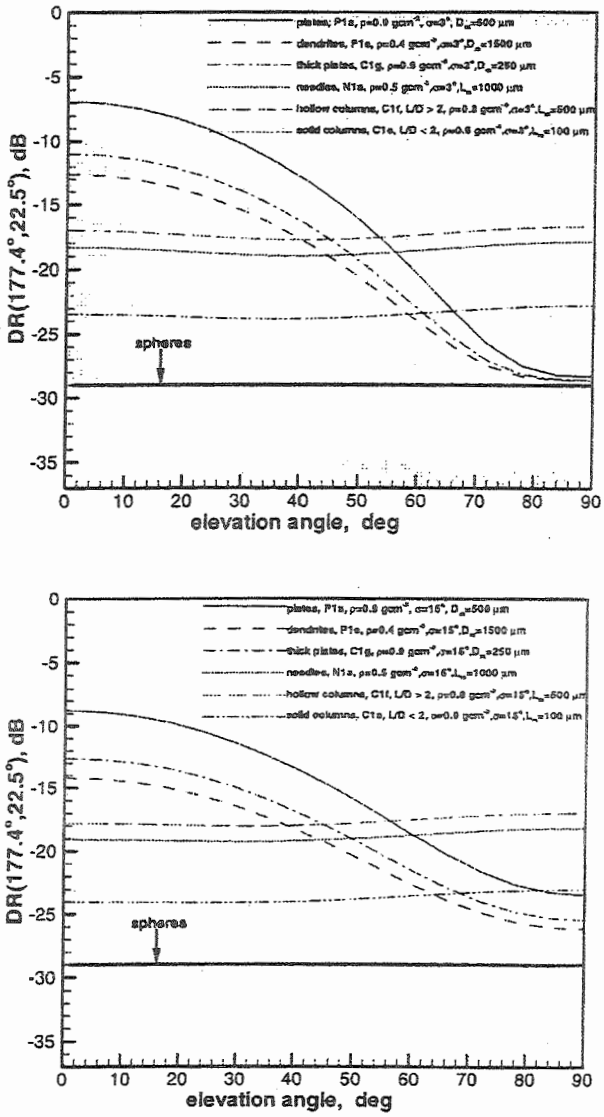

Fig. 1. Calculated depolarization ratio, SLDR*-45 = DR (177.4°,22.5°) (dB) as a function of antenna elevation angle χ (°) for basic planar and columnar ice crystal types specified according to their Magono and Lee classification, for (top) σ_θ = 3° and (bottom) σ_θ = 15°.

aircraft, and CLASS sondes. For brevity, only the depolarization measurements are presented.

Figure 2 shows the measured SLDR*-45 caused by crystals of the basic regular growth habits. The graph shows constant altitude values from RHI scans through the clouds. Not only were planar and columnar crystal categories identified, the fundamental planar plates and dendrites, and the long (L/D > 2) and short (L/D < 2) columns were also clearly differentiated.

Since drizzle-sized droplets (spheres) do not produce a depolarized backscattered signal, the measurement is indeed independent of χ, and well separated from all the signatures of the crystals of regular habits. The drizzle in this case was observed below a bright band and was warm. All of the SLDR*-45 values in Fig. 2 match within about 2 dB the corresponding calculated curves of SLDR*-45(χ) in Fig. 1. Near zenith, where SLDR*-45 of planar crystals is somewhat sensitive to σ_θ, the differences suggest that σ_θ was very small for the hexagonal plates (near 3° as in Fig. 1a) and considerably larger for the dendrites (near 15° as in Fig. 1b). Actual values of σ_θ are largely unknown, so the relative insensitivity of SLDR*-45 to σ_θ indicates that this DR will be a useful measurement parameter for the hydrometeor identification. Ice particles do frequently occur in pristine form, especially early in glaciation processes, so the curves in Figs. 1 and 2 are relevant to practical identification of these particles and their distinction from drizzle. Fig. 2 also shows that these clouds were homogeneous with regard to particle type in the vicinity of the radar.

Ice particles usually evolve to more complex and irregular forms. Figure 3 shows measurements of SLDR*-45(χ) for such particle forms, and for a case of drizzle that was verified as supercooled to -7 to -11 °C by a temperature sounding. The droplets had a median size of ~150 μm, recorded with a 2DGC probe at the summit. They presented an icing hazard, and their SLDR*-45 signature was distinguishable even from the irregular types of ice particles.

Aggregates of regular crystals are very irregular in bulk form. Matrosov et al. (1996) showed from scattering calculations and measurements of EDR that aggregation will reduce the depolarization of dendrites, but some of the variation in depolarization ratio with elevation angle will be preserved. This effect is observable with SLDR*-45 (Fig. 3) and allows nearly all aggregated ice forms to be distinguished from the -29 dB value for spheres. Elongated or "long-chain" aggregates, caused larger depolarizations with less dependence on χ as they mimicked long-columns (Fig. 2) although the samples at 2-5 cm lengths were immensely larger than columnar crystals.

The measured SLDR*-45 for conical graupel was ~ - 23 - -24 dB, some 6 - 9 dB above the signature for drizzle-sized droplets (Fig. 3). The separation of this magnitude made the graupel unambiguously separable from drizzle.

Of all the crystals sampled, heavily rimed branched planar crystals caused the least depolarization, resulting in the least distinction from drizzle. Nevertheless, the variation of SLDR*-45 with χ characteristic of planar crystals was still evident in the

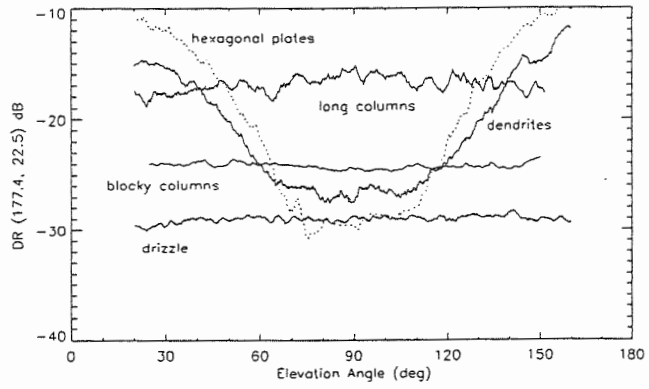

Fig. 2. Composite of measured curves of the function, SLDR*-45 (χ) (dB,°), for several different basic habits and drizzle droplets. The curves at χ > 90° approximate mirror images of those at χ < 90°, such that either half of each curve can be compared to the corresponding calculated curve in Fig. 1a or b. (Each measurement was at a constant altitude, h: Hexagonal plates (P1a), h = 2.2 km AGL, 1442 UTC 15 April 1999; dendrites (P1e); 1.4 km AGL, 1257 UTC 14 April; long columns (Cif + N1e), 0.3 km AGL, 1404 UTC 17 April; blocky columns (C1e), 0.4 km AGL, 1043 UTC 27 April; drizzle (warm), 0.2 km AGL, 1232 UTC 17 April 1999.)

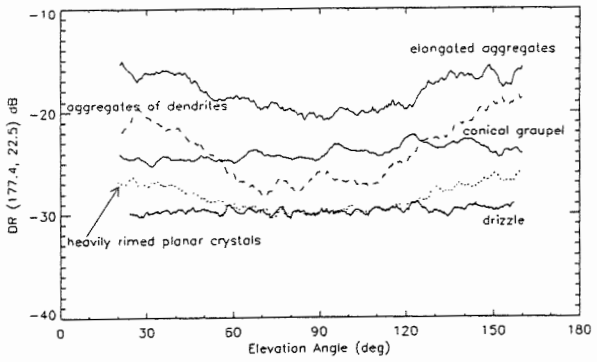

Fig. 3. Composite of measured curves of the function, SLDR*-45 (χ) (dB,°), for ice particles of irregular forms and drizzle; including aggregates of dendrites, h = 1.0 km AGL,1508 UTC 15 April 1999; elongated aggregates of dendrites, 1.6 km AGL, 1902 UTC 27 April; conical graupel (P4c), 1.5 km AGL 2110 UTC 20 April; heavily rimed planar crystals (R2b), 0.4 km AGL 1211 UTC 13 April; drizzle (supercooled), 0.5 km AGL, 2010 UTC 14 April 1999.)

signature, and at low χ, the separation rose to about 3 dB, which is readily measurable as seen in the figure.

4. CONCLUSIONS

Supercooled droplets of drizzle size are considered a potentially severe aircraft icing hazard. An optimal polarization state is being sought for differentiating among drizzle and the various types of ice particles. The optimization requires compromises due to tradeoffs between signal power in the weak cross-polarization channel, and the available dynamic range that determines DR differences between low DR ice crystals and drizzle and is set by polarization state.

Measurable differentiation among the crystals of the various regular habits, as predicted by theory, and among the various types of more irregular ice particles, and segregation of drizzle from all of these, was achieved with a 45°-slant, quasi-linear polarization. Overall, our observational experience has indicated that reasonable averaging of data will allow us to detect ice particles having DR values within about one or two dB of the value expected for water droplets. The 45° tilt and the slight ellipticity of the transmitted signal enhance the cross-polar return for ice particles relative to that obtainable in horizontal LDR which is strongly affected by the unknown spread in canting angle. The signatures of crystals in horizontal LDR will resemble spheres (and be indistinguishable from drizzle) if the scatters have zero canting angle and will change significantly when it is large. SLDR*-45, by comparison, is very stable, so it will minimize the potential errors in identification due to unknown variations in canting angle.

Is SLDR*-45 (ϵ = 0.02) the optimal state? The dynamic range reaches its minimum when ϵ = 0.5, so states near this are to be avoided. Pure linear or circular states sacrifice cross-polar return and weak-cloud sensitivity. New calculations by Matrosov et al. (2000) indicate that a state with ϵ = 0.97 would improve isolation of drizzle over SLDR*-45. Thus, states near to circular (e.g., ϵ = 0.92 -0.97) as SLDR*-45 is near to linear should also be considered.

5. ACKNOWLEDGMENTS

This research is in response to requirements and funding by the FAA. The views expressed are those of the authors and do not necessarily represent official policy of the FAA. Supporting data were provided by CRREL, NASA/GLEN, Spec, Inc., and NCAR.

6. REFERENCES

Ashendon, R., and J. D. Marwitz, 1997: Turboprop aircraft performance reponse to various environmental conditions. *J. Aircraft*, **34**, 278-287.

Kropfli, R. A., and colleagues, 1995: Cloud physics studies with 8-mm-wavelength radar. *Atmos. Res.*, **35**, 299-313.

Matrosov, S. Y., 1991: Theoretical study of radar polarization parameters obtained from cirrus clouds. *J. Atmos. Sci.*, **48**, 1062-1070.

Matrosov, S. Y., R. F. Reinking, R. A. Kropfli, and B. w. Bartram, 1996: Estimation of ice hydrometeor types and shapes from radar polarization measurments. *J. Atmos. Oceanic Technol.*, **13**, 85-96.

Matrosov, S.Y., R. F. Reinking, Robert A. Kropfli, B. E. Martner, and B. W. Bartram, 2000: The use of radar depolarization ratios for estimating shapes of ice hydrometeors. *J. Appl. Met.* (submitted).

Politovich, M. K., 1989: Aircraft icing caused by large supercooled droplets. *J. Appl. Met.*, **28**, 856-868.

Reinking, R. F., S. Y. Matrosov, B. E. Martner, and R. A. Kropfli, 1997a: Dual-polarization radar to identify drizzle, with applications to aircraft icing avoidance. *J. Aircraft*, *34*, 778-784.

Reinking, R. F., S. Y. Matrosov, R. T. Bruintjes, and B. E. Martner, 1997b: Identification of hydrometeors with elliptical and linear polarization K_a-band radar. *J. Appl. Met.*, **36**, 323-339.

Ryerson, C. C., and colleagues, 2000: Mt. Washington Icing Sensors Project: Conduct and Preliminary Results. *Paper # AAIA-2000-0488, Preprints, 38th AAIA Aerospace Sciences Meeting and Exhibit*, 10-13 January 1999, Reno, 10 pp.

TECHNIQUES FOR THE STUDY OF CLOUD MORPHOLOGY IN TWO AND THREE DIMENSIONS

Laura M. Hinkelman,[1] K. Franklin Evans,[2] Thomas P. Ackerman,[3] and Eugene E. Clothiaux[1]

[1]Department of Meteorology, The Pennsylvania State University, University Park, PA 16802
[2]Program in Atmospheric and Oceanic Sciences, University of Colorado, Boulder, CO 80309
[3]Pacific Northwest National Laboratory, Richland, WA 99352

1. INTRODUCTION

Radiative transfer and heating in the cloudy atmosphere depend on the specific three-dimensional structure of the clouds that are present. However, most cloud-imaging instruments (*e.g.*, radar, lidar, satellite sensors) are limited to making measurements in a plane. When one of these instruments is used, the third dimension is either ignored, assumed to be similar to one of the measured dimensions, or filled in using a limited number of values from a different instrument measuring in the third dimension. For this reason, it is not certain that the cloud fields used in such studies are accurate representations of the cloud types of interest.

An additional problem with most cloud measurements is that they sample only a small portion of the cloud or cloud field. FSSP, 2-DC, 2-DP, and other airborne instruments sample only a pencil-thin ray along the aircraft path. Integrating instruments, such as radiometers, cover much more area in an individual measurement, but still sweep out only a plane through the cloud field. Even cloud radars (assumed non-scanning) only measure cloud structure in a plane, although without integration in either direction. While each of these instruments provides valuable information about cloud structure, it is difficult to assess the degree to which the results are representative of the observed clouds due to their limited sampling volumes. This is especially the case for ground-based instruments, since they are restricted to sampling in the direction of the mean wind.

In this abstract, we describe methods we intend to use to analyze the spatial characteristics of three-dimensional cloud fields produced by cloud-resolving models. These techniques focus on the level of isotropy found in cloud structures, especially in the horizontal plane. They also provide statistics that describe the spatial distribution of cloud water. Example results demonstrate how these techniques can be used to estimate the level of variability that arises in cloud measurements due to the sampling strategy employed.

Corresponding author's address: Laura M. Hinkelman, Department of Meteorology, The Pennsylvania State University, University Park, PA 16802; e-mail: laura@essc.psu.edu

2. PROPOSED METHODS

Overhead cloud fraction is the simplest description of cloud fields that is useful for radiation budget studies. Given a three-dimensional cloud liquid water field from a model, a two-dimensional binary cloud mask, or "shadow" array, can be created by establishing a minimum liquid water content for which cloud is considered to occur in a grid cell. Positions in the cloud mask array are then marked as cloud covered if this threshold is exceeded at any point in the corresponding column of the original field. Sampling is then simulated by tracing lines across the array and calculating the percentage of cells along the lines that are cloud covered. The representativeness of the result obtained along any line can be determined by comparison to the average cloud-occurrence statistics over the whole array.

A more detailed description of cloud field structure can be obtained by performing a similar analysis over the entire cloud field. That is, thresholding can be used to convert the entire field to a three-dimensional binary array and sampling can be performed along lines in any direction through this array. This not only allows the results of sampling the cloud field in different directions to be compared for a given height but also makes it possible to analyze the change in the cloud coverage with height. Given the cloud fraction at each level, cloud overlap assumptions used in large-scale models can be tested. Total cloud fraction computed using maximum overlap, random overlap, and maximum-random overlap assumptions can be compared to the actual values obtained in the cloud masking procedure described above.

Statistics can also be calculated for actual cloud fields rather than the binary cloud occurrence arrays mentioned above. Sampling of liquid water content in three dimensions or integrated variables in a plane, such as liquid water path or optical depth, can also be simulated and results for an individual trajectory compared to the overall cloud field properties. In this case, more detail is provided by analyzing the distribution of values obtained along each path in addition to the average value.

Particular questions that arise in the context of ground-based measurements can also be addressed. An

important issue for long-term measurements at fixed locations is the representativeness of the measured data given that cloud fields measurements are only taken in the along-wind direction. This issue can be addressed by simulating measurements through any of the arrays listed above and comparing the results to the cloud field averages. If the distribution of results obtained for along-wind traces is compiled, the probability of obtaining a result characteristic of the total cloud from an single measurement can be computed. The respresentativeness of ground-based measurements is also uncertain because they sample moving cloud fields that evolve over time rather "frozen" clouds advecting by. These two sampling methods can be compared by analyzing a complete time series of model cloud fields.

3. EXAMPLE RESULTS

To illustrate the techniques proposed for this study, sample three-dimensional cloud fields were obtained from numerical simulations of cloud system development during the Global Atmospheric Research Program Atlantic Tropical Experiment (GATE) in 1974 performed by Grabowski *et al.* (1996, 1998). These output fields consisted of liquid water mixing ratios on a 200 x 200 x 35 grid with 2 km spacing in the horizontal directions and variable vertical spacing ranging from 100 m near the surface to 1052 m at the top (~20 km) of the domain. The corresponding three-dimensional velocity fields and the vertical density and pressure profiles were also employed for this study.

The three prototypical scenes shown in Figure 1 (Grabowski *et al.*, 1998) were examined. The first was a case of scattered convection, which occurred on 7 September 1974. This scene consists of small cumulus cells scattered across the model domain with a slight preference for organization in the SW-NE direction. The second included strong organized convection from 2 September 1974. In this case, the clouds are organized in large clusters with SW-NE orientations clearly evident. The last case simulated a fully-developed squall line that occurred on 4 September 1974. In this scene, the cloud structure is strongly anisoptropic with the squall line running nearly due west to east. These scenes were chosen for the initial study because they exhibit a wide range of structural organization in the horizontal plane. However, we plan to apply the techniques described here to a larger number of cases in order to determine typical cloud field properties at other locations.

Here, we present the results of a simple analysis of overhead cloud fraction. Two-dimensional cloud masks were created for each of the GATE cases using a mixing ratio threshold of 10^{-4} g kg^{-1} to define cloudy grid cells. Sampling was carried out in four directions: N-S, E-W, and along the two diagonals. Note that, although the same number of rays were used in the grid-parallel and diagonal directions, the diagonal traces did not sam-

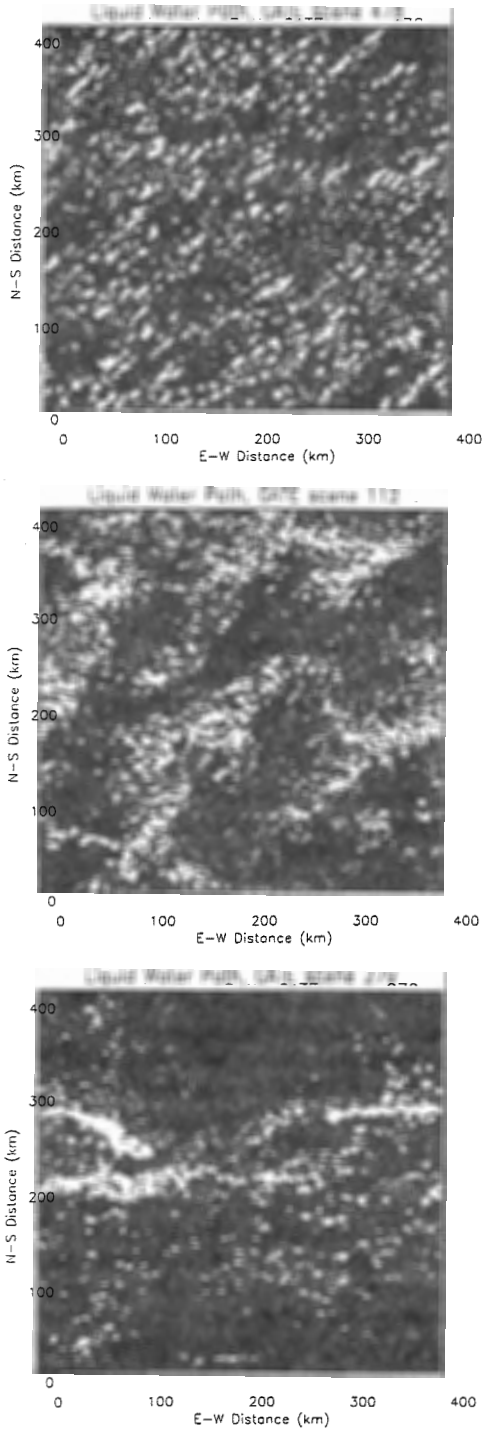

Figure 1. GATE cloud scenes displayed as horizontal projections of vertically-integrated water content (liquid water path). White corresponds to a liquid water path of 2000 gm^{-2} or more, black to near-zero values. a) Scene 478, scattered convection, 7 September 1974. b) Scene 112, organized convection, 2 September 1974. c) Scene 279, squall line, 4 September 1974.

Table I. Statistics of cloud occurrence in a column for sampling in four directions in the horizontal plane.

Cloud scene	478		112		279	
Direction	Mean	Variance	Mean	Variance	Mean	Variance
E-W	0.4219	0.0056	0.4848	0.0128	0.2654	0.0503
N-S	0.4219	0.0047	0.4848	0.0057	0.2654	0.0046
NW-SE	0.4358	0.0041	0.4831	0.0060	0.2925	0.0050
SW-NE	0.4226	0.0091	0.5038	0.0143	0.2889	0.0037
Whole plane	0.4219	–	0.4848	–	0.2654	–

ple all of the grid points. The diagonal lines contained between 142 and 284 points, for an average of 213 points, while the N-S and E-W lines each consisted of 201 samples.

The probability of observing a cloud in each column along all possible transects in the E-W, N-S, NW-SE, and SW-NE directions is given in Table I along with the variance in these results among all the paths in each direction. As can be seen from the mean values, the proportion of grid cells containing cloud water is much lower for case 279 than for the other two cloud fields. This is to be expected because the squall line has a much smaller horizontal extent than either of the cumulus cloud fields. Note that the mean values for the NS and EW directions are the same as the whole plane value while the diagonal means are not. This is because the N-S, E-W , and whole plane means are taken over the entire volume while some points are omitted from the diagonal analysis.

The variances presented in Table I show that the choice of sampling direction can significantly affect the fraction of cloudy grid cells detected. For the squall line, for example, the variance among results for measurements along E-W transects is ten times higher than for measurements in any other direction. This result is obvious from the cloud field structure shown in Figure 1c, since some E-W lines are entirely within the squall line region while others miss this structure altogether. However, there are cases where such sampling differences are less apparent. For example, while the clouds in scene 112 seem fairly well distributed, except for their alignment along the SW-NE diagonal, the variance in cloud occurrence is more than twice as high when sampling is done in the E-W direction than the N-S direction for this field. The diagonal alignment of the small cumulus of case 478 is also clearly evident in the variances of Table I.

The distributions of cloud fraction values obtained for all the rays in each direction were computed for the three cases. This allows us to provide a quantitative estimate of the likelihood of obtaining a value characteristic of the entire cloud field when sampling is done along one line in a given direction. The structure of the shallow convective cloud field is isotropic enough that 80% of all the trajectories calculated for each direction yield cloud fractions within ten percentage points of the mean value of 42%. For the squall line, however, ~60% of all measurements along either diagonal or on a N-S line fall within five percentage points of the mean value, but for measurements in a E-W direction, only 12% do. These results indicate that care must be used when devising plans for measuring cloud field structure with limited sample coverage.

4. CONCLUSIONS

A set of techniques for the analysis of cloud field morphology have been presented. Example results for the GATE cloud fields demonstrate the value of this approach. However, far more cloud scenes must be studied to determine the ubiquity of various cloud forms and range of cases in which sampling patterns are important. The next step in this work will be to obtain a large number of scenes from large eddy simulations carried out over a limited number of locations and at higher resolution. It is hoped that the results will enable us to better define the representativeness of cloud data obtained from long-term measurement projects, such as those underway as part of the Department of Energy's Atmospheric Radiation Measurement program.

5. ACKNOWLEDGMENTS

This material is based on work supported by a National Science Foundation graduate fellowship. Additional funding was provided by the Department of Energy through grant DE-FG02-90ER-61071.

6. REFERENCES

Grabowski, W. W., X. Wu, and M. W. Moncrieff, 1996: Cloud-resolving modeling of tropical cloud systems during phase III of GATE. Part I: Two-dimensional experiments. *J. Atmos. Sci.*, **53**, 3684-3709.

Grabowski, W. W., X. Wu, M. W. Moncrieff, and W. D. Hall, 1998: Cloud-resolving modeling of tropical cloud systems during phase III of GATE. Part II: Effects of resolution and the third spatial dimension. *J. Atmos. Sci.*, **55**, 3264-3282.

USING RADAR PROFILES AND PASSIVE MICROWAVE RADIANCES AS CONSTRAINTS FOR DERIVING MICROPHYSICAL PROFILES WITHIN TROPICAL CLOUD SYSTEMS

Edward J. Zipser[1], Stephen W. Nesbitt[1], Baike Xi[1], Gerald Heymsfield[2], and Robbie Hood[3]

[1]Department of Meteorology, University of Utah, Salt Lake City, Utah 84112 USA
[2]NASA Goddard Space Flight Center, Greenbelt, Maryland 20771 USA
[3]NASA Global Hydrology and Climate Center, Huntsville, Alabama 35806 USA

1. INTRODUCTION

The Tropical Rainfall Measuring Mission (TRMM) ground validation component involved the undertaking of five field programs during 1998-1999. During these programs, a large volume of data was collected from in situ microphysical instruments, and passive and active remote sensing instruments. One of the primary goals of these field campaigns was to obtain high resolution observations of tropical precipitating clouds to improve microphysical models of these storms. A better understanding of the microphysics will improve the utility of passive and active retrievals of rainfall (and therefore latent heating profiles), constraining retrievals made aboard the TRMM satellite.

This study will use two instruments flown aboard the NASA ER-2 high altitude aircraft during selected TRMM field campaigns: the ER-2 Doppler Radar (EDOP) and the Advanced Microwave Precipitation Radiometer (AMPR). The EDOP nadir reflectivity will degraded in resolution and converted to ice and liquid equivalent rain rate as input to a plane-parallel radiative transfer model developed by Kummerow (1993). The simulated radiances will then be compared to coincident observations made by AMPR. Both the similiarities and differences between the simulations and observations will improve our understanding of the microphysics of the precipitation system under examination.

2. DATA

2.1 Observational Data

The ER-2 aircraft flies at a nominal altitude of 20 km, above any cloud system. For this reason, it is an excellent platform to act as a surrogate for a satellite remote sensing platform. However, its position allows for high resolution, both for passive and active sensors.

EDOP has a wavelength of 3.12 cm (9.6 GHz), a vertical resolution of 37.5 m, and a horizontal along-track resolution of about 550 m at 10 km MSL and 1100 m at the ground. However, it samples every 150 m to provide significant oversample. It has a nadir and forward antenna; this study only employs the nadir reflectivity field as input to the radiative transfer model.

Corresponding author's address: Edward J. Zipser, 135 S 1460 E Rm. 819, Dept. of Meteorology, Univerisity of Utah, Salt Lake City, UT 84112-0110; E-mail: ezipser@met.utah.edu

AMPR is a four channel (10.7, 19.35, 37.1 and 85.5 GHz) cross-track scanning (±45° from nadir) passive microwave radiometer. At ER-2 altitude, it has a ground footprint size of 2.78, 2.78, 1.48, and 0.67 km for its four channels, respectively. The footprints are configured to be contiguous at 85 GHz, with oversampling at the other frequencies. The measured radiances can be converted to brightness temperatures.

Depressed brightness temperatures mainly at the high frequencies (37 and 85 GHz) are an indication of optical depths of ice hydrometeors scattering upwelling microwave radiation out of the field of view of the instrument, as well as scattering cold cosmic background into the field of view. This study will focus on the depression of T_b due to ice scattering as both cases occured over land (emission techniques to sense precipitation are only useful over a water surface).

2.2 Radiative Transfer Model

The one-dimensional plane parallel microwave radiative transfer model approach used in this study is detailed in Kummerow (1993). It approximates the sizes of ice and liquid hydrometeors as Marshall-Palmer spheres with densities of 1.0, 0.4, and 0.1 g m^{-3} for rain, graupel, and snow, respectively. Inputs for hydrometeor profiles are given by rain and equivalent ice rain rates which are used to calculate the extinction coefficient, single scattering albedo, and assymetry factor for each gridpoint. The model contains 1-km thick layers extending upward from the surface. A typical tropical thermodynamic sounding is used as input, with cloud liquid water specified as 0.1 g m^{-3} within the simulated cloud profile. The surface emissivity is set to 0.5 and the surface wind speed is 7 m s^{-1}.

3. HYDROMETEOR PROFILES

As a preliminary investigation, an admittedly crude method of determining liquid and frozen liquid rain rate profiles is employed. As is well known, variations in convective and stratiform precipitation hydrometeor particle dynamics yields significant differences in their respective drop size distributions. For this pilot study, however, we employ "merged" convective-stratiform particle size distributions that will serve as a control for future studies.

Below the freezing level (which is located below 5 km in both cases presented here), a combined

convective-stratiform Z-R relationship (Tokay and Short 1996) is used to calculate liquid rain rate:

$$Z = 221R^{1.43}$$

Above the freezing level, ice water content is first calculated from a hurricane composite Z-IWC relationship determined by Black (1990):

$$Z = 670(IWC)^{1.79}$$

For this experiment, the IWC was assumed to be composed of 25% graupel and 75% snow. The implications of this assumption will be discussed later. The rain rate is calculated using the following relation:

$$R = \frac{(IWC)}{\rho A dt}$$

where A and dt is the area and time increment for liquid accumulation. Converted to units of mm hr^{-1}, these relations give an approximation to the ice hydrometeor liquid rain rates.

For computational considerations, the input fields were degraded to 1 km resolution in the vertical and 500 m resolution in the horizontal. AMPR brightness temperatures were degraded accordingly. Future work will seek to improve the resolution of the inputs.

4. THE CASES

The first case (presented in Fig. 1) was sampled during the TEFLUN-B field campaign on 15 Aug 1998 over west-central Florida (21.4°N 81.1°W). It features a very strong convective element centered near x=95 km with the 30 dBZ echo extending to near 15 km in the vertical. A weaker convective feature is apparent around x=30 km. Stratiform rain exists elsewhere between the two cores and left of the weaker convective element.

The second case (Fig. 2) was observed on 23 Feb 1999 during the TRMM-LBA field campaign in Rondonia, Brazil (10.4°S 62.0°W). The convective cores produce maximum 30 dBZ heights extending only to near 7 km, with very weak stratiform rain extending to the left of the convective features.

4. DISCUSSION OF RADIATIVE TRANSFER RESULTS

4.1 TEFLUN-B Case (Fig.1)

The intense convective core evident in (a.) produced high concentrations of ice at high altitudes shown in (c.), exceeding 20 mm hr^{-1} up to 12 km. This produces minimum 85 GHz and 37 GHz brightness temperatures around 80 and 130 K, respectively. These are in agreement in magnitude with the minimum brightness temperatures observed by AMPR, but are displaced by about 5 km. In the weaker convective core to the left, there is much less ice calculated to be aloft in the cloud. The simulation produces minimum brightness temperatures at 85 and 37 GHz about 30 K warmer than the minumum values observed by AMPR, with those values displaced by about 10 km from each other. In the stratiform regions, simulated brightness temperatures are too low (by 10-30 K) except where the surface rainrates are > 5 mm hr^{-1}, where the observed temperatures are less then the simulations. These discrepancies are likely due to the fixed graupel fraction (25%) in our ice microphysical assumptions.

4.2 TRMM-LBA Case (Fig.2)

Here, the convective areas produce much less ice above the freezing level, extending much lower in height. The 10 mm hr^{-1} contour extends only to around 8 km (as compared to near 15 km in the TEFLUN-A case). This agrees with lower retrievals of core upward vertical velocity from EDOP in this case (not shown). The convection is also much less horizontally homogeneous, which introduces much more variability in the observational and simulation output. Here 85 GHz observations and simulations differ by more than 50 K in some cases. More agreement is present at 37 GHz. There is also some horizontal displacement of depressions evident, with some convective cores to the right of the line producing little brightness temperature response in the model. When comparing the modeled brightness temperatures, there seems to be more correlation between the height of the 1 mm hr^{-1} contour than the higher ice rain rate contours below (especially between 50 and 60 km). In the stratiform areas, as in the previous case, simulations are less than observations by about 30 K.

5. CONCLUSIONS

This pilot study argues strongly for several improvements to our model. First, more complex input assumptions need to be made (especially in the mixed phase region and between convective and stratiform areas of the clouds). Also, increased resolution in the vertical will aid this. Differences in spatial location of the brightness temperature depressions must be due to: (1) location error among the instruments, (2) time response of the instruments, or (3) differences between the altitude or location of the actual radiative forcing compared to where the model simulates the forcing. With improvements, these results do promise useful improvements to our microphysical understanding of precipitating systems.

6. REFERENCES

Kummerow, C., 1993: On the accuracy of the Eddington approximation for radiative transfer in the microwave frequencies. *J. Geophys. Res.*, **98**, 2757-2765.

Tokay, A. and D. A. Short, 1996: Evidence from tropical raindrop spectra of the origin of rain from stratiform versus convective clouds. *J. Appl. Meteor.*, **35**, 355-371.

Black, R. A., 1990: Radar reflectivity-ice water content relationships for use above the melting level in hurricanes. *J. Appl. Meteor.*, **29**, 955-961.

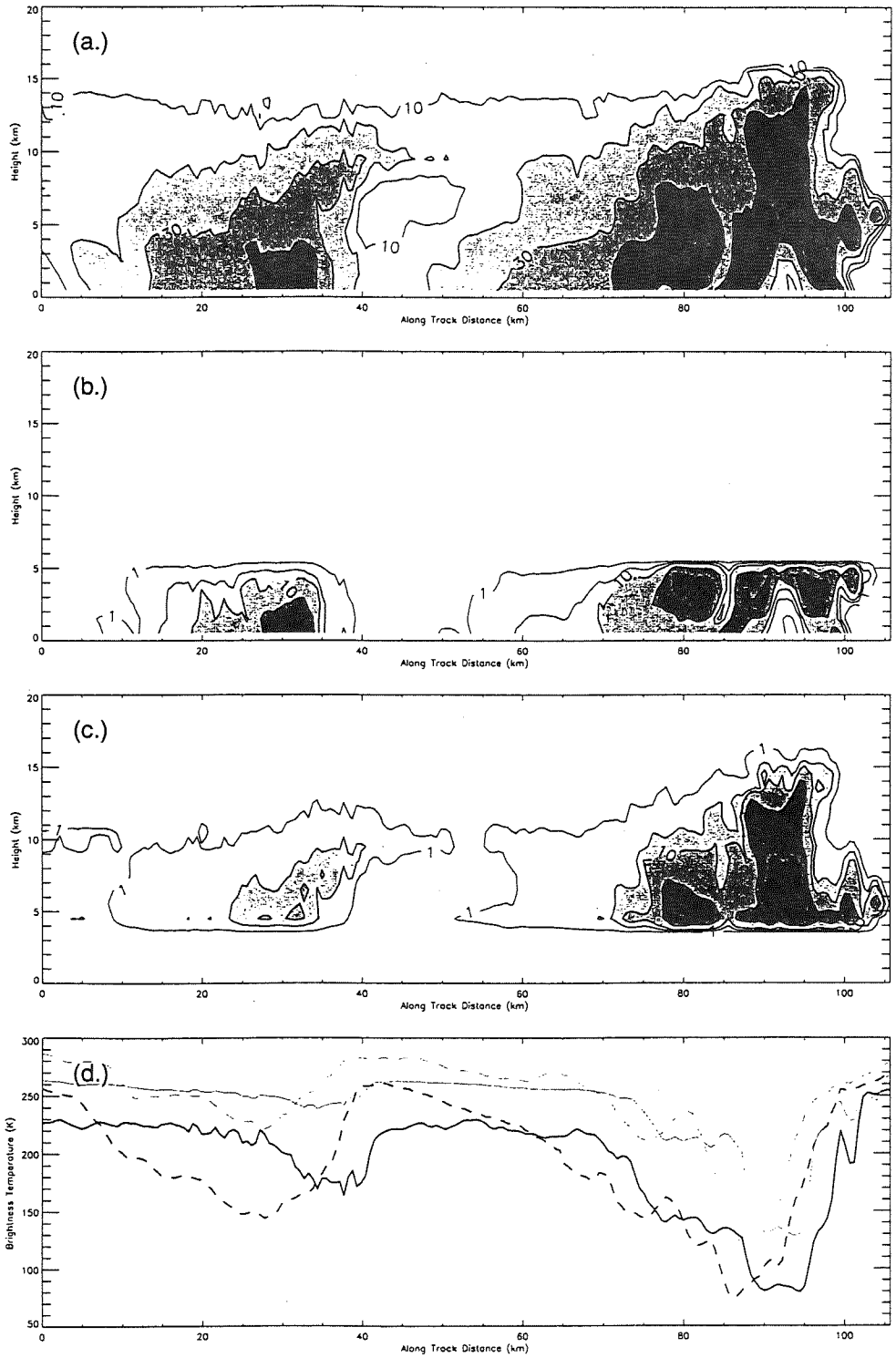

Fig. 1. 15 Aug 1998 22:23-22:30 UTC (a.) EDOP reflectivities contoured at 10, 20, 30, 40, and 50 dBZe, (b.) calculated liquid rain rates (mm hr^{-1}), (c.) calculated liquid equivalent frozen hydrometeor rain rates (mm hr^{-1}), and (d.) coincident observed AMPR 85 GHz (dark dashed line) and 37 GHz (grey dashed line) brightness temperatures and simulated 85 GHz (dark solid line) and 37 GHz (grey solid line) radiative transfer model results.

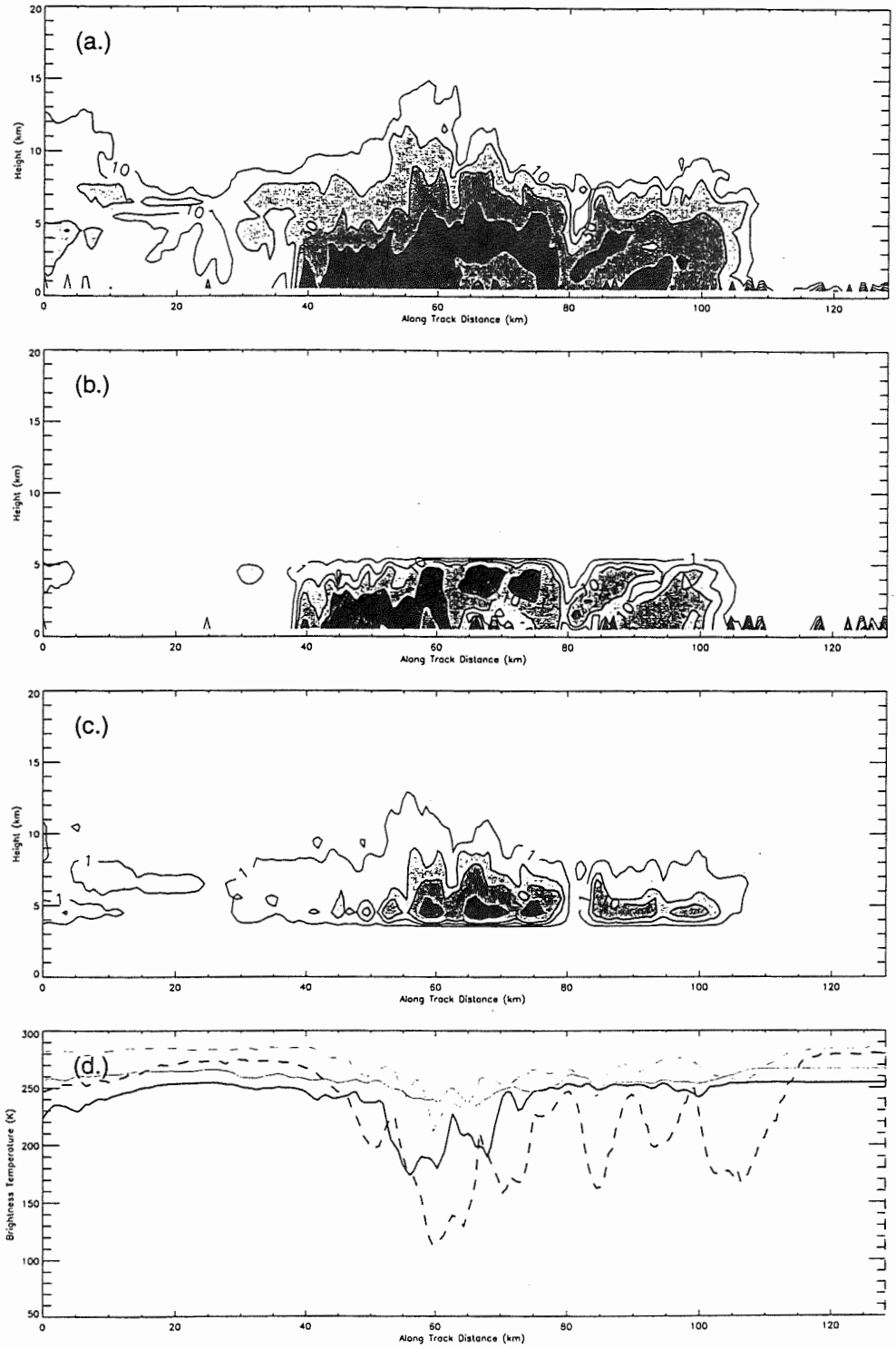

Fig. 2. 23 Feb 1999 20:55-21:02 UTC (a.) EDOP reflectivities contoured at 10, 20, 30, 40, and 50 dBZe, (b.) calculated liquid rain rates contoured at 1,5,10,25 and 50 mm hr^{-1}, (c.) calculated liquid equivalent frozen hydrometeor rain rates contoured at 1,5,10,25 and 50 mm hr^{-1}, and (d.) coincident observed AMPR 85 GHz (dark dashed line) and 37 GHz (grey dashed line) brightness temperatures and simulated 85 GHz (dark solid line) and 37 GHz (grey solid line) radiative transfer model results.

REFLECTIVITY AND VERTICAL VELOCITY PROFILES IN TROPICAL PRECIPITATION SYSTEMS, DERIVED FROM A NADIR-VIEWING X-BAND AIRBORNE RADAR

Bart Geerts

Dept of Atmospheric Sciences, University of Wyoming, Laramie WY

1. INTRODUCTION

Equivalent radar reflectivity (Z) profiles in a spectrum of tropical precipitation systems, including hurricanes, are analyzed. These profiles were obtained from the nadir beam of the ER-2 Doppler radar (EDOP) in a several field experiments, TEFLUN (Texas and Central Florida), CAMEX-3 (Atlantic Hurricanes), and TRMM-LBA (Brazil). Rain is classified as stratiform or convective according to a profile-based scheme similar to that employed for TRMM PR (Precipitation Radar) data. Further characterizations distinguish vigorous convection, a clear bright band (BB) vs a weak one, small vs large thunderstorms, stratiform and convective rain in hurricanes, warm rain, and rain not reaching the ground.
The definitions are on a beam-by-beam basis, i.e. the spatial structure is not used as an argument in the classification. We do not classify precipitating systems based on their size (eg MCS or smaller storm) or morphology (eg linear vs non-linear).

2. CONVECTIVE VS. STRATIFORM

The 'convective' type should include all precip that is of convective origin, even if, upon decay, it forms a BB. Only if some non-convective ascent is present (eg in a 'stratiform region' behind a squall line, or in a tropical depression) should the precip be labeled stratiform. In order to allow comparisons to TRMM, we use a V-method equivalent to TRMM's, with slight adaptations due to a better knowledge of the freezing level (FL), the higher resolution, and the absence of a 3rd (across-track) dimension. A H-method classification is included also, but because of the absence of a 3rd (across-track) dimension, it is not equivalent to TRMM's H-method, which is based on Steiner et al '95 (SHY).

V-method

The algorithm is as follows: first the beam profile data are filtered (to n=7, i.e. 250/37.5) to match the PR's best vertical resolution. Then one or more BBs are identified, based on these selection criteria:

- Find all local maxima ($dZ/dx = 0$ and $d^2Z/dx^2 < 0$)
- The BB must be within 750 m of the observed FL
- If any of the last 5 beams have a BB, then the BB must be at about the same level as the average BB of the 5 last beams (+/- 400 m)
- Z at 0.5 km above the BB (Z_{above}) must be at least 2 dB less, and the average Z between 0.5 and 1.0 km below the BB (Z_{below}) must be at least 1 dB less
- If more than one BB satisfies all 4 conditions above, the candidate BB must be within 400 m from the average height of all BBs on a flight leg. In the case of the PR, this seems to reduce the number of BBs to a single one.

If a BB is present, then the beam is **stratiform**.
If a BB is present, but Z_{max} >42 dB and $Z_{max} > Z_{BB}$, then the beam is **convective** (following the TRMM 2A23 algorithm)
If no BB is present, and $Z_{max} > 25$ dB, and, then the beam is **convective**. (for the PR this threshold is $Z_{max} > 39$ dB, producing an artificial fringe of H-stratiform and V-inconclusive around convection)
Else (i.e. if no BB exists and Z_{max} <25 dB), the pixel is **inconclusive** (non-convective and non-stratiform).
(Z_{max}: maximum reflectivity in the beam, at any level above the ground; Z_{BB}: the maximum reflectivity in the BB).

H-method

We apply the SHY technique, using low-level data (an average of levels 10-17 above the ground, ie between 375-638 m AGL). Because the horizontal resolution is constant (at any elevation), horizontal filtering (to n=2 or ~2 km) is not important and not implemented. A beam is **convective** if

- *Intensity*: $Z > 40$ dB
- *Peakedness*: $Z - Z_{bg} > 10 - Z_{bg}^2/180$ dB (where Z_{bg} is calculated between $-11 < x < 11$ km)
- *Vicinity*: beam is within convective radius (R_c) of a beam that is defined as convective thru its intensity or peakedness ($R_c = \max\{1, (Z_{bg} - 17)/5.2\}$)

Else, a beam is **stratiform**. There is no need for an 'inconclusive' type, which in the case of the PR is defined as Z near noise level (17 dB).

3. SPECIFIC TYPES

For hurricanes, both stratiform (common) and convective (rare) reflectivity profiles will be shown. We further characterize the following special types of precip:

Vigorous convection: subset of convective: a 39 dB reflectivity is found at 7 km or higher and $Z_{max} > 45$ dB . This criteria is arbitrarily chosen to include 3 cases in Brazil (1/25, 2/7, and perhaps 2/23) one in central Florida (8/20), and one hurricane case (9/22).

Stratiform: weak vs strong BB (Table 1)

Corresponding author address: B. Geerts, Dept. of Atmospheric Sciences, University of Wyoming, Laramie, WY 82071, USA ; email: geerts@uwyo.edu

Table 1	$Z_{BB} - Z_{above}$	$Z_{BB} - Z_{below}$
weak BB	2-4 dB	1-2 dB
(mediocre BB)	only 1 of the 2 criteria for a strong BB is satisfied	
strong BB	> 4 dB	> 2 dB

Warm rain: define $H_{top,0}$ as the 0 dB storm top height in the beam. If $H_{top,0}$ < FL, rain is considered 'warm'. The threshold reflectivity is picked arbitrarily, but physically is should be the lowest measurable reflectivity level. TRMM defines warm rain more restrictively, as $H_{top,18}$ <FL -2000 m, where 18 dB is the sensitivity threshold for the TRMM PR.

Additional criterion: if (FL- $H_{top,0}$)< 500 m, then a warm-rain beam cannot be adjacent to a deep-rain beam (ie $H_{top,0}$ <FL also in the next and previous beams). This is intended to exclude seeder-feeder growth, i.e. glaciation and growth just above the FL. Most warm rain is expected to be **non-convective and non-stratiform**, but it can be convective (as defined above), but not stratiform (because there is no BB).

Rain not reaching the ground: define Z_f as the reflectivity of the first pixel above and well-separated from the ground. Rain does not reach the ground when Z_f <0 dB but Z_{max} > 5 dB. This can be:

- Low-level or stratiform (BB present)
- High-level or anvil (no BB present and $H(Z_{max})$ > FL)
- Convective (no BB present and Z_{max} >25 dB and $Z_{f,\,FL}$ > 0 dB)

4. RESULTS

X-band attenuation is insignificant if Z_{max}< 40 dB or if the average dB over a few km depth is less than 35 dB. In the case of vigorous convection or a strong BB, attenuation correction is required. Over the ocean (most hurricane cases) nadir reflectivity is corrected by means of a combination of the Hitchfield-Borden (HB) and the Surface Reference techniques (SRT). This is fairly accurate, because the ocean surface has a fairly constant radar cross section, even over a rough ocean surface. The same method is used for the TRMM PR (Igushi and Meneghini 1994). Over land, the HB method may be used for correction in the nadir if the attenuation is small. For large attenuation, especially convective 'beasts', we can only correct thee attenuation in the forward beam, using the SRT, because the radar cross section at the surface varies a lot in the nadir beam. Drawbacks are that even the forward beam has a fair bit of variability, it may be sensitive to surface wetness, and it has a much coarser vertical resolution.

Using the EDOP nadir antenna data, we are compositing and comparing several variables for all rain types:

- contoured frequency by altitude diagrams (CFADs) of reflectivity
- the BB vertical structure for stratiform systems (an example is shown in **Fig 1**)
- storm top (at 0 dB and at 18 dB, the latter corresponds with TRMM PR storm top)
- measured radial velocity profile (CFAD)
- estimated air motion profile (CFAD)
- near-ground reflectivity (and derived rainrate)
- relation between rainrate and storm top height
- system length (along-track)

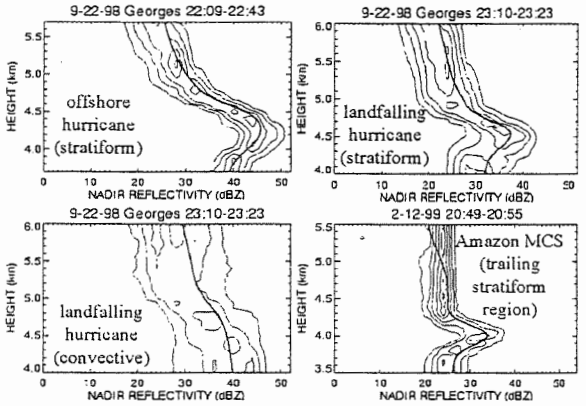

Figure 1. *Bright band comparisons. The height range of these CFADs is just 2 km. The upper two CFAD profiles are from Hurricane Georges, offshore (left) and onshore (right). The lower left profile is derived from a convective tower within Georges as it made landfall on Hispaniola (Geerts et al 2000). The lower right profile is based on the trailing stratiform region of a small MCS in Rondonia, Brazil.*

In the future we also plan to composite simultaneous data from other instruments on the ER-2: passive microwave brightness temperatures at 10, 37, and 85 GHz (mean and standard deviation), and derived rainrate; electric field and lightning frequency; and IR temperature (and sounding-derived cloud top height).

Acknowledgement: this work would have been impossible without Dr. G. Heymsfield (NASA GSFC).

REFERENCES

Geerts, B., G.M. Heymsfield, L. Tian, J.B. Halverson, A. Guillory, and M.I. Mejia, 2000: Hurricane Georges' landfall in the Dominican Republic: detailed airborne Doppler radar imagery. *Bull. Amer. Meteor. Soc.*, in print (May).

Igushi, T. and R. Meneghini, 1994: Intercomparisons of single-frequency methods for retrieving a vertical rain profile from airborne or spaceborne radar data. *J. Atm. Ocean Tech.*,**11**, 1507-1516.

Steiner, M., R.A. Houze Jr., S.E. Yuter, 1995: Climatological characterization of three-dimensional storm structure from operational radar and raingauge data. J. *Appl. Meteor.*, **34**, 1978-2007.

FORWARD MONTECARLO COMPUTATIONS OF POLARIZED MICROWAVE RADIATION

A. Battaglia[1] and C. Kummerow[2]

[1]University of Ferrara, Ferrara, 44100 Italy
[2] NASA Goddard Space Flight Center, Greenbelt, Maryland, USA

1. INTRODUCTION

Microwave radiative transfer computations continue to acquire greater importance as the emphasis in remote sensing shifts towards the understanding of microphysical properties of clouds and with these to better understand the non linear relation between rainfall rates and satellite-observed radiance.
A first step toward realistic radiative simulations has been the introduction of techniques capable of treating 3-dimensional geometry being generated by ever more sophisticated cloud resolving models. To date, a series of numerical codes have been developed to treat spherical and randomly oriented axisymmetric particles. Backward and backward-forward Monte Carlo methods are, indeed, efficient in this field, e.g. Roberti et al. (1999) Liu et al. (1996).
These methods, however, cannot deal properly with oriented particles, which seem to play an important role in polarization signatures over stratiform precipitation, see Heymsfield et al. (1996). Moreover, beyond the polarization channel, the next generation of fully polarimetric radiometers challenges us to better understand the behavior of the last two Stokes parameters as well.
In order to solve the vector radiative transfer equation, one-dimensional numerical models (e.g., Czekala et al. (1998), Evans et al. (1995), Wauben et al.(1992)) have been developed. These codes, unfortunately, consider the atmosphere as horizontally homogeneous with horizontally infinite plane parallel layers.
The next development step for microwave radiative transfer codes must be fully polarized 3-D methods. Recently Haferman et al. (1997) presented a 3-D polarized radiative transfer model based on the discrete ordinate method. Roberti and Kummerow (1999) developed a forward MC code that treats oriented non-spherical hydrometeors, but only for plane-parallel situations.

In this work, a 3-D forward Monte Carlo radiative transfer model for all 4 Stokes vector components has been developed in order to study the radiative properties of 3-D clouds containing non spherical water and ice particles; rather than adopting one of a host of backward, and backward-forward methods, this code is geared at the simplicity which can be gained from a pure forward model. In exchange for the simplicity, a fairly substantial computational penalty is payed, but the problem is manageable for microwave problems due to the relatively low optical depths in this region of the electromagnetic spectrum.

2. THE MONTE CARLO CODE

In the forward approach, photons are started from a scene in proportion to the total irradiance originating from each component of that scene (e.g. surface, atmosphere). The scene has to be taken large enough to cover all the regions from which photons are expected to arrive at the reception sensor and it is modeled with horizontally finite and vertically layered sub-clouds. A background plane parallel atmosphere then surrounds the cloud itself. Scattering properties - extinction and albedo (at different incident angles) and phase functions (at different incident and scattering angles) are computed for each finite cell as well as the plane parallel background.
Photons are released with the appropriate emission Stokes vector and are then traced forward using the usual random number techniques to simulate the distance of collision and the scattered direction. The photons' Stokes vector is multiplied by statistical weighting matrix to force all photons into scattering events only, thus avoiding absorption. This procedure further acts to remove statistical perturbation introduced by sampling the distance to collision from a biased probability distribution (Roberti (1999)). Scattering events are treated by sampling the outgoing direction randomly in the solid angle, computing the phase matrix (by interpolation from precomputed values) and multiplying the Stokes vector for a renormalised

[1] Corresponding author's address: A. Battaglia,
University of Ferrara, via Paradiso 12, 44100 Ferrara, Italy.
E-mail address: a.battaglia@isao.bo.cnr.it

scattering matrix (Chuah et al. (1989)). A good crosscheck for this technique is the average conservation of intensity in scattering events.
The process is tracked until either the intensity has become so weak that its contribution to the next scattering is negligible or until the photon is scattered out of the cloud.
Rayleigh-Jeans brightness temperatures have been computed at the top and at the bottom of the atmosphere. Brightness temperatures, however, can also be computed at any position within the cloud to accommodate aircraft radiometer studies.
Computational requirements remain a concern. This code is therefore structured primarily to provide a simple framework in which to test the effect of various issues associated with oriented particles. Even so, results with adequate accuracy can generally be obtained within a few hours on today's workstations if the optical thickness of the analyzed scene remains in the order of magnitude of 1.

2.1 VALIDATION OF THE MODEL

The model has been validated in its full Stokes treatment by comparing its results with benchmark results from Haferman et al. (1996) and from Wauben et al. (1992) and in its 3D version by comparisons with Roberti et al. (1999).
An example of validation is given in fig. 1: the fluctuation introduced by the Monte Carlo statistics is self evident.

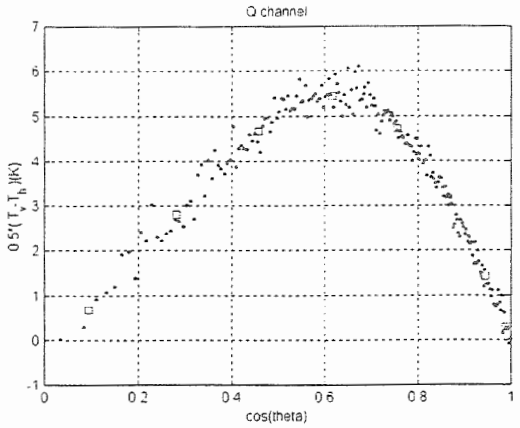

Figure 1: Comparison between upward polarization results from our code (dots) and from Haferman et al. (squares) for a two layer infinite atmosphere with ice and rain.

3. RESULTS

The radiative transfer simulations are carried out assuming both land and water surfaces because of their marked contrast in microwave radiometric properties: the land is modeled as a Lambertian surface with constant emissivity while the water is modeled as a Fresnel reflecting surface with the index of refraction of water varying with frequency, salinity, surface wind and temperature.

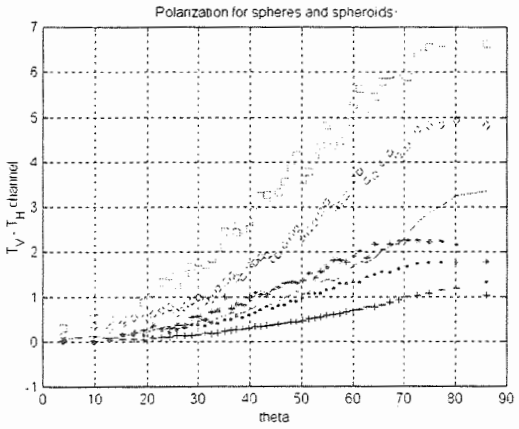

Figure 2: Upwelling polarization over Lambertian surface: +, • and * line are for spheres while continuous, ◊ and line for spheroids perfectly oriented correspondent to RR=5, 10, 20 mm/hr respectively.

As a simple example, a plane parallel 4-km layer of rain, modeled as a Marshall Palmer size distribution of prolate spheroids (with an axial ratio varying with size according to the literature), has been studied. Some results are presented at 19 GHz, although computations have been performed at 37 and 85 GHz also. At this frequencies a rainfall rate of 10 mm/hr corresponds to an optical thickness τ=0.8 and an albedo ω=0.18 while a rainfall rate of 20mm/hr corresponds to τ=1.7 and an albedo ω=0.22.
Computed intensities (not shown), follow the general behavior that is expected: upwelling T_B, over sea (cold) surfaces increases with increasing rain rates, reach a maximum and decreases for higher rain rates. Increasing cloud emissivity, and thus the upward shift of the layer that contributes most to the radiance causes the decrease. For land (warm) surfaces the increasing effect is practically absent.
Stronger and more detectable differences can be observed in the polarization signal T_V-T_H=2Q (see figs.2-4). For spheres, the radiation shows a positive polarization difference both upwelling and downwelling in the expected ranges. The effect is caused by the

symmetry breaking due to the finite vertical against the infinite horizontal dimension (e.g. Liu et al. 1996)

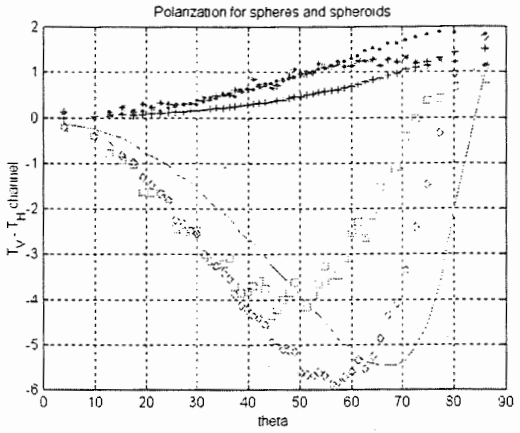

Figure 3: Same as fig.2 for downward polarization.

In the case of the non-spherical particles, the effect is significantly stronger and positive upward while negative in the downward direction.
With Fresnel surface the polarization pattern is complicated by the presence of the polarized surface. In this framework, however, Monte Carlo procedures are very useful because they can suggest which percentage of the signal is coming from the surface.
To better understand the polarization behavior we have studied in detail a particular situation (RR=20 mm/hr, Lambertian surface) by looking at the contributions to the polarization signal coming from different orders of scattering (fig.5).

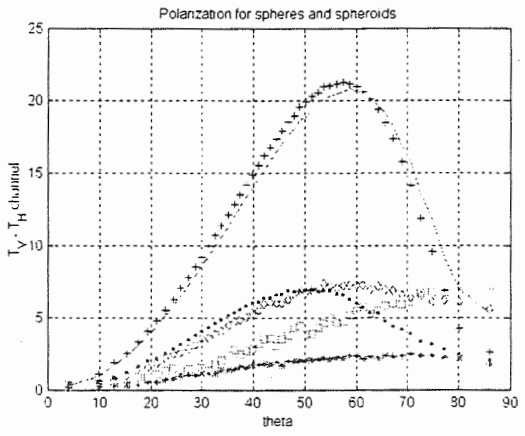

Figure 4: Same as fig.2 for Fresnel surface.

Without scattering the polarization signal is much lower in intensity and positive both upward and downward; in the upward direction the polarization is most pronounced at small angles because of the preferentially nadir-oriented photons coming from the surface. In this case, since no scattering is involved, the mechanism of polarization is essentially driven by angular dependent absorption coefficient. The polarization signature then becomes more and more evident as one moves off nadir. This is due to the decrease in the ratio between vertical and horizontal extinction coefficients.
Considering the first order scattering events only, losses in intensities become less pronounced while a significant decrease in the polarization occurs both in the upward and downward directions. Downward, where a significant contribution comes from scattered photons, the decrease is so pronounced that the signal becomes negative for a great part of the angular range. Scattered photons are therefore preferentially H-polarized. This is not due to the scattering itself (that is, to the phase matrix) but mostly to the fact that interacting photons are preferentially H-polarized ($K_{ext,H} > K_{ext,V}$).
If photons having had two scattering events are taken in account, then the signal is practically completely saturated.

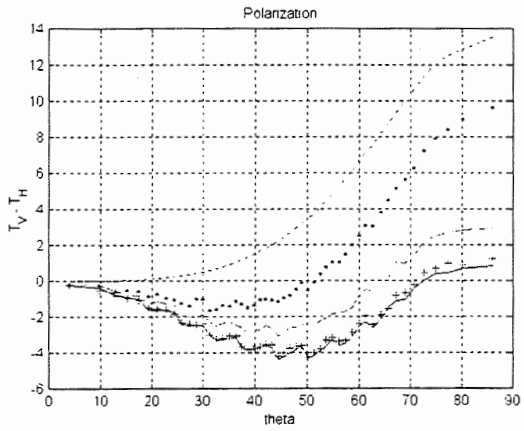

Figure 5: Different scattering order contributions to polarization downward: dotted, dashed and + line corresponds to 0,1,2 order; continuos line is multiple scattering solution and •line is solution without surface photons.

The effect of finiteness is studied by taking a 15x15 km horizontally extending cloud with the same physical properties as before. Temperatures are computed directly above the cloud, looking at φ=0.
In figs. 6-7, the 20-mm/h Fresnel surface case is analyzed. The results of finiteness is a net depression in intensity both upward and downward (not shown). This is as expected because of the leakages from the sidewalls and the contributions from the colder water surface.

On the other hand, upward polarization shows a much greater signature than for infinite cloud for the same reason: now the sensor is seeing much more polarized contributions from surface than before. This explains why negatively polarized signals from perfectly oriented raindrops are much more attenuated than for the infinite case.

For Lambertian surface (not shown), contributions from the non-polarized surface and leakages from the sidewalls will tend to smooth the polarization signal from cloud and to broaden it over a region larger than the top of the cloud itself.

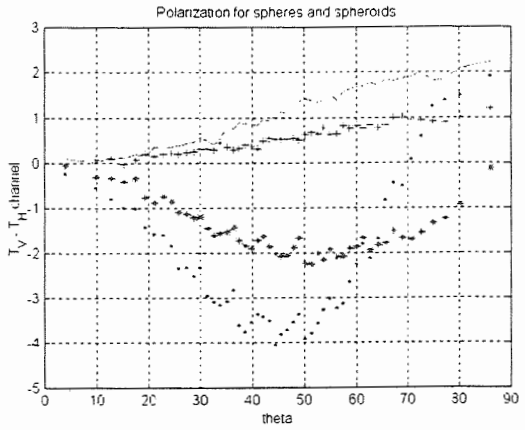

Figure 6: Downward polarization for finite (* line is for perfectly oriented spheroidal droplets, + line for spherical droplets) and infinite raining cloud (dashed line is for perfectly oriented spheroidal droplets, dotted line for spherical droplets)

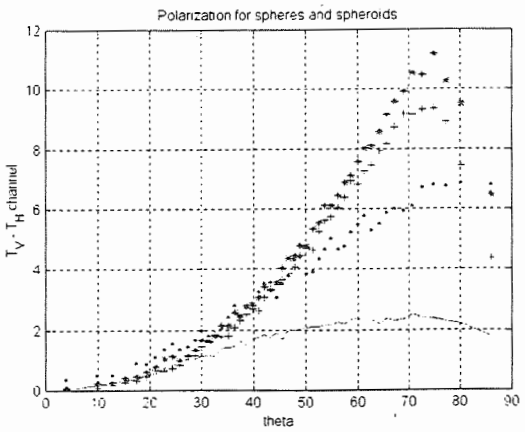

Figure 7: Same legend as fig. 6 for upward polarization.

Studies are now in progress to better understand the role of finite horizontal dimension and to find distinctive signatures of microphysical properties in water, ice and mixed phase clouds containing perfectly oriented particles.

Acknowledgements

This work has been partially funded by USRA and performed at NASA GSFC as part of the TRMM research program.

References

Czekala, H., and Simmer, C., 1998: Microwave radiative transfer with nonspherical precipitating hydrometeors, J. Quant. Spectr. Radiat. Transfer, 60, 365-374.

Chuah, H. T. and Tan H.S., 1989: A Monte Carlo Method for Radar Backscatter from a Half-Space Random Medium, IEEE Trans Geosci. Remote Sens., 27, 86-93.

Evans, K.F., and Vivekanandan, J., 1990: Multiparameter radar and microwave radiative transfer modeling of nonspherical atmospheric ice particles, IEEE Trans. Geosci. Remote Sens., 28, 423-437.

Evans, K.F., and Stephens, G.L., 1995: Microwave radiative transfer through clouds composed of realistically shaped ice crystals. II. Remote sensing of ice clouds, J. Atmos. Sci., 52, 2058-2072.

Haferman, J.L., Smith, T.F. and Krajewski, W.F. 1997: A multi dimensional discrete ordinates method for polarized radiative transfer. I. Validation for randomly oriented axisymmetric particles. J. Quant. Spectr. Radiat. Transfer, 58, 379-398.

Heymsfield, G.M., and Fulton, R., 1994 Passive microwave and infrared structure of mesoscale convective systems, Meteorol. Atmos. Phys., 54, 123-139.

Liu, Q., Simmer, C., and Ruprecht E., 1996: Three-dimensional radiative transfer effects of clouds in the microwave spectral range. J. of Geophysical Research, 101, D2, 4289-4298.

Roberti, L., and Kummerow, C., 1999: Monte Carlo calculations of polarized microwave radiation emerging from cloud structures. J. of Geophysical Research, 104, 2093-2104.

Wauben W. M. F. and Hovenier J. W., 1992: Polarized Radiation of an Atmosphere Containing Randomly-oriented spheroids, J. Quant. Spectr. Radiat. Transfer, 47, 491-504.

COHERENT PARTICLE SCATTER IN CLOUDS: REFLECTION CALCULATIONS BASED ON IN-SITU MEASUREMENTS

Victor Venema, Jan Erkelens, Herman Russchenberg, and Leo Ligthart

IRCTR, Delft University of Technology

Well-known radar scattering mechanisms are Rayleigh scattering (*incoherent particle scattering*), and clear-air scattering (*coherent air scattering*). This article discusses the importance in clouds of these two mechanisms compared to a third scattering mechanism: *coherent particle scattering*, which is caused by spatial variations in the liquid water content of the clouds. We will argue that for radars with a wavelength larger than a centimetre, coherent particle scatter can dominate Rayleigh scattering from individual droplets, both for cumulus and stratiform clouds. Coherent air scatter in clouds is probably less important than previously thought.

Incoherent particle scatter is due to particles that are randomly distributed within the radar volume. It is most important in atmospheric radars with a small wavelength. Coherent air scatter is caused by variations in the refractive index of atmospheric gases. It is normally dominated by spatial variations in humidity (Gossard and Strauch, 1980) and occurs mainly in radar measurements using a long wavelength (cm-waves or longer).

Erkelens et al. (2000) recently showed that coherent particle scatter, which is caused by variations in the liquid water content (LWC) of clouds, may be important in clouds. Like coherent air scatter this mechanism is mainly important in atmospheric radars with a long wavelength. Erkelens et al. showed that coherent particle scatter can explain the results of dual-wavelength radar measurements of cumulus clouds performed by Knight and Miller (1998) and those of a smoke plume done by Rogers and Brown (1997). In this article we explore the importance of this scattering mechanism for other radar systems and cloud types. Coherent particle scatter is compared in strength to the other two scattering mechanisms. As quantitative data is sparse, the discussion must be labelled as tentative, but for the sake of readability this is not stressed continuously.

2. THEORY OF COHERENT PARTICLE SCATTER

For a cloud with a mono-disperse drop size distribution with diameter (D) in which the particle mass variations are transported from large scales to small scales by isotropic homogeneous turbulence, the radar reflectivity factor (Z) is given by (Erkelens et al., 2000):

$$Z = ND^6 + 4.2\times10^{-3}\beta^2 L_0^{-2/3} N^2 D^6 \lambda^{11/3} \qquad (1)$$

Corresponding author's address: Victor Venema, IRCTR, ITS, TU Delft, Mekelweg 4, 2628 CD Delft, The Netherlands. Fax: +31-(0)15-2784046; Tel: +31-(0)15-2787860; e-mail: V.K.C.Venema@ITS.TUDelft.nl; http://irctr.et.tudelft.nl/~venema/

with N the ensemble average particle number density, L_0 the outer scale length of the inertial subrange of isotropic homogeneous turbulence, and λ the radar wavelength. The first term is the incoherent backscatter and the second term the coherent backscatter. The standard deviation of the spatial Liquid Water Content (LWC) variations is assumed to be a fraction (β) of the total LWC. The derivation is only briefly described in this article – as Erkelens et al. already did this in depth – and is new in the sense that the slope of the LWC variance spectrum is allowed to have various values.

In Van de Hulst (1981) the refractive index (n) of air with many small spheres is formulated as:

$$n = 1 + \frac{\pi}{4} K D^3 N \qquad (2)$$

with $K = (\varepsilon_r - 1)(\varepsilon_r + 2)^{-1}$, a constant that is determined by the relative permittivity of the particles (ε_r); the absorption is neglected.

Assuming that the standard deviations of the variations are a fraction of the mean LWC, i.e. $\sigma_{LWC} = \beta \cdot LWC$, or $\mathrm{var}(ND^3) = \beta^2 (ND^3)^2$, one can write:

$$\mathrm{var}\, n = \frac{\pi^2}{16} |K|^2 \,\mathrm{var}(ND^3) = \frac{\pi^2}{16} |K|^2 \beta^2 N^2 D^6 \qquad (3)$$

The radar backscatter is determined by the variance of the three-dimensional variance density spectrum ($\phi_n(\mathbf{k})$) in a small spectral band around half the radar wavelength in the radars direction ($\hat{\mathbf{k}}$). Following Ottersten (1969) we assume that the spatial variance spectrum integrated over the entire wave number (k) space is equal to the total spatial variance of the refractive index (var n):

$$\int \phi(k)\, dk = \mathrm{var}\, n \qquad (4)$$

To compute this three-dimensional power density integral, it is assumed that the energy spectrum of the LWC variations follows a power law.

Slopes different from –5/3 (the value for homogeneous isotropic turbulence in the inertial subrange) have been measured in clouds. That is why an equation for coherent particle scatter for slopes between –1 and –3 is derived here. According to Tatarski (1961), the three-dimensional spectral density (ϕ(k)) for isotropic turbulence is in this case given by:

$$\phi(k) = \frac{\Gamma(p+1)}{4\pi^2} \sin\left(\frac{\pi(p-1)}{2}\right) C_n^2 k^{-(p+2)} \qquad (5)$$

with $\Gamma(..)$ the gamma function, $-p$ the slope of the (LWC) variance spectrum. The structure constant of the refractive index (C_n^2) is a measure for the total amount of refractive index variations per unit volume.

L_0 (outer scale) and ℓ_0 (inner scale) are, respectively, the largest scale and the smallest scale of the inertial

subrange. Equation (4) can be computed by using Eq. (5) and by assuming that there are no variations at scales larger than L_0 or smaller than ℓ_0. C_n^2 is then given by:

$$C_n^2 = \frac{p-1}{2\Gamma(p+1)\sin(\pi(p-1)/2)}\frac{(2\pi)^p}{\left(L_0^{p-1}-\ell_0^{p-1}\right)^{-1}}\operatorname{var} n \quad (6)$$

The relation between C_n^2 and the radar reflectivity can be found by combining the expression,

$$\eta = \frac{\pi^2}{2}k^4\varphi(k) \quad (7)$$

from Ottersten (1969) with Eq. (5):

$$\eta = \frac{\Gamma(p+1)}{8}\sin(\pi(p-1)/2)k^{-p+2}C_n^2 \quad (8)$$

Combining this with Eq. (6) and substituting $k=4\pi\lambda^{-1}$ yields the radar reflectivity as a function of var n:

$$\eta = \frac{(p-1)\pi^2}{2^p}\left(L_0^{p-1}-\ell_0^{p-1}\right)^{-1}\lambda^{p-2}\operatorname{var} n \quad (9)$$

The radar reflectivity factor is defined by:

$$Z = \frac{\lambda^4}{\pi^5|K|^2}\eta \quad (10)$$

Finally, by combining (3), (9), and (10), the radar reflectivity factor for coherent particle scatter for a variance spectrum with $1<p<3$ is found:

$$Z = \frac{p-1}{16\pi\ 2^p}(L_0^{p-1}-\ell_0^{p-1})^{-1}\lambda^{p+2}N^2\beta^2D^6 \quad (11)$$

which will reduce to the second term on the right-hand side of Eq. (1) for p=5/3 and $\ell_0 << L_0$. For most slopes the term with the inner scale (ℓ_0) can be ignored, as the outer scale (L_0) is normally much bigger. However for p close to 1 the inner scale will become important.

3. SPATIAL VARIATIONS IN CLOUDS

A literature review of measured spatial variations and its sources and sinks is given in Venema et al. (1999). Davis et al. (1999) have measured LWC variations in stratocumulus clouds of 0.290 ± 0.167 g/m^{-3}, so the relative standard deviation is 58 %. Davis et al. (1996) found an average relative standard deviation of LWC of about 19 % in stratocumulus, but it varied highly per measurement; the lowest value found was 5 % and the highest 25 %. Politovich and Cooper (1988) have measured *humidity* variations in cumulus clouds; in the entrained regions the standard deviation was below 0.4 % and in the core of the cloud around 0.1 %.

For fully developed homogeneous isotropic turbulence the slope is –5/3 in the inertial subrange if the sources of the variations act on scales larger than the outer scale (L_0) and the sinks act on scales smaller than the inner scale (ℓ_0). For a passive *conservative* additive the slope of the variance spectrum of the additive is the same as the slope of the turbulent energy spectrum (Tatarski, 1961). However, both the amount of water vapour and liquid water are not conserved in clouds. One can expect the slope of the humidity or LWC variance spectrum to become more flat (steep) if there is an additional source (sink) of variations within the inertial subrange. Slopes that have been measured in situ or by radar are summarised in table 1. Note, that the slopes measured by dual wavelength radar may be incorrect as both the wavelengths may not lie in the inertial subrange

4. COHERENT PARTICLE AND COHERENT AIR SCATTER

Gossard and Strauch (1983) calculated that if the spatial variance of the water vapour content is equal to the spatial variance of liquid water content, the radar reflectivity due to the humidity variations should be about 28 times larger. The quantitative relations are:

$$10^{12}\cdot\operatorname{var} n_L = 2.09\cdot\operatorname{var} L$$
$$10^{12}\cdot\operatorname{var} n_V = 58.5\cdot\operatorname{var} V \quad (12)$$

with, respectively, var n_L and var n_V the variance of the refractive index due to Liquid water variations (var L) and water Vapour variations (var V). In other words, if the coherent particle scatter is to dominate the coherent air scatter, the spatial *standard deviation* of the LWC variations should be at least 5.3 times larger than the spatial standard deviation of the humidity variation.

The relative standard deviations in the spatial humidity variations measured by Politovich and Cooper (1988) in cumulus clouds are: 0.4 % and 0.1 %, see above. One can calculate that the magnitude of the relative liquid water variations in cumulus clouds can be easily more than 5.3 times, except near the cloud base [Venema et al., 1999]. In stratiform clouds the difference is much smaller and measurements should be made to attain a reliable answer.

In the above calculations the slopes of the LWC and humidity variations are assumed to be equal. If this is not the case, the results can be drastically different. Assuming that $\ell_0 << L_0$, and using Eq. (9) and Eq. (12)one can derive the following:

Cloud type	Slope	Additive	Measurement method	Source
Stratocumulus	–0.94 ± 0.10	LWC	In situ, at scales below 5 m	Davis et al. (1999)
Stratocumulus	–1.6 ± 0.1	LWC	In situ, at scales above 5 m	Davis et al. (1999)
Stratocumulus	–1.36±0.06	LWC	In situ	Davis et al. (1996)
Cumulus	–2.2	Humidity	Dual wavelength radar	Knight & Miller (1998)
Winter clouds	–0.9	LWC/hum.	Forward scattering radar	Gossard & Strauch (1981)
Low level clouds	–1.1 to –1.3	LWC/hum.	Dual wavelength radar	Gage et al. (1999)

Table 1. Slopes of the variance spectra in clouds.

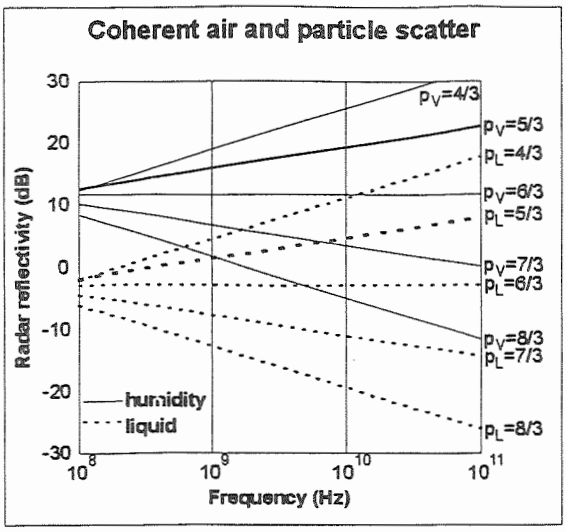

Figure 1. Calculation of the strength of coherent air and coherent particle scatter for different slopes of the humidity and LWC variance spectrum, using Eq. (11) and (13). The dashed line is the radar reflectivity from LWC variations and the drawn line from the humidity variations. The variances in humidity and LWC are equal, and L_0 is 10 m.

$$\frac{\eta_L}{\eta_V} = \frac{p_L - 1}{p_V - 1} 2^{-p_L + p_V} L_0^{-p_L + p_V} \lambda^{p_L - p_V} \frac{\mathrm{var}\, L}{28\, \mathrm{var}\, V} \qquad (13)$$

with η_L and η_V the radar reflectivity due to LWC variations and humidity variations, respectively, and $-p_L$ and $-p_V$ the slopes of respectively the LWC and humidity variance spectra.

In Fig. 1 η_L and η_V are compared for various slopes and wavelengths for identical variance of humidity and LWC and L_0 = 10 m. For a larger value of L_0 the differences will be larger. In Fig. 1 one can see that for equal slopes the coherent air scatter is 28 times (15 dB) more than the coherent particle scatter, as expressed by Eq. (12). When the slope of the humidity variations is steeper than that of the LWC variations, the lines can cross. For example, the radar reflectivity due to humidity variations (for a slope $-p_V$ of –2.2) and the radar reflectivity due to the LWC variations (for a slope $-p_L$ of –1.36) will be almost equal for an S-band radar (λ=0.1 m), in-stead of 28 times smaller.

5. COHERENT AND INCOHERENT PARTICLE SCATTER

To investigate how important incoherent scatter is compared to coherent particle scatter for various scenarios we illustrate the influence of the variables in Eq. (1) and (11) with a few graphs. Fig. 2a shows the relative strength of coherent particle scatter compared to incoherent particle scatter for different values of the relative spatial standard deviation of LWC (β).The high values may occur at cloud boundaries and the low ones in a cloud that is not very turbulent.

In Fig. 2b the relative strength of coherent particle scatter compared to incoherent particle scatter is investigated in relation to the number density (N). A number density of 1000 cm^{-3} is a high value for cumulus, 200 to 500 cm^{-3} is representative for stratus clouds, and the value of 10 cm^{-3} corresponds to some ice clouds. The other parameters are shown in the figure.

The value for the outer scale is uncertain; fortunately it is a less importance (Fig. 2c). VanZandt et al. (1978) used 10 m. L_0 is largest in turbulent regions with low hydrostatic stability (Gage, 1999). We included this graph with L_0 as independent variable to show that the spread is not very large compared to the other variables.

The influence of the slope (p) is plotted in Fig. 2d, using Eq. (11). The inner scale is assumed zero. The difference in reflectivity between the plotted slopes will become larger when a larger outer scale is chosen.

Concluding, the strength of coherent scatter compared to incoherent scatter is largely determined by the radar wavelength. For wind profilers coherent particle scatter will often dominate incoherent particle scatter. For typical number densities in ice clouds only a wind profiler may receive significant coherent scatter. For typical number densities and relative LWC variations found in stratocumulus clouds, coherent particle scatter (either from humidity or LWC variations) can dominate incoherent scatter for an S-band radar. For an X-band radar, coherent particle scatter can dominate only for the highest values of β and number densities. For mm-wave radars coherent particle scatter is not likely, although given the uncertainty in the variables (especially β and p) it cannot be ruled out. Note that the inner scale may be larger than half the wavelength in some situations. When the slope is flatter than –5/3, which occurs, as measurements have shown, the coherent particle scattering is several dBs stronger at typical radar wavelengths (see Fig. 2d).

6. CONCLUSIONS & RECOMMENDATIONS

This paper explored the possibility of significant coherent particle scatter in clouds. Measurements in literature have shown significant spatial variations in liquid water content and humidity in stratus, stratocumulus and cumulus clouds.

There is evidence from dual-wavelength measurements that the slope of the humidity spectrum can be steeper than the standard value of –5/3, while evidence from in situ measurements shows that the slope of the LWC spectrum can be flatter. This can have a significant impact on radar reflectivity.

Calculations show that coherent particle scatter can dominate coherent air scatter and incoherent particle scatter in the top part of cumulus clouds. In stratocumulus clouds coherent scatter can dominate, to determine whether the source of the coherent scatter is variations in LWC or humidity, simultaneous in-situ measurements of these parameters are needed.

To test the theory of coherent particle scatter, simultaneous measurements of LWC and humidity variations should be compared to measurements of coherent radar scatter.

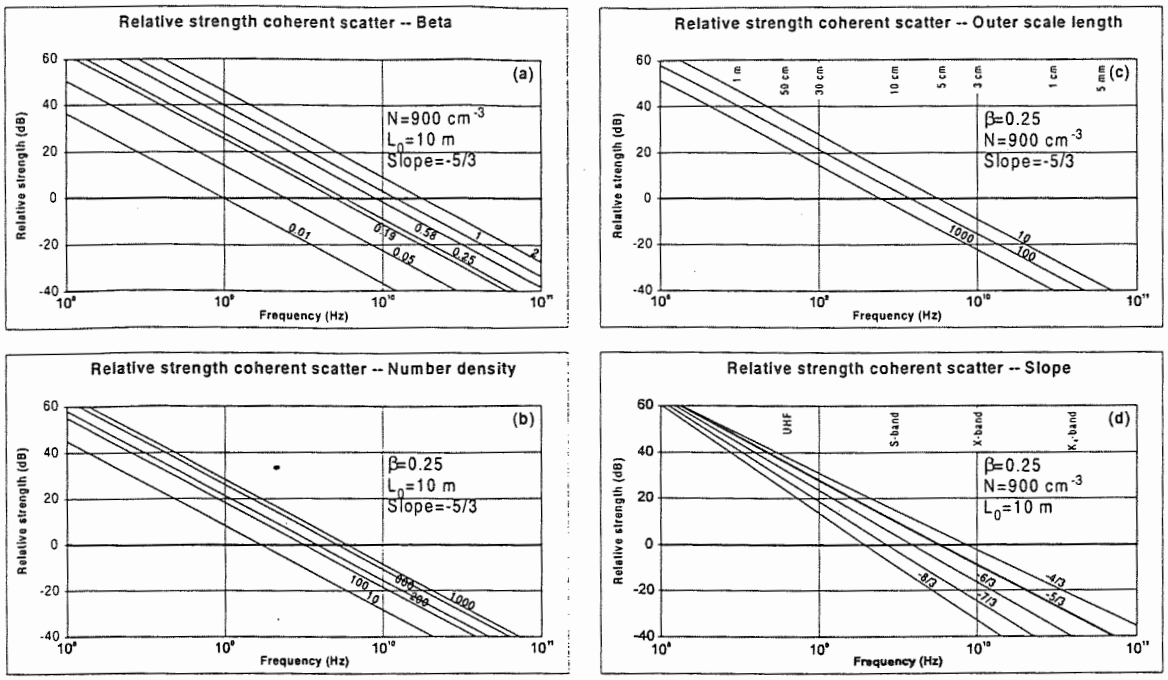

Figure 2. Plots of the relative strength of coherent particle scatter compared to incoherent particle scatter as a function of radar frequency. On the 0-dB level both mechanisms are equally strong.

To develop the theory further, small-scale in situ measurements should be made of humidity, LWC and temperature spectra, both of the (co-)variance and the slopes. Measurements of the LWC and humidity spectra should be made for a range of different cloud types, to determine which type of coherent scatter is important for which type of cloud. A theoretical expression for coherent particle scatter for LWC spectra with a slope flatter than −1 should be developed, especially since a slope of −0.9 has been observed.

REFERENCES

Davis, A.B., A. Marshak, H. Gerber, and W.J. Wiscombe, 1999: Horizontal structure of marine boundary layer clouds from centimeter to kilometer scales. *J. Geophys. Res.*, **104**, pp. 6123-6144.

Davis, A., A. Marshak, W. Wiscombe, and R. Cahalan, 1996: Scale Invariance of Liquid Water Distributions in Marine Stratocumulus. Part I: Spectral Properties and Stationarity Issues. *J. Atmos. Sc.*, **53**, no. 11, pp. 1538-1558.

Erkelens, J.S., V.K.C. Venema, H.W.J. Russchenberg, and L.P. Ligthart, 2000: Coherent scattering of microwaves by particles, evidence from clouds and smoke. Submitted to *J. Atmos. Sci.*

Gage, K.S., C.R. Williams, W.L. Ecklund, and P.E. Johnston, 1999: Use of Two Profilers during MCTEX for Unambiguous Identification of Bragg Scattering and Rayleigh Scattering. *J. Atmos. Sci.*, **56**, pp. 3679-3691.

Gossard, E.E., and R.G. Strauch, 1983: *Radar Observations of Clear Air and Clouds*. Elsevier, 280 p.

Gossard, E.E., and R.G. Strauch, 1981: The Refractive Index Spectra within Clouds from Forward-Scatter Radar Observations. *J. Atmos. Sci.*, **20**, pp. 170-183.

Van de Hulst, H.C., 1981: *Light scattering by small particles*. p. 67 & 70, Dover, New York, 470 p.

Knight, C.A., and L.J. Miller, 1998: Early Radar Echoes from Small, Warm Cumulus: Bragg and Hydrometeor Scattering. *J. Atmos. Sci.*, **55**, no. 18, pp. 2974-2992.

Ottersten, H., 1969: Radar Backscattering from the Turbulent Clear Atmosphere. *Radio Sci.*, **4** (12), pp. 1251-1255.

Politovich, M.K., and W.A. Cooper, 1988: Variability of the Supersaturation in Cumulus Clouds. *J. Atmos. Sci.*, **45**, no. 11, pp. 1651-1664.

Rogers, R.R., and W.O.J. Brown, 1997: Radar observations of a major industrial fire. *Bull. Am. Met. Soc.*, **78**, no. 5, pp. 802-814.

Tatarski, V.I, 1961: *Wave propagation in a turbulent medium*. McGraw-Hill, New York, 285 p.

VanZandt, T.E., J.L. Green, K.S. Gage and W.L. Clark, 1978: Vertical profiles of refractivity turbulent structure function: Comparison of the observations by the Sunset radar with a new model. *Radio Sci.*, **13**, pp. 819-829.

Venema, V.K.C., J.S. Erkelens, H.W.J. Russchenberg, and L.P. Ligthart, 1999: Some notes on scattering of radiowaves by clouds. *Proc. Symp. Remote Sensing of Cloud Parameters: Retrieval and Validation*, pp. 63-70, 21-22 Oct. Delft, The Netherlands.

Observations of supercooled water and of secondary ice generation by a vertically pointing X-band Doppler radar.

Isztar Zawadzki and Frédéric Fabry

Department of Atmospheric and Oceanic Sciences, J. S. Marshall Radar Observatory, McGill University

1. INTRODUCTION

Rimed snow is a common occurrence in winter storms when the prevailing temperature is relatively mild. Thus, the conditions for co-existence between snow and supercooled liquid cloud are often fulfilled in stratiform winter precipitation. Soundings such as the one in Fig. 1 are common during winter storms. In this particular case, a relatively warm quasi-isothermal saturated layer extends up to 650 mb and a moist adiabatic lapse rate is seen thereafter.

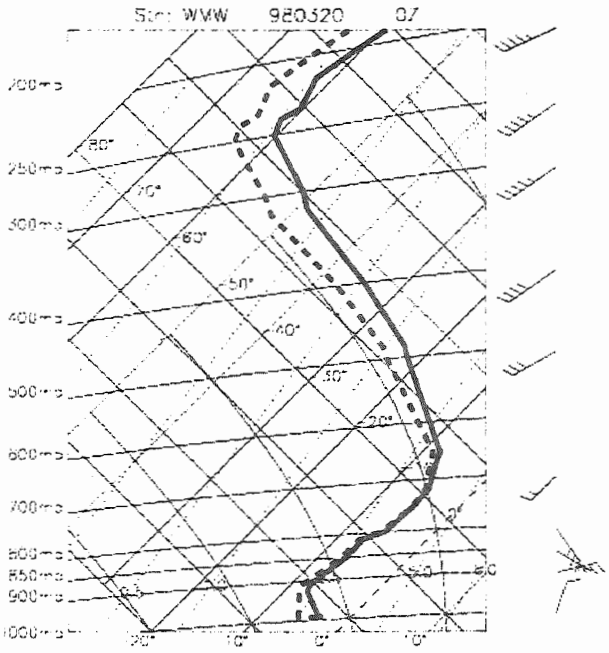

Fig. 1 –*Maniwaki sounding, 150 km NNW of Montreal, just before a snow storm passed over Montreal*

The rate at which water vapor (wv) is depleted by deposition is controlled by the supersaturation, and the number and size of particles. Because of the scarcity of freezing nuclei at $0 > T > -10$, few, if any, new freezing nuclei will be activated at these levels. Deposition on solid particles will hence mainly occur on snow falling from above 600mb. If the number of solid particles is too small to deplete the wv its pressure will increase until saturation is reached with respect to liquid water. At that point, condensation will occur and liquid cloud form. Therefore, when this number of snowflakes is small, the generation of excess of wv may become fast enough so that condensation occurs and riming follows (see for example Zawadzki et al, 1999).

If the rimed cloud droplets have sizes above 24 μm, laboratory experiments indicate that at these warm temperatures secondary ice generation may occur (Mossop 1976). At the same time, given the presence of the large cloud droplets, supercooled drizzle formation becomes possible. Sufficiently rapid secondary ice generation will prevent, or at least limit, the amount of drizzle generation by increasing the total rate of deposition. For a given snow content, it is clear that the rate of generation of excess of vw, determined by the intensity of the vertical air motion, will determine which of these two processes dominates. This may have a practical consequence since supercooled droplets, particularly those of drizzle size, cause aircraft icing.

2- RADAR OBSERVATIONS.

Figure 2 depicts a situation that we will analyze to illustrate the detection of supercooled water with a X-band Vertically Pointing Doppler Radar (VPDR, see Fabry and Zawadzki 2000). The upper air sounding corresponding to this snowstorm is the one shown in Fig. 1.

The time-height sections of reflectivity and of Doppler velocity are shown in the upper and middle panels, respectively. Vertical profiles of Doppler spectra and reflectivity at two times are shown in the bottom part of Fig. 2. Our objective is to understand the nature and the origin of the bi-modality seen in the spectra.

The reflectivity panel clearly shows the typical snow generating cells just above 5 km where the temperature is close to -20 C (see the upper air sounding in Fig. 1). There is some decrease in reflectivity with height between the level of snow generation and 4 km. It suggests that there is no upward vertical air motion within this one-kilometer

Correspondig author: Isztar Zawadzki, Dept. of Atmospheric and Oceanic Sciences, McGill University,805 Shrbrooke St W., Montreal, Quebec, Canada, H3A 2K6.

layer and some sublimation of snow is taking place. Just below 4 km the intensity of precipitation increases abruptly. Thus, it appears that a second level of precipitation generation is present.

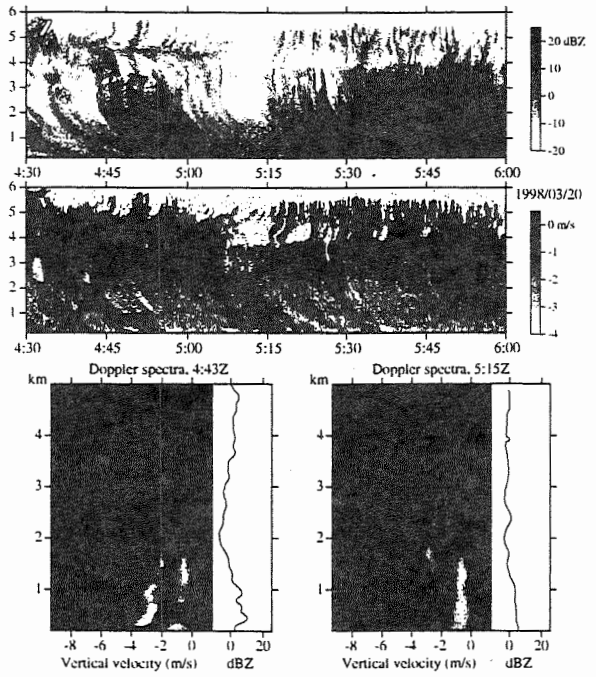

Fig. 2.-*Upper panel shows the time-height section of reflectivity; middle panel shows the mean Doppler velocity. Vertical profiles of Doppler spectra and of reflectivity are shown at the bottom.*

This can be better understood with reference to the sounding of Fig. 1. The temperature profile is quasi-isothermal and saturated up to 650 mb with temperatures between –6 C and –8 C. As mentioned above, the number of active freezing nuclei in this layer is very low and consequently few new ice particles can be initiated here. Above this layer the temperature profile is near moist adiabatic and below saturation. Any general uplifting in the stable layer below 650 mb will generate excess of water vapor with respect to saturation which will deposit on the existing snow. If the generation of excess of wv is faster than the rate of deposition the remaining vapor will condense into supercooled cloud.

A rapid increase in fall velocity (see the velocity panel) and to a lesser extent in reflectivity, is seen between 2 and 3 km. Spectral bi-modality starts at the bottom of this layer, at 2 km. The two Doppler modes are well separated indicating two types of hydrometeors originating through two distinct processes. From a first glance at the Doppler spectra in Fig. 2 it is tempting to associate the mode with the modal velocity of 1 m/s to snow and consequently the modal 2.5 m/s of the second Doppler mode with 0.5 mm droplets forming super-cooled drizzle. However, it is possible to trace the mode with the fastest fall velocity to the upper levels (5 km). First gradually and then rapidly the modal velocity increases from 1 m/s, typical of snow, to 3 m/s, while the lower velocity mode (peak of 1.1 m/s) only appears first at 2.5 km. Thus, the fastest falling particles are initially snow. Their rapid growth leading to velocities above 2 m/s can only be interpreted as riming. Thus, the slowest particles appear to be drizzle droplets of around 0.3mm diameter.

From these observations the following picture emerges. Dry snow is generated at the –20 C level. It freely falls into the isothermal region where the vertical velocity is sufficiently strong to produce excess of vw at a rate faster than can be depleted by deposition on existing snow and by initiation of a few new snow particles. To account for the increase in fall velocity we must assume that w is strong enough so that some liquid cloud is formed, and in the layer below 4 km snow grows by riming. This explains the rapid increase in reflectivity from 4 to 2.5 km and the accompanying rapid increase in modal velocity. However, the rate of riming cannot compensate the rate of cloud formation. Thus, eventually super-cooled drizzle droplets are formed by coalescence of cloud droplets giving rise to the second Doppler peak. Their fall velocity is 1 m/s plus whatever air velocity w is present.

A thin layer of ice covered the snow at ground after the event. This confirms unambiguously the presence of supercooled drizzle.

3. ALTERNATIVE ORIGIN OF THE BI-MODALITY.

There is an alternative explanation for the slower falling particles. The temperature conditions in which the riming takes place are ideal for the secondary generation of ice crystals by the process described by Mossop (1976). These crystals could have rapidly grown to snow size by the transfer of vapor from the supercooled cloud and attain the fall speed of snow. The question is then whether the low velocity mode is in fact due solely to drizzle, or to a mixture of drizzle and ice crystals produced by secondary ice generation.

There is no simple way to answer the question in this particular situation. However, in warmer air masses, in which the precipitation falls through the zero degree isotherm, it is possible to tell the difference between ice and water by the change in fall velocity as the precipitation goes through the melting layer. An abrupt change indicates melting of solid particles. Figure 3 illustrate that the two mechanisms can produce very similar bi-modality. Figure 3 shows two very different situations in which spectral bi-modality was observed above the freezing level. In the right-hand side the melting layer is at 4 km while the in left hand side case the melting level is at 2 km; eventually the melting layer.

The right-hand side Doppler spectra indicate snow formation at 8 km. At seven kilometers a rapid growth is seen accompanied by an increase in fall velocity from that of snow to values indicative of heavy riming. A second mode appears at ~5.5 km, with particles of speed increasing with fall distance again. When the zero degree isotherm is crossed the abrupt increase in modal velocity of both Doppler modes indicates that both populations of solid particles are melting. Thus the low velocity mode is very likely indicative of ice multiplication.

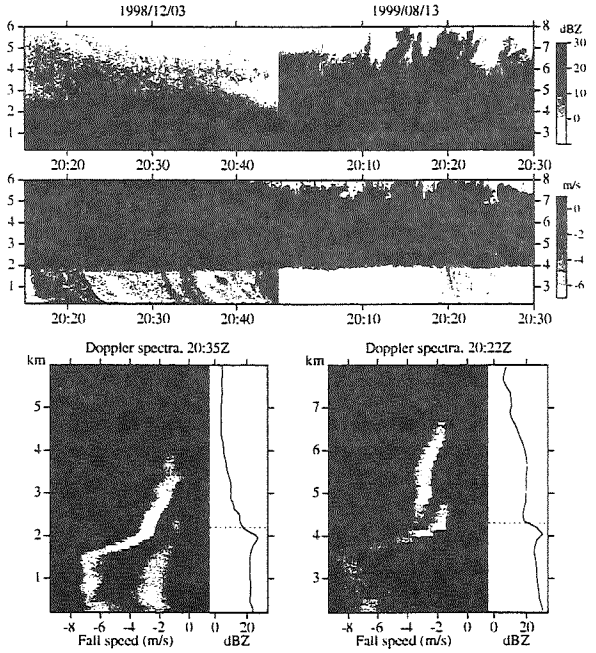

Fig. 3- *As in Fig 2 for two situations in which the bright band is present.*

In the case of 3/12/98 (left hand side Doppler spectra in Fig. 3) the faster Doppler mode, corresponding to snow, shows an increase in velocity and in reflectivity indicative of riming in the lower levels, from 3.5 km to the melting layer. The second Doppler mode appears just below 3 km. In contrast to the previous example, in this case the passage through the bright band shows that the fastest mode is associated with solid particles while the slower mode appears to be associated with drizzle. The change in fall velocity of the latter is gradual, and the smooth increase in velocity and reflectivity is indicative of low level growth rather than of phase change.

Why secondary ice generation is dominant in one case while formation of drizzle prevails in the other? A glance at the time-height velocity panels in Fig. 3 provides the clue.

In the case of 13/8/99, the increase in fall velocity of snow begins at 6.5 km indicating that riming is already happening. Values of fall velocity greater than 2 m/s, indicative of heavy riming, appear over a layer of 2.5 km. Heavy riming occurs over a deep layer. In the other case, some patches of upward vertical motion between 3.5 and 5 km indicates updraft in this layer. The heavy riming, as revealed by the increase in fall velocity and reflectivity, occurs in a much shallower layer near the bright band.

Both, the generation of drizzle and of secondary ice, depend on the presence of large cloud droplets. The rate of cloud conversion to drizzle increases with the square of the number of cloud particles. On the other hand, the rate of liquid water collection by riming increases linearly with the number of cloud particles and is proportional to snow content. If the number concentration of cloud droplets is large, few snow particles will not be sufficient to sweep away the cloud nor to produce appreciable amount of secondary ice, as it takes between 100 and 300 rimed cloud droplets to produce one secondary ice particle (Mossop 1976). The rate of riming has also bearing on the snow-vapor interaction. As shown in Zawadzki et al. (2000), the latent heat released during heavy riming decreases significantly the difference in saturation water pressure between the snow and the cloud liquid water. The deposition on snow is then appreciably slowed down. With sufficient riming, the wv pressure difference may even change sign and snow could then sublimate as a consequence of riming. In this situation, ice crystals originating in the secondary ice generation - not capable of riming because of their small size and poor collision efficiency - may be the only agents of the Bergeron process and therefore necessary for preventing drizzle formation.

With high cloud water content, such as needed for drizzle generation, and relatively few snow particles, each particle will have abundant water to collect. Consequently, rimed snow will be sufficiently warmed up by the latent heat released and will not inhibit the growth of the liquid phase by the Bergeron process. The not too abundant crystals generated by the riming may be insufficient as well. Thus, with high number concentration of cloud droplets and low snow content the formation of supercooled drizzle becomes possible. Only when both, the snow and cloud contents are large, heavy riming will generate enough secondary ice crystals and inhibit the growth of cloud particles to drizzle size by the transfer of wv from liquid to solid. The two situations depicted in Fig. 2 seem to be consistent with these ideas.

There is another situation of bimodal Doppler spectra that it is clearly associated with coexistence of snow and supercooled drizzle. Figure 4 shows bi-modal spectrum observed on the 13 of December 1999. The temperature profile was quasi-isothermal and above –10 C up to 700mb. The two modal velocities appear at the top of the detectable precipitation layer. Thus, it appears that there was no time for heavy riming to generate secondary ice and the slow mode peak is likely associated with drizzle

formed by the "warm process" at the same time as some ice was generated. This case resembles the one in Fig. 2: there is indication of generating cells at 5 km and a second level of generation at 4 km. At that height the two modes appear. The NASA Twin Otter aircraft passed overhead our instrument and reported presence of supercooled drizzle.

DISCUSSION.

An increase in vertical fall velocity of snow to values above 2 m/s is indicative of riming. In several occasions we observed that spectral bi-modality appeared right below the level where a fast riming rate had occurred. This can be interpreted as either secondary ice generation or formation of supercooled drizzle from the same cloud that feed the riming. We have shown that both processes are possible, although at any time one of them may be the dominant source of the second Doppler mode. To our knowledge, the case of stratiform precipitation of 13/8/99 in Fig. 3 is a first direct observation of occurrence of secondary ice generation concurrent with riming. In the case of 12/3/98 the auto-conversion of cloud to drizzle was the dominant process.

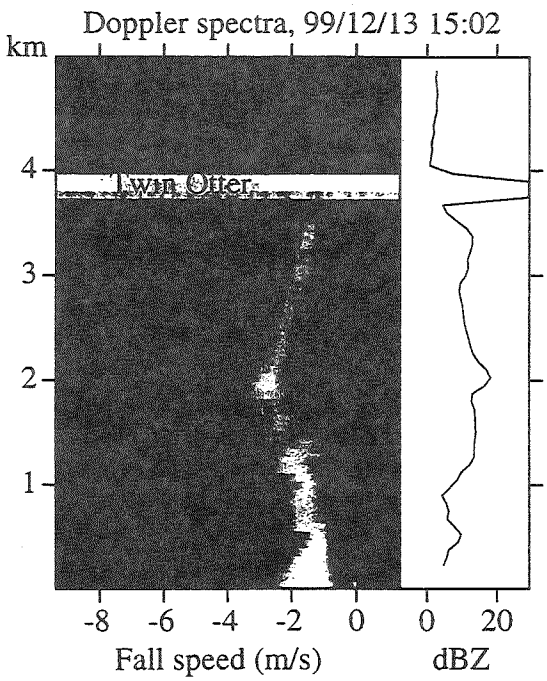

Fig. 4- *Example of a bimodal spectrum where the low velocity mode appears at the top of the detectable precipitation.*

Acknowledgments:

Thomas P. Ratvasky kindly provided the report on the drizzle observation during the Twin Otter flight.

References.

Fabry, F. and I. Zawadzki, 2000: Atmospheric physics as observed by a vertically pointing Doppler radar. These proceedings.

Mossop, S. C.,1976: Production of secondary ice particles during growth of graupel by riming. Quart. J. R. Met. Soc., **102**, 45-57.

Zawadzki, I., W Szyrmer, and, S. Laroche, 1999: Diagnostic of Supercooled Cloud from Single Doppler Observations in Regions of Detectable Snow. J. of Appl. Met. In print.

HYDROMETEOR CLASSIFICATION FROM POLARIMETRIC RADAR MEASUREMENTS: A FUZZY LOGIC SYSTEM AND IN-SITU VERIFICATION

V. Chandrasekar, Hongping Liu, and Gang Xu
Colorado State University, Fort Collins, CO 80523.

1. INTRODUCTION

A Fuzzy logic system for classification of hydrometeor type based on multiparameter radar measurements is described in this paper. The hydrometeor classification system is implemented by using Fuzzy Logic, where the fuzzy logic is used to infer hydrometeor type. Five radar measurements, namely, horizontal reflectivity (Z_H), differential reflectivity (Z_{DR}), differential propagation phase shift (K_{DP}), correlation coefficient ($\rho_{HV}(0)$), and linear depolarization ratio (LDR), along with the corresponding altitude have been used as input variables to the Fuzzy logic network. The output of the Fuzzy logic system is one of the many possible hydrometeor types, namely 1)drizzle, 2)rain, 3)dry and low density snow, 4)dry and high density crystals, 5)wet and melting snow, 6)dry graupel, 7)wet graupel, 8)small hail, 9)large hail, and 10)mixture of rain and hail. The Neuro-Fuzzy classifier is more advantageous than a simple Neural Network or a fuzzy logic classifier because it is more transparent (instead of a "black box"), and can learn the parameter of the system from the past data (unlike a fuzzy logic system). The Fuzzy logic hydrometeor classifier has been applied to several case studies and the results are compared against in-situ observations. A detailed description of this development can be seen in Liu and Chandrasekar (2000).

2. FUZZY LOGIC HYDROMETEOR CLASSIFIER

2.1 Configuration of a General Fuzzy Logic System

The Fuzzy logic system consists of four parts, fuzzification, rule inference, aggregation and defuzzification (Zadeh, 1989). The function of the various blocks in the fuzzy logic system are as follows:

(i) Fuzzification

The function of the "fuzzification" block is to convert the crisp inputs (or precise measurements) to the fuzzy sets with corresponding membership degree. The most important component in fuzzification is the *membership function*, which is used to describe the relationship of the crisp input and the fuzzy sets in the input domain.

(ii) Inference

In a fuzzy logic system, rules are used to describe linguistically the complex relationship between the input and output fuzzy variables in the form of IF-THEN statements. Typically, the rule is composed of several 'antecedents' in the IF statement and one or several 'consequents' in the THEN statement. The process of deducing the "strength" of these consequents from the "strength" of the antecedents is called rule *inference.*

(iii) Aggregation

Several rules (instead of a single rule) can be used to describe a fuzzy logic system. The set of rules is called a 'rulebase'. The complete knowledge about a fuzzy model is contained in its rulebase and the membership functions. We can use the inference methods to derive the "strength" of each rule, then an aggregation method can be used to determine an overall fuzzy region.

(iv) Defuzzification

The output of the aggregation process is a fuzzy set. In many applications, however, such as hydrometeor classification, it is necessary to find a crisp value which best represents the fuzzy output set. This process is called *defuzzification.*

2.2 Architecture of A Fuzzy Hydrometeor Classifier

To implement the hydrometeor classification using fuzzy logic (fuzzy hydrometeor classifier, hence forth referred as FHC), the four general blocks (*fuzzification*, IF-THEN rule *inference*, *aggregation* and *defuzzification*) need to be specified. The block diagram of the FHC is shown in Figure 1, Z_H, Z_{DR}, K_{DP}, LDR, ρ_{hv}, and altitude of the observation (H), are the 6 inputs, and the hydrometeor Class (C) is the output. The FHC will infer the hydrometeor

Table 1: Output of the fuzzy classifier system

Hydrometeor Type	Classifier Output C
drizzle	1
rain	2
low density dry ice crystal	3
high density dry ice crystal	4
wet ice crystal	5
dry graupel	6
wet graupel	7
small hail	8
large hail	9
rain + hail	10

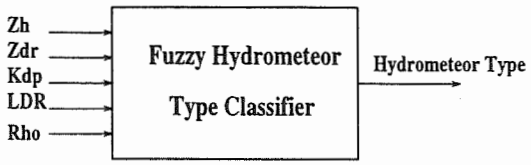

Figure 1: Block scheme of the fuzzy classifier

type C based on the rulebase from the 6 inputs. Table 1 lists the 10 classes used in inference of summer storms. The detailed block diagram of the Fuzzy Hydrometeor Classifier is shown in Figure 2.

2.3 Classification Procedure

The classification procedure of FHC shown in Figure 2 can be described as follows: First, the 5 radar measurements and altitude are fuzzified by using membership functions (MBFs). There are 10 MBFs for each of the input variables in the system. After fuzzification, the IF-THEN rule inference is carried out based on the rulebase for the classification system. To achieve the total effect of all the rules, rule aggregation is applied. The last step is defuzzification, which can convert the aggregation result into a single hydrometeor type.

3. PERFORMANCE EVALUATION OF THE FHC

The performance of the Fuzzy hydrometeor classifier is evaluated using radar data from CSU-CHILL radar.

3.1 Data Sources and Instrumentation

(i) CSU-CHILL Radar

The radar data used in this study were collected by the CSU-CHILL radar. CSU-CHILL is an S-band, dual polarization radar, which can measure a full set of polarimetric measurements.

(ii) In-Situ Observations

Hail Chase Van

An instrumented hail chase van with a roof-mounted net was constructed to intercept the

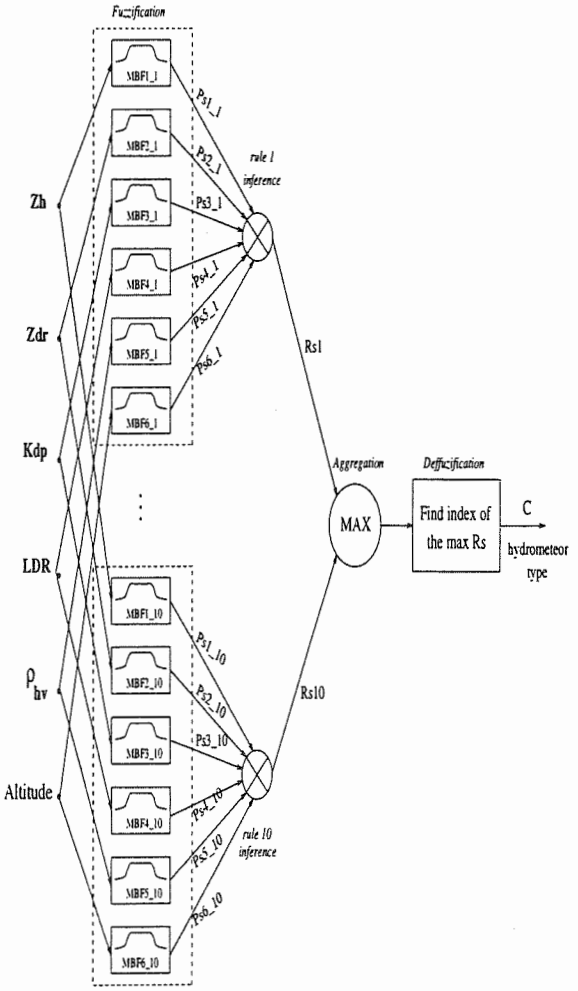

Figure 2: A Fuzzy System for Hydrometeor Type Classification

storms. This chase van is equipped with a rain/hail separator and a Young capacitance raingage. Hail was collected and quenched in chilled hexane and then stored in dry ice. The hail stones were eventually photographed using digital camera for post analysis. A detailed description of the hail chase van is given in Hubbert et al (1998).

3.2 In-situ Verification of Hydrometeor Classification

(i) The severe hail storm on June 7, 1995

On 7 June 1995, the CSU-CHILL radar observed a supercell structure, and a chase van with a roof-mounted hail collector net was sent to intercept the storm core and collect in-situ measurements. The 7 June 1995 storm turned out to be a severe hail storm. Figure 3 shows the radar measurements Z_h, Z_{dr}, K_{dp}, LDR, and ρ_{hv}, and Figure 4 shows the the classification result from the Fuzzy classification system. We can see from the hydrometeor classification result that hail and rain mixture, wet graupel, and rain are found on the ground as well as at low altitude, whereas ice crystals were inferred at high altitude. The vertical structure of the storm can be seen fairly well from the classification result. The in-situ ground observations were consistent with the result of the Fuzzy Hydrometeor classifier. The hail chase van collected some hailstones, and also observed rain mixed in the storm. The in-situ ground observations for this case are given in Hubbert et al (1998). The Fuzzy classification results agree very well with inference of Hubbert et al (1998).

(ii) The Snow Storm on February 18, 1997

On February 18, there was a light snow event in the vicinity of the CSU-CHILL radar. Figures 5 and 6 show a vertical section of the CSU-CHILL radar measurements through this storm. The radar measurements of Z_H, LDR and ρ_{HV} and the hydrometeor classification result are shown in Figures 5 and 6. The hydrometeor classification indicates wet snow below 1 km, dry snow and oriented ice crystal above 1 km. We can see a transition from rain to snow on the ground. This feature of rain to snow transition was observed on the ground in excellent agreement with radar based FHC inferences.

4. SUMMARY AND CONCLUSION

Polarimetric radars have been used for discriminating water and ice regions, detecting ice-crystal and hail regions in storms. In this paper, we have described an automatic classification system using fuzzy logic to classify the hydrometeors in storms.

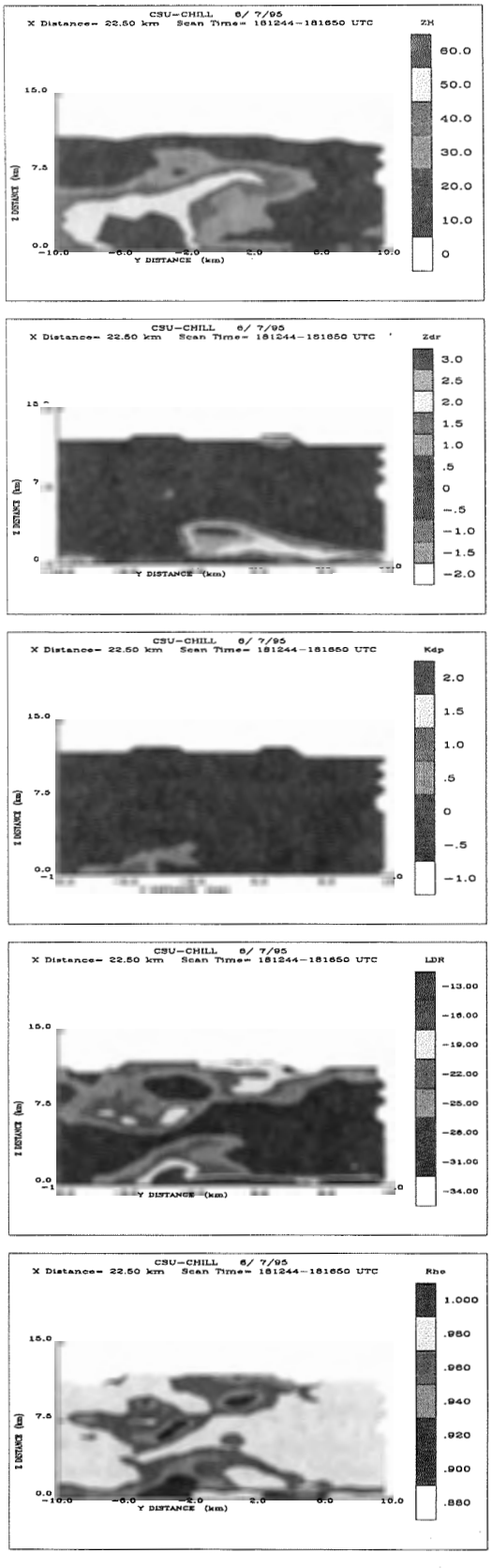

Figure 3: Radar measurements Z_H, Z_{DR}, K_{DP}, LDR and ρ_{HV}

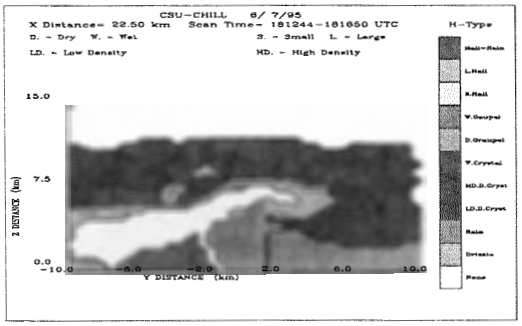

Figure 4: Hydrometeor Type Classification result corresponding to the case of June 7, 1995

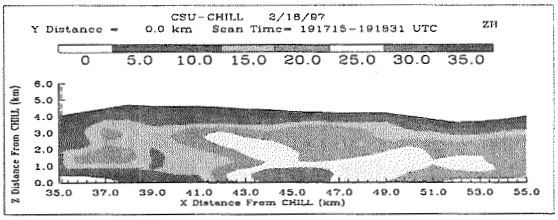

Figure 5: (a)Radar measurements Z_H for the storm on Feb. 18, 1997

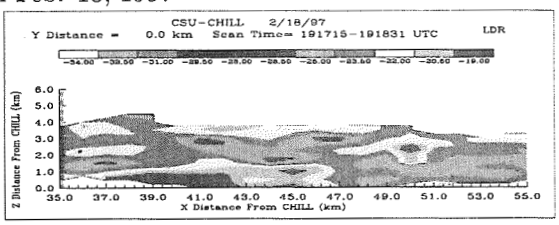

Figure 5: (b) Radar measurements LDR for the storm on Feb. 18, 1997

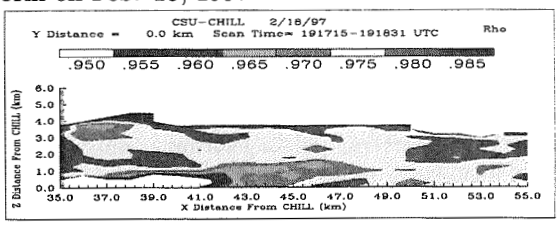

Figure 5: (c)Radar measurements ρ_{hv} for the storm on Feb. 18, 1997

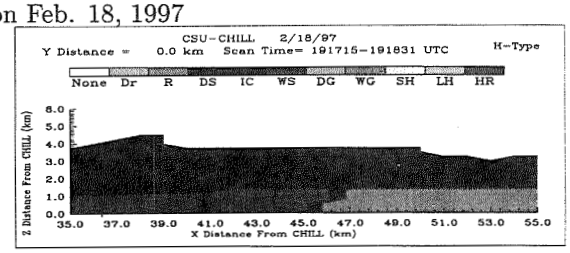

Figure 6: Hydrometeor type classification result: Dr. = Drizzle, R. = Rain, DS. = Dry Snow, IC = Oriented Ice Crystal, WS = Wet Snow, DG = Dry Graupel, WG. = Wet Graupel, SH = Small Hail, LH = Large Hail, HR = mixture of Hail and Rain.

The Fuzzy logic system developed in this work is robust and is not affected by measurement errors. The Fuzzy hydrometeor classifier has been applied to radar data and successfully compared against in-situ measurements. The fuzzy logic classification is currently being implemented in the product display in real time in the CSU-CHILL radar. Similar to any newly introduced systems, the Fuzzy Logic and Neuro-Fuzzy system will be evaluated, fine tuned and improved over time when more observations become available. However the basic frame work is very conducive to improvement and adjustment.

5. ACKNOWLEDGMENTS

This research was supported by the National Science Foundation (ATM - 9413453,9500108). The CSU CHILL radar is supported by the NSF (ATM - 9500108).

References

[1] Hongping Liu and V. Chandrasekar Classification of hydrometeors based on polarimetric radar measurements: development of fuzzy logic and neuro-fuzzy systems, and in-situ verification. In *Journal of Atmospheric and Oceanic Technology*, pages 140–164. February, 2000.

[2] Hubbert,J., Bringi,V.N., and Carey,L.D. CSU-CHILL Polarimetric Radar Measurements from a Severe Hail Storm in Eastern Colorado. *Journal of Applied Meteorology*, pages 749–775. Volume 37, August, 1998.

[3] Zadeh, L.A.. A computational approach to fuzzy quantifiers in natural languages. In *Computers and Mathematics*, Vol. 9(1), pp. 149-184, 1983.

IN SITU VERIFICATION OF POLARIMETRIC RADAR-BASED HYDROMETEOR TYPES

Sabine Göke,* Eszter Barthazy,◇ Scott M. Ellis,* Jothiram Vivekanandan,* and Zhaoxia Zeng+

*National Center for Atmospheric Research, Boulder, Colorado
◇Institute for Atmospheric Science (LAPETH), Swiss Federal Institute of Technology (ETH), Zurich, Switzerland
+Department of Atmospheric Sciences, University of Washington, Seattle, Washington

1. INTRODUCTION

One of the major recent field experiment in atmospheric sciences was the field phase of the Mesoscale Alpine Program (MAP), which took place in fall 1999. MAP was a coordinated international and interdisciplinary effort to explore the mesoscale effects of complex topography. One special focus (the so called 'Wet' MAP) was on the orographically induced heavy precipitation events including flash flood. It is well known that microphysical effects are profound in regions of complex terrain but nevertheless, the least well documented aspects of orographic precipitation are growth, development, and fall out of ice particles. Since the field phase ended recently the analyses of the data is in progress. But their quality is very encouraging in order to gain more insight into these aspects.

During MAP the microphysics was investigated in two different ways - remotely and *in situ*. *In situ* measurements were carried out on the ground or using research aircraft. They yield of course the most detailed information, but have the disadvantage of a poor spatial and temporal resolution. Remote measurements of the microphysics were performed using a new generation radar - a multiparameter polarimetric radar. It surveys a large volume of the atmosphere in high time and space resolution. Recently developed particle typing algorithm simplify the microphysical interpretation of polarimetric radar data. They have the advantage that a radar meteorologist may not be required to know the complicated details associated with polarimetric radar data processing. Although their results look promising, they have not been validated in a systematic way up to now. To verify radar-based microphysics using *in situ* observation is the purpose of the present study. A qualitative comparisons for one case study is presented as a first result.

2. *IN SITU* MEASUREMENTS

Three research aircrafts - the NOAA P-3, the NCAR Electra, and the CNRM Merlin - participated in the MAP field phase. They were equipped with Particle Measuring Systems (PMS), several one- and two-dimensional probes. The latter were mono probes in case of the Merlin and Electra, and grey probes in case of the P-3. Some missions included special microphysical flight modules. Measurements were collected within a radius of 50 km around the polarimetric radar for high resolution comparisons. At the same time the radar was scanning in the vicinity of aircraft location. Some tracks were aligned radial to the radar during the descending or ascending flights. For this case study a flight track at constant altitude was selected.

*Corresponding author address: S. Göke, Advanced Study Program, National Center for Atmospheric Research, P.O. Box 3000, Boulder, CO 80307-3000; e-mail: goeke@ucar.edu.

3. POLARIMETRIC MEASUREMENTS

The NCAR S-Pol was the only polarimetric radar involved in the MAP project. It was located close to the southern end of Lago Maggiore at about 300 m MSL. Different scan strategies were used: 360° volume scans, sector scans, and range height indicator (RHI) scans. Two different particle type classification techniques were implemented - one developed at the University of Washington (UW) and another at NCAR. They will be introduced briefly below.

3.2 The University of Washington Algorithm

The UW microphysical retrieval was developed by Zeng *et al.* (2000). It is based on a simple but robust algorithm implementing fixed rules. Microphysical informations are derived using four parameters of a full set of polarimetric parameters. This algorithm is empirically calibrated by making use of radar data obtained in rain-only situations. It identifies eight broad categories of particles and one ambiguous category. They are rain, attenuated rain and graupel, hail, hail and rain, graupel, graupel and rain, snow, and supercooled rain.

3.1 The NCAR Algorithm

A more sophisticated algorithm is the fuzzy logic approach developed by Vivekanandan *et al.* (1999) at NCAR. It identifies 17 different categories using the full set of polarimetric parameters. The authors chose the fuzzy logic approach, because the values of the radar observables that delineate different particle types overlap and are not sharply defined. It is computationally simple enough to run in real time. There are four rain categories including drizzle, light rain, moderate rain, and heavy rain; five solid phase categories including hail graupel and small hail, dry snow, oriented ice crystals, and irregular ice crystals; three mixed phase

categories including rain and hail, graupel and rain, and wet snow; and three non precipitation particle categories including ground clutter, birds, and insects. Finally there are the categories of super cooled liquid water droplets and cloud particles.

4. CASE STUDY

Persistent precipitation started in the Lago Maggiore region on 3 November 1999 and became heavier the next day. This precipitation was associated with a slow moving upper-level trough, becoming cutoff due to an orographic cyclogenesis process. Stratiform precipitation with embedded cellular structure was observed during the whole morning of 4 November, as seen in Fig. 1. It shows a plan position indicator (PPI) scan of the radar reflectivity recorded by S-Pol at 12:13 UTC. The elevation angle for that sweep was 3.8°. The radar data were preprocessed using a clutter filter. West of S-Pol at a distance of about 25 to 30 km the melting layer can be recognized as a layer of enhanced radar reflectivity - the bright band in dark gray.

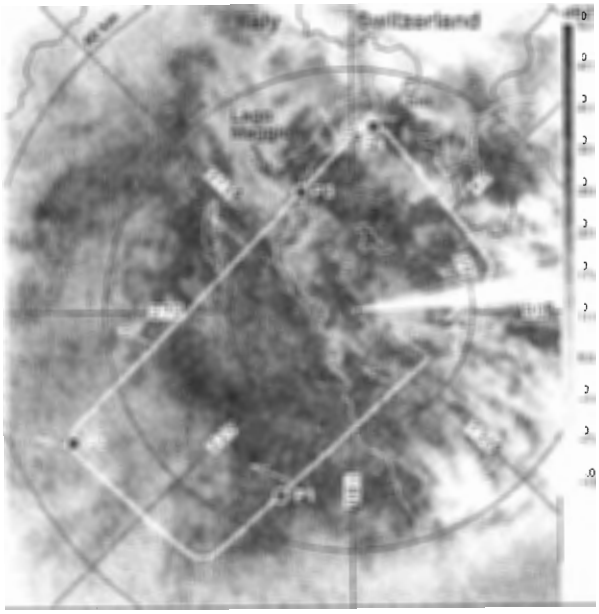

Figure 1: *The radar reflectivity at 12:13 UTC depicted as a PPI with elevation angle of 3.8°. The thick solid white line indicates the flight track of the P-3 performed between 11:46 UTC and 12:13 UTC. The points P1 up to P4 are points of special interest during the flight.*

A number of south-west to north-east oriented lines of precipitation bands moved into the Lago Maggiore area from the south-east. They intensified as they moved into the foothills region. The P-3 flew rectangular flight tracks to sample these lines of precipitation. One of the rectangles is shown in Fig. 1 as a solid thick white line. We started this track at 11:46 UTC and completed the rectangle 27 min later. The long edges of the rectangle are oriented parallel to the slope of the Alps. The north-western edge went straight along the foothills of the mountains. The aircraft was keeping nearly constant altitude during this track (3300 m MSL at the beginning, slowly descending to 3100 m MSL at the end). It was the lowest altitude which was allowed due to air traffic control guidelines. The temperature was about -5°C at this altitude. Four points are indicated in Fig. 1, P1 up to P4. *In situ* measurements in these points will be compared to results of the two different particle classification techniques discussed above.

4.1 Temperature Dependency of the Retrievals

It turns out, that the quality of the results of both microphysical retrievals depends on the temperature profile, particularly the freezing level. In order to obtain the most accurate estimate of the temperature profile, which was prevailing in the area the flight track took place, we reconstructed a profile interpolating several temperature measurements. Shortly before the aircraft started the flight track shown in Fig. 1 it was descending from 5500 m MSL. The precipitation system was relatively stable. This became obvious when we repeated the flight track a second time at the same altitude. We observed the same particles along the track as we did 27 min before. The temperature profile obtained during the descent could therefore be assumed to be valid within the region of our observation.

The height of the 0°C layer was estimated from S-Pol radar data that show a well developed bright band. At the same time a vertically pointing X-band Doppler radar, located 65 km north-west of S-Pol, recorded the bright band with a higher resolution (Barthazy . *et al.*, 2000). The height of the 0°C layer estimated from this radar agreed very well with the height estimated from the S-Pol data. Ground based temperature measurements were also available at the measuring site of the X-band radar.

4.2 At Point P1

Heading towards the south-west, we reached point P1 at 11:51 UTC. The cloud probe on board of the P-3 showed only columns capped with dendrites as depicted in Fig. 2. This situation remained about 40 s (which correspond to a distance of about 5.2 km). Little later we observed needles and their aggregates for a very short time period, and than a mixture of different aggregated particles.

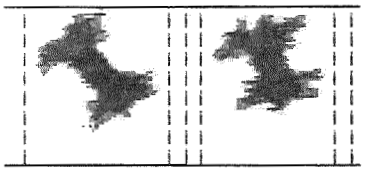

Figure 2: *Columns capped with dendrites recorded at 11:51 UTC. Their lengths are about 1.05 mm (right) up to about 1.15 mm (left).*

These findings were now compared to the results

of the two retrievals (Fig. 3). The radar was scanning the same volume of the atmosphere at 11:43 UTC in the PPI mode using an elevation angle of 5°. There was a time gap of 8 min between the radar measurements and the passage of the aircraft. As pointed out above, a comparison is nevertheless appropriate, since the precipitation was very stable.

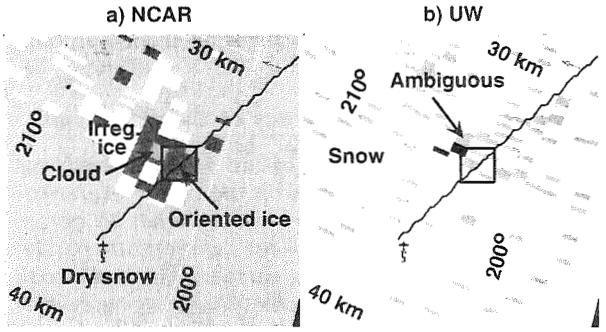

Figure 3: *The particle identifications of NCAR (a) and the University of Washington (b) depicted as PPI. The radar data are recorded at 11:43 UTC using an elevation angle of 5° and the box indicates the position of the aircraft at 11:51 UTC.*

The results of the NCAR algorithms are depicted in Fig. 3a. It clearly shows a little cell of mainly oriented ice crystal embedded in a wider region of dry snow, which is consistent with the *in situ* measurements. The P-3 flew through this cell at 11:51 UTC. The UW algorithm (Fig. 3b) shows the widespread region of snow as well. Small embedded cells classified as ambiguous can be recognized.

4.3 At Point P2

Reaching the foothills of the mountains at 11:58 UTC, the P-3 turned to the north-east. The probes recorded single dendrites and aggregates comprised of dendrites, only. Very large single crystals with maximum diameter of about 4.6 mm could clearly be recognized in the particle probe. Usually the resolution of this probe is too rough to resolve single crystals.

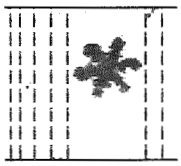

Figure 4: *Ordinary dendritic crystal recorded at 11:58 UTC. Its maximum diameter is about 4.6 mm.*

The radar was scanning the same volume at 11:41 UTC in the PPI mode using an elevation angle of 3°. Unfortunately, there were no radar data available within 17 min from the aircraft measurements. The NCAR and the UW algorithm, both depicted in Fig. 5, show that the aircraft is passing a more widespread region of dry snow. This is in good agreement with the *in situ* measurements. The backscattered intensity is dominated by the largest particles in the volume, which are, in this case, the aggregates.

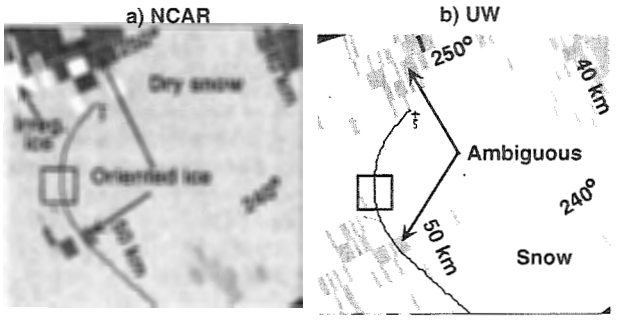

Figure 5: *The particle identifications of NCAR (a) and the University of Washington (b) depicted as PPI. The radar data are recorded at 11:41 UTC using an elevation angle of 3° and the box indicates the position of the aircraft at 11:58 UTC.*

4.4 At Point P3

At 12:04 UTC the aircraft was directly above Lago Maggiore heading towards the north-east. Both hot-wire probes - the King and the Johnson Williams probe - indicated that the liquid water content was increased in this region. Both 2D probes had severe problems due to icing. No particles were recorded. This may be due to icing or may indicate that only supercooled liquid water droplets were present. These droplets are mostly too small to be resolved by the cloud probe.

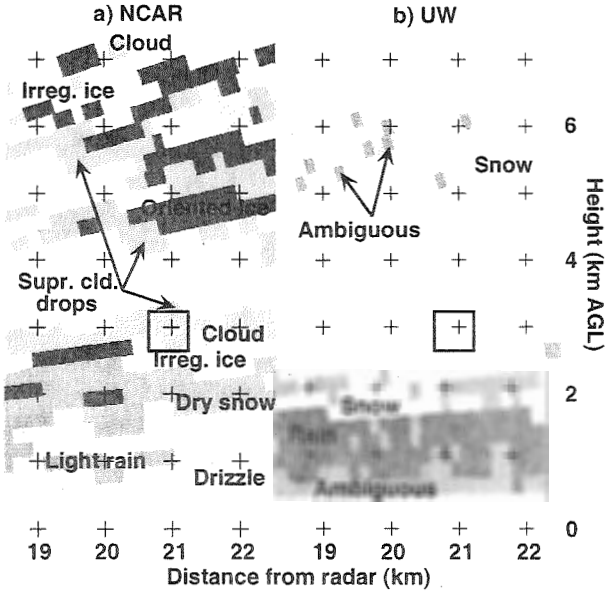

Figure 6: *The particle identifications of NCAR (a) and the University of Washington (b) depicted as RHI. The radar data were recorded at 12:07 UTC using an azimuth of 335° and the box indicates the position of the aircraft at 12:04 UTC.*

Three minutes later the radar was scanning the same volume in the RHI mode with an azimuth of 335°. The results of the particle classification technique are shown in Fig. 6. The NCAR algorithm (Fig. 6a) detected a layer of cloud particles in the region the aircraft was passing, which agrees with the *in situ* data. If the cloud particles were liquid or solid was not distinguishable from the radar data. The backscattered intensity was very weak. The UW algorithm (Fig. 6b) did not identify the particles in this region. Only when the backscattered echoes have a certain intensity, a classification is possible.

Another feature can be recognized in Fig. 6a which is due to weak echoes. No wet snow is detected at an altitude of about 2 km - the height of the melting layer. Taking a closer look at all polarimetric variables we could not found any of the typical bright band characteristics at that altitude. Thus we concluded that due to the weak precipitation the melting layer was possibly too thin to be resolved by the radar.

4.5 At Point P4

At 12:07 UTC the aircraft reached the northern most point of the flight track. The terrain below was relatively high and the aircraft was flying at the lowest altitude which was allowed over this terrain. Elementary needles and very few aggregates comprised of needles were recorded by the cloud probe in this region as shown in Fig. 7.

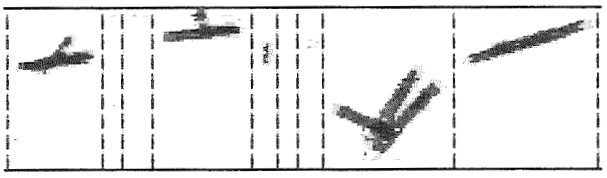

Figure 7: *Elementary needles and very few needle aggregates recorded at 12:07 UTC. Their lengths are about 0.6 mm (left) up to about 1.4 mm (right).*

Data of a RHI scan were available nearly at the same time (a time difference of only 1 min). The results of the two algorithms were depicted in Fig. 8. The NCAR classification (Fig. 8a) agrees nicely with the *in situ* measurements. The aircraft was flying through a layer of oriented ice crystals. The reflectivity threshold implemented in the UW algorithm (Fig. 8b) was barely reached, once again due to very weak echoes. The particles in the region of the aircraft were classified as snow and ambiguous.

5. SUMMARY AND OUTLOOK

This case study presents comparisons between *in situ* measurements and results of two microphysical retrievals, which use polarimetric radar data. The intensity of the precipitation was relatively weak. Under these conditions the algorithms were approaching generally their limits to yield reliable results. Nevertheless the NCAR results agreed well with aircraft observations of ice crystals, super cooled liquid water droplets, and snow. The UW algorithm performed also well in case of snow. Ambiguous types are common for super cooled droplets and low concentration of ice crystals. Although these results are very encouraging, this study presents only four different qualitative comparisons.

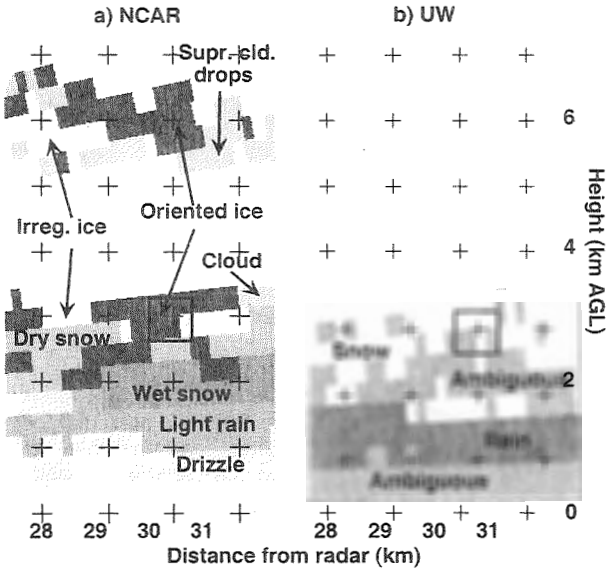

Figure 8: *The particle identifications of NCAR (a) and the University of Washington (b) depicted as RHI. The radar data were recorded at 12:08 UTC using an azimuth of 2° and the box indicates the position of the aircraft at 12:07 UTC.*

In a more systematic approach each flight track will be divided into unit sample volumes. Each volume will be classified in a first step with respect to the phase of the particles within the volume. These three categories include solid particles only, liquid particles only, and mixed phase particles. Than, in a second step, the focus will be on the largest particles within each unit volume. Their characteristics dominate the value of the polarimetric parameters. These particles will than be classified according to the radar-based hydrometeor types for verification purpose.

REFERENCES

Barthazy, E., S. Göke, Z. Zeng, J. Vivekanandan, and S. M. Ellis, 2000, *13th Int. Conf. on Clouds and Precip.*, Reno, NV, Int. Commission on Clouds and Precipitation.

Vivekanandan, J., D. S. Zrnic, S. M. Ellis, R. A. Oye, A. V. Ryzhkov, and J. Straka, 1999, *Bull. Amer. Meteor. Soc.*, **80**, 381-388.

Zeng, Z., S. E. Yuter, and R. A. Houze, 2000, *J. Appl. Meteor.*, submitted.

DEPOLARIZATION RATIOS FOR PARTIALLY ALIGNED POPULATIONS OF HYDROMETEORS WITH AXIALLY-SYMMETRIC SHAPES

O. Sturniolo [1], A. Battaglia [2], and F. Prodi [1,2]

[1]Institute ISAO-C.N.R., Clouds and Precipitation Group, Via Gobetti, 101, 40129, Bologna, Italy
[2]Department of Physics, University of Ferrara, Via Paradiso, 12, 44100, Ferrara, Italy

1. INTRODUCTION

Hydrometeors in ice clouds and ice precipitation have different shapes, sizes and bulk density. Knowledge of these characteristics and parameters is essential in studies of cloud microphysical properties, in cloud classification and in microphysics of precipitation. This work aims at computing the most important radar depolarization ratios for different ice and in particular for cirrus clouds. Since the latter are invisible to conventional radars operating in the centimetric band, our computations have been performed for radars operating in the microwave region at wavelengths of *3 - 4 mm* (*W*-band, 94 GHz).

For this purpose a code based on *T-matrix* approach for axially-symmetric population of hydrometeors has been modified. Starting from the computation of the *T-matrix* we have implemented an algorithm to analytically compute T, TT^* and TT^t averaged over orientations. Currently this code operates on randomly oriented particles since it originated among astrophysicist to solve cosmic dust light scattering problems. We decided to modify it into a new code able to compute averages over orientations, for population of particles with an arbitrary axis-symmetric probability density function. This approach is motivated by the fact that in a gravitation field ice crystals with larger dimensions greater than *0.1-0.2 mm* tend to be horizontally oriented and in general the interaction particle fluid leads to a preferred orientation for a given hydrometeor type.

For radar parameters computation purposes, we evaluated C_{ext}, C_{sca}, C_{abs}, $\dot{w}$ (albedo), $\langle \cos q \rangle$ (asymmetry parameter), the non-zero elements of Mueller matrix at backscattering region, C_{back}, attenuation coefficient A, effective reflectivity Z_e (expressed in *dBZ*), *IWC*, *LWC*, and the depolarization ratios *LDR*, *CDR* and *ZDR* in *dB*.

We have obtained radar response using perfect alignment and fluctuations from this state, described by different probability density functions.

Corresponding author's address: Franco Prodi, Institute ISAO-C.N.R., Clouds and Precipitation Group, Via Gobetti, 101, 40129, Bologna, Italy, E-mail: f.prodi@isao.bo.cnr.it

Hydrometeor shapes have been modelled by prolate and oblate homogeneous and statistically inhomogeneous spheroids.

The depolarisation ratios *LDR* and *CDR* have been computed for ice clouds populations using the Γ size distributions for different values of modal radius R_c, α parameter, elevation angle, axial ratio and standard deviation σ_β for gaussian distribution over orientation.

2. T- MATRIX COMPUTATION CODE

T-matrix computation codes for light scattering by non-spherical particles have acquired importance in the last years thanks to their greater ability of computing scattering properties with large size parameters and/or extreme geometries.

Mishchenko (1990) and Mischchenko and Travis (1994) developed a code able to compute T-matrix for axially symmetric particles with a plane of symmetry and from this matrix to analytically compute scattering properties of randomly oriented population of particles. This analytical approach developed in Mischchenko and Travis (1994) and Khlebtsov (1992) for randomly oriented axially oriented non spherical particles has been extended by Paramonov (1995) to arbitrary quadratically integrable orientation distribution function. The computational conversion of this theoretical work has the drawback that the formulas for computing the average of TT^* elements involve highly nested summations, so that their efficient numerical implementation is difficult.

To reduce the long computing time we have computed only backscattering matrices of axially symmetric particles, characterised, in the natural reference frame, by the well-known T-matrix symmetry:

$$T^{ij}_{mnm'n'} = \delta_{m,m'} T^{ij}_{mnmn} \qquad (1)$$

$$T^{ij}_{mnmn} = (-1)^{i+j} T^{ij}_{-m n -m' n'} \qquad (2)$$

The novelty, therefore, consists in having numerically implemented the formalism present in Paramonov (1995) for backscattering, using as input Mischenko's T-matrix. Mishchenko (1990) already implemented a similar code for forward scattering since his major interest is in radiative transfer theory. This is easier since, for this purpose, only averages of T matrix are involved.

3. ENSEMBLE OF HYDROMETEORS WITH AN ARBITRARY DISTRIBUTION OVER ORIENTATION

By using an approach similar to Holt (1984) and Sturniolo et al. (1995) (but for hydrometeor symmetry axis instead of particle's one), in the laboratory L frame, the hydrometeor symmetry axis OZ_H (with z_H z-axis of the hydrometeor frame *H*) is oriented in the direction (θ_{sym}, ϕ_{sym}) with θ_{sym} the "true canting angle" respect to the local vertical (see fig. 1).

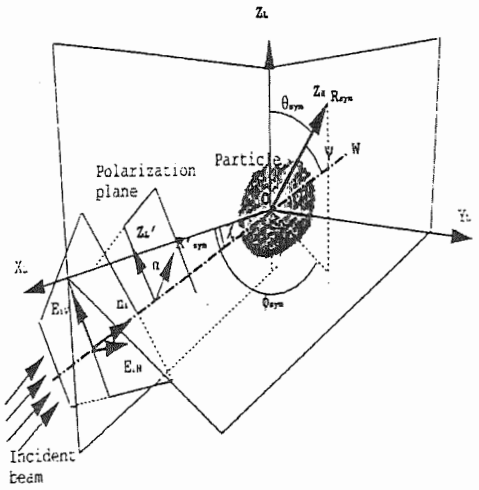

FIG.1: Scattering geometry

The orientation angle ψ of the symmetry axis respect to the direction of propagation, and the canting angle α in the polarisation plane (defined as the angle between the vertical polarisation axis and the projection of the direction of alignment onto the polarisation plane) are analytically connected to θ_{sym}, ϕ_{sym} and χ angles.

In T-matrix approach, transformation rules between two frames are accomplished by an Euler transformation. Consider two arbitrary co-ordinate systems having a common origin inside the scattering particle and let α, β, γ be the Euler angles of rotation that transform co-ordinate system 2 into co-ordinate system 1. The elements of the T-matrix are transformed according to:

$$ {}^{2}T^{ij}_{mnm'n'} = \sum_{m_1,m_2} [D^{n'}_{m'm_2}]^{*} {}^{1}T^{ij}_{m_1nm_2n'} D^{n}_{mm_1} \qquad (3) $$

where the argument (α, β, γ) of the Wigner functions are implicit.

Let (α, β, γ) be the Euler angles of the rotation that transforms *H* in natural *A* frame (that is, rotating z_H axis in the axis of symmetry of the particle), (α_2, β_2, γ_2) frame *L* in *A* and (α_L, β_L, γ_L) frame *H* in *L* [note that the angles of the inverse transformation are (π - γ_L, β_L, π - α_L)]. These Euler angles are connected to the azimuthal and polar angles of the Z_H direction by $\beta_L = \theta_{sym}$ and $\gamma_L = \pi - \phi_{sym}$.

With respect to reference *H*, we define a probability-density function over orientations, ${}^{H}p(\alpha, \beta, \gamma)$, square integrable in the closed domain [0, 2π] x [0, π] x [0, 2π], normalised by:

$$ \int_0^{2\pi} d\alpha \int_0^{\pi} \sin\beta \, d\beta \int_0^{2\pi} d\gamma \, {}^{H}p(\alpha,\beta,\gamma) = 1 \qquad (4) $$

It is possible to expand this function in a series of Wigner *D*-function:

$$ {}^{H}p(\alpha,\beta,\gamma) = \sum_{n,mm'} \frac{2n+1}{8\pi^2} {}^{H}p^{n}_{mm'} D^{n}_{mm'}(\alpha,\beta,\gamma) \qquad (5) $$

As orientation is typically axially symmetric, we will use as orientation function ${}^{H}p(\beta)/4\pi^2$ (β is the angle formed by the direction of axis of symmetry and the *z* direction of *H*), square integrable in the closed domain [0, π], normalised by:

$$ \int_0^{\pi} \sin\beta \, d\beta \; {}^{H}p(\beta) = 1 \qquad (6) $$

It is possible to expand this function in a series of Wigner function or, in a similar way, of Legendre polynomials P_n by writing:

$$ {}^{H}p(\beta) = \sum_{n=0}^{\infty} \frac{2n+1}{2} {}^{H}p_n P_n(\cos\beta) \qquad (7) $$

$$ {}^{H}p_n = \int_0^{\infty} \sin\beta \; {}^{H}p(\beta) d^{n}_{00}(\beta) \qquad (8) $$

Because of (6) ${}^{H}p_0 = 1$.

It is important to transform the probability density function over the orientation of the particles from the reference *H* to the reference *L*.

We do this, by using the addition theorem for Wigner *D*-functions, and we obtain:

$$ {}^{L}p = \sum_{n,m,m'} \frac{2n+1}{8\pi^2} {}^{L}p^{n}_{\dot{m}m'} D^{n}_{\dot{m}m'}(\alpha_2,\beta_2,\gamma_2) $$

$$ {}^{L}p^{n}_{\dot{m}m'} = [\sum_{m=-n}^{n} {}^{H}p^{n}_{mm'} D^{n}_{\dot{m}m}(\alpha_L,\beta_L,\gamma_L)] \qquad (9) $$

In particular, in the case that the distribution is axially symmetric respect to the reference *H*:

$$ {}^{L}p^{n}_{\dot{m}m'} = \delta_{m',0} \; {}^{H}p_n D^{n}_{0\dot{m}}(\alpha_L,\beta_L,\gamma_L) $$

$$ = \delta_{m',0} \; {}^{H}p_n D^{n}_{0\dot{m}}(\beta_L) e^{-i\dot{m}\gamma_L} \equiv {}^{L}p^{n}_{\dot{m}} \qquad (10) $$

Note that

$$ {}^{L}p^{n}_{-\dot{m}} = (-1)^{\dot{m}} e^{2i\dot{m}\gamma_L} \; {}^{L}p^{n}_{\dot{m}} = (-1)^{\dot{m}} [{}^{L}p^{n}_{\dot{m}}]^{*} $$

We give some examples of possible orientation functions:

- random orientation:

$$ p(\beta) = \frac{1}{2} \Rightarrow \begin{cases} p_0 = 1, \; p_n = 0 \text{ for } n \geq 1 \\ \langle \cos^2\beta \rangle = \frac{1}{3} \end{cases} \qquad (11) $$

- perfect alignment: for flattened particles (like oblate spheroids):

$$ p(\beta) = \delta(\cos\beta - 1) \Rightarrow \begin{cases} p_n = 1 \text{ for } n \in N \\ \langle \cos^2\beta \rangle = 1 \end{cases} \qquad (12) $$

while for elongated particles (like prolate spheroids):

$$p(\beta)=\delta(\cos\beta)\Rightarrow\begin{cases}p_{2n+1}=0.\\ p_{2n}=(-1)^n\dfrac{1\cdot3....(2n+1)}{2\cdot4..2n}\\ \langle\cos^2\beta\rangle=1\end{cases}\quad(13)$$

- gaussian alignment:

$$p(\beta)=Ce^{\frac{(\beta-\bar{\beta})^2}{2\sigma^2}}\begin{cases}\bar{\beta}=0\ \ for\ oblate\ particles\\ \bar{\beta}=\dfrac{\pi}{2}\ \ for\ prolate\ particles\end{cases}\quad(14)$$

4. DEPOLARISATION PARAMETERS AND SIZE DISTRIBUTION

In order to compute different scattering properties we have analytically computed the average over orientation for different combination of T-matrix elements in the laboratory reference frame *L* expressed as combinations of Clebsch-Gordon coefficients, T-matrix elements computed in the natural frame *A* and orientational coefficients of (9).
In our computations, the cloud contains particles and mirror particles in equal number, so that backscattering matrix in linear basis is characterised by 6 parameters.

For general backscattering matrix **S**, we can compute:

- differential reflectivity *ZDR* [dB], defined as the ratio between the fraction of horizontally polarised backscattering and vertically polarised backscattering:

$$ZDR=10log_{10}\frac{Z_{HH}}{Z_{VV}}=10log_{10}\frac{S_{11}+2S_{12}+S_{22}}{S_{11}-2S_{12}+S_{22}}\quad(15)$$

- linear depolarisation ratio *LDR* [dB], defined as the ratio of power backscattered at vertical polarisation to the power backscattered at horizontal polarisation for a horizontally polarised incident field:

$$LDR=10log_{10}\frac{Z_{VH}}{Z_{HH}}=10log_{10}\frac{S_{11}-S_{22}}{S_{11}+2S_{12}+S_{22}}\quad(16)$$

- circular depolarisation ratio *CDR* [dB], defined as the ratio of the power backscattered at left-hand circular polarisation to the power backscattered at right-hand polarisation for a left-hand circularly polarised incident field:

$$CDR=10log_{10}\frac{Z_{LL}}{Z_{RL}}=10log_{10}\frac{S_{11}-2S_{14}+S_{44}}{S_{11}-S_{44}}\quad(17)$$

Ice crystals, especially in cirrus clouds, take on a wide variety of shapes (plates, dendrites, columns, bullets, needles, etc.). Referring to Magono and Lee (1966) needles and hexagonal plates have the extremest axial ratios so that they present problems in T-matrix convergence; therefore, they have been substituted with extreme monoaxial population of prolate (a/b=0.1) and oblate (a/b=10) spheroids, respectively. Oblate spheroids represent both types of plates while prolate spheroids represent long columns or solid columns. For our ice crystals studies, we have taken the Γ size distribution defined by:

$$n(L)=\frac{n_0 b^{\alpha+1}}{\Gamma(\alpha+1)}L^{\alpha}e^{-bL}\quad(18)$$

where L is the maximum particle dimension, n_0 is the volume concentration and b is connected to the median L_m of the distribution by $b=(\alpha+3.67)/L_m$. Adequate representation of cirrus size distribution are obtained with α ranging from 0 to 2.

5. RESULTS AND DISCUSSION

Here we show only one meaningful case for prolate spheroidal (long columns in cirrus) ice hydrometeors, with equivolumic radius R_c = 200 μm, corresponding to $19.5 \le r_{eqv} \le 127$ μm, ρ = 0.917 gcm^{-3}, n_0 = 0.0007 cm^{-3}, refractive index m = 1.780532 - *i* 0.001943 at 94 GHz, α = 2. We have selected four different χ values: 15°, 45°, 60° and 90° and for any of these values σ_θ has been fixed at 6° (small degree of alignment), 30° and 90° (almost random orientation).

In Table 1 results for ice columns are illustrated.
In Figures 2 and 3, LDR and CDR contributes from component with different axial ratio in the size distribution indicate that radar depolarization parameters are predominantly affected by the most extreme particles (the biggest ones also), as expected. Curves show an increase in CDR and LDR when the standard deviation over orientation increases, (LDR values increase of 35% when σ_θ increase from 6° to 90°) besides CDR and LDR decrease with axial ratio approaching 1 (no depolarization at all). Not shown here, we note that CDR and LDR increase when the radar elevation angle increases [since oblate particles, not shown here, have an opposite behaviour, this constitutes a method for distinguishing between prolate and oblate hydrometeors, as already noted in Matrosov (1991) and Matrosov et al. (1996)].

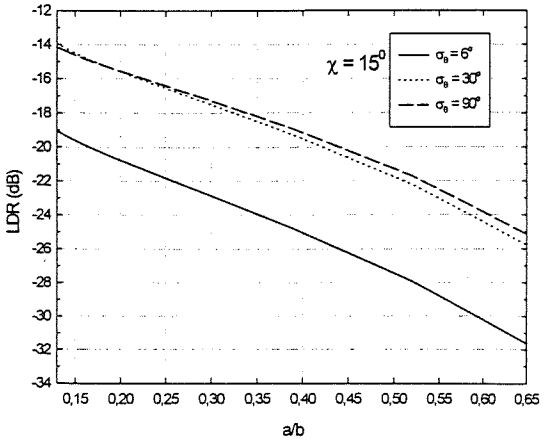

FIG. 2: LDR (dB) versus axial ratio a/b for elevation χ angle equal to 15° and for different σ_θ for gaussian distribution over orientation.

In general, with fixed orientation distribution (that is with fixed σ_θ), LDR values show, passing from χ = 15° to χ = 90° a greater variation than CDR ones. ZDR (not shown here) has a strong dependence both in axial ratio and in σ_θ. In the limit of randomly orientation clearly ZDR $\Rightarrow$ 0 and, in any way, by varying the elevation angle, ZDR approaches zero value with zenith looking geometry. For our prolate particles we have strong signals (as strong as 4 dB for 15° and even more for lower elevation angles) .

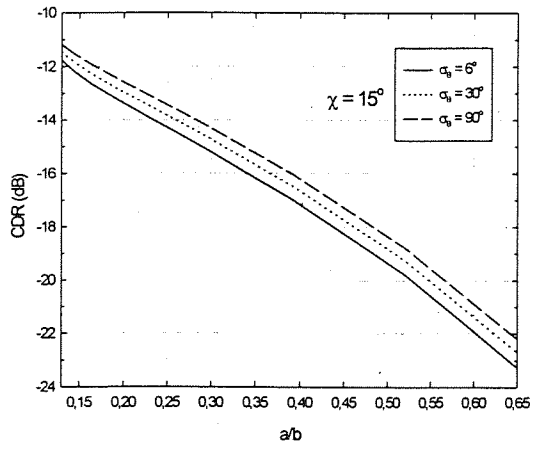

FIG. 3: CDR (dB) versus axial ratio a/b for elevation χ angle equal to 15° and for different σ_θ for gaussian distribution over orientation.

The variation of bulk density and therefore of refractive index, see Prodi et al. (1999), has the effect of increasing the depolarisation effect by including water (till 5 dB with 40% water inclusion) and of decreasing it by decreasing bulk density (till 5 dB with 40% air inclusion).

TAB. 1: Results for ice columns.

χ (deg)	σ_θ (deg)	CDR (dB)	LDR (dB)	ZDR (dB)
15°	6°	-12.26	-19.58	3.46
15°	30°	-11.92	-14.45	1.69
15°	90°	-11.60	-14.58	0.27
45°	6°	-11.41	-14.39	1.81
45°	30°	-11.43	-14.48	1.89
45°	90°	-11.50	-14.58	0.14
60°	6°	-10.75	-13.63	0.88
60°	30°	-11.07	-14.06	0.40
60°	90°	-11.45	-14.57	0.07
90°	6°	-10.06	-13.28	0.00
90°	30°	-10.81	-13.99	0.00
90°	90°	-11.40	-14.57	0.00

In conclusion, our numerical results, obtained using analytical average over arbitrary orientation distribution of scattering quantities, give interesting information in cloud cirri investigation using polarimetric radar at different elevation angles.

6. REFERENCES

Holt, A. R, 1984: Some factors affecting the remote sensing of rain by polarization diversity radar in the 3- to 35- Ghz frequency range. Radio Sci., 19, 1399-1412.

Khlebtsov, N. G., 1992: Orientational averaging of light-scattering observables in the T-matrix approach. Appl. Opt., 31, No. 25, 5359-5365.

Magono, C., and D.R. Lee, 1966: Meteorological classification of natural snow crystals. J. Fac. Sci., Hokkaido University, Ser. 7, 2, No. 4, 321-335.

Matrosov, S., 1991: Theoretical Study of Radar Polarization Parameters Obtained from Cirrus Clouds. J. Atmos. Sc., 48, No. 8, 1062-1070.

Matrosov, S., R. F., Reinking, R. A, Kropfli, and B.W., Bartram, 1996: Estimation of ice hydrometeor types and shapes from radar polarization measurements. J. Atmos. Oceanic Technol., 13, 85-96.

Mishchenko, M.I., 1990: Extinction and polarization of transmitted light by partially aligned nonspherical grains. Astr. J., 367, 561-574.

Mishchenko, M.I., and L. D., Travis, 1994: Light scattering by polydispersions of randomly oriented spheroids with sizes comparable to wavelengths of observation. Appl. Opt, 33, No. 30, 7206-7225.

Paramanov L. E., 1995: T-matrix approach and the angular momentum theory in light-scattering problems by ensembles of arbitrarily shaped particles. J. Opt. Soc. Am. A, 12, No.12.

Prodi, F., O., Sturniolo, A., Battaglia and R., Medini, 1999: Radar parameter simulation for populations of spherical and non-spherical hydrometeors: dependence on size distributions, shapes and composition. J. Quant. Spectrosc. Radiat. Transfer, 63, 677-699.

Sturniolo, O., A., Mugnai, and F., Prodi, 1995: A numerical sensitivity study on the backscattering at 35.8 GHz from precipitation - sized hydrometeors. Radio Sci., 30, No. 4, 903-919.

Use of Raman Lidar In the Study of Clouds

David Whiteman[1], Belay Demoz[2], David O'C. Starr[1], Geary Schwemmer[1], Keith Evans[2], Tim Berkoff[2], Ravindra Peravali[2]

[1]NASA Goddard Space Flight Center, Greenbelt, MD 20771
[2]Joint Center for Earth Technology, University of Maryland Baltimore County, Baltimore, MD

1. INTRODUCTION

Clouds play an important role in atmospheric radiation. Accurate remote measurements of cloud properties are needed to help validate model predictions and satellite observations. Accurate characterization of cloud boundaries is, for example, fundamental to understanding the radiative effect of clouds on climate. Cloud-radiation interactions impact the radiation budget of the Earth, both at the surface and in the atmosphere, and are the largest source of radiation budget uncertainty. These interactions depend on many variables, including cloud depth (both optical and geometrical), cloud top height, cloud liquid water content, water vapor profile, and solar zenith angle. The calculation of cloud optical depth, for example, requires accurate determination of cloud base and cloud top heights. Cloud geometry is also a primary factor that controls effective cloud fraction and is a major uncertainty in calculation of downwelling longwave flux at the surface. The Atmospheric Radiation Measurements (ARM) program established by the U.S. Department of Energy and the World Meteorological Organization's (WMO) World Climate Research Program's (WCRP) International Satellite Cloud Climatology Project (ISCCP) are indicators of the importance of clouds in the earth-climate system.

We report here Raman lidar measurements of cloud properties in varying conditions. We attempt to address the questions "*given clouds, what of radiation*" and "*given an environment, what of clouds.*" First, a description of the Raman lidar will be given and then its utility in cloud studies will be presented in subsequent sections.

2. THE GODDARD SCANNING RAMAN LIDAR

The Scanning Raman Lidar is a mobile lidar system designed to measure water vapor, aerosols, cloud liquid water, cloud droplet radius and number density, cloud base height and upper tropospheric temperature (see Whiteman et al. 1999 for details). The SRL detects light backscattered by molecules and aerosols at the laser wavelength as well as Raman backscattered light from water vapor (at 3657 cm^{-1}), nitrogen (2329 cm^{-1}), and oxygen (1555 cm^{-1}) molecules. The SRL employs two different lasers for its measurements; a XeF excimer laser (351 nm output) for optimized nighttime measurements and a tripled Nd:YAG laser for daytime measurements. The receiving telescope is a 0.76 m, F/5.2, variable field-of-view (0.25 - 2.5 milli-radians) Dall-Kirkham system mounted horizontally on a 3.7m optical table. The telescope field-of-view is steered with a large (1.2m x 0.8m), motorized flat mirror that rotates on a horizontal axis and is also mounted on the optical table. The entire system, including data acquisition electronics and workspace for several scientists, is housed in a single, environmentally controlled, mobile trailer. The optical table can be slid out the back of the trailer to allow atmospheric profiles to be acquired at any angle in the plane perpendicular to the trailer or continuously scanned from horizon to horizon. Alternatively, the lidar system may be operated with the optics completely inside the trailer by directing the output laser beam through one of three windowed openings in the trailer. This allows vertical measurements and measurements at 5-10 degrees above the horizon in either direction to be acquired. It also allows measurements to be made during rainfall. More information and photos on the lidar instrument is available at http://virl.gsfc.nasa.gov/srl/index.htm.

3. GIVEN CLOUDS WHAT OF RADIATION

3.1 Cirrus Cloud Optical Depth

The SRL was located on Andros Island in the Bahamas during August and September 1998 for the third Convection and Moisture Experiment (CAMEX-3). During the period of August 21-25, the water vapor and cirrus cloud environment at Andros Island was influenced by the nearby passage of Hurricane Bonnie. The cirrus clouds associated with Bonnie reached altitudes greater than 16 km and were characterized by temperatures in the range of -55 to -75C.

Raman lidar measurements of cirrus cloud backscattering coefficient (km^{-1} sr^{-1}) and optical depth (at 351 nm) acquired during this period on the night of August 23, 1998 are presented in figure 1. The influence of multiple scattering on these optical depth measurements was estimated using the technique of Eloranta (1998) and found to cause a decrease in optical depth of about 10% assuming particle sizes typical for the cold cirrus clouds studied here (10-20 microns). The optical depth values shown in figure 1 have been increased by 10% over the lidar-measured values to estimate the influence of multiple scattering.

The measurements of August 23 provide a convenient dataset to test the effect of cirrus clouds on satellite radiances because of the range of optical depths covered. On this night the measured optical depth at 351

nm ranged from a minimum of approximately 0.01 to a maximum of approximately 0.7.

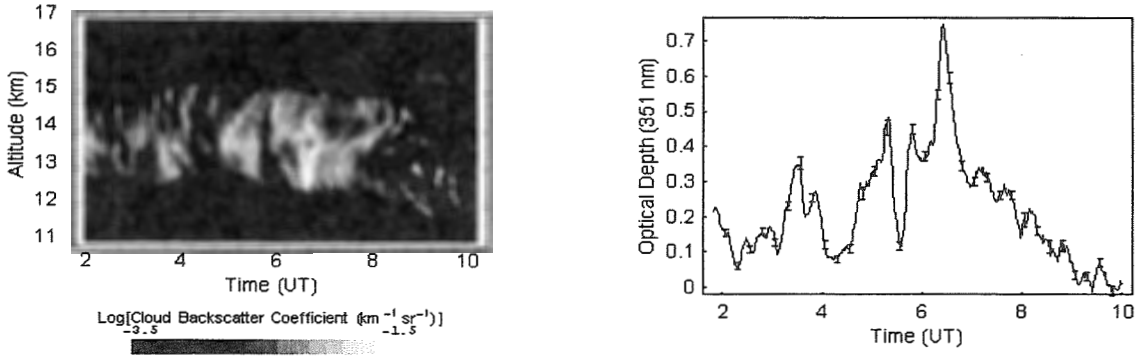

Figure 1 Cloud backscatter coefficient and optical depth at 351 nm as measured by the Scanning Raman Lidar on the night of August 23, 1998 at Andros Island, Bahamas. The optical depth values have been increased 10% over those measured to account for the effects of multiple scattering.

A simple radiative transfer model, which accounts for surface emissivity, surface temperature, cloud emissivity and cloud temperature was used to predict satellite radiances. The lidar optical depths were converted to IR (GOES channels) using a technique similar to Wylie et. al. (1995) and DeSlover et. al. (1999).

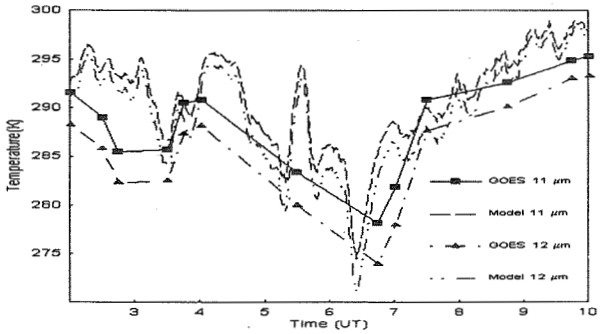

Figure 2 GOES satellite 11- and 12- micron channel brightness temperatures for the pixel over the lidar site are shown in closed boxes and triangles, respectively. Also plotted are the brightness temperatures predicted by the model equation using the lidar-measured, IR adjusted, optical depths.

The results of the comparison of model predicted brightness temperatures and actual GOES brightness temperatures are shown in figure 2. The brightness temperatures calculated from the model for both the 11- and 12-micron GOES channels are shown in long dash and dot-dot-dash lines, respectively. The GOES 11- and 12-micron channel brightness temperatures are shown using closed boxes and triangles.

It is apparent from the figure that, despite the sampling issues related to the comparison of 10-minute averages of lidar data and 10 km satellite pixels, these simple model calculations capture the main features observed in the satellite brightness temperatures. A comparison of the results using the adjacent satellite pixel to the east of the lidar site, and thus completely over the ocean, yielded very similar results to those shown indicating that the constant surface temperature assumption in the model retrievals is reasonable. That being the case, another point is that these data indicate that the variation in cirrus cloud optical depth is the dominant factor causing fluctuations in the satellite brightness temperatures.

Comparisons and errors in satellite retrieved skin surface temperature and total precipitable water will be presented at the conference and are the subject of Whiteman et al. (2000).

4. GIVEN ENVIRONMENT WHAT OF CLOUDS?

4.1 Convergence lines and Associated Clouds

Observational studies have shown that convective storms often form near boundary-layer convergence lines. For example, Wilson and Schreiber (1986) reported that up to 95% of intense storms over eastern Colorado (18 May to 15 August 1984) occurred in close proximity to radar-observed boundary-layer convergence (BLC). Previous studies of BLC lines used primarily dense networks of anemometers, satellite cloud images or Doppler radar. We present here an example of the utility of the SRL in BLC cloud formation studies.

On 28 September 1997, a confluence of northward moving moist air and a post-frontal cold/dry air-mass led to wide-scale cloud development over northern Oklahoma. Radiosonde measurements of wind indicated that the profile between 1.0-2.5 km at 0831 (1131), about 1.5 hrs prior to (following) the surface frontal passage, the zonal wind changed from westerly at about 10 m sec^{-1} ahead of the front to -10 m sec^{-1} after the frontal passage. The symmetric convergence in the zonal wind led to moisture-lifting and cloud formation over the site as observed by Raman lidar. A dramatic picture of the dynamics of the interaction between two different air masses is revealed by the lidar-measured water vapor mixing ratio profile which will be shown at the conference.

Cloud base height derived from the Raman lidar measured aerosol scattering ratio profile data and other remote sensors are shown in Fig. 3. The data compared well. It is striking to note that the cloud base altitude was the highest at or near the convergence line, right where the updraft is located (about 1100), and is a measure of the lifting associated with the convergent flow. More on these aspects of the case study will be presented at the conference.

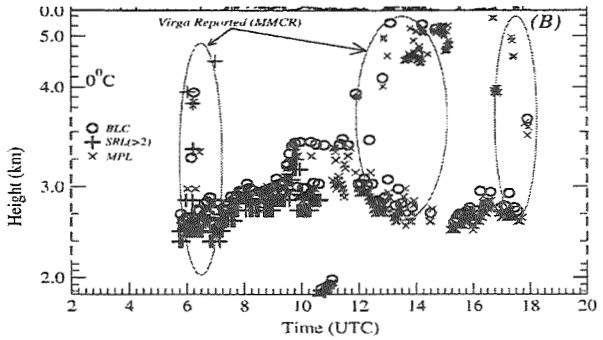

Figure 3. Cloud base height derived from Raman lidar aerosol scattering ratio profiles measured on 28 September 1997. Details of the cloud base derivation are reported in Demoz et al (2000). Note that Milli-Meter Cloud Radar (MMCR), Micro-Pulse Lidar and Belfort Ceilometer (BLC) derived cloud base heights agree well with Raman lidar.

mixing ratio in the cloud. The saturation-mixing ratio is subtracted from the combined water vapor+liquid water signal to yield the liquid water signal alone. An example of this is shown in figure 4. The water vapor mixing ratio was enhanced by up to 3 gm kg^{-1}, a measure of the liquid water content. The experimental capability to measure liquid and vapor separately in the cloud, and thus eliminate error sources in the current technique, is currently under development.

4.2. Cloud Base Detection Including Virga and Rain

Most techniques used for cloud base height detection search for zero crossings in the derivative of the lidar returned signal [Pal et al. 1992, Campbell et al. 1998, Gaumet et al. 1998], or search for a "threshold" value of signal shift from the background [Platt et al. 1994], or assume the peak in the signal return to be the cloud base level [Eberhard, 1986], or construct lidar clear-sky power return profiles from archived data to test for the presence of clouds [Clothiaux et al. 1998]. In practice, however, these simple definitions of cloud base height are not as straightforward as they might appear. Cloud base definition is influenced by the sensing instrument's wavelength, low signal-to-noise-ratio at very high cirrus altitudes, insects or other scatterers between the

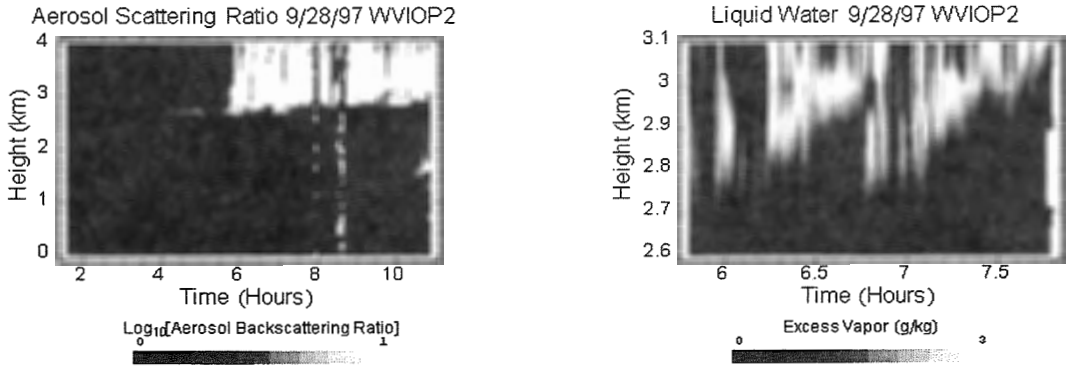

Figure 4 Aerosol scattering ratio (left) and cloud liquid water (right) quantified as excess vapor (g/kg) determined by subtracting mixing ratio from the combined vapor+liquid Raman scattered signal measured by the Scanning Raman Lidar on the night of September, 28 1997 in northern Oklahoma

Another capability of the Raman lidar is its ability to measure Raman scattering from liquid droplets in clouds. Due to the broadness of the Raman backscattered spectrum of liquid water, water vapor measurements made in a cloud will inevitably contain scattering from any cloud liquid water that is also present. A retrieval technique based on these measurements that quantifies the cloud droplet radius and number density has been developed recently (Whiteman et. al., 1999). In the retrievals to date, the liquid and vapor components of the combined signal have been separated using a measurement of temperature and pressure to establish the saturation-

instrument and cloud base and the fact that the definition of cloud base height itself may depend upon the particular research problem to be addressed. For surface radiation budget studies, for example, cloud base height may refer to the radiatively important part of the cloud and neglect any virga-associated excursions. For visibility applications, such as pilot/flight safety, alternative criteria may be required.

An example of data during such conditions, observed on 27 August 1998 at Andros Island, Bahamas, as part of the CAMEX-3 field campaign, is shown in Figure 5. Aerosol scattering ratio and water vapor mixing ratio profiles are shown at two selected times: at 0400 when precipitation reached the surface (Fig. 5A) and at 0745

(Fig. 5B). Rawinsonde measured dewpoint depression at 0745 is also plotted in Fig. 5C. At 0400, near-surface aerosol scattering ratio values were about five times the background, when precipitation was recorded at the ground. Aerosol scattering ratio increased monotonically to 4.2 km followed by a "dip" to a minimum at 4.6 km and then a peak at 5 km, before returning to near-background levels. This peak-dip-peak structure near the freezing level is the well-known lidar-dark band [Sassen and Chen 1995], which is associated with the structural collapse and accumulation of melted snowflakes and their transition to spherical drops. A similar shape in aerosol scattering ratio and water vapor mixing ratio profiles was also observed at 0745. Given only backscatter information (which is the case for most elastic lidars), the threshold technique of determining cloud base height will not work and most other algorithms will have difficulties. An alternative solution could utilize available radiosonde information or depolarization ratio [Platt et al. 1994]. With Raman lidar systems, however, the water vapor mixing ratio channel may be used. Note that the water vapor channel at 0400 (0745) provided usable data up to 5.1 (5.4) km, close to the peak above the lidar dark band in the aerosol scattering ratio profile. Above 5.1 (5.4) km, the lidar signals were severely attenuated (this occurs for optical depth greater than about 5). The lidar-derived relative humidity (using radiosonde temperature, not shown) indicated saturation was reached at an altitude of 5.2 km, slightly lower than the peak in aerosol scattering ratio. From the 0745 sonde, the altitude of the smallest dewpoint depression was 5.2 km, in agreement with the lidar-derived cloud base height, confirming the utility of the Raman water vapor signal for cloud base height detection even in rain (0400) or virga (0745) conditions.

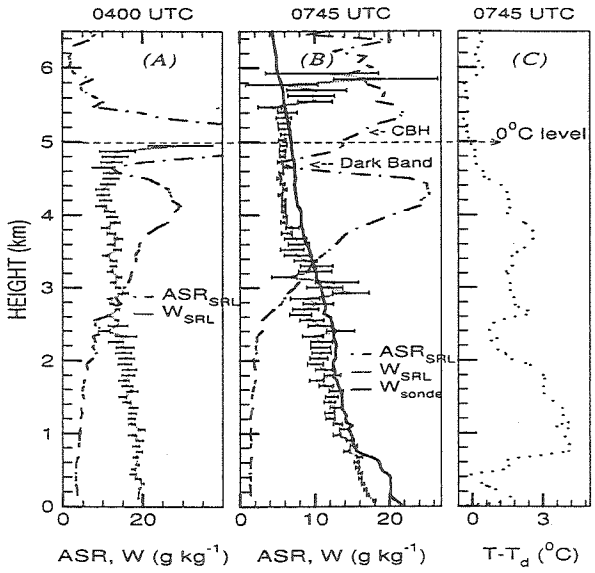

Figure 3. Typical profiles of SRL-measured aerosol scattering ratio (ASR, dash-dot) and water vapor mixing ratio (W, heavy solid) from (a) rain at 0400 UTC and (b) virga at 0745 UTC conditions for the 27 August, 1998 case. (C) Sonde derived profile of the dewpoint depression ($T-T_d$) at 0745 is plotted for comparison. The freezing level, cloud base height and lidar dark-band positions are also indicated.

5. Acknowledgement

The authors wish to acknowledge the support of the Department of Energy/Atmospheric Radiation Measurements program for participation in the Water Vapor IOP. In addition, we appreciate the support of Dr. Ramesh Kakar, head of NASA's Atmospheric Dynamics and Remote Sensing Program, which made the CAMEX-3 experiment possible.

6. *References*

Clothiaux, E. E., G. G. Mace, T. P. Ackerman, T. J. Kane, J. D. Spinhirne, and V. S. Scott, An automated algorithm for detection of hydrometer returns in micropulse lidar data. *J. Atmos. Oceanic Technol.*, **15**, 1035-1042, 1998.

Demoz, B. D. Starr, D. Whiteman, K. Evans, D. Hlavka R. Peravali, 2000: Raman LIDAR detection of cloud base. Accepted, *Geophysical Research Letters.*

DeSlover, D. H., W. L. Smith, P. K. Piironen and E. W. Eloranta, 1999: A methodology for measuring cirrus cloud visible-to-infrared spectral optical depth ratios, J. Atmos. Ocean. Tech., 16, 251-262.

Eberhard, W. L., Cloud signals from lidar and rotating beam ceilometer compared with pilot ceiling, *J. Atmos. Oceanic Technol.*, 3, 499-512, 1986.

Eloranta, E. W., Practical model for the calculation of multiply scattered lidar returns, Appl. Opt., 37,12, 2464-2472.
Gaumet, J. L., J. C. Heinrich, M. Cluzeau, P. Pierrard, J. Prieur, Cloud base height measurements with a single pulse erbium-glass laser ceilometer. *J. Atmos. Oceanic Technol.*, **15** 37-45, 1998

Platt, C. M., and Co-authors, The Experimental Cloud Lidar Pilot Study (ECLIPS) for cloud-radiation research. *Bull. Amer. Meteor. Soc.*, **75**, 1635-1654, 1994.

Whiteman, D. N. and S. H. Melfi, 1999: Cloud liquid water, mean droplet radius and number density measurements using a Raman lidar. *J. Geopphys. Res.*, **104**, pp. 31411-31419.

Whiteman, D. N., K. D. Evans, B. Demoz, D. O'C. Starr, D. Tobin, W. Feltz, G.J. Jedlovec, S. I. Gutman, G. K. Schwemmer, M. Cadirola, S. H. Melfi, F. J.Schmidlin 2000: Raman lidar measurements of water vapor and cirrus clouds during the passage of hurricane Bonnie. Submitted to JGR

Wilson, J. W. and W. E. Schreiber, 1986: Initiation of convective storms by radar-observed boundary layer convergent lines. *Mon. Wea. Rev.* **114**, 2516-2536.

Wylie, D., P. Piironen, W. Wolf, E. Eloranta, 1995: Understanding Satellite Cirrus Cloud Climatologies with Calibrated Lidar Optical Depths, J. Atmos. Sci, 52, 23, 4327-4343.

GLOBAL SCALE DETERMINATION OF CIRRUS CLOUD PHYSICAL PROPERTIES FROM TIROS-N VERTICAL SOUNDER INFRARED MEASUREMENTS

R. Holz [1], C. J. Stubenrauch[1], N. A. Scott[1], D. Mitchell[2] and P. Yang [3]
[1]Laboratoire de Météorologie Dynamique, École Polytechnique, Palaiseau, France
[2]Desert Research Institute, Atmospheric Sciences Center, Reno, USA
[3]NASA Goddard Space Flight Center, Greenbelt, USA

1. INTRODUCTION

The spectral dependence of infrared radiances measured by the High resolution InfraRed Sounder (HIRS) instrument, which is part of the TOVS system (Smith et al. 1979), allows us to detect reliably the presence of cirrus clouds and to derive some valuable information on their physical properties at a global scale (Stubenrauch et al., 1999a). Within the framework of the NOAA/NASA Pathfinder Program, eight years of TOVS data (NOAA-10 and NOAA-12) have been processed with the Improved Initialization Inversion (3I) algorithms (Scott et al., 1999), providing cloud and atmospheric properties at a spatial resolution of 1°.

Recently, several theoretical approaches such as finite-difference time domain (FDTD, cf. Yang et al, 1997), anomalous diffraction theory (ADT, cf. Mitchell et al., 1996), T-matrix (cf. Baran et al., 1999) and composite methods (cf. Fu et al., 1998) have been developed to describe more realistically the single scattering properties of complex shaped nonspherical ice crystals. These schemes enable us to simulate more precisely the interaction between cirrus clouds and infrared radiation and to investigate the influence of cloud microphysics on the spectral behavior of effective emissivities. We apply these simulations to enlarge the 3I cloud climatology by a global scale retrieval of effective particle sizes.

2. 3I CLOUD IDENTIFICATION

The High resolution InfraRed Sounder (HIRS) instrument measures radiation emitted and scattered from different levels of the atmosphere at 19 infrared wavelengths as well as at one visible wavelength. With the 3I algorithms we derive from these radiances atmospheric, cloud and surface properties. The algorithms are based on the fast line-by-line radiative transfer model "Automatized Atmospheric Absorption Atlas" (4A) of the Atmospheric Radiation Analysis group (ARA-LMD) and the Thermodynamic Initial Guess Retrieval (TIGR) data set which includes a huge collection of radiosonde measurements of temperature, humidity and pressure. Clouds are detected at HIRS spatial resolution ($18\ km$ at nadir) by a succession of threshold tests, which depend on the simultaneous Microwave Sounding Unit (MSU) radiance measurements that probe through the clouds. To insure more coherence with MSU, the HIRS radiances are averaged over clear and cloudy pixels within $100\,km \times 100\,km$ regions. Cloud parameters are determined from the averaged cloudy pixel radiances assuming that all cloudy pixels are covered by a single homogeneous cloud layer. The average cloud-top pressure (p_{cld}) and the average effective cloud amount over cloudy pixels ($N\epsilon$) are obtained from four radiances in the $15\,\mu m$ CO_2-band (with peak responses from 400 to $900\,hPa$ levels in the atmosphere) and one in the $11\,\mu m$ IR atmospheric window by minimizing a weighted χ^2 (Stubenrauch et al. 1999b). Empirical weights reflect the effect of the brightness temperature uncertainty within a TIGR airmass class on these radiances at the various cloud levels.

Figure 1 shows an example of the zonally averaged frequencies of cirrus clouds above three height levels obtained for summer (June, July, August) and winter (December, January, February) of 1990. In the midlatitudes high

1. Corresponding author's adress: Ralph Holz, LMD, École Polytechnique, RD 36, 91128 Palaiseau, France, e-mail: ralph@araf1.polytechnique.fr

clouds occur with a frequency of about 30 %. The ITCZ with a frequency of clouds above 310 hPa of about 60 % is clearly visible in the data.

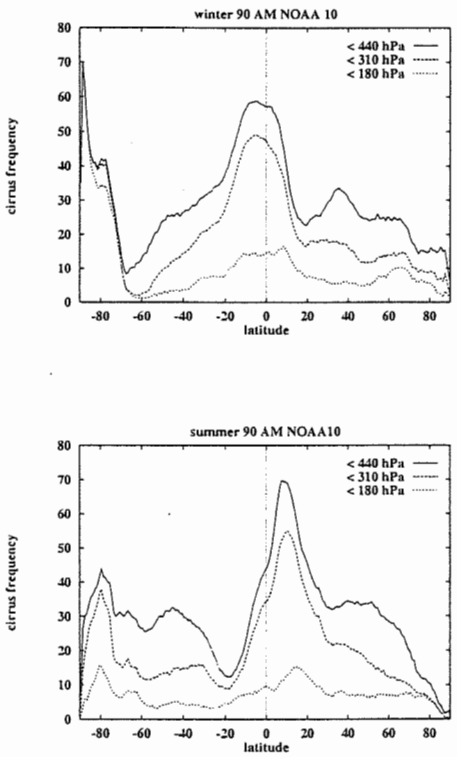

Figure 1. - Zonally averaged frequency of cirrus clouds above three different pressure levels. Measurements taken at 7h30 am local time.

3. DETERMINATION OF EFFECTIVE PARTICLE SIZES

Recently, several efforts have been undertaken to obtain a global scale satellite retrieval of cirrus microphysical properties. For example Han et al. (1997) use visible optical thicknesses from International Satellite Cloud Climatology Project (ISCCP) data (during day) in combination with a radiative transfer model treating ice crystals as hexagonal columns in order to derive ice crystal sizes. Baran et al. (1998b) consider measurements from the dual view instrument ATSR (1 km spatial resolution) and an ADT based radiative transfer model. In another study Baran et al. (1998a) demonstrate for selected cases the possibility to retrieve ice crystal size information at relatively low spatial resolution from TOVS observations.

As infrared sounders provide a good sensivity to high-level ice clouds we started to expand the ice crystal size retrieval from TOVS over the whole globe based on the 3I cirrus identification. After studying two months of NOAA-10 data (Stubenrauch et al., 1999c) we now establish a three year climatology (1989-1991). We compare the use of different theoretical approaches for the determination of single scattering properties (ADT, FDTD, T-matrix, Mie) in order to investigate the uncertainties that are related to data and theory respectively.

3.1. Effective cirrus cloud emissivities from 3I Data

For the large scale ice clouds that have been identified with the 3I cloud scheme we rerieve effective cloud emissivities ($\epsilon(\lambda)$) at wavelenghts of 3.7 μm (not shown here), 8.3 μm and 11 μm. The effective emissivities are related to the measured brightness temperatures T_b^m at these wavelengths, the cloud-top temperature T_{cld} and the surface temperature T_s by the ratio

$$\epsilon = \frac{B(T_b^m) - B(T_s)}{B(T_{cld}) - B(T_s)}$$

where $B(T)$ is the Planck function.

For the ice crystal size determination we select overcast high clouds ($p_{cld} < 440\ hPa$), with all HIRS pixels cloudy over an area of 1° latitude x 1° longitude. The influence of atmospheric water vapor on the radiances is taken into account by the use of the transmissivities that correspond to the 3I retrieved TIGR atmospheric profiles. The surface temperature as well as atmospheric water vapor and temperature profiles can only be retrieved when the clouds are not too opaque ($N\epsilon < 0.6$). In the case of highly opaque clouds, we use monthly averages of these variables.

For the calculation of clear sky radiances over land, we use the global scene type map created by the Surface and Atmospheric Radiation Budget (SARB) group in the framework of the CERES experiment (Rutan and Charlock, 1997) in order to distinguish the surface emissivities for 18 different surface types that varies in a range from 0.83 (8 μm) and 0.92 (11 μm) over barren to nearly one at both wavelengths over snow/ice sur-

faces. Over ocean, assumed surface emissivites are 0.98 at both wavelengths. In order to limit the uncertaintities due to the surface contributions we limit the retrieval to clouds with an $11\,\mu m$ emissivity larger than 0.4. For the ice crystal retrieval we calculate the measured ratio between the 8.3 and $11.1\,\mu m$ emissivities of the considered cirrus clouds to compare them to look-up tables of simulated values.

3.2. Simulated cloud emissivities

The radiative properties of ice crystals at IR wavelengths are treated under different hypotheses of complex shaped crystals such as hexagonal plates and columns, bullet rosettes and planar polycrystals. We combine the absorption coefficients from the anomalous diffraction theory with single scattering albedos and asymmetry factors from ray-tracing/T-matrix calculations and dinite-difference time domain calculations respectively.

In Stubenrauch et al. (1999) the scattering effects had been removed from the measured radiances and compared to emissivities obtained with the zero-scattering approximation. Here multiple scattering processes are directly taken into account in the simulation using the DISORT-based STREAMER radiative transfer code (Key and Schweiger, 1998). Furthermore, we incorporated into the STREAMER code the single scattering properties resulting from a FDTD and improved GOM for several shapes, as well as the parameterization resulting from the composite scheme of Fu et al. (1998), who fits GOM/FDTD results for hexagonal columns with a linear combination of Mie, GOM and ADT parameters.

In the case of ADT, analytical expressions describe the extinction and absorption coefficients as functions of size distribution parameters, ice crystal shapes, wavelength and refractive index. If the ice crystal geometry is properly represented, i.e. not approximated as a sphere, the absorption efficiency of photons inside the ice crystal exhibits varying degrees of dependence on mass (ice water path) and projected area (particle size). In the thermal spectrum between 6 and $20\,\mu m$, ice crystals show minimal absorption at $8.5\,\mu m$ and maximal absorption around $11\,\mu m$. At $8.5\,\mu m$ absorption changes from being mass to projected area dependent as the crystal sizes increase. For small ice crystals, ADT predicts more of a mass dependence which lowers emissivity, whilst large ice crystals have more of a projected area dependence which increases emissivity. At $11\,\mu m$, the absorption is mass dependent. This means that the absorption difference between both wavelengths increases with decreasing ice crystal size. Figure 2 demonstrates for example the ratios of 8 and 11 micron emissivities for different effective particle sizes that result from radiances simulated with absorbtion coefficients from ADT and single scatter albedos and asymmetrie factors from T-matrix calculations.

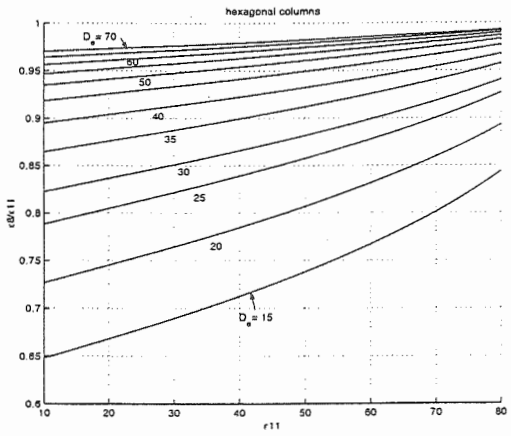

Figure 2. - Ratios of 8 over 11 micron emissivity for different effective particle sizes. Simulations are based on single scattering properties from ADT (Q_{abs}) and T-matrix/Ray-tracing (ω_0, g).

3.3. Retrieved particle sizes

The particle size retrieval is applied only to those cirrus cloud scenes that are overcast with an emissivity ($11\,\mu m$) greater than 0.4, to ensure that most of the signal reveals from the cloud itself. Due to the decreasing spectral signature for very high emissivities we also limit the retrieval to cases where $\epsilon(11\,\mu m)$ is less than 0.8.

Figure 3 shows the percentages of the total number of cirrus clouds detected over ocean during summer and winter of 1990 that satisfy these conditions. In the ITCZ about $80\,\%$ of the cirrus scenes are overcast and about $35\,\%$ remain after the emissivity cuts. Figure 4 show the zonally averaged effective particle sizes (D_e), which equals the ratios of the third over the second moment of the particle size distributions, that is obtained for the period of 1989-1991 by application of the look-up tables corresponding to figure 3.

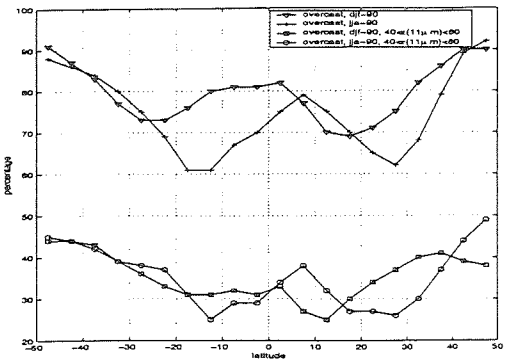

Figure 3. - Zonally averaged percentages of the total number of cirrus clouds scene that are taken into account for the particles size retrieval, (for 1990).

We oberve the same overall order of magnitude for the range of D_e $(30 - 45\,\mu m)$ as in Stubenrauch at al. (1999c). The observed particle sizes are higher during winter than summer. The interannual variabilies lie in a range of about 0 to $10\,\mu m$.

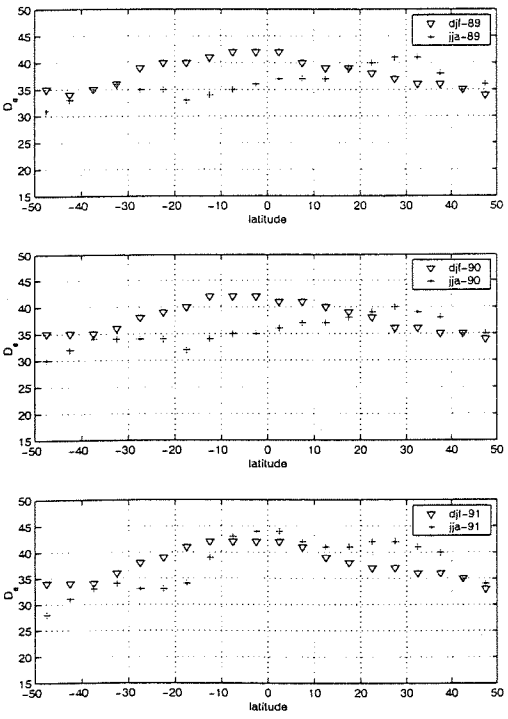

Figure 4. - Zonally averaged effective radii for overcast cirrus scenes, $0.4 < \epsilon(11\,\mu m) < 0.8$, observed over ocean in 1989, 1990 and 1991. Average over summer (jja) and winter months (djf).

REFERENCES

Baran A. J., J. S. Foot, and D. L. Mitchell, 1998a: The question of ice crystal absorption: A comparison between theory and implications for remote sensing, Appl. Opt., 37, 2207-2215.

Baran A. J., S. J. Brown, J. S. Foot, and D. L. Mitchell, 1998b: Retrieval of tropical cirrus thermal optical depth, crystal size and shape using a dual view instrument at 3.7 and $10.8\,\mu m$, J. Atmos. Sci., 56, 92-100

Baran A. J., and S. Havemann, 1999: Application of complex angular momentum theory to nonspherical particles: Implications for approximate theory and remote sensing, J. Quant. Spectrosc. Radiat. Transfer, 63, 499-519.

Fu Q, P. Yang and W. Sun, 1998: An accurate parameterization of the infrared radiative properties of cirrus clouds for climate models, J. Climate, 11, 2223-2237.

Han Q., J. Chou, and R. M. Welch, 1997: Ice cloud microphysics and its temperature dependence retrieved from satellite data, SPIE proceed., 3220, 39-47.

Key, J. and A. Schweiger, 1998: Tools for atmospheric radiative transfer: Streamer and FluxNet, Computers & Geosciences, 24(5), 443-451.

Mitchell, D. L., A. Macke and Y. Liu, 1996: Modeling Cirrus Clouds: II) Treatment of radiative properties, J. Atmos. Sci., 53, 2967-2988.

Rutan, D. A. and T. P. Charlock, 1997: Spectral reflectance, directional reflectance and broadband albedo of the Earth's surface. Proceedings of the AMS Ninth Conference on Atmospheric Radiation, Long Beach, 446-470.

Scott, N. A., A. Chédin, R. Armante, J. Francis, C. Stubenrauch, J.P. Chaboureau, F. Chevallier, C. Claud and Frédérique Chéruy, 1999: Characteristics of the TOVS Pathfinder Path-B Dataset, BAMS, 80, No 12, 2679-2701

Smith, W. L., H. M. Woolf, M. C. Hayden, D. Q. Wark, and L. M. McMillin, 1979: The TIROS-N Operational Vertical Sounder. Bull. Amer. Meteor. Soc., 60, 1177-1187.

Stubenrauch, C. J., A. Chédin, R. Armante, and N. A. Scott, 1999a: Clouds as seen by Infrared Sounders (3I) and Imagers (ISCCP): Part II) A New Approach for Cloud Parameter Determination in the 3I Algorithms. J. Climate, 12, 2214-2223

Stubenrauch, C. J., W. B. Rossow, N. A. Scott, and A. Chédin, 1999b: Clouds as seen by Infrared Sounders (3I) and Imagers (ISCCP): Part III) Combining 3I Cloud Parameters and ISCCP for better understanding of Cloud Radiative Effects. J. Climate,

Stubenrauch, C. J., R. Holz, A. Chédin, D. Mitchell and A. J. Baran, 1999c: Retrieval of cirrus ice crystal sizes from 8.3 and $11.1\mu m$ emissivities determined by the improved initialization inversion of TIROS-N Operational Vertical Sounder observations, J. Geophys. Res., 104, D24, 31,793-31,808.

Yang P. and K. N. Liou, 1996: Finite-difference-time-domain method for light scattering by small ice crystals in three dimensional space, J. Opt. Soc. Am. A, 13, 2072-2085.

Yang P., K. N. Liou and W.P. Arnott, 1997: Extinction efficiency and single scattering albedo for laboratory and natural cirrus clouds, J. Geophys. Res., 102, 21825-2135.

DISCRIMINATION OF HYDROMETEOR TYPE IN MIXED-PHASE CLOUDS USING RADAR DOPPLER SPECTRA

D. M. Babb,[1] N. Miles and J. Verlinde

[1]Department of Meteorology, The Pennsylvania State University, University Park, PA, 16802

1. INTRODUCTION

In many instances, knowledge of the cloud and precipitation size distributions is key to understanding cloud microphysical, dynamical, and radiative processes. This knowledge also must include the vertical structure and evolution of the size distributions and be based on a large observational data set. Therefore, it is imperative that observational techniques be developed to measure vertical profiles of the cloud and precipitation size distributions over large time domains.

Such observational requirements favor the use of remote sensors over *in situ* measurements. Specifically, cloud radar has shown great promise in cloud observations over long time periods (Miles et. al. 2000). In cases of liquid phase clouds, several studies have demonstrated that cloud radar can be used to retrieve the cloud drop size distribution (e.g. Babb et. al. 1999). However, a majority of the clouds, particularly in the mid-latitudes, fall into a category which do not contain a single hydrometeor type.

These mixed-hydrometeor (i.e. mixed-phase and/or multi-habit) clouds are difficult to measure because remote sensors integrate cloud properties across the measurement volume. Therefore, if a cloud contains a mix of hydrometeors, the resulting signal is a combination of signals from all the different types. What is needed is a way to differentiate the signals from the various hydrometer types. Some of the most promising work in this area involves using the Doppler power spectrum from a vertically pointing cloud radar.

The Doppler spectrum is a measure of the power received by the radar as a function of the Doppler phase shift between the transmitted and received signals. This phase shift is generated by the motions of the particles detected by the radar. For a vertically pointing radar, only the vertical motions (i.e. along the axis of the radar beam) contribute to the Doppler shift. Since the vertical motion of a given hydrometeor is determined by its quiet-air terminal velocity and the back-ground air motions, the Doppler spectrum can give information about the sizes of the various particles in the radar beam. In addition, the magnitude of power (e.g. radar reflectivity) received by the radar is a function of the sizes and numbers of these particles. Therefore, if one can determine the sizes of particles present, it is possible to determine the concentration of each size particle.

In cases where the radar volume contains a mixture of hydrometeor phases and shapes, using the Doppler spectrum should allow one to distinguish between the different fall velocity classes. This is because different hydrometers have specific fall velocity / reflectivity relationships. These different fall velocities produce multi-modal spectra; each mode representing a separate, identifiable class of hydrometeor. To demonstrate the feasibility of hydrometeor discrimination using the Doppler spectrum, we will start with a forward simulation of a Doppler spectrum based on an observed multi-phase, multi-habit size distribution.

Corresponding author's address: David M. Babb, Dept. of Meteorology, 503 Walker Bldg., University Park, PA 16802; E-Mail: dbabb@essc.psu.edu.

2. METHOD

The first step in the forward simulation is the collection of *in situ* observations from a cloud having multiple hydrometeor types. A data set collected during the Lake-Induced Convection Experiment (LAKE-ICE) was ideal for this purpose. During this experiment, several instrument platforms were used to study the formation and evolution of lake-effect snow bands over Lake Michigan. Among these instrument platforms was the Wyoming King Air aircraft which collected in-cloud measurements. Also used was the Penn State cloud radar that collected profiles of Doppler spectra as the snow bands moved over land. This data set was selected because there were several over-flights of the radar by the aircraft allowing for inter-comparisons between the two platforms.

A selection of ice crystal images from the 2-DP and 2-DC PMS probes is shown in figure 1. These images were first classified into the following categories: spheres, dendrites, small hexagonal, aggregates, and graupel. Once classified, the number concentrations for each category were generated (figure 2). In order to generate a simulated Doppler spectrum from the number concentrations, the diameter/fall-velocity and reflectivity relationships are needed. For this study, we used relationships previously cited in the literature (Locatelli and Hobbs 1974; Heymsfield and Kajikawa 1987). The relationships for fall velocity (v) and reflectivity (Z) are based on power laws with the following form:

$$v = \alpha D^{\beta}$$

$$Z = \gamma N D^{\sigma}$$

where D is the particle diameter, N is the number concentration, and the parameters (α, β, γ, σ) have the following values:

sphere: α=.0317; β=2.0; γ=1.0; σ=6.0
dendrite: α=0.62; β=0.33; γ=0.371; σ=3.38
hexagonal: α=2.973; β=0.86; γ=1.54; σ=4.49
aggregate: α=0.79; β=0.27; γ=0.0934; σ=2.09
graupel: α=1.3; β=0.66; γ=1.62E-2; σ=0.57

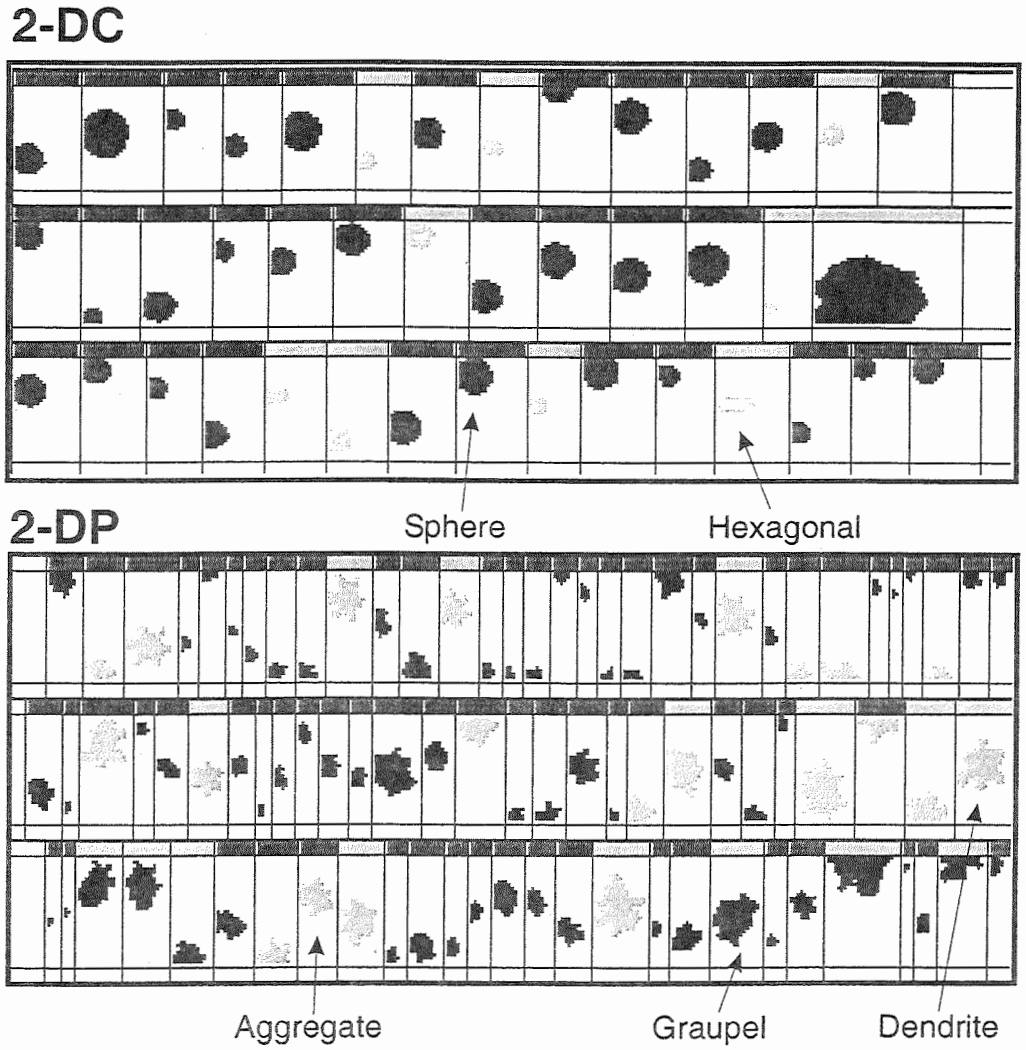

Figure 1. Sample images from the aircraft 2-DC and 2-DP particle probes. Examples from each of the major hydrometeor groups used in this study are also indicated.

Figure 3 shows the result of applying these relations to the distributions shown in figure 2. This is the simulated Doppler spectrum. We should note that since the aircraft sample volume was not immediately available, the volume dimension is assumed to be of unit value. Doing so causes a scale difference in the simulated power received by the radar.

3. RESULTS

Looking at the spectrum in figure 3, we see several distinct regions that are unique to a particular hydrometeor type, while other regions are represented by a combination of types. This shows that it is possible to distinguish between certain types of hydrometeors with large differences in fall velocities, such as graupel and dendrites, but distinguishing between other types with similar fall velocities – aggregates and dendrites for example – is considerably more difficult. By understanding in which of the various fall velocity classes that particular hydrometeor types are contained, one can use the physical situation to determine the predominate type represented by each mode of the Doppler spectrum.

To place the forward simulation in perspective, figure 4 shows an actual Doppler spectrum collected at the aircraft altitude during the time of the aircraft over-flight. We should point out that comparisons between aircraft and radar must be performed with caution because the sample volumes of the two instruments are dramatically different. Nevertheless, the actual Doppler spectrum contains several regions that resemble those predicted by the forward simulation.

This example suggests that it may be possible to determine the various hydrometeor types within a mixed-phase and/or mixed-habit cloud. Considerable work needs to be done to move from the forward problem to a retrieval algorithm. It is likely that certain mixtures of hydrometeors will be more readily separated than others. Any retrieval algorithm should be designed around these cases first, then expanded to include more difficult situations.

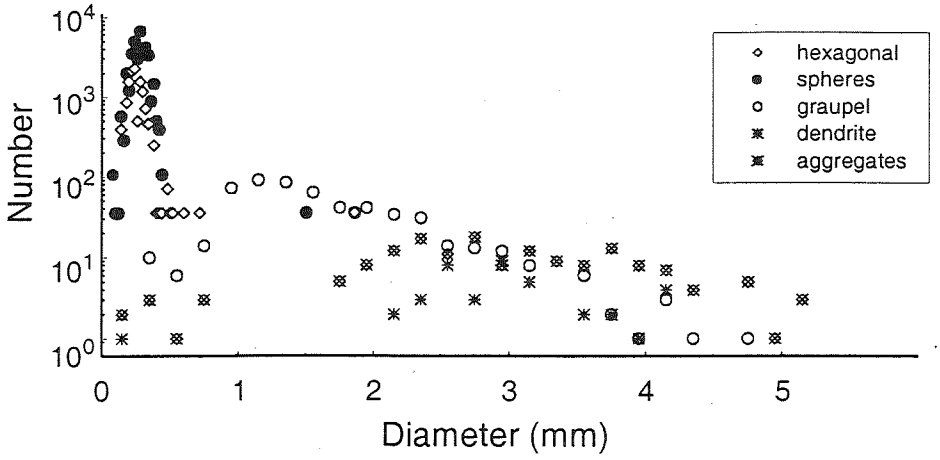

Figure 2. Numbers of particles in the aircraft sample volume as a function of hydrometeor type. Since the sample volume is unknown, the values are per unit volume.

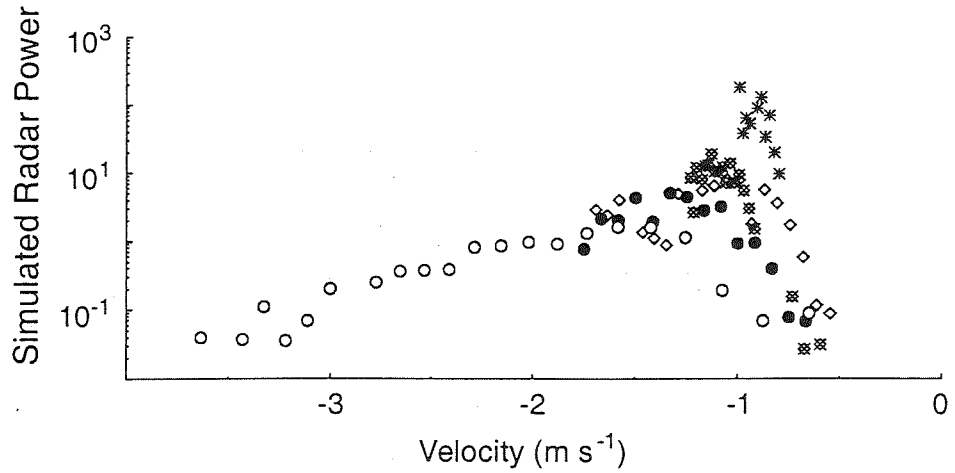

Figure 3. Particle concentrations are converted to a Doppler power spectrum using power law relationships for fall velocity and reflectivity. Here again the simulated radar power is not scaled properly due to the unknown sample volume.

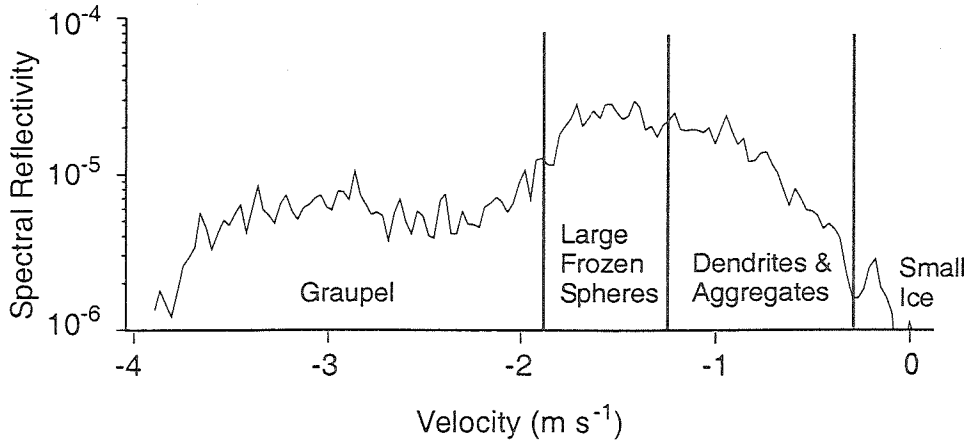

Figure 4. Actual radar Doppler spectrum collected during the same time period as the PMS probe data. Note the similarity between this spectrum and the simulated spectrum in figure 3.

4. ACKNOWLEDGEMENTS

We wish to thank H. Ochs and others at the University of Illinois for providing the image probe analysis software. This work was funded by the National Science Foundation (#ATM-9629343)

5. REFERENCES

Babb, D. M., J. Verlinde, B. A. Albrecht, 1999: Retrieval of cloud microphysical parameters from 94GHz radar power spectra. *J. Atmos. Oceanic. Technol.*, **16**, 489-503.

Heymsfield, A.J., and M. Kajikawa, 1987: Improved approach to calculating terminal velocities of platelike crystals and graupel. *J. Atmos. Sci.*, 44, 1088-1099.

Locatelli, J. D. and P. V. Hobbs, 1974: Fall speeds and Masses of solid precipitation particles. *Jour. Geophys. Res.*, **79**, 2185-2197.

Miles, N., D. M. Babb, and J Verlinde, 2000: Multi-scale analysis of in-cloud vertical velocity derived from 94-GHz Doppler radar. *Preprints: 13th ICCP*, Reno NV.

COMPARISON OF TWO HYDROMETEOR IDENTIFICATION ALGORITHMS OF THE S-POL RADAR WITH IN-SITU MEASUREMENTS OF HYDROMETEORS ON A MOUNTAIN

Eszter Barthazy*, Sabine Göke[1)], Zhaoxia Zeng[2)], Jothiram Vivekanandan[1)], Scott M. Ellis[1)]

Atmospheric Science, ETH , 8093 Zürich Switzerland
[1)]National Center for Atmospheric Research, Boulder, Colorado
[2)]University of Washington, Seattle, Washington

1 INTRODUCTION

Hydrometeor types above the melting layer are various and a good indication of the ongoing microphysical processes in their respective growth regimes. Also, the development of precipitation in the vertical (sedimentation) and in the horizontal (advection) is highly dependent on the hydrometeor types at subzero temperatures.

Time dependent three-dimensional fields of hydrometeor types have the potential to yield yet unknown details about the structure and evolution of precipitation systems, especially of stratiform and orographic types. Furthermore, the newest generation of numerical weather models have a horizontal resolution of only a few kilometers. Thus, quantities like hydrometer types above the melting layer become important when precipitation amounts are to be forecasted. This is especially true in complex orography, where it is important which valley is subject to what amount of precipitation to predict the danger of flooding.

Up to now, hydrometeor types have been investigated mainly by in-situ measurements. The methods are usually accurate but yield only poor information about spatial variabilities. Remote sensing of hydrometeor types opens up the possibility to study hydrometeors within a large volume. The most promising method is using a polarimetric radar.

During the Special Observing Period (SOP) of MAP (Mesoscale Alpine Programme, field phase autumn 1999) many different instruments were placed in Northern Italy to study the microphysics of precipitation. One of the key instruments was the S-Pol radar of NCAR. Within the range of the S-Pol radar a mountain station was run at 2800 m ASL equipped with instruments for observing microphysics. Formvar slides, on which solid precipitation particles are conserved, are used to deduce hydrometeor types in great detail.

The purpose of this study is to compare the detailed in-situ measurements obtained at the mountain station with the results of two different hydrometeor identification algorithms of the S-Pol radar.

2 INSTRUMENTAL SETUP

During the SOP of MAP, NCAR's S-Pol radar was set up at Vergiate in the Po valley south of the Alpine range. In a distance of 65 km northeast of the S-Pol radar, the experimental site of Macugnaga was located. In Macugnaga, two observing stations were set up. The bottom station was in the Anzasca valley at 1320 m ASL. Here, a vertically pointing X-band Doppler radar was operated together with a disdrometer and standard meteorological instruments. On Monte Moro, in a horizontal distance of 3.1 km from the bottom station, the top station was set up at 2800 m ASL. At the top station optical spectrometers were operated and Formvar replicas (Schaefer, 1956) of solid hydrometeors were taken.

*Corresponding authors adress: Atmospheric Science, ETH Hönggerberg HPP , CH–8093 Zürich, e–mail: eszter@atmos.umnw.ethz.ch

3 CLOUD MICROPHYSICS RETRIEVAL

Several studies have shown that polarimetric observables (both linear and circular) can be used to identify hydrometeor types (Vivekanandan *et al.*, 1999 and references therein, Zeng *et al.*, submitted). Linear polarimetric radars, like the one used in this study, transmit and recieve both horizontally and vertically polarized radiation, providing more information about the scattering media than conventional radar. Polarimetric radar observables depend on the microphysical characteristics of hydrometeors; namely, particle size, shape and orientation relative to the local vertical direction, phase (liquid or ice), and bulk density (wet, dry, aggregate, or rimed). In addition to traditional reflectivity (Z_{HH}) and Doppler measurements, linear polarimetric observables include differential reflectivity (Z_{DR}), linear depolarization radio (LDR), specific differential propagation phase (K_{DP}), and correlation coefficient (ρ_{HV}). By combining the different parameters of a linear polarimetric radar, many different particle types can be deduced. Two different philosophies exist to do this. One uses fixed thresholds for the different parameters, the other uses a fuzzy logic method to deduce particle types.

3.1 UW Algorithm

The Algorithm of the University of Washington (Zeng *et al.*, submitted, Zeng 1999) is a simple but robust algorithm for deriving the most certain microphysical information from a polarimetric radar. It combines reflectivity (Z), differential reflectivity (Z_{DR}), linear differential reflectivity (LDR), specific differential propagation phase shift (KDP) and a rain boundary in $Z - Z_{DR}$ space to distinguish hydrometeor types.

An important feature of the algorithm is that it is empirically calibrated by making use of radar data obtained in rain-only situations. This approach requires theoretical

relations to have a degree of physical consistency even in the absence of independent verification by in situ cloud physics measurements.

A vertical profile of temperature is need for the algorithm. Since no sounding stations were available close to Macugnaga, the temperature at the bottom station and the 0 °C level (extracted from the radar profiles) have been used to estimate the vertical temperature profile.

The algorithm is easy to apply and takes a conservative physically-based approach identifying only the most certain categories of precipitation types. There are 8 categories identified by the algorithm (listed below). The data are categorized as ambiguous type when the data are not identified as any of the other 8 categories by the algorithm.

ambiguous	hail+rain	graupel
rain	graupel+rain	hail
attenuated rain	supercooled rain	snow

3.2 NCAR Algorithm

The second algorithm, abbreviated to NCAR Algorithm is described in detail in Vivekananadan *et al.* (1999). The fuzzy logic–based method makes use of a smooth transition in polarimetric observable boundaries among precipitation types. This is usefull for precipitation which often shows mixed phases like melting ice particles or rain and hail mixtures. The hydrometeor types identified by the algorithm are summarized below:

cloud particles	dry snow
drizzle	wet snow
light rain	oriented ice crystals
moderate rain	irregular ice crystals
heavy rain	supercooled liquid water droplets
hail	insects
rain/hail mix	birds
graupel/small hail	clutter
graupel/rain	

4 TWO CASES FROM MAP

The ten weeks of the SOP of MAP consisted of several IOPs (Intensive Observing Period) where most of the instruments in the Alpine region were operating. In the following, two cases from two different IOPs will be discussed.

4.1 IOP-12

The first case is from IOP-12, 30 October 1999. At this day, precipitation started around noon and lasted until the evening. Fig. 1 shows the HTI (Height-Time Indicator) of the X-band Doppler radar and the rainrate measured by the disdrometer.

On Monte Moro, Formvar plates were replicated in intervals of 10 minutes between 11:45 and 17:30 UTC. By evaluating the Formvar plates the low precipitation rate is confirmed. Only few crystals can be found on the plates. In addition, the ambient temperature was barely below 0 °C and many of the coated plates show partly melted and unidentifyable particles. This can happen when the Formvar solution and/or the glass plates are not cold enough. However, Formvar plates between 15:00 and 15:30 UTC are good enough to be evaluated. Most of the ice crystals are of irregular type but some are of the broad branched stellar type as shown in Fig. 2. The riming degree of the ice crystals was calculated according to the six step scale of Mosimann *et al.* (1994) where a riming degree of 0 corresponds to unrimed crystals, 1 to lightly rimed, 2 to moderately rimed, 3 to densly rimed, 4 to heavily rimed and 5 to graupel. The average riming degree of the Formvar plates of the above mentioned 30 minutes was at most 1.

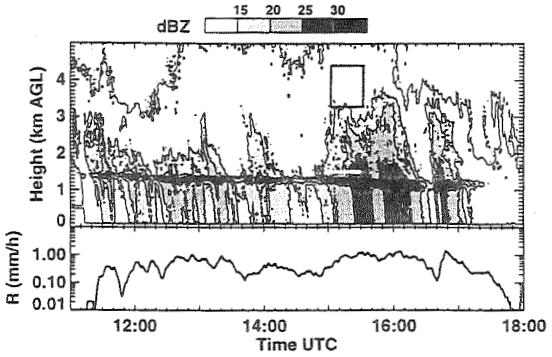

Figure 1: *HTI of radar reflectivity of the X-band Doppler radar. Below, the rainrate measured with the disdrometer is printed. The black rectangle indicates the time window and the vertical beamwidth of the S-Pol radar where data have been evaluated. The white line indicates the height of Monte Moro and the time period with reasonable Formvar data.*

Figure 2: *Formvar replicas of ice crystals from 30 October 15:20 UTC. The left picture shows some broad branched dendrites and a short column. The right picture shows a part of a small aggregate. Crystal types are not clearly visible but seem to be of columnar or planar type.*

To compare the in-situ measured type of ice crystals and the riming degree with the hydrometeor identification algorithms of the S-Pol radar, PPIs are used with an elevation angle of 4.09°. From these PPIs the section between 60 and 70 km range and roughly between 280 and 305° azimuth is used. At the location of Monte Moro, the radar beam is at 5160 m ASL and has a beam width of 1.1 km. The precipitation pattern was very stable during the time considered. Thus, average values of the radar quantities can be used. Fig. 3 shows the average radar reflectivity of the time period 15:00–15:30 UTC. As already seen in Fig. 1, the radar reflectivities at 5 km ASL are very low. There is a decrease of reflectivity roughly from South to North. This is on one hand because the radar beam is 400 m lower/higher at 60/70 km range than at 65 km. On the other hand, the orographic enhanced precipitation decreases to the North where the Alpine crest is located (the Monte Rosa Massive (4634 m ASL), one of the highest Alpine peaks, is close to where the 'S' for South is printed).

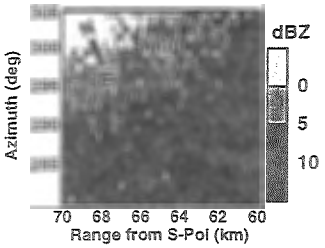

Figure 3: *Average radar reflectivity of the S-Pol radar taken from a PPI with an elevation angle of 4.09°. The North–South direction applies to the center of the image.*

The results of the particle identification algorithm of the University of Washington show, except of 'no data' either 'snow' or 'ambiguous' (Fig. 4). To obtain this figure, data of all PPIs from 15:00 to 15:30 have been summarized. Each pixel shows the particle type most often occuring at the same pixel in the original PPIs. The results of the algorithm are in good agreement with the in-situ observations.

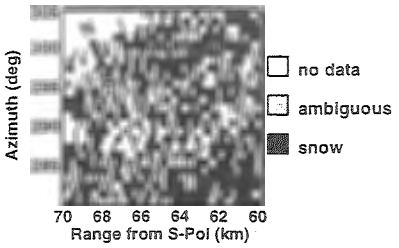

Figure 4: *Results of the UW algorithm of particle type identification for 30 October 1999.*

In the same manner, Fig. 5 shows the results of the NCAR algorithm. Here, more particle types are indicated. At the upper left corner 'cloud particles' are given which refer to very small particles (solid or liquid). This agrees with the very low radar reflectivity in this region. The rest of the image consists of 'irregular ice crystals', 'oriented ice crystals' and 'dry snow'. This is in very good agreement with the in-situ observations. When comparing results of the two algorithms with in-situ observations, it has to be noted that the radar samples roughly 2000 m above Monte Moro.

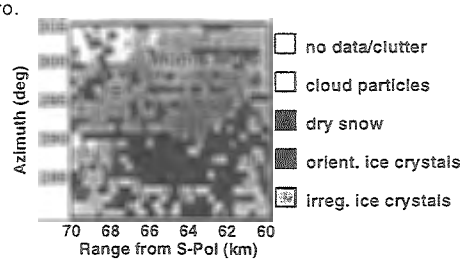

Figure 5: *Results of the NCAR algorithm of particle type identification for 30 October 1999.*

4.2 IOP-14

The second case is from IOP-14 where precipitation lasted for 48 hours with only short breaks. The most intense part of the precipitation was between 5:00 and 19:00 UTC on 4 November 1999. In Fig. 6 the HTI of the X-band Doppler radar and the rainrate is shown.

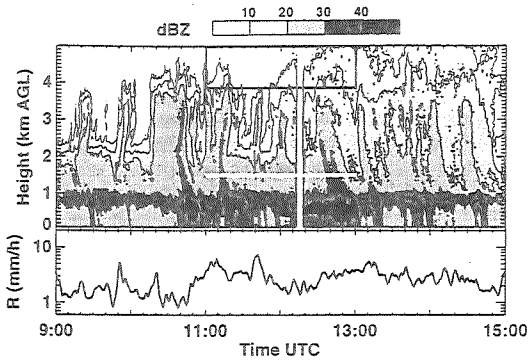

Figure 6: *X-band Doppler radar HTI and rainrate. the black rectange and the white line are like in Fig. 1.*

On Monte Moro, Formvar plates were replicated in intervals of 15 minutes between 6:45 and 15:00 UTC. For this case, the Formvar plates are of good quality and since rainfall rate was higher than in the first case, more crystals can be found on the plates. Most ice crystals of this day are needles. There are also aggregates of needles. Some are small, consisting of only a few crystals but some are rather large. Figs. 7 and 8 show an overview of the Formvar plates of IOP-14. Ice crystal types are constant throughout the day except for one hour. From 12:00 to 13:00 UTC some broad branched dendrites appeare and needles seem to be less frequent. The riming degree of the ice crystals is again very low, maximum riming degree is at most 1.

Figure 7: *Formvar replicas of ice crystals from 4 November. The left picture shows a large aggregate (10 mm) consisting of needles (11:00). The right picture shows some scattered needles (11:15).*

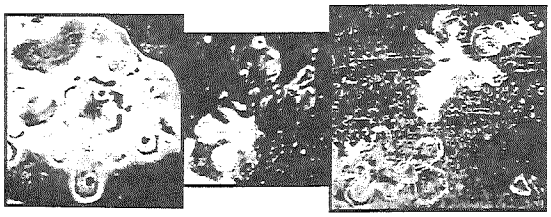

Figure 8: *Formvar replicas of ice crystals from 4 November. All three pictures show fragments of broad branched dendrites replicated at 12:45.*

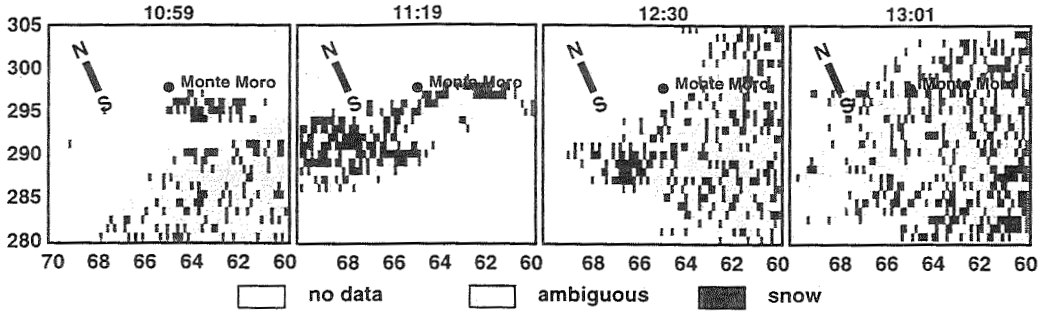

Figure 9: *Results of the UW algorithm of particle type identification for 4 November 1999.*

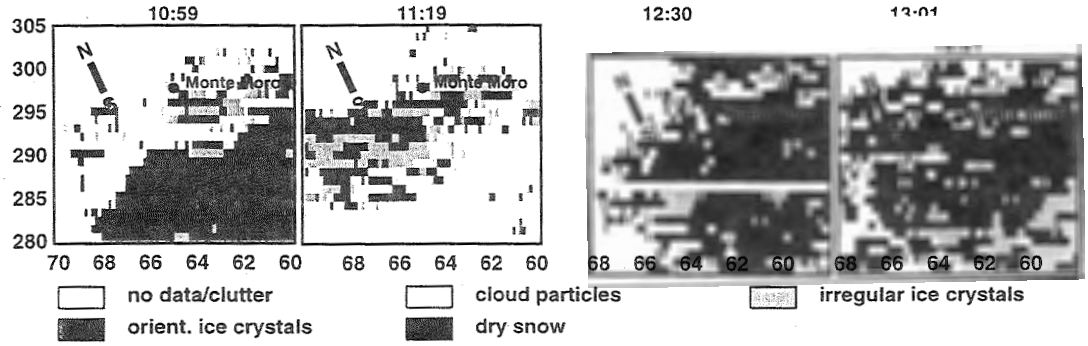

Figure 10: *Results of the NCAR algorithm of particle type identification for 4 November 1999.*

The precipitation pattern on 4 November is changing quickly and radar quantities cannot be displayed as averaged values as in IOP-12. PPIs are now taken with an elevation angle of 4.6 °, radar reflectivities are again lower than 15 dBZ. The results or the UW algorithm are displayed in Fig. 9. Four single PPIs have been chosen. The first two correspond to a time when rather large aggregates of needles are observed on Monte Moro. The last two were measured when some platelike crystals were observed. All four PPIs show mainly 'ambiguous' and some 'snow' pixels. This is generally in good agrrement with the in-situ observations although the amount of ambiguous pixels is rather high.

The results of the NCAR algorithm are displayed in Fig. 10. The identified particle type is here mainly 'oriented ice crystals' followed by 'irregular ice crystals', 'cloud particles' and 'dry snow'. Although there is a change of crystal type from the first hour to the second, this is not reflected by the NCAR algorithm. However, this is not surprising since the algorithm cannot differentiate between various ice crystal shapes. An interesting result is obtained, when the two IOPs are compared. In IOP-14, much more pixels are identified as 'oriented ice crystals' than as 'irregular ice crystals' whereas in IOP-12 this is vice versa. Therefore, the NCAR algorithm agrees with the in-situ observations of mainly irregular ice crystals in IOP-12 and of mainly needles in IOP-14.

5 CONCLUSION

The results of two different hydrometeor identification algorithms for the S-Pol radar have been compared to in-situ observations of solid hydrometeors. The data of two cases have been evaluated. Both cases were rather similar with mainly unrimed ice crystals and small aggregates. Both algorithms performed well. As a next step, the algorithms should be compared to in-situ observations of other types of hydrometeors, e.g. graupel, hail, wet snow, etc.

6 ACKNOWLEDGMENT

The authors would like to thank Richard A. Oye for his help in evaluating the S-Pol data.

7 REFERENCES

Mosimann, L., E. Weingartner, and A. Waldvogel, 1994: An analysis of accreted drop sizes and mass on rimed snow crystals. *J. Atmos. Sci.*, **51**, 1548–1558.

Schaefer, V. J., 1956: The preparation of snow crystal replicas-VI. *Weatherwise*, **9**, 132–135.

Vivekanandan, J., D. S. Zrnic, S. M. Ellis, R. Oye, A. V. Ryzhkov, and J. Straka, 1999: Cloud microphysics Retrieval using S-band dual-polarization radar measurements. *Bull. Amer. Met. Soc.*, **80**, 381–388.

Zeng, Z., 1999: Methodology for the identification of precipitation type by polarimetric radar. *M.S. Thesis*, Department of Atmospheric Sciences, University of Washington, Seattle, WA.

Zeng, Z., S. E. Yuter, and R. A. Houze: A simple empirical methodology for the identification of precipitation particle type by polarimetric radar. *J. Appl. Meteor.*, submitted.

IMPLICATION OF A STRATIFIED CLOUD MODEL FOR MW REMOTE SENSING OF PRECIPITATION

Jinli LIU[1], Zhehu CUI[2], Ling ZHANG[1], Xiankang DOU[3], and Daren LU[1]

[1]LAGEO, Institute of Atmospheric Physics, Chinese Academy of Sciences, Beijing 100029, China
[2]Chinese Academy of Meteorological Sciences, Beijing 100080, China
[3] University of Science and Technology of China, Hefei, Anhui Prov. 230026, China

1. INTRODUCTION

Space-borne Microwave (MW) radiometers have been actively used for global rainfall estimation, but the retrieval accuracy of rainfall rate still cannot meet the requirements of operational use and research, one of the main reasons is the highly complexity and rapid variation of the vertical structure of precipitating cloud. For improving the accuracy of retrieval rainfall rate, establishment of precipitating cloud model is one of the key steps.

By improving an existed stratified cloud model we revealed the fine vertical structure of the stratified precipitating cloud model. Combined this stratified cloud model with a vector radiative transfer model, the relationship between brightness temperature and ground rainfall rate was established.

In this paper, the influence of the melting layer in the cloud model and the pattern of hydrometeors size distribution in stratified precipitating cloud on radiative transfer characteristics were examined. Also, all the simulation results were compared with the real 'observed' data, which was obtained from ARMAR airborne radar-radiometer data during TOGA COARE IOP.

2. MODEL

Since tropical region covers large part of global oceans, remote sensing of rainfall in this area is of significance. Also rather homogeneous stratified rainfall is one of the main types of the rainfall in this area. Here we only focus on this kind of rainfall.

2.1 Stratified Precipitating Cloud Model

A dynamical cloud model developed by Hu & Yan (1986) was adopted and improved by incorporating melting layer microphysics. We used radio sounding data and ocean surface condition in TOGA COARE period as the input, and the output of the cloud model contained vertical structure of raindrops, cloud droplets as well as various kind of ice particles. Based on composition of radar observation and cloud model output of microphysics structure, the corresponding vertical structures of stratified precipitating cloud are established, and the resolution of vertical structure is 50 m.

2.2 Radiative Transfer Model

The radiative transfer (R-T) model developed by Evans et al (1995) was chosen in this study. Simulations were made for the following situations, range of rainfall rate: 0–20 mm/hr; ground surface: calm ocean; microwave (MW) channel: 13.8 GHz, which is the frequency of ARMAR aircraft

Corresponding author's address: Jinli LIU, LAGEO, Institute of Atmospheric Physics, Chinese Academy of Sciences, Beijing 100029, China; E-mail: jliu@linux2.iap.ac.cn.

radar/radiometer and it is also TRMM PR's channel.

3 Simulation Results

For investigating the radiative characteristics of stratified precipitating cloud, we did the simulation by using combined cloud model and radiative transfer model. The calculations were made for different melting situation and different pattern of particles size distribution (PSD). Three melting situations were considered in the stratified cloud model, i.e.:

1) 'No melting': do not consider melting process in stratified cloud model;

2) 'Without coating': consider melting process but ice particle without coated water;

3) 'With coating': consider melting process and ice particle with coated water.

Three kinds of particles size distribution are chosen as:

1) Marshall-Palmer (M-P) distribution were used for both liquid and ice particles.

$$N(D) = N_0 e^{-\lambda D} \qquad (1)$$

2) Gamma distribution

$$N(D) = N_0 D^{-\mu} e^{-\lambda D} \qquad (2)$$

3) Mixed distribution

Different spectra were chosen for different hydrometeor particles:

for cloud droplets,

$$dN(D) = N_0 D^2 e^{-\lambda D} dD \qquad (3)$$

for raindrop and graupel,

$$dN(D) = N_0 e^{-\lambda D} dD \qquad (4)$$

for ice crystal and aggregate,

$$dN(D) = N_0 D e^{-\lambda D} dD \qquad (5)$$

For comparison study, we analyzed the ARMAR (Durden et al 1994) airborne radar/radiometer observation data, which was measured over equatorial Pacific Ocean during TOGA/COARE Intensified Observation Period (IOP). Airborne radar observed vertical structure of radar reflectivity Z_e and the MW radiometer observed the brightness temperature of underneath cloud-ocean surface system. The radar observation revealed very clear stratified characteristics with brightband as well as relatively horizontal homogeneity of precipitating cloud. With Z_e profiles and the output of the cloud model, we produced vertical microphysical structure of the stratified precipitating cloud, which is the basis for radiative transfer simulation.

The influence of particle size distribution and melting situation on radiative transfer characteristics of precipitating cloud were investigated, simulation study were made by combined dynamic cloud model and radiative transfer model for above three different PSD and different melting situation. By using the real observed data comparison study were made.

3.1 Variation with Particle Size Distribution

Fig. 1 is the brightness temperature versus rainfall rate (Tb-R) obtained from both simulation and real observed data. Tb-R scattergram is the observed real data, brightness temperatures Tb are the observed brightness temperatures from airborne radiometer and the rainfall rates were derived from corresponding radar reflectivities with attenuation correction (Dou et al 1997). Three solid curves are the simulation results for three different PSD based on the combined cloud model structures and radiative transfer model for 'with coat' melting situation. From Fig.1 we can find the following results. 1) Large differences exist between three curves which means that the pattern of particle size distribution plays an

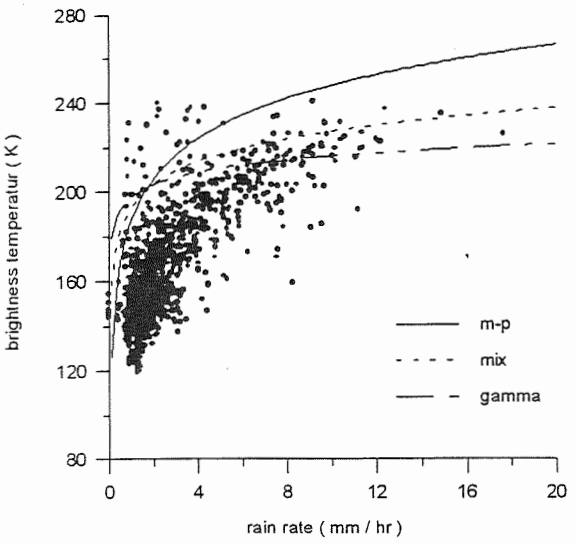

Fig.1 Brightness temperature versus rainrate for different particle size distribution when 'with coating' is chosen in cloud model.

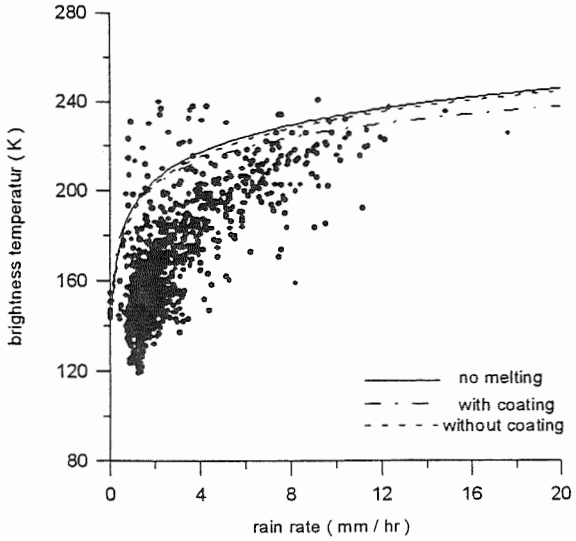

Fig.2 Brightness temperature versus rain rate for different melting situation when mixed distribution is chosen in simulation.

important role in retrieval rainfall rate, the biggest Tb difference of M-P and Gamma spectra reach 40 k for the rain rate of 20mm/hr. It indicates that we should be very careful to choose the pattern of PSD in radiative transfer simulation when we retrieve rain rate. 2) Comparison study of simulation results and the 'observed' data shows that the tendency of simulation curve for M-P spectra is consistence with the real observed data, but it is under-estimated the rain rate from the same brightness temperature. The simulation results of Gamma spectra are worse, not only the difference of the simulation and the observed data are considerable big, but also the dynamic range of brightness temperature in simulation is small refer to 0-20mm/hr. Mixed spectra is the best one in three spectra, it is the closest to the observed data. In this point, we may say mixed spectra are the closest real spectra in stratified precipitating cloud over Tropical Ocean area.

3.2 Variation with Melting Situation

As shown from the simulation results for different melting situation of the cloud model, different melting situations do influence the radiative transfer characteristics of stratified precipitating cloud, and different PSD have different influence of melting situation. Here we only show the simulation result for mixed PSD

Fig.2 is the brightness temperature versus rainfall rate for different melting situation when mixed PSD was chosen in simulation. Also, Tb-R scattergram is the 'observed' real data from ARMAR aircraft data, three solid curves are the simulation results for different melting situation chosen in cloud model. The following outcomes can be seen from Fig.2. 1) They do exist differences between three curves, it reveals that the different melting situation results in the different relationship of Tb-R. 2) In mixed PSD, the difference between 'no melt' (don't consider melting procedure in stratified cloud model) and 'without coating' (consider melting but ice particle without coated water) are very small, but the difference of these two situation and 'with coating' (consider melting and with coated water) is considerably large. 3) Comparison study shows that the melting procedures with coated water of ice particle are more closely to real observed data.

Simulations for the other two PSD also indicate that the 'with coating' is the best one.

In summary, simulation study by combined dynamic cloud model and radiative transfer model indicated that, different particle size distribution and different melting situation of stratified cloud model do influence the radiative transfer characteristics of precipitating cloud and may affect the retrieval accuracy of rainfall rate. Comparison study between simulation results and 'observed' data reveals that the improved stratified cloud model which consider melting process and ice particle with coated water is the best one for retrieval rainfall rate by combined cloud model and radiative transfer model; The mixed PSD seems be most closely to the real particle size distribution in tropical ocean area.

4. ACKNOWLEDGEMENT

This project is supported by the National Natural Science Foundation of China (No. 49885001 & 49705058).

5. REFERENCES

Dou, X.K., J. Testud, and P. Amayene, 1997: The study of the space-borne rain radar rainfall rate retrieval algorithms by simulations. Chinese Sci. Bull., Vol.42, No.3, 292-295.

Durden, S.L., E. Im, F.K. Li, W. Ricketts, A. Tanner, and W. Wilson, 1994: ARMAR: An airborne rain-mapping radar. J. Atmos. Oceanic Technol., vol.11, 727-737.

Evans, K.F., and G.L. Stephens, 1995: Microwave radiative through clouds composed of realistically shaped ice crystals, Part II: Remote sensing of ice clouds. J. Atmos. Sci., vol.52, 2058-2072.

Hu, ZhiJin and Caifan Yan, 1986: Numerical simulation of microphysical processes in stratiform cloud: Microphysical model. J. of Academy of Meteor. Sci., S.M.A., China, (1), 37-58.

On the Feasibility of identifying multi-spectral Visible/NIR signatures of clouds

T. P. DeFelice[1] & B. Wylie

RAYTHEON, Science Department, SAB, EROS Data Center, Sioux Falls, SD 57198
[1]Visiting Scientist, NCAR, RAP, Boulder, Co.

1. INTRODUCTION

Data from the original multispectral scanner (MSS), Thematic Mapper (TM) and most recently, the Enhanced Thematic Mapper Plus (ETM+) on the Landsat 7 have found applicability to problems in geology, land use/management, urban planning, ecology, oceanography, atmospheric science, and many other disciplines since the beginning of the Landsat program 25 years ago. The non-thermal spectral range, spectral resolution, and spectral coverage of these measurement platforms have recently been improved. One of the improvements sits on the EO-1 satellite platform tauting continuous, high spectral resolution (10 nm) readings in the 400–2500 nm spectral region, or 220 bands. In contrast, the ETM+ covers the spectral region between 400–2400 nm with a variable spectral resolution or six discrete bands and one panchromatic band. Four of the six discrete bands cover the visible and near infrared. This enhanced spectral information, especially below 1000 nm, enables us to assess whether it is feasible to improve the utility of solar spectrum atmospheric correction and cloud classification algorithms without using any thermal band information. Before such improvements can be utilized, we need to determine whether spectrally similar ground-based measurements demonstrate, (i) the ability to discriminate unique spectral features between various sky types, such as, sunny, cloud residual (areas of evaporating/evaporated clouds), cirrus, cirrostratus, cirrocumulus, optically thin altocumulus, and (ii) that more spectral bands can improve the discrimination between unique sky spectra. Ground-based measurements will be used to validate these atmospheric correction and cloud classification algorithms. If they fail to identify unique sky spectra in the visible to near infrared spectral region, then there is little cause to proceed.

2. BACKGROUND

A feasibility study was conducted at the EROS Data Center Terrestrial Ecosystem Assessment (TERESA) site to assess whether unique spectral signatures, using 4 bands between 440 and 940 nm, could be assigned to a variety of sky conditions using a handheld sunphotometer. Over 750 observations made during May through November 1999 have been included in this study. These data were also processed to simulate a 2 spectral band sensor and a different 4 band sensor.

Other studies had suggested that clouds and clear skies had different spectral signatures (e.g. Lindner and Isaac, 1990; King et al., 1992; Lindner and Isaacs, 1993; Goetz, 1994). Proprietary data from a precision agriculture company (DeFelice, unpublished) suggested that the reflectivity of optically thin clouds when viewed from an airborne sensor might include the reflectivity of the cloud plus that of the ground below.

3. METHODS

The sunphotometer spectral data were grouped according to sky type. Skytype was observed at the time of each sunphotometer observation. Local National Weather Service (NWS) data and the results of Haurwitz and others in Malone (1951) were used to verify the skytype. The sunphotometer data in each of its bands were summed, and corrected to the field of view for the pyranometer used by Haurwitz.

Part of our data analyses included a decision tree classifier and boosting. The decision tree classifier was used to establish a set of predictive spectral threshold rules to discriminate sky types. Decision trees use a hierarchical, nonparametric, nonlinear subdivision of large data sets and have been employed successfully for land cover discrimination (Hansen et al., 1996; Friedl and Brodley, 1997; Friedl et al., 1999). Decision tree classifiers are applicable since they (Hansen et al., 1996):

- are independent of the statistical distribution of class signature
- are able to utilize categorical data
- reveal the hierarchical structure of independent variables
- preserve discriminability during data reduction.

Boosting is a technique that forces decision trees to account for the more difficult cases by building multiple decision trees. It can reduce misclassification rates by 10-50% (Friedl et al., 1999). Ten boosted decision trees were used in this study. Rule sets which were generalized from the boosted decision trees (Feng and Michie, 1994) were used to make sky type estimates.

Sky type classes which had less then 20 observations were excluded from the analysis. Randomly, thirty percent of the remaining observations were removed from the data set and were used as an independent test data set for assessing the predictive accuracy of various boosted rule sets. Decision tree

Corresponding author's address: Thomas P. DeFelice, Raytheon, Science Department, SAB, EDC, Sioux Falls, SD 57198; E-Mail: defelice@edcmail.cr.usgs.gov.

analysis is prone to over fitting of the data. While the use of generalized rule sets reduces over fitting, decision trees can also be pruned back so that the entire training dataset will not fit perfectly. Various permutations of decision trees were obtained by systematically varying not only the severity of pruning (25%, 20%, and 15%) but also the number of observations per branch (2, 3, and 4). "Best" decision tree rule sets were obtained by minimizing misclassification errors in the independent test data. These techniques were repeated for each of three spectral data sets: (1) hand-held sunphotometer (Microtops II) spectral bands, (2) simulated LANDSAT bands, and (3) simulated AVHRR bands.

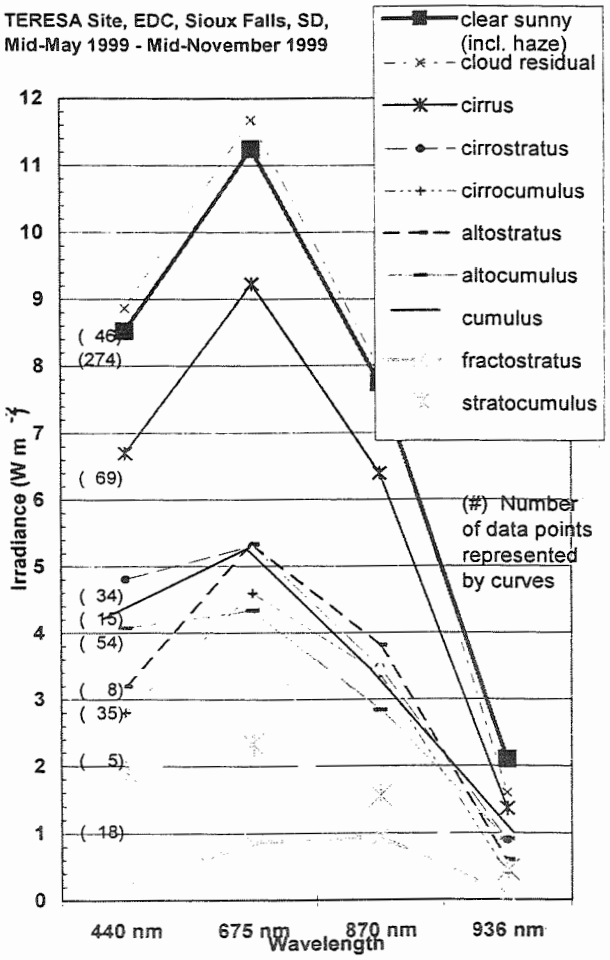

Figure 1 Sky spectra obtained from the Microtops II sunphotometer during mid-April through mid – November 1999 at the EROS Data Center Field Site for remote sensing data validation and development.

4. RESULTS

The results indicate the existence of unique spectral signatures for clear/sunny (including haze), evaporating cloud areas (cloud residual), cirrus, cirrostratus, cirrocumulus, and optically thin altocumulus clouds (Figure 1). There were insufficient data points to represent the other cloud types at a statistically significant level. The assignment of skytype was quality assured (Figure 2). Those sky types that fell more than 6 units away from the lines in Malone (1951) were primarily caused by the operational limitation of the sunphotometer, and the ability to accurately identify the actual sky type from the ground during such conditions. The 4 band data showed greater spectral uniqueness among the sky conditions than the two band data (Table 1). Multiple cloud layers, cloud thickness, cloud amount in the vicinity of the sun, mistaken cloud type assignment, and measurement error effected the significance of the results.

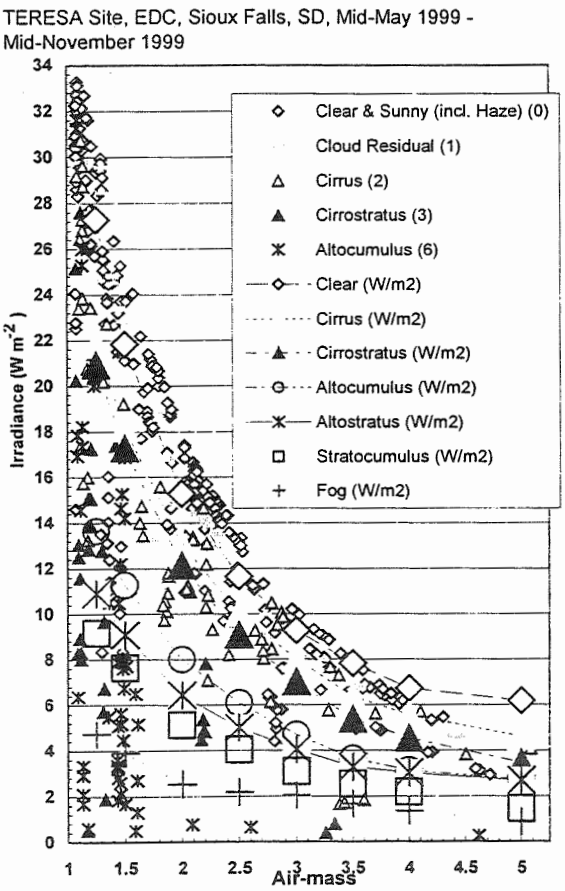

Figure 2 The comparison of the Microtops II data (symbols only) with those in Malone (1951). The field of view of the Microtops II has been corrected to that of the pyranometer used in Malone (1951).

Overall accuracies from the "best" Microtops, LANDSAT 5-like, and AVHRR-like band independent test data sets were 86, 84, and 80% respectively (Table 1). Despite drastic differences in spectral resolutions, the overall accuracies varied only 6% between the Microtops bands and the AVHRR bands. Only the percentage of sky type estimates that were correct are shown because we are primarily interested in the reliability of the estimates for subsequent applications. Highest sky type accuracies were for the sunny (including clear and hazy sky conditions), while

the lowest accuracies occurred for the Cirrostratus sky category data. We recognize that the number of observations per estimated class is sometimes quite small, however the results suggest fairly good sky type discrimination.

Table 1 Percent accuracies from the "best" Microtops, LANDSAT-like, and AVHRR-like band independent test

Sky Spectra -->	Clear to Sunny w/ Haze	Cloud Residual	Cirrus	Cirro-stratus	Cirro-cumulus	Alto-cumulus	Overall
Microtops II	92	90	73	60	88	86	86
LANDSAT-like	88	80	69	56	100	77	84
AVHRR-like	82	71	67	60	100	75	80

Notes: only 12-13 points for cirrocumulus, and a total of 148 data points.

5. DISCUSSION

We set out to see if it was feasible to identify unique spectral signatures of the various sky conditions (namely, clear/sunny, cirrus, cirrostratus, altostratus, altocumulus, cumulus).

Unique spectral signatures do exist for clear/sunny (including haziness), evaporating cloud areas, cirrus, cirrostratus, cirrocumulus, and optically thin altocumulus clouds. There were insufficient data points to represent the other cloud types at a statistically significant level.

The spectral signatures derived from the Microtops II data conservatively indicate a greater spectral uniqueness among clear to sunny (with haze), cloud residual, altocumulus and cirrus sky conditions compared to this information presented as two comparatively broader band data.

Multiple cloud layers, cloud thickness, cloud amount in the vicinity of the sun, mistaken cloud type assignment, and measurement error effected the significance of the results, since these conditions beg the accuracy of the instrument and the skytype observation.

The atmospheric correction of electro-optical satellite imagery and the validation of NWS Automated Surface Observation System (ASOS) sky condition reports may be potential applications for these sky spectra.

6. REFERENCES

Feng, C. and D. Michie, 1994: Machine learning of rules and trees. *In: Machine Learning, Neural and Statistical Classification*. Ellis Horwood, N,Y.,. 50-83.

Friedl, M.A., and C.E. Brodley. 1997: Decision tree classification of land cover from remotely sensed data. *Remote Sens. Environ.*, **61**, 339-409.

Friedl, M.A., C.E. Brodle, and A.H.Strahler. 1999. Maximizing land cover classification accuracies produced by decision trees at continental to global scales. *IEEE on Geoscience and Remote Sensing,* **37(2)**, 969-977.

Goetz, A.F.H., 1994: Characterization of Cirrus clouds from multi-pass AVIRIS data. *IEEE International Geoscience & Remote Sensing,* **32**, 41-43.

Hansen, M., R. Dubayah, and R. DeFries, 1996: Classification trees: an alternative to traditional land cover classifiers. *Int. J. Remote Sens.,* **17**(5), 1075-1081.

Kaufman, Y.J., D. Tanre, H.R. Gordon, T. Nakajima, J Lenoble, R. Frouin, H. Grassl, B.M. Herman, M.D. King, and P.M. Teilet, 1997: Passive Remote sensing of tropospheric aerosol and atmospheric correction for the aerosol effect. *J. Geophys. Res.,* **102D**, 16815-16830.

King, M.D., Y.J. Kaufman, W.P. Menzel, and D. Tanré, 1992: Remote sensing of cloud, aerosol, and water vapor properties from the moderate resolution imaging spectrometer (MODIS). *IEEE International Geoscience & Remote Sensing,* **30**, 2-27.

Lindner, B.L. and R.G. Issacs, 1990: Multispectral cloud property retrieval. *7th conf. Atmos. Radiation,* 23-27, July, AMS, Boston, 312-319.

Lindner, B.L. and R.G. Issacs, 1993: Remote sensing of clouds by multispectral sensors. *Appl. Optics,* **32**, 2744-2746.

Malone, T.F., 1951. *Compendium of Meteorology*. Amer. Meteorol. Soc., Boston, pp. 894.

FALLSPEEDS AND VERTICAL AIR MOTIONS IN STRATIFORM RAIN DERIVED FROM ER-2 DOPPLER RADAR OBSERVATIONS

G. M. Heymsfield
NASA/ Goddard Space Flight Center, Greenbelt, MD
L. Tian
USRA, Seabrook, MD

1. INTRODUCTION

The Tropical Rain Measuring Mission (TRMM) conducted several intensive field validation campaigns for improved understanding of Tropical precipitation systems (Zipser et al., this proceeding). Two of the campaigns (TEFLUN in Florida and Texas, and LBA in Brazil) utilized: the NASA ER-2 high-altitude (20 km) remote sensing aircraft instrumented with the ER-2 Doppler Radar (EDOP), the University of North Dakota Citation microphysics aircraft, and the NCAR S-POL polarization radar. This paper focuses on EDOP-derived fallspeeds and vertical velocities in the rain regions of two stratiform cases (5 September 1998 along the east coast of Florida, and 17 February 1999 in Amazonia in Brazil). These cases were sampled in situ microphysically by the Citation and reported elsewhere in this meeting; the main emphasis of this paper will be on the airborne radar measurements and inferences from them.

2. BACKGROUND AND APPROACH

EDOP is an X-band (9.6 GHz) nadir pointing Doppler radar. EDOP samples Doppler velocity, v_D, and reflectivity factor, Z, with a gate spacing of 37.5 m (vertical resolution) and at 0.5 s intervals (100 m along-track sampling frequency). The antenna beamwidth is about 3°, a footprint of about 1.2 km at the surface. Calibration accuracy of EDOP is about 1 dB. EDOP provides similar measurements to ground-based vertically pointing radars except that extensive regions can be covered in short times.

Doppler velocities v_D from a nadir-pointing airborne radar represent the sum of the mean reflectivity-weighted hydrometeor motion, the vertical air motion, and the aircraft vertical motion. Atlas et al. (1972) derived relations between Doppler velocity, reflectivity, and rain rate assuming an exponential size distribution for rain. Ulbrich (1994) expanded on this work assuming a Gamma size distribution.

Corresponding author address: Gerald M. Heymsfield, Goddard Space Flight Center, Greenbelt, MD 20771; e-mail: heymsfield@agnes.gsfc.nasa.gov

Retrieval of information on raindrop size distributions with the above method requires that air and aircraft motions be removed from the observed Doppler velocities.

The radar reflectivity factor Z in mm^6m^{-3} is given by:

$$Z = \int_{D_{min}}^{D_{max}} N(D)D^6 dD \qquad (1)$$

where D (cm) is particle equivalent spherical diameter, $N(D)$ in $m^{-3}cm^{-1}$ is number of raindrops per unit volume per unit size interval, D_o is the median particle diameter. For a Gamma size distribution, $N(D) = N_o D^{\mu} e^{-\Lambda D}$, where μ is the shape parameter, and $\alpha=\Lambda\ D_o = 3.67 + \mu + 10^{-0.3(9+\mu)}$. $N_o(\mu) \approx 6.4 \times 10^4 \exp(3.2\mu)$) has been shown observationally and theoretically by Ulbrich (1983). The integration limits D_{min} and D_{max} are assumed $0 \rightarrow \infty$, though several papers have dealt with truncated limits. The reflectivity-weighted Doppler velocity v_Z (ms^{-1}) is given by:

$$v_Z = \frac{\int_o^{\infty} v(D)N(D)D^6 dD}{\int_o^{\infty} N(D)D^6 dD} \qquad (2)$$

where $v(D)$ is the drop fallspeed. Furthermore, Ulbrich (1994) has derived the reflectivity-weighted Doppler velocity v_Z as a function of μ by assuming the Gunn-Kinzer fallspeed relation at ground level (1013 mb), i.e., $v(D) = 9.65 - 10.3\ e^{-6D}$. Assuming that vertical air motions are neglible, Eq. 2 can be given as a function of μ and Z:

$$v_Z(\mu) = 9.65 - 10.3\left\{1 + 6\left[\frac{Z}{N_o(\mu)10^6\Gamma(7+\mu)}\right]^{1/(7+\mu)}\right\}^{-(7+\mu)} \qquad (3)$$

This relation applies to ground level (1013 mb); v_Z at other altitudes is obtained by multiplying it by $[\rho_o/\rho]^{0.44}$ where ρ and ρ_o are the air density at the surface and measurement height, respectively. Eq. 3 has a major advantage over power law relations used extensively in the literature: v_Z is asymptotic with increasing reflectivity rather than increasing monotonically with Z.

Figure 1 shows the dependence of v_Z on μ using Eq. 3; a commonly used power law relation is also

plotted. At 40 dBZ, the variation of μ from -2 to 6. results a fairly substantial 4 ms^{-1} variation in v_Z. Figure 2 shows the Gamma size distribution corresponding to v_Z = 6, 8 ms^{-1} and μ =-2 to 4. The resulting range of generated curves are typical of reflectivities observed in EDOP data sets. Larger v_Z for a given μ implies larger D_o and a larger Z.

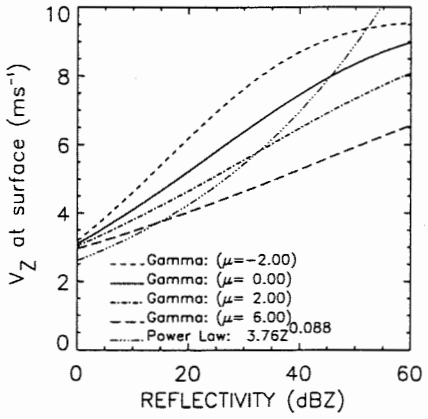

Figure 1. v_Z - Z relation as a function of μ.

3. EXAMPLES.

If one has large sample of v_D and Z measurements from the same region, then μ can be obtained by fitting Eq. 3. This requires the assumption that stratiform regions are fairly extensive. However, Eq. 3 must be modified with an additive constant C since widespread vertical motions can be present in the stratiform region that will bias fits to Eq. 3. Smaller scale vertical motions can also be present in the stratiform but are ignored in the following. Thus, the v_D – Z data from EDOP is fitted with the following:

$$\left(\frac{\rho}{\rho_o}\right)^{0.44} v_D = C + v_Z(\mu), \qquad (4)$$

where v_Z is obtained from Eq. 3, C is a constant which consists of the mean mesoscale vertical motion, positive (negative) C indicates downdrafts (updrafts), and the altitude dependence of the measurements are removed by the density term on the left side. This fitting method provides a global estimate of μ and C within some defined height interval, not a point-by-point estimate of the values. Besides the inhomogeniety

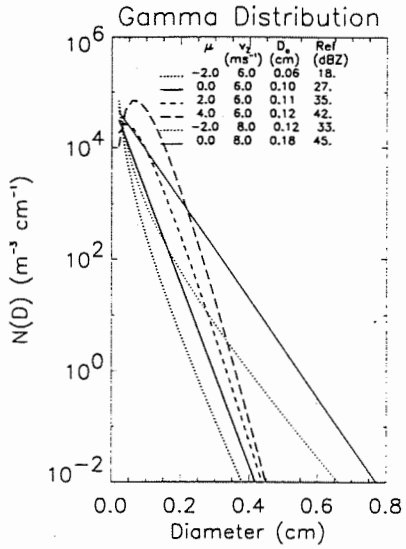

Figure 2. Gamma distribution for two values of v_z, assuming various values of the shape parameter μ.

of the size distribution over the analyzed region, a major source of error in this approach is the presence of small scale vertical air motions. In addition, small scale aircraft motions are not always fully removed from v_D resulting in an error in the calculation.

Figures 3 and 4 show an examples of applying Eq. 4 to stratiform regions in Florida during TEFLUN-B and Brazil during TRMM-LBA. The rain region between the surface and 400 m below the freezing level, is divided into approximately 500 m intervals and then fitted using a non-linear curve fitting routine. The vertical axis corresponds to observed Doppler velocities adjusted to the surface. The number of points used in Fig. 3 and Fig. 4 per layer are 6552 and 12000, respectively. It is noted that points above (below) the fitted curve are due to smaller scale downdrafts (updrafts) assuming aircraft motions have been removed. The scatter of the points around the fits is likely due to inadequate aircraft motion removal. Nevertheless, the fits are statistically significant, with an obvious increase in v_D with Z. The fitted curves in Fig. 3 for stratiform in Florida indicate that μ ranges from –1.4 at the top layer (2.74-3.19 km) to -0.4 at the bottom layer (0.3-0.75 km). Figure 4 indicates lower μ values (-3) which suggest a narrower size distribution than for the Florida flight line in Fig. 3. The calculated C ranges from about 1.5-2.0 ms^{-1} in the rain layers of Figs. 3 and 4 which suggests the presence of a mesoscale downdraft in both cases. Vertical reflectivity images for both cases suggest evaporation is possibly occurring for both cases which would account for the subsidence.

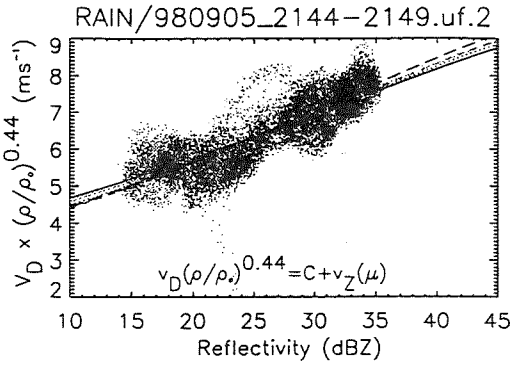

Bottom (km)	Top (km)	Npts	C (ms^{-1})	μ	N_o (m^{-3}cm$^{-1-\mu}$)
0.30	0.75	6552	1.7	−0.4	1.6E+04
0.79	1.24	6552	1.6	−1.0	3.0E+03
1.28	1.73	6552	1.6	−1.2	1.2E+03
1.76	2.21	6552	1.7	−0.9	3.3E+03
[illegible]					
2.74	3.19	6552	1.7	−1.4	6.5E+02

Figure 3. Observed measurements from stratiform on 5 September 1998 fitted with Eq. 4.

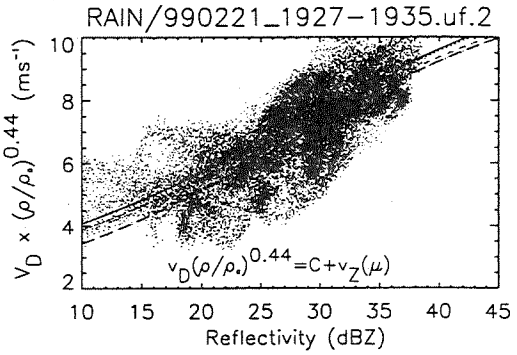

Bottom (km)	Top (km)	Npts	C (ms^{-1})	μ	N_o (m^{-3}cm$^{-1-\mu}$)
0.30	0.75	11812	2.0	−3.3	1.9E+00
0.79	1.24	11935	1.9	−3.4	1.2E+00
1.28	1.73	12119	1.8	−3.2	2.2E+00
1.76	2.21	12181	1.7	−3.1	2.7E+00
[illegible]					
2.74	3.19	12181	1.5	−3.5	9.0E−01

Figure 4. Same as Fig. 3 except for 21 February 1999 fitted with Eq. 4.

4. CONCLUSIONS.

A "global" fitting procedure has been presented to obtain layer values of μ in the Gamma distribution, and mean vertical air motions in stratiform rain regions. This approach facilitates a better understanding of the observational errors (aircraft motions) and the inhomogenieties in air motions and size distributions. The calculated μ for the two presented is less than 0, thus implying a narrow distribution of raindrops. This is in contrast to $\mu>0$ reported in the literature. The radar measurements and the approach presented will be explored further using insitu microphysics data and ground-based polarization radar data collected along with the EDOP measurements.

Acknowledgements

This work was supported by Dr. Ramesh Kakar of NASA Headquarters under the Tropical Rain Measuring Mission.

References.

Atlas, D., R.C. Srivastava, and R.S. Sekhon, 1973: Doppler radar characteristics of precipitation at vertical incidence. *Rev. Geophys. Space Phys.*, **11**, 1-35.

Heymsfield, G.M., et al., 1996: The EDOP radar system on the high-altitude NASA ER-2 aircraft. *J. Atmos. Ocean. Tech.*, **13**, 795-809.

Ulbrich, C.W., 1992: Algorithms for determination of rainfall integral parameters using radar reflectivity and mean Doppler fallspeeds at vertical incidence. . *J. Atmos. Ocean. Tech.*, **9**, 120-128.

Ulbrich, C.W., and P.B. Chilson, 1994: Effects of variations in precipitation size distribution and fallspeed law parameters on relations between mean Doppler fallspeed and reflectivity factor. *J. Atmos. Ocean. Tech.*, **11**, 1656-1663.

APPLICATION OF SATELLITE MICROPHYSICAL RETRIEVALS FOR ANALYSIS OF THE COAMPS MESOSCALE PREDICTION MODEL

Melanie Wetzel[1], Steven Chai[1], Marcin Szumowski[1], William Thompson[2], Tracy Haack[2], Gabor Vali[3] and Robert Kelly[3]

[1]Desert Research Institute, Reno, Nevada 89512-1095
[2]Naval Research Laboratory, Monterey, California 93943-5502
[3]University of Wyoming, Laramie, Wyoming 82071

1. INTRODUCTION

Prediction of boundary layer cloudiness is a difficult aspect of marine forecasting, due to the mesoscale variability of boundary layer dynamics and a lack of observations in many oceanic and coastal regions. Multichannel satellite remote sensing can provide near-continuous mapping of the mesoscale structure of stratus cloud layers (Lee et al., 1997). The use of radiative transfer retrieval methods for microphysical parameters such as cloud droplet size and cloud optical depth also allows satellite-based analysis of cloud climatology and cloud-aerosol interactions (Wetzel and Stowe, 1999). In this paper we demonstrate the application of satellite retrievals of cloud physical parameters for model verification and for development of methods to improve short-term forecasting.

2. THE COSAT '99 FIELD PROJECT

A collaborative field program, the COAMPS Operational Satellite and Aircraft Test (COSAT) was designed to demonstrate methods for integrating satellite remote sensing retrieval products with mesoscale model simulations of coastal stratus cloud layers. Model simulations from the Coupled Ocean/Atmosphere Mesoscale Prediction System (COAMPS) were compared to corresponding satellite and aircraft observations. Scientists from the Desert Research Institute (DRI), the Naval Research Lab (NRL), the University of Wyoming (UW) and Oregon State University (OSU) participated in the field experiment during 4-29 August 1999. Operations were based at the Corvallis airport in west-central Oregon. The University of Wyoming King Air instrumented aircraft was deployed from the Corvallis airport for several flights into the marine stratus and stratocumulus layers offshore. Satellite remote sensing analysis was conducted at the field site by DRI using digital processing and implementation of radiative transfer retrieval methods.

Mesoscale modeling using the COAMPS, carried out by NRL, provided several parameter fields in near-realtime. Oregon State University was also running the ARPS mesoscale model for the region during this period. The aircraft, satellite and modeling components of the field program each provided data for use in flight planning and case analysis. Figure 1 shows a GOES visible satellite image and the aircraft flight track for one of the study days.

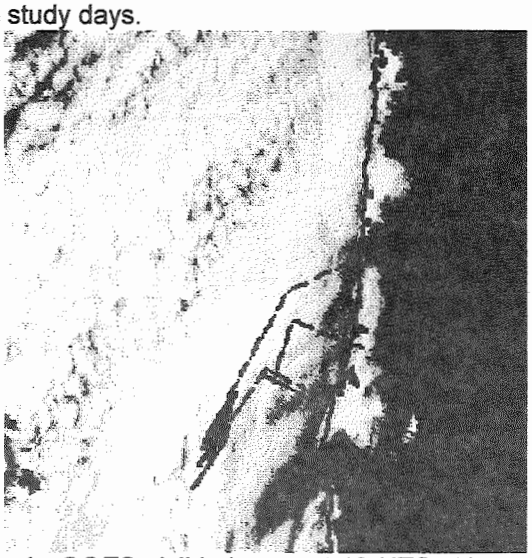

Fig. 1. GOES visible image at 18 UTC, 10 August 1999, with graphic overlays of the flight track (dashed) and central Oregon coastline (solid).

3. SATELLITE RETRIEVALS

3.1 Radiative Transfer Methodology

Remote sensing retrieval methods demonstrated by Wetzel et al. (1996) were used for satellite estimation of stratiform cloud droplet size and optical depth. Satellite data were

Corresponding author's address: Dr. M. Wetzel, Desert Research Institute, 2215 Raggio Parkway, Reno, NV 89512, USA: E-Mail: wetzel@dri.edu

obtained from the GOES geostationary Imager, primarily the visible Channel 1 (0.57-0.72 μm), the near-infrared Channel 2 (3.78-4.03 μm), and the thermal infrared window Channel 4 (10.2-11.2 μm).

From the satellite image data, cloud-covered pixels were selected using channel threshold tests, and the cloud optical depth (τ) and cloud droplet effective radius (Re) were found by interpolation from the observed satellite pixel reflectances in the visible and near-infrared channels to arrays of pre-calculated radiative transfer model reflectances.

Cubic spline interpolation was implemented to first estimate cloud optical depth from the AVHRR Channel 1 reflectances, then to retrieve cloud droplet effective radius from the cloud near-infrared reflectances. The thermal infrared channel data were used for subtraction of the thermal emission component from the near-infrared radiance. The Discrete Ordinates model (Stamnes et al., 1988; Meier et al., 1997) was used to produce tabular data for a wide range of Re, τ and solar/viewing geometry conditions, covering the possible image pixel viewing angles and cloud types.

The following parameterization (Stephens, 1978) was used to obtain the cloud liquid water path: LWP = (2/3) τ Re, where LWP has units (g/m2), the τ is non-dimensional and Re is expressed in microns. Figure 2 depicts the LWP distribution for 1800 UTC on 10 August 1999.

Fig. 2. Satellite-derived LWP, 18 UTC 10 August.

3.2 Validation of Re and LWP Estimates

Aircraft microphysical data were utilized for detailed analysis of vertical profiles of cloud droplet size and liquid water content, to evaluate the accuracy of the satellite estimation methods. The University of Wyoming's instrumented King Air (Vali et al., 1995) provided airborne characterization of the marine cloud structure and evolution. Multiple sensors recorded 1-Hz and higher frequency droplet size spectra and other microphysical parameters which were compiled for intercomparison with satellite retrieval results and mesoscale model simulations. In addition, the King Air high-resolution radar allowed interpretation of the fine-scale structure of cloud and precipitation reflectivity and Doppler velocity characteristics within the cloud and boundary layer.

Summary data for aircraft parameters such as cloud droplet effective radius, liquid water content and temperature were selected from ascent/descent flight legs as well as constant-altitude segments in order to evaluate the vertical profiles and horizontal structure of the cloud layers.

Case study datasets were obtained for 19 different aircraft sampling flights during the August 1999 field project. Examples will be presented here from a subset of these flight periods. Figure 3 depicts effective radii for a descent profile obtained during 1742-1746 UTC on 9 August. Individual flight segments such as these were directly matched by geographic location to the gridded and mapped satellite retrieval parameters for the closest available satellite image dataset (within 15 minutes).

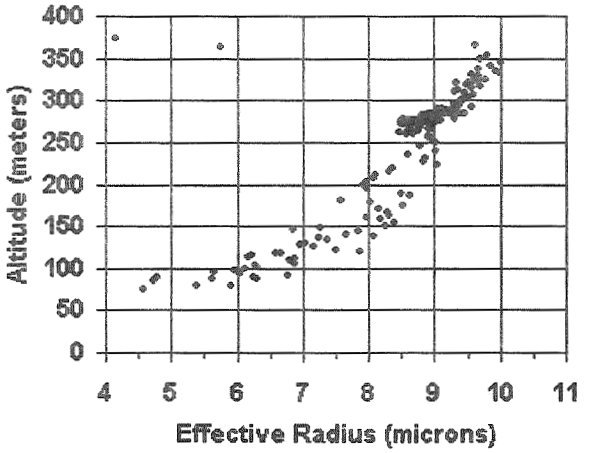

Fig. 3. Re values determined from the King Air droplet size spectra for the descent profile obtained 1742-1746 UTC, 9 August.

The satellite-retrieved values of effective radius along the 20-km aircraft track for this descent profile are all in the range of 8-9 μm, while the aircraft data indicated values at cloud top (the region of maximum Re) between 9 and 10 μm. This is within the range of agreement for two independent droplet size probe systems that were

operated on the aircraft (Gerber PVM and PMS FSSP. A series of similar intercomparisons were performed for several image dates and times. A list of aircraft and satellite-derived values of effective radius and liquid water path are shown below in Table 1. This summary indicates agreement between aircraft measurements and the satellite-estimated parameters.

Table 1. *Aircraft and satellite-derived values of effective radius (Re) and liquid water path (LWP) for specific ascent/descent profiles.*

Date / Time (UTC)	KingAir Re (μm)	GOES Re (μm)	KingAir LWP (g/m2)	GOES LWP (g/m2)
9 Aug 1700	9	9	40	30
9 Aug 1800	10	9	75	65
10 Aug 1600	10	11	95	65
10 Aug 1800	10	10	70	90
11 Aug 1600	15	16	70	75
11 Aug 1700	14	14	40	40
16 Aug 1630	14	12	80	45
16 Aug 1730	14	11	50	45
17 Aug 1600	10	10	25	25
17 Aug 1630	13	13	80	65

Variability in satellite-derived values of Re along the aircraft sampling track during the profile data collection segments was ≤ 2 μm, as was the variation in Re observed by the aircraft in the top 50-100 m of the cloud layers. Sensitivity tests on calculated reflectances for stratus clouds with vertically increasing droplet size (Wetzel and Vonder Haar, 1991) indicate that for the conditions of Re and liquid water content profiles described here, the satellite-estimated Re represents the actual Re in the top 100 meters of cloud to an accuracy of 1-2 μm. Variations in satellite-estimated LWP were 4-24 g/m2, and this corresponds to the magnitude of fluctuations which could be attributed to cloud top inhomogeneity.

4. COMPARISON WITH MODEL LWP FIELDS

COAMPS is a three-dimensional nonhydrostatic forecasting model developed at NRL (Hodur, 1997). The horizontal resolutions of the three nested domains used in this study were 81, 27 and 9 km. The bulk-water cloud microphysics scheme follows Rutledge and Hobbs (1983). Output data for the 9-km grid resolution was used in this analysis. The model prediction intervals closest to the satellite observation times were extracted for model-satellite comparisons. Vertical profiles of liquid water content were vertically integrated through the boundary layer, with pressure scaling from the model sigma levels, to obtain LWP.

Detailed analyses have been made for several case studies including multi-day sequences. Over the period of 9-11 August, the marine boundary layer deepened significantly, the horizontal scale of the cellular elements increased, and precipitation production was enhanced. The multi-day evolution of the COAMPS model cloud field compares well to the overall cloud distribution observed in the satellite imagery.

The COAMPS model was run in two modes for the 9-11 August sequence; first using 30 vertical levels in the 'operational' mode as was carried out for the realtime forecasting during the field project; and then using 45 levels in 'high resolution' research mode, with 60 m vertical resolution in the lower levels (to 1600 m altitude). Figure 4 shows the 'high resolution' COAMPS LWP forecast valid 18 UTC on 10 August. The model was initialized at 00 UTC on 10 August. There is close correspondence between the cloud field structure in the model simulation and the satellite data (see also Figure 2), but the model overpredicts LWP.

Fig. 4. *Forecast LWP at 18 UTC on 10 August.*

This higher-vertical resolution model prediction of LWP is significantly closer to the satellite-estimated (and aircraft-observed) LWP field than

the forecast from the 30-level model simulation, which had even larger LWP discrepancies. It is not operationally feasible to operate the COAMPS model with 45 vertical levels at all times, so the model-satellite LWP difference fields could be used to identify situations where the higher vertical resolution is warranted on a temporary basis.

5. FORECASTING APPLICATIONS

A variety of diagnostic procedures can be implemented by combining the satellite and model products for analysis of marine stratus, such as difference fields of model-satellite LWP. Temporal tendencies in satellite-observed parameters have also been mapped. Products such as the 2-hour tendency of LWP (Figure 5) are being created to show cloud layer evolution. Tendency fields which indicate increasing Re could be used for short-term prediction of precipitation onset. Temporal changes in droplet size could also reveal local fluctuations in aerosol concentration. Other applications include local climatologies of Re and LWP, and classification of meteorological scenarios by their observed evolution in Re and LWP distributions.

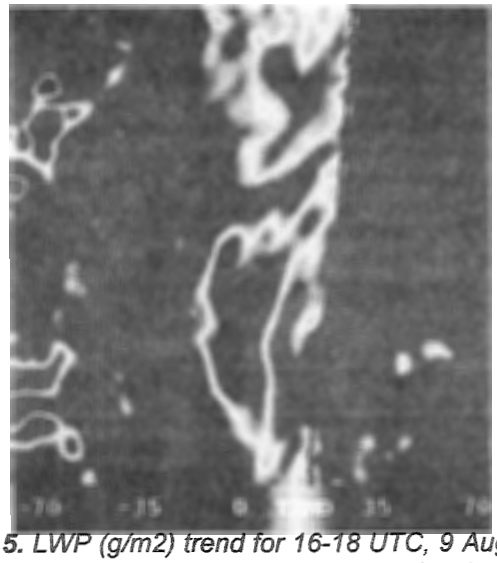

Fig. 5. *LWP (g/m2) trend for 16-18 UTC, 9 August. Positive tendencies are outlined in light shading, while negative tendencies are more solidly dark. Note the decreasing LWP over this two hour period (9-11 am LT) for the small bay along the coast.*

6. CONCLUSIONS

Analysis of case studies for coastal stratus offshore Oregon has been used to demonstrate satellite remote sensing methods for cloud droplet effective radius and liquid water path. Intercomparison of satellite-derived and COAMPS model fields of LWP indicate fairly good correspondence of model and satellite-observed cloud distribution and layer evolution, but also that COAMPS overpredicted the liquid water path. Satellite-derived LWP grids indicated that an increase in the vertical resolution used for COAMPS significantly improved the LWP forecast. Model-satellite LWP difference fields may thus be valuable in identifying periods or regions in which the higher model resolution is needed. The satellite retrieval methods provide Re and LWP fields with a spatial and temporal continuity which is not available from other sources.

7. ACKNOWLEDGEMENTS

This research was funded by DEPSCoR grants from the Office of Naval Research to DRI and to the University of Wyoming. Additional support was provided by the State of Nevada, the University of Wyoming, and the Naval Research Laboratory.

8. REFERENCES

Hodur, R.M., 1997: The Naval Research Laboratory's Coupled Ocaen/Atmosphere Mesoscale Prediction System (COAMPS). *Mon. Wea. Review*, **125**, 1414-1430.

Lee, T.F., F. J. Turk, and K. Richardson, 1997: Stratus and fog products using GOES-8-9 3.9-µm data. *Weather and Forecasting*, **12**, 664-677.

Rutledge, S.A. and P.V. Hobbs, 1969: The mesoscale and microscale structure and organization of clouds and precipitation in midlatitude cyclones. VIII: A model for the "seeder-feeder" process in warm-frontal rainbands. *J. Atmos. Sci.*, **40**, 1185-1206.

Meier, W.N., J.A. Maslanik, J.R. Key, and C.W. Fowler, 1997: Multiparameter AVHRR-derived products for Arctic climate studies. *Earth Interactions*, **EI009**, 43 pp.

Stamnes, K., S.C. Tsay, W. Wiscombe and K. Jayaweera, 1988: Numerically stable algorithm for discrete-ordinate-method radiative transfer in scattering and emitting layered media. *Appl. Opt.*, **27**, 2502-2509.

Stephens, G.L., 1978: Radiation profiles in extended water clouds. II: Parameterization schemes. *J. Atmos. Sci.*, **35**, 2123-2132.

Wetzel, M.A., R. D. Borys, and L.E. Xu, 1996: Satellite microphysical retrievals for land-based fog with validation by balloon profiling. *J. Appl. Meteor.*, **35**, 810-829.

Wetzel, M.A., and L.L. Stowe, 1999: Satellite-observed patterns in stratus microphysics, aerosol optical thickness, and shortwave radiative forcing. *J. Geophys. Res.*, **104**, 31287-31299.

Wetzel, M. A., and T.H. Vonder Haar, 1991: Theoretical development and sensitivity tests of a stratus cloud droplet size retrieval method for AVHRR-K/L/M. Rem. Sens. Env., 36, 105-119.

Vali, G., R.D. Kelly, A. Pazmany, and R.E. Macintosh, 1995: Airborne radar and in-situ observations of a shallow stratus with drizzle. Atmos. Res., 38, 361-380.

ATMOSPHERIC PHYSICS AS OBSERVED BY A VERTICALLY POINTING DOPPLER RADAR

Frédéric Fabry, and Isztar Zawadzki

Department of Atmospheric and Oceanic Sciences, McGill University, Montreal, Quebec, H3A 2K6, Canada

1. THE INSTRUMENT AND ITS USES

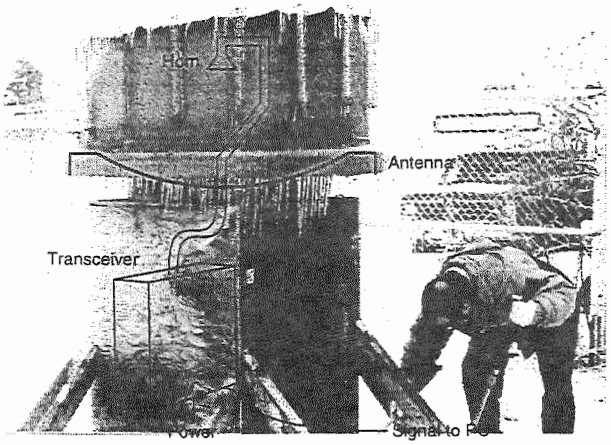

FIG. 1. The McGill vertically pointing radar after a freezing rain event.

Let us introduce to you the McGill vertically pointing radar (VPR, Fig. 1). It is a small, low cost, low maintenance, X-band (3 cm wavelength) radar. Originally assembled in 1989 to measure at high resolution the reflectivity patterns of precipitation (Fabry et al. 1992), the VPR has been upgraded to measure the distribution of the fall speed of targets in 1998. In the past 10 years, a considerable amount of data has been collected in a large variety of situations. In many instances, we have been fascinated by the information obtained by this instrument on various atmospheric physics phenomena, in particular for cloud and precipitation physics and small scale dynamics. We find that many of these images would make wonderful textbook or classroom material. In these few pages, we would like to share with you a bit of our enthusiasm about this instrument and its data.

2. WARM AND COLD RAIN PROCESSES

Despite the fact that radar observations in rain show considerable variety in the shape of echoes and in the resulting vertical reflectivity profiles, these profiles can generally be grouped in 5 classes (Fig. 2). The existance of these five classes of profiles is the direct result of the combination between the microphysical phenomena driving rain formation, warm rain (w) versus cold rain (c) processes, and storm dynamics, stratiform (S) versus convective (C) versus mixed (M).

Corresponding author's address: Frédéric Fabry, Dept. Atmospheric and Oceanic Sciences, McGill University, 805 Sherbrooke St. W., Montreal, Quebec, H3A 2K6, Canada; E-mail: frederic@radar.mcgill.ca.

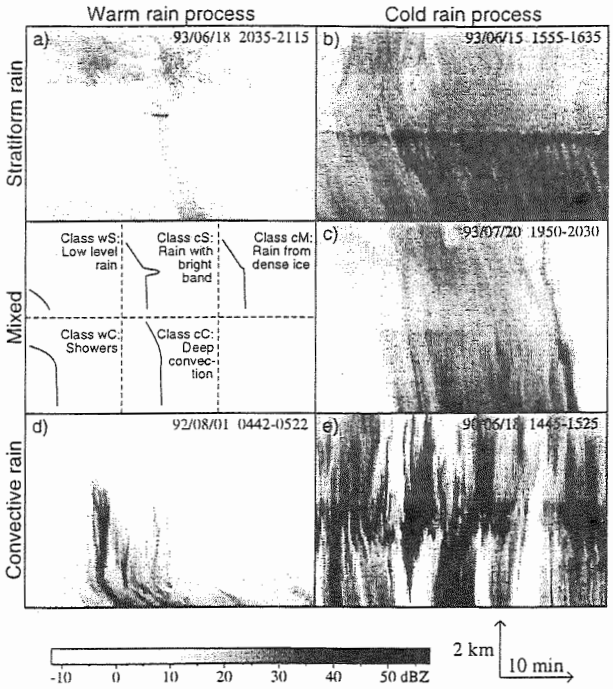

FIG. 2. Examples of the 5 classes of vertical reflectivity profiles in rain. All time-height sections span over 40 min and show echoes from 0.2 km to 7 km. a) Low level drizzle (bottom, class wS) accompanied by a palm-tree shaped echo with a bright band (class cS). Note how low the drizzle forms compared with the height of the 0°C isotherm indicated by the bright band. b) Rain with bright band (class cS). c) Rain from compact ice (class cM). Observe the increase in reflectivity at the same height as the bright band in b). d) Showers (class wC, 0450-0505) within drizzle echoes. e) Deep convection (class cC) from a squall line. Adapted from Fabry and Zawadzki (1995).

A more careful analysis of radar echoes from rain shows that, occasionally, rain falling at the ground at a given instant can originate partly from autoconversion process, and partly from the Bergeron process. A clear example is illustrated in Fig. 2a, when a 'cold' rain shaft passes through drizzle and both reach the ground together over a 5 min period. Another such case is presented in Fig. 3, where for a long period, drizzle and 'cold' rain coexist, as the two arise from large scale updrafts occurring at different levels. If one would measure the drop size distribution from such an event, a bimodal distribution would be found not because of some strange kind of drop-drop interaction, but simply because two types of precipitation of different origin are observed together. At other times, we have also observed supercooled drizzle formed directly via the warm rain process coexisting with snow (Zawadzki and Fabry 2000).

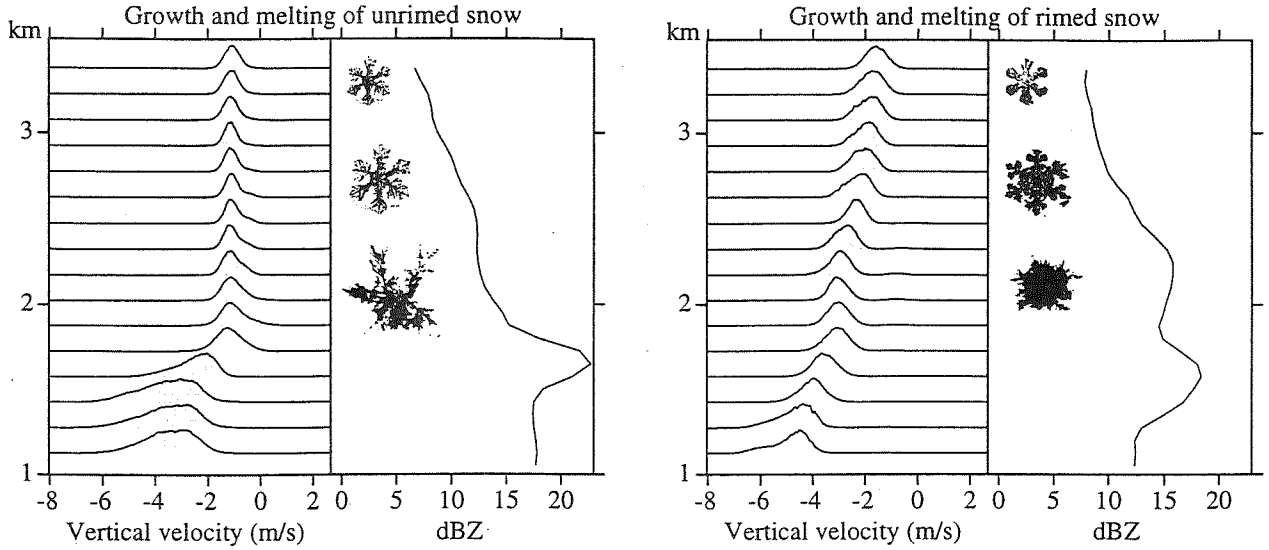

FIG. 5. Doppler spectra of echoes measured at vertical incidence by the VPR in the absence (left) and presence (right) of supercooled water accretion in snow. In the main window, each of the 16 curves shows the relative contribution to the reflectivity of targets moving at a given vertical velocity (upward when positive) as a function of height. The vertical profile of reflectivity is plotted at the right of the main window. Note the increase in fall velocity and the weaker bright band associated with the rimed snow case. Snowflake images are from Nakaya (1954).

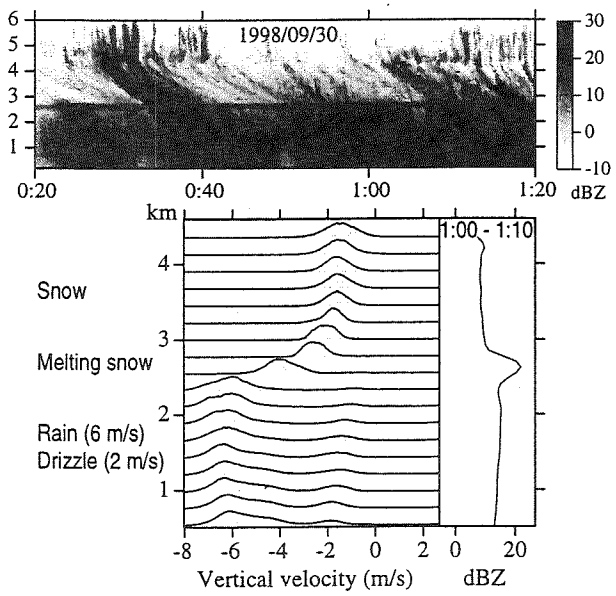

FIG. 3. Top: Time-height section of reflectivity taken by the VPR. This image suggests that all precipitation forms via the Bergeron process. Bottom: Fall speed spectra associated with the same case showing the coexistence of rain originating from snow and drizzle forming by autoconversion.

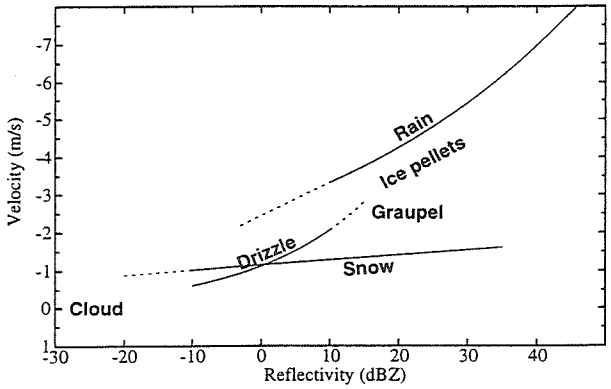

FIG. 4. Regimes of reflectivity and air-velocity associated with different types of hydrometeors.

3. PRECIPITATION

Thanks to the combination of velocity and reflectivity measurements, it is relatively easy to determine the type of hydrometeor being observed, as almost every target has a unique velocity-reflectivity combination (Fig. 4). This is, of course, true only when air velocity is negligible. As we will see in the next pages, this is far from always being the case.

In addition to helping us determine the mode of precipitation formation, the VPR is extremely useful to observe and study other microphysical processes related to rain and snow. Several of them, like snow generating cells, have been studied for a long time (Douglas et al. 1957). Newer topics of interest include the detection of accretion, or of the riming of snow. This interest is due both to the need to detect directly or indirectly the presence of supercooled water for aviation safety as well as the need to determine the effect of riming on snow microphysics and the resulting drop size distributions after melting. The effect of riming on snow is relatively easy to detect (Fig. 5). In unrimed snow, reflectivity increases steadily with height, while fall velocity remains relatively constant; when snow melts, a strong bright band is observed. In rimed snow, reflectivity increases more rapidly while velocity also increases with the rise in snow density associated with accretion. Then, the melting of this relatively dense ice results in a considerably weaker bright band.

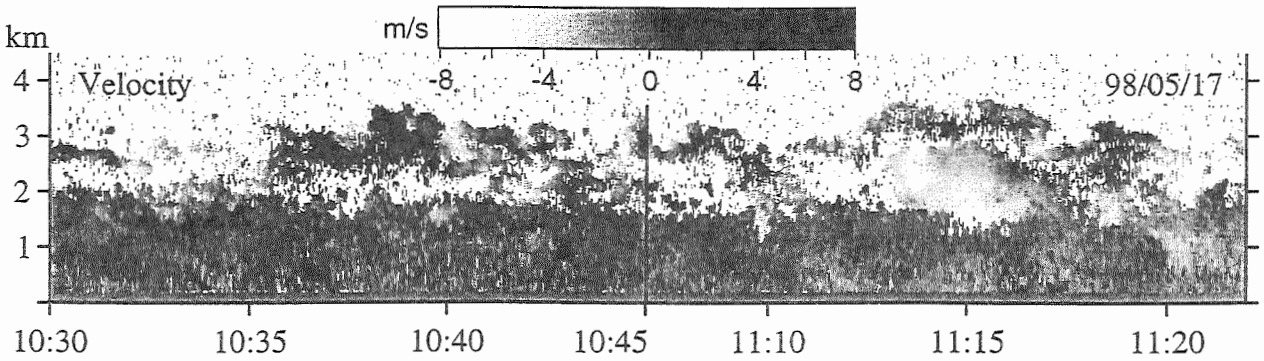

FIG. 6. Time-height image of vertical velocity measured in the boundary layer (0-2 km) and in cumulus clouds (above 2 km).

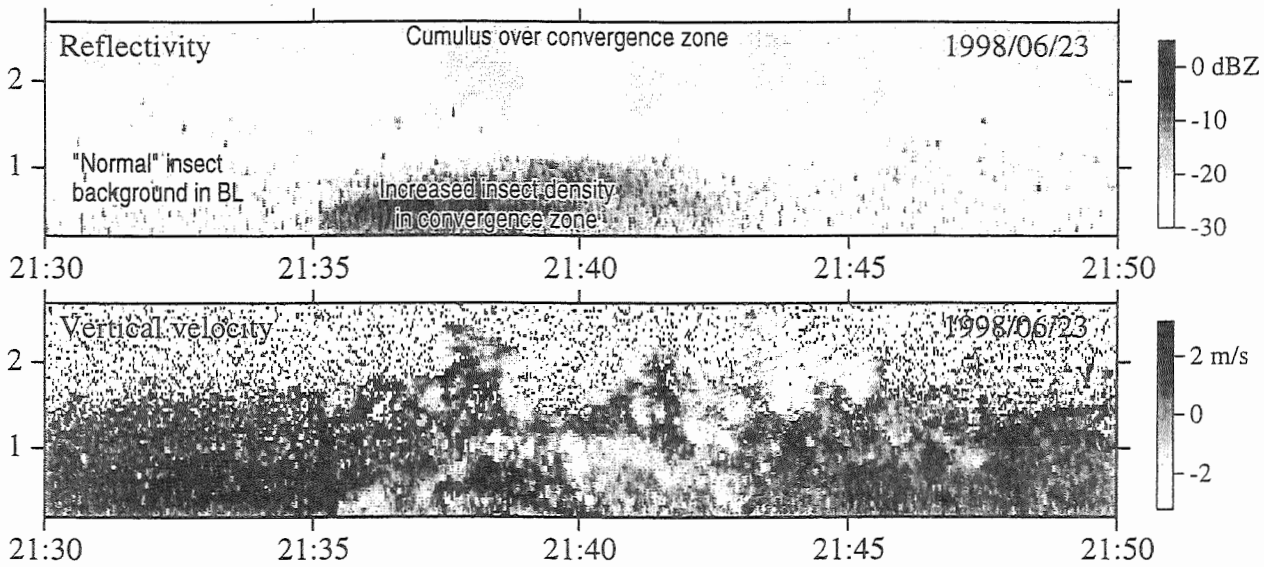

FIG. 7. Time-height image of reflectivity and vertical velocity measured during the passage of a front. Convergence at the frontal boundary forces the growth of cumulus clouds which can be observed at different stages of their life cycle.

4. BOUNDARY LAYER AND CLOUDS

Vertically pointing radars have been used extensively to study ice clouds, in particular cirrus, because they are relatively easy to detect. They are also well suited to take measurements in boundary layer, and to get very weak reflections related to cumulus clouds. These can be either related to Bragg scattering, most likely occurring at the interface between moist cloudy air and dry environmental air, or to Rayleigh scattering from growing droplets.

A first example of such data is shown in Fig. 6. At low levels, from the surface to 2 km, insect echoes fill the boundary layer. Convective updrafts and downdrafts of up to 1 m s^{-1} stimulated by solar heating can be observed. Above, a few cumulus clouds are present. The first main one, between 10:35 and 10:42, has updrafts up to 8 m s^{-1} in the main turret, with significant downdrafts around it. No precipitation is observed, though there is a suggestion from the reflectivity information (not shown) that drizzle-size droplets have formed in the main turret. A second significant cloud can be seen around 11:15. It is characterized by weaker updrafts observed near the top of the cloud. However, this cloud has already generated many large drops which fall around 6 m s^{-1}. This example illustrates well the very different nature of circulation in the neutrally stable boundary layer and in the unstable cumulus clouds.

The case illustrated in Fig. 7 may be more complex, but is an even more fascinating example. A front passes near the surface at 21:35, lifting air as well as insects. This lifting forces air parcels through the capping inversion of the boundary layer, and cumulus clouds form as a result. Five cumulus clouds can be observed in different stages of their evolution, the more mature clouds being the further away from the convergence line. The first two cumulus, barely visible on the velocity map at 21:35 and 21:36:30, are mere hot bubbles. The next one, centered around 21:38, is a vigorous cumulus cloud, with an updraft in its core and downdrafts at the periphery. The next one around 21:42 is at the early stages of dissipation with a few updrafts and a lot of downdrafts, while the last one (21:44) is collapsing rapidly. A complete history of cumulus growth in one picture! Unfortunately, the black and white images in this preprint do not do justice to these examples in general and to this one in particular.

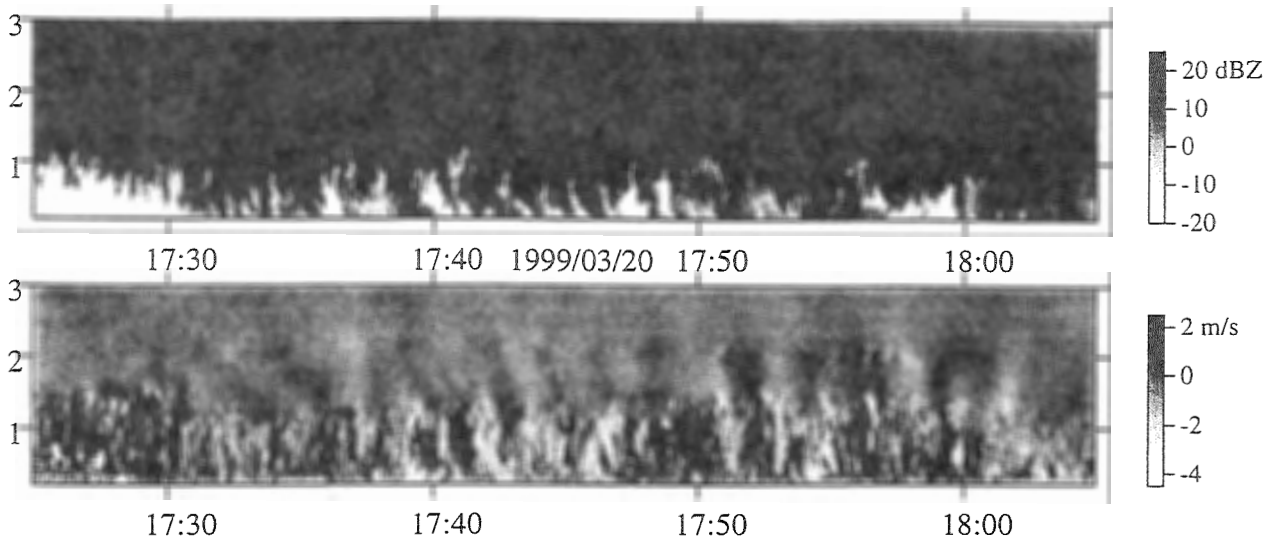

FIG. 8. Time-height image of reflectivity and vertical velocity measured at the onset of a snow storm.

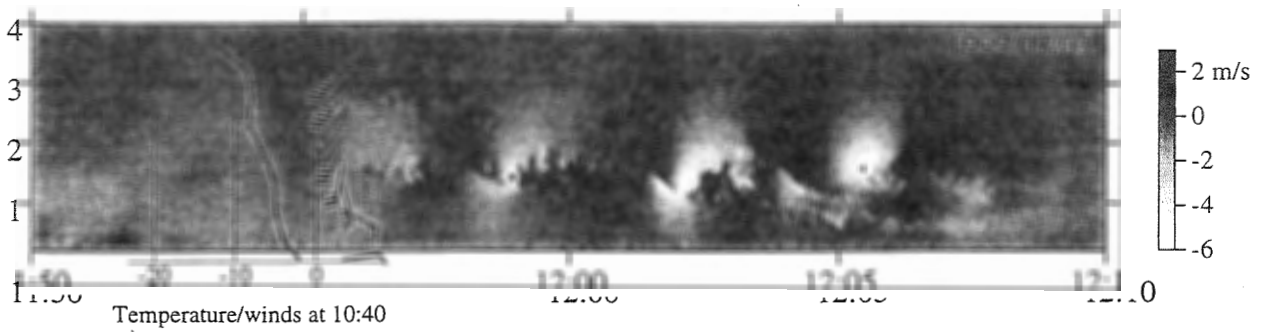

FIG. 9. Time-height image of vertical velocity measured during a snowstorm. The passage of a spectacular Kelvin-Helmoltz wave is noted. In inset, the temperature and wind profiles measured an hour before are shown.

5. WAVES AND SMALL SCALE DYNAMICS

With the Doppler capability, we can observe many high resolution examples of small scale dynamical phenomena, whether they are occurring by themselves or caused by microphysics. Two spectacular examples:

In the first case (Fig. 8), snowflakes trying to reach the ground are sublimating as they penetrate into dry air near the surface. In pockets where more snow is present, sublimation cooling becomes important, making these pockets denser than their surroundings. Downdrafts result. Conversely, snow-poor regions become warmer than their surroundings and updrafts are observed. The resulting circulation reinforce this situation, resulting in the appearance of "stalactites" in reflectivity. The velocity graph clearly shows that the stalactites are associated with downdrafts, while updrafts are observed in echo-free regions.

Last but not the least, we caught an extremely strong Kelvin-Helmoltz (KH) wave during a snowstorm (Fig. 9). The KH wave occurred in a region of strong shear on a frontal surface not well resolved by the temperature sounding. In this case, updrafts and downdrafts are strong enough that the snowflakes generally falling at 1.5 m s^{-1} were seen to fall at up to 6 m s^{-1} in some locations, while they were moving upwards at 3 m s^{-1} at others.

6. CONCLUSION

Thanks to a relatively simple remote sensing instrument, we have been able to observe a wealth of atmospheric phenomena over the past ten years. Due to the ruggedness of the VPR, we have been able to operate the radar almost continuously during this period, allowing us to catch most of these events while nobody was nearby. We are convinced the VPR has the ability to provide more research and class material for years to come.

6.1 References

Douglas, R.H., K.L.S. Gunn, and J.S. Marshall, 1957: Pattern in the vertical of snow generation. *J. Meteor.*, **14**, 95-114.

Fabry, F., G.L. Austin, and A. Singh, 1992: High resolution observations of precipitation with a vertically pointing radar. Proceeding, *11th Int. Conf. on Clouds and Precipitation*, Montreal, Canada, ICCP/IAMAS, 258-259.

Fabry, F., and I. Zawadzki, 1995: Long-term radar observations of the melting layer of precipitation and their interpretation. *J. Atmos. Sci.*, **52**, 838-851.

Nakaya, U., 1954: *Snow crystals, natural and artificial.* Harvard Press, Cambridge, 510 pp.

Zawadzki, I., and F. Fabry, 2000: Observations of supercooled water and of secondary ice generation by a vertically pointing X-band Doppler radar. Proceeding, *13th Int. Conf. on Clouds and Precipitation*, Reno, Nevada, ICCP/IAMAS.

LARGE SCALE VIEW OF THE EFFECT OF AEROSOLS ON THE ONSET OF PRECIPITATION USING SATELLITE DATA.

Itamar M. Lensky, Ron Drori and Daniel Rosenfeld

Institute of Earth Science, Hebrew University of Jerusalem, Jerusalem, Israel

1. INTRODUCTION

It is well known that aerosols serve as cloud condensation nuclei (CCN) and Ice Nuclei (IN), which interact with convective clouds and alter their microphysical properties. Rain formation processes on the microphysical scale are therefore impacted by these interactions and hence the rainfall (Rosenfeld, 1999). Recently Rosenfeld (2000) showed how rain and snow are suppressed by urban and industrial air pollution. In these two papers Rosenfeld used visible/infrared channels to retrieve the cloud microphysics, and radar data for the validation of the retrieval.

This paper will demonstrate how a single parameter, retrieved from standard operational visible/infrared satellite data can provide a large-scale look on the impact of different air masses characterized by different aerosol types, on convective clouds microstructure and precipitation formation processes through few case studies.

2. METHODOLOGY

The method presented in this paper is a third stage in a developing approach to retrieve cloud properties, using remotely sensed microphysical properties. In the first stage Rosenfeld and Gutman (1994) (RG), showed that the area of precipitation radar echoes from convective clouds are well correlated with the area delineated by a 14 μm threshold of the effective radius of cloud droplets (*Re*). In the second stage, Rosenfeld and Lensky (1998) (RL) analyzed convective cloud clusters and defined five different vertical zones that can be found in these clouds. Each of the five zones represents a different microphysical process, according to analysis of the growth of the cloud droplets effective radius with height (or temperature). Not all of the processes necessarily appear in every cloud. The five zones from cloud base to top are:

- Diffusional droplet growth zone
- Droplet coalescence growth zone
- Rainout zone
- Mixed phase zone
- Glaciated zone

To detect the large-scale impact of different aerosols on clouds, the RL algorithm was applied to running windows of 50 by 50 AVHRR pixels in satellite images of up to few thousands lines of 2048 samples. The running window samples every 25 AVHRR pixels. In each window, the temperature at which the effective radius exceeded the precipitation threshold of 15 μm (*T(Re=15)*) was calculated, using the RL technique (i.e. looking at the 50th percentile). The value of *T(Re=15)* was assigned to the center of the running window.

Interpretation of the meaning of *T(Re=15)* will be done assuming that the convective clouds that are analyzed have the same cloud base temperature. In cases where this cannot be assumed, the cloud base temperature must be retrieved explicitly. High *T(Re=15)* temperature indicates that efficient warm rain precipitation formation processes as coalescence and rainout are present already in the lower parts of the clouds in the cloud cluster. This is typical to clouds that grow in clean air mass such as maritime air mass, or air that its aerosols were washed out by previous precipitation. Low *T(Re=15)* temperatures are typical to clouds growing in continental air mass. Extremely low *T(Re=15)* temperatures are typical to clouds growing in polluted air. The classical distinction between continental and maritime air masses is the number of CCN per centimeter cube. 100

Corresponding author address: Prof. Daniel Rosenfeld, Institute of Earth Science, Hebrew University of Jerusalem, Jerusalem 91904, Israel
E-mail: daniel@vms.huji.ac.il

CCN per cc or less are typical values of clean maritime aerosols, few hundreds CCN per cc are typical values of continental, and few thousands for pollution aerosols. The number of CCN per cc also determines the cloud droplet size distribution (DSD) function near cloud base, and subsequently in higher altitudes. In the maritime case, the available cloud water is condensed on a small number of CCN. This implies a small number of larger droplets near cloud base, or in other words, a wide DSD for clean maritime aerosol. In the case of continental aerosol, the same amount of available cloud water is condensed on a much larger number of CCN. This implies a large number of small droplets near cloud base, or in other words, a narrow DSD. For effective coalescence, a wide DSD is required, therefore the effective radius of 15 μm threshold is expected to be reached in lower altitudes (or warmer *T(Re=15)*) in clean maritime air, while in polluted air, the *T(Re=15)* parameter is expected to be lower (colder). An exception is, when the window is fully covered only with high cloud tops. In this case the *T(Re=15)* parameter will show very low *T(Re=15)* temperature. To avoid such mistakenly low *T(Re=15)* temperatures, a criterion for the presence of cloud base in the window was added. Another criterion was added to avoid false interpretation in the case where multi layer clouds are present in the window, such as thin cloud layers, partly covering the convective cloud layer. The non convective clouds were screened out using the fact that the effective radius grows with height in convective clouds.

Aerosols are present everywhere, but their effect on clouds will reveal itself only where and when convection is triggered. The *T(Re=15)* parameter exist only in running windows where onset of precipitation was detected. For a large scale view of the effect of the aerosols on convective clouds, we would like to interpolate the *T(Re=15)* parameter to windows that did not pass the filtering and to windows outside the cloud clusters. This is done by giving weights to windows with valid *T(Re=15)* parameter within a predefined number of windows distance from the interpolated window. The number of windows that will take part in the interpolation depends on the size of viewing domain (2 to 10 windows). The weight is given in accordance to the reciprocal of the distance to the interpolated window. A minimum of two *T(Re=15)* values were required for the interpolation. The interpolated *T(Re=15)* parameter will be referred here as *T15*.

The *T15* parameter can be viewed also as a measure of the height of the onset of precipitation. High *T15* value represent efficient rain processes in the lower parts of the clouds. Low *T15* values means that clouds need to develop to heights with lower temperature to start precipitation. When plotting a surface of the *T15* parameter on a latitude longitude geographical projection, the decreasing *T15* represent loading of the air mass with aerosol, and therefor lifting the altitude where effective precipitation processes are initiated. Increasing *T15* represent cleaning of the air mass from the aerosol, therefore effective precipitation processes are initiated in lower altitude. The typical situation is of decreasing *T15* while movement of an air mass from the ocean inland. A further decrease of *T15* occurs when moving over heavy pollution sources such as densely populated cities or from biomass burning smoke. A slow increase of *T15* is seen when an air mass heavily loaded with aerosols moves away from the source of the aerosols over an ocean.

3. THE DATA

Data from the Advanced Very High Resolution Radiometer (AVHRR) on board the National Oceanic and Atmospheric Administration (NOAA) operational satellites is used for the two case studies presented in this paper. The *T15* was calculated using the effective radius and the 11 micron channel (Rosenfeld and Lensky 1998). The 0.65, 3.7, 11 and 12 micron Channels are used to retrieve the effective radius (Rosenfeld and Gutman, 1994). The data source for the case studies is from "the NOAA Satellite Active Archive". http://www.saa.noaa.gov/.

4. CASE STUDIES

The first case study is from 14 December 1997, over the Philippines. This case study was analyzed in the RL paper. Figure 8 in RL shows the satellite data, and figure 9 in RL shows an analysis of selected areas containing clouds in different air masses. In this paper, the analysis of the same data was taken one step further. Figure 1 shows the 0.9 μm image of the analyzed area (599 by 728 AVHRR pixels). In this figure, the clouds that are seen over the Philippines have different microphysical properties. Figure 2 shows the *T15* parameter – 23 by 29 windows.

The interpolation was done for distance of two windows from windows containing valid *T(Re=15)* data. This image "tells the whole story in a glance of the eye". The clean maritime air mass to the east of the island is seen to have high temperature values of *T15* (19°C). While going inland the value of the *T15* parameter decrease to 15°C, and a further decrease to 5°C in *T15* occurs when moving over Manila, which is a source for heavy pollution.

The second case study is from the 14 October 1997. In this case study the effect of smoke from biomass burning interacting with clouds over Sumatra and Kalimantan can be seen. Figure 3 shows the TOMS aerosol index. In this figure the smoke aerosol area is represented by the grayscale, the background is white for ocean and black for land. The larger aerosol index (dark) due to the smoke can be seen over Sumatra and Kalimantan. The *T15* plot (111 by 80 windows) is shown in figure 4. Because of the large domain, the interpolation was done for distance of 10 windows from windows containing valid *T(Re=15)* data. The bright colors represent maritime clouds with high *T15* of 15 to 20°C. These can be seen over South China Sea and Andaman Sea. The *T15* over land (Thailand and Vietnam) is slightly lower (10 to 15°C), with extreme low *T15* over Bangkok (-4°C), and 0 °C over Ho Chi Minh City (Saigon). Clouds influenced by the smoke aerosol are much darker and have much lower *T15* temperatures than clouds over rural areas (as low as –5°C). This indicates less efficient rain processes.

5. CONCLUSION

This paper presents a methodology and two case studies of an automatic detection of the cloud aerosol interactions on a mid to large-scale perspective. The advantage is that the results of the algorithm are clear and do not require special skill for the interpretation. Outside of the convctive cloud cluster the values of the *T15* parameter depend on the interpolation method. The extend of interpolation depends on the scale of the image. For large scale images interpolation was done up to 10 windows distance, while for mid scale, only 3 windows distance were considered.

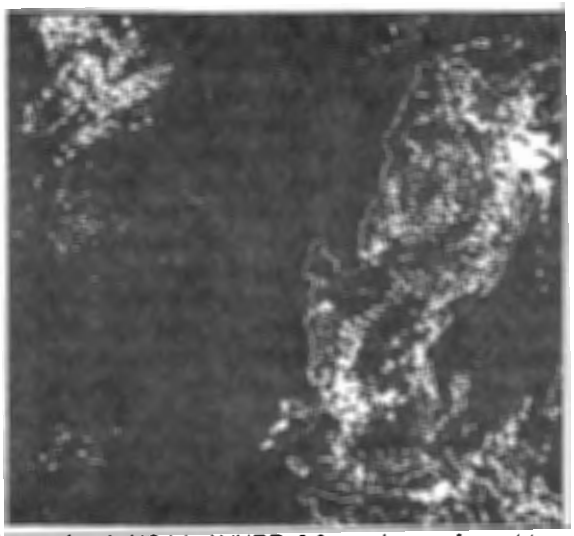

Figure 1. *A NOAA AVHRR 0.9 μm image from 14 December 1997, over the Philippines. The T15 for the clouds in this area is shown in figure 2.*

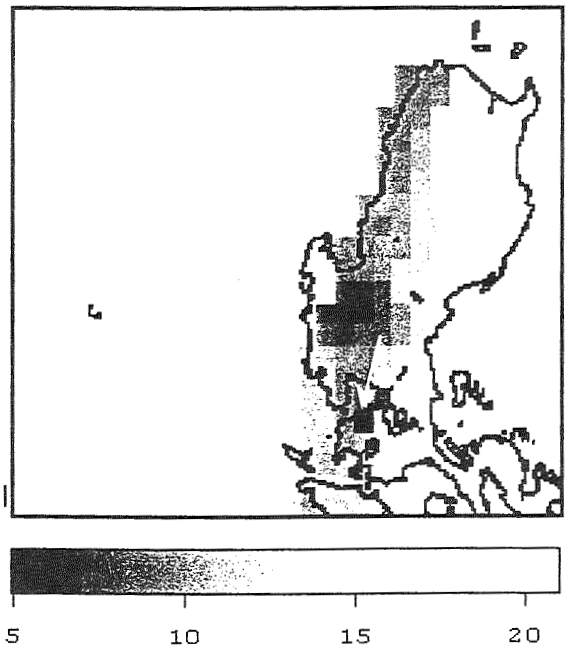

Figure 2. *The T15 results for area displayed in figure 1. The T15 temperature can be seen decreasing while going inland. The arrow is pointing to a minimum of 5°C that can be seen over Manila. Plain white is for no data.*

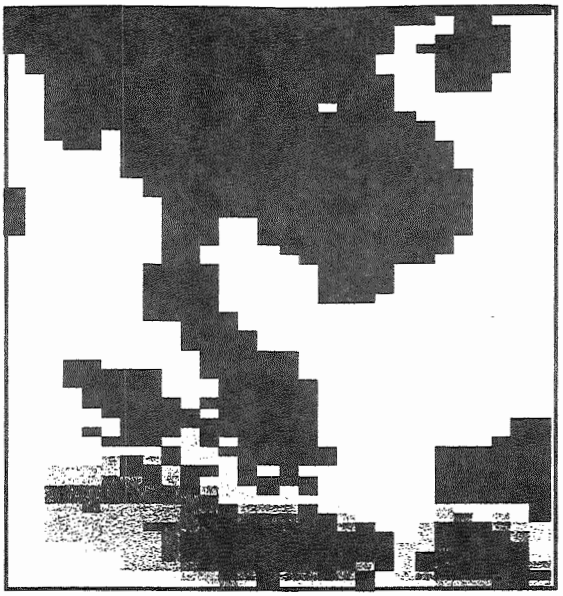

Figure 3. *A TOMS aerosol index image from 14 October 1997 of biomass burning smoke interacting with clouds over Indonesia.. The aerosol index is displayed in gray colors. The T15 for the clouds in this area is shown in figure 4.*

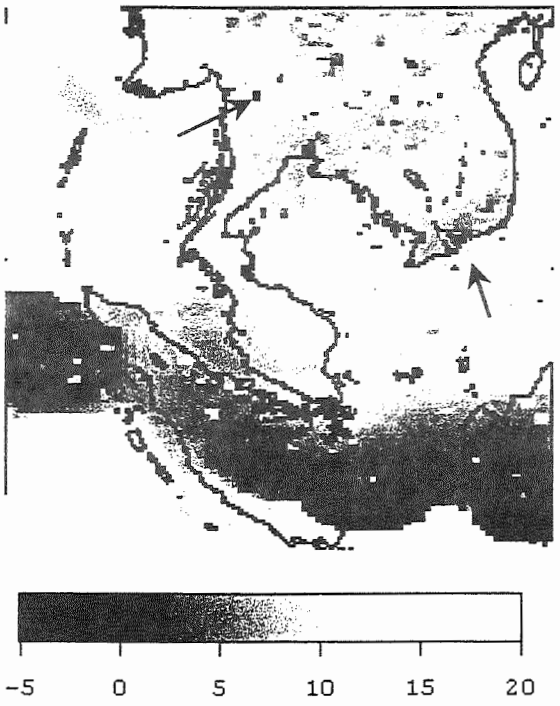

Figure 4. *The T15 results for area displayed in figure 3. The most maritime (clean) clouds are shown in bright color (20°C). Polluted clouds are shown in black The white arrow points to Bangkok (-4°C), The black arrows points to Ho Chi Minh City (0°C), and Chiang Mai (2°C). Plain white is for no data.*

6. REFERENCES

Rosenfeld, D., 1999: TRMM observed first direct evidence of smoke from forest fires inhibiting rainfall. *Geophys. Res. Lett.* **26,** 3105-3108.

Rosenfeld, D., 2000: Suppression of rain and snow by urban and industrial air pollution. *Science.* **287,** 1793-1796.

Rosenfeld, D., and I. M. Lensky, 1998: Satellite based insights into precipitation formation processes in continental and maritime convective clouds. *Bull. Amer. Meteor. Soc.,* **79,** 2457-2476.

Rosenfeld, D., and G. Gutman, 1994: Retrieving microphysical properties near the tops of potential rain clouds by multispectral analysis of AVHRR data. *J. Atmos. Res.*, **34,** 259-283.

DESIGN AND SENSITIVITY ESTIMATION OF A NEW AIRBORNE CLOUD RADAR

Dirk Klugmann and Manfred Wendisch

Institute for Tropospheric Research, 04318 Leipzig, Germany

1 INTRODUCTION

Continental clouds consisting of small droplets (effective droplet radius less than $10\,\mu$m) partly reveal systematic discrepancies between calculated and measured radiative cloud properties (Wendisch and Keil (1999)) that need to be resolved. One suspicion to explain these discrepancies are horizontal inhomogeneities of microphysical cloud properties. A promising tool to characterize the inhomogeneities is radar technique.

For clouds dominated by larger droplets, calculations and measurements (e. g. Clothiaux et al. (1995); Kropfli et al. (1995); Fox and Illingworth (1997)) have proven the ability of millimeter wave radar technique to retrieve multi-dimensional microphysical cloud properties. Airborne operation of this type of radar (Pazmany et al. (1994); Sadowy et al. (1997)) is a substantial supplement to ground based radar measurements. Though millimeter wave radars exclusively using semiconductor devices for power generation are still afflicted with a number of problems (Klugmann and Judaschke (1996)), first approaches of airborne operation of a radar using this technique have been reported by Bambha et al. (1998). We focus on detecting clouds dominated by small droplets. We show that a special design of such an airborne radar system is capable to detect these small droplets.

2 GOVERNING EQUATIONS

The sensitivity of a millimeter wave radar system to a cloud is determined by the clouds radar reflectivity factor Z. The calculation of Z is done by Rayleigh approximation, which simplifies the approach.

Corresponding author's address: Dirk Klugmann, Institute for Tropospheric Research, Permoserstraße 15, 04318 Leipzig, Germany; E-mail: klugmann@tropos.de

2.1 Derivation of radar reflectivity factor

The radar reflectivity factor Z of an ensemble of small droplets is defined by

$$Z = \int_0^\infty S_N(d)\, d^6 \mathrm{d}d \tag{1}$$

The number-size distribution $S_N(d) \equiv \mathrm{d}N(d)/\mathrm{d}d$, with d indicating the droplet diameter, describes the number concentration with respect to the diameter interval $\mathrm{d}d$. The incremental radar reflectivity is:

$$S_Z(d) \equiv \frac{\mathrm{d}Z(d)}{\mathrm{d}d} = S_N(d)\, d^6 \tag{2}$$

We apply the modified Gamma distribution to parameterize the cloud droplet size distribution:

$$S_N(d) = n_\mathrm{m} \cdot \left(\frac{d}{d_\mathrm{m}}\right)^\alpha \cdot \mathrm{e}^{(\alpha+6)\left(1-\frac{d}{d_\mathrm{m}}\right)} \tag{3}$$

The parameter d_m gives the location of the maximum of $S_Z(d)$ according to Eq. (2), while $n_\mathrm{m} \equiv S_N(d_\mathrm{m})$. The third parameter α gives the order of the modified Gamma distribution. It can be shown that the $\mathcal{O}$th moment of the modified Gamma distribution is given by

$$M_\mathcal{O} = \frac{n_\mathrm{m} \cdot d_\mathrm{m}^{(\mathcal{O}+1)} \cdot \mathrm{e}^{(\alpha+6)}}{(\alpha+6)^{(\alpha+\mathcal{O}+1)}} \cdot (\alpha+\mathcal{O})! \tag{4}$$

Using Eq. (4), $Z \equiv M_6$ yields

$$Z = \frac{n_\mathrm{m} \cdot d_\mathrm{m}^7 \cdot \mathrm{e}^{(\alpha+6)}}{(\alpha+6)^{(\alpha+7)}} \cdot (\alpha+6)! \tag{5}$$

Frequently the parameters accessed by *in-situ* measurements are neither n_m nor d_m, but total droplet number concentration

$$N_\mathrm{tot} \equiv M_0 \tag{6}$$

and effective radius

$$r_\mathrm{eff} \equiv \frac{1}{2} M_3/M_2 \tag{7}$$

Applying Eq. (4) to Eq. (6) and Eq. (7), respectively, and inserting the results into Eq. (5) yields

$$Z = N_{\text{tot}} \cdot f_\alpha \cdot (2r_{\text{eff}})^6 \quad \left(f_\alpha = \frac{(\alpha+6)!}{\alpha!\,(\alpha+3)^6} \right) \tag{8}$$

For $0 \leq \alpha \leq 8$, the overall variation of f_α is less than 30%, corresponding to a change of Z of about 1 dB. In our calculations we assume $\alpha = 2$. For the microphysical bulk parameter pairs r_{eff}, LWC (liquid water content) and N_{tot}, LWC, respectively, Z can also be expressed in a similar way.

2.2 Calculation of radar sensitivity

It is assumed that a droplet distribution leading to a given Z_{R_0} (according to Eq. (1)) is situated a distance R_0 from the radar. For Gaussian antenna illumination and monostatic antenna setting the received signal power P_{r,R_0} from that distance can be calculated:

$$P_{\text{r},R_0} = P_{\text{t}} \cdot \frac{\pi^5 G G_{\text{s}} |K|^2}{512 \cdot \ln 2 \cdot \lambda^2} \cdot \frac{\Delta R}{R_0^2} \cdot \frac{Z_{R_0}}{(1+F^4)} \tag{9}$$

Here P_{t} denotes the transmitted signal power, G the antenna gain, and ΔR is the range resolution. The radar wavelength is denoted by λ, system power gain by G_{s}, and $|K(\lambda = 3.2\,\text{mm})|^2 \approx 0.82$. The term $(1+F^4)$ invented by Lataitis et al. (1998) accounts for a near field correction. Detecting a scattered signal requires to distinguish this signal from instrumental noise and atmospheric emission, so $P_{\text{r},R_0} > \sigma_{P_{\text{n}}}$ ($\sigma_{P_{\text{n}}}$: noise power incertainy) must apply. Assuming $\sigma_{P_{\text{n}}} \approx P_{\text{n}}$, the threshold radar reflectivity factor at a given R_0 can be calculated using Eq. (9):

$$Z_{\text{thre}}(R_0) = \frac{P_{\text{n}}}{P_{\text{t}}} \cdot \frac{512 \cdot \ln 2 \cdot \lambda^2}{\pi G G_{\text{s}} |K|^2} \cdot \frac{R_0^2}{\Delta R} \cdot (1+F^4) \tag{10}$$

The noise power P_{n} is described by means of the noise temperature T_{n} at a given system temperature T_0:

$$P_{\text{n}} = k_{\text{B}} T_{\text{n}} B_{\text{D}} \quad \left(B_{\text{D}} = \frac{2\Delta v}{\lambda} \right) \tag{11}$$

with $k_{\text{B}} = 1.38 \cdot 10^{-23}\,\text{J K}^{-1}$ (Boltzmann constant), and B_{D} denoting the frequency band width over which the return signal is Doppler distributed due to the target velocity range Δv. Another concept for describing the system noise is the noise figure N_{n}, which links T_{n} to T_0 by

$$N_{\text{n}} = \frac{T_{\text{n}}}{T_0} + 1 \tag{12}$$

and is usually given in dB.

2.2.1 Near field correction

For $R_0\lambda > D_{\text{e}}^2$, where D_{e} denotes the effective diameter of the antenna related to the physical diameter D_{a} by $D_{\text{e}} \approx \sqrt{2/3} \cdot D_{\text{a}}$, the near field correction with

$$F = \frac{D_{\text{e}}}{\sqrt{\frac{8R_0\lambda}{\pi}}} \tag{13}$$

has to be applied in Eq. (9). Using $A_{\text{e}} = \pi D_{\text{e}}^2/4$ and the effective antenna area

$$A_{\text{e}} = \frac{G\lambda^2}{4\pi} \tag{14}$$

one finally ends up with

$$F^4 = \left(\frac{G\lambda}{8\pi R_0} \right)^2 \tag{15}$$

For $R_0/(G\lambda) = 0.1$, obtained at $R_0 \approx 50\,\text{m}$ for an antenna gain of $G = 52\,\text{dB}$ and $\lambda = 3.2\,\text{mm}$, the deviation of P_{r,R_0} from the far field value is $F^4 < 20\%$.

3 RESULTS

The calculation of Z from *in-situ* measurements has been performed for various cases (e. g. Fox and Illingworth (1997)), but up to now not for polluted boundary layer clouds. We concentrate on the detection limits for an airborne radar with regard to detecting small cloud droplets, which usually are found in continental polluted environments. We use recent *in-situ* measurements presented by Wendisch and Keil (1999).

3.1 Radar reflectivity factor

Wendisch and Keil (1999) show profiles of LWC, r_{eff}, and N_{tot} for several cases of heavily polluted boundary layer clouds. From these data, a vertical profile of Z_{bulk}, calculated with $\alpha = 2$ according to Eq. (8), is displayed in Figure 1 (crosses). In addition, values of Z_{dis} were calculated according to Eq. (1) from the drop size distribution, which also has been measured (circles). The average, minimum, and maximum values for $\Delta Z = Z_{\text{bulk}} - Z_{\text{dis}}$ (Z in dBZ) are also stated. Both methods of calculating Z are in reasonable agreement.

For the investigated non-precipitating, heavily polluted boundary layer clouds, Z seldom exceeded $Z =$

$-25\,\mathrm{dB}Z$. Values below $Z = -40\,\mathrm{dB}Z$ were not unusual, and even $Z = -50\,\mathrm{dB}Z$ has been be found. A radar system specifically designed to study these highly polluted continental cloud systems must be able to detect a significant portion of clouds within that range of Z at the distance of a few hundred meters.

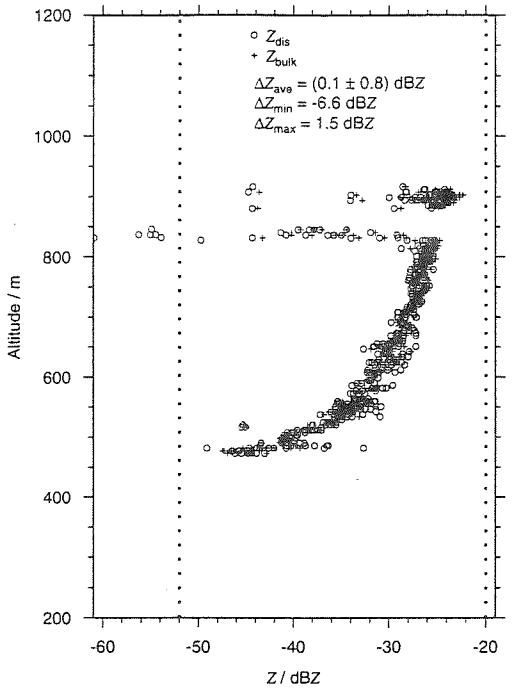

Figure 1: Radar reflectivity factor Z derived from measurements on December 9, 1996. Crosses: Values calculated from Eq. (8) with $\alpha = 2$. Circles: Results from Eq. (1). The average, minimum, and maximum difference between the results obtained by the two different methods is given in the upper part. Vertical dotted lines show Z_{min} and Z_{max} calculated from the minimal and maximal recorded bulk values.

4 RADAR SYSTEM

Due to the desired airborne operation, the 94-GHz Doppler radar system weight should not exceed a few kilograms, the size should be limited to 50 cm in all dimensions, and the power consumption should fit the airplane's power supply ($2 \times 28\,\mathrm{V}/70\,\mathrm{A}$). This is achieved, in part, by using semiconductor devices for transmitted power generation operated in FM-CW (Frequency Modulated Continuous Wave) mode (Strauch (1976)). A prototype of this robust and durable radar front end is described by Klugmann and Judaschke (1996). The modular design allows easy upgrading of individual components.

A block diagram of the radar front end can be found in Figure 2. The system is monostatic, with an average transmitted power of $P_{\mathrm{t}} \approx 350\,\mathrm{mW}$. The isolation between transmitting and receiving branch is better than 50 dB. The indicated low-noise amplifier (LNA) is optional and can be used to increase the system power gain G_{s} in Eq. (10). The mixer noise number (Eq. (12)) is $N_{\mathrm{n}} < 7\,\mathrm{dB}$, its conversion loss approximately 7 dB. The antenna gain G has to be optimized to cover performance and size / weight requirements. The actual antenna gain is $G \approx 42\,\mathrm{dB}$.

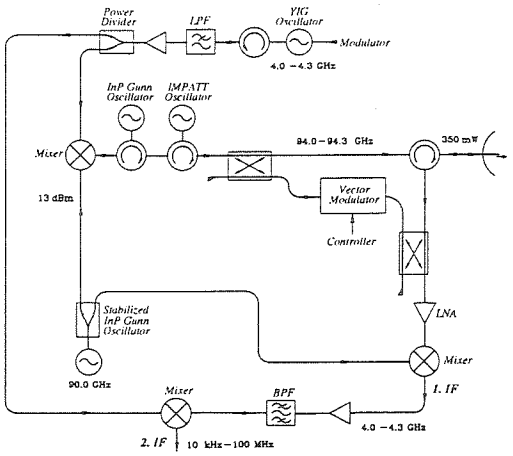

Figure 2: Block diagram of the radar front end.

An enhancement of the radar system by increasing the antenna gain to $G \approx 52\,\mathrm{dB}$, transmitting power to $P_{\mathrm{t}} \approx 1.6\,\mathrm{W}$, and applying the optional 15 dB low-noise amplifier is planned.

4.1 Sensitivity

From Eq. (10) Z_{thre} was calculated assuming $\Delta v \approx 2\,\mathrm{ms}^{-1}$, leading to $B_{\mathrm{D}} \approx 1250\,\mathrm{Hz}$ (Eq. (11)). The system noise figure (mixer and amplifier) $N_{\mathrm{n}} \approx 9.8\,\mathrm{dB}$, inserted in Eq. (12), leads to $T_{\mathrm{n}} \approx 2500\,\mathrm{K}$ for $T_0 = 290\,\mathrm{K}$. The sensitivity of a monostatic FM-CW Doppler radar also is determined by the cross talk from transmitting into the receiving branch, leading to a increasing phase noise power for decreasing R_0. The transmitting signal shows an e^{-1}-bandwidth of 23.3 kHz.

The results for $G = 52\,\mathrm{dB}$ and an unambiguous velocity range of $9.6\,\mathrm{m\,s}^{-1}$ can be found in Figure 3. In this figure the area in R_0-ΔR space where clouds with

$Z \geq -30$ dB can be detected is marked by the dark gray shading. The extension of this area by applying the additional 15 dB low-noise amplifier is shown by the light gray shading. Applying this amplifier, clouds of $Z = -45$ dB can be detected in the area in R_0-ΔR space marked by the dark gray shading.

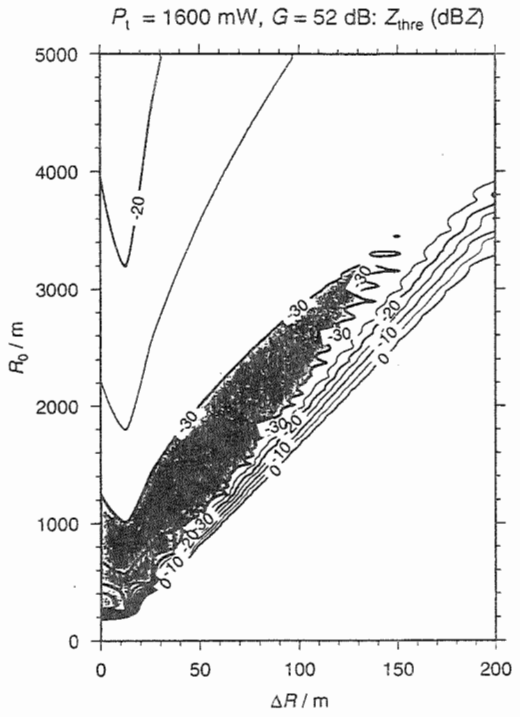

Figure 3: Sensitivity of the radar in final state.

5 CONCLUSIONS

An airborne radar system to investigate highly polluted boundary layer clouds has to accomplish a number of requirements. *In-situ* measurements in this type of clouds have revealed that typical radar reflectivity factors might be $Z < -40$ dBZ. Thus, the most important requirement is for high sensitivity at ranges R_0 of a few hundreds of meters. This has to be achieved with low power consumption and a compact and lightweight system.

The best compromise to yield the necessary system performance with the given restrictions can be achieved with a radar front end operating in FM-CW Doppler mode, generating transmitted power by semiconductor devices. The necessary sensitivity can be obtained by mounting a reasonable-sized antenna with a gain of $G \approx 50$ dB and applying an additional low-noise ($N_n \approx 7.5$ dB) preamplifier with a gain of approximately 15 dB. The radar system is set up in a modular design. This allows successive enhancements as better components become available in the future.

ACKNOWLEDGMENTS

The block diagram shown in Fig. 2 was provided by Dr. Rolf Judaschke, Technical University Harburg, Hamburg, Germany. We want to thank Prof. Dr. Jost Heintzenberg for his strong support of this project.

REFERENCES

Bambha, R. P. et al. A Compact Millimeter Wave Radar for Airborne Studies of Clouds and Precipitation. In *Preprints, IGARSS-98*, pages 443–445. IEEE, 1998.

Clothiaux, E. E. et al. An Evaluation of a 94-GHz Radar for Remote Sensing Cloud Properties. *J. Atmos. Oceanic Technol.*, 12(2):201–229, 1995.

Fox, N. I. and A. J. Illingworth. The Retrieval of Stratocumulus Cloud Properties by Ground-Based Cloud Radar. *J. Appl. Meteor.*, 36:485–492, 1997.

Klugmann, D. and R. Judaschke. A 94 GHz FM-CW-Doppler radar profiler using semiconductor technique. *Contrib. Atmos. Phys.*, 69(1):239–246, 1996.

Kropfli, R. A. et al. Cloud physics studies with 8mm wavelength radar. *Atmos. Res.*, 35:299–313, 1995.

Lataitis, R. J. et al. Near-field correction to the meteorological radar equation. In McKie, J., editor, *Extended Abstracts of the Fourth International Symposium on Tropospheric Profiling, Snowmass, Colorado*, volume 2, pages 188–198, Snowmass, Colorado, 1998.

Pazmany, A. et al. An Airborne 95 GHz Dual-Polarization Radar for Cloud Studies. *IEEE Transact. Geosci. Remote Sens.*, 32(4):731–739, 1994.

Sadowy, S. M. et al. The NASA DC-8 airborne cloud radar: Design and preliminary results. In *Preprints, IGARSS-97*, Singapore, 1997. IEEE.

Strauch, R. G. *Theory and Application of the FM-CW Doppler Radar.* PhD thesis, Graduate School of the University of Colorado, Department of Electrical Engineering, 1976.

Wendisch, M. and A. Keil. Discrepancies Between Measured and Modeled Solar and UV Radiation within Polluted Boundary Layer Clouds. *J. Geophys. Res.*, 104(D22):27373–27385, 1999.

A NOVEL METHOD FOR CLOUD DRIFT VELOCITY ESTIMATION BASED ON SEQUENTIAL IMAGE ANALYSIS

I. Genkova [1], G. Ganev [2] and V. Tsanev [1]

[1] Institute of Electronics - Bulgarian Academy of Sciences, Sofia, 1784, Bulgaria
[2] National Institute of Meteorology and Hydrology - Bulgarian Academy of Sciences, Sofia, 1784, Bulgaria

1. INTRODUCTION

The cloud motion wind (CMW) continuously engages the attention of the researchers during the last decades. The CMW vectors are derived mainly utilizing cross-correlation techniques using the IR cloud images, provided by the geostationary meteorological satellites. The topic is discussed in details by Henderson-Seller (1984) and Hayden et al. (1994). Three common problems arise during the cross-correlation techniques implementation. First, the necessity to select traceable targets, second, the difficulty to locate the position of the cross-correlation function diffuse maxima, and third, the assignment of cloud and wind vector heights. Numerous other methods for motion determination can be used for CMW estimation (Jahne, 1993).

The time mutability method (TMM) for drift velocity (DV) estimation of statistically non-homogeneous and non-stationary objects is suggested by Ferdinandov and Stoikova (1984) as an alternative of the cross-correlation techniques utilized in the laser remote sensing. The TMM was successfully applied for cloud field DV measurement during the last years in the Institute of Electronics at the Bulgarian Academy of Sciences (Mitev et al., 1992; Mitev et al., 1995a; Mitev et al., 1995b). The analysis of the obtained results and the systematic investigation of TMM (Pachedjieva et al., 1996a; Pache-djieva et al., 1996b; Pachedjieva et al., 1997) brought to its improvement (Genkova et al., 1999). Here we describe the results of cloud motion DV estimation obtained by the improved TMM handling of METEOSAT images registered on August 11, 1999 from 08:30 UT to 13:30 UT.

2. DESCRIPTION OF THE METHOD

The improved TMM utilization requires an ensemble of images registered in successive equidistant time moments over the regular set of space nodes, i.e.

$$\mathbf{S} \equiv \left\{ S(x_i, y_j; t_k) \; ; i=\overline{1,I} \; ; j=\overline{1,J} \; ; k=\overline{1,K} \; ; \right.$$
$$\Delta x = x_i - x_{i-1} = \Delta y = y_j - y_{j-1} = const \; ; \quad (1)$$
$$\left. \Delta t = t_k - t_{k-1} = const \right\} .$$

We suppose that the x-axis is horizontal with positive direction from left to right, whilst the y-axis is vertical and pointed upward. The TMM utilization requires:

(1) To pick out a common "initial" point (x_o, y_o) and build through it sections $\Xi(n,M)$, directionally defined by a set of vectors $\bar{\Xi}(n) \equiv \{\bar{\xi}_{n,g}, g=\overline{1,G(n)}\}$. Each section $\Xi(n,M)$ contains $M=2m+1$ points, m points at both sides of (x_o, y_o). The $G(n)$ vectors $\bar{\Xi}(n)$ are non-opposite. They have common starting point (x_o, y_o) and end-point situated on the square with center (x_o, y_o) and side equal to $2n$. For example, $G(1)=4$ and the set $\bar{\Xi}(1)$ consists of vectors $\bar{\xi}_{1,1}=(1,0)$, $\bar{\xi}_{1,2}=(1,1)$, $\bar{\xi}_{1,3}=(0,1)$ and $\bar{\xi}_{1,4}=(-1,1)$. The vectors $(-1,0)$, $(-1,-1)$, $(0,-1)$ and $(1,-1)$ do not belong to $\bar{\Xi}(1)$, because they are opposite to $\bar{\xi}_{1,1}$, $\bar{\xi}_{1,2}$, $\bar{\xi}_{1,3}$ and $\bar{\xi}_{1,4}$, correspondingly.

(2) To calculate estimations $\hat{I}(U;\bar{\xi}_{n,g})$ for each section $\Xi(n,M)$ as follows

$$(2) \quad \begin{cases} \hat{I}(\eta;\bar{\xi}_{n,g}) = \left\langle \left[S(\xi_l, t_k) - S(\xi_{l+\eta}, t_{k+1}) \right]^2 \right\rangle / (\Delta t)^2 , \\ \xi_l - \xi_{l-1} = \Delta\xi = \left| \bar{\xi}_{n,g} \right| ; \xi_{l+\eta} = \xi_l + \eta \, U_o \, \Delta t \; ; \\ U_o = \Delta\xi / \Delta t \; ; \; U = \eta \, U_o \; ; \; U' = \eta \; . \end{cases}$$

The space co-ordinate ξ varies along the section $\Xi(n,M)$ and has a zero value at the point (x_o, y_o). The positive direction of the ξ axis is obtained by clock-wise rotation from the positive direction of the x-axis. The symbol $\langle \; \rangle$ stands for averaging accounting all pairs $\{\xi_l, \xi_{l+\eta}\}$ registered at $\{t_k, t_{k+1}\}$ and belonging to the sections $\Xi(n,M)$ of the set (1). The averaged quantity in (2) describes "movement over the sections" with apparent velocity $U=\eta U_o$, i.e. translation from ξ_l to $\xi_{l+\eta}$. The corresponding dimensionless apparent velocity is $U'=\eta$. The estimations $\hat{I}(\eta;\bar{\xi}_{n,g})$ of the TM are calculated in accordance with (2) where $-(M-1) \le \eta \le +(M-1)$.

(3) To evaluate the position $\hat{U}_{min}(n,g)$ and the value $\hat{I}(\hat{U}_{min}(n,g);\bar{\xi}_{n,g})$ of the $\hat{I}(\eta;\bar{\xi}_{n,g})$-minimum.

(4) To find the direction $\bar{\bar{\xi}}_{n,g}$, where the value

Corresponding author's address: Iliana S. Genkova, Institute of Electronics-Bulgarian Academy of Sciences, 72 Tsarigradsko Chaussee, 1784 Sofia, Bulgaria,
E-Mail: tsanev@ie.bas.bg

$\hat{I}(\hat{U}_{min}(n,g);\bar{\xi}_{n,g})$ is minimized and to accept that the random field yielding images (1) is moving with DV $\hat{V}=\hat{U}_{min}(n,g)$ in the direction $\bar{\xi}_{n,g}$. Thus obtained DV estimation is two-fold averaged.

3. VERIFICATION BY NUMERICAL EXPERIMENTS

In order to evaluate the accuracy of the above described TMM we modeled sets (1) by scanning cloud photos and "cutting" consecutive shifted parts. In this way we obtained sets corresponding to uniform and non-uniform linear motion and also to rotation.

Fig. 1 First, third and the fifth images from set of ten modeled images with 256×256 pixels and $\Delta x=\Delta y=1\,m$, $\Delta t=1\,s$, simulating non-uniform linear motion from right to left with mean DV $V_{mod}=-25.22\,m/s$.

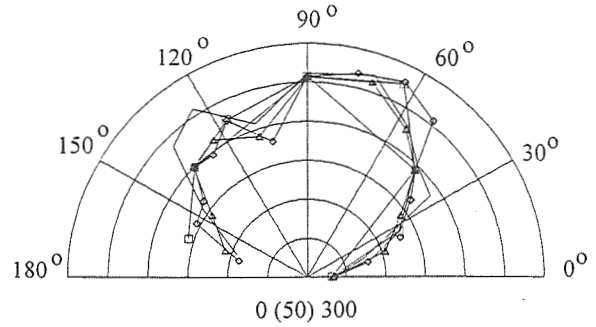

Fig. 2 Polar diagrams $\hat{I}(\hat{U}_{min}(n,g);\bar{\xi}_{n,g})$ for the sections $\Xi(1,241)$ (—O—), $\Xi(2,121)$ (—□—), $\Xi(3,81)$ (—△—), $\Xi(3,33)$ (——) and $\Xi(4,61)$ (—◊—) with common point $(x_o=128, y_o=128)$, evaluated for the set shown in Fig.1.

Fig.1 shows a set of modeled images with 256×256 pixels and $\Delta x=\Delta y=1m$, $\Delta t=1s$. They simulate non-uniform linear motion from right to left with mean DV $V_{mod}=-25.22\,m/s$. The following Fig.2 shows the polar diagrams $\hat{I}(\hat{U}_{min}(n,g);\bar{\xi}_{n,g})$ for the sections $\Xi(1,241)$, $\Xi(2,121)$, $\Xi(3,81)$, $\Xi(3,33)$ and $\Xi(4,61)$ with common point $(x_o=128, y_o=128)$, evaluated for the set shown in Fig.1 and for another similar set but with mean DV -*50.44 m/s*. A part of the obtained results is summarized in Table 1. The angle α shows DV inclination with respect to the left-to-right horizontal direction. All movements are non-uniform and V_{mod} is the mean DV. The negative V_{mod} -sign corresponds to the right-to-left movement. The TMM DV estimations are denoted with $\hat{V}_t$. Each modelled set is handled using different sections $\Xi(n,M)$. In some particular cases the section $\Xi(3,33)$ does not permit DV estimation, because due to its small volume $M=2m+1$ the TM has no minimum. These cases are indicated with "***" in Table 1. Lines 1, 2 and 4 correspond to sets (1) with consecutively increasing DV. The influence of statistical properties is outlined in lines 2 and 3 where the models are statistically different but are moving with equal DV. Lines 5 and 6 contain results of the experiments when the DV does not coincide with some of the permitted directions $\bar{\xi}_{n,g}$. The most complicated situation corresponds to the line 7 - DV direction varies within $\pm 10^o$, keeping its mean direction constant.

The analysis of the obtained results permits to draw the following conclusions: **(1)** The conditions

$$(3)\quad \begin{cases} \min\limits_{\Xi(n)}\{\hat{I}(\hat{U}_{min},\bar{\xi}_{ng})\}=\hat{I}(\hat{U}_{min},\bar{\bar{\xi}}_{ng}), \\ \hat{I}(\hat{U}_{min},\bar{\xi}_{ng}\neq\bar{\bar{\xi}}_{ng})>\hat{I}(\hat{U}_{min},\bar{\bar{\xi}}_{ng}) \end{cases}$$

always hold true. Here $\bar{\bar{\xi}}_{ng}$ is the vector from the set $\Xi(n)$, whose direction is the closest to $\bar{V}_{mod}$. The more vectors in the set $\Xi(n)$, the more precise the direction estimation. **(2)** The TMM leads to DV estimations with a relative error of the order of *3 %* when the investigated object moves linearly with velocity non-uniformity

Table 1 Results of the performed numerical experiments.

N	α	V_{mod}	$\hat{V}_t$ [m/s]					$(V_{mod}-\hat{V}_t)\,/\,V_{mod}\,100$ [%]				
[-]	[deg]	[m/s]	$\Xi(1,241)$	$\Xi(2,121)$	$\Xi(3,81)$	$\Xi(3,33)$	$\Xi(4,61)$	$\Xi(1,241)$	$\Xi(2,121)$	$\Xi(3,81)$	$\Xi(3,33)$	$\Xi(4,61)$
1	0	-25.22	-25.44	-25.46	-25.38	-26.25	-25.64	-0.87	-0.95	-0.63	-4.08	-1.67
2	0	-51.44	-50.22	-50.20	-49.38	-51.09	-48.48	+2.37	+2.41	+4.01	+0.68	+5.75
3	0	-50.44	-52.38	-52.32	-50.28	-	-50.32	-3.85	-3.73	+0.32	-	+0.24
4	0	-95.56	-99.04	-99.12	-98.79	***	-97.44	-3.64	-3.73	-3.38	***	-1.97
5	95	-51.44	-48.73	-48.58	-48.54	-49.98	-48.28	+5.27	+5.56	+5.64	+2.84	+6.14
6	140	-74.88	-76.51	-76.78	-70.14	***	-72.65	-2.18	-2.54	+6.33	***	+2.98
7	0 (rot)	-25.00	-19.49	-19.46	-19.29	-	-19.28	+22.04	+22.16	+22.84	-	+22.88

between the consecutive images less than *15 %*. **(3)** The TMM results essentially depend on the statistical properties of the observed object when its movement can be considered as a combination of translation and rotation. The TMM relative error is less than *25 %* if the DV varies within $\pm 10^{o}$ around its mean direction. The TMM is inapplicable in the presence of the observed objects velocity divergence and/or rotation. **(4)** The choice of the measuring section is a compromise between the accuracy of the DV value and direction estimations. **(5)** The TMM permits to measure the velocity space distribution of a statistically non-homogeneous and non-stationary object, e.g. a cloud field. This requires enough large images in the set (1), i.e. large *I* and *J* values. In this case it is possible to separate the images in the source to sub-images forming new sets where the movement is predominantly linear. The TMM can be utilized for DV estimation in such obtained sub-sets.

4. TREATMENT OF SATELLITE IMAGES

Further we describe the results of cloud DV estimation obtained by TMM handling of 10 consecutive IR METEOSAT images registered on August 11, 1999 from 09:00 UT to 13:30 UT. This was the day of the last observed total solar eclipse. The Mediterranean and the Balkan Peninsula were in the periphery of wide lifted anticyclone. The predominant air transportation in the Central and South Europe was from the Atlantic Ocean. Over the Balkan Peninsula there was a tendency of convergation. The surface wind field was diluted but with anticyclonal curvature. The data from six aerological stations were used to estimate CMW for the "brightest" clouds observed from the satellite. These are the winds in the layers where the humidity reached its maximum or its decrease was sharply outlined. The data are presented in Table 2. For simplicity here and further we omit the adjectives east (E) for longitudes and north (N) for latitude because the observed area is part of Europe.

Table 2 CMW moduli *V* in m/s and azimuths *A* obtained from six aerological stations in the area

Station	UT	λ	φ	*V*	*A*
Wien (W)	12:00	16.22°	48.15°	9	225°
Brindizi (BR)	11:00	17.58°	41.39	4	350°
Sofia (S)	12:00	23.38°	42.65°	15	265°
Bucuresti (B)	11:00	26.37°	44.50°	12	265

The source satellite images cover the area between 10° and 27° longitude and 32° and 50° latitude. Due to the nature of the geostatinary satellite data these images were first, transferred to a regular set of geographical coordinates using the ordinary Kriging with linear variogram model and second, transformed to cylindrical map coordinates. Thus we obtained the handled set of ten images that satisfy the relations (1). The transformed images covered the area between 7.66° and 20.68° longitude and 32° and 50° latitude and had *512 x 712* nodes and $\Delta x = \Delta y = 6.67\ km$. The TMM was applied for three sub-areas, where clouds were observed, and for seven 1.5-hour time sub-intervals. For example, the first interval started at 09:30 UT and finished at 10:30 UT. Four images were registered during it and the evaluated DV pertained to the middle, i.e. at 09:30 UT. This approach permitted to obtain the time behavior of the cloud DV. Each sub-area consisted of *81 x 81* nodes and we used the sections $\bar{\Xi}(3)$ for TMM calculation. The "initial" points were chosen as follows: point #1 (φ=46.78°, λ=14.28°) is near Wien (see Fig. 3); point #2 (φ=46.78°, λ=22.92°) is near Bucuresti; point # 3 (φ=41°, λ=18.6°) is near Brindizi. Aimed to distinguish the different cloud layers we analyzed the sub-image histograms together with image temperature scales and thus chose different intervals of gray levels (*q*) corresponding to the predominant cloud layers. Thus we selected $130 \geq q \leq 200$ for the sub-area around point # 1, $130 \geq q \leq 220$ for the sub-area around point # 2 and finally $130 \geq q \leq 250$ for the sub-area around point # 3. The described procedure is illustrated in Fig. 3.

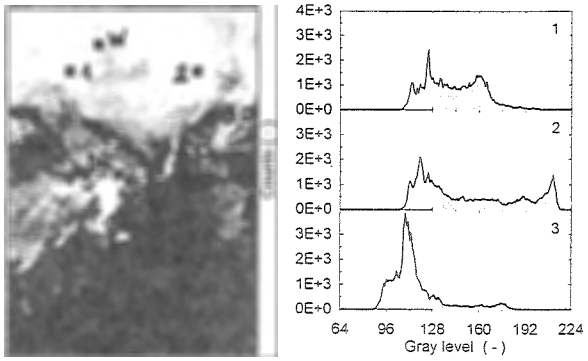

Fig. 3 One of the handled satellite images after the transformation to cylidrical map coordinates. The numbered squares denote the positions of the three "initial" points whilst the positions of the meteorological stations are denoted with abbreviations. The right plot presents the gray level histograms for the selected sub-areas. The "cloudy" intervals are shadowed.

The obtained estimations of the DV utilizing TMM for the three chosen points are summarized in Table 3.

Table 3 DV moduli *V* in m/s and azimuths *A* obtained utilizing TMM for the three chosen points

Time	Point # 1		Point # 2		Point # 3	
UT	V	A	V	A	V	A
09:45	2.57	326.3°	19.67	233.3°	16.68	315.4°
10:15	2.69	288.4°	20.65	233.3°	9.34	315.4°
10:45	3.12	288.4°	22.17	233.3°	7.03	341.8°
11:15	3.68	288.4°	23.45	233.3°	6.80	326.7°
11:45	7.91	236.3°	18.33	222.8°	10.96	315.4°
12:15	7.11	236.3°	19.86	222.8°	9.08	326.7°
12:45	4.76	236.3°	20.63	222.8°	14.44	341.8°
11:15	5.59	288.4°	21.30	233.3°	9.3	326.7°

Each line presents the results obtained using ten images, i.e. the mean DV during the time interval from first to tenth image registration. It is interesting to

discuss the significance of the chosen "cloudy" interval. There are only a few pixels (nodes) around point #3 with $q > 220$. If we repeat the calculations accounting only for nodes with $130 \geq q \leq 250$ during 09:00 UT to 13:30 UT the result is $V = 9.29\,m/s$ and $A = 151.3°$. The significant azimuthal difference is mainly due to the presence of rotation around point # 3.

We treated also the corresponding visible METEOSAT images. The obtained results differ within ± 5 % from the reported above.

5. DISCUSSION

1. The Eqs. (2) and (3) outline the essence of TMM. They can be interpreted as follows. An observer is "flying" over the set of images (1) along the "permitted traceable" directions ($\Xi(n)$) observing downward in the discrete moments t_k. Obviously the observer will not be able to detect any changes if he flies along the direction of the movement with apparent velocity equal to the drift velocity and if the observed cloud is "frozen", i.e. moves without evolution.

2. The Eq. (3) might be considered as calculating formula of the structure function if one neglects the denominator. This is a wrong judgment because the methods of averaging when calculating the time mutability function (TMF) and the structure function (SF) are quite different. The SF calculation is based on a pair of registered images. The averaging process accounts for all nodes shifted by the given lag-vector. Thus obtained velocity has to be considered as: **(a)** instantaneous and related to the middle of the time interval between the registrations of the used images; **(b)** averaged over the area of the used images. The TMF calculation is based on an ensemble of images registered in successive equidistant time moments (1). The averaging process accounts for the nodes that are situated along the sections $\Xi(n, M)$. The required number of numerical calculations is significantly reduced. Thus obtained velocity has to be considered as: **(a)** mean velocity related with a linear motion during the interval when the set (1) is registered; **(b)** averaged over the area of the used images.

3. The comparison of the velocities given in Tables 2 and 3 demonstrate the efficiency of the TMM utilization for cloud motion DV estimation. For example, around point # 1 at 11:45 UT the TMM gives $V=7.91\ m/s$ and $A=236.31°$ whilst the aerrological data for Wien are $V=9m/s$ and $A=225°$ at 12:00 UT. The coincidence at point # 2 is within (20-30)%. We ought to mention that there is significant influence of the Black See around the latter point.

4. The estimated accuracy by the numerical experiments is comparable with those of the obtained using satellite images. An important advantage of the DF estimations obtained using TMF is that they are insensitive to the spatial homogeneity of the observed clouds.

5. The fast and simple calculations for TMM allow its application in real time. The TMM evaluates cloud DV triple averaged: over the time interval (necessary for registration of the handled images); over the space regions containing cloud objects; over the temperature interval corresponding to the handled interval of gray levels. The obtained DV is related with observed clouds situated at a certain height. The suggested method should be considered promising in this respect.

6. The successful utilization of the TMM requires further investigations pointed to the automation of the calculations and to the selection of the informative temperature intervals.

6. REFERENCES

Ferdinandov, E.S. and E.V. Stoikova, 1984: Method of laser sounding of the atmospheric dynamics. Bulg. J. Phys., 11(1), 58-69.

Hayden, C.M., W.P. Mentzel, S.J. Nieman, T.J. Smith and C.S. Velden, 1994: Recent progress in methods for deriving winds from satelite data at NESDIS/CIMS. Adv. Space Res., 14 (3), 99-110.

Henderson-Seller, A. (ed.), 1984: Satellite sensig of a cloudy atmosphere: Observing the third planet. Taylor&Francis, London.

Jahne, B., 1993: Spatio-temporal image processing. Theory and applications. Springer-Verlag, Berlin.

Mitev, V.A., G.I. Sokolinov, 1992: Image velocimetry of atmospheric inhomogeneities using a statistical approach. Optics Comm., 90, 16-20.

Mitev, V.A., G.I. Sokolinov, 1995a: Image data-handling techniques for precise velocity measurements of atmospheric inhomogeneities. Appl. Opt., 34, 1867-1871.

Mitev, V.A., G.I. Sokolinov, 1995b: Remote cloud velocity measurements by image data processing. Proc. SPIE, 2506, 1995, 483-490.

Pachedjieva, B., V. Tsanev, and E. Ferdinandov, 1996a: Time mutability method for cloud field drift velocity measurements. Compt. Rend. de l'Acad. Bulg. Sci., 49(3), 49-51.

Pachedjieva, B., V. Tsanev, and E. Ferdinandov, 1996b: Influence of the measurement conditions on the accuracy of the time mutability method for cloud field drift velocity estimations. Compt. Rend. de l'Acad. Bulg. Sci., 49(5),47-50.

Pachedjieva, B., V. Tsanev, and E. Ferdinandov, 1997: Accuracy of the time mutability method for drift velocity estimations of non homogeneous and non-stationary objects. Compt. Rend. de l'Acad. Bulg. Sci., 50(8), 55-58, 1997.

Genkova, I., B. Pachedjieva, E. Ferdinandov, and V. Tsanev, 1999: Modification of the time mutability method for drift velocity estimation. Compt. Rend. de l'Acad. Bulg. Sci., 52(11), 31-34.

THE INFLUENCE OF DEEP CONVECTIVE MOTIONS ON THE VARIABILITY OF Z–R RELATIONS

Nikolai Dotzek[1] and Klaus D. Beheng[2]

[1]DLR–Institut für Physik der Atmosphäre, Oberpfaffenhofen, Germany
[2]Institut für Meteorologie und Klimaforschung, Universität/Forschungszentrum Karlsruhe, Germany

1. INTRODUCTION

The radar reflectivity factor at a certain height level is commonly used in radar meteorology to estimate the rain rate at the ground. Aside from other involved assumptions this method will only work if precipitation falls through purely horizontal air flow and fall speeds only depend on hydrometeor mass.

However, as noted by Battan (1976), Austin (1987), Atlas et al. (1995) and Yuter & Houze (1997) this is not the case in general. The precipitation rate (defined as the vertical hydrometeor mass flux density) is modified by convective up- and downdrafts within the precipitation core of deep convective clouds. Besides, the lower air density aloft leads to an enhanced precipitation rate for a given reflectivity factor compared to standard sea level conditions (Foote & du Toit, 1969). This paper aims at a quantification of either effect on the reflectivity factor–rain rate relations.

The problem is first addressed using analytical methods. The radar reflectivity factor Z and precipitation rate R are derived as functions of hydrometeor content ρq. The Z–R relation following from an elimination of ρq is then subjected to variations of R caused by changing air density and vertical motions.

The second part evaluates exemplary data obtained from a mesoscale simulation case study of a single Cb–cloud. The model contains a balance equation for ρq in which selfevidently effects of a vertical wind field w are considered. Also local variations of the hydrometeors' fall speed w_t due to changing air density ρ are included. Consequently, all information is available to calculate the rain rate and the Z–R relation in the most general case. As in the analytical study, the Z–R relation inherent to the cloud model formulation is first checked for the influence of variable air density and then for the effects of the modeled strong up- and downdrafts within the precipitation region of the mature shower cell.

2. ANALYTICAL APPROACH

The following normalized Γ–type spectrum is assumed for any hydrometeor class:

$$n(D) = N_0 \frac{\Gamma(4)}{\Gamma(\gamma+3)} \left(\frac{D}{D_0}\right)^{\gamma-1} e^{-D/D_0} \quad . \tag{1}$$

Here D denotes particle diameter, γ is a shape parameter, and N_0, D_0 are the spectral particle load and a measure of diameter, respectively. The parameter D_0 can easily be related to any specific measure of particle diameter, such as the volume median $D_v \approx (2.67+\gamma)\, D_0$. Note that both $n(D)$ and N_0 are given in units of m^{-4}, or conventionally in $\mathrm{mm}^{-1}\,\mathrm{m}^{-3}$. The normalization in Eq. (1) assures that the hydrometeor content ρq does not depend on the shape parameter γ:

$$\rho q = \pi \rho_h N_0 \, {D_0}^4 \quad . \tag{2}$$

Here, ρ_h denotes the hydrometeors' density. Moreover, for $\gamma = 1$ the exponential Marshall & Palmer (1948) spectrum is reproduced (Illingworth & Blackman, 1999). Eq. (2) can be used to eliminate either N_0 or D_0, depending on which spectral parameter is considered to describe the particle spectrum. We will only demonstrate elimination of D_0. For a complete discussion of both alternatives the reader is referred to Dotzek & Beheng (2000).

2.1 Radar reflectivity factor

The radar reflectivity factor (dimension m^3, or conventionally $\mathrm{mm}^6\,\mathrm{m}^{-3}$) for spherical particles under the assumption of Rayleigh's approximation is given by

$$Z = \Gamma(4)(\gamma+5)(\gamma+4)(\gamma+3) N_0 \, {D_0}^7 \quad .$$

By eliminating D_0 using Eq. (2) we arrive at the desired relationship between Z and ρq (cf. Kessler, 1969):

$$Z = \frac{\Gamma(4)}{[\pi\rho_h]^{7/4}} (\gamma+5)(\gamma+4)(\gamma+3)\, {N_0}^{-3/4} \, (\rho q)^{7/4} \quad . \tag{3}$$

In a next step we derive formulations for the rain rate and proceed from a situation with stagnant air via the case of a vertical variation of air density to consideration of up- and downdrafts.

2.2 Z–R Relation in a Deep Layer of Stagnant Air

The terminal velocity of the hydrometeors as a function of ρq will be computed by starting from a function

$$w_{t,00}(D) = w_0 \left(\frac{D}{\hat{D}}\right)^{\beta}$$

Here $\hat{D}$ is a unit diameter, usually 1 mm, and $\bar{w}_{t,00}(\rho q)$ then follows as a mass–weighted average from

$$\bar{w}_{t,00}(\rho q) = \frac{\pi \rho_h}{6 \rho q} \int_0^\infty n(D)\, w_{t,00}(D)\, D^3 \, dD$$

Corresponding author's address: Nikolai Dotzek, DLR–Institut für Physik der Atmosphäre, Oberpfaffenhofen, D–82234 Wessling, Germany; E–Mail: nikolai.dotzek@dlr.de.

However, the precipitation rate R, or vertical hydrometeor mass flux density in kg m^{-2} s^{-1} is given by

$$R = \frac{\pi}{6}\rho_h \int_0^\infty n(D) D^3 w_t(D)\, dD \quad .$$

We see further that

$$R = -w_t(\rho q)\, \rho q \qquad (4)$$

$$= -\bar{w}_{t,00}(\rho q) \left(\frac{\rho_{00}}{\rho}\right)^{0.4} \rho q \quad , \qquad (5)$$

is linked to both the terminal fall velocity and the hydrometeor content. We have split w_t from Eq. (4) into reference level value $\bar{w}_{t,00}$ and height dependence due to density stratification (Foote & du Toit, 1969). So

$$R(\rho q) = \frac{-w_0}{[\pi\rho_h]^{\beta/4}} \frac{\Gamma(\gamma+3+\beta)}{\Gamma(\gamma+3)} \hat{D}^{-\beta} {N_0}^{-\beta/4} (\rho q)^{1+\beta/4} \qquad (6)$$

is found after elimination of D_0. After some tedious calculation using Eqs. (3) and (6) the Z–R relation can be cast to the following form:

$$Z = a_{00} \left(\frac{\rho_{00}}{\rho}\right)^{-0.4\,[7/(4+\beta)]} R^{7/(4+\beta)} \qquad (7)$$

$$= a_{00}\, f(\rho)\, R^{7/(4+\beta)} = a\, R^b \quad .$$

The factor a_{00} consists of many terms depending on w_0, $\hat{D}$, N_0, and γ, but is a constant for a fixed hydrometeor spectrum. For $\beta = 1/2$, i. e. raindrops (Kessler, 1969), $Z = a_{00} f(\rho) R^{14/9}$ follows. So only the prefactor of the relation is affected by density variations $f(\rho)$. However, this $f(\rho)$–effect will be minor. The exponent b in the formal Z–R relation according to Eq. (7) can be used to schematically indicate different regimes of Z–R relations. An upper limit $b = 7/4$ follows for hydrometeors falling at a constant terminal velocity $w_{t,00}(D) = \text{const}$, i. e. $\beta = 0$. Most slopes of observed Z–R relations fall in the range $7/5 \le b \le 7/4$ where the value of $7/5$ corresponds to linear laws $w_{t,00}(D)$. The slope $b \simeq 1.55 \pm 0.05$ often reported in the literature corresponds to roughly $w_{t,00}(D) \propto D^{1/2}$, i. e. $\beta = 1/2$ and raindrop–dominated precipitation. Values of b lower than $7/5$ are seldom reported as they would correspond to $\beta > 1$ or other scarce meteorological conditions. The lower limit $b = 1$ follows both for equilibrium raindrop spectra (Sauvageot & Ochou, 2000) and spectra with a constant D_0 being also known to occurr only rarely (Waldvogel, 1974). Note that the same ranges of b were found by Dölling et al. (1998) from experimental data.

2.3 Z–R in Deep Convection

After imposing an external vertical velocity field w the precipitation rate reads

$$R = -\left[w + \bar{w}_{t,00}(\rho q) \left(\frac{\rho_{00}}{\rho}\right)^{0.4}\right] \rho q \qquad (8)$$

Without loss of generality we set

$$w = X\, \bar{w}_{t,00}(\rho q) \quad , \qquad -1 < X < \infty \quad ,$$

as any local value of w is a superposition of an imposed vertical wind and an additional downdraft component induced by the hydrometeor drag. Eq. (8) then becomes

$$R = -(X+1)\, \bar{w}_{t,00}(\rho q) \left(\frac{\rho_{00}}{\rho}\right)^{0.4} \rho q \quad . \qquad (9)$$

Inserting Eq. (9) in Eq. (7) leads to

$$Z = a_{00}\, f(\rho)\, (X+1)^{-7/(4+\beta)}\, R^{7/(4+\beta)} \qquad (10)$$

$$= a_{00}\, f(\rho)\, g(w)\, R^{7/(4+\beta)} \quad .$$

Note that again only the prefactor is affected. Compared to the $f(\rho)$–effect discussed above, $g(w)$ will modify the Z–R relation more strongly.

3. MODELING CASE STUDY

The 3D non–hydrostatic mesocale model KAMM (Adrian & Fiedler, 1991) was applied in a substantially revised and extended version. As described by Dotzek (1998, 1999) it now includes a bulk–microphysical scheme for precipitation, cloud water, and cloud ice. As for the analytical approach, all hydrometeor fall speeds in the model are subject to a variation due to density stratification according to Eq. (5) with $\rho_{00} = 1.225$ kg m^{-3}.

A single shower cloud was initiated by a moist and warm air mass; the horizontal resolution of the model was 1 km and varied in the vertical from 10 m near the ground to $\approx$ 500 m at the model top (18 km AGL). The model data analyzed here were taken from the point of maximum cloud development: the Cb–top exceeded 9 km AGL and the instantaneous rain rate at the ground was 420 mm h^{-1}. Even though Figs. 1–3 show Z–R relations for cloud ice and cloud water as well, the following evaluation is focused on the model–predicted precipitation.

3.1 Stagnant Air

Warm rain microphysics The model uses the terminal velocity formulation of Soong & Ogura (1973):

$$\bar{w}_{t,00}(\rho q) = -14.16 \left(\frac{\rho q}{\text{kg m}^{-3}}\right)^{0.1364} \text{m s}^{-1} \quad . \qquad (11)$$

Comparing to Eq. (6) this relation implies $\beta = 0.5456$, roughly in the middle of the accepted range $[0 \le \beta \lesssim 1]$ for $w_{t,00}(D)$ power laws.

While the analytical Z–R relation for rain from Eqs. (3) and (11) and the R–ρq relation in SI units read

$$Z = \frac{\Gamma(4)}{(\pi\rho_h)^{7/4}}\, 14.16^{-7/(4+\beta)} (\gamma+5)(\gamma+4)(\gamma+3)\, {N_0}^{-3/4}\, R^{7/(4+\beta)} \qquad (12)$$

$$R = 14.16 \left(\frac{\rho q}{\text{kg m}^{-3}}\right)^{1.1364} \quad . \qquad (13)$$

the same relations in conventional units for an exponential spectrum ($\gamma = 1$) and $N_0 = 8.0 \times 10^6$ m^{-4} become

$$Z = 205 \left(\frac{R}{\text{mm h}^{-1}}\right)^{1.54} , \quad R = 19.90 \left(\frac{\rho q}{\text{g m}^{-3}}\right)^{1.1364}$$

similar to Kessler (1969). The exponent $b = 7/4.5456 \simeq 1.54$ agrees very well with our analytical findings and the experimental data of Dölling et al. (1998).

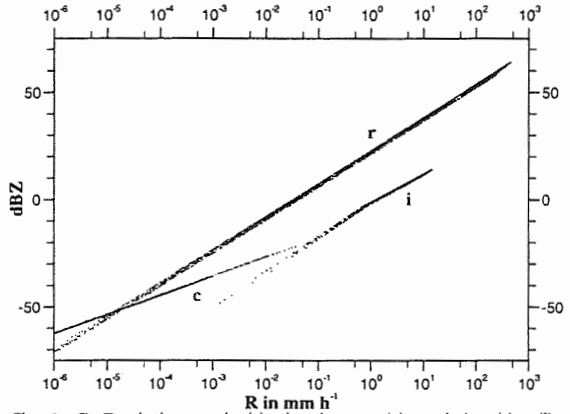

Fig. 1: Z–R relations: rain (**r**), cloud water (**c**), and cloud ice (**i**).

Fig. 1 shows this Z–R relation in a scatter plot of the model data. For all grid points within the cloud and the rain shaft, both Z and R were evaluated from the hydrometeor concentrations ρq and depicted as dots in the diagram. The letters **r**, **i**, and **c** denote the Z–R relations for rain, cloud ice, and cloud water, respectively. The latter two are only given for completeness and comparison (cf. Dotzek & Beheng, 2000).

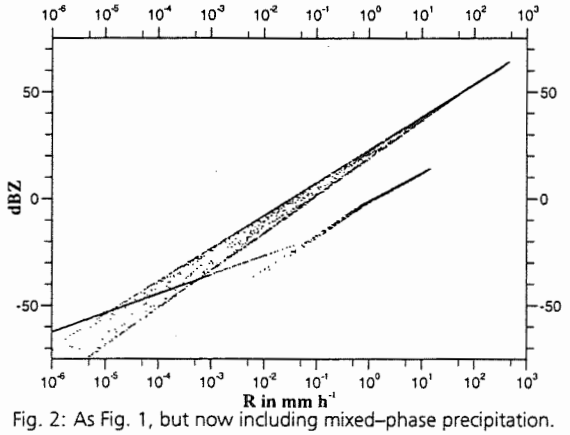

Fig. 2: As Fig. 1, but now including mixed–phase precipitation.

The KAMM model data show the above Z–R relation. Only the $f(\rho)$–effect introduces about ± 1.5 dBZ scatter for a given rain rate. Linear regression yields

$$Z = [175 \pm 25]\, R^{1.54 \pm 0.03} , \quad R = [22 \pm 2]\, (\rho q)^{1.13 \pm 0.03}$$

and shows that indeed mainly the prefactor is affected by the effects of density stratification. The small noise in the exponent must be attributed to be purely statistical — as the analytical reasoning showed, the exponent b remains unaffected by all the physical mechanisms studied here.

Mixed–phase precipitation The effects of mixed–phase precipitation were included in the model KAMM with the simple approach by Tartaglione et al. (1996): below the freezing level Eq. (11) according to Soong & Ogura (1973) is applied. For temperatures less than -35 °C a constant fall speed representative of snow/lump graupel is assumed:

$$\bar{w}_{t,00}(\rho q) = -2.5 \text{ m s}^{-1} \quad . \tag{14}$$

For $[-35°\text{C} < T < 0°\text{C}]$ a linear interpolation between Eqs. (11) and (14) is performed, while analytical evaluation with Eq. (14) yields

$$Z_e \simeq 437\, R^{7/4} , \qquad R \simeq 3.61 \frac{\rho q}{\text{g m}^{-3}} .$$

Fig. 2 depicts the consequences of the parameterization on the same data as in Fig. 1. The Z–R relation for precipitation particles is now split in two — an upper branch corresponding to Eq. (11) and a lower one with a steeper slope for the limiting case of Eq. (14). Both curves are close to another for high precipitation rates but start to diverge for $R \lesssim 1$ mm h^{-1}.

3.2 Deep Convection

The KAMM model also provides the field w at any grid point, so Eq. (8) can easily be evaluated. As the up- and downdraft speeds in the small Cb–cloud at that time were still in excess of 5 m s^{-1}, some portions of the hydrometeors were no longer falling to the ground but rising upward. These were not considered in the following evaluation. Naturally, slowly sedimenting hydrometeors like cloud ice and especially cloud water will suffer the largest loss of data points due to this effect.

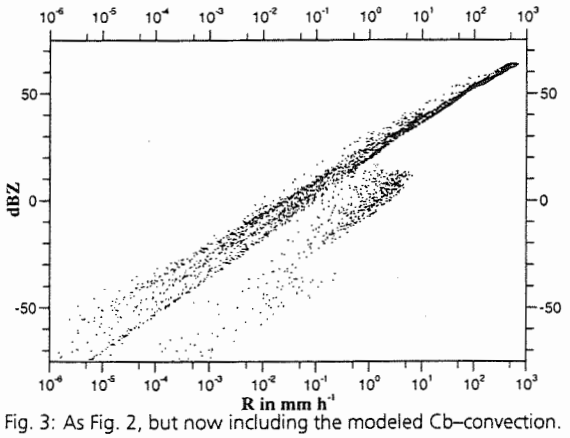

Fig. 3: As Fig. 2, but now including the modeled Cb–convection.

As shown in Fig. 3 for mixed–phase precipitation in the relevant range of $[0.1 \lesssim R \lesssim 420]$ mm h^{-1} the data from the two asymptotic cases of rain and snow/lump graupel collapse on a joint relation

$$Z = [230 \pm 100]\, R^{1.51 \pm 0.09} , \quad R = [18 \pm 7]\, (\rho q)^{1.14 \pm 0.14}$$

on average. Even for these rapidly falling hydrometeors the data are very noisy and have numerous outliers with high reflectivity factors at very small precipitation rates. These result from large hydrometeor contents within the main updraft core. For some of these data points the rain rate is reduced by a factor of 100 compared to the rain rate in air at rest. On the contrary, in the main downdraft within the rain shaft R is increased only by a factor of 2.

Comparison with Eq. (10) shows that these variations imply a range of X

$$[-0.99 \lesssim X \lesssim 2.00]$$

For more intense convective clouds with higher downdraft intensities this range would be expanded to higher positive X. But even this moderate variation in X suffices to introduce a standard deviation of ± 43 % in the prefactor of the average Z–R relation. This noise cannot be attributed to the different asymptotic relations for rain and snow: Fig. 2 shows that the spread between the two curves is small for relevant rain rates.

4. DISCUSSION

The results of the modeling study show that on average over the whole storm cloud, customary Z–R relations still hold in a statistical sense. This is also true for other stages of the 3D mesoscale simulation presented here: during cloud growth with updraft dominance more points in the Z–R scatterplot lie left of the mean relation, during decay the strong precipitation–induced downdrafts shift the data to the right of the mean state for stagnant air. While any average over a subset of the data may show significant deviations from this mean state, an average over the total storm volume will still be close to the standard Z–R relation.

Our findings coincide in principle with an experimental study of Z–R relations (Yuter & Houze, 1997). Their main conclusion was that though some far outliers may appear in a R, Z–diagram, on average the mean relationship between the two remains little affected. Furthermore, they suggested not to distinguish between "stratiform" and "convective" Z–R relations, as these tend to merge and collapse on a single relation. Also, they noted the dependence of experimentally derived Z–R relationships on the spatial scales under consideration. As noted by Atlas et al. (1995) and visible in Fig. 3 in the present study, considering only a limited volume of a storm to evaluate $R(Z)$ can produce almost any functional form.

5. CONCLUSIONS

We have studied the effects of vertical air motion and density stratification on the Z–R relation. Both analytical and mesoscale model results show that

1. Z–R relations originally applied to air at rest and sea level conditions are robust in a statistical sense even in deep convection.

2. vertical air motions as well as density variations affect the prefactor of standard Z–R relations by increasing both their average value and standard deviation.

3. for deep convection the typical variability among common Z–R relations can be accounted for by the combined effects of vertical air motions and the variation of air density with height.

4. for stratiform clouds with smaller vertical velocities and cloud depths notable differences among Z–R relations more likely stem from variations in hydrometeor spectra.

5. it is necessary to monitor the complete precipitation volume of a convective storm to obtain reliable Z–R statistics.

ACKNOWLEDGEMENTS

We are grateful to Drs. Martin Löffler–Mang, Ronald Hannesen, and Jürg Joss for many fruitful discussions.

REFERENCES

Adrian, G., F. Fiedler, 1991: Simulation of unstationary wind and temperature fields over complex terrain and comparison with observations. *Contr. Atmos. Phys.*, **64**, 27–48.

Atlas, D., P. Willis, F. Marks, 1995: The effects of convective up- and downdrafts on reflectivity–rain rate relations and water budgets. In *Proc. 27th Int. Conf. Radar Meteor.*, Vail, 19–22.

Austin, P. M., 1987: Relation between measured radar reflectivity and surface rainfall. *Mon. Wea. Rev.*, **115**, 1053–1070.

Battan, L. J., 1976: Vertical air motions and the Z–R relation. *J. Appl. Meteor.*, **15**, 1120–1121.

Dölling, I. G., J. Joss, J. Riedl, 1998: Systematic variations of Z–R–relationships from drop size distributions measured in northern Germany during seven years. *Atmos. Res.*, **47–48**, 635–649.

Dotzek, N., 1998: Numerische Modellierung topographisch induzierter hochreichender konvektiver Wolken. (In German). *Ann. Meteor.*, **37**, 465–466.

Dotzek, N., 1999: *Mesoskalige numerische Simulation von Wolken- und Niederschlagsprozessen über strukturiertem Gelände.* (In German). Dissertation, Univ. Karlsruhe, 127 pp. [Available at http://www.op.dlr.de/~pa4p/papers.html]

Dotzek, N., K. D. Beheng, 2000: The influence of deep convective motions on the variability of Z–R relations. Submitted to *Atmos. Res.*

Foote, G. B., P. S. du Toit, 1969: Terminal velocity of raindrops aloft. *J. Appl. Meteor.*, **8**, 249–253.

Illingworth, A. J., T. M. Blackman, 1999: The need to normalise RSDs based on the Gamma RSD formulation and implications for interpreting polarimetric radar data. In *Proc. 29th Int. Conf. Radar Meteor.*, Montreal, 629–631.

Kessler, E., 1969: *On the distribution and continuity of water substance in atmospheric circulation.* Meteor. Monogr., **10**(32), Amer. Meteor. Soc., Boston, 84 pp.

Marshall, J. S., W. M. K. Palmer, 1948: The distribution of raindrops with size. *J. Meteor.*, **5**, 165–166.

Sauvageot, H., A. D. Ochou, 2000: Equilibrium raindrop size distributions in heavy rain. In *Proc. 1st Conf. European Tornadoes and Severe Storms*, Toulouse, 1 p.

Soong, S.–T., Y. Ogura, 1973: A comparison between axisymmetric and slab–symmetric cumulus cloud models. *J. Atmos. Sci.*, **30**, 879–893.

Tartaglione, N., A. Buzzi, M. Fantini, 1996: Supercell simulations with simple ice parameterization. *Meteor. Atmos. Phys.*, **58**, 139–149.

Waldvogel, A., 1974: The N_0–jump of raindrop spectra. *J. Atmos. Sci.*, **31**, 1067–1078.

Yuter, S., R. A. Houze, 1997: Measurements of raindrop size distributions over the Pacific warm pool and implications for Z–R relations. *J. Appl. Meteor.*, **38**, 847–867.

CONCEPT AND FIRST TESTS OF A NEW AIRBORNE SPECTROMETER SYSTEM FOR SOLAR RADIATION MEASUREMENTS

Dörthe Müller[1], Manfred Wendisch[1], Jost Heintzenberg[1] and Dieter Schell[2]

[1]Institute for Tropospheric Research, Permoserstraße 15, 04303 Leipzig, Germany
[2]*enviscope* GmbH, Arnoldshainer Str.5, 60489 Frankfurt, Germany

1 INTRODUCTION

Aerosol particles and cloud droplets modify the transfer of solar radiation through the atmosphere by absorbing and scattering of radiation. However, there are still significant differences between the shortwave radiation measurements and the results of respective radiative transfer models, which have been extensively discussed in the literature, especially for cloudy atmospheres (*Stephens and Tsay* [1990], *Li et al. [1995]* , *Cess et al. [1995]*, *Wendisch and Keil [1999]*). Up to now the reasons for these discrepancies between measured and modeled radiation (so-called "enhanced absorption") have not been found. Two basic instrumental problems (among others) are discussed in this context: (a) missing spectral resolution of the radiation measurements, and (b) uncertainties of the irradiance measurements caused by changes of aircraft attitude during the flight.
To overcome these problems we have developed a new airborne spectrometer system with horizontally stabilized entrance optics to measure spectral up- and downwelling irradiances. The new spectrometer system (called "albedometer" in the subsequent text) covers the spectral range between 350 nm and 950 nm with a wavelength resolution of better than 2.4 nm. Unavoidable horizontal attitude changes during the flight are balanced by a stabilization system in order to get irradiances, which are generally related to a horizontal surface. Already small misalignments of the radiation sensor cause high uncertainties in measured irradiances, especially at lower sun positions. This fact is quantified in Figure 1, where the percentage deviations of irradiance measurements are shown as a function of horizontal misalignment of the entrance optics for different solar zenith angles. The calculations in Figure 1 are based on an ideal cosine response of the entrance optics and result from the relation $E[\%] = 100\frac{cos\theta - cos(\theta+\Delta\theta)}{cos\theta}$ with the solar zenith angle θ and the horizontal misalignment $\Delta\theta$.
To assure uncertainties in irradiance measurements due to misalignment of less than 1% for a wide variety of zenith angles, the irradiance sensor has to be positioned with a precision of 0.1 - 0.2 degrees relative to a horizontal plane.
The technical setup of the albedometer and preliminary results of a first aircraft field campaign carried out in November 1999 reported below for clear-sky conditions. Albeit are the major motivation for the development of the albedometer is to study cloud radiative properties.

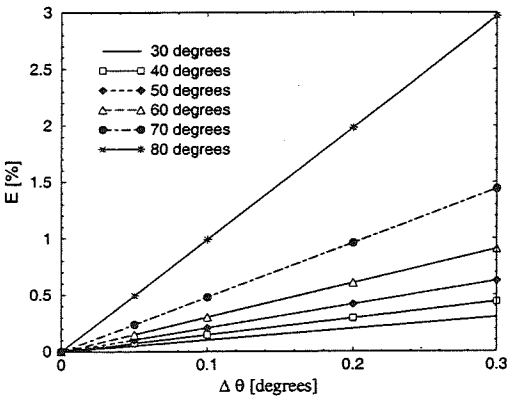

Figure 1: Percentage deviations of irradiance measurements E caused by horizontal misalignment $\Delta\theta$ of the radiation sensor for different solar zenith angles θ.

2 TECHNICAL SETUP AND TESTS

2.1 Radiation sensors

The albedometer consists of two nearly identical multichannel spectrometer modules with gratings

Corresponding author's address:
Dörthe Müller, Institute for Tropospheric Research, Permoserstraße 15, 04303 Leipzig, Germany, email: doe@tropos.de

and diode arrays designed for the visible and near-infrared spectral range. Both modules are connected via fiber optics with cosine diffusors as optical entrance, one is measuring downward and the other upward irradiances (manufactured by *Meteorologie Consult* GmbH). The upward looking cosine diffusor is horizontally stabilized and installed on the top of the aircraft, the downward looking component is fixed under the aircraft's fuselage. For technical reasons in the present version the downward looking sensor has not been stabilized yet.

The spectrometer system has been calibrated by using a 200 W tungsten halogen lamp that is traceable to an absolute standard maintained at the Physikalisch Technische Bundesanstalt with an absolute uncertainty of ± 3% in the visible and ± 5% in the UV regions. Furthermore the cosine error of the entrance optics has been determined in order to correct measurement errors caused by a non ideal cosine response of the instrument.

2.2 Stabilized platform

Even during research flights under stable meteorological conditions above the boundary layer, small roll and pitch movements of the aircraft are unavoidable. To compensate for these movements during irradiance measurements, a stabilized platform has been developed. It is a combination of a very fast and precise Artificial Horizon (AHZ), consisting of three fiber optical gyros and three accelerometers for accurate roll and pitch angles measurements, and a real-time controlled motor driven two-axis tilt-stage. Maximum range for each tilt-stage is ±6 degrees. The platform is stabilized with an accuracy of ±0.2 degrees as long as angular velocities of the aircraft movements do not exceed 4 degrees/sec.

To verify the performance of the stabilized platform in the lab, the radiation sensor on top of the two-axis tilt stage has been replaced by the sensor-head of the AHZ. In this way the AHZ was used for detecting movements of the platform. Then the tilt-stage was externally driven by a function generator to perform defined movements, which are then measured by the sensor head of AHZ. If the system is working perfectly, no differences between the generated and measured stage movements should be detected.

Several tests with artificial sinus and rectangular type movements have been performed. Each of them confirmed the proper operation of the system. Furthermore a simulation of real flight situations was carried out.

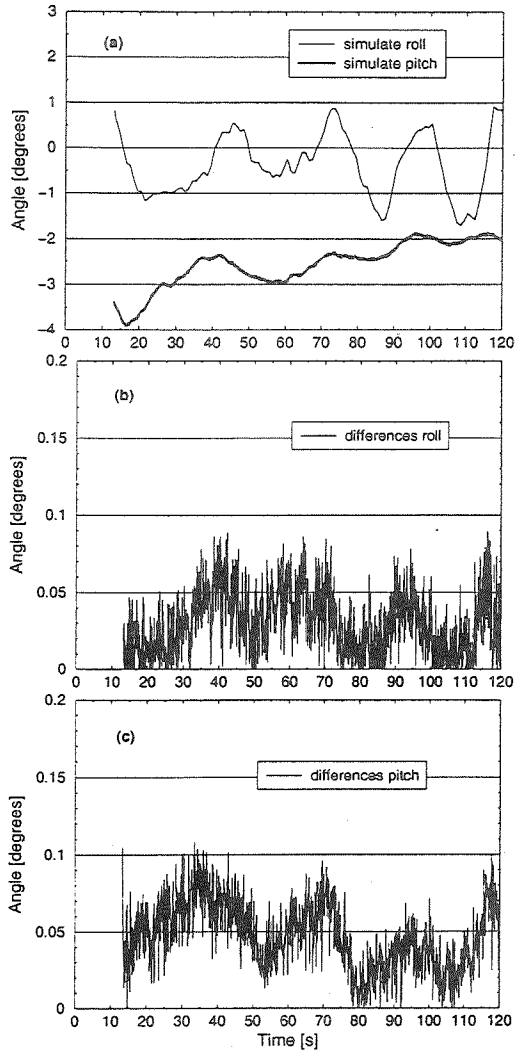

Figure 2: Lab simulation of a real flight situation under turbulent conditions. Comparison of the generated ("simulate") and detected movement of the two-axis tilt-stage (roll and pitch).

For this purpose attitude data previously recorded during actual flights have been used to move the tilt-stage according to the aircraft movements. Figure 2a shows the generated signal ("simulate") of the actual aircraft movements for both, roll and pitch axis during a short period of a flight in 3000 m altitude under stable meteorological conditions. Smooth pitch and roll angle changes are recorded. In Figure 2b and Figure 2c the absolute differences between generated (function generator)

and detected (AHZ) signals are shown for both roll and pitch angles. These deviations are mostly well below ±0.1 degrees for both angles.
A slightly different situation is depicted in Figure 3a, where the simulated data of a slow descent into the boundary layer with significant turbulence at around 1000 m altitude is shown. The roll and pitch variations are much faster compared to the previous example (see Figure 2a), which reflects the enhanced turbulence during this flight period. However, the differences between the generated angles and the response by the AHZ (Figures 3b and 3c) keep mostly below 0.15 degrees.

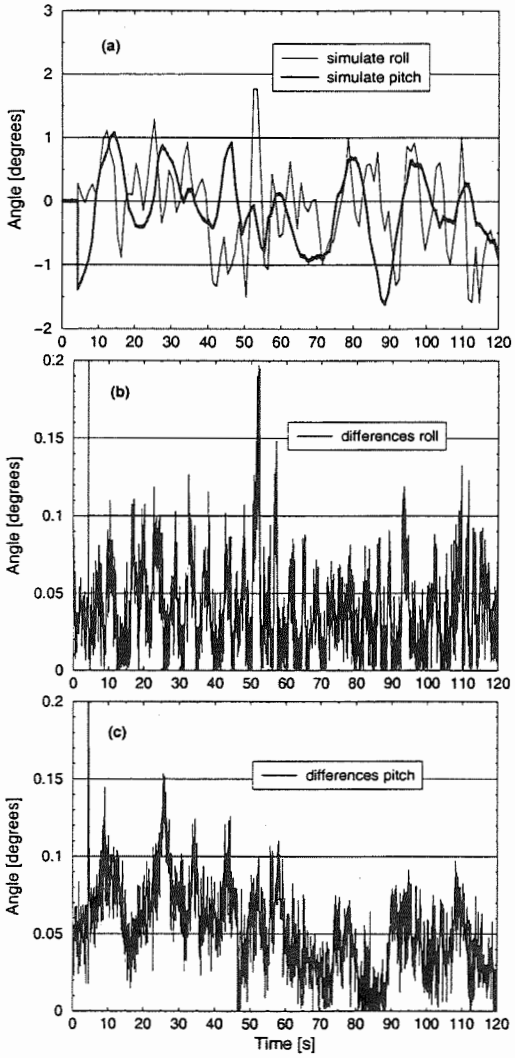

Figure 3: Lab simulation of a real flight situation under turbulent conditions. Comparison of the generated ('simulated') and detected movement of the two-axis tilt-stage (roll and pitch).

3 AIRCRAFT MEASUREMENTS

In November 1999 first field tests with the new albedometer were carried out north of Dresden, Germany (51.3N 14.1E). A small research aircraft of the type Partenavia P68B was used. Beside the albedometer and common meteorological instruments, the aircraft payload was complemented by an optical particle counter, measuring the number size distribution of aerosol particles, and several instruments measuring microphysical properties of clouds. Measurements of vertical profiles of downwelling spectral irradiances as well as microphysical parameters of particles under cloudless conditions from the ground up to an altitude of about 3000 meters are shown.

3.1 In-flight performance test

Special in-flight characterization experiments were performed in order to sound out the limits and capabilities of the horizontal stabilization platform under real flight conditions when external system accelerations occur. In one of these experiments both optical inlets were installed on top of the aircraft, one horizontally stabilized, and the other fixed. Under nearly clear-sky conditions a "dodecagon" flight pattern was carried out consisting of twelve long straight flight sections with different azimuthal orientations to the sun. Figure 4 shows the irradiance measurements during this flight at a constant altitude of 3200 meters.

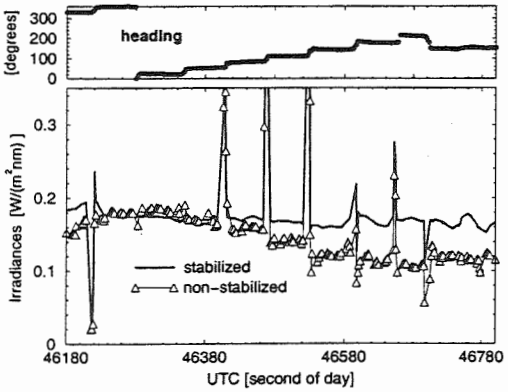

Figure 4: Comparison of downwelling spectral irradiances at 700 nm measured by stabilized and non-stabilized radiation sensors on a special dodecan flight pattern on November 16, 1999.

While the stabilized sensor delivers an almost constant irradiance level (a slight decline is attributed to the solar zenith angle change during the measurement period) the non stabilized sensor sensor clearly shows level jumps between the flight legs depending on its orientation to the sun.
Obviously, the non-stabilized sensor is also misaligned with respect to the horizontal plane. The irradiances are partly larger and partly less then those of the stabilized platform. The single conspicuous irradiance peaks correspond to sharp turns performed between the flight legs of the dodecagon in sun direction. During such drastic aircraft attitude changes the stabilization unit exceeds its limits and both sensors are not horizontally adjusted.

3.2 Measurement example

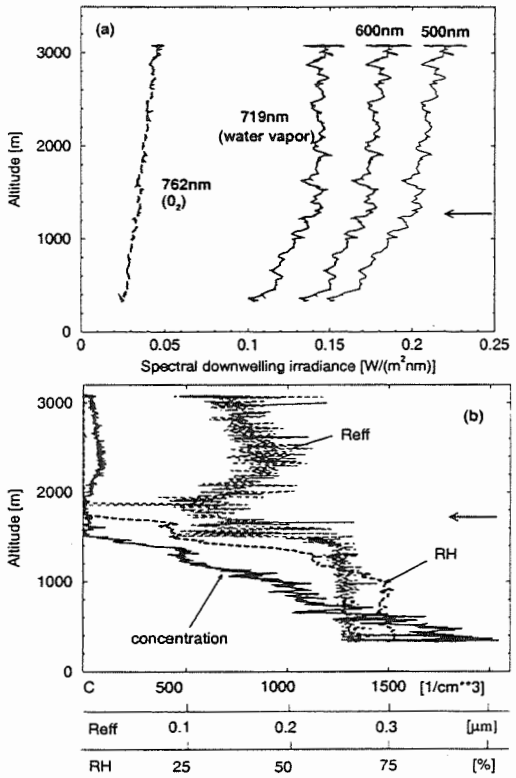

Figure 5: (a) Downwelling spectral irradiances at different wavelength's and (b) corresponding profiles of effective radius R_{eff} of aerosol particles, particle concentration C and relative humidity RH during a descent on November 17, 1999, 13:00-13:15 UTC.

We have performed descending flights under clear-sky conditions. In Figure 5a vertical profiles of downwelling spectral irradiances at aerosol (500 nm and 600 nm) as well as at gas absorption wavelengths (water vapor at 719 nm and oxygen at 762 nm) are presented. The vertical profiles of spectral irradiances at 719nm (water vapor) are obviously correlated with the relative humidity profile, which is related to the boundary layer (see RH-profile in Fig. 5b). On the other hand the aerosol channel irradiances (500 and 600 nm) show a similar strong decrease of irradiances within the boundary layer, which is a consequence of the vertical aerosol distribution, i.e. the vertikal profiles of R_{eff} and C (see Fig. 5b).
The oxygen channel (762 nm) shows less vertical variations, because O_2 absorption occures in upper atmospheric layers. As expected, there is no correlation with the boundary layer meteorological and aerosol properties.

4 CONCLUSIONS

Laboratory and first flight tests showed the possibility of airborne spectral irradiance measurements with the new albedometer system. The stabilization works properly within the given limits. Best results are achieved in stable flight situations above the boundary layer.

5 ACKNOWLEDGEMENTS

We are grateful to *meteorologie consult* GmbH for construction and help with the spectrometer system. We wish to thank U. Ihling for laboratory measurements and data processing.

6 REFERENCES

Cess, R.D. et al., Absorption of solar radiation by clouds: Observations versus models, *Science, 267*, 496–499, 1995.
Li, Z. et al., The variable effect of clouds on atmospheric absorption of solar radiation, *Nature, 376*, 486–490, 1995.
Stephens, G. L., and S.-C. Tsay, On the cloud absorption anomaly, *Q.J.R. Meteorol. Soc., 116*, 671–704, 1990.
Wendisch, M. and A. Keil, Discrepancies between measured and modeled solar and UV radiation within polluted boundary layer clouds, *JGR, 104*, 27373–27385, 1999.

RADIATIVE PARAMETERS FROM CLOUD PROFILING RADAR

Karine Caillault[1] and Jacques Testud

Centre d'étude des Environnements Terrestre et Planétaires, Vélizy, 78140, France

1. INTRODUCTION

Clouds play an important role in the dynamics of the global atmosphere through their influence on the radiative budget. But cloud layering and microphysics are not well represented in atmospheric Global Circulation Model (GCM).

Thus, it is necessary to operate spaceborne, airborne or ground-based instruments to obtain a large range of datasets that will allow to document the cloud characteristics.

This paper is focussed on the retrieval of the profiles of pertinent parameters to define radiative properties of clouds from a reflectivity profile measured by a single frequency cloud radar. These radiative parameters are: the liquid water content (LWC) or Ice Water Content (IWC) and the effective radius (r_e).

2. INVESTIGATING STATISTICAL PROPERTIES OF THE PSD

The physical characterization of an observed cloud particle size distribution (PSD) raises three questions:

(i) What liquid water content LWC (or ice water content IWC, if solid particles) corresponds to this PSD?

(ii) What is the "mean" particle diameter?

(iii) What is the "intrinsic" shape of the PSD?

The liquid water content relates to the cloud droplet size distribution $N(D)$ [D: droplet diameter] as:

$$LWC = \frac{\pi\rho_w}{6}\int_0^\infty N(D)D^3 dD \qquad (1)$$

where ρ_w is the density of water. The expression of the ice water content *IWC* is more complex since it depends on particle density and shape. We will use hereafter the formulation by Francis et al.(1998) who calculates the *IWC* from the microphysical observations as:

$$IWC = \frac{\pi\rho_w}{6}\int_0^\infty N(D_{eq})D_{eq}^3 dD_{eq} \qquad (2)$$

where D_{eq} is the "equivalent melted diameter", and $N(D_{eq})$ is the PSD in equivalent melted diameter. D_{eq} is empirically related to the cross sectional area A of the ice particle observed by the 2D probes through:

$D_{eq} = 1.097\ A^{0.50}$ if $A \le 0.0052$ mm^2

$D_{eq} = 0.615\ A^{0.39}$ if $A > 0.0052$ mm^2

The characterization of the mean particle size is more subjective. Ideally we should consider the effective particle radius r_e defined for a spectrum of liquid cloud droplets as:

$$r_e = \frac{3}{2}\frac{1}{\rho_w}\frac{LWC}{2A_c} = \frac{M_3}{2M_2} \qquad (3)$$

where A_c is the integral of A over the PSD, and M_3 and M_2 are respectively the third and second moment of $N(D)$. However, for ice the effective radius is written as:

$$r_e = \frac{3}{2}\frac{IWC}{3\rho_i A_c} \qquad (4)$$

which cannot be expressed simply in terms of "moments" of $N(D_{eq})$.

In the following we prefer characterizing the mean particle size by the "volume weighted mean diameter" (usually referred to as the "mean volume diameter" in the literature) defined as:

$$D_m = M_4 / M_3 \qquad (5)$$

where M_4 and M_3 denote the fourth and third moment of the PSD in D if liquid droplets, or in D_{eq} if ice particles.

Thus we defined the normalization of the PSD from the general form:

$$N(D) = N_0^* F(D/D_m) \qquad (6)$$

where N_0^* is the normalization parameter along concentration axis, D_m the normalization parameter along diameter axis and $F(X)$ is the "normalized PSD" describing the "intrinsic" shape of the PSD (noting $X = D/D_m$). For an ice particle spectrum D stands for D_{eq}.

By virtue of (6), $F(X)$ verifies:

$$\int_0^\infty F(X)X^4 dX = \int_0^\infty F(X)X^3 dX \qquad (7)$$

While (1) [or (2) for an ice particle spectrum] provides:

$$\int_0^\infty F(X)X^3 dX = \frac{6}{\pi\rho_w}\frac{LWC}{N_0^* D_m^4} \qquad (8)$$

In order to obtain a normalized function F independent of *LWC* and D_m, we should require that:

$$\int_0^\infty F(X)X^3 dX = C \qquad (9)$$

where C is an arbitrary constant.

[1] Corresponding author's address: Karine Caillault, CETP, 10-12 avenue de l'Europe; 78140 Vélizy; France
E-mail: caillault@cetp.ipsl.fr

A "natural" value to assign to the arbitrary constant C is $C = 6/(\pi\rho_w)$, such that the "normalized LWC" associated to the "normalized PSD" be equal to 1. However, we will show that this is not the best value for C, for the reason explained hereafter. It follows from (8) and (9) that N_0^* is defined by:

$$N_0^* = \frac{6}{C}\frac{1}{\pi\rho_w}\frac{LWC}{D_m^4} \quad (10)$$

When the PSD is an exponential of the form $N(D) = N_0 \exp(-\Lambda D)$, it may be easily shown that $F(X) = \exp(-4X)$, and that:

$$N_0^* = \frac{1}{C} N_0 \frac{\Gamma(4)}{4^4} \quad (11)$$

It is obviously interesting to define C such that N_0^* equals N_0 when the PSD is exponential, thus C should be set to:

$$C = \frac{\Gamma(4)}{4^4} \quad (12)$$

and:

$$N_0^* = \frac{LWC}{\pi\rho_w}\frac{4^4}{D_m^4} \quad (13)$$

3. NORMALIZED PSD IN ICE CLOUDS OBSERVED DURING CLARE98.

CLARE98 (CLoud And Radiation Experiment-1998) deployed various observing systems for clouds and radiation at Chilbolton (England) in October 1998 (Wursteisen and Illingworth,1999). The ground based experiment (including various meteorological radars and passive microwave observations) was coordinated with flights of three aircraft: the C130 of the UKMO[1], the Falcon of the German DLR[2], and the Fokker 27 "ARAT" of the French INSU[3]. For the purpose of this paper, we are particularly interested in the C130 flights. The C130 performed microphysical sampling from 2DP, 2DC and FSSP probes in ice clouds at various altitude levels.

In this section we would like to report some results obtained from analyzing cloud ice particle spectra observed from the C130 using the approach described in section 2.

Figure 1.-a and b show examples of normalized PSD obtained from ice particle spectra sampled at –32°C and –9°C, respectively. Each spectrum is integrated over 60s (i.e. 7.2 km). Note the remarkable stability of the PSD normalized shape between the various spectra collected at a given temperature. Meanwhile there is a significant difference in shape between –32°C and –9°C, which suggests to look for a model stratified in temperature.

[1] United Kingdom Meteorological Office
[2] Deutschen Zentrum für Luft- und Raumfahrt
[3] Institut National des Sciences de l'Univers

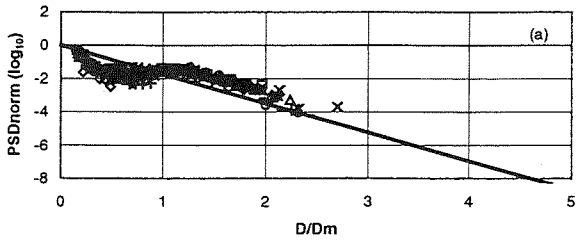

Figure 1-a: Normalized PSD for the legs of CLARE98 at -32°C

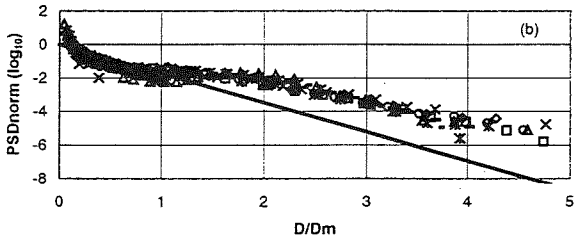

Figure 1.-b: Normalized PSD for the legs of CLARE98 at -9°C

At the opposite of this stability in shape, the normalization parameters N_0^* and D_m appear very variable and poorly correlated between themselves, as shown in the scatter plot of Figure 3 .

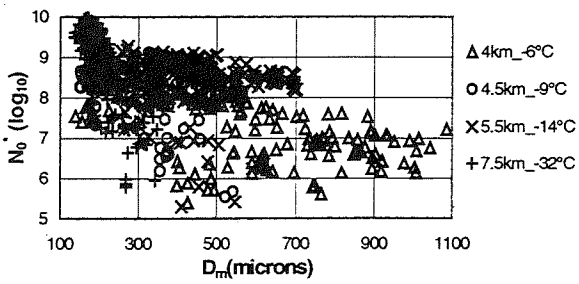

Figure 3: Scatter plot of N0 versus D_m for the CLARE98 microphysical database*

In future work it would be essential to check if the stability of the shape of the PSD found for the CLARE98 data set maintains when our analysis is applied to others data sets (with different cloud types, corresponding to different climatic zones, etc.). A key point in particular would be to check if the temperature suffices to define the shape of the normalized PSD.

4. INVERSE MODEL FOR RADAR RETRIEVAL

The radiative parameters retrieval is not possible from a single reflectivity profile, so it is necessary to build a microphysical model from in-situ microphysical data sets.

The data used in this study are, at the first step, the CLARE98 microphysical in-situ measurements.

From a fit of the observed scatter plot between the N_0^* and IWC displayed in Figure 5, we get a power law between these two parameters:

$$N_0^* = aIWC^b \quad (14)$$

where a and b are function of the temperature.

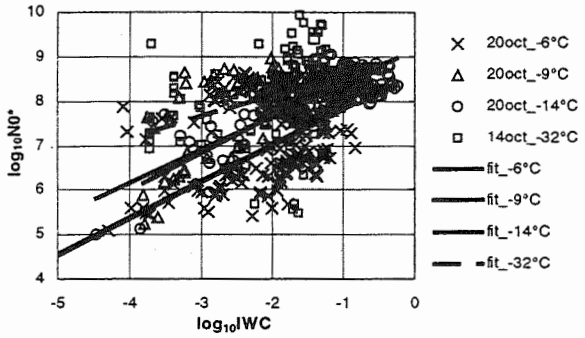

Figure 5: Scatter plot of N_0^* versus IWC from in-situ microphysical CLARE98 dataset

Combining Eq. (13) and (14), we get N_0^* and D_m as a function of IWC and thus the PSD. From the PSD, we can calculate every integrated parameter: physical parameters such as the effective radius or LWC and IWC, or instrumental parameters such as the equivalent radar reflectivity Z_e or the specific radar attenuation K that can also be expressed in term of PSD:

$$Z_e \propto \int N(D)\sigma_r(\lambda,D)dD \quad [mm^6.m^{-3}] \quad (15)$$

where σ_r is the backscattering cross section and λ the wavelength.

$$K \propto \int N(D)\sigma_a(\lambda,D)dD \quad [dB.km^{-1}] \quad (16)$$

where σ_a is the absorption cross section.

As we have seen in section 3, there is a systematic variation of the PSD shape with the temperature. Despite this fact, Figs 4-a, b and c show that for the CLARE98 dataset, the normalized relationships between Z_e and IWC, K and IWC, and K and Z_e are almost functional. This demonstrates the robustness of our inverse model, funded upon the following set of power-law relationships:

$$Z_e = c(N_0^*)^{1-d}IWC^d \quad (17)$$

$$K = e(N_0^*)^{1-f}IWC^f \quad (18)$$

$$K = p(N_0^*)^{1-q}IWC^q \quad (19)$$

where the power laws parameters are function of temperature.

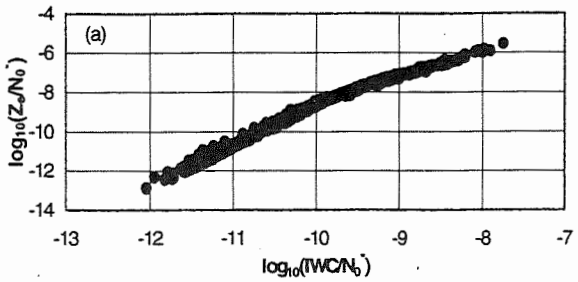

Figure 7-a: Scatter plot of normalized Z_e versus normalized IWC from in-situ microphysical CLARE98 dataset

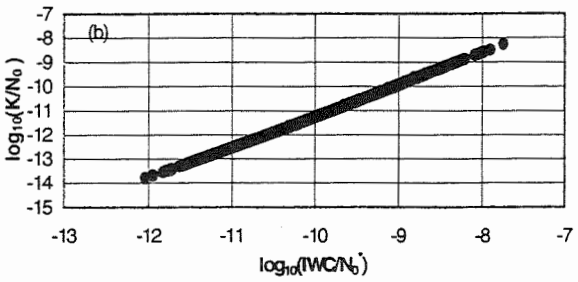

Figure 4-b: Scatter plot of normalized K versus normalized IWC from in-situ microphysical CLARE98 dataset

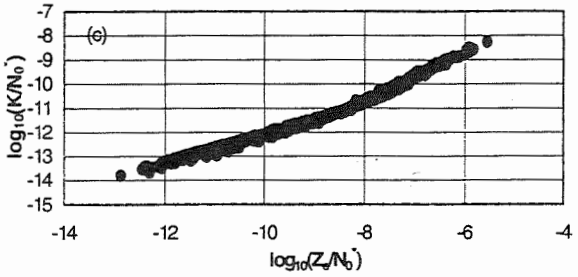

Figure 4-c: Scatter plot of normalized K versus normalized Z_e from in-situ microphysical CLARE98 dataset

The same kind of relationships can be established for combined instruments, in particular for studies based on radar-lidar measurements (Tinel and Testud, 2000). Indeed, the lidar extinction coefficient is also an integrated parameter and can be expressed as:

$$\alpha = \frac{\pi}{2}\int N(D)D^2.dD \quad (20)$$

An example of the normalized relationship between normalized α and the normalized radar specific attenuation K is given in Fig. 5 for the CLARE98 data.

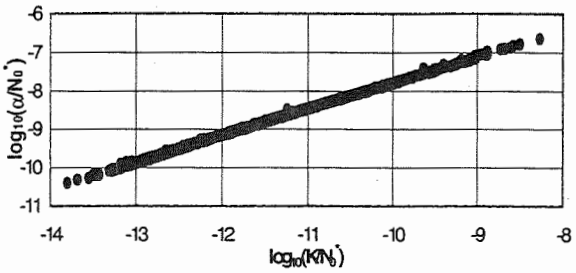

Figure 8: Scatter plot of normalized α versus normalized K from in-situ microphysical CLARE98 dataset

5. RADIATIVE PARAMETERS RETRIEVAL

Thanks to the inverse model, we can retrieve, from a reflectivity profile, the interesting parameters to appreciate the cloud effect on the radiative budget of the atmosphere: the LWC or IWC and the effective radius.

We show here the preliminary results of the radiative parameters retrieval. The chosen reflectivity profile displayed in Figure 9, has been measured by a zenith-pointing radar located in the South Great Plains site of the ARM (Atmospheric Radiation Measurements) program on 25 April 1998 at 1300 UTC.

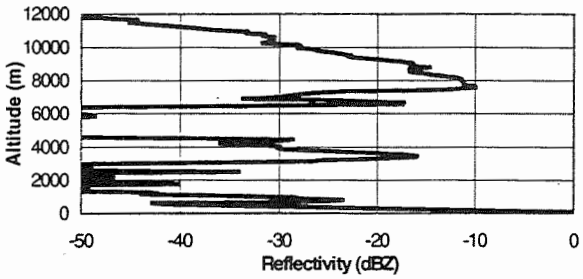

Figure 9: Reflectivity profile at ARM-SGP on 25 April 1998 at 13 UTC.

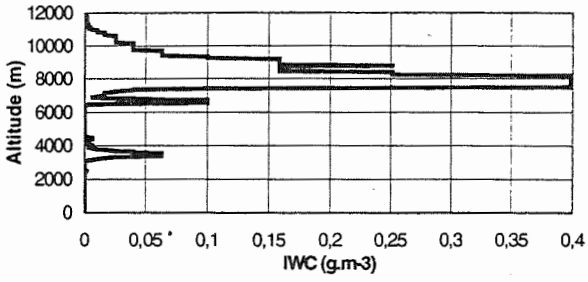

Figure 11-a: IWC profile corresponding to the reflectivity profile shown in Fig.6

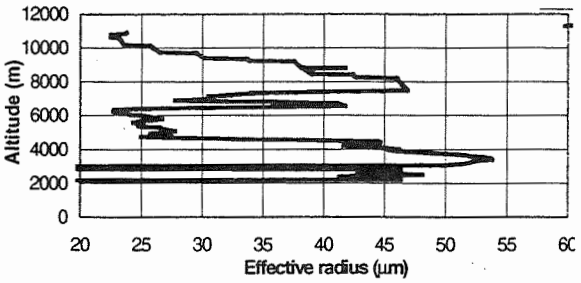

Figure 7-b: Effective radius profile corresponding to the reflectivity profile shown in Fig.6.

The retrieved radiative parameters corresponding to this profile are shown in Figure 11-a and b for IWC and effective radius respectively.

There is a good consistency between the radiative parameters profiles and the reflectivity profile. Values of IWC and effective radius are in good agreement are consistent with what it is usually observed in ice clouds.

6. CONCLUSION

The first results obtained in the radiative parameters retrieval are promising. They comfort the robustness of the inverse model, raised by the study of the normalized parameters relationships.

Further work will consist in extending the analysis to other microphysical data sets to test the degree of generality of the inverse model.

7. ACKNOWLEDGEMENTS

Reflectivity measurements were obtained from the Atmospheric Radiation measurements (ARM) program sponsored by the U.S. Department of Energy, Office of Science, Office of Biological and Environmental Research, Environmental Sciences Division.

8. REFERENCES

Francis, P. N., A. Jones, R. W. Saunders, K. P. Shine, A. Slingo and Z. Sun, 1994: An observational and theoretical study of the radiative properties of cirrus: Some results from ICE'89. *Q. J. R. Meteorol. Soc.*,**120**,809-848.

Tinel, C. and J. Testud, 2000: Synergy in ice clouds between airborne nadir-pointing radar and lidar. *Proceedings of the 13th International Conference on Clouds and Precipitation, Reno,Nevada.*

Wursteisen, P. and A. Illingworth, 1999: CLARE'98 Campaign Summary. Proceedings of the CLARE'98 International Workshop, ESTEC, Noordwijk, The Netherlansd, 13-14 September 1999, pp 9-13.

PLUDIX: AN X-BAND SENSOR FOR MEASURING HYDROMETEORS SIZE DISTRIBUTIONS AND FALL RATE

F. Prodi[1][2], A. Tagliavini[3], F. Pasqualucci[4]

[1] University of Ferrara, Dept. of Physics, Ferrara, Italy
[2] ISAO-CNR, Clouds and Precipitation Group, Bologna, Italy
[3] ADA Applicazioni Digitali e Analogiche, Bologna, Italy
[4] Raytheon Corporation, office of Rome, Rome, Italy

1. INTRODUCTION

The performance of a multi-hydrometeor sensor based on an low-power, continuos wave doppler radar is presented and discussed. The MW beam is backscattered by the hydrometeors (rain drops, groupel, hail, snowflakes etc) in free fall. The backscattered signal is formed by many different frequencies in dependence of fall velocity (doppler shift) while the amplitude depends on the refractive index of the hydrometeors and their concentration in the effective volume seen by the instrument.
The hydrometeors are classified in size ranges and in intensity as for the contribution in each size range.
The capabilities of discriminating among different hydrometeors is demonstrated and there is the possibility of using it as a "meteo sentinel" in ground networks of hydrological instruments.
The advantages with respect to other instruments based on different physical principles (simple maintenance, no effect of simultaneous hydrometeors, sensitivity to smallest sizes) are shown. Potential applications are also envisaged to radar calibration, agriculture, soil physics etc.

2. INSTRUMENT FUNCTIONS

Pludix is a multifunctional instrument for monitoring and characterising atmospheric precipitation on the ground with high sensitivity and fast response. It can be operated automatically and has low maintenance requirements

- Monitors precipitation.
- Identifies precipitation type (rain, snow, hail, drizzle).
- Provides hydrometeor size distribution (for drops, snowflakes, hailstones); this is called disdrometric function.
- Measures instantaneous rainfall rate.
- Gives the total rainfall in a given time interval.

The knowledge of hydrometeor size distribution (disdrometric function) is crucial in investigating, or forecasting, such events and occurrences as soil erosion and percolation, landslides, evapotranspiration, plant physiology, spring seepage etc., or in several other applications, such as in meteorological radar calibration, in defining reflectivity vs rainfall rate relationships, etc..

Corresponding author's address: Franco Prodi, Institute ISAO-C.N.R., Clouds and Precipitation Group, Via Gobetti, 101, 40129, Bologna, Italy, E-mail: f.prodi@isao.bo.cnr.it

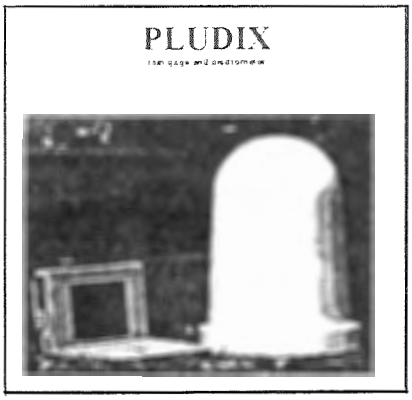

Fig. 1: The Pludix instrument

2.1 Characteristics of the instrument PLUDIX

It can operate automatically and can be connected in networks for operation in remote areas; it is highly reliable.
The detection and characterization of a precipitation and its characterization in PLUDIX is based on the fact that each precipitation type (rain, snow, hail) has its own Doppler spectrum. So for each precipitation type a different algorithm is selected to determine size distribution and intensity.
The instrument has a discdrometric function; it measures the size of the hydrometeors falling in a well defined volume (about 3 m high and 1 m wide) above it. The hydrometeors are classified in variable size intervals (e.g. 0.3 mm for intermediate size drops). In each size the average concentrations (m-3) and its contribution to the total precipitation intensity (in mm h-1) is given. It also has a rain gage function; by integration of the disdrometric function the instrument is providing the instantaneous rainfall rate and the total amount in a given time interval.
The instrument is made of a sensor located in a waterproof Fiberglass container to be placed outside, connected by a cable to the power supply/signal processing unit.

2.2 Characteristics of the sensor

The sensor is shown on the front cover page with a portable PC. The upper part of the container (dome) is shaped in order to minimize dry deposition and snowcover, and can be heated. The length of the cable connecting the sensor with the power supply/signal processing unit can be extended to several tens of meters. The sensor is an X band continuous wave, low power (10 mW) Doppler Radar (9.5 GHz frequency of operation). The radar electronics are hosted in a custom made microwave module tuned to the proper sensitivity to detect the weakest precipitation. The MW beam emitted by an upward oriented antenna is backscattered by hydrometeors in free fall. Near the ground each hydrometeor has reached an aerodynamic equilibrium and falls at a constant terminal velocity only as a function of its size. The backscattered signal at the receiving antenna is comprised of many components that are shifted in frequency from the transmitted signal depending on the hydrometeors' terminal velocities (Doppler effect). The amplitude of these components is a function of the reflectivity of the hydrometeors and their concentrations in the volume seen by the sensor. Since a given drop at terminal velocity is not generating a constant but rather a variable doppler echo depending on its position in space, a special algorithm has been developed which obtains the hydrometeor size distribution from the signal spectrum and hence the parameters characterizing the precipitation.
There is the possibility of updating the software to cope with the evolution of the signal processing algorithms.
Advantages:
With respect to optical disdrometers:

- simplicity and lack of maintenance;
- lower cost.

With respect to electromechanical disdrometers:

- no difficulty in distinguishing simultaneously or almost simultaneously falling drops;

With respect to rain gages

- low precipitation intensity detected;
- no clogging of the funnel by leaves, feathers and other objects;
- no maintenance (waterproof bell shaped container);
- specific response for snow and hail;
- disdrometric ability.

The signal processing unit communicates to the outside through a serial port RS232C, which can be used to connect the instrument to the data transmission system (in the field) or to a PC for archiving and visualization (in the lab).

PLUDIX has been patented n. MI 99A 001 906.

http://users.iol.it/nubila/plud_en.html
http://users.iol.it/nubila/

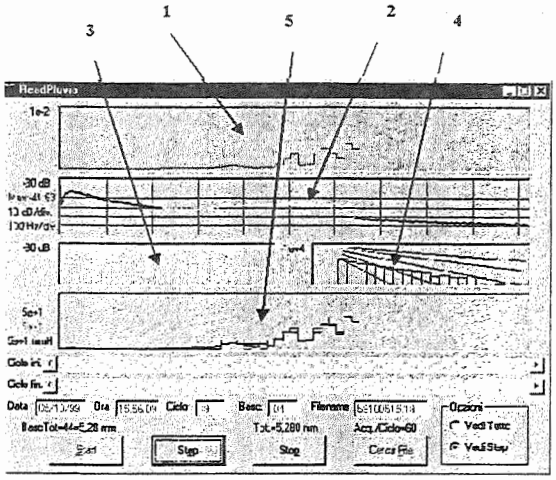

Figure 1

Fig. 2: Rainfall event instrument display

Rainfall event instrument display:

1. Total received power vs time (1 step, 1 min);
2. Power spectrum in the running time interval (1 min), 100 Hz/div in abscissa;
3. power spectrum in the size ranges;
4. Logarithmic presentation of drop concentration vs size. Note the agreement with the yellow line which shows the Marshall-Palmer distribution for the given precipitation intensity;
5. Precipitation intensity vs time (1 div, 1 min) superimposed with intensity measured by the tipping bucket rain gage.

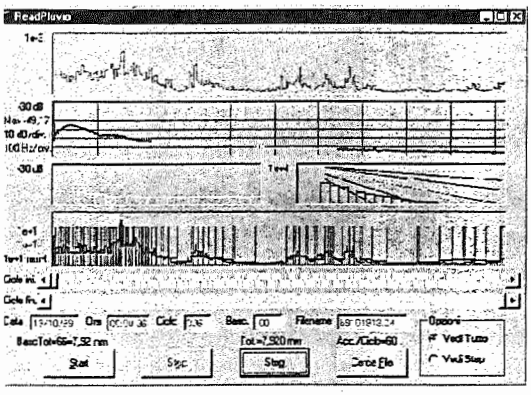

Figure 2

Fig. 3: Full duration rainfall event presentation (24 hours). In the lowest diagram the agreement of PLUDIX rainfall intensity (in red) with conventional tipping

ON REMOTE SENSING OF STRATIFORM CLOUDS: INSIGHT FROM LARGE-EDDY SIMULATIONS

Mikhail Ovtchinnikov and Yefim L. Kogan

School of Meteorology and Cooperative Institute for Mesoscale Meteorological Studies (CIMMS)
University of Oklahoma, Norman, Oklahoma

1. INTRODUCTION

Satellite and ground-based remote sensing is a basis for obtaining the global distribution of cloud properties needed for climatological studies. Despite the rapidly increasing number of retrieval algorithms using a variety of platforms (e.g., radar, lidar, passive microwave radiometer (MWR), etc.), verification of these retrievals remains a challenge. It has been impeded largely by the lack of in situ (aircraft) microphysical measurements taken in the same cloud volume as sensed by remote instruments. Such comparisons are hard to obtain because of fundamental differences between these probing techniques, including the enormous disparity in sampled cloud volumes as well as difficulties in accurate space-time coordination. An alternative approach to evaluate the performance of various retrieval algorithms and their assumptions is to use three-dimensional cloud model simulations.

In this study, droplet size distributions (DSD) generated by a large-eddy simulation (LES) model for a number of selected case studies are used to compute a 3-D field of the radar reflectivity factor (Z) and 2-D fields of visible optical depth (τ) and vertical liquid water path (P). From these, vertical profiles of cloud liquid water content (W) and effective radius (r_e) are retrieved and compared to the ones calculated directly from the simulated DSDs. In contrast to observational data, simulated fields have no errors introduced by instruments or inadequate sampling, since both Z and W are calculated from the same DSD. This approach therefore highlights discrepancies between the retrieved and true profiles that are purely due to assumptions and approximations included in the retrieval algorithms. The advantage over the earlier studies that used only measured DSD (e.g., Fox and Illingworth (1997)) is that having a complete and coherent three-dimensional cloud structure enables a more consistent comparison than those based on selective aircraft measurements.

* *Corresponding author address*: Mikhail Ovtchinnikov, CIMMS, University of Oklahoma, 100 E. Boyd, SEC, Rm.1110, Norman, OK 73019; e-mail: mikhail@ou.edu

Retrievals evaluated here are intended for use with millimeter wavelength radars. Detailed spatial resolution and high sensitivity of these so-called "cloud radars" contribute to broadening of their applications during the last decade, particularly in studies of boundary layer clouds. The Atmospheric Radiation Measurement (ARM) Program has employed several vertically pointing 35-GHz (wavelength of 0.86 cm) Doppler radar systems for continuous cloud observations at various locations around the globe.

2. MODEL AND CASE STUDY DESCRIPTION

A case study of the continental stratus layer observed on April 30, 1994 over north-central Oklahoma during the intensive Observation Period (IOP) of the ARM program was conducted using the CIMMS LES cloud model. The model combines the 3-D dynamics with explicit (size-resolving) formulation of the liquid phase microphysical processes (Khairoutdinov and Kogan, 1999). The thermodynamic state is described in terms of the virtual liquid water potential temperature and the total water mixing ratio. The one and a half order turbulence closure is based on the prognostic equation for the subgrid scale turbulent kinetic energy.

Cloud physics processes are treated based on the prediction equations for cloud particle spectra. The spectra of the basic cloud particles are taken into consideration: cloud condensation nuclei (19 categories), cloud and drizzle drops (25 categories). The equations for particle size distribution functions include processes of advection, sedimentation, turbulent mixing, and individual microphysical processes of nucleation, condensation/evaporation and stochastic coagulation. The solar heating and longwave cooling rates at each grid point and at each time step are calculated using the computationally efficient broadband radiation package. The model is initialized with environmental sounding, large-scale subsidence, and characteristics of the underlying surface including temperature or heat flux. The cloud microphysics is determined by the concentration and activation spectrum of cloud condensation nuclei that are either specified from measurements or parameterized using typical values for specific locations.

Earlier case studies showed that the model realistically reproduces dynamical, turbulence, radiative, and microphysical cloud parameters, including the position and magnitude of the maximum, as well as the overall shape of the observed droplet size distribution throughout the cloud (Khairoutdinov and Kogan, 1999).

The simulation was conducted with model resolution of 33 m in vertical and 75 m in both horizontal directions covering the 3 x 3 km^2 domain that is 2-km high. For comparison, the range resolution of the ARM cloud radar when sampling boundary layer clouds is 45 meters.

3. RETRIEVAL OF LIQUID WATER PROFILE

The basic parameter provided by radar measurements is a reflectivity factor Z as a function of distance, or, in the case of vertically pointing radar, height. While Z contains some information about cloud and precipitation particle spectra (namely, Z is proportional to the sixth moment of particle size), other measurements and/or assumption are needed to retrieve DSD. For many practical applications, clouds can be adequately described by several bulk or integrated parameters among which the liquid water content, W, is the most commonly used. A universal Z-W relation is often sought in the form of the power law

$$Z=aW^b. \qquad (1)$$

By varying coefficients a and b different algorithms can be obtained. When both coefficients are fixed, (1) represents a one-parameter retrieval algorithm in which LWC is determined by the reflectivity alone. Ovtchinnikov and Kogan (2000) showed that such algorithms lack versatility. They often can produce adequate results in one or several situations but perform poorly when cloud microphysical conditions change.

Some of these limitations can be eliminated by using an adjustable a in (1). This coefficient has been related to a second independently measured parameter such as cloud drop number concentration, N, (Liao and Sassen 1994) or vertically integrated liquid water path, P (Frisch et al. 1998). For example, if P is known, a mean W profile can be retrieved from Z by averaging individual profiles calculated from

$$W(h_i)=\frac{P}{\Delta h\sum_i[Z(h_i)]^{1/b}}[Z(h_i)]^{1/b}, \qquad (2)$$

where the summation is performed over the depth of the cloud layer and Δh is the distance between adjacent range gates of the radar, h_i. Parameter b still has to be specified *a priory*. It can be easily shown that if DSD has a lognormal or gamma distribution shape, and concentration and relative dispersion do not change with height, then b=2 (Frisch et al. 1998). In the two case studies representing typical marine and continental stratiform clouds, Ovtchinnikov and Kogan (2000) found that the retrieval errors are minimizing when b=1.32. The performance of these retrieval algorithms on the simulated data set is illustrated in Fig. 1 that shows the domain averaged LWC profiles.

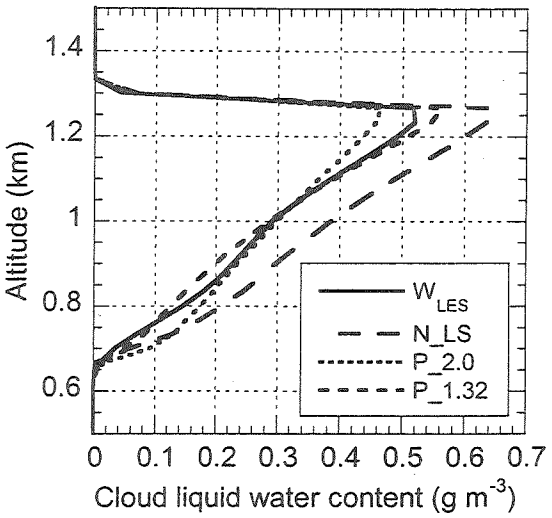

Fig. 1. *Cloud LWC profiles retrieved using algorithm (2) with b=1.32 (P_1.32) and b=2 (P_2.0). Liao and Sassen (1994) method using real N (N_LS) as well as the LES benchmark profile (W_{LES}) are also shown.*

4. RETRIEVAL OF EFFECTIVE RADIUS PROFILE

The droplet effective radius r_e defined as

$$r_e=\frac{\int r^3 n(r)dr}{\int r^2 n(r)dr}, \qquad (3)$$

where $n(r)$ is DSD. r_e is an important parameter in cloud-radiation parameterizations in mesoscale and general circulation models. Although it is recognized that the vertical variations of r_e may significantly affect outcome of such parameterizations, the assumption of constant r_e is commonly used in today's models. This simplification is caused in part by the limited data on the r_e-height dependence obtained primarily from expensive aircraft sampling of relatively small number of clouds. It is therefore important to be able to determine the vertical profile of r_e using remote sensing that has a potential to sample much larger cloud volumes.

Since W is a function of the third and the extinction coefficient ε is a function of the second moment of the DSD, r_e can be expressed as

$$r_e=\frac{3Q_e}{4\rho_w}\frac{W}{\varepsilon}, \qquad (4)$$

where ρ_w is the density of liquid water and Q_e is the extinction efficiency of the droplets (assumed constant independent of droplet size).

By assuming a power law relationship between Z and ε in the form

$$Z=c\,\varepsilon^{d}, \qquad (5)$$

the vertical profile of ε can be obtained from Z and the cloud optical depth τ:

$$\varepsilon(h_i)=\frac{\tau}{\Delta h\sum_i[Z(h_i)]^{1/d}}[Z(h_i)]^{1/d} \qquad (6)$$

We find that the best for the retrieval of ε using (6) is obtained for d=1.75 ($1/d$=0.57). The lognormal approximation of the droplet spectra yields d=3.

Using (4), the retrievals (2) and (6) can be combined to give the profile of r_e:

$$r_e(h_i)=\frac{3Q_e}{4\rho_w}\frac{P}{\tau}\frac{\sum_i[Z(h_i)]^{1/d}}{\sum_i[Z(h_i)]^{1/b}}[Z(h_i)]^{1/b-1/d}. \qquad (7)$$

The results of the r_e retrieval from simulated measurements are presented in Fig. 2. The difference between the two considered algorithms is insignificant; both give an accurate result.

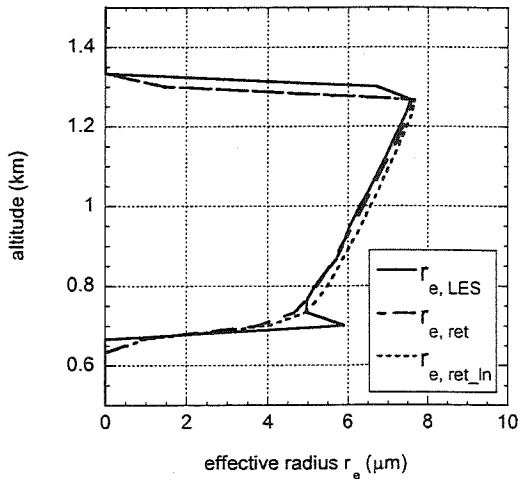

Fig. 2. *Retrieved profiles of the effective radius using algorithm (7) with b=1.32 and d=1.75 ($r_{e,\,ret}$) and b=2 and d=3 ($r_{e,\,ret\_ln}$). The LES benchmark profile ($r_{e,\,LES}$) is also shown.*

By calculating Z and r_e from cloud droplet spectra measured by the Forward Scattering Spectrometer Probe (FSSP), Fox and Illingworth (1997) found that the relation of the form

$$Z\sim r_e^{\,f}, \qquad (8)$$

is best fitted to points when f=4.09 although the scatter on their Z - r_e plot was large. For r_e averaged over 2.5-dBZ bins, they found that f=5.65 ensures higher correlation.

By comparing (7) and (8), we find that $f=bd/(d-b)$. Thus, for our algorithm, f=5.37 (b=1.32 and d=1.75), while under the lognormal approximation f=6 (b=2 and d=3). Fox and Illingworth's estimate lies between these values and, therefore, is equally appropriate.

For the 30 April 1994 case, the retrieval was tested using reflectivity measurements collected by the University of Massachusetts Cloud Profiling Radar System. P was derived using aircraft data. We used τ derived from the Geostationary Operational Environmental Satellite (GOES)-7 measurements. The average values of P_{avr} = 150 $g\ m^{-2}$ and τ_{avr} = 28 are used in the retrievals presented in Fig. 3. Cloud droplet spectra collected by the University of North Dakota (UND) Citation aircraft were used to calculate r_e directly.

The retrieved r_e overestimates the measured values by 0.5 to 1.5 μm, which is likely due to underestimated τ (see Fig. 4). There is pronounced increase of r_e by about 4 μm from cloud base to cloud top.

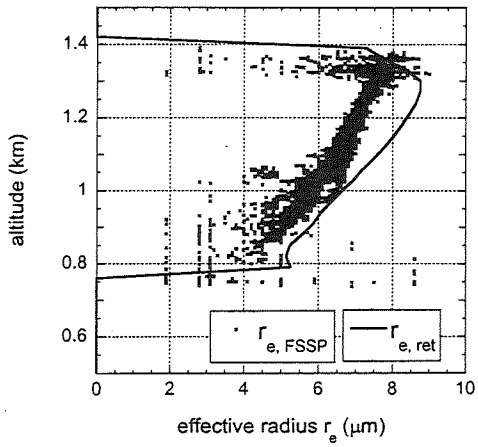

Fig. 3. *Effective radius calculated from the FSSP-measured droplet spectra ($r_{e,\,FSSP}$) on 30 April 1994. A solid line represents the profile retrieved using algorithm (7) with b=1.32 and d=1.75 ($r_{e,\,ret}$).*

5. DISCUSSION AND CONCLUDING REMARKS

An assessment of various cloud liquid water retrieval algorithms based on the simulated continental stratiform clouds is presented. It was shown earlier that retrieval algorithms based only on radar reflectivity rely, explicitly or implicitly, on a prescribed shape of the cloud droplet spectra and, therefore, lack versatility (Ovtchinnikov and Kogan, 2000). When cloud microstructure changes significantly these algorithms must be adjusted to produce reasonable results. Additional measurements are needed to constrain the

retrieved cloud water profile. In the presented case, the knowledge of the exact droplet concentration did not improve the accuracy of the profile retrieval because the assumed width of the cloud droplet spectrum remains fixed. In contrast, integrated liquid water path that can be obtained, for example, from microwave radiometer measurements is a robust constraint that ensures a more accurate retrieval.

It is possible to derive an analytical Z-W and Z-ε relation in the form (1) and (5) by assuming the shape of the DSD. It can be easily shown that b=2 and d=3 for a lognormal or gamma DSD with constant N and shape parameter. These assumptions often do not hold for continental stratus or in regions of active entrainment. Simulation results suggest that the reduced exponents b and d (in our case 1.32 and 1.75, respectively) yield significantly smaller errors in the retrieved W and ε, but have minor effect on the retrieved r_e.

According to (7), the retrieved r_e is inversely proportional to the cloud optical depth and directly proportional to the liquid water path. Consequently, the method requires the accurate estimates of these parameters. The sensitivity of r_e to the uncertainties in τ is illustrated in Fig. 4, which shows the retrieved profiles using the average optical depth τ_{avr} = 28 as well as this value plus and minus one standard deviation $\Delta\tau$ = 7.65 derived from GOES-7 measurements. It is clear that the uncertainties of this magnitude have a profound effect on the retrieved profiles.

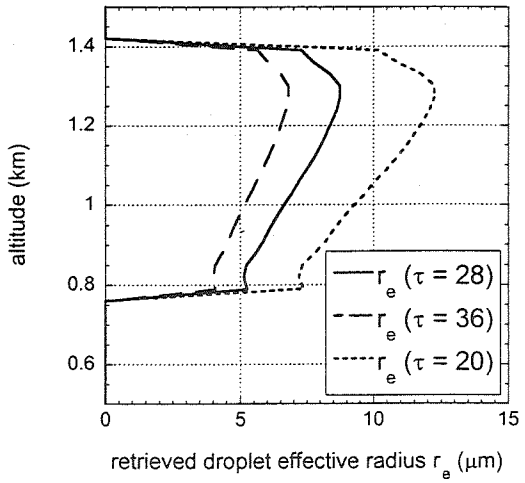

Fig. 4. *Retrieved profiles of the effective radius for three values of the cloud optical depth.*

Uncertainties in P are equally important. The difference between P retrieved using MWR and measured by the aircraft was quite significant (up to 100%) on 30 April 1994, although the source of the error was not identified (Sassen et al., 1999). This precluded the use of the MWR data in the case study.

Although the presented analysis based on LES simulations appears to be a valuable tool in evaluation of the retrieval algorithms, independent validation using aircraft measurements is still required. This validation remains a problem. For example, spirals performed by the UND Citation aircraft around the CF on 30 April 1994 were about 10 km in radius. Coincidentally, one of the most prominent features of the cloud structure (fluctuations of the cloud depth and liquid water path) was observed on the same scale. In addition, during even the fastest ramps attempted during the mission (ascent/descent rate of ~10 m/s), the aircraft covers a horizontal distance of several kilometers within a cloud and therefore does not represent very well vertical cloud profiles. These sampling and averaging issues must be taken into account in all algorithm validation studies.

6. ACKNOWLEDGEMENTS

This research was supported by the Environmental Sciences Division of the U.S. Department of Energy (through Battelle PNL Contract 144880-A-Q1 to the CIMMS) as part of the Atmospheric Radiation Measurement Program, by the ONR Grant N00014-96-0687, by the NOAA OGP Grant NA37RJ0203, and by the NASA Earth Science and Applications Division, Radiation Dynamics and Hydrology Branch, through Task 460-23-54-20.

7. REFERENCES

Fox, N. I. and A. J. Illingworth, 1997: The retrieval of stratocumulus cloud properties by ground-based cloud radar. *J. Appl. Meteor.*, **36**, 485-492.

Frisch, A. S., G. Feingold, C. W. Fairall, T. Uttal, and J. B. Snider, 1998: On cloud radar and microwave radiometer measurements of stratus cloud liquid water profiles, *J. Geophys. Res.*, **103**, 23,195-23,197.

Khairoutdinov, M. F., and Y. L. Kogan, 1999: A Large Eddy Simulation Model with Explicit Microphysics: Validation Against Aircraft Observations of a Stratocumulus-Topped Boundary Layer, *J. Atmos. Sci.*, **56**, 2115-2131.

Liao, L., and K. Sassen, 1994: Investigation of relationships between Ka-band radar reflectivity and ice and liquid water contents, *Atmos. Res.*, **34**, 231-248.

Ovtchinnikov, M., and Y. L. Kogan, 2000: Evaluation of radar retrieval algorithms in stratiform clouds using large-eddy simulations. *J. Geophys. Res.*, in press.

Sassen, K., G. Mace, Z. Wang, M. Poellot, S. Sekelsky, and R. E. McIntosh, 1999: Continental stratus clouds: A case study using coordinated remote sensing and aircraft measurements, *J. Atmos. Sci.*, **56**, 2345-2358.

STATISTICAL PROPERTIES OF PRECIPITATING CLOUDS USING UHF AND S-BAND PROFILERS ON MANUS ISLAND, PAPUA NEW GUINEA

Christopher R. Williams[1,2], Warner L. Ecklund[1,2], and Kenneth S. Gage[2,1]

[1] Cooperative Institute for Research in Environmental Science (CIRES), University of Colorado, Boulder, USA
[2] National Oceanic and Atmospheric Administration (NOAA), Aeronomy Laboratory, Boulder, Colorado, USA

1. INTRODUCTION

The NOAA Aeronomy Laboratory deployed two vertically-pointing Doppler profiling radars operating at 915 and 2835 MHz (UHF and S-band) on Manus Island, Papua New Guinea, to study the tropical Pacific precipitating cloud systems that advect overhead. The two profilers are sensitive to the rain drops near the surface as well as the larger ice particles above the melting level. These upper level ice particles may not contribute to the surface liquid-water mass flux but are important in balancing the radiation budget and redistributing the moisture lifted by deep convective cloud systems.

2. DATA SETS

The 915 MHz wind profiler was deployed in 1991 in support of the Topical Ocean-Global Atmosphere (TOGA) program for long term monitoring of the boundary layer winds. The 2835 MHz profiler was deployed next to the UHF profiler in February 1996 to monitor the precipitating ice particles that advected over the profiler. The S-band profiler was in position for two years before being moved to Nauru, Republic of Nauru, in support of the US Department of Energy (DOE) Atmospheric Radiation Monitoring (ARM) program. While the 915 MHz profiler operated in a beam-swinging mode alternating between oblique and vertical pointing directions (horizontal winds are estimated using the off-vertical directed beams), the 2835 MHz profiler observed only in the vertical direction.

The two profilers were configured to have the same range gate spacing and range resolution volume so that both radars illuminated the same volume of the atmosphere. Observing the same volume of the atmosphere with two profilers operating at different frequencies enables the scattering process to be identified as resulting from either Bragg or Rayleigh scattering. This identification is important to separate precipitating particles with weak intensities from turbulent motions especially near and below the melting level.

The simultaneous vertically-pointing 915 and 2835 MHz profiler observations from February 1996 to February 1998 are analyzed in this study. The Bragg and Rayleigh scattering processes were unambiguous identified by examining the difference in reflecitivity between the two profilers as described in Gage et al. (1999). Due to space limitations, only the 2835 MHz profiler observations are presented.

Corresponding author's address: Christopher R. Williams, CIRES/NOAA Aeronomy Laboratory, Mail Stop R/AL3, 325 Broadway, Boulder, CO 803-3-3328, USA; E-Mail: chris@al.noaa.gov.

3. PRECIPITATING CLOUDS ABOVE THE MELTING LEVEL

The 2835 MHz profiler precipitation reflectivity distribution above 5 km is shown in Figure 1. The panel on the left indicates the number of precipitation observations at each altitude. The curve is normalized such that the maximum occurrence at 10.5 km corresponds to 100% (15,918 observations). The right panel shows contours of the occurrence frequency distribution in the altitude and reflectivity dimensions. Contours are normalized such that the pixel with the most occurrences corresponds to 100% (794 observations). The contours of occurrence rate highlight the pattern of reflectivity versus altitude. There is an increase in occurrence rate with decreasing reflectivity and increasing altitude with the most frequent precipitation observation near 11 km and -15 dBZe. The pattern is consistent with aggregation and vapor deposition which increases the cross-sectional area of the particles and increases the reflectivity.

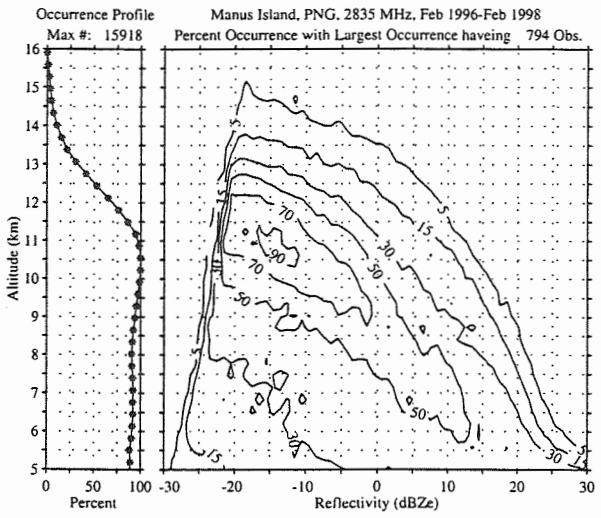

Figure 1. Precipitating cloud Reflectivity occurrence above 5 km. Left panel is the total number in each altitude expressed in percent (100% = 15,918 observations), and the right panel is the frequency distribution express in percent (100% is the pixel with 794 observations).

The frequency distribution shown in Figure 1 shows the distribution of the anvil precipitating clouds following the deep convective systems that lifted these particles from lower altitudes (first liquid than frozen particles). The frequency distribution does not show the intense reflectivity cores because these deep convective systems have a limited horizontal cross-section and are of short duration compared with the resulting anvil precipitating clouds. So statistically, the vertically pointing profiler will sample more of the precipitating anvils than the convective cores.

4. DOPPLER VELOCITY VERSUS REFLECTIVITY

It is very difficult to derive the properties of the precipitating particles using a single remote sensing instrument (Danne et al. 1999). One of the eluding parameters is the ambient air motion the particles are falling through. The measured reflectivity-weighted mean Doppler velocity is the summation of the ambient air motion and the reflectivity-weighted mean terminal velocity of the particle distribution. While it is difficult to estimate the ambient air motions with these individual observations, the systematic ambient air motions could be modeled given the average characteristics of these observed precipitating cloud systems (Orr and Kropfli 1999).

Figure 2 shows the mean Doppler velocity versus reflectivity at the four selected altitudes of 6, 8, 10, and 12 km. At each altitude, the observed quantities are shown with symbols, and the best fit is shown with lines. The best fit line is determined using the relation

$$V_{Doppler} = \alpha z^{\beta}$$

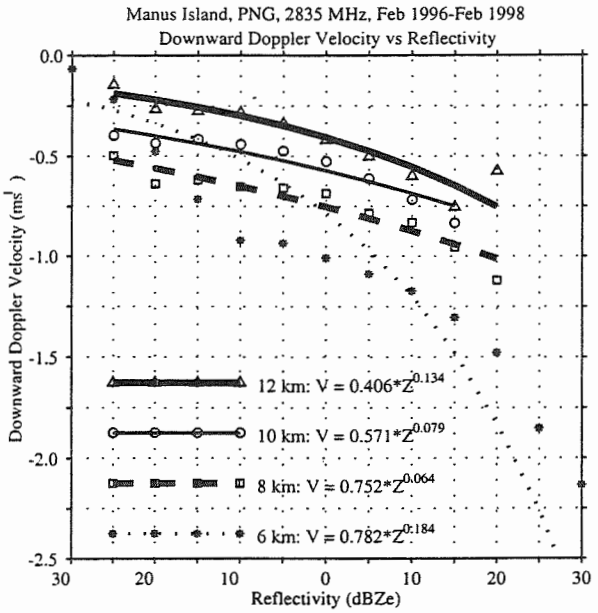

Figure 2. Reflectivity-weighted mean Doppler velocity versus reflectivity for the altitudes of 6, 8, 10, and 12 km. The symbols represent the mean observations, and the lines represent the best line fits.

where $V_{Doppler}$ is the observed Doppler velocity, z is the reflectivity in units mm^6m^{-3}, and α and β are two parameters. The relationship at 6 km is significantly different than the other three altitudes. This is due to the proximity of the zero degree Celsius level near 4.8 km. The particles are changing density as they approach the melting level. The best fit lines for the altitudes at 8, 10, and 12 km are very similar and represent the average Doppler velocity and reflectivity distributions for these altitudes. Over 12,000 individual observations at each altitude were used to construct these relations. Thus, these relations represent the mean of the distributions at each altitude.

5. CONCLUDING REMARKS

Observations from two years of vertically pointing UHF and S-band profilers are being analyzed to study the precipitating clouds above the melting level. Due to the sampling issues of a single point looking vertically, the frequency distribution of reflectivity represents the long lived anvil precipitating clouds resulting from short lived and small spatial scale deep convective precipitating cloud systems. Remote sensing instruments observe the characteristics of the ambient air and the precipitating particles. It is very difficult to separate the ambient air characteristics motion from the precipitating particles using a single remote sensing instrument. Relationships between the reflectivity-weighted mean Doppler velocity and reflectivity were estimated above the melting level using over 12,000 observations at each altitude.

5. REFERENCES

Danne, O., M. Quante, D. Milferstadt, H. Lemke, and E. Raschke, 1999: Relationship between Doppler spectral moments within large-scale cirro- and altostratus cloud fields observed by a ground-based 95-GHz cloud radar. *J. Appl. Meteor.*, **38**, 175-189.

Gage, K.S., C.R. Williams, W.L. Ekclund, and P.E. Johnston, 1999: Use of two profilers during MCTEX for unambiguous identification of Bragg scattering and Rayleigh Scattering. *J. Amos. Sci.*, **56**, 3679-3691.

Orr, B.W., and R.A. Kropfli, 1999: A method for estimating particle fall velocities from vertically pointing Doppler radar. *J. Atmos. Oceanic Technol.*, **16**, 29-37.

Polarization measurements of clouds by passive microwave radiometers

A.V. Troitsky[1], A.V. Korolev[2], J.W. Strapp[2], G. A. Isaac[2], A. M. Osharin[1]

[1]Institute of Radiophysics, Nizhny Novgorod, Russia
[2]Meteorological Service of Canada, Toronto, Canada

1. Introduction

It is generally accepted that thermal microwave atmospheric radiation, even in presence of clouds, is not polarized. This is the basic assumption for the interpretation of the measurements of thermal radiation characteristics of the atmospheric (Stepanenko et al. 1987; Jansen 1993). The effect of ice particles on the polarization was considered to be negligible, since the absorption in ice is three orders of magnitude less relative to water (Jansen 1993). However, Troitsky and Osharin (1999, 2000) have detected the polarization of 94GHz radiation in winter clouds. This study presents observations of the polarization of microwave radiation in winter clouds near Ottawa during the Alliance Icing Research Study (AIRS), during the period from December 1999 to February 2000.

2. Instrumentation

The brightness temperature of the microwave radiation was measured at two orthogonal polarizations (vertical and horizontal). The intensity of the received radiation, or the first Stokes parameter, is converted to liquid water path (LWP) in the cloud. The difference between the horizontal and vertical components describes the second Stokes parameter, and results from the polarization effects of clouds.

The measurements of the microwave radiation were made by dual-polarized 37GHz and 85GHz radiometers. The radiometers were inclined at 25° to the horizon and pointed in the same direction in order to receive radiation from approximately the same cloud volume. The measurements were made through a radiotransparent window. Thus the effect of precipitation accumulation on the environmental protection and antennae did not affect the measurements. The radiometers were mounted inside a special thermo-stabilized trailer to avoid any effect of temperature changes on the measurements. The signals were integrated over 10 seconds and recorded on a data acquisition system. The sensitivity of the measurements of the brightness temperature for 85GHz was about 0.2°K and that for 37GHz about 0.1°K for each polarization channel.

Total transmission coefficients for both channels were equalized with an accuracy not worse than 0.5% and controlled by the two unpolarized sources, i. e. the clear atmosphere and a black body, located in the far zone of the antenna and oriented perpendicular to the electric axis of the horn antenna. The temperature of the black body was maintained equal to the outside air temperature. The same sources were used as standards to calibrate radiometer channels for both the radio brightness and polarization contrast $\Delta T=T_h-T_v$ scales. The level of zero polarization contrast was taken to be the clear atmosphere radiation or that of the black body.

The absolute brightness temperature was measured with an accuracy of about 2°K, which corresponds to approximately 0.03 kgm^{-2} of LWP. The threshold sensitivity of the polarization contrast for 37GHz (ΔT_{37}) was 0.2°K and that of for 85GHz (ΔT_{85}) was 0.4°K.

The results of radiometric measurements were compared with *in situ* measurements of cloud microstructure made by the National Research Council (NRC) Convair-580. The NRC Convair-580 was instrumented for measurements of different microphysical parameters (e.g. liquid water content, ice water content, cloud particle shape, particle size distribution, particle number concentration etc.). The radiometer trailer was installed in the vicinity of the runway at the Ottawa Airport. The comparisons were conducted for periods of take-off and landing, when the airplane was ascending or descending over the radiometer site.

3. Results of measurements

The main data set was collected in stratiform clouds associated with frontal systems. The total observation time was 1736 hours, in which cloudy periods comprised about 640 hours (37%). Figures 1 and 2 show examples of measurements of LWP derived from 37GHz measurements (a), polarization contrast ΔT_{85} for 85GHz (b), and polarization contrast ΔT_{37} for 37GHz (c). The following conclusions result from the observations.

1. Polarization of the microwave radiation, beyond the threshold sensitivity, at frequencies 37GHz and 85GHz was observed during 188 hours, corresponding to approximately 30% of time clouds were observed.

2. The zones of polarization have a distinct cellular structure. The characteristic time for observations of polarization may vary from few minutes to few hours. Assuming that the wind speed is about 20kmh^{-1} the

characteristic spatial scale of polarized zones may be estimated as a few kilometers.

3. The polarization contrast $\Delta T = T_h - T_v$ was found to be both positive and negative. Figure 1bc demonstrates this phenomenon for both the 37GHz and 85GHz radiometers. The positive polarization contrasts were observed more frequently than negative ones. During the AIRS project negative contrasts were observed in approximately 10% of all polarization cases.

Figure 1. Example of measurements of (a) LWP derived from the 37GHz radiometer; (b) polarization contrast at 85GHz, (c) polarization contrast at 37Ghz. Measurements were collected near Ottawa during the AIRS project

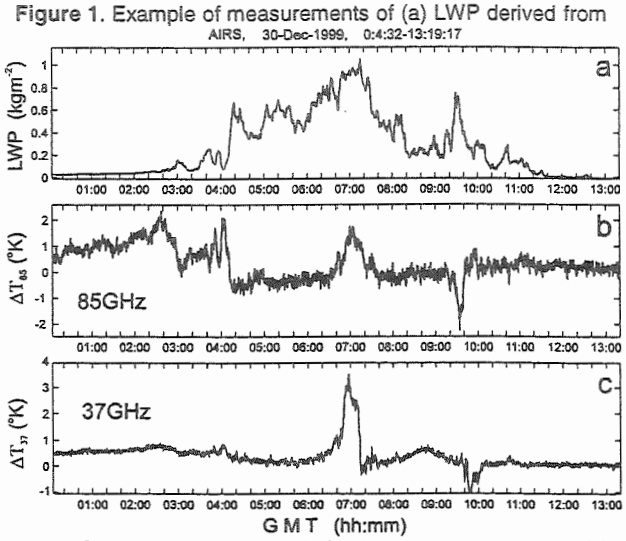

4. In absence of precipitation ΔT_{37} is usually 2-6 times less than ΔT_{85}, and the amplitude of ΔT_{37} did not exceed about 2°K. However, in the case of deep clouds with LWP>0.6 kgm^{-2} or during liquid precipitation, ΔT_{37} is usually higher than ΔT_{85} (Fig.1 at 7.00 GMT).

5. The polarization of clouds in the microwave range does not correlate with LWP. This can be clearly seen in Figs. 1 and 2. The correlation coefficient between LWP and ΔT typically varies from –0.3 to 0.3, indicating an absence of a relationship between these parameters. It should also be noted that there are a lot of cases where polarization ΔT>0.2°K was not observed in the presence of rather thick clouds with LWP of 0.1 kgm^{-2} to 1kgm^{-2}.

6. The polarization contrasts ΔT_{85} and ΔT_{37} are usually close to zero (below sensitivity threshold) for falling snow.

5. Discussion

The polarization of the thermal radiation from clouds due to scattering may be caused both by spherical particles and nonspherical ice particles. The effect of polarization in the microwave range may be described by the equation for the radiation transfer in a cloudy atmosphere containing ice particles that scatter radiation emitted by the atmosphere and the Earth (Troitsky and Osharin 2000)

$$\cos\theta \frac{d\mathbf{I}(\theta,\phi,z)}{dz} = -\mathbf{K}_{at}(\theta,\phi)\mathbf{I}(\theta,\phi,z) + \mathbf{J}(\phi,\theta,z) + \\ + \int_0^{2\pi} d\phi' \int_0^{2\pi} d\theta' \sin\theta' \mathbf{P}(\phi,\theta,\phi',\theta') I(\phi',\theta',z) \qquad (1)$$

Here θ, ϕ are zenith and azimuth angles, respectively, $\mathbf{I}(\theta,\phi,z) = \begin{pmatrix} I_v + I_h \\ I_v - I_h \\ U \\ V \end{pmatrix}$ is the vector of modified Stockes parameters, $\mathbf{K}_{at}$ is the matrix of attenuation, $\mathbf{P}(\theta, \phi, \theta', \phi',)$ is the phase matrix of scattering describing single scattering radiation coming from direction (θ, ϕ) and scattering into the direction (θ', ϕ'), $\mathbf{J}$ is the source of thermal emission.

Figure 3 shows the polarization contrast ΔT for 85GHz versus azimuth angle computed for horizontally oriented ice plates in a cloud layer with a thickness of 1km, containing liquid phase droplets. The modal diameter of the plates was D=500μm, the liquid water content W=0.1gm^{-3}. An increase of ice water content results in an increase of polarization contrast for all zenith angles. The polarization contrast rapidly decreases at angles θ >80° due to an increase of absorption of the cloudy atmosphere.

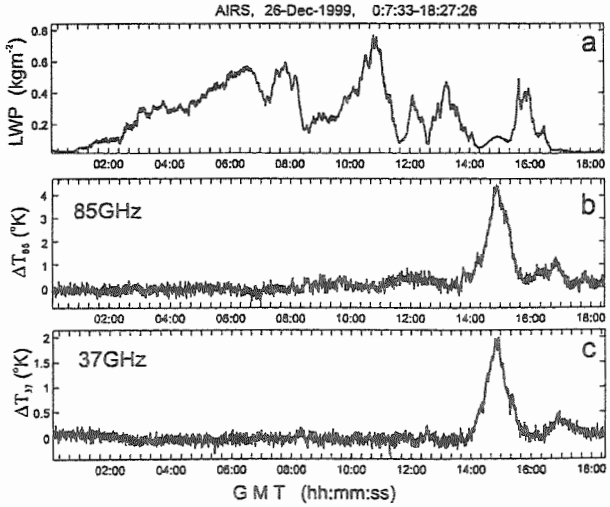

Figure 2. Same as Fig. 1. ΔT_{85} correlates with ΔT_{37}

The calculations have shown that the sign of the polarization contrast depends on the habits of the ice particles. Figure 4 shows the polarization contrasts ΔT_{85} and ΔT_{37} for ice spheres with modal diameter D=500μm, ice water content W_i=0.1gm^{-3}, and liquid water content W_l=0.1gm^{-3}. Flat ice particles (plates, stellar, dendrites) oriented horizontally, result in a dominance of the horizontal polarization over the vertical i.e. ΔT>0, as it is shown in Fig. 3. Spherical ice particles (Fig. 4) or needles having a preferential orientation may give a negative contrast i.e. ΔT<0. The frequency of occurrence of needles/columns in the troposphere averages about 5%, and that for spherical (liquid drops) or quasi-spherical particles (frozen drops, graupel, etc.) averages about 13% (Korolev et. al. 2000). Such occurrences of needles/columns and spheres may explain the observations of negative polarization contrast at LWP<0.6 kgm^{-2}. It is worth noting that irregularly shaped ice particles may also contribute to negative contrasts, depending on their preferred orientation in space.

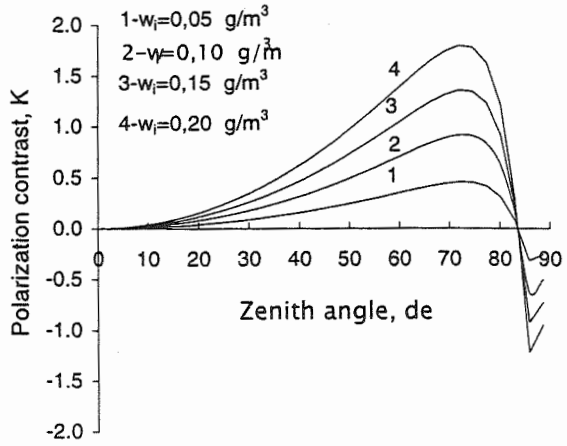

Figure 3. Polarization contrast at 85GHz for ice plates versus zenith angle. Liquid water content W_l=0.1gm^{-3}.

The value of the polarization contrast depends on the wavelength, ice particle size distribution and LWP. For the cases when LWP<0.6, the ΔT_{85} is usually higher than ΔT_{37}. An increase in the LWP results in an increase in the optical path at 85GHz, such that it may exceed unity, whereas that at 37GHz may still remain less than unity. Large optical paths may reduce the polarization contrast down to zero.

6. Conclusion

The current study, along with the work of Troitsky and Osharin (1999), represents some of the first observations of the polarization of clouds in the microwave range. Some preliminary results of data processing were presented here. The observations show that the polarization of microwave radiation by winter clouds is a rather common phenomenon. The amplitude of the polarization contrast was observed to reach several degrees Kelvin. Polarization of microwave radiation by clouds may be explained by scattering by ice particles of the microwave radiation emitted by the atmosphere and the Earth.. Further study towards the description of this phenomenon should consider scattering and polarization of microwave radiation by irregular ice crystals.

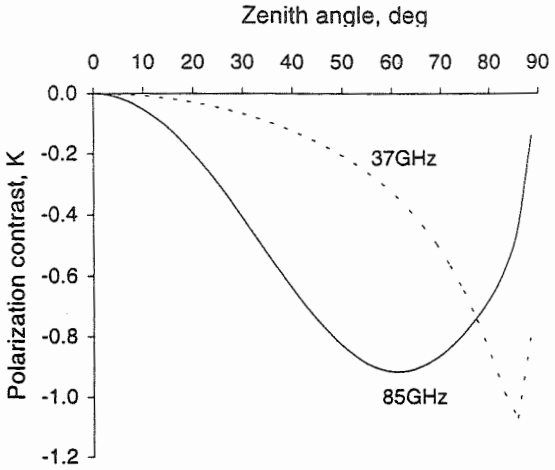

Figure 4. Polarization contrast for ice spheres. Liquid water content W_l=0.1gm^{-3}, ice water content W_i=0.1gm^{-3}

Acknowledgments

Meteorological Service of Canada (MSC), National Research Council (NRC), the National Search and Rescue Secretariat of Canada, NASA, Boeing Commercial Airplane Group, Transport Canada, the Canadian Department of National Defense provided funding for the AIRS project. This study was supported by RFBR grant No.00-02-16037. Special thanks to Mr. Ken Asmus of the Canadian Ice Service assisted in the data collection.

References

Jansen M. A. 1993: *Atmospheric Remote Sensing by Microwave Radiometry*. J.Wiley Sons. Inc.

Korolev, A., G. A. Isaac and J. Hallett, 2000: Ice particle habits in stratiform clouds. (ibid)

Stepanenko V.D., Schukin G.G., Bobylev L.P., Matrosov S.Yu. 1987: *Radiothermolocation in meteorology*. Gidrometeoizdat (in Russian).

Troitsky, A.V., and A.M. Osharin, 1999: Polarization of microwave radiation in cloudy atmosphere. *Proc. Conf. on Atmosper. Radiation,* St. Peterburg, Russia, July 12-15, 27-28

Troitsky AV., Osharin A.M. Polarization of the thermal microwave radiation of the cloudy atmosphere. Izvestija VUZov. Radiofizika, 2000 (in press).

REMOTE SENSING OF CLOUD LIQUID WATER CONTENT WITH OFF-BEAM LIDAR

Steven P. Love,[1] Anthony B. Davis,[1] Cheng Ho,[1] Charles A. Rohde,[1] Alan W. Bird[1]
Robert F. Cahalan,[2] Matthew J. McGill,[2] and Luis Ramos-Izquierdo[2]

[1]Los Alamos National Laboratory, Los Alamos, NM 87545, USA
[2]NASA's Goddard Space Flight Center, Greenbelt, MD 20771, USA

1. INTRODUCTION

For remote sensing of cloud properties, traditional lidar, which collects returns from only a very narrow field of view about the transmitted laser beam, yields only a small fraction of the information potentially available, and for the optically thick clouds typical of the boundary layer, is limited to providing the range to the first interface (ceilometry from ground, cloud-top geometry from airborne platforms). With some effort, information about the water phase can also be inferred by using multiple fields of view and depolarization measurements. It is important to recognize, however, that at most visible and NIR wavelengths lidar photons are not absorbed but merely scattered out of the beam. Much additional information exists in this light exiting the cloud far from the input beam. Since a pulsed laser is essentially a delta function in space and time, by measuring the complete spatial and temporal profiles of the returning light one is in effect measuring the Green functions of the cloud.

The extent of the temporal Green function, which is directly related to the distribution of photon path lengths, is dominated by physical cloud thickness, while the lateral extension of spatial Green function (i.e. its root-mean-square diameter) is influenced strongly by optical depth. These two cloud properties, of direct interest in a variety of meteorological applications, can be retrieved from off-beam lidar returns.

This also means that that one can remotely, hence cost-effectively, determine a volume-averaged liquid water content via the mean extinction coefficient (i.e., optical depth divided by cloud thickness) and an educated guess at the effective radius. We report here on the status of this emerging technology and its associated retrieval schemes.

2. OFF-BEAM CLOUD LIDAR THEORY

The schematic in Fig. 1 describes the geometry of off-beam cloud lidar observations. The key quantities are cloud optical depth (τ), physical thickness (Δ_z), asymmetry factor of scattering phase function (g), and range (δ_{obs}). The remotely observable radiative transfer Green's Functions (GFs) for a δ-source at the cloud boundary (G_{obs}) will depend parametrically on all of these cloud quantities as well as two independent variables for space and one for time. The spatial variables can be in Cartesian coordinates (x,y) cylindrical coordinates (ρ,φ), or polar angles (θ_ρ,φ). The temporal variable can be either time elapsed since the pulse impacted the cloud (t), or the "in-cloud" pathlength ($\lambda = ct$), noting that the "out-of-cloud" pathlength is simply $\delta_{obs}(1+1/\cos\theta_\rho)$.

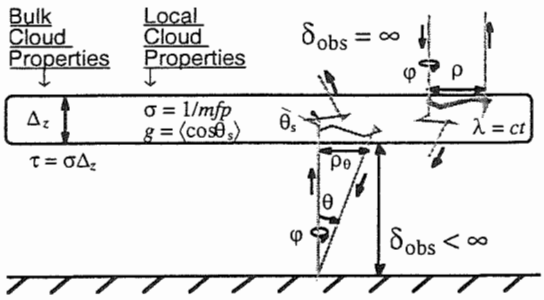

FIGURE 1. ***Geometry of Off-Beam Cloud Lidar.*** From left to right, illustrated meanings for: (1) cloud optical depth τ, physical thickness Δ_z, their ratio (extinction σ), and asymmetry factor g (mean cosine of scattering angle ≈ 0.85 for typical droplet populations); (2) independent variables angle (space) θ_ρ and time t, radiance $G_{obs}(\tau,g,\Delta_z,\delta_{obs};t,\theta_\rho,\varphi)$ for a ground-based WAIL system and a cloud at finite range δ_{obs}; (3) similarly, $G_{obs}(\tau,g,\Delta_z,\infty;t,\rho,\varphi)$ is measured during a LITE-like mission in space and has been extensively studied elsewhere (Winker 1997; Miller and Stephens, 1999).

Photon-escape GFs have straightforward interpretations in terms of probability of a photon to escape from the cloud into any direction at position (x,y) and time t, conditional to be either reflected or transmitted: e.g.,

$$G_R(t,x,y)dxdydt \,/\, R = \text{Prob}\{\text{ escape during } [t,t+dt), \text{ from } [x,x+dx)\otimes[y,y+dy) \text{ in reflection }\}, \quad (1)$$

where the normalization constant,

$$R = \iiint G_R(t,x,y)dxdydt, \quad (2)$$

is simply cloud albedo for normal incidence. Analogous relations can be written for transmission where, by conservation at most lidar wavelengths, we have $T = 1-R$. Normalized escape GFs can thus be treated as probability density functions and we can compute their moments. If detailed information about the space/time-dependent bi-directional properties of the cloud's radiative GFs is not available, then we make a standard Lambertian hypothesis:

$$G_R(t,x,y)dxdydt \approx \pi G_{obs}(t,\theta_\rho,\varphi)\sin\theta_\rho d\theta_\rho d\varphi dt. \quad (3)$$

The simplest in-cloud propagation characteristics of a laser pulse are: mean photon pathlength,

Corresponding author's address: Steven P. Love, Los Alamos National Laboratory, NIS-2, MS C323, Los Alamos, NM 87544, USA; E-Mail: splove@lanl.gov

$$\langle\lambda\rangle_R = c\langle t\rangle_R = c\iint dxdy\left[\int tG_R(t,x,y)dt\right] / R; \quad (4)$$

its 2nd-order moment (used in path variance $\langle\lambda^2\rangle_R - \langle\lambda\rangle_R^2$),

$$\langle\lambda^2\rangle_R = c^2\langle t^2\rangle_R = c^2\iint dxdy\left[\int t^2 G_R(t,x,y)dt\right] / R; \quad (5)$$

rms horizontal transport $\sqrt{\langle\rho^2\rangle_R}$, where

$$\langle\rho^2\rangle_R = \int dt\left[\iint (x^2+y^2)G_R(t,x,y)dxdy\right] / R \quad (6)$$

One can think of $\langle\rho^2\rangle_R^{1/2}$ as the gyration radius of the spot of diffuse light excited by the laser in cw mode. There are of course analogous quantities for transmission (subscript "T") that have been used in other studies, cf. Savigny et al. (1999). A major advantage of using the observables in Eqs. (4–6) is that there is no need for absolute calibration to estimate them from observations using Eqs. (1–3).

In absence of absorption, only two scales are required to determine the optical properties of a plane-parallel slab: the outer-scale Δ_z, and the inner-scale defined by the photon mean-free-path (MFP), $\ell = 1/\sigma = \Delta_z/\tau$. In the diffusion approximation, we are more interested in the "transport" MFP

$$\ell_t = \ell/(1-g) = 1/[(1-g)\sigma] \quad (7)$$

which is in essence the MFP for an effectively isotropic scattering; the rescaling by $(1-g)^{-1} \approx 6.7$ takes care of the propensity for forward scattering. One final parameter is introduced in diffusion theory to describe boundary conditions: the "extrapolation length" which we will denote $\chi\ell_t$. Here χ is an $O(1)$ numerical factor that can be used to minimize the approximation error.

A spatial-Fourier/temporal-Laplace solution of the non-stationary three-dimensional diffusion equation by Davis et al. (1999) with boundary/initial conditions describing a pulsed point-source leads to:

$$R = \frac{\Delta_z}{\Delta_z + 2\chi\ell_t} = \frac{(1-g)\tau}{(1-g)\tau + 2\chi} \quad (8)$$

for albedo in Eq. (2);

$$\langle\lambda\rangle_R = 2\chi\,\Delta_z\left[1 + C\left(\frac{\chi}{(1-g)\tau}\right)\right] \quad (9)$$

for mean pathlength in Eq. (4); and

$$\langle\lambda^2\rangle_R = \frac{4\chi}{5}\,\Delta_z^2(1-g)\tau\left[1 + C'\left(\frac{\chi}{(1-g)\tau}\right)\right] \quad (10)$$

for the 2nd moment of pathlength in Eq. (5); and

$$\langle\rho^2\rangle_R = \frac{8\chi}{3}\,\frac{\Delta_z^2}{(1-g)\tau}\left[1 + C''\left(\frac{\chi}{(1-g)\tau}\right)\right] \quad (11)$$

for the variance in horizontal transport defined in Eq. (6). The radiative quantities in (9–11) contain pre-asymptotic correction terms given by:

$$C(\varepsilon) = C''(\varepsilon) = \varepsilon(1+3\varepsilon)/(1+2\varepsilon), \quad (12a)$$

$$C'(\varepsilon) = \varepsilon(8+41\varepsilon+75\varepsilon^2+\varepsilon^3)/(1+2\varepsilon)^2; \quad (12b)$$

these corrections become small as

$$1/\varepsilon = (1-g)\tau/\chi = \Delta_z/(\chi\ell_t) \quad (13)$$

increases. Representative cloud parameters for a stratus layer are $g = 0.85$, τ in the range 7–70, hence $1 \le (1-g)\tau \le 10$, with Δ_z in the corresponding range 300–500 m. Using these values in Fig. 2 leads to an albedo R between 0.5 and 0.1, an rms "spot-size" $\langle\rho^2\rangle_R^{1/2}$ around 300 m, $\langle\lambda\rangle_R \approx$ 500–600 m, and the ratio $\langle\lambda^2\rangle_R^{1/2}/\langle\lambda\rangle_R$ falls between 1.5 and 2. Finally, we note that, apart from exact proportionality constants, the leading terms in (8–10) can be obtained from simpler arguments based on the fractal properties of the random walks of the photons in the finite slab that defines the cloud (Davis et al., 1997; Davis, 1999).

3. WIDE-ANGLE IMAGING LIDAR (WAIL)

We see from the above that, by combining the temporal and spatial information from off-beam lidar — the mean pathlength from the temporal Green function (Eq. 9) and the mean-square horizontal displacement from the spatial Green function (Eq. 11) — both the cloud thickness Δ_z and optical depth τ can be determined. While the primary spatial information lies in the radial displacement, the most informative realization of off-beam lidar would be one in which not only the radial and temporal distributions of the returning light are recorded, but its azimuthal dependence as well. This amounts to full time-resolved 2D imaging of the scattered radiation, in essence a high-speed movie of the light propagation. With such a system, not only are quasi-uniform cloud fields amenable to azimuthally averaged analysis, but complex scattering mechanisms (scattering between clouds, etc.) in highly non-uniform clouds and broken cloud decks may also be observed and interpreted.

This is the approach we are taking at Los Alamos National Laboratory, and it relies on an imaging detector technology developed at LANL, the Micro-channel Plate/Crossed Delay Line (MCP/CDL) detector, coupled with high-speed pulse absolute timing electronics. The MCP/CDL technology features photon-counting sensitivity, a large spatial format (4 cm diameter active area, effectively up to 1500^2 pixels, and ultra-high time resolution (100 ps). It consists of the MCP/CDL detector — a photo-cathode coated vacuum tube, intensified by micro-channel plates, read out by a crossed delay line anode — together with fast pulse-timing electronics. Each photo-electron is intensified a factor of 10^7, with positional information preserved, by the MCP. The electron cloud is collected by helically wound delay lines, producing in each line two counter-propagating current pulses which emerge from the ends. By measuring the arrival times of the pulses at the ends of the delay lines, the

position of the original photon event is determined; with two orthogonal delay lines, both the *x*- and *y*-coordinates are determined.

Its unique strategy for extracting spatial information distinguishes the MCP/CDL from other sensitive imagers such as CCDs in that it is intrinsically very fast, with photon arrival time automatically known to within 100 ps as a by-product of the imaging scheme, and in that it is not only capable of performing at very low light-levels, but actually requires them — too high a count rate ($>5\times10^6$/sec over the entire detector) confuses the timing-based imaging scheme.

These strengths and limitations drive the choice of laser for the imaging lidar system. The count rate limit demands a high repetition rate and averaging over many pulses. A repetition rate around 5-15 kHz is ideal, permitting maximal pulse averaging while avoiding the return from one pulse overlapping with the next. The MCP's spectral response makes a 532nm frequency-doubled Nd:YAG laser a good choice. Our current laser produces 0.2 to 0.5 mJ/pulse, at a variable rep rate (12 kHz is typical in our experiments), with pulsewidths ranging from 30 ns to 50 ns depending on operating conditions. The laser is triggered by a master clock, which also provides triggers the detector system electronics.

Our current nighttime WAIL implementation uses a 35mm f.l. camera lens on the detector, for a 60° full-angle field of view. One challenge in designing an imaging lidar system for clouds is the large dynamic range, several orders of magnitude, between the initial return (the traditional lidar signal) and the multiply scattered returns from locations at large displacements from the beam. The faint large-displacement returns require a band-pass filter, ~10nm wide for nighttime work, to reject as much background light as possible. This presents an apparent problem, given the wide field of view, since the band center for standard interference filters varies strongly with angle of incidence; over the 30° half-angle range of our system, the passband center wavelength shifts nearly 15 nm to shorter wavelengths as one moves from the center to the edge of the field. But this can be put to use to partially cancel the strong center-to-edge gradient intrinsic to cloud returns, if, instead of choosing a filter centered (at normal incidence) at the laser wavelength, one chooses a somewhat longer nominal filter wavelength. With proper choice of filter, light at large angles of incidence (i.e. from the edge of the field of view) will be near the angle-shifted center of the filter passband, while light near normal incidence (the bright central spot) will be in the wings of the filter passband and be strongly attenuated.

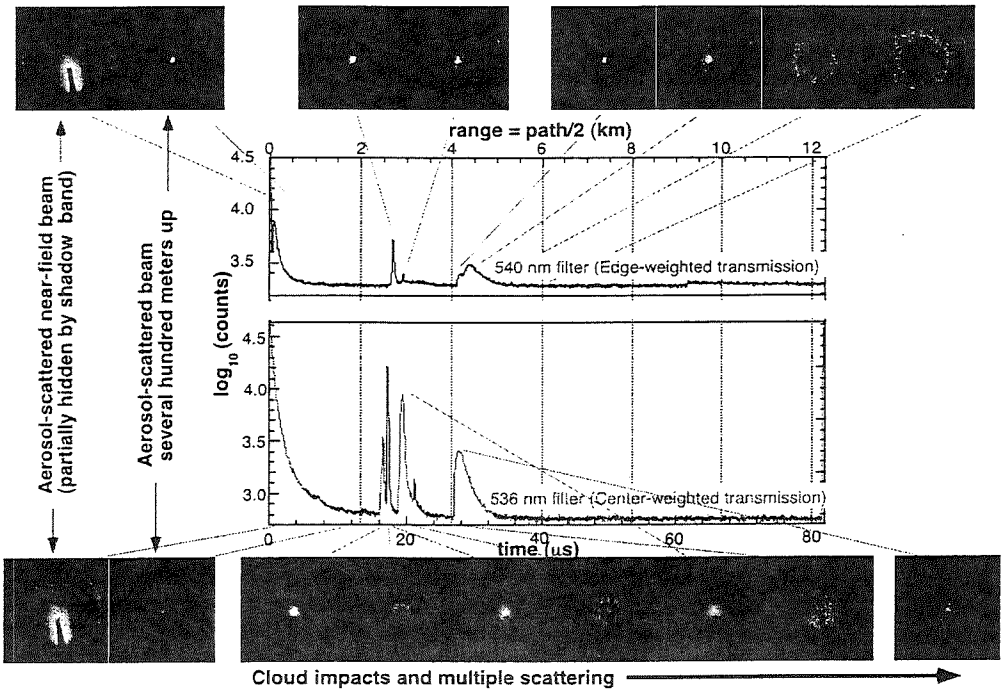

FIGURE 2. ***Nighttime WAIL results for a multi-layer cloud deck, obtained July, 1999.*** Shown here are the spatially integrated total return as a function of time (graphs), and a sequence of selected frames from the corresponding WAIL "movies," which show the spatial distribution of the returning light as a function of time. The full-angle field of view for each frame is approximately 60 degrees. Each sequence begins with the Rayleigh/aerosol-scattered beam as it leaves the laser (located off the bottom right side of the field of view); a shadow band blocks the brightest portion of this early return. Subsequent frames show the aerosol-scattered pulse several hundred meters up, the initial impact on the cloud deck, and subsequent spreading due to multiple scattering. For QuickTime movie versions of these and other datasets, see http://nis-www.lanl.gov/~love/clouds.html Two data sets for essentially the same cloud deck (taken a few minutes apart) are shown. These were obtained with two different filters on the optics, one which emphasizes the large-angle returns (top) and the other emphasizing the center region (bottom). (Narrow bandpass interference filters are generally used to reject background light. But because of their strong angular dependence of the bandpass center wavelength, these filters also affect the spatial response of the system.)

Figure 2 shows nighttime WAIL results for a multi-layer cloud deck, probed with two different filters on the detector, one (nominal band center 540 nm) which strongly suppresses the center spot, and the other (nominal band center 536 nm) providing a more uniform response across the field. In each case, the spatially integrated return as a function of time is plotted, along with representative frames of the spatial WAIL "movie," each frame showing the full 60° f.o.v. Here we see the initial near-field aerosol scattering, followed by multiple cloud-base impacts and spreading due to multiple scattering.

In Fig. 3, the analysis of section 2 is applied to WAIL data. Two methods for extracting cloud thickness and optical depth are shown. The two methods yield consistent results, but note that the combined space-time scheme provides a much less ambiguous measure of Δ_z and τ.

4. CONCLUSIONS AND FUTURE DIRECTIONS

We have shown that off-beam lidar, in the form of WAIL can be used to measure both the vertical thickness of clouds and their optical depth. Thus, with relatively straightforward assumptions on drop radii, the liquid water content can be estimated, using an optical measurement alone.

In previous work, it has also been demonstrated that similar information can be extracted from non-imaging, space-based lidar (Davis *et al.*, 1999b; 2000). While WAIL provides a very exhaustive data set, extrapolation to a space-based system presents many technical challenges. Therefore, parallel to the WAIL project, work underway at NASA Goddard is focused on schemes using more conventional detectors, and which preserve the radial information but average azimuthally. These approaches include using holographic filters or fiber optics to route light from pre-defined radial zones to several separate high-sensitivity photodetectors. Meanwhile, work currently underway at LANL is focused on implementing daylight WAIL, by means of ultra-narrow atomic line filters coincident with strong solar Fraunhofer aborptions.

Regardless of which of these schemes gains the widest acceptance, it is clear that off-beam lidar can provide a valuable new tool for remote probing of cloud properties.

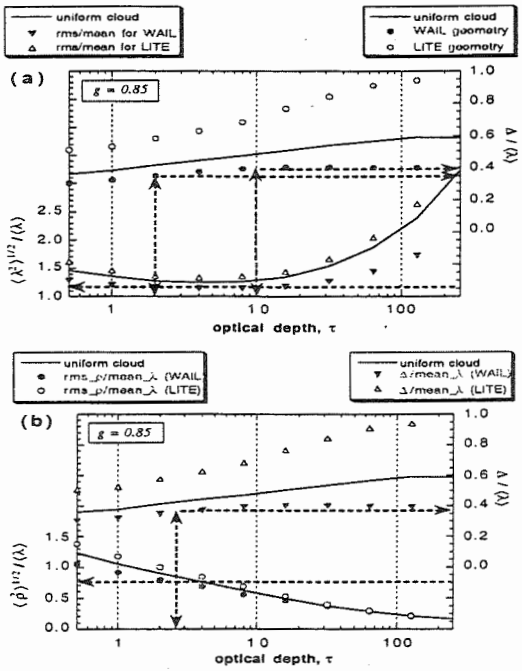

FIGURE 3. ***Inference of Cloud Properties from WAIL Data.*** (a) Time-only scheme. Lower curves show calculated ratios of the second to first moments of the pathlength distribution, vs. optical depth for a uniform cloud (solid line) and for a more realistic stratified cloud in the ground-based (solid symbols) and space-based (open symbols) geomtries. Upper curves similarly plot calculated ratios of the cloud thickness to mean path. Values measured with WAIL are indicated by the lower dashed line. The intersection with the lower curve determines the optical depth, and from the upper curve, the cloud thickness. (b) A similar plot illustrating the combined space-time scheme, which yields similar results as in panel (a), but with less uncertainty in the optical depth and thickness .

REFERENCES

Davis, A.B., D.M. Winker, A. Marshak, J.D. Spinhirne, R.F. Cahalan, S.P. Love, S.H. Melfi, and W.J. Wiscombe, 1997: Retrieval of physical and optical cloud thicknesses from space-borne and wide-angle lidar, *Advances in Atmospheric Remote Sensing with Lidar*, Eds. A. Ansmann et al., Springer-Verlag, pp. 193–196.

Davis, A.B., C. Ho, and S.P. Love, 1998: Off-Beam (Multiply-Scattered) Lidar Returns from Stratus, 2: Space-Time Measurements in a Laboratory Simulation, *19th International Laser Radar Conference Proceedings*, Eds. U. Singh et al., pp. 55–58, July 6–10, 1998, Annapolis (Md), NASA Center for Aero-Space Information (CASI).

Davis, A.B., R.F. Cahalan, J.D. Spinhirne, M.J. McGill, and S.P. Love, 1999a: Off-beam lidar: An emerging technique in cloud remote sensing based on radiative Green-function theory in the diffusion domain, *Phys. Chem. Earth (B)*, **24**, 757–765.

Davis, A.B., 1999b: Physical thickness and optical depth of stratocumulus from space-borne lidar, A moment-based diffusion method, *Technical Digest of OSA Topical Meeting on "Optical Remote Sensing of the Atmosphere"*, pp. 66–68, June 21–25, 1999, Santa Barbara (Ca), Optical Society of America, Washington (DC).

Davis, A.B., S. P. Love, C. Ho, D. M. Winker, M. Vaughan, and R. F. Cahalan, 2000: Cloud-Property Retrievals from Off-Beam/Multiple-Scattering Lidar Data Collected in Space and from Ground *20th International Laser Radar Conference Proceedings*

Marshak, A., A.B. Davis, W.J. Wiscombe, and R.F. Cahalan, 1995: Radiative smoothing in fractal clouds, *J. Geophys. Res.*, **100**, 26247–26261.

Miller, S.D., and G.L. Stephens, 1999: Multiple scattering effects in the lidar pulse stretching problem, *J. Geophys. Res*, **104**, 22205–22219.

Priedhorsky, W.C., R.C. Smith, and C. Ho, 1996: Laser ranging and mapping with a photon-counting detector, *Appl. Opt.*, **35**, 441–452.

Savigny, C., O. Funk, U. Platt, and K. Pfeilsticker, 1999: Radiative smoothing in zenith-scattered sky light transmitted through clouds to the ground, *Geophys. Res. Lett.*, **26**, 2949-2952.

Winker, D.M., R.H. Couch, and M.P. McCormick, 1996: An overview of LITE: NASA's Lidar In-space Technology Experiment, *Proc. IEEE*, **84**, 164–180.

Winker, D.M., 1997: Simulation and modeling of the multiple scattering effects observed in LITE data, *Advances in Atmospheric Remote Sensing with Lidar*, Eds. A. Ansmann et al., Springer-Verlag, pp. 185–188.

RADAR OBSERVATION OF LARGE ATTENUATION IN CONVECTIVE STORMS: IMPLICATIONS FOR THE DROPSIZE DISTRIBUTION

Lin Tian[1], G. M. Heymsfield[2] and R. C. Srivastava[3]

[1]University Space Research Association
[2]NASA Goddard Space Flight Center
[3]University of Chicago

1. Introduction

Airborne meteorological radars typically operate at attenuating wavelengths. The path integrated attenuation (PIA) can be estimated using the surface reference technique (SRT) [Meneghini et al., 1992, Iguchi and Meneghini, 1994]. In this method, an initial value is determined for the radar cross section of the earth surface in a rain-free area in relatively close proximity to the rain cloud. During subsequent observations of precipitation any decrease in the observed surface cross section from the reference value is assumed to be a result of the two-way attenuation along the propagation path.

In this paper we present selected instances of high PIA observed over land by an airborne radar. The observations were taken in Brazil and Florida during TRMM (Tropical Rainfall Measurement Mission) field campaigns. We compared these observations with collocated and nearly simultaneous ground-based radar observations by an S-band radar that is not subject to significant attenuation. In this preliminary evaluation, a systematic difference in the attenuation in the two storms is attributed to a difference in the raindrop size distributions; this is supported by observations of ZDR (differential reflectivity).

2. Field observations and equipment

The TRMM field experiment was held in the southwestern Amazon from January to February 1999 and Florida from August to September 1998. A variety of instruments were deployed during the field campaigns. Here we give a brief description of relevant instruments.

Corresponding author address: Lin Tian, NASA/GSFC, Code 912, MD 20771
email: tian@agnes.gsfc.nasa.gov

The NASA ER-2 Doppler radar (EDOP) mounted on ER-2 aircraft operates at the 3-cm wavelength and has two fixed antennas, one pointing at nadir and the second pointing approximately 33° ahead of nadir. The beam width of the antennas is 3° which defines a nadir footprint at the surface of 1 km. The ER-2 ground speed is nominally 210 ms^{-1} and the integration period used by the data system is 0.5 s. These two values imply that an estimate of the surface cross-section is obtained every 100 m along the flight track and so 10 samples are obtained during the travel of one beam width. The range resolution is 37.5 meters. Additional details of the radar and processing are described by Heymsfield et al. (1996). NCAR S-Pol (S-band Polarization) is a ground-based radar operated at 10 cm wavelength. The beam width of S-Pol antenna is 0.91° and range resolution is 150 meters. (http://www.atd.ucar.edu)

3. Observations

Fig. 1a shows the reflectivity observed by EDOP forward antenna from a deep convective storm on 10 February 1999 in Brazil. The 40 dB reflectivity reaches up to 8 km in height and the maximum reflectivity is about 45 dBZ. Fig. 1b shows PIA estimated from the surface reflectivity measured along the forward path (solid line). A maximum PIA of 30 dB occurred around 19 km distance. PIA from nadir measurement is not used because it is subject to large errors due to the high variability of the surface return over land at nadir incidence.

For this case, reflectivity data were obtained from the S-Pol radar located about 60 km from the storm and the volume scan nearest in time to the over-flight was interpolated to a grid coincident with the vertical plane mapped out by the EDOP radar. PIA was then estimated from the S-pol data using an empirical relation between the specific attenuation (k) and reflectivity (Z). The path of the

integration was along the path of the EDOP forward beam. The maximum PIA derived from the S-Pol reflectivity (dashed line in Figure 1b) shows a maximum of 13 dB which is less than half of that observed from the EDOP.

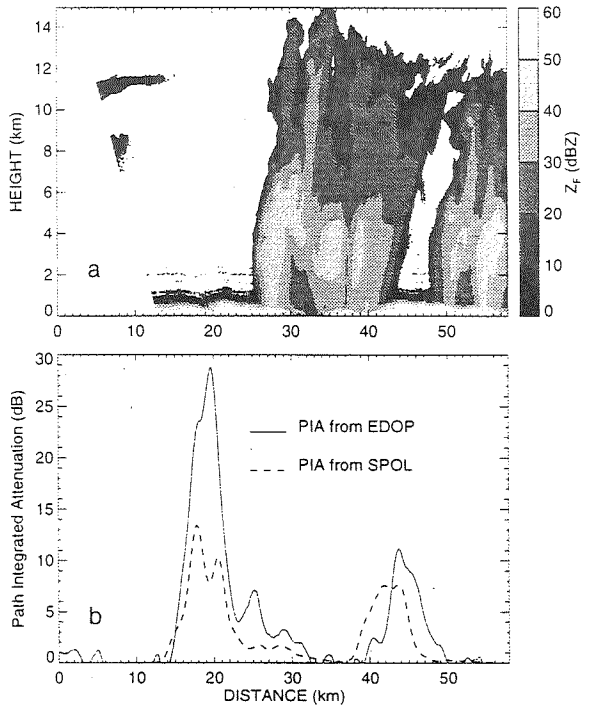

Fig. 1 a) Reflectivity observed by EDOP on February 10, 1999 during 1811-1819 UT in Brazil. b) PIA estimated by EDOP using surface reflectivity (solid line) and using an empirical relation between the specific attenuation and reflectivity obtained by SPOL (dashed line)

Fig. 2 is similar to Fig. 1 but the observation was taken in Florida on 15 August, 1998. The storm in Florida is more intense; The 40 dB reflectivity reaches up to 15 km (Fig. 2a) and the maximum reflectivity observed by EDOP is 55 dBZ. The maximum PIA observed by EDOP (solid line in Fig.2b is about 25 dB which is lower than the case in Brazil. The maximium PIA calculated from k-Z (specific attenuation and refllectivity) relation using reflectivity from S_Pol (dashed line in Fig. 2b) is about 15 dB. The actual value would be about 18 dB if the heightest elevation scan topped the storm.

How do we explain the large PIA observed in Brazil? Why is there a difference in PIA derived from k-Z relation and from the SRT? There are several possibilities: a) a non-typical raindrop size distribution, b) wetted ice particles such as snow aggregates, graupel, or hail, c) large non-spherical particles, d) error in the measurement of the surface return. In this paper, we will limit our scope on a) and discuss others briefly.

For the possibility of hail we examined reflectivity and ZDR from S_Pol. In general, ZDR is a measure of mean drop size and is positive

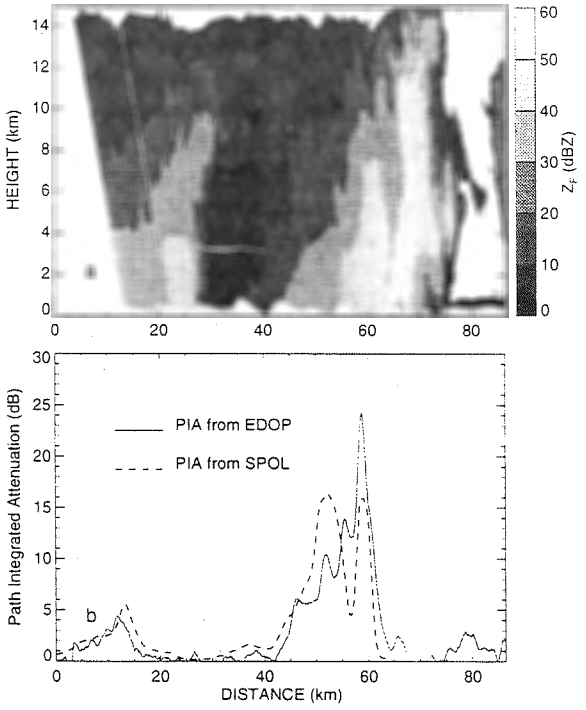

Fig. 2 Same as Fig. 1 but the observation is on August 15, 1998 during 2223-2230 in Florida.

for rain and near zero for hails. Also the reflectivity increases substantially with the presence of hail because the scattering cross section of hails are much larger than that of raindrops. Below the melting level, ZDR is about 1dB for the Brazil case, and 2 dB for the Florida case. The maximum reflectivity observed in the Brazil storm was 52 dBZ. Therefore significant hail is unlikely in the Brazil storm. The maximum reflectivities in the Florida storm exceeded 55 dBZ which means that hail was likely in that storm. Below the freezing level, where most of the attenuation occurs, any hail is likely to be wet due to melting and /or because of collisions with raindrops. The accumulation of water around an ice particle can stabilize it during fall preventing the tendency of the dry particle to tumble. That wet particle is also likely to have an ellipsoidal shape similar to large raindrops because of the tendency for the melted

water to collect around the middle part of the particle as it is swept around the particle by the airflow. This can explain the high ZDR in the Florida storm despite the presence of hail. However, the wet ice particle is likely to produce large attenuation which conflicts with the lower attenuation observed in the Florida storm. The role of ice particles as a possible factor in explaining the observed differences between the two storms needs to be further examined through analysis of other polarimetric variables, vertical air velocities and other features of the storms. We propose to make such a study in the future.

The errors in PIA estimated from surface return are less than 2 dB since the variability in the surface return over the land at large incidence angle is less then 2 dB (Tian et al., 1999). It should be emphasized that the absolute value of the surface echo is not critical for PIA since it is a difference of the surface return in adjacent rain-free and rain area. What is important, however, is that the surface echo does not change as a consequence of wetting from the rain since any changes in the surface cross-section are assumed to be a result of attenuation along the propagation path. In the cases studied so far with the EDOP radar, no significant change in the cross-section has been observed at the transition between rainy and clear conditions for non-nadir incidence.

Now we shall interpret the difference in PIA in terms of differences in the DSDs in the two storms.

4. Discussion

a) Theory

Attenuation greater than that given by empirical equation could be due to unusual rain drop size distribution, namely, predominately small drops (Tian and Srivastava, 1996). For an exponential drop size distribution,

$$N(D) = N_0 \exp(-\Lambda D) \qquad (1)$$

where *N(D)dD* is the number of drops of diameter between *D and D+dD* per unit volume. and the slope Λ can be written as

$$\Lambda = C_1 / D_0 \qquad (2)$$

where D_0 is the median drop diameter and $C_1 = 3.67$ if the maximum diameter of the drop $D_{\max} \to \infty$. The reflectivity factor is given by

$$Z = \int_0^\infty N(D) D^6 dD = 720 N_0 / \Lambda^7 \qquad (3)$$

Now suppose the extinction cross-section of a drop of diameter *D* is given by $Q_{ext} = CD^n$, where *C* and *n* are parameters depending on the refractive index of the drop and wavelength of the radar (Atlas and Ulbrich, 1974). Then the specific attenuation

$$k = \int_0^\infty N(D) Q_{ext}(D) dD = C_2 N_0 / \Lambda^{n+1} \qquad (4)$$

where C_2 is a numerical constant. Eliminate N_0 between (3) and (4), we have

$$k = C_3 N_0^{(6-n)/7} Z^{(n+1)/7} \qquad (5)$$

Where C_3 is a numerical constant. Suppose we have two exponential distributions with intercepts N_0 and N_{00}, such that they both give the same Z. Then we have

$$N_0 / \Lambda_0^7 = N_{00} / \Lambda_{00}^7 \qquad (6)$$

where Λ_0 and Λ_{00} are slopes for the two distributions. From the eq.(3), the ratio of k's (k_0 and k_{00}) for the two distribution will then be

$$k_0 / k_{00} = \left(N_0 / N_{00}\right)^{(6-n)/7} \qquad (7)$$

From (2) and (6), the ratio of the median volume diameter for the two distribution will be

$$D_0 / D_{00} = \left(N_{00} / N_0\right)^{1/7} \qquad (8)$$

From (7) and (8) we see that distribution with higher N_0 will have higher *k* and smaller median volume diameter. As an example, for the same Z, if $k_0 / k_{00} = 2$ then from eq. (7), assuming n = 4.5, we have $N_0 / N_{00} = 25.5$ and $D_0 / D_{00} = 0.63$. Therefore, the first distribution which has twice the attenuation has an intercept which is 26 times the intercept of the 2nd distribution; the first distribution also has a median volume diameter which is smaller; it is 0.63 times the median volume drop diameter of the 2nd distribution.

b) Observations

There were no coincident or near-coincident observations of DSD taken for the two flight lines due to the strong intensity of the storms. However, average drop size distributions from the ground-based distrometers suggest more smaller drops and less bigger drops in Brazil compared to Florida (personal communication, Tokay, 2000). The observed ZDR difference between the two cases also implies a smaller median volume drop

diameter in the Brazil storm if we assume that the reflectivity is dominated by raindrops in both storms.

Fig. 3 shows the frequency of ZDR for intervals of 4 dBZ and 0.5 dB in reflectivity and ZDR respectively. The data was limited to the area where the large PIA occurred and below the melting level. It shows a systematic difference in ZDR for given reflectivity between the Brazil (Fig. 3a) and the Florida (Fig. 3b) flight lines. For example, for given reflectivity of about 40 dBZ, there is a greater occurrence of ZDR of 1 dB in Brazil and 2 dB in Florida, corresponding to a median drop diameter of 1 mm and 1.8 mm respectively.

5. Future Work

In this paper, we suggest that the observed large PIA observed in Brazil is due to a substantial large number of smaller drops based on observation of DSD and ZDR. In the future we will (1) examine further the possible role of ice in the X-band attenuation using other polarization measurements from S-Pol; (2) conduct a more detailed comparison between the S-band (S-Pol) and X-band (EDOP) reflectivities, including vertical profiles; (3) Finally, we will try to explain why the drop sizes distribution may be different in the two places and study the possible role of ice particles and wet ice particles in explaining the differences in attenuation.

Acknowledgments: The authors thank Dr. J. Vivekanandan for his interest and many helpful comments. We also thank Dr. Ali Tokay for providing the drop size distribution observation. We appreciate Dr. Steve Bidwell and Ed Zenker for their engineering support. We also thank Bob Rilling for providing S-Pol data. This work is supported by Dr. R. Kakar of NASA Headquarters under NASA's Tropical Rainfall Measuring Mission. The work of Ramesh C. Srivastava in TRMM is supported by NASA NAG 5 4777.

6. Reference

Atlas, D., and C. W. Ulbrich, 1974: The physical basis for attenuation-rainfall relationships and the measurement of the rainfall parameters by combined attenuation and rainfall methods. *J. Rech. Atmos.*, **8**, 175-298.

Heymsfield, G.M., S.W. Bidwell, I.J.Caylor, S. Ameen, S. Nicholson, W. Boncyk, L. Miller, D. Vandemark, P.E. Racette, and L.R. Dodd, 1996: The EDOP radar system on the high-altitude NASA ER-2 aircraft. *J. Atmos. Oceanic Technol.*, **13**, 795-809.

Iguchi, T. and R. Meneghini, 1994: Intercomparison of single frequency methods for retrieving a vertical rain profile from airborne o spaceborne radar data. *J. Atmos. Oceanic Technol.*, **11**, 1507-1516.

Meneghini, R., T. Kozu, H. Kumagai, and W. C. Boncyk, 1992: A study of rain estimation methods from space using dual-wavelength radar measurements at near-nadir over ocean. *J. Atmos. Oceanic Technol.*, **9**, 364-382.

Tian, L., G. H. Heymsfield and S. W. Bidwell, 1999: Potential Application of the Surface Reference Technique Over Land at Large Incidence Angle. Preprints, *29th Conf. on Radar Meteor., Amer. Meteor. Soc.*, 748-750.

Tian, L., and R. C. Srivastava, 1997: Measurement of Attenuation at C Band in a Convective Storm by a Dual-Radar Method, *J. Atmos. Oceanic Technol.*, **14**, 184-196.

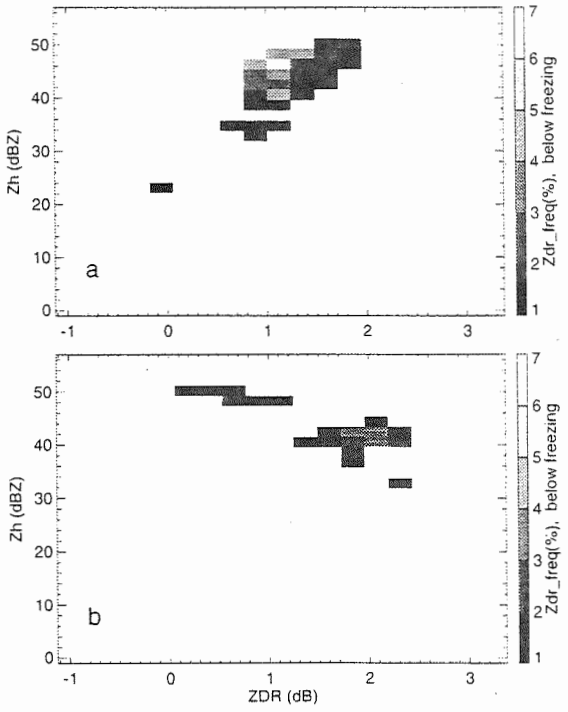

Fig. 3 Frequency occurrence of ZDR for given interval of reflectivity and ZDR observed by S_Pol in the region where high PIA is observed for the case shown in Fig. 1a (a) and Fig. 2b. (b).

PULSE DOPPLER WEATHER RADAR & ITS USE IN THE RESEARCH OF CLOUD AND PRECIPITATION PHYSICS

Huang, Jixiong

CAAC Beijing Meteorology Center, Beijing, China

Pulse Doppler Weather Radar works according to Doppler effect. Using the discrepancies of phase or frequency between signals sent and received, it estimates such physical values as average velocity, velocity spectrum and velocity spectrum width of scattering particles in the effective radiate objects, relative to the radar.

Since the introduction of Pulse Doppler Weather Radar, it has made great achievements in the detection of strong convection weather, in the research of clouds and fogs, in the precaution and short-period forecast of catastrophic weather like tornado, burst downdraft, etc. In recent years, dramatic advances have been made in computer technology. The large amount of information obtained by Doppler radar can be gathered, processed and displayed in real time and real place. Various radar secondary products get from further analysis are able to measure the vertical velocity, dripping spectrum distribution, turbulence spectrum width, horizontal wind field, wind shear of the atmosphere. They can also be used to get a variety of atmospheric physics parameters such as containing water quantity in the clouds, precipitation, and its intensity and condense ratio. Hence some light can be shed on the movement of airflow in the precipitation area and the turbulence structure in the surface boundary layer.

1. DESCRIPTION OF THE PULSE DOPPLER WEATHER RADAR THEORY

1.1 Extraction of the Doppler frequency spectrum

The key to put Doppler radar into practice is how to effectively extract the Doppler frequency information on time. There are several methods as follows:

1.1.1 Electronic spectrum analyzer method:

Use large number of short-term filter at different frequency center, according different echo information at different distance point, calculate the integral by time interval, then make output.

In this method, because there must be too many filters, it is too hard to put it into practice.

First Corresponding author's address:
Huang,Jixiong, 6914 Post-box,
Beijing,100621, P. R. China
Telephone: (China)010-65682455
E-mail: carson@bj.col.com.cn
Huhjx@sina.com

1.1.2 Fast Fourier Transform (FFT) method:

Use Fourier Transform to handle with the signal returned from the radar, get the frequency spectrum distribution, then calculate the spectrum parameter. If the radar received signal in one distance is f(nt), t is sample time interval, n is sample serial number. Use Discrete Fourier Transform (DFT) we can get the frequency spectrum of the return signal.

This method has high precision, and can get Doppler frequency spectrum, then average Doppler frequency, frequency spectrum density, etc. But in this method there is too many calculations so it is very hard to make processing on time.

1.1.3 Pulse Pair Processing (PPP) method:

For make it possible to processing on time, and keep high precision, under a kind of assumption, use Pulse Pair Processor to deal with a pair of continuous sample value in each distance library, then get the average frequency information etc. This is Pulse Pair Processing (PPP) method.

If the compound amplitude of the echo signal is:

A(t)=x(t)+iy(t)

Self related function of compound amplitude is:

$$R(t) = \overline{A(t)A^*(t+T)}$$

Average Doppler frequency floating:

$$\overline{F}_{DPPP} = \frac{1}{2\pi T} Arg[R(t)] = \frac{1}{2\pi T} \arctan\left[\frac{I_m R(t)}{R_e R(t)}\right]$$

The variance of Doppler frequency spectrum (frequency spectrum width)

$$\sigma_{FD}^2 = \frac{1}{\pi T}\left[1 - \frac{R(T)}{R(0)}\right]$$

As V=2f/λ, that is, Doppler frequency spectrum is equal to Doppler velocity spectrum of particles inside the effective radiate objects. So, Average Doppler radial velocity:

$$\overline{V} = \frac{1}{4\pi\lambda T} Arg[R(t)]$$

Velocity spectrum width:

$$\sigma_V^2 = \frac{1}{2\pi\lambda T}\left[1 - \frac{R(t)}{R(0)}\right]$$

1.1.4 Other method:

Concerned Memorial Filter method (CMF), Vector Phase Change method (VPC), Scalar Phase Change method (SPC), Time Dervative Change method (TDC).

All above method has its own special characteristics. When power density function of the precipitation echo signal obey Gauss distribution, PPP method is more practical.

1.2 Application of Doppler velocity spectrum width:

Doppler velocity spectrum width is the deviation of the Doppler velocity from the average value. It is caused by various radial velocities of scattering particles. There are four factors that affect the spectrum width of meteorological objects:

(1) Vertical wind shear of atmosphere;
(2) Horizontal wind movement caused by width of radar wave;
(3) Atmosphere turbulence;
(4) Final precipitating velocity of uneven particles.

Evidence show that the first two influences are relatively small. When radar makes horizontal detection, the particles' final precipitating velocity has no effect on the spectrum width. Therefore turbulence can be approximated by the spectrum width estimates. When radar makes vertical detection, the estimates of spectrum width can be approximately taken as the spectrum width of particles if turbulence is weak.

1.3 Detection parameters and methods of Weather Doppler Radar

Since the introduction of the first Doppler Radar in 1943, great achievements have been made in the detection of strong convection climate, in the research of clouds and fogs, in the precaution and short-period forecast of catastrophic weather like tornado and burst downdraft. Also great progress has been made in the research of windstorm, airflow structure and outcome of the precipitation system. Use single Doppler radar detecting technique as a sample, Now let me make briefly introduction of the detecting method and parameter of Doppler weather radar.

1.3.1 Plane Point scanning pattern detection (PPI)

By layered display form, we can get the distribution of average radial velocity in echo signal. Because velocity detected by Doppler radar is only the average Doppler velocity of all of particles in the radar radiate volume, the target object velocity detected by Doppler radar is the 2-D shape of radial heft which direction is the antenna direction. It has essential differences with the real 3-D wind field.

Therefore, on one hand, we should identify and analyze this kind of radial velocity, find out its rule, make Doppler velocity map of different kinds of weather system, then according to Doppler radial velocity map, determine the mid-small size weather system, get the inside airflow structure and characteristic of its development. For example, cyclone, reverse cyclone, gather, divergence, burst downdraft, tornado, bail cloud, frontal surface, gust front etc.

On the other hand, with the developing of computer technology and computer mathematics. By digital radar technology, people use radial Doppler velocity products make 3-D real wind field simulation, then put them into practice.

1.3.2 Vertical detection

(1) Detection of atmosphere vertical velocity.()
(2) Measuring the rain drip spectrum.()

1.3.3 Detecting Horizon flow filed and precipitation with VAD technology.

When using VAD method, the radar antenna scanning with a fixed angle of elevation α, at the same time, make record of dripping particles' radial velocity at distance R and radial velocity $V_R(\beta)$ at angle β, make display of velocity angle. (map omitted)

VAD method can make detection of large wind field centered by radar. When the wind field is even, it can get the horizontal wind direction, wind velocity, and average Doppler vertical velocity at detected height.

Horizontal: $\overline{V}_h = \dfrac{V_1 - V_2}{2\cos\alpha}$

Vertical: $\overline{V}_f = \dfrac{V_1 + V_2}{2\sin\alpha}$

When angle β=0, $\overline{V} = V_1$, when β=180° , $\overline{V} = V_2$

When wind field is not even, make Fourier progression spread out with the detect value can get wind direction, wind speed of horizontal wind, and horizontal air gather, divergence, wind field deformation etc. Make assumptions under some kinds of condition, use VAD method and other sounding values together, can measure condense ratio of precipitation and precipitation intensity.

1.4 Maximum unambiguous velocity and maximum unambiguous distance

1.4.1 Maximum unambiguous velocity and velocity fold

The rationale of pulse Doppler radar is: Use the feature of Doppler frequency floating between moving particles and radar (the difference between reflex frequency of moving particle with radar sent frequent beam and radar sent frequency) is in direct proportion to particle radial velocity, to make detection of particle velocity. That is:

$$f_d = \frac{2V_r}{\lambda} = \frac{\Delta\Phi}{2\pi T} = \frac{\Delta\Phi}{2\pi}F \Rightarrow V_r = \frac{\lambda F \Delta\Phi}{4\pi}$$

In above equation: *F* also named as *PRF*, is pulse repeat frequency, $\Delta\Phi$ is the phase difference between adjacent cycle echo pulse signal and coherent vibration signal It's a cyclic function of 2π. When $\Delta\Phi = n \cdot 2\pi$ the velocity fold will happen. For it is possible to have velocity value which is less than zero, therefore, the unfold maximum unambiguous velocity is:

$$V_{\max} = \pm\frac{1}{4}\lambda F$$

That is, when the radial velocity between real wind field and radar is larger than maximum unambiguous velocity $V_{\max}$, the radar detected velocity map will fold.

1.4.2 Maximum unambiguous distance

When use pulse Doppler radar itself get samples from non-adjacent time period, It is caused not continuous of maximum detectable distance space. The maximum unambiguous distance is the longest distance from one pulse's start to its return before next pulse's start.

$$R_{MAX} = \frac{1}{2}CT = \frac{C}{2F}$$

1.4.3 The relationship between maximum unambiguous velocity and maximum unambiguous distance

According to the facts we mentioned above, we can know that the radar pulse repeat frequency is in direct proportion to maximum unambiguous velocity, in opposite proportion to maximum unambiguous distance. For a constant radar pulse repeat frequency (*PRF*), the non-blur velocity and distance detected by radar is a pair of contradictory value. There is equation as follows:

$$R_{MAX} \cdot V_{MAX} = \frac{C\lambda}{8} = Const \quad \textit{(for a specified radar)}$$

For a specified radar, λ firm, *PRF* firm, according to this theory, it's impossible to make benefit for both velocity and distance at the same time. Therefore, in next step we must use digital radar technology to expand the range of non-blur velocity. This is what usually people said: "Doppler velocity unfold technology".

2. DIGITAL RADAR TECHNOLOGY AND DOPPLER DATA ANALYSIS FORECASTING METHOD.

2.1 Doppler radar velocity unfold technology

2.1.1 Hardware Double *PRF* method.

Two different kinds of pulse repeat frequency work alternately, use PPP method to calculate the difference between the auxiliary co-variance axle angle, then get expended velocity value after computer process.
For example, when the launched time between two pulse T1:T2=2:3, the maximum non-blur velocity can be extended twice, when T1:T2=4:3, the maximum unambigiuous velocity can be extended three times.

2.1.2 Application velocity's successive and its logical determination, using software to expand velocity.

Scanning Doppler velocity map point by point from radial direction. When blur happens, two adjacent velocity grade gradient change to two times of maximum unambiguous velocity, That's not fall in the truth. Tuning one of all the adjacent velocity grade $2V_{MAX}$ to expand velocity.
In our daily work, velocity folding occurs popularly. If velocity changing from positive infinite to negative infinite fluently, there is no zero line during it, then the velocity fold once. If there is zero line and "opposite" folding district, then the velocity fold twice. The first folding district real radial wind direction is the opposite direction of the displaying radial wind direction. The real radial wind velocity should plus $2V_{MAX}$. The second folding district real radial wind direction is the same direction with displaying radial wind direction. The real radial wind velocity also should plus $2V_{MAX}$. This is different from against the wind region. (against the wind region is the real radial wind field in small district opposite with surrounding radial wind field.) For example, the velocity map of May 3, 1997(map omitted), the small structure 40kms southwest of local field is second velocity fold, not head wind area.

2.2 3-D real wind field simulation

After Doppler radial velocity echo unfolding, and have it fore-processing, we can simulate real wind field. For a single Doppler radar, there must be some assumption to extend radial velocity free space, typically it s local small district one wind field assumption. Simulate radial wind as multi space 2-D horizontal wind field and Vertical wind field, then use computer graphic technology make 3-D real wind field simulation.

2.3 Identification, tracking and evolution of strong convection.

Use radar make identification, tracking strong convection weather system, forecasting its moving direction, next position, strength change, and make danger zone alert. Together with mid-small size weather system data mode, mid-large cloud map

message, put multi station inspecting, identifying, tracking together, to identify a system strength changing and inside structure alternating during its happening, developing, and dying.

For digital processing, Identify strong convection weather system like windstorm as the 3-D constant area which reflective ratio factor, velocity factor and volume is bigger than valve value. Use multi changeable parameter to identify, justify system. According to the map change between adjacent two time point, merge a same system by gravity tracking method. According to its merging and splitting status and time period, use liner method, history route tracking, map tracking, velocity tracking, guide airflow tracking, and many other kinds of data model forecasting, tracking the next system position and status, display its output with animation.

2.4 Digital conclusion of cloud physics parameters

Use data calculation method, identify the rising air flow and sinking airflow thickness of mid-size cyclone, together with radar velocity azimuth display (VAD) technology and velocity volume display (VVP) technology, identify horizontal and vertical wind velocity and wind direction in clouds and its divergence, deformation, aixs of dilation, district average reflectivity etc. Together with theshold value detect wind shear in the low air, gust front, onflow in cloud, burst downdraft, tornado, bail, then get its quantitative parameter and structure.

2.5 Analyses of atmosphere motion an onflow in cloud

Use Doppler velocity pulse — Doppler velocity spectrum width to identify the atmosphere turbulence and wind shear of the atmosphere.

3. DOPPLER WEATHER RADAR AT BEIJING CAPITAL INTERNATIONAL AIRPORT

3.1 System description

The TDR—3600HP Doppler radar at Beijing Capital International Airport is bought from Kavouras Corp. August, 1995. This is a new C wave band Doppler weather radar. Working frequency is tunable at 5600MHz, 5620MHz, and 5650MHz ($\lambda \cong$ 5.4cm). It has strong penetrate ability, and high sensitive, maximum power $\geq$ 250KW, pulse width is tunable between 0.125μs—18μs, pulse repeat frequency PRF is continuously tunable between 150Hz — 3000Hz, Receiver minimum detectable signal (MDS) is –123DB when pulse width is 18μs.

3.2 Working mode

(1) Alert status

The radar regularly make low angle of elevation scan between 400KM — 250 KM, when the echo signal has been detected notify meteorological forecaster and air traffic controller, change to second mode.

(2) 200km mode

When echo signal is mainly between 100KM — 200 KM, working tasks 200KM — VOL, 200KM — SIP, 100KM — SIP.

(3) 100km mode

When echo signal is mainly less than 100KM, working tasks 100KM — VOL, 100 KM — SIP, 200KM — SIP.

In the above, VOL volume scan task is from highest to lowest multi angle of elevation assembled original message working package. Mainly it is weather forecasting people make service and keep the message integrity of radar information. SIP simple mission is fast working package of low angle of elevation simplify. Mainly it is air traffic control service, and make low angle of elevation graphic runs faster, keep radar map on time.

3.3 Second production

PPI (plan position indicator product)
RHI (range height indicator)
TOPS (echo tops)
CAPPI (constant altitude plan position indicator)
MAX (maximum reflectivity)
XSECT (cross section)
SHEAR (wind shear)
VIL (vertically integrated liquid)
VVP (velocity volume processing)
WARN (warning/centroid)
RAIN1,RAINN (1, n—hour rain accumulation)

3.4 Real sample analysis ( )

3.5 The combination of using Doppler weather radar and wind shear outline radar ( )

4. SUMMARIES AND CONCLUSION

There is a great potential of new Doppler weather's use in the research of cloud and precipitation physics. Therefore more attention should be paid to the further development and applications of it.

REFERENCES()

Spatial Distribution of Mean Raindrop Shape from Polarimetric Radar Observations

Eugenio Gorgucci, Gianfranco Scarchilli[1], Chandrasekar and V. N. Bringi[2]

[1]Istituto di Fisica dell'Atmosfera (CNR), Area di Ricerca Roma-Tor Vergata
Via del Fosso del Cavaliere, 100 - 00133 Rome, Italy, E-mail: gorgucci@radar.ifa.rm.cnr.it
[2]Colorado State University, Fort Collins, Colorado 80523-1373

1. Introduction

The mean shape of raindrops plays a critical role in the interpretation of the polarimetric radar measurements. The shapes of raindrops have been studied theoretically by Beard and Chuang (1987), experimentally in wind tunnels by Pruppacher and Beard (1970), and in natural rainfall using aircraft probes by Chandrasekar et al., (1988) and Bringi et al., (1998). All of the above studies as well as polarimetric radar measurements at multiple polarizations show that the shape of raindrops can be approximated by an oblate spheroid, described with an axis ratio (b/a) and equivolumetric spherical diameter D, where a and b are the major and the minor axes of the drop, respectively. A commonly used approximation relating the axis ratio of a raindrop to the diameter is given by (Pruppacher and Beard, 1970)

$$\frac{b}{a} = 1.03 - 0.062D \qquad (1)$$

In addition non linear relations are also available to model axis ratios of raindrops (Andsager et al., 1999). It would be very useful to obtain an estimate of the mean shape-size relation from polarimetric radar measurements in order to study any variability in the mean shape of the raindrops in different storms as well as in different regions of storm. This paper presents an algorithm to estimate the mean shape of raindrops from polarimetric radar data as well as spatial variability of this estimate using CSU-CHILL polarimetric radar data.

2. Mean raindrop shape model

The shape versus size relation can be approximated by a straight line given by

$$r = 1.03 - \beta D \qquad (2)$$

In equation (3) r=1 when $D \le 0.03/\beta$, where β is the magnitude of the slope of the shape-size relationship given

$$\beta = -\frac{dr}{dD} \qquad (3)$$

The approximation given by (1) corresponds to β=0.062 mm^{-1}, which is close to the equilibrium shape-size relation, and therefore we denote it by β_e. $\beta > \beta_e$ indicates that raindrops are more oblate than equilibrium, whereas $\beta < \beta_e$ indicates raindrops are less oblate (or closer to spherical) than equilibrium.

3. Polarimetric radar measurements: Sensitivity to shape-size relation

The three commonly used polarimetric radar parameters are reflectivity factor at horizontal polarization (Z_h), differential reflectivity (Z_{dr}) and specific differential propagation phase (K_{dp}). Both cloud model and measurements of Raindrop Size Distribution (RSD) at the surface and aloft show that a Gamma distribution model adequately describes many of the natural variations in RSD (Ulbrich, 1983):

$$N(D) = n_c f(D) \qquad (m^{-3}mm^{-1}) \qquad (4)$$

where N(D) is the number of raindrops per unit volume per unit size interval, n_c is the concentration and f(D) is the Gamma probability density function. N(D) can also be written to normalize the water content with respect to an equivalent exponential distribution as (Testud et al., 2000)

$$N(D) = N_w g(\mu) \left(\frac{D}{D_0}\right)^{\mu} e^{-\Lambda D} \qquad (5)$$

$$g(\mu) = \frac{6}{(3.67)^4} \frac{(3.67+\mu)^{\mu+4}}{\Gamma(\mu+4)} \qquad (6)$$

where D_0 is the volume weighted median diameter and Γ indicates the Gamma function..

According to (1), raindrops become more oblate when the size is large. Therefore, the effect of varying shape-size relationship should be more evident in the presence of larger drops. The volume weighted median drop diameter D_0 is a good indicator of the mean size of drops in the distribution. The effect of varying shape-size relation of raindrops is illustrated by the following analysis. For a given RSD we compute the radar measurements Z_h, Z_{dr} and K_{dp}, at S-band frequency, for various β in the range of 0.02 to 0.1 in steps of 0.01. Fig. 1 shows the normalized variation of Z_{dr} (linear scale) with respect to Z_{dr} obtained from the

equilibrium relation (1) as a function of β for different values of D_0. For nearly spherical particles ($\beta \cong 0$), Z_{dr} value should be zero dB or unity in linear scale. The normalized bias for $\beta \cong 0$ in comparison to β_e is determined by the value of Z_{dr} at β=0.062 so that it increases as D_0 increases. The range of Z_{dr} difference between nearly spherical drops (β=0.02) to equilibrium shape drops varies between 0.84 dB to 1.89 dB depending on D_0. Similar arguments can also be made when β>0 so that normalized bias of Z_{dr} increases with D_0 as we move farther from $\beta \cong 0$. Similar analysis can also be made for K_{dp}.

4. Algorithm to estimate raindrop shape-size relation

The result of section 3 indicates that the observations of Z_{dr} and K_{dp} are sufficiently sensitive to β, so that it can be turned around into measurement. The estimator of β is developed using the following procedure. Firstly, a large number of Gamma RSD is simulated over a wide range of the parameters chosen randomly in the following intervals:

$-1<\mu<4$, $10^2< N_w<10^5$ (m^{-3} mm), $0.5<D_0<2.5$ (mm).

In addition, for each RSD Z_h, Z_{dr} and K_{dp} are computed for various values of β ranging between 0.02 to 0.1. The above computations are done at S-band frequency. Subsequently, non linear regression analysis is performed to evaluate various functional forms to estimate β. The above analysis yields the estimator for β, at S-band, given by Gorgucci et al. (2000)

$$\hat{\beta} = 2.08 Z_H^{-0.365} K_{DP}^{0.380} 10^{0.0965 Z_{DR}} \qquad (7)$$

A scattergram between $\hat{\beta}$ and the true value of β is shown in Fig. 2; it can be noted that (7) estimates β fairly well. The data used in Fig. 2 yield a correlation of 0.996 with a normalized standard error (the root mean square error normalized with the mean) of 3.6%.

4a. Shape-size relation estimate in the presence of measurement errors

The estimate given by (7) uses Z_h, Z_{dr} and K_{dp}. These three measurements have completely different error structure. Z_h is based on absolute power measurement and has a typical accuracy of 1 dB. Z_{dr} is a relative power measurement and is the differential power estimate between Z_h and Z_v. It can be estimated to an accuracy of 0.2 dB. K_{dp} is the slope of the range profile of differential propagation phase Φ_{dp}, which can be estimated to an accuracy of few degrees. The subsequent estimate of K_{dp} depends on the procedure used such as a simple finite difference scheme or a least square fit. Using a least square estimate of Φ_{dp} profile the standard deviation of K_{dp} can be expressed as (Gorgucci et al., 1999)

$$\sigma(K_{dp}) = \sqrt{3}\frac{\sigma(\Phi_{dp})}{N\Delta r}\sqrt{\frac{N}{(N-1)(N+1)}} \qquad (8)$$

where Δr is the range resolution of Φ_{dp} estimate and N is the number of range samples within the path. For large N we can see that $\sigma(K_{dp})$ decreases as $N^{-3/2}$. For a typical 150 m range spacing, and 2.5 degrees accuracy of Φ_{dp}, K_{dp} can be estimated, over a path of 3 km, with a standard error of 0.32 deg km^{-1}. Thus, the three measurements Z_h, Z_{dr} and K_{dp} have completely different error structure. In addition, the measurement errors of Z_h, Z_{dr} and K_{dp} are nearly independent. In the following we use simulations to quantify the error structure of the estimate of β. The simulation is done as follows. Various rainfall values are simulated varying the parameters (μ, N_w, D_0) of the Gamma RSD over a wide range of values, as defined above. For each RSD the corresponding Z_h, Z_{dr} and K_{dp} are evaluated. The random measurement errors are simulated using the procedure described in Chandrasekar et al., (1986). The principal parameters of our simulation are as follows: a) wavelength λ=*11 cm*, b) sampling time *PRT=1 ms*, c) number of samples pairs *M=64*, d) Doppler velocity spectrum width σ_v=*2 m* sec^{-1}, e) cross correlation between *H* and *V* signals ρ_{hv}=*0.99*, f) range sample spacing over the path where K_{dp} is estimated is 150 m and g) K_{dp} is estimated over a path of 50 range samples, as a least square fit on Φ_{dp} measurements. The above simulation was used to estimate the standard deviation of K_{dp} in the presence of measurement errors. The results of this analysis show that the slope of the shape-size relation β can be estimated to an accuracy of about 9 % in the presence of measurement errors in Z_h, Z_{dr} and K_{dp}.

Bias errors in Z_h and Z_{dr} can affect the estimate of β. Typically in a well maintained system bias error in Z_{dr} is less than 0.2 dB and bias in Z_h is less than 1 dB. Under these conditions $\hat{\beta}$ can be estimated within 10% accuracy under those biases of Z_h and Z_{dr}.

5. Data Analysis

The algorithm to estimate the mean shape-size relation is applied to the CSU-CHILL radar data collected in convective rain showers. Figure 3a shows an RHI of reflectivity through the storm, whereas Fig. 3b shows β. The region between 32 and 34 km consists of down draft with ice melting to rain

whereas, the region between 34 to 38 km is the updraft region (inferred from Z_{dr} profiles). In the down draft region, there is a steady decrease in β as with height indicating that spherical particles melt into raindrops. In addition the β values near the surface are around 0.058 indicating near equilibrium conditions, perhaps due to slight oscillation. On the contrary, in the ranges between 36 to 38 km where it could be dominated by the presence of larger drops, the average β is higher and it is of the order of 0.07. This could be due to two reasons, namely a narrow distribution of the large drops which alone yield a high value of β, or it may be that in updraft regions raindrops are more oblate than equilibrium. Careful in-situ analysis may be needed to further explore this.

6. Summary

The mean shape-size relation of raindrops plays an important role in the interpretation of polarimetric radar measurements. The polarimetric radar algorithms available in the literature have been developed for equilibrium axis ratios. A simple model was developed to describe the shape-size relation of raindrops in terms of the slope (β) of the linear approximation to the shape-size function. Subsequently, theoretical analysis was utilized to quantify the variability in Z_h, Z_{dr} and K_{dp} due to changes in β. The sensitivity of Z_h,. Z_{dr} and K_{dp} to deviation from equilibrium shape-size relation β_e was studied. It was found that both Z_{dr} and K_{dp} were fairly sensitive to changes in β, whereas Z_h was insensitive as expected. There was enough sensitivity to β in Z_{dr} and K_{dp}, that it could be turned around to a measurement. An algorithm to estimate the slope of the shape-size relation was derived. The algorithm can be used to estimate β from measurements of Z_h, Z_{dr} and K_{dp}. Polarimetric radar data collected by the CSU-CHILL radar was used to estimate β. β provides a shape size relation that varied between updraft and down draft regions. In down draft regions, the β was close to equilibrium, whereas in updraft $\beta > \beta_e$. This could be due to domination of large drops, and the mean shape corresponds to large drops only.

7. Acknowledgments

This project was supported by the National Group for Defense from Hydrological Hazards (CNR, Italy), by the Italian Space Agency (ASI), by the NSF and by NASA/TRMM. The CSU-CHILL is supported by the National Science Foundation (ATM-9500108).

References

Andsager K., K. V. Beard, and N. F. Laird, 1999: Laboratory measurements of axis ratios for large raindrops. *J. Atmos. Sci.*, **56**, 2673-2683.

Beard, K. V., and C. Chuang, 1987: A new model for the equilibrium shape of raindrops. *J. Atmos. Sci.*, **44**, 1509-1524.

Bringi, V. N., V. Chandrasekar, and R. Xiao, 1998: Raindrop axis ratio and size distributions in Florida rainshafts: an assessment of multiparameter radar algorithms. *IEEE Trans. Geosci. Remote Sensing*, 36, 703-715.

Chandrasekar, V., V. N. Bringi, and P. J. Brockwell, 1986: Statistical properties of dual polarized radar signals. Preprints, *23rd Conf. on Radar Meteorology*, Snowmass, Colorado, Amer. Meteor. Soc., 154-157.

Chandrasekar, V., W. A Cooper, and V. N. Bringi, 1988: Axis ratios and oscillation of raindrops. *J. Atmos. Sci.*, **45**, 1325-1333.

Gorgucci, E., G. Scarchilli, and V. Chandrasekar, 1999: A procedure to calibrate multiparameter weather radar using properties of the rain medium. *IEEE Trans. Geosci. Remote Sensing*, 37, 269-276.

Gorgucci, E., G. Scarchilli, and V. Chandrasekar, 2000: Measurement of Mean Raindrop Shape from Polarimetric Radar Observations. *J Appl. Meteor. (in press)*

Pruppacher, H. R and K. V. Beard, 1971: A wind tunnel investigation of the internal circulation and shape of water drops falling at terminal velocity in air. *Q. J. R. Meteorol. Soc.*, **96**, 247-256.

Seliga, T.A., and V.N. Bringi, 1976: Potential use of the radar reflectivity at orthogonal polarizations for measuring precipitation. *J. Appl. Meteor.*, **15**, 69-76.

Testud, J., E. L. Bouar, E. Obligis, and M. Ali-Mehenni, 2000: The rain profiling algorithm applied to polarimetric weather radar. *J. Atmos. Oceanic Technol.*

Ulbrich, C. W., 1983: Natural variations in the analytical form of raindrop size distributions. *J. Climate Appl. Meteor.*, **22**, 1764-1775

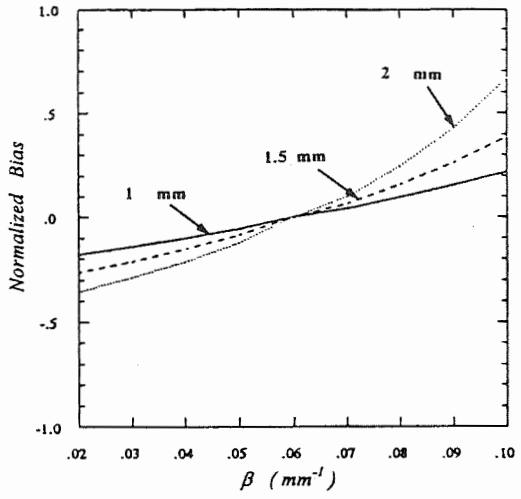

Fig. 1 Normalized bias of Z_{dr} with respect to Z_{dr} obtained from equilibrium model of (1), as a function of β for different values of D_0 (1 mm, 1.5 mm and 2 mm). Note that the bias is zero when β = 0.062.

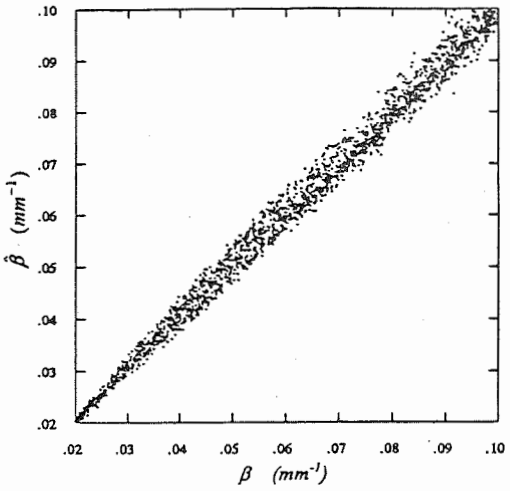

Fig. 2 Scatter diagram of the estimate versus β for various RSD. The correlation coefficient and normalized standard of error of the scatter-gram are 0.996, 3.6 % respectively.

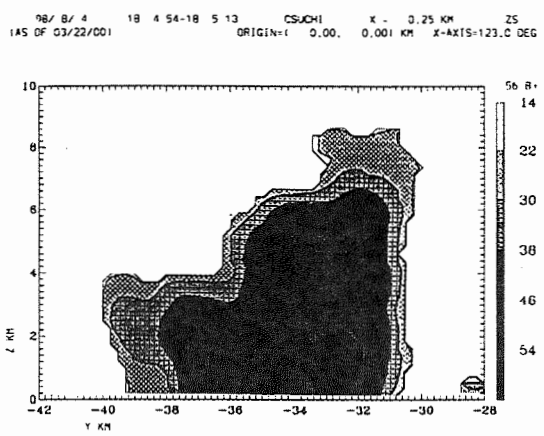

Fig. 3a RHI of reflectivity through a storm cell observed by the CSU-CHILL radar on Aug. 4, 98.

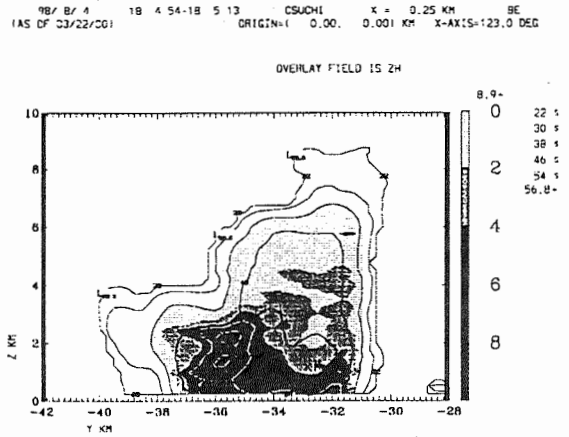

Fig. 3b Vertical structure of β evaluated with overlaid reflectivity contours.

OBSERVATION OF THE INTERACTION BETWEEN CONTRAILS AND NATURAL CIRRUS CLOUDS

M. Kajikawa, K. Saito and C. Ito

Faculty of Engineering & Resource Science, Akita University, Akita 010-8502, Japan

1. INTRODUCTION

Physical properties of contrails, as well as of cirrus clouds, are important to investigate their radiative effects (e.g., Liou, 1986; Sassen, 1997). Although lidar observations of the structure of those clouds have been performed by many researchers (e.g., Freudenthaler et al., 1995, 1998), there are much less data available on the interaction between contrails and natural cirrus clouds. Sassen and Hsueh (1998) pointed out that contrails can be distinguished from natural cirrus due to their tendency to remain thin, and to generate strong laser backscattering and depolarization.

Observations of contrails and cirrus clouds with a ground-based lidar were made at Akita University campus (39°43' N, 140°08' E, 10 m, a.s.l.) during the spring and summer seasons of 1995 to 1997. In this paper the interaction between the contrails formed from aircraft exhausts and natural cirrus clouds will be analyzed and discussed.

2. METHOD OF OBSERVATION

The lidar system used in this observation is equipped with a Q-switched 532 nm Nd:YAG laser as transmitter, with a pulse energy of 0.16 J and a pulse repetition rate of 10 Hz. It is a fixed, vertically pointing system with a 20 cm-diameter telescope. Backscatter signal is converted to electric ones by a photomultiplier tube and recorded by a digital oscilloscope. The vertical resolution of backscattering measurement is 15 m and the vertical profile of backscattering power is obtained by moving average of 75 m.

The scattering ratio (R) of contrails or natural cirrus clouds was made an approximation with the ratio of total (contrails/cirrus clouds and molecular) backscattering power to molecular backscattering ones. The molecular backscattering power was estimated from the vertical profile (the approximate equation obtained by the least squares method) of it except the contrails/cirrus clouds layer. The depolarization ratio (δ) is derived from the ratio of the perpendicular- to parallel-polarized returned powers at each altitude.

Corresponding author's address: Masahiro Kajikawa, Department of civil & Environmental Engineering, Faculty of Engineering & Resource Science, Akita University, Akita 010-8502, Japan; E-mail: kajikawa@ipc. akita-u. ac. jp.

Contrails from commercial jet traffic in an north-south aerial route drifted eastward and then probed by the lider when overhead within about 5~20 minutes after the generation. The young contrails which become the object of this observation are could be identified because of their linear north-south features (Sassen et al., 1998). Contrails primarily were formed at the range of altitude and air temperature, 6.6~12.5 km and −19.8~−59.5 ℃ in respectively.

3. RESULTS AND CONSIDERATION

An example of the obtained vertical profile of R and δ is shown in Fig. 1. In this case a contrail was accompanied with a cirrostratus in higher altitude. The distinction of altitudes of contrails and natural clouds was decided by the existence of shadow of contrails.

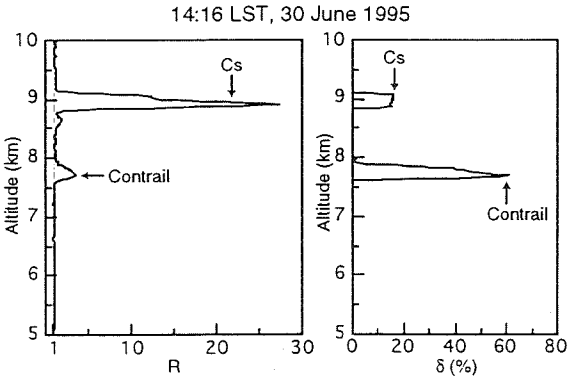

Fig. 1. An example of vertical profiles of scattering ratio (R) and depolarization ratio (δ).

Figure 2 shows the relationship between the maximum value (R_{max}) of scattering ratio and the maximum value (δ_{max}) of depolarization ratio in various cases of contrails and natural cirrus clouds. In this figure the contrails accompanied by cirrus or cirrostratus in higher altitude are indicated with the marks of *i* or *s*, respectively. A double contrail is also attached *d*. The range of differences in altitude of Rmax of contrails and cirrus clouds was from 1.2 km to 1.5 km.

R_{max} of isolated contrails and contrails with cirrus (Ci) or cirrostratus (Cs) in lower altitude proves to be the analogous values of thin natural cirrus clouds from this figure. δ_{max} of the double contrail is larger than that of other contrails. It is clear that R_{max} of contrails with Ci or Cs in higher altitude is considerably larger

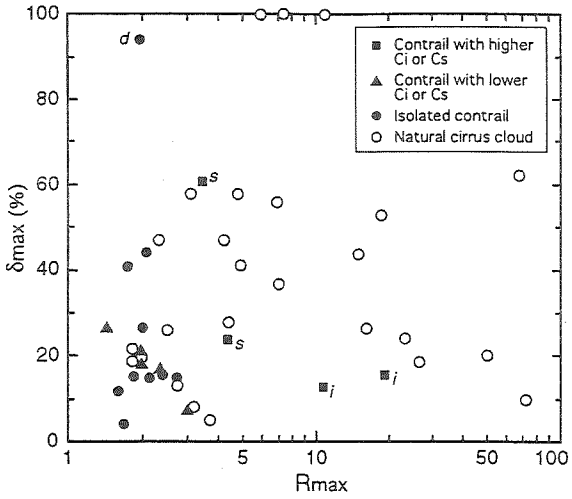

Fig. 2. The relationship between the maximum backscattering ratio (Rmax) and the maximum depolarization ratio (δ) in various contrails and natural cirrus clouds.

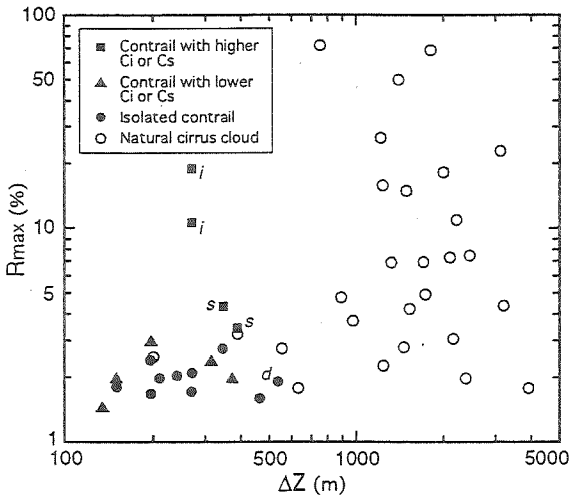

Fig. 3. The relationship between the thickness (ΔZ) and the maximum backscattering ratio (Rmax).

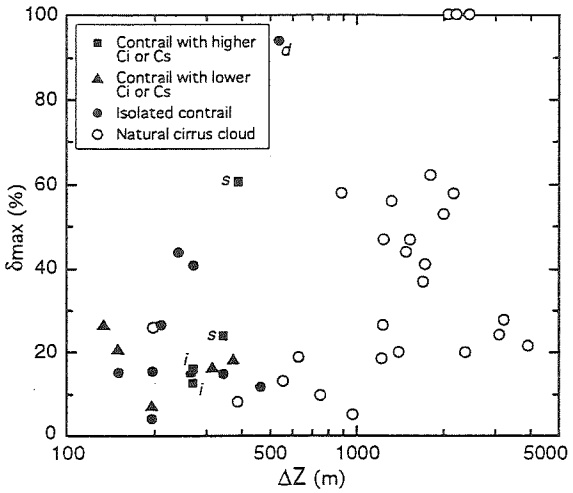

Fig. 4. The relationship between the thickness (ΔZ) and the maximum depolarization ratio (δ).

than that of isolated contrails and contrails with Ci or Cs in lower altitude, although δmax is not always smaller. This fact suggests that the internal structure of those contrails changed by the seeding effect of overlying cirrus or cirrostratus.

The relationship between the physical thickness (ΔZ) and Rmax is shown in Fig. 3 in various contrails and cirrus clouds. The thickness was defined as the continuous layer of R>1 containing the altitude of Rmax (Fig. 1). It can be seen from this figure that ΔZ (about 150～500 m) of various contrails is considerably smaller than that of natural cirrus clouds (Sassen et al., 1998). Rmax of contrails with Ci in higher altitude, in particular, larger than that of other contrails in the same thickness. This suggest again that the effect of interaction between cirrus clouds and contrails.

Figure 4 shows the relationship between ΔZ and δmax of various contrails and cirrus clouds. δmax of the double contrail is much larger than that of other contrails in the same thickness.

4. CONCLUDING REMARKS

The observation of exhaust contrails and natural cirrus clouds using a backscatter-depolarization lidar (532 nm in wavelength) was conducted at Akita University campus during spring and summer seasons of 1995～1997. Contrails primarily formed at the range of height and air temperature, 6.6～12.5 km and −19.8～−59.5 °C, in respectively.

In the case of contrails with cirrus or cirrostratus in higher altitude, the maximum value of scattering ratio is considerably larger than that of isolated contrails, although the physical thickness of them is not always larger. This fact suggests that the interaction between contrails and natural cirrus clouds.

REFERENCES

Freudenthaler, V., F. Homburg and H. Jäger, 1995: Contrail observation by ground-based scanning lidar: cross-sectional growth. Geophys. Res. Let., 22, 3501-3504.

Freudenthaler, V., F. Homburg and H. Jäger, 1996: Optical parameters of contrails from lidar measurements: Linear depolarization. Geophys. Res. Let., 23, 3715-3718.

Liou, K. N., 1986: Influence of cirrus clouds on weather and climate processes: A global perspective. Mon. Wea. Rev., 114, 1167-1199.

Sassen, K., 1997: Contrail-cirrus and their potential for regional climate change. Bull. Amer. Meteor. Soc., 78, 1885-1903.

Sassen, K., and C. Hsueh, 1998: Contrail properties derived from high-resolution polarization lidar studies during SUCCESS. Geophys. Res. Let., 25, 1165-1168.

THE OBSERVATION AND ANALYSIS OF THE PRECIPITATING STRATIFORM CLOUD STRUCTURE OVER ONORTHERN CHINA AREA

Duan Ying, Yang Baodong and Wu Zhihui

Weather Modification Office of Hebei Province
No.178, Tiyu South Street, Shijiazhuang, P.R.China.
Email: hbwmo@public.sj.he.cn Postal code 050021

1.Introduction

Since 1980'late, artificial precipitation enhancement operation is proceeding in northern China area. In order to update the science and technology level on artificial precipitation, the study of the characteristics of precipitating stratiform cloud has been completed. Some technical equipment was used in the study period, such as satellite, radar, Particle Measurement System (PMS), ground-based dual-channel microwave radiometer and radiosonde observations.

Duan Ying et al. (1994) reported their researched results on cloud seeding conditions of aircraft-artificial precipitation enhancement operation. Wu zhihui et al. (1994) reported their results of micro-physical structure of stratiform cloud. Shi lixin et al. (1994) reported their results of macro-characteristics on the stratiform clouds in Hebei province of China. Duan ying (1999) published his paper about atmospheric integral vapor and liquid water distribution characteristics, based on the continuous microwave radiometer observational data.

In this paper, the data of sixty-two cases of cloud system during 1990-1994 over Hebei province of northern China obtained by the aircraft, radar, radiometer probed are used to analysis the characteristic of the precipitating stratiform clouds and it's macro-micro structure.

2.Macro-structure of precipitating stratiform cloud

Based on the data of sixty-two cases of cloud system during 1990-1994 obtained with the aircraft, radar, satellite, radiosonde and dual-channel microwave radiometer probed, the macro-structure of precipitating stratiform cloud was analyzed over Hebei province of northern China. The analysis results indicate

Corresponding author' s address: Duan ying et al.,
No.178, Tiyu South Street, Shijiazhuang, P.R.China.
Email: hbwmo@public.sj.he.cn Postal code 050021

that the cloud system has multi-layers structure in vertical direction. It is mainly cirrus-altostratus-stratocumulus or cirrus-altocumulus-nimbostratus cloud layer structure from upper to lower level. The thickness of precipitating cloud system is generally greater than three kilometers and the height of cloud base is lower than two kilometers. The median thickness of warmer layer is 2500 meters in the cloud. The median thickness of colder layer is 2000 meters in the cloud(temperature lower than 0° C). The cloud top temperature is from -50° C to -20° C range. The ground average rainfall intensity is 0.82mmh^{-1} according to the data of the sixty-two cases in this study. The macro characteristic of stratiform cloud is given as follows table.

The table of macro-characteristics of cloud system

Cloud system	Case	Percentage (%)	Median height of cloud base (meter)	Median Thickness of cloud (meter)	Average rain Intensity (mmh^{-1})
Ci-As-Sc	36	58	1270	3800	0.86
Ci-Ac-Sc	19	31	950	4400	1.53
Asop	4	6	3060	2510	0.30
Scop	3	5	1830	2360	0.59
Total or Average value	62	100	1527.5	2367.5	0.82

3. Micro physical characteristic of cloud

According to the data of FSSP probed by the Particle Measuring System (PMS) at the seeding aircraft. The synthetic study result shows that the mean value of liquid water content (LWC) is 0.04 gram per cubic meter in the cloud. But, the cases of 67%indicates that LWC value are greater than 0.1 gram per cubic meter and the maximum value is 0.4 gram per cubic meter in precipitating stratiform cloud. The mean cloud droplet concentration is 62 per cubic centimeter, the mean diameter is 9 micrometer and maximum droplet concentration is 838 per cubic centimeter. The larger cloud droplet is lack of in cloud that the cloud droplet diameter is greater than 50 micrometer, this indicates that collision growths of cloud droplet has no advantage in the process of precipitation.

In other words, it is difficult for this type of cloud to produce precipitation through the warm rain process, the cold rain process plays a dominant role in the formation of precipitation. Therefore, it is the typical characteristics for continental cloud system. Based on the data of 2D-C probed, the mean ice crystal concentration is 15.6 per liter, the concentration of ice crystal in 49 percent samples are less than 10 per liter. For gaining the optimum effectiveness of stratiform cloud precipitation, the ice crystals are far too few in cloud, this mean that there exist seed-ability of

cloud condition for stratiform clouds over Hebei province of northern China.

4.The relative distribution of vapor and liquid water in cloudy atmospheric

It is well known that the water in the atmosphere basically exists in gaseous phase that can not form rainfall directly. From the point of cloud seeding, it is regarded that the resource condition of cloud seeding is the liquid water that it is also not converted to precipitation in cloud by natural process. For this reason, the amount of atmospheric vapor content can not reflect the resource condition of cloud seeding. So it is important to have some knowledge about the relative distribution of atmospheric vapor and liquid water content under cloudy condition.

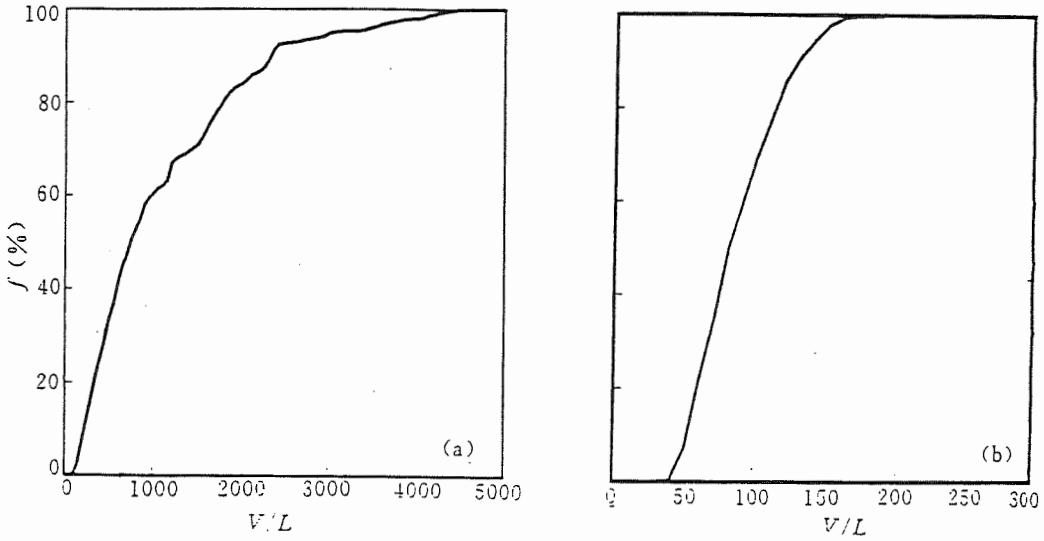

The figure (a) is the ratio of vapor to liquid water (V/L) under cloudy condition, and the figure (b) is the ratio of vapor to liquid water (V/L) under rainy condition

Above figure shows the ratio of atmospheric vertical integral vapor to liquid water (V/L) from April to June of 1992—1994 under rainy and cloudy conditions. The data were obtained by dual channel microwave radiometer continuous observation. When it is cloudy, the ratio of vapor to liquid water (V/L) is generally 100-4000, the median is 750, indicating that the amount of liquid water in atmospheric water is less than 1%. Whereas it rains, the ratio of vapor to liquid water (V/L) is generally 50-150, the median is 80,indicating that the amount of liquid water in the total atmospheric water is less than 2%. For two weather conditions stated above, the available liquid water resource for cloud seeding is only a small fraction of the water vapor content in atmosphere.

References

Duan ying et al., 1994: Observational research on cloud seeding conditions of aircraft artificial precipitation, WMO workshop on cloud, micro-physical and application to global change, 10-14 August, 1992, Toronto, Canada, WMO/TD, No.537, 235-240.

Duan ying et al., 1994: The observation and analysis of the cloud system in the southwest vortex process in an artificial precipitation operation, a study proceedings, 69-82, China Meteoro. Press, Beijing (in Chinese).

Duan ying et al., 1996: An analysis for the precipitation structure of the stratiform cloud system in North China, 12th International conference on cloud and precipitation, 19-23 August, 1996, Zurich, Switzerland

Duan ying, 1999: Estimation of artificial precipitation enhancement resource condition and cloud seeding potential by ground-based remote sensing data, ACTA, Meteorologica Sinica, Vol.13, No.1, 103-114, China Meteor. press, Beijing.

Shi lixin et al., 1994: The macro-characteristics of the stratiform clouds in artificial precipitation operation in Heibei province, A study proceedings, 53-62, China Meteoro. Press, Beijing (in Chinese).

Wu zhihui et al., 1994: Case study of the micro-physical characteristics of the returning cloud system in Hebei province spring, A study proceedings, 112-117, China Meteoro. Press, Beijing (in Chinese).

Wu zhihui, 1994: Primary study of the micro-physical structure of stratiform clouds in Spring and Summer in Hebei province and their artificial precipitation potential, A study proceedings, 83-88, China Meteoro. Press, Beijing (in Chinese).

Microstructures and Precipitation Processes in a Stable Orographic Snow Cloud over the Mikuni Mountains in Central Japan

Masataka MURAKAMI[1], Mizuho HOSHIMOTO[1], Narihiro ORIKASA[1], Ken-ichi KUSUNOKI[1] and Yoshinori YAMADA[2]

[1]Meteorological Research Institute, Tsukuba, JAPAN
[2]Japan Meteorological Agency, Tokyo, JAPAN

1. INTRODUCTION

In winter, a cold airmass from the Eurasian Continent receives a great amount of heat and moisture and forms a convective mixed layer while it crosses the warmer surface of Japan Sea. Snow clouds developed in the mixed layer land the west coast of Japan Island and bring snowfall over the coastal areas. And the airmass is forced up the divide of Japan Islands with the peak of 2,000 m, producing further condensate and snowfall. The mountain area (windward slopes of the divide in northern and central parts of Japan Islands) is one of heaviest snowfall areas in the world. Although orographic modifications of snow clouds are clearly responsible for the heavy snowfall, and should be investigated to improve the precipitation forecasts in mountainous area and to determine the design of seeding experiments, no systematic study on orographic snow clouds, which covers microscale and mesoscale aspects, has been carried out so far.

Meteorological Research Institute, Japan Meteorological Agency and Tone River Dams Integrated Control Office, Ministry of Construction have been carring out the orographic snow cloud project over the western slope of the Mikuni Mountain (the divede of central parts of Japan Island) since 1994 (Murakami et al., 1998; Miyao et al., 1998).

In this paper, thermodynamic, kinetic and microphysical structures of snow clouds modified by a complex terrin, the Mikuni Mountain, are described on the basis of observation data collected by an instrumented aircraft, hydrometeor videosonde, X-band and Ka-band Doppler radar, ground-based microwave radiometers, etc.

2. OBSERVATION FACILITIES

Field program on orographic snow cloud study was carried out arround the Mikuni Mountains. The topography is not as simple as an isolated mountain and two-dimensional one, but of complicated and three-dimensional. Windward slope of the mountain are very steep, with altitudes increasing from 300 m MSL to 2,000 m MSL over a horizontal distance of 100 km (see Fig. 1).

The primary instrumentation is an instrumented aircraft, which was operated from Niigata Airport and provides us with microphysical, thermodynamic and kinetic measurements. On the ground, we deployed X-band and Ka-band Doppler radar, three ground-base microwave radiometers, an instrumented 4-wheel-drive van, hydrometeor videosonde (Murakami and Matsuo, 1990)

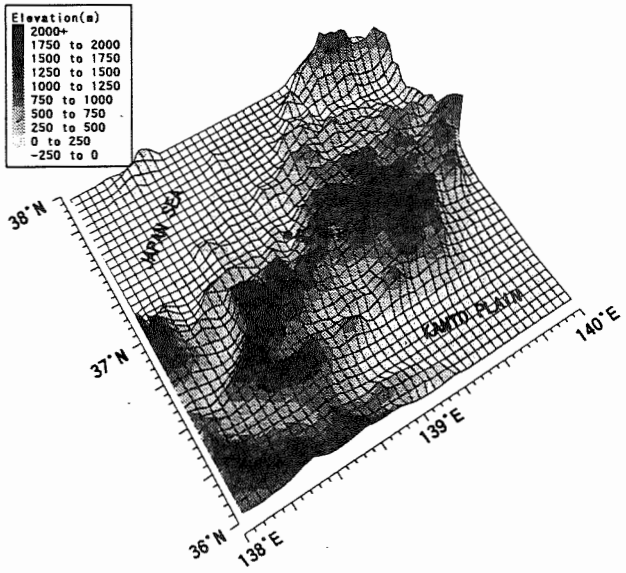

Fig. 1 Topography around the observation area.

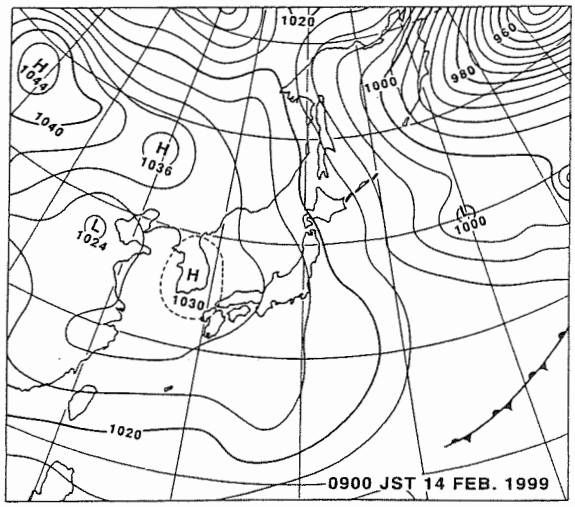

Fig. 2 Surface weather map at 0900 JST 14 Feb. 1999.

Corresponding author's address: Masataka Murakami, Meteorological Research Institute, Tsukuba, Ibaraki 305-0052, Japan; E-Mail: mamuraka@mri-jma.go.jp

and rawinsonde system. X-band and Ka-band Doppler radar were disposed at the eastern foot of the Uonuma Hills, from which the radar are able to obtain the unobstracted view of snow clouds over the mountains. Three dual frequency (23 GHz and 31 GHz) microwave radiometers were disposed at Shiozawa basin (site B), windward slope (site C) and leeward slope (site D) of the mountains. The microwave radiometers were pointed toward the zenith and measured liquid water path passing overhead every 1 min. Hydrometeor videosonde and rawinsonde were launched at the site B to measure the vertical profiles of cloud and precipitation particles and meteorological data. Automobile measurements of liquid water path (with a microwave radiometer) and precipitation particle images (with 2D-P gray probe) are also available.

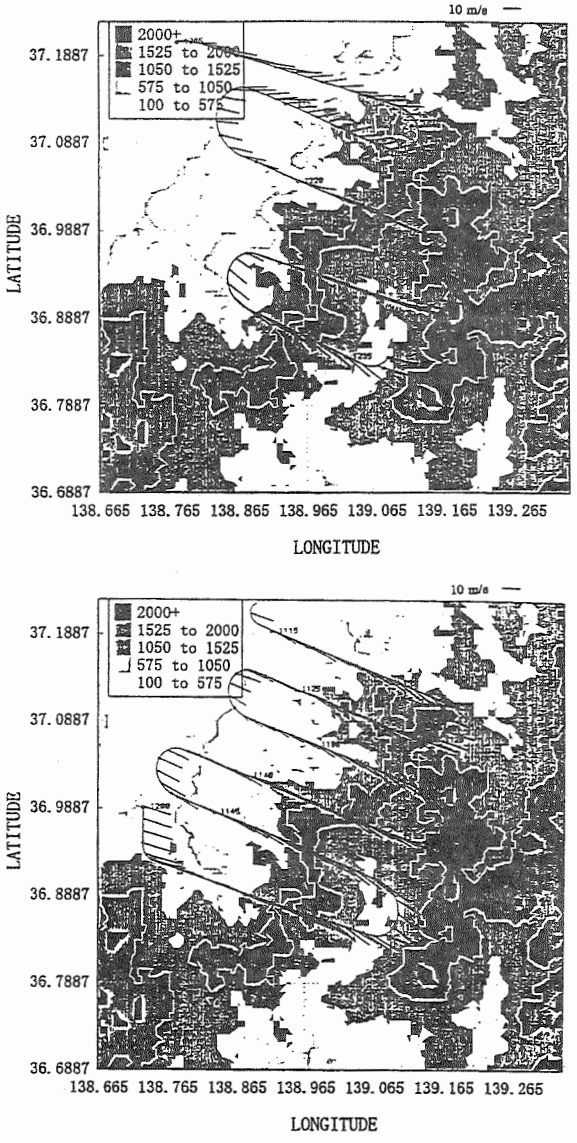

Fig. 3 Horizontal wind vectors along flight tracks at 3.3 km (upper panel) and 2.7 km (lower panel).

3. OBSERVATION RESULTS

3.1 Synoptic and Mesoscale Features

An orographic snow cloud was investigated over the Mikuni Mountains on Feb. 14, 1999. The cloud formed during a moderate cold airmass outbreak under the synoptic pressure pattern of winter monsoon shown in Fig. 2. Aircraft measurements were made during the time periods between 1100 JST and 1300 JST.

GMS visible image at 1200 JST (not shown) showed that snow bands with NW-SE orientation invaded from the sea into the northern part of the observation area. Another snow bands with E-W orientation moved into the area and merged with the former ones. These snow bands bring about snowfall of 0.5 ~ 1.0 mm/hr in the norhtern part of the study area.

An aircraft sounding taken over the Shiozawa basin at 1040 showed that a strong temperature inversion existed at 3.6 km and prevent the clouds from developing upward. The thermal stratification between 1.5 and 3.6 km was stable. Below 1.5 km, it was neutral according to radiosonde measurement made immediately before the aircraft measurements. Therefore cloud tops have rather flat shapes and their height and temperature were 3.6 km and –25C, respectively.

Wind speeds were 10 ~ 15 m s^{-1} in the cloud layer and increased to more than 30 m s^{-1} above the cloud top whereas wind directions did not show any significant changes and were roughly WNW between 1.5 and 4.5 km.

3.2 Horizontal Cross Section

Horizontal wind vectors along the fight tracks at 2.7 and 3.3 km are overlain on topography contours in Fig. 3. Horizontal winds at 2.7 km were roughly WNW over most of the domain although they changed to NW leeward of the crest line. Wind speeds increased over the peaks of the Uonuma Hills and the Mikuni Mountains. Horizontal cross sections of wind speeds at 2.7 and 3.3 km (not shown) clearly indicate weaker wind regions windward of the crest line.

Horizontal wind field at 3.3km was qualitatively similar to that at 2.7 km except for the westerly in the northern part of the domain. This westerly seemed te be influenced by airflow structures in the snow band with E-W orientation.

Figure 4 shows horizontal distributions of vertical velocities at 2.7 km (middle panel) and 3.3 km (upper panel) together with topography contours (lower panel). The horizontal distributions of physical parameters were derived by interporating the data along the flight tracks shown in Fig. 3. Star marks in the lower panel indicate the observation sites B and C. Weak updrft regions extended ~ 20 km windward of the crest line and moderate updrafts of 1 ~ 2 m s^{-1} were found around 10 km windward of the crest. Airflow was much more turbulent leeward of the crest and the magnitude of downdraft exceeded 2 m s^{-1} although on the average, downdraft regions extended several kilometers leeward of the crest line.

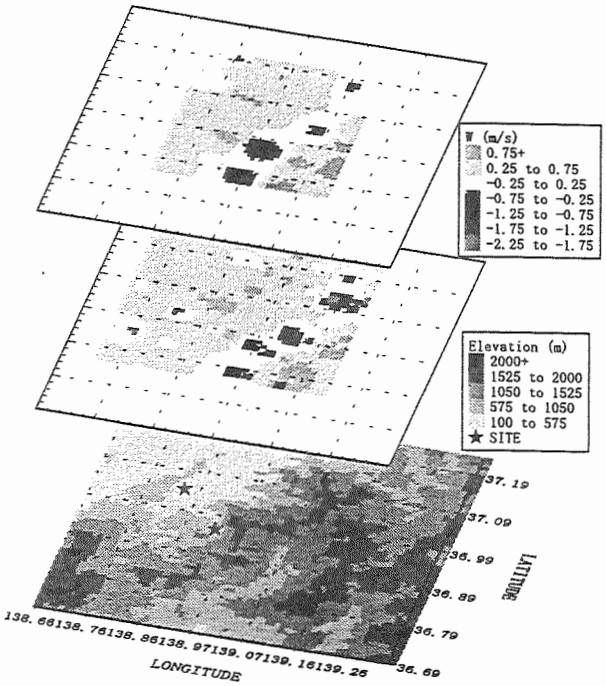

Fig. 4 Horizontal cross sections of vertical velocities at 3.3 km (upper panel) and 2.7 km (middle panel) and topography (lower panel).

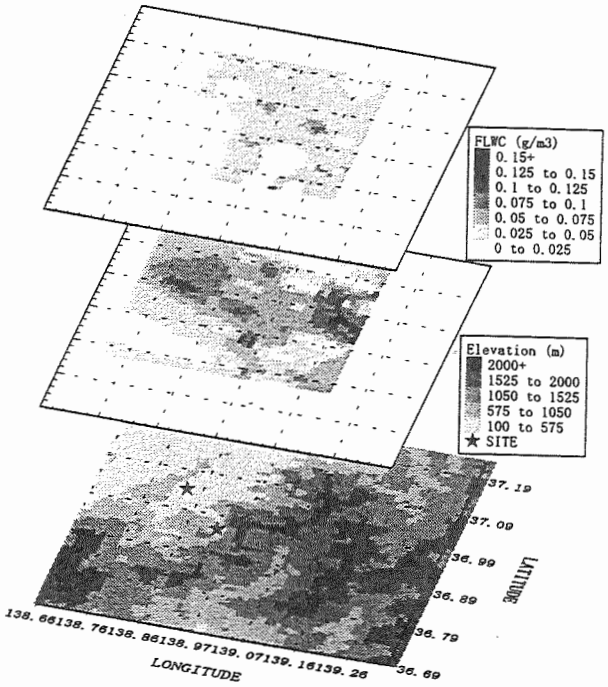

Fig. 5 As Fig. 4 except for cloud water contents.

Horizontal distributions of cloud water contents almost coincide with those of updrafts and relatively large values (0.1 ~ 0.3 g m^{-3}) were found windward of the crest line at 2.7 km. A distribution pattern of cloud water contents at

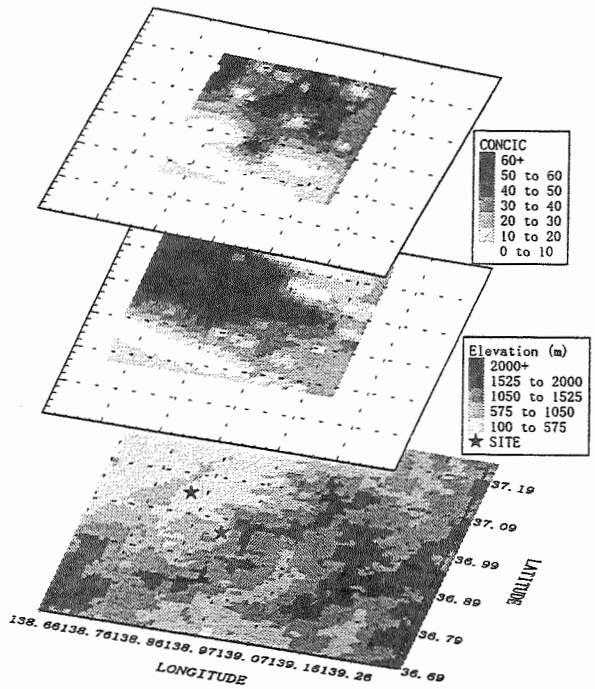

Fig. 6 As Fig. 4 except for 2D-C concentrations.

3.3 km was similar to that at 2.7 km, but the absolute values are one third of those at 2.7 km (Fig.5).

At 2.7 km, high concentrations (~ 30 particles/L) of ice crystals and snow particles larger than 25 • m (measured with 2D-C probe) distributed windward of the crest while the concentrations decreased leeward of the crest due to the sublimation of smaller particles in downdraft regions. At 3.3 km, just below cloud tops, high concentrations of ice crystals were found over the windward slopes of the hills and the mountains (Fig.6).

3.3 Vertical Cross Section

RHI cross section of reflectivities and Doppler velocities for azimuth angle of 140° , which is measured with Ka-band radar, are shown in Fig. 7. Radar data showed that the cloud was not convective but rather stratiform and the low-level weak wind layer produced by blocking effect of the mountain barrier was evident below 1 km.

Aircraft measurements in the vertical cross section along the valley also showed high concentrations of ice crystals over the windward slopes of the hills and the mountains and significant cloud water contents between cloud top and the 2.5 km level. HYVIS observations made at 1356 confirmed that supercooled cloud droplet layer existed above 2.5 km and that ice crystals rapidly grew during their descent from the cloud top to the 2.5 km level, and did not show any significant growth from 2.5 km to 1.5 km. Below 1.5 km, sizes and concentrations of snow particles decreased with decreasing altitude.

During the time of aircraft measurements, liquid water paths at sites B and C ranged from 0.1 to 0.3 mm, being

consistent with aircraft measurements that cloud water contents of 0.1 ~ 0.3 g m^{-3} widely distributed windward of the crest line in the upper layer of 1 km thick in the cloud.

4. PRECIPITATION MECHANISMS

As clearly shown in RHI cross section of Doppler velocities in Fig. 7, there was a weak wind region due to the blocking in lower levels, especially below 1 km windward of the Mikuni Mountains. The oncoming airflow rose over the low-level, weak wind layer. This produced a diffuse, gentle updraft regions extended ~ 20 km windward of the crest line as shown in the horizontal cross section of vertical velocities. Cloud droplet regions with water contents of 0.1 ~ 0.3 g m^{-3} were almost collocated with the updraft regions.

Spatial distributions of ice crystal concentrations suggested that ice nucleation likely occurred near the cloud tops over the windward slopes of the Uonuma Hills and the Mikuni Mountains. From the fact that high concentrations of ice crystals occurred in coexistence with supercooled cloud droplets, most likely mechanism of ice nucleation in the present cloud was the freezing of cloud droplets (condensation-freezing and/or immersion freezing mechanisms). Ice crystals generated in upper parts of clouds rapidly grew by vapor deposition and accretion of cloud droplets in the cloud water regions with horizontal scale of ~ 20 km during their descent.

The blocking effect of the mountain barrier on low-level winds can extend updraft regions farther upstream from the mountain barrier than would otherwise occur, and allowed snow particles to continue the rapid growth for longer time in coexistence of supercooled cloud droplets. Thus it is suggested that the blocking effect could further strengthen the precipitation enhancement due to orographic lift.

5. CONCLUSIONS

A stable orographic snow cloud was investigated over the Mikuni Mountains with peaks of ~ 2 km, the divide of central parts of Japan Islands, with an instrumented aircraft, hydrometeor videosonde, three ground-based microwave radiometers, X-band and Ka-band Doppler radar and automobile equipped with a microwave radiometer and a 2D-P gray probe.

The snow cloud had its top height (temperature) of 3.6 km (-25C) and was confined to below a strong temperature inversion. The cloud layer was characterized by a stable thermal stratification and a strong unidirectional wind shear across the cloud top.

Aircraft observations and Doppler radar observations showed that there existed a weak wind region windward of the crest line, especially below 1 km, due to the blocking effect. Air parcels moving toward the mountains upglided over the weak wind layer and produced a diffuse, gentle updraft regions extended ~ 20 km windward of the crest line. Moderate updrafts (1~2 ms-1) were found over the windward slopes of the Uonuma Hills and the Mikuni Mountains while a mixture of strong updraft and downdraft existed leeward of the Mikuni

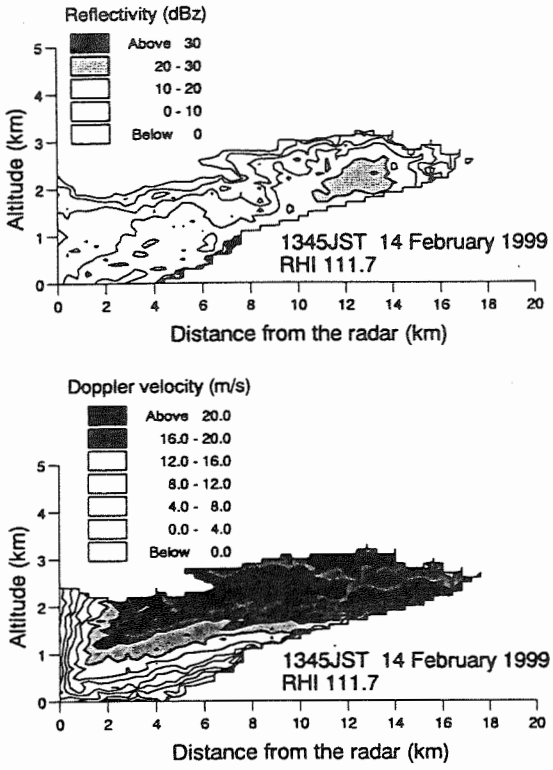

Fig. 7 RHI cross sections of reflectivities (upper panel) and Doppler velocities (lower panel) for azimuth angle of 111.7° at 1345 JST.

Mountains.

Regions with cloud water contents of 0.1 ~ 0.3 g m^{-3} were collocated with the updraft regions, above 2.5 km. Ice crystals generated near the cloud top over the windward slopes grew rapidly by vapor deposition and accretion of cloud droplets in the supercooled cloud water region with a horizontal extent of ~20 km during their descent from cloud top to the 2.5 km level.

Microphysical structures mentioned above were confirmed with HYVIS observations and ground-based microwave radiometer measurements.

6. REFERENCES

Miyao, M., M. Murakami, N. Orikasa, Y. Yamada and K. Soeda, 1998: Precipitation mechanism of orographic snow clouds with warm top temperatures. *Preprints of the Conf. on Cloud Physics*, 419-442.

Murakami, M. and T. Matsuo, 1990: Development of hydrometeor videosonde. *J. Atmos. Oceanic Tech.*, 7, 613-620.

Murakami, M., M. Miyao, N. Orikasa, Y. Yamada, H. Mizuno and K. Soeda, 1998: Seedability of orographic snow clouds in central Japan. *Preprints of 14th Conf. on Planned and Inadvertent Weather Modification.* 569-572.

SIMULATION OF A WARM PRECIPITATION EVENT OVER OROGRAPHY WITH A TWO-MOMENT MICROPHYSICAL SCHEME

Jean-Pierre PINTY, Stéphanie COSMA,
Jean-Martial COHARD and Evelyne RICHARD

Laboratoire d'Aérologie, Toulouse, France

1. INTRODUCTION

Many numerical simulations have focused on the microphysical impact of changing CCN concentrations in low cloud layers (mainly to analyse radiative effects and induced modifications on precipitation). However, because such studies are computationally expensive, they are restricted to idealized cloud conditions such as those reproduced by 2D moist LES codes. A good illustration is the explicit simulation of drizzle from stratocumulus decks owing the use of detailed microphysical schemes with several tens of bins. In order to extend such approach to 3D real case simulations in mesoscale models, it is worth to take a keen interest in simplified precipitation bulk schemes for obvious practical reasons. The minimal approach that is supported here, considers a two-moment warm microphysical scheme with prediction of the concentrations and mixing ratios of both cloud droplets and raindrops. In the scheme, any sensitivity to CCN properties is accounted for explicitly by using a CCN activation parameterization which establishes a strong dependence between aerosol (CCN) and cloud droplet concentrations. The first part of the paper contains a rapid overview of the scheme. The second part is devoted to the simulation of observed precipitation bands over the Cevennes ridge in France at high resolution. This case study is a first attempt to test the sensitivity of precipitation patterns and intensities to initial CCN characteristics.

2. A BRIEF REVIEW OF THE SCHEME

2.1 The two-moment warm scheme

The original warm cloud scheme (hereafter referenced as C2R2) which is implemented in the French 3D non-hydrostatic mesoscale model MésoNH, is extensively described in Cohard and Pinty (2000a), with first results shown in Cohard and Pinty (2000b). The scheme is grounded on the classical partition between cloud droplets ($D < 80\mu$m) and raindrops ($D > 80\mu$m) for which both mixing ratios (r_c and r_r) and number concentrations (N_c and N_r) are the respective prognostic variables. An assumption of the scheme is to consider generalized γ-functions as size distribution functions, in the normalized form given below (with $x \in \{c, r\}$) for fixed dispersion coefficients α_x and ν_x,

$$\gamma_x(D) = \frac{\alpha_x}{\Gamma(\nu_x)} \lambda_x^{\alpha_x \nu_x} D^{\alpha_x \nu_x - 1} exp\left(-(\lambda_x D)^{\alpha_x}\right) \quad (1)$$

D is the drop/droplet diameter and λ_x, the slope parameter computed from the third and zeroth moments of (1) corresponding to r and N. The microphysical scheme itself is summarized in the diagramm of Fig. 1.

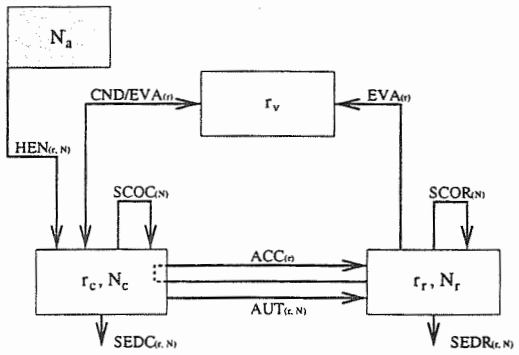

Figure 1: Warm microphysical processes included in the C2R2 scheme (see text for the acronyms and explanations).

The heterogeneous nucleation (**HEN**) selects the formation of the first cloud droplets by CCN activation from the aerosol reservoir N_a. The reversible condensation/evaporation process (**CND/EVA**) is the result of an implicit adjustment to water saturation (no prediction of supersaturation). The growth of the raindrops is made through the coalescence processes which involve the autoconversion (**AUT**), the accretion (**ACC**) and the self-collections (**SCOC, SCOR**). A raindrop breakup efficiency, with an exponential decrease with D, limits the SCOR term. The sedimentation terms (**SEDC, SEDR**) affect the concentrations and

* *Corresponding author address*:
Jean-Pierre Pinty, Laboratoire d'Aérologie, OMP, 14 av. E. Belin, 31650, Toulouse, France;
e-mail <pinjp@aero.obs-mip.fr>.

mixing ratios and so crudely account for size sorting phenomenon. Finally, the evaporation of the raindrops (**EVA**) is integrated from the vapor diffusion growth equation including the ventilation effect. It is important to recall that the bulk representation of the microphysical processes in C2R2 proceeds mostly from analytical integration using (1). This is also the case for the CCN activation scheme which is shortly described now.

2.2 The CCN activation scheme

This process is treated following Cohard et al. (1998). The scheme is based upon the concept of activation spectrum relating the cumulative number of activated CCN to the surrounding field of water vapor supersaturation s. The originality of the scheme relies on an elaborate function to shape activation spectra $N_{CCN}(s)$ in the place of classical power laws. The $N_{CCN}(s)$ function, expressed by

$$N_{CCN}(s) = Cs^k F(\mu, \frac{k}{2}, \frac{k}{2}+1; -\beta s^2) \qquad (2)$$

where F is the hypergeometric function and $[C, k, \mu, \beta]$, four adjustable coefficients, has two remarkable properties. First, the number of activated CCN can be computed with (2) following the formulation of Twomey (see Pruppacher and Klett, 1997) for which a analytical integration can be obtained. Secondly, the mathematical expression (2) with a finite limit as s goes to infinity, adheres closely to activation spectra produced by lognormally distributed aerosols. Exploiting further this property, Cohard et al. (2000c) were able to calibrate the four tunable coefficients of (2), from known properties of aerosol populations (modal radius $\overline{r}$, standard deviation $\ln(\sigma)$, concentration N_a, solubility, etc...). In conclusion, the CCN activation scheme in C2R2 provides a reasonnable estimate of N_c given the vertical velocity field (the source of supersaturation) computed by the mesoscale model and for specified aerosol properties. This makes the "CCN sensitive" C2R2 scheme suitable to 3D studies.

3. FINE SCALE SIMULATION OF PRECIPITATING BANDS

3.1 Introduction

South-East facing slopes of the Massif Central, the Cevennes ridge in France (see Fig. 2 for a geographical location), are exposed to intense precipitation events that can lead locally to severe flash flooding. The meteorological situation at the origin of these events is well understood. The precipitation forms after a forced ascent of warm moist air flowing from the Mediterranean sea in response to an eastward moving upper level trough approaching

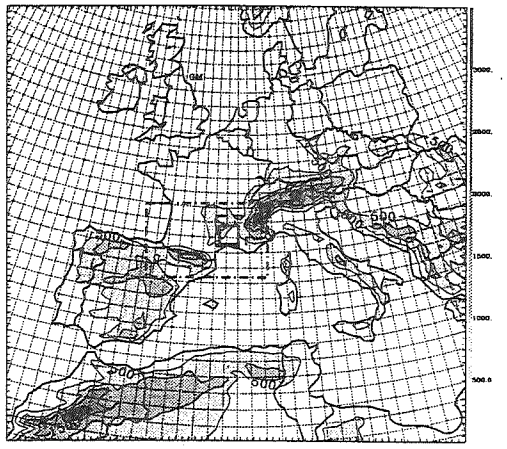

Figure 2: Domains used for the nested simulations with a background map at a 50 km resolution (height contours every 500 m). The 10, 2 and 1 km inner meshes are marked by dashed-dot, dashed and solid rectangles, respectively.

the French Atlantic coast. A first investigation of this phenomenom has been made during the fall seasons of 1986-1988 by French hydrologists to estimate the feasability of integrating over small scale watersheds rainfall rates derived from radar reflectivities. The radar observations (not detailed here) indicate that cloud tops remain below the freezing level.

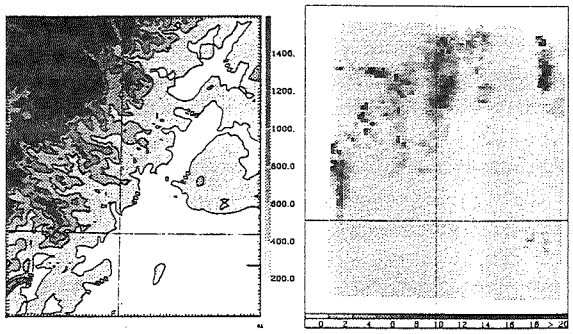

Figure 3: 1 km scale relief with contours every 200 m (left). Mean radar rainfall rates between 11:00 and 12:00 (right).

Due to small scale topographical features superimposed on the main slope of the terrain (Fig. 3), precipitations over the Cevennes ridge are often organized in narrow bands that evolve with a time scale of one hour, approximately. Simulations made with idealized orography (a constant slope with aligned bell-shape mountains) confirm that these bands result from an enhanced convergence in the lee-side after flow deflection around upstream obstacles. This preliminary study reveals also that these precipitating bands are better simulated at high horizontal resolution (1 km). Consequently, the Cevennes

area seems to be a rather favourable location for testing a hypothetic sensitivity of small scale warm precipitations to the aerosol load of the incoming airmasses.

3.2 The 13-15 Nov. 1986 case study

The simulations are carried out with the MésoNH model (Lafore et al., 1998) and its full physical package. The initial (14 Nov. 1986, 00Z) and boundary conditions of the large scale run at 50 km, are obtained from the 6 hour ECMWF analyses. A multi-scale strategy is then adopted to run the 10, 2 and 1 km scale simulations. The one-way nesting procedure (Fig. 2) allows for a high refreshment rate of the boundary conditions for the simulations performed on the inner domain. A first run is made with a standard Kessler scheme and the two other runs use the C2R2 scheme with maritime ($N_a = 66$ cm^{-3}, $\overline{r} = 0.133$ μm and $\ln(\sigma) = 0.4835$) and enhanced maritime ($N_a \times 4$) CCN spectra.

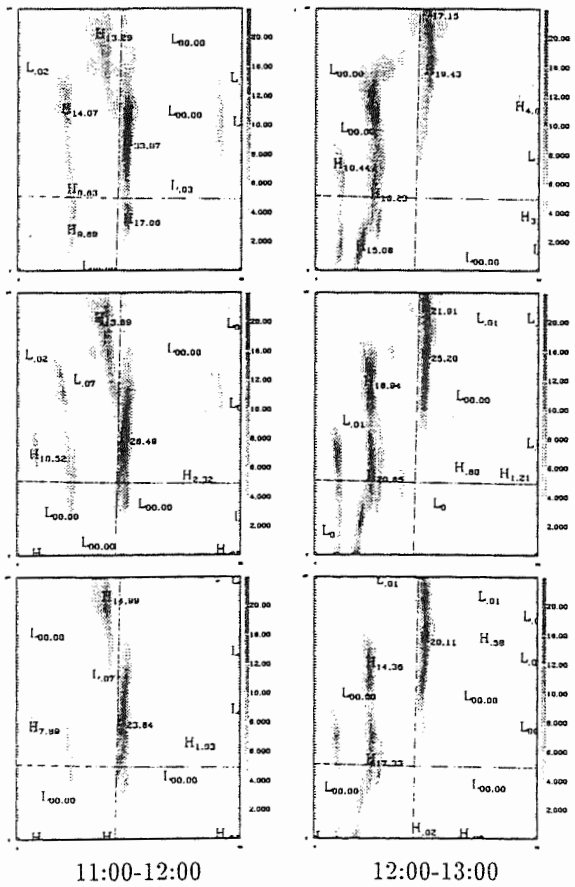

Figure 4: Simulated mean rainfall rates with the Kessler scheme (top) and with the C2R2 scheme for N_a (middle) and $N_a \times 4$ (bottom) aerosol concnentrations.

For the C2R2 simulations, N_c is initialized as the number of activated CCN at $s = 0.1\%$ in cloudy areas while the initial N_r is deduced from r_r assuming a Marshall-Palmer law ($N_0 = 10^7$ m^{-4}). This ensures a continuous lateral forcing of all the microphysical fields in the domain of simulation.

3.3 Simulation results

The hourly averaged simulated rainfall rates (RR) are reproduced in Fig. 4. All the simulations give a similar location of the rainbands but with different intensities. The best correlation with the observations (shown in the interval 11-12Z in Fig. 3) is obtained for the interval 12-13Z. This delay is partially due to the time needed for the hydrometeors to reach the ground because the radar rainfall rates were estimated at a constant site angle and also due to the rapid temporal evolution of the precipitation patterns. A cross-comparison between the three 1 km simulations reveals that the Kessler

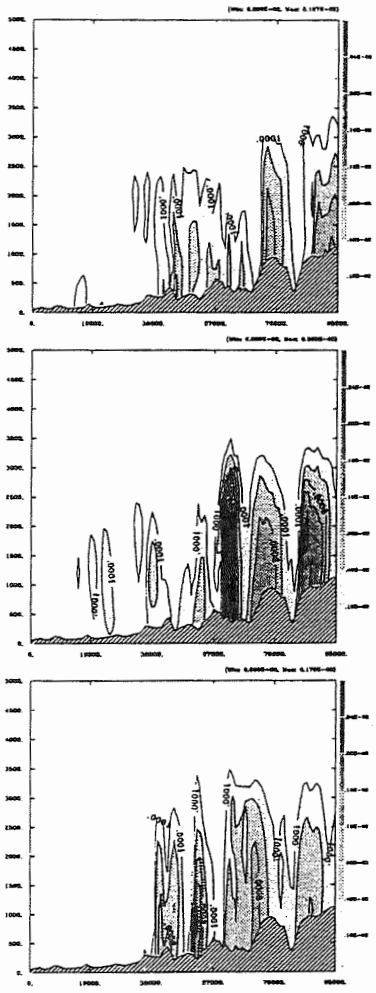

Figure 5: Cross section of rain mixing ratios, r_r, at 12:20 along Meridian 4°E (N-S axis drawn in Fig. 3).

scheme leads to $RR_{max} = 33.1$ mm decreasing to 19.4 mm one hour later while the C2R2 scheme produces more steady precipitation ($RR_{max} = 28.5$ mm and then 25.2 mm). Increasing the initial aerosol concentration N_a by a factor 4 leads to a mean decrease of 25 % in the precipitation. This result is fully explained by less autoconversion efficiency in presence of high cloud number concentration.

Another interesting feature that can be observed between the different simulations, is the slight shift of the precipitation to the north obtained with the C2R2 scheme as better illustrated in Fig. 5. For the selected cross-section, it appears that the precipitable rainwater has been pumped out by the Kessler scheme in contrast to the C2R2 scheme where rainwater is still available (max $r_r \sim 3$ g/kg in the "N_a" case) for the high valleys of the ridge. This effect is also visible in Fig. 6 where the cloud water mixing ratios have been plotted along the same axis but 20 mn later. Now the maximum value of r_c reaches 2.3 g/kg for the "$N_a \times 4$" case compared to 1.3 g/kg for the "N_a" case, both with the C2R2 scheme. This analysis illustrates that a fine tuning of the autoconversion rates affects the evolution of a precipitating system and the cloud lifetime.

4. CONCLUSIONS

The study presented in this paper aims to show that 3D real case simulations of orographically forced precipitating rainbands can be achieved at high resolution using a two-moment warm microphysical scheme that explicitly incorporates the activation of the CCN. An important result is that changing the CCN activation spectrum of typical maritime airmasses may induce a significant change in the precipitation patterns. These modifications, commensurate to the scale of the watersheds, are attributable to the different autoconversion efficiencies that result from variations of the CCN activation spectra in the C2R2 scheme. The run made with the Kessler scheme seems to produce too much upwind precipitation. The C2R2 scheme with a more accurate representation of the autoconversion leads to a more progressive downwind spreading of the precipitation.

The lack of very accurate data prevents us to more firmly conclude on the realism of the simulations presented in this study. However, as encouraging results have been shown on the sensitivity of CCN spectra to precipitation at small scale, routine measurements of aerosol spectra will be needed in the near future to objectively initialize CCN properties that can be dealt by warm microphysical schemes like C2R2.

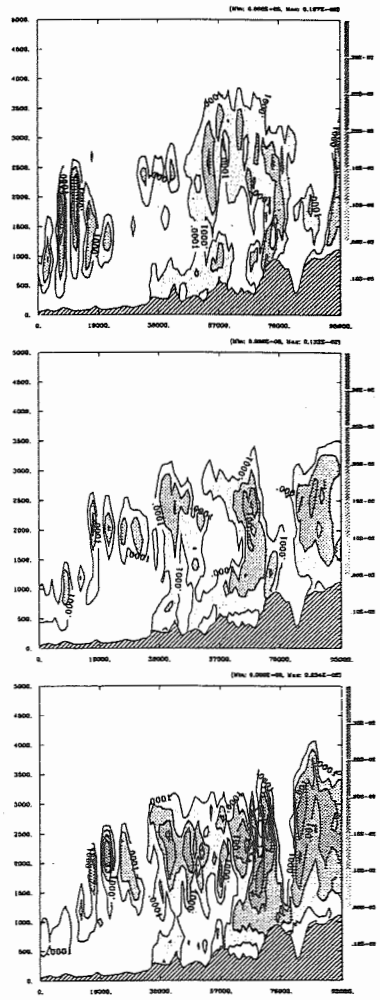

Figure 6: As in Fig. 5 but for the cloud droplet mixing ratios, r_c at 12:40.

5. REFERENCES

Cohard, J.-M., J.-P. Pinty and C. Bedos, 1998: Extending Twomey's analytical estimate of nucleated cloud droplet concentrations from CCN spectra. *J. Atmos. Sci.*, **55**, 3348-3357.

Cohard, J.-M. and J.-P. Pinty, 2000a: A comprehensive two-moment warm microphysical bulk scheme. Part I: Description and tests. *Quart. J. Roy. Meteor. Soc.*, , July issue.

Cohard, J.-M. and J.-P. Pinty, 2000b: A comprehensive two-moment warm microphysical bulk scheme. Part II: 2D experiments with a non-hydrostatic model. *Quart. J. Roy. Meteor. Soc.*, , July issue.

Cohard, J.-M., J.-P. Pinty and K. Suhre, 2000c: On the parameterization of activation spectra from CCN microphysical properties.*J. Geophys. Res.*, , May issue.

Lafore, J. P., J. Stein, N. Asencio, P. Bougeault, V. Ducrocq, J. Duron, C. Fischer, P. Hereil, P. Mascart, J. P. Pinty, J. L. Redelsperger, E. Richard, and J. Vila-Guerau de Arellano, 1998: The Meso-NH Atmospheric Simulation System. Part I: Adiabatic formulation and control simulations. *Annales Geophysicae*,16,90-109.

Pruppacher, H. R., and J. D. Klett, 1997: *Microphysics of Clouds and Precipitations.* 2nd Ed. D. Reidel, 954 pp

On the Difference between Maritime and Continental Clouds

Harold D. Orville, Chengshu Wang, and Richard D. Farley

Institute of Atmospheric Sciences, South Dakota School of Mines & Technology, Rapid City, SD, 57701-3995, USA

1. INTRODUCTION

The renewed interest in hygroscopic seeding has emphasized the differences in maritime and continental clouds (Mather *et al.* 1996) and the processes by which rain and hail are formed. Partly, this is because the purpose of hygroscopic seeding is to make a continental-type cloud more maritime like. The aim of this paper is to examine some of the microphysical and dynamic differences between the two types of clouds, using extreme examples of maritime and continental-type clouds.

To look at the differences we simulate both types of clouds, changing only the ease with which coalescence rain is formed in the maritime cloud compared with the continental cloud. The focus is on the development of precipitation in two extreme situations, a maritime cloud in which coalescence is allowed to act as soon as any cloud water is formed, causing the immediate formation of precipitation, and a continental cloud in which the coalescence process is prohibited, so that precipitation formation is delayed and forms via various ice processes.

2. BRIEF DESCRIPTION OF CLOUD MODEL

The numerical model used for this study is a modified version of the three-dimensional bulk-water model developed by Clark (1977, 1979) and Clark and Farley (1984). The model microphysics was updated by Farley *et al.* (1992) to include the bulk-water parameterization method by Orville and Kopp (1977) and Lin *et al.* (1983) with secondary ice production parameterization according to the method of Aleksić *et al.* (1989). This version includes five categories for water and ice particles such as cloud water, rain, cloud ice, snow, and graupel/hail fields.

The five categories of water and ice particles interact with each other and water vapor through the physical processes of condensation/evaporation, collision/coalescence, aggregation, accretion, melting/freezing, and deposition/sublimation. The model also includes graupel/hail formation via snow accreting supercooled water drops as described by Farley *et al.* (1989). The rain, snow, and graupel/hail particles are assumed to follow inverse exponential size distributions. These particles also have their respective terminal fall velocities. Cloud water and cloud ice particles are assumed to have zero terminal velocity. As a result, these smaller particles travel with the air.

Corresponding author's address: Dr. Harold D. Orville, Institute of Atmospheric Sciences, South Dakota School of Mines & Technology, 501 East Saint Joseph Street, Rapid City, SD 57701-3995,
E-Mail: horville@ias.sdsmt.edu.

A non-nested version of the cloud model is applied to a moderate size convective cloud case from CCOPE* and a more vigorous cloud case from a North Dakota experiment. Convection is initiated at time zero in a bubble-like fashion. A maximum temperature perturbation of 2°C is used. Relative humidity is the same inside and outside the bubble.

3. RESULTS

Two cloud situations are simulated. The first simulation uses atmospheric conditions that were observed during the CCOPE experiment on 19 July 1981. Many papers concerning this day are in the literature. Farley *et al.* (1992) simulated this day using Clark's 3D model. A moderate convective cloud forms in this case, having maximum updrafts of 20 to 25 m s^{-1}. The second cloud situation comes from a strong thunderstorm day observed in the North Dakota Thunderstorm project, June 28, 1989. The clouds on this day developed maximum updrafts of 40 to 45 m s^{-1}.

3.1 CCOPE moderate cloud case

We have run the simulations with extreme maritime and continental conditions imposed, as discussed above. Only a few of the results are presented here. The moderate cloud case radar echoes are shown in Fig. 1 for the first cycle of growth of the cloud. The left column shows results for the continental cloud simulation, the right column for the maritime simulation. The earlier precipitation (mainly rain) in the maritime cloud is clearly evident. More rain and graupel/hail fall from the maritime cloud as compared with the less efficient continental cloud (608 vs. 374 ktons of rain, 25.8 vs. 9.2 ktons of graupel/hail).

Figure 2 shows why the maritime cloud is the more efficient precipitator. For the maritime cloud this figure shows the rapid formation of rain from coalescence of the cloud water, the early graupel initiation from probabilistic freezing of the rain drops, the cloud ice formation via the Hallett-Mossop mechanism (involving the collision of graupel and large cloud droplets), and the rather inconsequential formation of snow. The sequence of events for the maritime cloud is: cloud water (5 min) -> rain water (5+ min) -> graupel (6 min) -> cloud ice (6 min) -> snow (7 min).

Figure 2 shows a very different story for the continental cloud. Copious amounts of cloud water form first, cloud ice and snow form next, mainly from the nucleation of cloud ice at the -15°C temperature level, and finally rain forms from the melt of snow and later

* Cooperative Convective Precipitation Experiment

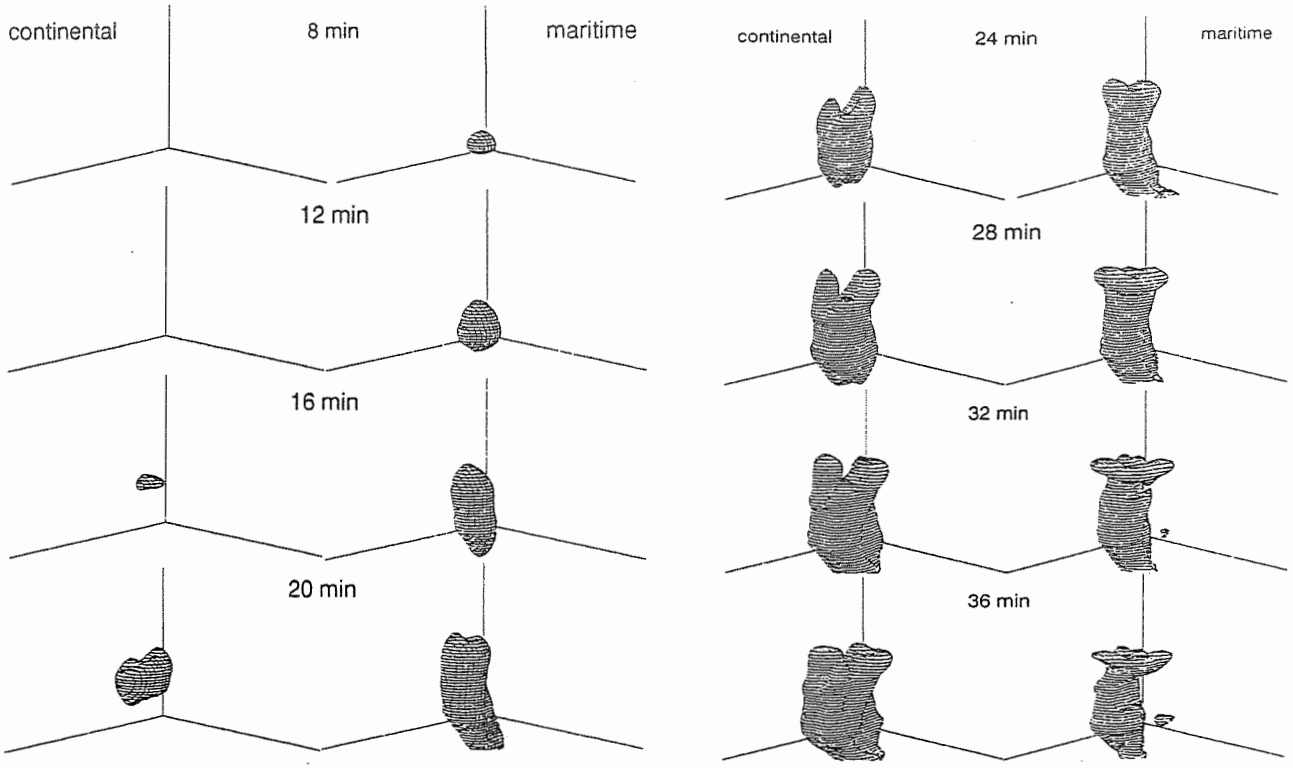

Figure 1. 3D perspective depictions of the simulated radar reflectivity for the initial growth cycle of the CCOPE case. The perspectives are viewed from the northeast and are produced by plotting the surface of the radar reflectivity at 10 dBz. The left panel is for the continental cloud while the right is for the maritime cloud.

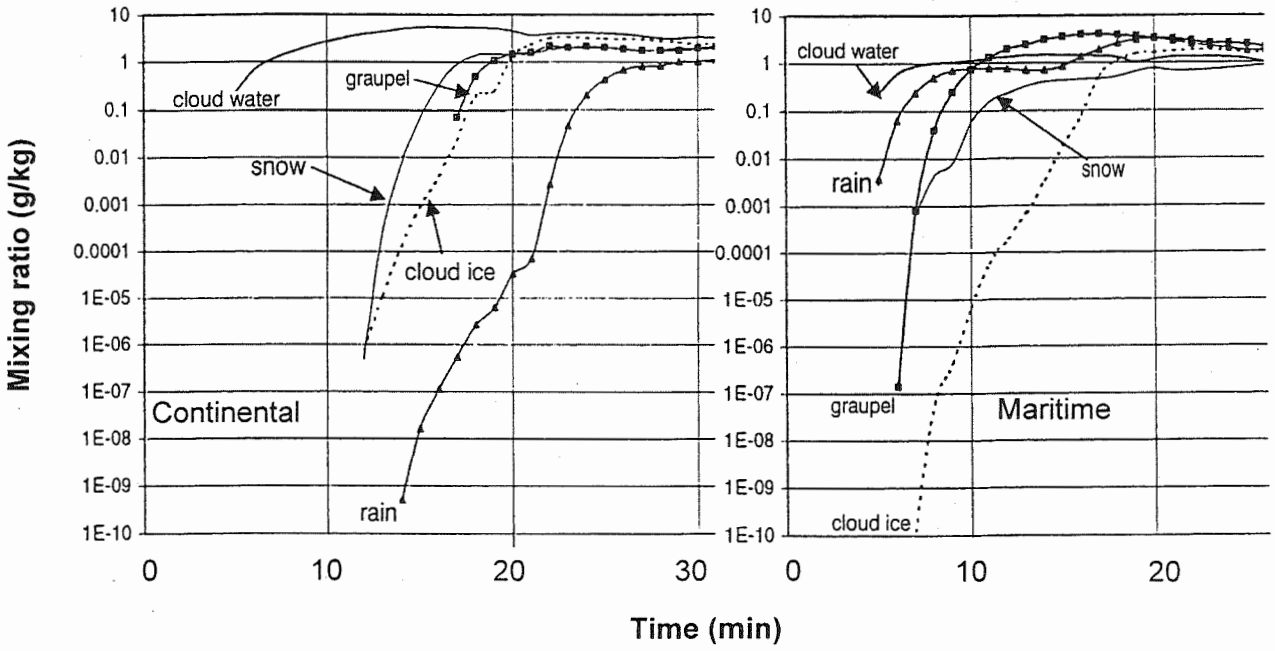

Figure 2. Plot of the maximum mixing ratio of various water substance forms versus time for the CCOPE case. The logarithmic scale is used to better illustrate differences in the initial stages.

graupel. The sequence of events for the continental cloud is: cloud water (5 min) -> cloud ice (12 min) -> snow (12 min) -> rain water (14 min) -> graupel (17 min). In this moderate size continental cloud cell the precipitation forms too late to fully participate in sweeping the cloud water and cloud ice out of the cloud.

3.2 North Dakota strong convective case

The general outline of the continental and maritime cloud system is shown in Fig. 3. The cloud system develops more vigorously in the continental model run compared with the maritime cloud run. A squall line develops and moves east out of the grid in both runs. The maximum vertical velocity is initially developed in the maritime cloud cell, but the later developing continental cells build up even stronger updrafts. The sequence of events concerning precipitation formation is similar to the CCOPE case and so we show the development of maximum mixing ratios in Fig. 4.

Figure 4 shows the cloud water developing first in each run but rapidly converting to rain in the maritime cloud. The rain then transforms to graupel/hail as it is carried to subfreezing regions of the cloud. A maximum of nearly 8 g kg^{-1} is formed in the maritime cloud at about 40 min. The rain maximum follows the graupel curve, indicating the importance of graupel melting during fallout to the production of rain. Cloud water, cloud ice, and snow all vary around 1.0 to 2.0 g kg^{-1}, as they are the raw material for the graupel and rain fields.

The continental cloud shows a much different sequence in its precipitation development. The cloud water increases steadily in the beginning, reaching a value greater than 6 g kg^{-1} at about 20 min. Cloud ice then forms and interacts with the cloud water to form snow and graupel. Rain does not form until the snow and graupel fall below the melting level, near 30 min. The graupel/hail has copious amounts of supercooled cloud water to accrete and increases to more than 10 g kg^{-1} at 45 min.

The maritime clouds in this ND case produce less rain and hail than the continental clouds (5700 vs. 6500 ktons of rain and 30 vs. 88 ktons of graupel/hail).

4. DISCUSSION AND CONCLUSIONS

These results indicate earlier formation of precipitation, but not necessarily more precipitation, in the maritime clouds compared with the continental clouds. The total amount of precipitation depends on the subsequent development of cloud cells and the interactions among them. The strength of the updrafts and downdrafts controls the amount of precipitation. The updraft is initially stronger in the maritime cloud aloft, due to the unloading of the precipitation and the release of latent heat of fusion during the freezing of rain and formation of cloud ice at an early stage. The cloud ice is formed earlier in the maritime clouds due to the Hallet-Mossop process. However, the continental clouds may catch up regarding the vigor of the dynamics, if the atmosphere is unstable enough to allow the updraft to carry the supercooled cloud water to its freezing level. The heterogeneous freezing of copious amounts of liquid releases latent heat of fusion at a higher level than in the maritime clouds. More hail invariably forms in the vigorous continental clouds. It is possible for the continental clouds to process more of their condensate through the ice phase, because the maritime clouds lose some of their liquid to fallout before freezing. Also, the early fallout of the rain in the maritime cloud may inhibit the inflow of moisture to the updraft, reducing its strength further.

For the CCOPE moderate, less efficient continental cloud situation, the transformation to a more maritime cloud condition results in both more rain and more graupel/hail because more of the condensate is processed to precipitation in the maritime clouds.

5. Acknowledgments

Funding for this project was provided bgy NSF grant ATM-9630008. We thank Ms. Connie Crandall for assistance in compiling and typing this abstract.

6. References

Aleksić, N.M., R.D. Farley and H.D. Orville, 1989: A numerical cloud study of the Hallett-Mossip ice multiplication process in strong convection. *Atmos Res.*, **23**, 1-30.

Clark, T.L., 1977: A small scale dynamic model using a terrain following coordinate transformation. *J. Comput. Phys.*, **24**, 186-215.

Clark, T.L., 1979: Numerical simulations with a three-dimensional cloud model: Lateral boundary condition experiments and multi-cellular severe storm simulations. *J. Atmos. Sci.*, **36**, 2191-2215.

Clark, T.L., and R.D. Farley, 1984: Severe downslope windstorm calculations in two and three spatial dimensions using anelastic interactive grid nesting: A possible mechanism for gustiness. *J. Atmos. Sci.*, **41**, 329-350.

Farley, R. D., P. E. Price, H. D. Orville and J. H. Hirsch, 1989: A note on the numerical simulation of graupel/hail initiation via the riming of snow in bulk water cloud microphysical models. *J. Appl. Meteor.*, **28**, 1128-1131.

Farley, R. D., S. Wang and H. D. Orville, 1992: A comparison of 3D model results with observations for an isolated CCOPE thunderstorm. *J. Meteorol. Atmos. Physics*, **49**, 187-207.

Lin, Y-L., R.D. Farley and H.D. Orville, 1983: Bulk parameterization of the snow field in a cloud model. *J. Climate Appl. Meteor.*, **22**, 1065-1092.

Mather, G.K., M.J. Dixon and J.M. de Jager, 1996: Assessing the potential for rain augmentation - the Nelspruit randomised convective cloud seeding experiment. *J. Appl. Meteor.*, **35**, 1465-1482.

Orville, H.D., and F.J. Kopp, 1977: Numerical simulation of the life history of a hailstorm. *J. Atmos. Sci.*, **34**, 1596-1618.

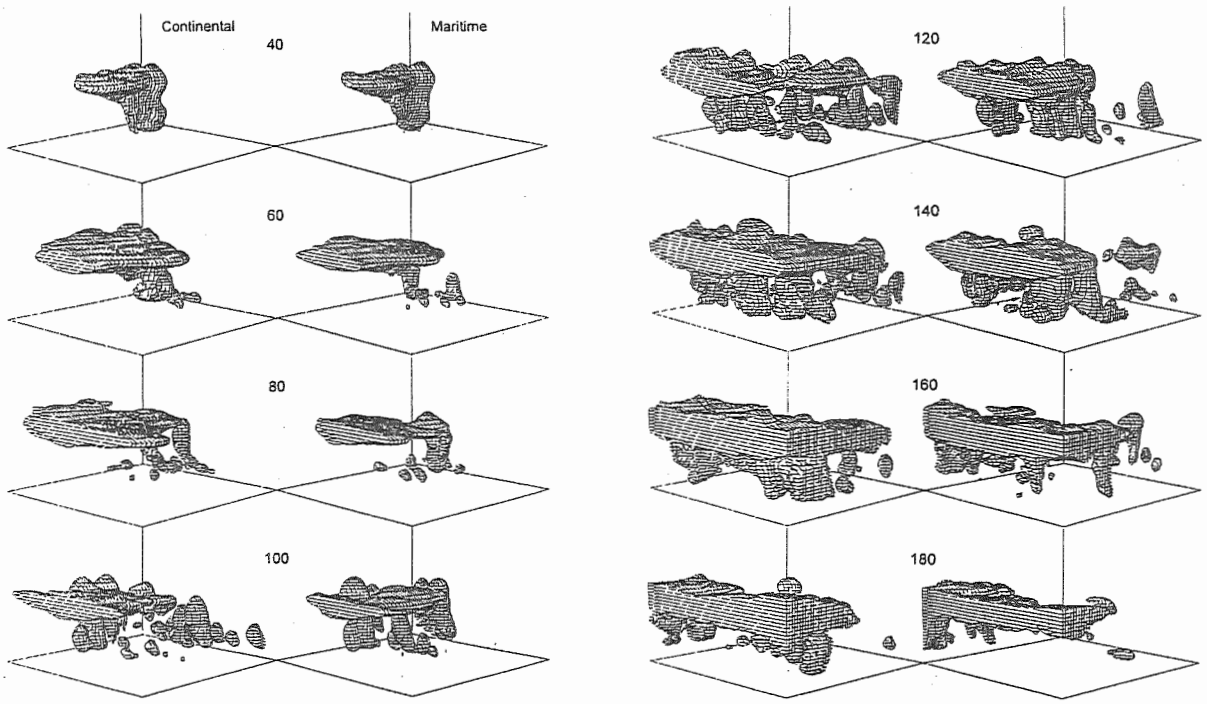

Figure 3. Three-dimensional perspective depictions of the simulated cloud for North Dakota case. The left panel is for the continental cloud and the right for the maritime cloud. The perspectives are viewed from northeast and do not include precipitation and are produced by plotting the surface of the combined cloud water and cloud ice field at $q_{cw} + q_{ci} = 0.1$ g/kg.

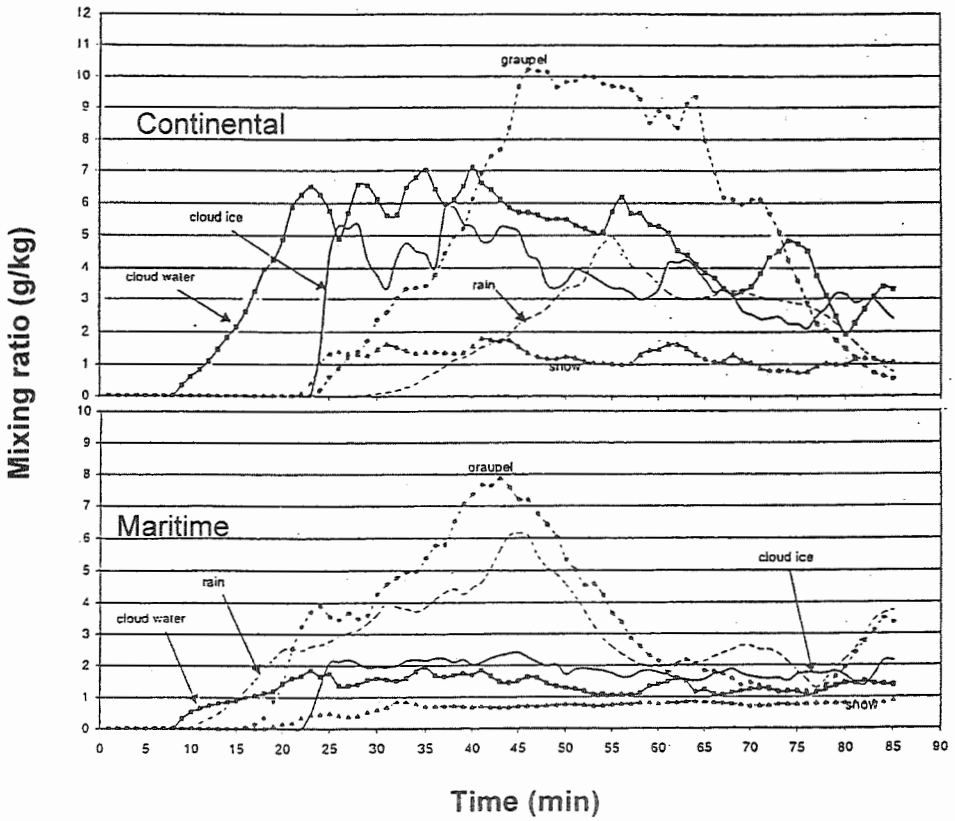

Figure 4. Similar to Fig. 2, but for the North Dakota case on a linear scale.

SUMMER CONVECTIVE PRECIPITATION DURING MONSOON FLOW AGAINST MEXICO'S SIERRA MADRES

Janice L. Coen and Roelof T. Bruintjes

National Center for Atmospheric Research *, Boulder, CO

1. INTRODUCTION

The water supply in the reservoirs of north central Mexico near Torreon depends on convective precipitation produced from late June to early October as monsoon flow crosses rolling hills and reaches the steep slopes of the Sierra Madre. Due to steadiness in the monsoon moisture flow, regular diurnal cycle, and light upper air motions, convective clouds form predictably in certain locations, providing a dependable experimental framework for cloud microphysics investigations.

Here, we use observations collected during annual field experiments and high resolution numerical modeling studies using the nonhydrostatic, anelastic Clark Model to examine the dynamics, microphysical processes and orographic features that control the timing, quantity, scales, and distribution of precipitation. We contrast these studies with previous work from the Arizona Program (Bruintjes et al., 1994; Coen et al 1996), which showed how precipitation distributions during winter storms were controlled not only by the orientation of the changing large-scale flow, but also specific terrain features.

2. MODEL DESCRIPTION

The three-dimensional, nonhydrostatic anelastic meteorological model described by Clark (1977), Clark and Hall (1991), and Clark et al. (1996), exploits features such as two-way interactive grid nesting and vertically-stretched terrain-following coordinates. The model uses Kessler's (1969) warm rain treatment, with the option of using Simpson and Wiggert's (1969) autoconversion formula, and the Koenig and Murray (1976) ice microphysical scheme. It uses the quasi-analytical method of treating supersaturation, as described in Clark (1973). The model carries microphysical variables of water vapor, cloud water mixing ratio, rain water mixing ratio, and number concentration and mixing ratio for two types of ice particles.

Corresponding author's address: Janice L. Coen, NCAR, P.O. Box 3000, Boulder, CO, 80307; ph: (303)497-8986. E-Mail: janicec@ncar.ucar.edu .

*NCAR is sponsored by the National Science Foundation.

The following modifications or parameters were set to tailor the model for these experiments:

- Simpson and Wiggert's (1969) form of Berry's (1968) autoconversion formula was used (except where Kessler's (1969) formula is specifically identified and used for comparison). The droplet concentration was set to 600 cm^{-3}, reflecting the high drop concentrations measured by research aircraft.
- In addition to the surface sensible heat flux (set to an average of 600 W/m^2), a surface moisture source was added at half that flux.
- Ice microphysics were not included in these preliminary experiments.

3. EXPERIMENTAL DESIGN

We have designed these experiments to focus on the development of fine-scale convective features near the complex terrain of the Sierra Madre. Rising dramatically from the north central plains at about 1 km above sea level westward to sharp peaks of 3 km within the experiment area, before dropping sharply to the Pacific Ocean, these finely-featured mountains have a profound effect on the distribution of precipitation in the watershed of the Presa Lazaro Cardenas reservoir (25.61 deg N, 105.05 deg W). Here, we simulate several hours of the summer monsoon convection that occurred on Aug. 13, 1999.

3.1 Domain Setup

Two nested domains (horizontal grid spacings: 2 km and 0.67 km) located over the El Palmito Radar (25.76 deg N, 104.91 deg W) and the reservoir's mountainous watershed were initialized using the 9:15 AM LST Durango sounding. These domains were dimensioned 503 x 48 x 31 km and 275 x 280 x 17 km, respectively, with 50 m vertical grid spacing near the surface stretching to 750 m at higher levels.

3.2 Topography

Three arc sec topography (approx. 100 m resolution) from the Defense Mapping Agency has been averaged to 12 arc sec to produce the fine topography needed for these simulations. The topography for domain 2 is shown in Fig. 1.

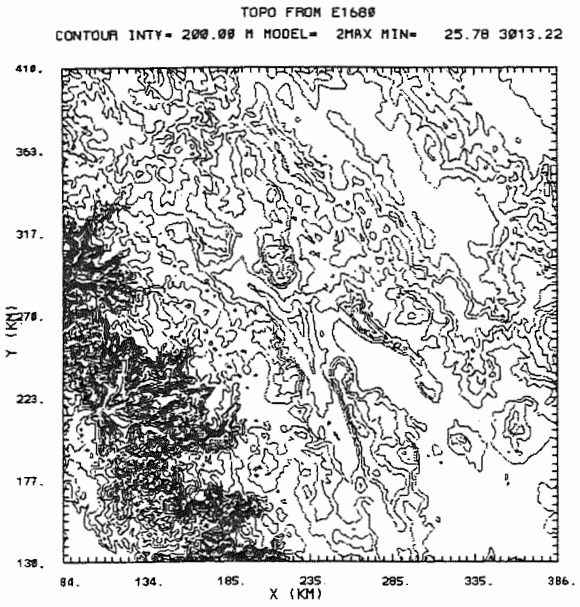

Fig. 1. Topography for model domain 2. Contours every 200 m.

3.3 Meteorological Conditions

The environment on August 13, 1999, was characteristic of the summer monsoon conditions, containing a deep layer of warm, moist air drifting at very low speeds from the northeast towards the perpendicularly-oriented mountain range, beneath light upper air motions. Driven by a strong diurnal cycle (characterized by 600 W/m^2 of sensible heating from the surface, and about half that in latent heating), convective clouds formed predictably in certain locations nearly every afternoon.

For these simulations, we used a single sounding from the Durango airport to establish the background environment. The sounding is shown in Fig. 2. We believe that initialization using an single upstream

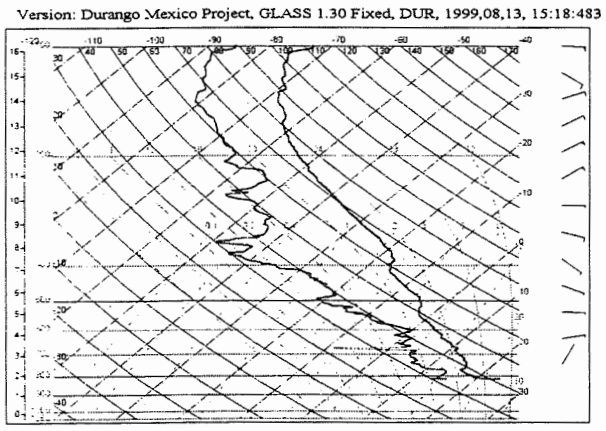

Fig. 2. 8/13/99 9:18 am sounding at Durango, used to initialize simulations.

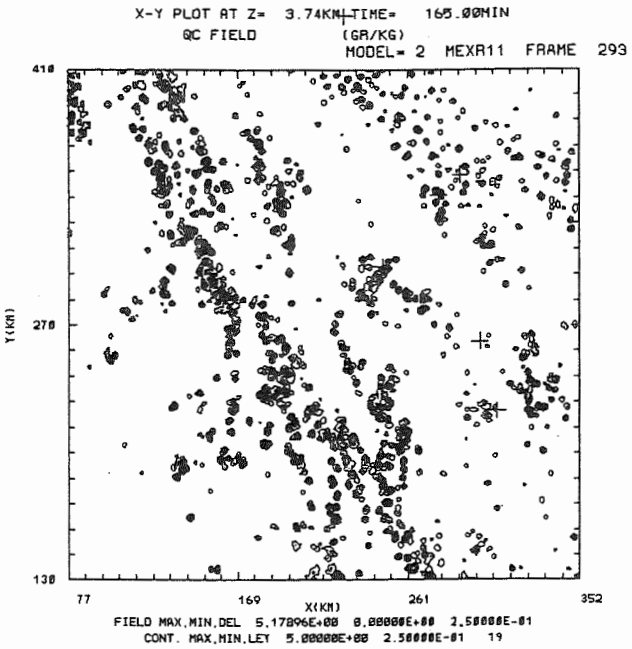

Fig. 3. Horizontal cross section of cloud water mixing ratio at 3.74 km above ground level. Contours every 0.25 g/kg.

sounding is adequate for these simulations because of the steady conditions and its representativeness over a wide area. Taken at Durango (surface pressure, 818 mb) it has been extrapolated with a constant vapor mixing ratio (12 g/kg) and the near-surface potential temperature lapse to 304 K at 1013 mb, to fill in the background environment at lower elevations.

4. RESULTS

The simulations show a very structured region of convection, generally organized into clusters of strongly convective clouds (updrafts up to 10 m/s) in a band along the tallest peaks. Within this band as well as in smaller bands along less dramatic ridges, there are enhanced convective clusters in locations clearly tied to specific mountain features, ranging from lone mountains to dead-end canyons. Cloud organization and depth increased with time, as solar heating increased.

4.1 Structure and distribution of clouds

The cloud field is organized into isolated and strong clusters 2-3 km in diameter containing of 3-5 strong updrafts of 5-9 m/s, with downdrafts about half as strong. A plot of the cloud water mixing ratio distribution in domain 2 is shown in Fig. 3. Along with the long band of clumps of clouds, we can easily identify specific clusters within this band associated with ridges and isolated features, and clear regions with valleys.

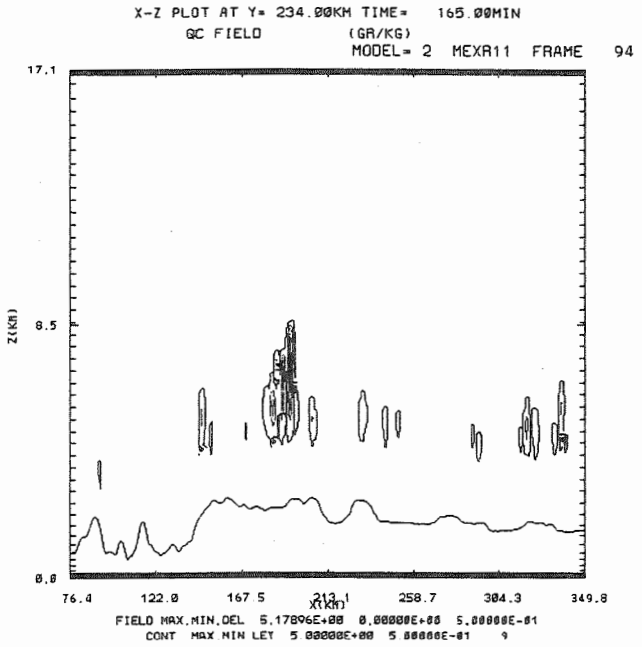

Fig. 4. Vertical cross section of cloud water mixing ratio. Contours every 0.5 g/kg.

Cloud water reached its maximum at a height of about 5.5 km. Mixing ratios in these clouds reached values of 4-5 g/kg. By examining the tephigram in Fig. 2, we see this agrees well with the adiabatic liquid water mixing ratios of about 4 g/kg at this height. Rainwater mixing ratios reached values of 2 g/kg, increased by the plentiful cloud water, but limited due to the high cloud droplet concentration.

4.2 Comparison Simpson-Wiggert: Kessler autoconversion

Rainwater production in warm clouds due to collisions between cloud water droplets is controlled in this and many other numerical models with parameterized microphysics by the 'autoconversion' process. We compare results using two common autoconversion schemes: Kessler (1969), and

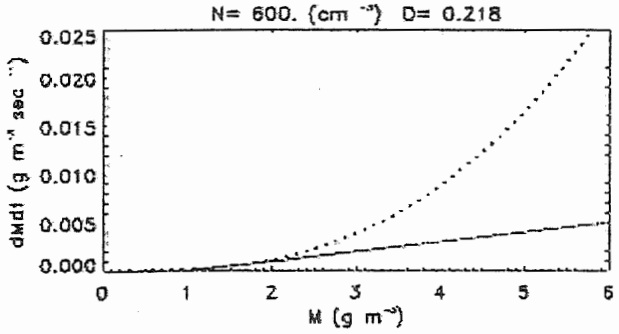

Fig.5. Autoconversion rates as a function of cloud water content for the Simpson-Wiggert autoconversion formula (dotted) and Kessler scheme (solid.).

Simpson and Wiggert's (1969) version of the Berry (1969) scheme (SW).

Both schemes produce rainwater faster at larger cloud water contents. Kessler's linear scheme requires a threshold cloud water content ; cloud water above this amount will be converted to rainwater at a prescribed rate ("autoconversion rate parameter"). SW does not have a threshold – the autoconversion rate is a smooth function that depends, in addition to cloud water content, on the specified droplet concentration and dispersion. The autoconversion rates for a Kessler threshold 1 g/m^3 and 10^{-3} g/m^3/sec, and SW rates for a droplet concentration of 600 cm^{-3} and dispersion of 0.218 are shown in Fig. 5. At the ~5 g/m^{-3} cloud water contents of these clouds, the SW scheme's rainwater production rate are a factor of 6 larger.

While choosing a higher Kessler autoconversion rate parameter would produce qualitatively similar autoconversion rates, how would one choose it? While we might be fortunate enough to have information to guide the selection of SW droplet spectra parameters, it would be difficult to collect data to identify this important parameter, and far different results may be obtained. In this case, after 1 hour of simulation, a run with the SW scheme had produced clouds with 1.8 g/kg maximum rain water mixing ratio, compared to one with the Kessler scheme, 1.4, (a 25% difference). (Cloud water contents at this time were 3.1 and 2.8 g/kg respectively.)

5. CONCLUSIONS

We have examined simulations of warm rain production in convective clouds during monsoon flow as it reached the barrier of the Sierra Madre. These convective clouds were seen to organize in small clusters of narrow clouds with strong updrafts and downdrafts, strongly tied to overall and specific mountainous features. These scales and locations closely match those in radar images (not shown).

The sensitivity to the parameters governing our rainwater production through collisions between cloud droplets suggests this aspect of the model should be examined carefully.

6. ACKNOWLEDGEMENTS

This work is supported by a grant from the Secretaria Agricultura, Grenaderia, y Desarollo Rural of the Government of the State of Durango.

7. REFERENCES

Berry, E. X., 1968: Modification of the warm rain process. Proc. 1st. Intl. Conf. on Wea. Mod. Albany, NY. Apr 28-May 1. Amer. Meteor. Soc. 81-85.

Bruintjes, R. T., T. L. Clark, and W. D. Hall, 1994: Interactions between topographic airflow and cloud/

precipitation development during the passage of a winter storm in Arizona. J. Atmos. Sci., 51, 48-67.

Clark, T. L., 1973: Numerical modelling of the dynamics and microphysics of warm cumulus convection. J. Atmos. Sci. 30, 857-878.

Clark, T. L., 1977: A small scale numerical model using a terrain following coordinate transformation. J. Comput. Phys., 24, 186-215.

Clark, T. L. and W. D. Hall, 1991: Multi-domain simulations of the time dependent Navier Stokes equation: Benchmark Error analyses of nesting procedures. J. Comp. Phys., 92, 456-481.

Clark, T. L., W. D. Hall, J. L. Coen, 1996: Source code documentation for the Clark-Hall Cloud-scale model: Code version G3CH01. NCAR Tech. Note. NCAR/TN-426+STR. 174 pp.

Coen, J. L., R.T. Bruintjes, W. D. Hall, T. L. Clark, and R. F. Reinking, 1996: Numerical simulation of wintertime precipitation development in gravity wave and upslope flow in Arizona's Verde valley. 12th Intl. Conf. on Clouds and Precip. 19-23 Aug. 1996, Zurich, 778-781.

Kessler, E., 1969: On the distribution and continuity of water substance in atmospheric circulations. Meteor. Monogr. No. 32, Amer. Meteor. Soc., 84 pp.

Koenig, L. R., and F. W. Murray, 1976: Ice-bearing cumulus cloud evolution: Numerical simulation and general comparison against observations. J. Appl. Meteor., 15, 747-762.

Simpson, J, and V. Wiggert, 1969: Models of precipitating cumulus towers. Mon. Wea. Rev. 97:471-489.

RELATIONSHIP BETWEEN RAINDROP SIZE DISTRIBUTION AND PRECIPITATION CLOUD TYPE

Akihiro Hashimoto and Toshio Harimaya

Division of Earth and Planetary Sciences, Graduate School of Science,
Hokkaido University, Sapporo, 060-0810, Japan

1. INTRODUCTION

Information on raindrop size distribution (RSD) is fundamental for remote sensing techniques (e.g., radar) and for understanding of precipitation processes. RSD shows different properties depending upon precipitation processes. Waldvogel (1974) and Tokay and Short (1996) reported that there are different properties between RSDs in convective and stratiform precipitations. RSD in convective precipitation may change with the growth stage of the cloud.

The aim of this study was to investigate the different properties between RSDs in convective and stratiform precipitations and between RSDs in stages of convective cloud by using a large amount of RSD data and doppler radar data simultaneously obtained.

2. INSTRUMENTATION AND DATA

The data for analysis were obtained from three observations TREX (1996), X-BAIU-98 (1998) and X-BAIU-99 (1999). The periods of three observations and the locations of instruments are shown in Figure 1. RSD data were obtained using an optical raindrop spectrometer (ORS), which measures the number and diameters of the raindrops which are passing through the measuring area in a sampling period. The minimum diameter of raindrop that could be measured was 0.4 mm. The resolvable time and size were 10 seconds and 0.1 mm, respectively. The measured number of raindrops were converted to space number concentration ($m^{-3}mm^{-1}$) by using of the results of Gunn and Kinzer (1949).

Corresponding auther's address: Akihiro Hashimoto, Division of Earth and Planetary Sciences, Graduate School of Science, Hokkaido University, Sapporo, 060-0810, Japan; E-Mail: hashi@taiki.ep.sci.hokudai.ac.jp.

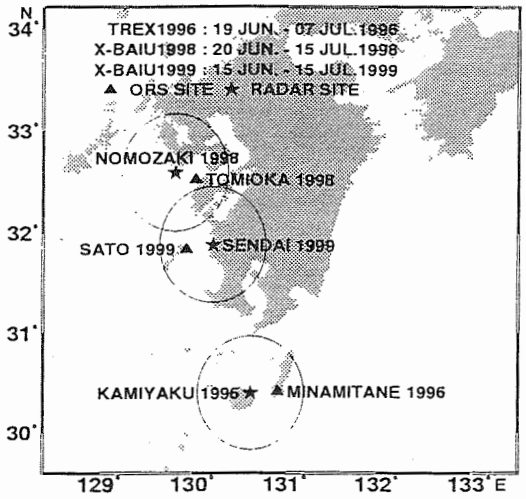

Figure 1. Periods of three observations and locations of instruments. The circles show the detectable ranges of doppler radars.

3. ANALYSIS AND DISCUSSION

3.1 Principal Component Analysis

A large amount of RSD data were objectively analyzed by principal component analysis to extract the modes of RSD variation. Observed RSDs were averaged over 2 minutes. The part of RSD ranging from 0.4 mm to 2.4 mm in diameter was separated into 10 bins at 0.2-mm intervals. The logarithmic number concentrations of each bin were used as the variables for principal component analysis.

The following analyses were performed with special attention given to the first and second principal components because the cumulative proportion of these components was larger than 80%.

The first mode of RSD variation represents an increase in the number concentration over all sizes with

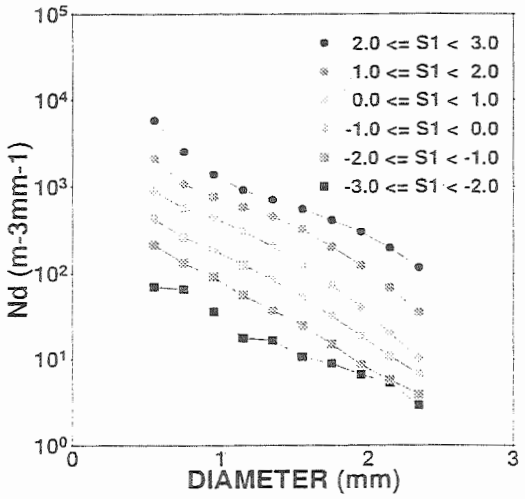

Figure 2. Averaged RSDs over each range of S1

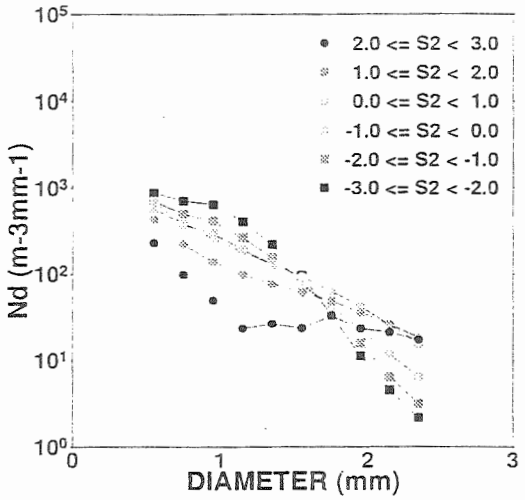

Figure 3. Averaged RSDs over each range of S2

an increase in the score of the first principal component ($S1$) (Figure 2). The second mode represents broadening (or steeping) of RSD with an increase (or decrease) in the score of the second principal component ($S2$) (Figure 3).

3.2 Characteristics of RSDs in Convective and Stratiform Precipitations

Precipitations were classified into convective and stratiform categories based on the results of analysis of radar reflectivity. Precipitation that had a bright band in the vertical cross section of reflectivity was classified as stratiform, and precipitation that had a vertical structure and no bright band was classified as convective. In cases where the reflectivity was complicated, making accurate classification difficult, the data were excluded.

Figure 4 shows the properties of RSD in convective and stratiform precipitations by using $S1$ and $S2$. The property of RSD in convective precipitation is represented by the lower right cluster corresponding to large $S1$ and small $S2$, and the property of RSD in stratiform precipitation is represented by the upper left cluster corresponding to small $S1$ and large $S2$. RSDs were approximated by the exponential function $N = N_0 \exp(-\lambda D)$ in order to obtain the RSD parameters of N_0 and λ. Because there are good correlations between $S1$ and rain water content (RWC) and between $S2$ and λ (Figure 5), it is indicated that the convective category has greater λ (steeper RSD) than does the stratiform category for a given RWC.

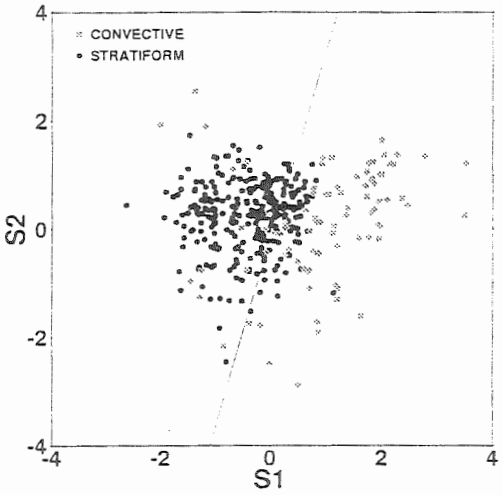

Figure 4. Scattering plot for comparing RSDs in convective and stratiform categories. Solid line shows the boundary.

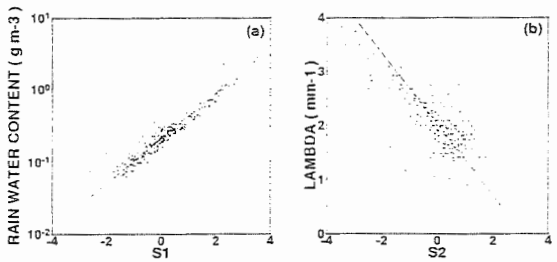

Figure 5. (a) Relationships between S1 and RWC, (b) Relationship between S2 and λ

One possible reason for the different properties of RSDs in convective and stratiform precipitations is the difference in the kinds of hydrometer above freezing level. It seems reasonable to assume that a strong

updraft in convective clouds generates graupel particles above the freezing level by accretion, while a weak vertical motion in stratiform clouds causes formation of large snowflakes due to aggregation.
In order to clarify whether the difference in the kinds of hydrometer above freezing level is one of the reasons for the difference in RSD on the ground, we estimated the values of the parameters of RSDs produced by the melting of graupel particles and snowflakes by using of the results of Yagi et al. (1979). Yagi et al. (1979) observed size distributions of graupel particles and snowflakes in Niigata Prefecture, central Japan in 1978 and 1979, and they obtained the relationships of $N_0 - S$ (snowfall rate) and $\lambda - S$. Figure 6 shows the relationships of $N_0 - RWC$ and $\lambda - RWC$, which were derived from the relationships reported by Yagi et al. (1979), assuming that graupel particles and snowflakes melt under no break-up and no evaporation processes. The value of λ of graupel particles is larger than that of snowflakes in the range of a sufficiently large RWC. This property is the same as that of λ being greater in the convective category than in the stratiform category for a given RWC (Figures 4 and 5) and shows that the difference in the kinds of hydrometer above freezing level is one possible reason for the difference between RSDs in convective and stratiform precipitations.

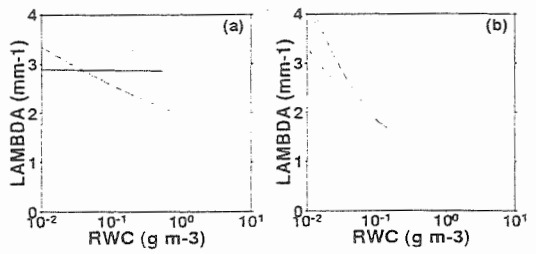

Figure 6. (a) RWC and λ converted from 1978 data in the report by Yagi et al. (1979). (b) Same as (a) except for 1979 data. Solid and broken curves show graupel particles and snowflakes, respectively.

3.3 Relationship between RSD and Growth Stage of Precipitation Clouds

Convective clouds were classified into three stages by tracking time variation in the cross section of radar reflectivity. Case where the echo core was rising were classified as clouds in the developing stage, cases in which the echo core did not change the altitude were classified as clouds in the mature stage, and cases in which the echo core was falling were classified as clouds in the dissipation stage. In cases where the structure of reflectivity was complicated, so making classification difficult, the data were excluded. Since were few cases that were classified as being in the developing stage, only the properties of RSDs in the mature and dissipation stages will be described below. The maximum reflectivity in the life of each convective cloud (Z_{ml}) was obtained. Averaged convergence (C_{av}) over the range of altitude from 1.5 km to 4.5 km was obtained from the vertical profile of divergence calculated by the one elevation VAD method with doppler velocity data observed in X-BAIU-99. The difference between the time when the cloud passes over the ORS site and the time when the cloud passes over the radar site was considered in the analysis. It seems reasonable to assume that convergence in the mature stage is larger than that in the dissipation stage.

Figure 7 shows relationships between Z_{ml} and scores in the mature and dissipation stages. In the mature stage, $S1$ increases with increases in Z_{ml}, while $S2$ does not vary with increases in Z_{ml}. In the dissipation stage, however, $S1$ does not change with increases in Z_{ml}, while $S2$ increases with increases in Z_{ml}. If we assume that Z_{ml} and C_{av} are indices representing the degree of convective activity, the same trend was also found in the relationships between C_{av} and scores (Figure 8). Therefore it was shown that the number concentration over all size increases with increase in convective activity in the mature stage and the broadening of RSD in the dissipation stage occurs with increases in convective activity.

These findings are interpreted as follows from a microphysical point of view. The vigorous updraft in the mature stage, which allows nucleation and collision-coalescence processes to coexist and be in balance, increases the number concentration over all sizes, while broadening of the RSD in the dissipation stage, in which the collision-coalescence process is dominant although the nucleation process simultaneously exists, is produced by collision-coalescence of the raindrops grown in a stronger updraft in the stage before dissipation.

4. SUMMARY

The relationship between RSD and precipitation cloud type was investigated using data obtained by

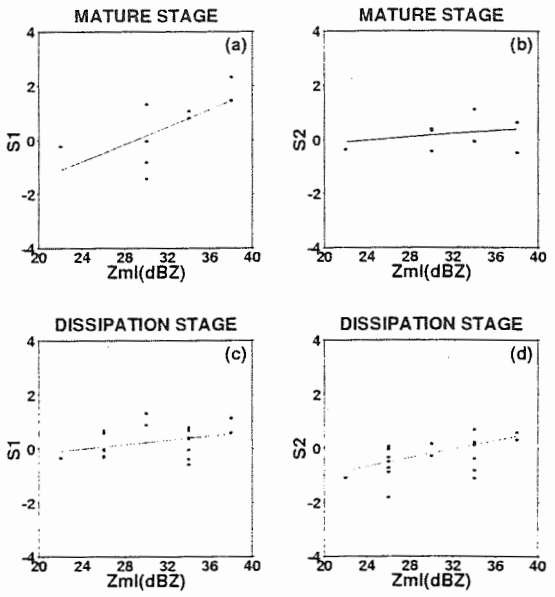

Figure 7. (a) Z_{ml} and $S1$ in the mature stage, (b) Z_{ml} and $S2$ in the mature stage, (c) Z_{ml} and $S1$ in the dissipation stage, (d) Z_{ml} and $S2$ in the dissipation stage.

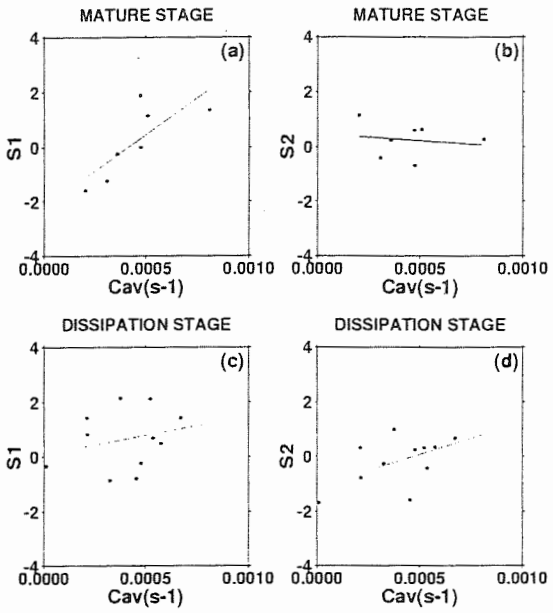

Figure 8. (a) C_{av} and $S1$ in the mature stage, (b) C_{av} and $S2$ in the mature stage, (c) C_{av} and $S1$ in the dissipation stage, (d) C_{av} and $S2$ in the dissipation stage.

three observations: TREX (1996), X-BAIU-98 (1998) and X-BAIU-99 (1999).

Convective precipitation has a steeper RSD than does stratiform precipitation for a given RWC. The difference in the kinds of hydrometer above freezing level might be one of the reasons for the difference in RSDs of convective and stratiform precipitations.

Different properties were found by comparing RSDs in the mature and dissipation stages of convective clouds. In the mature stage, the number concentration over all size increases with increases in convective activity, while in the dissipation stage, broadening of the RSD occurrs with increases in convective activity. These findings are interpreted as follows from a microphysical point of view. These nucleation and collision-coalescence processes which are allowed to coexist and be in balance by a vigorous updraft, cause an increase in the number concentration over all sizes in the mature stage, while the only collision-coalescence process, which is dominant in an updraft that begins to weaken, causes broadening of the RSD in the dissipation stage.

ACKNOWLEDGMENTS

The authors are very gratefull to Y. Fujiyoshi and all the operaters of the doppler radar at the Institute of Low Temperature Science in X-BAIU-98 for providing doppler radar data in 1998. We would also like to thank the X-BAIU-99 observation group for providing doppler radar data in 1999. Thanks are also extended to the doppler radar observation group at the Meteorological Research Institute of the Japan Meteorological Agency for providing doppler radar data during TREX observation in 1996. The SAS used in the principal component analysis was provided by the Hokkaido University Computing Center.

REFERENCES

Gunn, R. G., and G. D. Kinzer, 1949: The terminal velocity of fall for warter droplets in stagnant air. *J. Meteor.*, **6**, 243–248.

Tokay, A., and D. A. Short, 1996: Evidence from tropical raindrop spectra of the origin of rain from stratiform versus convective clouds. *J. Apple. Meteor.*, **35**, 355–371.

Waldvogel, A., 1974: The N_0 jump of raindrop spectra. *J. Atmos. Sci.*, **31**, 1067–1078.

Yagi, T., H. Ueda, and H. Seino, 1979: Size distribution of snowflakes and graupel particles observed in Nagaoka, Niigata prefecture. *J. Fac. Sci., Hokkaido Univ. Ser. VII (Geophysics)*, **VI**, 79–92.

EFFECT OF VERTICAL DRAFTS IN CONVECTIVE CLOUD ON THE RAINDROP SIZE DISTRIBUTION

Pavlos Kollias* and B. A. Albrecht

MPO/RSMAS University of Miami
4600 Rickenbacker Causeway, Miami, FL 33176

1. INTRODUCTION

In addition to the microphysical processes (collisional effects and evaporation) that modify the shape of the raindrop size distribution, vertical drafts also can alter the raindrop spectra by drop sorting due to the different fall velocities of the raindrops. Several authors (Srivastava, 1971; Feingold et. al., 1988; Hu and Srivastava 1995) investigate the evolution of raindrop spectra under the action of various physical processes. Different modeling efforts give similar equilibrium size distributions. On the observational side, despite the substantial development of active and passive remote sensors over the past 40-50 years, the increasing number of observations and the different observing strategies (ground and airborne Doppler radar, satellites, microwave radiometers, wind profilers, disdrometers, and aircraft penetrations) the connection to the modeling is weak. The natural variability of precipitation and the uncertainties related with the instruments' accuracy limit this effort. Here, an unexpected application of millimeter radars first mentioned by Lhermitte (1988) is applied to convective clouds observed in South Florida. The method allows accurate retrievals of air motion and subsequently the raindrop distribution from the Doppler spectrum (Kollias et al., 1999). In this paper we focus on observations taken in a convective core. The air motion retrieved by the cloud radar reveals updraft and downdraft structures and the associated raindrop spectra field is discussed with emphasis on the sorting effect of the drafts.

2. BACKGROUND

Doppler radars and wind profilers provide means for observing the structure and evolution of precipitating clouds, although the retrieved microphysical parameters are subject to large errors. The uncertainties are largely due to the direct coupling of the vertical air motion to the retrieval of the raindrop size distribution and spectral broadening due to small-scale turbulence that smears the Doppler spectrum. The limitations imposed by the lack of accurate measurements of the vertical air motion and turbulence can result in substantial errors (Atlas et. al., 1973). The noisy nature of the Doppler spectrum due to atmospheric and instrument sources makes the deconvolution of turbulence extremely difficult and biases the estimate of the velocity range of the terminal fall velocities of raindrops.

Although the use of wind profilers seem promising due to the existence of the Bragg scattering peak on the observed spectrum, several problems make the use of wind profilers difficult and the retrieval questionable. Despite these obstacles in the retrievals, it is apparent that wind profilers are capable of revealing details about the structure of tropical precipitating systems and provide meaningful ways to classify precipitation clouds in convective and stratiform types. Observations of both the vertical air velocities and the raindrop fall speeds are very rare. Aircraft observations are capable of this type of measurement, but lack vertical resolution and are difficult to make near the surface. In addition, aircraft measurements sample a very small volume (1-2 m^3) over a large horizontal path (typically 1 km). Disdrometers also have relatively small sampling volumes and are limited to measurements at ground level.

Millimeter radars have been primarily used as cloud radars due to their increased sensitivity to small droplets and their ability for high-resolution detection of weak targets. The use of millimeter radars under convective rain is limited due to the strong attenuation. Under such conditions, millimeter radars loose their main advantages over centimeter wavelength radars. But the transition from the Rayleigh to Mie scattering regime offers new possibilities and advantages for air motion and precipitation studies. In the Rayleigh regime, the backscattering power is proportional to the

*Corresponding author address: Pavlos Kollias, Rosenstiel School of Marine and Atmospheric Science, Division of Meteorology and Physical Oceanography 4600 Rickenbacker Causeway of Miami, Florida 33149-1098.

sixth power of the diameter and thus monotonically increases with droplet size. In the Mie regime, the backscattering power oscillates with consecutive maximum and minima with increasing size. The location of these local minima and maxima is well predicted by Mie theory. For raindrops at 94 GHz, these oscillations are apparent in the observed Doppler spectrum and therefore can be used as reference points for the retrieval of vertical air motions and raindrop size distributions. Furthermore, the side-by-side operation of a wind profiler and 94 GHz radar with mesoscale coverage from a centimeter radar (WSR-88D) can be used as powerful observing systems for the observational analysis of convective cloud systems.

Kollias et. al., (1999) applied a method first described and demonstrated by Lhermitte (1988) to study a shallow convective system, and illustrate how Doppler spectra from a 94 GHz radar can be used to obtain air vertical velocities and DSDs that are unbiased by the air vertical velocities. Besides giving air motions to an accuracy of 0.1 ms^{-1}, cloud radars operating in a vertical pointing mode have additional advantages. The sampling volume of the cloud radar, due to its narrow beam width (0.25°) and high-resolution temporal sampling, is very small compared with other radars (wind profilers, weather radars). But at the same time the radar sampling volume is relatively large compared with the volume sampled by disdrometers or raingauges. The high temporal and spatial resolution of the cloud radar can improve our knowledge of the physical foundations of rainfall statistics. Moreover, the high temporal variability of the drop size distribution in convective regimes and stratiform regimes can be observed and used to investigate cloud processes.

3. OBSERVATIONS

During the summer and autumn of 1999 a combination of instruments that included the University of Miami 94 GHz radar and a 915 MHz wind profiler was used to observe over-passing convective and stratiform precipitating systems. The data presented here were collected on September 7 and 8 1999, at the Rosenstiel School of Marine and Atmospheric Science, Miami, Florida. Fig.1 shows a time-height section of the reflectivity mapping of the convective core of the precipitating system.

The convective system formed inland from the site and was observed for almost 3 hours with a substantial stratiform trail. The rainfall rate measured by a rain gauge collocated with the radars during the passage of the high reflectivity core was between 30-80 mmh^{-1}.

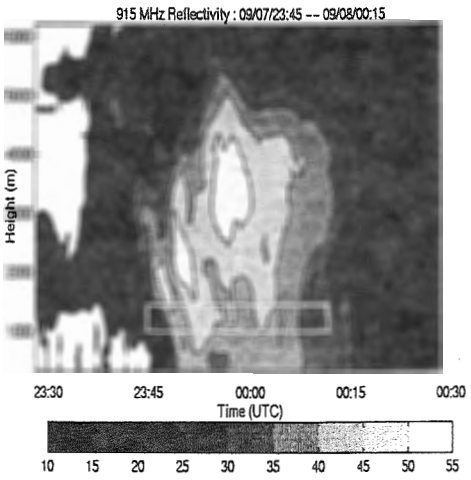

Fig 1. 915-MHz radar reflectivity mapping of the convective core. The reflectivity exceed 50 dBZ at levels between 1.5 and 4 km. The box defined by the white lines indicates the area where the millimeter radar data were used for microphysics and air motion retrievals.

The reflectivity values observed by the wind profiler were verified by the Miami WSR-88D (KAMX) located about 25 km from the radar site.

The cloud radar Doppler spectra were analyzed and the shifting of the first Mie minima relative to its location in still air conditions was estimated to provide retrievals of the air motion field (Figure 2) within the white box shown in Figure 1.

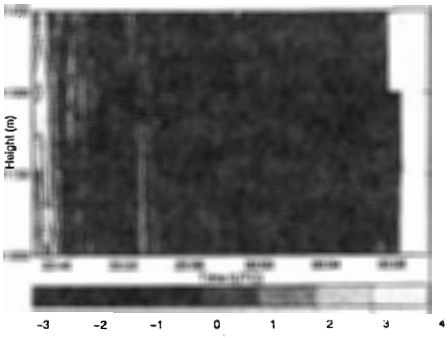

Fig. 2. Vertical air motion field retrieved by the millimeter radar.

The vertical resolutions of the cloud radar is 60 m, and since the temporal resolution is 4.8 sec, about 300 profiles of Doppler spectra were used to obtain the air motion field. The accuracy and stability of the retrieval technique were tested under stratiform conditions. The technique exhibits highly correlated (~ 0.9) cross sections of vertical air motion with

amplitudes less than 0.5 ms^{-1}. Each Doppler spectra is analyzed independently without any input from nearby Doppler spectra in the height - time domain. The results show a narrow updraft at the approaching side of the convective core. The interior of the convective system at these levels is dominated by two weak downdrafts separated by a narrow, weak updraft area. The magnitude of the updraft reaches 4 ms^{-1} and the main downdraft approaches – 3 ms^{-1}. After retrieving the vertical air motion, the Doppler spectrum is used to retrieve raindrop size distributions. Despite the narrow beam, turbulence, especially under strong drafts, can smooth the observed spectra. Thus we apply an iteration scheme involving a gamma drop size distribution convoluted with a Gaussian filter in order to account for the turbulence effects.

The retrieved raindrop size distributions illustrate the different nature of the two downdrafts. Figure 3, shows the retrieved medium volume diameters at two different levels with a spatial and temporal resolution that is difficult to duplicate with other instruments.

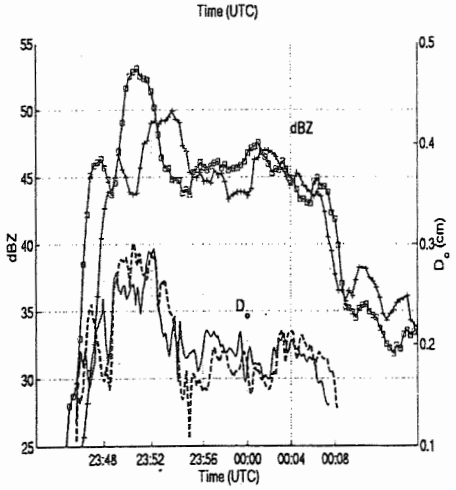

Fig. 3. Cross section of radar reflectivity from the wind profiler at 2 km (squares) and 1.35 km (crosses) and D_o at levels of 1.45 km (solid) and 1.15 km (dashed).

The results clearly demonstrate the drop-sorting effect of vertical drafts. The elevated high reflectivity core is consistent with the suspension of raindrops at high levels until they reach terminal velocities large enough to overcome the upward motion. These very large raindrops (D_o > 2.4 mm) are observed for a time period of 3 min inside the area of the first weak downdraft. The vertical air motion retrieved from the wind profiler also supports this. Titled updrafts are not favorable for the generation of very large raindrops, but this is just a snapshot of the air motion field and the raindrop could be generated at earlier stages of the development. Szumowski et al. (1998) observed the same behavior using combined radar and aircraft data. In the area of the main downdraft, the raindrops have much smaller sizes and the maximum observed sizes did not exceed 3 mm in diameter. In addition to the variability of D_o induced by the drafts, higher variability on the D_o, time series is observed. Other processes and especially the turbulent nature of the interior of the convective core may contribute to this variability. The retrievals are independent of the reflectivity measurements. Therefore, the fact that the D_o variability retrieved by the cloud radar follows the reflectivity values from the wind profiler indicates the quality of the retrievals.

The main downdraft is associated with much lower D_o values and higher rainfall rates at the surface (not shown). In an effort to recover any systematic variability in the interior of the main downdraft we isolated the area where the main downdraft reaches the lower level analyzed (23:57 – 00:00 UTC).

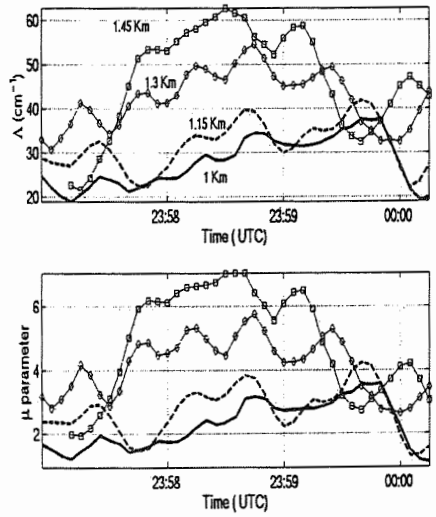

Fig. 4. Cross section of $\Lambda(cm^{-1})$, slope of the gamma function fitted to the retrieved raindrop spectra and μ, the shape parameter at four different levels (1.45, 1.3 1.15 and 1 Km).

The results (Figure 4) show a systematic variability of the gamma function parameters used to describe the observed raindrop size distributions with altitude. Estimating the cloud base height at 1.3 km, we see that during descent the slope of the distribution becomes steeper reaching values around 50 – 60 cm^{-1} at the lowest level. Further, the distribution spreading is diminished. It is difficult to account for the physical

processes responsible for this modification of the shape of the raindrop spectra.

Nevertheless, the steep slopes of the observed spectra at the tail of the large drops and the lack of raindrops greater than 3 mm at high rainfall rates are findings of special importance for the modeling community.

4. CONCLUSIONS

Strong evidences of drop sorting effects due to the kinematics of the interior of the convective core is presented in this paper. It is apparent that convective cores have internal variability. A large D_o jump is observed between the narrow transition area between the two downdrafts. Mass loading may have induced the observed downdrafts, especially in the first one observed where very large drops where observed and evaporation is limited. In the main downdraft, the systematic variability of the gamma distribution parameters with height indicates that other processes like breakup and evaporation are involved.

The results clearly demonstrate the capability of millimeter radars for the study of precipitation processes. The data presented here and the analysis of several other cases illustrates that such instruments can retrieve fine structures of the vertical air motion and raindrop spectra. With a sampling volume of a few hundred m^3 and excellent temporal and spatial resolution, millimeter radars can be used as precipitation sensor as well. Besides the value of the retrieval technique as a tool, this type of data can be used for refining the retrieval of other widely used radar systems for precipitation studies (e.g. wind profilers).

Fine scale variability of the precipitation field can be observed and physical processes as those described in this paper can be addressed.

5. REFERENCES

Atlas, D., R. S. Srivastava, and R. S. Sekhon, 1973: Doppler radar characteristics of precipitation at vertical incidence. *Rev. Geophys. Space. Phys.*, **11**, 1-35.

Feingold, G., S. Tzivion and Z. Levin, 1988: Evolution of raindrop spectra. Part I: Solution to the stochastic collection/breakup equation using the method of moments. *J. Atmos. Sci.*, **45**, 3387-3399.

Hu, Z., and R. C. Srivastava, 1992: Evolution of Raindrop Size distribution by coalescence, breakup and evaporation: Theory and observation., *J. Atmos. Sci.*, **52**, 1761-1783.

Kollias, P., R. Lhermitte and B.A. Albrecht, 1999: Vertical air motion and raindrop size distributions in convective systems using a 94 GHz radar. *Geophys. Res. Letters*, **26**, 3109-3112.

Lhermitte R., 1988: Observations of rain at vertical incidence with a 94 GHz doppler radar: an insight of Mie scattering., *Geophys. Res. Lett.*, **15** 1125-1128.

Srivastava, R. C., 1971: Size Distribution of Raindrops Generated by their Breakup and Coalescence. *J. Atmos. Sci.*, **28**, 410-415.

Szumowski, M. J., R. B. Rauber, H. T. Ochs III and K. V. Beard, 1998: The microphysical structure and evolution of Hawaiian rainband cloud. Part II: Aircraft measurements within rainbands containing high reflectivity cores. *J. Atmos. Sci.*, **55** , 208-226.

AN ANALYSIS OF THE EVOLUTION CHARACTERISTICS AND PHYSICAL CAUSE OF FORMATION ABOUT FORTY YEARS NATURAL RAINFALL IN HEBEI PROVINCE

An Yuegai, Guo Jinping, Duan Ying and Deng Yupeng

Weather Modification Office of Hebei Province
No.178, Tiyu South Street, Shijiazhuang, P.R.China
Email:hbwmo@public.sj.he.cn, Postal code 050021

1.Introduction

Since 1980s in northern China, the lack of water source has become more and more serious. Especially in Hebei province the situation of Hai and Luai river basin is much worse, which limited economic progress. In recently 40 years air temperature was tending to increase with the change of climate, but at the same time rainfall was decreasing.

Based on representative eleven stations' long sequence rainfall, air temperature and visibility data, with the ice nuclei data, the evolution characteristics about forty years natural rainfall and relation between rainfall and air temperature in Hebei province area, as well as the rainfall characteristics are analyzed. According to the changing tendency of visibility and ice nuclei concentration, results indicate that the weight of rainfall increases in winter half year, while decrease in summer half year in Hebei province area.

2. Change of rainfall and air temperature

1) Rainfall

The table1 mean rainfall in Huber (mm)

	1950s	1960s	1970s	1980s	1990s
Mean in all province	579	562	541	502	520
Hill of Yan mount	658	728	722	654	642
South plain	601	575	515	499	504
Middle plain	585	558	514	553	565
North plain	504	436	438	405	428

According to the table 1 from 1950s to 1980s mean rainfall dropped by 26mm every 10 years. It climbed up 18mm in 1990s than that in 1980s, but still less than in 1950s. The change of each part is similar though rainfall in Zhangjiakou in the north and in the south plain cut down 99mm and 102mm respectively. All these add the possibility of becoming into desert in the northwest. The hill of Yan mount usually is a region where rainfall is very high, but it lessened 86mm in 1990 than that in 1960s.

2) Air temperature

Annual mean temperature was the lowest in 1960s in Hebei province, and then stepped up to the highest in 1990s. Every 10 years it increases about 0.23°C. In winter mean annual lowest temperature also appeared in 1960s and it moved up in late 1970s until 1990s' 1.9°C higher than in 1960s. Every 10 years it increases 0.63°C. But in summer it changes a little, with the lowest in 1970s and rising up in late 1980s.

According to the table 2, we find that annual mean temperature stepped up in late 1970s to the highest in 1990s. It is becoming warmer and warmer.

3.Correlation between air temperature and rainfall

In Hebei province the temperature is tending to increase while the rainfall is inclining to decrease in recent 40 years. There is some correlation between them. By analyzing long sequence rainfall and temperature data, the correlation coefficient is 0.62 as all mean situations in Hebei province.

4.Statistic of rainfall characteristic value

Based on statistic of total rainfall and each year's rainfall, we find the tendency that days of slight rain in winter increase as time goes by. By analyzing weighting of slight rain in winter half year and in summer half year respectively, the result is in table 3.

From the table, we find weighting of slight rain is fluctuant in winter half year in south of Baoding, but as a whole it is tendency to increase. It is contrary in summer half yea

The table 2 annual, summer and winter mean temperature(°C)

	1950s	1960s	1970s	1980s	1990s
Annual mean	9.9	9.6	9.8	10.0	10.3
Summer mean	23.7	23.5	23.1	23.3	23.6
Winter mean	- 5.2	- 5.8	- 5.1	- 5.1	- 3.9

The table 3 weighting of slight rain in winter half year

	1950s	1960s	1970s	1980s	1990s
Zhangjiakou	34	31	40	25	33
Chengde	37	32	37	35	23
Tangshan	41	36	60	45	34
Qinghuangdao	41	35	42	47	35
Langfang	31	37	47	44	41
Baoding	36	47	41	46	58
Cangzhou	35	43	46	55	55
Shijiazhuang	48	52	50	51	60
Hengshui	46	46	51	54	58
Xingtai	44	49	50	60	57
Handan	54	43	59	59	61

5. Analyzing the reason

The precipitation mechanism should be thought in research of rain factor except for the dynamical and thermodynamic reason. The aerosol particle in atmosphere affects cloud micro physical structure and precipitation process by accelerating water phase to change. The number of CCN affects precipitation process in warm cloud while the number of ice nuclei affects precipitation process in cold cloud. Some times there is interaction.

In recent several decades along with human activity and society development, atmosphere visibility falls down markedly. By deducing relation between visibility and content of ice nuclei, the content of ice nuclei is likely to increase by geminating and now the ice nuclei data just prove it. The content of ice nuclei increased about 15 times in last 30 years in Beijing.

On the other hand, CCN also rose up that causes the amount of drops in cloud. It can be conferred that cold rain process is likely to be strengthened while warm rain process be restrained because of ice nuclei and CCN increasing with human activity and society development.

Reference

Zhang Chengchang et al., 1995: "Teaching material about atmospheric aerosol", China Meteoro. Press, Beijing (in Chinese).

Shi Anying et al., 1980:Ice nuclei and snow crystal, Hebei People Press, Shijiazhuang (in Chinese).

RAINDROP SPECTRA OBSERVATIONS FROM CONVECTIVE SHOWERS IN THE VALLEY OF MEXICO

F. García-García[1, 2] and Julio E. González [2]

[1] Centro de Ciencias de la Atmósfera, Universidad Nacional Autónoma de México
[2] Posgrado en Ciencias de la Tierra, Universidad Nacional Autónoma de México

1. INTRODUCTION

One of the quantities most commonly used to characterize rain is drop size distribution. The importance of the observation and study of raindrop spectra comes from the fact that they contain basic information regarding cloud microphysical processes and their interactions with the dynamical aspects of precipitation development. Thus, radar meteorology and cloud modeling are but two of the fields in atmospheric science that most benefit from the knowledge of raindrop size distributions.

The most widely used description for raindrop size distributions is that of Marshall and Palmer (1948), in which the number concentration is assumed to be an exponential function of the drop diameter. Although other, not so simplified distributions have also been proposed, such as lognormal and gamma functions (see for example Pruppacher and Klett 1997), there generally exist discrepancies between measured and theoretical spectra. This is due in part to the fact that numerous field observations indicate that raindrop spectra exhibit a multipeak behavior (for a summary, see Steiner and Waldvogel 1987). Thus, proposed functions are able to describe general trends in different cases, but it is basically impossible to solve all the discrepancies for all situations with a single functional form.

Numerical models with detailed microphysics used for warm rain processes calculations (Valdez and Young 1985, List *et al.* 1987) predict a multipeak behavior of the spectra, as those observed in the field. These processes are of great importance in the tropics where warm-based convective clouds are common, but also play a role in midlatitude summer precipitation where collision-coalescence mechanisms take place below cloud base. This latter case may also apply to Mexico City due to its particular geographical characteristics of high altitude.

With the purpose of better understanding the microphysical characteristics of precipitation in the Valley of Mexico, a series of ground-based field measurements was performed using two Optical Array Spectrometer Probes (OAP´s, by Particle Measuring Systems, Knollenberg 1981). García and Montañez (1992) have reported previous results for the region, at a site located at the southern end of the city. In the present study, the probes were mounted on a van for in-motion measurements as opposed to the previous case, in which the spectrometers were operated in a stationary mode. The details of the experiment and the preliminary results are described in what follows.

2. INSTRUMENTATION AND METHODOLOGY

Raindrop size distributions were measured with two OAP's (a 2D-C and a 2D-P) mounted side-by-side in a horizontal orientation (as on an aircraft) in a specially designed structure on a Ford Pick-Up truck. A cup anemometer and a wind vane were located besides the spectrometers to determine the sampling speed. Care was taken to locate the probes above and ahead of the front of the van in an attempt to minimize airflow distortion caused by the moving vehicle. The site chosen for the present study was a 2 km-long stretch of a paved, low vehicular traffic, local road located inside the main campus of the National University of Mexico. During sampling, the van was driven at a constant speed of 15 m/s, thus performing continuous penetrations through the precipitation shaft.

The particles image data were reduced by means of an objective software routine specifically developed for the particular sampling conditions, with a reconstruction algorithm based on a center-in technique (Alvarez and Torreblanca 1992). Laboratory performance tests and calibrations

Corresponding author's address:
Fernando García-García.
Centro de Ciencias de la Atmósfera.
Universidad Nacional Autónoma de México.
Circuito de la Investigación Científica,
Ciudad Universitaria. Del. Coyoacán.
04510 México, D.F. México.
e-mail: ffgg@ccaunam.atmosfcu.unam.mx

were conducted on the OAP's prior to the field data collection. The results, along with the given characteristics of the software routine, indicate that these particular 2D-C and 2D-P probes are in principle capable of detecting drops in the ranges from 20 to 835 μm (resolution 24 μm) and from 140 to 7360 μm (resolution 198 μm), respectively. Details on the peripheral equipment, its operation and on data reduction can be found in Montañez and García (1992).

The measurements took place during September 1995 and included three precipitation events, two of them being of convective nature. Due to the preliminary nature of the results only one case study, corresponding to measurements obtained with the 2D-P during the event of 11 September 1995 (hereafter Case 1), is discussed in the present paper. It is analyzed as time-series of two minutes duration. Rainfall rates were derived from the precipitation water content, which in turn was obtained by integrating over all drop diameters of the measured spectrum, i.e., over the range of the spectrometer. Temperatures recorded during the field observations ranged from 16 to 20°C, under generally calm wind conditions (maximum wind gust of about 2 m/s).

3. RESULTS AND DISCUSSION

Rainfall rates, R, for each of the individual, two-minute duration rainshaft penetrations realized during the two convective events occurred on 11 and 14 September 1995, ranged between less than 1 and 28 mm/h. For analysis purposes the data were stratified in terms of R in four categories: $R < 1$, $1 \le R < 5$, $5 \le R < 10$ and $R \ge 10$ mm/h. In order to determine the shape of the entire sample, raindrop spectra so obtained were analyzed by performing a least-squares data fit, assuming an exponential distribution of the Marshall-Palmer (MP) type:

$$N(D) = N_o \exp(-\Lambda D) \ ,$$

where N is the number concentration [cm^{-3} μm^{-1}], D [μm] is the mean diameter of each drop size category, $N_o = 10^{-5}$ cm^{-3} μm^{-1} (from the fit) and Λ is a function of R. As it can be appreciated in Figure 1, the data agree well with MP distributions within the range $400 < D < 3000$ μm. Also, there are very few drops larger than about 3 mm, possibly indicating that collision-coalescence-breakup processes are underway.

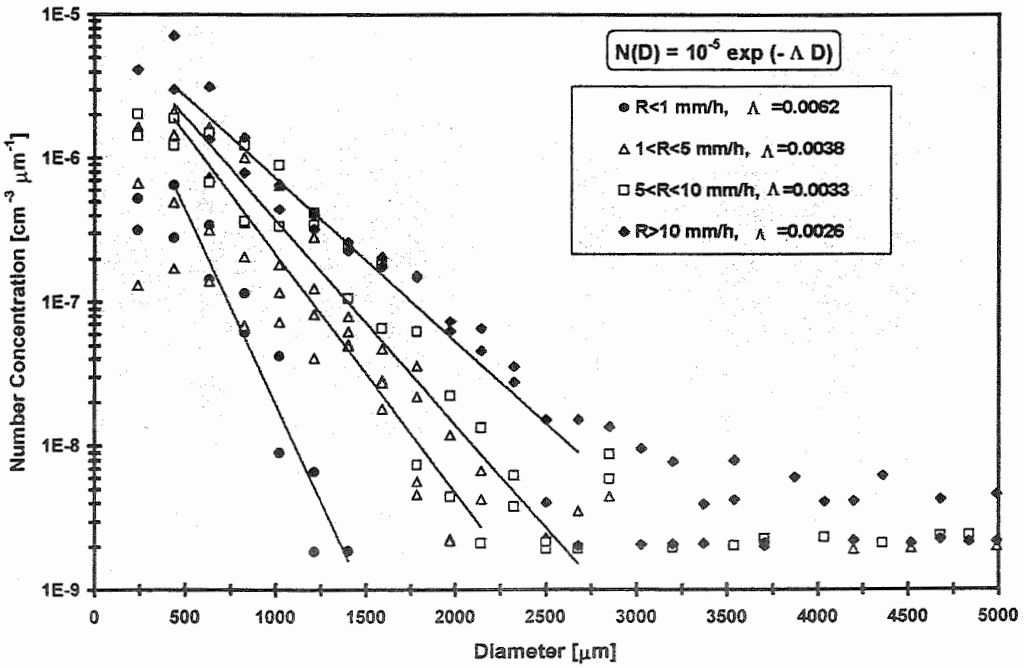

Figure 1. Raindrop spectra for two-minute rainshaft penetrations measured in Mexico City. Data include two rainfall events and are stratified in terms of rainfall rate, R. Lines represent least-squares fits to Marshall-Palmer distributions.

Figure 2 presents a time-series of raindrop spectra obtained for Case 1 (total precipitation time of 40 minutes) consisting of five, two-minute long rainshaft penetrations. For discussion purposes, spectra normally expressed as number of drops per unit volume of air and per unit size interval, are presented in Figure 3 in terms of the natural logarithm of D [N = a(l) dl, where l = ln D], and in Figure 4 in terms of mass concentration [g(l) dl]. (See List *et al.* 1987). The multimodal characteristics of the spectra can be appreciated in these figures and, in spite of the small size of the sample, a consistent pattern starts to emerge.

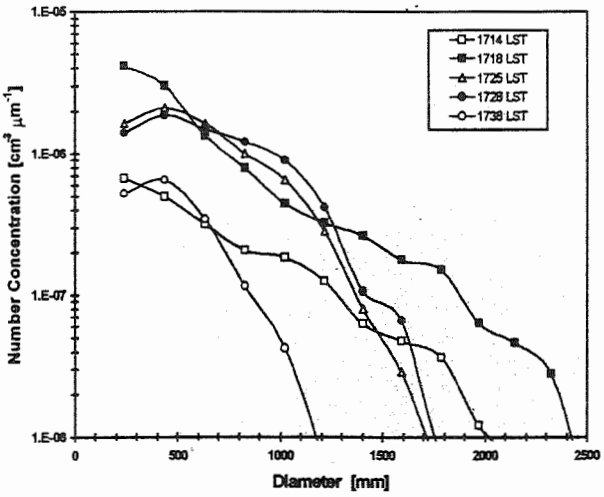

Figure 2. Time-series of raindrop spectra for two-minute rainshaft penetrations measured in Mexico City on 11 September 1995.

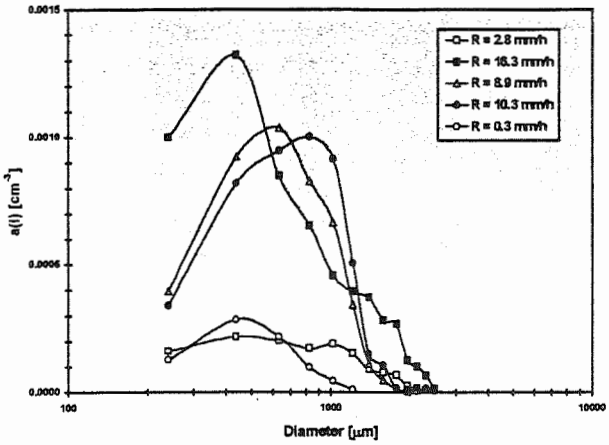

Figure 3. As in Figure 2, but in terms of logarithmic coordinates: N = a (l) dl, where l = ln D.

At the beginning of rain (penetration at t = 0), there is an indication of the appearance of two relative maxima at 1024 and 1787 μm. Four minutes later (t = 248 s) the number concentration of small droplets increases in one order of magnitude, presenting a distinctive peak at 438 μm, and the larger peak in mass concentration diminishes in magnitude. For t = 642 s and t = 857 s, the rainfall rates remain relatively constant: the smaller peak in number concentration is well defined, the maximum in mass concentration shifts to 1593 μm, and an emerging, third peak oscillates between 830 and 1024 μm. By t = 1432 s, the precipitation event has roughly ended, but the smaller maximum in number concentration can still be appreciated. The observations stated here can be discussed in view of the predictions given by currently available numerical models.

First, Valdez and Young (1985) and by List *et al.* (1987) predict three peaks roughly in the ranges between 0.2 and 0.3, 0.8 and 0.9, and 1.8 and 2.0 mm. The first one was not observed in the present investigation, since it falls within the limits of the OAP-2D-P. The two others are observed at different stages of rain development within the instrument limitations. It should be noted that the relative maximum at 438 μm has been consistently reported by several investigators (for a summary, see Steiner and Waldvogel 1987) using different sampling techniques.

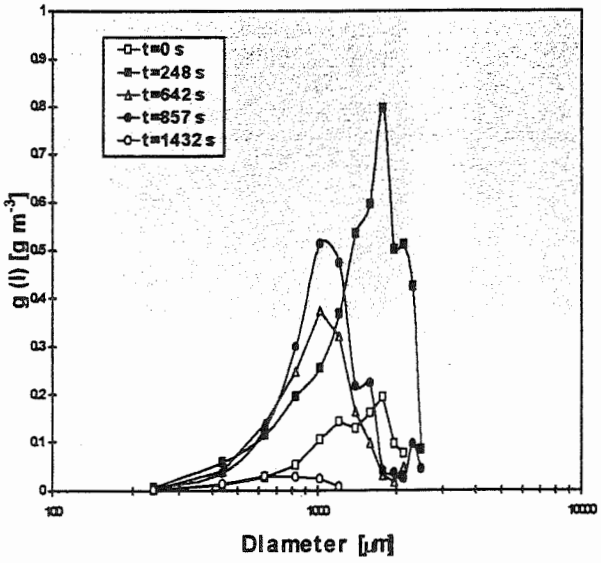

Figure 4. As in Figure 2, but in terms of mass concentration M = g (l) dl, where l = ln D.

Second, the three-peak distribution is not observed simultaneously at every time during rain development. This reflects, in part, separation in arrival times by sedimentation, but it may also have to do with the detailed microphysical processes that give way to the creation of the different drop sizes (List and McFarquhar 1990a). On the other hand, for the period in which simultaneous multipeak behavior persists, the conditions seem to duplicate the theoretical ones for equilibrium distributions All these observations support the predictions by List and McFarquhar (1990b).

4. SUMMARY AND CONCLUSIONS

Raindrop size distributions were measured at the ground in Mexico City, making use of two, in-motion, optical array spectrometer probes. The data were analyzed both as single precipitation events and as time-series. The results indicate that a Marshall-Palmer exponential form describes the data reasonably well and that the drop size distributions show a multipeak behavior. The observational data support several predictions stated by numerical models with detailed microphysics.

Further research is planned to consider the larger data set available, including the analysis of drop spectra obtained with the OAP-2D-C. This will help to better discriminate between the most probable peaks and to explore the existence of the maximum predicted by the smaller sizes. It will be interesting to compare the distributions obtained in both mobile and fixed fashions. Finally, it is expected that this research will improve our understanding of the microphysical processes that take place during the different stages of evolution of precipitation formation under the very specific conditions of high altitude of Mexico City, and to compare the results with those of numerical, dynamical simulations.

Acknowledgments.

The authors appreciate the continuous technical support provided by Messrs. J. Escalante, R.A. Montañez, A. Rodríguez and V. Zarraluqui.

REFERENCES

Álvarez P., J.M., and J. Torreblanca B., 1992: *Desarrollo de un Sistema de Software para Interpretación y Análisis de Datos de Espectrómetros de Gotas.* Tesis de Licenciatura. Departamento de Computación, Facultad de Ingeniería, Universidad Nacional Autónoma de México. 150 pp.

García-García, F., and R.A. Montañez, 1992: Ground-based raindrop spectra observations for the analysis of summer convective showers in Mexico City. *Proc. 11th Int. Conf. Clouds Precip.* IAMAP/ICCP, **1**, 151-153.

Knollenberg, R.G., 1981: Techniques for probing cloud microstructure. *Clouds: Their Formation, Optical Properties, and Effects*, P.V. Hobbs and A. Deepak (Eds.), Academic Press, 15-91.

List, R., and G.M. McFarquhar, 1990a: The role of breakup and coalescence in the three-peak equilibrium distribution of raindrops. *J. Atmos. Sci.*, **47**, 2274-2292.

List, R., and G.M. McFarquhar, 1990b: The evolution of three-peak raindrop size distributions in one-dimensional shaft models. Part I: Single-pulse rain. *J. Atmos. Sci.*, **47**, 2996-3006.

List, R., N.R. Donaldson and R.E. Stewart, 1987: Temporal evolution of drop spectra to collisional equilibrium in steady and pulsating rain. *J. Atmos. Sci.*, **44**, 362-372.

Marshall, J.S., and W. McK. Palmer, 1948: The distribution of raindrops with size. *J. Meteor.*, **5**, 165-166.

Montañez, R.A., and F. García-García, 1992: Instrumented vehicle for ground-based microphysical observations. *Proc. 11th Int. Conf. Clouds Precip.* IAMAP/ICCP, **2**, 972-974.

Pruppacher, H.R., and J.D. Klett, 1997: *Microphysics of Clouds and Precipitation, Second Edition.* Kluwer Academic Publishers, Dordrecht, 954 pp.

Steiner, M., and A. Waldvogel, 1987: Peaks in raindrop size distributions. *J. Atmos. Sci.*, **44**, 3127-3133.

Valdez, M.P., and K.C. Young, 1985: Number fluxes in equilibrium raindrop populations: A Markov chain analysis. *J. Atmos. Sci.*, **42**, 1024-1036.

EMPIRICAL ANALYSIS OF THE CONTINUUM LIMIT IN RAIN

S. Lovejoy[1], N. Desaulniers-Soucy[1], M. Lilley[1], D. Schertzer[2]

[1]McGill University, Dept. of Physics, 3600 University St., Montréal, Québec, Canada, H3A 2T8
[2]L. M. M./C.N.R.S., BP 162, Université Pierre et Marie Curie, 4 Place Jussieu F-75252 Paris Cedex 05, France

1. INTRODUCTION:

Clouds and precipitation are composed of particles; however for most purposes it is more convenient to treat them as continuous fields, much in the same way as in standard continuum mechanics we treat molecules collectively, ignoring the particulate nature of bulk matter. The standard continuum hypothesis used in cloud physics (e.g. for modelling drop growth, aggregation or the interpretation of radar reflectivities), is homogeneity. This has many implications including the prediction that in the limit of large enough numbers of particles, that the spatial distribution should be Poissonian and that the drop size statistics should be independent of the measuring volumes. In spite of its importance, neither the approach to the continuum limit nor its nature has ever been systematically empirically investigated in precipitation. This is true in spite of the fact that due to turbulence, homogeneity may never be reached until small scales of the order of the typical interparticle distance. On the contrary, turbulent cascade models predict a multifractal continuum and analysis of aircraft data of liquid water in clouds ([*Lovejoy and Schertzer*, 1995], [*Davis et al.*, 1996]) show that the statistics are indeed multifractal down to at least 10m; lidar measurements in rain ([*Lovejoy and Schertzer*, 1991]) take this down to 3m. This report is a summary of work presented in the phD. thesis [*Desaulniers-Soucy*, 1999].

A brief overview of the classical and scaling continuum hypotheses is based on the following schematic:

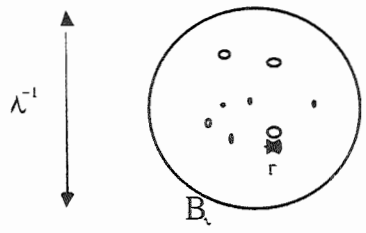

Fig. 1: Particles inside a sphere B_λ of radius λ^{-1}.
Let $n_\lambda(r)$ be the particle number density in a region of size λ^{-1} N_λ=total number of particles. The classical continuum hypothesis states that $n_\lambda(r)$ is independent of λ over a large range (density = uniform) so that:

$$N_\lambda \propto vol(B_\lambda)$$

This implies (via the central limit theorem) that the probability of total liquid water V_λ is:

$$P(V_\lambda) \propto e^{\frac{\langle N_\lambda \rangle}{2\langle v^2 \rangle}\left(\frac{V_\lambda}{\langle N_\lambda \rangle}-\langle V_\lambda \rangle\right)^2} \underset{\langle N_\lambda \rangle \to \infty}{\to} \delta\left(V_\lambda - \langle V_\lambda \rangle\right)$$

where $\langle v^2 \rangle$ is the variance of the drop volume. In contrast, the scaling continuum hypothesis predicts:

$$P(V_\lambda) = \lambda^{-c(\gamma)}; \quad \gamma = \frac{\log\left(V_\lambda / \langle V_\lambda \rangle\right)}{\log \lambda}$$

valid for large enough number of particles, $c(\gamma)$ is the codimension function. Equivalently, in terms of the statistical moments of the liquid water in a region diameter λ^{-1}, we have:

$$\langle V_\lambda^q \rangle = \lambda^{K(q)}$$

where the moment scaling exponent K(q) is related to $c(\gamma)$ by a Legendre transform. For various technical reasons, the moments are a bit easier to analyse; we will therefore attempt to estimate them from the data described in the following.

2. DESCIPTION OF THE EXPERIMENTAL SET-UP

At McGill, we have used various techniques, including chemically coated blotting paper [*Lovejoy and Schertzer*, 1990], and lidar [*Lovejoy and Schertzer*, 1991], in an effort to determine the size and position of hydrometeors. It was finally concluded that the optimum method for reconstructing both the size and location of hydrometeors in three dimensional space was stereophotography using three large format (Hasselblad) cameras and high powered Xenon flash lamps. The set-up is shown schematically in fig. 2. Each of the flashlamps emits 1kJ of energy in about 30μs, thus effectively freezing the drops. The experimental region is about $10m^3$.

Over a period of 2 years, over 450 image triplets were acquired in various rain and snow conditions. Once

the pictures were taken, the negatives were scanned on a special high resolution scientific scanner (approximately 10,000X10,000 pixels/negative) with 14 bit dynamic range (so as to accurately determine subtle variations in the photographic density. There were then two basic problems in the analysis. The first was to unambiguously identify the same drop in at least two of the three images. This involved the accurate alignment of the images correcting for very small discrepancies in the relative rotations and rescalings which occurred during the developing and scanning process; this involved a 27 parameter optimization problem and was possible using 50 or so large reference drops. This matching was done on the basis of proximity, the shape and intensity of the drop images and involved a sophisticated pattern matching, sorting and intercomparison algorithm. Of the six triplets fully analyzed so far (during two different storms), over 90% of the drops were identified. Each of these triplets (from rains of roughly 10mm/hr) had 20,000 – 50,000 identified drops, of which 10,000 -20,000 were in the central test region with adequate lighting and sharp enough focus.

Once the identification was accomplished, the positions were estimated to within roughly 1mm in the cross view direction and to 2cm in depth. The second

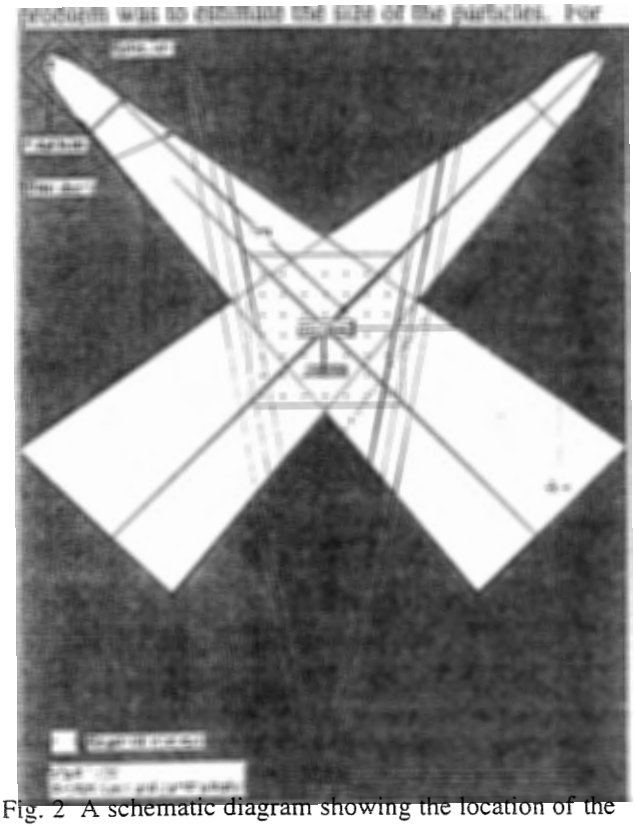

Fig. 2 A schematic diagram showing the location of the flashlamps and three coplanar cameras.

the large drops (roughly >1mm diameter), this was usually possible by talking advantage of the fact that for these, images of the two flash lamps were usually discernable (the drops act as lens) and for these, it was found that the distance in the image between brightness maxima was a highly accurate method of diameter determination. For the smaller drops, the size was estimated by correlating the albedo with the size using the fact that the location was known; this required that the illumination field be well estimated and the phase function for light scattering from spherical drops. The brightness field was estimated by using the large "double peaked" drops as reference "candles" and using them to map out the illumination field. The overall result was that drops with diameters in the range 0.2mm-1mm had diameters estimated to within ±50%. Drops smaller than 0.2mm were below the available resolution.

3. ANALYSIS

Extensive analyses of the triplets is given in [*Desaulniers-Soucy*, 1999], including probability distributions, and energy spectra. The main difficulty was that in spite of the seemingly large number of hydrometeors that were identified, the maximum range of scales which might display continuum statistics of any kind was less than an order of magnitude. This is due to the requirement that many drops be in a volume before convergence to the continuum is possible; the mean interparticle distance among the set of detected raindrops was about 10cm, and the largest sphere fully contained within the experimental region had a diameter of only about 2m. In order to estimate the statistics of the liquid water, 5000 random locations were chosen within the experimental region. From each, the total

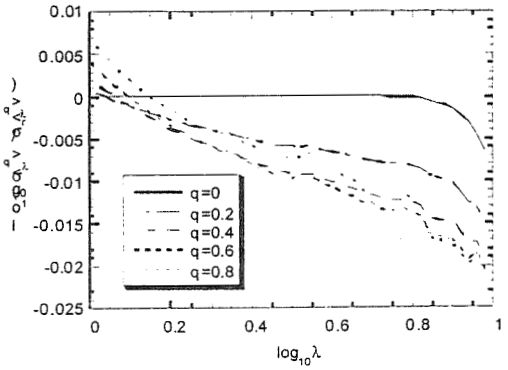

Fig. 3a $\log_{10}\langle V_{\lambda,data}\rangle / \langle V_{\lambda,ran}\rangle$ as a function of sphere size $\log_{10}\lambda$=R/r where R=0.97 is the largest radius, r the actual radius (large spheres on the left, small on the right). $V_{\lambda data}$ is the measured liquid water in a sphere radius r, $V_{\lambda ran}$ is with randomized coordinates.

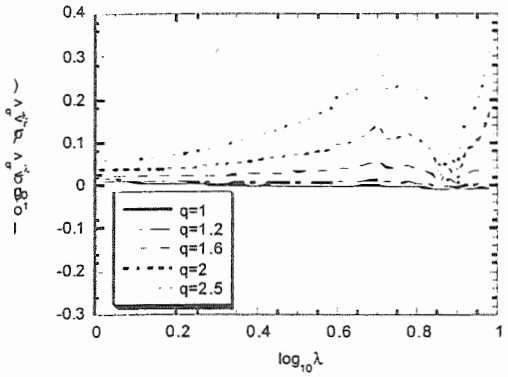

Fig. 3b: Same as 3a but for q>1.

liquid water in spheres of increasing radii were determined. Many of the larger spheres went outside the region; as long as the corresponding fraction was less than 50% of the total sphere volume, the statistics were kept, but were corrected by using the density of the measured part of the sphere. The results were raised to a series of powers q and averaged over all spheres of the same radius. In order to improve the statistics, averages over three triplets from the same rain were performed.

In order to see if the results favored the multifractal continuum hypothesis, the resulting moments were compared with those of the same drops and rains but with uniformly randomized (Poisson) locations (the classical continuum hypothesis). Fig. 3a, b show the results for various moments. Resimulating the randomized data shows that the relatively linear trends (implying scaling) are real and not spurious. Starting with q=0 (the number density) we can also note that the scaling continuum limit is apparently reached at scales which increase (λ decreases) as q increases. For q= 0, it occurs at about 15cm radius, for q=2, it is already about 25cm. This is to be expected since the number of drops needed to get accurate higher order moments is large. Note a slight inflection in the linear trends when λ is nearly 1; this is probably an artifact of the imperfect algorithm for correcting the large spheres which go outside the experimental region.

Although these slopes seem small the K(q) obtained is nearly the same as that estimated for liquid water from aircraft [*Lovejoy and Schertzer*, 1995]. In both cases, the statistics were found to be near the universal multifractal form:

$$K(q) = \frac{C_1}{\alpha - 1}\left(q^{\alpha} - q\right)$$

With α near 2 (log-normal statistics), and $C_1 \approx 0.05$. With another scanner, and another seven triplets from another rain, a value $C_1 \approx 0.045$ was obtained showing that the result is robust.

4. CONCLUSIONS:

We have presented analyses of three of the 450 triplets taken during an experiment designed to empirically investigate the continuum limit in rain – both the convergence to the limit and the type of limit (homogeneous /classical) or scaling (multifractal). Although the statistics are over a small range of scales, small but systematic scaling departures from the classical limit were observed, and were characterized by exponents of the same order as those found in the wind field e.g. [*Schmitt et al.*, 1992] (C_1=0.076, α=1.5). If further analysis of other triplets corroborates these findings, then systematic scale dependent corrections will be necessary to all radar ([*Lovejoy et al.*, 1996]) andr rain gage measurements ([*Tessier et al.*, 1993]).

5. REFERENCES:

Davis, A., A. Marshak, W. Wiscombe, and R. Cahalan, Scale Invariance of liquid water distributions in Marine Stratocumulus. Part I: Spectral properties and stationarity issues., *J. Atmos. Sci.*, *53*, 1538-1558, 1996.

Desaulniers-Soucy, N., Empirical Test of the multifractal continuum limit in rain, phD thesis, McGill, Montreal, 1999.

Lovejoy, S., M. Duncan, and D. Schertzer, The scalar multifractal radar observer's problem, *J. Geophys. Res.*, *31D*, 26,479-26,492, 1996.

Lovejoy, S., and D. Schertzer, Fractals, rain drops and resolution dependence of rain measurements, *Journal of Applied Meteorology*, *29*, 1167-1170, 1990.

Lovejoy, S., and D. Schertzer, Multifractal analysis techniques and the rain and clouds fields from 10^{-3} to 10^{6}m, in *Non-linear variability in geophysics: Scaling and Fractals*, edited by D. Schertzer, and S. Lovejoy, pp. 111-144, Kluwer, 1991.

Lovejoy, S., and D. Schertzer, How bright is the coast of Brittany?, in *Fractals in Geoscience and Remote Sensing*, edited by G. Wilkinson, pp. 102-151, Office for Official Publications of the European Communities, Luxembourg, 1995.

Schmitt, F., D. Lavallée, D. Schertzer, and S. Lovejoy, Empirical Determination of Universal Multifractal Exponents in Turbulent Velocity Fields, *Physical Review Letter*, *68*, 305-308, 1992.

Tessier, Y., S. Lovejoy, and D. Schertzer, Universal Multifractals: theory and observations for rain and clouds, *Journal of Applied Meteorology*, *32* (2), 223-250, 1993.

Corresponding author's address: Shaun Lovejoy, Physics dept., 3600 University St., Montreal, Que. H3A 2T8, Canada; E-Mail: lovejoy@physics.mcgill.ca.

MESOSCALE SIMULATIONS OF HEAVY PRECIPITATION EVENTS IN SOUTHERN CALIFORNIA DURING THE 1997-98 EL NIÑO

Charles Jones [1], David Danielson [2], David Gomberg [2] and Brent Bower [2]

[1]Institute for Computational Earth System Science (ICESS),
University of California, Santa Barbara, CA 93106-3060
[2] National Weather Service, Los Angeles/Oxnard Office, Oxnard, CA 93030

1. INTRODUCTION

The terrain of southern and central California is one of extremes. For example, Los Angeles County alone is arguably the most terrain diverse county in the Nation. It encompasses the islands of Santa Catalina and San Clemente–20 to 50 miles offshore in the Pacific Ocean, the broad expanses of the L.A. Basin and the San Fernando Valley, the Santa Monica Mountains that reach over 3000 feet, the San Gabriel Mountains that exceed 10,000 feet, and the dry and sparsely populated Antelope Valley of the Mojave Desert.

Like the terrain, the weather of central and southern California is one of extremes. The complex coastal topography, for example, can induce mesoscale circulations responsible for heavy precipitation. For instance, some of the heaviest 24-hour precipitation totals ever reported in the entire state of California were recorded in southern California. Goodridge (1992) reports 26.12" of rain fell in just 24 hours in the San Gabriel Mountains of Los Angeles County in 1943. In fact, the U.S. Department of Commerce (1998) estimates the maximum probable 24-hour precipitation is 38" for the mountains in Santa Barbara County, 42" for Ventura County and over 48" for the mountain ranges of Los Angeles and San Bernardino Counties. Current operational models from the National Centers for Environmental Prediction (NCEP) are of insufficient resolution (30 to 40 km or greater) to accurately capture both the complex weather/terrain interactions and the intense gradients of temperature and humidity which are so important for providing daily, critical forecasts for the millions of central and southern Californians.

In a collaborative project between the University of California Santa Barbara (UCSB) and the National Weather Service Los Angeles/Oxnard Office, high-resolution daily real-time forecasts are produced with the Pennsylvania State University/National Center for Atmospheric Research (PSU/NCAR) Mesoscale Model 5 Version 3 (MM5-V3). The objective of this presentation is to investigate the skill of MM5 forecasts during heavy precipitation situations in southern California.

Corresponding author's address: Dr. Charles Jones, ICESS – University of California, Santa Barbara, CA 93106-3060 Mail: cjones@icess.ucsb.edu

2. MESOSCALE MODEL EXPERIMENTS

The El Nino of 1997-1998 was the strongest El Nino/Southern Oscillation (ENSO) event in the instrumental record. It caused significant climatic anomalies worldwide especially over North America. Four major storms during that winter season produced individually over 10 inches of rain in Southern California–along with extensive flooding. We specifically analyze the events of 5-6 December, 2-3 February, 6-7 February and 23-24 February 1998.

The MM5-V3 model is a non-hydrostatic mesoscale model in sigma vertical coordinates. The model configuration includes three nested grids of 36 km, 12 km and 4 km and 23 sigma vertical levels. Figure 1 shows the nested domain configuration, while Fig. 2 shows the topography resolution for the finest nested grid. The current UCSB real-time model configuration uses Schultz (1995) cloud microphysics scheme, which account for ice and graupel/hail processes. Additionally, Kain-Fritsch cumulus parameterization in the outermost two grids (36 km and 12 km) and simple radiational cooling in the atmosphere are used. The planetary boundary layer scheme from the Medium Range Forecast (MRF) global model from NCEP is used for all three grids. The model configuration also includes a five-layer soil model. Additional details on model physics and parameterizations are discussed in Grell et al (1993).

Initial and boundary conditions were created by interpolation from global fields from National Centers for Environmental Prediction/National Center for Atmospheric Research (NCEP/NCAR) reanalysis. For each of the four extreme precipitation cases (5-6 Dec, 2-3 Feb, 6-7 Feb and 23-24 Feb), the model was initialized at 00Z and integrated for 48 hours. Model outputs for the finest grid (4 km) were saved every hour.

3. DISCUSSION

This presentation will discuss the skill of the high resolution MM5-V3 mesoscale model in producing quantitative precipitation estimates during the extreme events during the El Niño of 1997-98. Hourly precipitation totals from weather stations distributed throughout southern California are used for comparison with MM5-V3 estimates of precipitation. Mean biases, root-mean square errors and correlation coefficients were computed between observed and simulated precipitation estimates.

ACKNOWLEDGEMENTS

This project is partially supported by the Cooperative Program for Operational Meteorology, Education and Training (COMET Outreach) (S00-19119). Partial support is also acknowledged to the National Science Foundation (ATM-9712855), the Water Resources Center-Centers for Water and Wildland Resources, University of California, Riverside (W-905). Data support from Scientific Computing Division (SCD) and the Mesoscale and Microscale Meteorology (MMM) Division from the National Center for Atmospheric Research (NCAR, which is sponsored by the National Science Foundation) is greatly appreciated.

REFERENCES

Goodridge, J.D., 1992, A Study of 1000 Year Storms in California, *Ninth Annual PACLIM Workshop*, Pacific Grove, CA, 67 pp.

Grell, G., A., J. Dudhia, and D. R. Stauffer, 1993: A description of the fifth generation PENN STATE/NCAR MESOSCALE MODEL (MM5), NCAR/TN-398+IA, National Center for Atmospheric Research, Boulder, Co, 116pp.

Kalnay, E., and Coauthors, 1996: The NCEP/NCAR 40-year reanalysis project. *Bull Amer. Meteor. Soc.*, **77**, 437-471.

U.S. Department of Commerce, 1998: Probable Maximum Precipitation for California, *Hydrometeorological Report No. 58*, National Oceanographic and Atmospheric Administration, and US Department of the Army, Corps of Engineers.

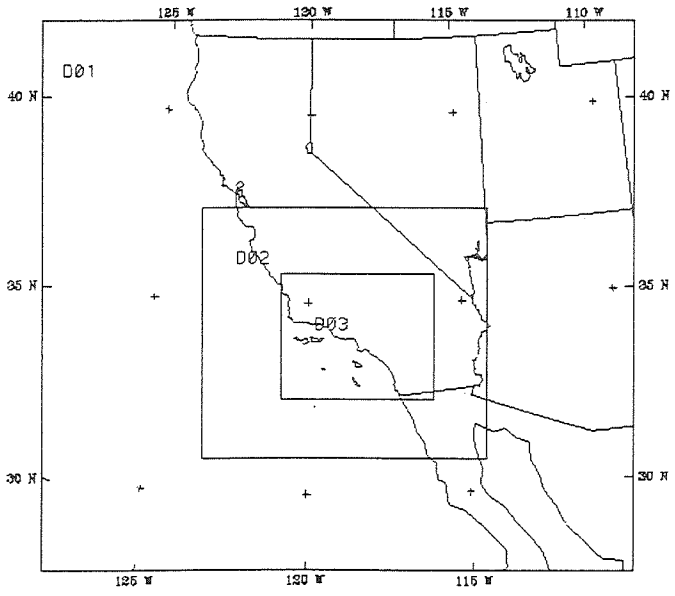

Figure 1. Nested configuration used by the Model (MM5-V3). The grid resolutions for the domains are: 36, 12 and 4 km.

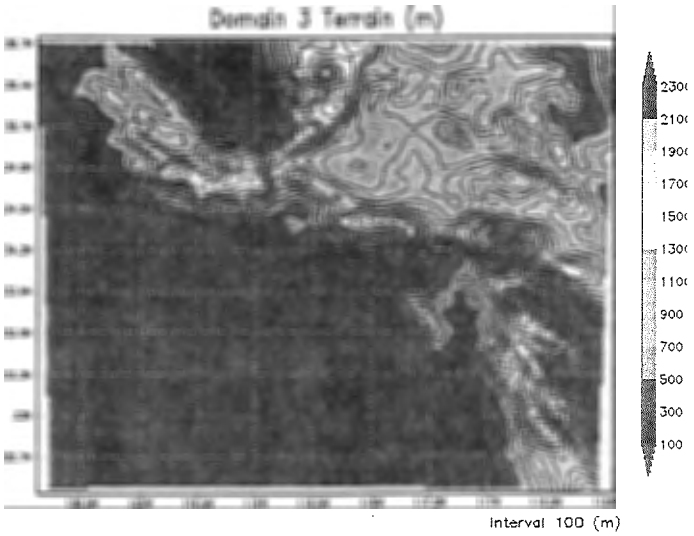

Figure 2. Topography resolution for the finest MM5-V3 domain.

SIMULATION RESEARCH ON HEAVY RAINSTORM IN HUBEI PROVINCE IN 1998 WITH 3-D CLOUD MODEL

Li Dun[1] Xu Guirong Fang Chunhua

(Meteorology Research Institute of Hubei Province)

ABSTRACT

Based on the research on macro-and-meso-scale synoptic process, a numerical simulation in meso-and-micro-scale was performed with 3-D quasi-elastic meso-and-micro-scale atmosphere cloud model, which simulated the heavy rainstorm process happened in Wuhan region of Hubei province on July 12,1998, in order to research the internal structure of strong precipitus, macrophysical and microphysical process and precipitation mechanism in the period. The research showed that 3-D cloud model could fairly reappearance the actual development of southern strong precipitus, and the simulation results were consistent with the radar and surface observations. The simulation content was more prolific and meticulous, which redeemed the shortage of mesoscale model.

INTRODUCTION

A heavy flood happened again in the whole Changjiang River area in 1998 since 1954.The main reason is that the precipitation was exceptional heavy and strong. Precipitation of a day reached several hundred millimeters in most areas of Hubei province. The interaction of various scales synoptic system resulted the heavy rainstorm process. Research results on the process are various, depending on methods and scales, such as synoptic scale, subsynoptic scale and meso- -scale . In this article, a 3-D numerical simulation on the "98" heavy rainstorm process in Wuhan region was performed in meso- -scale, in order to disclose the internal physical mechanism and various physical conditions favorable to the "98" heavy rainstorm in viewpoint of cloud scale. The 3-D cloud model can fairly fully perform various atmospheric phenomenon happened in the scale, and it is very important for realizing and researching most generation and development of natural process, such as, from isolated cumulus to strong storm.

BRIEF INTRODUCTION OF MODEL

The model adopted 3-D quasi-elastic atmosphere model, and the sound wave speed was replaced by the Cs which less than it in the continuity equation. It is showed as follow:

$$\frac{\partial p}{\partial t} + C_s^2\left(\frac{\partial \rho u}{\partial x} + \frac{\partial \rho v}{\partial y} + \frac{\partial \rho w}{\partial z}\right) = 0$$

In the equation, p is atmospheric pressure, is air density. Here, fetching in the quasi-elastic supposing reduced the calculation quantity and increased the calculational stability. In calculation, not only the integral time step was lengthened but also the equation was still kept as a whole. And six water elements, which are vapor, cloud water, ice crystal, dew, hail and rainwater, and the transforms among them were considered in the microphysical process in the model.

There are 34 grid points in west-east direction, 30 grid points in north-south direction and 25 grid points in vertical direction. The horizontal grid length, X= Y=1.2km the vertical grid length, Z=0.7km the long time step, T=10 seconds the short time step, t=1 second. The method of thermodynamic bubble lifting is adopted in the model starting. To guarantee the calculational stability, the

[1] Corresponding author's address: Li Dun, Meteorology Research Institute of Hubei Province, Wuhan, Hubei, 430074, China;
E-Mail: Ld99@public.wh.hb.cn

lateral boundary must let the wave motion in simulation area pass out as much as possible to reduce the reflection to least. For that, we adopt radiation boundary condition. The base boundary condition is $W|_{Z=0}=0$, the normal advection of other variables are calculate with upstream scheme when streaming out and the normal derivative is zero when streaming in. Finite-difference method is adopted to resolve the system of equations. Variables locate in staggered grid scheme. Basal difference analogue is leapfrog scheme.

3-D NUMERICAL SIMULATION ON THE HEAVY RAINSTORM

We processed a ninety-minute-long 3-D simulation on the heavy rainstorm process in Wuhan region on July 21,1998, and the maximal simulant precipitation was 65mm/hour, which was contiguous with the maximal actual precipitation 88.4mm/hour. The simulant cloud base height was 2.1km, cloud top height was 9.8km, and the maximal simulant ascending velocity in the cloud was 12m/s, which were consistent with the radar observations.

Figure 1 is the vertical cross-section diagram of QC (quantity of cloud water) along north-south direction in 30 minutes.

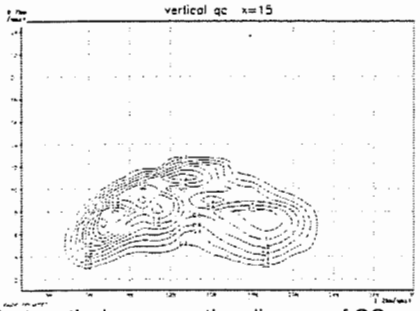

Fig.1 vertical cross-section diagram of QC

And figure 2 is the vertical cross-section diagram of QR (quantity of rainwater) along north-south direction in 30 minutes.

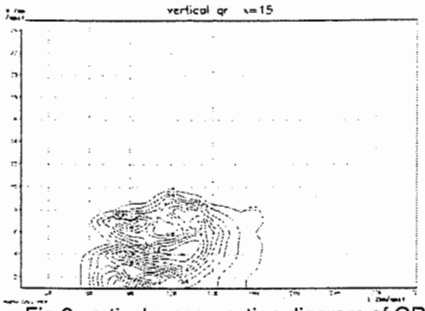

Fig.2 vertical cross-section diagram of QR

Figure 3 is the vertical cross-section diagram of streamline field in cloud along north-south direction in 30 minutes,

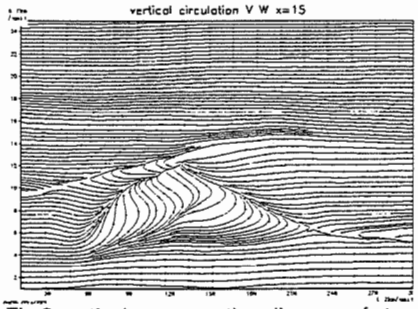

Fig.3 vertical cross-section diagram of streamline field along north-south direction

and figure 4 is along west-east direction.

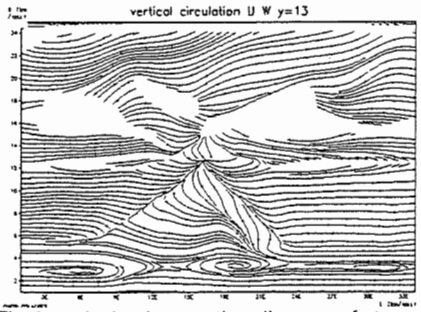

Fig.4 vertical cross-section diagram of streamline field along west-east direction

From the figures, we can see that the diameter of cloud object has reached above 20km in the middle period of development. The analytic result shows that the cloud object developed mainly along north-south direction, with a "vault" in the middle-below part of it, which was worked by the oblique ascending flow. Rainwater was generated above 6.3km height or so, which was higher, so there was an enough height before raindrop reaching the ground and enough time to generate a bigger one. With sufficient vapor, although the generated big raindrops were shattered in various extents, the concentration of big raindrops didn't decrease still. The transform and collection

between cloud water and rainwater contributed chiefly to it, and the other microphysical process did briefly. The cross-section diagrams of streamline field show that the wind blew mainly along southeast direction below 3km height, and along west above 3km height. Near the condensation level, the strong shear formed. The continuous shear provided sufficient vapor, which was favorable for the heavy rainstorm. The simulation researches in other days were similar. The simulation researches showed: the distributing of various particles in cloud had their characters, and the concentrations of various particles in cloud were relatively higher in the mass, especially the raindrop's diameter and quantity density were bigger and higher than those in general precipitations, which caused bigger precipitation intensity, and it was also one character of the heavy rainstorm.

BRIEF SUMMARY

1. 3-D cloud model provided the results approximately close to the actual observations and "reappearanced" the formation and development of isolated cloud object in the "98" heavy rainstorm better and described the fairly detailed internal structure of heavy rainstorm.

2. In the "98" heavy rainstorm in Wuhan region, the transform and collection between cloud water and rainwater were more important than the other microphysical process.

3. Continuous surface vapor providing was one of the main reasons resulted the heavy rainstorm.

4. The cloud layer depth in the heavy rainstorm process had no more noticeable advantage than in the other general precipitation process.

5. The higher concentration of big raindrops is one of important reasons caused the heavy rainstorm in short time.

6. 3-D quasi-elastic model can satisfy the precision request of meso-and-micro-scale atmosphere model at present.

REFERENCES

1.Hu Zhijin, Zhou Guangyuan: *Atmospheric Non-static Equilibrium Model and Elastic Trade-off,* China Science, B, 1991(5).

2.Wang Qian, Hu Zhijin: *3-D Elastic Atmospheric Model and Simulation of Observed Strong Storm,* Meteorological Science, 1990, 48(1).

3.Wu Cuihong, Yang Hongping, Wang Yufa: *Quantitated Featrues of Cloud-Rain for "98.7" Extremely Torrential Rain in the East Hubei,* Torrential Rain·Disaster, 1991.1.

MICROPHYSICAL CHARACTERISTICS OF CUMULONIMBUS RAINFALL IN THE REGION OF HARBIN

Li Dashan[1], Zhang Xinling[2], Fan Ling[1], Zhang Yunfeng[1], and Li Zihua[2]

[1]Heilongjiang Office of Weather Modification, Harbin 150001, P.R.China
[2]Nanjing Institute of Meteorology, Nanjing 21004, P.R.China

1. INTRODUCTION

Observation of the rainfall events was undertaken in the region of Harbin and its surroundings by means of a GBPP-100 raindrop collector in May – July, 1999, with the data presented in Table 1. This article concerns the study of the microphysical parameters of the rainfall from cumulonimbus clouds with special reference to the fluctuation of the microphysical parameters.

The Model GBPP-100 is an optical array probe (OAP) which has been configured for characterizing rainfall on the ground. In their study with an absorbent-paper technique and the GBPP-100 raindrop collector, Liu and You (1994) discovered that the number of GBPP-100 raindrops are bigger (hence greater rainfall intensity) on the side of large drops, which is due to its overestimating the contribution of large raindrops that comes from their deformation and superimposition. As regards the relationship between the size and deformation, Pruppacher and Pitter (Wang and Li, 1989) showed that with b/a denoting the ratio of the major to minor radius of a deformed drop and a^0 the radius of a corresponding spherical drop, they found

$$b/a = 1.05 - 0.131a_0 \quad (1)$$

and from

$$(4/3)\pi a^2 b = (4/3)\pi a_0^3 \quad (2)$$

they got

$$a = (1.05 - 0.131a_0)^{-1/3} a_0 \quad (3)$$

with which we correct the deformation error of drops, >3 mm across.

As a rule, the GBPP-100 samples continuously for a 10 to 30 seconds, depending on rainfall intensity. Analysis was done in connection with satellite imagery, radar, *in situ* clouds and weather observations. Cumulonimbus precipitation was dealt with from the comprehensive analysis of these data.

Table 1. Sampling date, period, interval and number.

date	Period	Interval	samples
99.05.27	7:52~8:59	10s	394
99.06.07	15:04~16:03	10s	335
99.06.23	7:06~8:18	10s	418
99.06.24	17:05~18:20	10s	321
99.06.26	23:05~24:00	10s	236
99.07.07	15:58~16:28	30s or 10s	48

2. GENERAL CHARACTERISTICS OF MICROPHYSICAL PARAMETERS OF THE PRECIPITATION

Table 2 presents averaged microphysical parameters, of which N and I are the spatial density of rain drops and precipitation intensity, respectively; D1, D2 and D3 are the mean diameter and those of *rms* and root of mean cube of raindrops, respectively; D_{max} the maximal diameter; D_0 the volumetric median diameter. As seen from the table, the intensity and density of raindrops are very big, differing greatly from one event to another of the precipitation in such a way that the minimal (maximal) intensity arrives at 4.43 (27.14) mm h^{-1} and the minimum (maximum) density at 10^3 (10^4) drops per m^3; large drop sizes average ~3 mm, with individual sizes attaining 9 mm in diameter and, however, the mean diameter is around 0.3 mm, averaging 0.32 mm. Though the density of drops is quite great, the drops, <1 mm across, constitute, on average, 98% and contribute 10% to rainfall intensity in sharp contrast to the corresponding figures of 2 and 90% for raindrops, >1 mm across, implying that the high rainfall intensity is related largely to large drops; the high density of cumulonimbus raindrops comes dominantly from the contribution of numerous droplets; 0.14~0.34 mm in

Table 2. Averaged microphysical parameters

date	N (m^{-3})	I (mm/h)	Q (g/m^3)	D1 (mm)	D2 (mm)	D3 (mm)	D_{max} (mm)	D_0 (mm)
5.27	2950	5.91	0.30	0.31	0.43	0.59	2.58	1.54
6.07	1814	4.47	0.19	0.31	0.41	0.58	2.73	2.16
6.23	3652	7.92	0.39	0.30	0.41	0.56	2.71	1.53
6.24	5766	16.6	0.72	0.31	0.42	0.59	3.21	1.62
6.26	11900	26.50	1.09	0.39	0.47	0.61	3.02	2.00
7.07	24788	27.14	1.10	0.22	0.26	0.36	2.72	1.62
7.24	2181	4.43	0.22	0.33	0.42	0.54	1.74	1.31
Average	5015	10.96	0.50	0.32	0.42	0.57	2.75	1.71

Table 3. Fitted values of the parameters for the M-P and Γ distributions in the study of 1999 seven events of cumulonimbus rainfall.

	M-P distribution		Γ distribution		
date	n_0	λ	n_0	λ	μ
99.05.27	979.5	1.8	359.0	0.9	-2.3
99.06.07	196.2	1.3	90.2	0.3	-2.8
99.06.23	1442.3	1.9	633.1	1.1	-1.9
99.06.24	1946.7	1.7	1096.3	1.1	-1.5
99.06.26	1145.8	1.3	704.2	0.5	-2.4
99.07.07	328.5	1.1	133.6	0.01	-3.2
99.07.24	889.7	1.9	235.1	0.8	-2.3
average	1106.2	1.7	527.1	0.8	-2.3

diameter, form 88% of total density. And the great number of such tiny droplets have a very small mean diameter.

3. MEAN RAINDROP SIZE DISTRIBUTION

In the context of the mean size distribution of raindrops from cumulonimbus observed in 1999, we made the least square fit of it to the M-P and Γ distributions, obtaining the fitted values of the parameters given in Table 3. Fig.1 depicts the mean distribution over 7 events of cumulonimbus rainfall and their fitted spectra, showing a multi-modal form in the large drop band of the mean distribution. The cumulonimbus drops do not obey the exponential law and the M-P distribution deviates remarkably from the measured distribution, especially in the bands of rain drops, <0.34 and >3 mm across but the Γ distribution gives the results close to the measured at the two bands, findings similar to Chen et al. (1998).

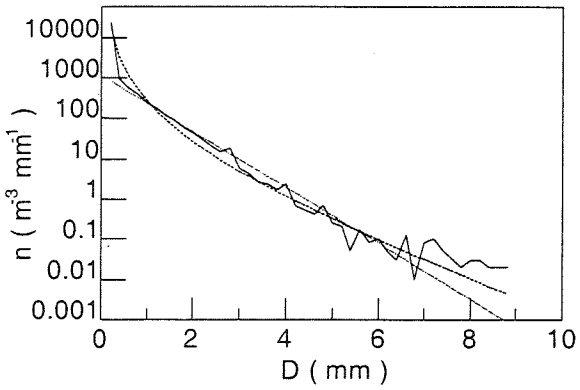

Fig.1. Mean size distribution (solid line) and fitted distribution using the FM-P (dotted) and • schemes (dashed) for raindrops from the rainfall events.

It follows that Γ distribution is a most effective scheme for describing the size distribution of cumulonimbus precipitation.

Fig.2 depicts that in the initial and terminal intervals the size ranges are narrow with few or no big drops emerging and the density of tiny drops is not high whereas in the prime period the size range is wide, showing a multi-modal structure and much greater density of tiny drops compared to the other stages.

4. FLUCTUATION FEATURES OF MICROPHYSICAL PARAMETERS OF THE RAINFALL EVENTS

As shown in Fig.3, the parameters fluctuate dramatically in the first half an hour; remarkable fluctuation happens to I, N and D_{max} more than tenfold; the instantaneous maximal (minimal) rainfall intensity is above 200 (below 1) mm h-1; the maximum (minimum) density is > 10^5 (<10^1) raindrops m^{-3}, differing by 4 orders of magnitude and bigger 1~2 orders than the density of raindrops from the Meiyu front (Xu et al., 1987); particularly, D_{max} undergoes marked change,

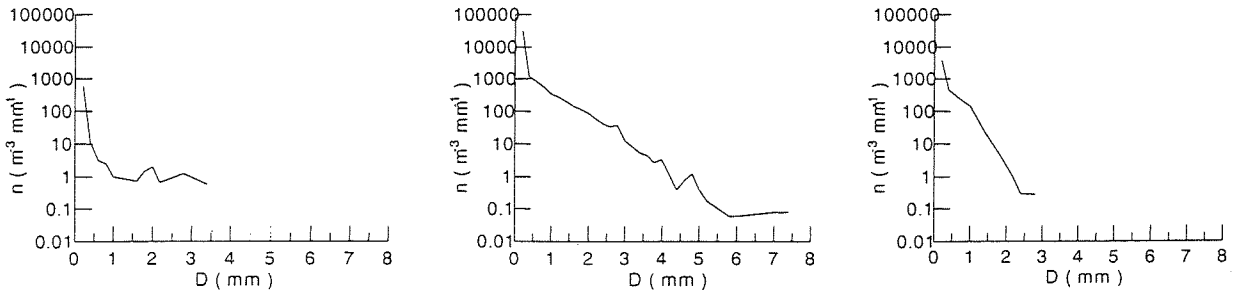

Fig.2. Size distribution at the initial (a), prime (b) and terminal period (c) of precipitation on June 24, 1999.

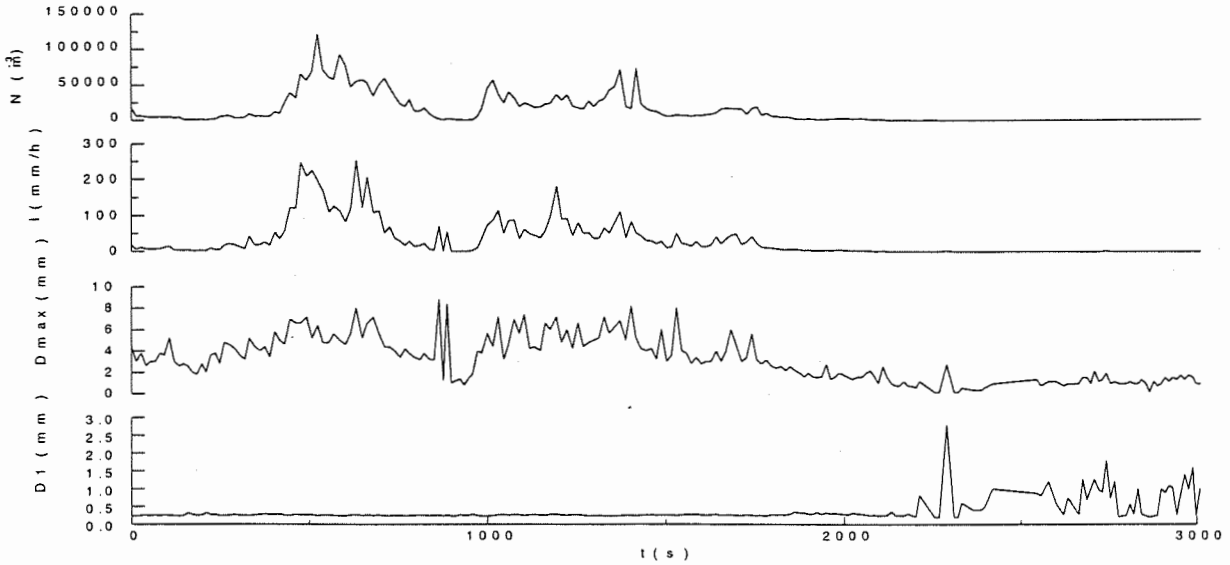

Fig.3. Evolution of microphysical parameters.

peaking at 8 mm in diameter several times and minimizing at as short as 1 mm.

To quantitatively investigate the fluctuations of the study rainfall we made approach to the fluctuation of the microphysical parameters •(x) (see Zhan et al., 1965) by setting

$$\delta(x) = \sigma(x) / \mu(x) \qquad (4)$$

where•(x) denotes the mean square deviation of a parameter and •(x) the expectation value. In calculation, we allowed for the fluctuations arising from the limited sample size and we give here the actual fluctuations.

Results show that N and I fluctuate significantly, maximizing at ~200%, averaging >100%. The greater the rainfall intensity and the grain density, the bigger•(N) and•(I), implying that the fluctuations of N and I bear a relation to their values. The fluctuation of the mean diameter is small (<11~89%), averaging 39%.

To examine the effect of raindrop size on the fluctuation, we separated the diameters into 4 groups, i.e., 0~1, 1~2, 2~3 and >3 mm, to find the fluctuation of the grain density and rainfall intensity for each of them, where we see that the group of drops, 1~2 mm across, fluctuate little but those beyond the scope vary greatly. Large drops come mainly from coalescence growth and many big drops change to a great number of tiny drops by breaking up from collision and deformation in their descent to ground. The above findings indicate that the fluctuation of coalescence in the cumulonimbus leads to the increased fluctuation in the number of large and tiny raindrops at ground.

5. CONCLUSIONS

From the foregoing analysis, we come the conclusions as follows.

High is the cumulonimbus precipitation intensity, to which drops, 1~3 mm across, make >60% contribution. The density is between 10^3 to 10^4 drops m^{-3} of which tiny drops, >1 mm in diameter (the mean being on the order of 0.3 mm) constitute ~98%.

Γ distribution fitted size spectrum is found close to the measured and thus superior to the M-P given distribution.

The related microphysical parameters fluctuate greatly. The variation is >100%, on average, in the intensity and density and between 11 to 89% for the mean diameter of drops.

The fluctuation is great for the drops, <1 and >3 mm across, suggesting that the remarkable variation in the coalescence growth and breaking up in descent.

REFERENCE

Liu Yanggang and You Laiguang, 1994:Error analysis of GBPP probe, *Atmos. Res.*, 34, 379~387.

Wang Pengfei and Li Zhihua, 1989: Microphysical Cloud Physics, China Meteorological Press, pp.401-410 (in Chinese).

Chen Baojun et al., 1998: Modeling of size distribution of drops from precipitating cloud of third class, *Acta Meteoro. Sinica,* 56(4), 506-512 (in Chinese).

Xu Shaozu et al., 1987: Microphysical features of Meiyu frontal precipitation in the region of Nanjing, *J. Nanjing Univ.*, 23(3), 175-185 (in Chinese).

Zhan Lishan et al., 1965: Preliminary study of the fluctuation in the microphysical parameters observed in clouds over the Taishan and Nanyue Mountains, in Research on Microphysics of Rainfall, China Scientific press, Beijing, pp.30-40 (in Chinese).

DYNAMICS, CLOUD PHYSICS, AND PRECIPITATION

Q. Jiang *and R. B. Smith
Yale University, New Haven, Connecticut

1. INTRODUCTION

One of the most important influences of mountain barriers on human life is their enhancement of precipitation. Although an extensive literature can be found on this subject, surprisingly, even some very fundamental questions are still left unanswered. For example, given mountain shapes and heights, what percentage of moisture can be carried over a mountain barrier? Can moisture flow around peaks and make its way downstream? This study is motivated by such "simple" questions. Understanding these issues are not only critical to meteorology, but also important to other areas, such as regional climatology, hydrology, agriculture, ecology, and even geology. The complexity of this problem lies in the fact that it involves nonlinear interactions among flow dynamics, thermodynamics, and cloud physics.

Particularly, we try to answer the following questions:

1. How does moisture influence flow splitting and gravity wavebreaking?

2. Can a moist non-dimensional mountain height serve as a useful measure of flow splitting, wave breaking and general flow non-linearity?

3. How does flow stagnation influence orographic precipitation amount and spatial distribution?

4. What microphysical processes are most critical to orographic precipitation? How sensitive are they to control parameters?

5. Can one define a "microphysical time scale" for comparison with the dynamical time scale ($\tau_a = a/U$) as diagnosing precipitation location, release rate, spill-over, and by-pass?

The outline of this paper is as the follows. In section 2, the numerical setup is described. Moist mountain flow stagnation is discussed in section 3. The influence of stagnation on precipitation is discussed in section 4. The relevant time scales and their control of precipitation are examined in section 5. A summary is given in section 6.

2. NUMERICAL SETUP

A mesoscale model, "Advanced regional prediction system (ARPS)", is used for this study. ARPS is a 3-Dimensional non-hydrostatic model developed at the Center for Analysis and Prediction of Storms (CAPS) . The full nonlinear (momentum, continuity, and thermodynamic) equations are solved on finite grid points. The terrain following vertical coordinate is further stretched to allow higher vertical resolution in the lower troposphere. ARPS has both 2nd and 4th order advection options, leapfrog time differencing and split-explicit treatment of gravity and acoustic modes, and vertically implicit options (Xue et al, 1995).

The model domain is 103×103 with 33 vertical layers. The spatial resolutions are $DX = DY = 2000m$ and $DZ = 500m$. The vertical coordinate is stretched using a cubic function with $\delta Z_{min} = 100m$ between the lowest two layers. Zero gradient boundary condition is applied to all lateral boundaries. Solid wall condition is applied to the lower bottom and the top with Rayleigh damping near the top. At H=12000m, the terrain-following coordinate transformation becomes flat.

The model is initialized using a single sounding. The temperature profile is specified with a constant "N_d", the buoyancy frequency for dry air, and a constant surface temperature "T_o". For this study, we choose a stable atmosphere, i.e. $N_d^2 > 0$, and a fixed surface temperature, $T_o = 270K$, as a representation of typical mid-latitude wintertime situations.

The moisture is specified with a constant relative humidity in conjection with the temperature profile. The upstream wind is unsheared and unidirectional with a constant wind speed "U_o". The physics options include Lin's ice cloud physics (Lin et al, 1983) and 1.5 order TKE closure scheme. The topography is a 3-D ideal Gaussian type mountain specified by

$$h(x,y) = h_m exp\left(-(x^2+y^2)/a^2\right) \qquad (1)$$

where h_m is the maximum mountain height and "a" is the half mountain width.

3. MOIST FLOW STAGNATION

As stratified flow passes a high isolated 3-D mountain, a number of nonlinear phenomena can occur in the vicinity of the mountain, such as flow blocking, flow splitting, flow reverse, and wave breaking. Generally, this type of nonlinearity can be well

*Corresponding author address: Qingfang Jiang, Yale University, Dept. of Geology, New Haven, CT06520-8109; email: qingfang.jiang@yale.edu

described by the non-dimensional mountain height (i.e. $M = Nh_m/U_0$). As $M << 1$, flow is linear, and as $M > 1$, nonlinear dynamics becomes important. In addition to 'M', two useful indices are the non-dimensional velocity minimas aloft over lee slope (see Fig 1) and on the windward slope. U_A/U_0 indicates flow deceleration due to nonlinear wave steepening, and $U_A/U_o = 0$ suggests gravity wave overturning and the onset of gravity wave-breaking. U_B/U_o indicates flow deceleration related to mountain blocking effect, and for a 3-D topography, $U_B/U_o = 0$ suggests center streamline splitting.

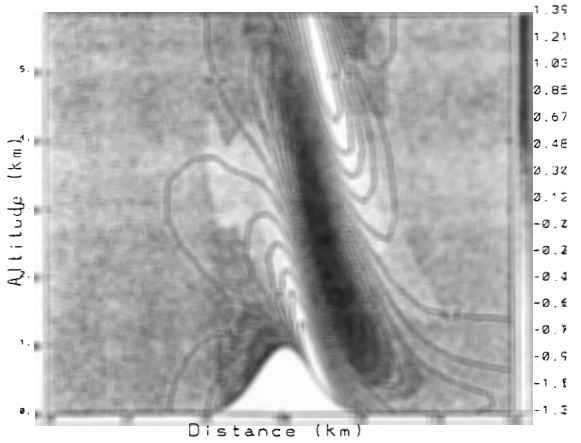

Fig 1. Velocity along the vertical section through the center streamline. U component is contoured and W component is shaded

With moisture, clouds can form both in front of the mountain due to mountain lifting and over the leeside due to gravity wave lifting. For our case, the clouds refer to cloud water (Fig 2), and cloud ice. On the other hand, clouds and snow may be sublimated or re-evaporated wherever air flow descended. With cloud/snow formation and re-evaporation, the latent heating/cooling may modify flow solutions, as well as the universal curves discovered by Smith and Gronas (1993).

Based on four groups of runs to steady state, four pairs of flow deceleration curves were constructed, which correspond to different wind speed, mountain width, and static stability. The results can be summarized as the following:

- The addition of moisture delays flow stagnation at both windward side and leeside. Its influence on windward stagnation is much more significant, however.
- The flow deceleration curves are insensitive to both mountain width and wind-speed, and quite sensitive to static stability.
- The moisture effect can be understood using the concept of moist stability. Two separate moist "N" can be derived for windward flow blocking and leeside wave steepening, however, which suggested that there is no a single moist nondimensional mountain height to indicate the general nonlinearity of moist mountain flow.
- The moisture effect can be understood using linear theory with specified heating/cooling sources (similar to Smith and Lin, 1982).

The details of the derivation, formulation, and discuss can be found in Jiang and Smith (2000).

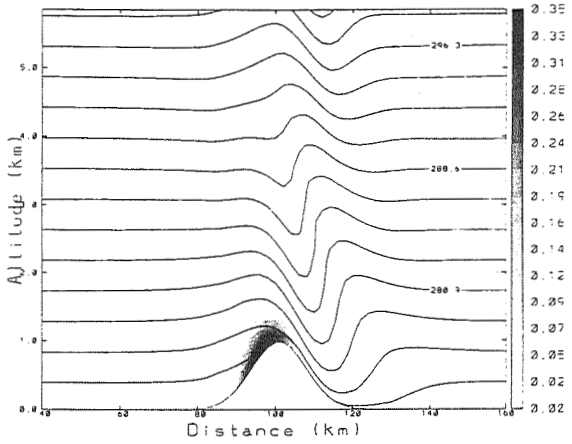

Fig 2. Potential temperature (contoured) and cloud water mixing ratio (shaded) along the same vertical section as in Fig 1.

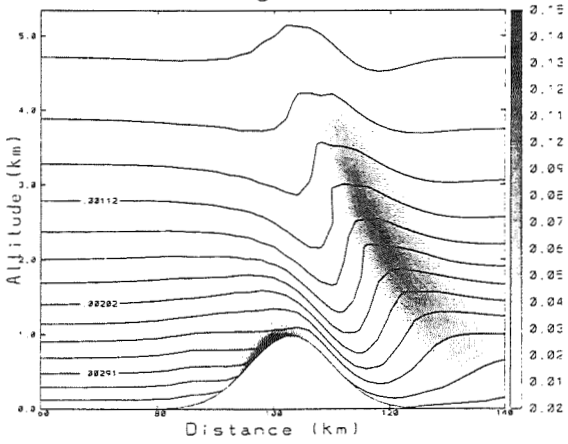

Fig 3. Water vapor mixing ratio (contoured) and snow mixing ratio (shaded) along the same vertical section as in Figs 1 and 2.

4. DYNAMICS AND PRECIPITATION

How does flow stagnation influence the distribution and amount of orographic precipitation? To answer this question, we carried out dozens of runs with varied combination of parameters. In addition, we developed a "slab" model as a reference (Jiang and Smith, 2000). The slab model suggests that the precipitation rate is proportional to windspeed

and mountain height. Some results are displayed in Fig 4. The ARPS model predictions of the precipitation maxima follows the "slab" model prediction quite well for low mountains. However, as the mountain becomes higher, less flow climb over the mountain peak, and therefore, the increase of precipitation maxima with mountain height was slow down. The same tendency can be observed in all four groups of runs with varied control parameters. At some mountain heights, which are roughly the same critical mountain heights for flow splitting, precipitation rate maxima started to decrease or stopped to increase with increasing mountain height.

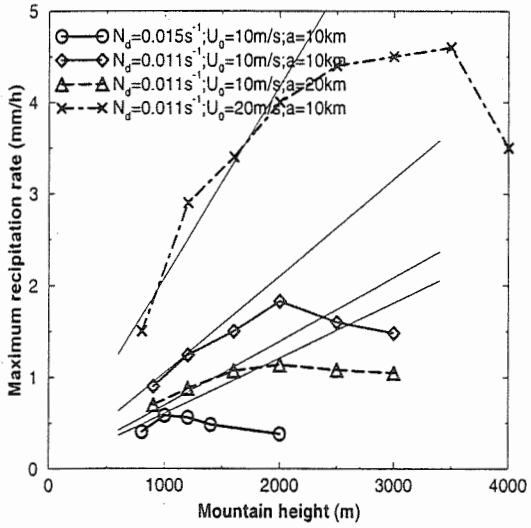

Fig 4. The plot of local precipitation rate maxima (mm/h) versus mountain height (m). Four groups of runs and their corresponding "slab" model results are plotted. Those symbols lying off curves represent a second precipitation rate maxima as double peak structure occurs in the precipitation field.

5. MICROPHYSICS AND PRECIPITATION

Orographic precipitation involves the interactions among flow dynamics, thermodynamics, and microphysics. In this section, we try to examine the effect of dynamics and cloud physics on precipitation features such as release rate and spill-over based on the diagnosis of model predictions. Our motivation is to find answers to the question 4 and 5 listed in the introduction. Here we only give two examples. Readers interested in the details are referred to the full paper Jiang and Smith (2000).

5.1 "Flow chart"

There are six water categories in Lin's cloud scheme, namely, water vapor, cloud water, rain water, cloud ice, snow, and hail (Lin at al, 1983). For our problem, the formation of rain water and hailstone is not important. This allows us to identify the most important process by creating some simple flow charts (Fig 5). The conversion rates between each pair of water species (water vapor (w.v.), cloud water (c.w.), cloud ice (c.i.), and snow) were integrated. Both integrated conversion rated and precipitation rate (integrated over the whole domain) were scaled by the total "loss" of water vapor as 100.

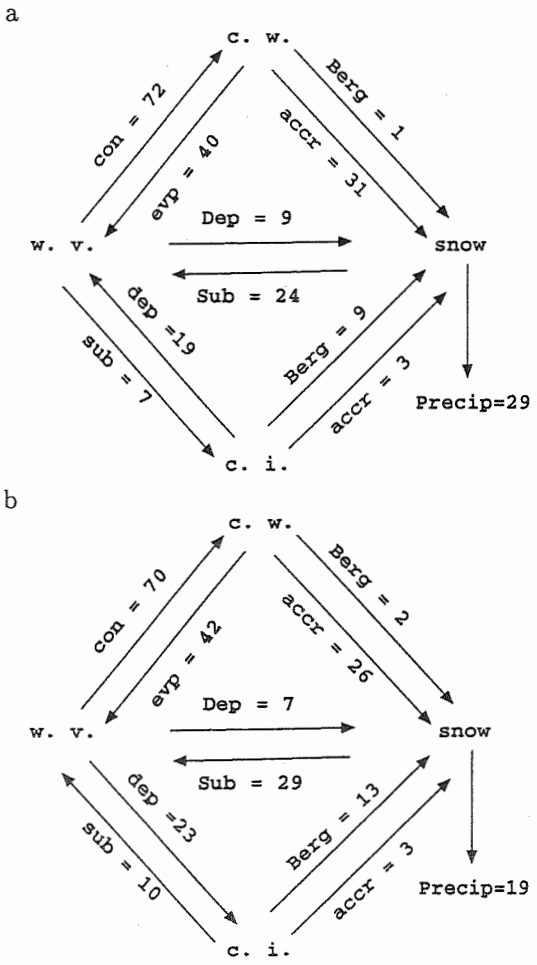

Fig 5. Interaction "flow chart" for a. $N = 0.011s^{-1}, U = 10m/s$; b. $N = 0.011s^{-1}, U = 20m/s$. $h_m = 1000m$ and $a = 10km$. The following processes are included: condensation (con), deposition (dep), evaporation (evp), accretion (accr), Bergeron process (Berg), sublimation (sub), and precipitation (precip).

From Fig 5-a, we can see that for given parameters, the most important path to produce snow is "water vapor → cloud water → snow", which accounts for 60% of total snow generation. The second important path is "water vapor → cloud ice → snow", which accounts about 23%. Direct deposition of water vapor on snow accounts for the rest of

snow production.

From Fig 5-b, with doubled wind-speed, there are the following changes in the "flow chart":

- The first path is reduced, but is still the most important. It produces about 50% of total snow. The second path becomes more important.
- The precipitation rate decreases from 29% to 19% with doubled wind-speed.
- The total rate of snow generation is unchanged (53% for both cases).
- There are 30% snow sublimated with $U_0 = 10m/s$, and about 55% snow sublimated with $U_0 = 20m/s$.

5.2 "Microphysical time scales"

We define the following time scales:

Advection time scale $\tau_a = a/U_0$; Average conversion time scale $\tau_{AB} = \frac{\int \rho_a A dv}{\int \rho_{air} \tau_{AB} dv}$ for conversion from species A to B; Average falling time scale of snow $\tau_f = \hat{h}/\hat{v_s} = \int \rho q_s z dz / \int \rho q_s v_s dz$. where ρ_a is air density, τ_{AB} is the local conversion rate from A to B, q_s is snow mixing ratio, and v_s is the falling speed of snowflakes.

If those time scales are well defined, we should have the following relations:

$$\begin{aligned} Q_s &= Q_v(1-e^{-\tau_a/\tau_{vc}})(1-e^{-\tau_a/\tau_{cs}}) \\ &+ Q_v(1-e^{-\tau_a/\tau_{vi}})(1-e^{-\tau_a/\tau_{is}}) \\ &+ Q_v(1-e^{-\tau_a/\tau_{vs}}) \qquad (2) \\ P &= Q_s(1-e^{-\tau_a/\tau_f}) \qquad (3) \end{aligned}$$

where Q_s and Q_v are total snow and saturated water generation rate, P is precipitation rate, and τ_{vc}, τ_{cs}, τ_{vi}, τ_{is}, and τ_{vs} are time scales for conversion between, saturated water vapor (v), cloud water (c), cloud ice (i), snow (s). Equation (2) and (3) allows us to estimate the release rate (i.e., P/Q_v). Based on numerical runs, for the examples given above, we have the following time scales:

Table 1. Microphysical time scales (seconds)

U_0	τ_{vs}	τ_{vc}	τ_{vi}	τ_{cs}	τ_{is}	τ_a	τ_f
10	14000	75	2700	1700	470	1000	1100
20	7000	80	740	1110	417	500	1340

The estimated release rate from Table 1 and equations (2-3) is around 30% for $U_0 = 10m/s$ and 22% for $U_0 = 20m/s$, which is close to the value derived from the flow charts. Similarly, these time scales can be used to estimate cloud amount, spill-over ratio, and so on (Jiang and Smith, 2000). These results suggest that even complicated microphysical processes may be well described by a few time scales. It should be pointed out, however, none of the conversion time scales in the examples are "universal". They at least change with wind speed. Further discussion can be found in Jiang and Smith (2000).

6. SUMMARY

A number of issues of moist mountain flow dynamics and its influence on orographic cloud formation and precipitation enhancement are addressed in this model based idealized study. The relations between flow dynamics and precipitation, and microphysics and precipitation are examined. Several predictions and arguments (e.g., the influence of flow splitting on amount and distribution of precipitation, the time scales and their control of release rate and spill-over) have been proposed to be tested in the future field observations.

7. ACKNOWLEDGMENTS

This research was supported by NASA/ADRO (NAG5-3972) and by the National Science Foundation, Division of Atmospheric Sciences (ATM-9711076). Dr. Skubis helped with graphics. The simulations were made using the Advanced Regional Prediction (ARPS) developed by the Center for Analysis and Prediction of Storms (CAPS), University of Oklahoma. CAPS is supported by the National Science Foundation and the Federal Aviation Administration. The computing was done on a SGI Origin 200 at Yale Center for Earth Observation.

8. REFERENCE

Jiang, Q. and R. B. Smith, 2000: Moist air flow over 3-D mountains, in preparation.

Lin, Y. L., R. D. Farley, and H. D. Orville, 1983: Bulk parameterization of the snow field in a cloud model. J. Climate and Appl. meteor., 22, 1065-1092.

Smith, R. B., and Y. L. Lin, 1982: The addition of heat to a stratified air stream with application to the dynamics of orographic rain. Quart. J. R. Met. Soc., 108, 353-379

Smith, R. B., and S. Gronas, 1993: Stagnation points and bifurcation in 3-D mountain airflow. Tellus, 45A, 28-43

Xue, M., K. K. Droegemeier, V. Wong, A. Shapiro, and K. Brewster, 1995: ARPS Version 4.0 User's Guide. Center for Analysis and Prediction of Storms, [Available from CAPS, Univ. of Oklahoma, 100 E. Boyd St., Norman OK 73019], 380 pp.

RAINBAND PRECIPITATION AND EVOLUTION IN 2D AND 3D NUMERICAL MODELS WITH DETAILED MICROPHYSICS

Tetsuya Kawano* and Tsutomu Takahashi†

* Department of Earth and Planetary Sciences, Kyushu University, Fukuoka, 812-8581, Japan
† School of International Studies, Obirin University, Machida, Tokyo, 194-0294, Japan

1. INTRODUCTION

Rainbands are the primary producer of precipitation (Houze and Hobbs, 1982). The inclusion of such rainbands in climate model will be one of the important task to increase our understanding of global water circulation. However, those rainbands may react differently on precipitation with different microphysics. The first step for such research will be to identify the precipitation processes by describing the spatial distribution of precipitation particles in rainbands.

Recently, videosonde system which sends images of precipitation particles in clouds was devised and many sondes have been sent into the various rainbands at many different geographical locations. The data have shown the existence of different precipitation mechanisms in rainbands occurring in different geographical locations (Takahashi, 1990; Takahashi and Kuhara, 1993; Takahashi et al. 1995a,b; Takahashi, 1996). Results show that warm rain-freezing processes dominate in rainbands over the Western Pacific, close to the equator, and that graupel are the dominant precipitation particles over a semi-arid area of continental China. Both cool rain and warm rain processes are assumed to be held together in Asian winter monsoon rainbands.

The purpose of the present work is to examine how such different precipitation processes may affect the evolution of rainbands clouds and rain.

2. THE MODEL

2.1 Model formulation

The models are deep two-dimensional (2-D) and three-dimensional (3-D), non-hydrostatic and anelastic. The dynamic and thermodynamic equations used in Takahashi (1988) were rewritten in deep convection. Eddy coefficients are calculated by solving a prognostic eddy diffusion equation (Klemp and Wilhelmson, 1978). The present models are characterized by including detailed microphysics (Takahashi, 1976b). Briefly, cloud nuclei are activated to predetermined cloud droplet sizes when supersaturation over water is calculated. Supersaturation is calculated prognostically as Clark (1973). The employment of his method is essential in deep cloud model to minimize the overestimation of condensation growth rate by the calculation of falsely high supersaturation in usual method. The cloud nuclei which can potentially grow cloud droplets are 300 cm^{-3} in maritime case and 1000 cm^{-3} in continental case. The cloud droplet size distributions calculated at the cloud base in one dimensional cloud nuclei are employed (Takahashi, 1976a). The droplets then grow through both condensation and collection processes.

Above the freezing level, ice nuclei are activated and form pre-determined plate-like ice crystal sizes at the supersaturation over ice. The potentially nucleated ice nuclei is 1 cm^{-3}. Ice crystals are also formed by both secondary ice multiplication (Hallett and Mossop, 1974) and freezing of small particles. The freezing probability of supercooled drops was recently modified (Takahashi and Asuma, 1992). Ice crystals grow in diameter during deposition and increase thickness during riming. When the thickness is equal to the diameter, the particles are treated as graupel. Ice crystals in the least rimed class can grow snowflakes within the same thickness class. Densities of graupel are the function of the median cloud drop volume diameter, particle terminal velocity and environmental temperature. When calculated densities are over 0.7 gcm^{-3}, they are transferred to hail class. Below the freezing level, ice particles melt.

Drops are grouped exponentially by mass into 45 classes. Ice crystals are grouped into 21 diameter classes and five thickness classes, while both graupel (density, 0.3 gcm^{-3}) and hail (density, 0.9 gcm^{-3}) were grouped into 45 classes.

2.2 Environmental and initial conditions and calculations

The vertical thermodynamic structure is conditionally unstable with convective available potential en-

*Corresponding author's address: Tetsuya Kawano, Department of Earth and Planetary Sciences, Kyushu University, 6-10-1, Hakozaki, Higashi-ku, Fukuoka, 812-8581, Japan; E-Mail: kawano@weather.geo.kyushu-u.ac.jp

ergy (CAPE) of $\sim$ 2700 Jkg^{-1} (Fig. 1). As is shown in Fig. 2, low-level wind shear has been used to simulate the long-lived rainbands. In 3-D calculations, also, southerly wind, 0.5 msec^{-1} was given above 2 km in height.

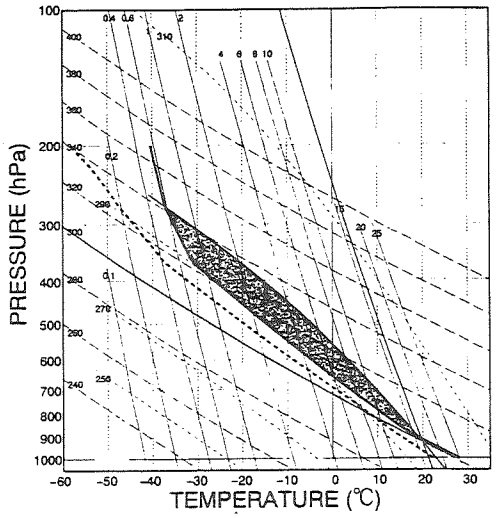

Figure 1 : Model vertical thermodynamic structure. Positive potential energy area is shaded.

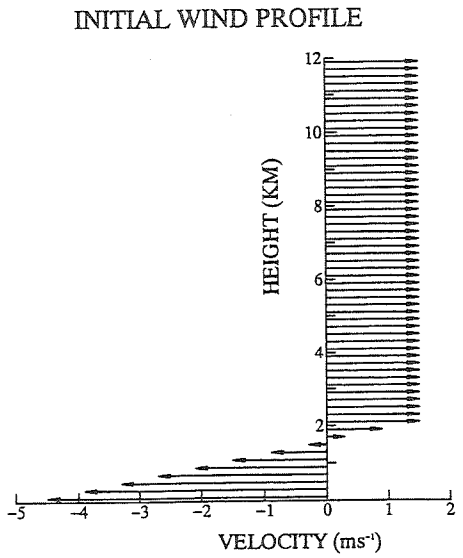

Figure 2 : x-component linear wind profile.

Open boundary conditions are used for all lateral sides of domain. The upper and lower boundaries are taken as rigid with free slip conditions. In 2-D model, the calculation domain is subdivided into 111 $\times$ 61 in the horizontal (x) and vertical (z) and a grid interval of 400 m in x and 200 m in z. In 3-D model, the grid, with a grid length of 400 m in x, 400 m in y and 200 m in z, has dimensions of 56 $\times$ 56 $\times$ 61.

An initial impulse in the form of a buoyant parcel of air has been given to the potential temperature.

2.3 Calculations and rainband types

Five rainband types are selected with microphysical properties differing in kind and number of nuclei. 1) Maritime-Ice (M-I) : representative of Asian monsoon rainbands. Potentially active cloud condensation nuclei (CCN) at 300 cm^{-3} and potentially active ice nuclei at 1 cm^{-3} are equally distributed over all grid spaces. 2) Maritime-Warm (M-W) with 300 cm^{-3} CCN, no ice nuclei, and no drop freezing. 3) Maritime-Frozen (M-F), which may represent equatorial rainbands over the Western Pacific with 300 cm^{-3} CCN and no ice nuclei. In this case it is assumed that all drops larger in diameter than 200 μm and colder than -5°C froze, as has been reported by Takahashi et al. (1995a). Smaller drops remained unfrozen. 4) Continental-Ice (C-I), assumed to represent continental rainbands, with CCN increased to 1000 cm^{-3} and ice nuclei at 1 cm^{-3}. 5) Continental-Warm (C-W) with CCN again at 1000 cm^{-3}, no ice nuclei, and no drop freezing.

3. RESULTS

3.1 2-D results

Both of the patterns of precipitation and the dynamic structures of the clouds differed greatly with different microphysics (Takahashi and Kawano, 1998).

3.1.1 Maritime-Ice

In the very early stage of development the airflow pattern was characterized by an updraft tilted to the rear and a downdraft along the rear boundary of the cloud. At T = 15 min, raindrops had developed through recirculation (Takahashi, 1988). At T = 30 min, a downdraft, formed by the raindrop drag force, produced low-level circulation, enhancing new cell development at the front of the cloud. Ice crystals began to grow at cloud top and the cloud increased in height as additional heat was released during development of the ice phase. Graupel falling from the upper cloud collected supercooled drops transported from the forward cell. Hail formation was thus accelerated and heavy rain fell at the rear (T = 45 min). The heavy rain induced a rear-to-front flow near the surface, triggering new cells at the front that eventu-

ally merged with the main cell (Fig. 3).

It is interesting to note that the low-level circulation, formed through the strong downdraft, expanded forward with time, enhancing development of a cloud cell moving from front to rear. Heavy rain fell from this cell. At T = 90 min, the low-level circulation formed by heavy rain in the center of the rainband had again extended toward the front of the cloud and triggered another cell. Hail formation was enhanced and another rain peak appeared (T = 105 min). These processes were repeated, and in time the rain area extended to the rear of the cloud. By T = 120 min it was raining over 25 km from the front of the cloud rearward. The airflow was characterized by strong front-to-rear, horizontal winds near the freezing level and relatively strong updraft at the rear of the main cloud domain.

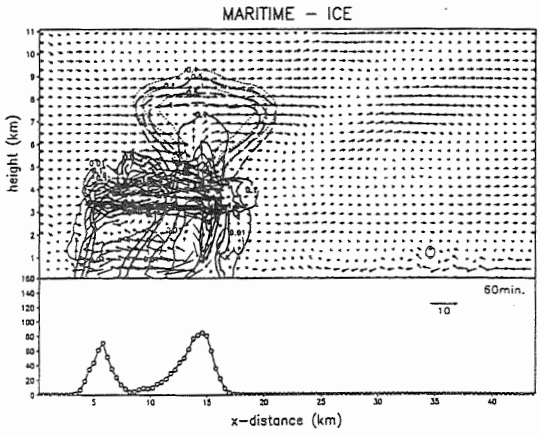

Figure 3 : Maritime-Ice rainband, airflow, mixing ratio and surface rainfall intensity at T=60 min. Thin solid line: cloud droplet mixing ratio (0.01 gkg^{-1}); thick solid line: raindrops; thin dashed lines: ice crystals; thick long-dashed line: graupel; thick short-dashed lines: hail. Mixing ratios at 0.1, 1, 5, 10, 20 gkg^{-1}.

3.1.2 Maritime-Warm

In the early stage, the evolution of rain in this rainband was the same as that in the M-I band, although here the cloud-top height was much lower.

Recirculation of drops enhanced raindrop formation. Major production of rain occurred only at the front of the cloud. In the previous, M-I case, strong, low-level convection formed in association with heavy rain but this did not occur in this case.

3.1.3 Maritime-Frozen

Up to T = 30min, the evolution of rain in this case was similar to that in M-I case, although, in the absence of the latent heat released during ice crystal growth, the cloud top was lower. The rainfall intensity was also weaker without the graupel and hail formation of the M-I case. Because of weak rainfall from the main cell, the low-level circulation remained weak.

3.1.4 Continental-Ice

The drop condensation rate was slower in this case and the consequent weak release of latent heat retarded cloud development. After T = 60min, the rear-most cell began to produce graupel with very rapid hail formation occurring near the freezing level. As was seen in the M-I case, the low-level circulation associated with heavy rain extended forward and enhanced cloud development in the center of cloud band, which also produced heavy rain. In this case, however, the new low-level circulation accelerated cell development at the rear of the band instead of reducing it as had been seen in M-I case.

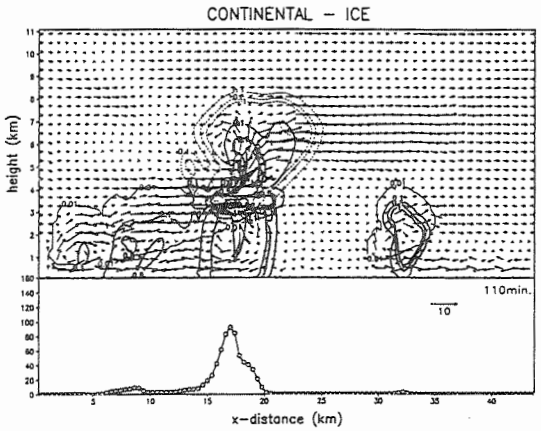

Figure 4 : Continental-Ice rainband at 110 min as Fig. 3.

3.1.5 Continental-Warm

In the early stage, the evolution of rain in this case was similar to that in C-I case. Because of no ice, however, the cloud-top height was shallow at 5 km and no heavy rain was produced.

3.2 3-D results

The evolution of rain through the interaction of front and rear cloud cells was similar to that in 2-D M-I rainband. However, cloud cell development is much three dimensional. Outflow by the rainfall produced two cells to the sides at the front. Drops were fed from those cells to the main rain cell at the rear, producing heavy rainfall (Fig. 5).

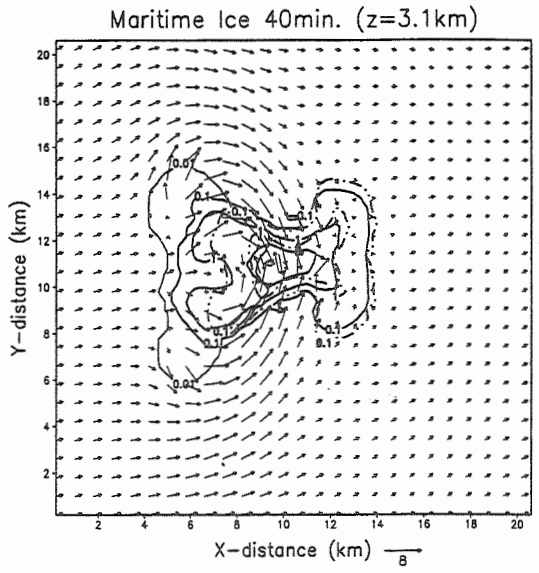

Figure 5 : x-y cross section at z=3.1 km of mixing ratios for 3-D Maritime-Ice rainband at T=40 min. Thin solid line: cloud droplet mixing ratio (0.01 gkg^{-1}); thick solid line: raindrops; thin dashed lines: ice crystals; thick long-dashed line: graupel; thick short-dashed lines: hail. Mixing ratios at 0.1, 1, 5, 10, 20 gkg^{-1}.

4. CONCLUSIONS

Not only rain evolution but cloud cell activity varied greatly depending on the microphysical processes. Clouds without ice nuclei were shallow and most of the precipitation was produced in the forward cell through drop recirculation and the warm rain process. With the addition of the ice phase the additional release of latent heat through drop freezing and ice crystal growth produced active development at the rear of the cloud.

5. REFERENCES

Clark, T. L., 1973 : Numerical modeling of the dynamics and microphysics of warm cumulus convection. *J. Atmos. Sci.*, **30**, 857–878.

Hallett, J., and S. C. Mossop, 1974 : Production of secondary ice particles during the riming process. *Nature*, **249**, 26–28.

Houze, R. A., Jr., and P. V. Hobbs, 1982 : Organization and structure of precipitating cloud systems. *Advances in Geophysics*, Vol. 34, Academic Press. 225–315.

Klemp, J. B., 1987 : Dynamics of tornadic thunderstorms. *Ann. Rev. Fluid Mech.*, **19**, 369–402.

——, and R. B. Wilhelmson, 1978 : The simulation of three dimensional convective storm dynamics. *J. Atmos. Sci.*, **35**, 1070–1096.

Takahashi, T., 1976a : Warm rain, giant nuclei and chemical balance – a numerical model. *J. Atmos. Sci.*, **33**, 269–286.

——, 1976b : Hail in an Axisymmetric Cloud Model. *J. Atmos. Sci.*, **33**, 1579–1601.

——, 1988 : Long-lasting trade-wind rain showers in a three-dimensional model. *J. Atmos. Sci.*, **45**, 3333–3353.

——, 1990 : Near absence of lightning in torrential rainfall producing Micronesian thunderstorms. *Goephys. Res. Lett.*, **17**, 2381–2384.

——, 1996 : Precipitation processes in Asian monsoon rainbands. *Seventh Conf. on Mesoscale Processes*, Reading, United Kingdom, Amer. Meteor. Soc., 339–341.

——, and Y. Asuma, 1992 : Cool rain in a three-dimensional shallow-cloud model. *J. Meteor. Soc. Japan*, **70**, 739–748.

——, and K. Kuhara, 1993 : Precipitation mechanisms of cumulonimbus clouds at Pohnpei, Micronesia. *J. Meteor. Soc. Japan*, **71**, 21–31.

——, and T. Kawano, 1998 : Numerical sensitivity study of rainband precipitation and evolution. *J. Atmos. Sci.*, **55**, 57–87.

——, K. Suzuki, M. Orita, M. Tokuno and Robert de la Mar, 1995a : Videosonde observations of precipitation processes in equatorial cloud clusters. *J. Meteor. Soc. Japan*, **73**, 509–534.

——, K. Suzuki, C. Wang and C. Guo, 1995b : Precipitation mechanisms of cloud systems developed in a semi-arid area of Pingliang, China. *J. Meteor. Soc. Japan*, **73**, 1191–1211.

COUPLING BETWEEN RIMING AND THE DYNAMICS OF PRECIPITATING CLOUDS

M. Wüest[1], W. Schmid[1] and J. Joss[2]

[1]Institute for Atmospheric Science, ETH Zürich, Switzerland
[2]Swiss Meteorological Institute, Locarno-Monti, Switzerland

1 INTRODUCTION

Riming is the collection of supercooled cloud droplets by falling snow crystals. It is the second of the three basic growth processes of snow (deposition of water vapor, riming and aggregation to flakes). Riming is the link between the cloud and the precipitation, therefore, the key process for the mass balance and pollutant scavenging mechanisms.

Riming may be the dominating growth process in convective towers whereas water vapor deposition reigns over stratiform snowfall. However, field experiments demonstrated that riming is - besides vapor deposition - an important particle growth process in widespread precipitation (Mosimann et al. 1994a). During moderately to heavily rimed snowfalls the contribution of accreted cloud water to the snow mass reaches 30% to 60% (Mitchell et al. 1990; Harimaya and Sato 1989). They find the rimed mass fraction to be significantly higher when graupel is observed.

Barthazy et al. (2000) noted that riming is associated with variations of vertical particle motions. This is also known from extreme riming in hailstorms where updrafts are of the order of several meters per second. In stratiform precipitation vertical air motions can be as weak as a few centimeters per second. Caused by the superposition of particle fall speeds and the air motion in observed Doppler velocities from vertical pointing radars (VPR), a quantification of the vertical air motion is a difficult task.

Microphysical field experiments for the AMDOP project (Analysis of Multiple-DOPpler radar data) in winter 1999 with broad instrumental effort, provided the study in hand with data to investigate the coupling between riming and the dynamics of the precipitating cloud.

2 AMDOP FIELD EXPERIMENTS

The year 1999 will remain in our memory, also because of its exceptional snow- and rainfalls in northern Switzerland. The snow masses in February caused fatal avalanches in the Alps. Floods in May led to large damage. In the framework of the project AMDOP a microphysical field campaign near Zürich with broad instrumental effort was carried out. Two scanning C-band radars provided a dual-Doppler configuration for the wind retrieval. Three vertically pointing radars at Ka-, X- and L-band, together with a Joss-Waldvogel distrometer and other meteo instruments, were set up in Birmensdorf at 545 m a.s.l. At a horizontal distance of three kilometers from the VPRs on the top of Üetliberg (870 m a.s.l.) two optical distrometers measured size distributions as well as the fall velocities of precipitation particles. In addition, Formvar replicas were taken to conserve probes of the falling snow.

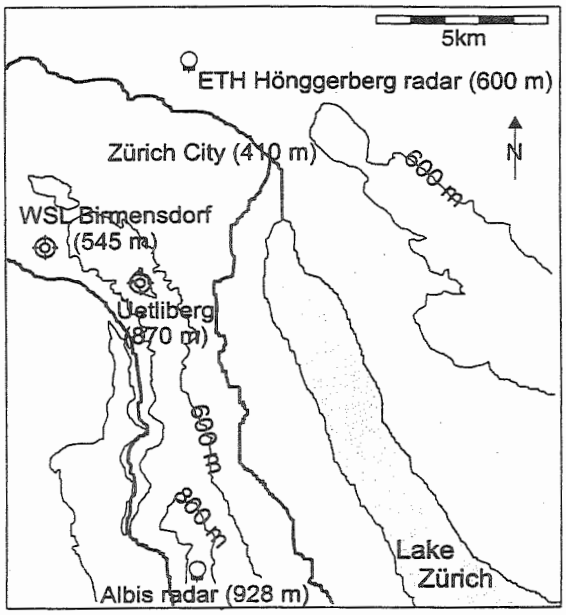

Figure 1: Geographical overview of the AMDOP field experiment setup. Thin lines are contour lines (height a.s.l.), thick lines are rivers.

The field campaign succeeded to catch a series of ten events, some of which with exceptional snow- and/or rainfall. Five snowfall events will provide the data for the following investigations: The 9 February was a very long-lasting and stratiform snowfall. The 28 January started with stratiform character which changed caused by the passage of a frontal system. The 11 January and the 17 February were events with convective cells embedded, the snowfall on the 5 February was inhomogeneous and of convective character. Figure 2 shows an RHI scan (azimuth 219°) of the ETH Hönggerberg radar at 1254 LT on the 17 February 1999 with a wavelike structure having a wavelength of approximately 10 km. The image

Corresponding author's address: Marc A. Wüest, Institute for Atmospheric Science ETH, CH-8093 Zürich, Switzerland;
E-mail: marc.wueest@atmos.umnw.ethz.ch.

indicates weak small-scale structure. The wave, however, may induce significant vertical motion. A similar wave was reported by Wüest (1998), which produced a raindrop spectrum typical for the riming mechanism (small drops, steep spectrum).

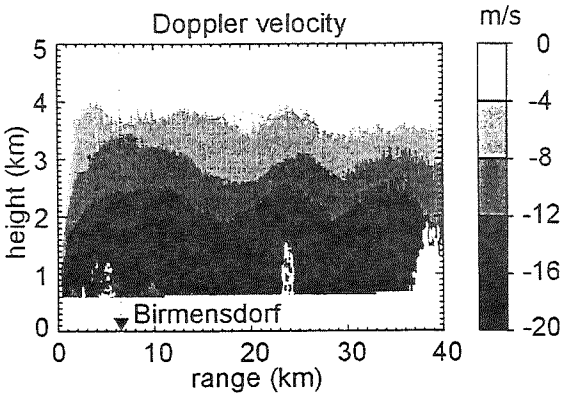

Figure 2: RHI scan of Doppler velocity from the ETH Hönggerberg radar in the direction of Birmensdorf (at 6.6 km range). The image shows a wavelike structure with a wavelength of approximately 10 km. A corresponding wave is also found in the reflectivity RHI.

3 OBSERVATION

In the majority of the events the mean horizontal wind on the lowest couple of kilometers height was roughly west. Figure 1 indicates that in this case Birmensdorf, where the VPRs are located, is upstream of Üetliberg equipped with the microphysical instruments. This is a good setting for comparing the remote sensing data recorded at Birmensdorf with the in-situ measurements on Üetliberg. The overall "stratiform" character of most events provides a certain continuity also when the wind direction is not ideal.

Table 1: The six riming degrees defined by Mosimann (1994a). A detailed description can be found there.

riming degree	description
0	unrimed
1	lightly rimed
2	moderately rimed
3	densely rimed
4	heavily rimed
5	graupel

The riming degree observed during the snowfalls was determined from Formvar probes. All probes of the five snowfall events were considered, except those where melting disallowed for an analysis. The riming degrees were determined using the classification scheme with the six riming levels given in Table 1 (Mosimann 1994a).

A half-hour time period is chosen for each Formvar probe starting at half an hour before the probe was taken. This period together with a height range from 0.87 km a.s.l. (Üetliberg) to 3.0 km a.s.l. determines a window in the HTI (height-time-indicator) of the X-band VPR. Figure 3 shows the riming degree versus the standard deviation of the Doppler velocity in each HTI window. 55 probes are included in the statistics. A couple of things catch our eye: the snow of the 9 February is mostly unrimed or weakly rimed and shows a low variation of the vertical Doppler velocity. The other events vary in snow type and velocity variation showing a trend to find higher riming degrees connected to a stronger variation of the vertical Doppler velocity. The linear fit (and its error range) in Figure 3 and the correlation of 0.78 strengthen this finding.

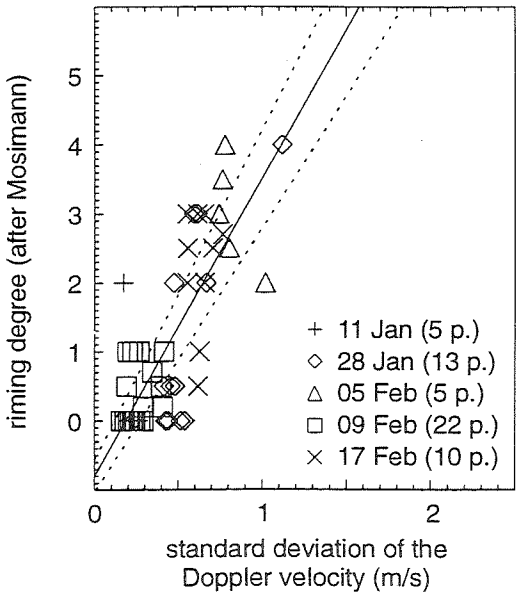

Figure 3: The riming degree of the Formvar probes versus the standard deviation of the Doppler velocity measured by the X-band VPR in a HTI window given in the text. The solid line is a linear fit, the dotted lines its error range. The number of probes per day is given in brackets behind the date.

4 INTERPRETATION

We see two explanations for this correlation of the riming degree and the vertical Doppler velocity. The first is the stronger variation of the terminal fall speed caused by the mass increase and the structure change of rimed crystals (Mosimann 1994b), the second one is the effect of turbulence. Pinsky and Khain (1998) found in theoretical experiments that cloud turbulence leads to increased particle collisions from which an increase in the rates of riming is expected.

4.1 Particles' terminal fall speeds

In order to investigate the effect of the fall speed variation, the data from the optical distrometer on Üetliberg is considered. This instrument measures size distributions by evaluating the shadow cast by the snow particles when falling through a horizontal light beam. If averages over several minutes are considered, we expect the variation of the fall speed of the 25 particle sizes (classes of the instrument) to be a reasonable estimate (assuming spherical particles, the orientation of the snow flakes being lost by averaging). Since the measuring area of the optical distrometer is about 20 cm off the ground and wind-shielded, there is no direct effect of turbulence or wind on the estimated velocity, neither by orientation nor by superposition of vertical air motion.

For each Formvar probe the standard deviation of the fall speed is computed from a spectra average over ten minutes centered on the observation time of the Formvar probe. The standard deviation is calculated from the velocities of all particle size classes. With this measure we expect to estimate the contribution of the fall speed variation to the variation of the Doppler velocity in Figure 3.

Figure 4 plots the riming degree from the Formvar probes versus the standard deviation of the fall speed estimated from the distrometer (thin symbols). For most of the probes, the standard deviation is between 0.3 and 0.5 m/s regardless of the riming degree. The 5 February is an exception showing higher standard deviations up to 0.7 m/s connected to riming degrees larger than two. The correlation between the two data rows is merely 0.3, a distinct trend is not identifiable.

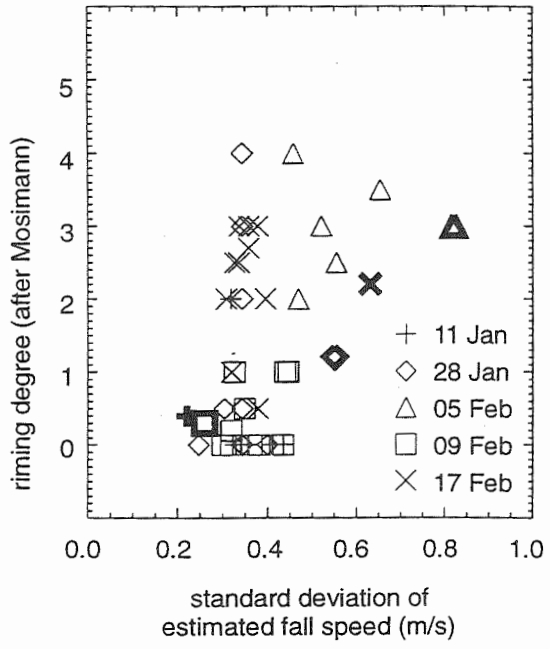

Figure 4: Thin lines: The riming degree from the Formvar probes is plotted versus the standard deviation of the fall velocities estimated from the optical distrometer data located at the same place (Üetliberg). The thick symbols are the averages for each day from Figure 3.

Assuming that we measure on Üetliberg the particles from the cloud parts seen by the VPR and comparing the variation of the fall speed to Figure 3 (thick symbols in Figure 4 are daily averages of Figure 3), we find the variation of the fall speed of the snow particles not completely explaining the trend of higher Doppler spread with higher riming.

4.2 Turbulence effect

Caused by the superposition of the particles' fall speed and the vertical air motion, the Doppler velocity observations from the VPR are difficult to interpret. In order to get more information about the dynamics of the clouds, we include RHI (range-height-indicator) scans from the ETH Hönggerberg radar into the analysis. The RHIs were scanned at an azimuth of 219° thus pointing over the VPR in Birmensdorf (at 6.6 km range). The time series of RHIs allow simulating HTIs over Birmensdorf. These are comparable to the HTIs of the VPR as far as reflectivity is concerned. The Doppler velocity, however, provides the "horizontal" (radial) wind component. This Doppler velocity is – depending on the elevation – only weakly affected by the fall speed of the scatterers.

In order to calculate the turbulence from these data we choose the following procedure. The spectral width observed by the RHI scan over Birmensdorf is a superposition of turbulence and horizontal wind shear within the pulse volume. The size of this pulse volume is roughly $6 \cdot 10^6$ m^3, about 100 times larger than the VPR pulse volume. The horizontal wind shear can alternatively be estimated by averaging the radial gradient from the RHI Doppler velocity at the location (range) of Birmensdorf over the height window (0.87-3.0 km a.s.l., see Section 3). Hence, the difference between the mean spectral width in the window and the horizontal wind shear yields a measure for the turbulence in the volume.

Table 2 and Figure 5 hold the results from this procedure. The quantities were calculated and averaged for characteristic periods (two to five hours long) on the five AMDOP events, respectively. Table 2 indicates negligible influence by the horizontal wind shear in all cases. As a consequence the mean spectral width of the horizontal Doppler velocity provides a measure for the turbulence.

Though there are few data points, the thick symbols in Figure 5 indicate a trend similar to the one in Figure 3 (shown in Figure 5 with thin symbols). The "turbulence" amplitude is - amongst instrumental and dynamic reasons - larger than the one in Figure 3 because the fall speed is not compensating and the volume of the "horizontal" radar is larger.

Table 2: The mean spectral width (msw), the influence of the horizontal wind shear (hws) and the square root of its quadratic difference (diff) calculated from the Hönggerberg RHIs over Birmensdorf as described in the text (v in m/s). RD gives the mean riming degree for the period with the Formvar probes and radar data.

m/s	11 Jan	28 Jan	5 Feb	9 Feb	17 Feb
msw	1.22	1.76	2.25	1.08	1.3
hws	0.03	0.00	-0.20	0.12	-0.16
diff	**1.22**	**1.76**	**2.24**	**1.07**	**1.29**
RD	**1.0**	**2.0**	**3.5**	**0.5**	**2.2**

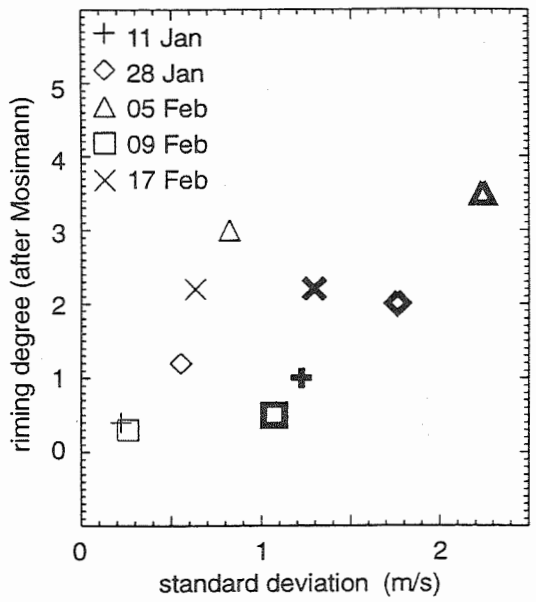

Figure 5: The bold symbols mark the riming degree averaged for the periods in Table 2 versus the "turbulence" width estimated as described in the text. The thin symbols are taken from Figure 3 but averaged for each event. Note that the mean riming degrees are not equal caused by different periods (data availability).

5 CONCLUSIONS

We have shown various ways to judge if (and how) the dynamics in a stratiform winter cloud correlates with the rate of riming of snow crystals. A first approach compared the variation of Doppler velocities from a VPR with the riming degree observed downstream. The good correlation of this relationship needed to be analyzed and explained, because two effects (particles' fall speed and turbulence) could be responsible.

An estimation of the variation of the fall speeds of the snow particles results in relatively low standard deviations. The latter helps to explain the observed variation of the vertical Doppler velocity.

To obtain independent information on the turbulence in the cloud, RHI scans from a horizontally scanning radar are included in the analysis. The influence of the horizontal shear on the spectral width is negligible. Therefore, the spectral width allowed to estimate other influences in the cloud, such as turbulence, without being affected by particles' fall speeds. Again, a good correlation between the riming degree and the turbulence in the cloud upstream is found.

In short, the findings of this study indicate that the rate of riming in stratiform precipitation is related to the turbulence in the cloud. This is in agreement with theoretical studies of Pinsky and Khain (1998) who found an increased collision efficiency caused by turbulence.

6 REFERENCES

Barthazy, E., W. Henrich, A. Waldvogel, and J. Joss, 2000: On the formation of raindrop spectra in widespread rain. Submitted to *J. Atmos. Sci.*

Harimaya, T., 1975: The riming properties of snow crystals. *J. Atmos. Sci.*, **26**, 522-531.

Mitchell, D. L., R. Zhang, and R. L. Pitter, 1990: Mass-dimensional relationships for ice particles and the influence of riming on snowfall rates. *J. Appl. Meteor.*, **29**, 153-163.

Mosimann, L., E. Weingartner, and A. Waldvogel, 1994a: An analysis of accreted drop sizes and mass on rimed snow crystals. *J. Atmos. Sci.*, **51**, 1548-1558.

Mosimann, L., 1994 : Die Bestimmung der Verreifung von Schneekristallen mittels vertikalem Dopplerradar. *Diss. ETH Nr. 10510.*

Pinsky, M.B., and A. P. Khain, 1998: Some effects of cloud turbulence on water-ice and ice-ice collisions. *Atmos. Res.*, **47-48**, 69-86.

Wüest, M., 1998 : Validation of a single-Doppler variational analysis technique with a dual-Doppler wind retrieval method. *Diploma thesis*, ETH Zürich.

EVOLUTION OF DROP SIZE DISTRIBUTION IN TROPICAL RAINFALL: NUMERICAL STUDY

Ryohei Misumi[1], Koyuru Iwanami[1], Masayuki Maki[1], Yoshiaki Sasaki[2], T. D. Keenan[3], Hiroshi Uyeda[4] and Chiharu Takahashi[4]

[1]National Research Institute for Earth Science and Disaster Prevention, Tsukuba, Japan
[2]Akita Prefectural University, Akita, Japan
[3]Bureau of Meteorology Research Centre, Melbourne, Australia
[4]Hokkaido University, Sapporo, Japan

1. INTRODUCTION

Raindrop size distribution (DSD) at the surface reflects precipitation mechanism in the upper level. Waldvogel (1974) found that stratiform and convective rainfall were characterized with large-drop and small-drop spectra, respectively, and that the shift from the former to the latter occurred very quickly even when rainfall intensity had been almost constant. Similar phenomena was observed in Japan by Harimaya and Okazaki (1993) and over the tropical Pacific by Tokay and Short (1996). It is considered that the difference in types of ice particles (graupel or snow) above the melting layer would cause such DSD shift. However, details of the physical process have not been made clear.

Recently Maki et al. (1999) analyzed 15 cases of tropical continental squall lines in Darwin and showed systematic difference in raindrop size spectra between convective and stratiform regions, which is consistent with Waldvogel (1974). In the present study we perform a numerical simulation of a tropical continental squall line using a time-dependent cloud model with explicit ice-phase microphysics. Results are analyzed with particular attention on the DSD characteristics of convective and stratiform precipitation, and discuss the relationship between precipitation mechanism and raindrop spectra.

Corresponding author's address: Ryohei Misumi, National Research Institute for Earth Science and Disaster Prevention, Tsukuba, 305-0006, Japan; Email: misumi@ess.bosai.go.jp

2. MODEL

One-dimensional (vertical coordinate only) and time dependent model is used in this study. The dynamic and thermodynamic frameworks follow Wisner et al. (1972). The micophysical processes are based on the bin method of Reisin et al. (1996) which includes detailed ice-phase microphysics. Hydrometeors are classified into four types; drops, ice crystals, snow particles and graupel, and each type of particles are divided into 34 size categories. The processes included are nucleation of CCN, collision breakup and spontaneous breakup of drops, nucleation of ice nuclei, ice multiplication, drop freezing, diffusion growth/ evaporation of ice and drops, collision coalescence of ice-ice and ice-drops (riming, aggregation, etc.) and melting of ice particles. For simplicity, we assume that one ice particle forms the same mass of one drop in the melting process. All the microphysical processes are solved by the two-moment technique (Reisin et al., 1996). The upper boundary of the model is at the 20 km level, and the grid interval and time step are 200 m and 2.5 s, respectively.

3. CASE STUDY ON 21 JANUARY 1999

3.1 Characteristics of the squall line

We chose the case of a tropical continental squall line on 21 January 1999 in Darwin, which was observed by the network of the Japan Australia Tropical Mesoscale Experiment (JATMEX; Iwanami et al., 1999). The squall line was organized about 20 km southwest to Darwin. At the mature stage, convective and stratiform regions well developed and they were divided by a transition zone where was almost echo

free. The DSD was recorded using RD-69 disdrometer every minute. The raindrop spectra were fitted with the exponential distribution given as

$$N(D)=N_0 exp(-\lambda D), \qquad (1)$$

where $N(D)dD$ is the number density of drops in diameter of D to $D+dD$. Time variation of rainfall intensity and parameters N_0 and λ are shown in Fig.1. Maximum rainfall 66 mmh^{-1} was recorded at 1031 UTC associated with the passage of the convective band. After 1230 UTC weak and continuous rainfall was recorded corresponding to the stratiform region. It is obvious that rainfall from convective band shows larger N_0 and λ although they highly fluctuate. The averaged N_0 and λ of convective rainfall (from 1024 to 1132 UTC) are 6.4×10^4 $mm^{-1}m^{-3}$ and 4.2 mm^{-1}, respectively, while they are 2.5×10^3 $mm^{-1}m^{-3}$ and 2.9 mm^{-1} for the stratiform rainfall (from 1226 to 1518 UTC). These results are not changed if we use a gamma distribution fit.

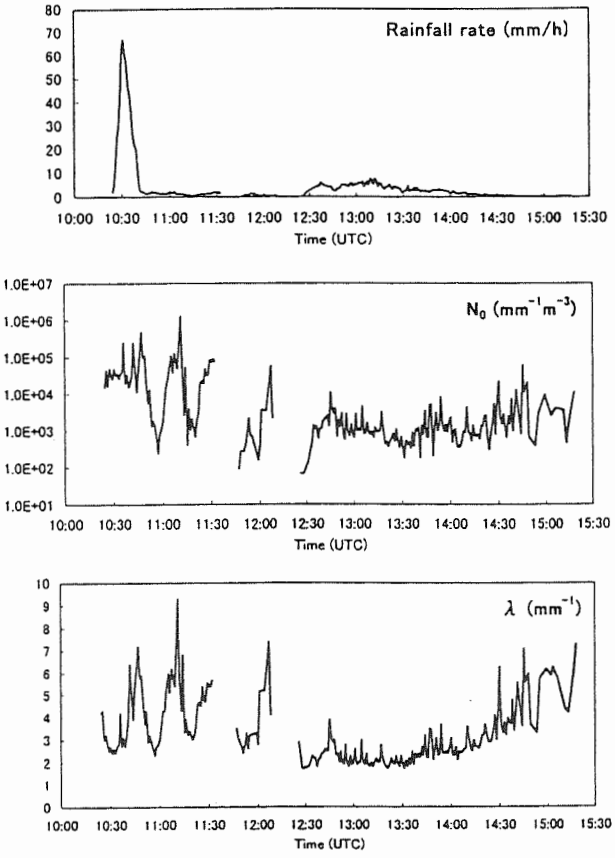

Fig.1 Time variation of rainfall rate, N_0 and λ on 21 January 1999 observed at Darwin.

3.2 Results of the simulation

As the initial condition of the simulation, we used the upper-air observation at Darwin at 1200 UTC. At this moment the convective region of the squall line has already passed over Darwin, but we selected it because there is no sounding data for the pre-storm environment. In order to make a favorable condition for convection, we modified the surface temperature to be 31°C.

The time variation of rainfall rate and parameters N_0 and λ are shown in Fig.2. The maximum rainfall rate of 63 mmh^{-1} is good correspondence to the observation. N_0 shows extremely small value at the beginning of rainfall due to the sorting of drops by the effect of the updraft. N_0 reaches maximum (1.7×10^5 $mm^{-1}m^{-3}$) when the rainfall rate is at the peak. After that N_0 decreases gradually, and it reaches almost steady state after 90min when rainfall rate is still decreasing. λ also shows its maximum at the rainfall peak, then slowly decreases until 90 min and increase again. The large N_0 and λ around the rainfall peak, small and steady N_0 and slow increment of λ in the later stage are well consistent with the observation.

The time height cross section of the hydrometeor contents and DSD parameters are shown in Fig.3. The DSD parameters for ice particles are calculated using equivalent liquid-water diameter. Graupel particles prevail above the 6 km from 20 min to 80 min, while snow particles are dominant after 90 min. Large N_0 and λ are found only where the content of raindorps is very high. It should be noted that both graupel and snow have relatively small N_0 ($\sim 10^3$ $mm^{-1}m^{-3}$) and λ (~ 3 mm^{-1}).

The size spectra of hydeometeors are shown in Fig.4. At 40 min the slope of the fitted lines is gentle above the melting level (8000 m) which indicates large-particle spectra of graupel. However, the lines become steeper in the lower level (4000 m). This suggests a drastic change of DSD below the melting

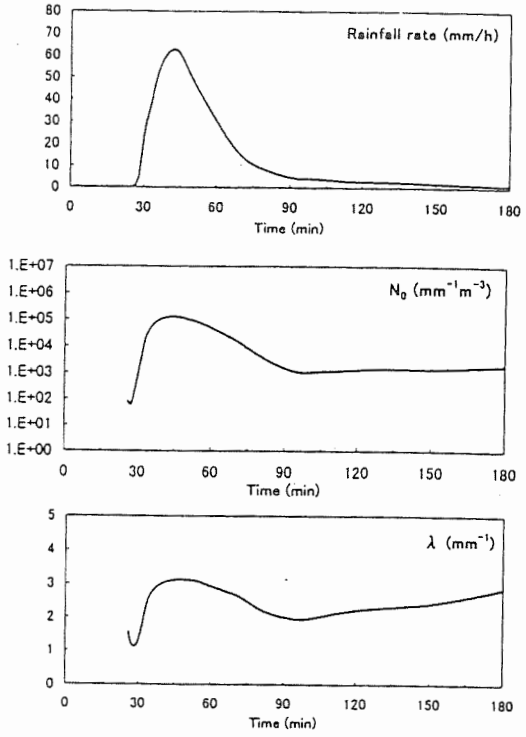

Fig.2 Time variation of simulated rainfall rate, N_0 and λ at the surface.

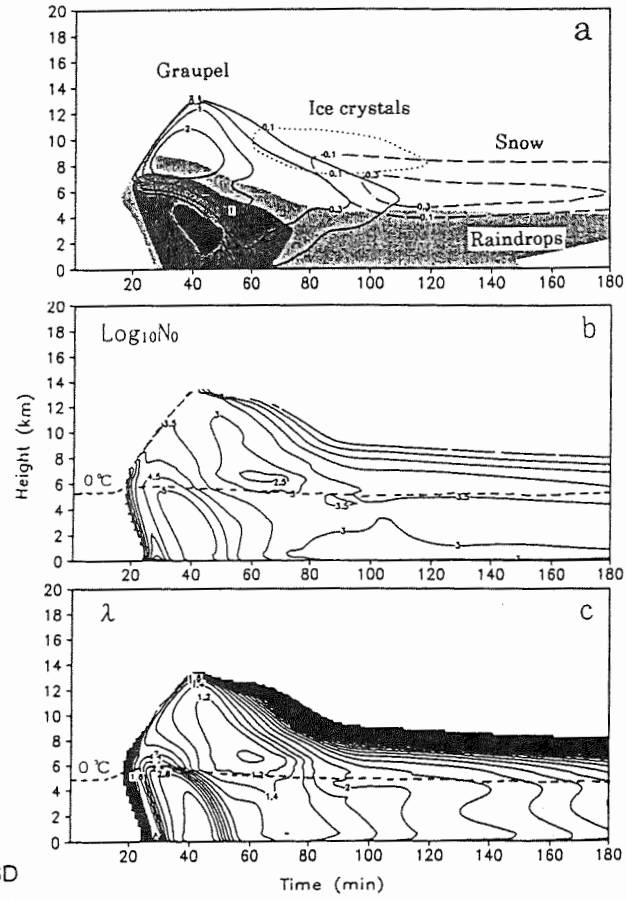

Fig.3 Time height cross section of (a) contents of hydrometeor (gm^{-3}) larger than 0.1 mm in equivalent liquid-water diameter (contour levels for raindrops are 0.1, 1 and 5 gm^{-3}), (b) $Log_{10}N_0$ and (c) λ (mm^{-1}).

level. On the other hand, the slope of the DSD becomes gentle below the melting level (4000 m) at 120 min.

The increasing rate of number density of large hydrometors are shown in Fig.5. At the 7000 m level (above the melting level) large particles are increased by the effects coalescence of supercooled drops and riming growth before 60 min, and by deposition growth and ice aggregation after 90 min. At the 5000 m level (just below the melting level) coalescence and collision breakup are dominant before 60 min, which suggests that collision breakup prohibits the formation of large drops. After 60 min its effect is very small.

4. SUMMARY

Results of the simulation show graupel particles have relatively small N_0 and λ (large-particle spectra), but when they reach below the 0°C level, number of large particles quickly decreases due to collision breakup, thus small-drop spectra are created in convective rainfall. On the other hand, snow particles get small N_0 and λ (large-particle spectra) just above the melting level by the effects of deposition growth and aggregation, and this spectrum is maintained below the melting level because collision breakup is not effective to the melted snow. These results explain the difference in DSD between convective and stratiform rainfall.

However, the simulation results do not explain the sudden change of DSD (N_0 jump). In the observation the large N_0 is found even when rainfall is very weak (around 1100UTC in Fig.1), while simulated N_0 decreases slowly with the decrease of rainfall. More realistic simulation of squall line using two- or three-dimensional model is necessary to explain the large N_0 in the weak rainfall region.

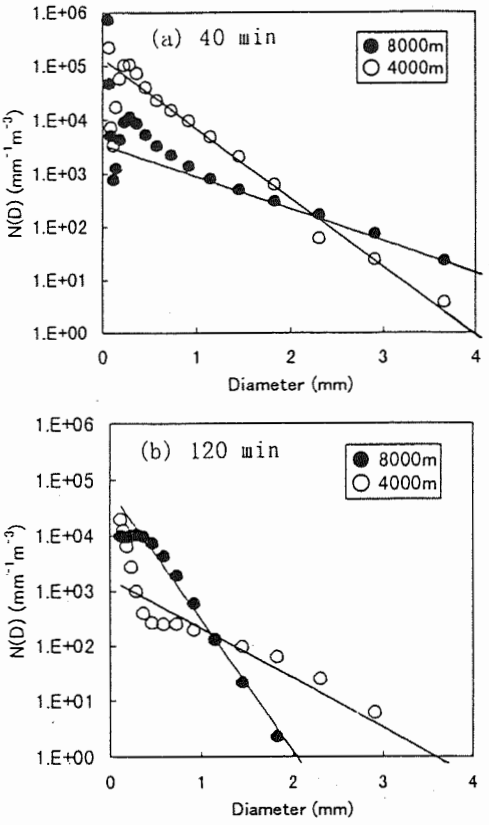

Fig.4 Variation of DSD with height at 40 min and 120 min.

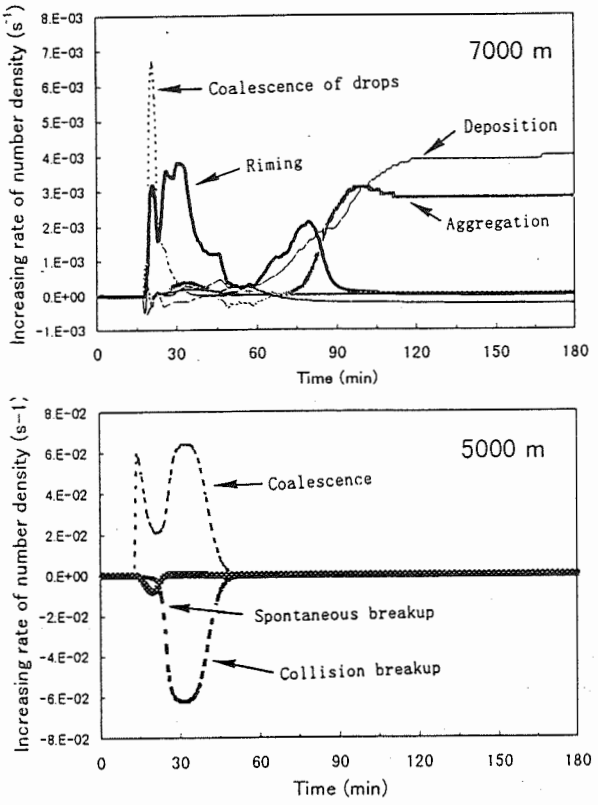

Fig.5 Contribution of each factor to the increasing rate of number density of hydrometeors larger than 2.5 mm in equivalent liquid-water diameter. The values are normalized with number density.

REFERENCES

Harimaya, T. and K. Okazaki, 1993: A comparison of the raindrop size distributions from stratiform clouds with those from convective clouds. *J. Fac. Sci., Hokkaido Univ., Ser. VII (Geophysics)*, **9**, 341-353.

Iwanami, K., M. Maki, R. Misumi, Y. Sasaki and T. D. Keenan, 1999: Multiple Doppler radar observation of tropical precipitation systems in JATMEX. *Preprints, 29th Int. Conf. Radar Meteorology*, Montreal, Canada, Amer. Meteor. Soc., 400-403.

Maki, M., T. D. Keenan, Y. sasaki and K. Nakamura, 1999: Spatial variability of raindrop size distribution in tropical continental squall lines. *Preprints, 29th Int. Conf. Radar Meteorology*, Montreal, Canada, Amer. Meteor. Soc., 651-654.

Reisin, T., Z. Levin and S. Tzivion, 1996: Rain production in convective clouds as simulated in an axisymmetric model with detailed microphysics. Part I. Description of the model. *J. Atmos. Sci.*, **53**, 497-519.

Tokay, A. and D. A. Short, 1996: Evidence from tropical raindrop spectra of the origin of rain from stratiform versus convective clouds. *J. Appl. Meteor.*, **35**, 355-371.

Waldvogel, A., 1974: The N0 jump of raindrop spectra. *J. Atmos. Sci.*, **31**, 1067-1078.

Wisner, C., H. D. Orville and C. Meyers, 1972: A numerical model of a hail bearing cloud. *J. Atmos. Sci.*, **29**, 1160-1181.

HEAVY RAINFALL PRODUCED BY A LONG-LIVED LINE-SHAPED PRECIPITATING CONVECTIVE-CLOUD SYSTEM

S. Kanada, G. Biao, H. Minda, K. Tsuboki and T. Takeda

Institute for Hydrospheric-Atmospheric Sciences, Nagoya University, Nagoya 464-8601, Japan

1. INTRODUCTION

Heavy rainfall is very often caused in subtropical humid-climate region by a meso-scale precipitating convective cloud system, the formation and development of which are subject to orographic effect. The Kyushu District located in the southern part of Japan Islands is a typical area where the orographic enhancement of rainfall is often observed during the Baiu period. For example, monthly rainfall amount at Hiyoshi station in the center of the Kyushu District reached 1600 mm in June in 1993.

During the Baiu period in 1997 dual-Doppler radars of Nagoya University were installed in the Nagasaki Peninsula and Amakusa in the Kyushu District, respectively, in order to study the relationship between an orographically modified convective-cloud system and heavy rainfall.

The locations of radar-sites are shown in Fig. 1. The radar-observation area can be often dominated by warm and moist air during the Baiu period. There are two high mountains, whose tops exceed 1000m, around radar sites.

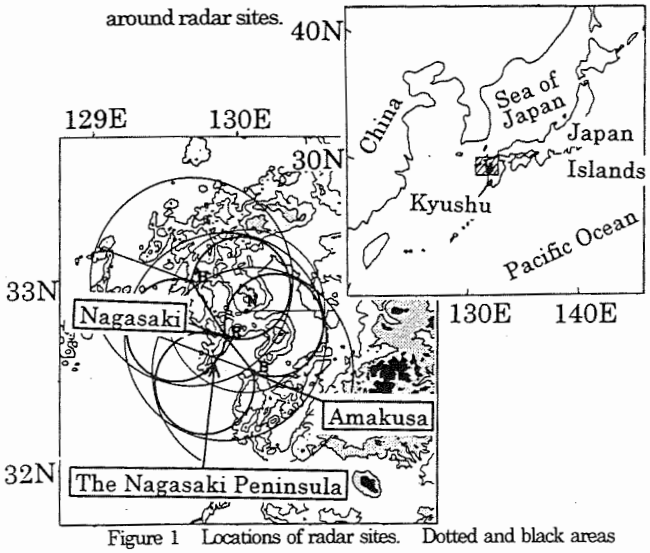

Figure 1 Locations of radar sites. Dotted and black areas indicate area s over 500 and 1000,respectively.

Corresponding author's address: Sachie Kanada, Institute for Hydrospheric-Atmospheric Sciences, Nagoya University, Nagoya 464-8601, Japan; E-Mail: kanada@ihas.nagoya-u.ac.jp

2. BRIEF DESCRIPTION OF AN ANALYZED CASE

On July 11 in 1997 an extremely heavy rainfall was concentrated in the narrow area in the Nagasaki Peninsula in the Kyushu District. The horizontal distribution of total rainfall amount from 0900 LST on July 11 to 0300 LST on July 12 is shown in Fig. 2 on the basis of the data of raingage stations of the Japan Meterological Agency (JMA) in the peninsula.

A large rainfall amount was observed around Isahaya city. The largest amount of 176 mm was recorded at Meotogi station located almost at the base of the peninsula. It is noted that total rainfall amounts larger than 10 mm were observed only in the limited area around the base of the peninsula. Total rainfall amount at a few km north around from Meotogi station was only 3 mm.

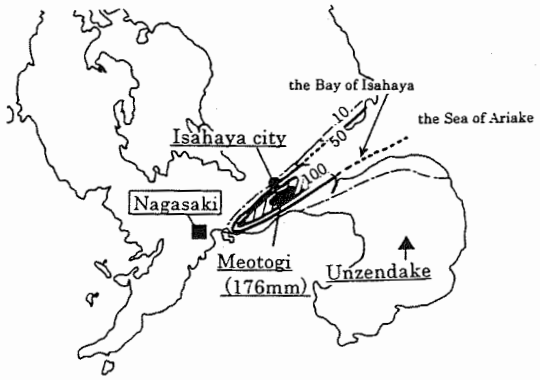

Figure 2 Horizontal distribution of total rainfall amount from 0900 LST on July 11 to 0300 LST on July 12.

3. THREE-DIMENSIONAL STRUCTURE OF A RADAR-ECHO BAND

The horizontal distribution of rainfall shown in Fig. 2 was produced by a long-lived line-shaped convective cloud system which was maintained for about 18 hours almost in the same place and which extended in the direction of low-level ambient winds.

The length and width of its radar-echo band were over 60 km and about 10 km, respectively. Interestingly its length extended with period of 2 to 3 hours.

The three-dimensional structure of this radar-echo band was observed by the dual-Doppler radars of Nagoya University. Figure 3 shows the example of the horizontal distribution of radar-echo intensity (10logZ). The radar-echo band was composed of many convective cells whose radar-echo tops were about 6 km. Most of them formed successively in the upwind side of the band and moved along its direction. Cellular-echoes had a tendency to be intensified, moving in the downwind direction, especially in three areas fixed geographically.

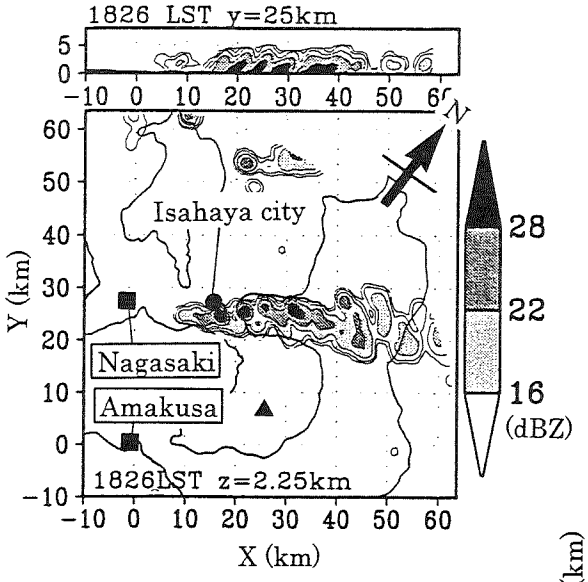

Figure 3 Horizontal distribution of radar-echo intensity at 1.25 km level.

Figure 4 shows the horizontal distribution of time-averaged radar-echo intensity at 1.25 km level. The western end of radar-echo region over 10 dBZ was at X = 6 km, that is, around the base of the Nagasaki Peninsula. The line-shaped radar-echo region extended eastward, becoming wider with distance away from the base of the peninsula.

The intensification of radar-echo was seen in three areas around X = 20 km, 24 km and 30 km, that is, 'the base of Nagasaki Peninsula', 'the Bay of Isahaya' and 'the Sea of Ariake'.

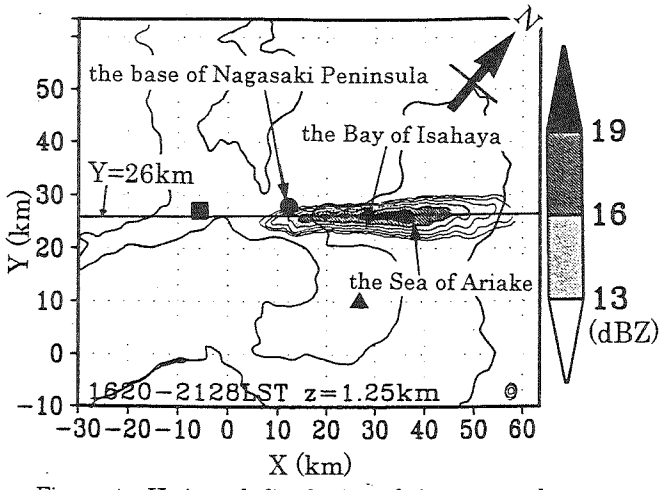

Figure 4 Horizontal distribution of time-averaged radar-echo intensity at 1.25 km level.

The distributions of time-averaged radar-echo intensities in vertical sections along and normal to the line are shown in Fig. 5a and 5b, respectively. The position of Fig. 5a is shown in Fig. 4. The height of echo top defined by 10 dBZ was about 5 km. Three intensive echo areas shown in Fig. 4 are seen in Fig. 5a. As shown in Fig. 5b, radar-echoes were tilted south-southwestward in sections normal to the line. Time-averaged radar-echo intensity were intensified from X = 10 to 30 km. Around X = 40 km (over the Sea of Ariake) radar-echoes tended to become weaker and their echo-top became lower. These features imply that convective clouds were in more developing stage in the Bay of Isahaya than over the Sea of Ariake.

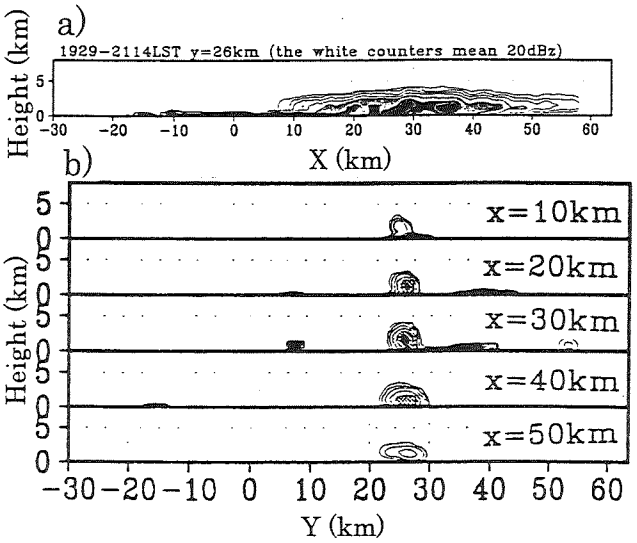

Figure 5a,bDistributions of time-averaged radar-echo intensities in vertical sections along and normal to the band.

As mentioned above, the length of the radar-echo band extended with period of 2 to 3 hours. Figure 6 shows the t-x cross section of radar-echo intensity at 1.25 km level. In this figure the periodicity of the band is clearly revealed and it was intensified at least three times from 1622 to 2130 LST. Constituent radar-echoes of the band seems to have formed around X = 0 ~ 10 km (around the base of Nagasaki Peninsula). The west-southwestern end of the band moved to the upwind side, that is, west-southwestward. These features were also seen during other periods.

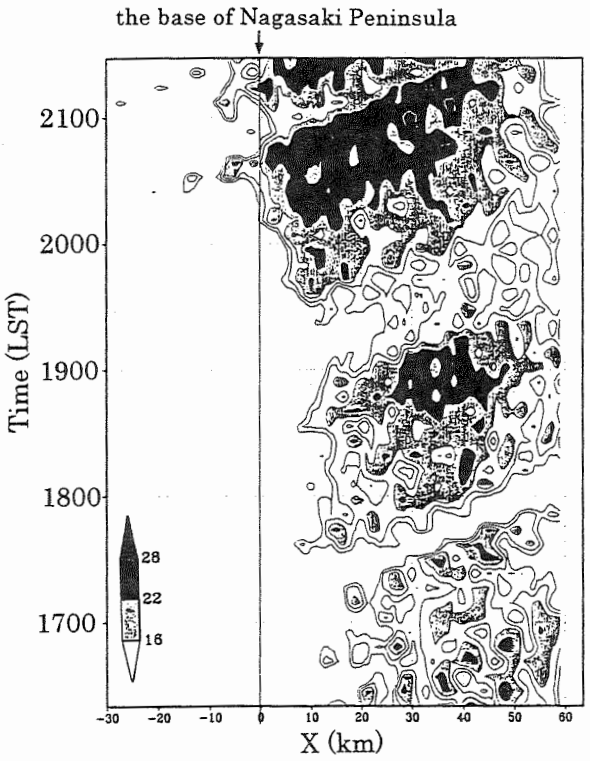

Figure 6 Time-x cross section of radar-echo intensity at 1.25 km level.

4. DISTRIBUTION OF AIRFLOWS

The three-dimensional distribution of airflows were observed by the dual-Doppler radars. Figure 7 shows the horizontal distribution of time-averaged winds at 1.50 km level. As shown in the figure, low-level winds in the radar-echo band and its surrounding area had the characteristic features which are strongly dependent upon the topography of the peninsula. Interestingly these features correspond with three intense radar-echo areas shown in Fig. 4.

In the base of the Nagasaki Peninsula, there was the stagnation region of airflows where southwesterly winds became weaker. New cellular radar-echoes formed often in this region. In the Bay of Isahaya, southerly winds which turned around the western slope of Unzen-dake caused horizontal convergence together with southwesterly winds, which was not much influenced by the orography around the base of the Nagasaki Peninsula. Since there are two high mountains whise tops are over 1000 m level, most of low-level winds go though the Bay of Isahaya toward the Sea of Ariake. As shown in the figure, winds became stronger in the Bay of Isahaya and winds diverged in the Sea of Ariake.

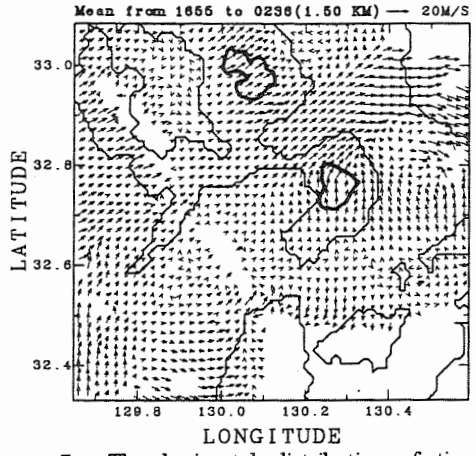

Figure 7 The horizontal distribution of time-averaged winds at 1.50 km level.

The vertical profiles of time-averaged horizontal winds along and normal to the band are shown in Figs. 8a and b, respectively. As shown in Fig. 4, there were three notably intense echo areas in 'the base of Nagasaki Peninsula', 'the Bay of Isahaya' and 'the Sea of Ariake'. Winds averaged in each of these three places are shown in the figures.

In the base of Nagasaki Peninsula and the Bay of Isahaya, strong southwesterly wind of about 20 m/s were predominant. The most intense southwesterly winds of about 22 m/s were seen at 4.0 km level. Winds were stronger in the base of Nagasaki Peninsula than in the Bay of Isahaya.

The vertical profile of winds along the band in the Sea of Ariake was much different from the profile of winds along the band in the other regions and strong winds were located was observed 2.25 km level.

As shown in Fig.8b, northeasterly winds were seen in the Sea of Ariake, although southwesterly winds were seen in the base of Nagasaki Peninsula and the Bay of Isahaya. These northeasterly winds in the Sea of Ariake caused convergence together with southerly winds which turned around the eastern slope of Unzen-dake and let to sudden expansion of radar-echo in the direction normal to the band.

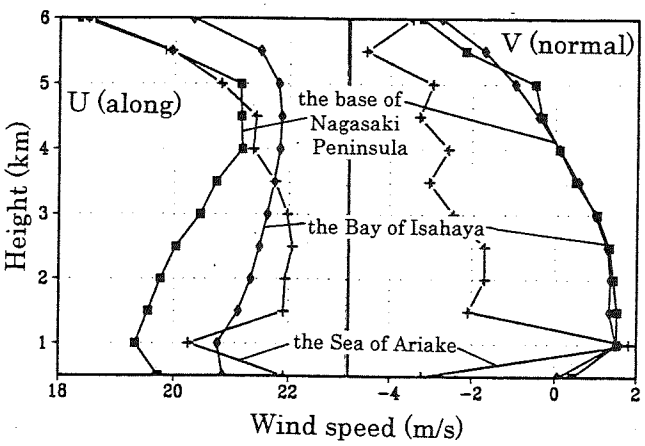

Figure 8 The vertical profiles of time-averaged horizontal winds, along and normal to the radar-echo band, respectively, in each area.

5. SUMMERY AND DISCUSSION

From 0900 LST on July 11 to 0300 LST on July 12, a long-lived line-shaped convective system was observed in the Nagasaki Peninsula. It was maintained for about 18 hours almost in the same place to bring an extremely huge rainfall amount.

Cellular radar-echoes had a tendency to be intensified, moving in the downwind direction along the line, especially in three areas. Its length extended with period of 2 to 3 hours.

As shown in Figs. 2, 4 and 7, the horizontal distributions of rainfall amount and winds were strongly affected by the topography of the Nagasaki Peninsula.

Radar-echoes were intensified .especially in three areas.

The horizontal distribution of time-averaged winds shows following notable features which are strongly dependent upon the topography of the peninsula;

1) the stagnant region of airflows in the base of the peninsula
2) the convergent and strong winds in the Bay of Isahaya
3) the divergent winds in the Sea of Ariake

It can be said that rainfall in the line-shaped convective cloud system was intensified by following processes.

1) Low-level horizontal winds became slower in the base of Nagasaki Peninsula by the upwind effect of the peninsula. New convective clouds formed and developed in this area and these were drifted to the downwind side .

2) In the Bay of Isahaya there was another convergence zone which was caused by the confluence of predominant ambient winds and southerly winds modified by Unzen-dake. Convective clouds developed in this area and they were drifted to the downwind side by strong southwesterly winds.

3) In the Sea of Ariake strong southwesterly winds diverged. These winds caused convergence together with southerly wind which turned around the eastern slope of Unzen-dake.

Interestingly, when low-level southerly winds became stronger, the radar-echo band was also intensified. This fact supports above-mentioned processes.

One more interesting feature was the periodic extension of the long-lived line-shaped convective system. The same periodicity was seen in the time variation of pressure field.

The results of more detailed analysis will be presented together with the results of numerical simulation on airflows and precipitating convective clouds around the Nagasaki Peninsula.

RAINDROP SIZE DISTRIBUTIONS OF TROPICAL DEPRESSIONS OBSERVED DURING THE R/V MIRAI CRUISE AND TYPHOON 9918 (BART)

[1]Kenji Suzuki

[1]Department of Biological Science, Yamaguchi University, 1677-1 Yamaguchi, 753-8515, Japan

1. INTRODUCTION

In order to understand the mechanism of the torrential rainfall, it is important to know how efficiently the precipitation processes work and raindrops are formed in clouds. Takahashi et. al. (1995) found that the warm rain process was dominate in the maritime convective clouds at Manus in TOGA-COARE, using the videosonde system. Large raindrops (>4mm in diameter) were also observed in the convective shallow clouds. They concluded that raindrops grown through the warm rain process froze just above freezing level and continued to grow by collecting supercooled drops. Since they don't need to break up as raindrops do, they keep growing and produce heavy rainfall. It was also found that the precipitation particle distributions varied in different climatological regions, depending on the precipitation processes (Suzuki and Takahashi, 1996).

For measuring the raindrop size distribution, the portable disdrometer was developed. In this paper, the raindrop size distributions from different rainfall events observed by this disdrometer in 1999 are reported, which are two maritime tropical depressions observed during the R/V Mirai cruise, and the mature stage of Typhoon 9918 (Bart).

2. OBSERVATIONS

2.1 Disdrometer

Portable video disdrometer was developed for measuring the raindrop size distribution. This was improved from a videosonde (Precipitation Particle Image Sensor; Takahashi, 1990) and consists of a CCD camera, an IR sensor, a strobe, and a signal control unit. When a raindrop interrupts the IR sensor beam, the strobe flashes and the image of the raindrop is recorded on a VTR tape.

2.2 Tropical Depressions observed during the R/V Mirai cruise

The portable disdrometer was set up on the navigational bridge deck of the R/V Mirai (JAMSTEC: the Japan Marine Science and Technology Center) from June 8 to July 17, 1999. This cruise was meant for the participation into the international field experiment Nauru99. On the way back to Japan after Nauru99 IOP, rainfalls from two tropical depressions were observed on July 8 and July 13, 1999. The cruise track overlapped GMS image on 00UTC July 9, 1999 is shown in Figure 1. The total rainfall amounts were 12.9mm and 25.4mm, respectively.

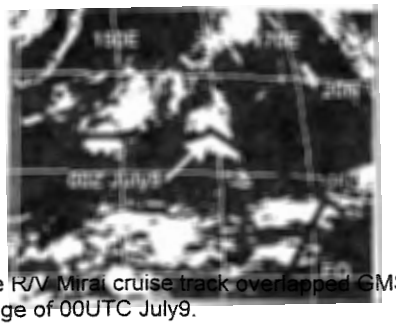

Figure 1. The R/V Mirai cruise track overlapped GMS image of 00UTC July9.

2.3 Typhoon 9918 (Bart)

Typhoon 9918 (Bart) appeared at 00UTC September 19 over the East China Sea, and moved northward. It struck Kyushu area around 21UTC September 23, and landed again at Yamaguchi just before 00UTC September 24 from the Inland Sea after crossing Kyushu (Figure 2). The total rainfall at Yamaguchi was 117.0 mm. The portable disdrometer was set on the rooftop of a building of Yamaguchi University, and continued to record raindrop images until the power o

Fi line indicates the track of Typhoon Bart.

Corresponding author's address: Kenji Suzuki, Department of Biological Science, Yamaguchi University, 1677-1 Yamaguchi, 753-8515, Japan;
E-mail: ksuzuki@agr.yamaguchi-u.ac.jp

3. RESULTS AND DISCUSSION

3.1 Case of July 8, 1999

The R/V Mirai was at (14N, 160E) on July 8 and encountered the rainfall from the small tropical depression. The total rainfall amount was 12.9mm from 2000UTC July 8 through 0030UTC July 9. 10-minute rainfall amount from 18UTC to 03UTC is shown in Figure 3. There were clearly two different rains, which were the short-time moderate rain at the beginning of the rain and subsequent weak rainfall. This was also shown in the radar reflectivity observed by the C-band Doppler radar of the R/V Mirai (not shown here).

The disdrometer data are shown in Figure 4(a) as number of drops within 0.2-mm size category. More than 80% of the drops were between 0.2 and 1.2 mm in diameter. Figure 5 shows the frequency distribution of convective (2058-2105UTC) and stratiform (2300-2339UTC) precipitation. The former distribution has higher peak and narrower width. As Tokay and Short (1996) have demonstrated, the raindrop concentrations may have been higher in the convective region because of small drops generated by collisional breakup. They concluded that this could perhaps be due to enhanced growth of aggregates, leading to a larger supply of bigger raindrops after melting. According to Takahashi et. al. (1995), large raindrops concentrated at the level of 1-2 km in the tropical convective clouds, while smaller drops were predominant near the surface. This suggested that the breakup process works at the lower level in the convective clouds.

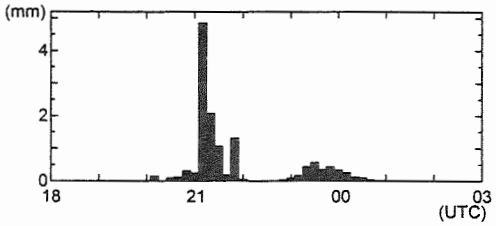

Figure 3. 10-minute rainfall amount observed by Young Raingauge set on the flying deck of the R/V Mirai.

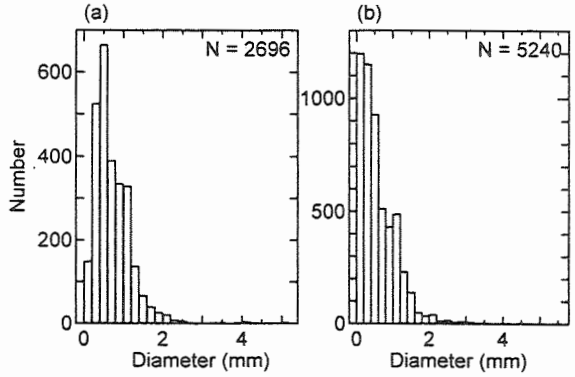

Figure 4. Raindrop size spectra from disdrometer data presented as number of drops in each 0.2 mm interval. (a)2025 - 2339UTC July8, 1999 (b)2210 - 2257(UTC) September 23, 1999.

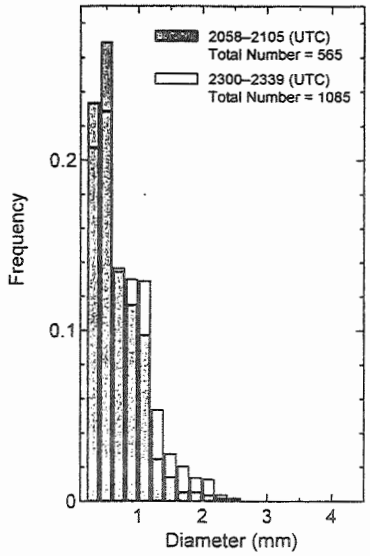

Figure 5. Frequency distributions for convective (shaded) and stratiform precipitation (clear).

3.2 Case of September 23, 1999

Figure 6 shows the meteorological factors observed at Yamaguchi Meteorological Station. The total rainfall amount was 117.9mm and the maximum rainfall intensity and wind speed were 81.8mm/hr and 20.2m/s (2340UTC), respectively.

The disdrometer data are shown in Figure 4(b). Compared with the distribution of the case of July 8, the distribution is broadened and fewer medium size raindrops are characterized.

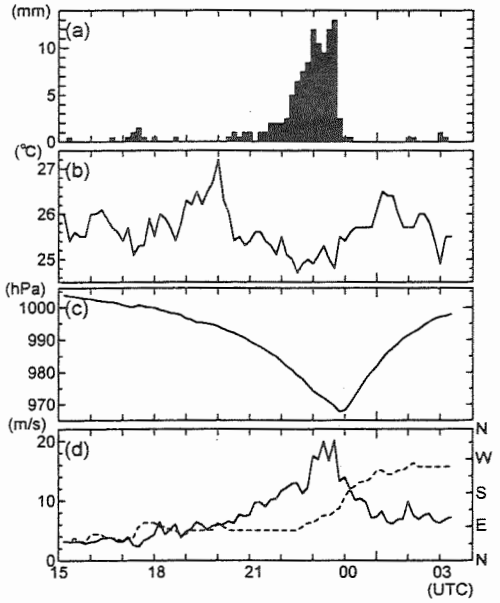

Figure 6. (a)10-minute rainfall amount, (b)Temperature, (c)Sea level pressure, (d)Wind speed (solid line) and wind direction (dashed line) observed at Yamaguchi meteorological station.

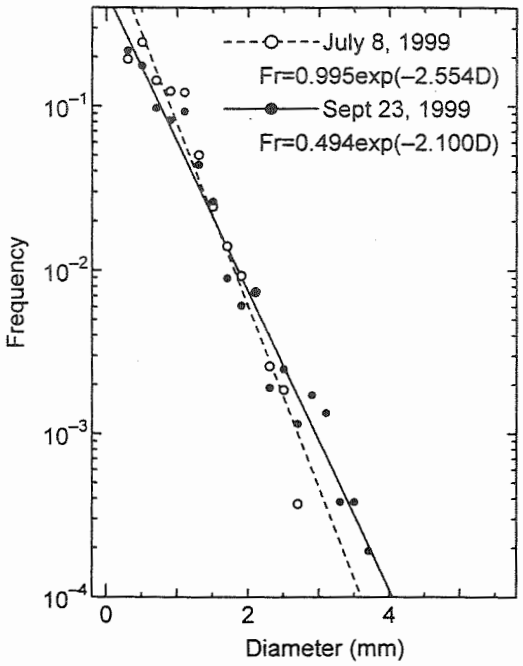

Figure 7. Drop size distribution of Typhoon 9918 (Bart) (solid line) and Tropical depression (dashed line).

Figure 7 shows the frequency distribution for the cases of July 8 (dashed line) and September 23 (solid line). The distribution for Typhoon clouds had higher frequency at larger drop size and lower at smaller drop size. The distribution differences between the July 8 and September 23 cases are probably related to the type of rainfalls. The data from July 8 were collected within maritime clouds having light-moderate rainfall, whereas the data from September 23 originated in stronger rainfall with the typhoon passage.

It is supposed that the raindrops efficiently formed in the typhoon clouds and that its formation processes at the upper level play important role to make heavy rainfall. In the case of July 8, the raindrops might be mainly formed through the warm rain process, which size distribution was sharper peak and narrower by the collision breakup of raindrops. On the other hand, in the typhoon clouds, which caused heavy rainfall, large raindrops might be formed through the warm rain-freezing process as mentioned by Takahashi et. al. (1995). Raindrops formed at lower levels might be carried up to the freezing level by the strong updraft. Then raindrops might freeze and grow by collecting supercooled drops. When they fell through lower warm atmosphere, they melt, but it might be difficult to breakup because of the existence of ice core in the raindrops. Furthermore, due to the supposed strong updraft in the typhoon cloud, the ice crystal and graupel formation process might be active. These precipitation particle formations at upper level might be important for the raindrop size distribution at the surface.

4. Acknowledgements

This work was partially supported by the R/V Mirai MR99-K03 cruise of JAMSTEC. The author also wishes to thank Captain Akamine and his crew of the R/V Mirai for their skilful help.

5. References

Cober, S. G., J. W. Strapp and G. A. Isaac, 1996: An example of supercooled drizzle drops formed through a collision-coalescence process. J. Appl. Meteor., **35**, 2250-2260.

Marshall, J. S. and W. M. Palmer, 1948: The distribution of raindrops with size. J. Meteor., **5**, 165-166.

Smith, P. L., D. J. Musil, A. G. Detwiler and R. Ramachandran, 1999: Observations of mixed-phase precipitation within a CaPE thunderstorm. J. Appl. Meteor., **38**, 145-155.

Suzuki, K. and T. Takahashi, 1996: Rainband precipitation processes in different climatological areas. Proc. of the Int. Conf. on Water Resour. Environ. Res. **2**, 595-601.

Takahashi, T., 1990: Near absence of lightning in torrential rainfall producing Micronesian thunderstorms. Geophys. Res. Lett., **17**, 2381-2384.

Takahashi, T., K. Suzuki, M. Orita, M. Tokuno and R. de la Mar, 1995: Videosonde observation of precipitation processes in equatorial cloud clusters. J. Meteor. Soc. Japan, **73**, 509-534.

Tokay, A. and D. A. Short, 1996: Evidence from tropical raindrop spectra of the origin of rain from stratiform versus convective clouds. J. Appl. Meteor., **35**, 355-371.

Tokay, A. and K. V. Beard, 1996: A field study of raindrop oscillations. Part I: Observation of size spectra and evaluation of oscillation cases. J. Appl. Meteor., **35**, 1671-1687.

Tokay, A., D. A. Short, C. R. Williams, W. L. Ecklund and K. S. Gage, 1999: Tropical rainfall associated with convective and stratiform clouds: Intercomparison of disdrometer and profiler measurements. J. Appl. Meteor., **38**, 302-320.

Yuter, S. E. and R. A. Houze Jr., 1997: Measurements of raindrop size distributions over the Pacific warm pool and implications for Z-R relations. J. Appl. Meteor., **36**, 847-867.

STRUCTURE OF PRECIPITATION SYSTEMS AND FORMATION PROCESS OF PRECIPITATION DERIVED FROM DUAL-DOPPLER RADAR ANALYSIS AND WATER VAPOR BUDGET DURING GAME/HUBEX IOP

T. Maesaka and H. Uyeda

Graduate School of Science, Hokkaido University, Sapporo, Japan.

1. INTRODUCTION

During June and July 1998, GEWEX Asian Monsoon Experiment (GAME) / Huaihe River Basin Experiment (HUBEX) was carried out in Anhui province, China, in order to gain an understanding of the energy and water circulation around the Meiyu front (Zhao and Takeda, 1998). Meiyu is the rain in the season when plum is ripe and caused by predominant sub-tropical front. Most of the precipitation during the Intensive Observation Period (IOP) of GAME/HUBEX was concentrated from June 29 to July 3, 1998 and consisted of two events. The first event was associated with the generation of a meso-α scale low on the Meiyu front, and the second was associated with a lingering of the Meiyu front, which was aligned from west to east (Maesaka and Uyeda, 1999).

In this paper, we describe our analysis of the structure of precipitation systems with dual-Doppler radar data and our comparison of the water vapor budget with the sounding data. We also discuss the contribution of the water vapor convergence and condensation to the development of these systems.

2. METHOD OF ANALYSIS

Dual-Doppler radar analysis is used to determine the detailed structure of the precipitation systems. In the IOP of GAME/HUBEX, Doppler radars at Shouxian, Fengtai, and Huainan, Anhui province, China (Fig. 1) acquire volume scan data of the reflectivity and Doppler velocity every seven minutes synchronously. The best combination of two of three radars is used to retrieve three-dimensional wind fields by using a mass continuity equation with the anelastic approximation. To understand the development of the precipitation systems, it is important to know where water vapor comes from, and where it converges, and where it condenses. We thus analyze the water vapor budget by using high-resolution (for the most part, sampled every six seconds) upper-air sounding data. During the IOP, a radiosonde was launched every six hours. The high-resolution sounding points used in this analysis are shown in Fig. 1. We calculate the apparent moisture sink (Q_2) by using this sounding data to estimate the water vapor condensation (Yanai et al., 1973).

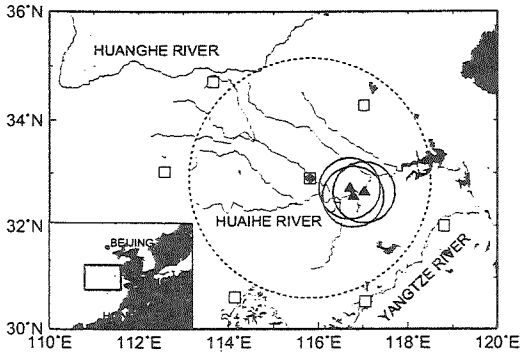

Figure 1: GAME/HUBEX observation area. Three solid triangles indicate the Doppler radar sites (Huainan, Shauxian, Fengtai) and their observation ranges (64 km) are encircled by solid line. A solid diamond indicates the conventional meteorological radar site (Fuyang) and its observation range (250 km) are encircled by dashed line. Squares indicates upper-air sounding sites.

In estimating of precipitation water content from radar reflectivity, it is important that the accuracy of the reflectivity value is verified. So we compare the reflectivity of the HUML (Hokkaido University, Meteorological Laboratory) radar installed at Huainan with the reflectivity of the TRMM–PR (Tropical Rainfall Measurement Mission – Precipitation Radar), a space-borne radar. Before this comparison, attenuation correction (Doviak and Zrnić, 1984) is applied to the HUML radar reflectivity. In the work reported in this paper, we corrected the reflectivity of the HUML radar by linear regression because the reflectivity obtained with the TRMM–

Corresponding author address: Takeshi Maesaka, Earth and Planetary Sciences, Graduate School of Science, Hokkaido University, Sapporo, 060-0810, Japan.
TEL: +81–11–706–2761, FAX: +81–11–746–2751.
e-mail: msaka@ep.sci.hokudai.ac.jp

PR coincide well with the reflectivity observed by the Disdromater installed at Huainan (data not shown).

3. STRUCTURE AND WATER VAPOR BUDGET OF PRECIPITATION SYSTEMS

3.1 Cold Frontal Type

During the morning of June 29 a meso-α scale low was generated; it moved eastward on the Meiyu front around the Huaihe river basin. With this low generation, warm and cold frontal precipitation system appeared over the Doppler radar sites. In this section, we mention the structure and water vapor budget of the cold frontal system because the cold frontal system caused heavier rainfall than the warm frontal system.

Six hours after the passage of the warm frontal system, a convective precipitation system like a cold front appeared in the region observed by the Doppler radar network. Figure 2a shows a horizontal plane (z =2 km) of dual-Doppler radar analysis at 1842 BST (Beijing Standard Time, BST=UTC+8). A linear convective system formed along SW–NE line corresponding to the shear line of a southwesterly (ahead of the system) and a westerly (behind the system), and new convective cells are generated at the southwest end of the line. Figure 2b shows a vertical cross-section of dual-Doppler radar analysis (storm relative) along the A–A' line of Fig. 2a. A strong inflow to the convective cell is predominant ahead of the cell, where a large quantity of water vapor is advected by the southwesterly. Furthermore, the height at which this strong inflow is observed is below 2 km in height. This suggests that the precipitation is forming in the lower layer, because lower air contains a large quantity of water vapor, and that only a little lifting is enough to elicit condensation.

Figure 3 shows the apparent moisture sink calculated from upper-air sounding data for 20 BST, 29 June. Around linear precipitation system (area A), the peak of apparent moisture sink is estimated around 800 and 400 hPa layer. The lower peak well corresponded to the precipitation formation at heights below 2 km.

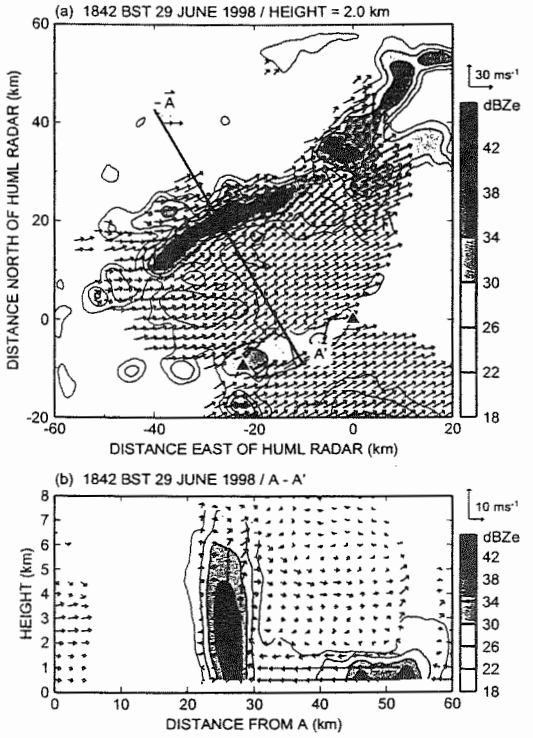

Figure 2: Dual-Doppler radar analysis for 1842 BST 29 June 1998. a) Horizontal plane at 2.0 km in height. b) Vertical cross-sections along A–A' lines in (a). The vector denotes the wind on the plane. Vectors of (b) are subtracted from the average wind. The shading denotes the radar reflectivity.

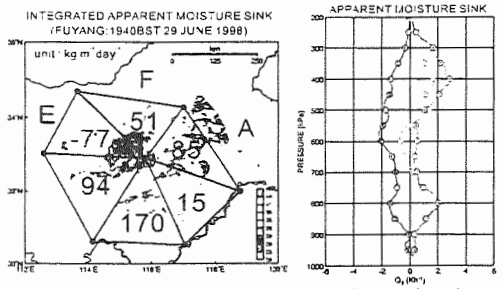

Figure 3: Apparent moisture sink in each triangular area estimated from sounding data at 20 BST 29 June 1998. a) Vertical integrated (975–200 hPa) apparent moisture sink. Gray scale shows the reflectivity of Fuyang radar. b) Vertical profiles of apparent moisture sink.

3.2 Meso-vortex Type

On July 2, a southwesterly synoptic winds around the sub-tropical high southeast of the observation area and a northeasterly from a weak high north of the area converged to form the Meiyu front. In the horizontal shear zone, vigorous convective clouds with meso-β or γ scale vortexes formed. So, we name this a meso-vortex type precipitation system. Figure 4 shows horizontal plane of the dual-Doppler radar analysis near a vortex. Figure 5 shows the vertical cross sections of the convective area (22 minutes before the time corresponding to the data shown in Fig. 4) along W–E and S–N lines. In the verti-

cal cross section along the W–E line, a strong inflow to the convective cell is located ahead of the cell, where large amount of water vapor are adveced by the southwesterly. In the vertical cross section along the S-W line, the lower northerly is remarkable and converges with the southerly to form a convective zone in the south part of the Meiyu front. Furthermore, a stratiform zone is formed behind the convective zone. In both the cold frontal and meso-vortex type system, the strong inflows to the convective cell are ahead of the cell, but the level of inflow in the meso-vortex type is higher.

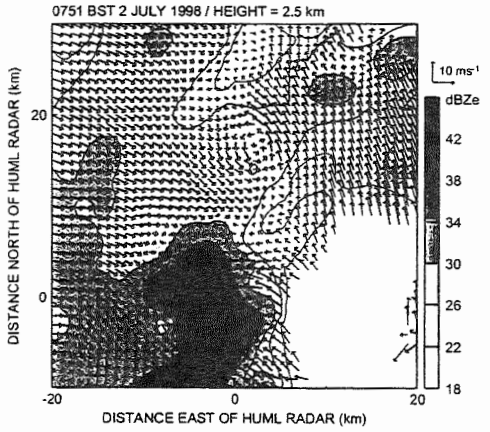

Figure 4: Horizontal plane of dual-Doppler radar analysis at 2.5 km in height at 0751 BST 2 July 1998. Details are the same as in Fig. 2a but vectors are subtracted from the averaged wind.

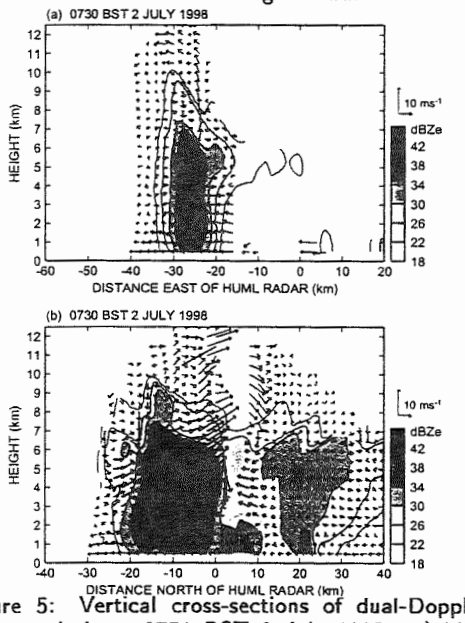

Figure 5: Vertical cross-sections of dual-Doppler radar analysis at 0751 BST 2 July 1998. a) Vertical cross-section along W–E line. Details are the same as in Fig. 2b. b) Vertical cross-section along S–N line. Details are the same as in Fig. 2b.

Figure 6 shows the apparent moisture sink calculated from upper-air sounding data for 08 BST, 2 July. A tremendous apparent moisture sink is calculated to be at 800–400 hPa ahead of the system (area A). It is remarkable that this larger apparent moisture sink is calculated to be at an altitude higher than other apparent moisture sinks observed during the IOP. The layer in which the strong apparent moisture sink is calculated to be, corresponds to the layer in which dual-Doppler radar analysis showed that strong ascending motion occurred and heavy precipitation formed. In the stratiform region behind the convective region (area E), an apparent moisture source is calculated to be in all layers. It is considered that the apparent moisture source in the stratiform region enhances the lower northerly, because the lower northerly comes through the stratiform region.

4. TIME VARIATION OF INFLOW AND PRECIPITATION FORMATION

In this section, we discuss the time variation of inflow to the convective cell and of the formation of precipitation in cold frontal system. Figure 7 shows a time–height cross-sections of averaged reflectivity, horizontal divergence, vertical velocity, southeasterly inflow and northwesterly inflow around the linear (along SW–NE) convective system. The warm and moist inflow ahead the system (from southeast of the system) was predominant at heights below 2 km. As time passes, strong reflectivity gradually appears in higher level, and horizontal convergence and vertical velocity peak level appears also in higher level. When the horizontal convergence peak level reaches about 4 km in height, the inflow from the northeast of system observed at 4 km level. Following the northeasterly inflow, descending motion prevails in the convective cell and the system fades. It is

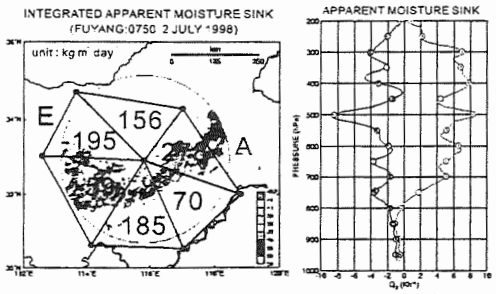

Figure 6: Apparent moisture sink in each triangular area estimated from sounding data at 08 BST 2 July 1998. Details are the same as Fig. 3.

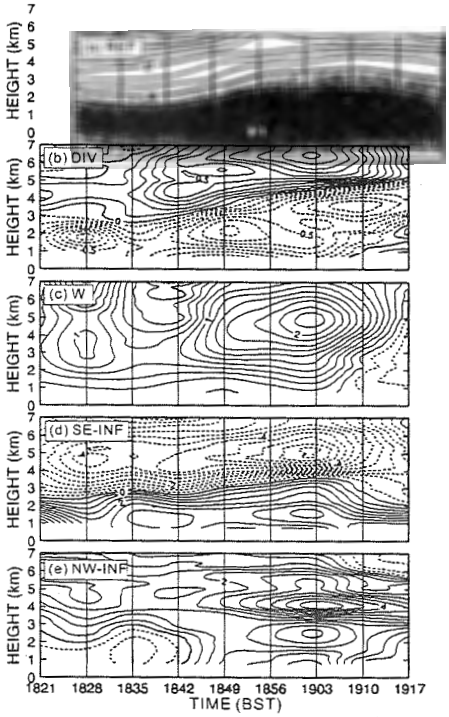

Figure 7: Time–height cross-sections of a) reflectivity (dBZ_e), b) horizontal divergence ($\times 10^{-3}$ s^{-1}), c) vertical velocity (ms^{-1}), d) southeasterly inflow (ms^{-1}) and e) northwesterly inflow (ms^{-1}). These profile are averaged in the area where reflectivity is larger than 30 dBZ_e at 2.0 km in height. Shaded area indicates negative value.

considered that the northeasterly inflow is very dry.

Figure 8 shows a vertical profile of the increasing rate of precipitation water content (area averaged; $>$ 30 dBZ_e at 2 km in height) estimated by

$$\frac{Dm}{Dt} = \frac{\partial m}{\partial t} + u\frac{\partial m}{\partial x} + v\frac{\partial m}{\partial y} + \left(w + V_F\right)\frac{\partial m}{\partial z}, \quad (1)$$

where m is precipitation water content, V_F is fall velocity, (u, v, w) is wind velocity derived by dual-Doppler radar analysis. V_F is estimated by Rogers (1964) using reflectivity, m is estimated by Z–R relation by Fujiwara (1965). The profile in Fig. 8 shows that most precipitation is formed at heights below 2 km.

5. Conclusion

It is considered that distribution of the condensation and evaporation areas were formed by the precipitation system and intensified the Meiyu front itself through latent heating or cooling to develop and maintain the long-term (several hours) rainfall. The structure determined from the dual-Doppler radar

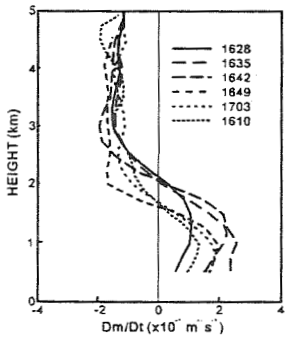

Figure 8: Vertical profile of increasing rate of precipitation water estimated by equation (1) in 29 June 1998. These profiles are averaged in the same area in Fig. 7.

data corresponded well with water vapor budget estimated by using sounding data. The analysis reported here revealed that the moisture advection by the southwesterly was important and necessary for developing and maintaining each of these precipitation systems, although the transformation of water vapor to precipitation was different in these systems. In particular, the low-level inflow like the cold frontal system causes heavy rainfall because even a little lifting triggers the condensation.

Acknowledgments

We are grateful to the GAME/HUBEX Project Office for providing the upper-air sounding data. For the Doppler radar observation, we thank Prof. Takao Takeda, Dr. Kazuhisa Tsuboki, Dr. Biao Geng (Nagoya University) and Prof. Yasushi Fujiyoshi (Hokkaido University). Furthermore, Prof. WenZhong Ge (Nanjing University) and the China Meteorological Administration contributed greatly to the continuous acquisition of Fuyang weather radar data. Finally, we note that Prof. Katsuhiro Kikuchi (Hokkaido University) gave us encouragement throughout this study.

References

Doviak, R. and D. S. Zrnić, 1984: Doppler Radar and Weather Observations. Academic Press, pp458.

Fujiwara, M., 1965: Raindrop-size distribution from individual storms. *J. Atmos. Sci.*, 585–591.

Maesaka, T. and H. Uyeda, 1999: Structure of precipitation systems derived from dual-Doppler radar analysis in comparison with water vapor budget during GAME/HUBEX IOP. *Proc. of the Workshop on Meso-scale Systems in Meiyu/Baiu Front and Hydrological Cycle.*

Rogers, R. R., 1964: An Extension of the Z–R relationship for Doppler radar. *Proc. of 11th Wea. Radar Conf.*, 158–161.

Yanai, M., S. Esbensen, J. Chu, 1973: Determination of Bulk Properties of Tropical Cloud Clusters from Large-Scale Heat and Moisture Budgets. *J. Atmos. Sci.*, 611–627.

Zhao, B. and T. Takeda, 1998: Huaihe river basin experiment (GAME/HUBEX). pp24.

THE INFLUENCE OF METEOROLOGICAL PROFILES AT A LOCAL SCALE IN RAINFALL OVER CAMAGÜEY. CUBA.

Daniel Martínez[1], Léster Alfonso[2], Reynaldo Báez[1] and Ieng Jo[1].

[1] Instituto de Meteorología. La Habana, Cuba

[2] Universidad Autónoma de Mexico. Ciudad Mexico

1. INTRODUCTION.

The prevalence of convective rainfall in the rainy season for the tropical regions is widely accepted (Riehl, 1979), and this particularly applies to Cuba (Rivero and Medvedev, 1987). In addition to synoptic factors, the intensity of convective processes is conditioned by local factors, as static stability, moisture content in the atmosphere, vertical wind shear and mesoscale wind convergence. The objective of this paper is to study the influence of the first three local factors mentioned above, on rainfall over Camagüey, Cuba. These factors can be estimated from an atmospheric sounding. Static stability has traditionally been parameterized by means of the stability indices, some of which also contain information about tropospheric moisture content (Peppler and Lamb, 1989). In the last two decades, intergral parameters as Convective Available Potential Energy (CAPE), Convective Inhibition Energy (CINE), Bulk Shear (BS), Bulk Richardson Number (BRN) and mean relative humidity have also been widely used to parameterize the local meteorological profiles. (Weisman and Klemp, 1982; Williams and Rennó, 1993; Rasmussen and Straka, 1998).

2. DATASETS

Meteorological profiles were obtained from the afternoon soundings of the Camagüey Rawinsond Station, located at 21°25'N and 77°10'W, near the center of the Camagüey province, an almost flat region in the central-eastern part of Cuba. This province extends from the northern to the southern coast of Cuba, and has an area of 15837 km^2, and a maximum width of nearly 170 km from coast to coast. The total sample consisted on 408 valid soundings. The sounding time ranged from 1200 LST to 1400 LST, though in most cases it was very close to 1300 LST (1800 UTS). Most of them (338) corresponded to the Cuban rainy season (May-October, that will be conventionally called "summer"

in this paper). The rest (70) correspond to the less rainy season, that will be conventionally called "winter", and were included in the analysis mainly for comparison.

Corresponding author's address: Daniel Martínez
Instituto de Meteorología. Ap. 17032, La Habana 17
C.P. 11700. Cuba. E-mail: dan@met.inf.cu

The observation period extended from 1982 to 1991. A subset of the soundings did not arrive to the equilibrium level (EL), but reached levels higher than 6 km. In these cases, the sounding was considered valid, and all variables could be calculated but CAPE and EL. Table 1 shows the obtained parameters and the number of valid cases for each of them. Most definitions can be found in the references, mainly in Peppler and Lamb, (1989) and Rasmussen and Straka, (1998). Particularly, Htmod is cloud top height, as predicted by a simple stationary cloud model, of the type used by Simpson and Wiggert (1969) and ΔTmax, HΔTmax are the maximum parcel excess temperature by pseudoadiabatic ascent and the corresponding height at which it takes place.

Table 1. Parameters obtained from Camagüey afternoon meteorological soundings to be used as rainfall covariants.

Symbol	Denomination	N
SI	Showalter index	408
LI	Lifted index	408
TT	Total-totals index	408
K	George index	408
LCL	Lifting condensation level (km)	408
CINE	Convective inhibition energy (J/kg)	408
Tc	Convective temp. (°C)	408
ΔTmax	Parcel temp. excess.(°C)	408
HΔTmax	Height of Δtmax. (km)	408
EL	Equilibrium level (km)	245
CAPE	Convective available potential energy (J/kg).	238
BS	Bulk vertical wind shear (m/s)	317
SS	Wind shear between surface and 300 m (m/s).	323
Htmod	Model predicted cloud top height (km)	408
RH6km	Averaged relative hum. from surface to 6 km (%)	408
RH1500	Averaged relative hum. from surface to 1.5 km (%)	408

Rainfall data are those of the Camagüey Basic Network of the National Institute for Hydraulic Resources (INRH), consisting in 263 raingauge stations, uniformly covering all the area of the province. The instruments were read every day at 0800 LST, corresponding to 24-hour totals. Three rainfall parameters were used for the study; the first is daily area mean rainfall (PMEAN), calculated as the simple mean rainfall value (in mm) for all valid readings on each day in the area. The second is daily maximum rainfall (PMAX), defined as the maximum reading for a day, and the third is fractional area rain cover (FRAREA), calculated as the simple ratio between number of stations with non-zero rainfall and the total number of valid readings for a day.

3. ANALYSIS AND DISCUSSION

To find relations between the sounding derived parameters and the rainfall estimates, Pearson correlation analysis and linear discriminant analysis by progressive stepwise multivariate linear regression were applied. Preliminarily, a linear correlation matrix between all the parameters was calculated. Correlation coefficients of CAPE and EL with stability indices, as for example, LI were as high as –0.88 and –0.89 respectively, with signification levels higher than 99.9%. Taking into account that the inclusion of this two integral parameters in the general analysis would have sensibly diminished the number of cases, and so, the significance of the results, it was decided to eliminate this variables from the analysis. Table 2 shows correlation matrixes between the rest of the sounding parameters and the rainfall estimators. The first tree data columns correspond to the total sample, excluding CAPE and EL, and the other two groups of three columns correspond to the summer and winter subsets.

Table 2. Correlation matrixes between sounding parameters shown in Table 1 (except CAPE and EL) and rainfall estimates, for the whole sample, and for the summer and winter samples. Correlation coefficients greater than 0,20 (0.40 for the winter sample) are significant at more than the 99.5% level, and those greater than 0.10 (0.20) are significant at more than 95% level.

	Total sample(313 cases)			Summer (251 cases)			Winter (62 cases)		
	FRAREA	PMEAN	PMAX	FRAREA	PMEAN	PMAX	FRAREA	PMEAN	PMAX
SI	-0.34	-0.30	-0.38	-0.22	-0.18	-0.16	-0.33	-0.27	-0.24
LI	-0.19	-0.16	-0.33	0.08	0.07	0.02	-0.37	-0.29	-0.38
TT	0.29	0.25	0.34	0.14	0.11	0.11	0.33	0.28	0.26
K	0.49	0.43	0.46	0.44	0.38	0.29	0.46	0.40	0.31
LCL	-0.30	-0.26	-0.27	-0.25	-0.23	-0.16	-0.28	-0.20	-0.30
CINE	-0.04	-0.04	0.01	-0.08	-0.06	-0.03	0.16	0.12	0.24
Tc	-0.07	-0.05	-0.02	-0.14	-0.12	-0.11	-0.22	-0.17	-0.29
ΔTmax	-0.01	-0.02	0.13	-0.20	-0.17	-0.10	0.25	0.13	0.21
HΔTmax	0.03	0.00	0.19	-0.22	-0.22	-0.10	0.20	0.08	0.17
Htmod	0.08	0.05	0.16	-0.06	-0.06	-0.02	0.30	0.20	0.26
RH6km	0.59	0.52	0.47	0.57	0.49	0.36	0.46	0.36	0.34
RH1500	0.37	0.34	0.32	0.34	0.32	0.26	0.31	0.23	0.23
BS	0.01	-0.01	-0.08	0.03	0.01	-0.04	0.21	0.24	0.17
SS	-0.04	-0.06	-0.05	-0.04	-0.06	-0.04	-0.05	-0.11	-0.10

Correlation coefficients between instability indicators and rainfall estimates for the whole sample are significant at the 99.5%, but for the summer they are not, and in some cases, even negative (according to the definition of LI, the instability indicator would be –LI). However, in the winter, they are positively correlated, as well as for the whole sample. An exception could be K, but it contains information not only of instability, but mainly about midtropospheric moisture content. This problem can be analyzed from Fig. 1, showing scatterplots of Pmax vs. LI and Pmax vs. RH6km. As can be seen, the summer and winter dots form two distinct clusters, especially in the LI plot. This means that the relatively high correlation Pmax-LI for the whole sample is mainly due to a seasonal effect, and hence, instability is an important factor in the difference in rainfall between the two seasons. The linear and quadratic fits for the summer and the winter samples are shown separately. For the LI summer plot, linear and quadratic fits are substantially different, and the quadratic curve shows that Pmax increases with LI for very negative LI values. However, the RH6km plot does not show a great difference

between the linear and the quadratic plot. Fore the winter both plots are roughly linear. This means that, while more moisture is always associated with more rain, the same does not hold for instability. When instability reaches extreme values, it seems to be associated with an average decrease in rainfall. The explanation of this fact is related with the efficiency of precipitation. Rosenfeld and Gagin (1989) have found a similar effect in convective rainfall at storm scale in South Africa and Israel. They found that for very high instability, the intensity of updrafts in convective clouds was too high, so that the time of coalescence drop grow was reduced. Recently, Rasmussen and Straka (1998) studied characteristic thermodynamic profiles for three different types of supercell storms, finding that more CAPE was associated to more rainfall only to a certain limit, beyond which the effect was reversed.

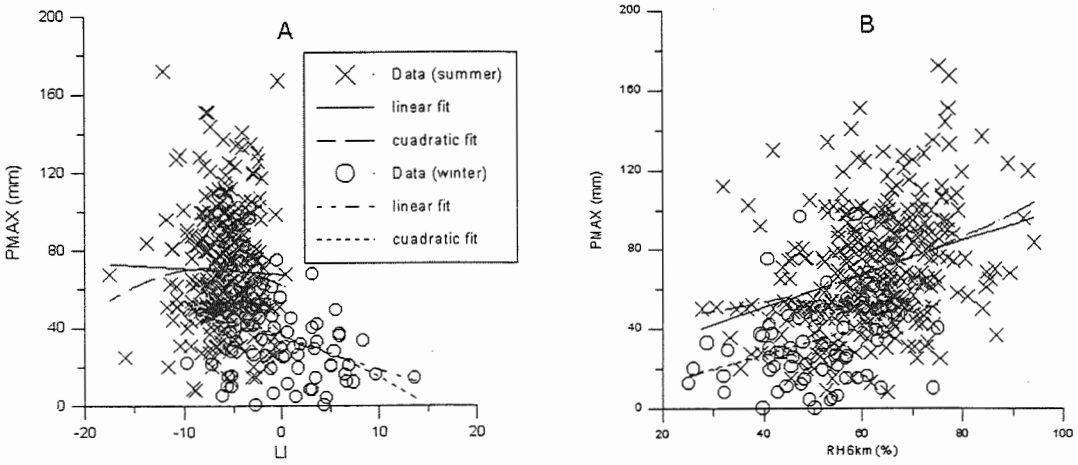

Fig. 1. Scatterplots of Pmax vs LI and Pmax vs RH6km. Summer and winter cases are differentiated, so as the linear and cuadratic fits for each period.

To investigate the possibility to classify rainfall amount as a function of sounding parameters, linear discriminant analysis by forward stepwise regression was applied. A grouping variable was defined for each of the rainfall estimates for each season, as follows:

For the summer:

CLPMAX = 1 if PMAX ≤ 70 mm (=2 otherwise)
CLPMEAN = 1 if PMEAN ≤ 2 mm (= 2 otherwise)
CLAREA = 1 if FRAREA ≤ 0.15(=2 otherwise)

For the winter:

CLPMAXW = 1 if PMAX ≤ 30 mm (=2 otherwise)
CLPMEAW = 1 if PMEAN ≤ 1.5 mm (=2 otherwise)
CLAREAW= 1 if FRAREA ≤ 0.1 (=2 otherwise)

The following discriminant equations were obtained:

F_{CLPMAX} = .051 RH6km –.054 Htmod –2.80
$F_{CLPMEAN}$ = .093 RH6km -.076 ΔTmax –5.01
F_{CLAREA} = .117 RH6km -.088 Htmod –6.54
$F_{CLPMAXW}$= -.187 LI + .402 BS +.017 CINE -.894
$F_{CLPMEAW}$= .125 RH6km +.444 BS + .333 SS –7.08
$F_{CLAREAW}$= .12 K +.46 BS +.030 CINE -.158 SS –3.0

In all cases $F_X > 0 \Rightarrow$ Group 2.

Classification matrices were constructed for each variable and season, in which the real and predicted grouping variables were compared. The best predicted grouping variables were CLPMEAW and CLAREAW, with 82 and 81% of correct choices, while the worst was CLPMAX, with 63% correct choices.

The application of multivariate analysis imposes that variables in the right hand side of the regression equation do not correlate with each other. So, the parameters in the discriminant equations are not necessarily the most informative, but only the most informative which do not correlate with any other parameter in the equation. To evaluate the behavior of each individual parameter as a rainfall covariant, the first criterion is the correlation coefficient. Table 2 shows that many of the sounding parameters have significant correlations with rainfall. The parameters which correlate best with rainfall estimates for the two seasons are both related with moisture: RH6km, and K. For the winter, the other three traditional stability indexes (LI, SI and TT), and also Htmod and LCL, have correlations greater than 0.3 with some or all of the rainfall parameters. In terms of described variance, mean relative humidity describes more than 30% of the variance of rain cover for the summer and 21% for the winter, and from 12% to 21% of the variance of mean and maximum rainfall for the two seasons. The K index describes from 8% to 21% of the rainfall parameters variance, which is consistent with the results of Peppler and Lamb (1989) and higher than most of the references in that paper. The application of the Student test and the evaluation of the individual variability of each parameter allow to assess which of them have significantly different mean values for the

different groups of cases, and for each grouping variable. A range of values was also found for each parameter to be used by itself as a rainfall covariant. Table 3 shows the results for the most informative parameters.

Table 3. Mean and threshold values for the most informative covariants, for each of the grouping variables, and each group

Cov.	Gr. var.	Gr. 1		Gr. 2	
		Mea.	Thre.	Mea.	Thre.
K	CLPMAX	28	≤25	31.5	≥36
	CLPMEAN	25.5	≤25	31.5	≥36
	CLAREA	26	≤27	32	≥34
RH6km	CLPMAX	59	≤54	65	≥71
(%)	CLPMEAN	56	≤57	65.5	≥66
	CLAREA	56	≤57	66	≥66
K	CLPMAXW	14.5	≤9	18	≥26
	CLPMEAW	14	≤13	23	≥26
	CLAREI	14	≤12	21	≥26
RH6	CLPMAXW	47	≤43	53	≥58
(%)	CLPMEAW	47	≤47	57	≥58
	CLAREAW	47.5	≤47	56	≥57
LI	CLPMAXW	1	≥3	-0.8	≤-4
	CLPMEAW	1	≥1	-2.2	≤-4
	CLAREAW	1	≥3	-1	≤-4
SI	CLPMAXW	7.8 n	≥11	6.5 n	----
	CLPMEAW	7.8	≥9	5.5	----
	CLAREAW	7.5 n	≥10	6.2 n	----
TT	CLPMAXW	3,6 n	≤32	37.5	----
	CLPMEAW	3.6	≤34	39	----
	CLAREAW	3.6 n	≤28	38 n	----
Htmod	CLPMAXW	4.2 n	≤2	5 n	----
(km)	CLPMEAW	4.3	≤3	6	≥7.2
	CLAREAW	4.2	≤2.6	5.2	≥7.2
LCL	CLPMAXW	1.52	≥1.7	1.35	≤1.1
(km)	CLPMEAW	1.47	≥1.6	1.31	≤1.1
	CLAREAW	1.52	≥1.6	1.27	≤1.2

Note: All means are different at more than 95% of significance, except the ones with an "n" besides the value. Group discernment and threshold values are significant at the 85%, except the ones with a bar in place of the threshold value.

Some case studies were analyzed, using a one dimensional time-dependent cloud model with parameterized microphysics (Alfonso et al., 1998). The results (not included for lack of space) show that high environmental moisture in convective cloud development favors rainfall by being related to longer cell lifetime, while high instability is related with higher cloud tops. In most cases, the model predicted rainfall qualitatively well, on a high-low scale. Anyway, in some cases with moderate moisture content and instability, high maximum precipitation was measured in the area, and this could not be explained by the model. The model also failed in some cases with very high instability and not so high rainfall.

5. ACKNOWLEDGEMENTS.

This research was developed under financial support of projects No. 97-RG/PHYS/LA, of the Third World Academy of Sciences, and 1999-014 of the Cuban Environment Agency. The paper was prepared under financial support of the UNESCO International Centre for Theoretical Physics. We also thank the Camagüey Delegation of the National Institute for Hydraulic Resources for access to daily rainfall data.

6. REFERENCES

Alfonso L., Martínez D. and Pérez C., 1998: Numerical simulations of tropical convective clouds over Cuba using a one-dimensional and time-dependent cloud model. *Atmospheric Research*, 47-48, 343-354.

Peppler R. A. and Lamb. P. J., 1989: Tropospheric stability and Central North American growing season rainfall. *Mon. Wea. Rev.*, 117: 1156-1180.

Rasmussen E. N. and Straka J. M., 1998:.Variations in supercell morphology. Part I: Observations of the role of upper-level storm-relative flow. *Mon. Wea. Rev.*, 126: 2406-2421.

Riehl H., 1979: *Climate and weather in the tropics.* London. Academic Press. 595 pp.

Rosenfeld D. and A. Gagin., 1989: Factors governing the total rainfall yield from continental convective clouds. *Journ. App. Meteor.*, 28: 1015-1030.

Rivero, R., and G. A. Medvedev., 1987: Peculiarities of the atmospheric aerological during the KETO-82 experiment. regime (In Russian. Spanish translation available at the Atmospheric Physics Center in The Institute of Meteorology, Cuba) In: *Tropicheskaya Meteorologia. Trudy II Mezhdunorodnovo Simpoziuma.*, 135-141.

Simpson J.S., and V. Wiggert., 1969: Models of precipitating cumulus towers. *Mon. Wea. Rev.*, 97: 471-489.

Weisman M.L., and J. B. Klemp, 1982: The dependence of numerically simulated convective storms on vertical wind shear and buoyancy. *Mon. Wea. Rev*, 110, 504-520.

Williams E., and N. Rennó, 1993: An analysis of the conditional instability in the tropical atmosphere.. *Month. Wea. Rev*, 121: 21-36.

EAULIQNG: THE SECOND GENERATION OF CLOUD MICROPHYSICS AND FRACTIONAL CLOUDINESS IN THE CSU GENERAL CIRCULATION MODEL

Laura D. Fowler and David A. Randall

Department of Atmospheric Science
Colorado State University
Fort Collins, Colorado, USA.

1. INTRODUCTION

In the last decade, parameterizations of fractional cloudiness in general circulation models (GCMs) have focused on prognosing consistently water vapor, condensates (mainly, cloud water, cloud ice) and the horizontal fractional area that they occupy in a GCM grid-box (Tiedtke 1993, Sud and Walker 1999).

Until now, our parameterization of stratiform cloudiness (EAUliq) developed for the Colorado State University General Model (CSU GCM; Fowler et al. 1996) assumed that, once formed, clouds occupied the entire area of the GCM grid-box, regardless of the amount of water and ice condensates present in the box. In turn, this assumption forced us to make arbitrary changes in some of the microphysical parameters used. In particular, we had to reduce the autoconversion thresholds to values drastically smaller than those recommended by Rutledge and Hobbs (1983) and Lin et al. (1983).

We have formulated a generalized version of EAUliq. The new version, called EAUliqNG (Randall and Fowler 1999), has the following enhancements:

- A prognostic stratiform cloudiness, similar to that of Tiedtke (1993).
- Separate prognosis of the thermodynamic properties of the cloudy and clear fractions of the GCM grid cell.
- Fully consistent interaction with convection, as convection affects microphysical variable and the cloud amount.
- Diagnosis of distinct vertical motion fields for the cloudy and clear portions of each grid cell, formulated in such a way that the stratiform cloud tends to remain neutrally buoyant through time.

The chief equations driving EAUliqNG are described below.

2. MODEL EQUATIONS

The horizontal grid domain of a grid cell is divided into three sub-regions, as shown in Fig. 1. These are the clear sub-region of fractional area A_{clr}, the sub-region filled with a stratiform cloud of fractional area A_{cld}, and the cumulus sub-region of horizontal area A_{cu}. The total area of the grid-cell, A, is

$$A = A_{clr} + A_{cld} + A_{cu} \tag{1}$$

Following the approach of Margolin et al. (1997), we allow each of the three sub-regions to exchange mass laterally with the other two. This mass exchange can occur inside the grid cell under consideration, and in addition, each sub-region can exchange mass with neighboring grid cells.

Corresponding author's address: Laura D. Fowler,
Dept. Atmospheric Science, Colorado State University,
Fort Collins, CO 80523, USA. E-Mail: laura@atmos.colostate.edu

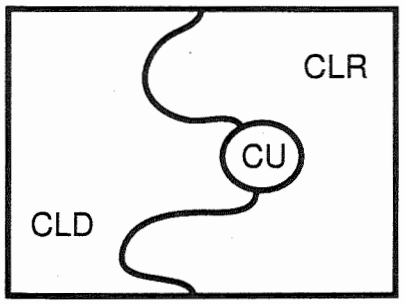

FIG. 1. Schematic showing the horizontal cross section of a grid cell containing a clear region (CLR), a stratiform cloudy region (CLD), and a cumulus region (CU).

Consider an arbitrary intensive variable h, and let S_h denote the source or sink of h, which can include the effects of small-scale turbulence, radiation, and cloud microphysical processes. We can write the following budget equations for each GCM grid-box:

$$\frac{\partial}{\partial t}(mh_{clr}A_{clr}) = E_{cld,clr}h_{cld} + E_{cu,clr}h_{cu} - (E_{clr,cld} + E_{clr,cu})h_{clr} - \frac{\partial}{\partial z}(mw_{clr}h_{clr}A_{clr}) + (S_h)_{clr}A_{clr} \tag{2}$$

$$\frac{\partial}{\partial t}(mh_{cld}A_{cld}) = E_{clr,cld}h_{clr} + E_{cu,cld}h_{cu} - (E_{cld,clr} + E_{cld,cu})h_{cld} - \frac{\partial}{\partial z}(mw_{cld}h_{cld}A_{cld}) + (S_h)_{cld}A_{cld} \tag{3}$$

and

$$\frac{\partial}{\partial t}(mh_{cu}A_{cu}) = E_{clr,cu}h_{clr} + E_{cld,cu}h_{cld} - (E_{cu,clr} + E_{cu,cld})h_{cu} - \frac{\partial}{\partial z}(mw_{cu}h_{cu}A_{cu}) + (S_h)_{cu}A_{cu} \tag{4}$$

In Eqs. 2, 3, and 4, m is the mass of dry air, per unit area. $E_{clr,cld}$ and $E_{cld,clr}$ represent lateral exchanges of mass between the cloud-free and stratiform-cloudy fractions of the grid-box. $E_{cu,clr}$ and $E_{clr,cu}$ ($E_{cu,cld}$ and $E_{cld,cu}$) simulate lateral exchanges of mass between the cloud-free (stratiform-cloudy) and convective environments. The third and fourth terms on the right-hand-side of Eqs. 2, 3, and 4 are vertical mass exchanges and sources/sinks of h. w_{clr}, w_{cld}, and w_{cu} are the vertical velocities in the

cloud-free, stratiform-cloudy, and cumulus sub-regions, respectively.

When applied to EAUliqNG, Eqs. 2 to 4 are solved for the temperature, and water vapor, cloud water, cloud ice, rain, and snow mixing ratios, respectively.

A_{clr}, A_{cld}, and A_{cu} are obtained using the continuity equations corresponding to Eqs. 2, 3, and 4. When setting $h \equiv 1$ and $S_h = 0$ we get:

$$\frac{\partial}{\partial t}(mA_{clr}) = E_{cld,clr} + E_{cu,clr} - (E_{clr,cu} + E_{clr,cld}) - \frac{\partial}{\partial z}(mw_{clr}A_{clr}) \quad (5)$$

$$\frac{\partial}{\partial t}(mA_{cld}) = E_{clr,cld} + E_{cu,cld} - (E_{cld,clr} + E_{cld,cu}) - \frac{\partial}{\partial z}(mw_{cld}A_{cld}) \quad (6)$$

and

$$\frac{\partial}{\partial t}(mA_{cu}) = E_{clr,cu} + E_{cld,cu} - (E_{cu,clr} + E_{cu,cld}) - \frac{\partial}{\partial z}(mw_{cu}A_{cu}) \quad (7)$$

Details on the computation of the lateral and vertical exchange terms, and interactions between the cloud-free, stratiform cloudy, and convective areas of the GCM grid-box can be found in Randall and Fowler (1999). Details on the horizontal advections of the different water species and cloud fractions are also described in Randall and Fowler (1999).

3. SIMULATIONS

Two simulations run with the CSU GCM will be compared. In the CONTROL simulation, our EAUliq parameterization of stratiform cloudiness without fractional cloudiness was used. In the EAUliqNG simulation, our prognostic parameterization of fractional cloudiness was applied. Improvements in the climate of the CSU GCM with EAUliqNG are highlighted.

ACKNOWLEDGMENTS:

This research was sponsored by the National Science Foundation under the grant ATM-9812384, by the U.S. Department of Energy under the grant DE-FG03-95ER61968, and by the National Aeronautics and Space Administration under the grants NAG1-1266 and NAS1-98125.

REFERENCES

Fowler, L.D., D.A. Randall, and S.A. Rutledge, 1996: Liquid and ice cloud microphysics in the CSU General Circulation Model. Part I: Model description and simulated microphysical processes. *J. Climate*, **9**, 489-529.

Lin, Y.-L, R.D. Farley, and H.D. Orville, 1983: Bulk parameterization of the snow field in a cloud model. *J. Climate Appl. Meteor.*, **22** , 1065-1092.

Margolin, L., J.M. Reisner, and P. Smolarkiewicz, 1997: Application of the volume-of-fluid method to the advection-condensation problem. *Mon. Wea. Rev.*, **125** , 2265-2273.

Randall, D.A., and L.D. Fowler, 1999: EAUliq: The next generation. Department of Atmospheric Science Paper no. 673. Department of Atmospheric Science, Colorado State University, Fort Collins, Colorado, 65pp.

Rutledge, S.A., and P.V. Hobbs, 1983: The mesoscale and microscale structure and organization of clouds and precipitation in mid-latitude cyclones. VIII: A model for the "feeder-seeder" process in warm-frontal rainbands. *J. Atmos. Sci.*, **40** , 1185-1206.

Sud, Y.C., and G.K. Walker, 1999: Microphysics of clouds with the Relaxed Arakawa-Schubert scheme (McRAS). Part I: Design and evaluation with GATE Phase III data. *J. Atmos. Sci.*, **56** , 3196-3220.

Tiedtke, M., 1993: Representation of clouds in large-scale models. *Mon. Wea. Rev.*, **121** , 3040-3061.

Corresponding author's address: Laura D. Fowler,
Dept. Atmospheric Science, Colorado State University,
Fort Collins, CO 80523, USA. E-Mail: laura@atmos.colostate.edu

FREEZING DRIZZLE AND SUPERCOOLED LARGE DROPLET (SLD) FORMATION IN STABLY STRATIFIED LAYER CLOUDS: RESULTS FROM DETAILED MICROPHYSICAL SIMULATIONS AND IMPLICATIONS FOR AIRCRAFT ICING

Roy Rasmussen[1] and Istvan Geresdi[2]
[1]National Center for Atmospheric Research,Box 3000,Boulder, CO USA
[2] University of Pecs, Hungary

1. Introduction

It is well established that Supercooled Large Droplets (SLD, cloud droplets > 50 μm diameter) and freezing drizzle (droplets between 200 and 500 μm diameter, subset of SLD) can be a significant safety hazard to aviation due to the potentially dangerous icing it can produce on aircraft. A number of turbo-prop aircraft accidents have been attributed to the formation of ice on un-protected regions of the wing during SLD and freezing drizzle conditions (Marwitz et al. 1996, Pike 1995). Due to its hazardous nature, regions with SLD and freezing drizzle are generally avoided by most pilots if possible. In order for them to do this, however, accurate forecasts of SLD and freezing drizzle are required. Forecast quality, however, is limited by a proper physical understanding of the mechanisms by which SLD and freezing drizzle forms. Freezing drizzle and SLD are generally recognized to form via an all water process through collision-coalescence of cloud droplets at temperatures below freezing, or the so called "supercooled warm rain" process (Ohtake 1963, Kajikawa et al. 1988, Huffman and Norman 1988, Rasmussen et al. 1995, Cober et al. 1996). The major bottleneck to the formation of freezing drizzle and SLD is the creation of cloud droplet sizes greater than 40 μm in diameter in order for the collision efficiency between droplets to be sufficiently high to initiate the collision-coalescence process. Otherwise, the formation of droplets > 40 μm in diameter through diffusional growth alone is a slow process (Pruppacher and Klett, 1997).

The processes causing cloud droplet broadening in stably stratified clouds are currently not well understood. Initial studies suggested that shear induced mixing near cloud top may be responsible for this broadening effect (Pobanz et al. 1994). However, more recent studies have found significant amounts of SLD and freezing drizzle in clouds with none to minimal shear near cloud top (Cober et al. 1996, Bernstein 2000). Since many cases of freezing drizzle formation involve frontal situations, it may be that wind shear is associated with the front and not the formation of SLD or drizzle.

Observational studies by Murakami et al. (1992), Rasmussen et al. (1995), and Cober et al. (1996) have suggested that low concentrations of CCN may be responsible for the rapid broadening of cloud droplets diameters to sizes large enough to initiate the collision-coalescence process in these types of stably stratified clouds. Another possible mechanism for cloud droplet broadening is radiative cooling of the individual cloud droplets (Roach 1976). This effect has been mainly studied in the context of fogs and stratocumulus clouds (Roach 1976, Chen and Cotton 1987, Caughey and Kitchen (1984)). In these types of clouds radiative cooling of the individual drops has been shown to broaden the spectra.

In this paper we evaluate the role of : 1) low Cloud Condensation Nuclei (CCN) conditions, and 2) preferred radiative cooling of large cloud drops as compared to small cloud drops near cloud top, on cloud droplet broadening and subsequent drizzle and SLD formation in stably stratified layer clouds. The evaluation is performed by simulating cloud formation over a two-dimensional idealized mountain using a detailed microphysical model implemented into the NCAR/Penn State MM5 mesoscale model. The height and width of the two-dimensional mountain was designed to produce an updraft pattern with extent and magnitude similar to observed freezing drizzle cases (Rasmussen et al. 1995, Cober et al. 1996, Bernstein 1997, Bernstein 2000). In addition, we also evaluate the effect of the Meyers et al. (1992) and Cooper (1986) methods of ice initiation on freezing drizzle formation

Corresponding Author: Roy Rasmussen
NCAR, Box 3000, Boulder, CO 80307
e-mail: rasmus@ucar.edu

2. Description of the Detailed Microphysical Model

A detailed microphysical scheme was developed to simulate the formation of freezing drizzle and various ice species in stably stratified clouds based on the model of Geresdi (1998). A key improvement over the previous Geresdi (1998) model is the implementation of the moment conserving technique (Reisen 1996) for calculation of the time evolution of the hydrometeor size distributions. The moment conserving technique has been demonstrated to accurately model the evolution of hydrometeor distributions by Tsvion et al. (1999, 1987). The main achievement of moment conserving technique is the prevention of artificial broadening of the hydrometeor distribution by numerical diffusion. In addition, the moment conserving technique conserves mass and number concentration independent of time step and bin size.

The modified model simulates five different types of hydrometeors: water drops, pristine ice crystals, rimed ice crystals, snowflake aggregates, and graupel. Thirty six size bins are used to describe the evolution of the size spectra for each of these five hydrometeor types, with the next largest bin having a mass double that of the previous bin. The mass range for all five hydrometeor types is: 1.5979×10^{-14} - 0.001098 kg, with $m_{k+1} = 2m_k$. Equations are also given for the interaction of the various hydrometeor types. Cloud droplets are initialized based on specified equations for Cloud Condensation Nuclei (CCN) as a function of supersaturation over a flat water surface. In this study we use CCN spectra typical of maritime and continental air masses.

Ice is initiated in the pristine ice category using equations that produce ice by deposition, condensation-freezing, immersion and contact *nucleation*. Two types of equations are used for deposition and condensation freezing; an equation by Meyers et al. (1992) based on laboratory measurements of natural ice nuclei using a continuous flow diffusion chamber, and a fit to in-situ ice crystal measurements by Cooper (1986). A given simulation will use one or the other of these equations. The Meyers equation is given by:

$$N_{i,Meyers} = \exp(-0.639 + 0.1296 S_i)$$

and the Cooper equation by:

$$N_{i,Cooper} = 5.0 \exp(0.304 (T_o - T))$$

where S_i is the supersaturation with respect to ice, T_o is equal to 273.15 K, and T is the ambient temperature in degrees Kelvin. In both cases, pristine ice crystals are initiated only if the temperature is less than –5 C and water saturation is reached. At temperatures less than –27 C both schemes are set to the ice concentration value at –27 C to prevent the formation of unrealistically high values of pristine ice crystals at colder temperatures.

A key new aspect of the model is the inclusion of radiative cooling effects of the drops when calculating diffusional growth.

3. Results

In order to evaluate the above two drizzle formation processes under typical supercooled drizzle conditions, we used a 2D bell shaped mountain to force a mesoscale uplift of 4-10 cm/s over a distance of approximately 200 km. This was achieved with the MM5 mesoscale model using the sounding shown in Fig. 1. This sounding has a moist layer to –10 C, and drying above that level, typical of freezing drizzle soundings. The wind speed impacting the barrier is 15 m/s, resulting in a vertical motion field as shown in Fig. 2. The formation of cloud liquid water (Fig. 3) and freezing drizzle is simulated in the vertical motion field on the upstream side of the mountain (Fig. 4).

Simulations were performed in which the ice phase was turned on and off for both continental and maritime CCN distributions, radiative cooling on and off, and with the Meyers and Cooper ice schemes.

The maximum cloud water and drizzle water content for a cloud with ice processes turned off are shown in Fig. 5 as a function of time from the start of the simulation. Cloud water increases in both the maritime and continental CCN cases in a similar manner during the first hour. After this time, drizzle water starts to form in the maritime simulation, depleting cloud water mixing ratio. As a result, maximum cloud water for the entire simulation is reached after only 2 hours of simulation and has a value of approximately 0.4 g/kg. At the same time, the drizzle water content increases to values near 0.1 g/kg. Thus, the drizzle formation process is relatively rapid in this cloud, with large amounts of drizzle appearing after only two hours of simulation time.

The continental cloud, on the other hand, takes nearly 5 hours to form drizzle amounts comparable to that of the maritime cloud. The cloud water content in this case increases to near 0.75 g/kg before drizzle starts to form. This value is nearly twice the magnitude of the maximum maritime cloud water mixing ratio. This is due to the narrower size distribution and smaller mean

diameter in the continental case, requiring significantly more liquid water in the distribution before the tail of the distribution exceeds 40 μm diameter, while the broader maritime distribution with larger mean diameter requires much less liquid water before the droplets in the tail of the distribution start to exceed 40 μm diameter. Thus, stratified layer clouds with low CCN and warm cloud top temperatures can form drizzle rapidly (in less than 2 hours), while clouds with high CCN takes nearly 5 hours. It is interesting to note, however, that clouds with continental CCN can also form drizzle given sufficient amount of time to grow the tail of the size distribution to sizes larger than 40 μm.

Simulations with the Meyers and Cooper ice initiation schemes show that the above drizzle formation scenario is unaffected by use of the Cooper scheme, while the Meyers scheme produces significantly more ice crystals (factor of 10 more) that deplete the liquid water content and as a consequence significantly reduces the drizzle water content.

Simulations with preferred radiative cooling of large drops as compared to small drops (only at cloud top) revealed that this mechanism effectively broadened the droplet size distribution of the continental cloud near cloud top. However, the effect on the timing and amount of maximum liquid water was relatively small. Thus, processes that act on cloud surfaces, such as cloud top, may not be as effective in producing drizzle as volume processes such as low CCN. The above results have been compared with observed freezing drizzle cases and good agreement was found. Further results will be presented at the conference.

4.0 Acknowledgements

The authors acknowledge the assistance of Eli Karplus, Greg Thompson, and Kevin Manning for this study. This research is in response to requirements and funding by the Federal Aviation Administration (FAA). The view expressed are those of the authors and do not necessarily represent the official policy of the FAA. This research was also supported by the Hungarian Research Fund (number: T30857)

5.0 References

Bernstein, B., T.A. Omeron, F. McDonough, and M.K. Politovich, 1997: The Relationship between Aircraft Icing and Synoptic-Scale Weather Conditions. *Weather and Forecasting*, **12**, 742 762.

Bernstein, B, T.A. Omeron, M.K. Politovich, and F. McDonough, 1998: Surface weather features associated with freezing precipitation and severe in-flight icing. *Atmos. Res.*, **46**, 57 – 73.

Bernstein, B., 2000: Regional and local influences on freezing drizzle, freezing rain and ice pellet events, Accepted for Pubication in Weather and Forecasting.

Chen, C. and W.R. Cotton , 1987: The physics of the marine stratocumulus-capped mixed layer, *J. Atmos. Sci.*, **44**, 2951 – 2977.

Cober, S. G., J.W. Strapp, and G.A. Isaac, 1996: An Example of Supercooled Drizzle Drops Formed through a Collision-Coalescence Process. *J. Appl. Met.*, **35**, 2250 – 2260.

Cooper, W. A., 1986: Ice initiation in natural clouds. AMS Meteor. Monograph, **21**, {R.G. Braham, Jr., Ed.}, Amer. Meter. Soc., Boston, Mass., 29-32.

Geresdi, I., 1998: Idealized simulation of the Colorado hailstorm case: Comparison of bulk and detailed microphysics. *Atmos. Res.*, **45**, 237 – 252.

Huffman, G.J., and G.A. Norman, Jr., 1988: The supercooled warm rain process and specification of freezing precipitation. *Mon. Wea. Rev.*, **116**, 2172 – 2182.

Kajikawa, M., Sakurai, K., Kikuchi, K., 1988. Characteristic features of supercooled raindrops in the midwinter season of Arctic Canada, *J. Meterol. Soc. Japan*, **62**, 393 – 398

Meyers, M.P., P.J. DeMott, W.R. Cotton, 1992: New Primary ice-nucleation parameterization in an explicit cloud model. *J. Appl. Met.*, **31**, 708 – 721.

Marwitz, J., M. Politovich, B. Bernstein, F. Ralph, R.Ashenden and J. Bresch, 1996: Meteorological conditions associated with the ATR72 Aircraft accident near Roselawn, Indiana, on 31 October 1994. *Bull. Amer. Meteor, Soc.*, **78**, 41-52.

Murakami, M. Y. Yamada, T. Matsuo, H. Mizuno, and K. Morikawa, 1992: Microphysical structures of warm-frontal clouds. The 20 June 1987 case study. *J. Meteor. Soc. Japan*, **70**, 877 – 895.

Ohtake, 1963: Hemispheric Investigation of Warm Rain by Radiosonde Data. J. Applied Met., 2, 594 – 607.

Pike, W.S., 1995: Extreme warm frontal icing on 25 February 1994 causes an aircraft accident near Uttoxeter., *Meteor. Appl,*. **2**, 273 – 279.

Pobanz, B. M, J.D. Marwitz, and M.K. Politovich, 1994: Conditions associated with large-drop regions. *J. Appl. Meteor.*, 33, 1366 – 1372.

Pruppacher, H.R. and J.D. Klett, 1997: Microphysics of Clouds and Precipitation. Kluwer Academic Publishers, 945 pp.

Rasmussen, R.M. et al., 1992: Winter Icing and Storms Project (WISP), *Bull. Amer. Met. Soc.*, **73**, 951-974

Rasmussen, R.M., B. Bernstein, M. Murakami, G. Stossmeister, B. Stankov, 1995: The 1990 Valentine's Day Arctic Outbreak. Part I: Mesoscale and Microscale Structure and Evolution of a Colorado Front Range Shallow Upslope Cloud. *J. Appl. Met.*, **34**, 1481 – 1511.

Reisin, T., Z. Levin, and S.Tzivion, 1996: Rain production in convective clouds as simulated in an axisymmetric model with detailed microphysics. Part I. Description of the model. J. Atmos. Sci., 53, p. 497.

Roach, W.T.R., 1976: On the effect of radiative exchange on the growth by condensation of a cloud or fog droplet. *Q.J.R.Meterol. Soc.*, **102**, 361– 372.

Tzivion, S., G. Feingold, and Z. Levin, 1987: An efficient numerical solution to the stochastic collection equation, *J. Atmos. Sci.*, **44**, p. 3139.

Tzivion, S., T. Reisin, and Z. Levin, 1999: A numerical solution of the kinetic collection equation using high spectral grid resolution: A proposed reference. *J. Comp. Physics*, **148**, 527 – 544.

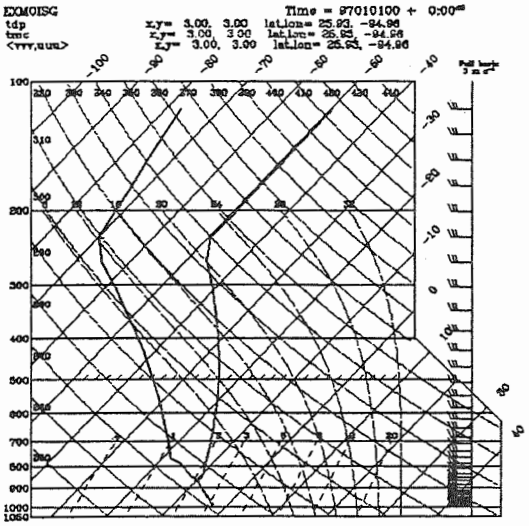

Figure 1 Sounding used to initialize the model

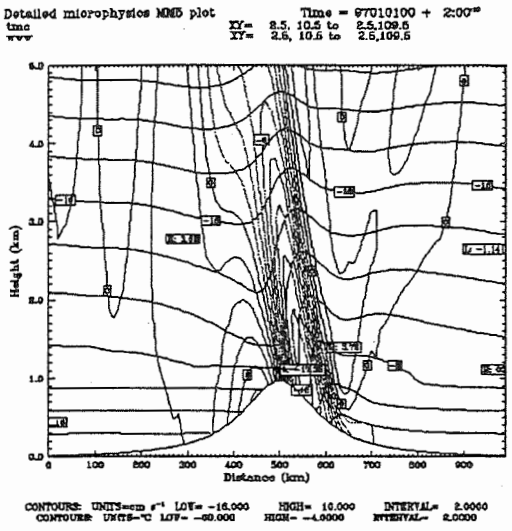

Figure 2 Vertical velocity (cm/s) and temperature C

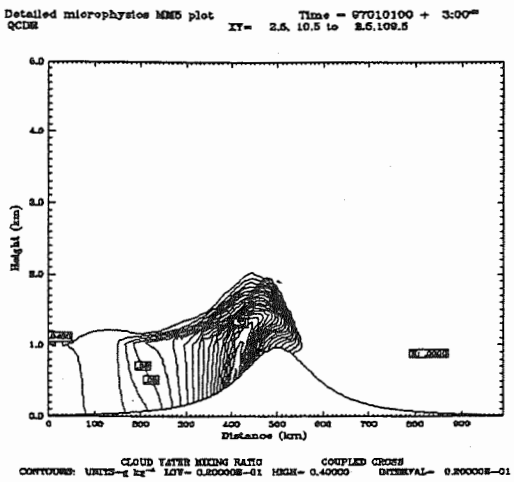

Figure 3 Cloud Water Mixing Ratio at 3 hours

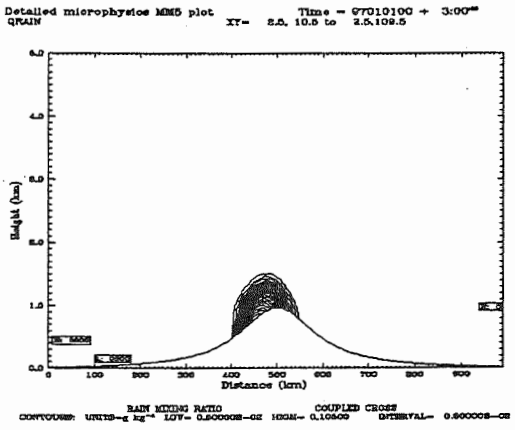

Figure 4 Rain Water Mixing Ratio at 3 hours

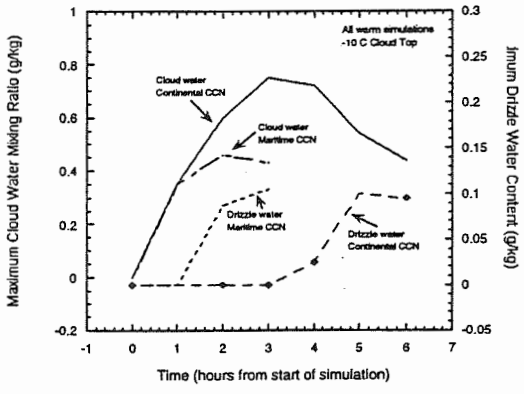

Figure 5 Time series of maximum drizzle water and cloud water mixing ratio for the maritime and continental model simulations

THE INFLUENCE OF SUB-GRID SCALE VARIABILITY OF CLOUDS AND RELATIVE HUMIDITY ON RADIATION IN A CLIMATE MODEL.

J. C. Petch *; J. M. Edwards and M. E. B. Gray

The Met. Office, Bracknell, Berkshire, UK.

1. INTRODUCTION

Many types of clouds, including those described as stratiform, exhibit considerable horizontal variability on the scales less than typical Climate Model or General Circulation Model (GCM) grid boxes (e.g. Hignett and Taylor, 1996; Barker, 1996; Oreopoulos and Davies, 1998). Often, this sub-grid scale variability is represented in GCMs by having cloudy and cloud free regions in the model. Typically, no allowances are made for variability of in-cloud water and ice contents which can have a strong influence on the averaged radiative properties of clouds over a grid box. This variability is likely to be very important when parametrizing the radiative properties of clouds in a GCM and may also be important when considering the influence of radiation on the development of the cloud itself.

There are two main reasons why cloud inhomogeneities can influence domain averaged radiative properties calculated in a GCM or climate model. Firstly, by using a domain averaged cloud field, no allowance can be made for the horizontal transport of photons, thus passing through regions of different cloudiness. This is particularly important at high zenith angles where a cloud can effectively cast a large horizontal shadow. This effect would be missed by any domain average calculation or by any model which uses plane parallel radiative transfer calculations such as a two stream scheme. Recent work has suggested that on the scales of a GCM grid box over periods of a day or more that this effect may not be very important (Fu et al., 2000).

The second influence of the cloud inhomogeneities on radiative transfer is caused by the nonlinear dependence of a clouds optical properties on cloud water and ice contents. This can introduce a systematic bias to the radiative properties of a cloud because the averaged cloud properties will always over estimate the optical thickness of a cloud. Unlike the plane parallel bias, this systematic bias is likely to have a large influence on the scales of a GCM grid box. This problem can be investigated with the use of a plane parallel radiation scheme and is the focus of this study. Figure 1 shows the upward Top of Atmosphere (TOA) solar irradiance for a standard tropical atmosphere with a range of cloud ice contents between 500 and 250 mb. From Figure 1 it can be seen that 2 equal sized clouds which have an ice contents of 0.1 and 0.4 gkg^{-1} would have an average TOA upward irradiance of 620 Wm^{-2}. However, if the average ice content (0.25 gkg^{-1}) is used to calculate the irradiance, it would be 690 Wm^{-2}, an overestimation of 70 Wm^{-2}.

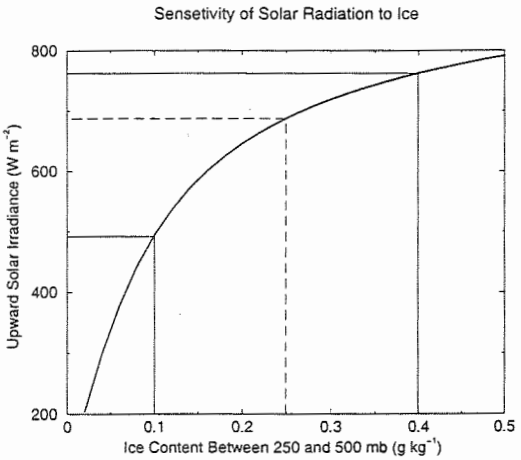

Figure 1. The Influence of various ice contents between 250 mb and 500 mb on TOA upward solar irradiance.

In the work presented here, Cloud Resolving

*Corresponding author's address: Jon Petch, Atmospheric Processes Research, The Met. Office, London Road, Bracknell, Berkshire, RG12 2SZ; E-Mail jpetch@meto.gov.uk

Model (CRM) simulations of a 6 day period of the Tropical Ocean Global Atmosphere-Couple Ocean Atmosphere Response Experiment (TOGA-COARE) have been used to show the influence of radiation on the development of a tropical convective system. Offline calculations on datasets produced by these simulations can then be used to investigate errors in the radiative properties of clouds in GCMs through not representing the horizontal variability of cloud water and ice.

The 6 day period is between 20th and 26th of December, has been used in a model intercomparison project (Krueger and Lazarus, 1999), and is chosen because of its convective nature. The CRM used in this study was the Meteorological Office Large Eddy Model (LEM; Shutts and Gray, 1994). For the results shown here, the model had 60 levels in the vertical, 128 by 128 grid points in the horizontal with a 2 km grid length; this resolution is typical of many other CRM simulations of this region. The CRM used an interactive radiation scheme (Edwards and Slingo, 1996) which included the effect of all hydrometeors in its calculation of the radiative heating rates. The off-line single column radiation calculations described later also used this radiation scheme.

2. The Influence of Radiation on the Convective System

To show the strong influence of radiation on the convective system, the 6 day TOGA-COARE simulation is done with and without radiation included. Figure 2 shows the 6 day time mean upward convective mass flux from the two simulations. For this plot, an updraught is defined as 'convective' if the vertical velocity is greater than 1 ms^{-1}. It is clear from Figure 2 that radiation plays a major role in driving the convective system, particularly notable is the secondary peak in the mass flux between 8 and 12 km. At these altitudes the mass flux with radiation included is over double that of the no radiation simulation.

Several other fields, which will not be shown here, such as hydrometeor content and relative humidity also show large responses to including radiative heating. Given the importance of the radiation on the development of the system, two major issues

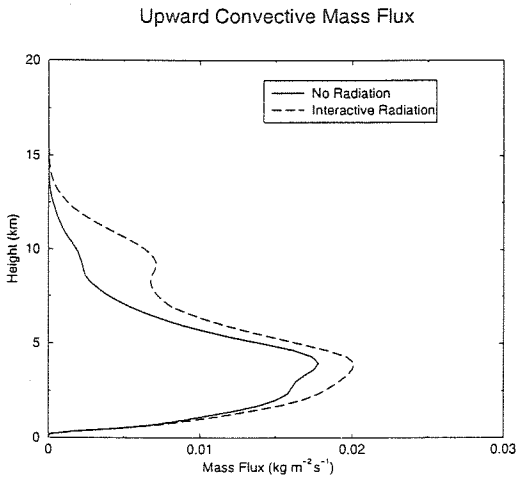

Figure 2. Profile of upward convective mass flux from the 6 day TOGA-COARE simulation with and without radiation included.

related to the parametrization of clouds and radiation in a GCM will be addressed in this report. Firstly, it is important to understand how accurate a GCM calculates the domain average heating without any knowledge of sub-grid scale variability of cloud water. This can be addressed using offline datasets from the CRM and is discussed in the following section. It is also important to consider how the sub-grid scale variability in the radiative heating influences the development of the system. This requires further CRM simulations and is described in section 4.

3. GCM Calculations of Radiative Heating Rates

To investigate the radiative importance of the horizontal variability of cloud water in a GCM, we can use off-line datasets from the CRM and compare the domain averaged heating rates (LEM) with single column (SCM) radiation calculations. The SCM calculation is a single calculation using domain averaged cloud water, cloud fraction, temperature and water vapour fields from the CRM. It is also important to separate out the influence the horizontal variability of cloud water from other potential causes of differences between domain aver-

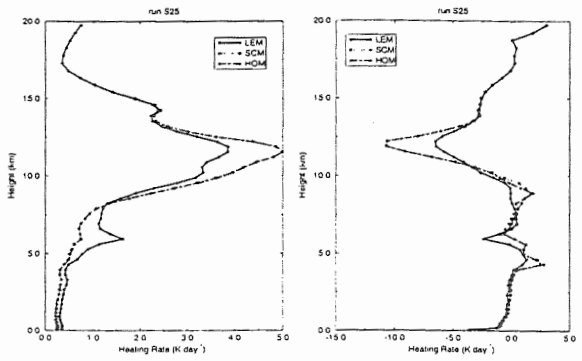

(a) Solar (b) Infra-red

Figure 3. Plots of (a)solar and (b) infra-red heating rates from 0Z on day 3 of the TOGA-COARE simulation. Shown are results from the 2-D LEM, from single column calculations [SCM] and from the 2-D LEM using homogeneous cloud [HOM].

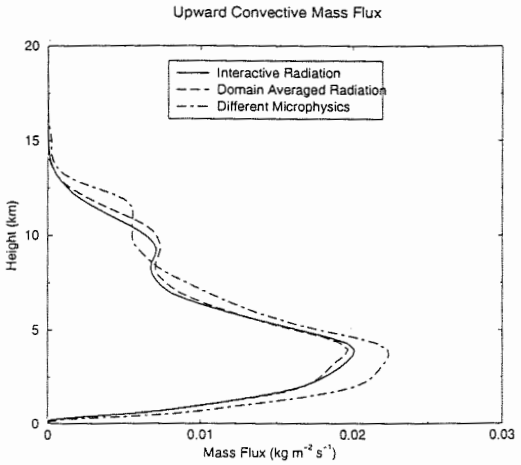

Figure 4. Profile of upward convective mass flux from the 6 day TOGA-COARE simulation with (i) Interactive radiation, (ii) Domain average radiation and (iii) interactive radiation using a different microphysical scheme.

age and single column heating rates. This can be done by doing full radiative transfer calculations on an CRM dataset which has had the cloud 'homogenized' (HOM). This involves changing the cloud water and ice contents on every 'cloudy' grid point in the CRM dataset to be the in-cloud mean value. This technique does not change the domain averaged properties of the cloud.

Figure 3 shows the (a) solar and (b) infra-red heating rates from an off-line radiation calculation using an instantaneous dump from the CRM at 0Z on day 3 (December 23rd 1992). The solar heating was calculated using a zenith angle of 60^o. It can be seen that the infra-red and solar heating rates from the SCM calculation differ significantly from the domain average (LEM). However, when the cloud is homogenized in the CRM dataset (HOM), the heating rates are very close to the SCM calculations. For the solar spectrum (left plot) the HOM and SCM heating rates lie on top of each other suggesting that the errors in the SCM calculations are almost entirely due to the sub-grid scale variability of the cloud water and ice.

Figure 3 shows that a GCM would typically overestimate the atmospheric solar heating rate by about 1.5 K day^{-1}(30%) through much of the cloud and overestimate the infra-red cloud top cooling by 5K day^{-1} (100%). Although not shown here, the TOA upward solar irradiance would be overestimated in a GCM by 80 Wm^{-2} and the OLR underestimated by 25 Wm^{-2}. These errors are very large which is why the horizontal variability of cloud water and ice in a GCM should be parametrized using techniques such as those suggested by Barker et al. (1996).

4. The Influence of The Distribution of Radiative Heating on the Convective System

In this section, two 6 day simulations of TOGA-COARE are compared, both with interactive radiation. In one run, the radiative heating is calculated and applied locally at every grid point in the CRM, as was done in section 2. This is then compared to a run where the radiation is calculated at every point but then the domain average of the heating rate is applied at all points. The difference in these will show how the horizontal variability in the radiative heating rate effects the convective system.

Figure 4 shows the 6 day mean upward convective mass flux for interactive radiation (solid line) and domain average radiation (dashed line) from

the TOGA-COARE simulation. Also included for comparison is a run with a change to the fall rate of ice in the microphysical scheme (dot-dashed line). From Figure 4 it can be seen that the influence of the sub-grid scale variability in the radiative heating is to reduce the mass flux above about 6 km and increase it below this level. However, the changes in the mass fluxes are small (<5%) and when compared with changes due to the fall rate of ice in the microphysics are not significant. This suggests that in the modelling of a tropical convective system it is important to get the domain average radiative heating rate correct but the sub-grid sale distribution of this is less important.

5. Acknowledgements

The authors would like to thank Steve Cusack and Steve Derbyshire for help during this work. The development of the radiation code used in this work was supported by DETR under contract PECD 7/12/37.

6. References

Barker, H. W., 1996: A parametrization for computing grid-averaged solar fluxes for inhomogeneous marine boundary layer clouds. Partă1: Methodology and Homogeneous Biases. *J. Atmos. Sci.*, **53**, *2289-2303*

Barker, H.W., B.A. Wielicki and L. Parker, 1996: A parameterization for computing grid-averaged solar fluxes for inhomogeneous marine boundary layer clouds. Part II: validation using satellite data. *J. Atmos. Sci., 53, 2304-2316*

Edwards, J. M. and A. Slingo, 1996: Studies with a flexible new radiation code I: Choosing a configuration for a large scale model. *Q. J. R. Meteorol. Soc., 122, 689-719*

Fu, Q., M. C. Cribb, H. W. Barker, S. K. Krueger and A. Grossman, 2000: Cloud Geometry Effects on Atmospheric Solar Absorption. *J. Atmos. Sci. (In press)*

Hignett, P. and J. P. Taylor, 1996: The radiative properties of inhomogeneous boundary layer cloud: Observations and modelling. *Q. J. R. Meteorol. Soc., 122, 1341-1364*

Krueger, S. K. and S. M. Lazarus, 1999: Intercomparison of multi-day simulations of convection during TOGA COARE with several cloud-resolving and single-column models. *Proceedings of the CLIVAR/GEWEX COARE98 Conference, Boulder, CO. 351-352.*

Oreopoulos, L. and R. Davies, 1998: Plane parallel albedo biases from satellite observations. Part 1: Dependence on resolution and other factors. *J. Climate, 11, 919-932*

Shutts, G. J. and M. E. B. Gray, 1994: A numerical modelling study of the geostrophic adjustment process following deep convection. *Q. J. R. Meteorol. Soc., 120, 1145-1178.*

The Intercomparison of numerical cloud models with INTACC data.

D. Figueras-Nieto , J. Cardwell and C.P.R. Saunders
Physics Department, UMIST, Manchester, M60 1QD

1. INTRODUCTION

Ice crystals play a major role in our skies. Apart from their effect on precipitation which is well documented it is also thought that they could affect the thermodynamics and dynamics of clouds through latent heat release. Another effect which has been recently been spoken about is the effect of ice crystal on the earth's radiation budget, which is vital for climate studies.

In the recent literature there has also been some debate on the importance of ice crystal sizes and shapes. There has also been a debate on what type of crystals form most of the clouds. It is the main aim of this project to look at the importance of the different crystal shapes in the total ice content of the cloud. It is clear that at different temperatures the habit of crystals changes and that the growth rate of ice crystals is dependent on the habit. However, it is not clear what happens if a crystal starts to grow in a specific habit and then is moved to a different habit growth region.

2. THE INTACC PROJECT

In September and October 1999 the Meteorological Office Hercules C-130 flew several missions in the North of Sweden under the project scheme An Investigation Into the Interaction of Aerosol and Cold Clouds (INTACC). The aim of the flights was to look at how ice crystals are formed in the stationary orographic cirrus clouds associated with mid-latitude frontal systems.

One of the main objectives of the INTACC project was to develop parametrisations of the glaciation processes in clouds for inclusion in large scale models, but to achieve this aim we first need to look at cloud models. This paper looks at two different microphysics explicit models and compared their respective outputs with the data obtain from the campaign.

3. THE MODELS

The first model used is the UMIST Multilayer model with explicit mixed phase microphysics. The first model as the name suggests is a mixed phase model with variable bin size. For primary nucleation it uses the Meyers *et al.* (1992) scheme for heterogeneous nucleation and the Heymsfield and Sabin (1989) scheme for Homogeneous nucleation. It also includes the Hallet-Mossop process as a secondary nucleation process. It also uses the capacitance model for the diffusional growth of ice crystals considering only plates. The Model also includes riming and the Korvetz and Olund (1969) aggregation scheme.

The second model is a single layer model with explicit microphysics and multiple ice crystal shape considerations. This single layer model considers 11 distinct growth regions under 5 different crystal shapes, which include both different shaped plates and columns. It uses the same bin arrangement and riming scheme as the

Corresponding author's address: Daniel Figueras-Nieto, Physics Department, UMIST, PO BOX 88, Manchester, M60 1QD, UK; e-mail: mccphdf2@stud.umist.ac.uk

first model. It only includes primary nucleation under the Meyers *et al.* (1992) scheme and the Heymsfield and Sabin(1969) scheme as adapted from Spice *et al.* (1999), but neglects secondary nucleation schemes as they were thought to have minimal consequences at the level of cirrus clouds.

The Second model has also closely looked at the different ice crystal terminal fall velocity schemes.

Three schemes where compared:

- Ji (1991) and Wang and Ji(1992)
- Miller and Young (1979)
- Middleton (1971)

As it can be seen from figure 1 the three models give similar results. It has been subsequently found that the scheme of Ji (1991) and Wang and Ji(1992) is only valid for relatively small crystals and would not be able to be used for a full cloud model.

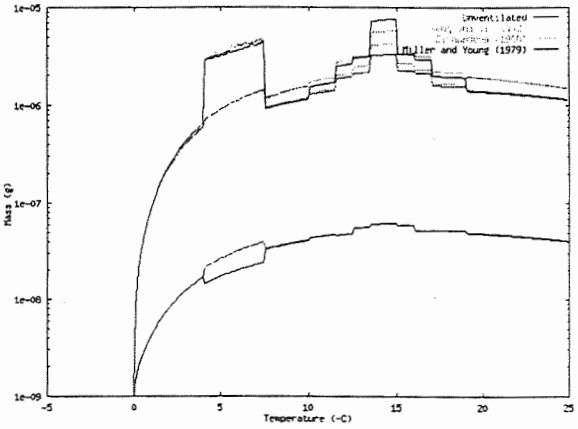

Figure 1 *Graph of Mass versus Temperature between 0°C and -25°C for the three ventilation schemes as well as the unventilated case after 60s and 600s into the model run dt=0.1s.*

4. EXAMPLE CASE

One of the Cases studied is the Case A728 R5.2 which represents a train of wave clouds at a height of approximately 4100m. The Starting Relative Humidity is of 95% at 4100m with a temperature of –19°C. From the figures below we can first see the temperature variation with time. It can clearly be seen that the parcel follows a wave pattern as is expected to exist in the lee of hills

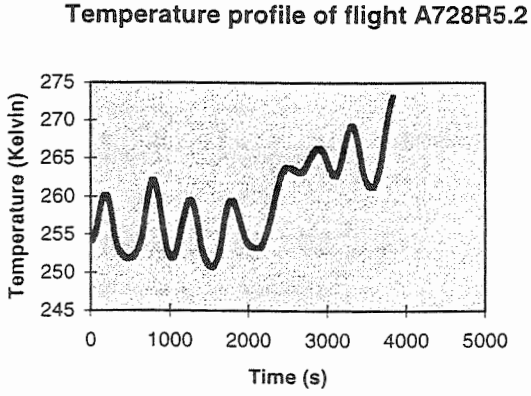

Figure 2 *Profile of the Temperature versus time for the A728R5.2 case.*

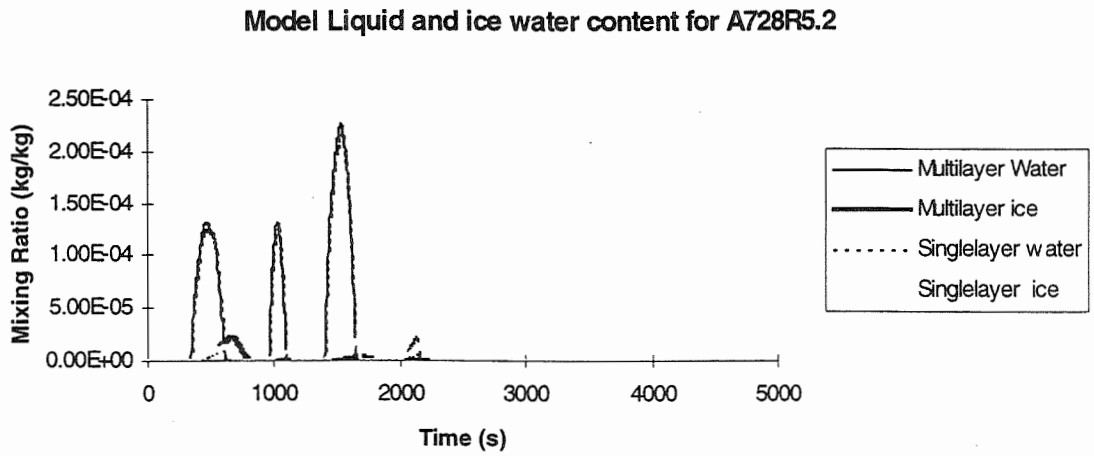

Figure 3 *Plot of the Models output of Ice water and liquid water content of the parcel for the A278R5.2 case.*

Figure 3 shows the ice water content and the Liquid water content of both models. We can see that both models see four clouds. In the Case of the multi-layer model two of those clouds are only constituted by liquid water, however, the single layer model does give some ice in this two clouds. The other large difference between the output of both models is in the forth cloud where the multi-layer model suggest that this cloud is liquid water only while the single layer model suggest that it is mainly ice. Nonetheless in both cases we can see that ice trails the water content which would suggest that the nucleation is mainly due to contact nucleation instead of deposition nucleation. Comparing figure 2 and 3 shows that the clouds follow closely the temperature profile as is expected for wave clouds.

5. REFERENCES

Heymsfiled A.J. and Sabin R.M., 1989: Cirrus Crystal Nucleation by Homogeneous Freezing of Solution Droplets, *J. Atmos. Sci.*, **46**, 2252-2264

Ji W. 1991: *PhD thesis*, Dept. Met., Univ Wisconsin

Korvetz A and Olund B. 1969: The effect of oalecence on rain formation in a cloud of finite vertical extent, *J. Atmos. Sci.*, **26**,1060-1065

Meyers M.P., DeMott P.J. and Cotton W.R. 1992: New Primary Ice-Nucleation Paremeterizations in an Explicit Cloud Model, *J. App. Met.*, **31**, 708-721.

Middleton J.R. 1971: *A numerical model of ice crystal growth within a predicted cap cloud*, **Report AR101**, University of Wyoming, pp.33

Miller T.L. and Young K.C. 1979: A numerical simulation of ice crystal growth from the vapour phase, *J. Atmos. Sci.*, **36**, 458-469

Spice A., Johnson D.W., Brown P.R.A., Darlinson A.G. and Saunders C.P.R. 1999: Primary ice-nucleation in orographic cirrus clouds: A numerical simulation of the microphysics, *Quart. J. Royal. Met. Soc.*, **125**, 1637-1667

Wang P.K. and Ji W. 1992: A numerical Study of the Diffusional Growth and Rimming Rates of Ice Clouds, *Proceeds. 12th Int. Conf. Clouds Precip.*, Montreal, Canada, 76-77

SENSITIVITY STUDIES WITH A NUDGED VERSION OF THE ECHAM4 GENERAL CIRCULATION MODEL FOR THE PURPOSE OF CLOUD VALIDATION

Hans-Stefan Bauer and Lennart Bengtsson

Max Planck Institute for Meteorology, Bundesstrasse 55, 20146 Hamburg, Germany

1 INTRODUCTION

About 60 % of the Earth's surface is covered by clouds. They exert a major impact on the hydrological cycle and affect the dynamics of the atmosphere through complex coupling between radiative, thermodynamic, and dynamic processes. The different treatment of cloud processes in GCMs is still one of the main reasons for their differences in climate sensitivity (Cess et al., 1996).

Due to the appearance of clouds over a wide range of spatial scales, many of them smaller or even much smaller than the normal grid boxes of today's climate models, it is necessary to parameterize clouds and their effects on the climate system. Although the horizontal resolution is going to be higher in future model versions due to more powerful computers, microphysical processes as well as the radiative effects of clouds will remain highly parameterized. Therefore the continuous development of parameterization schemes is one of the main targets in climate modeling.

For climate models validation is only done for long-term means, for example by comparing to a monthly mean value of cloud cover and liquid water. This temporal averaging hides model weaknesses occurring on shorter time scales. In this study the development of synoptic-scale cloud systems in the general circulation model ECHAM4 will be investigated in a high temporal and spatial resolution.

As examples the development of an extraordinary strong East Coast storm between the 12th and 14th of March 1993 (hereafter referred to as "blizzard case") and a blocking situation over the North Atlantic ("blocking case") are investigated.

To enable the comparison with "real" synoptic systems, it is necessary to force the model to the observed state. Therefore a dynamical adjustment based on the nudging technique (Krishnamurti et al., 1993; Jeuken et al., 1996) is used. It provides the model with excellent spin-up characteristics compared to a standard data assimilation by adding a small, non-physical relaxation term to the model equations at every time step rather than a strong impact every few hours, as it is done in todays forecast systems. This ensures a more gradual forcing of the model dynamics, reducing the excitation of gravity waves due to the forcing.

Compared to observations, the synoptic-scale features are well reproduced by the model for both synoptic situations. This is true even for variables which are not adjusted to the observed state, such as for the different precipitation patterns. The general features of the horizontal and vertical cloud distribution are reproduced for the development of cyclone. Nevertheless, systematic differences as compared to observations of ISCCP occur. The model underestimates clouds in low and middle levels of the troposphere and therefore total cloud amounts. Low-level clouds are most obviously underestimated behind the cold front of the developing cyclone. The underestimation of mid-level cloudiness seems to be a more general feature, which occurs in frontal as well as non-frontal regions. On the other hand, thin upper-level cirrus anvils in pre-frontal regions seem to be overestimated. In the blocking situation larger differences to the observations occur, since even the distribution of low level clouds is different as compared to ISCCP observations.

In section 2 the experiments are described briefly before the results of the comparisons are presented in section 3. In section 4 main conclusions from the experiments are given.

Corresponding author's address: Hans-Stefan Bauer, Max Planck Institute for Meteorology, Bundesstrasse 55, 20146 Hamburg, Germany
E-mail: stefan.bauer@dkrz.de

2 EXPERIMENTS

The sensitivity studies, described in the following sections, are carried out to investigate the influence of different cloud descriptions on the repre-

sentation of synoptic-scale cloud systems.

In the first experiment the standard stratiform cloud scheme is replaced by the newer, more sophisticated scheme PCI, developed by Lohmann and Roeckner (1996). It treats cloud liquid water and cloud ice with two different prognostic equations, including more physical processes as compared to the CONTROL scheme.

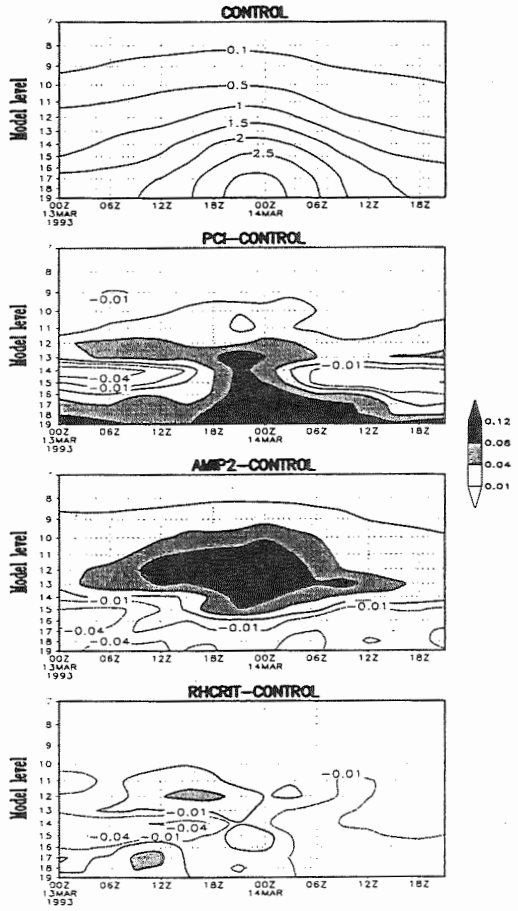

Figure 1: Height-time section of the specific humidity $[gkg^{-1}]$ (spatially averaged over the region 85°W to 65°W and 35°N to 55°N in which the strongest development of the cyclone occur) in the blizzard case of the CONTROL simulation and differences to the sensitivity studies. In shaded regions of the difference plots larger values occur in the sensitivity study, while lower values are simulated in contoured regions. Contours are drawn for -0.08, -0.04, -0.01, 0.01, 0.04, 0.08 and 0.12 gkg^{-1}.

The second experiment is a simulation using the changes with respect to AMIP2. A large part of the introduced changes is expected to have no influence on the investigated systems, either due to the too short integration time or due to a small influence in midlatitudes. Of particular importance are a changed numerical implementation of parts of the cloud scheme (Lenderink et al., 1998), a stronger detrainment of convective cloud water into the level above the main detrainment layer and different values for some of the tuning parameters used in the cloud scheme.

In the third experiment the vertical profile of the "critical relative humidity" in the cloud scheme is changed as compared to the CONTROL scheme. It determines the partial cloud cover within the grid box and therefore the onset of condensation. It is changed from an exponential to a polynomial profile with the intention to increase the amounts of low and mid-level clouds and to impede condensation in the upper troposphere. This would lead to a better agreement with ISCCP observations.

All experiments are carried out in the T106 horizontal resolution for both synoptic situations. They are started a few days in advance of the developing system, so that the atmosphere can reach a new balanced state.

3 RESULTS

The experiments exert virtually no changes on the representation of the large-scale dynamics. On the other hand systematic differences occur in the representation of cloud related processes.

The more sophisticated **PCI** scheme (Lohmann and Roeckner, 1996) leads to a moister lower troposphere. This is true for the specific humidity (Figure 1) as well as for the liquid water content (Figure 2). As a consequence larger cloud amounts are simulated in the lower troposphere, improving the representation of clouds in the blizzard and especially in the blocking case (Figure 3). Furthermore, an enhanced precipitation efficiency in middle levels of the troposphere is simulated, removing moisture from the troposphere more efficiently than in the CONTROL simulation. This is illustrated by Figure 2, showing larger amounts of cloud liquid water in middle levels of the troposphere and smaller values in the upper troposphere during the strongest development of the cyclone. Therefore, cloud amounts in the upper-troposphere are reduced. An intensification of the precipitation efficiency in the middle troposphere is therefore a feasible method to reduce the overestimation of cirrus in the upper troposphere. On the other hand

the removal of ice crystals is reduced in the PCI scheme. The reason for this is, that the precipitation development over the ice phase is less efficient as compared to the sedimentation of ice crystals in the CONTROL scheme for small amounts of ice crystals (Lohmann and Roeckner, 1996b). Before and after the strongest development of the cyclone, larger amounts of cloud ice occur in the upper troposphere.

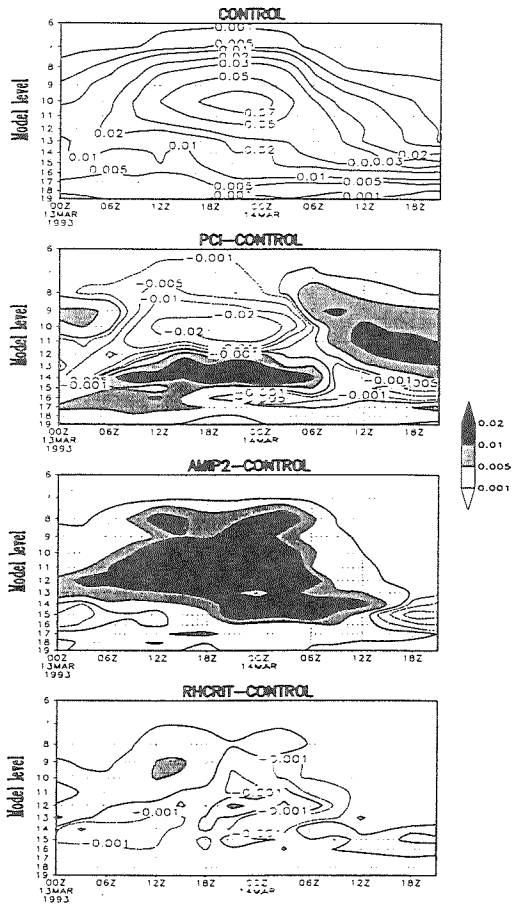

Figure 2: Same as Figure 1 but for the cloud water content (liquid + ice) $[gkg^{-1}]$. Contours are drawn for -0.02, -0.01, -0.005, -0.001, 0.001, 0.005, 0.01 and 0.01 gkg^{-1}.

AMIP2 simulates a moister middle and upper troposphere in frontal regions (Figures 1 and 2). Therefore, clearly larger cloud amounts are simulated in the three cloud layers of the developing cyclone. This leads to well represented cloudiness along the fronts with consistent overcast sky. The modified description of the detrainment of convective cloud water leads to higher cloud tops along the cold front during the life-cycle of the extratropical cyclone (not shown). This agrees better to ISCCP observations. On the other hand, AMIP2 induces the smallest changes into the cloud distribution in the blocking situation. This is a surprising result, since Lenderink et al. (1998) introduced the numerical changes to improve the representation of stratocumulus clouds.

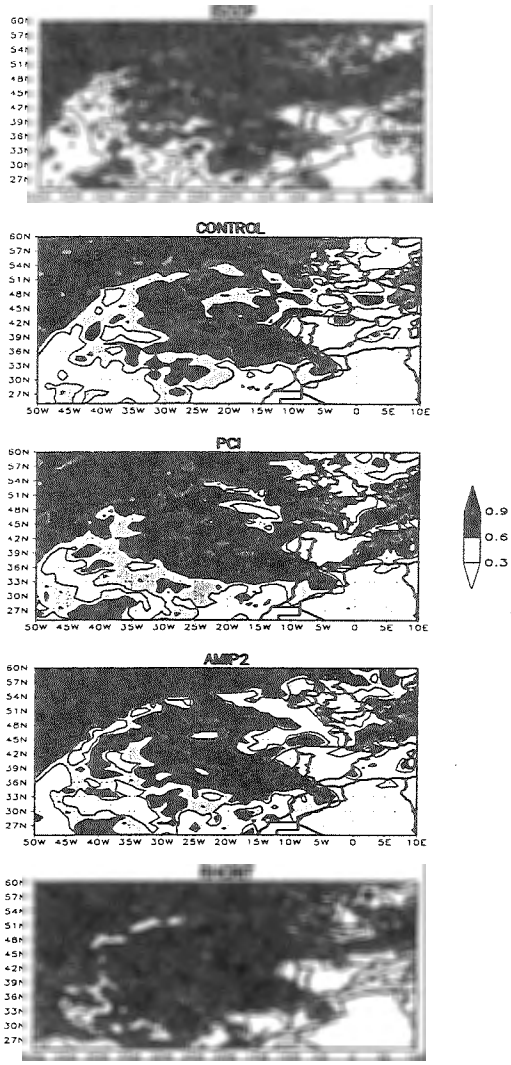

Figure 3: Total cloud cover [*fract.*] for one time step in the blocking case of ISCCP DX, the CONTROL simulation and the different sensitivity experiments [12Z, 19th of February 1993].

In the **RHCRIT** experiment, the changed condensation profile leads to a strongly improved cloud

distribution in the blocking case (Figure 3). Furthermore, the fastest reaction to the forcing from the environment is introduced illustrated by the strongest diurnal cycle in the representation of low-level clouds (not shown). This is not surprising, because smaller changes of the relative humidity are necessary to cause changes in cloud cover.

In the blizzard case the smallest changes of all experiments are induced. The specific humidity is slightly enhanced in the lower and upper troposphere in the first half of the development. In the second half on the other hand a slight reduction occurs (Figure 1). The cloud water content (Figure 2) is slightly enhanced in the middle and upper troposphere in the first part of the development, while enhancements occur in the lower troposphere after the strongest development of the cyclone.

However, this leads to frontal regions being more pronounced, in accordance with cloud optical thickness observations of ISCCP. This demonstrates, that midlatitude cloudiness in lower and middle levels of the troposphere is very sensitive to the condensation profile and that the profile used in CONTROL simulation might be the cause for the erroneous cloudiness. However, the changed profile does not reduce the overestimated cloudiness in the upper troposphere, indicating that it is stronger influenced by other processes such as for example the sedimentation of ice crystals. However, the influence of the changed condensation profile in the upper troposphere is larger in the tropics (Roeckner, personal communication).

4 CONCLUSIONS

In this investigation the representation of synoptic-scale cloud systems in the ECHAM4 model using different cloud descriptions has been investigated. It was the purpose to find changes in the cloud description which clearly improves the representation of clouds.

All experiments lead to an improved representation of clouds. But their influence on the different cloud levels and the two synoptic situations is different. Therefore it is not possible to draw a general conclusion about what is the best change for a most realistic representation of clouds. While RHCRIT leads for example to the most realistic representation in the blocking situation, its influence in the blizzard case is relatively small (but positive). AMIP2 on the other hand strongly improves the cloudiness in the blizzard case while smallest (but also positive) changes are introduced in the blocking case. PCI improves the representation of the blocking case, whereas it shows some weaknesses in the blizzard case.

An encouraging result is that the changed condensation profile in the RHCRIT experiment, which is a small modification as compared to the other two experiments, leads to positive changes in both synoptic situations, in particular in the blocking situation.

5 ACKNOWLEDGMENTS

The ISCCP DX data were obtained by the NASA Langley Research Center EOSDIS Distributed Active Archive Center.

6 REFERENCES

Cess, R. D. et al., 1996: Cloud feedback in atmospheric general circulation models. An update. *J. Geophys.Res.*, **101**, 12791-12794.

Jeuken, A.B.M., P.C. Sigmund, L.C. Heijboer, J. Feichter and L. Bengtsson, 1996: On the potential of assimilating meteorological analysis in a global climate model for the purpose of model validation. *J. Geophys. Res.*, **101**, 16939-16950.

Kocin, P.J., P.N. Schumacher, R.F. Morales Jr. and L. W. Uccellini, 1995: Overview of the 12-14 March 1993 superstorm. *Bull. Amer. Meteor. Soc.*, **76**, 165-182.

Krishnamurti, T.N., J. Xue, H. Bedi, K. Ingles and D. Oosterhof, 1991: Physical initialization for numerical weather prediction over the tropics. *Tellus*, **43AB**, 53-81.

Lenderink, G., E. van Meijgaard and A.A.M. Holtslag, 1998: Evaluation of the ECHAM4 cloud turbulence scheme for stratocumulus. Preprints 98-13, KNMI, De Bildt, The Netherlands, submitted to *Contributions to Atmospheric Physics.*

Lohmann, U. and E. Roeckner, 1996: Design and performance of a new cloud microphysics scheme developed for the ECHAM general circulation model. *Clim. Dyn.*, **12**, 557-572.

Lohmann, U. and E. Roeckner, 1996b: Influence of different parameterizations of ice clouds on climate sensitivity in a general circulation model. *Proceedings of the 12th International Conference on Clouds and Precipitation*, 1228-1231, Zürich, Switzerland.

EVALUATION OF THE CARACTERISTICS OF MIDLATITUDE CYCLONIC CLOUD SYSTEM SIMULATED IN A GENERAL CIRCULATION MODEL

Cheng-Ta Chen[1] AND Erich Roeckner[2]

[1]Dept. of Earth Sciences, National Taiwan Normal University, Taipei, Taiwan
[2]Max Planck Institute for Meteorology, Hamburg, F. R. Germany

1. INTRODUCTION

The evolution of extratropical cyclone and the distribution of cloud and precipitation associated with frontal system have long been the focus of synoptic meteorology. Studies and conceptual models depict the air-flow pattern and rainbands associated with the development of midlatitude circulation system can be found from the early Norwegian school (Bjerknes and Solberg, 1926) to the more recent review papers and textbooks (Houze and Hobbs, 1982; Cotton and Anthes, 1989; Carlson, 1991; Houze, 1993; To name a few). With the aid of recent compilation of satellite cloud climatology, the cloud structure associated with midlatitude synoptic-scale system has been revisited from a climatological perspective in the work by Lau and Crane (1995; hereafter LC). The composite picture of satellite cloud patterns and the concurrent atmospheric dynamics are found in good agreement with traditional conceptual frameworks for organization of cloud properties near the midlatitude frontal zone (LC). Since the prognostic cloud water scheme is now used in many current generation of general circulation model (Sundquist, 1978; Tiedtke, 1993 and many others), the organization of cloud properties associated with the midlatitude circulation system in the model can be traced in the same fashion and evaluated with observations.

It is expected to find some discrepancies in the model cloud simulation due to the highly parameterized cloud schemes used in the general circulation model (GCM). They are also quite model dependent (Weare et al., 1995). However, it is of interest to know, from GCM's perspective, what are the general characteristics of cloud systems produced in the model's large-scale dynamical and moisture fields using the carefully designed cloud parameterization. It may be different from the current knowledge of observed cloud fields associated with circulation system. The information of cloud system evolution, such as revealed in this study, would provide some valuable insights for the modification of cloud scheme in the GCM from cloud system model's view. Moreover, the complete hydrologic, and dynamical picture from the model integration can clearly depict not only the atmospheric structure and cloud fields, but also the impact of the circulation system on the ambient moisture transport and energy distribution.

2. MODEL DATA

The model data used in this study are taken from the fourth generation atmospheric GCM at Max Planck Institute for Meteorology (ECHAM4). A detailed model description and the simulation of present-day climate in ECHAM4 have been documented by Roeckner et al. (1996).

The model has been integrated with monthly observed sea surface temperature (SST) and sea ice for the period 1979-1993. The model data analyzed in this study are limited to the 7 year period between 1986 and 1993. The length of data-analyzed period is the same as in LC. It is easier for the intercomparison. For study focused on the synoptic-scale midlatitude cyclone, it is also quite ample to collect enough events. The structure of atmospheric circulation is inferred from model's daily mean horizontal wind, pressure velocity, temperature, geopotential height, specific humidity, cloud water content at 1000, 925, 850, 700, 500, 400, 300, 250, 200, 150, 100, 70, 50 hPa interpolated from the hybrid vertical levels. The data grids have a horizontal resolution of roughly 2.8° in latitude and longitude. In addition to these level data, the daily mean precipitation, total cloud cover, total precipitable water, total cloud water path, energy fluxes are also obtained for a more complete depiction of interactions among circulation, water, and energy cycle.

3. CHAHARACTERISTICS OF TEMPORAL AND SPATIAL VARIABILITY OF CLOUD PROPERTIES IN THE EXTRATROPICS

3.1 Time series, frequency distribution function

The time series of daily mean total cloud water path (CWP, hereinafter; CWP represents vertical integrated cloud water content) are shown in Fig. 1 for the winter half year (from October to March) for the period 1986-1993 at a grid point (38°N, 65°W) situated in the North Atlantic storm track region. There are strong fluctuations in the total cloud water path during the year. The "spiky" appearance of CWP time series suggest a discrete process being alternately switched on and off at typical time interval of 2-8 days. By diagnosing the properties of cloud and circulation fields common to these pulse-like episodes at reference dates and subtracting the time-mean values in the background, we can highlight the temporal and spatial

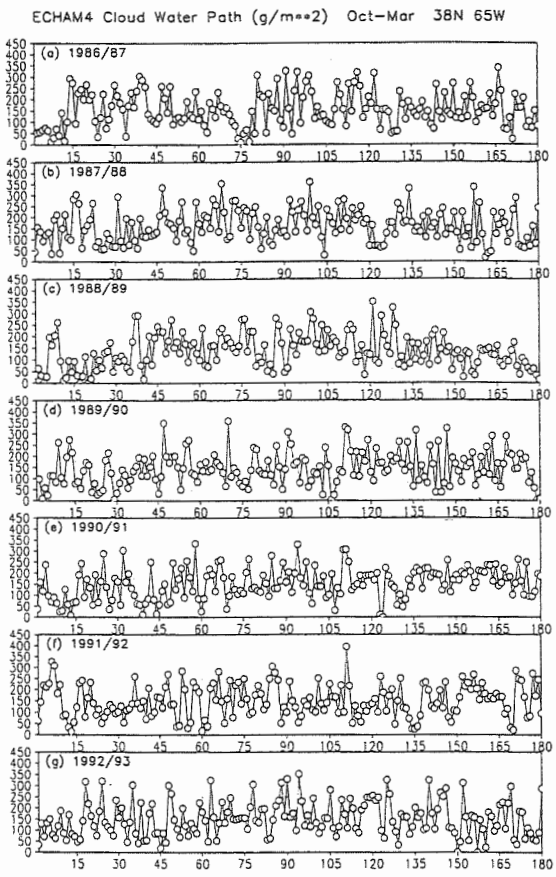

Fig. 1 Time series of daily means of simulated cloud water path at 38N, 65W during winter half year of (a) 1986/87, (b) 1987/88, (c) 1988/89 (d) 1989/90, (e) 1990/91, (f) 1991/92, and (g) 1992/1993.

variability in the cloud and circulation fields associted with the larger CWP events in the model

3.2 Composite charts

The composite chart of CWP, as constructed by arithmetic averaging over the chosen key dates (hereafter referred to as "day 0"), obtained from the above method, is shown in the middle panel of Fig. 2. To describe the temporal evolution of individual feature in these patterns, the composite procedure has been applied to the data for the day before day 0 (hereafter referred to as "day 1", see Fig. 2a), and the day after day 0 ("day +1", see Fig. 2c). For all patterns shown in Fig. 2, the composite signals are presented as departures from the local background level, which is estimated by 5 days mean CWP values centered at day 0.

The area of enhanced CWP centered at reference site on day 0 (Fig. 2b) is more like a circle with a northwest extension as compared to the southwest-northeast orientation in the observed cloud optical depth enhancement (LC). The radius is about 1000km. The shape of this feature is resemble to the familiar cloud shield associated with a typical occluded midlatitude frontal system often seen in the satellite imagery. The negative CWP zones located on the two size of positive CWP area are also with a similar round shape with weak extensions on the southwest and northeast directions. The characteristic wavelength and the propagation speed of this composite pattern are approximately 4000-5000 km and 12 ms^{-1}, respectively. These wave structures are similar to those in LC. Although in principle the simulated CWP and retrieved cloud optical depth should be proportional to each other, they are not equivalent due to the nature of different data sources. In addition, there are variations in the composite methods used in two studies. It's expected to obtain some differences in the patterns of cloud properties.

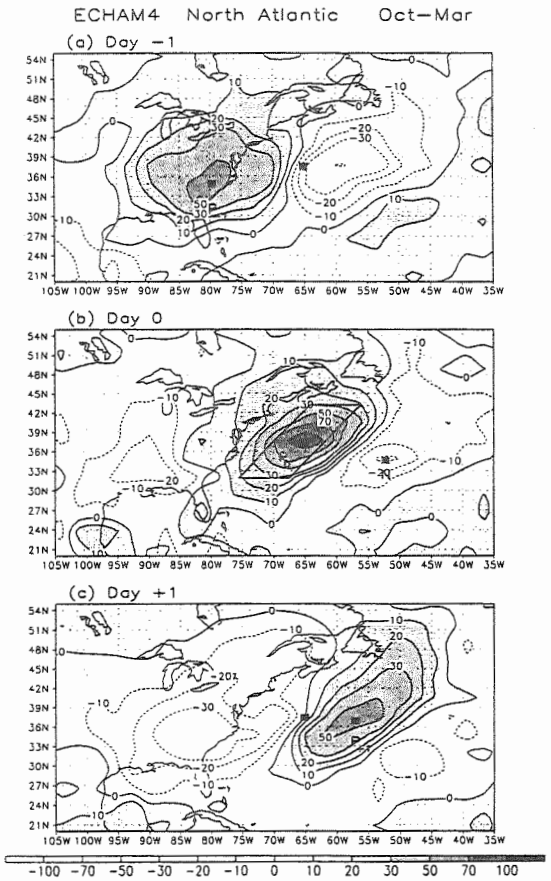

Fig. 2 Composite charts of simulated cloud water path for North Atlantic region as constructed on the basis of outstanding cloudy events at reference site 38N, 65W. Composite pattern for the key date is shown in the middle panel. For one day before (after) is in the upper (lower) panel.

4. CLOUD FIELDS AND CIRCULATION ASSOCIATED WITH EXTRATROPICAL DISTURBANCES IN THE MODEL

4.1. Composite patterns of cloud fields, precipitation and the near surface circulation

The distribution of surface pressure and the 1000 hPa horizontal wind and CWP, as constructed by merging the corresponding composite charts on day 0 for the chosen North Atlantic site. It is evident that the outstanding episodes of large CWP at the reference site are accompanied by well-define patterns of surface pressure and atmospheric circulation. The increased CWP area near the reference site has a some extension toward the northwest. There are also indications of tail-like extension toward the southwest of the reference site, especially in the precipitation and total precipitable water. The comma-shape of this area of enhancement is similar to the description of the cloud patterns and rain bands associated with extratropical cyclone (Carlson, 1991), satellite images of baroclinic troughs (Anderson et al., 1995) and the pattern constructed from the ISCCP cloud-type climatology and ECMWF circulation data (LC). In the center of comma shape, southerly airstreams originated from lower latitudes prevails. Local maxima of suppressed CWP, cloud cover, and precipitation in day 0 are found in the midst of the northerly flows located behind the low centers and ahead of the surface high pressure centers. The distinct spatial relationships between the composite features coincide with the classical model of extratropical cyclone structure (Bjerknes and Solberg, 1926).

4.2. Composite patterns along vertical cross section

To provide a more detailed description of the vertical structure of the feature described in the preceding subsections, composite pictures of selected variables are complied at each of available pressure levels following the same procedure described previously

The contours in Fig. 3 described the composite patterns of (a) cloud cover, (b) moisture, (c) temperature, and (d) geopotential height for the vertical plane along a line segment from the south-west to the north-east of the composite center of enhanced CWP. The wind vectors (arrows) along the east-west orientated cross section are reproduced in all panels. These composite patterns in Fig. 3 exhibit the familiar structure characteristics of a baroclinic wave and correspond well to the patterns depicted in LC from the observed counterpart. The maximum enhancement in cloud water content are located slightly higher than that for cloud cover. There is eastward displacement with increasing altitude for the composite patterns in Fig. 3a. The larger positive departure values for cloud fields are coincided with the low center near the surface and

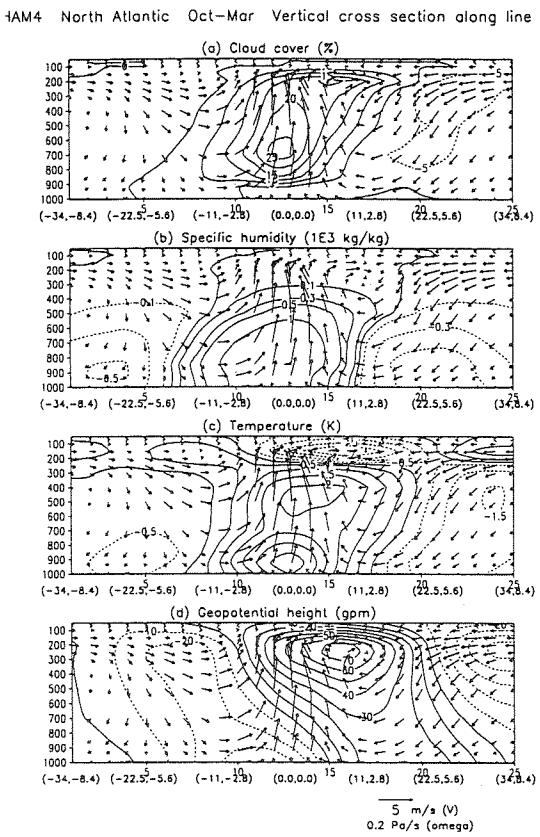

Fig.3 Distrubition of (a) cloud cover, (b) specific humidity, (c) temperature, (d) geopotential height in the vertical cross section taken along the line segment across composite maximum of CWP. Wind vector represents the zonal wind and negative pressure velocity (scale represent 5 m/s and 0.2 Pa/s, respectively)

with ridge in the upper troposphere (Fig. 3d). The systematic reduction of both cloud-top altitude and cloud optical depth from the comma region toward west is found in the observation (LC). Compared to the observed pattern, the eastward tilting and extension of cloud fields in the upper troposphere is less in the model. Above the surface low pressure center, there are increases in cloud cover and water content and weak westerly flow prevails. Ahead the surface low, there is a transitional zone for cloud fields from the suppressed to the enhanced region. The altitude of transition zone increase toward the east. The maximum ascending motion are also located ahead of the surface low. Behind the surface low, there are slight increases in cloud cover and water content in the lower troposphere. Colder temperature, drier air, and subsidence are found to the west of low center. The enhancement in cloud fields occurs preferentially ahead of surface low center where ascending, warm, moist, and southerly air currents develops.

5. SUMMARY

Following a composite technique to depict the synoptic-scale organization of cloud properties associated with midlatitude circulation system (LC), we construct the spatial and temporal variability of simulated cloud fields in conjunction with the concurrent three dimensional atmospheric structure and dynamical processes near a reference site in the North pacific. The similarities in the composite methods are intended for an easy comparison with the already published observational study. Nevertheless, one should keep in mind the differences between observations and model generated data (e.g., cloud properties retrieved from satellite and those produced by physical parameterization in the model).

As also shown in the observation, the simulated cloud variations over the midlatitude oceanic region are primarily associated with the passage of developing baroclinic waves as clearly depicted by the atmospheric structure. The westward displacement of the low center and eastward tilting of the cold core with altitude are evident in the model data. The composite charts show a slight eastward displacement in the upper tropospheric cloud cover and cloud water content from the center of upward motion at 500 hPa. However, this tilting is not as distinct as revealed in the observation. The vertical cross sections along the wave propagating direction and the warm and cold sectors reveal the more complete three dimensional structure of various fields and their interrelations. The eastward displacement of the moisture convergence and dominant moisture transport with altitude well explains the vertical tilting in cloud cover and water content anomalies pattern. All these features are in good agreement with the classical model of extratropical cyclone structure (Bjerknes and Solberg 1926) and more recent depiction of the cloud and air flow pattern associated with the development of extratropical cyclones (Carlson, 1980; Hirschberg and Fritsch, 1991).

Contrasting these composite patterns to those shown in the observational study brings an unique way to evaluate the ensemble mean of a particular cloud and system in the model. The deficiencies in the simulated cloud distribution and its association with dynamical and thermal atmospheric structure from this view could provide additional valuable informations for the improvement in the cloud parameterization than only comparing the statistical properties of cloud fields in the model. It is, therefore, also possible to extend this study to other type of organization of cloud cover in the well-documented circulation systems in different climate regimes. Other independent cloud system models developed in GCSS project would certainly improve our understanding of detailed physical processes within the cloud system and help in shaping the cloud scheme in climate model. Since the cloud parameterization and simulation in different GCMs are quite different, the result discussed here may not apply to other models. It is, however, very easy to use a similar approach to find out the association of cloud system and circulation fields in other climate model.

Acknowledgements

We thank Drs. N.-C. Lau and Stephen Klein for helpful discussion. This work is supported by National Science Council of Taiwan under grant NSC 87-2621-P-003-001, NSC 88-2111-M-003-001-AGT, NSC 89-2111-M-003-001-AGT, NSC 8801PPP08, and NSC 88041870.

6. REFERENCE

Anderson, R. A., T. N. Carlson, and J. R. Grant, 1995: Synoptic-scale cloud and moisture patterns. *Images in weather forecasting-A practical guide for interpreting satellite and radar images*, M. J. Bader, G. S. Forbes, J. R. Grant, R. B. E. Lilley, and A. J. Waters, Eds., Cambridge University Press, 70-137.

Bjerknes and Solberg, 1926: Life cycle of cyclones and polar front theory of atmospheric circulation. *Geofys. Publ.*, **3**, 1-18.

Carlson, T. N., 1991: *Mid-latitude Weather Systems*. Harper Collins Academic, 507pp.

Cotton, W. R., and R. A. Anthes, 1989: *Storm and Cloud Dynamics*. Academic Press, 883pp.

Hirschberg, P. A., and J. M. Fritsch, 1991: Tropopause undulation and development of extratropical cyclones. Part II: Diagnostic Analysis and conceptual model, *Mon. Wea. Rev.*, **119**, 518-550.

Houze, R. A., Jr., 1993: *Cloud Dynamics*. Academic Press, 573pp.

Houze, R. A. and Hobbs, 1982: Organization and Structure of precipitating cloud systems. *Advances in Geophysics*, Vol. **24**, Academic Press, 225-315.

Lau, N.-C., and M. W. Crane, 1995: A satellite view of the synoptic-scale organization of cloud properties in midlatitude and tropical circulation systems, *Mon. Wea. Rev.*, **123**, 1984-2006.

Roeckner, E., K. Arpe, L. Bengtsson, M. Christoph, M. Claussen, L. Dümenil, M. Esch, M. Giorgetta, U. Schlese, U. Schulzweida, 1996: *The atmospheric general circulation model ECHAM4: Model description and simulation of present-day climate*, Rep. 218, Max-Planck-Institut für Meteorologie, Hamburg, Germany, 90pp.

Sundquist, H., 1978: A parameterization scheme for non-convective condensation including prediction of cloud water content. *Q. J. R. Meteorol. Soc.*, **104**, 677-690.

Tiedtke, M., 1993: Representation of clouds in large-scale models. *Mon. Wea. Rev.*, **121**, 3040-3061.

Weare, B. C., I. I. Mokhov, and Project Members, 1995: Evaluation of total cloudiness and its variability in the Atmospheric Model Intercomparison Project. *J. Climate*, **8**, 2224-2238.

SIMULATIONS OF UPDRAFTS IN A DEEP CONVECTIVE SYSTEM WITH A MULTI-THERMAL MICROPHYSICAL MODEL – A COMPARISON WITH THE UKMO CLOUD-RESOLVING MODEL

V.T.J.Phillips[1], A. Blyth[2], P.S. Brown[3], T.W.Choularton[1] and J. Latham[1]
[1]University of Manchester Institute of Science and Technology (UMIST), UK.
[2]New Mexican Institute of Mining and Technology (NMIMT), USA.
[3]Meteorological Office, UK.

1. INTRODUCTION

Cloud-Resolving Models (CRMs) with bulk microphysical parametrisations resolve the 3D fluid dynamics of the cloud. The microphysical problem is simplified by assuming that size distributions of hydrometeors always conform to continuous gamma or exponential functions. In a double-moment scheme, the size distribution of a species of particle is uniquely defined by its total mixing ratio and particle concentration. These scalars are advected with the 3D flow.

In the case of the Multi-Thermal Microphysical Model (MTMM), the dynamical field of the CRM is used to run a more detailed representation of the cloud microphysics. This field of air velocity allows trajectories of groups of hydrometeors to be traced through the storm. Continuous growth of particles occurs along these trajectories.

This paper documents a model inter-comparison between the United Kingdom Meteorological Office (UKMO) CRM and the MTMM at UMIST, for a storm observed over New Mexico on the 10th August 1987.

2. MODEL DESCRIPTION

A description of the UKMO CRM is provided by Swann (1998). The MTMM is an extended version of the model by Blyth and Latham (1997). It involves the continuous interaction between the ice, cloud-water, rain and vapour components during a simulation. Primary nucleation of ice occurs via the activation of condensation-freezing ice nuclei in cloud droplets with the formula provided by Meyers et al. (1992). The processes of primary and secondary nucleation of droplets are represented in the MTMM, with a prescribed aerosol activity spectrum.

Growth of ice particles occurs by vapour deposition and by the riming of cloud-water. Collision efficiencies for riming are based on data from Wang and Ji (1992) for planar and columnar crystals, and from Bohm (1994) for spheroidal graupel. Formulae for the density of accreted rime are from Levi et al. (1991) for riming crystals and from Heymsfield and Pflaum (1985) for graupel particles. Growth of rain-water occurs via the accretion of liquid water, while condensational growth is applied to rain- and cloud-water.

Corresponding author's address: Vaughan T.J. Phillips, Department of Physics, UMIST, Manchester, M60 1QD, United Kingdom; E-Mail: mccpgvp2@fs2.ee.umist.ac.uk

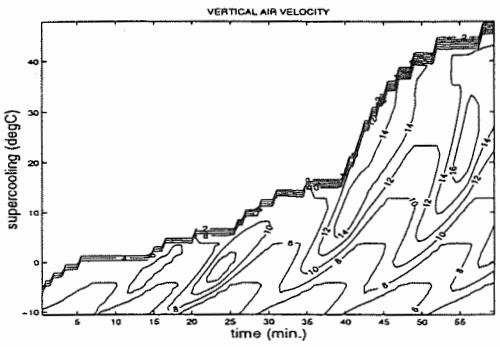

Figure 1. The vertical air velocity (m/s) along the vertical axis of the updraft in the MTMM over time (min). The vertical coordinate is supercooling (°C).

The dynamical evolution of the field of vertical air velocity, *W(x,z)*, in the updraft of the MTMM has been matched with the CRM simulation of this case. There is no environmental shear and the updraft has no slope in the MTMM. A sequence of thermals is prescribed within the updraft. These are shown in Figure 1. The width of the updraft increases with altitude as thermals expand during ascent. The cloud-base altitude is 3 km. MSL (10 °C). The cloud-top ascends to a maximum level of 12 km. MSL (-48 °C) during the 60 minutes of the simulation. The peak updraft velocity inside thermals increases from 6 m/s. at the cloud-base to 21 m/s. at 11 km. MSL altitude.

A height-dependent horizontal velocity of 3 - 8 m/s is applied in the tops of thermals, sweeping particles towards and into a downdraft. The downdraft is a region of uniform descent of 6 m/s. Particles in the downdraft that have descended by at least 1 km. are recycled back into the updraft below the –5 °C level.

Hallett-Mossop (H-M) ice multiplication occurs when ice particles rime in the –3 to –8 °C region. Micron-sized splinters of ice, hereafter termed 'H-M splinters' are emitted at a fixed rate of 350 per mg. of accreted rime. This matches the rate assumed by the bulk parametrisation in the CRM.

Raindrop-freezing occurs via (1) collisions between drops and ice particles, and (2) heterogeneous nucleation, from the activation of condensation-freezing ice nuclei inside raindrops. Heterogeneous nucleation of drops only occurs at temperatures colder than -5 °C. As soon as raindrops freeze they commence riming and soon become graupel.

Rain and ice particles are advected by the 2D field of $W(x,z)$ on the vertical plane coinciding with the updraft and downdraft. Vapour and groups of cloud droplets are advected together by a 1D vertical velocity profile, $\langle W \rangle (z)$. This is the area-average of W over the horizontal area of the updraft at level z. Homogeneous freezing of these droplets occurs at temperatures colder than around -36 °C. Whenever the mean diameter of cloud-water exceeds a critical value, d_{wo}, the auto-conversion scheme of Kessler (1969) converts cloud droplets to rain. A similar scheme exists in the UKMO CRM. In the MTMM, the Kessler scheme is applied at all levels from the cloud-base up to the anvil base, whenever sufficient cloud-water exists,

$$\partial_t Q_r = A_{wo} (Q_w - Q_{wo})$$

when,

$$d_w > d_{wo}$$

where $A_{wo} = 10^{-3}$ sec.$^{-1}$. Here, Q_{wo} is the critical threshold of the cloud-water mixing ratio that corresponds to a population of droplets of critical size d_{wo} at the same concentration as the actual cloud-droplet population.

3. RESULTS OF THE MODEL INTERCOMPARISON

Figure 2 shows the vertical profiles for the mixing ratio of graupel and snow. The mixing ratio of graupel is much weaker in the CRM than in the MTMM, especially at upper levels. Both simulations predict the same altitude for the local maximum in graupel mixing ratio at the -6 °C level.

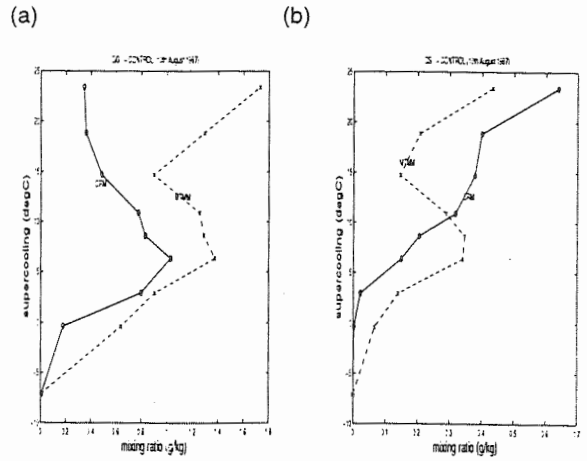

Figure 2. Vertical profiles from the updraft of the time-averaged mixing ratio (g/kg) of (a) graupel and (b) snow, for the CRM (full line) and MTMM (dashed line) simulations. The vertical coordinate is supercooling (°C). The time-averaging at each level is performed over the period of the simulation for which cloudy air is present.

The definition of snow in the MTMM is set to agree with that in the CRM: all ice particles larger than 500 microns and with less than 50% of their mass consisting of accreted rime are classified as snow. In both models there is a general trend of increasing mixing ratio of snow with height. In the MTMM, however, there is an 'S-curve' superimposed on this trend. A similar S-curve is seen in the profile of graupel mixing ratio in the MTMM. This reflects the fact that recently frozen raindrops larger than 500 microns are classed as snow in the MTMM.

There is a steady decrease with height in the mixing ratio of graupel between the –6 and –15 °C levels in both models. However, above the –15 °C level there is an increase in graupel mixing ratio with height in the MTMM. This is due to the growth by riming of a second generation of frozen drops in the MTMM. This generation of frozen drops is formed by collisions between liquid drops and H-M splinters emitted by frozen drops at lower levels. Liquid drops exist in the MTMM at such cold temperatures, albeit with very short life-times, owing to the auto-conversion of cloud-water to rain whenever $d_w > d_{wo}$.

Figure 3 shows the particle concentrations of graupel and snow. The maximum graupel concentration is located at -6 °C in the CRM. The corresponding local maximum in graupel concentration in the MTMM occurs at the -10 °C level. This confirms that drop-freezing is the major source of graupel particles in both models. The altitude of maximum concentration of graupel particles is somewhat higher in the MTMM than in the CRM, due to the classification of recently frozen drops as snow in the MTMM.

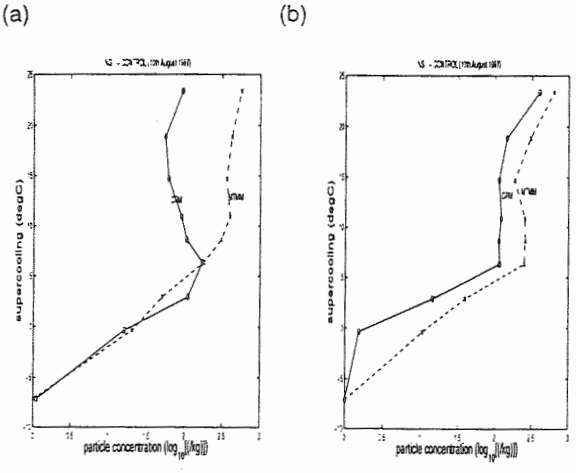

Figure 3. Vertical profiles of particle concentration ($\log_{10}$[(/kg)]) of (a) graupel and (b) snow, plotted as in Figure 2.

A striking difference between the models is the relatively low concentration of graupel particles at most levels above the H-M generation region in the CRM. The rate of precipitation of graupel out of the updraft core seems more marked in the CRM than in the

MTMM. The updraft in the MTMM is fixed and has no slope in this simulation, whereas the slope of the updraft in the CRM fluctuates in the 3D turbulent flow. In the MTMM, there is an increase in graupel concentration with height at levels above –15 °C. This is due to auto-conversion of cloud-water to rain aloft followed by immediate drop-freezing.

Figure 4 shows the vertical profiles of the mixing ratio of cloud- and rain-water. Below the freezing level, the cloud-water mixing ratios are similar for both models. However, in the -10 to -20 °C region, the mixing ratio of cloud-water is around 0.2 g/kg smaller in the MTMM than in the CRM. This is due to the riming of graupel at upper levels in the MTMM where the mixing ratio of graupel is much larger than in the CRM.

The mixing ratio of rainwater above the –6 °C level is < 0.05 g/kg in the MTMM and is almost zero in the CRM. Thus, most of the mass of rain-water upwelled in the updraft freezes between 0 and –5 °C in both models. The rain-water mixing ratio is much larger below the freezing level in the CRM than in the MTMM. Probably fluctuations in 3D of the slope and position of the updraft tend to allow fall-out of drops and melting ice into the updraft from upper levels in the CRM.

(a) (b)

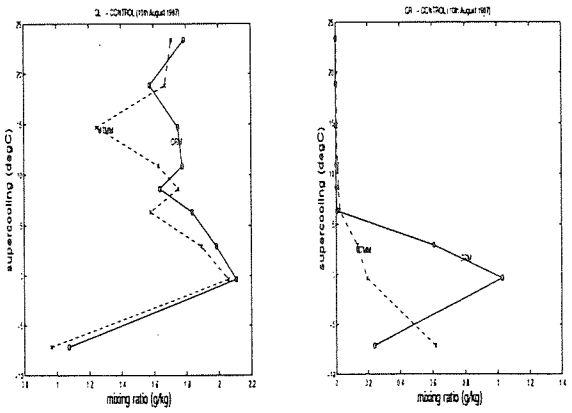

Figure 4. Vertical profiles of the mixing ratio (g/kg) of (a) cloud- and (b) rain-water, plotted as in Figure 2.

At vertical levels above –6 °C, the time-averaged raindrop concentrations (not shown) are of the order of 0.01 – 0.1/L in the MTMM and are practically zero in the CRM. In the MTMM, clearly drops continue to form by coalescence at upper levels.

Figure 5 shows the vertical profile of the particle concentration for pristine ice. It is evident that the rates of H-M ice multiplication are stronger than in the CRM than in the MTMM. It is probable that there is a difference in riming rates between the models. Firstly, graupel concentrations are much higher in the CRM case between –3 and –6 °C. Secondly, the density of graupel is fixed at 300 kg/m^3 in the CRM, and is around 600 kg/m^3 in the MTMM. Consequently, there may be a higher total cross-sectional area for riming of graupel

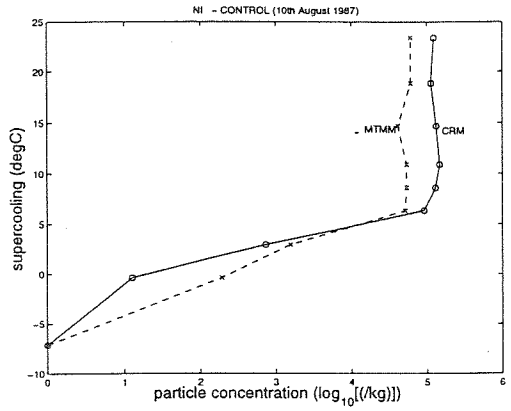

Figure 5. A vertical profile of the concentration ($\log_{10}$[(/kg)]) of pristine ice, plotted as in Figure 2.

particles in the CRM than in the MTMM at –3 to –8 °C.

4. RESULTS FROM VALIDATION OF THE MTMM WITH AIRCRAFT DATA

The results from first 35 minutes of the control simulation from the MTMM were compared with the period 19:00 to 19:35 from the aircraft observations of the storm observed on the 10th August 1987. In the aircraft observations, the updraft was defined as the region of $W > 2$ m/s and FSSP concentrations > 40 /cm^3.

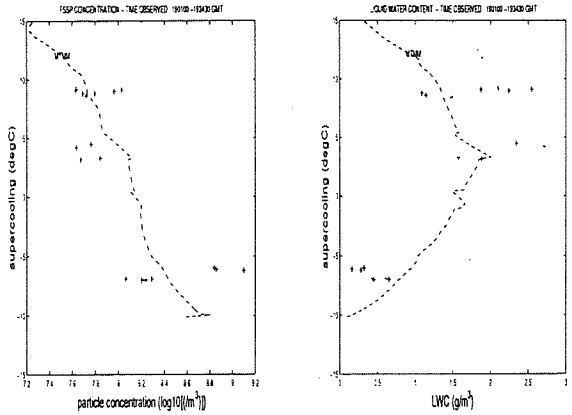

Figure 6. The vertical profile of (a) FSSP concentration and (b) FSSP-inferred liquid water content, from the model (dashed line) and from observations (+).

Satisfactory agreement at the cloud-base between observed and predicted FSSP concentrations in the updraft is seen in Figure 6(a) . This confirms that the prescribed aerosol spectrum is reasonable: the concentration of droplets activated at supersaturations less than s is given by $N = 1000\ s^{0.8}$ in the model. The

FSSP-inferred liquid water content from the aircraft data is compared with the MTMM prediction in Figure 6(b).

Small particles < 0.8 mm are measured by the aircraft with the 2DC probe. The 2DC concentration is predicted by the MTMM and compared with the observations in Figure 7. Large particles > 1 mm are only measured by filtering the 2DP data. The comparison between the MTMM and the observations is presented in Figure 8.

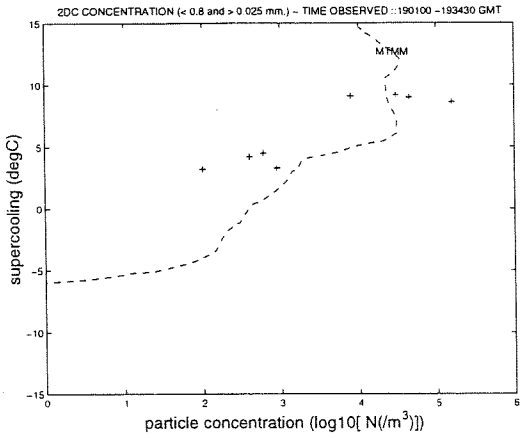

Figure 7. The vertical profile of 2DC particle concentrations, plotted as in Figure 6.

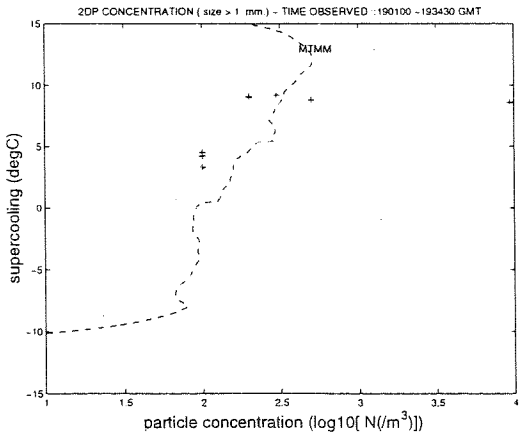

Figure 8. The vertical profile of 2DP particle concentrations, for particle sizes > 1 mm., plotted as in Figure 6.

4. CONCLUSIONS

Raindrop-freezing accounts for most of the graupel formed in both models. There is less persistence of graupel particles above their level of formation near the freezing level in the CRM compared to the MTMM. There is probably less auto-conversion of cloud droplets to rain above the –10 °C level in the CRM than in the MTMM, which further restricts graupel concentrations aloft in the CRM. Indeed, snow is the major component of the total ice mixing ratio in the CRM at upper levels. This is not true for the MTMM. Sensitivity studies are currently being conducted to assess the effect of variations in the parameters of the Kessler scheme for auto-conversion of cloud-water to rain.

Identical schemes for H-M ice multiplication were used in both models. Thus, the higher rates of H-M ice multiplication in the CRM seem connected with the higher graupel concentration between the –3 and –6 °C levels. Rain-water mixing ratios and drop concentrations just above the freezing level are higher in the CRM compared to the MTMM, explaining this difference in graupel concentrations between the models. Fall-out of melting ice and drops into the updraft is probably more marked in the CRM for dynamical reasons. This difference in riming rates between the models is currently being investigated.

4.1 Acknowledgements

The author thanks Dr. J. Cardwell, Dr K. Bower and Dr C. Saunders at UMIST for their advice. The author is grateful to Dr. P. Smolarkiewicz at NCAR for his advice on the implicit scheme for vapour advection implemented in the MTMM.

4.2 References

Blyth, A.M., and J. Latham, 1997: A multi-thermal microphysical model of cumulus glaciation via the Hallett-Mossop process. *Q.J.R. Met. Soc.*, **123**, 1185-1198.

Bohm, 1994: Theoretical collision efficiencies for riming and aerosol impaction. *Atmos. Res.*, **32**, 171-187.

Heymsfield, A.J., and J.C. Pflaum, 1985: A qualitative assessment of the accuracy of techniques for calculating graupel growth. *J. Atmos. Sci.*, **42**, 2264-2274.

Kessler, E., 1969: On the distribution and continuity of water substance in atmospheric circulations. *Meteor. Monogr.*, **10**, No.32.

Levi, L., Nasello, O.B., and F. Prodi, 1991: Morphology and density of ice accreted on cylindrical collectors at low values of impaction parameter: fixed deposits. *Q.J.R. Met. Soc.*, **117**, 761-782.

Meyers, M.P., De Mott, P.J., and W.R. Cotton, 1992: New primary ice-nucleation parametrisations in an explicit cloud model. *J. Appl. Meteor.*, **31**, 708-720.

Swann, H.A., 1998: Sensitivity to the representation of precipitating ice in CRM simulations of deep convection. *Atmos. Res.*, **47**, 415-435.

Wang, P.K., and W. Ji, 1992: Preprints Cloud Phys. Conf., p. 76, Montreal, McGill University.

NUMERICAL SIMULATIONS OF CLOUD MICROPHYSICS AND DROP FREEZING AS FUNCTION OF DROP CONTAMINATION

Sabine Wurzler[1] *, Andreas Bott[2]

[1]Institute for Tropospheric Research, Leipzig, Germany
[2] Institute for Meteorology, University of Bonn, Germany

1. INTRODUCTION

Cloud-aerosol interactions play a key role in many aspects of cloud physics and chemistry such as the evolution of drop spectra, efficiency of rain formation, chemical characteristics of cloud and rain water, optical properties of the cloud and cloud processing of aerosols. The atmospheric aerosol is a heterogeneous mixture of particles of different chemical compositions.

When these particles enter a cloud, they can serve, depending on their size and chemical composition, as cloud condensation nuclei. Subsequently, the newly formed drops inside the cloud can have different chemical compositions. Even drops of the same size can have different contaminations owing to the heterogeneous physico-chemical properties of the aerosols. Field measurements as well as numerical simulations with a two component model (drops and aerosols) have shown that even precipitation sized drops of similar sizes, which have been formed by collision and coalescence of drops, must not necessarily contain similar amounts of aerosols. Furthermore, the freezing behavior of drops depends not only on their sizes but also on their contamination. In-cloud measurements show that supercooled drops can exist in clouds at very low temperatures and that liquid and frozen drops of similar sizes can coexist.

The traditional treatment of detailed microphysics in cloud models, where e.g. the contamination is predicted as function of the drop size, implies that drops of the same size have the same contamination and will therefore have the same freezing behavior. Using a two component description of the cloud microphysics allows that drops of the same size can have different contaminations and owing to these different contaminations drops of the same size can have different freezing temperatures.

Comparisons between the two and one dimensional distribution functions are presented and the importance of the additional information obtained is discussed. Results from calculations of the drop freezing process inside a cloud using the traditional treatment of the microphysics and using the above mentioned two component treatment of the microphysics will be reviewed.

* *Corresponding author address:* Sabine Wurzler, Institute for Tropospheric Research, Permoserstrasse 15, 04318 Leipzig, Germany; e-mail:wurzler@tropos.de

2. METHODS

Two entraining air parcel models with detailed description of the cloud microphysics and the interactions between the aerosol particles and the hydrometeors are employed. Both models treat the activation of aerosol particles to drops, impaction scavenging of aerosols by drops, collision and coalescence of drops and are currently extended to the freezing of drops.

One of the cloud models (Wurzler et al., 1995) treats the cloud microphysics as function of the drop and particle radii in the traditional way.

The other air parcel model with a two component treatment of the cloud microphysics (Bott, 1997, Bott, 1999, Reisin et al., 1998) is currently extended to the treatment of drop freezing.

3. PRELIMINARY RESULTS

The models have been extended to the drop freezing in dependency of the drop contamination. In both model we have included the freezing point depression as function of the drop contamination and the freezing time of the drops following Pruppacher and Klett (1997) and Brdicka (1958). We are aware that this approach to the freezing behaviour is rather simplified, but is a very useful first step to investigate the influence of different contaminations of similar sized drops. Some preliminary results of our model calculations are shown in Figs. 1 and 2. Fig. 1 shows an example result of the two component distribution of drops and aerosols. From Fig. 2 can be seen how the two component drop–aerosol population becomes intersected into a part which could freeze at a certain temperature (here -15 C) and into drops which could not freeze at that temperature. In the classical treatment of the cloud microphysics, for the present example all drops with radii larger than 50 μm would be frozen.

4. CONCLUSIONS

Numerical simulations of the evolution of a two dimensional distribution function of drops and aerosol particles due to microphysical and chemical processes are

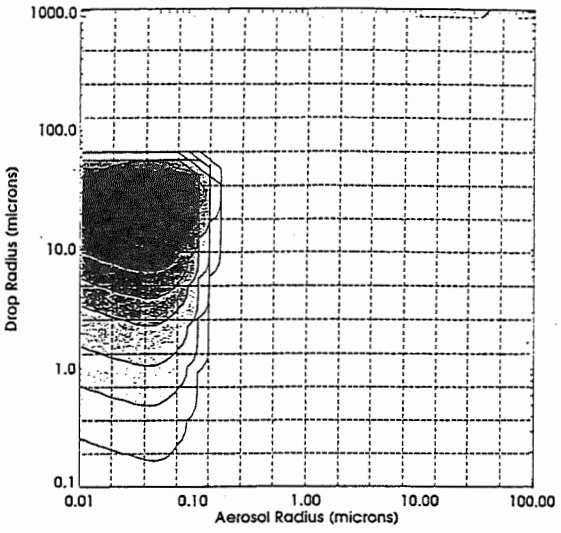

Figure 1: Example of a two component distribution. Displayed is the liquid water mass in g cm^{-3}.

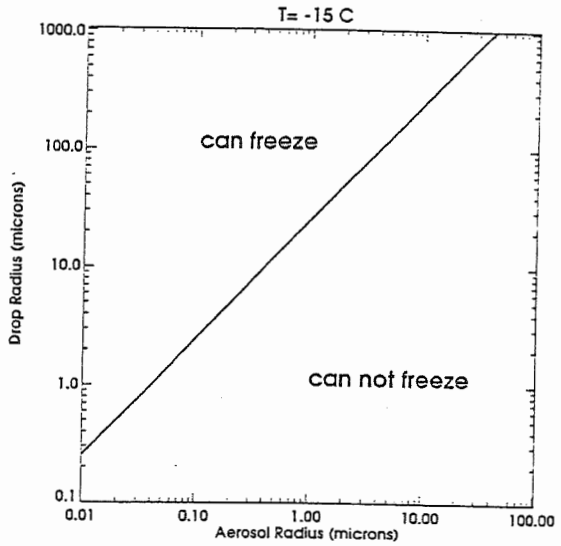

Figure 2: Example of the intersection of the model domain into areas where the drop-aerosol population can freeze and those where they can not freeze at -15 C

presented. In comparison to one dimensional functions, multidimensional distributions provide a more realistic description of the distribution of dissolved atmospheric pollutants inside the drop populations. The one dimensional distribution functions implicitely assume that drops of the same size have the same contamination. This does not agree with observations. In the atmosphere, drops of the same size can have different chemical compositions, depending on the physico chemical characteristics of the aerosol particles which have been activated to drops. Treating the cloud microphysics as two component functions lead to a drop population where frozen and liquid drops can coexist.

ACKNOWLEDGEMENTS

This work is supported by the AFS-program of the BMBF.

REFERENCES

Bott, A., 1997: A numerical model of the cloud topped planetary boundary layer: Impact of aerosol particles on radiative forcing of stratiform clouds. Quarterly Journal of the Royal Meteorological Society, 123, 631-656

Bott, A., 1999: A numerical model of the cloud-topped planetary boundary-layer: Chemistry in marine stratus and the effects on aerosol particles. Atmospheric Environment, 33, 1921-1936.

Brdicka,R., 1958: Grundlagen der physikalischen Chemie. VEB Deutscher Verlag der Wissenschaften, Berlin.

Pruppacher, H.R., and J.D. Klett, 1997: Microphysics of clouds and precipitation. Kluwer Academic Publishers, Dordrecht, The Netherlands.

Reisin, T.G., S.C. Wurzler and A. Bott. 1998: A new insight into cloud-aerosol interactions: Numerical simulations using a two-dimensional distribution function. Journal of Aerosol Sciences, Suppl. 1, 29, S785-S786

Wurzler, S., A.I. Flossmann, H.R. Pruppacher and S.E. Schwartz (1995). The scavenging of nitrate by clouds and precipitation: I. A theoretical study of the uptake and redistribution of NaNO3 particles and HNO3 gas by growing cloud drops using an entraining air parcel model. Journal of Atmospheric Chemistry, 20, 259-280

APPLICATION OF AN EXPLICIT CLOUD MICROPHYSICS ALGORITHM IN A NON-HYDROSTATIC MESOSCALE MODEL

Dirk Klugmann

Institute for Tropospheric Research, 04318 Leipzig, Germany

1 MOTIVATION

Common mesoscale forecasting models usually apply a parameterized treatment of grid-scale cloud and precipitation processes. The frequently used parameterization according to Kessler (1969) does not take into account aerosol properties at all. Clouds are generated by adjusting the water vapor saturation to 100%. The amount of water vapor exceeding this percentage is converted to liquid water immediately. Generation of precipitation is parameterized depending on cloud water/ice content (CWC/CIC). These parameterizations often do not describe atmospheric processes in a sufficient way.

Algorithms basing on findings by Twomey (1959) at least regard basic properties of different simple aerosol size distributions. However, all of these parameterizations are in need of verification and, in part, of enhancement. The intention of the presented work is to investigate the influence of aerosols on the development of clouds and precipitation as well as on atmospheric dynamics.

This will be done by replacing the parameterized microphysics in a mesoscale model by an explicit cloud microphysics algorithm. In addition, the modified model can be coupled with a chemistry transport model (CTM) to provide the droplet size distributions requested by the CTM for calculating wet phase chemistry processes, or provide the input data for 3-dimensional radiative transfer calculations.

2 MODEL DESCRIPTION

The applied model is the Lokal-Modell (Local Model, LM) of the German Weather Service (DWD). LM (Doms and Schättler (1998)) is a non-hydrostatic limited area atmospheric prediction model on the meso-γ and meso-β scale (horizontal resolution: 14 to 2.5 km). The model equations are formulated in rotated geographical coordinates and a generalized terrain following height coordinate. In the standard version of LM, grid-scale clouds and precipitation are treated optionally by a warm rain scheme (Kessler (1969)), or a one-category (liquid water and snow) or two-category (additional ice) ice scheme bulk parameterization. The generation of precipitation is parameterized by the CWC/CIC.

The standard version of LM will serve as an reference for the planned investigations.

3 PRELIMINARY INVESTIGATIONS

Prior to implementing the explicit cloud microphysics scheme into the LM, investigations with a one-dimensional dynamical cloud model featuring a similar explicit cloud microphysics algorithm (Schimmel (1998)) have been made.

Model runs with different aerosols (one component or two internally mixed components) were performed. The aerosol data were taken from Jaenicke (1993). A sample result is displayed in Fig. 1.

These investigations have shown the significance of aerosol properties on the development of meteorological variables inside of clouds, and of the clouds themselves. For explicitly soluble aerosols, the influence of aerosol size distribution was more significant than that of chemical composition.

Further studies have been performed applying a box model based on the explicit cloud microphysics module YAMCM (Yet Another Microphysical Cloud Module). YAMCM was developed to replace the original grid scale cloud parameterization

Author's address: Dirk Klugmann, Institute for Tropospheric Research, Permoserstraße 15, 04318 Leipzig, Germany; E-mail: klugmann@tropos.de

in the LM and is based on the diffusive growth of single drops. It features the explicit activation and de-activation of cloud droplets from dry aerosol particles, but does not regard for haze droplets. The diffusion growth is described thermodynamically. The dependence of droplet solution activity on molality is taken from publications (e. g. Pilinis and Seinfeld (1987)) or fits to published data.

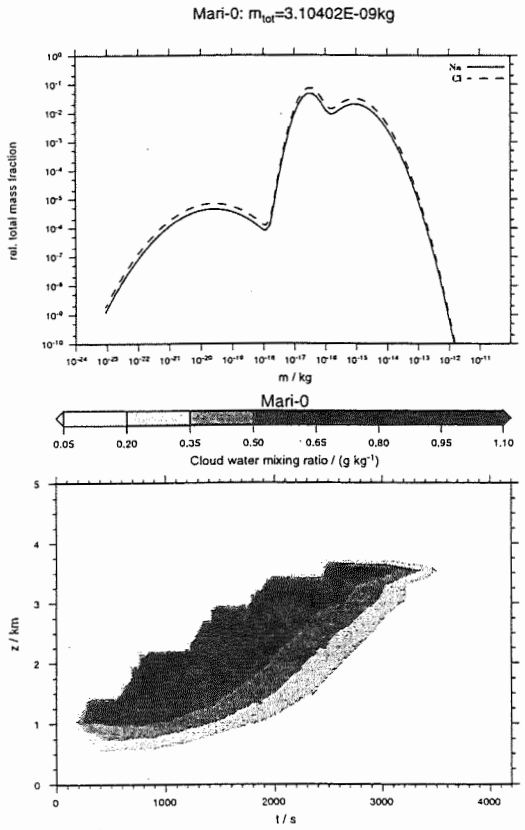

Figure 1: Cross section of CWC (bottom) calculated with the one-dimensional dynamical cloud model from a maritime aerosol size distribution composed from Sodium Chloride (top).

These studies yielded results similar to that before, but applying the enhanced formula to calculate solution activity slightly increases the influence of the chemical aerosol composition.

4 MODIFICATIONS TO THE LM

As can be seen from Fig. 2, the LM has to be changed in two parts to enable explicit microphysical modeling. The first part is the dynamics module, responsible for transport in horizontal and vertical direction, and over the model boundaries. This module has been changed in order to allow the transport of explicit aerosol and droplet size distributions instead of just bulk water.

For the second part, the Kessler scheme bulk parameterization has been replaced by an explicit warm rain cloud microphysics algorithm based on YAMCM. This algorithm handles nucleation and diffusion growth according to the grid-scale ambient conditions. Droplet collision and coalescence, and sedimentation of cloud droplets and aerosol particles are neglected for the moment. The generation of precipitation is parameterized on CWC by using the original LM routines. Meteorological situation and initialization data are taken from data sets provided by DWD.

Up to two pure or internally mixed aerosol components are allowed, that also can mix internally (dry case) or be incorporated in a single drop. A three-dimensional wet aerosol size distribution field is assigned to each model grid cell. It is spanned by the variables m_{ae1}-m_{ae2}-r_{d}, where $m_{\mathrm{ae}x}$ denotes the mass of the x^{th} aerosol component and r_{d} the droplet diameter. The variables stored in this field are droplet number concentration N (units: m^{-3}), mass density of the incorporated aerosol components $M_{\mathrm{ae}x}$ (units: $\mathrm{kg\,m}^{-3}$), and LWC (units: $\mathrm{kg\,m}^{-3}$).

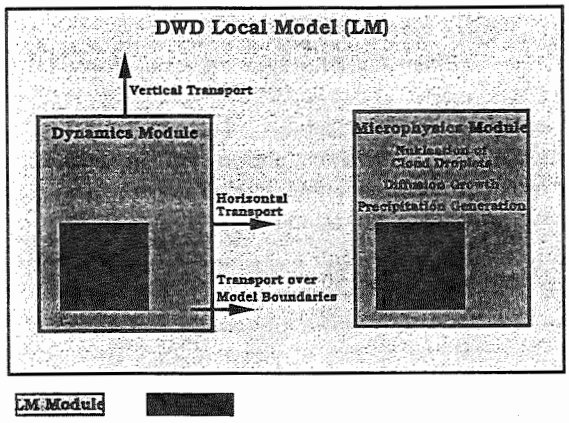

Figure 2: Intended changes to the LM.

For the initialization of LWC, also the data sets from DWD are used. The initial DSDs in the model domain grid cells are calculated as follows:

1. The critical supersaturation S_{crit} of the aerosol particles in each bin is calculated.

2. The critical radius r_{crit} of the aerosol particles in each bin of the wet aerosol size distribution field is calculated. Then $S_{\mathrm{crit}}$is compared to the ambient supersaturation S_{amb}:

   $S_{\mathrm{crit}} > S_{\mathrm{amb}}$: Aerosol particles of this bin stay dry (no haze droplets allowed) with $r_{\mathrm{d}} = 0$.

   $S_{\mathrm{crit}} \leq S_{\mathrm{amb}}$: Aerosol particles of that bin are assigned a cloud droplet of $r_{\mathrm{d}} = r_{\mathrm{crit}}$.

3. The overall LWC in each grid cell of the model domain is calculated.

4. The overall LWC in each grid cell is adjusted to the value qc given by the initialization data set provided by DWD:

   LWC $> qc$: Number concentration N in each size bin of the wet aerosol size distribution field is reduced by multiplication with $C_{>} = (qc/\mathrm{LWC})$. This simulates that not all aerosol particles that are able to act as CCN already nucleate cloud droplets, but some remain interstitial aerosol.

   LWC $< qc$: The radius r_{d} in each size bin of the wet aerosol size distribution field is multiplied with $C_{<} = (qc/\mathrm{LWC})^{(1/3)}$ and re-assigned to the proper size bin. This simulates a wet aerosol size distribution that has grown for some time since nucleation of the cloud droplets.

5 TEST RUNS FOR DRY AEROSOL TRANSPORT

Model runs with a horizontal grid resolution of 14 km for testing the dry aerosol transport (release experiment) have been performed. The topography of the model area is shown in Fig. 3. Aerosol size distributions $N(r, x, y, 0)$ at sea level were calculated according to Jaenicke (1993). For each grid cell at height z, the formula $N(r, x, y, z) = N(r, x, y, 0) \cdot \mathrm{e}^{-\frac{z}{H_0}}$ with a characteristic scale height of $H_0 = 3000$ m was applied. Isosurface plots of N at height level $z = 5$ for the initial state and after three hours can be seen in Fig. 4.

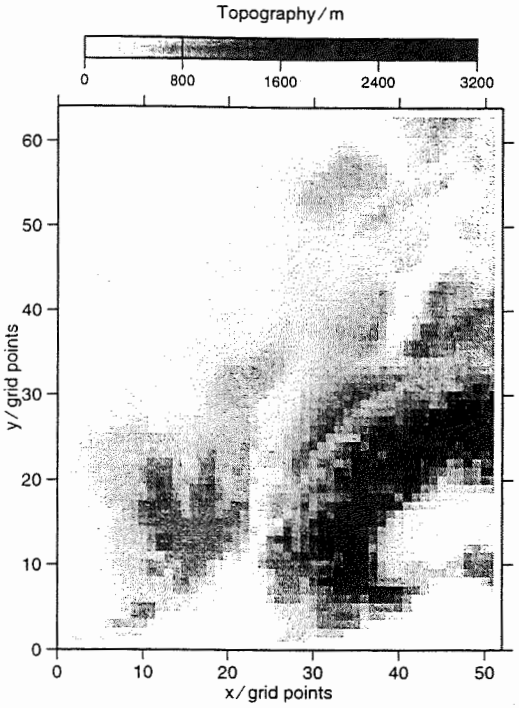

Figure 3: Topography of the model area.

6 CONCLUSIONS AND OUTLOOK

The influence of aerosols on the development of clouds and precipitation as well as on atmospheric dynamics shall be investigated. For this purpose, the parameterized microphysics in the mesoscale model LM was replaced by an explicit microphysical algorithm. Preliminary studies with detailed microphysical algorithms have shown the significance of the aerosols for the investigated atmospheric processes. A test run of the modified LM for dry aerosol transport (release experiment) have been presented.

The modified LM will be used for sensitivity studies to determine the influence of aerosols on the development of clouds and precipitation as well as on atmospheric dynamics. Model runs of the unchanged LM will serve as reference. Further applications of the modified LM will include the intercomparison between model runs and measurements from field experiments.

Planned enhancements are the handling of rain generation by a collision / coalescence mechanism, introduction of an explicit ice microphysics scheme,

refinement of the applied explicit cloud microphysics algorithm, and enabling case studies of sub-grid-scale clouds.

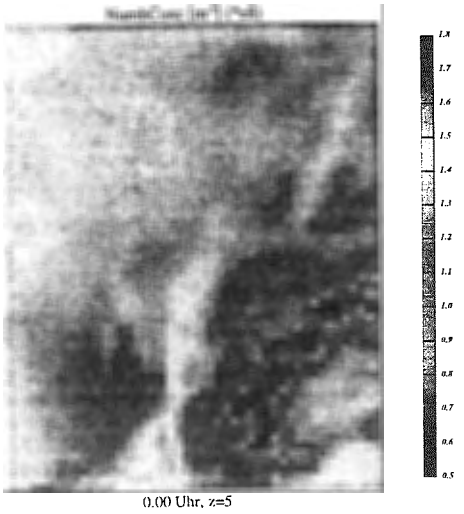

Figure 4: Number concentration at model initialization (top) and after three hours (bottom).

The modified LM will be applied for testing and enhancing parameterizations used in standard mesoscale models. The LM will be coupled to an CTM, which will use LM generated DSDs as input for liquid phase chemistry calculations. Furthermore, DSDs from the LM can be used as input for radiative transport models.

ACKNOWLEDGEMENTS

Thanks to Dr. Frank Müller (Meteorological Institute of the University Hamburg, Germany) for providing the one-dimensional dynamical cloud microphysics model developed under his supervision, and for his advice concerning it's application.

REFERENCES

Doms, G. and U. Schättler. The Nonhydrastatic Limited-Area Model LM (Lokal-Modell) of DWD; Part I: Scientific Documentation. Technical report, Deutscher Wetterdienst, D-63004 Offenbach, Germany, 1998.

Jaenicke, R. Tropospheric Aerosols. In Hobbs, P. V., editor, *Aerosol-Cloud-Climate Interactions*, chapter 1, pages 1–31. Academic Press, Inc., San Diego, California, 1993.

Kessler, E. *On the Distribution and Continuity of Water Substance in Atmospheric Circulations*, volume 10 of *Met. Monograph.* AMS, Boston, 1969.

Pilinis, C. and J. H. Seinfeld. Continued development of a general equilibrium model for inorganic multicomponent atmospheric aerosols. *Atmospheric Environment*, 21(11):2453–2466, 1987.

Schimmel, F. Parametrisierung der Wolkentropfenbildung für mehrdimensionale Atmosphärenmodelle. Master's thesis, Meteorologisches Institut der Universiät Hamburg, Bundesstraße 55, 20169 Hamburg, Germany, 1998.

Twomey, S. The nuclei of natural cloud formation part ii: the supersaturation in natural clouds and the variation of cloud droplet concentration. *Geofis. Pura et Appl.*, 43:243–249, 1959.

Some Statistical Properties of Cumulus Convection over the SGP ARM site derived from 3-D cloud-resolving modeling

Marat F. Khairoutdinov and David A. Randall

Department of Atmospheric Science
Colorado State University
Fort Collins, Colorado 80526, U.S.A.

1. Introduction

Cloud Resolving Models (CRMs) are run for long simulation times (on the order of ten days) in a computational domain large enough to represent individual convective systems (on the order of hundreds of kilometers), but with a grid fine enough to resolve individual clouds. High computational cost of a three-dimensional dynamical framework has been a major reason for popularity of two-dimensional CRMs. However, recent progress in microchip technology, and shift to massively parallel computing have made three-dimensional CRMs quite affordable.

The CRMs can be used as a tool to evaluate cloud parameterizations used in General Circulation Models. They can also test various assumptions in foundation of those parameterizations. In this study, we analyze the statistical properties of the simulated deep cumulus convection with the emphasis on the budget of the second statistical moments such as variances and covariances of the wind velocity and scalar fields. Such an analysis is very important for development and validation of one-dimensional higher-order closure schemes of deep convection. To our knowledge, such a detailed budget analysis derived from a 3-D cloud resolving modeling has not been done before.

2. The Model

Colorado State University's three-dimensional CRM (CSU-3d) employs the Message Passing Interface (MPI) to efficiently run on such massively parallel computers as the Cray T3E, IBM SP-1, and SGI Origin 2000. A global computational domain is cut into a number of subdomains with their number matching the number of processors, or processing elements (PEs). Each PE runs one copy of the model for each subdomain, so that the subdomain's data can *only* be accessed *directly* by its own PE's CPU. The subdomains exchange the lateral boundary information needed to compute the horizontal advection and diffusion by sending packets of information or *messages* to each other over a network connecting the PEs.

The model uses the anelastic approximation for the momentum equations. The thermodynamic state is prescribed in terms of three prognostic variables: generalized liquid/ice static energy, total non-precipitating water (cloud water + cloud ice + vapor), and precipitating water (snow + rain). The model employs the Kessler-type bulk microphysics. The subgrid-scale (SGS) parameterization is based on the prognostic SGS turbulent kinetic energy. The surface fluxes are parameterized following the Monin-Obukhov similarity theory. The model's numerics are formulated on a fully staggered Arakawa C-type grid. The second/forth-order central differences in flux form are used for the momentum advection, while a monotonic positive-definite advection scheme is utilized for the advection of all scalars. The 3rd-order Adams-Bashforth scheme with a variable time step is used for the time integration of the momentum equations.

3. Model Simulations

The simulations represent the summertime continental deep convection observed over the Southern Great Plains Cloud and Radiation Testbed (SGP CART) during the Atmospheric Radiation Measurement (ARM) June-July 1997 Intensive Observation Period IOP). This IOP was used by the GEWEX Cloud System Study's (GCCS) Working Group 4 as the Case 3 of the CRM intercomparison project. This IOP period was divided into several sub-periods, or subcases. The deep convection events correspond to the Subcases A, B, and C. The Subcase A was 4-day long, and the Subcases B and C - 5-day long. The model was initialized with the observed sounding and forced throughout a simulation by prescribing the surface sensible/latent heat fluxes and the large-scale advective tendencies of temperature and moisture derived from observations. The numerical domain was 256 x 256 x 28 km^3 in size with 128x128x64 grid points. The vertical resolution gradually varied with height - from 100 m near the surface to 500 m above. The time step was 10 sec. It took just slightly more than 1 hour of the wall-clock time to simulate one day of evolution running the model on 32 processors of the SGI Origin 2000 supercomputer.

4. Results

Figure 1 shows the vertical profiles of the bias, RMS error, and the temporal correlation of the simulated temperature and water vapor mixing ratio with respect to observations for each of the subcases. The worst temporal correlation is observed near the tropopause and near

the surface. The latter can be explained by possibly large errors in the specified surface fluxes. Figure 2 shows the vertical budgets of the following second moments:

Perturbation Kinetic Energy $e = 0.5\bar{\rho}u_i'u_i'$

$$\frac{\partial \bar{e}}{\partial t} = -\frac{\partial}{\partial z}\overline{w'e'} - \frac{\partial}{\partial z}\overline{w'p'} - \bar{\rho}\overline{u'w'}\frac{\partial \bar{u}}{\partial z} - \bar{\rho}\overline{v'w'}\frac{\partial \bar{v}}{\partial z} + \bar{\rho}\beta\overline{w'\theta'_v} - \bar{\rho}\varepsilon$$

Horizontal x-Momentum Flux

$$\bar{\rho}\frac{\partial}{\partial t}\overline{u'w'} = -\frac{\partial}{\partial z}\bar{\rho}\overline{w'^2u'} - \bar{\rho}\overline{w'^2}\frac{\partial \bar{u}}{\partial z} + \bar{\rho}\beta\overline{u'\theta'_v} - \frac{\partial}{\partial z}\overline{u'p'} + \overline{\frac{p'}{\bar{\rho}}\left(\frac{\partial \bar{\rho}w'}{\partial x} + \frac{\partial \bar{\rho}u'}{\partial z}\right)}$$

Total Water Variance

$$\frac{\partial}{\partial t}\overline{q_T'^2} = -\bar{\rho}^{-1}\frac{\partial}{\partial z}(\bar{\rho}\overline{w'q_T'^2}) - 2\overline{w'q_T'}\frac{\partial \bar{q}_T}{\partial z} - 2\overline{q_T'Q_p} - \varepsilon_{qq}$$

Passive-Tracer Variance

$$\frac{\partial}{\partial t}\overline{S'^2} = -\bar{\rho}^{-1}\frac{\partial}{\partial z}(\bar{\rho}\overline{w'S'^2}) - 2\overline{w'S'}\frac{\partial \bar{q}_T}{\partial z} - \varepsilon_{SS}$$

Total Water Flux

$$\frac{\partial}{\partial t}\bar{\rho}\overline{w'q_T'} = -\frac{\partial}{\partial z}\bar{\rho}\overline{w'^2q_T'} - \bar{\rho}\overline{w'^2}\frac{\partial \bar{q}_T}{\partial z} + \bar{\rho}\beta\overline{q_T'\theta'_v} - \overline{\bar{\rho}q_T'\frac{\partial p'}{\partial z\rho}} - \bar{\rho}\overline{w'Q_p}$$

Passive-Tracer Flux

$$\frac{\partial}{\partial t}\bar{\rho}\overline{w'S'} = -\frac{\partial}{\partial z}\bar{\rho}\overline{w'^2S'} - \bar{\rho}\overline{w'^2}\frac{\partial \bar{S}}{\partial z} + \bar{\rho}\beta\overline{S'\theta'_v} - \overline{\bar{\rho}S'\frac{\partial p'}{\partial z\rho}}$$

Each profile was averaged over a 7-hour time period during the deep convection event in the Subcase A simulation. One of the most intriguing features of the budgets shown in Figure 2 is that the production of momentum and scalar fluxes seem to be dominated by two terms - buoyancy and pressure production/destruction; however, one can see that the transport and shear/gradient production terms remain important for the variance budgets.

Acknowledgments. This research was supported by the U.S. Department of Energy Grant DE-FG03-95ER61968 as part of the Atmospheric Radiation Measurement Program, and by the National Science Foundation Grant ATM-9812384. The computational resources provided by the Climate and Global Dynamics (CGD) Division of the National Center for Atmospheric Research are greatly appreciated.

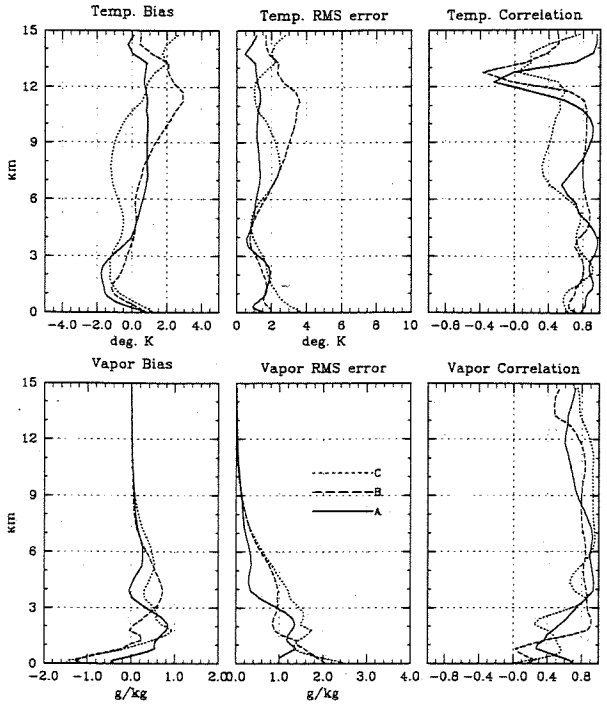

Figure 1. The vertical profiles of the bias, RMS error, and temporal correlation with respect to observations of the simulated temperature and water vapor mixing ratio for the Subcases A, B, and C.

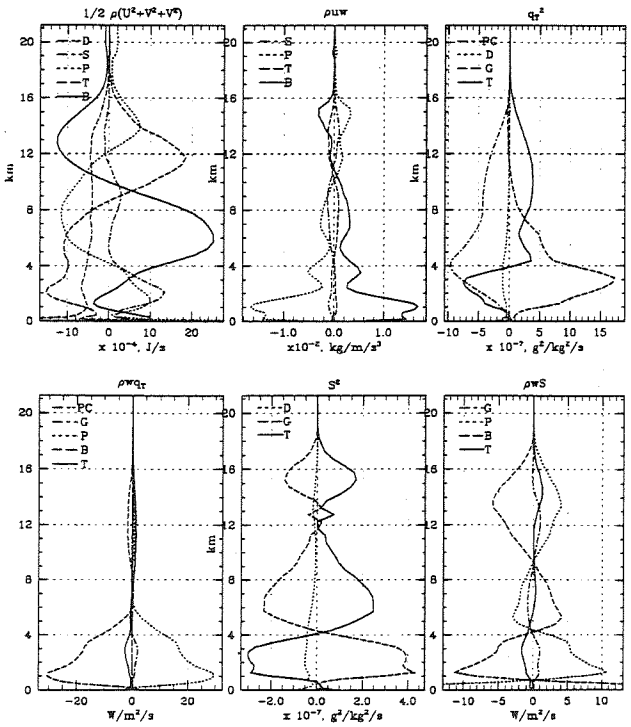

Figure 2. The vertical budgets of the second moments for the deep-convection event. The profiles are averaged over a 7-hour time period. Here: T - advective transport, P - total pressure production, B - buoyancy production, D - dissipation, PC - production due to precipitation.

SIGNIFICANT FEATURES FOUND IN SIMULATED TROPICAL CLIMATES USING A CLOUD RESOLVING MODEL

C.-L. Shie[1,2], W.-K. Tao[1], J. Simpson[1], and C.-H. Sui[1]

[1]Laboratory for Atmospheres
NASA/Goddard Space Flight Center, Greenbelt, Maryland
[2]Science Systems and Applications, Inc., Lanham, Maryland

1. INTRODUCTION

Cloud resolving model (CRM) has widely been used in recent years for simulations involving studies of radiative-convective systems and their role in determining the tropical regional climate. The growing popularity of CRMs usage can be credited for their inclusion of crucial and realistic features such like explicit cloud-scale dynamics, sophisticated microphysical processes, and explicit radiative-convective interaction (genuinely reviewed by Sui et al., 1994 and Tao et al., 1999, hereafter S94 and T99, respectively). For example, by using a two-dimensional cloud model with radiative-convective interaction process, Held et al. (1993), found a QBO-like (quasi-biennial oscillation) oscillation of mean zonal wind that affected the convective system. Accordingly, the model-generated rain band corresponding to convective activity propagated in the direction of the low-level zonal mean winds; however, the precipitation became "localized" (limited within a small portion of the domain) as zonal mean winds were removed. Two other CRM simulations by S94 and Grabowski et al. (1996, hereafter G96), respectively that produced distinctive quasi-equilibrium ("climate") states on both tropical water and energy, i.e., a cold/dry state in S94 and a warm/wet state in G96, have later been investigated by T99. They found that the pattern of the imposed large-scale horizontal wind and the magnitude of the imposed surface fluxes were the two crucial mechanisms in determining the tropical climate states. The warm/wet climate was found associated with prescribed strong surface winds, or with maintained strong vertical wind shears that well-organized convective systems prevailed. On the other hand, the cold/dry climate was produced due to imposed weak surface winds and weak wind shears throughout a vertically mixing process by convection.

In this study (related to Shie et al., 2000), considered as a sequel of T99, the model simulations to be presented are generally similar to those of T99 (where a detailed model setup can be found), except for a more detailed discussion along with few more simulated experiments. There are twelve major experiments chosen for presentations that are introduced in section two. Several significant feature analyses regarding the rainfall properties, CAPE (Convective Available Potential Energy), cloud-scale eddies, the stability issue, the convective system propagation, relative humidity, and the effect on the quasi-equilibrium state by the imposed constant radiation or constant surface fluxes, and etc. will be presented in the meeting. However, only three of the subjects are discussed in section three. A brief summary is concluded in the end section.

Corresponding author address: Chung-Lin Shie, Code 912, NASA/GSFC, Greenbelt, MD 20771; e-mail: shie@gert.gsfc.nasa.gov.

2. SENSITIVITY EXPERIMENTS

The major characteristics of the twelve sensitivity experiments presented (all with a 25-day integration period reaching a quasi-equilibrium state) are listed in Table 1. For example, in experiment "S4M" an initial sounding of S94 ("S"), a minimum surface wind speed of 4 ms^{-1} ("4") in the bulk formulas and a mixed-wind shear condition ("M") are applied. Soundings in S94 are generally found drier aloft than that in G96. The horizontal wind profile is vertically well mixed with time by convective processes (as in S94) in the mixed-wind shear runs, while it is relaxed to its initial value in the counterpart experiments with nudging (similar to G96). Three levels of minimum surface wind speed (1 ms^{-1}, 4 ms^{-1} and 7 ms^{-1}) are applied to test their effects on climate change through produced (computed) surface fluxes. The middle value 4 ms^{-1} is picked following S94 to account for the gustiness effect in the boundary layer. Details of the characteristics of the three major components can be found in T99. The two special pairs of experiments (R4M versus R4N, and F4M versus F4N) are performed with prescribed time-invariant radiation and surface fluxes, respectively. R4M has the same set-up as S4M except that the former uses the time-averaged shortwave and longwave radiation of the latter. With radiation being kept constant, only a one-way interaction between clouds and radiation is allowed throughout the entire integration in R4M. Its purpose is to examine whether a variation (varying or constant with time) in radiation pattern would be critical in changing the cloud modeled climates. R4N is similar to R4M except that the nudging wind shear is installed. Similarly, an application of the time-averaged surface fluxes of S4M to the paired experiments F4M and F4N (throughout their integration) is intended to study whether the climate status would be altered with a change from a time-fluctuating to a time-invariant surface flux.

3. RESULTS

Only three of several major features to be presented in the meeting are discussed in the following three sub-sections, respectively. First is the characteristic of rainfall properties, followed by the CAPE feature, and the effects on quasi-equilibrium states by the variously imposed radiation and surface fluxes patterns.

Table 1: Setups for the twelve experiments conducted.

Run Name	Sounding	Minimum Wind Speed	Vertical Wind Shear	Radiation	Surface Fluxes
S1M	S94	1 ms^{-1}	Mixed	Variant	Variant
G1M	G96	1 ms^{-1}	Mixed	Variant	Variant
S4M	S94	4 ms^{-1}	Mixed	Variant	Variant
S7M	G96	7 ms^{-1}	Mixed	Variant	Variant
R4M	S94	4 ms^{-1}	Mixed	Constant	Variant
F4M	G96	4 ms^{-1}	Mixed	Variant	Constant
S1N	S94	1 ms^{-1}	Nudging	Variant	Variant
G1N	G96	1 ms^{-1}	Nudging	Variant	Variant
S4N	S94	4 ms^{-1}	Nudging	Variant	Variant
S7N	G96	7 ms^{-1}	Nudging	Variant	Variant
R4N	S94	4 ms^{-1}	Nudging	Constant	Variant
F4N	G96	4 ms^{-1}	Nudging	Variant	Constant

3.1 Rainfall Properties

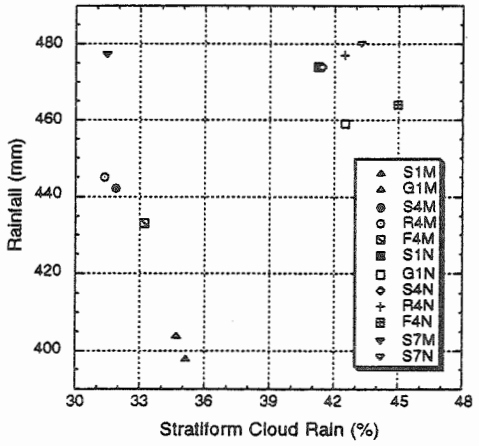

Figure 1. Scatter diagram of 25-day surface rainfall versus rainfall contribution by stratiform clouds (in %) for the twelve experiments.

Scatter diagram of 25-day surface rainfall versus the rainfall contribution by stratiform clouds (in %) for the twelve experiments is shown in Fig. 1. It first indicates that the experiments with mixed-wind shear have less rainfall contribution by stratiform clouds (between 30 to 36%), while the nudging experiments favor stratiform clouds that contribute more (between 41 to 45%) rainfall. The total rainfall intensifies with an increase in minimum surface wind for cases with mixed-wind shear whereas the contribution by stratiform clouds generally weakens. It also implies that, without the existence of a significant shear, the larger surface fluxes driven by a stronger surface wind have emerged as the dominant heat and moisture source that enhances the convective clouds as well as their contribution to the increased rainfall. On the other hand, for cases with nudging shear, they all produce large rainfall amount (with a greater role by stratiform clouds as mentioned), which however is independent of the embedded surface wind. Third, the convective clouds (55 to 70%) are still considered as the leading resource over the stratiform clouds (30 to 45%) in terms of the rainfall contribution among all the experiments.

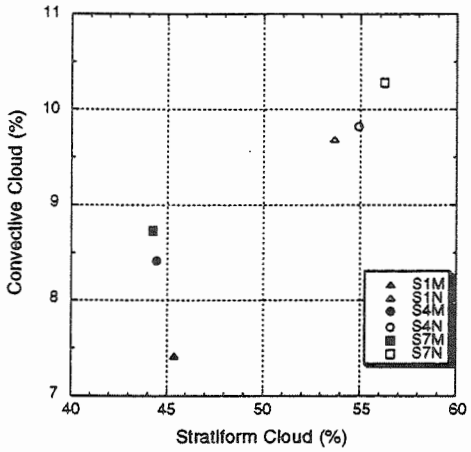

Figure 2. Scatter diagram of 25-day convective cloud coverage (in %) versus stratiform cloud coverage (in %) for three pairs of experiments.

However, the stratiform clouds dominate the cloud area coverage which is defined as a fraction of cloud region (with or without precipitation) over the entire domain, e.g., a 44.4% coverage by stratiform clouds to an 8.4% by convective clouds in S4M, a run with mixed-wind shear (see Fig. 2). This dominance by stratiform clouds elevates as the nudging shear is applied, e.g., a 54.9% coverage by stratiform clouds to a 9.8% by convective clouds in S4N. In other words, the total cloud area coverage (including both stratiform and convective clouds) enlarges by 22.5% (from 52.8% to 64.7%) due to the nudging effect. Furthermore, this cloud area enlargement due to nudging is greater with a higher minimum surface wind, i.e., a 20.1% of area increase from S1M to S1N, while a 25.7% area expansion from S7M to S7N. On the other hand, for those experiments with a mixed-wind shear, the convective cloud coverage is increased with an increased minimum surface wind (i.e., from 7.4% to 8.4%, and then 8.7%), while the stratiform cloud coverage slightly diminishes (i.e., from 45.4% to 44.4%, and then 44.2%). It again indicates that the surface latent heat flux has played a decisive role on the formation of the erect convective clouds when environment does not favor producing organized clouds; however, it does not alter the total cloud coverage which remains at about 52.8%. For the nudging cases, both the stratiform and convective clouds expand their area coverage as the minimum wind

speed increases, though the well-organized stratiform cloud dominates (53.7% to 56.2%) the convective cloud (9.7% to 10.3%) in area coverage. Apparently, the nudging wind shear performs a significant impact on the cloud system by enhancing the large-scale forcing process that generates more well-organized clouds as well as strengthening the surface flux process that generates more convective clouds.

3.2 Wet-bulb Potential Temperature & CAPE

Using the GISS GCM, Ye et al. (1998) produced a realistic linear relationship between CAPE and Θ_W in the surface layer and suggested that the CAPE variation is mostly determined by the moisture variation in the boundary layer over the tropical ocean. We found a similar linear pattern in our study using data at the end of the simulation period (Fig. 3). However, our CAPE is smaller than theirs for large Θ_W, yet larger for small Θ_W. Above all, both CAPE and Θ_W are found larger in the warm/wet cases than in the cold/dry cases that provides a consistent evidence for our finding based on a stability analysis. Accordingly, the warm/wet cases have involved in a more pseudo-adiabatic unstable environment, while the cold/dry cases have been associated with a more stable one. An additional finding from a relative humidity analysis also supports the same argument.

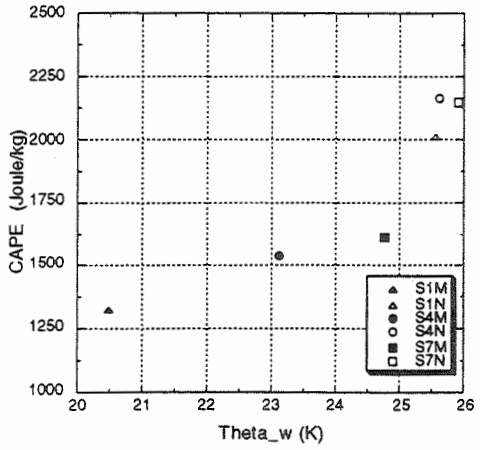

Figure 3. Scatter diagram of CAPE versus wet-bulb potential temperature at the end of simulation period for three pairs of experiments.

3.3 Constant Radiation and Surface Fluxes

In this section, whether the way (time-variant or time-invariant) radiation or surface fluxes treated in the model would be critical to alter the quasi-equilibrium state of energy and water vapor is discussed. First, by comparing R4M and S4M (or R4N and S4N), it is found that the paired experiments share the same climate regime mild/moist (or warm/wet) for the mixed-wind shear (or the nudging-wind shear) case regardless how the radiation is treated, i.e., time-variant or time-invariant (figure not shown). It implies that neither a two-way (time-variant) nor a one-way (time-invariant) radiative-convective interaction would alter a climate state, but how much the total amount of net radiation is involved could still be crucial. As a matter of fact, it is found that the equilibrium state moves up (warmer and moister) when radiation is completely shut off in our pilot runs (not shown) by considering that the net radiation would have been negative with a larger longwave cooling over a smaller shortwave heating, had them been included. Note that, the constant radiation implemented in both R4M and R4N was the time-averaged radiation obtained from S4M.

Regarding experiments associated with prescribed constant surface flux, a similar feature is found by the contrast of F4M and S4M (or, F4N and S4N). Namely, whether the surface layer interacts with the cloud system one-way (time-invariant fluxes) or two-way (time-variant fluxes) has no critical effect on the climate change. However, the surface fluxes embedded in the system are very important for the convective system to develop and reach a quasi-equilibrium state, especially for those mixed-wind shear cases while the large-scale forcing is weak. In our pilot runs excluding the surface fluxes (not shown), both temperature and water vapor are greatly reduced without reaching a quasi-equilibrium state after twenty-five days of simulation for a mixed-wind shear case. It is however found that various treatments of imposed surface fluxes more or less modify the cloud structure through the nudging effect, but not large enough to alter the quasi-equilibrium state.

4. SUMMARY

Besides the three major features discussed here, few more significant features will also be presented during the conference meeting. Even our simulations have been performed based on an environment that is more idealized than realistic, but the major features that have been found reasonable can be considered as realistically constructive. However, since the modeled quasi-equilibrium states have been found sensitive particularly to the two large-scale conditions (magnitude of the prescribed minimum wind speed and pattern of the imposed vertical wind shear), a more realistic and careful approach should be considered in our cloud-resolving model for our future research works. Further studies aiming at a better and thorough understanding of the mechanisms of the physical processes involving both the energy and water vapor budgets are also desired.

5. REFERENCES

Grabowski, W. W., M. W. Moncrieff, and J. T. Kiehl, 1996: Long-term behavior of precipitating tropical cloud systems: A numerical study. *Quart. J. Roy. Meteor. Soc.*, **122**, 1019-1042.

Held, I. M., R. S. Hemler, and V. Ramaswamy, 1993: Radiative-convective equilibrium with explicit two-dimensional moist convection. *J. Atmos. Sci.*, **50**, 3909-3927.

Shie, C.-L., W.-K. Tao, J. Simpson, and C.-H. Sui, 2000: A sensitivity study of equilibrium states simulated by a cloud-resolving model. *J. Climate.* (submitted)

Sui, C.-H., K. M. Lau, W.-K. Tao, and J. Simpson, 1994: The tropical water and energy cycles in a cumulus ensemble model. Part I: Equilibrium climate. *J. Atmos. Sci.*, **51**, 711-728.

Tao, W.-K., J. Simpson, C.-H. Sui, C.-L. Shie, B. Zhou, K. M. Lau, and M. Moncrieff, 1999: Equilibrium states simulated by cloud-resolving models. *J. Atmos. Sci.*, **56**, 3128-3139.

Ye, Bing, A. D. Del Genio, and K. K.-W. Lo, 1998: CAPE variations in the current climate and in a climate change. *J. Climate,* **11**, 1997-2015.

TOWARD CLOUD-RESOLVING MODELING OF CLIMATE: A GLOBAL CLOUD MODEL

Piotr K. Smolarkiewicz*, Wojciech W. Grabowski and Andrzej Wyszogrodzki
NCAR†, Boulder, Colorado

Contemporary atmospheric general circulation models (AGCMs) demonstrate convincingly that clouds play an essential role in the climate system through their impact on radiative fluxes and on the hydrologic cycle. However, the role of cloud physics per se is still unclear. Present AGCMs are incapable of addressing this issue, a priori, due to the way they treat cloud processes. For the most part this is because the spatial resolution of AGCMs is too coarse for cloud processes in general, and for convective dynamics in particular. This situation has to change if one aims to study the role of clouds in the climate system in more detail, for instance, to consider the indirect impact of atmospheric aerosols, or cloud-radiation interactions.

This is the first of two companion papers that report the development of numerical tools enabling the inclusion of elements of cloud dynamics and microphysics in modeling the atmospheric general circulation. Here we present our nonhydrostatic anelastic *global cloud model*—an incompressible Boussinesq-type Navier-Stokes' solver, suitable for modeling a broad range of idealized moist (and precipitating) atmospheric flows past an irregular lower boundary in a thin spherical shell.

The dynamic core of the global cloud model is discussed in detail in Smolarkiewicz et al. (1999, 2000). It is an extension (straightforward except for the semi-implicit treatment of internal gravity waves) of a Cartesian, small- to mesoscale nonhydrostatic anelastic model to a rotating mountainous sphere. Because of its small-scale heritage, our global model dispenses naturally with the traditional meteorological simplifications of hydrostaticity, gentle terrain slopes, and weak rotation. A unique feature of our models is the parallel implementations of nonoscillatory forward-in-time (NFT) semi-Lagrangian and Eulerian approximations (Smolarkiewicz and Pudykiewicz 1992, Smolarkiewicz and Margolin 1993), options which are selectable by the user. This approach has been employed in a variety of geophysical applications and the quality of results suggest that NFT methods are superior to the more traditional centered-in-time-and-space schemes in terms of accuracy, computational efficiency, flexibility and robustness (cf. Smolarkiewicz and Margolin 1997, 1998).

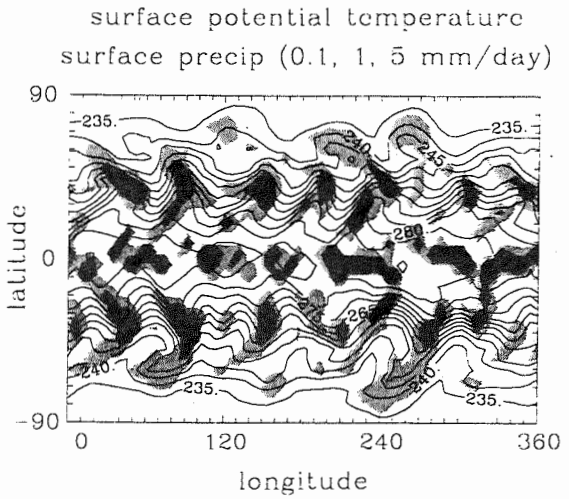

Figure 1: Spatial distribution of the surface precipitation (gray scale with light, intermediate, and dark gray representing surface precipitation rates between 0.1 and 1 mm/day, between 1 and 5 mm/day, and above 5 mm/day, respectively) and the surface potential temperature (isolines, contour interval of 5 K) for the moist HS global flow test at day 400.

The foundation of the global cloud model is the implementation of the moist precipitating thermodynamics which follows the strategy developed for cloud models and leads to an appropriate dynamical/thermodynamical framework for a cloud-resolving AGCM. However, at spatial resolutions available for present climate studies (rarely exceeding 1 degree in latitude and longitude), the main issue is how to deal with the disparity between the time scales of the fluid flow and the much shorter time scales associated with phase-change processes and precipitation fallout. Our approach is based on the method of averages (MOA; Nadiga et al. 1997), where fast processes are evaluated with adequately small time step (and lower accuracy) along flow trajectories to provide an accurate approximation to the large-time-step trajectory integral of a stiff process. This approach allows for stable integrations when cloud processes are poorly resolved

* *Corresponding author address*: Dr. Piotr K. Smolarkiewicz, NCAR, PO Box 3000, Boulder, CO 80307; e-mail: smolar@ncar.ucar.edu.

† NCAR is sponsored by the National Science Foundation.

(a situation typical in current global models), and it converges to the formulation standard in cloud models when the spatial and temporal resolutions reach values typical for cloud-resolving simulations ($\sim$ 1 km, $\sim$ 1 min). The cloud microphysics scheme selected for the initial tests is the simple yet robust scheme of Grabowski (1998) which considers just two classes of condensed water: cloud condensate (either cloud water or cloud ice depending on the ambient temperature) or precipitation (rain or snow).

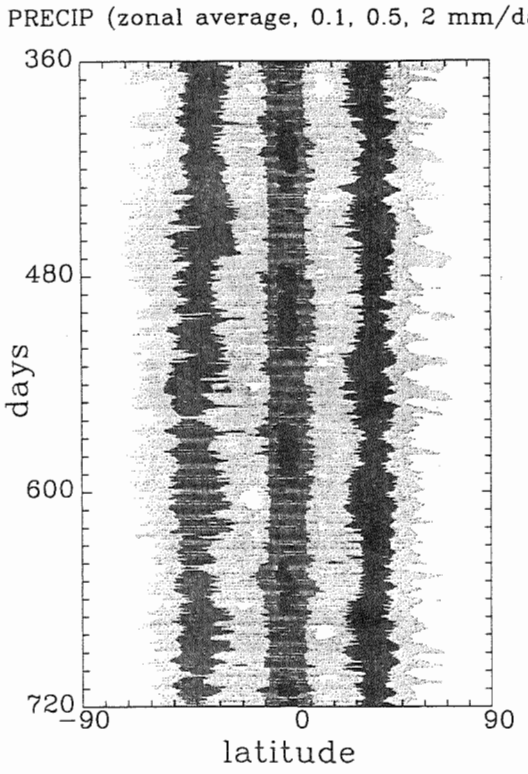

Figure 2: Hovmöller diagram of the zonally-averaged surface precipitation rate for the period of days 360 to 720 of the moist HS test. The gray scale with light, intermediate, and dark gray represents surface precipitation rates between 0.1 and 0.5 mm/day, between 0.5 and 2 mm/day, and above 2 mm/day, respectively.

We illustrate the above developments with an application of our global cloud model to the moist extension of the Held-Suarez (HS) test (originally dry; Held and Suarez 1994). The HS test considers flow on a smooth sphere (i.e., no topography) with the same size and rotation rate as the Earth. The global-scale flow is driven by prescribed meridional and vertical distribution of temperature which is maintained by a simple relaxation procedure. In addition, the lower tropospheric winds are relaxed toward the vanishing flow to mimic the effect of surface friction. The moist extension of the HS test adds a relaxation term to the conservation equation for the water vapor. The water vapor field is relaxed toward the water vapor distribution which corresponds to 90% relative humidity with respect to the prescribed ambient temperature.

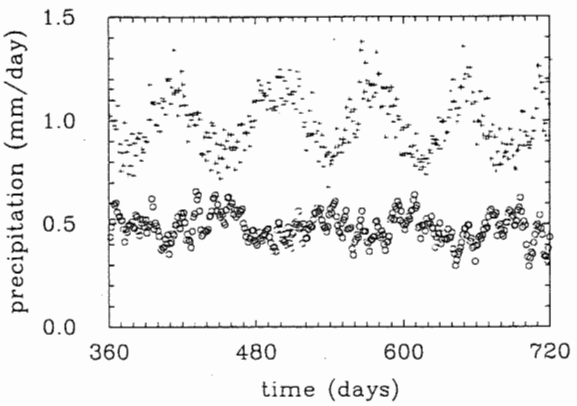

Figure 3: Evolution of the instantaneous surface precipitation rate averaged over the equatorial belt (from 20°S to 20°N, plus signs) and over the midlatitudes (from 60°S to 20°S and 20°N to 60°N, circles). Precipitation is sampled once every day. Equatorial values are increased by 0.25 mm/day to separate equatorial and midlatitude precipitation rates in the figure.

Figures 1 and 2 show examples of model results from a low-resolution simulation applying a grid of (64,32,24) in (longitude,latitude,vertical), with a vertical grid spacing of 0.8 km. The global model time step is 40 min. A 10-min time step is applied to the MOA representation of cloud microphysics and an implicit advection scheme is used for the precipitation sedimentation. An Eulerian variant of the global model is employed. The simulation is run for 720 days. Figure 1 shows a snapshot of the spatial distribution of the surface precipitation and isolines of the surface potential temperature at day 400. Figure 2, on the other hand, shows the Hovmöller diagram of the zonally-averaged surface precipitation rate for the period of day 360 to 720. Both figures show that the surface precipitation is associated with two distinct cloud systems. Near the equator, model analogs of the tropical convective cloud systems develop in response to the very low stability of the HS temperature profiles there. The low stability associated with an almost dry adiabatic ambient temperature profile results in large-scale moist convective overturning. Frontal cloud systems, associated with baroclinic eddies, develop in the midlatitudes. As illustrated in figure 2, these two distinct cloud systems are separated by zones of suppressed surface precipitation, mimicing subtropical highs in terrestrial global circulation. Another feature of the large-scale flow is a pronounced

low-frequency variability (LFV), with a period of about 70 days, associated with fluctuations of the zonally averaged surface precipitation. The LFV is most apparent in the equatorial surface precipitation as illustrated in Fig. 3. Fig. 3 also shows that the averaged precipitation rates in the tropics and midlatitudes are negatively correlated, i.e., the maximum averaged surface precipitation rates in the tropics correspond to the minimum surface precipitation in midlatitudes.

REFERENCES

Grabowski, W. W., 1998: Toward cloud resolving modeling of large–scale tropical circulations: A simple cloud microphysics parameterization. *J. Atmos. Sci.*, **55**, 3283–3298.

Held, I. M., and M. J. Suarez, 1994: A proposal for intercomparison of the dynamical cores of atmospheric general circulation models. *Bull. Amer. Meteor. Soc.*, 75, 1825–1830.

Nadiga, B.T., M.W. Hecht, L.G. Margolin, and P.K. Smolarkiewicz, 1997: On simulating flows with multiple time scales using a method of averages, *Theor. Comp. Fluid Dyn.*, **9**, 281–292.

Smolarkiewicz, P. K., and J. A. Pudykiewicz, 1992: A class of semi-Lagrangian approximations for fluids. *J. Atmos. Sci.*, **49**, 2082–2096.

Smolarkiewicz, P. K., and L. G. Margolin, 1993: On forward-in-time differencing for fluids: Extension to a curvilinear framework, *Mon. Wea. Rev.*, **121**, 1847–1859.

Smolarkiewicz, P. K., and L. G. Margolin, 1997: On forward-in-time differencing for fluids: An Eulerian/semi-Lagrangian nonhydrostatic model for stratified flows. *Atmos. Ocean Special*, **35**, 127–152.

Smolarkiewicz, P. K., and L. G. Margolin, 1998: MPDATA: A finite-difference solver for geophysical flows, *J. Comput. Phys.*, **140**, 459-480.

Smolarkiewicz, P. K., V. Grubišić, L. G. Margolin, and A. A. Wyszogrodzki, 1999: Forward-in-time differencing for fluids: Nonhydrostatic modeling of fluid motions on a sphere. *Proc. 1998 Seminar on Recent Developments in Numerical Methods for Atmospheric Modelling*, Reading, UK, ECMWF, 21-43.

Smolarkiewicz, P. K., L. G. Margolin, and A. Wyszogrodzki, 2000: A class of nonhydrostatic global models. *J. Atmos. Sci.* (submitted).

TOWARD CLOUD-RESOLVING MODELING OF CLIMATE: APPLICATION OF THE CLOUD-RESOLVING CONVECTION PARAMETERIZATION (CRCP) TO GLOBAL MODELING

Wojciech W. Grabowski*, Piotr K. Smolarkiewicz and Mirosław Andrejczuk
NCAR†, Boulder, Colorado

Smolarkiewicz et al. (2000b) presents a brief description and selected results from the *global cloud model*—a two-time-level nonoscillatory forward-in-time (NFT) Navier-Stokes solver in spherical geometry, suitable for modeling a broad range of idealized atmospheric flows, including flows with moisture and precipitation, past an irregular lower boundary. The model contains congruent semi-Lagrangian or Eulerian NFT approximations for fluids, selectable by a user.

Computational resources available today, however, do not permit cloud-resolving simulations of global-scale flows for planets similar to Earth. This is particularly true for flows featuring deep moist convection (e.g., in the tropics), where a horizontal resolution of $\sim$ 1 km is required (e.g., Grabowski et al. 1998, among many others). It is also well recognized that tropical deep convection is organized on a wide range of spatial scales, from a cloud system scale (tens of kilometers) up to the scale of the intraseasonal oscillation (thousands of kilometers), e.g., Nakazawa (1988). Despite vigorous research in this area in the last decade, the specific mechanisms behind the observed organization of tropical convection (or, more generally, behind the coupling of tropical convection with the large-scale flow) remain ambiguous.

This paper illustrates the application of the cloud-resolving convection parameterization (CRCP, Grabowski and Smolarkiewicz 1999) to modeling global moist precipitating flows. The CRCP technique represents subgrid scales of the global model by imbedding a 2D cloud-resolving model in each column of the global model. In the spirit of classical convection parameterization which assumes scale separation between convection and the large-scale flow, the cloud-resolving models from neighboring columns interact with each other only through the large-scale dynamics. The CRCP approach is perfectly suited for distributed memory architectures and it requires one to two orders of magnitude fewer computations than the cloud-resolving global model.

* *Corresponding author address*: Dr. Wojciech W. Grabowski, NCAR, PO Box 3000, Boulder, CO 80307; e-mail: grabow@ncar.ucar.edu.

†NCAR is sponsored by the National Science Foundation.

The modeling setup is a constant SST aquaplanet (with the same size and rotation as Earth) in radiative-convective equilibrium. The global model is that of Smolarkiewicz et al (2000a). It has low resolution in the E-W and N-S directions (32×16) and uses 51 levels with a uniform gridlength of

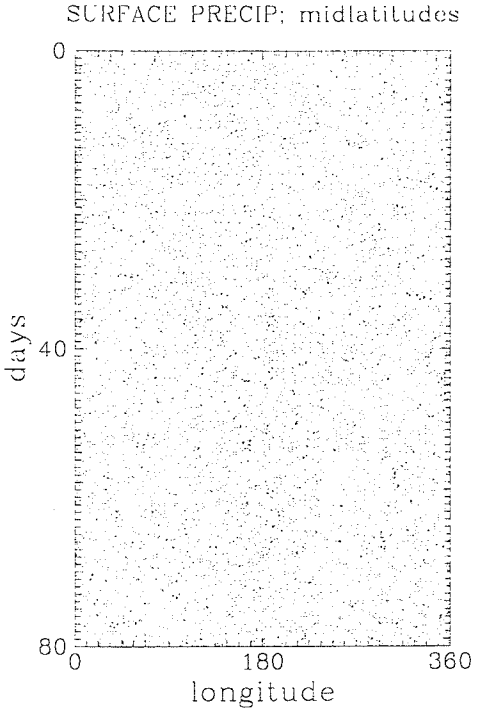

Figure 1: Hovmöller diagram of the surface precipitation rate in midlatitudes for the global CRCP model. For each time level, the surface precipitation rate combines precipitation rates from all CRCP 2D cloud models along a selected midlatitude belt.

0.5 km. The global model time step is 12 min. The 2D cloud-scale models in each column of the global model are aligned in the E-W direction and have a horizontal periodic domain of 200 km with a 2-km gridlength. The vertical grid is the same as in the global model, and the time step is 30 sec. The globally uniform SST is 30°C, and the effects of radiative processes are prescribed by applying a constant-in-time cooling rate profile (1.5 K/day be-

low 12 km, linearly decreasing from 1.5 K/day to zero between 12 and 15 km, and zero above 15 km). The global CRCP simulation was run for 80 days.

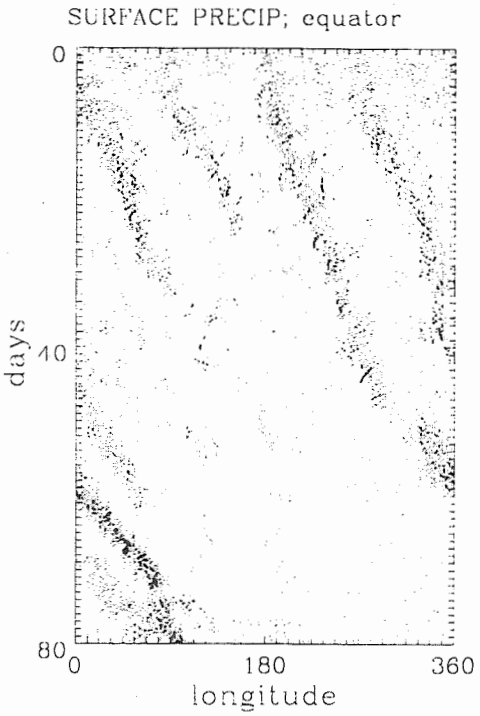

Figure 2: As Fig. 1, but for the surface precipitation on the equator.

Figure 1 and 2 show the Hovmöller diagrams of the surface precipitation in midlatitudes and on the equator, respectively, for the entire simulation. The precipitation outside the equatorial waveguide does not feature any large-scale organization and the zonal flow is weak (not shown). Near the equator, on the other hand, large scale-organization of convection is evident. Four eastward-propagating structures dominate during the first three weeks of the simulation. The convective clouds (or cloud systems) within these structures propagate towards the west. The subsequent merging of the eastward-propagating structures results in a strong solitary feature which dominates the surface precipitation on the equator in the last three weeks of the simulation. The solitary feature travels around the globe in about 60 days. The spatial structure of the surface precipitation and the large-scale flow is illustrated in Fig. 3 which shows the surface precipitation and zonal winds at day 80.00 of the CRCP global simulation. The solitary feature is characterized by strong surface precipitation on the leading edge of strong surface westerly winds (up to 35 m s^{-1}). Such a pattern of deep convection and surface flow is reminiscent of the Madden-Julian Oscillation and an associated westerly wind burst observed in the terrestrial tropical atmosphere.

REFERENCES

Grabowski, W. W., X. Wu, M. W. Moncrieff, and W. D. Hall, 1998: Cloud resolving modeling of tropical cloud systems during Phase III of GATE. Part II: Effects of resolution and the third spatial dimension. *J. Atmos. Sci.*, **55**, 3264–3282.

Grabowski, W. W., and P. K. Smolarkiewicz, 1999: CRCP: A cloud resolving convection parameterization for modeling the tropical convecting atmosphere. *Physica D*, **133**, 171–178.

Nakazawa, T., 1988: Tropical super clusters within intraseasonal variations over the western Pacific. *J. Met. Soc. Japan*, **66**, 823–839.

Smolarkiewicz, P. K., L. G. Margolin, and A. Wyszogrodzki, 2000a: A class of nonhydrostatic global models. *J. Atmos. Sci.* (submitted).

Smolarkiewicz, P. K., W. W. Grabowski, and A. Wyszogrodzki, 2000b: Toward cloud-resolving modeling of climate: A global cloud model. *In this volume.*

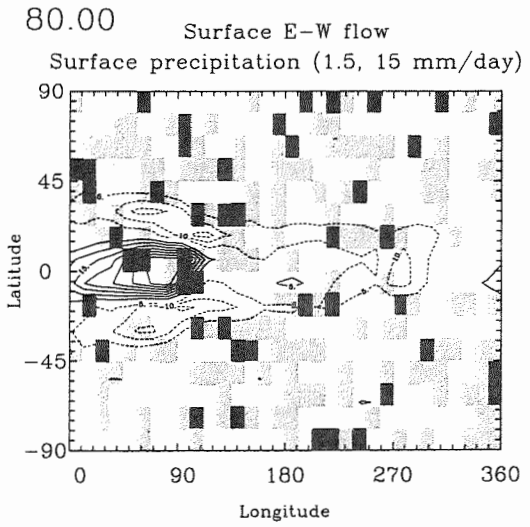

Figure 3: Spatial distribution of surface precipitation rate (gray scale, light and dark gray represents surface precipitation rate between 1.5 and 15 mm/day, and above 15 mm/day, respectively) and surface zonal winds (solid and dashed contours, contour interval of 5 m s^{-1}) at day 80.00 of the CRCP global simulation of the constant-SST aquaplanet in radiative-convective equilibrium. The mean surface precipitation is derived by averaging 2D cloud-resolving model precipitation inside each global model column.

A 1-D bulk-updraught model of deep convection

Hugh Swann
The Met. Office.

1. INTRODUCTION

Deep convection parametrization schemes used in weather and climate prediction models currently have very simplistic representation of updraught properties. The properties of convective updraughts are reasonably well approximated by a moist adiabat ascent, but water loading, latent heat due to freezing and the effect of mixing with environment air can effect virtual temperatures in the updraught by several degrees. Cloud Resolving Model results are used to quantify these processes. SCM simulations of convective atmosphere show the sensitivity of the modelled temperature and humidity profiles to the representation of these processes.

Given a supply of moisture, moist convection acts to remove instability where it exists, ie. the virtual temperature of the environment is adjusted towards that of the convective updraughts. Therefore, a deep convection parametrization (be it a mass flux or adjustment-type scheme) must accurately predict updraught virtual temperature in order to correctly predict the temperature profile of the convecting atmosphere.

Variability of atmospheric water vapour is the most important atmospheric feedback in present climate models. It is shown that varying the microphysics assumptions in a bulk-updraught mass-flux convection scheme has significant effect of the simulated humidity profiles.

2. THE UPDRAUGHT MODEL

Cloud Resolving Model (CRM) used in this study was The Met. Office's Large Eddy Model, described by Shutts and Gray (1994). The three-phase, five-category, double-moment microphysics scheme is described by Swann (1998). Two cases of deep (glaciated and precipitating) convection are used to derive the bulk-updraught model. A handful of cells are active at a given time and statistic are averaged over several cell lifetimes (about 3 hours). The bulk-updraught properties are defined here as the average over the *cloud core*, points that are both cloudy and buoyant.

Case SE3 was observed at 11pm on 5^{th} July, 1991. This case has an initial CAPE of 1000J/kg, most of which is removed during the 3 hour simulation. Cloud base temperature is 10°C and cloud top temperature is -42°C. The simulation used a 90x90x60 gridpoint domain with 500m horizontal resolution.

Case SE2 was observed at midday on 10^{th} May, 1990. The convective precipitation in this simulation was in balance with the surface moisture flux (assumed to be a constant 200W/m^2), the CAPE did not exceed 50J/kg. Cloud base temperature is 0°C and cloud top temperature is -33°C. The simulation used a 90x90x60 gridpoint domain with 333m horizontal resolution.

The cases are decribed in more detail by Swann (1998). More case studies will be required to ensure that the updraught model is valid over a broad range of convective conditions.

2.1 Mixing with the environment

The treatment of the interaction between updraught and environment (entrainment and detrainment) receives much attention in the literature. Conceptual models of entrainment and detrainment are one of the main distinguishing features between the various Mass Flux convection schemes used in forecast and climate models (Tiedtke 1989, Kain and Fritsch 1990 and Gregory and Rowntree 1990). The subject is discussed and entrainment and detrainments are quantified elsewhere (Swann 2000).

This study shows that the effect of entrainment and detrainment on bulk-updraught properties can be represented quite simply and is assumed to be independent of the shape and magnitude of the mass flux profile:

The mean buoyancy of the bulk-updraught is a constant fraction (0.5) of the buoyancy of an undilute parcel due to mixing between the updraughts and the environment. This implies that that the buoyant cloud core extends to the height of neutral buoyancy of an undilute plume, in agreement with CRM simulation (Figures 1a,2a). The effects of freezing and water loading are assumed to be the same for the undilute ascent and the bulk-updraught and are described in the following paragraphs.

In mass flux convection schemes it is necessary to make additional assumptions about the properties of air entering and leaving the updraught at each height in order to predict the updraught mass flux and the proportion of detrained cloud compared to precipitation production. A mass flux scheme based on an entraining plume must selectively detrain air which is cooler than the mean bulk-updraught in order to accurately predict the updraught temperature, as proposed by Yanai *at al.* (1973) and employed in The Met. Office Unified Model (Gregory and Rowntree 1990).

Corresponding author's address: Hugh Swann, Hadley Centre, The Met. Office, Bracknell, RG12 2SY, England.
E-mail: hswann@meto.gov.uk

2.2 Water loading

Water loading or precipitation drag is the effect on virtual temperature due to condensate in the updraught. Mass flux schemes often either ignore this term or only consider the updraught cloud mixing ration, neglecting the precipitation content of the updraught. CRM results (Figures 1c,2c) suggest that /bf Water loading is a constant fraction (0.3) of the adiabatic condensate.

2.3 Liquid Cloud Mixing ratio

In glaciated, precipitating convection liquid cloud is depleted primarily by freezing and collection by precipitation (we wont consider warm, non-precipitating convection where entrainment of dry air is the dominating process). **The liquid cloud mixing ratio is the product of a temperature-dependent time-scale and the condensation rate,** $q_L = \tau w \partial q_s / \partial z$ (Figures 1f,2f). The time scale, τ is 260s below the freezing level, 180s at the freezing level, falling to 100s at -40°C. **The velocity velocity squared increases with height in proportional to the buoyancy** (Figures 1g,2g).

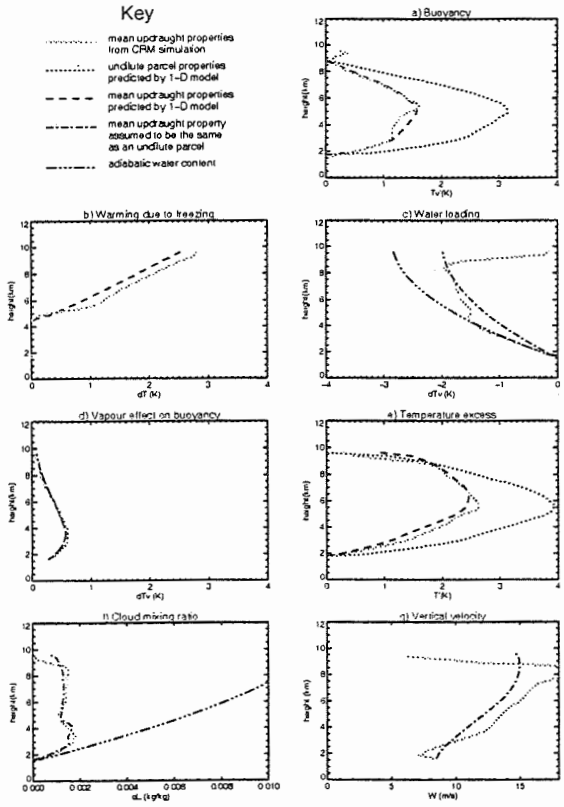

Figure 1: Updraught properties from the simulation of the SE3 case compared to those predicted by the 1–D bulk-updraught model.

2.3 Freezing

All precipitation produced at temperatures below O°C is frozen. (Figures 1b and 2b). In some cases (but not those used in this study) super cooled rain forms at temperatures as low as -10°C, this is neglected in this updraught model. An assumption regarding entrainment of dry air is required to predict the rate of precipitation production per unit mass flux, this updraught model assumes a fractional entrainment rate of $2/Z_{cloud}$ at cloud base, falling linearly with height to zero at cloud top (Swann 2000).

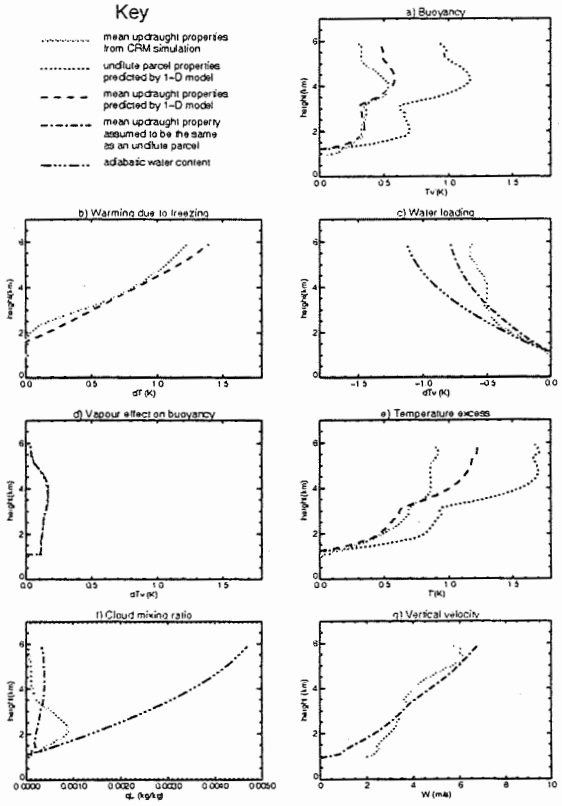

Figure 2: Updraught properties from the simulation of the SE2 case compared to those predicted by the 1–D bulk-updraught model.

3. APPLYING THE BULK-UPDRUAGHT MODEL TO A MASS FLUX CONVECTION SCHEME

The microphysics in the updraught model described may seem very simplistic *especially to those attending the ICCP!*. Many factors which may effect the subtleties of updraught microphyysics are not considered, such as the wind profile. No distiction is made between ice precipitation and cloud ice, which must be considered when including the updraught model with a downdraught and cloud model in a convection parametrization. The model will be refined by validating and tuning it to a wider range of cases.

However, water-loading due to precipitation and the dependence of liquid cloud mixing ratio on condensation rate are neglected or treated *even more crudely* in convection parametrizations. This is despite their undoubted effect on the bulk-updraught virtual temperature and water content which are fundamental quantity in determining the temperature and humidity profiles of the convecting atmosphere.

The notion that an entraining/detrainment plume should predict the presence of buoyant air right up to the level of neutral buoyancy for an undilute plume is also often disregarded in deep convection parametrizations. Representations of bulk-updraughts usually have no consideration of the relatively undilute air within the plumes which will rise to cloud top.

4. FUTURE WORK

The updraught model provides the basis for modifying aspects of the convection scheme in The Met. Office's Unified Model. The sensitivity of the SCM simulations to each aspect of the updraught microphysics changes can then be gauged.

References

Gregory and Rowntree 1990: A mass flux convection scheme with representation of cloud ensemble characteristics and stability dependent closure. *Q. J. R. Meteorol. Soc.* **118** ,1483-1507.

Kain, J. S. and J. M. Fritsch, 1990: A One-Dimensional Entraining Plume Model and Its Application in Convective Parameterization. *J. Atmos. Sci.* **47** ,2784-2802.

Swann, H., 1998: Sensitivity to the Representation of Precipitating Ice in CRM Simulations of Deep Convection. *Atmos. Res.* **48** ,415-435.

Swann, H., 2000: Evaluation of the mass flux approach to the parameterization of deep convection. *Quart. J. Roy. Meteorol. Soc. (in print)*

Tiedtke, M., 1989: A comprehensive mass flux scheme for cumulus parametrization in large-scale models. *Mon. Weather Rev.* **117** ,1779-1800.

Yanai, M., S. Esbensenn and J. Chu, 1973: Determination of Bulk Properties of Tropical Cloud Clusters from Large-Scale Moisture Budgets. *J. Atmos. Sci.* **30** ,611-627.

A NUMERICAL METHOD FOR THE SOLUTION OF THE STOCHASTIC COLLECTION EQUATION USING TWO PROGNOSTIC MOMENTS

M. Simmel[1], N. Mölders, and G. Tetzlaff

Leipziger Institut für Meteorologie (LIM), Leipzig, Germany

1 INTRODUCTION

In future, more powerful computers using parallelization techniques will allow weather forecast models to be run with high spatial resolution. One consequence may be that the bulk parameterization schemes that are used for the calculation of cloud microphysical processes at the moment will be replaced by explicit (or spectral) representations. This includes the difficulty of solving the stochastic collection equation (SCE), which describes the collisions between existing drops. Finally, this process leads to the formation of rain drops.

In the literature, various methods are known to solve the SCE numerically (Seeßelberg et al. 1996, Tzivion et al. 1999). Further references and a more detailed description of the method used can be found in Simmel (2000).

2 STOCHASTIC COLLECTION EQUATION

The SCE can be written in the form (e. g. Pruppacher and Klett 1997)

$$\frac{\partial n(x)}{\partial t} = \frac{1}{2}\int_0^x n(x-y)n(y)K(x-y,y)dy - n(x)\int_0^\infty n(y)K(x,y)dy \qquad (1)$$

where $n(x)dx$ is the number of drops $\epsilon\ [x, x+dx]$ per unit volume and $K(x,y)$ is the collection kernel. Note that $n(x) = n(x,t)$ is a function of time, too.

For the numerical solution of the SCE, a logarithmic mass discretization using J_{Max} bins is applied. A single drop of mass x belongs to bin k if

$$x_k \leq x < x_{k+1} \qquad (2)$$

with $x_{k+1} = px_k$ and $p = const > 1$. In our simulations we use $p = 2, 2^{1/2}, 2^{1/4}$, and x_1 corresponds to a drop with a radius $r_1 = 1\ \mu$m.

The lth moment of the distribution function $n(x)$ in bin k is defined as

$$M_k^l = \int_{x_k}^{x_{k+1}} x^l n(x)dx \qquad (3)$$

After multiplying (1) with x^l and integrating over each bin k, one obtains a set of prognostic equations for the moments in each bin k (Tzivion et al. 1999):

$$\frac{dM_k^l}{dt} = \qquad (4)$$
$$\frac{1}{2}\int_{x_k}^{x_{k+1}}\int_{x_1}^{x} n(x-y)n(y)K(x-y,y)dydx$$
$$-\sum_{j=1}^{J_{MAX}}\int_{x_k}^{x_{k+1}} x^l n(x)dx \int_{x_j}^{x_{j+1}} n(y)K(x,y)dy$$

The first term on the right-hand side describes the gain of bin k due to collisions that result in drops belonging to bin k (gain term). The second term describes the loss of bin k caused by the collision of a drop of bin k with any other drop (loss term). This set of equations has to be solved numerically.

3 LINEAR DISCRETE METHOD (LDM)

The 0^{th} moment ($M_k^0 = N_k$, number concentration in m^{-3}) and the 1^{st} moment ($M_k^1 = M_k$, liquid water content in kg m^{-3}, see eq. (3)) in each bin k are the prognostic fields used. Gain and loss terms are calculated seperately. The interaction term for two drops out of the bins i and j is

$$WM_{ij}^l = \int_{x_i}^{x_{i+1}} x^l n(x)dx \int_{x_j}^{x_{j+1}} n(y)K(x,y)dy \qquad (5)$$

which can be approximated by

$$WM_{ij}^0 = K_{i,j}N_iN_j \quad \text{for} \quad l=0 \qquad (6)$$
$$WM_{ij}^1 = K_{i,j}M_iN_j \quad \text{for} \quad l=1 \qquad (7)$$

[1] Corresponding author's address:
Martin Simmel, Leipziger Institut für Meteorologie (LIM), Stephanstr. 3, 04103 Leipzig, Germany,
E-mail: smartie@dynamics.meteo.uni-leipzig.de

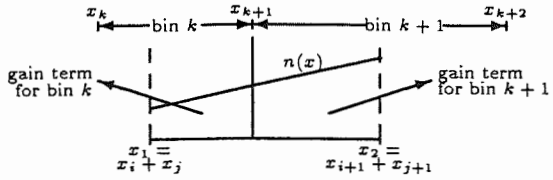

Figure 1: *Schematic view of the linear approximation to the distribution of the interaction terms of bins i, j that is used to calculate the gain terms for the bins k and $k+1$ caused by the interaction ($i \neq j$).*

This interaction results in a loss of the considered quantities for the bins i and j and in a gain for the bin k with $x_k = x_i + x_j$ and $x_{k+1} = x_{i+1} + x_{j+1}$ (if $j = i$) or for the bins k and $k+1$ with $x_k < x_i + x_j$ and $x_{k+2} > x_{i+1} + x_{j+1}$ (if $j \neq i$). If $j \neq i$, for the gain interval a linear distribution (Chen and Lamb 1994) will be used to calculate the time-dependent relative part of the two gain bins k and $k+1$ (Fig. 1).

4 RESULTS

We did simulations for different resolutions ($p = 2$, $p = 2^{1/2}$, and $p = 2^{1/4}$) for the Golovin kernel (Golovin 1963) and for the hydrodynamical kernel after Hall (1980). As initial distribution we use the same exponential function as Tzivion et al. (1987, 1999).

$$n(x) = 4\frac{N_0 x}{x_0^2}\exp[-2x/x_0] \qquad (8)$$

with $N_0 = 3 \cdot 10^8$ m^{-3} and $x_0 = 3.33 \cdot 10^{-12}$ kg for the simulations with the Golovin kernel and $N_0 = 10^8$ m^{-3} and $x_0 = 10^{-11}$ kg for the Hall kernel. This corresponds to a liquid water content of 1 g m^{-3} in both cases.

4.1 Golovin kernel

Using the Golovin kernel, the SCE can be solved analytically for various initial distributions (Golovin 1963, Scott 1968). The Golovin or "sum of mass" kernel is given as

$$K(x, y) = b(x + y) \qquad (9)$$

with $b = 1.5$ m^3 s^{-1} kg^{-1} and x, y the mass of the colliding drops. Out of all kernels for which an analytical solution of the SCE is known, the Golovin kernel is the closest to the hydrodynamical kernel and therefore it is a good test for the numerical method used.

Figure 2 shows the mass distribution for different resolutions p after an integration time of 15, 30, 45, and 60 minutes. For the lowest resolution used ($p = 2$), LDM slightly overestimates the growth. For the higher resolutions ($p = 2^{1/2}$ and $p = 2^{1/4}$), the analytical solution is approximated almost perfectly.

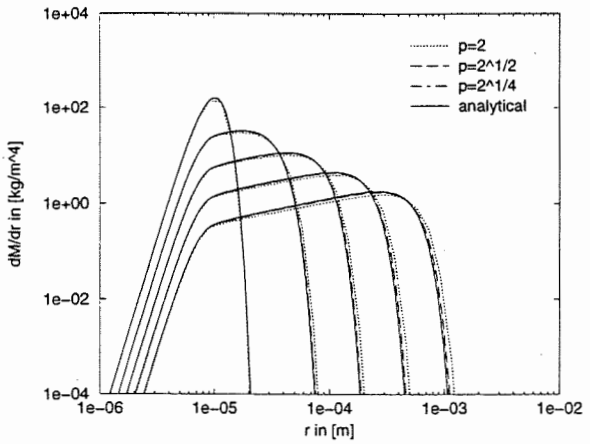

Figure 2: *Mass distribution for the Golovin kernel with $p = 2$ (dotted line), $p = 2^{1/2}$ (dashed line), and $p = 2^{1/4}$ (dot-dashed line) compared to the analytical solution (solid line). Results are shown after 0 (initial distribution), 15, 30, 45, and 60 min, respectively. Time step was 1 s.*

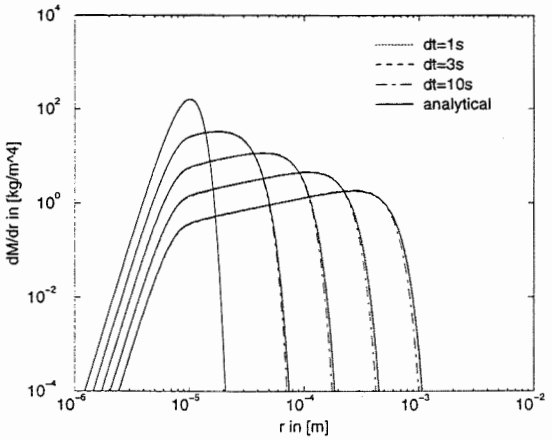

Figure 3: *Mass distribution for the Golovin kernel with $p = 2^{1/4}$ compared to the analytical solution (solid line). Results are shown after 0 (initial distribution), 15, 30, 45, and 60 min, respectively. Time steps were 1 s (dotted line), 3 s (dashed line), and 10 s (dot-dashed line).*

Figure 3 shows the simulation results using $p = 2^{1/4}$ for different time steps. The largest time step (10 s) leads to a slight underestimation of the growth, whereas the simulations using the smaller

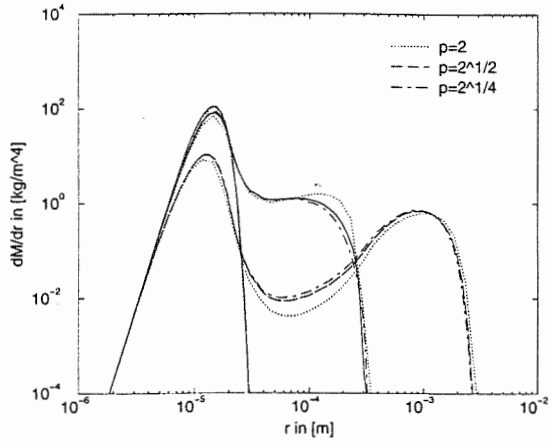

Figure 4: *Mass distribution for the hydrodynamical kernel with $p = 2$ (dotted line), $p = 2^{1/2}$ (dashed line), and $p = 2^{1/4}$ (dot-dashed line). Results are shown after 0 (initial distribution), 20, and 40 min, respectively. Time step was 1 s.*

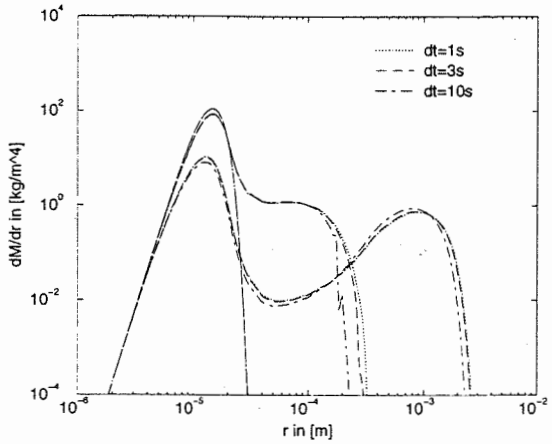

Figure 5: *Mass distribution for the hydrodynamical kernel with $p = 2^{1/4}$. Results are shown after 0 (initial distribution), 20, and 40 min, respectively. Time steps were 1 s (dotted line), 3 s (dashed line), and 10 s (dot-dashed line).*

time steps (1 s and 3 s) show almost the same results as the analytical solution.

These results for the Golovin kernel are comparable to those presented by other authors using different numerical methods (e. g. Kovetz and Olund 1969, Berry and Reinhardt 1974, Tzivion et al. 1987, 1999, Seeßelberg et al. 1996, Bott 1998).

4.2 Hydrodynamical kernel

The hydrodynamical kernel is defined as

$$K(x,y) = \pi(r_x + r_y)^2 E(x,y)|v_x - v_y| \qquad (10)$$

with the terminal fall velocity v and the collection efficiency $E(x,y)$. For our simulations we choose one of the most used datasets for the collision efficiency which is the one of Hall (1980). The coalescence efficiency is assumed to be unity and the terminal velocity is taken from Beard (1976). For the hydrodynamical kernel, no analytic solution is available.

Figure 4 shows the mass distribution for different resolutions p after an integration time of 20 and 40 minutes. Compared to the higher resolutions $p = 2^{1/2}$ and $p = 2^{1/4}$, which show almost the same result, the low resolution $p = 2$ only slightly overestimates the growth.

Figure 5 shows the simulation results using $p = 2^{1/4}$ for different time steps. Using a large time step (10 s) again leads to an underestimation of the growth compared to the runs using the smaller time steps (1 s and 3 s) which show almost the same results. The results for the 10 s time step show numerical problems after 20 minutes integration time (which disappear after 40 min), which is due to a too large time step.

An upper limit for the time step can be derived via the assumption that the loss for each moment and bin is limited by the existing moment itself (see eqs. (6) and (7))

$$\sum_{j=1}^{J_{MAX}} W M_{i,j}^l \Delta t_{MAX} = M_i^l \qquad (11)$$

which leads to

$$\Delta t_{MAX} = \left(\max_{i=1,J_{MAX}} \left(\sum_{j=1}^{J_{MAX}} N_j K_{i,j} \right) \right)^{-1} \qquad (12)$$

Due to the time dependence of N_j, Δt_{MAX} is time-dependent, too. This fact explains the vanishing of the numerical problems after 40 min, because then the total number concentration N is smaller than at 20 min.

5 CONCLUSIONS

Simulation results are presented for the Golovin and the hydrodynamical kernel after Hall (1980). For the Golovin kernel, the numerical solutions show a very good agreement with the analytical solution even for low resolution ($p = 2$) and are hardly to distinguish by visual inspection for higher resolutions ($\leq 2^{1/2}$). For the hydrodynamical kernel, an analytical solution is not available. The differences between solutions using different

resolutions are still small, but larger than for the Golovin kernel. Additionally, an upper limit for the time step was derived. Mass is conserved for all runs except for numerical inaccuracies.

Finally, we can conclude, that the numerical method presented is able to describe the coalescence process in a way which is appropriate to the requirements of spectral cloud models even when using the lowest resolution ($p = 2$). This fact is important because the computation time grows fast with the number of bins used.

At the moment, the model is extended to the ice phase, using theoretically derived collision kernels for various water-ice and ice-ice interactions as well as the corresponding terminal fall velocities (see Böhm 1999 and citations therein).

Acknowledgements

This work was supported by the Deutsche Forschungsgemeinschaft (DFG) under contract TE 51/11-1 and TE 51/11-3.

References

Beard, K. V. (1976). Terminal velocity and shape of cloud and precipitation drops aloft. *Journal of the Atmospheric Sciences 33*, 851–864.

Berry, E. X. and R. L. Reinhardt (1974). An analysis of cloud drop growth by collection. Part I: Double distributions. *Journal of the Atmospheric Sciences 31*, 1814–1824.

Böhm, J. P. (1999). Revision and clarification of "A general hydrodynamic theory for mixed-phase microphysics". *Atmospheric Research 52*, 167–176.

Bott, A. (1998). A flux method for the numerical solution of the stochastic collection equation. *Journal of the Atmospheric Sciences 55*, 2284–2293.

Chen, J.-P. and D. Lamb (1994). Simulation of cloud microphysical and chemical processes using a multicomponent framework. Part I: Description of the microphysical model. *Journal of the Atmospheric Sciences 51*, 2613–2630.

Golovin, A. M. (1963). The solution of the coagulation equation for cloud droplets in a rising air current. *Bull. Acad. Sci. USSR Geophys. Ser. 5*, 783–791.

Hall, W. D. (1980). A detailed microphysical model within a two-dimensional dynamic framework: Model description and preliminary results. *Journal of the Atmospheric Sciences 37*, 2486–2507.

Kovetz, A. and B. Olund (1969). The effect of coalescence and condensation on rain formation in a cloud of finite vertical extent. *Journal of the Atmospheric Sciences 26*, 1060–1065.

Pruppacher, H. R. and J. D. Klett (1997). *Microphysics of clouds and precipitation.* Kluwer Academic Publisher.

Scott, W. T. (1968). Analytic studies of cloud droplet coalescence. *Journal of the Atmospheric Sciences 25*, 54–65.

Seeßelberg, M., T. Trautmann, and M. Thorn (1996). Stochastic simulations as a benchmark for mathematical methods solving the coalescence equation. *Atmospheric Research 40*, 33–48.

Simmel, M. (2000). Two numerical solutions for the stochastic collection equation. *Wissenschaftliche Mitteilungen aus dem Institut für Meteorologie der Universität Leipzig und dem Institut für Troposphärenforschung e. V. Leipzig 17*, 61–73.

Tzivion, S., G. Feingold, and Z. Levin (1987). An efficient numerical solution to the stochastic collection equation. *Journal of the Atmospheric Sciences 41*, 1648–1661.

Tzivion, S., T. G. Reisin, and Z. Levin (1999). A numerical solution of the kinetic collection equation using high spectral grid resolution: A proposed reference. *Journal of Computational Physics 148*, 527–544.

An improved parameterization for simulating autoconversion, accretion and selfcollection based on a double-moment scheme

AXEL SEIFERT AND KLAUS D. BEHENG

Institut für Meteorologie und Klimaforschung, Universität Karlsruhe/Forschungszentrum Karlsruhe, 76021 Karlsruhe, Germany

1 Introduction

Most numerical models of the atmosphere treat clouds and precipitation by simple parameterizations. Based on heuristic considerations, Kessler (1969) has introduced equations describing the evolution of cloud water and rainwater mass concentration by the basic coagulation processes autoconversion and accretion. However, as has been shown by Beheng and Doms (1986), Kessler's method is unable to reproduce the time development of rainwater mass if different size distributions of cloud droplets with same liquid water content are considered.

In order to eliminate this deficiency Beheng (1994) has presented a double-moment parameterization explicitly taking into account the spectral width of a cloud droplet size spectrum as well as additionally formulating rate equations for the number densities of cloud droplets and raindrops. Note that Beheng (1994) based his parameterization on evaluating results obtained by numerically solving the so-called stochastic collection equation (SCE) describing the time rate of change of a drop spectrum.

The SCE is widely accepted to represent the microphysics of droplet coagulation in greatest detail (Pruppacher and Klett 1997). However, the inclusion of such a detailed formulation into a multidimensional numerical cloud model is very expensive. The aim of this paper is to close the gap between the heuristic parameterizations and the detailed but computationaly costly spectral modelling. Following the work of Beheng and Doms (1986), the SCE is taken as a reference to derive improved rate equations for the number concentrations and the liquid water contents of both cloud droplets and raindrops. In contrast to Beheng's (1994) original ad-hoc ansatz, the parameterization given here relies on a theoretical investigation using the collection kernel of Long (1974) and a fundamental scaling relationship of the SCE (Srivastava 1988).

2 Autoconversion, accretion and selfcollection based on Long's kernel

The SCE is originally formulated for a size distribution function $f(x)$ with drop mass x. By multiplication with x^k, $0 \leq k \in \mathbb{N}$, and integration, rate equations for the power moments $M^{(k)} = \int_0^\infty x^k f(x)\,dx$ result in the form

$$\frac{\partial M^{(k)}}{\partial t} = \frac{1}{2}\int_0^\infty\int_0^\infty f(x)f(y)K(x,y) \times \left[(x+y)^k - x^k - y^k\right] dx\,dy. \quad (1)$$

The collection kernel $K(x,y)$ is a nonnegative symmetric function of the masses x and y of drops undergoing binary collisions. Specifying $k = 0, 1, 2$ the first three moments are the number density N, the liquid water content L and a quantity Z which is - except a constant factor - equal to the radar reflectivity (in Rayleigh domain), respectively.

In order to derive rate equations for the partial coagulation mechanisms autoconversion, accretion and selfcollection, the complete size range of drops is formally splitted into a cloud droplet and a raindrop part (Beheng and Doms 1986). This procedure demands a collection kernel according to the partitioning concept. To this end, the piecewise polynomial collection kernel derived by Long (1974)

$$K(x,y) = \begin{cases} k_c(x^2+y^2), & x \wedge y < x^* \\ k_r(x+y), & x \vee y \geq x^*. \end{cases} \quad (2)$$

is applied, which is a mathematically simple, but sufficiently good approximation to a detailed formulation of the collection kernel. Here $x^* = 2.6 \times 10^{-7}$ g is the drop mass separating the cloud portion from the rain portion corresponding to a separating drop radius of 40 μm. For K in cm^{3}s^{-1} the constants are $k_c = 9.44 \times 10^9$ cm^{3}g^{-2}s^{-1} and $k_r = 5.78 \times 10^3$ cm^{3}g^{-1}s^{-1} as proposed by Long (1974). Inserting Eq. (2) in Eq. (1), the following rate equations for N, L and Z result

$$\frac{\partial N}{\partial t} = -k_c N_c Z_c - k_r(N_c L_r + N_r L_c + N_r L_r) \quad (3)$$

$$\frac{\partial L}{\partial t} = 0 \quad (4)$$

$$\frac{\partial Z}{\partial t} = 2k_c L_c M_c^{(3)} + k_r(L_c Z_r + L_r Z_c + L_r Z_r). \quad (5)$$

Note that the l.h.s. represent rates of change for the *complete* moments of $f(x)$ as defined above, while on the

Corresponding author's address: Axel Seifert, Institut für Meteorologie und Klimaforschung, Forschungszentrum Karlsruhe, 76021 Karlsruhe, Germany; E-Mail: axel.seifert@imk.fzk.de

r.h.s. the *partial* moments of $f(x)$ occur due to the partitioning concept of the drop spectra and the specific mass relations in Eq. (2). It should be noted that the first terms on the r.h.s. comprise contributions by both autoconversion and selfcollection, the second and third terms refer to accretion and the last terms are due to selfcollection by raindrops. Obviously the system of Eqs. (3) - (5) is subject to a severe closure problem and cannot be solved without further assumptions.

Since the structure of a drop spectrum largely determines its time evolution, it is reasonable to prescribe appropriate mathematical representations for the cloud droplet and the raindrop part, respectively, of the spectrum. We assume for cloud droplets a Gamma distribution function reading $f_c(x) = Ax^{\nu}e^{-Bx}$, ν = const., and for raindrops the traditional exponential formulation $f_r(D) = \alpha e^{-\beta D}$ with $D\,(\propto x^{1/3})$ = drop diameter.

Moreover, in order to facilitate evaluation, especially of the autoconversion rate, it is provisionally assumed that the cloud droplet spectrum $f_c(x)$ does not contain a significant number of droplets with masses almost equal to or larger than x^* (referred to as undeveloped cloud droplet spectrum in the following). In this case corresponding integrations can be extended beyond x^* to infinity without considerable error: the number density of cloud droplets N_c, e.g., is then

$$N_c = \int_0^{x^*} f_c(x)\,dx = \int_0^{\infty} f_c(x)\,dx = \frac{A\,\Gamma(\nu+1)}{B^{\nu+1}}, \qquad (6)$$

where Γ is the Gamma function. At first an approximation to the autoconversion rate is derived by evaluating Eq. (5). With f_c and f_r as formulated above it yields $Z_c = (\nu+2)L_c^2/[(\nu+1)N_c]$ as well as $Z_r = 20\,L_r^2/N_r$ and differentiation of the l.h.s. of Eq. (5) can easily be performed. Considering then $L_c = \bar{x}_c\,N_c$ ($\bar{x}_c$ = mean cloud droplet mass), $L_r \approx x^*\,N_r$ and $\partial L_r/\partial t = -\partial L_c/\partial t$ [from Eq. (4)] it follows in good approximation with $\bar{x}_c \ll x^*$

$$\frac{\partial L_r}{\partial t} = \frac{1}{20\,x^*}\left(\frac{\partial Z}{\partial t} + \bar{x}_c^2\,\frac{\nu+2}{\nu+1}\,\frac{\partial N_c}{\partial t}\right). \qquad (7)$$

This equation is now tailored more specifically to the autoconversion process by specifying $\partial Z/\partial t \equiv \partial Z/\partial t|_{au,sc} \approx 2k_c L_c M_c^{(3)}$ (cf. Eq. (5)) and $\partial N_c/\partial t \equiv \partial N_c/\partial t|_{au,sc} \approx -k_c N_c Z_c$ (cf. Eq. (3)) so that Eq. (7) finally results in

$$\left.\frac{\partial L_r}{\partial t}\right|_{au} = \frac{k_c}{20\,x^*}\,\frac{(\nu+2)(\nu+4)}{(\nu+1)^2}\,L_c^2\,\bar{x}_c^2. \qquad (8)$$

which shows a certain similarity to the autoconversion rate of Beheng (1994) obtained, however, by an ad-hoc ansatz.

Evidently the assumption of an undeveloped cloud droplet spectrum is generally not valid. For, as shown by Beheng and Doms (1990), selfcollection of cloud droplets (which so far has not been taken into account) leads to a broadening of the cloud droplet spectrum. For such a spectrum simple integrations as demonstrated by Eq. (6) are no longer permitted. Consequently the autoconversion relation Eq. (8) has to be modified as will be shown in the subsequent section.

Next the approximations of the accretion rate and the selfcollection rate of raindrops following from application of Long's kernel are given. By direct evaluation of the corresponding integral expressions from Beheng and Doms (1986) and furthermore assuming an undeveloped Gamma distributed cloud droplet spectrum one easily arrives at

$$\left.\frac{\partial N_r}{\partial t}\right|_{sc} = -k_r N_r L_r \qquad (9)$$

$$\left.\frac{\partial N_c}{\partial t}\right|_{ac} = -k_r N_c L_r \left(1 + \frac{\bar{x}_c}{\bar{x}_r}\right) \approx -k_r N_c L_r \qquad (10)$$

$$\left.\frac{\partial L_c}{\partial t}\right|_{ac} = -k_r L_c L_r \left(1 + \frac{\nu+2}{\nu+1}\,\frac{\bar{x}_c}{\bar{x}_r}\right) \approx -k_r L_c L_r \qquad (11)$$

with $\bar{x}_r = L_r/N_r$ = mean raindrop mass. Due to $\bar{x}_r \gg \bar{x}_c$, terms proportional to the ratio of the mean masses can be neglected. Similar equations have been derived by Ziegler (1985). Note that the approximate equations are not restricted to Gamma distributed cloud spectra.

It should be noticed that implicit in the kernel formula Eq. (2), a collision efficiency of one has been assumed for the intermediate drop sizes (Pruppacher and Klett 1997, p. 621), which is a valid approximation only for coagulation of relatively large raindrops with relatively large cloud droplets. Thus, it is expected that Eq. (11) has also to be corrected for effects by smaller collision efficiency values to be accounted for in case of raindrops collecting relatively small cloud droplets.

3 Similarity solutions and universal functions

In this section a new method is outlined to account for effects by broadening of the cloud spectrum due to selfcollection on the autoconversion and consequently the accretion rates.

Starting point is the fact that the stochastic collection equation is invariant under stretching transformations, i.e. each solution $f(x,t)$ has similarity solutions of the form

$$\tilde{f}(x,t) = cf(x,ct) \qquad (12)$$

with a positive constant c. In adopting the idea of Srivastava (1988), we choose for c the ratio of the liquid water contents of the solutions f and $\tilde{f}$. This also suggests the existence of an internal time scale of the coagulation process τ which is inversely proportional to the total liquid water content $L = L_c + L_r$. Specifically we set

$$\tau = 1 - \frac{L_c(t)}{L} \qquad (13)$$

being zero for $L_r = 0$ occuring mostly at the beginning of coagulation growth and one for $L_c = 0$ corresponding to a situation when nearly all clouds droplets have been converted to raindrops. With this dimensionless time scale,

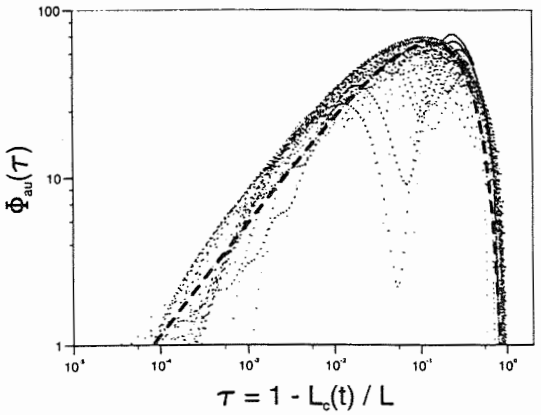

Figure 1: Scatterplot of the numerical results for the universal function $\Phi_{au}(\tau)$ as function of internal time scale τ as well as the curve according to Eq. (16) [thick dashed line]; all quantities in dimensionless units.

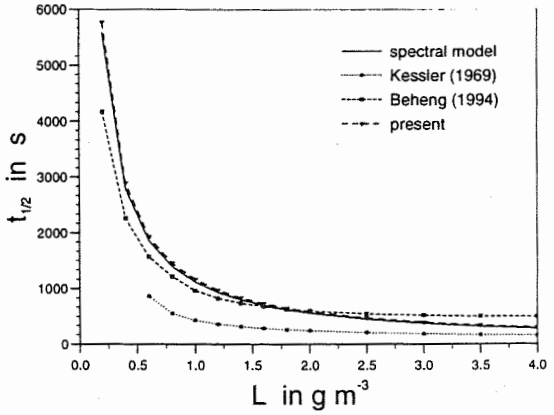

Figure 2: Halftime of coagulation $t_{1/2}$ in s as function of the total liquid water content L in g m^{-3} derived from SCE results and different parameterizations.

the approximation of the autoconversion rate Eq. (8) can be corrected by use of a universal function Φ_{au} depending only on τ. In detail we set

$$\left.\frac{\partial L_r}{\partial t}\right|_{au} = \frac{k_c}{20\,x^*}\,\frac{(\nu+2)(\nu+4)}{(\nu+1)^2}\,L_c^2\,\bar{x}_c^2 \times\left[1+\frac{\Phi_{au}(\tau)}{(1-\tau)^2}\right]. \quad (14)$$

Since Eq. (8) should also be valid for an undeveloped cloud spectrum, this implies $\Phi_{au}(0)= 0$. In this form the autoconversion rate is an extension of Eq. (8) by introducing an additional term varying solely via $\Phi_{au}(\tau)$.
For reasons mentioned at the end of the previous section, a correction of the accretion rate given by Eq. (11) is also necessary. Consequently we set

$$\left.\frac{\partial L_c}{\partial t}\right|_{ac} = -k_r\,L_c\,L_r\,\Phi_{ac}(\tau). \quad (15)$$

Here it is expected that $\Phi_{ac}(\tau) \to 1$ as $\tau \to 1$.
In order to find estimates of Φ_{au} and Φ_{ac}, we performed a series of numerical experiments where SCE is numerically solved applying empirical collection kernels (for details cf. Beheng 1982). The initial values (subscript '0') defining each cloud droplet spectrum ranged between $0.1\,\mathrm{g\,m^{-3}} \le L \le 3.0\ \mathrm{g\,m^{-3}}$ (implying $L_{r,0} = 0$) and $8\,\mu\mathrm{m} \le r_0 \le 20\,\mu\mathrm{m}$, $r_0 \propto \bar{x}_{c,0} = L_{c,0}/N_{c,0}$. For the constant width parameter we chose $0 \le \nu \le 3$.
The results for $\Phi_{au}(\tau)$ are shown in Fig. 1. Despite some scattering, which is also due to numerical deficiencies, the scaling, derived from the considerations above, works quite well. The shape of $\Phi_{au}(\tau)$ shows a clear maximum at about $\tau_{max} = 0.1$ and can be fitted by

$$\Phi_{au}(\tau) = 600\,\tau^{0.68}\left(1-\tau^{0.68}\right)^3. \quad (16)$$

Thus, the correction of effects by the broadening of the cloud droplet spectrum can amount to a factor of 60 compared to the case of an undeveloped cloud droplet spectrum.

As expected, the universal function for accretion, derived from the simulation results,

$$\Phi_{ac}(\tau) = \left(\frac{\tau}{\tau + 5\times 10^{-4}}\right)^4 \quad (17)$$

provides a considerable contribution only for very small τ.

4 Results and comparison with other parameterizations

In order to check the performance of different microphysical parameterizations we compare the halftime of coagulation $t_{1/2}$ defined as the time needed to convert 50 percent of the cloud water to rainwater. Accordingly Fig. 2 shows this time measure as function of the total liquid water content derived from (i) SCE results, from (ii) the above parameterizations and from (iii) the parameterizations of Kessler (1969) and Beheng (1994). In all cases an initial mean radius of $r_0 = 13\,\mu$m and a width parameter of $\nu = 0$ has been applied. For Beheng's parameterization, which is based on a radius representation of the cloud droplet spectrum, $n = 9.59$ has been used, corresponding to an equal reflectivity assumption.
A list of all conversion rate equations applied is given in the Appendix.
As can be seen, the new parameterization scheme is able to reproduce the SCE results. Kessler's scheme overestimates the speed of the coagulation process for $L > 0.5$ g m^{-3} by more than a factor of two. Due to the threshold value in his autoconversion rate, there is no evolution tendency for smaller liquid water contents. Beheng's parameterization performs quite well, but the dependency of the autoconversion rate on the liquid water content is not strong enough, leading to an overestimation for small and an underestimation for large liquid water contents.
A comparison of SCE results and the parameterization

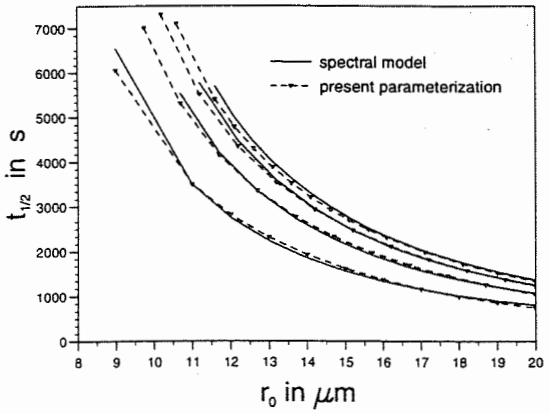

Figure 3: The halftime of coagulation $t_{1/2}$ in s as a function of the initial mean radius r_0 in μm and the width parameter ν ($\nu = 0, 1, 2, 3$ from bottom to top), $L = 0.5$ g m^{-3}.

presented, taking into account different mean radii r_0 and different widths of the initial cloud spectrum, is depicted in Fig. 3, showing the halftime of coagulation for $L = 0.5$ g m^{-3}. Only for small mean radii and large ν the speed of coagulation is slightly overestimated. Note that in the actual parameterization the only dependency on the width parameter ν is the simple term in Eq. (14).

5 Summary and conclusions

Based on the partitioning concept and Long's piecewise polynomial kernel, a new parameterization scheme describing coagulation in warm clouds has been directly derived from the stochastic collection equation. Using a similarity theory approach, subscale processes like the broadening of the cloud spectrum are included by universal functions, which have been derived from numerical data. The results of simulations calculated by this parameterization scheme strongly resemble those of spectral modelling.

The question remains how the similarity theory, which is exact for the zero-dimensional system, is affected when other processes like sedimentation are included. A comparision of spectral and parameterized microphysics in a one- or multi-dimensional cloud model would be necessary. On the other hand parameterization of sedimentation leads to additional problems as shown by Wacker and Seifert (2000). Future research will also include a breakup parameterization and the extension to a double-moment parameterization of mixed clouds.

Appendix
List of all parameterization equations

Autoconversion, accretion and the selfcollection of raindrops can be parameterized using equations (9), (14) and (15) with the universal functions (16) and (17). The remaining rate equations are:

$$\left.\frac{\partial L_c}{\partial t}\right|_{au/ac} = -\left.\frac{\partial L_r}{\partial t}\right|_{au/ac}$$

$$\left.\frac{\partial N_c}{\partial t}\right|_{au} = \frac{2}{x^*}\left.\frac{\partial L_c}{\partial t}\right|_{au}$$

$$\left.\frac{\partial N_c}{\partial t}\right|_{ac} = \frac{1}{\bar{x}_c}\left.\frac{\partial L_c}{\partial t}\right|_{ac}$$

$$\left.\frac{\partial N_r}{\partial t}\right|_{au} = -\frac{1}{2}\left.\frac{\partial N_c}{\partial t}\right|_{au}$$

$$\left.\frac{\partial N_c}{\partial t}\right|_{sc} = -k_c\frac{(\nu+2)}{(\nu+1)}L_c^2 - \left.\frac{\partial N_c}{\partial t}\right|_{au}$$

The last equation follows directly from equation (3) with everything else identical to Beheng (1994).

References

Beheng, K. D. (1982). A numerical study on the combined action of droplet coagulation, ice particle riming and the splintering process concerning maritime cumuli. *Beitr. Phys. Atmosph. 55*, 201–214.

Beheng, K. D. (1994). A parameterization of warm cloud microphysical conversion processes. *Atmos. Res. 33*, 193–206.

Beheng, K. D. and G. Doms (1986). A general formulation of collection rates of cloud and raindrops using the kinetic equation and comparison with parameterizations. *Beitr. Phys. Atmosph. 59*, 66–84.

Beheng, K. D. and G. Doms (1990). The time evolution of a drop spectrum due to collision/coalescence: A numerical case study on the effects of selfcollection, autoconversion and accretion. *Meteor. Rundsch. 42*, 52–61.

Kessler, E. (1969). *On the distribution and continuity of water substance in atmospheric circulations.* Meteor. Monogr. 32, Amer. Meteor. Soc., Boston.

Long, A. B. (1974). Solutions to the droplet collection equation for polynomial kernels. *J. Atmos. Sci. 31*, 1040–1052.

Pruppacher, H. and J. Klett (1997). *Microphysics of Clouds and Precipitation.* Kluwer Academic Publishers, Dordrecht.

Srivastava, R. (1988). On the scaling of equations governing the evolution of raindrop size distributions. *J. Atmos. Sci. 45*, 1091–1092.

Wacker, U. and A. Seifert (2000). On shock-type-solutions for the precipitation concentration in models with parameterized microphysics. *This proceedings.*

Ziegler, C. L. (1985). Retrieval of thermal and microphysical variables in observed convective storms. Part 1: Model development and preliminary testing. *J. Atmos. Sci. 42*, 1487–1509.

A HIGHLY ACCURATE ADVECTION ALGORITHM FOR CALCULATING TRANSPORT WITHIN NUMERICAL CLOUD MODELS

Chris J. Walcek*
Atmospheric Sciences Research Center, State University of New York, Albany, New York, 12203, U. S. A.

1. INTRODUCTION

For many physical science applications it is necessary to calculate the transport of fluid properties or trace constituent concentrations C using:

$$\frac{\partial C}{\partial t} = -\frac{\partial (uC)}{\partial x} \qquad (1)$$

For most atmospheric applications, numerical approximations of (1) are required to quantify advection. Unfortunately, numerical solutions suffer from numerous undesirable traits: oscillatory behavior near steep gradients, unphysical non-monotonic behavior, including negative concentrations, and appreciable numerical diffusion when small features are being advected.

Here a simple, absolutely monotonic numerical advection algorithm with extremely low numerical diffusion is presented and tested. Compared with more complex and computationally expensive higher-order schemes, the method described here is significantly more accurate yet less computationally intensive.

2. ALGORITHM DESCRIPTION

Eq. (1) can be expressed in terms of conservative mixing ratio Q (=C/ρ, where ρ is the fluid density):

$$\frac{\partial (\rho Q)}{\partial t} = -\frac{\partial (u \rho Q)}{\partial x} \quad . \qquad (2)$$

Using a forward-time difference approximation to the time derivative, and evaluating the space derivative at time t, mixing ratios at time t+Δt can be numerically estimated in terms of the initial Q distribution using:

$$Q_i^{t+\Delta t} = \frac{D_{d-1} Q_i^t - \left[(u \Delta t \rho Q_f)_+ - (u \Delta t \rho Q_f)_- \right] / \Delta x_i}{D_d} \qquad (3)$$

where the bracketed quantities refer to fluxes evaluated at the "higher-i" $()_+$ and "lower-i" $()_-$ cell edges (shown in Fig. 1), and ρ is the initial fluid density.

This scheme evaluates fluxes using the 2nd-order accurate van Leer (1977) approach, which is identical to Bott (1992) L=1, but several modifications that enhance the accuracy of these well-tested schemes are made. A linear distribution of tracer is assumed within each cell, and the gradient across the cell $\partial Q/\partial x = (Q_{i+1} - Q_{i-1})/2\Delta x$. Under these assumptions, the average mixing ratio in the fluid transported across the i+1/2 cell face during time step Δt, shown schematically in Fig. 1, is:

$$Q_f = \begin{cases} Q_i + (Q_{i+1} - Q_{i-1})(1-c)\alpha/4 \;, & u \geq 0 \\ Q_{i+1} + (Q_i - Q_{i+2})(1-c)\alpha/4 \;, & u < 0 \end{cases} \qquad (4)$$

where c is the local Courant number at the cell edge where fluxes are being calculated (=|u|Δt/Δx). α is a "sharpening factor" set to 1 most of the time. Setting α=0 yields simple upstream advection. As described below,

*Author address: ASRC, 251 Fuller Rd., Albany, NY 12203-3649. (Email: walcek@asrc.cestm.albany.edu)

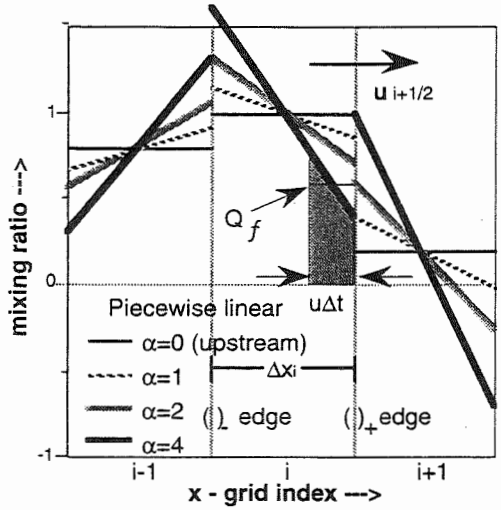

Fig 1. Schematic of piecewise-linear distribution through tracer distribution.

setting α>1 at two cells surrounding each local extreme greatly reduces numerical diffusion.

The D_d terms in (3) are dimensionally-dependent fluid densities, which change even in incompressible flows due to the "operator splitting" method of solving 2- or 3-D calculations one dimension at a time. D_{d-1} is the density at the beginning of the time step or dimensional step, and D_d is the density at the end of the time or dimensional step. These densities are given by:

$$\begin{aligned} D_0 &= (\rho)_i \;, \\ D_1 &= D_0 - [(\rho u)_{i+1/2} - (\rho u)_{i-1/2}]\Delta t/\Delta x_i \;, \\ D_2 &= D_1 - [(\rho v)_{j+1/2} - (\rho v)_{j-1/2}]\Delta t/\Delta y_j \;, \\ D_3 &= D_2 - [(\rho w)_{k+1/2} - (\rho w)_{k-1/2}]\Delta t/\Delta z_k \;. \end{aligned} \qquad (5)$$

D_0 and D_1 are used at the beginning and end of an x-advection step of a 3-D calculation. D_1 and D_2 are used at the beginning and end of the y-advection step, and D_2 and D_3 are used during z-advection. u, v, and w in (5) are the x, y, and z-direction velocities.

Monotonic constraints: Monotonicity is guaranteed through two steps. First, Q_f in (4) is constrained to fall within the range of the mixing ratios on either side of the cell interface where fluxes are being calculated.

$$\min(Q_i, Q_{i+1}) < Q_f < \max(Q_i, Q_{i+1}) \;. \qquad (6)$$

Second, updated mixing ratios are never allowed to exceed the highest mixing ratio allowed, nor can they fall below the lowest mixing ratio allowed. Thus

$$\min(Q_i, Q_{i-1}) < Q_i^{t+\Delta t} < \max(Q_i, Q_{i-1}) \qquad (7a)$$

if winds are positive (u≥0), and

$$\min(Q_i, Q_{i+1}) < Q_i^{t+\Delta t} < \max(Q_i, Q_{i+1}) \qquad (7b)$$

if winds are negative (u<0).

If $Q^{t+\Delta t}$ calculated using (3) ever violates the constraints in (7), then the outflowing flux [e. g. $(cpQ_f)_+$ in (3) if u>0] is adjusted upward or downward so that the $Q^{t+\Delta t}$ meets the limits in (7). The outflowing flux for updating mixing ratios at one cell becomes the inflow flux for updating mixing ratios at the next higher grid cell.

Limiting numerical diffusion: Overall numerical diffusion is limited by adjustment of the sharpening factor α in (4) near local extremes during calculation of fluxes so that mass is "aggregated" around local maximums, as shown in Fig. 1. If there is a local extreme at the cell immediately downwind of the edge where fluxes are being calculated, α should be:

$$\alpha = 1.75 - 0.45c \qquad (8a)$$

If the cell two cells upwind of the face where fluxes are being calculated is a local extreme, α in (4) should be:

$$\alpha = \max(1.5,\ 1.2 + 0.6c) \qquad (8b)$$

At all other cells, α is set to 1. A local extreme exists at cell "i" if $Q_i \geq \max(Q_{i+1}, Q_{i-1})$ or $Q_i \leq \min(Q_{i+1}, Q_{i-1})$.

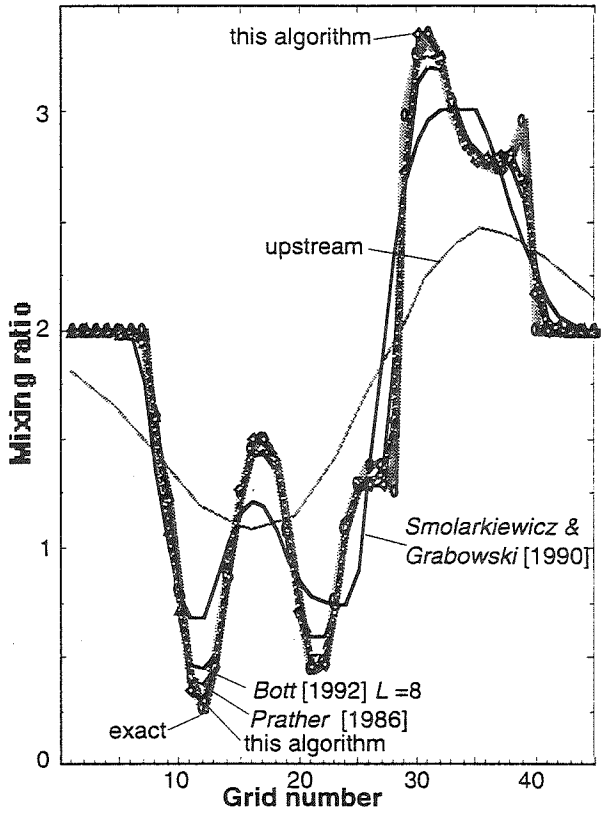

Fig 2. Advection test for irregular signaladvected 50 grid cells at Courant number 0.2. This algoritm compared with several algorithms used in atmospheric sciences.

Table 1. Computational Time and Errors for Fig. 2 test

Algorithm	Relative Computation Time	Mean rms Errors for Fig 2 shape, %
Upstream	1	17.04
Bott [1992] *L*=2	2.3	7.97
This algorithm	**2.9**	**2.80**
Bott [1992] *L*=4	3.1	5.77
Smolarkiewicz [1983]	4.0	11.12
Bott [1992] *L*=8	5.1	4.62
Prather [1986] (monotonic)	6.6	2.94

3. RESULTS & CONCLUSIONS

Results: Fig. 2 compares this scheme with other extremely high-order accurate approaches for an irregular signal used in previous advection tests. Table 1 summarizes the computational time and errors of this scheme showing that diffusion errors if this scheme are appreciably smaller than most higher-order and more computationally expensive approaches. The only scheme that produces errors for this test that are just slightly worse than this algorithm, the multi-moment Prather (1986) scheme, requires more than double the computation time and 3-10 times the memory requirements.

Conclusions: A simplified but very accurate method for calculating advection of mixing ratios in a mass conservative and monotonic manner in divergent multidimensional flows is presented. This scheme uses a flux adjustment near local extremes to greatly reduce unrealistic numerical diffusion around small features. Advection errors are reduced by a factor of 2-3 relative to higher-order schemes when advecting features that are resolved by fewer than 10-20 grid cells. Features resolved by more than 10-20 grid cells are advected with extremely low errors that are sometimes very slightly worse than existing higher-order schemes. Negative values can be advected by this scheme with no modifications. Because of its simplicity, the number of calculations required per time step are significantly lower than higher-order schemes. For modeling applications where features smaller than 10-20 grid cells in size are being advected, this scheme will yield significantly more accurate advection calculations than existing higher-order, more complex numerical advection schemes.

REFERENCES

Bott A., 1992: Monotone flux limitation in the area-preserving flux-form advection algorithm. *Mon. Wea. Rev.* **120,** 2592-2602.

Prather, M. J., Numerical advection by conservation of second-order moments, *J. Geophys. Res., 91*, 6671-6681, 1986.

Smolarkiewicz, P. K., and W. W. Grabowski, The multidimensional positive definite advection transport algorithm: Nonoscillatory option, *J. Comp. Phys., 86*, 355-375, 1990.

van Leer B., 1977: Toward the ultimate conservative difference scheme. IV: A new approach to numerical convection. *J. Comp. Phys.* **23,** 276-299.

INTERCOMPARISON OF DIFFERENT CLOUD MICROPHYSICS SCHEMES IN FORECASTS OF WINTER STORMS

Anna Glazer and André Tremblay

Meteorological Service of Canada, Dorval, Quebec, H9P 1J3, Canada

1. INTRODUCTION

The ability to forecast precipitation amount and types, as well as clouds and their phase, is becoming a necessity. In particular, forecasts of supercooled liquid water are essential to predict icing in clouds and freezing precipitation. Such forecasts are not possible with the current operational cloud scheme at the Canadian Meteorological Center (CMC). Moreover, the way that microphysical processes are treated within this scheme does not allow an easy implementation of new findings in the cloud physics domain. To improve this aspect of the operational forecasting system, the evaluation of the impact of cloud microphysics on the quality of mesoscale predictions was undertaken, and a number of simulations were performed using four different cloud schemes.

2. CLOUD SCHEMES

The evaluated cloud schemes are currently available within the CMC/RPN (Recherche en Prevision Numerique) library (Mailhot *et al.*, 1998). Each scheme has a different degree of complexity in the representation of cloud microphysics.

The explicit moisture scheme EXMO (Zhang, 1989; Hsie *et al.*, 1984) uses two prognostic variables. The first variable describes cloud water or ice in suspension and the second variable is introduced for the precipitation in the form of rain or snow. The solid phase (ice or snow) is predicted below 0 °C, the liquid phase (cloud water or rain) above 0 °C.

The KY scheme (Kong and Yau, 1997) introduces four prognostic variables. The cloud water in suspension is defined for all temperatures, allowing the existence of supercooled cloud droplets. The precipitating liquid water can exist for any temperature, giving both warm and freezing rain. Two types of solid precipitating particles are considered: ice crystal or snow, and graupel.

The MIXPHAS scheme (Tremblay *et al.*, 1996; Tremblay and Glazer, 2000) attempts to model the natural continuum of hydrometeors. The 3-D fields of cloud ice, supercooled cloud water, cloud water, freezing rain and rainwater are specified using only one predictive variable.

The SUND scheme (Sundqvist *et al.*, 1989) considers one predictive variable for suspended hydrometeors that are either liquid or solid, depending on the air temperature.

3. INTERCOMPARISON

3.1 MC2 model

To compare the behavior of the different cloud schemes on the mesoscale and their potential in numerical weather prediction applications, the simulations of winter storms were performed with the Canadian Mesoscale Compressible Community (MC2) model. The MC2 model is fully compressible, three-dimensional, non-hydrostatic, semi-implicit and semi-Lagrangian (Robert *et al.*, 1985; Benoit *et al.*, 1997). Model domain covering continental US and a large portion of Canada was selected for the current study. A 216 x 154 35-km resolution grid was used with 33 levels in the vertical. Below 5 km the levels had an equal spacing of 250 m. Above, the resolution was gradually decreased up to the model top at 25 km. For all simulations, a 6-minute time step was used to obtain the 48-hour integration. Each simulation was initialized and laterally driven by 35-km CMC objective analysis.

3.2 Cases

Sixteen winter storms were selected during the period from Dec. 10th 1996 to Feb. 13th 1997. Each storm was characterized by a wide range of surface conditions, including snow, rain, freezing rain or drizzle, ice pellets and icing in clouds. Such situations appear ideal for testing multi-phase cloud microphysics schemes. To have a well-balanced simulation set an equal number of integration were initialized at 00 UTC and 12 UTC.

3.3 Methodology

Anna Glazer, Meteorological Service of Canada,
Dorval, Quebec, H9P 1J3, Canada;
E-mail: anna.glazer@ec.gc.ca

Model results will be compared with satellite-derived cloud top pressure, surface precipitation, and upper-air data.

The satellite data can be used to infer the localization of cloud top. The pressure level of cloud top at a given pixel is determined by matching satellite infrared temperature (obtained from the 11 μm IR channel) with a three-dimensional analysis of observed pressure and temperature (Garand, 1993; Yu *et al.*, 1997). The cloud top pressure can be also derived from the model output. An infrared sensor detects radiation from a cloud down to a depth corresponding to an emissivity approaching unity. The emissivity depends on both liquid and ice water path and monotonically increases with them. Starting from the model top the combined emissivity of both liquid and solid phase clouds was determined for each model level until it reached the value 0.99. This level was considered as cloud top. Cloud top pressure derived from model output was subsequently compared with the satellite derived cloud top pressure.

Surface precipitation was verified directly from observations of conventional synoptic station reports using CMC standard procedures. For each forecast, modeled and observed 24-hour accumulations of precipitation were broken down into specific precipitation categories, and contingency tables were constructed. In general, each validation period includes about 500 reports of precipitation.

For the evaluation of temperature and humidity distribution the radiosonde dataset including aerologic stations of the WMO North American network contained within the model domain was used (approximately 100 soundings per verification time). Each station records at synoptic hour measurements of temperature, dew point, geopotential height, wind speed and direction at mandatory pressure levels (100, 250, 500, 700, 850, 925 and 1000 mb). The scores are calculated directly from the CMC verification package that follows the recommendations of the Commission for Basic Systems (WMO, 1998). This procedure is as proposed by Côté *et al.* (1998) and used for validation of the operational CMC forecast model. The scores of temperature and moisture (in term of dew point depression DPD = $T - T_d$) will be discussed.

4. RESULTS

4.1 Cloud top pressure (CTP)

The most abundant cloud species observed during the simulation period (Fig. 1) were middle level clouds (MLC: 400 < CPT ≤ 700 mb), followed by upper level clouds (ULC: 100 < CTP ≤ 400 mb). The low-level clouds (LLC: 700 < CTP ≤ 1000 mb) were rarely detected. The extent of observed free of clouds (FOC: CTP = 1000 mb) region (about 30% of the GOES8 domain) is much less than that forecasted. All schemes overforecast the FOC region by about a factor 2. Thus, in general there is a lack of clouds in the forecast model.

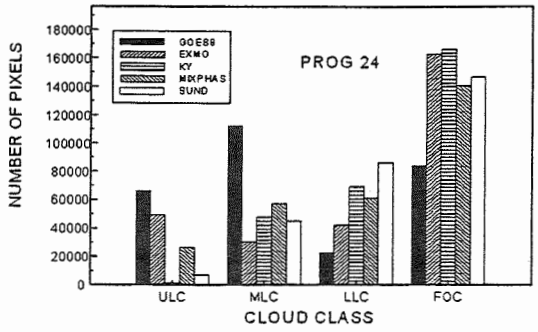

Fig. 1: Distribution of cloud top pressure for each scheme, 24-hour forecasts.

ULC were underforecast by all schemes. The situation is particularly critical for KY and SUND with ULC being quasi-absent for these schemes. MLC are also underforecasted in particular by the EXMO scheme. KY, MIXPHAS and SUND have better MLC forecasts than EXMO but underestimate the extent of these clouds by a factor 2. All schemes overforecast LLC. Such a systematic behavior is indicative of problems in other parts of the model physics, but a discussion of these issues is beyond the scope of this paper (Garand and Nadon, 1998). It can be said that in general EXMO and MIXPHAS have better cloud forecasts than KY and SUND, although there are apparent deficiencies in these schemes. The comparison of 48-hour forecast of cloud top pressure distribution with satellite data (not shown) confirms the conclusions formulated above.

4.2 Precipitation

Surface observations of accumulated precipitation for 00-24 h period are compared with model results (Fig. 2).

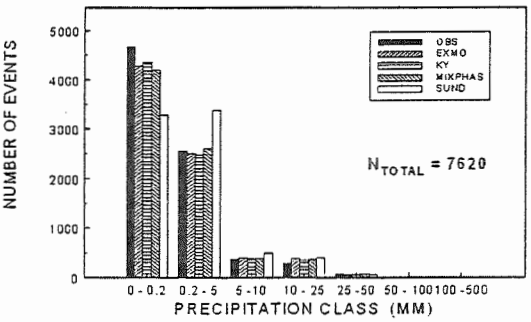

Fig. 2: Distribution of accumulation of precipitation for each scheme for 00-24 h period.

The SUND scheme systematically underforecasts the area of no precipitation (0 - 0.2 mm), but overforecasts the next class (0.2 – 5.0 mm). The precipitation trace of the SUND scheme is too wide. In comparison, the three remaining schemes have a better performance, with the number of events in each class closer to observations. For higher categories, the number of reports decreases and the statistics should be considered with caution. Nevertheless, it can be noted that in general the three microphysics schemes tend to produce better forecasts then the SUND scheme. The differences between the three schemes are small and it is difficult to determine the best performance. The same conclusions can be drawn from an examination of the 24-48 h period (not shown).

4.3 Temperature and moisture scores

Model results were also compared with available radiosonde observations in terms of temperature (Fig. 3) and DPD biases (Fig. 4).

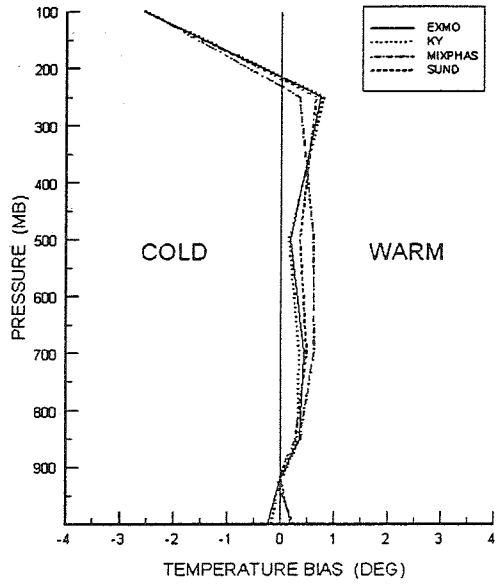

Fig. 3: Temperature bias for all simulations, 48-hour forecasts.

These statistics indicate that the distribution of temperature is weakly affected by cloud physics. Each simulation develops a weak (and almost uniform with altitude) temperature bias (≈ 1 °C) at the end of the 48-hour integration. The DPD bias score is affected by the cloud scheme under consideration. In general, the model tends to develop a dry bias with time in the middle atmosphere for all selected cloud schemes. The amplitude of the DPD dry mid-atmosphere bias is weakly affected by cloud scheme. It could be linked to other aspects of model physics. In general, the microphysics schemes are slightly better than the SUND scheme, particularly the KY scheme. These schemes improve the DPD bias score between 700 and 400 mb over the SUND scheme, although EXMO and MIXPHAS tend to develop a moist bias near 250 mb. However, DPD errors at low levels (high specific humidity) have much more influence on the hydrologic cycle than those at high levels (low specific humidity). The incorporation of the homogenous condensation-freezing nucleation mechanism in MIXPHAS removes the moist bias around the 250-mb level.

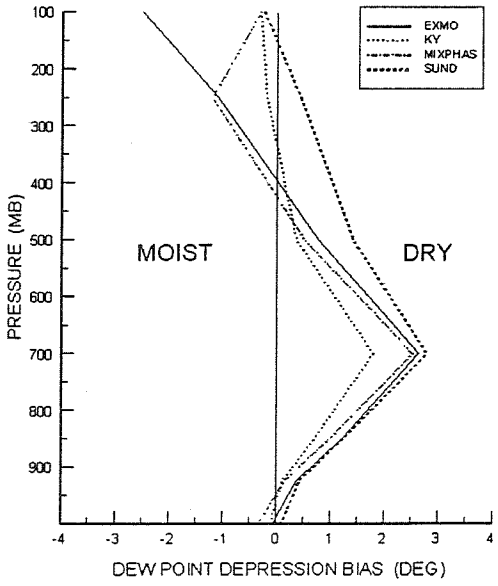

Fig. 4: Dew point depression bias for all simulations, 48-hour forecasts.

5. SUMMARY

All schemes underpredict the cloud cover and particularly the upper and mid level clouds. The low level clouds, (below 700 mb), however, are overpredicted by all schemes. The operational CMC scheme tends to systematically overforecast precipitation accumulation during the considered period. The remaining schemes have a comparable skill and are better than the operational scheme. Comparisons with radiosondes have shown that temperature is weakly affected by the choice of the cloud physics scheme. The distribution of moisture is more realistic for detailed microphysics schemes than for the operational CMC scheme. In general, the model tends to develop a dry bias with time in the middle atmosphere for all selected cloud schemes.

Two of the four analyzed schemes explicitly predict the occurrence of supercooled liquid water. One of them, the mixed-phase cloud scheme, better reproduces typical cloud structures. Its computational cost is equivalent to the actual operational scheme and it shows a superior forecast skill for winter storms. It has better cloud, precipitation and moisture forecasts.

6. ACKNOWLEDGMENTS

The authors are grateful to the National Search and Rescue Secretariat of Canada for a financial assistance. The authors would like to acknowledge Mr. André Méthot and Mrs. Monique Loiselle for their assistance with the CMC model validation package. Special thanks to Dr. Louis Garand for his help with the algorithm for cloud top pressure from model output.

7. REFERENCES

Benoit, R., M. Desgagne, P. Pellerin, S. Pellerin, Y. Chartier, and S. Desjardins, 1997: The Canadian MC2: A semi-Lagrangian, semi-implicit wideband atmospheric model suited for finescale process studies and simulation. *Mon. Wea. Rev.*, **125**, 2382-2415.

Côté, J., J.G. Desmarais, S. Gravel, A. Méthot , A. Patoine, M. Roch, and A. Staniforth, 1998: The operational CMC-MRB Global Environmental Multiscale (GEM) Model. Part II: Results. *Mon. Wea. Rev.*, **126**, 1397-1418.

Garand, L., 1993: A pattern recognition technique for retrieving humidity profiles from Meteosat or GOES imagery. *J. Appl. Meteor.*, **32**, 1592-1607.

Garand, L. and S. Nadon, 1998: High-resolution satellite analysis and model evaluation of cloud and radiation over the Mackenzie Basin using AVHRR data. *J. of Climate*. **11**, 1976-1996.

Hsie, E.Y., R.A. Anthes, and D. Keyser, 1984: Numerical simulation of frontogenesis in a moist atmosphere. *J. Atmos. Sci.*, **41**, 2172-2182.

Kong, F. and M.K. Yau, 1997: An explicit approach to microphysics in MC2. *Atmosphere-Ocean*, **35**, 257-291.

Mailhot, J., S. Bélair, R. Benoit, B. Bilodeau, Y. Delage, L. Filion, L. Garand, C. Girard, and A. Tremblay, 1998: Scientific description of RPN physics library – Version 3.6 –. Document available at: http://www.cmc.ec.gc.ca.

Robert, A., T.L. Yee, and H. Ritchie, 1985: A semi-Lagrangian and semi-implicit numerical integration scheme for multilevel atmospheric models. *Mon. Wea. Rev.*, **113**, 388-394.

Sundqvist, H., E. Berge, and J. E. Kristjansson, 1989: Condensation and cloud parameterization studies with a mesoscale numerical weather prediction model. *Mon. Wea. Rev.*, **117**, 1641-1657.

Tremblay, A. and A. Glazer, 2000: An Improved Modeling Scheme for Freezing Precipitation Forecasts. *Mon. Wea. Rev.*, **128**, 1289-1308.

Tremblay, A., A. Glazer, W. Yu, and R. Benoit, 1996: An explicit cloud scheme based on a single prognostic equation. *Tellus*, **18A**, 483-500.

World Meteorological Organization, 1998: Commission for Basic Systems. Extraordinary Session. Karlsruhe, 3-Sept. – 9 Oct. 1998. WMO-No. 893.

Yu, W., L. Garand, and A.P. Dastoor, 1997: Evaluation of model clouds and radiation at 100 km scale using GOES data. *Tellus*, **49A**, 246-262.

Zhang D.L., 1989: The effect of parameterized ice microphysics on the simulation of vortex circulation with a mesoscale hydrostatic model. *Tellus*, **41A**, 132-147.

A NEW METHOD FOR THE SOLUTION OF THE STOCHASTIC COLLECTION EQUATION IN CLOUD MODELS WITH MULTI-COMPONENT MICROPHYSICS

Andreas Bott
Meteorologisches Institut, Universität Bonn, Germany

1. Introduction

In a recent paper Bott (1998) presented a new flux method for the numerical solution of the stochastic collection equation (SCE). The method is mass conservative and consists of a two step procedure. In the first step cloud droplets with water masses $m_{w,i}$ and $m_{w,j}$ collide thus forming new drops with mass $m'_w = m_{w,i} + m_{w,j}$. This mass is entirely added to grid box k of the numerical grid mesh with $m_{w,k} \leq m'_w \leq m_{w,k+1}$. In the second step of the procedure a certain fraction of the water mass in grid box k is transported to $k+1$. This mass transport is calculated by means of an advection procedure. In different numerical case studies Bott compared the new approach with the model of Berry and Reinhardt (1974) and found very good agreement between the two methods. He also showed that with the flux method a numerical timestep of 10 s may be used without significant loss of accuracy so that the method is computationally very fast.

In cloud models with one-dimensional droplet distributions the flux method is an efficient and accurate approach for the solution of the SCE. In the microphysical stratus model MISTRA of Bott et al. (1996) and Bott (1997) cloud microphysical processes are considered by treating unactivated aerosols and cloud droplets in a joint two-dimensional size distribution. Each particle is characterized by the mass of its dry aerosol nucleus and by its water mass. Due to the use of a two-dimensional particle spectrum the treatment of collision/coalescence processes is not yet possible because to the author's knowledge in the literature a corresponding coalescence model for two-dimensional particle spectra is not yet available. In order to fill this gap, in the present paper the flux method will be extended for the solution of the SCE in cloud models with two-dimensional microphysics.

Corresponding author's address: Andreas Bott, Meteorologisches Institut, Universität Bonn, Auf dem Hügel 20, D-53121 Bonn, Germany; E-Mail: a.bott@uni-bonn.de

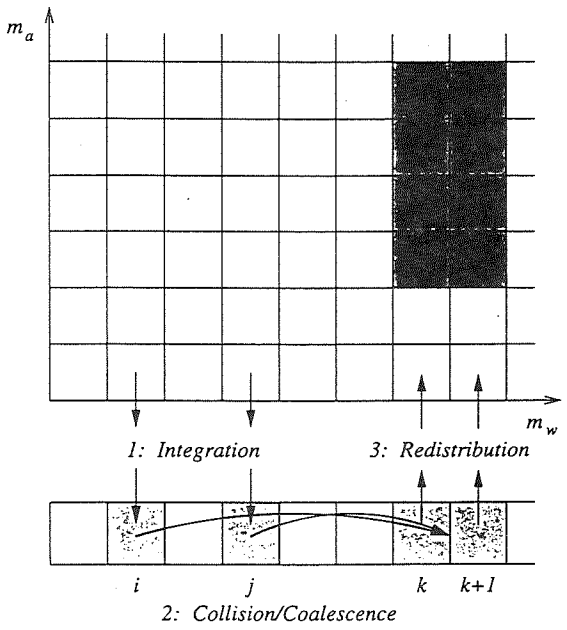

Figure1: Schematic illustration of the two-dimensional flux method.

2. Model description

A fundamental assumption of the new approach is that the probability for the collision of two cloud droplets only depends on their water mass m_w and not on the mass of their aerosol nucleus m_a. This assumption is justified since $m_a \ll m_w$. Based on this assumption the collision/coalescence process is calculated in the following way, see Figure 1:

i) The two-dimensional particle spectrum is integrated over the aerosol mass grid yielding a one-dimensional droplet spectrum as function of the water mass.

ii) For this distribution the SCE is solved by means of the one-dimensional flux method of Bott (1998). The collision of drops at grid

point i with drops at j yields a change in the mass distributions g_i, g_j and produces new drops $g'(i,\ j)$ with mass $m'_w(i,\ j) = m_{w,i} + m_{w,j}$. Since usually $m_{w,k} \leq m'_w(i,\ j) \leq m_{w,k+1}$ the mass density $g'(i,\ j)$ will be split up in grid boxes k and $k+1$. In the first step $g'(i,\ j)$ is entirely added to grid box k yielding the intermediate value $g'_k(i,\ j) = g_k + g'(i,\ j)$. In the second step a certain fraction of $g'_k(i,\ j)$ is transported into grid box $k+1$. The mass flux through the boundary $k+1/2$ is determined by means of exponential functions. For more details on the one-dimensional flux method see Bott (1998).

iii) The new two-dimensional particle spectrum is reconstructed from the one-dimensional intermediate distribution. Since the mass of the dry aerosol nucleus is negligble in comparison to the total mass of the drops, the corresponding weighting functions for the redistribution into the two-dimensional aerosol-water grid may be easily calculated.

3. Results

In the one-dimensional water grid space the flux method yields very similar results in comparison to the method of Berry and Reinhardt (1974). This is demonstrated in Figure 2 showing a comparison between the two methods.

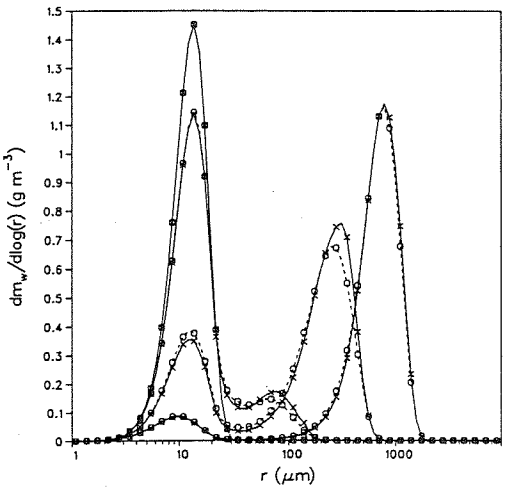

Figure 2: Spectral distribution of the water mass at the times indicated in the figure. Comparison between the method of Berry and Reinhardt (full curves) and the flux method (dashed curves).

Figures 3a–c show the time evolution of the water mass within the two-dimensional aerosol-water grid. The initial water mass is mainly carried by drops with radii smaller than 30 μm. The two local maxima of the contour plot are due to the bimodal structure of the initial aerosol size distribution. From Figures 3b,c it can be seen that with increasing time the main liquid water mass is continuously moving towards larger values of a and r whereby the newly formed drops are more or less concentrated along a straight line.

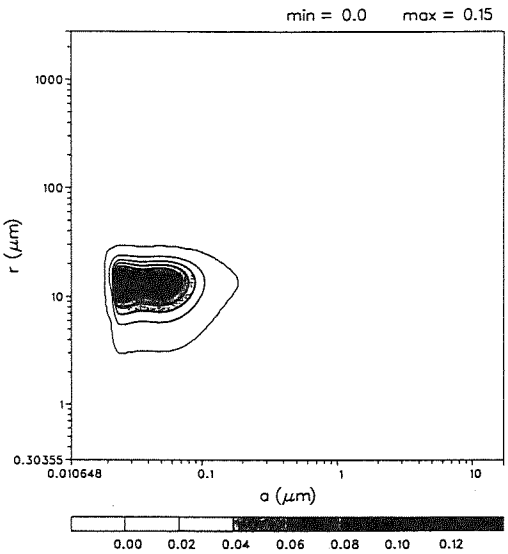

Figure 3a: Contour plot of the initial water mass distribution within the aerosol-water grid.

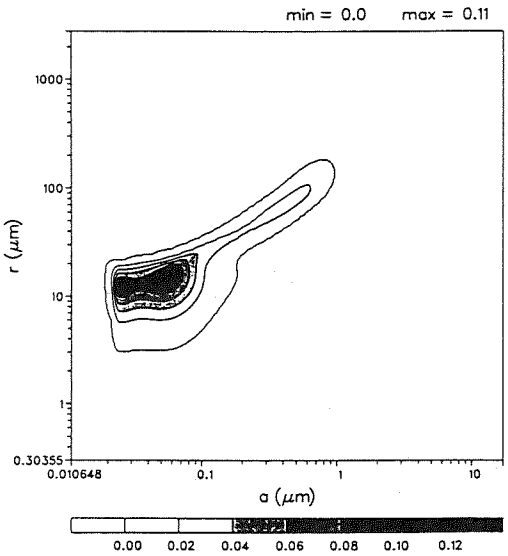

Figure 3b: Same as Figure 3a but after 30 min.

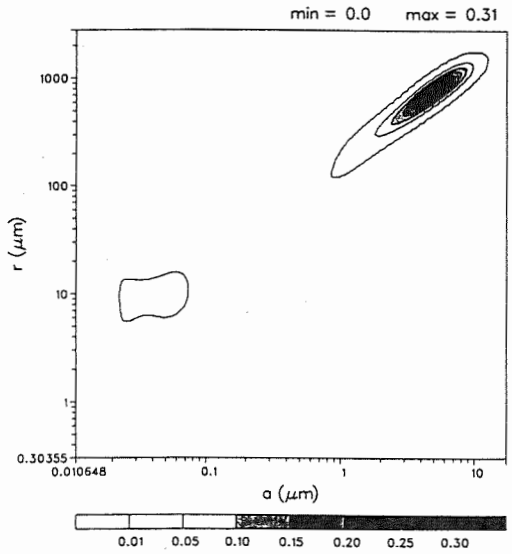

Figure 3c: Same as Figure 3a but after 60 min.

Figures 4a–c show the contour plots of the aerosol mass at different times. After 30 minutes a third mode has already evolved at the upper right edge of the mass spectrum depicting the newly formed drops, (Figure 4b).

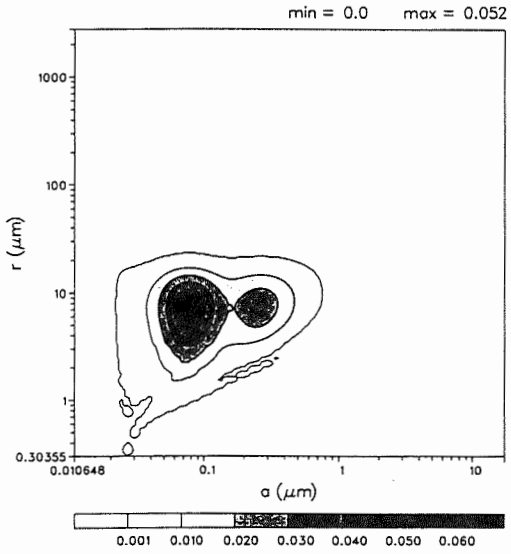

Figure 4a: Contour plot of the initial aerosol mass distribution within the aerosol-water grid.

Since at this time the aerosol mass of these drops is still relatively small, in the 30 minute curve of Figure 3 b this new mode is not yet visible but is expressed by a broadening of the second

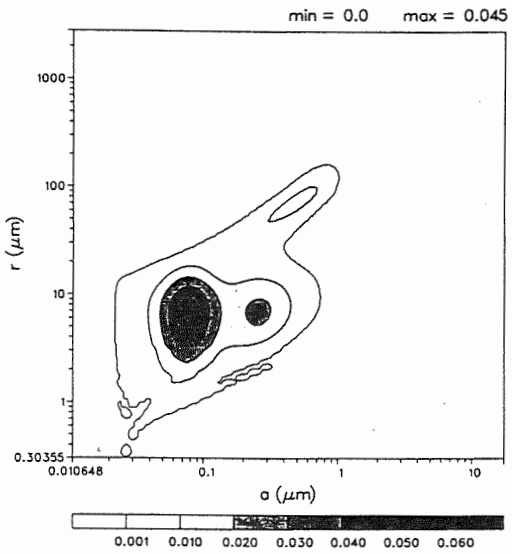

Figure 4b: Same as Figure 4a but after 30 min.

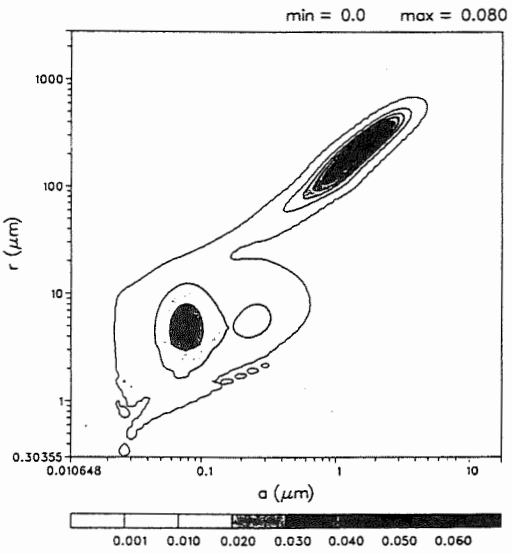

Figure 4c: Same as Figure 4a but after 60 min.

mode of the initial aerosol mass distribution. With increasing time more and more aerosol mass is transferred from the initial two modes into the third mode, (Figures 4b,c). After one hour collision/coalescence time most of the aerosol mass is found in the big rain drops. The time evolution of the mass distribution shown in these figures demonstrates how efficient the aerosol mass is removed from the atmosphere by falling rain drops.

4. Conclusions

In this paper a two-dimensional flux method for the solution of the stochastic collection equation has been presented. The method may be used in cloud models dealing with two-dimensional cloud microphysics. It is based on the one-dimensional exponential flux method of Bott (1998). The basic assumption of the approach is that the collision of two drops only depends on their water mass and not on the mass of their aerosol nucleus. Due to this assumption it is possible to reduce the two-dimensional solution of the SCE to a one-dimensional approach. In the first step of the procedure the two-dimensional particle spectrum is integrated over the aerosol mass grid yielding a one-dimensional distribution as function of the water mass. For this intermediate spectrum the SCE is solved by means of EFM. In the last step the new one-dimensional drop spectrum is redistributed into the two-dimensional aerosol-water grid.

From the numerical results it is seen that in the one-dimensional water grid space the flux method yields very similar results in comparison to the method of Berry and Reinhardt (1974). In the two-dimensional aerosol-water grid the drop distributions move from initially small radii (a, r) towards larger values whereby the drops are always concentrated along a straight line.

A more detailed description of the two-dimensional flux method may be found in Bott (2000).

Acknowledgements

This research is funded by the German Bundesministerium für Bildung und Forschung, BMBF. A FORTRAN code of the flux method is available upon request via E-mail from the author at a.bott@uni-bonn.de.

References

Berry, E. X, and R. L. Reinhardt, 1974: An analysis of cloud droplet growth by collection: Part I. Double distributions. *J. Atmos. Sci.*, **31**, 1814–1824.

Bott, A., T. Trautmann, and W. Zdunkowski, 1996: A numerical model of the cloud-topped planetary boundary-layer: Radiation, turbulence and spectral microphysics in marine stratus. *Quart. J. Roy. Meteor. Soc.*, **122**, 635–667.

Bott, A., 1997: A numerical model of the cloud-topped planetary boundary layer: Impact of aerosol particles on radiative forcing of stratiform clouds. *Quart. J. Roy. Meteor. Soc.*, **123**, 631–656.

Bott, A., 1998: A flux method for the numerical solution of the stochastic collection equation. *J. Atmos. Sci.*, **55**, 2284–2293.

Bott, A., 2000: A flux method for the numerical solution of the stochastic collection equation: Extension to two-dimensional particle distributions. *J. Atmos. Sci.*, **57**, 284–294.

SCALE ANALYSIS OF NON-CONVECTIVE CLOUDS IN LARGE SCALE AND IN GCM

Wang Bizheng Zeng Qingcun

(Laboratory of Numerical Modeling for Atmospheric Sciences and Geophysical Fluid Dynamics, Institute of Atmospheric Physics, Chinese Academy of Sciences, Beijing, 100029, China)

1. INTRODUCTION

Scale analysis of non-convective clouds in large scale and in GCM provides a method of comparing the magnitudes of the various terms of the non-convective clouds' equation. However, because non-convective clouds' distribution is discontinuous in large scale, classic method of scale analysis is not applied to the non-convective clouds' equation. In this study, another method of functional space characteristic scale, provided by Zeng Qingcun(1979), is used for solving the problem. In this paper, we will summarize the results with this method.

2. THE DIMENSIONLESS EQUATION IN FUNCTIONAL SPACE

In this study, we make the physical assumption that non-convective clouds' field is controlled by wind and temperature in large scale, and we do not consider the reaction of cloud field on the wind and temperature in the large scale during the scale analysis' time. This assumption is reasonable from the view of physics.

In spherical curvilinear coordinates the equation of the various phase non-convective cloud is

$$\frac{\partial}{\partial t}q_x + \frac{v_\theta}{a}\frac{\partial}{\partial \theta}q_x + \frac{v_\lambda}{a\sin\theta}\frac{\partial}{\partial \lambda}q_x + \dot{\sigma}\frac{\partial}{\partial \sigma}q_x = P + F_h + F_v, \quad (1)$$

where θ is co-latitude, λ is longitude, and σ is the vertical coordinate and is defined as

$$\sigma = \frac{p - p_t}{p_s - p_t}. \quad (2)$$

where p is the pressure at any level, p_t is the pressure at model top level, and p_s is the pressure at the surface, q_x is the cloud water mixing ratio including water cloud, ice cloud and mixing phase cloud, P is microphysics terms including precipitation, F_h is the horizontal turbulent term, and F_v is the vertical turbulent term, v_θ is velocity along θ direction, v_λ is velocity along λ direction, $\dot{\sigma}(=\frac{d}{dt}\sigma)$ is vertical velocity.

Although the microphysics process of non-convective clouds and precipitation is very complex, Wang Bizheng(1997) has demonstrated that the microphysics term P in (1) can be expressed as according to observation data

$$P = \pm\frac{q_x}{\tau} \quad (3)$$

where τ is a parameter, '+' represents cloud generation, and '-'represents cloud dissipation.

The F_h and F_V in (1) can be expressed as

$$F_h = \frac{k_h}{a^2\sin\theta}\left[\frac{\partial}{\partial\theta}\sin\theta\frac{\partial}{\partial\theta} + \frac{1}{\sin\theta}\frac{\partial^2}{\partial\lambda^2}\right]q_x \quad (4)$$

$$F_V = \frac{k_V}{(\Delta Z)^2}\frac{\partial^2}{\partial\sigma^2}q_x \quad (5)$$

where k_h is the horizontal turbulent coefficient, k_v is the vertical turbulent coefficient, and $\Delta Z = \frac{p_s}{\rho g}$.

Because q_x is not smooth in large scale, classic scale analysis method can not be used. The reason is as follows: If q_x is not smooth, then $\frac{\partial q_x}{\partial x}$ exists in the sense of generalized function, and can be written

Corresponding author's address: Wang Bizheng, Laboratory of Numerical Modeling for Atmospheric Sciences and Geophysical Fluid Dynamics, Institute of Atmospheric Physics, Chinese Academy of Sciences, Beijing, 100029, China;
E-mail:wbz@lasgsgi4.iap.ac.cn.

$$\frac{\partial q_x}{\partial x} = c\delta(x-b) \tag{6}$$

Where b is the point of discontinuity, and c is the constant. Thus, we use another method by Zeng Qingcun (1979). Characteristic scale F of any function f in the domain Ω of the non-convective cloud at any time can be defined as

$$F = \left\{ \frac{1}{V(\Omega)} \iiint_{\Omega} f^2 a^2 \sin\theta d\theta d\lambda d\sigma \right\}^{1/2} \tag{7}$$

where V(Ω) is the volume of the domain Ω .Mathematical difficulty of function's discontinuity can be avoided with this method. According to (7),characteristic time scale T is

$$T = \frac{\|q_x\|}{\left\| \frac{\partial}{\partial t} q_x \right\|} \tag{8}$$

characteristic horizontal scale L is

$$L = \frac{\|q_x\|}{\left\| \frac{1}{2a} \nabla_2 q_x \right\|} \tag{9}$$

where $\nabla_2 = \left(\frac{1}{a}\frac{\partial}{\partial\theta}, \frac{1}{a\sin\theta}\frac{\partial}{\partial\lambda} \right)$, and characteristic vertical scale H is in the sense of the coordinate σ

$$H = \frac{\|q_x\|}{\left\| \frac{\partial q_x}{\partial\sigma} \right\|} \tag{10}$$

Then let

$$t = Tt_1, q_x = \|q_x\| q_{x,1}, V_\theta = Uv_1,$$
$$V_\lambda = Uv_2, \dot{\sigma} = W\dot{\sigma}_1$$
$$\frac{1}{a}\frac{\partial q_x}{\partial\theta} = \frac{1}{L}\|q_x\|\frac{\partial}{\partial\theta} q_{x,1},$$
$$\frac{1}{a\sin\theta}\frac{\partial q_x}{\partial\lambda} = \frac{1}{L}\|q_x\|\frac{1}{a\sin\theta}\frac{\partial q_{x,1}}{\partial\lambda},$$

$$\frac{\partial}{\partial t} q_x = \frac{\|q_x\|}{T}\frac{\partial q_{x,1}}{\partial t_1}, \frac{\partial}{\partial\sigma} q_x = \frac{\|q_x\|}{H}\frac{\partial q_{x,1}}{\partial\sigma_1},$$
$$\frac{\partial^2}{\partial\sigma^2} q_x = \frac{\|q_x\|}{H^2}\frac{\partial^2 q_{x,1}}{\partial\sigma_1^2}, \frac{1}{a^2}\Delta_2 q_x = \frac{\|q_x\|}{L_1^2}\Delta_2 q_{x,1}.$$

We obtain the dimensionless equation of non-convective cloud

$$\begin{aligned} &\frac{\partial}{\partial t_1} q_{x,1} + \frac{UT}{L}\left(v_1\frac{\partial}{\partial\theta} q_{x,1} + v_2\frac{\partial}{\partial\lambda} q_{x,1} \right) \\ &+ \frac{WT}{H}\dot{\sigma}\frac{\partial}{\partial\sigma_1} q_{x,1} = \pm\frac{T}{\tau} q_{x,1} \\ &+ \frac{k_h T}{L^2}\Delta_2 q_{x,1} + \frac{k_v T}{D^2}\frac{\partial^2}{\partial\sigma_1^2} q_{x,1}, \end{aligned} \tag{11}$$

where $D = \Delta Z$ $H = \frac{Hp_s}{\rho g} = 10^3$ m is the cloud characteristic scale in the vertical direction. Zeng Qingcun(1979) has proven that the magnitude of each of the terms in (11) is determined by the coefficients of the terms in (11).Therefore, the magnitude of $\frac{UT}{L}$, $\frac{WT}{H}$, $\frac{T}{\tau}$, $\frac{k_h T}{L^2}$ and $\frac{k_v T}{D^2}$ represents the relative importance of horizontal advection of non-convective cloud, vertical advection, local change, horizontal turbulent change term , and vertical turbulent change term of non-convective cloud respectively.

According to observation data, Wang Bizheng (1997) has demonstrated that $T = \tau$ is the reasonable approximation.

3. THE RESULTS OF SCALE ANALYSIS OF NON-CONVECTIVE CLOUDS

3.1 The Result of Scale Analysis of High Cloud

For high cloud, the characteristic values are

$T = \tau = 3.6\times10^1$ s, $L = 1.0\times10^6$ m, $U = 30$ ms^{-1},
$W = 3.0\times10^{-6}$ s^{-1}, $k_h = 0.5\times10^6$ m^{2}s^{-1},
$K_v = 1.0\times10$ m^{2}s^{-1}, $D = 1,000$ m

with these values, we obtain

$$\frac{UT}{L}\sim 1.0,\frac{WT}{H}\sim 1.0,\frac{T}{\tau}=1.0$$
$$\frac{k_h T}{L^2}=1.8\times 10^{-2},\frac{k_v T}{D^2}=0.36. \quad (12)$$

From(12), the various terms except the horizontal turbulent exchange term in (12) are important.

3.2 The Result of Scale Analysis of Middle Cloud

For middle cloud, the characteristic value are

$T=\tau=3.6\times 10^{4}$ s, $L=1.0\times 10^{6}$ m, $U=15$ ms^{-1},
$W=3.0\times 10^{-6}$ s^{-1}, $k_h=0.5\times 10^{6}$ m^{2}s^{-1},
$K_v=1.0\times 10$ m^{2}s^{-1}, $D=1,000$ m

with these values, we obtain

$$\frac{UT}{L}\sim 0.5,\frac{WT}{H}\sim 1.0,\frac{T}{\tau}=1.0$$
$$\frac{k_h T}{L^2}=1.8\times 10^{-2},\frac{k_v T}{D^2}=0.36. \quad (13)$$

From(13), the various terms except the horizontal turbulent exchange term in (13) are important.

3.3 The Result of Scale Analysis of Ns

For Ns,the characteristic values are

$T=\tau=1.08\times 10^{4}$ s, $L=1.0\times 10^{6}$ m, $U=10$ ms^{-1},
$W=3.0\times 10^{-6}$ s^{-1}, $k_h=5.0\times 10^{6}$ m^{2}s^{-1},
$K_v=1.0\times 10$ m^{2}s^{-1}, $D=1,000$ m

with these values, we obtain

$$\frac{UT}{L}\sim 10^{-1},\frac{WT}{H}\sim 3.2\times 10^{-1},\frac{T}{\tau}=1$$
$$\frac{k_h T}{L^2}=0.54\times 10^{-2},\frac{k_v T}{D^2}=10^{-1}. \quad (14)$$

From(14), the microphysics term and local change term in (11) are important.

3.4 The Result of Scale Analysis of Marine St and Sc

Marine St and Sc is very important for climate and GCM. Their characteristic values are

$T=\tau=1.08\times 10^{4}$ s, $L=1.0\times 10^{6}$ m, $U=5$ ms^{-1},
$W=10^{-6}$ s^{-1}, $k_h=5.0\times 10^{6}$ m^{2}s^{-1},
$K_v=10^{2}$ m^{2}s^{-1}, $D=1,000$ m

with these values, we obtain

$$\frac{UT}{L}\sim 5.0\times 10^{-2},\frac{WT}{H}\sim 10^{-1},\frac{T}{\tau}=1$$
$$\frac{k_h T}{L^2}=0.54\times 10^{-2},\frac{k_v T}{D^2}=1.0. \quad (15)$$

From(15), local change term and the vertical turbulent exchange term in (11) are important.

4. REFERABLE TO THE DESIGNING OF NON-CONVECTIVE CLOUDS IN GCM

According to above results, we have some suggestions for designing of clouds in GCM.

First, the horizontal advection distance of high cloud and low cloud is UT=1,000 km and UT=500 km respectively, and both of the vertical advection distance of them is WT=1,000 m. Thus, they should be represented explicitly in GCM.

Secondly, all of the horizontal advection distance of Ns, St and Sc is UT=50 km. Thus, the horizontal grid distance should be 12.5 km in order to represent horizontal advection. However, this is difficult for the present GCM. They should considered in the future GCM.

Thirdly, the vertical advection distance of Ns is WT=320 m, and one of St and Sc is 108 m. Thus, More vertical layers in future GCM will be necessary in order to represent vertical advection in GCM.

Acknowledgements. Project 49805005 and Project 49735160 Supported by National Natural Science Foundation of China.

REFERENCES

Wang Bizheng, 1997: The dynamics of non-convective clouds in GCM and its computational problems. Ph. D. Dissertation, Institute of Atmospheric Physics, Chinese Academy of Sciences, 157pp.

Zeng Qingcun, 1979: Physical-Mathematical Basis of Numerical Weather Prediction. Vol. 1., Sciences, Press, Beijing, 543 pp.

MESOSCALE STRATIFORM CLOUD MODEL AND THE NUMERICAL EXPERIMENTS

Zhou Yuquan Huang Yimei

Henan Provice Meteorological bureau 110 Jingshui Road, Zhengzhou , 450003, P.R.China

1. Introduction

Stratiform colud system is usually accompanied by large or mesoscale weather system, its dynamic procedure depends on large or mesoscale atomospheric movement. Only by building mutually coupled complete stratiform cloud model of dynamics and cloud physics, we can completely and accurately forecast the developing and evolving law of atomospheric cloud and rainfall. In mesoscale weather forecast model, use reasonable cloud rainfall display scheme to replace previous convection parameterization scheme, which is the hot spot of research and development in international meteorological field. Whereas, the shortcoming is that the presently used display scheme is comparatively simple. The paper nests Hu Zhijin's detailed three dimension stratiform cloud model into MM4 mesoscale model, a perfect three dimensional mesoscale cloud model has been built up, and on the basis, a real-time mesoscale cloud field and rainfall field forecast system has been set up, the forecast system is organically connected with local real-time material system. The forecast system has been running in the central part of China for over one year, and has provided many numerical instruction products for local rainfall and cloud field forecast and artificial cloud spreading experiment. The paper makes a brief introduction to the three aspects of model, real-time forecast system development and the operational application of product:

2. Three dimensional mesoscale cloud model

Mesoscale model dynamic structure selects and uses NCAR/PSUMM4 model, and makes locally reforming to its data preprocessing part, based on this, leads into Hu Zhijin's detailed double parameter microphysical model, to form a three dimensional mesoscale cloud system model. The model integrates 1440 minutes, from which a 10 kinds mesoscale macrofield and a microphysical field of cloud in 6 types and 10 kinds, totally over 20 kinds of model forecast products of 24 hours may be obtained.

2.1 Dynamical equation set

Detail dynamical set is omitted.

In which, the actual expression of potential diagnosis equation is:

$$\frac{\partial \varphi}{\partial L_n\left(\sigma + P_t / \rho^*\right)} = -\frac{RT_v}{1+Q_c+Q_r+Q_i+Q_s}$$

The source-sink of heat equation dQ/dT considers the phase change potential heat of water, i.e.

$$\frac{dQ}{dT} = (Svc+Svr)\cdot Lv + Ls\cdot(Svi+Svs) + Lf(Mic+Msc+Msr+Ccs)$$

2.2 Cloud microphysical model

Using double parameters to describe the microphysical procedures of cloud-water particle groups, i.e. cloud-water, cloud-ice, snow, rain and graupel, etc. totally including 3 phases, 5 types and over 20 kinds.

Cloud drops and rain drops are divided by the diameter of 200 μ m; Ice crystals and snow balls are divided by the diameter of 340 μ m.

Their detailed particle spectrum distribution and all microphysical equations are omitted.

2.3 Others

Model scope: large mesh $\triangle x=\triangle y=90$km, mesh points number 30×25, time step length $\triangle T=93$s;

points number 30 × 25, time step length △T=93s; small mesh △x=△y=30km, mesh points number 23 × 23, time step length △T=93/3s,in vertical direction, by unequal distances, divided into 15 layers (the top layer 150hpa), mainly refined close to 0° layer. Bidirectional nesting method is used.

Mesh point structure: horizontal mesh point and vertical mesh point both use: "stagger" scheme. The horizontal stagger scheme is ArakawaB scheme.

The horizontal flow and fall of rainfall use improved near wind difference, the horizontal flow of other variables use the leapfrog scheme of time and the central difference of space, for the calculation of source-sink item, time leapfrog scheme and space central difference are used, and in vertical direction, σ coordinate is used.

3. Design and development of real-time forecast system

In order to put above set up brand new mesoscale stratiform cloud model into real-time operation, we specially developed the model data preprocessing and after processing system, as well as the distributing system for services of product.

Data preprocessing system: a data real-time acquisition and transmission system has been set up, from network, various data is obtained, and automatically carry out primary processing for large and small meshes.

Model operation system: start at fixed time, automatically operate model, operate on Dell 400MT work-station for 110 minutes, and then finished.

Model afterprocessing system: composes of a perfect icon display software package and a comprehensive processing and analysis system of output products.

Product service and test system: a model product distribution, service and actual status information feedback system has been built up, which composes of approach, telecommunication and comprehensive analysis console, etc. In general, from acquisition of initial data—model operation—result icon display—comprehensive analysis—product distribution—actual situation test, automatically complete all procedures. A real-time numerical forecast system with high automatization is formed.

4. Real time operational application

The mesoscale model real-time forecast system, since March of 1999, has been operated for real-time operation in the central part of China for one year. Every day at fixed time, output various macro and micro physical quantities and the forecast instruction products such as artificial catalytic potential, etc. here, a brief introduction is made to the forecast of the amount of precipitation, cloud field and artificial catalytic potential.

4.1 Forecast precipitation field

(a) Statistics estimation of partitioned precipitation forecast.

Divide the small mesh test area of Henan, China into 5 districts, I. II. III. IV and V, shown as Fig.1.

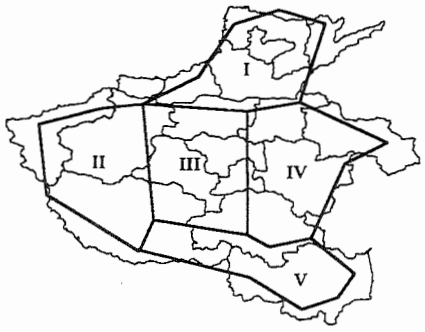

Figure 1 The 5 test districts of Henan, China

It is stipulated that, in some area, if at more than 2/3 mesh points rain is forecasted, then the area is forecasted to rain, otherwise the area is forecasted no rain. For actual situation, if at some part of an area

precipitation occurred, then the area is regarded actually rained. According to the stipulation, to carry out TS giving marks and tests, the results is shown in table1.

Table 1. Partitioned forecast TS marks for 6-hour with or without precipitation (season average)

Periods of time	Districts				
	I	II	III	IV	V
06—12h	0.81	0.84	0.89	0.86	0.79
12—18h	0.79	0.80	0.83	0.78	0.77
18—24h	0.65	0.69	0.72	0.67	0.60
Average	0.75	0.78	0.81	0.77	0.72

From the table above, it may be seen that using the mesoscale cloud system model to make partitioned with or without precipitation forecast, TS marks may reach over 0.70, the highest marks may be over 0.80. It should be said having high forecast accuracy.

(b) Statistics estimation of graded precipitation forecast.

In order to further investigate the model's forecast ability to forecast different grade precipitation, using the precipitation amount of 12 hours, by three grades of ⩾1.0mm, ⩾10.0mm and ⩾25.5mm, made further test, the result is shown in table 2.

Table 2 Graded forecast TS marks for 12-hour precipitation

TS marks	Rainfall grade		
	⩾1.0mm	⩾10.0mm	⩾25.5mm
	0.82	0.75	0.58

From here we may see that the model has a high forecast ability to light—moderate rain.

4.2 Cloud field forecast

By accumulating the hourly output micrograins (Qc, Qr, Qi, Qs, Qg) in cloud, the total amount of water condensed mater in cloud is obtained, that is, the hourly varying situation of modeled cloud field has been obtained. By hourly comparing modeled cloud field with actual measurment satellited could picture and radar echo, it is found that there is comparatively uniform developing trend. Take 99.04.08 as an example, see figure 2 and figure 3.

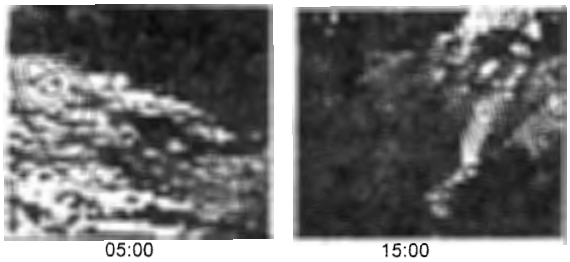

(04/08/1999)

Figure 2. Comparision between modeled total cloud water (isoline g/kg) and actually measurment satellited could picture

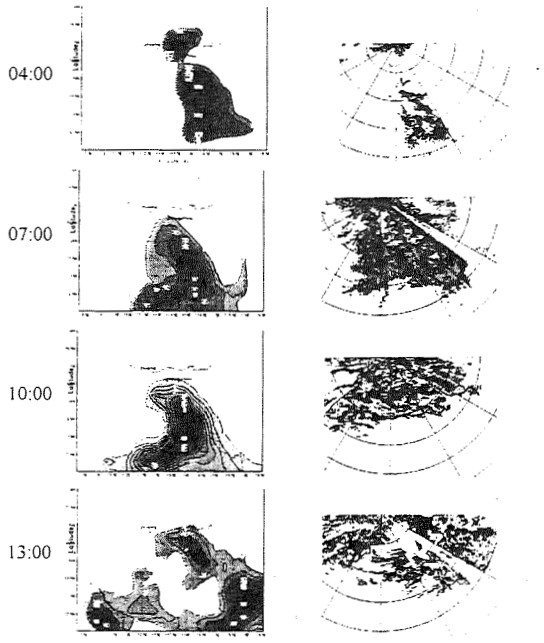

(04/08/1999)

Figure 3. Comparision between modeled cloud field (a) and actually measurment radar echo (b) developing trend.

From here we may see that the mesocale cloud model has good forecast ability to cloud system

developing trend.

4.3 Forecast of artificially increasing rain potential

The artificial catalytic potential mainly depends on cloud field microphysical structure, i.e. the configuaration of overcold cloudwater and content of ice-crystal, timely forecast out future microstructure of cloud body, provide the different spaces and places to carry out artificial catalysis, and the potential of the catalysis, which has a great significance to give instructions for influencing weather. Figure 4 has shown the opportunities, places and area of model cloud field catalytic potential area by comparision between modeled cloud field vertical section and actually measurment radar echo RHI.

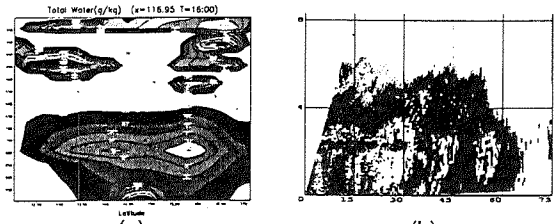

(a) (b)

(07:00 04/08/1999)

Fig4. Modeled cloud field vertical section (a) and actually measurment radar echo RHI (b) .

5. Conclusion:

At the same time with respectively leading-in mesoscale model and cloud microphysics model, a dynamic—microphysics mutually coupled mesoscale cloud model has been developed and built up, on the basis of this, combining with the actual situations of the central part of China, a real-time forecast operation system about mesoscale cloud system has been set up. The system has been real-time professionally operated for over one year in the local area. It may provide the forecast products about the aspects of precipitation field, cloud field and artificial influence ability. From the statistics test, hourly comparing and tracing test to its major forecast products, we may know:

(1) The forecast system has a high forecast accuracy to with or without precipitation.

(2) The forecast system has a strong forecast ability to the stable precipitation of light—moderate rain quantity grade.

(3) Forecasted cloud field has good uniformity with the actually tested cloud system made by satellite and radar. With these conventional indirect cloud physical observation data, we may make real-time inversion of cloud parameter field, and make real-time test and modification to modeled cloud field.

(4) The model has a certain instructive ability to cloudlayer selection and seeding scheme selection for artificially influencing weather operation.

In one word, the model has a certain use value for many fields, such as weather forecast, cloud physics research, artificial influencing weather service and atmospheric environment prediction, etc.

6. Thanks

I hereby express my thanks to Hu Zhijin research fellow for his many instructions to the work; At the same time, I earnestly express my thanks to comrade Bao Shaowu for his help in the aspect of model.

7. Reference

Heimann D. Three-dimensional modeling of synthetic cold fronts approaching the alps. Meteor Atmos Phys.1990,42:197-219

Hu Zhijin, Yan Caifan, Numerical simulationy for the stratiform cloud microphysical process(1) Microphysical mode, Journal of the Meteorological Science Research Institute,1986-01-01.

Liu Gongbo, Hu Zhijin, case simulationy of the middle size lower eddy cloud system in the mode of floating optical mixing phase strtiform cloud system, Meteorological Journal, 1994-01.

A PREDOMINANT MASS PRESERVING SCHEME FOR THE MICROPHYSICS OF CONVECTIVE CLOUDS

Gustavo G. Carrió [1] and Matilde Nicolini

Departamento de Ciencias de la Atmósfera / Universidad de Buenos Aires, Centro de Investigaciones del Mar y la Atmósfera / CONICET, Buenos Aires, Argentina

1. INTRODUCTION

A two-moment microphysical parameterization has been developed for a mixed phase convective cloud model in use at the Atmospheric Sciences Department of the University of Buenos Aires. It prognoses the mixing ratios and concentrations of five condensed water species: cloud droplets, rain drops, pristine ice crystals, snow and graupel-hail.

Two-moment microphysical schemes appear to be a compromise solution between the description detail associated to explicit treatments and computational expedience of "Kessler-type" schemes. Therefore, these multimoment treatments are becoming a standard, among them, Ziegler (1985), Ferrier (1994), Walko et al. (1995), and Meyers (1997) et al..

The general structure of the proposed scheme share some common characteristics with the above mentioned schemes such as the use of pre-calculated matrices of interaction for the collisional mechanisms. They are computed by numerical integration of the corresponding stochastic collection equations and stored in look-up tables for later interpolation respect to the mean or characteristic sizes of the interacting spectra. The melting of the solid species, raindrop freezing, heterogeneous and homogeneous ice nucleation as well as vapor diffusion processes, among others, are also computed using look-up tables for computational economy.

The proposed two-moment microphysical parameterization includes some new features that may improve the treatment of various collective mechanisms as well as other processes such as spontaneous raindrop freezing. The main distinctive characteristics lie on the fact that the number concentration tendencies are considered dependent on the predominant mass changes for various processes. A similar procedure has been applied by Carrió and Nicolini (1999) to parameterize the raindrop number change due to autoconversion. Additional matrices of interaction are precomputed to evaluate the predominant mass change of the destination specie. These matrices, are related to the second mass moment of the particles generated after the collision or freezing. The predominant mass of the generated particles is used to determine the destination specie for some collective mechanisms instead of relating this decision to mixing ratios or mean masses of the interacting spectra.

In the present communication, the treatment of the collisional processes is briefly described putting special emphasis on the main distinctive features.

2. BRIEF DESCRIPTION

2.1 Treatment of the collisional processes

The scheme prognoses the mixing ratios and number concentrations of five condensed water species are considered: cloud droplets, rain drops, pristine ice crystals, snow and graupel-hail. Each mass distribution is assumed to follow a gamma (Pearson type III) spectrum, and it can be written for a generic specie "j" as

$$N_j(m_j,t)= N_{jt}\, n_j\,(m_j, M_j) = N_{jt}\,(\nu_j+1)^{\nu_j+1}\,(m_j / M_{fj})^{\nu_j} / [M_{fj}\,\Gamma\,(\nu_j+1)]\,\exp[-(\nu_j+1)\, m_j / M_{fj}] \qquad (1)$$

[1] * *Corresponding author address:* Gustavo Carrió, Departamento de Ciencias de la Atmósfera, Facultad de Ciencias Exactas y Naturales, Ciudad Universitaria, Pabellón II-2P, 1428 Buenos Aires, Argentina; email: carrio@at1.fcen.uba.ar

where $N_j(m_j,t)$ represents the number concentration of particles of the specie "j" with masses between m_j and m_j+dm_j at time t, N_{jt} is the total number concentration, M_{fj} is the mean mass if the spectrum, ν_j is the width parameter, assumed to be a constant, and $n_j(m_j, Mf_j)$ denotes the corresponding normalized distribution.

The procedure to evaluate the effect of collective processes can be summarized as follows. The changes in the prognostic variables of the colliding species X and Y (as well as those corresponding to a third Z when the collision gives rise to a particle of a third specie) are evaluated in terms of three quantities. They are: the rate of the total number of binary collision (ΔN_{xy}) and the involved masses of each interacting spectrum (ΔM_x and ΔM_y). The integral expressions for these rates are given in the following expressions (eqs.2-4) based on the corresponding stochastic collection equations.

$$\Delta N_{xy} = N_{xt} N_{yt} IN_{xy} \quad (2)$$

$$IN_{xy} = \int_0^\infty \int_0^\infty n_x (m_x, M_{fx}) K[m_x, m_y] n_y (m_y, M_{fy}) dm_x dm_y$$

$$\Delta M_x = N_{xt} N_{yt} IM_x \quad (3)$$

$$IM_x = \int_0^\infty \int_0^\infty n_x (m_x, M_{fx}) K[m_x, m_y] n_y (m_y, M_{fy}) m_x dm_x dm_y$$

$$\Delta M_y = N_{xt} N_{yt} IM_y \quad (4)$$

$$IM_y = \int_0^\infty \int_0^\infty n_x (m_x, M_{fx}) K[m_x, m_y] n_y (m_y, M_{fy}) m_y dm_x dm_y$$

where $K[m_x,m_y]$ is the collision kernel for a particle "x" with mass m_x to and a particle "y" with mass m_y

As these expressions are linear respect to each number concentration, IN_{xy}, IM_x and IM_y are numerically computed for a large number of M_{oj} and M_{oj} values to construct the interaction matrices. In eqs. (5-8) the resulting tendencies are given for the case in which X particles collect Y particles, those corresponding to the case in which destination specie is other that X or Y, in eqs. (9-12).

$$dN_{xt}/dt = 0 \quad (5)$$
$$dQ_x/dt = -\rho^{-1} N_{xt} N_{yt} IM_y^* \quad (6)$$

$$dN_{yt}/dt = -N_{xt} N_{yt} IN_{xy}^* \quad (7)$$
$$dQ_y/dt = -\rho^{-1} N_{xt} N_{yt} IM_y^* \quad (8)$$

$$dN_{xt}/dt = - N_{xt} N_{yt} IN_{xy}^* \quad (9)$$
$$dQ_x/dt = -\rho^{-1} N_{xt} N_{yt} IM_x^* \quad (10)$$

$$dN_{yt}/dt = - N_{xt} N_{yt} IN_{xy}^* \quad (11)$$
$$dQ_y/dt = -\rho^{-1} N_{xt} N_{yt} IM_y^* \quad (12)$$

$$dN_{zt}/dt = N_{xt} N_{yt} IN_{xy}^* \quad (13)$$
$$dQ_z/dt = -\rho^{-1} N_{xt} N_{yt} (IM_y^* + IM_x^*) \quad (14)$$

where dN_{xt}/dt, dQ_x/dt, dN_{yt}/dt, dQ_y/dt, dN_{zt}/dt, dQ_z/dt are the time rates of change of the number concentrations and mixing ratios due to X-Y collisions, and * denotes interpolated values.

2.1 Calculations preserving predominant masses

The distribution of a given specie "z" is mainly characterized by three quantities: the mass (mixing ratio), the mean mass and the mass about which most of the mass is concentrated, called following Berry (1974), the predominant mass. These three quantities cannot be "strictly" computed as they are not independent within a treatment in which the spectrum has two degrees of freedom (constant value for the width parameter are assumed).

The predominant mass (M_{gz}) is equal to the ratio between the second and first mass moments of the distribution, and it is linearly related to the mean mass (M_{fz}) under this constraint ($M_{gz} = [1+ 1/(1+ \nu_z)] M_{fz}$)

For number concentration tendencies (of the type eq.(13)) that "preserve" the number concentration (and implicitly the mean mass of the specie Z), the inclusion of a large number of small particles to a given spectrum "z" and the attendant reduction in M_{fz} leads to an artificial decrease of M_{gz} when what actually occurs is a spectrum widening. As the width parameter is not a prognostic variable within this framework, in this scheme, these tendencies are considered dependent on the rate of change of M_{gz} in order to preserve this more physically meaningful quantity. This procedure has been applied by Carrió and Nicolini (1999) to compute the raindrop number concentration change due to autoconversion and lead to an improved performance in simulation radar reflectivities within a warm cloud.

The rate of change of M_{gz} is expressed as a function of the predominant mass of the new Z particles ($\mathcal{M}_{gz}$) generated during the time step as

$$\mathcal{M}_{gz} = \int_0^\infty \mathcal{N}_z(m)\, m^2 dm \,/ \int_0^\infty \mathcal{N}_z(m)\, m\, dm \qquad (15)$$

where is $\mathcal{N}_z(m)$ is the spectrum of these new Z particles and is given by eq(16).

$$\mathcal{N}_z(m) = \left\{ N_{xt} N_{yt} \int_0^m A(M_{fx}, M_{fy})\, dm_x\, dm_y \right\} \Delta t \qquad (16)$$

in which,

$$A(M_{fx}, M_{fy}) = n_x (m_x, M_{fx})\, K[m_x, m-m_x]\, n_y (m-m_x, M_{fy})$$

The predominant mass that corresponds to the Z spectrum after a time step ($M_{gz}(t+\Delta t)$) is

$$M_{gz}(t+\Delta t) = \left\{ \int_0^\infty [N_z(m,t) + \mathcal{N}_z(m)]\, m^2 dm \right\} X \qquad (17)$$

$$\left\{ \int_0^\infty [N_z(m,t) + \mathcal{N}_z(m)]\, m\, dm \right\}^{-1} = (1+\nu_z)^{-1} M_{fz}$$

The denominator of eq (17) is the mass content per unit volume, thus $M_{gz}(t+\Delta t)$ can be written as in the following equation (18) from which the resulting dN_{zt}/dt can be easily equated.

$$\alpha\, \rho\, [Q_z(t) + \Delta Q_z]\, [N_{zt}(t) + dN_{zt}/dt \Delta t]^{-1} =$$

$$= [Q_z(t)\, M_{gz}(t) + \Delta Q_z\, \mathcal{M}_{gz}]\, [Q_z(t) + \Delta Q_z]^{-1} \qquad (18)$$

where $\alpha = 1 + (1+\nu_z)^{-1}$,
and $\Delta Q_z = dQ_z/dt\, \Delta t$

The values of the predominant mass of the generated Z particles are computed as a function of the mean masses of the colliding species (M_{fx} and M_{fy}) as done with eqs. (2-4). The corresponding matrices are computed by numerical integration of the composition of eqs. (15) and (16) to determine $\mathcal{M}_{gz}$ by interpolation.

A similar procedure can be applied for raindrop spontaneous freezing. The "number-conserving" tendency equation to take into account the corresponding graupel number concentration change is given in the eq. (19), and the corresponding expression for the mixing ratio in eq. (20).

In this case the predominant mass of the new generated graupel particles can be computed with eq.(21) and tabulated as a function of the mean mass of the raindrop spectrum and the temperature. And again, an alternative computation for the corresponding dN_{zt}/dt can be determined interpolating $\mathcal{M}_{gz}$ and using an equation homologous to eq.(18). The difference between these two calculation procedures is a function of the ratio between the predominant and mean masses of the new particles.

$$dN_{gt}/dt = N_{rt} \int_0^\infty n_r (m_r, M_{fr})\, P[m_r, T]\, dm_r \,/\, \Delta t \qquad (19)$$

$$dQ_g/dt = N_{rt} \int_0^\infty n_r (m_r, M_{fr})\, P[m_r, T]\, m_r\, dm_r \,/\, \Delta t \qquad (20)$$

where the subscripts **g** and **r** denote graupel and rain, respectively. $P[m_r, T]$ is the freezing probability within a time step for an drop of mass m_r at a temperature T.

$$\mathcal{M}_{gz} = \left\{ \int_0^\infty n_r (m_r, M_{fr})\, P[m_r, T]\, m_r^2\, dm_r \right\} X \qquad (21)$$

$$\left\{ \int_0^\infty n_r (m_r, M_{fr})\, P[m_r, T]\, m_r\, dm_r \right\}^{-1}$$

The ratio between predominant mass changes that correspond to each procedure of calculation can be written as:

$$r = [\Delta Q_z / (Q_z + \Delta Q_z)]\, [(M_{fz} + \beta/\alpha\, \mathcal{M}_{fz}) / (M_{fz} + \mathcal{M}_{fz})] \qquad (22)$$

where $\mathcal{M}_{fz}$ is the mean mass of the of the new Z particles, α, β are the ratios between predominant and mean masses of the Z spectrum and new Z particles, respectively.

As said above, the difference between these two procedures lies on the quotient between the predominant and mean masses of the new Z particles. Figure 1, the value of β for raindrop freezing is plotted as a function of the mean mass radius of raindrop distribution and T.

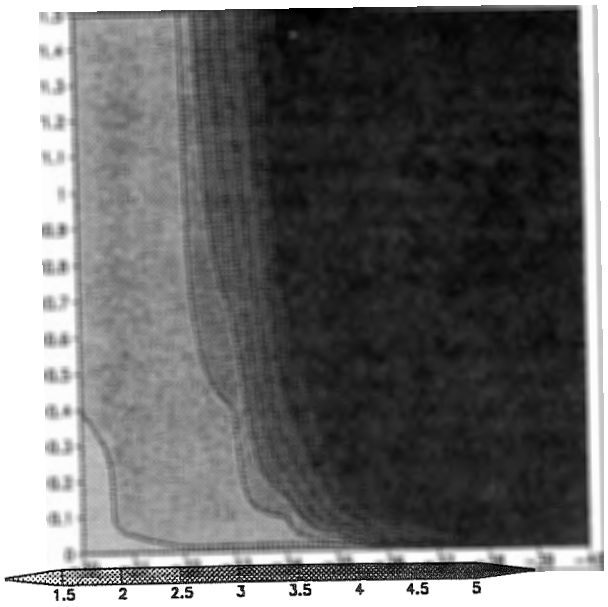

Figure 1 M_e/M_r for frozen drops during a time step. Celsius temperature in the X axis and mean mass radii in the Y axis

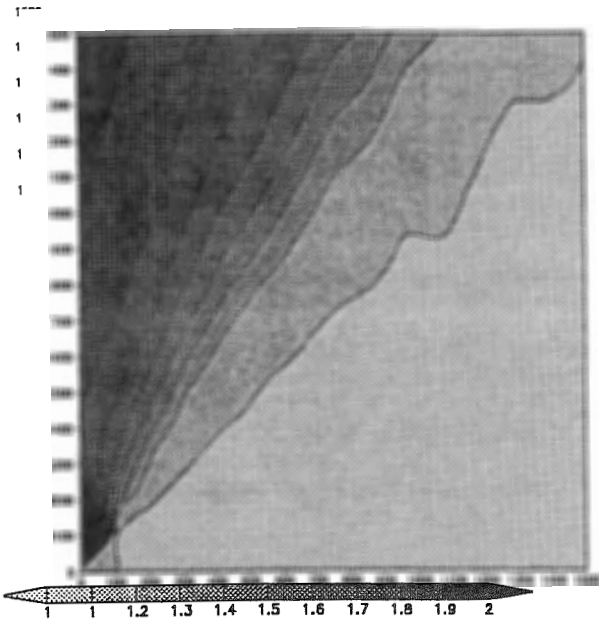

Figure 2 Ratio between changes of predominant and mean masses for graupel collecting drops as a function of the mean masses radii of the spectra. Raindrop and graupel in X axis and Y axis, respectively.

For various accretional processes, a number concentration tendency equation can be considered for the collector (see eq(5)). The corresponding rates are again considered dependent on the predominant mass change. The ratio between time rates of change of the predominant and mean mass gives, for accretional processes, a direct measure of the difference between predicting predominant mass change instead of number concentration. As an example, in figure 2, this ratio is plotted for the case of graupel collecting raindrops as a function of the mean masses of the spectra. The corresponding rates are evaluated pre-computing and tabulating and interpolating the time rates of change of collector specie as a function of both mean masses.

COMMENTS

Additional matrices of interaction are pre-computed to predict the physically more meaningful predominant masses instead of predicting number concentrations (that implicitly preserve mean masses)

Preliminary results indicate that the cloud model exhibits a significant sensitivity to the choice and that this alternative may improve the performance of double-moment bulk schemes.

ACKNOWLEDGEMENTS

The authors wish to thank UBA and CONICET for financial support.

REFERENCES

- Berry, E. X. and Reinhardt, R.L., 1974: An analysis of cloud drop growth by collection: Part II. Single initial distributions. J. Atmos. Sci., 31, 1825-1831.
- Carrió, G. G. and Nicolini, L., 1999: A double moment warm rain scheme: description and test within a kinematic framework. Atmos. Res., 52, 1-16.
- Ferrier, B. S., 1994. A double moment multiple-phase four-class bulk ice scheme. Part 1 Description. J. Atmos. Sci.,51: 249-280.
- Meyers, M.P., Walko, R. L. Harrington, J.Y. and Cotton, W.R., 1997: New RAMS cloud microphysics parameterization. Part II The two-moment scheme. Atmos. Res. 45: 3-39.
- Walko, R .L., Cotton W.R., Meyers M.P and Harrington J.Y.1995. New RAMS cloud microphysics parameterization .Part 1: The single- moment scheme., Atmos. Res., 38: 29-62.
- Ziegler, C. L., 1985: Retrieval of thermal and microphysical variables in observed convective

THE INFLUENCE OF INTERNAL GRAVITY WAVES ON CONVECTION AND CLOUDS IN THE LOWER ATMOSPHERE

Andrzej A. Wyszogrodzki[1]

[1] Institute of Geophysics, Warsaw University, Warsaw, 02-093, Poland

1. INTRODUCTION

The 3D nonhydrostatic Navier-Stokes model has been used to perform numerical simulations investigating the interaction between the convective eddies in the boundary layer, cumulus clouds convection and tropospheric gravity waves.

The unstable boundary layers under thermal forcing evolve into a variety of organization modes. The simplest is the classical Rayleigh-Bérnard thermal instability of a fluid at rest heated uniformly from below. In general the convection modes within boundary layer are known as a *Rayleigh modes*. Above supercritical heating value (critical value of non-dimensional Rayleigh number R_a) infinitesimal flow perturbations tend to grow and lead to formation of convective cells within boundary layer. Inclusion of the mean horizontal flow (e.g. Ekman layer flow) increases the complexity of the convective patterns. Without shear, Rayleigh modes take the form of hexagonal cells. In presence of shear, the horizontal symmetry is broken and the preferred cell organization is in the form of horizontal roll vortices that are aligned mainly with the mean wind shear direction (e.g. Brown, 1970; Le Mone, 1973; Ettling and Brown, 1993).

When the convection penetrates areas above the LCL (Lifting Condensation Level), clouds provide visible evidence of boundary layer organization (e.g. so called "cloud streets" for the case of the roll vortices). In the presence of shear, the top of the cloud streets (or fair weather cumuli and even clear air thermals) experiences a differential wind speed. Conserving part of their horizontal momentum cloud acts as an obstacle to the sheared environmental flow. In result the gravity wave spectrum rises in the stable free atmosphere above boundary layer. The wave excitation efficiency is governed to a great extent by the strength and vertical distribution of the shear.

Haman (1962), as one of the firsts made the theoretical suggestion of the possibility of excitation gravity waves by boundary-layer convection. In the later studies, Townsed (1966) demonstrated that horizontally propagating gravity waves are excited by perturbations of the convective updrafts on the lower surface of the stable tropospheric layers. Related studies by Townsed (1968) and Stull (1976) showed that the penetrative convection excite both horizontal interfacial waves at the inversion layer and external gravity waves in the stable atmosphere above. These vertically propagating gravity waves transfer momentum and heat from the boundary layer to tropospheric and stratospheric altitudes. Thus they have strong impact on the structure and circulation of the middle atmosphere (e.g. distribution of zonal mean winds and temperatures, semi-annual and quasi-biennial oscillations, chemical composition of the mesosphere) - Fovell et al. (1992). The dynamical coupling of the troposphere and stratosphere across the tropopause has also some effect on the circulation of the troposphere and down to the boundary layer.

The hypothesis that scale selection in boundary layer convection can be modulated by gravity waves propagating in the free troposphere was initially formulated in a series of papers by Clark et al. (1996), Balaji and Clark (1988), Hauf and Clark (1989). Numerical simulations performed by these authors and analytical solutions to linearized system of atmospheric equations by Sang (1991, 1993) show that gravity waves, initially excited by boundary layer convection, acted as a *feedback mechanism* to organize the temporal and spatial scales of the convective activities in the boundary layer itself. Clouds grow in the stable air just above the convective boundary layer and are exposed to the impact of thermals from below and gravity waves from above, which may lead to variety of convective systems. If a conditionally unstable environment exists, convection waves can provide enough ascents to both trigger and organize deep tropospheric convection.

Numerical simulations performed by Bretherton and Smolarkiewicz (1988) show that gravity waves fulfil a major role in the redistribution of heat and moisture in the field of deep convective clouds. The concept of CAPE (Convective *Available Potential Energy*) and CIN (*Convective Inhibition*) describes property of the environment in which convective systems are developed. Recent works by Lane and Reeder (1999) show in 2D simulations that gravity waves are responsible for the changes in CAPE and reduction in CIN. The maximum far-field perturbation in CAPE and CIN was found to be approximately 15% and 33% of initial background values respectively. The development and organization of the convective activity in the boundary layer and lower atmosphere is then a non-local problem, which require extend the range of the research to the full troposphere and even lower stratosphere.

Corresponding author address:
Andrzej A. Wyszogrodzki, Institute of Geophysics, Warsaw University, Warsaw, 02-093, Poland;
E-mail: andii@fuw.edu.pl; fax: [48](22) 822-23-87

2. MODEL EQUAQTIONS

The numerical model used in this study is suitable for modeling a wide range of natural (rotating, stratified, precipitating, turbulent, etc.) atmospheric flows, broadly documented in the literature. It is representative of a class of nonhydrostatic atmospheric models that solve the anelastic equations of motion in the Cartesian coordinates. Moist processes are governed by the standard bulk, warm-rain parameterization of small-scale atmospheric thermodynamics (Kessler 1969, Lipps and Hemler 1982, Grabowski and Smolarkiewicz, 1996). The governing anelastic equations of moist motion may be written compactly as follows:

The momentum equation:

$$\frac{du_i}{dt} = -\frac{\partial \pi}{\partial x_i} + \delta_{i_3} g \left(\frac{\theta - \theta_e}{\theta} + \varepsilon(q_v - q_{ve}) - q_c \right) + D_{u_i}$$

the anelastic conservation of mass equation:

$$\frac{\partial}{\partial x_i}(\bar{\rho} u_i) = 0$$

where Cartesian tensor notation has been used.

The conservation of potential temperature θ:

$$\frac{d\theta}{dt} = \frac{L\theta_e}{c_p T_e} C_d + D_\theta$$

the conservation of water vapor q_v and cloud water q_c mixing ratio:

$$\frac{dq_v}{dt} = -C_d + D_{q_v}$$

$$\frac{dq_c}{dt} = C_d + D_{q_c}$$

In the above equations overbars refer to the anelastic reference state, subscript e represents hydrostatically balanced environmental profiles (thus $\varphi''=\varphi-\varphi_e$ is the time dependent perturbation from environmental profile). The other symbols appearing in equations have the following meaning: $d/dt = \partial/\partial t + u_i \partial/\partial x_i$ is total (substantial) derivative, where u_i denotes velocity vector; π is pressure perturbation with respect to hydrostatically balanced environmental profile normalized by the anelastic density $\bar{\rho} = \bar{\rho}(z)$; $\varepsilon = R_v/R_d - 1$ is the ratio of gas constant for water vapor R_v=461 [J/kg·K] and dry air R_d=287.04 [J/kg·K]. L denotes latent heat of condensation; c_p is the specific heat at constant pressure; T_e is the environmental temperature profile. C_d symbolizes condensation of water vapor into cloud water. Bulk condensation C_d is defined implicitly based on two assumptions: the water vapor is saturated in the presence of cloud water and the cloud water evaporates instantaneously in unsaturated conditions (Grabowski and Smolarkiewicz, 1990).

$D_\varphi = D_\varphi^{Dyf} + D_\varphi^{\alpha}$ terms appearing in all prognostic equations symbolize viscous forcing. The subgrid-scale turbulence parametrization D_φ^{Dyf} is based on the Smagorinsky (1963) model or in the second approach the subgrid-scale turbulence energy satisfies prognostic equation with parameters given by Schumann (1991). The gravity-wave absorber D_φ^{α} (i.e. "Raylegh friction" - a linear drag law) is employed in the vicinity of the model boundaries.

The elliptic pressure equation derives from the anelastic incompressibility equation of the mass conservation imposed on the discretized momentum equation. It is solved (subject to boundary conditions imposed on normal components of contravariant velocity) by using the generalized conjugate residual methods. Algorithmic details are discussed in Smolarkiewicz and Margolin (1994).

3. RESULTS FROM NUMERICAL EXPERIMENTS

Illustration of the coupling between gravity waves and convection is presented in the two- and three-dimensional "dry" numerical simulations (LES). In all simulations cyclic boundary conditions are specified in the horizontal direction and the lower boundary is heated with uniform net heat flux. The vertical length scale of the convective activity is connected with the transmission of the heat from the lower surface to the higher altitudes.

3.1 2D simulations

Exemplary results from two-dimensional simulations are presented on Figure 1. Vertical shear of the mean wind with value of 3 (m/s)/km is set in the areas where convection penetrates stable layer above. The horizontal domain size is 40 km, vertical extent of the model is 5 km for the upper picture and 13 km for the lower. The horizontal and vertical resolution is 200m and 150 m respectively. On the bottom surface the uniform net heat flux H=0.2 Km/s is specified.

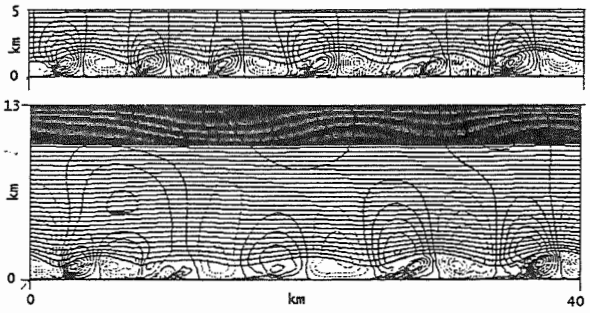

Figure 1: The evolution of convective activity after 4 hours of the simulation. The potential temperature distribution is represented by horizontal isolines with interval of 2 K. The circular continuous (updrafts) and dashed (downdrafts) contour with interval of 0.5 m/s represent vertical velocity field (i.e. convection cells).

Differences in the boundary layer evolution due to change of the model domain height are clearly seen in these figures. This can be explained in the following manner. Increasing the model domain height up to 13 km and taking into consideration full troposphere and lower part of the stratosphere allows for development

of the convection waves in these areas. Thus larger horizontal scale modes become prevailing (dominant eigenmodes of the troposphere). As the wave moves over the convective boundary layer certain scales are enhanced whereas other are suppressed resulting in a selection of the spatial distance between convective cells and its size. Finally in the "shallow" simulations we see 6 convective cells in the boundary layer versus 5 in the "deep" simulation.

3.2 3D simulations

In the two-dimensional model, thermal convection always lead to roll-like solutions. Inclusion of the third spatial dimension introduces various directional effects, which have a great impact on the structure of the convective eddies. An interesting point is examination of the existence of explicit relations of the wave number selection in the fully three-dimensional solutions, which is essential to developing of the further parametrization approach.

Sang (1993) solved theoretically and numerically the linearized system of atmospheric equations for two-layer model. Convection waves were composed of trapped waves. The selected wave numbers in the wave field was determined by the interaction between convective boundary layer and the overlying stable layer (*layer interaction*).

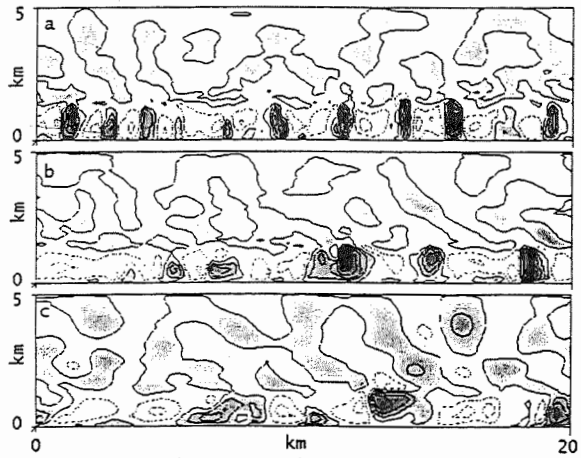

Figure 2: Vertical cross-section of the vertical velocity field distribution in the 3D simulations after 3-hour simulation. Contour interval is 0.5 m/s, gray scale with continuous isolines represent updrafts and dashed isolines - downdrafts.

The explicit relation of wave-number selection define pattern of the boundary layer convection, which may appear as cloud streets, cellular convection or convective thermals and the transition between them. The common form of analytical solution was found for a wide range of the large-scale atmospheric conditions: thermal forcing, mean wind shear (wind speed and directional turning), thermal stabilities and temperature jump across the interface.

Current three-dimensional numerical simulations of the convective boundary layer evolution are the attempt to revise theoretical Sang's results with the aid of nonlinear fluid dynamic model. An example presented in Figure 2 shows how sensitive are the results on the inclusion of different magnitudes of the environmental wind within the boundary layer. Consecutive panels on Figure 2 represent following wind magnitudes: a) u=0m/s, b) u=2m/s, c) u=5m/s. Shear of the mean wind is set above 1000m with the magnitude of 1 (m/s)/km. Lower surface is heated with uniform net heat flux H=0.2 Km/s. The horizontal extent of the model domain is 20 km and vertical 5 km with resolution of 250 m and 100 m respectively.

In the sheared flow the top of the clear air thermals act as obstacles, which result in the excitation of the gravity waves in the stable free atmosphere above boundary layer as well as the waves trapped in the inversion. The wave excitation efficiency and wave number selection may be related to the strength and vertical distribution of the wind shear and other flow parameters. Increasing the mean environmental wind have the impact on aspect ratio of the boundary layer convection which changes from hexagonal cells in Figure 2a) to more broaden structures in Figure 2c). The roll-like structures and strongest environmental wind tend to excite stronger waves as seen in Figure 2c). Further extension of the model domain height will give possibility to explore the *feedback mechanism* between convective tropospheric gravity waves and boundary layer convection.

4. CONCLUSIONS

Gravity waves are often excited by a pure thermal convection with cumulus clouds formed over convectively active boundary layer acting as an obstacle to the sheared environmental horizontal flow. Gravity waves initially forced by the boundary layer eddies lead to a feedback mechanism that acts to reorganize the convective activities and to tune up the spacing of the boundary layer eddies and the cumulus clouds above. In the presence of gravity waves the character of fair weather convection is then a non-local problem. Boundary layer dynamics can no longer be considered as being governed only by local parameters. This must lead to extension of the research problem to include dynamical processes from altitudes above the boundary layer.

In recent years, a number of new computers based on a massively parallel processing (MPP) architecture consisting of hundreds or thousands of processors are enabled for numerical computing. By use these architectures we have a chance to increase the size of the problem that can be solved. But the computation of the fine mesh resolution atmospheric flows with inclusion of the multiscale effects on relatively big domain is still out of the scope in present research. This can lead to alternative solution e.g. construction a sort of parametrization schemes which will describe the gravity wave - convection feedback mechanisms.

5. ACKNOWLEDGMENTS

This work is supported by the KBN (Komitet Badań Naukowych) under Grant № 6 PO4D 02418. The numerical simulations were performed on the Nec SX-4B/2A and Cray T3E supercomputers at the ICM (Interdisciplinary Center for Mathematical and Computational Modeling) at Warsaw University.

6. REFERENCES

Balaji, V. and T.L. Clark, 1988: scale selection in locally forced convective fields and the initiation of deep convection cumulus. *J. Atmos. Sci.*, **45**, 3188-3211.

Bretherton, C.S. and P.K. Smolarkiewicz, 1988: Gravity Waves, compensating subsidence and detrainment around cumulus clouds. *J. Atmos. Sci.*, **46**, 740-759.

Brown R.A., 1970: A secondary flow model for the planetary boundary layer. *J. Atmos. Sci.*, **27**, 742-757.

Clark, T.L, T. Hauf and J.P. Kuettner, 1986: Convectively forced internal gravity waves: Results from two-dimensional numerical experiments. *Quart. J. Roy. Meteor. Soc.*, **112**, 899-925.

Etling, D. and R.A. Brown, 1993: Roll vortices in the planetary boundary layer: A review. *Boundary-Layer Meteorol.*, **65**, 215-248.

Fowell, R., D. Durran and J.R. Holton, 1992: Numerical simulations of convectively generated stratospheric gravity waves. *J. Atmos. Sci.*, **49**, 1427-1442.

Grabowski, W.W. and P.K. Smolarkiewicz, 1990: Monotone finite difference approximation to the advection-condensation problem. *Mon. Wea. Rev.*, **118**, 2082-2097.

Grabowski, W.W. and P.K. Smolarkiewicz, 1996: Two-time-level semi-lagrangian modelling of precipitating clouds. *Mon. Wea. Rev.*, **124**, 487-498.

Haman, K., 1962: On some possible causes of clear air turbulence. *Acta Geophys. Pol.*, **10**, 335-357.

Hauf, T. and T.L. Clark, 1989: Three-dimensional experiments on convectively forced internal gravity waves. *Quart. J. Roy. Meteor. Soc.*, **115**, 303-333.

Kessler, E., 1969: On the distribution and continuity of water substance in atmospheric circulations. *Meteor. Monogr.*, **32**, No. Amer. Meteor. Soc. 84 pp.

Kuettner, J.P., P.A. Hildebrand and T.L. Clark, 1987: Convection waves: Observations of gravity wave systems over convetively active boundary layers. *Quart. J. Roy. Meteor. Soc.*, **113**, 445-467.

Lane, T.P and M.J. Reeder, 1999: Convectively generated gravity waves and their effect on the cloud environment. *Appleid Mathematics Reports and Preprints*. 99/22. subm. to *J. Atmos. Sci.*

Le Mone, M.A., 1973: The structure and dynamics of horizontal roll vortices in the planetary boundary layer. *J. Atmos. Sci.*, **30**, 1077-1091.

Lipps, F.B. and R.S. Hemler, 1982: A scale analysis of deep moist convection and some related numerical calculations. *J. Atmos. Sci.*, **39**, 2192-2210.

Sang, J.G., 1991: On formation of convective roll vortices by internal gravity waves: A theoretical study. *Meteorol. Atmos. Phys.*, **46**, 15-28.

Sang, J.G., 1993: On the dynamics of convection waves. *Quart. J. Roy. Meteor. Soc.*, **119**, 715-732.

Schumann, U., 1991: Subgrid length-scales for large-eddy simulation of stratified turbulence. *Theor. Comput. Fluid Dyn.*, **2**, 279-290.

Smagorinsky, J., 1963: General circulation experiments with the primitive equations. Part I: The basic experiment. *Mon. Wea. Rev.*, **91**, 99-164.

Smolarkiewicz, P.K. and L.G. Margolin, 1994: Variational solver for elliptic problems in atmospheric flows. *Appl. Math. and Comp. Sci.*, **4**, 527-551.

Stull, R.B., 1976: Internal gravity waves generated by penetrative convection. *J. Atmos. Sci.*, **33**, 1279-1286.

Townsed, A.A., 1966: Internal waves produced by a convective layer. *J. Fluid Mech.*, **24**, 307-320.

Townsed, A.A., 1968: Excitation of internal waves in a stably stratified atmosphere with considerable wind shear. *J. Fluid Mech.*, **32**, 145-171.

COMPRESSIBLE AND ANELASTIC CONTINUUM EQUATIONS FOR CLOUDY AIR

Peter R. Bannon *and Jeffrey M. Chagnon

The Pennsylvania State University, University Park, PA, 16802 USA

1. INTRODUCTION

A fundamental issue in the modeling of cloud systems is the choice of the governing equations. Studies of deep, nonhydrostatic, precipitating clouds require the use of the fully compressible equations or an anelastic set that filters sound waves.

Cloudy air contains water vapor, liquid drops, and ice particles. The liquid drops and ice particles may have different temperatures from that of the air. They may also move relative to the air. Thus the system is not only multi-phase but also multi-velocity and multi-temperature. Numerical models require that the physics be expressed as continuum equations. We present general continuum equations for cloudy air. For simplicity of the presentation we ignore ice particles and include only liquid droplets.

2. CONTINUUM HYPOTHESIS

We assume the dry air, vapor, and liquid drops are "interpenetrating continua" (Aris, 1962). The molecules of the dry air and the water vapor are sufficiently small and numerous that the continuum assumption is valid. The distribution of water drops is more discrete and the assumption is not as good. For an arbitrary control volume there may be "boundary drops" that require special care.

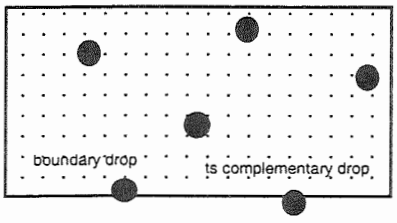

These boundary drops are treated by the principle of complementarity whereby the net effect of a complementary pair is equivalent to one interior drop (Crowe et al., 1998).

*Corresponding author address: Peter R. Bannon, Pennsylvania State University, Department of Meteorology, University Park, PA 16802 USA; e-mail: bannon@ems.psu.edu.

3. GENERAL APPROACH

We consider a fixed volume, V, in space with surface S. Let χ describe the amount of a flow property per unit volume. The change in the property in the volume V is given by

$$\int_V \frac{\partial \chi}{\partial t} dV = - \int_S \chi \, \mathbf{u}_\chi \cdot d\mathbf{S} + \int_V \dot{\chi} \, dV ,$$

where $\mathbf{u}_\chi$ is the velocity with which χ is being transported and $\dot{\chi}$ describes the rate at which property χ is being created per unit volume. Using the divergence theorem we have

$$\int_V \frac{\partial \chi}{\partial t} dV = - \int_V \nabla \cdot (\chi \, \mathbf{u}_\chi) \, dV + \int_V \dot{\chi} \, dV ,$$

and since the volume V is arbitrary we have

$$\frac{\partial \chi}{\partial t} + \nabla \cdot (\chi \, \mathbf{u}_\chi) = \dot{\chi} ,$$

where $\dot{\chi}$ is the source rate for property χ. As a specific example of the formalism, we let the flow property of interest be the mass of dry air. Then χ is the density ρ_a of the dry air with velocity $\mathbf{u}_a$ and there are no sources or sinks of dry air. Substituting we have the statement of the conservation of dry air

$$\frac{D\rho_a}{Dt} = - \rho_a \nabla \cdot \mathbf{u}_a ,$$

where the material derivative is defined following a dry air parcel

$$\frac{D}{Dt} \equiv \frac{\partial}{\partial t} + (\mathbf{u}_a \cdot \nabla) .$$

In general, the property χ may move with a velocity $\mathbf{u}_\chi$ that is different than the velocity $\mathbf{u}_a$ of the dry air. Let

$$\mathbf{u}_\chi = \mathbf{u}_a + \mathbf{v}_\chi \ ,$$

where $\mathbf{v}_\chi$ is the velocity relative to the air velocity $\mathbf{u}_a$. Then our conservation statement for χ is

$$\frac{D}{Dt}\left(\frac{\chi}{\rho_a}\right) = \frac{\dot{\chi}}{\rho_a} - \frac{1}{\rho_a}\nabla\cdot(\chi\,\mathbf{v}_\chi) \ .$$

This equation states that χ/ρ_a will change following the dry air if there is a source of χ or if there is a convergence of χ moving relative to the air parcel. The latter process we call fallout since we anticipate that there will typically be divergence of χ relative to the dry air.

We apply this approach to the various flow properties of interest.

4. CONTINUITY EQUATIONS

The equation for the water vapor and liquid water mixing ratios may be found by letting χ equal the vapor and liquid water densities ρ_v and ρ_l with velocities $\mathbf{u}_a = \mathbf{u}_v$ and $\mathbf{u}_l$ respectively. We find

$$\frac{D\,r_v}{Dt} = -\dot{r}_{cond} \ ,$$

$$\frac{D\,r_l}{Dt} = +\dot{r}_{cond} - \dot{r}_{fallout} \ ,$$

where r denotes a mixing ratio (for example, $r_v = \rho_v/\rho_a$) and $\dot{r}_{cond}$ is the condensation rate. We assume the condensation rate is known from cloud microphysical considerations. The liquid water fallout is defined as the divergence of the flux of liquid water relative to the dry air parcel

$$\dot{r}_{fallout} \equiv \frac{1}{\rho_a}\nabla\,(\rho_a\, r_l \mathbf{v}_l) \ .$$

There is no water vapor fallout since the vapor moves with the velocity of the dry air. The sum of these equations states that, relative to the dry air parcel, there can be a loss of water due to the fallout of the drops.

5. IDEAL GAS LAW FOR MOIST AIR

The equation of state has the traditional form

$$p = \rho_a R\,T + \rho_v \frac{R}{\varepsilon} T = \rho_a R\,T\,(1 + r_v/\varepsilon) \ ,$$

where R is the ideal gas constant for dry air and $\varepsilon = 0.622$ is the ratio of the mean molecular weight of water vapor to that of dry air. The dry air and the water vapor have the same temperature, T.

6. ENTROPY EQUATIONS

We next let the fluid property of interest be the entropy of cloudy air. Then $\chi = \rho_a s_a + \rho_v s_v + \rho_l s_l$ where s is the specific entropy. Then the entropy equation for cloudy air is

$$\frac{Ds_a}{Dt} + r_v\frac{Ds_v}{Dt} + r_l\frac{Ds_l}{Dt} = (1+r)\frac{q_{rad}}{T} - \left[\, s_v\frac{Dr_v}{Dt} + s_l\frac{Dr_l}{Dt} + \dot{s}_{fallout}\,\right] \ ,$$

where q_{rad} is the radiative heating rate per unit mass of cloudy air and the total water mixing ratio is $r = r_v + r_l$. The left side is the time rate of change of the entropy per unit mass of dry air following an air parcel. The right side describes the sources of entropy due to radiative heating, changes in water content, and fallout. The fallout of entropy is given by

$$\dot{s}_{fallout} = +\frac{1}{\rho_a}\nabla\cdot(\rho_a\, r_l\, s_l\, \mathbf{v}_l) \ .$$

Note that the only explicit external entropy source is that due to the convergence of the radiative flux into the control volume V.

7. ENTROPY EQUATIONS FOR EACH COMPONENT

The rate of change of the specific entropies of each component is described by the following set of equations.

$$\frac{Ds_a}{Dt} = c_{pa}\frac{Dln\,T}{Dt} - R\frac{Dln\,p_a}{Dt} = c_{pa}\frac{Dln\,\theta_a}{Dt} \ ,$$

$$\frac{Ds_v}{Dt} = c_{pv}\frac{Dln\,T}{Dt} - \frac{R}{\varepsilon}\frac{Dln\,e}{Dt} \ ,$$

$$\frac{Ds_l}{Dt_l} = c_l\frac{Dln\,T_l}{Dt_l} \ ,$$

where c_{pa}, c_{pv}, and c_l are the specific heats for dry air, water vapor, and liquid water, respectively. Here the subscript on the material derivative in the last equation indicates a time rate of change following the liquid drop.

The specific entropies of water substance are related by the enthalpy of vaporization, l_v, sublimation, l_s, and fusion, l_f, by

$$s_{v_{sat}} - s_l = \frac{l_v}{T} \quad , \quad s_{v_{sat}} - s_i = \frac{l_s}{T} \quad , \quad s_l - s_i = \frac{l_f}{T} \quad ,$$

and

$$l_s = l_v + l_f \quad .$$

These relations hold only at the time of the phase change. Thus they describe the vapor entropy relative to the liquid entropy when the vapor is saturated. The equations indicate that the water entropies are interrelated and share a common constant

We define the vapor and liquid water entropies relative to their values at the triple point. The triple point, denoted by a subscript tp, has vapor pressure e_{tp} = 6.11 mb and temperature T_{tp} = 273.17 K.

$$s_l(T) = s_l(T_{tp}) + c_l ln\left(\frac{T}{T_{tp}}\right) \quad ,$$

$$s_v(T, e) = s_v(T_{tp}, e_{tp}) + c_{pv} ln\left(\frac{T}{T_{tp}}\right) - \frac{R}{\varepsilon} ln\left(\frac{e}{e_{tp}}\right) \quad .$$

We take the common constant to be the entropy of ice at the triple point. Defining

$$s_0 \equiv s_i(T_{tp}) \quad ,$$

we have

$$s_l(T_l) = s_0 + \frac{l_f(T_{tp})}{T_{tp}} + c_l ln\left(\frac{T_l}{T_{tp}}\right) \quad ,$$

$$s_v(T) = s_0 + \frac{l_s(T_{tp})}{T_{tp}} + c_{pv} ln\left(\frac{T}{T_{tp}}\right) - \frac{R}{\varepsilon} ln\left(\frac{e}{e_{tp}}\right) \quad .$$

The temperature dependence of the enthalpy of vaporization is described by Kirchhoff's relation

$$\frac{dl_v}{dT} = c_{pv} - c_{pl} \quad .$$

Since the dry air undergoes no phase changes, an air reference entropy is not needed.

8. ADIABATIC SATURATED ASCENT

For the case of adiabatic saturated flow of a closed cloud parcel, there is neither radiative heating nor fallout, and the vapor pressure is the saturated value, r_{sat}. Then continuity is

$$\frac{Dr_{sat}}{Dt} = -\frac{Dr_l}{Dt} \quad ,$$

and the entropy equation becomes

$$\frac{Ds_a}{Dt} + r_{sat}\frac{Ds_v}{Dt} + r_l\frac{Ds_l}{Dt} = -(s_v - s_l)\frac{Dr_{sat}}{Dt}$$

$$= -\frac{l_v}{T}\frac{Dr_{sat}}{Dt} \quad ,$$

or

$$c_p\frac{Dln\,\theta_a}{Dt} + \frac{l_v}{T}\frac{Dr_{sat}}{Dt}$$

$$+\left(r_{sat}\,c_v + r_l\,c_l - \frac{l_v\,r_{sat}}{T}\right)\frac{Dln\,T}{Dt} = 0 \quad ,$$

where we have used the entropy definitions for the components and the Clausius-Clapeyron equation

$$\frac{R}{\varepsilon}\frac{Dln\,e_{sat}}{Dt} = \frac{l_v}{T}\frac{Dln\,T}{Dt} \quad .$$

Our result agrees with the standard exact expression.

9. EVAPORATION OF RAINDROPS

In this case the heat equation for a raindrop is

$$\frac{DT_l}{Dt_l} = -\left(\frac{T_l - T}{\tau_c}\right) + \frac{l_v\,\dot{r}_{cond}}{c_l\,r_l} + \dot{T}_{rad} \quad ,$$

where τ_C is a conductive/ventilative time scale, l_v is the enthalpy of vaporization, and T is the ambient air temperature. Here $\dot{T}_{rad}$ is the radiative warming rate of the drop.

Then the entropy of the moist air is given by

$$\frac{Ds_a}{Dt} + r_v\frac{Ds_v}{Dt} = (1 + r)\frac{q_{rad}}{T} - \frac{r_l c_l \dot{T}_{rad}}{T_l}$$

$$-\left[\frac{r_l c_l(T - T_l)}{\tau_c\,T_l} + (s_{v_{sat}}(T_l) - s_v)\,\dot{r}_{cond}\right]$$

Since the temperature of the raindrop is typically less than that of the ambient air, the first term in the square brackets represents the cooling of the air as the droplet evaporates. The second term is a correction for the fact that the ambient air need not be saturated.

If the ventilative time scale is small compared to the dynamical time scale, then the first term in the heat equation may be ignored and the entropy equation for the moist air simplifies to the familiar form

$$\frac{Ds_a}{Dt} + r_v\frac{Ds_v}{Dt} \cong (1 + r)\frac{q_{rad}}{T} + \frac{l_v(T_l)}{T_l}\dot{r}_{cond}$$

10. MOMENTUM EQUATION

The momentum per unit volume is $\chi = \rho_a \mathbf{u}_a + \rho_v \mathbf{u}_a + \rho_l \mathbf{u}_l$. Then the momentum equation for cloudy air is

$$(1+r)\frac{D\mathbf{u}_a}{Dt} + r_l\frac{D\mathbf{v}_l}{Dt} = -\frac{1}{\rho_a}\nabla p + (1+r)\mathbf{g} - \left[\mathbf{u}_a\frac{Dr_v}{Dt} + (\mathbf{u}_a + \mathbf{v}_l)\frac{Dr_l}{Dt} + \dot{\mathbf{u}}_{fallout}\right] .$$

Note that the only explicit sources of momentum acting on the control volume are those due to the body force of gravity, $\mathbf{g}$, and the surface forces due to the air pressure. We assume that the viscous forces only act between the air and the droplets. The momentum fallout is

$$\dot{\mathbf{u}}_{fallout} = +\frac{1}{\rho_a}\frac{\partial}{\partial x_j}(\rho_a r_l \mathbf{u}_l v_{lj}) .$$

The momentum equation for a cloud droplet of density ρ_p is

$$\frac{D\mathbf{u}_l}{Dt_l} = -\frac{1}{\rho_p}\nabla p + \mathbf{g} - \frac{(\mathbf{u}_l - \mathbf{u}_a)}{\tau_v} ,$$

where the viscous decay time

$$\tau_v = \left[\frac{6\pi a\,\mu_a}{m_p}\left(\frac{C_D N_{Re}}{24}\right)\right]^{-1} ,$$

is a function of the dynamic viscosity, particle mass, drag coefficient, and Reynolds number.

11. LIQUID WATER LOADING

Substituting the particle momentum equation into that for the cloudy air yields

$$(1+r_v)\frac{D\mathbf{u}_a}{Dt} = -\frac{1}{\rho_a}\left(1 - \frac{\rho_l}{\rho_p}\right)\nabla p + (1+r_v)\mathbf{g} + r_l\left(\frac{\mathbf{u}_p - \mathbf{u}_a}{\tau_v}\right) - \mathbf{v}_l\dot{r}_{cond} .$$

If the particle motion relative to the air is given by the terminal velocity $\mathbf{v}_T$

$$\mathbf{v}_T = +\tau_v\left(\mathbf{g} - \frac{1}{\rho_p}\nabla p\right) \cong -\tau_v g\,\frac{(\rho_p - \rho_s)}{\rho_p}\hat{\mathbf{z}} ,$$

then

$$(1+r_v)\frac{D\mathbf{u}_a}{Dt} = -\frac{1}{\rho_a}\nabla p + (1+r_v)\mathbf{g} + r_l\mathbf{g} - \mathbf{v}_T\dot{r}_{cond} .$$

The second to last term is the "liquid water loading". The last term represents an acceleration reaction due to the condensation of the vapor into a liquid.

12. CONCLUSIONS

We have formally derived the equations for cloudy air subject to the assumption of a continuum hypothesis and the principle of complementarity. The equations require expressions for the microphysical processes such as the condensation rate and equations describing the change in cloud particle entropy and momentum. The equations may be readily extended to include the ice phase and/or a distribution of cloud particles. Future research will address how these equations are modified when the anelastic approximation is made.

Acknowledgements. Partial support for this research was provided by the National Science Foundation under grant ATM-9820233.

REFERENCES

Aris, R., 1962: *Vectors, Tensors, and the Basic Equations of Fluid Mechanics.* Dover, 286 pp.

Crowe, C., M. Sommerfeld, and Y. Tsuji, 1998: *Multiphase Flows with Droplets and Particles.* CRC Press, 471 pp.

HYDROSTATIC AND GEOSTROPHIC ADJUSTMENT IN RESPONSE TO RAPID LOCALIZED DIABATIC HEATING

Jeffrey M. Chagnon* and Peter R. Bannon

Department of Meteorology, The Pennsylvania State University,
University Park, PA, 16802, U.S.A.

1. INTRODUCTION

Atmospheric flows exhibit a tendency toward hydrostatic and geostrophic balance. However, the atmosphere isn't always observed to be in a hydrostatic and geostrophic state, particularly on scales less than or equal to the synoptic scale. Diabatic heat sources, such as those provided by clusters of convection, can produce a hydrostatic and geostrophic imbalance. An adjustment process is induced in response to the imbalance. The adjustment is characterized by the production of a spectrum of acoustic, buoyancy, and Rossby-gravity waves, and a tendency of the flow toward a new hydrostatic and geostrophic state.

In the present study, we consider analytical solutions to a linearized hydrostatic and geostrophic adjustment problem forced by the imposition of an instantaneous diabatic heating function. This particular problem is used as a prototype problem for comparing several compressibility approximations and for assessing the effects of different vertical boundary conditions.

2. STEADY STATE SOLUTION

2.1 The Model

The governing equations for fully compressible, inviscid atmosphere with background rotation linearized about an isothermal resting base state are

$$\rho_s \frac{\partial u'}{\partial t} = -\frac{\partial p'}{\partial x} + \rho_s f v' \,, \tag{1}$$

$$\rho_s \frac{\partial v'}{\partial t} = -\frac{\partial p'}{\partial y} - \rho_s f u' \,, \tag{2}$$

$$\rho_s \frac{\partial w'}{\partial t} = -\frac{\partial p'}{\partial z} - \rho' g \,, \tag{3}$$

$$\frac{\partial \rho'}{\partial t} = -w \frac{\partial \rho_s}{\partial z} - \rho_s \left(\frac{\partial u'}{\partial x} + \frac{\partial v'}{\partial y} + \frac{\partial w'}{\partial z} \right) \,, \tag{4}$$

$$\frac{\partial \theta'}{\partial t} + w \frac{\partial \theta_s}{\partial z} = \dot{\Theta} \,, \tag{5}$$

$$\frac{\theta'}{\theta_s} = \frac{p'}{\gamma p_s} - \frac{\rho'}{\rho_s} \,. \tag{6}$$

where a superscript prime denotes a perturbation from the base state and a subscript 's' denotes a static base state quantity. The base state satisfies the relations

$$\begin{aligned} T_s &= T_* = 288\ K \,, \\ \theta_s &= \theta_* \exp(\kappa z / H_s) \,, \\ p_s &= p_* \exp(-z / H_s) \,, \\ \rho_s &= \rho_* \exp(-z / H_s) \,, \end{aligned} \tag{7}$$

where $\kappa = R / C_p$ and the scale height H_s is defined as

$$H_s = R T_s / g \,.$$

The diabatic heating function in (5) is defined as

$$\dot{\Theta} = \frac{\theta_s}{\rho_s C_p T_s} Q \,, \tag{8}$$

where the heating is

$$Q = \frac{C_v}{R} \Delta p \left[H(z+a) - H(z-a) \right] G(x,y)\, \delta(t) \,.$$

Here δ denotes the Dirac delta function, H is the Heaviside step function, and G is an arbitrary function representing the horizontal structure of the heating.

In addition to studying the fully compressible solution to these equations, we consider several common compressibility approximations and their solution to the adjustment problem. These approximations are the anelastic approximation (Bannon 1996), the pseudo-incompressible approximation (Durran 1989), and the modified compressible approximation (Klemp and Wilhelmson 1978). The most general way of denoting these approximations is by rewriting the mass conservation equation (4), using (5) and (6) to obtain

$$\nabla \cdot \mathbf{u_h}' = \frac{w'}{\gamma H_s} + \delta_1 \frac{\dot{\Theta}}{\theta_s} - \delta_2 \frac{1}{\gamma p_s} \frac{\partial p'}{\partial t} \,. \tag{9}$$

We solve (1) - (3), (5), (6), with (9) to produce the most general solution for comparing the compressibility approximations. The values of the δ's are used to denote the appropriate approximation - e.g., compressible ($\delta_1 = 1$, $\delta_2 = 1$), pseudo-incompressible

Corresponding author's address: Jeffrey M. Chagnon, The Pennsylvania State University, Department of Meteorology, 503 Walker Building, University Park, P.A., 16802; Email: chagnon@essc.psu.edu

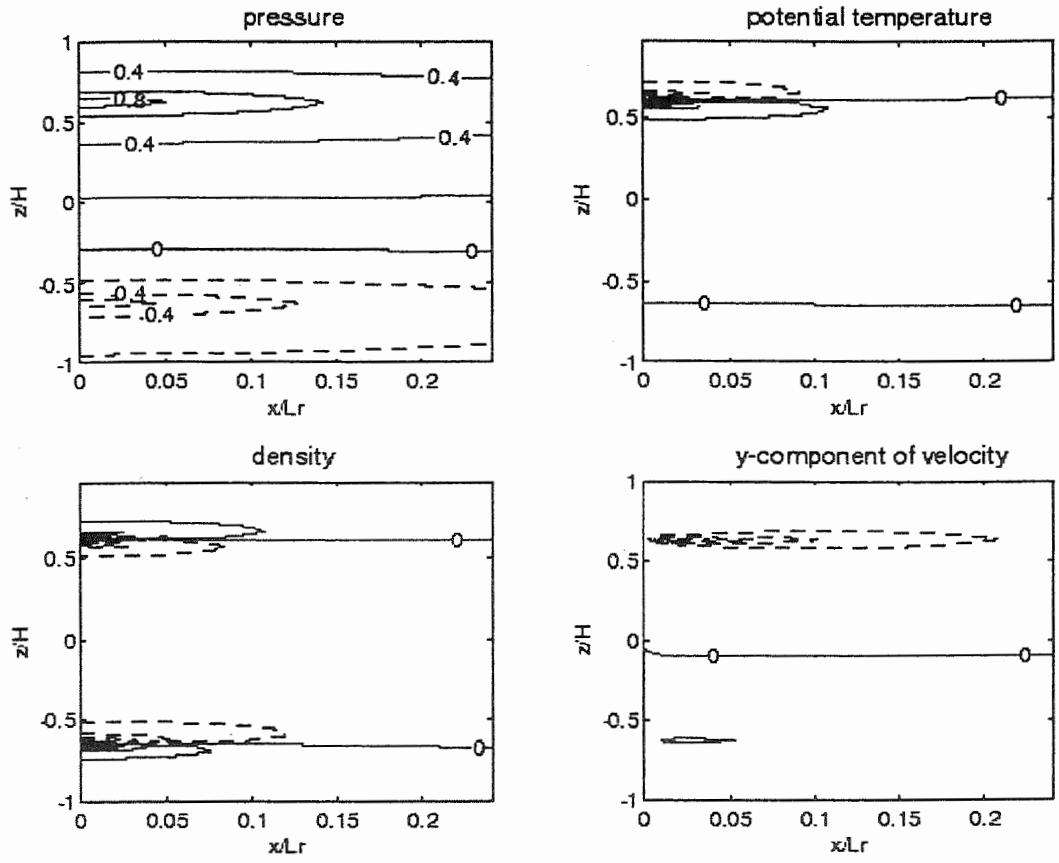

FIG. 1. Steady state perturbation fields contoured in the x-z plane. Dashed(solid) contours denote negative(positive) values. Fields are normalized such that the maximum value in each field is 1.

($\delta_1 = 1$, $\delta_2 = 0$), modified compressible ($\delta_1 = 0$, $\delta_2 = 1$), and anelastic ($\delta_1 = 0$, $\delta_2 = 0$, with $\gamma = 1$ in (9) and (6)).

2.2 Steady State Fields

The steady state solution to (1) - (6) is solved using the principle of potential vorticity conservation and the Fourier transform. An inverse fast-fourier transform was used to invert the analytical solutions. The diabatic heating function was prescribed such that

$$G(x) = \frac{d}{x^2 + d^2} ,$$

where d = 20 km.

The steady state pressure, density, potential temperature, and velocity anomaly fields are contoured in figure 1. The steady state is characterized by a dipole in the pressure anomaly field. A region of anomalously high(low) pressure remains at the top(bottom) of the initially warmed layer. This structure is consistent with the initial dipole potential vorticity anomaly induced by the heating. The velocity field exhibits a low level cyclone and upper level anticyclone consistent with the structure of the pressure field. A vertical asymmetry exists in the velocity field which is attributable to the negative exponential profile of density in the basic state. The potential temperature field exhibits a warm anomaly within the heated layer. A negative potential temperature anomaly persists above the heated layer, indicating that there has been a net upward expansion of the heated layer. This net expansion of the heated layer is also evident in the density anomaly field. Positive(negative) density anomalies persist outside(inside) of the heated layer. All steady state field anomalies decay with respect to horizontal distance from the heating center. The horizontal e-folding decay

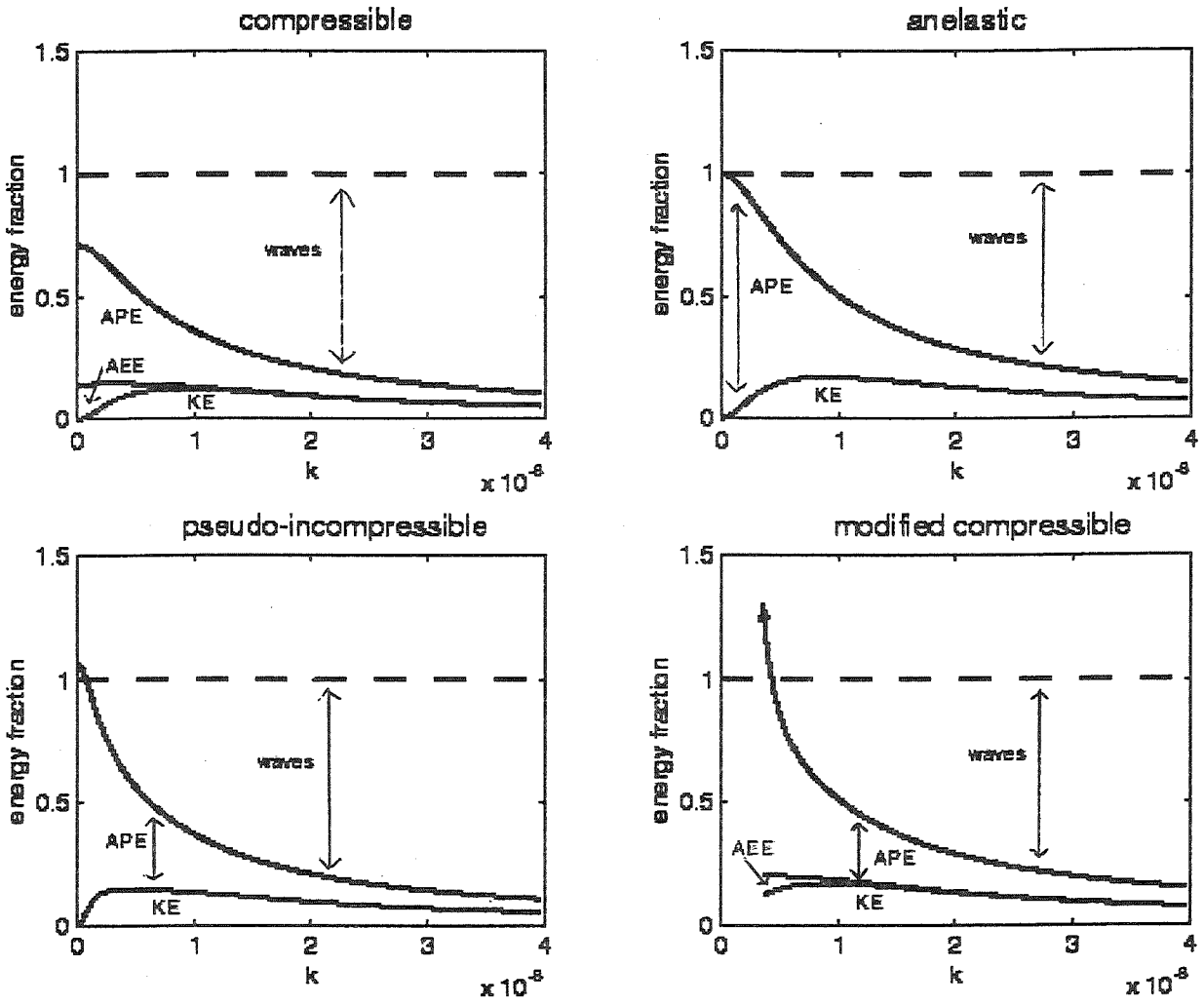

FIG. 2. Steady state energetics as a function of wavenumber. Regions between curves represent relative fractions of energy contained in APE, AEE, KE, or waves and are labeled as such. k is equivalent to $2\pi / L$, where L is the dimensional wavelength (m).

length scales with the Rossby radius of deformation, which has been approximated by

$$L_R = \frac{2 a N_s}{f}$$

3. ENERGETICS

An energy conservation equation can be derived from the governing equation in section 2.1 . The generalized energy conservation equation is

$$\frac{\partial}{\partial t}\left[\frac{1}{2}\rho_s \mathbf{u}\cdot\mathbf{u} + \frac{\rho_s}{2N_s^2}\left(\frac{g\theta}{\theta_s}\right)^2 + \delta_2\frac{p^2}{2\gamma p_s}\right] = - \nabla\cdot(p\,\mathbf{u}) + \dot{\theta}\left[\frac{\rho_s g^2 \theta}{N_s^2\,\theta_s^2} + \delta_1\frac{p}{\theta_0}\right] \quad (10)$$

We recognize the terms on the left hand side of (10) as the kinetic energy (KE), available potential energy (APE) and available elastic energy (AEE), respectively. The terms on the right hand side represent the energy due to wave generation and the initial energy projected onto AEE and APE.

The steady state energetics are displayed in figure 2 for the compressible, anelastic, pseudo-incompressible, and modified compressible atmospheres. At each horizontal wavenumber the initial energy projected onto the AEE and APE is computed

and considered the total energy at that wavenumber. The steady state KE, APE, and AEE are then computed and normailzed by the total energy residing in that wavenumber. The wave energy fraction is inferred as the remaining difference between the initial and final state energetics. Since this method removes the total energy dependence on wavenumber, it is equivalent to the "white noise" response.

4. DISCUSSION

Figure 2 demonstrates that in the presence of diabatic heating, the modified compressible and pseudo-incompressible systems are not energy conserving. In the modified compressible atmosphere there is no projection of heating energy onto initial AEE, but there is AEE in the steady state. In the pseudo-incompressible atmosphere there is no AEE in the steady state energy balance, but there is a projection of heating energy onto initial AEE. On the other hand, the anelastic approximation removes AEE from both the final state and initial state in the energy balance. This consistency allows for energy conservation under diabatic conditions.

The errors made in the energetics by each approximation are largest at the largest scales. The role of AEE in the adjustment process is only significant at scales larger than approximately 5000 km - scales much larger than those relevant to cloud dynamics. At scales on the order of the mesoscale, most of the initial energy is projected onto waves. It is therefore necessary to partition the wave energetics in order to provide useful information about the adjustment process on scales less than or equal to the mesoscale. Our present goal is to solve the time dependent adjustment problem and to partition the wave energetics between acoustic and gravity modes.

5. REFERENCES

Bannon, P.R., 1995: Hydrostatic adjustment: Lamb's problem. *J. Atmos. Sci.*, **52**, 1743-1752.

———, 1996: On the anelastic approximation for a compressible atmosphere. *J. Atmos. Sci.*, **53**, 3618-3628.

Durran, D. R., 1989: Improving the anelastic equation. *J. Atmos. Sci.*, **46**, 1453-1461.

Klemp, J. B., and R. B. Wilhelmson, 1978: The simulation of three-dimensional convective storm dynamics. *J. Atmos. Sci.*, **35**, 1070-1096.

Acknowledgments. Financial support for this work was provided by the NSF under NSF grant ATM-9820233

THE VALIDATION OF DRIZZLE PARAMETRIZATIONS USING AIRCRAFT DATA

Robert Wood

Meteorological Research Flight, The Met. Office, Farnborough, Hants, UK

1. INTRODUCTION

The climatological impact of precipitation formation in marine stratiform clouds is poorly understood. In order to improve our knowledge of the connections between drizzle and stratocumulus cloud climatology, better representation in climate models of the processes of precipitation formation in warm stratocumulus cloud is required. In this paper a number of commonly used parametrizations of autoconversion and accretion are examined using aircraft data from 11 flights. Only flights in which the cloud deck was sampled with good vertical and horizontal resolution were chosen for this study. In several of the cases improved vertical sampling was obtained using sawtooth runs from cloud-base to cloud-top. These data were obtained in marine stratocumulus cloud spanning a wide range of cloud thickness h, liquid water paths LWP and droplet concentrations N_d (see table 1). Also in the table is given the cloud-base height z_b and the ratio of the liquid water path observed to that in an adiabatic cloud with the same thickness. The droplet concentrations range from 25-710 cm^{-3} and liquid water paths from 80-360 g m^{-2}.

2. DRIZZLE LIQUID WATER CONTENTS.

The drizzle liquid water content q_D is defined as the liquid water content in droplets larger than 20 μm radius. Droplets smaller than this do not contribute significantly to the precipitation rate. Drizzle liquid water contents were calculated for each 1km section of flight. Figure 1(a) shows that the drizzle liquid water content is generally greater in the cleaner (low N_d) clouds. Figure 1(b) shows that clouds with high drizzle liquid water contents are more depleted in liquid water content.

Table 1: Details of C-130 flights used. Values given are mean values for entire flight.

Flight Month; Location	z_b [m]	h [m]	N_d [cm^{-3}]	LWP [g m^{-2}]	LWP/LWP_{adiab}
H511 April; UK	950	320	710	120	0.93
H526 July; UK	400	400	100	170	0.65
H564 Dec; UK	200	670	35	205	0.44
A049 Dec; UK	750	700	285	260	0.52
A209 Jun; Azores	275	425	120	170	0.79
A439 Feb; UK	750	400	90	115	0.66
A641 Dec; UK	400	750	320	360	0.83
A644 Dec; UK	150	1600	55	90	0.07
A648 Feb; UK	200	850	25	85	0.22
A649 Feb; UK	450	300	60	80	0.61
A693 Jul; UK	100	300	200	80	0.64

Corresponding author's address: Robert Wood, Meteorological Research Flight, Y46 Building, DERA, Farnborough, Hants, GU14 0LX, UK; email: robwood@meto.gov.uk

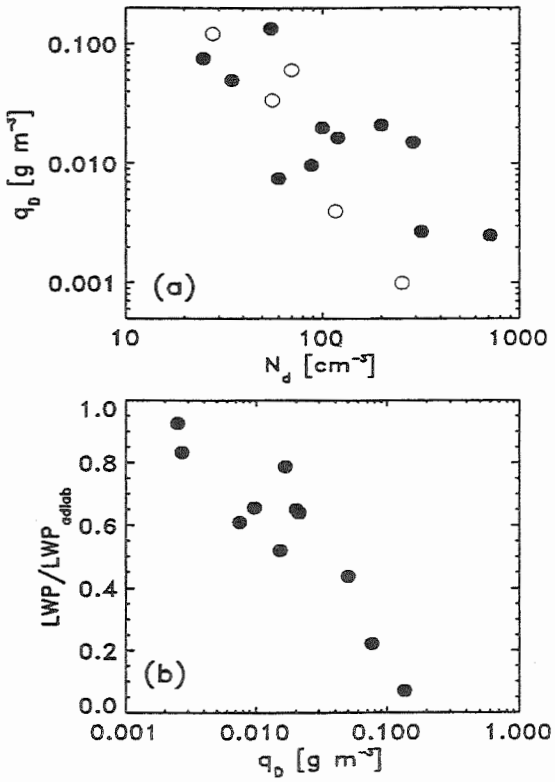

Figure 1.(a) Mean in-cloud drizzle liquid water content against cloud droplet concentration (solid circles). Results from Yum et al. (1998) are also shown (open circles). (b) Degree of adiabaticity as a function of drizzle liquid water content.

Figure 2 shows the mean vertical distribution of the drizzle liquid water content within cloud for flights A049-A693. Height-partitioned data were not available for cases H511-H564 as data for these flights is from Nicholls and Leighton (1986). The height in cloud is normalised using the cloud-base and top heights so that 0 represents cloud-base and 1 cloud-top. The abscissa is plotted using a logarithmic scale to show the large range of drizzle liquid water contents encountered. Table 2 shows the mean and standard deviation in-cloud drizzle liquid water content over the normalised height range 0.2-0.8 (to avoid the inclusion of cloud-free regions), which ranges from 2.7×10^{-3} to 7.5×10^{-2} g m^{-3}. The standard deviation gives an idea of the variability of the drizzle liquid water content within the cloud. The ratio of the standard deviation to the mean drizzle liquid water content (Table 2) ranges from 0.46-1.89 and this variability is mainly a result of horizontal variability rather than any systematic trend of the drizzle liquid water content with height. The parameter $F_{v/h}$ (Table 2) is the ratio of the standard deviation in the linear regression of drizzle liquid water content with height to the total standard deviation. In all cases except

A644 the systematic variation with height represents less than 20% of the total variability. In the case A644 there was a considerable increase in the drizzle liquid water content with height in cloud.

Table 2. Mean and standard deviation of observed in-cloud drizzle liquid water content. Standard deviations are not available for flights H511-H564. Also shown is the ratio of the standard deviation to the mean. The final column shows $F_{v/h}$ which is the ratio of vertical to horizontal variability in q_D.

Flight	$\overline{q_D}$ [x10^{-3} gm^{-3}]	σ_{q_D} [x10^{-3} gm^{-3}]	$\sigma_{q_D}/\overline{q_D}$	$F_{v/h}$
H511	2.5	-	-	-
H526	20.0	-	-	-
H564	30.1	-	-	-
A049	15.1	12.1	0.80	0.20
A209	16.5	15.4	0.93	0.01
A439	9.7	6.9	0.71	0.12
A641	2.7	5.1	1.89	0.06
A644	92.9	162.2	1.75	0.48
A648	76.0	123.0	1.62	0.10
A649	7.5	13.1	1.75	0.03
A693	21.0	9.6	0.46	0.15

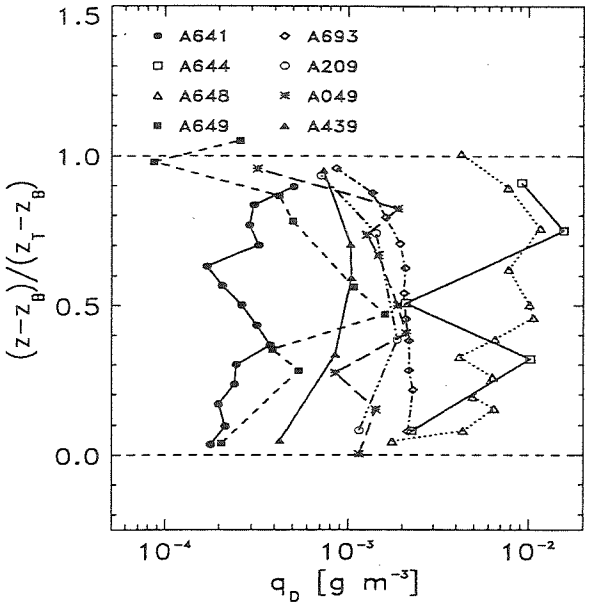

Figure 2. Variation of drizzle liquid water content with height in cloud (0=base; 1=top) for cases A049-A693.

3. HETEROGENEITY of DRIZZLE LWC

Table 2 indicates that the ratio of the standard deviation of q_D to the mean is roughly constant. Clouds with high drizzle liquid water contents exhibit considerable inhomogeneity, with regions of relatively weak drizzle interspersed among strongly drizzling regions. The probability distribution function (pdf) of drizzle within cloud is of considerable interest because the coupling between microphysical and dynamical processes is strongly affected by precipitation formation (Stevens et al., 1998). We find that the cases examined here have pdfs of drizzle liquid water content that are approximately lognormal in character with geometrical mean and standard deviation fitted well using

$$\text{geometrical mean} = 0.034\left\{1 - \exp\left(-27.0\overline{q_D}\right)\right\}$$
$$\text{geometrical s.d.} = 2.43 + 51.12\overline{q_D} \qquad [1]$$

This indicates that if the mean drizzle liquid water content in a grid-box is known then the subgrid variability is predictable to a reasonable accuracy.

4. PRECIPITATION RATE

The precipitation rate is of prime importance to the prediction of drizzle in both large and small scale numerical models. The precipitation rate P (g m^{-2} s^{-1}) of a population of drops can be written as

$$P = w_{FALL} q_D \qquad [2]$$

where w_{FALL} is the fall speed (m s^{-1}). The precipitation rate is derived from observed droplet size distributions using the terminal velocity relationships of Rogers and Yau (1989). We find that the mean fall velocity for all our clouds is 0.37 ± 0.09 m s^{-1}.

5. MODEL

A simple model is used to predict drizzle liquid water contents. The model assumes that the removal of precipitation from the cloud-base is balanced with an equal turbulent flux of water vapour into the cloud from below. It is also assumed that the depletion of CCN by drizzle drops falling to the surface is negligible over the timescale of the observations (3-6 hours). There was no evidence of a systematic reduction in droplet concentration during the course of the observations in any of the cases. The equilibrium assumption therefore allows the use of a constant liquid water and droplet concentration profile. The input profiles are obtained from the entire observational dataset at 20 levels from the surface to the inversion. At each level the rate of change of drizzle liquid water content is given by

$$\frac{\partial q_D(z)}{\partial t} = Auto(q_C, N_d) + Acc(q_C, q_D) + \frac{\partial P}{\partial z} \qquad [3]$$

where *Auto* is the autoconversion rate, a function of cloud liquid water content (q_C, r<20 μm) and Acc is the accretion rate, a function of both the cloud and drizzle liquid water contents.

All microphysical data were averaged over 10 second intervals to allow for sufficient sampling of the larger drizzle-size particles. The precipitation rate P is calculated as function of q_D using the fall speed from equation [2]. Autoconversion and accretion are parametrized using three different commonly used schemes shown in table 3.

The observed and model drizzle liquid water contents are shown in table 4 and for T+C and K+K in figure 3. All results were taken in-cloud from normalised height 0.2-0.8. There are several important features to note:

(i) The T+C scheme overestimates the drizzle liquid water content by a large amount in almost all cases apart for those clouds with low liquid water path and low droplet concentration. Especially poor are the predictions for thick polluted clouds for which q_D may be overestimated by up to three orders of magnitude. The observed drizzle liquid water contents are strongly influenced by droplet concentration but those of T+C are not.

Table 3. Details of the formulations for autoconversion and accretion used in the different parametrizations examined in this study. The values of A-F are approximately constant having only some weak dependency upon air density. H(x) is the Heaviside step function and ρ is the air density. All liquid water contents expressed in kg kg^{-1} and droplet concentrations in m^{-3}.

Scheme	$\left.\frac{dq_D}{dt}\right\|_{Auto}$ [kg kg^{-1} s^{-1}]	$\left.\frac{dq_D}{dt}\right\|_{Acc}$ [kg kg^{-1} s^{-1}]
Kessler (1969) [KES]	$A.max(q_C - q_{thresh})$ A=10^{-3} s^{-1} q_{thresh}=5x10^{-4} kg kg^{-1}	$D\rho^{7/8}N_d^{1/8}q_Cq_R^{7/8}$ D=0.29
Tripoli and Cotton (1980) [T+C]	$Bq_C^{7/3}N_d^{-1/3}H(q_C - q_{thresh})$ B=3268$\rho^{4/3}$ (E_C=0.55) q_{thresh} assumes r_{cm}=7μm	Eq_Cq_R E=4.7
Khairoutdinov and Kogan (2000) [K+K]	$Cq_C^{2.47}N_d^{-1.79}$ C=7.42x10^{13}	$F(q_Cq_D)^{1.15}$ F=67.0
Beheng (1994) [BEH]	$Gd^{-1.7}q_C^{4.7}N_d^{-3.3}\rho^{3.7}$ d is width parameter (d=9.9 for N_d<200 cm^{-3} d=3.9 for N_d>200 cm^{-3}) G=4.8x10^{14}	$Jq_Cq_R\rho$ J=6.0

(ii) The K+K scheme generally underpredicts the drizzle liquid water content, although the agreement is far better than that of T+C. In addition, the highest predicted drizzle liquid water contents are in the clouds with the highest observed drizzle liquid water contents suggesting that the K+K scheme has a realistic dependency upon droplet concentration.

(iii) The Beheng scheme generally underestimates the drizzle liquid water content as does K+K, but the discrepancies are generally worse than K+K but in general, BEH accounts reasonably well for the wide range of droplet concentrations. There appears to be too large a dependence upon liquid water content as the A641 drizzle liquid water content is considerably overpredicted.

(iv) The Kesler scheme, having an autoconversion threshold of 0.5 g m^{-3}, results in no drizzle production at all in most of the clouds. In the cases where drizzle is predicted by KES the rates are far too high and would in reality result in a complete depletion of the cloud liquid water within 10-20 minutes in cases A049 and A641. The lack of a dependence upon droplet concentration is also a limiting feature of this parametrization.

6. EFFECT OF HETEROGENEITY UPON AUTOCONVERSION AND ACCRETION

The three formulations presented here were intended for use in cloud-resolving models (CRMs). As such they represent the production of drizzle liquid water content on a *local* scale (the resolution of the CRM). In contrast, GCMs have grid-boxes which may be many times the scale for which the autoconversion and accretion parameterizations were intended. It is therefore important to assess how heterogeneity in the cloud on scales from 1 km upward would affect the production of drizzle liquid water content. This has been investigated previously (Larson et al., 1999) for clouds observed during the ASTEX campaign. Because there is sub-grid variability in liquid water content and droplet concentration, applying the autoconversion and accretion parametrizations to the grid-box mean parameters leads to biases in estimates of autoconversion and accretion rates. It is shown in Larson et al. (1999) that such biases can in some cases be large.

To give an idea of the bias caused by having a distribution of liquid water contents and droplet concentration at a model level, we examine the autoconversion and accretion using all the 1km data over a short height range close to the cloud-top.

Table 4. Observed and predicted mean in-cloud drizzle liquid water contents using the three different autoconversion and accretion schemes.

Flight	$\overline{q_D}$ [x10^{-3} g m^{-3}]				
	OBS.	K+K	T+C	KES	BEH
H511	2.5	0.04	0.0	0.0	0.003
H526	20.0	3.8	320.9	182.4	2.4
H564	30.1	6.2	145.8	0.0	3.3
A049	15.1	1.2	1407	23230	5.2
A209	16.5	2.3	329.4	685	0.1
A439	9.7	0.9	85.8	0.0	0.1
A641	2.7	2.9	2882	38310	16.5
A644	92.9	40.0	37.2	0.0	22.0
A648	76.0	32.8	15.7	0.0	51.8
A649	7.5	2.0	49.7	0.0	1.2
A693	21.0	0.2	31.5	0.0	0.02

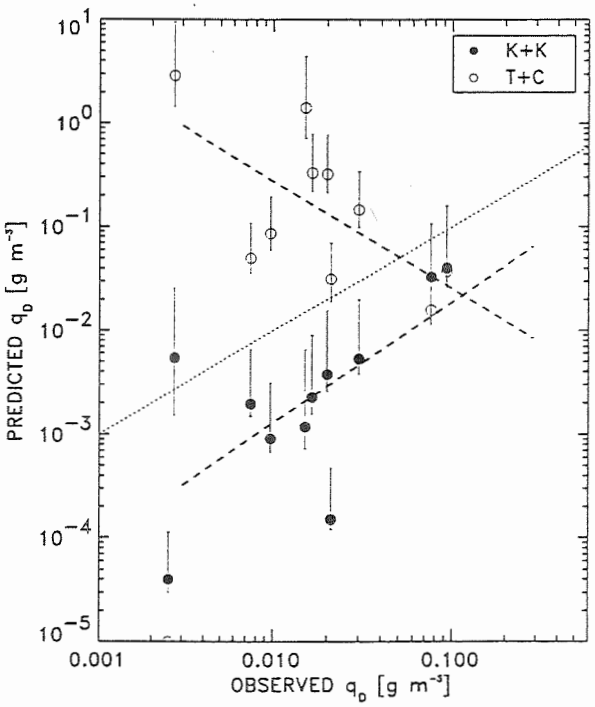

Figure 3. Observed and predicted cloud-mean drizzle liquid water contents. Only the T+C and K+K results are shown as KES predicted zero q_D for most of the cases. The error bars represent both the uncertainty in the fall speed, the droplet concentration and the liquid water content. In addition, the upper limit of the predictions has been extended to account for the effect of heterogeneity in the clouds (see section 6). The dotted line represents perfect agreement. The dashed lines are the best fits for the T+C (upper line) and K+K parametrization (lower line).

The ratio between the mean value of the autoconversion and the value of the autoconversion calculated using the level mean parameters varies from 1.15 (A439) to 1.80 (A644) with a mean of 1.58. For the accretion this ratio varies from 1.01 (A209) to 2.11 (A648) with a mean of 1.36. For all flights these ratios are greater than unity indicating that a model estimating the mean autoconversion and accretion at a level will underpredict these rates, with the greatest discrepancy being in the autoconversion. Inclusion of the effects of these biases (by raising the autoconversion and accretion rates) in the model increases the mean in-cloud drizzle liquid water contents by a factor of 2.2 for the K+K parametrization. The mean autoconversion and accretion ratios for T+C are 1.42 and 1.18, which would lead to a mean increase in the predicted drizzle liquid water contents of approximately 60%. The biases for BEH are also significant and result in a mean increase in drizzle liquid water content of some 80%.

The biases are somewhat less with the T+C and KES formulations because there is less dependency upon the droplet concentration. The error bars in figure 3 have been adjusted to account for this systematic underprediction. Inclusion of the heterogeneity of the clouds reduces the discrepancy between K+K and the observations, but increases it in the case of T+C and KES.

7. DISCUSSION

Eleven flights have been intensively observed to study the processes involved in drizzle formation in warm stratocumulus clouds. The results suggest that the production of drizzle is highly dependent upon the cloud droplet concentration and that parametrizations of autoconversion and accretion should account for this dependency. In addtion, this paper has reported an attempt to validate three autoconversion/accretion parametrizations used in GCMs using aircraft data from 11 intensively observed cases of stratocumulus cloud which varied considerably in cloud thickness, droplet concentration and drizzle liquid water content.

A simple equilibrium model of drizzle autoconversion, accretion and fallout was initialised using the observed, height resolved values of droplet concentration and liquid water content. The same fallout relationship was used throughout but the accretion and autoconversion terms differed. The most accurate predictions were those made by a scheme (Khairoutdinov and Kogan, 2000) derived using LES with explicit microphysics, but results from Beheng (1994) are also encouraging. The Tripoli and Cotton (1980) scheme generally predicted drizzle liquid water contents which were too high and the dependence of autoconversion upon droplet concentration appears to be too weak. The Kessler (1969) scheme either did not predict any drizzle at all (due to the inclusion of a threshold cloud liquid water content) or values far too high. This scheme is fundamentally limited for predictions the climatological impact of increasing aerosol loadings due to the lack of dependence of drizzle production upon cloud droplet concentration. This dependence appears to be significant – the observed drizzle liquid water contents (and hence precipitation rates) correlate strongly and negatively with the cloud droplet concentration as shown in figure 1(a). The autoconversion rate depends strongly upon droplet concentration in K+K (exponent = –1.79) and Beheng (exponent = –3.33), which accounts for the better predictions. However, these exponents still differ considerably.

The scaling up of a parametrization of local processes for use in climate and large scale numerical models requires considerable further attention. The use of mean liquid water contents and droplet concentrations in the simple model presented here results in sizeable underpredictions of the autoconversion and accretion rates. This bias is expected to be a function of both the observational averaging length (in this case 1 km) and the grid-box length. This bias is also expected to depend crucially upon cloud morphology, i.e. how variable the liquid water content and droplet concentration are in space.

ACKNOWLEDGEMENTS

Thanks to all staff and aircrew of the Met. Research Flight for their dedication in obtaining the data presented here.

REFERENCES

Beheng, K. D., 1994: A parameterization of warm cloud microphysical processes. Submitted to *Atmos. Res.*, **33**, 193-206.

Larson, V. E., Wood, R., Field, P. R., Golaz, J.-C., Vonder Haar, T. H., and Cotton, W. R., 1999: Systematic biases in the microphysics and thermodynamics of numerical models that ignore subgrid-scale variability. Submitted to *J. Atmos. Sci.*, November 1999.

Kessler, E., 1969: On the distribution and continuity of water substance in atmospheric circulations. *Meteor. Monogr.*, **32**, Amer. Meteorol. Soc., 1-84.

Khairoutdinov, M. and Kogan, Y. L., 2000: A new cloud physics parametrization in a large-eddy simulation model of marine stratocumulus. *Mon. Wea. Rev.*, **128**, 229-243.

Nicholls, S. and Leighton, J., 1986: An observational study of the structure of stratiform cloud sheets: Part I. Structure. *Quart. J. Roy. Meteorol. Soc.*, **112**, 431-460.

Stevens, B., Cotton, W. R., Feingold, G., Moeng, C.-H., 1998: Large-eddy simulations of strongly precipitating, shallow, stratocumulus-topped boundary layers. *J. Atmos. Sci.*, **55**, 3616-3638.

Rogers, R. R. and Yau, M. K., 1989: A first course in cloud physics. Third edition, Pergamon Press, Oxford, UK.

Tripoli, G. J. and Cotton, W. R., 1980: A numerical investigation of several factors contributing to the observed variable intensity of deep convection of south Florida, *J. Appl. Meteorol.*, **19**, 1037-1063.

Yum, S. S., Hudson, J. G. and Xie, Y., 1998: Cloud condensation nuclei and drizzle. *Proc. AMS Conf. Cloud Phys.*, Everett, USA, 1998, 267-270.

CONSIDERATIONS FOR THE PARAMETRIZATION OF CLOUD MICROPHYSICAL PROPERTIES IN NUMERICAL MODELS

D.R. Wilson

The Met. Office, London Road, Bracknell, RG12 2SZ, UK

1. INTRODUCTION

Large-scale models of the atmosphere are used for numerical weather prediction and climate change prediction. One such model is the `Unified Model' (UM), run at The Met. Office. Several factors constrain their formulation, not least the requirement for predictions to be reasonable. This paper reviews these considerations and methods for validating the large-scale precipitation scheme. The important observational quantities to measure are also reviewed.

Examples shown here are using the UM, reviewed by Cullen (1993), with the large-scale precipitation scheme given by Wilson and Ballard (1999).

2. PARAMETRIZATION CONSIDERATIONS

2.1 Computing

Numerical weather prediction models are required to run at great speed, especially for short range (a day or less) forecasts, in order that the forecast can reach customers whilst it is still useful. This has led to the use of ever-faster computers, which allows the resolution and complexity of the models to be increased. However, there is always a limit to the time available for the forecast and models usually run to extremely tight time constraints. This means that development of new physical parametrization schemes must always keep increases in run-time as small as possible.

Climate prediction models can afford to be slightly less severe on the run-time allowed. However, the models used for climate prediction are essentially the same as global numerical weather prediction models, except they run at reduced horizontal resolution.

Such models have an enormous number of lines of code and are usually under development. The easy maintenance and use of this code places additional restrictions on the formulation of the schemes and development timescales.

2.2 Subgrid-scale

A climate model may have grid-boxes of size 300 km x 300 km in horizontal dimension, and several hundred metres in the vertical. There is much that may occur in the atmosphere within these scales, as demonstrated by the radar cross section in figure 1. The model will typically know only gridbox mean values of temperature, winds, pressure and moisture variables and, depending upon the model, the volume coverage of cloud within the gridbox.

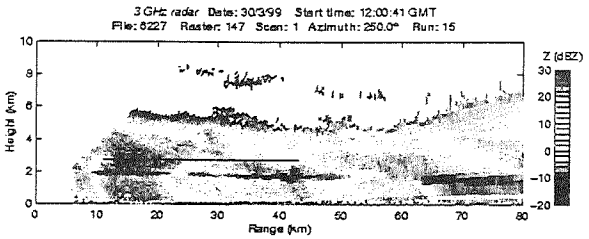

Figure 1. A vertical scan of radar reflectivity (dBZ). (University of Reading). The horizontal line marks the flight path of The Met. Office's C-130 aircraft.

From these average quantities the effect of physical processes must be calculated. The distribution of these quantities within the gridbox and their correlation in the vertical is critical in determining the behaviour of a physical parametrization.

A physical parametrization scheme must contain a `subgrid model' which estimates how the physical quantities are distributed. Aircraft data can be used to investigate this. By altering the subgrid model the predictions of the model can be significantly changed. A distribution of vertical velocities within a gridbox, rather than a uniform distribution, has been shown to result in different transfer rates between vapour, liquid and ice. This results in different profiles of water contents, shown in figure 2. Particularly sensitive is the Hallett-Mossop region of secondary ice production between –3 and –8 degrees Celsius.

2.3 Microphysics

A large-scale cloud and precipitation scheme will contain assumptions about the nature of the microphysical aspects of cloud and precipitation. Such quantities include fall speeds of particles and particle size distributions. These parametrizations will effect the evolution of the model. As an example, figure 3 shows an aircraft measurement of a particle size distribution for ice, and the size distribution in the Unified Model for that temperature and ice water content.

Corresponding author's address: Damian R. Wilson, Hadley Centre for Climate Prediction and Research, The Met. Office, London Road, Bracknell, RG12 2SY, UK.; E-Mail: drwilson@meto.gov.uk

The observations show many particles of the smallest sizes and a bimodal nature to the distribution. These features are not modelled. The absence of the small particles in the model will reduce the growth and evaporation rate of ice predicted by the model.

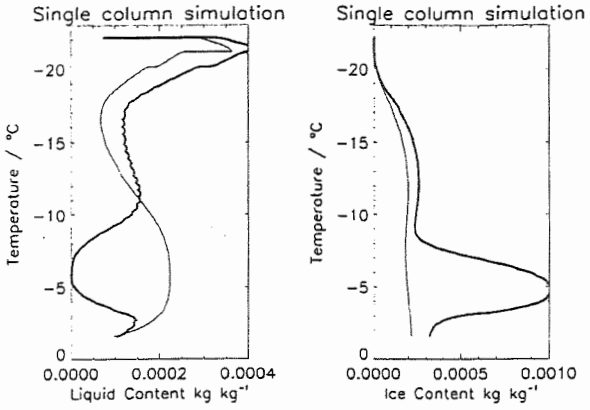

Figure 2. Predictions of a microphysically detailed single column model. Liquid contents (left) and ice contents (right) for a continuous updraft (thin) and a pulsed updraft (thick). (UMIST).

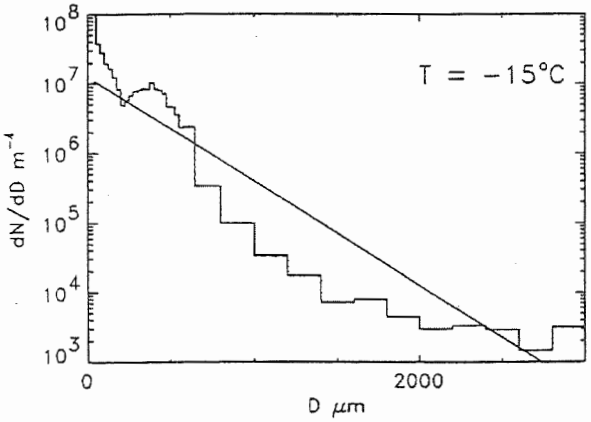

Figure 3. An aircraft measured ice particle size distribution (stepped line) and the equivalent distribution (straight line) which would be inferred by the UM for the same ice water content and temperature.

2.4 Robustness

Many parametrizations are based upon observational datasets. Although this may seem an essential feature of reasonable parametrizations, it often brings problems of robustness.

Usually data is collected for equilibrium conditions, or at least in a mature phase of the cloud. But a model must be able to grow and decay clouds reasonably as well. Often a parametrization of particle size in a microphysical scheme will not adequately deal with these parts of the lifecycle of a cloud, yet they are essential for the correct modelling of a cloud system.

Sometimes parametrizations that look reasonable when compared to observations can fail spectacularly when tried in a model. It is essential that any model parametrization behaves in a sensible way (even if not quantitatively accurate) *whatever the imposed model state and forcing.*

The above reason suggests that parametrizations should not be based around particular cloud types, but should be applicable in all circumstances, unless there is a clear *physical* difference between different regimes. This requirement extends into climate change simulation. If a model parametrization is dependent upon regime then one must be very sure that the same regimes still apply under a climate change scenario. Otherwise a feedback process is missing. For example, it is not allowed that a parametrization should depend on geographical location, since we cannot be sure that particular locations would behave in the same way under climate change.

Similarly, it is desirable for the parametrizations themselves to be based around physical mechanisms, so that feedbacks under climate change can occur.

2.5 Model simulation

The model simulation of the bulk, gridbox mean quantities, such as the liquid water and ice water contents, must be acceptably close to the truth. A numerical weather prediction model can be verified by comparison with surface synoptic observations of temperature and precipitation etc. Model predictions can also be verified by comparison with observations on a case-study basis or by comparisons of modelled and observed climatology. A variety of data sources can be used for such a comparison, including remote sensing by radar, lidar and satellite, or insitu verification using aircraft.

Figure 4 shows Special Sensor Microwave Imager (SSM/I) brightness temperatures and those simulated by a radiative transfer model operating on some UM fields. Discrepancies may be related to inaccuracies in the model predictions, for example whether the model simulates too much or too little liquid water content. However, discrepancies may also be due to shortcomings in the radiative transfer model.

Radar can also provide validation. Figure 5 shows the simulated radar reflectivity from a mesoscale model for the case observed in figure 1. Although the reflectivities within the ice region are broadly similar, the model cannot capture the observed variability. This makes direct comparison of model and observations difficult.

A requirement for coupled ocean-atmosphere climate change modelling is that the radiation budget is balanced. If it is not, the ocean will continually warm or cool in response to the imbalance. It is common practice to `tune' parameters in the model in order that this is the case. Although this is not desirable from a physical point of view, it is unavoidable. Much of the tuning involves clouds, since these have a very large impact on the radiation budget. Often it is the ice fall

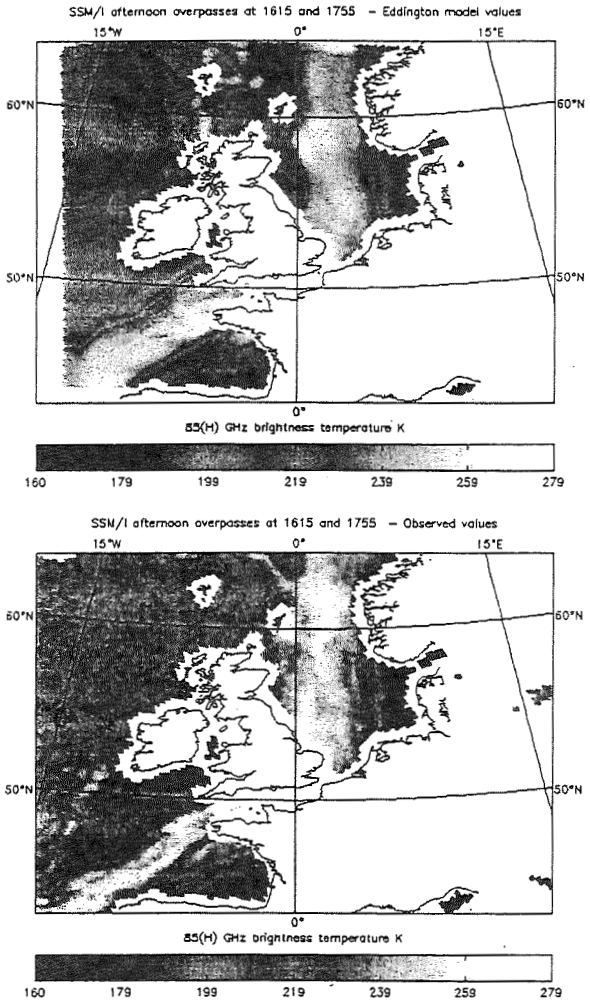

Figure 4. Modelled SSM/I (top) at 85 GHz horizontal polarization and observations (bottom).

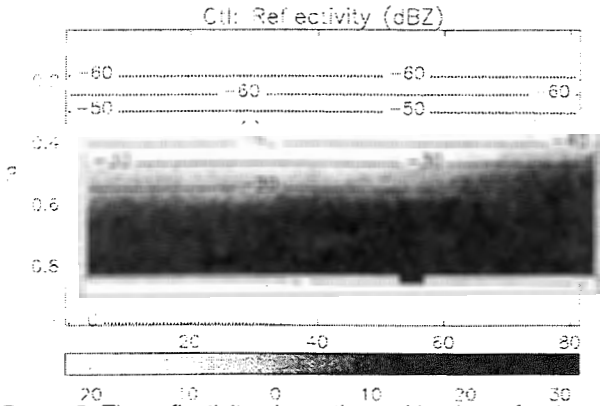

Figure 5. The reflectivity above the melting layer for the same cross-section as figure 1. The dotted lines are temperature in degrees Celsius and the vertical coordinate is pressure divided by surface pressure. The grid spacing of the model is 12 km.

speeds or precipitation generation efficiencies that are adjusted.

3. CRITICAL ASPECTS OF LARGE-SCALE CLOUD AND PRECIPITATION SCHEMES.

There are many critical comparisons which could be performed (if sufficient data is available) between the nature of the model and observations. However, it is worth concentrating on aspects of the parametrization which have a large influence on the model predictions. The basic factors are the ice and liquid water contents, and the fractional area of cloud cover within the model. These have a large effect on the radiation within the model, with corresponding feedbacks on surface and the general circulation.

3.1 Sensitive model parameters

The model parameters which most significantly effect the ice water content are those which give the fall speed of ice. Within the UM, the fall speed is determined by the parametrization of fallspeeds directly and the particle size distribution. The parametrization of the aggregation process has a significant role in determining the ice particle sizes.

The factors that influence the liquid water content are the parametrization of the 'warm rain' collision/coalescence mechanism, and the subgrid-scale model for liquid clouds. The parametrization of the collision/coalescence mechanism is usually extremely crude, whereas the real mechanism has dependencies upon the nature of the cloud condensation nuclei and the time history of the cloud system.

3.2 Surface conditions

Surface conditions are also affected by the nature of the parametrization scheme. Notably, if the scheme is unable to correctly distinguish between liquid and ice cloud then the predicted surface conditions may be incorrect. A particularly bad example is shown in figure 6. This shows the fractional coverage of fog in the model between runs where ice is incorrectly allowed to form from only a small supercooling of water drops (b) and where it does not (a).

3.3 Observational requirements

Critical requirements for observations are therefore to obtain estimates of liquid and ice contents. Measurements (with an error estimate) of ice contents are particularly lacking. Figure 7 shows the wide difference in simulated water paths from the UM using two different large-scale precipitation schemes. These differences are expanded on in Wilson (2000).

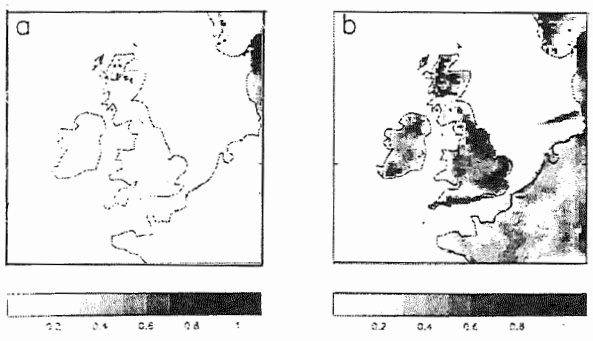

Figure 6. The fractional coverage of fog from a mesoscale model run with: (a) a large-scale precipitation scheme which grows ice using a deposition term; (b) a large-scale precipitation scheme which uses a linear function of temperature to partition condensate between liquid and ice.

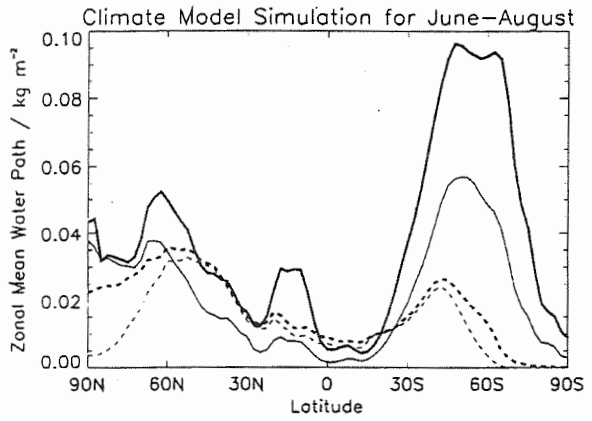

Figure 7. Zonal mean ice water contents (solid) and liquid water contents (dashed) for two different large-scale precipitation schemes (one shown thick, the other thin).

There is also a requirement to carefully investigate the nature of real distributions of physical quantities. Specifically for clouds, these relate to the horizontal distribution and vertical overlap of ice cloud, liquid cloud and precipitation.

4. SUMMARY

This paper has shown that there are several requirements of a large-scale parametrization scheme. The scheme must be fast; it must be robust to all possible situations; it must account for subgrid variability; it must be physically plausible; it must give sensible model predictions. Such a balance takes care to achieve.

Development work should concentrate upon the subgrid-scale problems and key parameters of water contents and ice contents.

To successfully measure ice, water and subgrid-scale quantities, in a way useful to the model and with an appropriate error estimate, is not trivial but is very desirable.

4.1 Acknowledgements

The author thanks Sue Ballard for initial work with the large-scale precipitation scheme, Paul Field and Rob Wood at MRF for the aircraft validation, David Jones for the SSM/I work, Robin Hogan and Anthony Illingworth at the University of Reading for the radar data, John Cardwell and Tom Choularton at UMIST for the detailed single column comparison and Roy Kershaw and David Gregory for general help with the work.

4.2 References

Cullen, M.J.P., 1993: The unified forecast/climate model. Meteorol. Mag., 122, 81-94

Wilson, D. R., and S. P. Ballard, 1999: A microphysically based precipitation scheme for the Meteorological Office Unified Model. Q. J. R. Meteorol. Soc., 125, 1607-1636

Wilson, D.R., 2000: The impact of a physically based microphysical scheme on the climate simulation of the Meteorological Office Unified Model. Accepted by Q.J.R. Meteorol. Soc.

VERIFICATION AND SENSITIVITY EXPERIMENTS FOR THE MIXED-PHASE SCHEME FORECASTS. – PRELIMINARY RESULTS

André Tremblay[1], Paul A. Vaillancourt, Stewart G. Cober and George A. Isaac.

Cloud Physics Research Division, Meteorological Service of Canada, Dorval, Quebec, Canada.

1. INTRODUCTION

Clouds and precipitation are among the most important products of modern numerical weather prediction (NWP) systems. Accurate qualitative precipitation forecasts (QPF) are highly desirable and have important impacts on human activity. In many sectors (aviation, ground transportation, electrical networks, etc.), forecasts of precipitation types (rain, snow or freezing precipitation) have important economical consequences. Precise forecasts of the three-dimensional distribution of clouds and their phases (liquid, ice, supercooled or mixed-phase) are of primary importance for aircraft operations. Unfortunately, since the treatment of cloud microphysics is oversimplified in many operational NWP modeling systems, it is often difficult to fulfill forecasting needs.

The production of realistic clouds and precipitation forecasts with detailed cloud microphysics mesoscale models is a difficult task. Increasing the microphysics complexity implies the specification of a number of adjustable parameters and processes, which requires extensive research and numerical experimentation. Furthermore, a large number of predictive equations and microphysical processes severely increases the computational time and thus limits the use of complex cloud microphysics schemes in operational applications.

The mixed-phase cloud (MXP) scheme proposed by Tremblay et al. (1996) and described in Tremblay and Glazer (2000) was developed with the intention of incorporating more detailed microphysics in NWP mesoscale models. In order to minimize uncertainties and the number of adjustable parameters associated with complex cloud microphysics formulations and to optimize computational efficiency, only the most important microphysical processes relevant to mesoscale systems were included in the scheme. The scheme has only one prognostic variable for the total water content and parameterizes the essential ingredients to allow mixed-phase clouds and freezing precipitation forecasts.

In order to evaluate and potentially improve the MXP scheme, a series of mesoscale simulations is being performed for selected situations taken during the Third Canadian Freezing Drizzle Experiment (CFDE3 –Isaac et al., 1999). For these cases, aircraft measurements of various microphysics parameters are available and can be used to evaluate the quality of forecasts produced by the MXP scheme.

To obtain meaningful comparisons between model results and aircraft measurements, numerical experiments were performed with the Canadian Mesoscale Compressible Community model (MC2 – Benoit *et al.*, 1997) using a nesting strategy (Fig. 1). Some comparisons and verifications will be discussed for a selected case (15 Jan 1998 from CFDE III). In this paper, only the low resolution (35km) run is briefly presented. Results of high-resolution runs (10 and 3 km) will be discussed at the conference.

2. SIMULATED CFDE III CASE: 15 JAN 98

The GOES8 visible image displayed in Fig. 1a is valid Jan 15 1700 UTC and outlines the meteorological situation near the beginning of the flight. A major synoptic system was centered near the north shore of the Gulf of Mexico with a trough extending to the Great Lakes. A weaker low-pressure system was located over the Canadian prairies. There was an extensive cloud shield associated with these systems and an important portion of the continental U.S. and Canada was covered with clouds. An examination of the associated infrared image (not shown) has revealed high level clouds (cloud top temperature CTT ≈ -50°C) near the two low-pressure systems. Over the Great Lakes region, where the flight was conducted, the clouds were confined to lower levels (CTT ≈ -10°C to -20°C). An 18h forecast of the vertically integrated supercooled liquid water content (SLWC) is depicted in Fig. 1b. A comparison with Fig. 1a shows that the SLWC signal is well correlated with the observed clouds suggesting the horizontal extent of clouds was correctly forecasted. The maximum value of the integrated SLWC is around 0.2 mm which is small compared to liquid water paths typically inferred in extratropical cyclones. In the present simulation, the liquid water path peaks around 1 mm, suggesting that the SLW signal is weak.

[1] Andre Tremblay, Meteorological Service of Canada, Dorval, Quebec,H9P 1J3, Canada;
e-mail: andre.tremblay@ec.gc.ca

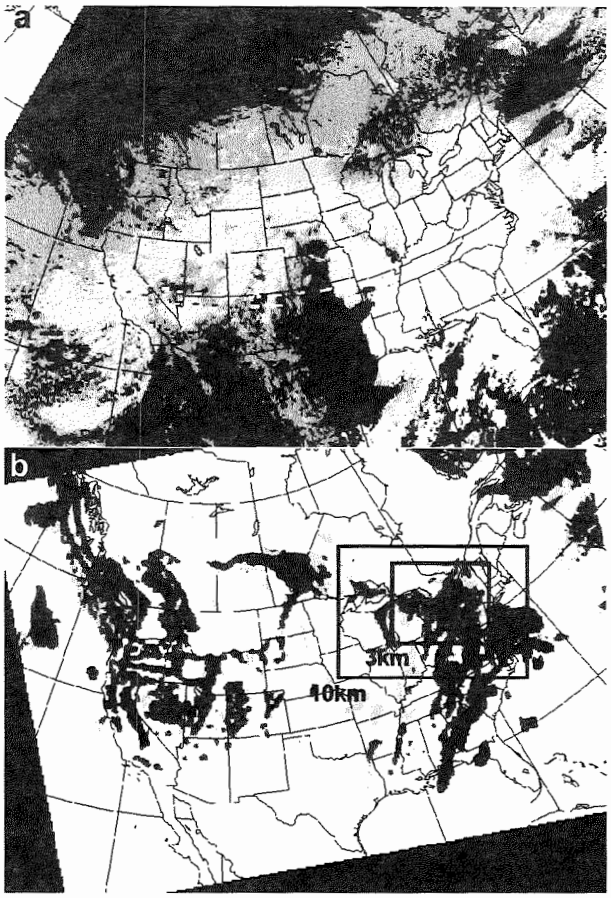

Fig. 1: a) GOES 8 visible image 15 Jan 98 17 UTC. b) A forecast of vertically integrated SLW valid 15 Jan 98 18 UTC (gray shading: .001, .01, .1 and .2 mm) . Outlines of high resolution runs are included.

Aircraft measurements of LWC, IWC are potentially important to evaluate model microphysics. Fig. 2 shows the microphysical structure of the clouds in the region sampled by the aircraft. The map shows a horizontal projection of the aircraft trajectory on which the measured cloud phase is superimposed. It is seen that in the sampled clouds, mixed and supercooled phases were much more abundant than the ice phase. In particular, in the region included between points B and D, a supercooled freezing drizzle cloud was present at low levels over Lake Erie as seen from the aircraft altitude time series.

Fig. 3 shows a vertical cross-section through the center of Lake Erie at 2100 UTC. At that time the aircraft was located somewhere between points C and D and the highest and lowest altitude along the CD leg were used to construct the box displayed in Fig.3. In this region, the model has forecasted a weak zone of SLW and maximum values of SLWC are just above 0.1 g/kg. The model cloud was mixed and the proportion of ice within the box varied from 0.5 to 0.7 for temperatures colder than the freezing point. The vertical extent of SLWC and IWC are coincident and it can be seen from

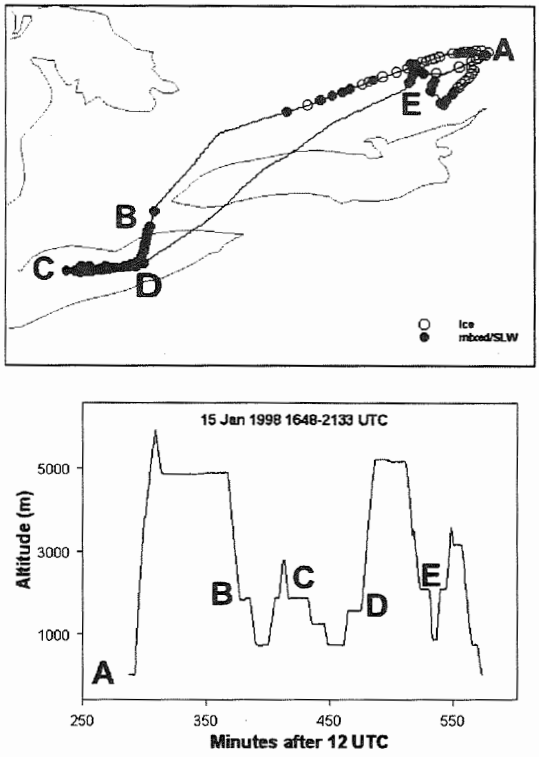

Fig. 2: A map showing cloud phases (SLW and ice black and white circles respectively) measured by the Convair-580 research aircraft on Jan 15 1998 (flight 11, Canadian Freezing Drizzle Experiment III). A plot of altitude vs time for this flight is also displayed.

Fig. 3 that model CTT is between -8°C and -12°C which is in reasonable agreement with satellite observations at this time and location. It should be noted that the model tends to develop a warm layer near the melting point within the sampled box. Such warm temperatures are

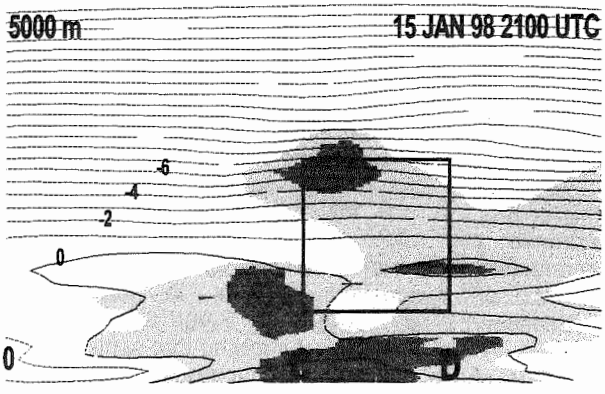

Fig. 3: A cross-section of model temperature and LWC (contoured at .005, .01 and .1 g/kg) passing through the center of Lake Erie. The box indicates the area of the aircraft corresponding to the CD leg.

however not detected by the aircraft (Fig. 4 – see Vaillancourt *et al.*, 2000 for details on the construction of model series). The time series depicted in Fig. 4 indicate

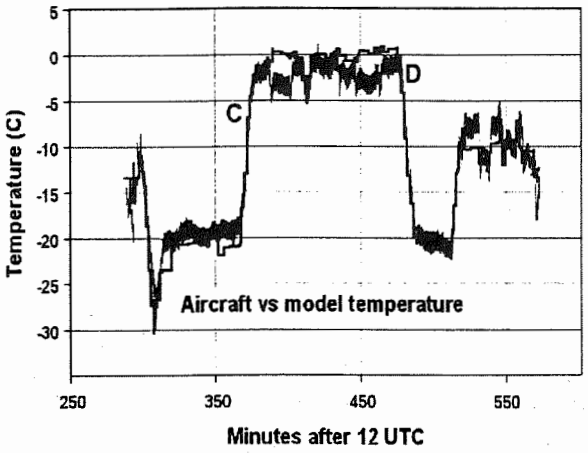

Fig. 4 Time series of aircraft and model temperature. The absolute error (±1C) of temperature measurement is indicated.

that the model is systematically too warm at low levels. According to aircraft measurements, the temperature at these levels remains within the 0°C to -5°C range and the model curve has clearly a warm bias greater than the instrument error range. Thus, in several occasions a warm cloud (T > 0°C) forecast is issued where a cold cloud (T < 0°C) is observed. Since the physics of mixed-phase clouds and warm rain processes are totally different, this certainly points to problems in the model physics that must be addressed for meaningful numerical experimentation. It should be noted that these problems are not necessarily related to the cloud microphysics and other aspect in the physics of the atmospheric model should be investigated as well.

Times series of aircraft and model LWC and IWC are given in Fig. 5 and 6. In these figures, the IWC has been multiplied by –1 to facilitate visualization. These figures demonstrate that the high amplitude SLW signal detected by the aircraft is not well reproduced by the model. There are many possible reasons for this behavior, in particular one should note the coarse resolution used for this simulation. High-resolution runs (10 km and 3 km – not shown) tend to produce higher liquid water content and the comparison with observation is improved. There are also a number of microphysics issues that should be considered. For example the MXP scheme uses a Kessler-type parameterization of the warm rain process that limits the growth of suspended droplets in the domain (Vaillancourt *et al.*, 2000). Figs. 5 and 6 also suggest that the IWC is overforecast implying that some aspects of mixed-phase microphysical processes built into the MXP scheme should be examined.

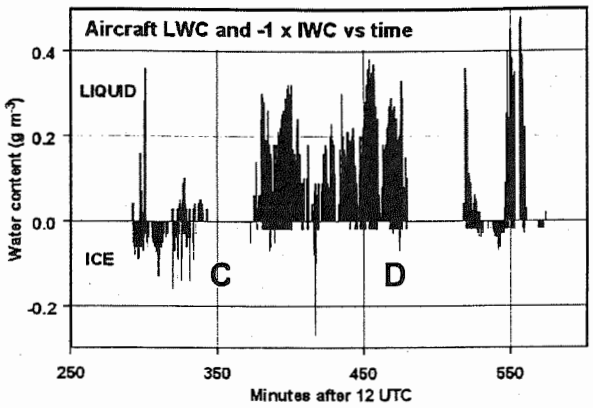

Fig. 5: Time series of aircraft measurements of LWC and IWC.

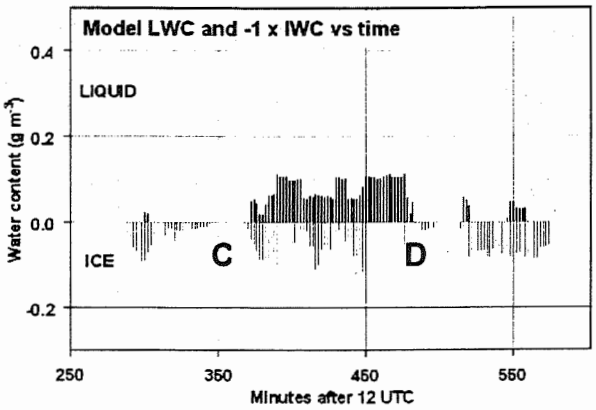

Fig. 6: As in Fig. 5 but for model.

3. SUMMARY

A series of high resolution numerical experiments is under construction with the objective of validating and improving SLW forecasts from a detailed comparison with aircraft observations taken during the Canadian Freezing Drizzle Experiment. The target cloud scheme is the mixed-phase scheme (Tremblay *et al.*, 1996) that will be implemented in the next version of the Canadian Forecast System. The MXP scheme has been verified against surface observations (Tremblay and Glazer, 2000) and compared to more detailed cloud microphysical schemes (Glazer and Tremblay, 2000).

4. ACKNOWLEGMENTS

The authors would like to acknowledge the financial support of the National Search and Rescue Secretariat, Transport Canada, and Boeing. Measurements were made by the technical and scientific staff of MSC and the National Research Council of Canada (NRCC) using the NRCC Convair-580 research aircraft.

5. REFERENCES

Benoit R., M. Desgagne, P. Pellerin, S. Pellerin, Y. Chartier and S. Desjardins, 1997: The Canadian MC2: A semi-lagrangian, semi-implicit wideband atmospheric model suited for finescale process studies and simulation. *Mon. Wea. Rev.*, **125**, 2382-2415.

Glazer A., and A. Tremblay, 2000: Intercomparison of different cloud microphysics schemes in forecasts of winter storms. *Proceedings of the 13th International Conference on Clouds and Precipitation*, Reno, Nevada.

Isaac, G.A., S.G. Cober, A.V. Korolev, J.W. Strapp, A. Tremblay, and D.L.Marcotte, 1999: Canadian Freezing Drizzle Experiment. *37th Aerospace Sci. Meeting, Reno Nevada,* 11-14 January 1999.

Tremblay A., A. Glazer, W. Yu and R. Benoit, 1996: A mixed-phase cloud scheme based on a single prognostic equation. *Tellus*, **48A**, 483-500.

Tremblay A. and A. Glazer, 2000: An improved modeling scheme for freezing precipitation. *Mon. Wea. Rev.*, **128**, 1289-1308.

Vaillancourt P., Tremblay A., Cober S.G. and G.A. Isaac, 2000: Evaluation of a mixed-phase cloud scheme's ability at forecasting supercooled liquid water in clouds. *Proceedings of the 13th International Conference on Clouds and Precipitation*, Reno, Nevada.

A new approach to parameterization of cloud physics processes

Yefim L. Kogan and Alexei A. Belochitski

Cooperative Institute for Mesoscale Meteorological Studies, University of Oklahoma, Norman OK

1. Introduction[1]

The conventional cloud physics parameterizations (Kessler, 1969) divide the total liquid water into cloud water (transported with an airflow) and rain water (having its own fall speed). The division is artificial, as observational, as well as modeling data do not show a distinctive gap between small and large drops (cloud and rainwater). As a result the autoconversion and accretion rates are quite sensitive to the value of the threshold radius dividing cloud and rain water. The severity of the errors depends on cloud type, however, the problem is better posed when the artificial division of total water into two parts is avoided altogether (Kogan 1998).

We describe a parameterization of cloud physics processes based on the full moments of the drop size distribution (DSD) function, as opposed to partial moments used in Kessler-type parameterizations. As shown below, the new parameterization is more accurate and, most importantly, easier to generalize for all cloud types.

The parameterization is based on the following set of total moments of the DSD representing, correspondingly: M_0 – cloud drop concentration N, M_2 – cloud drop geometrical cross-section S, M_3 – cloud liquid water content Q, M_4 – drizzle sedimentation flux P, and M_6 – radar reflectivity Z. The ratio of M_3 to M_2 is related to the drop effective radius, an important parameter needed for radiative transfer calculations.

The time derivatives showing the rate of change of each moment due to various microphysical processes are calculated from the explicit microphysical model. The CIMMS Large Eddy Simulation (LES) explicit microphysics model used in the study predicts both CCN and cloud drop distribution functions (DSD). We simulated a marine drizzling cloud layer observed during the ASTEX field experiment on June 12, 1992. The stratus cloud evolved in a clean air mass. During the six hour long simulation drizzle was gradually increasing, resulting in a breakup of the solid cloud deck and transforming it by the end of simulation into a field of small Cu with cloud cover of about 60%. We, therefore, divided the whole simulation into two periods: the first one representing moderate drizzle (drizzle rates at the surface of 0.2 mm/day) and the second representing heavy drizzle (drizzle rates at the surface of 1.0 mm/day). We note that model results have been tested against and found in good agreement with integrated observations of microphysical, radiative, and turbulence parameters (Khairoutdinov and Kogan 1999).

[1] *Corresponding author address:* Dr. Yefim L. Kogan, Cooperative Institute for Mesoscale Meteorological Studies, University of Oklahoma, 100 E. Boyd, Norman, OK 73019. E-mail: ykogan@ou.edu

The role of the explicit model is two-fold: first, it serves as a source of the 3D distributions of drop spectra needed for calculation of exact process rates; second, it is used as a test-bed for comparison of derived bulk parameterized expressions with a benchmark explicit formulation.

2. Parameterization of the coagulation process

The coagulation process in the new parameterization replaces artificial processes of autoconversion and accretion. The rate of change for each moment due to coagulation is determined using regression analysis of the exact coagulation rates. The parameterized coagulation rates are sought as functions of the moments N, S, P, and Z.

Figure 1 presents scatter plots that compare the parameterized and exact rates for the heavy drizzle regime. In order to save space, the moments are normalized by arbitrary constants in order to allow two different moments be shown on the same plot. The errors of parameterized expressions are 8-10% for moderate drizzle case (not shown), while slightly higher for the heavy drizzle case (10-16%). Note that these errors are an order of magnitude less than, e.g., autoconversion rates errors in a conventional Kessler type parameterization.

3. Parameterization of the condensation process

The drop condensational growth equation can be written in a simplified, but sufficiently accurate for bulk parameterization form

$$\frac{\partial r}{\partial t} = SG / r$$

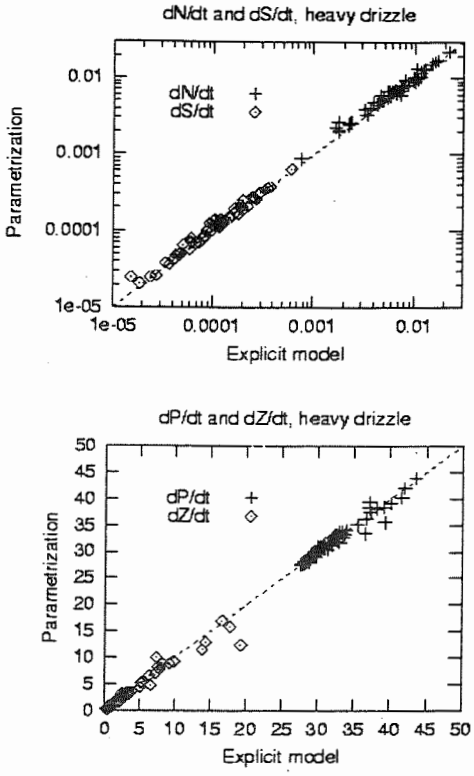

Figure 1. The scatter plots of the parameterized coagulation rates for moments N, S, P, and Q versus the benchmark explicit model values.

Here S is supersaturation, and G is a function of temperature and pressure (see, e.g., Rogers and Yau 1991). The condensation-evaporation rate is

$$\left(\frac{\partial M_i}{\partial t}\right)_{cond/evap} = iSGM_{i-2}$$

Note that $\left(\frac{\partial N}{\partial t}\right)_{cond/evap} = 0$ and that $\left(\frac{\partial Q}{\partial t}\right)_{cond/evap}$ is proportional to the first moment, i.e., the total mean radius. Using regression analysis, the latter can be parameterized quite accurately as a function of moments N, S, and Q. For instance, for the heavy drizzle case the parameterized expression $M_1 = M_0^{0.42} M_2^{0.82} M_3^{-0.21}$ has an error of only 4.3%.

4. Parameterization of the sedimentation process

The parameterized expressions for fall velocities V_i corresponding to the moment M_i are presented in Tables 1 and 2.

Table 1. Parameterized fall velocities for the moderate drizzle case

V_i	Fall velocity for moment M_i	ε, %
V_2	$4581.0\ S^{-0.88}\ P^{0.74} + 24289.0\ S^{-2}Q^{1.78}$	6.7
V_3	$6278.0\ Q^{-1.72}\ P^{1.54}$	9.8
V_4	$6182.0\ P^{-0.80}\ Z^{0.71}$	10.4
V_6	$3245.0\ Q^{0.5}\ P^{-0.9}\ Z^{0.48}$	8.6

Table 2. Parameterized fall velocities for the heavy drizzle case

V_i	Fall velocity for moment M_i	ε, %
V_2	$7292.0\ S^{-1.71}Q^{1.48}$	9.5
V_3	$9193.0\ Q^{-1.55}\ P^{1.43}$	7.3
V_4	$19334.0\ P^{-0.67}\ Z^{0.65}$	10.6
V_6	$5590.0\ Q^{0.41}\ P^{-0.92}\ Z^{0.56}$	7.6

The fall velocity for the zero-th moment, N, is of the order of 1-2 cm/s and can be safely neglected. An example of the scatter plot of the parameterized fall velocities for the heavy drizzle case versus benchmark values from the explicit model is shown in Fig. 2. The fall velocities are parameterized within the 10% error.

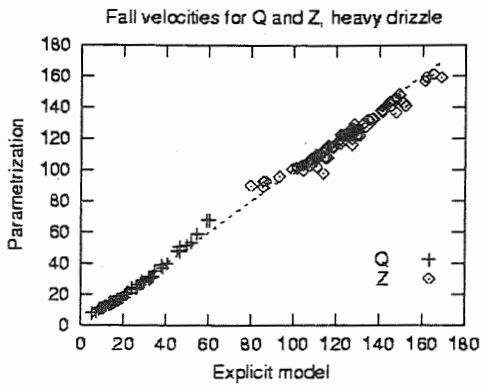

Figure 2. The scatter plots of the parameterized fall velocities for the 3rd and 6th moments Q and Z versus the exact values from the explicit model.

5. Conclusions

The CIMMS explicit microphysics model was used to provide a data set of drop spectra characteristic for drizzling stratocumulus clouds. We simulated a marine boundary layer cloud observed during the ASTEX field experiment on June 12, 1992. The stratus cloud evolved in a clean air mass and was categorized by two drizzle regimes: the first one of moderate drizzle (drizzle rate at the surface of 0.2 mm/day) and the second of heavy drizzle (drizzle rate of 1.0 mm/day).

The drop spectra provided by the LES model were used as input to various explicit microphysical modules in order to calculate the parameterized expressions for coagulation rates and fall velocities for the following integral moments of the spectra: : M_0 – cloud drop concentration N, M_2 – cloud drop geometrical cross-section S, M_3 – cloud liquid water content Q, M_4 – drizzle sedimentation flux P, and M_6 – radar reflectivity Z. The derived parameterizations approximate the exact rates and fall velocities within the 10-15% error which is significantly better than the corresponding

errors for the Kessler-type parameterizations. The work is currently underway to include the parameterizations into the LES dynamical framework. The resulting bulk microphysical version of the LES model will be compared with the benchmark solution provided by the explicit model. The comparison results will be presented at the 13th ICCP conference.

Acknowledgments. This research was supported by the ONR Grants N00014-96-1-0687 and N00014-96-1-1112 and by the Environmental Sciences Division of U.S. Department of Energy (through Battelle PNR Contract 144880-A-Q1 to the Cooperative Institute for Mesoscale Meteorological Studies) as part of the Atmospheric Radiation Measurement Program.

References

Kessler, E., 1969: On the distribution and continuity of water substance in atmospheric circulations. *Meteor. Monogr.*, 10, No. 32, Amer. Meteor. Soc., 84 pp.

Khairoutdinov, M. F. and Y. L. Kogan, 1999: A Large Eddy Simulation Model with Explicit Microphysics: Validation Against Aircraft Observations of a Stratocumulus-Topped Boundary Layer. *J. Atmos. Sci.*, **56**, 2115-2131

Kogan, Y.L., 1998: Parameterization of cloud physics processes in mesoscale models of stratocumulus cloud layers. Preprints, *AMS Conference on Cloud Physics,* 17-21 August 1998, Everett, WA.

Rogers, R.R. and M. K. Yau, 1989*: A Short Course in Cloud Physics*, Third edition, Pergamon Press.

A GCM PARAMETERIZATION OF BIMODAL SIZE SPECTRA FOR MID-LATITUDE CIRRUS CLOUDS

Dorothea Ivanova[1], David L. Mitchell[1], W. Patrick Arnott[1] and Michael Poellot[2]

[1]Division of Atmospheric Sciences, Desert Research Institute, Reno, Nevada, 89512, U.S.A.
[2]Dept. of Atmospheric Science, Univ. of North Dakota, Grand Forks, ND, 58202, U.S.A.

1. INTRODUCTION

The solar radiative properties of ice clouds are primarily a function of the ice water content (IWC) and the effective diameter (Mitchell et al. 1998; Wyser and Yang 1998), defined as

$$D_{eff} = IWC / (\rho_i P_t) , \qquad (1)$$

where ρ_i = bulk ice density corresponding to refractive index measurements (0.92 g/m^3) and P_t = projected area of size distribution, SD. However, D_{eff} cannot be determined from the SD alone, but also depends on ice crystal shape and associated mass and area properties (Mitchell et al. 1998).

To date, the representation of D_{eff} for the ice phase in GCMs has been highly uncertain, and is sometimes treated as constant or nearly constant. The aim of this work is to provide a means of estimating SDs and D_{eff} for mid-latitude cirrus clouds, the latter estimated with some informed assumption about ice particle shape. We parameterize SDs as bimodal, with both the small and large particle modes expressed as a gamma distribution having the form

$$N(D) = N_o D^{\nu} \exp(-\lambda D) , \qquad (2)$$

where D is maximum dimension, while the SD parameters are estimated as a function of temperature and IWC.

2. SMALL ICE CRYSTALS AND THE FSSP

The role of small ice crystals in cirrus continues to be uncertain, although new evidence shown here indicates the Forward Scattering Spectrometer Probe, or FSSP, may, given some criteria, at least approximately measure the small ice crystal mode for D < 50 μm. In a cloud chamber at DRI, ice crystals were sampled by the DRI Cloudscope (CS), where ice crystals were aspirated and impacted onto a lens 1 mm wide, having a high collection efficiency for D > 10 μm (Schmitt and Arnott 1999). Simultaneously, the same ice cloud was sampled by the FSSP, where sizing is based on the forward scattering lobe, primarily due to diffraction which is determined by a particle's area cross-section. The FSSP uses Mie theory for spheres to describe this forward lobe, and it is unclear to what degree it may be distorted by nonsphericity. The mean SD from 11 samples is shown in Fig. 1 for each probe, where all crystals were hexagonal columns, and D = maximum dimension regarding the CS. The probe measured optical depth over a 2 m path was 0.04, corresponding to a number concentration of about 60 cm^{-3} (exceeding FSSP concentrations in natural cirrus). Errors due to distortion of the forward scattering lobe through nonspherical effects appear marginal, since FSSP and CS spectra are in relatively good agreement. Similar good agreement was found when hexagonal plates were sampled.

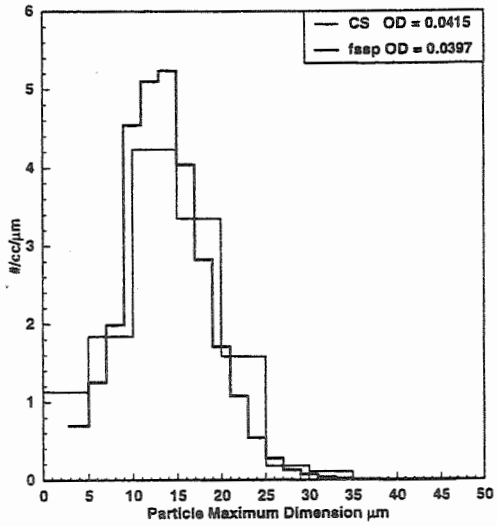

Fig. 1. Comparison of size spectra measured by the Cloudscope and FSSP for hexagonal columns in a laboratory grown ice cloud.

Point of contact: Dorothea Ivanova, Desert Research Institute, 2215 Raggio Parkway, Reno, NV 89512-1095; E-mail: dorothea@dri.edu Phone:775-674-7171

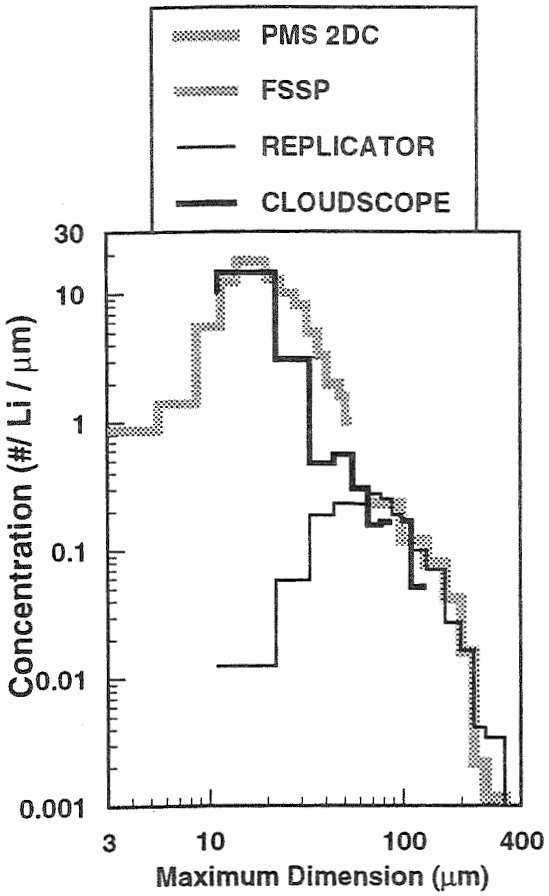

Fig. 2. Size spectra from 26 September 1997, DOE-ARM IOP, Hurricane Nora outflow,19:09:15 - 19:11:00 UTC, -48.3 C to -50.3 C, 11.95 km to 12.18 km, T.A.S. = 118.5 m/s.

The two probes were also compared when collocated on the Citation aircraft during and an ARM IOP, sampling cirrus blowoff from Hurricane Nora. Size spectra are shown in Fig. 2, where the CS, FSSP, DRI replicator, and 2DC probes are intercompared. The CS and 2DC clearly indicate bimodal spectra, with the FSSP in fair agreement with the CS, especially at the peak concentration near 15 μm. The replicator collection efficiency apparently falls off rapidly for D < 50 μm. In Gardinar and Hallett (1985), the FSSP and replicator were intercompared, with concentration differences reported up to a factor of 300. Since the replicator collection efficiency appears to decay rapidly for D < 50 μm, about the largest size the FSSP measures, it is not surprising that concentration differences between these two instruments can be quite large. For more details on intercomparisons between the CS, FSSP, replicator and 2DC, the reader is encouraged to read the paper by Arnott et al., this preprint volume.

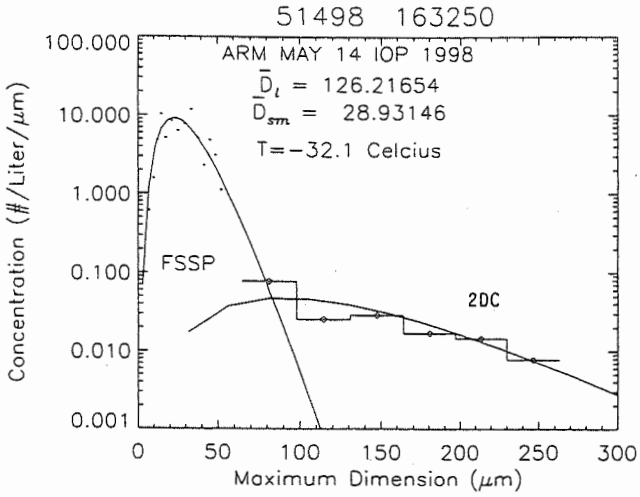

Fig. 3. Example of FSSP and 2DC size spectra, their parameterized gamma fits, and how FSSP data was extrapolated to larger sizes via its gamma fit to test for continuity with 2DC spectra.

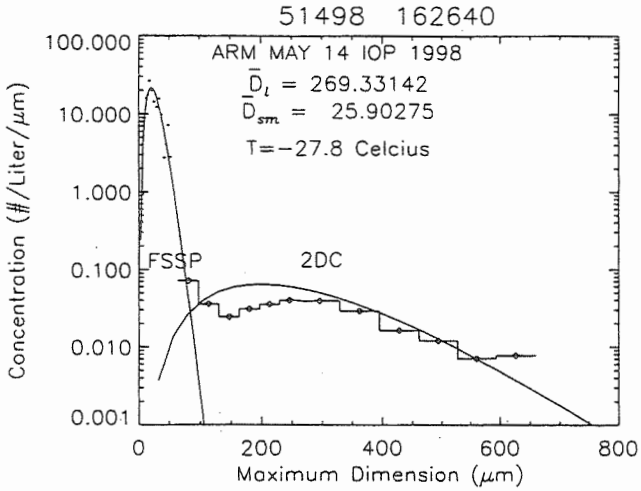

Fig. 4. As in Fig. 3, but for a different size distribution.

Twohy et al. (1997) found that IWCs measured by the CVI and FSSP in wave clouds were in good agreement. Also, the FSSP and 2DC were intercompared by Gayet et al. (1996), who found good agreement in the overlap region near 50 μm when SD were narrow (i.e. contrail cirrus where D ≤ 100 μm). In natural cirrus with broader SDs, measured SDs from the two probes were discontinuous in their overlap region, and these authors recommended using overlap criteria as a means of accepting or rejecting SDs from the FSSP. This policy was adopted in this study to the extent possible. An exact overlap was not obtainable since the maximum size bin of the FSSP was 52.4 μm, while the smallest reliable

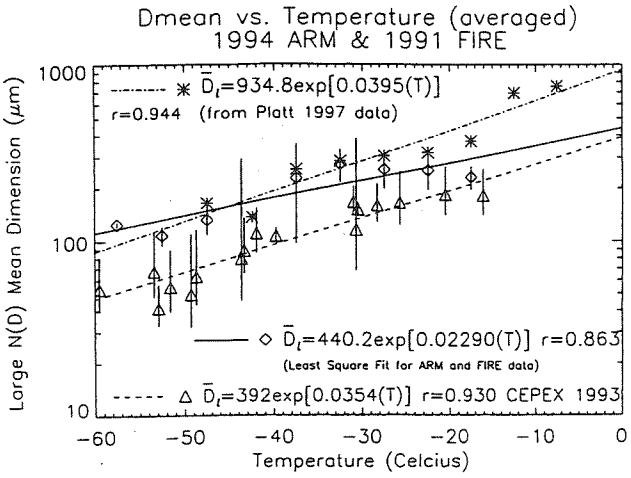

Fig. 5. Mean dimension measured by the 2DC vs. sampling temperature for this study (ARM & FIRE data), mid-latitude cirrus from Platt (1997), and tropical anvil cirrus (CEPEX). Vertical bars are standard deviations.

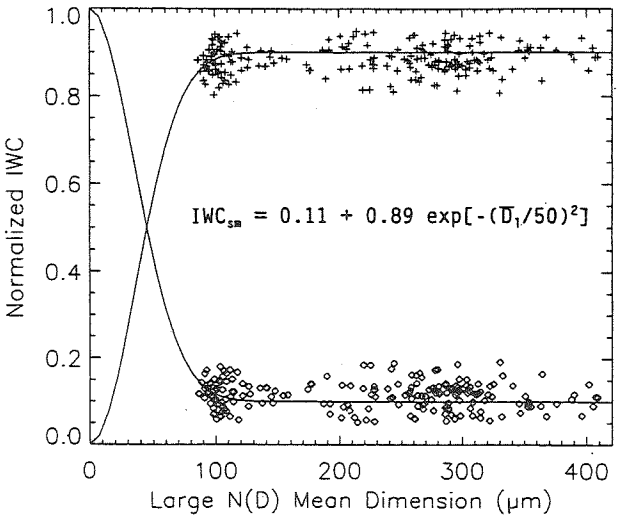

Fig. 6. Normalized IWC calculated from the FSSP (◇) and 2DC (+), related to $\bar{D}_l$. The IWC partitioning between the large and small SD modes is described by the equation.

2DC bin was centered on 81.5 μm. To estimate concentrations between these two sizes, the FSSP SD was parameterized as described in Mitchell (1991), using (2):

$$\nu = [(\beta + 0.67)\bar{D} - D_m]/(D_m - \bar{D}) , \quad (3)$$

$$\lambda = (\nu + 1)/\bar{D} , \quad (4)$$

$$N_o = IWC\ \lambda^{\beta+\nu+1}/\alpha\Gamma(\beta+\nu+1) , \quad (5)$$

where β refers to the ice particle mass-dimension power law $m = \alpha D^\beta$, $\bar{D}$ is the SD mean D, and D_m is the SD median mass dimension. The choice of m-D relation does not matter so long as one is consistent, and IWC, $\bar{D}$ and D_m were determined from the measured SD. The criteria used for accepting FSSP data was that the parameterized FSSP SD had to intersect the measured 2DC SD in either the 1st or 2nd usable bin (centered at 81.5 or 114.5 μm). Examples are shown in Fig. 3 and 4. Since this parameterization scheme conserves IWC, $\bar{D}$ and D_m , the extrapolation to D = 81.5 μm appears reasonable.

3. PARAMETERIZATION FOR MID-LATITUDE CIRRUS

This parameterization is based on flights during intensive observation periods (IOP) over the Southern Great Plains ARM CART site as well as some flights during FIRE II, totaling 17 flights between 1994 and 1998. SDs measured were based on a 10 s sampling interval where true air speeds (T.A.S.) were about 120 m s^{-1}. After screening each SD using the above criteria, 996 SDs were used in this parameterization. However, since this is work in progress, the relationship between $\bar{D}$ and cloud temperature T, shown below, is based on only 357 SDs. The method for obtaining gamma distribution parameters for the small mode, measured by the FSSP, has already been described. The same method was used to obtain these parameters from the large mode, measured by the 2DC probe. Since this approach conserves IWC, $\bar{D}$ and D_m, the SD area and mass, which radiative properties are based on, are accurately represented by the parameterized SD.

The parameterization was derived as follows. First, the measured $\bar{D}$ of the large mode, $\bar{D}_l$, was correlated with T as shown in Fig. 5, resulting in the correlation

$$\bar{D}_l = 440.2\ \exp(0.02290\ T) , \quad (6)$$

where T and $\bar{D}_l$ are in Celsius and μm. Over the range of T in this work, our data agree well with the $\bar{D}_l$ -T relation described in Platt (1997) for mid-latitude cirrus, also shown. For comparison, the $\bar{D}_l$ -T relation for the three CEPEX tropical anvil cases described in McFarquhar and Heymsfield (1996) is also shown (D > 100 μm).

Next, the measured $\bar{D}_l$ was related to the IWC of the parameterized FSSP and 2DC SDs, assuming planar polycrystals. These IWCs for the small and large modes were normalized by their sum, the total IWC. These normalized IWCs are plotted against $\bar{D}_l$ in Fig. 6, with "+" indicating the large mode and "◇" indicating the

small mode. It is seen that the normalized small mode IWC, IWC_{sm}, is described fairly well by the expression:

$$IWC_{sm} = 0.11 + 0.89 \exp(-(\overline{D}_l/50)^2), \qquad (7)$$

where $\overline{D}_l$ is in microns. The normalized large mode IWC, IWC_{lg}, is simply 1 - IWC_{sm}. Since these IWCs are normalized, they do not depend on initial assumptions of crystal shape used to derive them. The true IWC for each mode is given by multiplying each normalized IWC by the total IWC.

Given cloud temperature T and total IWC, we now have expressions for $\overline{D}_l$, IWC_{sm}, and IWC_{lg}. For closure, we still need expressions for $\overline{D}_{sm}$, ν_{sm} and ν_{lg}. Most fortuitously, the standard deviations associated with the mean values of these quantities are sufficiently small to regard them as constant: $\overline{D}_{sm} = 27.4 \pm 2.9$ μm, $\nu_{sm} = 3.24 \pm 1.41$ μm, $\nu_{lg} = 2.64 \pm 1.65$ μm. Based on the first few bins of the 2DC, Mitchell et al. (1996a) also found $\overline{D}_{sm}$ was constant. To calculate λ and N_o for each mode, (4) and (5) may be used for a given ice crystal shape (which effects only N_o).

Equations (6) and (7) and the findings above provide closure for estimating bimodal size spectra as a function of total IWC and temperature. Moreover, D_{eff} can be determined from (1) by noting $P_t = P_{sm} + P_l$, and that

$$P_x = \frac{\sigma_x \Gamma(\delta_x + \nu + 1)}{\alpha_x \Gamma(\beta_x + \nu + 1)} IWC_x \lambda_x^{\beta_x - \delta_x}, \qquad (8)$$

where x refers to either the "l" or "sm" subscript, Γ denotes the gamma function, and σ and δ refer to the projected area of an ice crystal, given as

$$P = \sigma D^{\delta}. \qquad (9)$$

Values of σ, δ, α and β for different crystal shapes corresponding to $N(D)_{sm}$ and $N(D)_l$ are given in Mitchell (1996) and Mitchell et al. (1996b).

Acknowledgments: This research was funded entirely by the DOE-ARM program, which is gratefully thanked for its support.

References

Gardiner, B.A., and J. Hallett, 1985: Degradation of in-cloud forward scattering spectrometer probe measurements in the presence of ice crystals. *J. Atmos. Ocean. Tech.*, **2**, 171-180.

Gayet, J.-F., G. Febvre, and H. Larsen, 1996: The reliability of the PMS FSSP in the presence of small ice crystals. *J. Atmos. Ocean. Tech.*, **13**, 1300-1310.

McFarquhar, G.M., and A.J. Heymsfield, 1996: Microphysical characteristics of three anvils sampled during the Central Equatorial Pacific Experiement. *J. Atmos. Sci.*, **53**, 2401-2423.

Mitchell, D.L., 1991: Evolution of snow-size spectra in cyclonic storms. Part II: Deviations from the exponential form. *J. Atmos. Sci.*, **48**, 1885-1899.

Mitchell, D.L., 1996: Use of mass- and area-dimensional power laws for determining precipitation particle terminal velocities. *J. Atmos. Sci.*, **53**, 1710-1723.

Mitchell, D.L., S.K. Chai, Y. Liu, A.J. Heymsfield, and Y. Dong, 1996a: Modeling cirrus clouds. Part I: Treatment of bimodal size spectra and case study analysis. *J. Atmos. Sci.*, **53**, 2967-2988.

Mitchell, D.L., A. Macke and Y. Liu, 1996b: Modeling cirrus clouds. Part II: Treatment of radiative properties. *J. Atmos. Sci.*, **53**, 2967-2988.

Mitchell, D.L., J.M. Edwards and P.N. Francis, 1998: GCM sensitivity of globally averaged albedo and OLR to ice crystal shape. ARM Science Meeting, San Antonio, Texas, 3-7 March 1997.

Platt, C.M.R., 1997: A parameterization of the visible extinction coefficient of ice clouds in terms of the ice/water content. *J. Atmos. Sci.*, **54**, 2083-2098.

Schmitt, C.G., and W.P. Arnott, 1999: Infrared emission (500-2000 1/cm) of laboratory ice clouds. *J. Quantitative Spectroscopy and Radiative Transfer*, **63**, 701-725.

Twohy, C.H., A.J. Schanot, and W.A. Cooper, 1997: Measurement of condensed water content in liquid and ice clouds using an airborne Counterflow Virtual Impactor. *J. Atmos. Ocean. Tech.*, **14**, 197-202.

Wyser, K., and P. Yang, 1998: Average ice crystal size and bulk short-wave single-scattering properties of cirrus clouds. *Atmos. Res.*, **49**, 315-335.

ASSESSING THE RELATIONSHIP BETWEEN ICE CRYSTAL EFFECTIVE SIZE AND TEMPERATURE

Gultepe, I., G. A. Isaac, and S. G. Cober
Cloud Physics Research Division
Meteorological Service of Canada, Toronto, Ontario

1. INTRODUCTION

The purpose of this study is to analyze ice crystal effective size (D_{eff}) versus temperature (T) for Arctic clouds. Observations collected during the First International Regional Experiment (ISCCP) Arctic Cloud Experiment (FIRE.ACE) are used in the analysis. FIRE.ACE flights were conducted over the Arctic Ocean during April of 1998. A detailed study of particle effective size versus T can be found in Wyser (1998). Using observations from the study of Heymsfield and Platt (1984), D_{eff} versus T relationship for cirrus clouds for T between -20 and -60°C has been obtained by Ou and Liou (1995). While the Ou and Liou relationship was obtained for cirrus clouds, it has been used beyond its suggested T interval and cloud type (Lohmann et al. 2000).

Number concentration of ice crystals (N_i) is an important parameter when used in effective radius calculations (Gultepe et al. 2000). Particle shape is also important in the effective radius calculations (Gultepe et al. 1998; Korolev et al. 2000). Korolev et al. (2000) showed that the majority of ice crystals have an irregular shape, while only a small fraction appears pristine. Gultepe et al. (2000) suggested that because of large unknowns in N_i versus T parameterizations, the effective radius calculations in the earlier studies may have significant error.

2. OBSERVATIONS

Observations in the present study represent T between 0 and -50°C. Ice crystal number concentrations are obtained using measurements from a 2D-C mono probe. Glaciated regions are identified using a similar technique to that discussed in Gultepe et al. (2000). In order to represent horizontal variability within the observed clouds, only observations collected at constant-altitude flight legs are used in the analysis. Uncertainties related to 2D-C probe analysis can be found in Gultepe et al. (2000). In the present study, particle maximum dimensions (L) greater than 100 μm are used in the calculations.

3. METHOD

3.1. D_{eff} versus T from earlier studies

Using columnar particle shape, Ou and Liou (1995) suggested a D_{eff}-T relationship for cirrus clouds as

$$D_{eff} = \sum_{n=0}^{3} c_n T_c^n, \quad (1)$$

where c_0=326.3, c_1=12.42, c_2=0.197, and c_3=0.0012. They stated that the rms error in D_{eff} is 12.5 μm, and the T range is between -20 and -60°C. D_{eff} ranges between 35 and 130 μm. Definition of the mean effective size is the ratio of the third to second moments of the ice crystal size distribution.

Using theoretical particle size distributions for 2 sub-size ranges as a function of maximum size, Wyser (1998) suggested the following equation for r_{eff}:

$$r_{eff}=377.4+203.3B+37.91B^2+2.3696B^3, \quad (2)$$

where B is defined as a function of ice water content (IWC) and T as

$$B=-2+10^{-3}(273-T)^{1.5}\log(IWC/IWC_o). \quad (3)$$

In Eq. (3), T is in K, IWC in g m^{-3}, and IWC_o=50 g m^{-3}. This equation did not consider particle shape. In the present study, the r_{eff} is converted into D_{eff} using

$$D_{eff}=(4/3)r_{eff}. \quad (4)$$

3.2. D_{eff} calculation

Based on an ice crystal width (D) and length (L) relationship, and assuming columnar particle shape, effective diameter is given by Ou and Liou (1995) as

$$D_{eff} = \frac{\int_{L\min}^{L\max} D^2 Ln(L)dL}{\int_{L\min}^{L\max} DLn(L)dL} \quad (5)$$

Takona and Liou (1989) showed that they were unable to reliably interpret the observed solar albedo values involving cirrus clouds when they assumed that the particles were spherical.

The present study uses the D-L relationship for solid columns given by Heymsfield (1972):

$$D=0.1973L^{0.414},\ L>0.2\ mm. \quad (6)$$

D_{eff} can be calculated using Eqs. 5 and 6, and assuming all particles have a columnar shape.

D_{eff} can also be obtained from Francis (1995):

$$r_{eff} = \frac{3}{4}\frac{IWC}{\sum_i n_i A_i}, \quad (7)$$

where IWC is in g m^{-3}, A is the cross sectional area in m^2, and n_i is the number concentration in m^{-3}. IWC is obtained from

$$IWC = \sum n_i M_i . \quad (8)$$

Francis (1995) suggested that the following relationship (Locatelli and Hobbs 1974) can be used for irregular particles:

$$M_i = 0.037 D_i^{1.9}, \quad (9)$$

where M_i is the particle mass in mg and D_i is the measured diameter of an ice crystal in mm.

In the present study, the cross sectional area (A) is obtained from the maximum particle size as:

$$A = 4\pi\xi\left(\frac{D_i}{2}\right)^2, \quad (10)$$

where ξ is the irregularity factor which is assumed as 0.7 for irregular particles and 1 for circles. Mass and size relationship for circles and needles are also used in the analysis. Their mass-length relationships were taken from Heymsfield and Kajaikava (1987) as

$$M_i = 0.028 D_i^{2.5} \text{ for plates and circles}, \quad (11)$$

and

$$M_i = 0.0049 L_i^{1.8} \text{ for needles}, \quad (12)$$

where D and L are in mm and M is in mg. Collectively, Eqs. 7-12 can be used to obtain D_{eff} versus T for each shape. After obtaining occurrence of particle shape, D_{eff} is weighted for N_i and habit ratio as

$$D_{eff}=(P_{irr}N_{irr}D_{effirr}+P_{nee}N_{nee}D_{effnee}+P_{cir}N_{cir}D_{effcir})/N_{it}, \quad (13)$$

where P, N, N_{it}, irr, nee, and cir are for occurrence of frequency, number concentration, total number concentration, irregular particles, needles, and circles, respectively. This equation is used in the calculation of D_{eff} versus T.

4. RESULTS

In the present study, in-situ observations from the ten FIRE.ACE flights are used in the analysis. Fig. 1 shows the particle spectra for the 25 April 1998. Irregular particle spectra are shown in Fig. 1a where particles are found at all size ranges. Particle spectra for circles including plates are given in Fig. 1b. Needles are seen at sizes less than 300 μm (Fig. 1c). Fig. 1d shows all particles excluding rejected particles. Habit ratios for the same case are given in Fig. 2 which shows that irregular particles account for approximately 60 to 80% of the classified particles, while circles and needles represent less than 30% and 10%, respectively.

These results indicate that the assumption of hexagonal columns for effective radius calculations is not a good assumption to be used in GCMs (Zhang et al. 1999) or remote sensing studies (Key and Intrieri, 2000).

The calculation of effective diameter (radius) can be made using an assumption of particle shape as done in the earlier studies e.g. columns in Ou and Liou (1995), and irregulars in Francis (1995). In the present study, D_{eff} is calculated using both Eq. 5 and Eq. 13. The results are shown in Fig. 3. Results from Eq. 5 based on a columnar assumption are found to be comparable with those of Ou and Liou (1995), and Wysler (1998). The study of Wysler used maximum particle size in the calculations. Results from Eq. 13 (triangles) which utilizes Eqs. 7-12 are found to be smaller than the others. The best fit to the data is found as

$$D_{eff}=28.96e^{0.006T} \text{ with } R=0.33. \quad (14)$$

Fig. 3 (dashed line) shows that if only irregular particles were used, D_{eff} would be less than 60 μm. Use of mass-length relationships for each shape, which is approximately related to the 2nd power of maximum diameter, likely resulted in the low values of D_{eff} (triangles in Fig. 3). Also, as shown in Gultepe et al. (2000), N_i doesn't change significantly with T.

5. DISCUSSION AND CONCLUSIONS

5.1. Comparisons

Comparisons show that mass-length relationships are very important for accurate calculations of D_{eff}. As shown in Fig. 3, the parameterizations of Ou and Liou (1995) are comparable with the present results when particle habit is assumed as columns. When all particle shapes are included in the calculations, D_{eff} is estimated to be lower than those of Ou and Liou (1995), and Wyser (1998). Wyser (1998) did not considered particle shape, but covered the size range from 20 to 1000 μm. In his calculations, maximum size is used in D_{eff} calculation. Without knowing accurate values of small particle concentration for sizes less than 125 μm and large particle concentration for sizes greater than 800 μm, D_{eff} can have a large uncertainty in the colder and warmer T regions. The reason is that more small particles at colder T and more large particles at warmer T are expected to occur. Overall, the results obtained from Eq. 13 indicate that D_{eff} is smaller than those obtained without shape consideration. This is consistent with Wyser (1998). It is important to clarify that satellite retrievals either use Eq. 5 (Key and Intrieri, 2000) or Eq. 7 (Francis et al. 1999).

5.2. Implications for nucleation rate

Ice crystal number concentration is related to particle effective size and T in large-scale models. The following equation is given by Levkov et al. (1992) for the calculation of ice crystal nucleation rate:

$$Q_{nuc} = \frac{3\rho q_i^{dep}}{4\pi\rho_i r_i^3}\frac{1}{\Delta t} \quad (15)$$

where r_i is related to ice crystal effective, Δt the time period, ρ_i the ice crystal density, ρ the air density. This equation shows that if there is an uncertainty in r_i of about 2 μm, the nucleation rate will be in error by about 1 order of magnitude. This uncertainty is very significant when optical parameters and precipitation rates are calculated in the modeling studies.

5.3. Implications for climate change

Using r_{eq}, representing the equivalent spherical radius of an ice crystal for a mono-type particle size distribution with a constant value of ice water content equal to 0.06 g m^{-3}, and one order of magnitude uncertainty in N_i, r_{eq} approximately changes from 150 to 50 μm or vice versa. As shown by Gultepe et al. (1998), a 50% uncertainty in r_{eq} may cause a 10 W m^{-2} change in net radiative cloud forcing. Using a prognostic scheme for microphysics in a National Center for Atmospheric Research (NCAR) Community Climate Model (CCM2), Ghan et al. (1997) stated that changing N_i=100 m^{-3} to 1000 m^{-3} resulted in the short wave cloud forcing (SWCF) changing from -44.5 W m^{-2} to -31.9 W m^{-2}. These studies demonstrate that more information on cloud microphysical parameters is needed to better understand the energy budget of Earth's atmosphere.

6. REFERENCES

Francis, P. N., J. S. Foot, A. J. Baran, 1999: Aircraft measurements of the solar and infrared radiative properties of cirrus and their dependence on ice crystal shape. *J. Geophy. Res.*, **104**, 31685-31695.

Francis, P., 1995: Some aircraft observations of the scattering properties of ice crystals. *J. Atmos. Sci.*, **8**, 1142-1154.

Ghan, S. J., L. R. Leing, and Q. Hu, 1997: Application of cloud microphysics to NCAR community climate models. *J. Geophy. Res.*, **102**, D14, 16507-16527.

Gultepe, I., G. A. Isaac, S. G. Cober and J. W. Strapp, 2000: Ice crystal number concentration versus temperature, *Inter. Journal of Climate., submitted.*

Gultepe, I., G. A. Isaac, A. Korolev, S. Cober, and J. W. Strapp, 1998: Effects of ice crystal shape on the radiative characteristics of low level ice clouds. Preprints, *Conference on Cloud Physics*, 17-21 August, Everett, Washington, 372-375

Heymsfield, A. J., and C. M. R. Platt, 1984: A parameterization of the particle size spectrum of ice clouds in terms of the ambient temperature and ice water content. *J. Atmos. Sci.*, **53**, 126-138.

Heymsfield and Kajikava, 1987: An improved approach to calculating terminal velocities of plate-like crystals and graupel. *J. Atmos. Sci.*, **44**, 1088-1099.

Heymsfield, A. J., 1972: Ice crystal terminal velocities. *J. Atmos. Sci.*, **29**, 1348-1357.

Key, J. and J. Intrieri, 2000: Cloud particle phase determination with the AVHRR, *J. Appl. Meteor.*, accepted.

Korolev, A., G.A. Isaac, and J. Hallett, 2000: Ice particle habits in stratiform clouds. *Q. J. Roy. Meteor. Soc.*, accepted.

Levkov, L., B. Rockel, H. Kapitza, and E. Raschke, 1992: 3D mesoscale numerical studies of cirrus and stratus clouds by their time and space evolution, *Beitr. Phy. Atmos.*, **65**, 35-58.

Locatelli, J. D., and P. V. Hobbs, 1974: Fall speeds and masses of solid precipitation particles. *J. Geophy. Res.*, **79**, 2185-2197.

Lohmann, U., J. Humble, W. R. Leaitch, and G. A. Isaac, 2000: Simulations of ice clouds during FIRE.ACE using the CCCMA single column model. *J. Geophy. Res.*, submitted.

Ou, S. C, and K. N. Liou, 1995: Ice microphysics and climatic temperature feedback. *Atmos. Res.*, **35**, 127-138.

Takona, C. S., and K. N. Liou, 1989: Solar radiative transfer in cirrus clouds. Part I: Single scattering and optical properties of hexagonal ice crystals. *J. Atmos. Sci.*, **45**, 3-19.

Wyser, K., 1998: Effective radius in ice clouds. *J. Climate*, **11**, 1793-1802.

Zhang, Y., A. Macke, and F. Albers, 1999: Effect of crystal size spectrum and crystal shape on stratiform cirrus radiative forcing. *Atmos. Res.*, ***52***, 59-75.

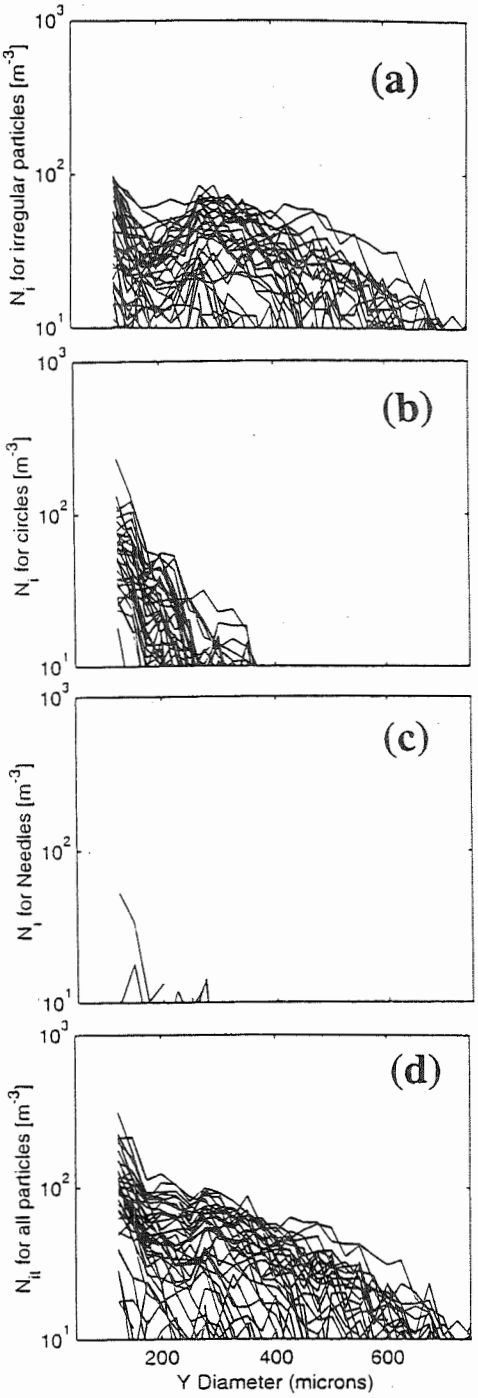

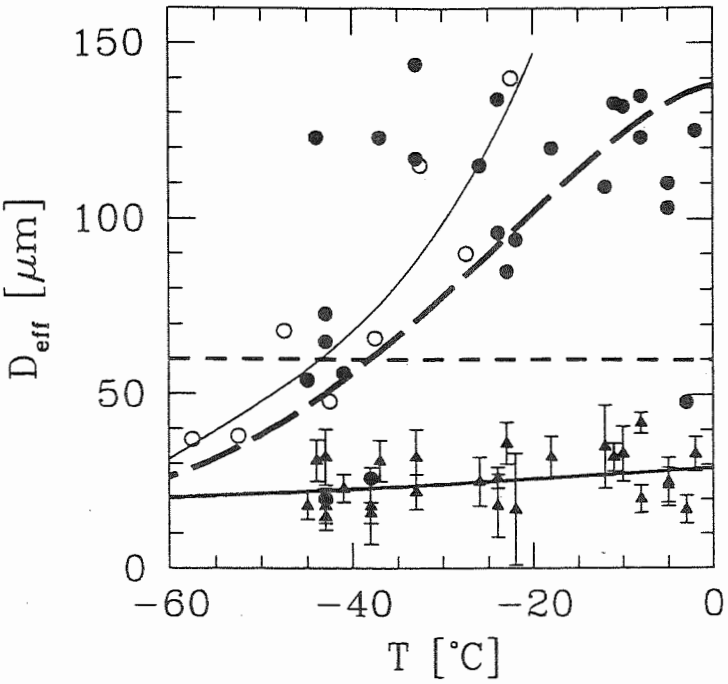

Figure 3: Effective diameter versus temperature. Solid thin line and blank circles are from Ou and Liou (1995). Filled circles are from the present study, assuming all particle are columns. Dark dashed line is from Wyser (1998) assuming IWC=0.005 g m^{-3}. Triangles are from the present study for FIRE.ACE, which is based on use of all particle shapes given in Fig. 1. Solid line over the triangles is the best fit. Bars are for standard deviation. Horizontal dashed line is for the upper limit of D_{eff} if only irregular particles are used in the calculations.

Figure 1. Ice crystal number concentration versus size for the April 25, 1998, FIRE.ACE data: Irregular particles in (a), circles in (b), and needles and columns (c). Total number concentration versus size is shown in (d).

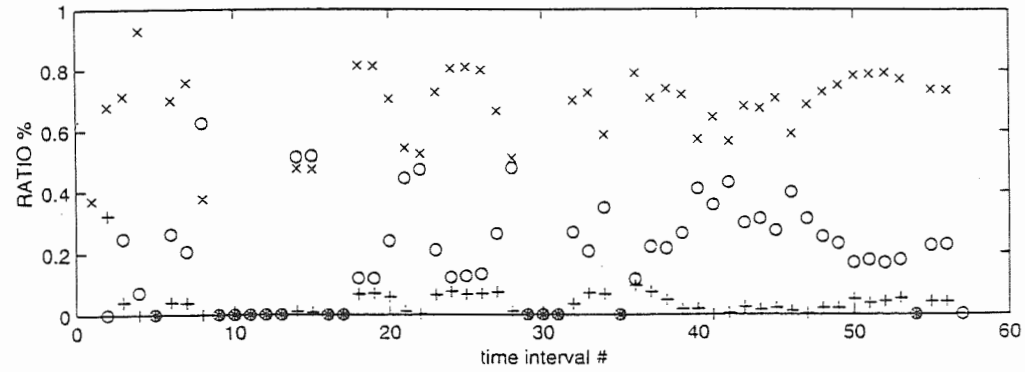

Figure 2. Habit ratio versus time interval for the April 25, 1998, FIRE.ACE data. Each time interval represents a 300 s sampling average. Irregular particles are shown by (x), needles by (+), and circles by (o).

A NEW MICROPHYSICAL PARAMETERIZATION FOR MARINE STRATOCUMULUS CLOUDS IN REGIONAL FORECAST MODELS

David Mechem[1], Yefim Kogan[2], and Fanyou Kong[1]
[1]Coastal Meteorology Research Program,
[2]Cooperative Institute for Mesoscale Meteorological Studies,
The University of Oklahoma, Norman, OK

1. INTRODUCTION*

Most current warm-rain microphysical parameterizations included with NWP models are based on the Kessler (1969) scheme. The advantage of this scheme is that it is conceptually simple, is computationally efficient, and gives reasonable results for situations in which vigorous rainfall is produced. The limitations of the parameterization mainly stem from high sensitivity to the semiempirical parameters defining the parameterization. For example, the autoconversion threshold which in the original formulation was set to 1 gkg^{-1}. This value is far too large for marine stratocumulus where liquid water content, depending on boundary layer conditions, may vary in the 0.2 -0.8 gkg^{-1} range but only rarely exceeds 1 gkg^{-1}. Furthermore, the scheme is unable to account for the differences in ambient CCN concentration between clean and polluted environments which are known to affect boundary layer thermodynamics and cloud microstructure.

To better represent these ubiquitous stratocumulus layers, a new 4-moment microphysical scheme (Khairoutdinov and Kogan 1999, hereafter referred to as the KK drizzle scheme), containing mixing ratios and concentrations of cloud water and drizzle, was recently implemented into the U.S. Navy Coupled Ocean-Atmosphere Modeling System (COAMPS). The scheme has been tested against the solution provided by an LES model which treats the microphysical processes in an explicit manner.

2. IDEALIZED SIMULATIONS IN CLEAN AND POLLUTED ENVIRONMENTS USING COAMPS

Initial conditions for the idealized three-dimensional simulations were based on the measurements obtained during the ASTEX A209 flight on 12 June 1992. Horizontal and vertical grid spacings were 75 m and 25 m. Initial values of CCN were set to 45 cm^{-3} and 400 cm^{-3} for the clean and polluted cases, respectively, and were homogeneous over the entire domain. The drizzle water concentration produced in the clean case is two orders of magnitude larger than in the polluted case, and surface drizzle rates shown in figure 1a reflect this difference. The drizzle scheme produces the expected decrease of in-cloud liquid water with time, visible in figure 2a, and a gradual thinning of the cloud field,

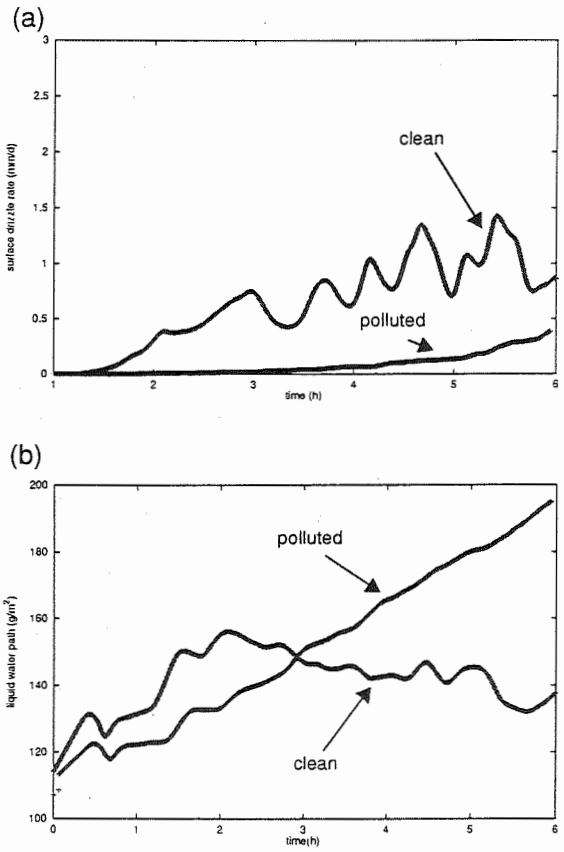

Figure 1. For clean and polluted cases. (a) Domain-average surface drizzle rates. (b) Domain-average liquid water path.

*Corresponding author's address: David Mechem, Coastal Meteorology Research Program, University of Oklahoma, 100 E. Boyd, Room 1034, Norman, OK 73019. Email: dmechem@ou.edu.

but only after the drizzle rate becomes significant. In contrast, the LWP in the polluted case steadily increases, a result of the constant surface moisture flux.

Trends in boundary layer stability brought about by drizzle evaporation are apparent in vertical profiles of θ_{vl} and total liquid water, and indications of boundary layer decoupling are evident in the profiles of vertical velocity variance (not shown here). Cloud droplet concentration decreases with time as the small cloud droplets either coalesce or accrete to the larger drizzle drops. Drizzle production efficiency is much smaller In the polluted case, and very little change in cloud characteristics and boundary layer thermodynamic structure occurs over the course of the 6 hour simulation.

3. APPLICATION OF THE SCHEME IN A MESOSCALE SETTING

As a test of the KK drizzle scheme at mesoscale resolutions, COAMPS was run over an area of the eastern Pacific containing the California coastal region. The model was run at a coarse horizontal resolution (18 km) with a fine vertical resolution in the boundary layer (10 m - 50 m). The model produced a broad region of drizzling stratocumulus, the spatial coverage of which is in agreement with satellite observations. The stratocumulus cloud top height slopes downward toward the coast and is strongly correlated with SST, which varies slowly in time. Surface drizzle rate after 12 hours (figure 2) seems to be correlated with LWP, with reasonable drizzle rates (.25-1.75 mmday^{-1}) being produced in locations where LWP is less than 200 gm^{-2} and significantly larger rates in locations of thicker cloud.

At the coarse horizontal grid spacing employed, the effects of drizzle are only readily apparent in the temperature and moisture fields. Vertical profiles of temperature taken in the drizzling portion of the cloud are cooler than those from the operational Kessler scheme, a case of the subcloud air being cooled by drizzle evaporation. The evaporation also results in a subcloud layer more moist than that using the operational scheme. This moistening effect is easily seen by comparing the surface relative humidities for the two schemes (figure 3a and 3b). The higher relative humidity near the coast in figure 3a is a result of cooler temperatures near the coast (and hence, smaller values of q_{vsat}), but the difference in humidity in the middle of the drizzling region is directly attributable to evaporative cooling of the falling drizzle.

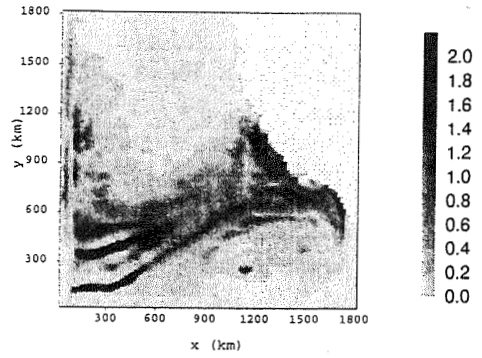

Figure 2. Surface drizzle rate (mm day^{-1}). The California coast in the top right corner is not explicitly drawn.

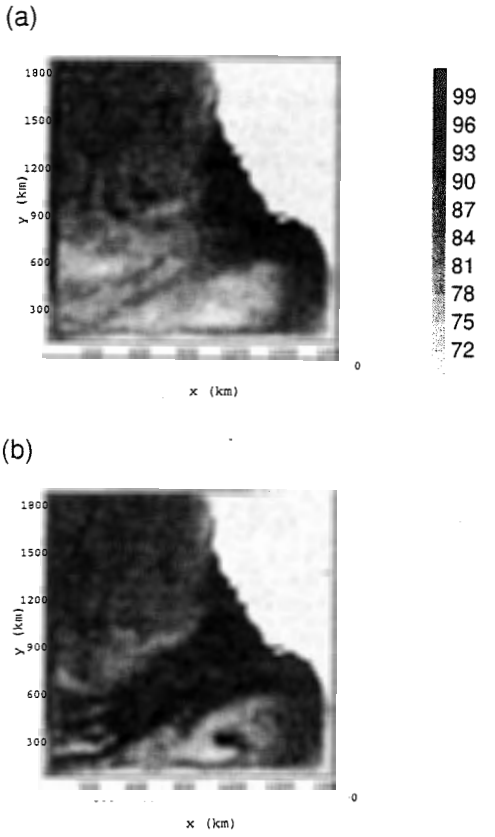

Figure 3. Surface relative humidity. (a) operational Kessler scheme. (b) KK drizzle scheme.

Over the course of a 24 hour simulation, much of the boundary layer CCN may be scavenged by precipitation processes. As the CCN concentration decreases, drizzle production efficiency increases, rapidly depleting the liquid water in the cloud and eventually leading to cloud breakup. This is an accepted property of drizzling stratocumulus, but it appears to occur too rapidly in these simulations. In the model, the CCN can be replenished by advective processes, assuming the upstream CCN concentrations can be ascertained. At the higher horizontal resolutions in the idealized simulations, partial replenishment of the boundary layer CCN occurs through entrainment of air above the inversion, but whether this is a process which is common in nature or whether it is merely an artifact of an initially homogeneous CCN concentration is not yet understood. It is not a process occurring at the coarse resolutions presented here, since the resolved eddies which are responsible for the entrainment are nonexistent and the parameterized cloud top entrainment appears to be underestimated. What is needed is an accurate formulation in the model of CCN source terms.

4. SUMMARY

Results from idealized simulations of stratocumulus using COAMPS with the new bulk microphysical scheme appear physically consistent with the results from the CIMMS LES model and show a realistic response to different CCN loads.

For the mesoscale case, since the drizzle growth efficiency is so fundamentally dependent upon the ambient CCN, it seems imperative to be able to account for CCN sources in a reasonable manner. A diurnal variation in the cloud characteristics is likely present but is overwhelmed by the cloud breakup caused by drizzle processes.

Although preliminary coarse grid results for the mesoscale case have been presented here, the study is proceeding by first concentrating on high resolution grids and then moving to coarser meshes. The reasoning is that the higher resolution simulations should be the easiest to comprehend since they will best correspond to the well-verified idealized experiments already performed. From there, the investigation can progress upscale, where more of the motion must be parameterized.

Acknowledgments. This research was supported by the ONR Grants N00014-96-1-0687 and N00014-96-1-1112.

REFERENCES

Khairoutdinov. M. and Y. L. Kogan, 2000: A new cloud physics parameterization for large-eddy simulation models of marine stratocumulus. *Mon. Wea. Rev.*, **128**, 229-243.

Kessler, E., 1969: On the distribution and continuity of water substances in atmospheric circulations. *Meteor. Monogr.*, **10**, No. 32, Amer. Meteor. Soc., 84 pp.

A CLOUD MICROPHYSICAL PARAMETERIZATION FOR HIGHER-ORDER TURBULENCE CLOSURE MODELS

Shouping Wang[1] and Qing Wang[2]
[1] *Universities Space Research Association, Huntsville, Alabama*
[2] *Naval Postgraduate School, Monterey, California*

1. INTRODUCTION

There have been continued efforts in improving cloud representation in turbulence closure models. These efforts include both bulk and bin microphysical approaches (e.g., Sigg, 2000 and Bott et al., 1996). Notably, Wang *et. al.* (1998) presented a bin-microphysics parameterization coupled with a 3rd-order turbulence closure model. A significant feature of this coupled model is an explicit representation of turbulence generated activation and condensation/evaporation (CE) processes, which is an important step forward compared with those of previous similar models. This model provides a framework of parameterizing bin-microphysics in a higher order turbulence closure model. Because it must predict mean droplet number and relevant turbulence statistics on each bin, the model requires intensive computing power, which clearly is a disadvantage for a turbulence closure model.

This study is a further development of the work of Wang *et al.* (1998). A log-normal distribution function is used to represent cloud droplet spectrum. CE rate is formulated based on the distribution and relevant turbulence statistics. Furthermore, effects of activation of cloud droplets on the turbulence statistics are also parameterized.

2. MODEL OUTLINE

The model includes two parts, one is a 3rd-order turbulence closure model (Wang and Wang, 1994), the other is cloud microphysics parameterization. The main objective is to predict 6 mean variables ($\overline{u},\overline{v},\ \overline{q}_t,\overline{\theta}_l,\overline{q}_l,\overline{N}$) [The last two variables are liquid water content mixing ratio, and cloud droplet number mixing ratio]. For this purpose, the model predicts second- and third-moments of the turbulence variables. For example, we need to predict ($\overline{w'q_l'},\overline{w'N'}$) for ($\overline{q}_l,\overline{N}$). All q_l- and N-related predictive equations have two major parts: turbulence part and microphysical part. The turbulence part is handled by the turbulence closure model, the microphysical part is derived in the next section. The main feature of the microphysical model is the use of a log-normal distribution function, which is inspired by the work of Feingold *et. al.* (1998) and Khairoutdinov and Kogan (2000). No gravitational settling of cloud droplets is considered in the model.

3. CONDENSATION AND EVAPORATION

The starting point for the CE parameterization is the equation for the change of droplet spectrum due to CE:

$$\left(\frac{\partial n}{\partial t}\right)_{ce} = -\frac{\partial}{\partial r}\left(\frac{G(T,p)\,S}{r}\right), \tag{1}$$

where $n(r)$ is the droplet size distribution function, $G(T,p)$ a weak function of temperature and pressure, S supersaturation [$S=(q_t-q_l-q_s)/q_s$], and r radius of a single cloud droplet. A third-moment integration gives the CE rate

$$\left(\frac{\partial q_l}{\partial t}\right)_{ce} = 4\pi G\rho_l RS, \tag{2}$$

where R is the integrated radius. Applying Reynolds averaging operation gives the following ensemble mean CE rate:

$$\left(\frac{\partial \overline{q_l}}{\partial t}\right)_{ce} = 4\pi G(\overline{T},\overline{p})\rho_l(\overline{R}\,\overline{S}+\overline{R'S'}), \tag{3}$$

Now, we need to express $\overline{R}$ in terms of $\overline{q}_l$ and $\overline{N}$. For this purpose, log-normal distribution function is used and is written as

$$n(r,r_g,\sigma)=\frac{N}{\sqrt{2\pi}\ln(\sigma)r}\exp\left[\frac{(\ln r-\ln r_g)^2}{2\ln^2\sigma}\right], \tag{4}$$

Corresponding author Address: Shouping Wang, USRA, 977 Explorer Blvd, Huntsville, AL 35806
wangsx@vmcs.msfc.nasa.gov

where σ and r_g are the two parameters to completely define the distribution. For the current parameterization, we require that σ be specified externally. Based on this distribution function, following relationship can be obtained:

$$R=\frac{Exp(-\ln^2\sigma)}{(4/3\pi\rho_l)^{1/3}}\left[q_l N^2\right]^{1/3}. \quad (5)$$

Since σ is assumed constant (1.25), we can expand above expression at $(\overline{q_l}, \overline{N})$ using Taylor series and derive following expressions:

$$\overline{R}\cong R_b+\frac{R_b}{9}\left(-\frac{\overline{q_l'^2}}{\overline{q_l}^2}+\frac{2\overline{N'q_l'}}{\overline{N}\,\overline{q_l}}-\frac{\overline{N'^2}}{\overline{N}^2}+.....\right), \quad (6a)$$

$$R'=\frac{R_b}{3}\left(\frac{q_l'}{\overline{q_l}}+\frac{2N'}{\overline{N}}\right) \text{ and} \quad (6b)$$

$$R_b=\frac{\exp(-\ln^2\sigma)}{(4/3\pi\rho_l)^{1/3}}\left[\overline{q_l}\,\overline{N}^2\right]^{1/3}. \quad (6c)$$

The fluctuating S, S', is given by

$$S'\cong\frac{1}{\overline{q_s}}\left(q_t'-\frac{c_p\gamma}{L}\theta_l'-(1+\gamma)q_l'\right), \quad (7)$$

where $\gamma=L/c_p\,dq_s/dT$.

Substituting (6) and (7) in (3), we can obtain the mean CE rate. By subtracting (3) from (2), we may also have fluctuating CE rate, which is also needed to formulate prognostic equations of q_r related turbulence variables. For example, we have prognostic equations for $(\overline{q_l}, \overline{w'q_l'})$ as

$$\frac{\partial\overline{q_l}}{\partial t}=-\frac{\partial\overline{w'q_l'}}{\partial z}+4\pi C\rho_l\left[\overline{R}\,\overline{S}+\frac{R_b}{3}\left(\frac{\overline{q'S'}}{\overline{q_l}}+\frac{2\overline{N'S'}}{\overline{N}}\right)\right] \quad (8)$$

$$\frac{\partial\overline{w'q_l'}}{\partial z}=-\frac{\partial\overline{w'w'q_l'}}{\partial z}-\overline{w'^2}\frac{\partial\overline{q_l}}{\partial z}+(1-C_7)\overline{\theta_v'q_l'}-\frac{C_6}{\tau}\overline{w'q_l'}$$
$$+4\pi G\rho_l\left[\overline{R}\,\overline{w'S'}+\frac{R_b\overline{S}}{3}\left(\frac{\overline{w'q_l'}}{\overline{q_l}}+\frac{2\overline{w'N'}}{\overline{N}}\right)+....\right] \quad (9)$$

where "....." denotes the higher order terms ignored in the present model, τ the dissipation time scale. We clearly see that a source term is included in the turbulence flux equation. All other q_l - related turbulence variables can be derived in a similar fashion. In the present model, all the second-moments of q_l include a similar source term, while the third-moments do not.

When S < 0, the droplets with radius less than the critical value (r_{cri} = 1 μm) completely evaporate. Assuming that *S* has a triangle distribution $f(S,\overline{S},\sigma_s)$, the complete evaporation is given by

$$\left(\frac{\partial\overline{N}}{\partial t}\right)_{eva}=-\frac{\int_{-\infty}^{0}f(S,\overline{S},\sigma_s)dS\int_{0}^{r_{cri}}n(r,r_g,\sigma_r)dr}{\Delta t} \quad (10)$$

Cloud fraction is diagnosed following Wang and Wang (1999):

$$CF=1-EXP\left(-k\frac{\overline{q_l}}{\sqrt{\overline{q_l'^2}}}\right).$$

4. ACTIVATION

Using the relationship between activated CCN number N_a and S formulated by (Khairoutdinov and Kogan, 2000), we can obtain the total mean activated CCN number from

$$\overline{N}_a=\int_0^\infty f(\overline{S},\sigma_s)CCN\sqrt{Min(\frac{S}{S_{\max}},1)}\,dS. \quad (11)$$

Then the activation tendency is given by

$$\left(\frac{\partial\overline{N}}{\partial t}\right)_{act}=\frac{Max\left(\overline{N}_a-\overline{N},0\right)}{\Delta t}. \quad (12)$$

A corresponding term is also included in the liquid water equation (8).

The number activation may also affect *N*–related turbulence statistics (such as $\overline{w'N'}$), because activation is likely to occur in turbulent updrafts. This process is parameterized in terms of mass flux transport concept (Wang and Albrecht, 1986, Randall *et al.*, 1992). It is assumed that all the activation occurs in the updrafts and all the turbulence fluctuations follow Gaussian distribution. After some algebraic manipulation, we can obtain

$$\left(\frac{\partial\overline{\phi'N'}}{\partial t}\right)_{act}=C(w,\phi')\sqrt{\frac{2}{\pi}}\sqrt{\overline{\phi'^2}}\left(\frac{\partial\overline{N}}{\partial t}\right)_{act}, \quad (13)$$

where ϕ is any variable, and *C(w, ϕ')* the correlation coefficient between *w* and ϕ'. Corresponding

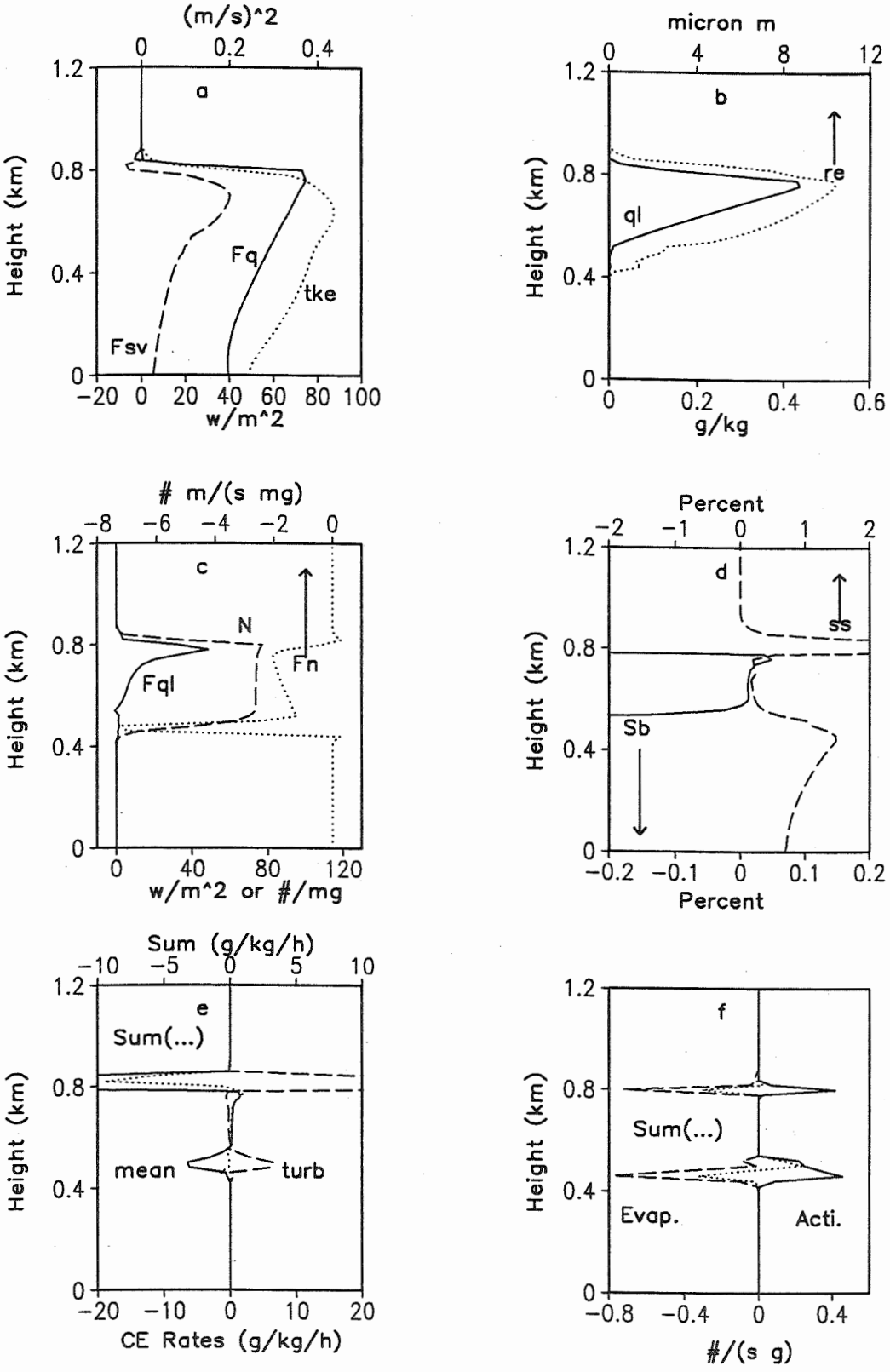

a: Buoyancy flux (Fsv), total water flux(Fq), TKE (tke);
b: mean radius (re), liquid water (ql)
c: liquid water flux(Fql), number(N), number flux (Fn);
d: mean S(Sb), standard deviation of S (SS)
e: CE from the Mean (mean), CE from the turbulence (turb), and Sum (Sum);
f: droplet number activation (Acti), evaporation (Evap.), and sum (Sum).

terms are also included in q_l - related turbulence variable equations.

5. A TEST RUN

The stratocumulus cloud case of GCSS (Betchtold *et al.*, 1996) is used here to test the model. All the initialization and model setup are the same as in that paper. The model is run for 5 hours with time step 1 s. Some results are shown on the figure.

The simulated total water flux, buoyancy flux, and TKE profiles (Fig. a) show common shapes as expected from our experiences. As shown in Fig. b., the maximum liquid water content is higher than those reported in Bechtold *et al.* (1996). The mean droplet radius increases linearly from the cloud base and reach to 10 μm. This profile is consistent with many other LES model simulations, although the maximum value is relatively small probably due to lack of the collection process in the model.

As shown in Fig.c, liquid water flux is zero at the cloud base and increases to the cloud top due to the source term in (9). The droplet number flux has negative maximum at the cloud base, maintains negative within the cloud layer, and obtains weak a positive value near the cloud top, indicating strong down-gradient characteristics in spite of "updraft-activation" parameterization (13). A key to understand the microphysical structure is profiles of the mean S and standard deviation of S due to turbulence. The mean S is negative at the cloud base, becomes positive about 50 m above, and increases to reach the maximum value 0.05% at the cloud top, which results from strong radiative cooling there. The standard deviation shows two maxima. One is at the cloud base, resulting from intense turbulent updrafts; the other is at the cloud top, resulting from the inversion. Therefore, even though the mean S is negative at the cloud base, condensation can still occur due to the turbulence generated positive S'.

The two terms (the mean and turbulence contributions) in the CE term in (8) are shown in Fig. e. The mean CE term is negative at the cloud base and positive in the middle and upper levels, and becomes strongly negative again at the cloud top. Opposite to the mean profile, the turbulence contribution is positive at the cloud base, and zero in the mid levels, and becomes very positive at the cloud top. The turbulence generated condensation at the cloud base results from saturated turbulent updrafts. The net profile shows weak evaporation at the cloud base, and condensation in the middle and upper levels, and finally gives significant evaporation at the top of cloud layer. These CE profiles are consistent with our basic understanding of cloud structure.

The activation and evaporation of the droplet number (Figs.f) show maxima at the cloud base and top, respectively. These features clearly result from the supersaturation profiles shown in Fig. d as discussed previously. The activation at the cloud base leads to the quasi-constant profile of N (Fig.c) within the cloud layer.

It should be emphasized that the microphysics related turbulence statistics (mainly S' related statistics) play essential roles in regulating the simulated cloud structure [as shown in Eq. (8) and (9)]. For example, without the turbulence contributions, it would not be possible to obtain the constant N profile and positive liquid water flux in the cloud layer. Therefore, any turbulence closure model that tends to simulate cloud microphysical structure must realistically parameterize these terms.

6. ACKNOWLEDGMENT

Shouping Wang was supported by NASA/ FIRE ACE, EOS projects, Atmospheric Dynamics and Remote Sensing program and NSF Grant ATM-9900496, Qing Wang was supported by NSF Grant ATM-9900496.

7. REFERENCES

Bott, A., *et al.*, 1996: A numerical model of cloud-topped planetary boundary-layer: Radiation, turbulence and spectral microphysics in marine stratus. *Quart. J. Roy. Meteor. Soc.* **122**, 635-667.

Khairoutdinov, M., and Y. Yogan, 2000: A new cloud physics parameterization in a large-eddy simulation model of marine stratocumulus. *Mon. Wea. Rev.*, **128**, 229-243.

Feingold, G., *et al.*, 1998: Simulations of marine stratocumulus using a new microphysical parameterization scheme. *Atmos. Res.*, **47-48**, 505-523.

Randall, D., *et al.*, 1992: A second-order bulk boundary layer model. *J. Atmos. Sci.*, 49, 1903-1923.

Siggs R., 2000: Use of pseudoadbatic adjustment of turbulence for a simplified night-time stratocumulus case: A one-dimensional study. *Mon. Wea. Rev.*

Wang, Q., *et al.*, 1998: A new turbulence closure model with explicit microphysics for marine stratocumulus. *Conf. On Cloud Physics*, Preprint, 325-328. 17-21 August, 1998.

Wang, S., and B. Albrecht, 1986: A stratocumulus model with an internal circulation. *J. Atmos. Sci.*, **43**, 2374-2391.

Wang, S., and Q. Wang, 1994: Roles of drizzle in a one-dimensional third-order turbulence closure model of the nocturnal stratus-topped marine boundary layer. *J. Atmos. Sci.*, **51**, 1559-1576.

Wang, S., and Q. Wang, 1999: On condensation and evaporation in turbulence cloud parameterizations. *J. Atmos. Sci.*, 56, 3338-3344.

SIMPLE PARAMETERIZATION OF SHALLOW CONVECTIVE CLOUDS BASED ON TWO-DIMENSIONAL NUMERICAL MODELLING

Gueorgui V. Mostovoi

Hydrometeorological Centre of Russia, Moscow, 123242, Russia

1. INTRODUCTION

All off the well known schemes of shallow convection parameterization use one-dimensional cloud models. In the simplest case such a model is identical to the parcel method and thermodynamic parameters of cloud air are described by the moist adiabat. It characterizes temperature and humidity changes in an isolated rising air parcel without mixing with the enviroment.

We suggest to refine the parcel method by taking into account terminal sizes of a cloud and its deformation during a life cycle. This will permit overcoming essential limitations of the well known cumulus parameterization methods (e.g., Tiedke, 1989) connected with representation of clouds by vertical columns of fixed section with constant lateral mixing.

2. NUMERICAL EXPERIMENTS

To solve the task formulated above, some numerical experiments, reproducing evolution of small cumulus clouds, have been carried out (Mostovoi, 1999a). A two-dimensional nonhydrostatic model (Pielke et al., 1992) with fine spatial resolution of 30 m is used. The choice of such resolution was caused by the necessity of the explicit treatment of large eddies responsible for cloud destruction. The integration domain was 3.6 km vertically and 2.4 km horizontally. Model variables are as follows: mixing ratio for total moisture content $q_t = q + \ell$, where q and ℓ are mixing ratios for water vapor and liquid water content (LWC), liquid water potential temperature θ_ℓ, pressure and velocity components.

Conservation properties of q_t and θ_ℓ can provide a useful Lagrangian framework for the analysis of the numerical experiments results. A Lagrangian approach makes more clear a formation of any cloud variable field at a fixed points from the viewpoint of parcel history (Mostovoi, 1997).

Vertical movements were initiated by a hot semicircular spot of radius R placed at the bottom of the integration domain. Inside the spot the air temperature decreased from its centre upward, having Gaussian distribution on both coordinates with a characteristic half-width G, set in grid steps, and an amplitude A. A similar overheated dome in the atmospheric boundary layer may be produced by a local heating of the surface. The rise of the dome is accompanied by the formation in its head of an isolated compact area of positive buoyancy, or a thermal. In all our experiments the thermal played the role of a certain initial dynamic trigger, only providing the rise of overlying layers necessary for reaching condensation. The direct contribution of the initially overheated area to the buoyancy of a cloud was negligible. Numerical experiments were conducted with different values of the forcing parameters R, G and A in order to simulate natural variability of small cumulus.

It should be noted that the initiation of a cloud cell by only one thermal is a certain simplification in comparison with natural cloud formation. We share Saunders' (1961) opinion that an improved knowledge of the behavior of individual thermals will benefit our understanding of both small and large cumulus.

Large-scale thermodynamic profiles, used for numerical experiments reflected various atmospheric stratification conditions in the tropics and midlatitudes during the development of small cumulus. Their brief characteristic and initial data for experiments are given in a contribution of Mostovoi (1999b).

The model equations were integrated for 50 min. During this period the cloud cell attained a stage of maximum development, at which the leading edge of the cloud rose to a maximum height.

3. RESULTS

Numerical experiments have shown, that after reaching the terminal size (it takes about 10-15 minutes from the start of condensation) a small isolated cloud begins to be destroyed by the organized inflow in its base of nonsaturated air parcels. The given mechanism is related to the explicitly resolved component of motion, causing gradual dilution of the core part of a cloud by parcels, descending along lateral boundaries and then coming into its base. Notice that this forced transport is connected only with a closed circulation arising around any cloud cell. The filling of the central part of a cloud with these parcels is clearly seen in Fig. 1 as a sharp rise of the 0.1 g/kg LWC isoline at 20 min from 0.6 km to 1.2 km in experiment with Voves data (Hicks et al., 1990). A similar process of the cloud filling was observed in all experiments. It proceeded at different rates, as follows from Fig. 2, which shows a set of curves, reflecting time dependent of the cloud integral LWC. The latter was determined by summing up LWC values in an x-z plane.

In Fig. 1, dotted lines show the time variation of

E-mail: most@rhmc.mecom.ru

q_t / q_{t0} on the centreline of the integration domain, where q_{t0} is the mixing ratio for total moisture air content at the surface. The destruction of the cloud core evidently displayes through a decrease with time in q_t / q_{t0}. The cause is that the total moisture content is a conservative quantity in the absence of subgrid mixing. Therefore, the isolines of the normalized values of total moisture content q_t / q_{t0} in Fig. 1 are quasi-material lines consisting of the same air parcels. Their configuration reflects the deformation of initially horizontal air layers caused by ascent of a small thermal (cloud).

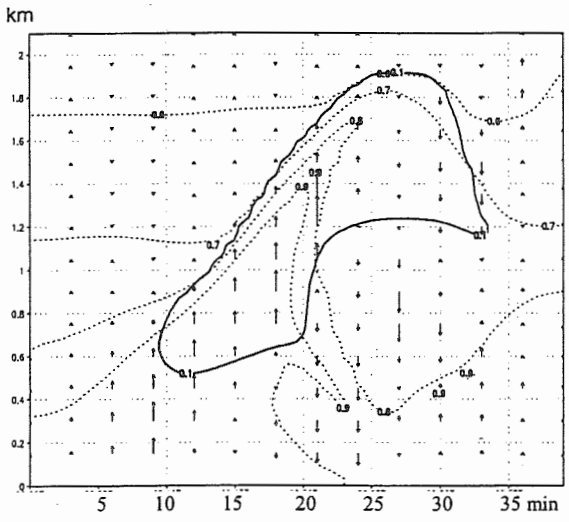

Fig. 1 Time variations of the total moisture content (dotted line) on the centreline of the integration domain, 0.1 g/kg LWC value(solid line) and vertical velocity component.

Figure 1 is also of interest since it clearly demonstrates the influence on the cloud evolution of two mixing components: diffusive and organized, connected with an explicitly resolved flow component. The subgrid diffusion results in rather smooth dilution of the cloud air, which is confirmed by the uniform narrowing of the area of maximum q_t / q_{t0} with time and height. It should be emphasized, that the organized dilution as a factor limiting cloud growth plays a basic role in comparison with diffusion. Its action leads to a supply of unsaturated particles to a rear part of a cloud cell as it ascents upward. Their influence creates a local minimum on the vertical profile of q_t / q_{t0}, providing a typical bend of the curves in Fig.1, which gives the space-time distribution of the normalized total moisture content a form of an overturning wave.

To sum up this section, it should be noted that the critical contribution to the destruction of a small cumulus cloud is made by the circulation arising around it. It causes us to consider the cloud environment in any horizontal layer as consisting mainly of air portions orderly ascending from below rather than coming from above through the cloud top. A cloud dilution in the active growth stage due to mixing on the top and lateral edges, does not appear to be as significant as commonly recognized. It becomes essential only at the stage of dissipation and the complete disappearance of a cloud, when its vertical development is suppressed by stable stratification of the enviroment. In this connection the role of diffusive mixing, as a factor limiting the growth of a small cumulus cloud seems to be exaggerated. Therefore, for practical purposes of LWC parametrization in numerical large-scale atmospheric models the entrainment through the lateral boundaries may be neglected.

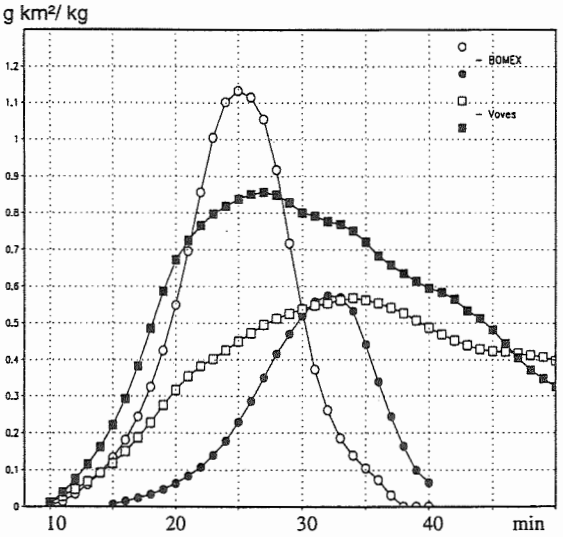

Fig.2. Time variations of the integral LWC. Circles correspond to experiments with BOMEX data, squares - Voves data for the different sets of *R*, *G* and *A* (open or closed markers).

4. MOIST ADIABAT & LWC RESTORATION

We consider now how to use features found in the life cycle of an isolated cloud cell in formulating the parametrization. Following Anthes (1977), the basic contribution to the diabatic heating of the atmosphere Q_c from shallow convection is assumed to be connected with the direct release of the heat of condensation in cumulus clouds. Therefore, designating by overbar the variables averaged over a grid cell of the large-scale model, the diabatic heating can be written as

$$Q_c = \frac{L}{C_P}\frac{\Delta \overline{C}}{\Delta t}, \qquad (1)$$

Where ΔC represents change in a cloud LWC during the time step Δt in a large-scale atmospheric model.

To caculate diabatic heating from (1) the following simplified representation of $\overline{C}$ is used: $\overline{C} = a\tilde{\ell}$, where a is a percent area, occupied by cumulus clouds inside a large-scale grid cell. The tilde

designates lifetime averaging for clouds prevailing in the cloud population. If we assume, that a is known, then cumulus cloud parameterization reduces to definition of $\overline{\ell}$. A method of a estimation will be discribed in a separate paper.

Consider the proposed method of estimating the LWC vertical profile $\overline{\ell}$ necessary for calculation of diabatic heating. The analysis of the cumulus modeling results obtained with different initial data has shown that vertical profiles of virtual potential air temperature $\overline{\theta}_v$ and total moisture content $\overline{q}_t$, formed during a life cycle of a small cumulus cloud are rather simple for analytical approximation. After applying the approximation procedure and thus obtaining the values of variables $\hat{\theta}_v$ and $\hat{q}_t$ (the hat designates approximation) LWC profile be easily calculated from the relation of $\hat{q}_t$ and $\hat{\theta}_\ell$ conservation. The given reasons form a basis for the proposed LWC parameterization.

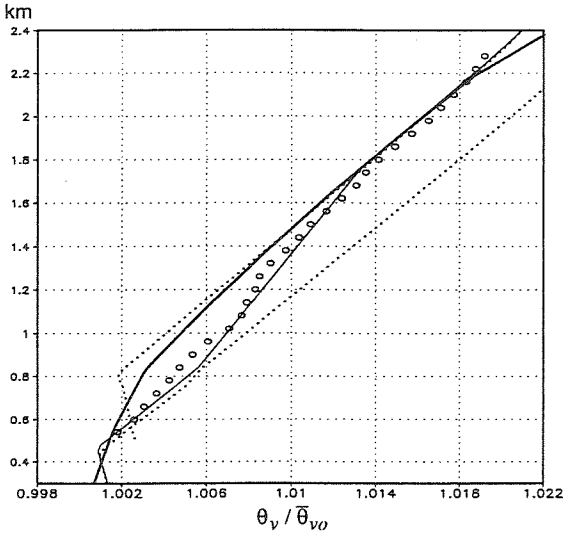

Fig. 3. Virtual potential temperature averaged over the life time of a cloud (circles). Stratification in the environment (thick line), approximation of the temperature profile (thin line), moist adiabats for air parcel rising from different levels (dotted line).

Consider the procedure of $\overline{\theta}_v$ approximation. We now turn to Fig. 3, where $\overline{\theta}_v$ profiles , normalized by the values $\overline{\theta}_{v0}$ at the surface and obtained in the experiment with Vovess initial data are shown. It is seen that the upper and the lower part of the $\overline{\theta}_v$ distribution with height almost coincide with strait dotted lines which are adiabats.

We will use this peculiarity of the profile for parameterization and approximate the vertical $\overline{\theta}_v$ profile by a combination of two reversible moist adiabats. Each of them characterizes θ_v changes in adiabatically rising parcels starting from different levels. One particle rises from a near-surface level with pressure P_b. It has adiabatic $\theta_v^b(p)$ distribution and is appropriate for description of the lower part of the vertical $\overline{\theta}_v$ profile, connected with an initial phase of a cloud cell growth.

The other particle rises from an overlying level, with a pressure P_{top}. The virtual potential temperature of this particle $\theta_v^{top}(p)$ can be used for approximating the upper part of the $\overline{\theta}_v$ profile. The adiabat $\theta_v^{top}(p)$ characterizes a stage of the filling of a cloud cell with parcels, descending from the overlying levels and orderly involved in a cloud through its base. In the filling stage the cloud cell begins to dissolve.

We emphasize, that the proposed approximation is not formal and qualitatively reproduces a principle feature of the life cycle of an isolated cloud, representing it by particles, rising from different levels.

Given these reasons, the following expression for estimating the vertical $\overline{\theta}_v$ profile is suggested :

$$\hat{\theta}_v = \begin{cases} \hat{\theta}_v^b(p), & p \geq P_{top}^s \\ \hat{\theta}_v^b(P_{top}^s) - \beta(P_{top}^s - p), & \\ & P_{top}^s - \delta p_1 \leq p < P_{top}^s \\ \hat{\theta}_v^{top}(p), & p < P_{top}^s - \delta p_1 \end{cases} \qquad (2)$$

$$\text{Where } \beta = \frac{\hat{\theta}_v^b(P_{top}^s) - \hat{\theta}_v^{top}(P_{top}^s - \delta p_1)}{\delta p_1},$$

P_{top}^s is the pressure at a level where a rising parcel from the level P_{top} reach saturation; δp_1 is the thickness of an intermediate layer between adiabats $\theta_v^b(p)$ and $\theta_v^{top}(p)$.

The proposed approximation (2) for $\overline{\theta}_v$ involves three layers. In the upper and lower layers $\overline{\theta}_v$ is replaced respectively by adiabats $\theta_v^b(p)$ and $\theta_v^{top}(p)$, and in the intermediate layer of thickness δp_1 we use a linear change for $\overline{\theta}_v$. A satisfactory agreement between $\hat{\ell}$ and $\overline{\ell}$ profiles is provided, even with the use of a constant δp_1 for all considered cases of clouds development.

To calculate an approximate $\hat{\theta}_v$ profile from (2) it is necessary to set P_b and P_{top} also. As an estimate

for P_b, we can take the pressure at a height of 200-300 m above the surface. The analysis of the $\bar{\theta}_v$ and $\hat{\theta}_v^{top}$ profiles has shown that pressure P_{top} is related to the adiabat $\hat{\theta}_v^{top}(p)$, which maximum difference $\bar{\theta}_v$ - $\hat{\theta}_v^{top}$ in a 1.5-2.5 km atmospheric layer proves to be closest to 0.3K. Given the monotone character of $\bar{\theta}_v$, it is easy to find this adiabat by the trial-and-error method, consecutively examining various P_{top} until the specified condition for maximum buoyancy is satisfied. The proposed approach provides the uniqueness of choice of P_{top}.

Consider briefly a way of determining of the $\hat{q}_t$ profile. Leaving aside the vertical profile of $\bar{q}_t$, it should be noted that, because of quasi-conservation of the total moisture content, the profile has a simpler form than the $\bar{\theta}_v$ distribution. It can be described by a linear relationship in the layer between P_b and P_{top} - δP_2, where δP_2 - ajusted parameter.

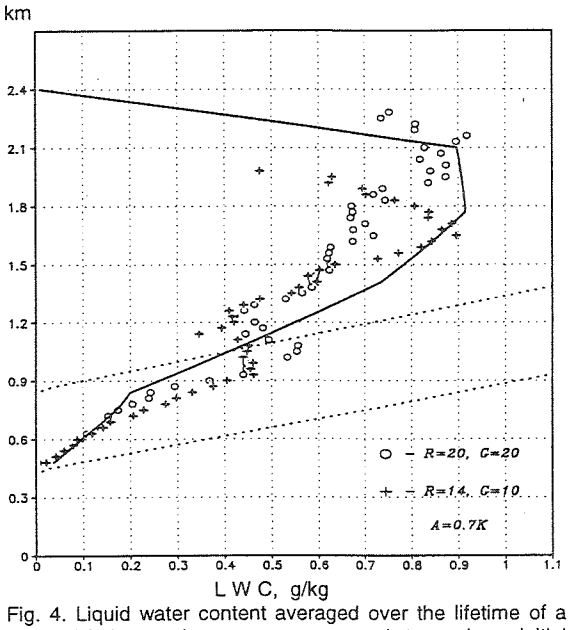

Fig. 4. Liquid water content averaged over the lifetime of a cloud (circles and crosses correspond to various initial forcing). Results of restoration of cloud LWC profile (solid line).

Figure 4 shows the vertical profile of $\hat{\ell}$ restored from the corresponding $\hat{\theta}_v$ (thin line without marker in Fig.3) and $\hat{q}_t$ values and simulated distributions of $\bar{\ell}$ in experiments with Voves data (Hicks et al., 1990). For calculating $\hat{\ell}$, we use the values of δP_1 and δP_2 equivalent to 900 and 600 m. Comparison of $\hat{\ell}$ and $\bar{\ell}$ profiles in Fig.4 demonstrates their qualitative coincidence. The dotted lines in Fig. 4 show adiabatic variations of LWC in air parcels ascending from the surface and from the height of 600 m. It should be emphasized that the difference between the averaged LWC profiles predicted in the experiments with various *R* and *G* (see circles and crosses in Fig.4) are of the same magnitude as the deviations between restored and predicted LWC profiles.

5. CONCLUSIONS

The new scheme for estimating cumulus cloud thermodynamic properties is proposed. The scheme takes into account the terminal size and deformation of small cumulus clouds. It allows one to consider the mixing between cumulus cloud and environment almost explicitly and to resolve the cumulus vertical structure more adequately, representing the cloud by the population of particles elevated from various levels.

6. ACKNOWLEDGEMENTS

This research was sponsored by INTAS grant 96-2074. Numerical experiments were performed during the visit to Foundation for Meteorology and Hydrology (FUNCEME), Ceara State of Brazil. We would like to thank the Mesoscale Group of FUNCEME for access to the RAMS software.

7. REFERENCES

Anthes R.A.,1977: A cumulus parameterization scheme utilizing a one-dimensional cloud model. Mon.Wea. Rev., , v. 105, 270-286.

Hicks E., Pontikis C. and Rigaud A., 1990: Entrainment and mixing processes as related to droplet growth in warm midlatitude and tropical clouds. J. Atm. Sci., 47, 1589- 1618.

Mostovoi G.V., 1999a: Numerical modeling of cumulus humilis clouds for their parameterization in large-scale atmospheric models. Met. & Hydrology (in Russian), 11, 13-23.

Mostovoi G.V., 1999b: Numerical modeling of a moist rising thermal: application for small cumuli parameterization. Res. Activities in Atm. & Oceanic modelling, Rep. N 28, TD N942, 4.17-4.18.

Mostovoi G.V., 1997: Two-dimensional Lagrangian model of a rising thermal:application for a liquid water content spatial variability of a warm cumulus cloud. Atm. Res., 43, 233-252.

Pielke R.A. et al., 1992: A comprehensive meteorological modeling system - RAMS. Met. Atmos. Phys., 49, 69-91.

Saunders P.M., 1961: An observational study of cumulus. J. Meteor., 18, 451-467.

Tiedtke M., 1989: A comprehensive mass flux scheme for cumulus parameterization in large-scale models. Mon. Wea.Rev., 117, 1779-1800.

PHYSICALLY-BASED TWO-MOMENT BULK-WATER PARAMETERIZATION FOR WARM CLOUD MICROPHYSICS

J.-P. Chen, S.-T. Liu and M.-H. Luo

Department of Atmospheric Sciences, National Taiwan University

1. INTRODUCTION

Traditional (Kessler-type) bulk-water parameterization schemes divide the water substance in cloud into water vapor, cloud drops, raindrops, and a few more categories for the ice-phase particles (Kessler, 1967; 1969). The conversion rates of water between different categories are derived either empirically or theoretically into rather simple forms. Because of their computation efficiency, such parameterization schemes have been widely applied in mesoscale cloud models (e.g. Tripoli and Cotton, 1982; Lin et al., 1983). However, because of their inherent weakness, traditional bulkwater parameterization schemes inevitably have critical limitations. First of all, in order to derive the conversion rates theoretically, a fixed form of particle size distribution (such as the Marshal-Palmer or log-normal distributions for raindrops) must be assumed. In reality, the size distribution may deviate significantly from the assumed functional forms either in time or space. The specification of particular functional forms necessary put artificial constraint on the conversion rates. Another important limitation stems from the omission of particle number concentration in many bulkwater schemes. Without number concentrations, these schemes cannot properly resolve processes such as the raindrop breakup or obtain parameters such as the effective radius.

In this study we developed a new bulkwater parameterization scheme for warm cloud microphysics following the statistical approach of Lee (1989; 1992). Lee's method groups the results (mixing ratios and conversion rates) from a detailed (multi-bin) cloud microphysical model into much less number of categories in a way similar to that of the traditional bulkwater schemes. The formulas of bulk conversion rates can be obtained by a regression analysis of the results from the detailed model, then expressing them in terms of the moments of the bulk species. In this way, no assumptions on the drop size distribution are necessary. Such a parameterization scheme is physically based, with accuracy approximate the detailed models and yet comparable in computation efficiency to the traditional bulk-water schemes. However, Lee (1989) provided parameterizations for only one moment of the bulk categories -- the mixing ratios. In this study, we built a set of parameterization scheme that considers not only the mixing ratio but also the number concentration of cloud drops and raindrops.

Corresponding author's address: Professor Jen-Ping Chen, Department of Atmospheric Sciences, National Taiwan University, No. 61, Ln. 144, Sec. 4, Keelung Road, Taipei, Taiwan 106, R. O. C.; E-mail: jpchen@water.as.ntu.edu.tw

2. METHOD

Developing parameterizations following Lee's (1989) statistical approach requires a large data set generated from a detailed microphysical model. Since the accuracy of the parameterization scheme is limited by the preciseness of the data set, it is essential to use a microphysical model that can realistically simulate the evolution of cloud particle size spectra under all kinds of conditions. Here we use the multi-component model of Chen and Lamb (1994, 1999) which treats the microphysical processes with great details. In this model cloud particles are classified into many categories (bins) according to not only the water mass but also the solute mass. For this study we describe the drop spectrum with 45 bins in both the water and solute components. A method-of-moments type scheme is used to ensure number and mass conservation, as well as to minimize numerical diffusion. The warm cloud processes included are the activation of cloud drops, drop growth by vapor diffusion, collision coalescence and breakup.

Similar to the traditional bulkwater schemes, we categorize liquid-phase cloud particles into two bulk categories -- cloud drops and raindrops. Here, the 50-μm radius is chosen as the separation criterion between cloud drops and raindrops in the detailed model. The distinction between cloud drops and interstitial aerosol particles is not straightforward. Theoretically, one should be able to use the critical radius of the Köhler curves to determine if a CCN is activated into cloud drops. However, the largest CCN may never reach their critical radii and remain as "giant haze drops," and yet they are normally the largest drops during the early stage of cloud formation and act as rain embryos (Chen and Lamb, 1999). So, we have relaxed the criterion by treating drops with radius greater than either 2.5 μm or their critical radius as cloud drops.

To convert the results of the detailed model into bulkwater parameterizations, we need to group particles in the 45 x 45 bins of the detailed model into two coarse categories defined above. The key work of this bulk parameterization scheme is to obtain formulas for the conversion rates between the bulk categories. So the rates of all transformations between categories in detailed model are also classified accordingly.

Besides using a more detailed microphysical model, we also apply a somewhat different principle in developing the parameterization than Lee's (1989) method. That is, we minimize the level of parameterization by analyzing the theoretical equations and segregate out parameters that are independent of the bulk parameters (see Table 1 for variable definition). Let's take the equation of diffusion growth (process *1* in

Table 2) for example:

$$\left.\frac{dm}{dt}\right|_{dif} = \frac{\Delta S}{A} r \qquad (1)$$

where m is drop mass, ΔS is the supersaturation, A is a function of air temperature and pressure, and r is drop radius (cf. Pruppacher and Klett, 1997, p. 511). The group conversion rate for all cloud-drop bins in the detailed model is then

$$\theta_{C,dif} = \frac{1}{\rho_a}\sum_i n_i \left.\frac{dm_i}{dt}\right|_{dif} = \frac{\Delta S}{\rho_a A}\sum_i n_i r_i \equiv B \cdot C \qquad (2)$$

where ρ_a is air density, i is the bin index, n is the number concentration, $B \equiv \Delta S / (\rho_a A)$, and $C \equiv \Sigma n_i r_i$. One can see that C is a function of the droplet properties only, whereas B is independent of them. So a modified bulk conversion rate can be expressed as a function of the bulk properties N_C and Q_C without carrying B in the parameterization:

$$\theta'_{C,dif} \equiv \theta_{C,dif} / B = C \approx f_1(N_C, Q_C), \qquad (3)$$

where $f_1(N_C, Q_C)$ is the parameterization (fitting function) we intend to get. Note that ΔS and A actually change slightly with particle size because of the solute and curvature effects (for ΔS) and the gas-kinetic effect (for A), but the minor dependence can be absorbed into $f_1(N_C, Q_C)$. Equation (3) can also be used for the diffusion growth of raindrops (process 2). The other relevant process we considered is the conversion of cloud drops into raindrops by diffusion growth (process 3), which turned out to be insignificant for most cases.

The bulk conversion rate for the collision-coalescence processes can be written as:

$$\theta_{X,col} \approx f(N_Y, N_Z, Q_Y, Q_Z), \qquad (4)$$

where X, Y, and Z represent the resulted drop group, the collector drop group, and the collected drop group, respectively. The five combinations of X, Y and Z for the collision processes are shown in Table 2. Note that a combination of processes 3 and 8 may represent the "autoconversion" process that commonly used in the traditional bulkwater schemes in describing the generation of raindrops from cloud drop. However, the former process is ignored here because it is insignificant compared with the later in all of our tests.

After establishing the basic mathematical forms of the conversion rates, the parameters Q, θ, N and ν are generated using a Lagrangian air parcel model with Chen and Lamb's (1994) microphysics. A curve-fitting software is then used to obtain the parameterization function f. Scenarios with varying updraft speeds, CCN distributions and cloud-base temperature and pressure are designed to increase the range of applicability and statistical meaning of the results.

Table 1: Variable names for the bulkwater properties and conversion rates: Q represents mixing ratio and N is the number concentration; $\theta \equiv dQ/dt$ and $\nu \equiv dN/dt$ are their conversion rates. The subscripts V, C and R stand for water vapor, cloud drops and raindrops.

	mixing ratio		number concentration	
	bulk property	conversion rate	bulk property	conversion rate
water vapor	Q_V	θ_V		
cloud drops	Q_C	θ_C	N_C	ν_C
raindrops	Q_R	θ_R	N_R	ν_R

Table 2: Microphysical processes for the interaction between bulkwater types Y and Z, and the resulted bulkwater type X.

	microphysical process	X	Y	Z
1	diffusion growth of cloud drops	C	C	V
2	diffusion growth of raindrops	R	R	V
3	raindrop formation due to the diffusion growth of cloud drops	R	C	V
4	cloud drop self-collection	C	C	C
5	raindrop formation due to the coalescence of cloud drop	R	C	C
6	raindrops collect cloud drops	R	R	C
7	raindrop self-collection	R	R	R
8	raindrop collision breakup	R	R	R

3. PARAMETERIZATION

In this section we will first demonstrate why the number concentration is an important parameter to consider. Figure 1 shows the relationship between the conversion rate $\theta_{C,dif}$ and cloud drop mixing ratio Q_C for three different updraft speeds (U = 0.5, 1.0 and 1.5 m s^{-1}). It is clear that the relationship between $\theta_{C,dif}$ and Q_C is not one to one. From Eq. (1) we can see the reason behind it: the diffusion growth rate of cloud drops is proportional to their number concentrations and radii, not their masses. Furthermore, both the drop number concentration and radii change with time during cloud formation, and their product vary differently with the mixing ratio. Let us take the outer most curve (U = 1.5 m s^{-1}) in Fig. 1 to describe the evolution history of the two parameters. Both the mixing ratio (Q_C) and growth rate ($\theta_{C,dif}$) of cloud drops increase with time during the earlier stage (the upper portion of the curve) then decreases with time during the later stage (the lower portion of the curve) but with different magnitudes. Initially (after the activation stage), the number concentration of cloud drops remain relatively unchanged, so the growth rate increases with time because the drops are getting bigger. After a while, however, the growth rate does not increase as rapidly because of the inverse proportionality of "drop-size growth rate" with the drop size itself. The coalescence among the cloud drops causes a decrease in their number concentration and an increase of drop sizes, but with much slower rates. This tends to reduce the growth rate $\theta_{C,dif}$ while the mixing ratio is still increasing. Later, raindrops form and their accretion of cloud drops is to significantly reduce the number concentration n_i but not the drop size r_i in Eq. (1), thus causing a decrease of Q_C and $\theta_{C,dif}$ at about the same rates. So the evolution history presents itself as a

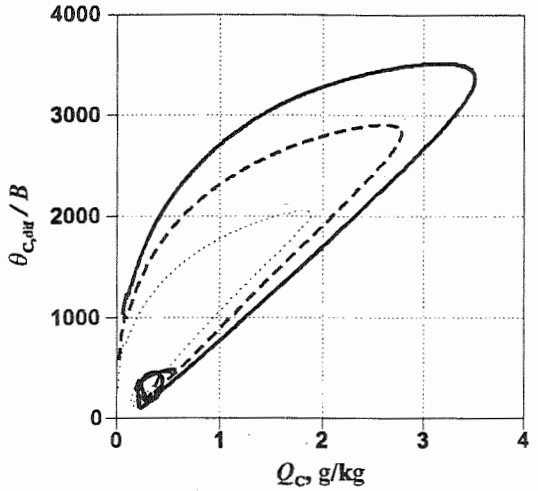

Figure 1: Relationship between the conversion rates and mixing ratios for the diffusion growth of cloud drops from a parcel simulation. The three curves (from outside in) correspond to updraft speeds of 0.5, 1.0 and 1.5 m s^{-1}.

straight line that is rather different from the track during the initial stage. Note that the tracks in Fig. 1 seem to be making circles toward the end. This is due to the reactivation of interstitial (previously unactivated) aerosol particles into new cloud drops, which repeats the process but with a much faster pace. Such an evolution cycle cannot be resolved with a one-moment scheme.

The best fitting of $\theta_{C,dif}$ as a function of Q_C gives a correlation (r^2) of 0.79 only, which reflects the inherent limitation of the one-moment parameterization. Parameterizations for other processes also have similar problems. Improvement can be achieved by considering a second moment of the drop size distribution -- the number concentration. Figure 2 shows the conversion rates $\theta_{C,dif}$ (same as those in Fig. 1)

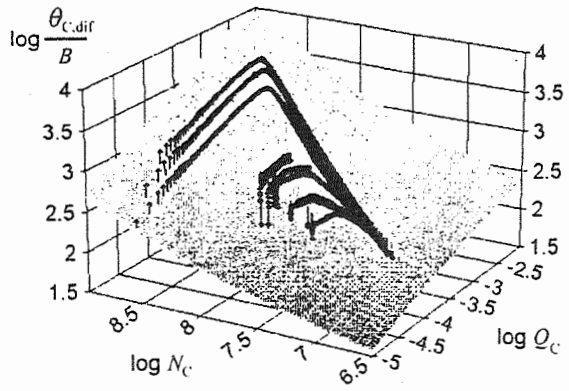

Figure 2: Conversion rate $\theta_{C,dif}$ plotted as a function of drop mixing ratio and number concentration. The differences between model results (diamond symbols) and regression results (shaded surface) are indicated by the vertical bars.

Table 3: Parameterization for the bulk conversion rates of mixing ratio (f) and number concentration (g), as well as the correlation coefficient of the fitting. The units for the variables are: Q in kg-H_2O/kg-air, N in #/kg-air, R in m, θ in kg-H_2O/kg-air/s, ν in #/kg-air/s, and B in m^2/s*kg-H_2O/kg-air.

	fitting formula	r^2
f_1	$\log\theta/B = a + b\log R_C + c\exp(-\log N_C)$	0.989
f_2	$\log\theta/B = a + b\log Q_C + c/(\log N_C)^{0.5}$	0.994
f_5	$\log\theta/N_C^2 = a + b/(\log R_C)^2 + c/(\log N_C)^2$	0.962
f_6	$\log\theta/(N_C N_R) = a + b\log R_C + c(\log R_R)^3$	0.979
g_4	$(\log\nu/N_C^2)^{-1} = a + b\log R_C + c(\log N_C)^3$	0.964
g_5	$\log\nu/N_C^2 = a + b\log R_C + c(\log N_C)^3$	0.918
g_6	$\log\nu/(N_C N_R) = a + b\log R_C + c\log R_R$	0.953
g_7	$\log\nu = a + b\log Q_R + c\log N_R \ln(\log N_R)$	0.992
g_8	$\nu^{-1} = a + b/Q_R^2 + c/N_R^2$	0.920

plotted against both the mixing ratio and number concentration of cloud drops. The fitting function $f_1(N_C, Q_C)$ in Eq. (3) is shown as the shaded surface. By applying an additional moment, the model results can now be fitted quite well with a much improved correlation coefficient of $r^2 = 0.97$. The results can be improved a bit further ($r^2 = 0.99$) if one use the parameter R_C to replace Q_C, where $R_C \equiv (Q_C/N_C)^{1/3}$ represents the mass averaged mean radius.

The two-moment parameterizations for other warm cloud processes are obtained in a similar way. Table 3 is a list of the regression parameterizations and correlation coefficients that we have analyzed so far. The coefficients for these formulas are given in Table 4. Note that we have ignored process 3. Also, processes 7 and 8 do not cause a change in mixing ratio (i.e., cannot be resolved with a one-moment scheme), whereas processes 1 and 2 do not alter the number concentration. The high correlation coefficients shown in Table 3 indicate that the statistical two-moment parameterization should produce bulkwater properties very close to those of the detailed model.

Table 4: Coefficients for the formulas listed in Table 3. All variables are expressed in mks units.

	a	b	c
f_1	0.99540139	1.1218478	3.8242432E2
f_2	0.03910668	4.3109146E-3	7.2155758
f_5	-5.0526467E1	4.1804354E2	-3.4968642E2
f_6	-1.0393636	3.9713803	0.1457898
g_4	-9.7815444E-2	-1.6890287E-2	8.7783931E-5
g_5	-3.5058222	1.215388E1	-0.059877085
g_6	-2.1008384	-1.8863793	0.93778732
g_7	-1.0578732	0.80296541	0.86316533
g_8	1.0783195E-3	1.4220864E-7	2.1601144E5

4. DISCUSSION AND CONCLUSION

The statistical-physical parameterization applied in this study produced well-behaved regression formulas when two moments of the bulkwater (i.e., mixing ratio and number concentration) are taken into account and when bulkwater-unrelated parameters are excluded from the parameterizations. Such a physically sound and easy to use parameterization scheme could be useful for improving the microphysical representation of mesoscale and cloud-scale models.

Based on the high correlation coefficients shown in Table 3, it is reasonable to assume that our scheme could produce results approximate those from the detailed microphysical model. However, we still need to do more tests by applying this scheme in different models to ensure its computation integrity. We shall first design a more rigorous set of scenarios to generate and test the parameterization formulas. Then the parameterization scheme will be tested against existing bulkwater parameterization schemes and the detailed microphysical model of Chen and Lamb (1994).

Some of the formulas in Table 3 are not in their simplest forms, and will be reorganized if possible. In addition, Table 3 does not include the production of cloud drops by CCN activation. To derive parameterizations for this process, the size distribution and chemical properties of CCN is needed. If these parameters are available, then the number concentration produced during activation can be derived directly by calculating the supersaturation. Our other future tasks include the parameterization for ice-phase particles and aerosol particles, as well as the group fall speeds of the bulkwaters.

Acknowledgments: This research was supported by the National Science Council under Grant NSC 89-2111-M-002-014.

REFERENCE

Chen, J-.P. and D. Lamb, 1994b: Simulation of cloud microphysical and chemical processes using a multicomponent framework, Part I: Description of the microphysical model. *J. Atmos. Sci.*, **51**, 2613-2630.

Chen, J-.P., and D. Lamb, 1999: Simulation of cloud microphysical and chemical processes using a multicomponent framework. Part II: Microphysical evolution of a wintertime orographic cloud. *J. Atmos. Sci.*, **56**, 2293-2312.

Kessler, E., 1967: *On the Continuity of Water Substance.* National Severe Storms Laboratory, Norman, Okla., ESSA Technical Memorandum IERTM-NSSL 33.

Kessler, E., 1969: On the distribution and continuity of water substance in atmospheric circulation. *Meteorol. Mongraph*, Amer. Meteorol. Soc., **10**, 84 pp.

Lee, I. Y., 1989: Evaluation of cloud microphysics parameterizations for mesoscale simulations. *Atmos. Res.*, **24**, 209-220.

Lin, Y.-L., R. D. Farley, and H. D. Orville, 1983: Bulk parameterization of the snow field in a cloud model. *J. Climate Appl.*, **22**, 1065-1092.

Pruppacher, H. R., and J. D. Klett, 1997: *Microphysics of clouds and Precipitation.* Kluwer Academic Publishers, Dordrecht/Boston/London, 954 pp.

Tripoli, G. J., and W. R. Cotton, 1982: The Colorado State University three-dimensional cloud/mesoscale model-1982, Part I: General theoretical framework and sensitivity experiments. *J. Rech. Atmos.*, **16**, 185-220.

EVALUATION OF THE KAIN-FRITSCH CUMULUS PARAMETERIZATION THROUGH HIERARCHICAL MODELING OF TROPICAL CONVECTIVE SYSTEMS

Changhai Liu, Mitchell W. Moncrieff and Wojciech W. Grabowski

National Center for Atmospheric Research, Boulder, CO

1. INTRODUCTION

The evaluation of convective parameterizations has traditionally used either a semi-prognostic approach or a fully prognostic approach. In the former, observed estimates of the large-scale tendencies, surface fluxes and radiation heating drive a one-time-step prediction of the convective tendencies, and the instantaneous estimates of heating and drying by cumulus ensembles are compared to the budget residuals diagnosed from observations. This approach has serious deficiencies, especially in the tropics where the convective tendencies are residuals of two dominant terms in the budget equations. Consequently, a seemingly good comparison between the predicted and observed apparent heat and moisture sources may still have significant errors in the local tendencies. Also, feedbacks beyond one time step are not permitted, so the corresponding deficiencies cannot be uniquely identified. There is an additional problem in validating parameterization schemes designed for mesoscale numerical models; that is, the resolved rainfall can be comparable in amount to the parameterized, whereas in the semi-prognostic approach it is assumed to be generated by the parameterization alone.

In the fully prognostic approach, the parameterization is applied in a numerical weather prediction model or a climate model, whose performance is assessed by making comparisons with observations. However, model performance depends as much on surface fluxes, subgrid diffusion, radiative fluxes, boundary conditions and numerical discretization, as on convective parameterization. This makes it difficult, it not impossible, to isolate errors in the convection scheme.

Recognizing the deficiencies in the traditional approaches, Liu et al. (1999, 2000) developed a hierarchical approach that uses the same nonhydrostatic numerical code for: (i) cloud-resolving simulation; (ii) coarse-grid simulations in which convection is explicit and (iii) coarse-grid simulations in which convection is parameterized. Parameterization schemes (in iii) are evaluated against the cloud-resolving, explicit modeling and observational analysis (in i and ii). Using this approach, we evaluated the Kain and Fritsch (1993) convective parameterization in simulations of cloud systems observed during December 19-26 1992 period in TOGA COARE.

Corresponding author's address: Changhai Liu, National Center for Atmospheric Research, Boulder, Co 80307, U. S. A.; E-Mail: chliu@ucar.edu

2. NUMERICAL MODEL

We use the two-dimensional Eulerian version of the nonhydrostatic Eulerian/semi-Lagrangian model (Smolarkiewicz and Margolin 1997). The computational domain is 900km x 30km with a constant vertical grid length of 300 m. The boundary conditions are periodic at lateral boundaries and free-slip at top and bottom of the domain. The model physics includes a bulk warm rain parameterization and a two-class ice parameterization, a radiative transfer parameterization, a bulk surface flux algorithm and the Kain-Fritsch cumulus parameterization. The model is driven by the evolving large-scale forcing for temperature and moisture, and evolving large-scale horizontal winds averaged over the COARE Intensive Flux Array (IFA).

Two categories of simulations are conducted. One is the cloud-resolving simulation having a 2-km grid length (CRM), and another is identical to the first except for a 15-km grid length and the application of the Kain-Fritsch parameterization (IMP).

3. CLOUD SYSTEM REALIZATIONS

The Hovmoller diagram of surface precipitation in Fig. 1 shows strong convective activity on 20, 21, 22 and 24 December and weak or no convection during the remaining period. These features are broadly consistent with radar observations. By comparison, the parameterization tends to produce shorter-lived and intermittent convection. In addition, some small-scale features in CRM do not appear in IMP because of the inadequate resolution.

In spite of the systematic cold bias, the domain- and time-averaged bias profiles in temperature exhibit similar vertical distribution between the two simulations, but significant differences exist at the surface and above 13 km with a 2K-maximum at 16 km (Fig. 2a). The respective bias in water vapor has similar patterns but also notable differences (Fig. 2b). For instance, IMP generates a moister bias below 4 km and a drier bias above.

The surface fluxes and precipitation have similar evolutions in CRM and IMP and are comparable to observations (Fig. 3a, b). The 8-day mean latent heat flux is 159 W m^{-2} in IMP, which is slightly larger than in CRM (156 W m^{-1}) and the satellite estimate (150 W m^{-1}). The mean sensible heat flux reaches 42 W m^{-1} in IMP and 34 W m^{-2}, which is significantly greater than either the satellite-derived value (11 W m^{-2}) or the buoy measurements (16 W m^{-2}). The poor sensible heat flux prediction is presumably a consequence of the cold temperature bias near

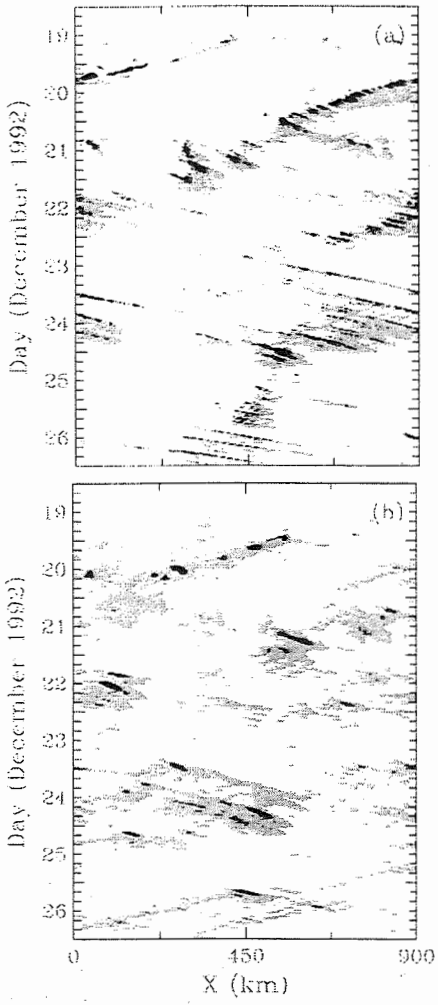

FIG. 1. Time-space plot of surface precipitation for (a) the 2-km explicit simulation (CRM) and (b) the 15-km simulation with parameterized convection (IMP). The light and dark shading correspond to the intensity greater than 1 and 10 mm h^{-1}, respectively.

the surface.

The temporal variability and mean-value of the precipitation in CRM and IMP are in good agreement with the satellite-derived estimate during the weak forcing episodes (Fig. 3b). In the satellite estimate, significant peaks occur during the strong forcing episodes on 20, 22 and 24 December, and therefore its mean value is about 20% too large. In contrast to the cloud-resolving simulation, the precipitation in IMP contains both grid-scale (explicit) and subgrid (parameterized) contributions. The parameterized part accounts for about half the total rainfall with a larger contribution during the weak forcing periods.

Apart from the spin-up period, the modeled OLR time series (Fig. 4) resembles observations. The 8-day average is 194 W m^{-2} in CRM, and 178 W m^{-2} in IMP. The difference is correlated with the more extensive cirrus in IMP (see Fig. 5). The cloud fraction profiles also suggest that the parameterized convection penetrates to altitudes higher than the resolved convection.

4. PARAMETERIZATION ISSUES

The agreement between the simulations and observations suggests an overall capability of the Kain-Fritsch scheme to represent tropical convection. However, important deficiencies do exist. Of note are the upper-level cold bias arising from the parameterized cooling, the low-level moist bias and the cirrus cloud overprediction. For the most part, we attribute these uncertainties to how the convective mass flux is represented in the parameterization by a single penetrative entraining plume model.

Figure 6 compares the profiles of the mass fluxes derived from the parameterization in IMP with the explicit values provided by CRM. The mass fluxes in active convective cores are distinguished from weak ascent and descent in the stratiform region and from gravity waves by requiring the vertical velocity to exceed 1 m s^{-1} and the total condensate to exceed 0.01 g kg^{-1}.

The updraft mass flux in CRM has a significant maximum in the 2-5 layer produced primarily by two dominant cumulus types – penetrative cumulonimbus and moderately deep convection with tops around the melting level (i.e., cumulus congestus). The parameterized convective

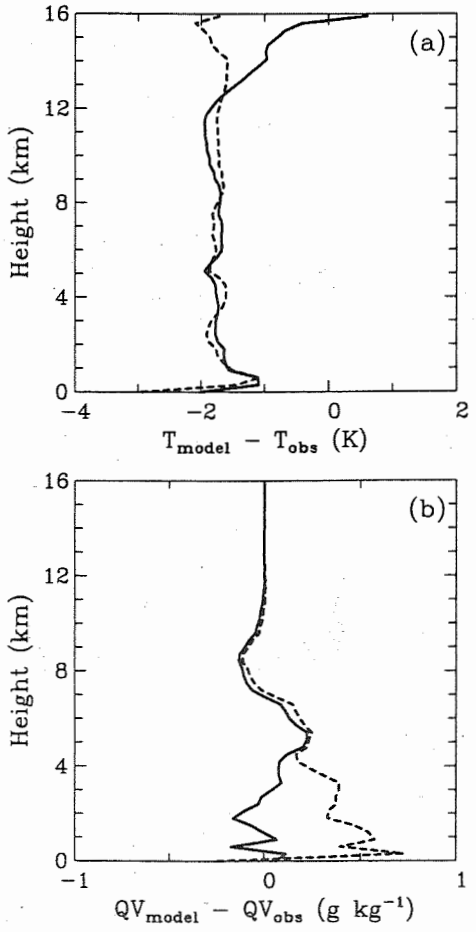

FIG. 2. Profiles of the domain- and time-averaged bias (model minus observation) for (a) temperature and (b) water vapor mixing ratio in CRM (solid) and IMP (dashed).

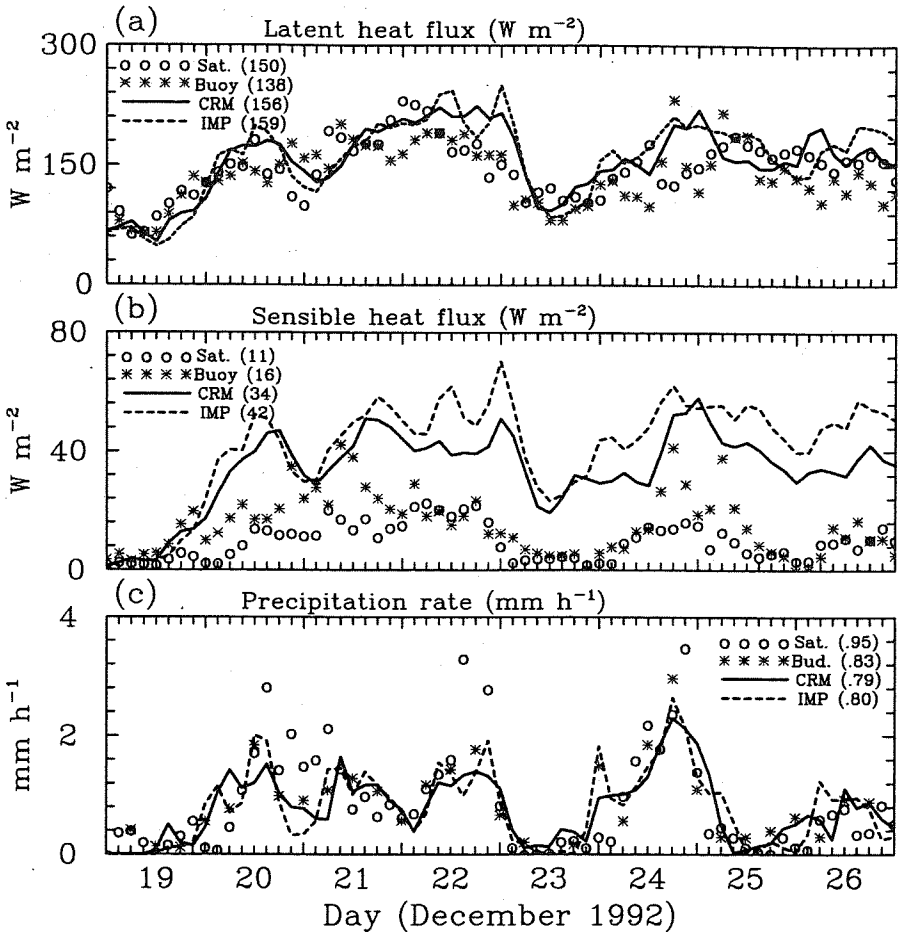

FIG. 3. Evolution of (a) domain-averaged surface latent heat flux, (b) sensible heat flux and (c) precipitation in CRM (solid) and IMP (dashed). Circles represent the satellite observation (Curry et al. 1999), and stars represent the buoy observation in (a) and (b) and the budget estimate in (c) (Lin and Johnson 1996). Numbers in the brackets are mean values

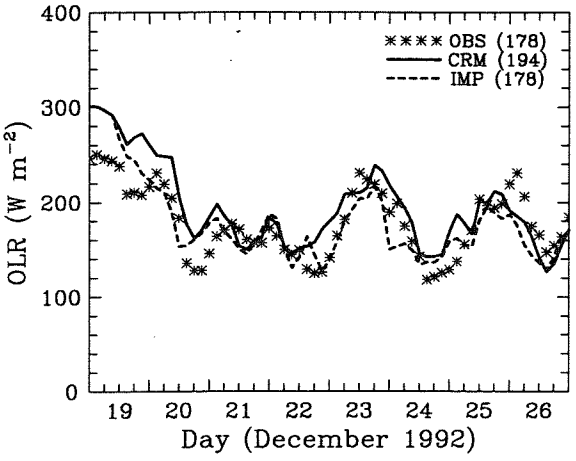

FIG. 4. Evolution of the domain-averaged OLR in CRM (solid) and IMP (dashed). Stars represent observations (Rossow and Zhang 1995), and numbers in the brackets are mean values.

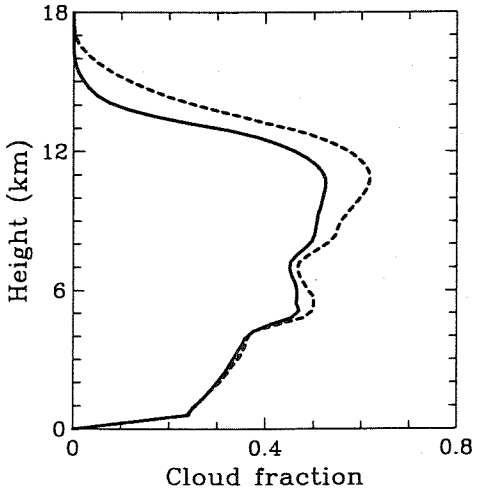

FIG. 5. Profiles of (a) the domain- and time-averaged cloud fraction in CRM (solid) and IMP (dashed).

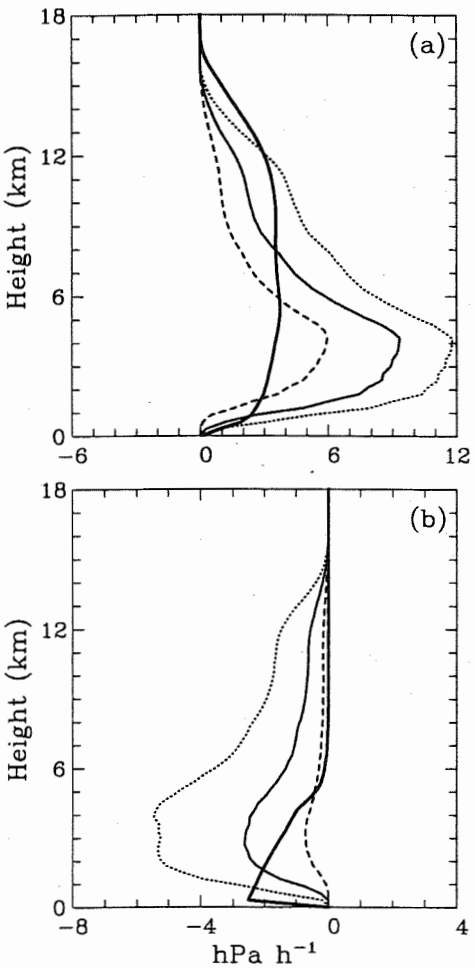

FIG. 6. (a) updraft and (b) downdraft mass fluxes in CRM when the condensate exceeds 0.01 g kg^{-1} and the absolute value of vertical velocity exceeds 1 m s^{-1} (solid), 2 m s^{-1} (dashed) and 0.5 m s^{-1} (dotted). The thick solid line represents the parameterized mass flux in IMP.

mass flux in IMP is much more uniform in the vertical and substantially smaller (larger) below (above) 8 km than in CRM. Only the penetrative cumulonimbus type is parameterized by the single entraining plume in the Kain-Fritsch scheme, so the absence of the cumulus congestus most likely contributes to the overprediction of low-level moisture. The large parameterized mass flux at upper levels imply deeper and stronger penetrative convection and a correspondingly larger moisture detrainment. We conclude that the overshoot-generated cooling in the parameterization is responsible for the cold bias. The attendant excessive detrainment is responsible for the overprediction of cirrus.

The convective downdrafts in CRM extend throughout the troposphere and the mass flux has a distribution similar to the updraft but of smaller magnitude. In IMP the parameterized downdraft mass flux is concentrated below 6 km and is smaller except in the lowest one kilometer where it is affected by the threshold on downward vertical velocity.

The relative humidity in the downdraft also affects the convective parameterization. The averaged relative humidity in CRM ranges from more than 90% near the melting level to less than 80% near the surface. In the Kain-Fritsch parameterization, a minimum 90% is used for the relative humidity in downdrafts. Consequently, the parameterized downdrafts will be moister than those in CRM. Sensitivity tests show that the low-level moist bias is reduced by lowering the minimum relative humidity.

5. CONCLUSIONS

We examined issues involving the Kain-Fritsch parameterization by employing a hierarchy of two-dimensional simulations of cloud systems during December 19-26, 1992 of TOGA COARE. Despite of the overall favorable comparison among the simulations and observations, specific shortcomings of the Kain-Fritsch scheme are identified. We quantified these biases in terms of the convective mass flux and attendant detrainment/entrainment.

A more realistic representation of middle-level detrainment by cumulus congestus is ultimately required. This suggests either a computationally expensive spectral cloud model or a more realistic model of detrainment/entrainment *and* aspects of convective organization. An improved treatment of downdrafts is also needed. In the short term, empirical modifications are advocated: (i) the cirrus cloudiness overprediction could be addressed by using an increased terminal velocity for ice particles; (ii) the lower troposphere moist bias could be alleviated by employing a lower threshold on the relative humidity of the downdraft (the CRM results suggest a range from 80% to 90%); (iii) the overshooting cloud tops would also be alleviated by increasing the entrainment rate; and (iv) an increase in midtropospheric detrainment would at least partly represent the cumulus congestus cloud type evident in the cloud-resolving simulations and observations.

6. REFERENCES

Kain, J. S., and J. M. Fritsch, 1993: Convective parameterization for mesoscale models: The Kain-Fritsch scheme. The representation of cumulus convection in numerical models. K. A. Emanuel and D. J. Raymond, Eds., Amer. Meteor. Sco., 246pp.

Liu, C.-H., M. W. Moncrieff, and W. W. Grabowski, 1999: Hierarchical modeling of tropical convective systems with explicit and parameterized approaches. Quart. J. Roy. Meteor. Soc., submitted.

———, ———, and ———, 2000: Explicit and parameterized realizations of convective cloud systems in TOGA COARE. Mon. Wea. Rev., submitted.

Smolarkiewicz, P. K., and L. G. Margolin, 1996: On forward-in-time differencing for fluids: an Eulerian/Semi-Lagrangian nonhydrostatic model for stratified flows. Atmos. Ocean Special,, 35, 127-152.

PARAMETERIZATION OF TRANSIENT SHALLOW CONVECTION IN THE CCCMA GENERAL CIRCULATION MODEL

K. von Salzen and N.A. McFarlane

Canadian Centre for Climate Modelling and Analysis
University of Victoria, Victoria, British Columbia, V8W 2Y2, Canada

1. INTRODUCTION

Nonprecipitating shallow cumulus clouds contribute considerably to the mixing of heat, moisture, and tracers in the trade wind regions. The large impact of these clouds on the large-scale atmospheric dynamics requires to parameterize these effects in General Circulation Models (GCMs). In order to account for shallow convection in the GCM of the Canadian Centre for Climate modelling and analysis (CCCma), a new parameterization of transient shallow convection is being developed.

A major motivation for the development of the parameterization was that observations show a striking tendency for air mixtures sampled in clouds to fall along a straight line connecting environmental air near cloud base with air at altitudes and above those at which the measurements where made (e.g., Paluch 1979). Parameterizations assuming laterally entraining plumes, which are currently in use in many models, are usually not consistent with these observations.

The parameterization proposed here uses a bulk representation for sub-grid scale cloud ensembles. It is based on the assumption that the cloud life cycle comprises two phases. In the initial growth phase the cloud grows by ascend of positively buoyant air from the mixed layer below the cloud. The physical properties of the rising air parcels are modified by entrainment of environmental air at the cloud top and in addition by entrainment at the lateral boundaries of the cloud. While the mixing events are assumed to be episodic in nature, a statistical approach for the cloud properties is introduced. The growth phase is terminated by the collapse of the cloud. During the infinitesimal collapse phase, the air in the cloud is detrained into the environment (e.g., Fraedrich 1973, Cho 1977).

This study presents the fundamental theoretical concept of the proposed parameterization. Currently, first tests and applications of the parameterization are being performed using results for the large-scale heat and moisture budgets over the tropical Atlantic Ocean during Phase 3 (22 to 30 June 1969) of the Barbados Oceanographic and Meteorological Experiment (BOMEX).

Corresponding author's address: Knut von Salzen, Canadian Centre for Climate Modelling and Analysis, University of Victoria, PO Box 1700, STN CSC, Victoria, British Columbia, V8W 2Y2, Canada; E-mail: KnutvonSalzen@ec.gc.ca.

2. MODEL DESCRIPTION

The budget equations for mass and a general scalar χ are given using the Boussinesq approximation:

$$\rho \frac{\partial a}{\partial t} = -\frac{\partial}{\partial z}\left(\rho a w_c\right) + E - D \quad , \tag{1}$$

$$\rho \frac{\partial}{\partial t}\left(a\chi_c\right) = -\frac{\partial}{\partial z}\left[\rho a\left(w_c\chi_c + \overline{w'\chi'}^c\right)\right] + E\chi_e - D\chi_c + \rho a S_\chi \quad . \tag{2}$$

In (1) and (2) ρ is the air density, a is the fractional cloudiness, w_c is the mean vertical velocity in the cloud, E and D are the entrainment and detrainment rates, χ_c and χ_e are the mean mixing ratios of χ in the cloud and in the environment, and the term S_χ represents the sources and sinks if χ is a non-conservative property. Subgrid-scale fluxes $\overline{w'\chi'}^c$ in the cloud are calculated from the mean cloud properties:

$$\overline{w'\chi'}^c = \alpha w_c\left(\chi_c - \chi_e\right) \quad , \tag{3}$$

where the overbar denotes an average over the cross-sectional area of the cloud. The parameter α depends on the distribution of the in-cloud properties and will be specified in the following.

Conserved moist thermodynamic variables considered in the parameterization are the total water mixing ratio q and the moist static energy $h = c_p T + L_v q_v + gz$, where c_p refers to the heat capacity of water vapor, T to the temperature, L_v to the latent heat of vaporization, q_v to the water vapor mixing ratio, g to the gravitational acceleration, and z to the hight above ground. In addition to q and h, the kinetic energy $k = \frac{1}{2}w^2$ is considered. For k, the source term in (2) has

the form

$$S_k = \frac{B_c w_c + \overline{B' w'}^c}{1+\gamma} \quad ,$$

with the buoyancy B. The factor $\gamma = \frac{1}{2}$ accounts for the effects of drag and pressure gradients in the cloud (Simpson and Wiggert 1969).

It is assumed that mixing of h, q, and k can be treated with a cloud property independent mixing parameter α according to (2) and (3). The kinetic energy in the environment is approximated by $k_e = 0$.

The buoyancy is given as a function of the density temperature T_ρ of the air in the cloud and the density temperature $(T_\rho)_e$ of the environmental air:

$$B = g\frac{T_\rho - (T_\rho)_e}{(T_\rho)_e} \quad , \tag{4}$$

with the density temperature given by (e.g., Emanuel 1994)

$$T_\rho = T\frac{1+q_v/\varepsilon}{1+q} \quad ,$$

and $\varepsilon = R_d/R_v$, with the gas constants R_d and R_v of dry air and of water vapor.

To solve (1) and (2), the fractional cloudiness a is defined as the difference of two heaviside functions $\mathcal{H}$,

$$a = a_0\left[\mathcal{H}\left(\frac{t-t_\star}{\tau}\right) - \mathcal{H}\left(\frac{t-\tau}{\tau}\right)\right] \quad , \tag{5}$$

where $t_\star$ refers to the time at which the cloud top reaches a certain hight above the cloud base and the cloud life time τ after which the cloud collapses. The parameter a_0 is determined by the solution of (1) and (2).

We further assume that the entrainment occurs both at the cloud top and at the lateral boundaries of the cloud. The detrainment occurs only while the cloud collapses:

$$E = E_0\,\delta\left(\frac{t-t_\star}{\tau}\right) + \lambda M_c \quad , \tag{6}$$

$$D = D_0\,\delta\left(\frac{t-\tau}{\tau}\right) \quad . \tag{7}$$

The parameters E_0 and D_0 depend on a, τ, and α as will be shown later. The contribution of lateral entrainment (second term on the right hand side of 6) is parameterized proportional to the mean vertical mass flux $M_c = \rho a w_c$, with the proportionality factor given by λ.

We finally assume that the properties w, χ are quasi steady in the cloud and in the environment while the cloud grows and that the buoyancy can be expressed in terms of the moist static energy,

$$B \approx \beta\,(h - h_n) \quad . \tag{8}$$

h_n refers to the value of the moist static energy at neutral buoyancy of the air in the cloud. This parameter and the factor β are calculated from (4) at each level in the cloud. While the approximation of B is not essential in the context of the cloud model described here, it considerably simplifies the numerical solution of the equations.

With the assumptions in (5) to (8), solutions of (1) and (2) are obtained using the definitions

$$\tilde{\chi} = \chi_c + \frac{\overline{w'\chi'}^c}{w_c} \quad ,$$
$$M_0 = \rho a_0 w_c \quad .$$

The solutions for budgets of mass and in-cloud properties are then given by

$$\frac{\partial M_0}{\partial z} = \lambda M_0 \quad , \tag{9}$$

$$\frac{\partial \tilde{h}}{\partial z} = \lambda\left(h_e - \tilde{h}\right) \quad , \tag{10}$$

$$\frac{\partial \tilde{q}}{\partial z} = \lambda\left(q_e - \tilde{q}\right) \quad , \tag{11}$$

$$\frac{\partial \tilde{k}}{\partial z} = \frac{\beta}{1+\gamma}\left(\tilde{h} - h_n\right) - \lambda\tilde{k} \quad . \tag{12}$$

Similar equations can be added for passive and reacting chemical constituents, if needed.

Additionally to these solutions, a relation for $t_\star$ is obtained:

$$\frac{\partial t_\star}{\partial z} = \frac{1}{w_c}\left(\frac{1}{1+\alpha}\right) \quad . \tag{13}$$

The cloud life time τ is defined as the time at which the cloud top reaches the height z_t,

$$\tau = \int_{z_b}^{z_t} \frac{\partial t_\star}{\partial z}\,dz \quad , \tag{14}$$

where z_t and the height of the cloud base z_b need to be specified. A consistent approach is to take z_b as the lifting condensation level of the air parcel that initiates the cloud. In the current version of the parameterization, z_t is taken to be the level at which $\alpha = 0$, corresponding to a top-hat profile of the in-cloud properties.

Finally, the parameters E_0 and D_0 in (6) and (7) are given as:

$$E_0 = \frac{M_0}{\tau w_c}\left(\frac{\alpha}{1+\alpha}\right) \quad , \tag{15}$$

$$D_0 = \frac{M_0}{\tau w_c} \quad . \tag{16}$$

Solutions for w_c, χ_c, and α can be obtained after introducing an approach for the distribution of the

subgrid-scale properties in the cloud. Owing to a lack of observations, the in-cloud distributions are highly uncertain and have to be prescribed in a consistent way.

Using the solutions (9) to (13) the effects of cloud on the large scale properties are obtained by integration over τ:

$$\rho\langle\frac{\partial\chi_e}{\partial t}\rangle = -\frac{\partial}{\partial z}\left[\langle M_c\rangle\left(\chi_c - \chi_e\right)\right] + \rho\langle a\rangle S_\chi \quad ,$$

where the bracketed terms ($\langle\ldots\rangle$) refer to time averaged values. For example, for a, the following relation applies:

$$\langle a\rangle = \frac{1}{\tau}\int_0^\tau a\,dt = a_0\left(1 - \frac{t_*}{\tau}\right) \quad .$$

Accordingly, the mean cloud mass flux, entrainment and detrainment rates are given by

$$\begin{aligned} \langle M_c\rangle &= M_0\left(1 - \frac{t_*}{\tau}\right) \quad , \\ \langle E\rangle &= E_0 + \lambda\langle M_c\rangle \quad , \\ \langle D\rangle &= D_0 \quad . \end{aligned}$$

3. CONCLUSIONS

Characteristic features of the parameterization are currently being investigated using prescribed steady vertical profiles of environmental temperature and water vapor mixing ratios. In the future, the parameterization will be tested in simulations with the GCM. For this, a closure for the mass flux at the cloud base will be introduced and tested.

Comparisons of results with results from LES simulations and observations during BOMEX will be presented at the Conference.

4. REFERENCES

Cho, H.-R., 1977: Contributions of cumulus cloud life-cycle effects to the large-scale heat and moisture budget equations. J. Atmos. Sci., 34, 87-97.

Emanuel, K. A., 1994: Atmospheric Convection. Oxford University Press, New York, pp. 580.

Fraedrich, K., 1973: On the parameterization of cumulus convection by lateral mixing and compensating subsidence. Part I. J. Atmos. Sci., 30, 408-413.

Paluch, I. R., 1979: The entrainment mechanism in Colorado cumuli. J. Atmos. Sci., 36, 2462-2478.

Simpson, J.,and V. Wiggert, 1969: Models of precipitating cumlus towers. Mon. Wea. Rev., 97, 471-489.

MICROPHYSICS OF CLEAN AND POLLUTED CLOUDS IN THE INDIAN OCEAN REGION: OBSERVATIONS AND PARAMETERIZATIONS.

Greg M. McFarquhar and Andrew J. Heymsfield

[1]National Center for Atmospheric Research (NCAR)*, Boulder, CO

1. INTRODUCTION

The emission of anthropogenic aerosols into the atmosphere alters the Earth's radiative forcing directly through absorption of outgoing longwave radiation and indirectly through enhanced solar reflection associated with a reduction in cloud droplet size or with an increase in cloud lifetime. Large uncertainties are associated with the magnitude of this effect with estimates ranging from -0.45 W m^{-2} to -2.2 W m^{-2} in the global mean.

Improved parameterizations of how cloud particle size is affected by emissions of sulfates and aerosols are developed using observations of cloud microphysical properties acquired during the Indian Ocean Experiment (INDOEX), which was conducted out of Male, Republic of Maldives from February 14, 1999 to March 26, 1999. During INDOEX, the prevailing winds blew from the Indian subcontinent to the Indian Ocean, allowing pristine air south of, and polluted air north of, the Intertropical Convergence Zone to be sampled.

In this paper, differences in cloud microphysical properties between pristine and polluted clouds are reviewed, and a parameterization of cloud effective radius, r_e, is developed in terms of cloud liquid water content, LWC, and aerosol number, CN. This is convenient because many parameterizations of cloud radiative properties (e.g., optical depth, single-scattering albedo, asymmetry parameter) are represented in terms of LWC and r_e. The sensitivity of cloud albedo to changes in cloud number concentration is also calculated.

2. MICROPHYSICAL MEASUREMENTS

Microphysical measurements were made using instruments installed on the NCAR C130 aircraft. The size distribution of cloud droplets is obtained by combining data from the forward scattering spectrometer probe (FSSP), covering the range 3 to 55 μm, with data from the one-dimensional cloud probe, covering larger sized drops with diameters greater than 55 μm. The FSSP measurements were processed to reflect post-project size and sample-volume calibrations, obtained from comparison with King probes and a Gerber particle volume monitor; corrections for particle losses due to coincidence and deadtime were also applied. The LWC, r_e, total number concentration (N_{tot}) and median volume radius (r_v) were then derived from the composite size distributions. The concentration of aerosols with sizes larger than 0.02 μm is derived from the NCAR TSI 3760 condensation nucleus (CN) counter and should include all particles in the accumulation mode of the aerosol size distribution. Because droplet shattering on the probe dramatically increased the measured CN inside cloud, CN values in cloud were given by an average of values measured immediately before or after each cloud penetration. The C130 was assumed to be in cloud whenever N_{tot} was greater than 50 cm^{-3} for at least 3 seconds, or approximately 300 m. Using the 1 Hz data, this gives 1022 cloud penetrations consisting of 5441 data points representing 603 km inside cloud.

The INDOEX cloud data are partitioned into three regimes according to the measured CN concentration: clean or pristine (CN $<$ 500 cm^{-3}); intermediate or transition 500 cm^{-3} $<$ CN 1500 cm^{-3}); and polluted (CN $>$ 1500 cm^{-3}). There were 859, 2295, and 1221 data points measured in these three regions respectively for clouds with altitudes lower than 2 km. Figure 1 shows histograms of occurence frequency of 1 Hz r_e values for the 3 different regimes. Although there are only minor differences between the polluted and intermediate regions, the r_e are significantly larger for the clean clouds because fewer cloud condensation nuclei (CCN) are available, and therefore fewer drops to compete for the available water. There is also a tail representing the occurrence of large r_e values in the clean cloud distribution because larger drops, associated with the occurrence of drizzle, occur more frequently under these conditions. Average number concentrations range from 122 to 214 to 265 cm^{-3} and the frequency of drizzle occurence ranges from 9.5% to 3.0% to 4.8% for pristine, transition, and polluted clouds. However, LWCs only change from 0.20 to 0.14 to 0.17 g m^{-3}, and cloud horizontal sizes from 429 to 441 to 530 m for the three regions, showing that the structural and dynamic properties in different regions are similar.

3. PARAMETERIZATION OF R_E

Many recent studies (e.g., Martin et al., 1994) have parameterized r_e as a function of the cube root of LWC divided by N_{tot} through the relation

$$r_e = \left(\frac{3LWC}{4\pi\rho_w k N_{tot}}\right)^{1/3}, \qquad (1)$$

* NCAR is sponsored by the National Science Foundation.

Corresponding author address: Dr. Greg M. McFarquhar, NCAR/MMM, P.O. Box 3000, Boulder, CO. 80307-3000, mcfarq@ncar.ucar.edu

where ρ_w is the density of water and the parameter k, which is unity for monodisperse size distributions, is called the spectral shape parameter. Figure 2 illustrates the relationship between r_e^3 and LWC/N_{tot} for the pristine and polluted INDOEX cloud data, using every fifth data point. The thick solid line represents the k = 1 curve, which is equivalent to $r_e = r_v$. The data points from the polluted clouds lie further from this line showing the lower k values that are associated with such clouds. The average k values calculated from the INDOEX data are 0.84±.07 for the pristine clouds and 0.73±.07 for the polluted clouds.

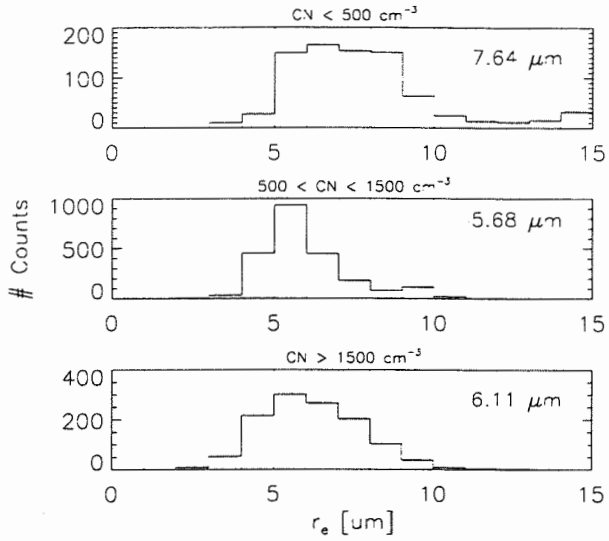

Figure 1. Frequency distribution of r_e, derived from FSSP and 1DC measurements, sorted by CN counts. Each count represent 1 s averaged r_e for all clouds penetrated at altitude < 2 km. Median r_e plotted in upper right corner.

The findings of different investigators are summarized in Fig. 2. A clear transition from high values of k for the maritime air masses (0.80) measured by Martin et al. (1994) to lower values of k in continental air masses (0.67, Martin et al. 1994) and even lower values measured in stratocumulus embedded in a smoky haze enveloping Brazil during the biomass-burning season (Reid et al. 1990) during the Smoke, Clouds, and Radiation-Brazil (SCAR-B) field project is seen. Similarly, slopes and k values comparable to the Martin et al. (1994) continental clouds are associated with air masses sampled off the east coast of the United States in polluted air masses during the Tropospheric Aerosol Radiative Forcing Experiment (TARFOX) (Reid et al., 1999) and with marine stratus within 50 km of shore over the Gulf of Maine and the Bay of Fundy during the North Atlantic Regional Experiment (NARE) (k of 0.72, Gultepe et al., 1996). Since the INDOEX measurements were obtained a minimum of 100 miles from India, this shows the substantial spread of anthropogenic pollutants in this region.

Other data sets do not seem to fit trends quoted above at first glance. Very low values of k are associated with the clean marine cumulus and cumulus congestus sampled during the Atlantic Stratocumulus Transition Experiment (ASTEX) (Reid et al., 1999), whereas larger values of k are associated with congestus of similar sizes in the more polluted environments sampled during SCAR-B and TARFOX. The lower k values during ASTEX are associated with larger drop sizes and r_e found in these clouds. Figure 6 in Reid et al. (1999) shows that the r_e were much larger in the clean marine ASTEX clouds than in the polluted SCAR-B and TARFOX clouds sampled. Similar behavior is seen during INDOEX with lower k values of 0.60 for pristine drizzle clouds compared to 0.85 for pristine non-drizzling clouds, where larger r_e values are associated with the drizzle clouds.

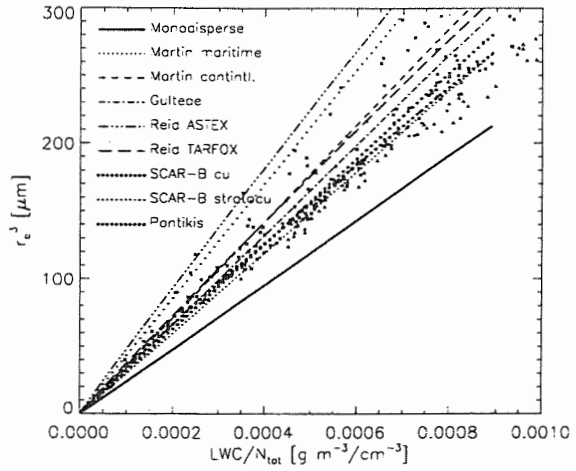

Figure 2. Relationship between r_e^3 and LWC/N_{tot} observed or parameterized by different investigators. Triangles and asteriks represent INDOEX cloud data for pristine and polluted clouds, as classified by CN values.

To apply the parameterization in models with aerosol number and LWC as prognostic variables, N_{tot} can be given as a function of CN. Examining the data, N_{tot} increased approximately linearly as CN increased until CN reached values of about 1100 cm^{-3}, where N_{tot} asymptoted to approximately 200 cm^{-3} (figure not shown). The fraction of CN nucleating increased with updraft strength, and can be accounted for by using velocity dependent coefficients in the above linear fits (paper under preparation).

The adequacy of the parameterization was assessed by comparing the predicted and observed r_e. For 22 cases where cloud was penetrated immediately before or after sub-cloud sampling, Figure 3 compares r_e measured in cloud with that predicted from the observed CN and LWC (circles). Despite considerable scatter, the INDOEX parameterization offers a good fit to the data within 20%. Other symbols represent r_e predicted from other parameterizations, many of which represent conditions very different than those sampled during INDOEX.

4. RADIATIVE IMPACTS

Cloud susceptibility measures the sensitivity of cloud albedo to changes in CCN concentration and has a multi-dimensional dependence on cloud optical depth, τ, and particle size. Platnick and Twomey (1994) define cloud susceptibility as the derivative of albedo with respect to N_{tot} under the condition of constant LWC. With further assumptions of constant cloud geometric depth (Δz), constant spectral breadth (i.e., $\tau \propto N_{tot}^{1/3}$), and conservative scattering in visible wavelengths (i.e., single-scatter albedo is one and asymmetry parameter constant with radius), they wrote susceptibility as

$$\frac{dA}{dN_{tot}} = \frac{\partial A}{\partial \tau}\frac{\tau}{3N_{tot}} = \frac{A(1-A)}{A(\chi^{1/3}-1)+1}\frac{4\pi\rho_w}{9LWC}r_v^3, \quad (2)$$

where A is cloud albedo.

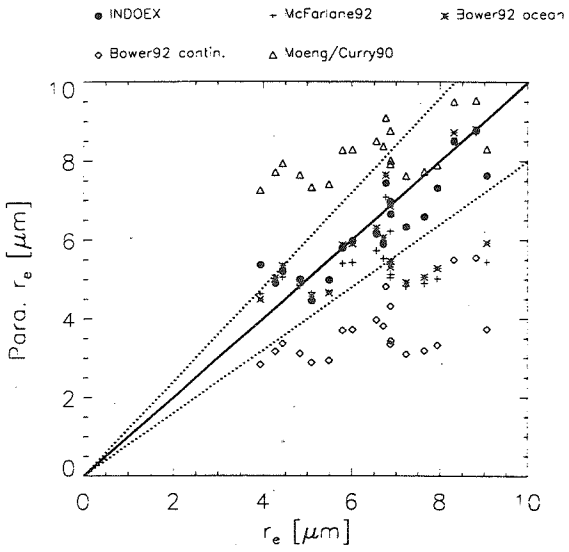

Figure 3. Average r_e calculated from cloud observations for specified CN and LWC ranges, as function of r_e calculated by applying parameterization equations. Different symbols represent application of different parameterizations.

Both skewness and dispersion, which give some measure of droplet spectral breadth, increase in more polluted clouds (e.g., 0.25 ±.06 and 0.36 ±.06 dispersions and -0.15 ±.52 and 0.41 ±.69 skewnesses for pristine and polluted clouds). Since $\tau = Q_{ext}\ A_c\Delta z$ where $Q_{ext} \approx 2$ for visible wavelengths, and A_c is the observed cross-sectional area, the approximate relationship between τ and N_{tot} is determined by assuming that Δz does not vary with N_{tot}. Figure 4 shows the variation of the natural logarithm of A_c against the natural logarithm of N_{tot}. Despite the scatter, the best fit offers a reasonable approximation to the data. The slope of the line is 0.86 ± 0.02 with a χ^2 of 0.28, very close to the 0.83 slope suggested by Feingold et al. (1997), who used a box model of stochastic collection to examine the relationship between τ and N_{tot}. The calculated slopes increased from 0.78 to 0.92 as LWC increased, but is not accounted for in the susceptibility calculations. Eq. (2) is hence rewritten as

$$\frac{dA}{dN_{tot}} = = \frac{A(1-A)}{A(\chi^{0.86}-1)+1}\frac{1.15\pi\rho_w}{LWC}r_v^3 \quad (3).$$

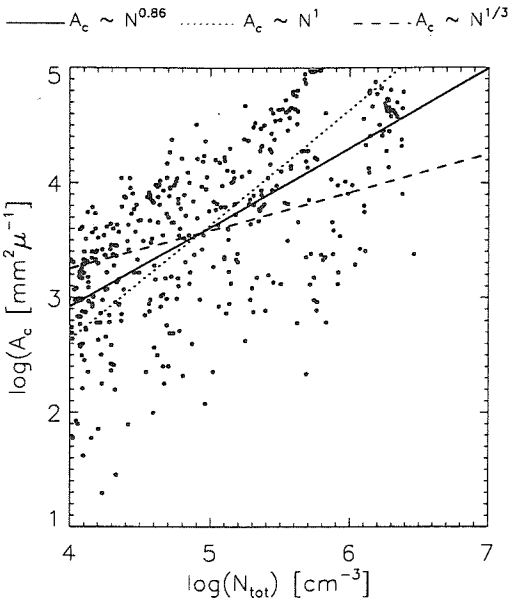

Figure 4. Logarithm of A_c as function of logarithm of N_{tot} for all clouds penetrated with altitude < 2 km during INDOEX. Solid line represents best fit to data, dotted and dashed lines represent Platnick and Twomey (1994) and Feingold et al. (1997) fits respectively.

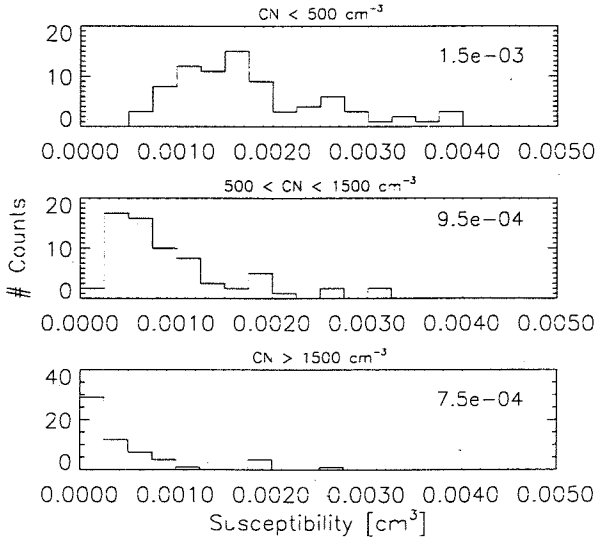

Figure 5. Frequency distributions of cloud susceptibility, computed using observed relationship between A_c and N_{tot}, sorted by CN counts. Median susceptibility plotted in upper right corner of panel.

Using observed cloud droplet distributions, single-scattering properties prediced by Mie theory,

and a plane parallel Monte Carlo radiative transfer model, it can be shown that cloud susceptibilities vary by less than 10% for different wavelengths. Hence, visible susceptibilities are assumed to represent potential radiative effects of the INDOEX clouds. Figure 5 shows the frequency of occurence of susceptibility for pristine, transition and polluted clouds assuming an albedo of 0.5, which gives an upper bound. The susceptibilities range from 1.5×10^{-3} cm^3 for pristine clouds to 0.75×10^{-3} cm^3 for polluted clouds. Susceptibilities as large as 4.0×10^{-3} cm^3 can be seen for clean clouds, but the tail cuts off at a much lower value, 2.5×10^{-3} cm^3, for polluted clouds. These calculations imply that for the pristine clouds, on average, an increase of 66 cm^{-3} particles is needed to increase albedos by 10%; given average N_{tot} for pristine and polluted clouds, such an effect should be ideally observable. However, the trade cumulus observed during INDOEX in the polluted regimes were typically embedded in a highly absorptive haze layer which would substantially decrease the above effect. Nevertheless, the magnitude of cloud susceptibility is a meaningful quantity because it allows a determination of an upper bound for indirect radiative forcing. For example, with an increase of 50 cm^{-3} in cloud number concentration and the calculated susceptibilties, there would be an approximately 7.5% increase in reflection, representing an increase in shortwave radiative forcing of approximately 4.5 W m^{-2}. Modeling studies are needed to provide better estimates of indirect radiative forcing.

5. DISCUSSION AND SUMMARY

Observations of cloud microphysical properties acquired during INDOEX have been used to develop a parameterization for effective radius, r_e, which can be used to represent cloud properties in both large scale and cloud modeling studies. Although the coefficients differ dramatically for pristine and polluted clouds, the nature of the relationship between variables does not change and is similar in format to relations developed for stratus clouds in geographically diverse regimes. The nonvarying form of the parameterization suggests that it may be applied universally in large scale models. This parameterization should only be applied for the conditions for which it was developed. It is not applicable to cases where drizzle occurs frequently, or to cases with substantially different cloud and aerosol properties than those sampled during INDOEX.

A new method of calculating cloud susceptibility, based on an empirical relation between total number concentration and the projected area of the cloud droplet distribution, yields values 2.6 times larger on average than those obtained with the original definition. As expected, the pristine clouds are most susceptible to the addition of cloud particles because the polluted clouds have already been modified.

Future studies should concentrate on an examination of conditions under which drizzle occurs and causes of changing cloud lifetimes because of their effects on the developed relationships. Due to the necessarily statistically limited sample and the complex nature of these issues, it is likely that a modeling study is required to address these issues. The effects of the absorptivity of the aerosol also need to be examined.

6. ACKNOWLEDGMENTS

We are grateful to Darrel Baumgardner of NCAR for his assistance in interpreting the cloud microphysical data for this study. This research was sponsored by the Center for Clouds, Chemistry and Climate at the Scripps Institution of Oceanography.

7. REFERENCES

Bower, K.N., and T.W. Choularton, 1992: A parameterisation of the effective radius of ice free clouds for use in global climate models. *Atmos. Res.*, **27**, 305–339.

Feingold, G., R. Boers, B. Stevens, and W. R. Cotton, 1997: A modeling study of the effect of drizzle on cloud optical depth and susceptibility, *J. Geophys. Res.*, **102**, 13527–13534.

Gultepe, I., G. A. Isaac, W. R. Leaitch, and C. M. Banic, 1996: Parameterizations of marine stratus microphysics based on in situ observations: implications for GCMs, *J. Climate*, *9*, 345–357.

Martin, G. M., D. W. Johnson, and A. Spice, 1994: The measurement and parameterization of effective radius of droplets in warm stratocumulus clouds, *J. Atmos. Sci.*, *51*, 1823–1842.

McFarlane, N.A., G.J. Boer, J.-P. Blanchet, and M. Lazare, 1992: The Canadian Climate Centre second-generation general circulation model and its equilibrium climate. *J. Climate*, **5**, 1013–1044.

Moeng, C.-H., and J. Curry, 1990: The senstivity of large eddy simulations of a stratus topped boundary layer to cloud microphysis. *Proc. Conf. Cloud Physics*, San Francisco, Amer. Meteor. Soc., 115–121.

Platnick, S., S. Twomey, 1994: Determining the susceptibility of cloud albedo to changes in droplet concentration with the Advanced Very High Resolution Radiometer, *J. Appl. Meteor.*, **33**, 334–347.

Reid, J. S., P. V. Hobbs, A. L. Rangno, and D. A. Hegg, 1999: Relationships between cloud droplet effective radius, liquid water content, and droplet concentration for warm clouds in Brazil embedded in biomass smoke, *J. Geophys. Res.*, **104**, 6145–6153.

On Shock–Type–Solutions for the Precipitation Concentration in Models with Parameterized Microphysics

ULRIKE WACKER[1] AND AXEL SEIFERT[2],

[1]Institut für Meteorologie und Geophysik der Universität Frankfurt a.M., 60054 Frankfurt a.M., Germany

[2]Institut für Meteorologie und Kimaforschung, Universität Karlsruhe/Forschungszentrum Karlsruhe, 76021 Karlsruhe, Germany

1 Introduction

In complex numerical prediction models, the effects of cloud microphysical processes are described for the sake of computational efficiency in parameterized form. In familiar schemes like e.g. those described by Lin et al. (1983), Dudhia (1989), Reisner et al. (1998), few variables are considered to characterize the ensembles of condensate particles. Most schemes, designed for water or mixed phase clouds, are based on the ideas presented by Kessler (1969), in which an ensemble of rain drops is characterized in terms of mass concentration, such as to express e.g. the sedimentation flux only in terms of that variable. This is doubtlessly a severe restriction, and research on the development of two– and more–variable schemes is going on, e.g. Seifert and Beheng (2000).

In this paper, a general problem connected to schemes with mass concentration as single prognostic variable to characterize the population of precipitation particles is discussed. The resulting budget equation for precipitation mass concentration is of the form of a quasi–linear advection equation with sources. Such types of prognostic equations have been widely investigated in nonlinear wave dynamics, see e.g. Whitham (1974) and LeVeque (1992). An essential feature of these equations is that they describe breaking of the signal, thus giving rise to multivalued solutions, which is obviously unphysical for a concentration variable. However, it is possible to find a so–called weak solution for the transient signal, if the problem is treated according to shock waves, whereby the multivalued solution is replaced by a discontinuous one.

The evolution of the vertical profile of precipitation concentration under the impact of sedimentation has been recently discussed within the context of breaking and shock waves by Wacker (2000). Here we will concentrate on transient precipitation profiles which develop shocks from either initially continuous or discontinuous ('Riemann problem') initial conditions. To this end, we will present analytic solutions to a simplified model for rain drop sedimentation using a Kessler–type parameterization. The results will be compared with numerical solutions, and finally to reference solutions resulting from a model describing microphysical processes in detail to estimate the ability of the parameterization model to describe all inclusively the microphysical processes.

Corresponding author's address: Dr. Ulrike Wacker, Institut für Meteorologie und Geophysik der Universität Frankfurt a.M., 60054 Frankfurt a.M., Germany

2 Breaking and Shock Solutions for the Precipitation Profile

To analyse the effect of sedimentation on the evolution of the vertical profile of precipitation, we consider a model, in which the partial density of rain water $\rho_p[\vec{r},t]$ changes only due to the divergence of the (downward) sedimentation mass flux F_p, while horizontal inhomogeneities, convective fluxes, as well as any source, are neglected (the form $Z[x]$ denotes the dependency of Z on some quantity x) . The differential form of the budget equation for rain water mass then reads

$$\frac{\partial \rho_p}{\partial t} - \frac{\partial F_p}{\partial z} = 0 \,. \tag{1}$$

We assume a familiar Kessler (1969)–type parameterization with only one variable (i.e. ρ_p) to characterize the rain drop population, a dependency of sedimentation velocity on drop diameter D according to $v_T[D] = \eta D^y$ (with parameters $\eta = \eta[\rho]$ and $y = \text{const.}$), as well as a self–preserving drop size distribution function in terms of the exponential Marshall–Palmer–spectrum $f[D] = n_0 \exp(-\lambda D)$ (with parameters n_0 and λ; here: $n_0 = \text{const.}$). Then we finally arrive at the following parameterization equation for the rain water mass flux:

$$F_p = \chi \rho_p^{\delta} \tag{2}$$

The coefficient χ and the exponent δ are determined as functions of the parameters; note $\delta = 1 + y/4 \geq 1$.

For the following we assume air density ρ to be constant. Then the sedimentation flux F_p (2) is a function of the rain water partial density ρ_p only. This result suggests that $\partial F_p/\partial z$ should be rewritten in terms of the vertical gradient of ρ_p. By introducing a quantity $\tilde{v}$

$$\tilde{v} := \frac{\partial F_p}{\partial \rho_p} = \chi \delta \rho_p^{\delta - 1} \,, \tag{3}$$

the prognostic equation (1) can be casted into the form

$$\frac{\partial \rho_p}{\partial t} - \tilde{v}[\rho_p] \frac{\partial \rho_p}{\partial z} = 0 \,. \tag{4}$$

This quasi–linear source–free advection equation (4) with an apparent advection velocity $\tilde{v}$ describes pure propagation of the signal $\rho_p[z,t]$ with a velocity $\tilde{v}$ depending on

ρ_p itself. The velocity $\tilde{v}$ defines a curve $z[t]$, the characteristic, in the t, z–plane with slope

$$\frac{dz}{dt} = -\tilde{v}[\rho_p] \,. \tag{5}$$

The rate of change of ρ_p along a characteristic, that is $d\rho_p/dt := \partial\rho_p/\partial t - \tilde{v}[\rho_p]\partial\rho_p/\partial z$, vanishes,

$$\frac{d\rho_p}{dt} = 0 \,. \tag{6}$$

Hence the rain water concentration ρ_p remains constant along the characteristic defined by (5), which is accordingly run through by an invariant velocity $\tilde{v}[\rho_p]$ defined in Eq. (3). The equation for a characteristic $z[t; z_0]$ passing through the level $z = z_0$ at initial time $t = t_0$ with initial concentration $\rho_{p0}[z_0]$ follows immediately as

$$z[t; z_0] = z_0 - \chi\delta\rho_{p0}^{\delta-1}[z_0](t - t_0) \,. \tag{7}$$

The solution to Eq. (4) can be constructed by determining the characteristic (7) for any given $\rho_{p0}[z]$ and assigning each point z the partial density ρ_{p0} at the matching initial position z_0:

$$\rho_p[z[t; z_0], t] = \rho_{p0}[z + \chi\delta\rho_{p0}^{\delta-1}[z_0](t - t_0)] \tag{8}$$

As is well known from nonlinear wave dynamics (Whitham 1974), solutions of nonlinear advection equations like (4) are subject to a serious problem. While the maximum and minimum values are preserved, the shape of the signal is distorted during progress in time. In any compressive part of the signal, the characteristics will ultimately cross. When this happens for the first time t_b, the function $\rho_p[z, t]$ takes an infinite slope; the signal is said to 'break' by analogy to waves in a fluid. Later on, the solution $\rho_p[z, t]$ is triple–valued.

As an example, Figure 1 shows the evolution of an initially smooth rain water concentration profile during 1000 s. It is calculated using $y = 0.5$ and $\eta = 1300$ cm$^{0.5}$/s for the terminal velocity relationship as used in Kessler (1969), hence $\delta = 1.125$. As to be expected, the maximum value is shifted downward, yet retaining its absolute value. The profile is sharpened on the downward side of the hump; finally it breaks and the solution becomes multivalued, which becomes clearly visible for $t = 1000$ s. As a multivalued concentration does not make sense, there is no physically meaningful solution of the PDE (4) beyond the time t_b of first breaking.

In order to determine a physically relevant solution, we follow the shock wave concept (for more details see Whitham (1974) or LeVeque (1992)) and take the integral form of the budget equation for precipitation mass instead of the differential form (4) as basis. The position of the shock is then calculated from the condition that the multivalued and the discontinuous solutions satisfy mass conservation. Hence the discontinuity must cut off lobes of equal area. The propagation speed of the shock v_s is determined by the so–called Rankine–Hugoniot–condition,

$$v_s\Delta\rho_p = \Delta F_p \,, \tag{9}$$

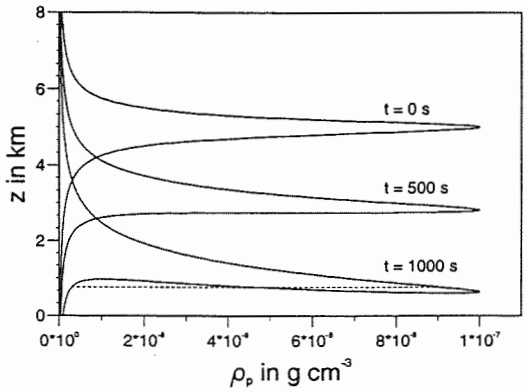

Figure 1: Evolution of the vertical profile of the precipitation concentration ρ_p in g/cm^3. Continuous solution (———) with breaking and shock solution (– – – –) for $t = 1000$ s.

where $\Delta\rho_p$ and ΔF_p mark the jump in the respective quantity. This shock solution is also indicated in Figure 1 for $t = 1000$ s.

It is already noted here and will be proved in Section 4, that the solution of the spectral budget equation provides always a single valued concentration profile without shocks. Hence breaking and shocks must be interpreted as an artifact of the parameterization, and will be discarded; instead we will concentrate in the following on the shock wave.

3 Riemann Problem and Square Wave

In this section we will investigate shock solutions of the source–free budget equation (1) for discontinuous initial conditions

$$\rho_p[z, t_0] = \begin{cases} \rho_t, & z \geq z^* \\ \rho_b, & z < z^* \,, \end{cases} \tag{10}$$

i.e. the Riemann problem, for which a rigorous mathematical theory exists (Chang and Hsiao 1989). It is widely discussed in e.g. gas dynamics. The Riemann problem can be treated analytically, because the PDE (4) as well as the initial condition are invariant to stretching transformations. Introducing the similarity coordinate

$$\zeta = \frac{z^* - z}{t} = \frac{\Delta z}{t} \tag{11}$$

the PDE can be reduced to the ODE

$$(\tilde{v}[\rho_p] - \zeta)\,\frac{d\rho_p[\zeta]}{d\zeta} = 0 \tag{12}$$

with boundary conditions

$$\rho_p[\pm\infty] = \rho_{t/b}. \tag{13}$$

From (12) it follows either $\rho_p = $ const. or $\zeta = \tilde{v}[\rho_p]$. Thus ρ_p can only change with ζ, if the slope of the characteristic equals $\zeta = \tilde{v}[\rho_p]$. With Eq. (3) this yields the

solution of the Riemann problem

$$\rho_p[z,t] = \begin{cases} \rho_t, & \text{if } \chi\delta\rho_t^{\delta-1} \geq \frac{\Delta z}{t} \\ \left(\frac{1}{\chi\delta}\frac{\Delta z}{t}\right)^{\frac{1}{\delta-1}}, & \text{if } \chi\delta\rho_t^{\delta-1} < \frac{\Delta z}{t} < \chi\delta\rho_b^{\delta-1} \\ \rho_b, & \text{if } \chi\delta\rho_b^{\delta-1} \leq \frac{\Delta z}{t}. \end{cases} \tag{14}$$

Note that $\delta \geq 1$ for drop sedimentation. Concerning the intermediate section of the solution (14), two cases are to be distinguished. For $\rho_b \geq \rho_t$ the domains with ρ_p = const. are connected by a monotonically increasing function, the so–called rarefaction wave. This solution is continuous. For $\rho_b < \rho_t$, however, this region does not exist. Using the concept of weak solutions, the solution turns out as a single discontinuity propagating with a shock speed v_s according to the Rankine-Hugoniot-condition (9).

Now we will focus on the square wave problem given by the PDE (1) with initial condition

$$\rho_p[z,t_0] = \begin{cases} \rho_0, & \text{if } z_2 > z > z_1 \\ 0, & \text{otherwise.} \end{cases} \tag{15}$$

Due to the hyperbolic character of the PDE the square wave problem can be decomposed into two independent Riemann problems, as long as the waves evolving from the two sides of the square wave do not intersect.

Figure 2 shows the initial condition of the square wave problem and the analytical solution for $t = 400$ s together with two numerical approximations using different mesh sizes. For the numerical solution of the PDE we have used a higher order Godunov method based on a third order ENO reconstruction step (Harten et al. 1987). For η and y again the values of Kessler (1969) have been applied.

At the upper bound of the precipitation profile the initial discontinuity is smoothed by the evolving rarefaction wave as described above. But at the lower bound the discontinuity remains unchanged while propagating downward with the Rankine-Hugoniot speed v_s. The structure of the analytical solution is resolved accurately on the fine grid, while on the coarse grid numerical diffusion makes it difficult to distinguish between the wave types.

4 Comparison with the Reference Solution

In order to estimate the applicability of the parameterization concept, the profiles presented in the last section will now be compared to the reference solutions. They are calculated by solving the spectral budget equation for the drops size distribution function $f[D,z,t]$, simplified with respect to the sedimentation problem:

$$\frac{\partial f[D,z,t]}{\partial t} - \frac{\partial(v_T[D]f[D,z,t])}{\partial z} = 0 \tag{16}$$

with $v_T[D]$: sedimentation velocity of particle with diameter D. This PDE is, in contrast to Eq. (4), a *linear* source free advection equation, because here D and z

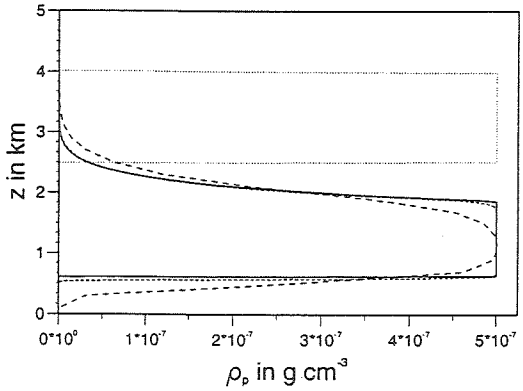

Figure 2: Vertical profile of the precipitation concentration ρ_p in g/cm^3 for the square wave problem with $z_1 = 2.5$ km and $z_2 = 4$ km. Initial profile (· · · · ·), analytic (———) and numerical solution with mesh sizes of 25 m (- - - - -) and 200 m (– – – –) at time $t = 400$ s.

are independent coordinates. Equation (16) describes the propagation of the signal $f[D,z,t]$ with a velocity $v_T[D]$ depending on particle diameter, but not on the signal f. Hence the solution for a selected D will describe a pure downward translation of the profile $f[D,z,t]$ in the course of time without change in shape, whereby only the translation speed depends on the respective particle size D.

Using as in Section 2 the characteristic method, we find the solution to the PDE (16) to read

$$f[D,z,t] = f_0[D, z + v_T[D](t - t_0)] \tag{17}$$

for an initial particle size distribution $f_0[D,z]$.

The vertical profile of partial density ρ_p is gained by integration over the entire spectrum,

$$\rho_p[z,t] = \int_0^\infty m f[D,z,t] dD \tag{18}$$

with m: particle mass. As the PDE (16) is linear, breaking and shocks in the profile of $f[D,z,t]$ are excluded and will be so for the matching profile of ρ_p.

For the square wave problem this reference solution $\rho_p[z,t]$ is given in Figure 3 to be compared with the analytic solution gained from the parameterized model. The initial size distribution has been chosen as to exactly match with the assumed Marshall–Palmer–size distribution prescribed in the parameterization.

The initial distribution is smoothed more rapidly for the reference solution, whereby the region with an appreciable precipitation concentration, i.e. the upper and lower flanks, is broadened and the maximum is damped in the course of time. This results from the description of the particle population as being actually composed of a spectrum of particles falling at different sedimentation speeds, whereas in the parameterization model the particle population is treated as falling at a uniform speed, namely the mass weighted mean fall velocty that depends only

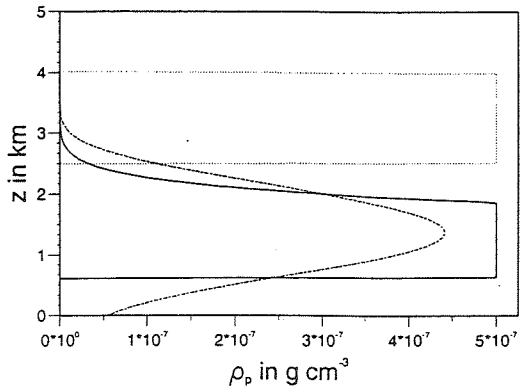

Figure 3: Vertical profile of the precipitation concentration ρ_p in g/cm^3. Comparison of analytic (———) and reference solutions (– · – · –·).

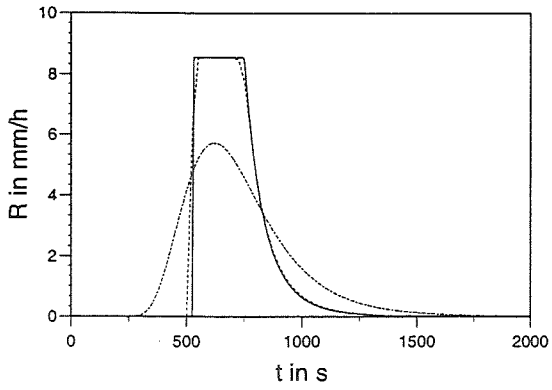

Figure 4: The surface precipitation rate R in mm/h as function of time t in s. Analytic solution (———), numerical solution for $\Delta z = 25$ m (- - - - -), and reference solution (– · – · –·).

on the mass concentration ρ_p of the population.
'Gravitational sorting' of precipitation particels smears the ρ_p–signal similar to a diffusion–effect. This leads to the unexpected result that the coarse grid numerical approximation given in Fig. 2 compares best with the reference solution, while as numerical accuracy is increased, larger deviations and the formation of an unphysical shock solution occur.
Concerning the surface precipitation rate shown in Figure 4, the spectral model again provides a smoother temporal distribution than the parameterized model, because large (small) drops arrive much earlier (later) at the surface than those of mean size. As the precipitation event lasts longer, the maximum rain intensity is considerably reduced.

5 Summary

The preceeding analysis has shown that the budget equation (1) for precipitation mass has time dependent solutions for the concentration profile, which may develop breaking waves or shock waves. These features are basically connected to the nonlinear parameterization equation (2) for the precipitation flux F_p as follows from a familiar one–variable parameterization scheme. F_p comes out as a linear function in ρ_p only, if either the terminal velocity is assumed to be independent of particle size or the slope parameter λ in the Marshall–Palmer–spectrum is set constant – both questionable assumptions. On the other hand, the reference solution derived on the basis of the microphysical description level reveals neither a breaking signal nor discontinuities. Hence breaking and shocks have to be considered as mathematical artifacts, that are basically connected to the parameterization assumptions.

Acknowledgement Parts of this paper are funded by the Deutsche Forschungsgemeinschaft (grant WA1334/1–1).

References

Chang, T., and L. Hsiao (1989). *The Riemann Problem and Interaction of Waves in Gas Dynamics.* Harlow: John Wiley and Sons.

Dudhia, J. (1989). Numerical study of convection observed during the winter monsoon experiment using a mesoscale two–dimensional model. *J. Atmos. Sci. 46*, 3077–3107.

Harten, A., B. Enquist, S. Osher, and S. Chakravarthy (1987). Uniformly high order accuracy essentially non-oscillatory schemes III. *J. Comp. Phys. 71*, 231–303.

Kessler, E. (1969). *On the distribution and continuity of water substance in atmospheric circulations*, Meteor. Monogr. 32, Boston: Amer. Meteor. Soc.

LeVeque, R. J. (1992). *Numerical Methods for Conservation Laws.* Lectures in Mathematics. Basel: Birkhäuser.

Lin, Y.-L., R. D. Farley, and H. Orville (1983). Bulk parameterization of the snow field in a cloud model. *J. Clim. Appl. Meteorol. 22*, 1065–1092.

Reisner, J., R. M. Rasmussen, and R. T. Bruintjes (1998). Explicit forecasting of supercooled liquid water in winter storms using the MM5 mesoscale model. *Q. J. R. Meteorol. Soc. 124*, 1071–1107.

Seifert, A., and K. Beheng (2000). An improved parameterization for simulating autoconversion, accretion, and selfcollection based on a double–moment scheme. *This proceedings.*

Wacker, U. (2000). Influence of the type of condensate particles on cloud physical properties. *Geophysical Research Letters* (in press).

Whitham, G. (1974). *Linear and Non-linear Waves.* New York: John Wiley and Sons.

THE IMPORTANCE OF EMBEDDED CONVECTION AND THE HALLETT MOSSOP PROCESS TO THE PARAMETERISATION OF DEEP LAYER CLOUDS

J. R. Cardwell and T. W. Choularton

Department of Physics, UMIST, Manchester M60 1QD, UK

1. INTRODUCTION

The UK Meteorological Office Unified Model (UM) is used for both climate and weather prediction and the work presented is aimed at improving the parameterisation of deep layer clouds with embedded convection. This type of cloud produces much of the precipitation in mid-latitude regions and is one of the more predominant clouds in these regions where baroclinic storms are the major source of precipitation. Hence these clouds are important to the precipitation and radiation budgets.

Comparisons are made between the UM microphysics and the UMIST microphysics, and between non-embedded and embedded cloud simulations.

The UM is unable to resolve embedded convection and its reliance on an inferred ice spectrum will cause it to miss features such as bimodality. These issues are discussed by Wilson in these ICCP proceedings, more results from the UMIST explicit model are also shown.

2. MODEL DESCRIPTION

2.1 The dynamical framework

Comparisons between the UM and UMIST microphysics were made using the same dynamical frameworks. There were two different simulations. The first is most akin to a UM simulation of stratified clouds and is a cloud of many layers all lifted by the same updraft velocity. The second builds on the first by the addition of periodic embedded thermals, which more closely simulates a real cloud.

2.1.1 The homogeneous stratified cloud simulation

The stratified cloud is effectively modelled by using a large number of Lagrangian parcel models. Each parcel represents a layer of cloud with a thickness depending on the resolution required (20 to 35m), the number of layers is fixed and is the number needed to model the required cloud depth. Each parcel rises adiabatically at the same fixed ascent rate, which is the specified cloud updraft velocity (0.25m/s). Once a parcel reaches cloud top it is lost and a new parcel is created at cloud base.

Corresponding author's address: John R. Cardwell, Physics Dept. UMIST,Manchester, M60 1QD. UK;
E-Mail: John@cloud2.phy.umist.ac.uk

2.1.2 The embedded convection simulation

Embedded convection is simulated by allowing periodic thermals to rise through the existing layer cloud, and after 5 or 6 thermals the cloud reaches a dynamic equilibrium. The thermal is treated in the same way as the background cloud described in the preceding section except that it ascends faster. In this study the background cloud layers are lifted by an updraft of 0.02m/s and thermal layers are lifted by an updraft of 0.5m/s. The thermal duration is 10 minutes and their separation is 20 minutes. The choice of the thermals duration and their separation is representative of the width and spatial variability of embedded convection.

Making the approximation that the cloud properties are similar to that of the thermal, the thermal base becomes the new cloud as the thermal rises, allowing successive thermals to rise through the debris of their predecessor.

2.2 The microphysics

The UM microphysics scheme is described by Wilson and Ballard (1999). The ice is assumed to be distributed exponentially across a spectrum of particle sizes with an intercept which depends upon the air temperature. The fall speed and densities of the ice particles are parametrised as a power function of their diameters. The Hallett Mossop process is not normally operational, but has been implemented for this study by increasing the deposition rate by a factor dependent upon the temperature and the amount of liquid water present. Growth by deposition and riming are solved explicitly and primary nucleation is from Fletcher (1962).

The UMIST explicit ice microphysical scheme, represents the ice spectrum by the use of discrete bins. The source of ice particles in the UMIST scheme is the temperature and saturation dependent Meyers (1992) scheme, and a secondary ice source of Hallett Mossop (1974) (200 splinters/mg of rime). Ice growth by vapor deposition, riming (growth by droplet collection) and Aggregation (ice collecting ice) are simulated.

The UMIST water microphysics fixes concentration of droplets at 500/cc and uses the droplet growth equation from Rogers and Yau (1989). It is applied to both schemes, although when in interaction with ice the UM and UMIST microphysics apply different droplet spectra.

3 RESULTS

Figure 1 and 2 show the total water/ice path for four simulations of a cloud (base –1°C, top –23°C). The non embedded (stratified) cases have an initial peak in ice and water and then settle back to remain at a constant value. The embedded cases oscillate with driving thermals. After the models have spun up to dynamic equilibrium (~200mins) time, it can be seen that embedded convection increases the ice loading of the clouds, as the thermals push ice back into the cloud that would otherwise precipitate out.

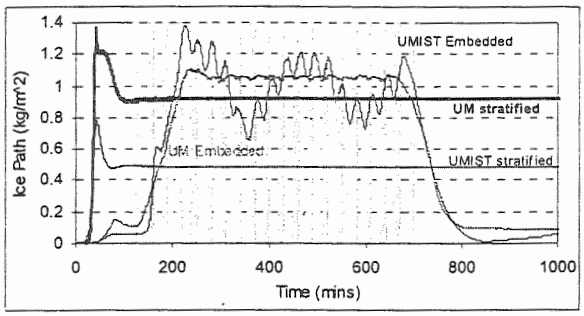

Figure 1. The evolution of the ice paths for UM microphysics with/without Embedded Convention and UMIST with/without Embedded Convection. The shaded area indicates the times when a thermal is being forced through cloud base.

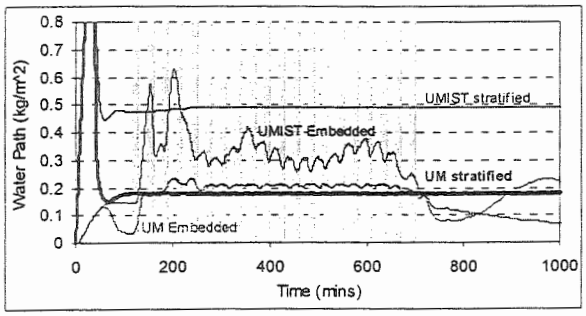

Figure 2. As Fig 1 but Water Paths

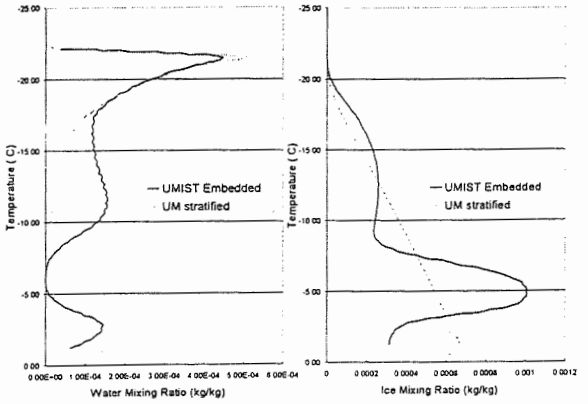

Figure 3 Time averaged (over steady state period) temperature profile of Ice & water mixing ratio for the UMIST embedded and UM non-embbeded case

The UM cases have almost the same liquid water. Both have considerably less water than that of the UMIST cases, because the UM ice spectrum assumes more middle size ice particles. This causes a greater amount of riming in lower cloud levels and prevents water from reaching to higher levels in the cloud.

The periodicity in the UMIST embedded thermal case is due to the Hallett Mossop process (-3 to –8°C). Periodically it produces so much ice in the cloud that it no longer has enough water to continue, thus the process stops until enough ice has been lost to allow liquid water to return so that the process can start again.

The Hallett Mossop process is also responsible for the difference between UMIST cases. Without embedded convection ice cannot be recycled to make the process efficient, allowing more water to survive.

Figure 3 shows the sharp difference between the non-embedded UM case and the embedded case. It is clear the UM cannot reproduce the peak of ice content in the Hallett Mossop region as it cannot produce a bimodal spectrum, therefore all the ice produced is seen as large and falls out quickly. However the compensating error of too larger riming rates, produces more ice, but as a consequence removes much more water.

4 SUMMARY

The UM is in reasonable agreement with the UMIST embedded convection simulation, for the bulk properties of the cloud. However the distribution of hydrometeors within the cloud is significantly different.

Embedded convection increases the amount of water reaching mid and higher levels in a cloud and increases the ice loading of the cloud. It is also important in recycling ice produced by the Hallett Mossop process, so that this process can be come more effective at glaciating the cloud.

4.1 Acknowledgments

This work was funded in part by the Department of the Environment, Transport and the Regions and the Met. Office

4.2 References

N. H. Fletcher, 1962: The physics of rain clouds., C.U.P.

J. Hallett and S.C. Mossop, 1974: Production of secondary ice particles during the riming process. Nature, 249, 26-28

R. R. Rogers and M. K. Yau, 1989: A short course in cloud physics. Pergamon Press

D. R. Wilson, and S. P. Ballard, 1999: A microphysically based precipitation scheme for the Meteorological Office Unified Model. Q. J. R. Meteorol. Soc., 125, 1607-1636

WHICH SIZE DISTRIBUTION FUNCTION TO USE FOR STUDIES RELATED TO EFFECTIVE RADIUS

Yangang Liu [1] and Peter H. Daum

[1]Department of Applied Science, Brookhaven National Laboratory, Upton, NY 11973-5000

1. INTROCUTION

Effective radius r_e (defined as the ratio of the third to the second moment of a droplet size distribution) is one of the key variables that are used for calculation of the radiative properties of liquid water clouds (Hansen and Travis 1974). The inclusion and parameterization of r_e in climate models has proven to be critical for assessing global climate change (Slingo 1990; Dandin et al, 1997). There has been increasing evidence for parameterizing r_e as a 1/3 power law of the ratio of the cloud liquid water content (L) to the droplet concentration (N) (Pontikis and Hicks, 1992; Bower and Choularton 1992; Bower et al. 1994; Martin et al. 1994; Liu and Hallett 1997; Reid et al. 1998). The "1/3" power-law takes the form

$$r_e = \alpha\left(\frac{L}{N}\right)^{1/3}, \qquad (1)$$

where r_e is in μm, L in gm^{-3}, and N in cm^{-3}. The only difference among different power-laws lies in the specification of the prefactor α.

On the other hand, different analytical functions are often used to describe size distributions (Liu et al. 1995). From these analytical size distributions, we can derive "1/3" power-laws. In this work, existing expressions are compared and analyzed using the data collected during two Intensive Observation Periods (IOPs) conducted at the ARM (Atmospheric Radiation Measurements) program SGP (Southern Great Plain) site in Oklahoma, in the spring and fall of 1997.

2. EXPRESSIONS FOR α

For clouds with a monodisperse droplet size distribution as described by a delta function $n(r)=N\delta(r-r_e)$, $\alpha = 100(3/4\pi)^{1/3} \approx 62.04$; the multiplier 100 is introduced to keep the units of r_e, L and N in μm, $g\ m^{-3}$ and cm^{-3}, respectively. This value of α was used by Bower and Choularton (1992), and Bower et al. (1994) to estimate the r_e of layer clouds and small cumuli. Martin et al. (1994) derived estimates of α of 66.83 for maritime, and 70.89 for continental stratocumulus clouds based upon analysis of in situ microphysical data. These expressions with fixed values of prefactor totally ignore the dependence of α on the spectral broadening processes. Pontikis and Hicks (1992) analytically derived an expression (PH) that relates α to the spectral dispersion d (defined as the ratio of the standard deviation to the mean radius of the corresponding droplet size distribution). Liu and Hallett (1997) derived another "1/3" power-law to allow for the effect of turbulent entrainment and mixing (WB) from the Weibull size distribution which itself derived from the systems theory proposed in Liu et al. (1995).

Besides the Weibull distribution, cloud droplet size distributions are often represented by the Gamma (GM) and lognormal (LN) distributions (Liu et al. 1995). More expressions can be easily derived from these two analytical size distributions. Table 1 summarizes all the prefactor expressions.

3. COMPARISON OF PREFACTORS

Figure 1 shows α as a function of d. Also shown in this figure are the α's for a monodisperse size distribution (MO), and Martin's values for continental (MC) and maritime clouds (MM). Substantial differences between these prefactor expressions are exhibited in Fig. 1.

[1] Corresponding author: Yangang Liu, Brookhaven National Laboratory, Bldg. 815E, Upton, NY 11973 lyg@bnl.gov

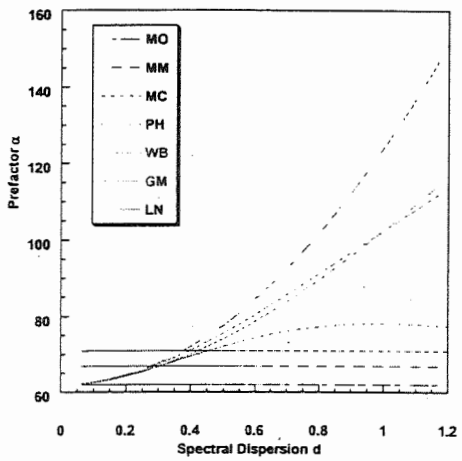

Fig. 1. Prefactor α as a function of the spectral dispersion of the cloud droplet size distribution.

To address the question of their accuracy, these expressions are compared to those calculated from droplet size distributions collected with a FSSP during two recent IOPs at the ARM SGP site in northern Oklahoma in the spring and fall of 1997, respectively. During the two campaigns Data from six flights in (broken) stratocumulus were analyzed. Figure 2 compares the measurements averaged over all the data sets with these different prefactor expressions, indicating that the WB and GM best fit the measurements, which are so close to each other that it is difficult to distinguish between them from these data sets. It is evident that the PH expression underestimates while the LN overestimates when droplet size distributions are broad, respectively. The PH, WB, GM and LN are almost equivalent for very narrow size distributions. The MO, MM and MC only represent cases with specific values of d.

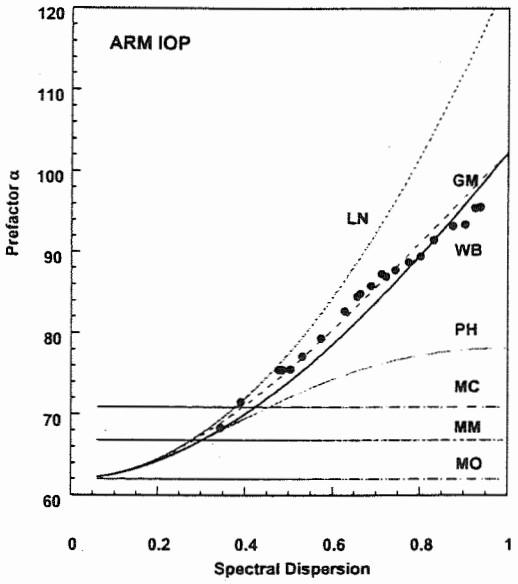

Fig. 2. Comparison of prefactors calculated from the different expressions listed in Table 1 as a function of the spectral dispersion. The solid dots represent those derived from the FSSP-measured cloud droplet size distributions.

4. COMPARISON OF MEASURED AND PARAMETERIZED r_e

This section further illustrates the performance of these different parameterization schemes by comparing values of r_e measured by the FSSP (r_{em}) with those estimated from the different parameterization schemes. As indicated in Fig. 3, the WB and GM schemes obviously outperform the others. The PH tends to underestimate while the LN tends to overestimate re.

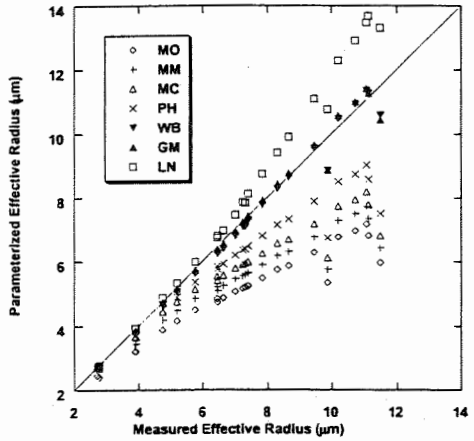

Fig. 3. The cloud droplet effective radius estimated from the five different parameterization schemes as a function of the measured effective radius.

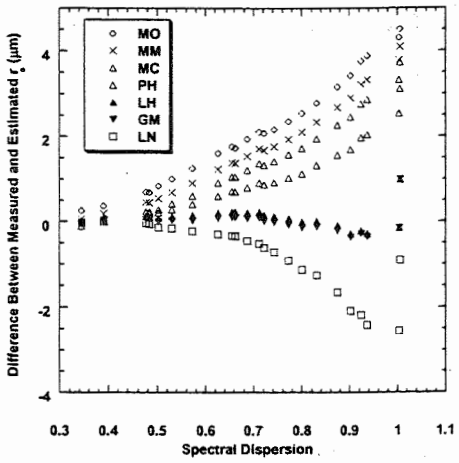

Fig. 4. The difference between measured cloud droplet effective radius and those estimated from different parameterization schemes as a function of the spectral dispersion. Note the substantial reduction of errors by the WB and GM parameterizations.

It is expected form Eq. (1) that the differences in r_e estimated from the different parameterizations are due to the treatment of the dependence of α on d. This result can be better understood by examining the differences between r_{em} and parameterized r_e as a function of spectral dispersion. As shown in Fig. 4, the bias of the estimated re from the measured values increases with d for all the parameterizations except for the WB and GM scheme. At large values of d, the bias of r_e could be larger than 2 μm, which is large enough to cause noticeable errors in climate models (Slingo 1990).

5. WHY IS THE LH SCHEME MOST ACCURATE?

By a simple mathematical analysis, a universal "1/3" power-law can be derived (Martin et al., 1994; Liu and Yu 1998)

$$r_e = 62.04 \frac{\left(1+3d^2+sd^3\right)^{2/3}}{1+d^2}\left(\frac{L}{N}\right)^{1/3}$$

where s is the skewness of the size distributions. From Eq. (2), all the 7 schemes can be derived as special cases by substituting the corresponding "functions" between s and d. Therefore, to demonstrate why the WB and GM schemes parameterize r_e more accurately becomes to show that both schemes describe the s-d relationship more accurately. The result is evident from Fig. 5.

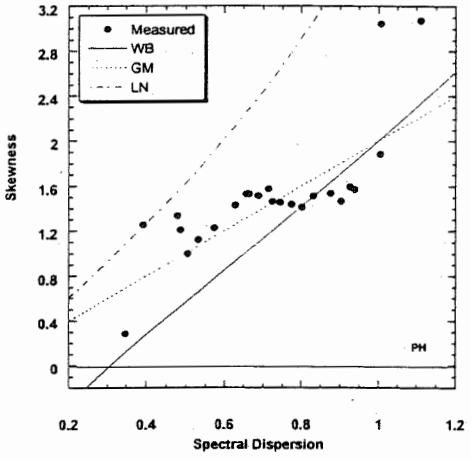

Fig. 5. The relationship between the skewness and spectral dispersion. The dots represent the data points calculated from measured droplet size distributions.

6. CONCLUSIONS

Existing "1/3" power-law expressions for parameterizing r_e are compared and analyzed using data collected during two recent IOPs over the ARM SGP site. It is found that the Weibull-based and Gamma-based schemes most accurately represents the dependence of α on d, and hence most accurately parameterizes r_e because of its accuracy in describing the dependence of s on d. It is also demonstrated that the bias of r_e by the parameterization schemes that have been widely used in current climate models could be large enough to cause serious problems. The result suggests that either Weibull distribution or Gamma distribution should be used to represent cloud droplet size distributions, particularly for studies related to the effective radius.

The state-of-art cloud parameterization in climate models is to predict L and N from which r_e is then determined using a "1/3" power-law with a fixed value of prefactor such as Martin's expression (Ghan et al. 1997; Lohmann et al. 1999). This study suggests that the prefactor is important as well. Accurately representing r_e in climate models requires predicting the prefactor in addition to liquid water content and droplet concentration. This study also suggests the convergence and consistence of microphysics parameterization in climate models with that in smaller-scale models such as cloud-resolving models: they also need to find the appropriate analytical size distribution for describing cloud droplet size distributions. In fact, finding an appropriate analytical size distribution itself is a fundamental change to cloud physics community.

ACKNOWLEDGEMENTS

The discussions with Dr. S. E. Schwartz at Brookhaven National Laboratory are stimulating. This research was supported by the Environmental Sciences Division of the US Department of Energy, as part of the Atmospheric Radiation Measurement Program and was performed under contract DE-AC02-98CH10886.

REFERENCES (INCOMPLETE)

Bower, K. N. and T. W. Choularton, 1992: A parameterization of the effective radius of ice-free clouds for use in global climate models. Atmos. Res., **27**, 305 – 339.

Bower, K. N., T. W. Choularton, J. Latham, J. Nelson, M. B. Baker, and J. Jensen, 1994: A parameterization of warm clouds for use in atmospheric general circulation models. J. Atmos. Sci., 51, 2722-2732.

Dandin, P., C. Pontikis, and E. Hicks, 1997: Sensitivity of a GCM to changes in the droplet effective radius parameterization. Geophys. Res. Lett., 24, 437-440.

Table 1. Expressions for Prefactor α

MO	$\alpha = 62.04$
MM	$\alpha = 66.84$
MC	$\alpha = 70.91$
PH	$\alpha = 62.04 \frac{\left(1+3d^2\right)^{2/3}}{\left(1+d^2\right)}$
WB	$\alpha(b) = 64.52 \frac{\Gamma^{2/3}(3/b)}{\Gamma(2/b)} b^{1/3}$, $d = \left[\frac{2b\Gamma(2/b)}{\Gamma^2(1/b)} - 1\right]^{1/2}$
GM	$\alpha = 62.04 \frac{\left(1+2d^2\right)^{2/3}}{\left(1+d^2\right)^{1/3}}$
LN	$\alpha = 52.04\left(1+d^2\right)$

VARIABILITY OF THERMODYNAMIC PROPERTIES OF CLOUDS

Vincent E. Larson*[1], Robert Wood[2], Paul R. Field[2], Jean-Christophe Golaz[3], Thomas H. Vonder Haar[1], William R. Cotton[3]

[1]Cooperative Institute for Research in the Atmosphere, Colorado State University
[2]Meteorological Research Flight, Farnborough, UK
[3]Colorado State University

1. INTRODUCTION

Clouds vary on smaller scales than those that can be resolved by atmospheric numerical models. Therefore several properties of clouds ought to be parameterized.

One such property is the fraction of a grid box that is occupied by cloud. In large-scale models of climate, fractional cloud cover of a grid box greatly affects radiative transfer within the grid box. Even for models with smaller grid boxes, cloud cover is still important for calculating cloud microphysical processes. The rates of microphysical processes depend on *within-cloud* properties, and if cloud fraction is unknown, the model only knows about *grid box average* properties. The in-cloud values and grid box average values may differ markedly.

Even when a grid box is entirely occupied by cloud, it still may be advantageous to parameterize within-cloud variability. Ignoring subgrid variability can lead to errors when computing the rate of a microphysical process that is nonlinear. To compute the rates of such nonlinear processes, a model that ignores subgrid variability would first compute the grid box average properties and then insert these averages into a microphysical formula. The result so obtained differs, in general, from the quantity we desire, which is the microphysical rate averaged over the grid box.

To parameterize microphysical processes, what is needed is the probability density function (pdf) of the relevant microphysical properties over the grid box. In principle, if the relevant pdf were known and a local microphysical formula were formulated with perfect accuracy, then the grid box average microphysical rate could be parameterized with perfect accuracy. Therefore we believe that a key to cloud parameterization is the pdf of microphysical properties.

Considering the fundamental place of pdfs in parameterization, few authors have used boundary layer observations to compute pdfs of conserved variables. (An exception is the paper of Wood and Field (2000).) Several studies have used satellite retrievals to calculate pdfs of cloud optical depth (see e.g. Wielicki and Parker 1994; Barker et al. 1996). However, to parameterize microphysical processes, what is most useful is pdfs of conserved variables. Such pdfs have been simulated by numerical models (Lewellen and Yoh 1993; Xu and Randall 1996b; Wyngaard and Moeng 1992), but obtaining pdfs from models has a disadvantage over obtaining pdfs from observational data: namely, the range of scales that can be simulated is still rather limited by computational cost. For example, the domain of large eddy simulations is still usually limited to several kilometers, whereas variability of scalars in boundary layers often maximizes at larger scales (Cotton and Anthes 1989, pp. 373–383). Therefore, a large eddy simulation may not produce the full variability that should be accounted for within, say, a 50-km mesoscale model grid box. With the data used in the present paper, we examine pdfs with scales ranging from 2 km to 50 km.

In the present paper, we will study pdfs associated with boundary layers topped by stratocumulus, cumulus, and cumulus rising into stratocumulus. Our primary goal is to characterize these pdfs so that they may be parameterized in numerical models and used, for instance, to compute cloud fraction. Since a pdf is completely determined once all its moments are known, one might expect that using more moments in a fitting formula would lead to a better fit. We will address the question of how many moments are needed to provide a satisfactory fit, and find specific families of pdfs that fit the observed pdfs well.

2. THEORETICAL BACKGROUND

Cloud fraction can be diagnosed if we know the pdf of the conserved variable s that is defined by Lewellen and Yoh (1993). s is a measure of the deviation from a state in which air is saturated but no liquid is present. s is useful because (1) it can be predicted by a numerical model in terms of pressure and conserved variables; and (2) s approximately equals the specific liquid water content, q_l, if (and only if) the total water content, q_t, exceeds saturation.

Given the pdf of s, $P(s)$, the cloud fraction, cf, is given by:

$$cf = \int_{-\infty}^{\infty} ds\, P(s)H(s), \qquad (1)$$

where $H(s)$ is the Heaviside step function. This formula states that the cloud fraction equals that portion of the area under $P(s)$ that corresponds to q_t in excess of saturation, i.e. the area with $s > 0$.

3. PARAMETERIZATIONS OF PDFS OF s

* *Corresponding author address:* Vincent E. Larson, Cooperative Institute for Research in the Atmosphere, Colorado State University, Fort Collins, CO, 80523-1375. E-mail: larson@cira.colostate.edu

If a numerical model can predict $P(s)$ explicitly, then it can also parameterize cloud fraction. But predicting a pdf is difficult and computationally expensive. Instead, we will suppose that the numerical model predicts several moments of s. Then we will assume a functional form for $P(s)$ that depends on several parameters. Given the values of the moments of s in a particular grid box, $P(s)$ for that grid box can then be determined. This approach to parameterization, the "assumed pdf" method, has been used by Sommeria and Deardorff (1977), Randall et al. (1992), Frankel et. al (1993), and Lappen (1999), among others.

The shape of a pdf is fully determined if all of its (infinitely many) moments are specified (Burington and May 1970, pp. 81–82). However, numerical models can feasibly predict only a small number of moments (e.g. 1, 2, or 3). Therefore, it is of practical importance to ascertain whether a small number of moments and an assumed functional form of the pdfs provide sufficient accuracy and generality to characterize atmospheric pdfs. If so, the assumed pdf method offers the promise of providing a rather general subgrid parameterization, one that is based firmly on rigorous mathematics and testable empiricism, and one that can be systematically improved by either increasing the number of moments predicted or refining the assumed functional form of the pdf.

We will use observational data to evaluate 8 different families of functions, listed below, that can be used to parameterize $P(s)$.

(1) Single Delta Function (1 parameter). This "parameterization" is simply the assumption that there is no subgrid variability. This is what models with no explicit pdf parameterization effectively assume. This parameterization provides a baseline against which we can measure the quality of the more sophisticated parameterizations that follow.

(2) Single Gaussian (2 parameters). This parameterization has the virtue of depending on only two moments, the mean and variance; but it cannot represent skewed pdfs.

(3) Generalized Gamma Function (3 parameters). This parameterization allows for skewed pdfs but not bimodal pdfs.

(4) Double Gaussian (5 parameters). This parameterization is the sum of two Gaussians:

$$P_{dg5}(s) = \frac{a}{\sqrt{2\pi}\sigma_1} e^{-\frac{1}{2}\left(\frac{s-s_1}{\sigma_1}\right)^2} + \frac{1-a}{\sqrt{2\pi}\sigma_2} e^{-\frac{1}{2}\left(\frac{s-s_2}{\sigma_2}\right)^2}. \tag{2}$$

Here s_1 and σ_1 are the mean and standard deviation, respectively, of one Gaussian with area a; s_2 and σ_2 are the mean and standard deviation of the other Gaussian. At the present time, predicting 5 moments in a numerical model is prohibitive. However, we include this pdf in our comparison in order to ascertain the best possible fit that can be expected from the double Gaussian functional form.

(5) Double Delta Function (3 parameters). This parameterization consists of two delta functions. The locations and relative amplitude of each can be determined analytically, given three moments (see Randall et al. 1992, Lappen 1999). This parameterization is equivalent to a commonly-used double-plume scheme in which each plume is assumed to be uniform (Randall 1987).

(6) LWFGVC1 (3 parameters). This pdf parameterization resembles the double delta function parameterization, except that we broaden the delta functions into Gaussians that have the same non-zero width. Specifically, in (2), we set $\sigma_1 = \sigma_2 = 0.6\sigma$, where σ is the standard deviation of the pdf as a whole. This parameterization is more realistic than the double delta function pdf, but the simple assumption of equal widths still allows us to solve for a, s_1, and s_2 analytically, unlike in the Lewellen-Yoh or LWFGVC2 parameterizations below. LWFGVC1 does not reduce to a single Gaussian when skewness vanishes.

(7) Lewellen-Yoh (3 parameters). Lewellen and Yoh (1993) assume a double Gaussian pdf and then eliminate two parameters so that the resulting pdf depends only on the mean, variance, and skewness of s. When the skewness vanishes, their pdf parameterization reduces to a single Gaussian, but when skewness approaches infinity, their pdf consists of one Gaussian with infinitesimal width, and the other Gaussian with width σ.

(8) LWFGVC2 (3 parameters). LWFGVC2 is similar to the Lewellen-Yoh parameterization except that LWFGVC2 can be easily modified if a later dataset warrants such modification. LWFGVC2 again assumes a double Gaussian pdf and again eliminates two parameters. Specifically, it assumes:

$$\frac{\sigma_1}{\sigma} = 1 + \gamma \frac{Sk}{\sqrt{\alpha + Sk^2}} \qquad \frac{\sigma_2}{\sigma} = 1 - \gamma \frac{Sk}{\sqrt{\alpha + Sk^2}}. \tag{3}$$

where we choose $\alpha = 2$ and $\gamma = 0.6$, and Sk is the skewness of s. This parameterization, like Lewellen and Yoh (1993), ensures that when skewness vanishes, the pdf reduces to a Gaussian (i.e., σ_1/σ and σ_2/σ approach unity).

4. COMPARISON OF PARAMETERIZATIONS OF THE PDF OF s

This section tests how well the aforementioned 8 parameterizations predict cloud fraction.

The data used to calculate observed pdfs were obtained during the Atlantic Stratocumulus Transition Experiment (ASTEX) field experiment, which studied the transition from stratocumulus to cumulus boundary layers over the North Atlantic Ocean in June 1992 (Albrecht et al. 1995), and the First ISCCP (International Satellite Cloud and Climatology Project) Regional Experiment (FIRE) field experiment, which studied marine stratocumulus off the coast of California in June and July of 1987 (Albrecht et al. 1988). In ASTEX, the boundary layers often contained cumulus rising into stratocumulus, and sometimes contained only cumulus clouds. In FIRE, the boundary layers

were shallower and usually contained only stratocumulus cloud. We test the parameterizations separately on the ASTEX and FIRE datasets, rather than combining the two. Furthermore, we form a third group of transects consisting of all ASTEX transects that contain some cloud and that occurred on flights during which, according to the observers' notes, the C-130 sampled pure cumulus layers. This set of transects is denoted "ASTEX cumulus cloud-layer transects" in Fig. 1. We formed this third grouping of transects because we want to test whether the 8 parameterizations are sufficiently general to model pdfs in both stratocumulus and cumulus layers.

Fig. 1 compares the predictions of cloud fraction for the 8 parameterizations. To construct Fig. 1, we first truncated all transects within a dataset to the same length, e.g. 50 km. Then we computed observed and parameterized cloud fraction for each transect. Next we computed the standard deviation of [parameterized cloud fraction minus observed cloud fraction] for all transects of a given length within the dataset. Finally we repeated the process for different transect lengths. Fig. 1 also includes the cloud fraction parameterization of Xu and Randall (1996a), a 2-parameter pdf which uses relative humidity and q_l as predictors. The Xu-Randall parameterization was originally developed for deep convective regimes, but here we test whether it can be extended for use in cloudy boundary layers.

The errors in cloud fraction for all parameterizations are fairly small. This is partly because cloud fraction is an integral of $P(s)$, and hence positive and negative areas partially cancel. From Fig. 1, we see that the single delta function parameterization performs worst: i.e., accounting for subgrid variability using any of our subgrid parameterizations is better than assuming no variability. The next best parameterizations are the 2-parameter Xu-Randall and 3-parameter double delta function parameterizations. Better than these two are the other 3-parameter parameterizations (Lewellen-Yoh, LWFGCV2, LWFGCV1, and generalized gamma distribution). Better than the 3-parameter parameterizations is the 5-parameter double Gaussian parameterization. The 3-parameter generalized gamma parameterization performs slightly worse than Lewellen-Yoh, LWFGCV2, and LWFGCV1, in part because for large skewness, the generalized gamma parameterization has an (integrable) singularity. This renders the scheme sensitive to bin placement.

The errors in cloud fraction prediction show little dependence on transect length. This implies that although variance and skewness may depend strongly on scale, the families of pdfs we test are more or less equally valid for all scales shown. Therefore pdf parameterizations may be largely independent of grid spacing from 2 km to 50 km.

In summary, we find that, as expected, the more parameters a parameterization uses, the better it fits $P(s)$. If only two parameters (e.g. mean and variance of s) are available to a numerical model, the (unskewed) single-Gaussian parameterization probably

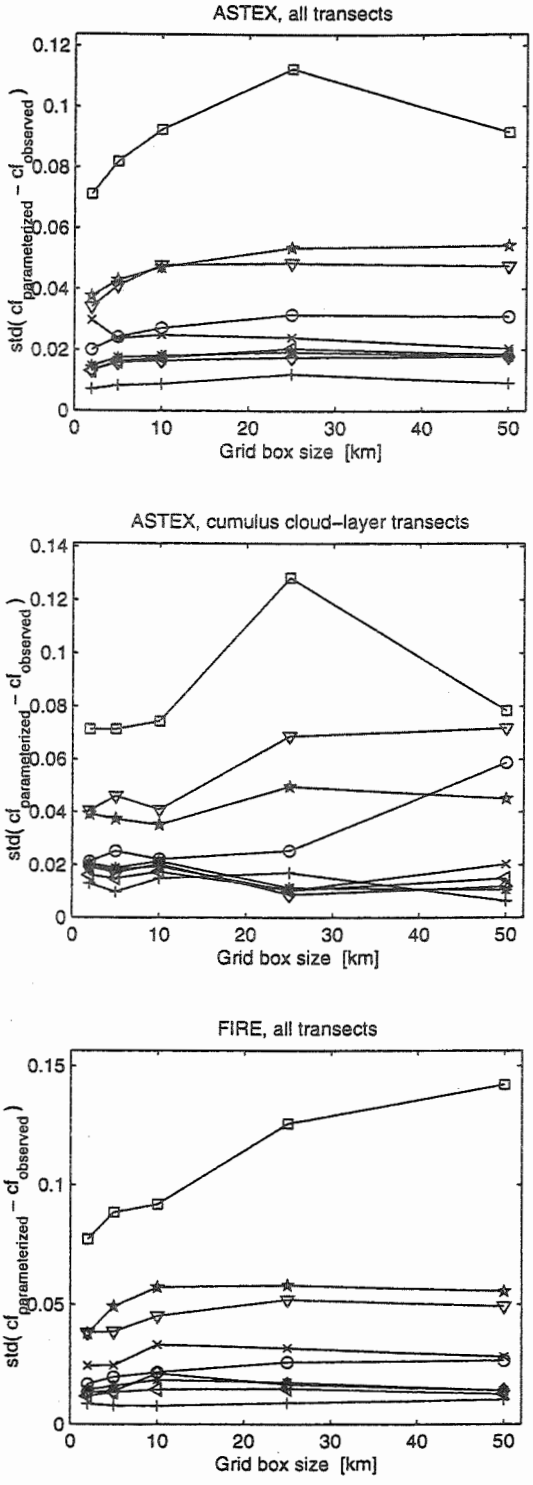

Figure 1: Single delta function, squares; single Gaussian, circles; generalized gamma function, x-marks; 5-parameter Gaussian, pluses; double delta function, stars; LWFGVC1, left-pointing triangles; Lewellen-Yoh, diamonds; LWFGVC2, asterisks; Xu-Randall, downward-pointing triangles.

performs as well as one can hope for, given that observed skewnesses in ASTEX and FIRE can be either negative or positive, with a near-zero average. However, the single-Gaussian distribution does perform poorly for cumulus cloud layers when large grid boxes ($\sim$ 50 km) are used. In these cases, the skewnesses are usually large and positive.

If mean, variance, and skewness of s are available to the parameterization, then a significant improvement over the single-Gaussian parameterization can be made. With the exception of the double delta function parameterization, all 3-parameter parameterizations perform better than the single-Gaussian parameterization. In particular, the Lewellen-Yoh, LWFGCV1, and LWFGCV2 parameterizations appear to be general enough and accurate enough to adequately represent the rather complex pdfs in stratocumulus and cumulus boundary layers. Although the prediction of an additional parameter, e.g. kurtosis, would improve the fit in some cases, the overall improvement would be fairly modest.

5. CONCLUSIONS

We have used observational data to calculate pdfs (probability density functions) for stratocumulus, cumulus, and cumulus-rising-into-stratocumulus layers. The observed pdfs are complex. Although many of the pdfs are Gaussian, others are strongly bimodal, highly positively skewed, or highly negatively skewed. The highly skewed pdfs tend to have a long tail, rather than a double-delta-function shape.

Despite this complexity, the observed pdfs can be adequately modeled by simple parameterizations. When only two parameters are available to a model, the model may use the single-Gaussian parameterization, which fits most of the data fairly well. But the single-Gaussian parameterization provides poor fits to cumulus-layer pdfs when the grid box size is large (e.g. 50 km). In contrast, pdf parameterizations that depend on three parameters (e.g. mean, variance, and skewness) appear to be general enough to model both stratocumulus and cumulus-layer pdfs. The Lewellen-Yoh, LWFGVC2, and LWFGVC1 parameterizations provide particularly good fits. Remarkably, these schemes offer uniformly good diagnoses of cloud fraction over length scales ranging from 2 km to 50 km, with no change in tuning coefficients. Hence these parameterizations may be satisfactory over a wide range of grid box sizes. These results suggest that it may be worthwhile to seek ways of predicting mean, variance, and skewness of s in numerical models.

Acknowledgements. The authors would like to thank the RAF aircrew and MRF staff involved in the planning and execution of the ASTEX field campaign. V. E. Larson acknowledges financial support from the National Oceanic and Atmospheric Administration, contract NA67RJ0152. J.-Ch. Golaz acknowledges support by the National Science Foundation under contract ATM-9904128.

REFERENCES

Albrecht, B. A., D. A. Randall, and S. Nicholls, 1988: Observations of marine stratocumulus clouds during FIRE. *Bull. Amer. Meteor. Soc.*, **69**, 618–626.

Albrecht, B. A., C. S. Bretherton, D. Johnson, W. H. Schubert, and A. S. Frisch, 1995: The Atlantic stratocumulus transition experiment — ASTEX. *Bull. Amer. Meteor. Soc.*, **76**, 889–904.

Barker, H. W., B. A. Wielicki, and L. Parker, 1996: A parameterization for computing grid-averaged solar fluxes for inhomogeneous marine boundary layer clouds. Part II: Validation using satellite data. *J. Atmos. Sci.*, **53**, 2304–2316.

Burington, R. S. and D. C. May, Jr., 1970: *Handbook of Probability and Statistics with Tables.* 2nd ed. McGraw-Hill Book Co., 462 pp.

Cotton, W. R., and R. A. Anthes, 1989: *Storm and Cloud Dynamics.* Academic Press, 883 pp.

Frankel, S. H., V. Adumitroaie, C. K. Madnia, and P. Givi, 1993: Large eddy simulation of turbulent reacting flow by assumed pdf methods. *Fluids Engineering Conference on Engineering Applications of Large Eddy Simulations*, FED 12, pp. 81–101.

Lappen, C.-L., 1999: The unification of mass flux and higher-order closure in the simulation of boundary layer turbulence. Ph. D. dissertation, Colorado State University, 329 pp.

Lewellen, W. S., and S. Yoh, 1993: Binormal model of ensemble partial cloudiness. *J. Atmos. Sci.*, **50**, 1228–1237.

Randall, D. A., 1987: Turbulent Fluxes of Liquid Water and Buoyancy in Partly Cloudy Layers. *J. Atmos. Sci.*, **44**, 850–858.

Randall, D. A., Q. Shao, and C.-H. Moeng, 1992: A second-order bulk boundary-layer model. *J. Atmos. Sci.*, **49**, 1903–1923.

Sommeria, G., and J. W. Deardorff, 1977: Subgrid-scale condensation in models of nonprecipitating clouds. *J. Atmos. Sci.*, **34**, 344–355.

Wielicki, B. A., and L. Parker, 1994: Frequency distribution of cloud liquid water path in oceanic boundary layer cloud as a function of cloud fraction. Preprints, *Eighth Conference on Atmospheric Radiation*, Nashville, TN, Amer. Meteor. Soc., 415–417.

Wood, R., and P. R. Field, 2000: Relationships between total water, condensed water and cloud fraction examined using aircraft data. Accepted to *J. Atmos. Sci.*

Wyngaard, J. C., and C.-H. Moeng, 1992: Joint Probability Density. *Bound.-Layer Meteor.*, **60**, 1–13.

Xu, K.-M., and D. A. Randall, 1996a: A semiempirical cloudiness parameterization for use in climate models. *J. Atmos. Sci.*, **53**, 3084–3102.

Xu, K.-M., and D. A. Randall, 1996b: Evaluation of statistically based cloudiness parameterizations used in climate models. *J. Atmos. Sci.*, **53**, 3103–3119.

RAINDROP SIZE SPECTRA: REPRESENTATION BY NORMALISED GAMMA FUNCTIONS.

Anthony J. Illingworth

JCMM, Department of Meteorology, University of Reading, RG6 6BB, UK

1. INTRODUCTION

A knowledge of the naturally occurring hydrometeor size distribution is important in understanding the mechanisms involved in the growth and formation of clouds and precipitation and also in correctly representing the many possible interactions between different categories of clouds and precipitation particles in bulk parameterisation schemes used in numerical models for forecasting weather and climate. A knowledge of hydrometeor size spectra is also important in interpreting radar reflectivity data.

Marshall and Palmer proposed the use of an exponential to describe naturally occurring raindrop spectra:

$$N(D) = N_o \exp(-\lambda D) \qquad (1)$$

where $\lambda = 3.67/D_o$, D_o is the equivolumetric median drop diameter and N_o is approximately constant with a value 8000 m^{-3} mm^{-1}. Naturally occurring raindrop spectra have fewer of the very large and the very small drops than given by equation (1) and Ulbrich (1983) explored the use of a gamma function to represent this:

$$N(D) = N_g D^{\mu} \exp(-\lambda D) \qquad (2)$$

where $\lambda = (3.67+\mu)/D_o$ and N_g has the units m^{-3} $mm^{-1-\mu}$. Values of μ=0 reduce to the exponential in equation (1) but for +ve μ the spectrum is more monodispersed.

Swann (1998) examined the effect of using μ= 0 and 2.5 in the graupel size spectrum for simulations of deep convection. Errors arise in estimating rainfall rate from radar reflectivity because radar reflectivity (Z) is proportional to ΣND^6 but rainfall rate (R) varies nearly as $\Sigma ND^{3.67}$ so changes in raindrop size spectra will lead to uncertainty when R is derived from Z. Smith (1998) has questioned the use of gamma functions for computing Z-R relationships noting that changing μ from 0 to 6 only changes the predicted rainfall by 40% which is less than the usual scatter in Z-R relationships. However, the changes in the value of μ are important when polarisation parameters such as differential reflectivity (Z_{DR}) and specific differential phase shift (KDP) are used; such techniques essentially respond to the mean shape (and therefore size) of the raindrops and so should reduce the error in derived rainfall to less than 40%.

Corresponding author address: Anthony Illingworth, JCMM, Dept of Meteorology, Univ of Reading, Reading RG6 6BB, UK. e-mail: A.J.Illingworth@reading.ac.uk.

In this paper we consider the range of naturally occurring raindrop spectra obtained by fitting observed spectra to normalised gamma functions. We note that the use of equation (2) leads to a spurious correlation between N_g and μ which vanishes if equation (2) is normalised. All measured raindrop spectra are subject to some errors because of instrumental imperfections and, more importantly, sampling limitations. As a result of these errors the value of μ can depend upon the application of the spectrum; if the use is for deriving effective radius or optical depth then the smaller diameter drops are more important, but for radar computations the contribution of the larger drops dominates. This leads to a counter intuitive conclusion: different values of μ being derived from the same observed spectrum dependent upon the subsequent use of the spectrum.

2. REPRESENTATION OF RAINDROP SIZE SPECTRA BY GAMMA FUNCTIONS.

Kozu and Nakamura (1991) and Tokay and Short (1996) have confirmed that equation (2) is an excellent representation of naturally occurring raindrop spectra: they fitted observed spectra to the equation by forcing the third, fourth and sixth moments of the spectrum to be equal to the integral of equation (2) with appropriate weighting and found that R calculated from the fitted values of λ, μ and N_g agreed to within 0.02dB (0.5%) of the value of R derived from the raw spectra. The values of μ were in the range 0 to 30, much larger than those predicted by Ulbrich. The values of N_g however, covered 15 orders of magnitude in agreement with Ulbrich. Ideally, in equation (2) changing μ should alter the shape of the drop size spectra independently of the drop concentration, but as equation (2) stands if μ is increased and N_g and λ are kept the same then the D^{μ} term leads to a massive fall in the value of N(D). Because this does not happen in natural drop spectra, we have the oft-reported correlation of N_g with μ to compensate.

Raindrop size spectra may be better represented by a normalised gamma function (Smyth et al, 1999; Illingworth and Blackman, 1999):

$$N(D) = \frac{N_L\, 0.03\, D_o^4 \lambda^{\mu+4} (D)^{\mu}}{\Gamma(\mu+4)} \exp(-\lambda D) \qquad (3)$$

rather than the simpler form in equation (2). The normalisation factors are introduced so that even if μ is varied the liquid water content stays the same. The factor

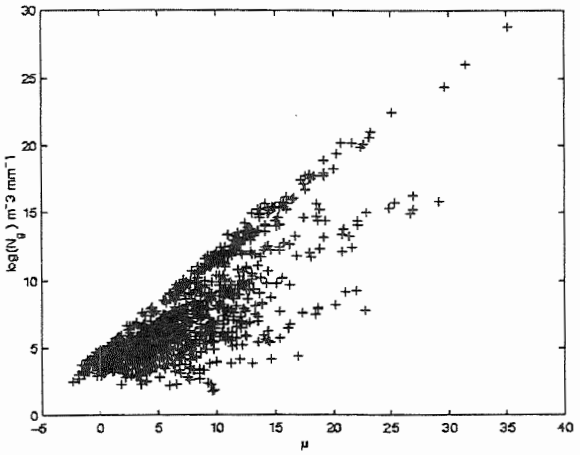

Figure 1. Values of μ and Ng (the non-normalised concentration - Equation (2) covering 25 orders of magnitude for the 1260 spectra in July 1998.

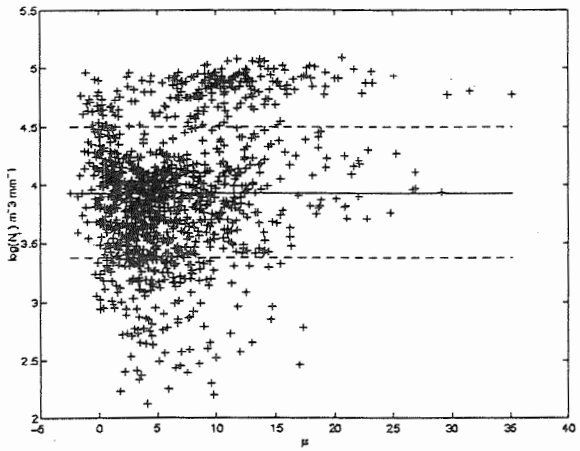

Figure 2. As for Figure 1 but fitted to the normalised gamma function of Equation. Mean $\log(N_L)$=3.93: solid line. Dotted lines are one standard deviation.

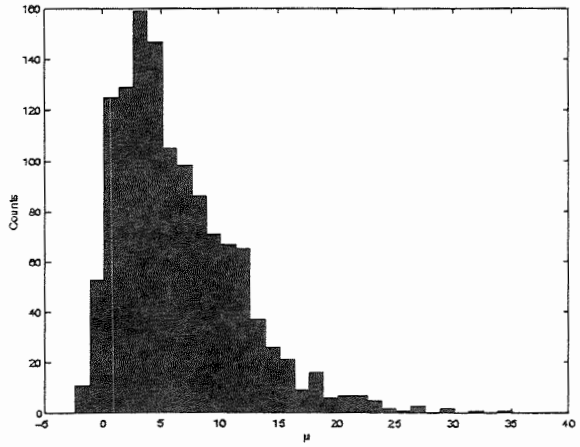

Figure 3. Histogram of μ for rainfall for the month of July 1988. Mean value is 6.43 and standard deviation 5.27. 99% of the values lie within two standard deviations.

$0.03\ D_o^4$ ensures that if μ=0 then (3) reduces to the standard Marshall-Palmer distribution with $N_L = N_o$. A final advantage is that the units of N_L and N_o are the same and are physically reasonable.

3. NORMALISED FITS TO NATURAL DROP SPECTRA.

In order to demonstrate the increased realism of equation (3) for representing naturally occurring raindrop spectra we have fitted the 1260 spectra recorded for every 30 second period of rainfall during the month of July 1988 in the UK. Figure 1 displays the well known correlation of μ with the non normalised concentration factor N_g in equation (2) obtained by fitting the sixth, fourth and third moments of the distribution. As found by Kozu and Nakamura (1991) and Tokay and Short (1996) values of μ range from zero to nearly 30 whilst the values of N_g range over fifteen orders of magnitude. This should be contrasted with the fit to equation (3) shown in Figure 2. The values of μ are of course unchanged, but are now uncorrelated with N_L. $\text{Log}(N_L)$ does not vary with μ but has a mean value of 3.93 (solid line in the Figure), or 8511 m^{-3} mm^{-1}, remarkably close to the Marshall Palmer value of 8000. The standard deviation of $\log(N_L)$ is 0.56 (or a factor of 3.6, dashed lines in the Figure) and 96% of the data lies within two standard deviations (a factor of thirteen) of the mean value. To test the sensitivity the exercise was repeated normalising the gamma function with respect to total drop concentration (N_T) as suggested by (Chandrasekar and Bringi, 1987) but in this case there is still a correlation of N_T and μ. However, if normalisation is carried out with respect to rain rate, N_R, (which involves replacing the number four in the gamma function and powers in equation (3) with 4.67, and the numerical factor is 0.0341 rather than 0.0331), then, as expected, the values of N_R are virtually identical to those of N_L. The mean of $\log(N_R)$ is still 3.93.

A histogram of the values of μ is plotted in Figure (3) and is similar to those found by Kozu and Nakamura (1991) and Tokay and Short (1996). The mean value of μ is 6.43 with a standard deviation of 5.27 and 99% of the values lying within two standard deviations of the mean. Figure 4 shows that μ is not correlated with rainfall rate, although once μ is above 30mm/hr the values of μ do seem to be less scattered and are restricted to the range 4 to 8. The values of D_o rise with rainfall rate, as would be expected, but there is some scatter, with values for R>30mm/hr in the range 2.3 to 3.3mm but values of N_L are lower and are within a factor of two of 2000 m^{-3} mm^{-1}. It is this size (or D_o) variability which is responsible for the errors in a simple Z-R relationship.

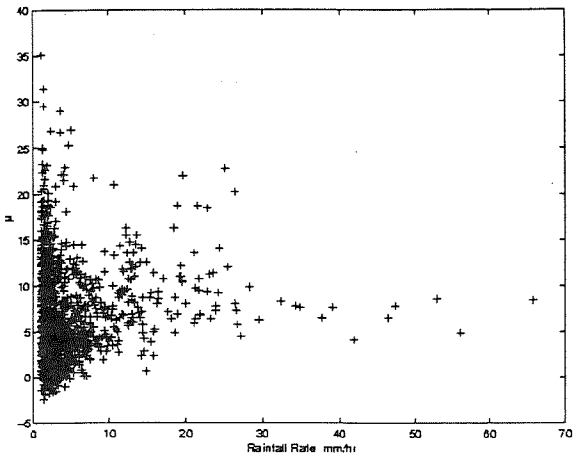

Figure 4. Values of μ as function of rainfall rate for the month of July 1988.

We conclude that equation (3), the normalised gamma function with respect to liquid water content, has the required properties of representing naturally occurring raindrop spectra, with the three parameters now becoming independent, with μ representing the shape of the spectrum, N_L the overall drop concentration, and λ or D_o, the equivolumetric median drop size.

6. CONCLUSIONS

Analysis of naturally occurring raindrop spectra reveals that if they are fitted to a normalised gamma function then for rain the mean value of μ=5 and the concentration, N_L, is no longer a function of μ. These values are obtained by forcing the third, fourth and sixth moments of the observed spectrum to be equal to the integral of the normalised gamma function with appropriate weightings. Such a fit is appropriate if radar reflectivity is being related to either liquid water content or to rainfall rate. If a relationship is sought between effective radius, optical depth and liquid water content, then it would be more appropriate to force the first, second and third moments to be equal to the integral of the weighted normalised gamma function. This leads to slightly lower values of μ

A similar fitting procedure could also be applied to ice particle spectra to deduce the optimum values of μ to be used in bulk parameterisation schemes.

ACKNOWLEDGEMENTS.

We thank the staff at Chilbolton and the RCRU at RAL for providing the disdrometer data. Financial support was provided by NERC and the Environment Agency grant EA 0331057.

REFERENCES

Chandrasekar, V. and V.N. Bringi, 1987: Simulation of radar reflectivity and surface measurement of rainfall *J.Atmos.Ocean.Tech.*, **4**, 464-478.

Illingworth, A.J. and Blackman T.M. 1999: The role of raindrop shape and size spectra in deriving rainfall rates using polarisation radar. 29th Int Conf on Rad Meteorol., 301-304. AMS.

Kozu, T. and K. Nakamura, 1991: Rainfall parameter estimation from dual-radar measurements combining reflectivity profile and path integrated attenuation. J. *Atmos. Ocean.Technol*, **8**, 259-270.

Smith P.L., 1998: Raindrop size distributions: Exponential of gamma - does it make a difference? Conf on Cloud Physics, Everrett, WA, AMS, Boston, Mass p399-402.

Smyth T.J., T.M.Blackman and A. J. Illingworth, 1999: Observations of oblate hail using dual polarisation radar and implications for hail-detection schemes. *Q. J. Roy. Meteorol. Soc.*, **125**, 993-1016..

Swann, H, 1998: Sensitivity to the representation of precipitating ice in CRM simulations of deep convection. *Atmos Research,* **48**, 415-435.

Tokay, A. and D.A. Short, 1996: Evidence from tropical raindrop spectra of the origin of rain from stratiform versus convective clouds. *J. Appl. Meteor.*, **35**, 355-371

Ulbrich,C.W., 1983: Natural variations in the analytical form of the raindrop size distribution. *J.Clim Appl.Met.*, **22**, 1764-1775.

A CONSISTENT MICROPHYSICAL PARAMETERIZATION FOR MULTI PHASE CLOUDS

Marcin J. Szumowski[1], David L. Mitchell[1], and Wojciech W. Grabowski[2]

[1] Division of Atmospheric Sciences, Desert Research Institute, Reno, NV
[2] National Center for Atmospheric Research, Boulder, CO

1. INTRODUCTION

Predicting heavy snow and rainfall events in complex terrain has been particularly challenging partly due to inadequate microphysical parameterizations and erroneous representation of terminal velocities of rain and snow in synoptic and mesoscale prediction models. We propose a new parameterization based on the Snow Growth Model (SGM) developed by Mitchell (1994). SGM has been diagnostically tested in nine different case studies and showed very good agreement with observations (e.g., Mitchell et al. 1996). In SGM ice number concentrations are diagnosed from two other known variables: ice water content, and the slope parameter (λ). Ice particle growth by diffusion, aggregation, and riming is treated explicitly in the SGM, and ice particle fall speeds (and the resulting snowfall rates) are sensitive to the relative importance of the three growth mechanisms and the broadness of the droplet size distribution. A new prognostic scheme based on the SGM is in the process of development and implementation in cloud and mesoscale models. The microphysical equations in the SGM, in addition to treating snowfall, can be adapted to predict the evolution of raindrop size distributions. However the applicability of SGM-based scheme to warm precipitation needs to be tested. In this paper we describe a test designed to evaluate SGM performance in warm rain situations. Preliminary results of these sensitivity tests will be presented at the conference.

2. KINEMATIC TEST FRAMEWORK

A simple but realistic framework used to test warm rain microphysical packages has been designed for the 4th International Cloud Modeling Workshop and documented by Szumowski et al. (1998).

Corresponding author address: Marcin Szumowski
2215 Raggio Parkway, Reno, NV, 89512-1095.
mszumow@dri.edu

This framework allows for efficient comparisons of various microphysical formulations, ranging from bulk to mass-resolving explicit schemes with a large number of mass categories, without the influence of dynamical-microphysical interactions, but with the influence of advective processes. The two-dimensional, time-evolving, prescribed flow is based on dual-Doppler syntheses of the kinematic structure of convective updrafts within offshore Hawaiian rainbands (Szumowski et al. 1997). A detailed discussion of the test framework can be found in Szumowski et al. (1998), or on the web at: http://misty.sws.uiuc.edu/wmoworkshop/Case1/Warm_Rain_Development.html.

3. DETAILED (MASS RESOLVING) MODEL

The detailed model used in the comparisons with the SGM parameterizations simulates drop activation, growth by condensation and collision-coalescence, but ignores breakup. The model uses 36 mass categories encompassing drop diameters from 3.5 microns to 6.25 mm. Droplet activation (similar to that described by Stevens et al. 1996) is followed by growth by vapor diffusion (or evaporation) including ventilation effects (after Tzivion et al. 1989), and growth by stochastic collision-coalescence using the multi-moment technique of Tzivion et al. (1987). In simulating the collision-coalescence process, we have implemented a new set of semi-empirical collection efficiencies (Beard and Ochs, personal communication), based on the work of Beard and Ochs (1984). Microphysical scheme very similar to the one outlined here was tested in the kinematic framework described in Section 2 by Reisin et al. (1998), and have been implemented in two- and three-dimensional large eddy simulation (LES) models (e.g., Stevens et al. 1996).

4. WARM RAIN PARAMETERIZATION BASED ON THE SGM

Applying the SGM-based scheme to simulate warm rain physics requires, among other considerations, different efficiencies in treating collision-coalescence and different coefficients in the mass and fall speed relationships.

The general unique feature of the two-moment SGM scheme is that it is not based on a prognostic equation for ice crystal nucleation, but rather on ice water content (IWC), with changes in the IWC driving the formulation of the growth processes. These processes predict the slope parameter (λ) of a gamma size distribution (Mitchell 1994):

$$N(D) = N_0 D^{\nu} \exp(-\lambda D) \qquad (1)$$

The dispersion parameter ν is generally assumed constant, while N_0 relates λ and ν to the IWC (or N). The SGM methodology may be adapted to treat warm clouds by predicting both λ and N_0 from the appropriate growth processes and advection. We apply mass- and fall speed-dimensional power law relations to spherical water drops instead of ice particles, substituting ice collection efficiencies with those corresponding to drop interactions. When used in this capacity the SGM becomes a rain growth model (RGM).

The RGM is applied in the context of a bulk formulation of the Rutledge and Hobbs (RH, 1983) single moment scheme that provides the cloud liquid water mixing ration (q_c) through bulk condensation and initial rain water mixing ratio (q_r) through the autoconversion process. Although we still utilize the RH parameterization of the autoconversion, we treat the interactions of rainwater and cloud water differently. The key difference between the RH scheme and the RGM scheme, is that the raindrop spectrum evolves during each time step according to (1) with adjustable N_0 and λ. Therefore the accretion (collection of cloud droplets by rain) process is treated differently, and the resulting raindrop spectrum and its mean terminal velocity vary from those in RH.

5. COMPARISON METHODOLOGY

In comparing simulations with detailed microphysics to those with the SGM-based scheme we will examine the temporal and spatial evolution of the following variables: cloud water (e.g., Fig. 1), rainwater, rainfall rate (e.g., Fig 2), radar reflectivity factor, and accumulated precipitation at the surface (e.g., Figs 3 and 4). Additionally drop size distribution obtained from the mass-resolving model will be compared to the RGM parameterization at selected times and places within the model domain. The preliminary results of these comparisons will be presented at the conference. Sample plots of the temporal evolution of cloud water, rainfall rate, and surface precipitation in the middle of the test domain are shown below. The bulk model predictions of rainfall rate and surface precipitation are both unrealistically high (Fig. 3). These values tend to be much lower for a mass-resolving model because of size dependence of terminal velocities and collection efficiencies (e.g., see Fig. 4 – note the scale change).

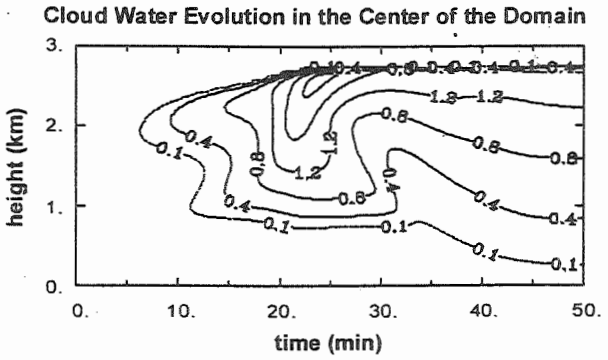

Fig. 1. Temporal evolution of the cloud water mixing ratio vertical profile in the center of the test domain simulated using bulk microphysics. The contour interval is 0.4 m s^{-1} (dashed line is 0.1 m s^{-1}).

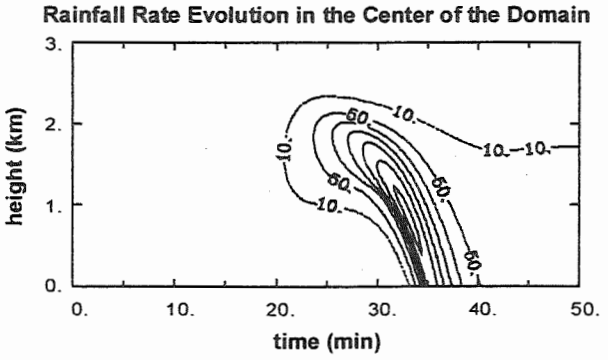

Fig.2. Same as Fig. 1 except for the maximum rainfall rate. The contour interval is 50 mm h^{-1}, except for the first contour at 10 mm h^{-1}.

6. ACKNOWLEDGEMENTS

The authors wish to thank Dr. Graham Feingold for providing the condensation and coalescence code and

for valuable comments. This work is sponsored in part by NSF under grant NSF ATM 9908995.

7. REFERENCES

Beard, K.V., and H.T. Ochs, 1984: Collection and coalescence efficiencies of accretion. *J. Geophys.* Res., **89,** 7165-7169.

Mitchell, D.L., 1994: A model predicting the evolution of ice particle size spectra and radiative properties of cirrus clouds. Part I: Microphysics. *J. Atmos. Sci.*, **51**, 797-816.

Mitchell, D.L., S. Chai, Y. Liu, A. Heymsfield and Y. Dong, 1996: Modeling cirrus clouds. Part I: Treatment of bimodal size spectra and case study analysis. *J. Atmos. Sci.*, **53**, 2952-2966.

Rutledge, S.A., and P.V. Hobbs, 1983: The mesoscale and microscale structure and organization of clouds and precipitation in midlatitude cyclones. VIII: A model for the "Seeder-Feeder" process in warm-frontal rainbands. *J. Atmos. Sci.*, **40**, 1185-1206.

Stevens, B., G. Feingold, W.R. Cotton, and R. L. Walko, 1996: Elements of the microphysical structure of numerically simulated nonprecipitating stratocumulus. *J. Atmos. Sci.*, **53**, 980-1006.

Szumowski, M. J., R. M. Rauber, H. T. Ochs, and L. J. Miller, 1997: The microphysical structure and evolution of Hawaiian rainband clouds. Part I: Radar observations of rainbands containing high reflectivity cores. *J. Atmos. Sci.*, **54**, 369-385.

Szumowski, M. J., W. W. Grabowski, and H. T. Ochs, 1998: Simple two-dimensional kinematic framework to test warm rain microphysical models. *Atmos. Res.*, **45**, 299-326.

Tzivion, S., G. Feingold, and Z. Levin, 1987: An efficient numerical solution to the stochastic collection equation. *J. Atmos. Sci.*, **44**, 3139-3149.

Tzivion, S., G. Feingold, and Z. Levin, 1989: The evolution of raindrop spectra. Part II: Collisional Collection/Breakup and Evaporation in a Rainshaft. *J. Atmos. Sci.*, **46**, 3312-3327.

Reisin, T.G.,Y. Yin, Z. Levin, S. Tzivion, 1998: Development of giant drops and high reflectivity cores in Hawaiian clouds: numerical simulations using a kinematic model with detailed microphysics. *Atmos. Res.*, **45**, 277-298.

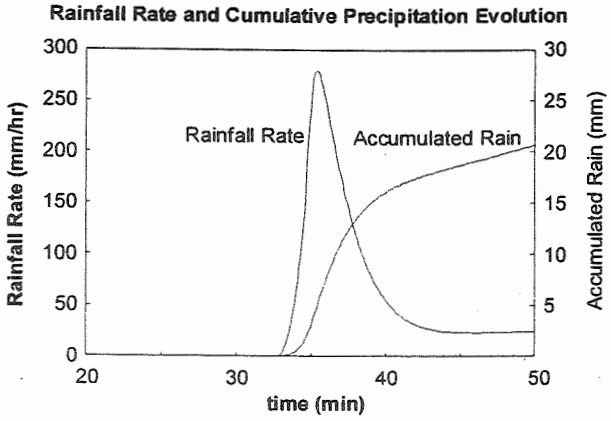

Fig. 3 Surface rainfall rate (mm h^{-1}) and accumulation of rain (mm) in the center of the domain.

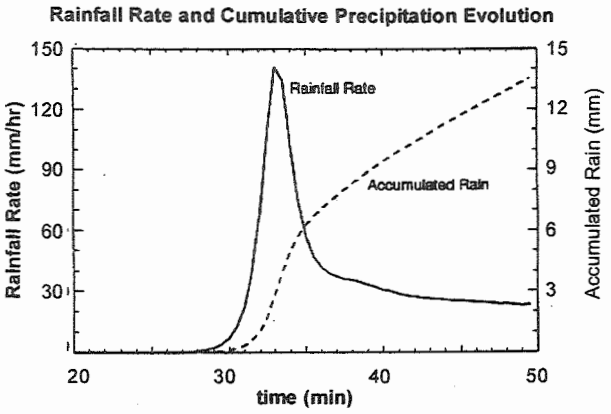

Fig. 4. Same as Fig. 3 except adapted from Reisin et al. (1998) for a simulation with detailed microphysics including drop breakup.

Sensitivity of Radiation Models to Parameterization of Arctic Cloud Ice Water Content Versus Particle Area and Length

F. S. Boudala [1], G. A. Isaac [2], Q. Fu [1], S. G. Cober [2], and A.V. Korolev [2]

[1] Department of Oceanography, Dalhousie University, Halifax, Nova Scotia, B3H 4J1, Canada

[2] Meteorological Service of Canada, Toronto, Ontario, M3H 5T4, Canada

1. INTRODUCTION

General circulation model (GCM) studies indicate that ice clouds have a major impact on earth's climate through their influence in the radiation balance (*Ramanhathan et al.*, 1983). However, GCM simulations require realistic treatment of the single scattering properties (SSP) of clouds for radiative transfer calculations. Ice clouds contain mainly non-spherical ice crystals and using models such as the geometric ray tracing method to calculate SSP is time consuming and as a result it is not applicable for GCMs. A parameterization developed by *Fu* (1996, hereafter Fu96) for ice clouds is one of the promising approaches to estimate SSP including the extinction coefficient (β), single scattering albedo (ϖ) , and asymmetry factor (g) . The extinction coefficient (β) can be given for example in a form:

$$\beta = \frac{4(3)^{1/2} IWC}{3\rho_{ic} D_{ge}} \qquad (1a)$$

where ρ_{ic} is the density of pure ice , IWC is the ice water content, and D_{ge} is the generalized mean effective size defined by:

$$D_{ge} = \frac{2(3)^{1/2} IWC}{3\rho_{ic} A_c} \qquad (1b)$$

where A_c is the total cross sectional area of ice particles per unit volume. In F96, the ϖ and g are parameterized as function of D_{ge} . Therefore, these two parameters, D_{ge} and IWC are needed to simulate radiative properties of cirrus clouds. The IWC could be a prognostic variable in GCM. The GCM predicted IWC, however, need to be validated from the in-situ aircraft measurements. In addition, parameterization of D_{ge} in terms of GCM predicted variables is also necessary, which also requires in-situ measurements of IWC.

Corresponding Author: F. S. Boudala, Dalhousie, University, Halifax, Nova Scotia, Canada, B3H 4J1

In this study, the focus will be on the uncertainties of IWC derived from aircraft observations of area and particle distributions, and their effects on radiative properties of ice clouds.

The customary practice for estimating IWC is via parameterization with area (A) and D measured with 2D probes (*Brown and Francis*, 1995; *Francis et al.*, 1994; *Francis*, 1995; *Francis et al.* 1998). These parameterizations are based on mass to particle size relationships determined by experiments (*Cunnigham*, 1978, hereafter Cu78, *Locatelli* and *Hobbs*, 1974, hereafter, LH74; *Mitchell*, 1990, hereafter, M90). In this paper, these parameterization schemes used to estimate IWC are compared using particle size and projected area measured with 2DC and 2DP probes during the FIRE Arctic Cloud Experiment (FIRE.ACE) and the Beaufort and Arctic Storms Experiment (BASE) in various glaciated clouds in the polar regions. The IWC parameterization schemes are tested against the measurements obtained with a total water content (TWC) probe (Korolev et al., 1998). Finally, the estimated IWC and D_{ge} from these schemes were used to calculate absorption coefficients in the IR and asymmetry factor in the visible bands, and possible effects on radiative transfer calculations are discussed .

2. THE PARAMETERIZATION SCHEMES

The following two relationships were determined by experiments:

$M_{ij} = a_j D_{ij}^{b_j}$ (Locatelli and Hobs, 1974) (2a)

$\mathrm{Deij} = a_j A_{ij}^{b_j}$ (Cunnigham, 1978) (2b)

where M_{ij} is the mass of particle with size i and habit j , D_{ij} is the maximum dimension of ice particles for given i and j, De_{ij} is the equivalent melted diameter for given i and j, A_{ij} is the projected area for given i and j and a and b are some constants for a given habit j. Using the expressions in equations 2a and b, IWC is calculated using the equations:

$$IWC = \frac{4}{3}\pi\rho ic\sum_{ij} Nij(De/2)^3 \quad \text{(Francis et al., 1994)} \quad (3a)$$

$$IWC = \sum_{ij} Nij Mij \quad \text{(Heymsfield and Mcfarquhar} \quad (3b)$$

where Nij is the concentration of ice particles in a given bin size i and habit j. Similar expressions to 3a , but with D in equation 2a taken as a mean diameter of given ice particle habit (Francis, 1995, hereafter F95), or as the mean of the maximum chord lengths measured parallel and perpendicular to the photo diode probe (maximum mean diameter) (*Brown* and *Francis,* 1995, hereafter BF95) have been used. F95 and BF95 have assumed equation 2a corresponding to the habit j=1 to be aggregates of unrimed plates, side planes, bullets and columns (*Locatelli and Hobbs*, 1974, hereafter LH74). *Francis et al.* (1994, hereafter F94) have assumed the habit to be bullet-rosette and they have only considered the particle size in the range 25 to 800 μm measured using a 2DC probe. In *Francis et al.* (1998, hereafterF98), a and b were estimated from an assumed exponential size distribution for N in equation 3a that best fit the measured IWC using their TWC probe (F95). The *Heymsfield and McFarquhar* (1996, hereafter HMc96) scheme was based on a maximum diameter. However, in their model 12 different particle habits were used based on an algorithm developed from Central Equatorial Pacific Experiment (CEPEX) observations. In this work, only four different particle habits were identified based on an algorithm developed by *Cober et al.*, (2000). The particle habits identified are circles, needles, dendrites (2DP) and irregular shapes. Using this information, similar parameterization schemes also were developed. The parameterization scheme that is based on HMc96 (equations 2b and 3a) is represented by HM96. Finally, we modify F98 scheme, to consider four different habits, which is called F98habit here. Therefore, F98habit scheme is an extension of F98 scheme.

For the HM96 scheme, constants (a & b) for the four identified particle habits were obtained from LH74 and M90. The irregular particles are assumed to be aggregates of unrimed plates, bullets, planes and columns (M90), and the circular particles are represented by ice spheres by adjusting the constants (a & b) for water drops obtained in *Heymsfield,* (1977) to spherical ice particles. Constants (a & b) for needles and dendrites are based on M90 and LH78 respectively.

The constants (a and b) used by F98 were used for irregular particles only in F98habit, and the other 3 particle habit classifications were based on Cu78. In this scheme, the best agreement with measurements using TWC probe were found when the circular images were assumed to be small and large snow.

3. THE DATA ANALYSIS SCHEMES

The measurements were taken during FIRE.ACE covering the dates from 21 to 29 of April, 1998 and during BASE from 4 to 29 of September, 1994. Instruments used for measuring particle size and area were the PMS 2DC and 2DP probes. The TWC content was measured using the Nevzorov TWC and LWC probes. The glaciated clouds were identified based on 2D images and the Nevzorov probes. From 2DC and 2DP data, particle distributions in terms of maximum diameter, mean diameter, maximum mean diameter and area diameter were calculated. Using these particle size distributions, 4 parameterization schemes (F94, F98, F95 and BF95) along with two modified schemes (HM96 and F98habit) were tested. During the analysis, particle sizes in the range $25 \le D \le 725$ μm (2DC) and in the range $800 \le D \le 6400$ μm (2DP) measurements were used. The 2DC probe seems to underestimate particle concentrations for diameter less than 100 μm and as a result the IWC derived in this region can be underestimated.

4. PRELIMINARY RESULTS AND DISCUSSION

4.1 The IWC and mean effective size

The derived IWC from several of the parameterization schemes were compared against the F98 scheme. All schemes generally show similar trends, although the derived ice water contents differ by al least a factor of 2 due to using different schemes.

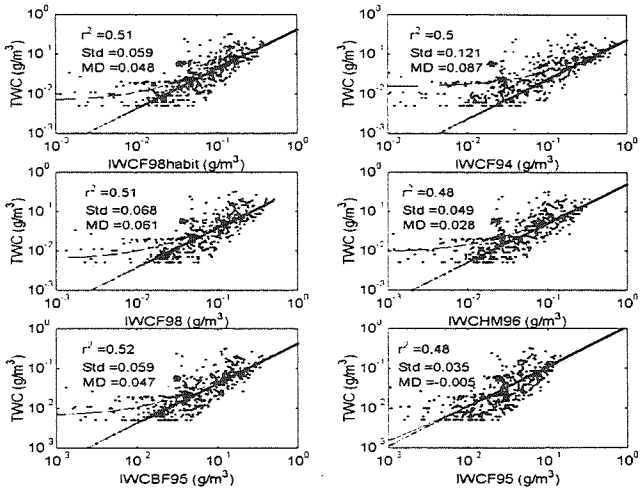

Figure 1. The estimated IWCs are plotted against TWC.

The validity of these parameterization schemes can only be tested against directly measured IWC, which is not possible at this stage. However, in glaciated clouds, measured TWC can be assumed to represent IWC. Data plotted in the figures are identified as measured in ice clouds based on the 2D images, but sometimes it is hard to differentiate between circular ice and liquid drops. The parameterization schemes were tested, against the measured TWC for various combinations of TWC and altitude (Figure 1). For BASE data the best correlation was found for conditions of TWC ≥ 0.005 g//m^3 and LWC $\le 0.6 * TWC$ g//m^3 . The figure also indicates that the

agreement seems to be better for higher IWC (TWC>g/m^3) .

In the figure, the best fit line is represented by the thin line, and the thick line is when the best fit line is forced to cross at the center. As can be seen in the figure, the difference between these two lines becomes more significant in regions of low TWCs . The poor correlation in these regions of low IWC may be partly the effects of missing small particles in the schemes in relatively low IWC clouds, but instrument errors could also be a factor.

The correlation coefficient (r^2), standard deviation of the difference between estimated and measured (Std), and the mean difference (MD) are also given in the figure. The r^2 s are similar for all schemes, near 0.5 for BASE data (Figure 1) , for FIRE.ACE data (not shown here), the r^2 values are significantly lower. The Std and MD can vary however (see Figure 1). The scheme F94 gave the highest MD (0.121 g//m^3) and the scheme F95 gave the lowest MD (-0.005 g//m^3). Generally however, for both FIRE.ACE and BASE data, the parameterized IWC were higher than the measured TWC by about a factor of 2. The exceptions are for F94 and F95; the mean ratios to TWC for these schemes were found to be 3 and 0.8 respectively suggesting that the F94 scheme overestimates the measured TWC by at least a factor of 3 and that there is no significant difference between TWC and the F95 scheme. BF95 found a good correlation between their TWC probe measurements and estimated IWC for cirrus cloud. They claimed that the TWC probe overestimated the parameterized IWC in the region where IWC is greater than 0.07 g//m^3. Note that their measurements were performed at higher altitude where the clouds are usually dominated by small ice particles. This study also indicated a significant improvements between the parameterization schemes and TWC probe measurements at higher altitudes (Figure 2).

4.2. Radiation

The radiative energy budget is modulated by the clouds through there single scattering properties including extinction , absorption, and the asymmetry factor. Since the extinction coefficient is largely determined by ice particle cross sectional areas which are directly measured by the 2DC and 2DP, the uncertainty in the IWC has a little effects on the extinction coefficient. Therefore, the solar albedo is sensitive to the IWC through its effect on asymmetry factor (g) ,which is a function of D_{ge} . Since the radiative properties of ice clouds in the infrared dominated by absorption (*Fu et al.*, 1997), the IWC effect can be seen through absorption coefficient (β_a) .

Asymmetry factor is a measure of the relative strength of forward scattering and it is expected to vary with ice crystal habit and size. It is believed that for typical terrestrial clouds this parameter ranges 0.75 < g <0.9 (*Stephens,* 1984), although based on limited observations, lower value of 0.7 has been suggested (*Stephens et al.*, 1990). F94 have found a better agreement with observations when g = 0.8. Thus, the influence of ice cloud on climate is strongly affected by choice of a value for g (F94). In order to see the variations of SSP by choice of a certain parameterization, we have calculated the g in the visible and β_a in the infrared using the D_{ge} and IWC derived from the parameterization schemes. To calculate these two parameters, the D_{ge} and IWC estimated from all 30 second averaged BASE data were averaged vertically for every 180 meters and these are given in the first two panels of Figure 2. The calculations were performed using the parameterization schemes given in Fu96 and *Fu et al.*, (1998, hereafter Fu98). These schemes were obtained based on numerical fitting to exact light scattering models (Fu96). The calculated values of g and β_a are given in the last two panels of the Figure 2.

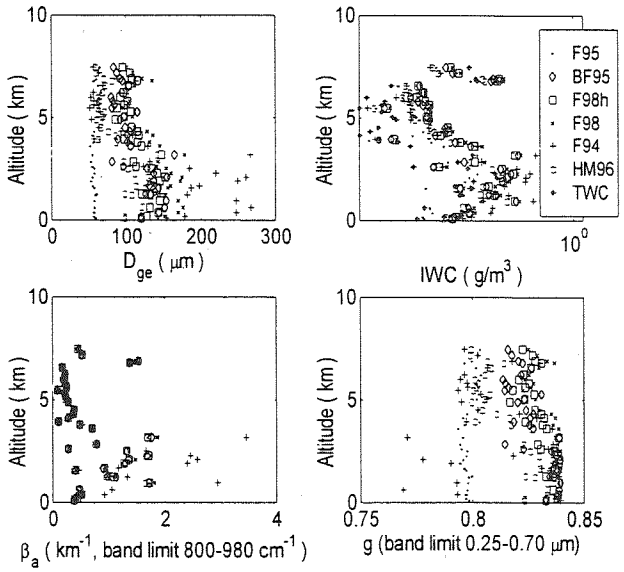

Figure 2. Vertical distributions of asymmetry factor in the visible, absorption coefficient in the IR (the last two panels), and D_{ge} , and parameterized IWC and TWC (the first 2 panels).

As can be seen in the figure, the asymmetry factor can vary from 0.77 to 0.84 for altitudes below about 4 km, and 0.8 to 0.84 above this level , depending on the scheme used. These variations in g can introduce significant errors in model calculations of the atmospheric radiation budget and this will be investigated in the later stages of this work. It is interesting also to note however that the scheme F95 gave a constant value of about 0.8 for all heights in agreement with the observation (F94). As indicated in the figure, generally no significant variations in β_a , particularly above 4 km have been observed.

5. CONCLUSIONS

Several parameterization schemes were used to derive the IWC from aircraft measurements of ice particle area and particle number distributions in stratiform ice clouds, during the Beaufort and Arctic Storms Experiment (BASE) and FIRE Arctic Cloud Experiment (FIRE.ACE). The ice cloud microphysics measurements were made using PMS 2D optical probes, and Nevzorov total water and liquid water content probes. To study the sensitivity of these parameterizations to the model radiative calculations, the asymmetry factor in the visible and the absorption coefficient in IR have been determined from the estimated IWCs and mean effective size (D_{ge}) using the parameterizations given in Fu (96, 98).

The derived IWC from these schemes varied by a factor of 2. Significant correlation (r^2 = 0.5), between measured TWC in the ice clouds and IWC estimated from parameterizations have been observed for BASE, although, all of the schemes have overestimated the measured TWC by a factor 2 except the F95 scheme, which gave similar values. However, the correlation between measured and estimated IWC is weak for FIRE.ACE. The result showed some improvements at higher altitudes.

There was no evidence of any significant improvements when more habits were used in the parameterization schemes as compared to the schemes that assumed a single habit. However, this are just a preliminary result and more research is required to get a better agreement between measured and estimated IWCs, which is highly dependent on the accuracy of the instruments and parameterization schemes used.

The calculated. asymmetry factors from each parameterization schemes can vary from 0.77 to 0.84 for altitudes below about 4 km, and 0.8 to 0.84 above this level , depending on the assumed scheme

6. REFERENCES

Brown A.R.P. and Francis N. P. (1995) Improved measurements of the ice water content in cirrus using a total-water probe. *J. Atmos. Oceanic Technol.,* **12,** 410-414.

Cober, S.G., G.A. Isaac, A.V. Korolev, and J.W. Strapp, (2000:) Assessing the relative contributions of liquid and ice phases in winter clouds. *Proceedings 13th Intl. Conf. on Clouds and Precipitation*, Reno Nevada, 14-18 August 2000.

Cunningham M. R. (1978) Analysis of particle spectral data from optical array (PMS) 1D and 2D sensors. *American . Meteorological Society, Fourth Symposium . Meteorol. Obs. Instrument.* Denver, USA, April 10-14, 1978, 345-350.

Francis N. P., Hignett P. and Macke A. (1998) The retrieval of cirrus cloud properties from aircraft multi-spectral reflectance measurements during EUCREX'93. *Q.J.R. Meteorol. Soc.* , **124**, 1273-1291.

Francis N. P. (1995) Some aircraft observations of the scattering properties of ice crystals. *J. Atmos. Sci.*, **52**, 1142-1154.

Francis N. P., Jones A., Sauders W. R., Shine P. K., Slingo A. And Sun Zhian (1994) The observational and theoretical study of radiative properties of cirrus: results from ICE'89. *Q.J.R. Meteorol. Soc.* , **120**, 809-848.

Fu Q., Yang P., and Sun B. W. (1998) An accurate parameterization of the infrared radiative properties of cirrus clouds of climate models. *J. Climate* , **11,** 2223 - 2237.

Fu Q., Liou N. K., Cribb C. M., Charlock P.T. , and Grossman A. (1997) Multiple scattering parameterization in thermal infrared radiative transfer. J. Atmos. Sci., **54**, 2799 - 2812.

Fu Q. (1996) The accurate parameterization of the Solar radiative properties of Cirrus Clouds for climate models. *J. Climate*, **9**, 2058 - 2082.

Heymsfield J. A. and McFarquhar M. G. (1996) High albedos of Cirrus in the Tropical Pcific warm pool: Micro-physical interpretations from CEPEX from Kwajalein, Marshall Islands. *J. Atmos. Sci.*, **53,** 2424-2551.

Heymsfield J. A. (1977) Precipitation development in stratiform ice clouds: A micro-physical and dynamical study. *J. Atmos. Sci.*, **34,** 367-381.

Locatteli J. and Hobbs V. P. (1974) Fall speeds and masses of solid precipitation particles. *J. Geophys. Res.*, **20**, 2186-2197.

Korolev V. A., Strapp W. J., and Isaac A. G. (1998) The Nevzorov airborne hot wire LWC-TWC probe: Principle of operation and performance. J. *Atmos. Oceanic Technol.* , **15,** 1495-1510.

Stephens G. L. (1984) Parameterization of radiation for numerical weather prediction and climate models. *Mon. Wea. Rev.*, **112,** 827 - 867.

Stephens, G. L., Tsay S. C. , Stackhouse P. W. , and Flatau P. J. (1990) Relevance of micro-physical and radiative properties of cirrus clouds to climate and climatic feedback. *J. Atmos. Sci.*, **47**, 1742 – 1753.

Michel L. D., Zhang R. and Pitter R. (1990) Mass-diamensional relationship for ice particles and the influence of riming on snowfall rates. *J Appl. Meteorol.* **29,** 153-163.

Ramanathan V. , Pitcher J., Malone R. C., and Blackmon M. L. (1983) The response of a spectral general circulation to refinements in radiative processes. *J. . atmos. Sci.* , **40**, 605 - 630.

A NEW MICROPHYSICAL PARAMETERIZATION FOR CLOUD RESOLVING MODELS

Vanda Grubišić and David L. Mitchell
Division of Atmospheric Sciences, Desert Research Institute, Reno, Nevada

1. INTRODUCTION

Accurate prediction of the amount and spatial distribution of precipitation remains a difficult forecasting problem, particularly in regions of complex terrain. Substantial errors in precipitation forecasts result in part from inadequate representation of microphysical processes in mesoscale atmospheric models. Better formulation of the microphysical processes is especially important for predicting precipitation in winter mountain storms, where errors in riming rates, mean terminal velocities, and trajectories of the falling snow can result in serious over- and under-prediction of precipitation amounts on windward and leeward mountain slopes, respectively.

As a first step in developing a new microphysical parameterization for mesoscale models, we have implemented a new scheme in a cloud-resolving model. Existing double-moment ice microphysical schemes for mesoscale models generally treat ice crystal nucleation explicitly whereas the ice crystal size is inferred based on the information on nucleation and ice water content (IWC). These schemes also contain prognostic equations for IWC for various categories of hydrometeors such as cloud ice, snow and graupel, resulting in additional increase of computer time requirements. The two-moment microphysical scheme employed in this work differs in both of these aspects.

2. MICROPHYSICAL MODEL

Instead of explicit treatment of nucleation, which introduces large uncertainties into predicted microphysical fields, the new scheme employs a prognostic equation for the slope parameter λ of the gamma size distribution

$$N(D) = N_0 D^{\nu} \exp -(\lambda D) \ , \qquad (1)$$

where ν is the disperson parameter of the distribution (assumed constant), D is the ice particle dimension, and N_0 relates λ and ν to the number concentration N. The slope parameter λ is a measure of the ice particle size since it related to the mean dimension D_m of distribution (1) through $D_m = (\nu+1)/\lambda$. The equation for the slope parameter has the form

$$\frac{d\lambda}{dt} = \left(\frac{d\lambda}{dt}\right)_{diff} + \left(\frac{d\lambda}{dt}\right)_{agg} + \left(\frac{d\lambda}{dt}\right)_{rim} \ , \qquad (2)$$

where the three terms on the RHS of Eq. (2) account for contributions to ice particle growth by vapor diffusion, aggregation and riming. While this model alleviates issues of nucleation, it requires input on the total IWC and its spatial and temporal changes. Provided the total IWC and λ predicted via Eq. (2), the model solves for the ice particle number concentration using mass conservation.

The scheme is based on the snow growth model (SGM) of Mitchell (1994), which has realistically predicted evolution of ice size spectra in nine case studies of cirrus and frontal clouds. This suggests that using a prognostic equation for the slope parameter, rather than ice particle number concentration, can greatly reduce uncertainties arising from assumptions about the nucleation process. Our approach also eliminates the need for ice hydrometeor categories, since a single size distribution is evolved through all growth processes considered. Since the ice particle number concentration is determined through mass conservation, various cloud ice categories are not needed for determining precipitation.

Another unique aspect of this scheme is its treatment of ice particle shape and fall speed through the use of mass- and area- dimensional power law relations. Theoretical predictions of the fallspeed scheme used, described in Mitchell (1996), fall within 20% of the observed fallspeeds for various particle types, covering various sizes, shapes and phases. The power laws in the fallspeed equation are determined as a function of riming. Hence, mass fluxes predicted by the model are not only linked to the riming process through added mass from accretion, but also through the impact of riming on fallspeeds. Although a single collection efficiency is used for calculating riming amounts, this efficiency is based on the median mass dimension of the size distribution

Corresponding author's address: Dr. Vanda Grubišić, DRI/DAS, 2215 Raggio Pwky, Reno, NV 89512–1095; E-mail: grubisic@dri.edu.

for ice and cloud droplets determined explicitly following Mitchell (1990).

3. CLOUD RESOLVING MODEL

This new microphysical scheme has been incorporated into an Eulerian variant of the cloud resolving model EULAG—a semi-Lagrangian/Eulerian cloud-resolving model documented in Smolarkiewicz and Margolin (1995), and tested in a number of complex geophysical fluid dynamics problems (Grubišić et al. 1996, Grubišić and Smolarkiewicz 1997, Grubišić and Moncrieff 2000). This model is representative of a class of nonhydrostatic atmospheric models that solve the anelastic equations of motion in the standard nonorthogonal terrain-following coordinates. The model is fully second-order accurate in space and time, and its two-time-level temporal discretization, employing consistently the same non-oscillatory forward-in-time transport methods for all model variables, distinguishes it from similar models.

4. PARAMETERIZATION IMPLEMENTATION

The implementation of the new microphysical scheme is based on a predictor-corrector algorithm (Fig. 1). A simple bulk scheme constitutes the predictor step, which provides a necessary input on IWC. Within the corrector step, the SGM-based scheme is invoked to solve the transport equation for the slope parameter and account for the forcing terms from Eq. (2), thus predicting the evolution of the size spectra taking into account various growth processes. Information about the size spectra is in turn used to modify IWC, which is, together with the snowfall rate, returned to the parent model upon the completion of the corrector step.

In the presentation, snowfall rates obtained employing the new microphysical parameterization will be compared to rates obtained with standard microphysical schemes in idealized cloud resolving simulations of wintertime orographic precipitation. We will also comment on the computational efficiency of the new scheme.

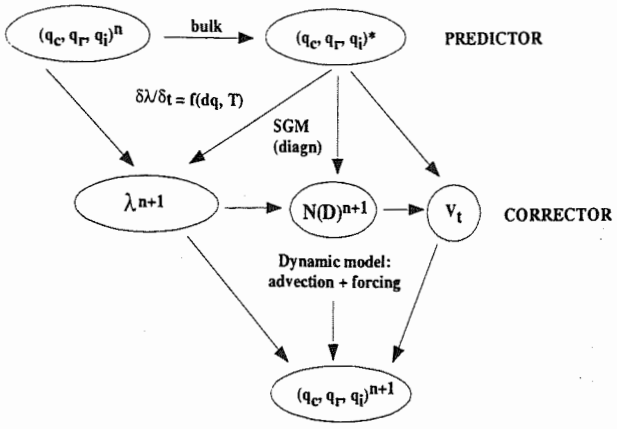

Figure 1: The implementation of the predictor/corrector microphysical scheme into a prognostic model. The predictor step is achieved solely using bulk microphysics. The corrector step evolves the size distribution and yields a new IWC and snowfall rate (or mass flux) at each gridpoint.

5. ACKNOWLEDGMENTS

This research has been funded in part through the U.S. Weather Research Program, NSF Grant ATM–9908995.

6. REFERENCES

Grubišić, V., P. K. Smolarkiewicz, R. M. Rasmussen, and R. E. Carbone, 1996: Hawaiian Rainbands: Effects of thermal forcing on the rainband dynamics. *12th Int. Conf. on Clouds and Precip.*, 19–23 August 1996, Zürich, Switzerland, 741–743.

Grubišić, V., and P. K. Smolarkiewicz, 1997: The effect of critical levels on 3D orographic flows: Linear regime. *J. Atmos. Sci.*, **54**, 1943–1960.

Grubišić, V., and M. W. Moncrieff, 2000: Parameterization of convective momentum transport in highly baroclinic conditions. *J. Atmos. Sci.*, in press.

Mitchell, D. L., 1990: Evolution of snow-size spectra predicted by the growth processes of diffusion, aggregation and riming. *Preprints. Conf. on Cloud Physics*, AMS, July 23–27 1990, San Francisco, CA, 270–272.

Mitchell, D. L., 1994: A model predicting the evolution of ice particle size spectra and the radiative properties of cirrus clouds. Part I: Microphysics. *J. Atmos. Sci.*, **51**, 797–816.

Mitchell, D. L., 1996: Use of mass- and area-dimensional power laws for determining precipitation particle terminal velocities. *J. Atmos. Sci.*, **53**, 1710–1723.

Smolarkiewicz, P. K., and L. G. Margolin, 1995: On forward-in-time differencing for fluids: An Eulerian/semi-Lagrangian nonhydrostatic model for stratified flows. *Atmosphere-Ocean Special*, **35**, 127–152.

Parameterization of drop effective radius in drizzling marine stratus for large-scale models

Zena N. Kogan and Yefim L. Kogan

Cooperative Institute for Mesoscale Meteorological Studies, University of Oklahoma, Norman OK

1. INTRODUCTION[1]

The cloud drop effective radius, R_e, is one of the most important parameters in calculations of cloud radiative properties. Numerous formulations of the effective radius have been developed for use in numerical models (see, e.g., review in Gultere et al. 1996), however, to the best of our knowledge, they all were designed for non-drizzling clouds. The objective of this paper is to derive a parameterization of R_e for precipitating boundary layer clouds.

The R_e parameterization is necessary a function of cloud prognostic variables used in a specific numerical model. To this regard, we note that the majority of current formulations of cloud processes in numerical models are based on partial moments of the drop distribution function: Q_c, cloud water and Q_r, rain water mixing ratios (Kessler, 1969). Kogan and Belochitski (2000) argue that a better-posed problem can be formulated based on the total moments of the drop size distributions (DSD). In this paper we describe R_e parameterizations based on total, as well as partial moments of the DSD. In the latter case we use the following set of variables: N - total drop concentration, Q - total liquid water content, and Q_r drizzle liquid water content, while in the former case - radar reflectivity Z is used instead of Q_r. By using multiple nonlinear regression analysis, we seek R_e in the form: $(R_e)_{par} = D\, N^A\, Q^B\, Z^C$. In the case of partial moments, the parameterization uses Q_r instead of Z.

2. APPROACH AND MODEL

The study was based on microphysical data obtained from simulations made by the CIMMS LES model. The model explicitly predicts CCN and DSD functions (Kogan et al. 1995). We simulated the case of a cloud layer observed during the ASTEX field experiment on June 12, 1992. The marine cloud layer evolved in a clean air mass producing moderate (0.2 mm/day) to heavy drizzle (1.0 mm/day). The boundary layer was well mixed with a stratocumulus base at 250-300 m and a capping inversion at 700-800 m. Cloud layer parameters evolved quite significantly during the six hour long simulation period. Drizzle was gradually increasing, resulting in a breakup of the solid cloud deck and transforming it eventually into a field of small Cu with cloud cover of about 60%. We, therefore, divided the whole simulation into two periods: the first one represented moderate drizzle case (referred to as case M), while the second represented heavy drizzle (referred to as case H). Simulations were made in a domain of 3x3x1.25 km using resolution 75x75x25 m, respectively. From each simulation we extracted about 4,000 to 6,000 DSD that comprised the data set used for deriving the parameterization, as well as a benchmark for its verification.

Finally, we would like to mention that the simulation results have been tested against and found in good agreement with integrated observations of microphysical, radiative, and turbulence parameters (Khairoutdinov and Kogan 1999).

3. TWO AND THREE VARIABLE PARAMETERIZATIONS OF EFFECTIVE RADIUS

Martin et al (1994) using empirical data obtained a parameterization for R_e in the form $R_e^3 = k^{-1} R_{vol}^3$ where $k=0.8$ for non-drizzling marine clouds. This expression can also be written in the form $R_e=66.7(Q/N)^{1/3}$. As Fig. 1 shows, this parameterization performs reasonably well for the

[1] *Corresponding author address*: Dr. Zena Kogan, Cooperative Institute for Mesoscale Meteorological Studies, University of Oklahoma, Norman OK 73019 email: zkogan@ou.edu

moderate drizzle case (rms error of 4.7%), but rather poorly for the case of heavy drizzle (rms error of 12%).

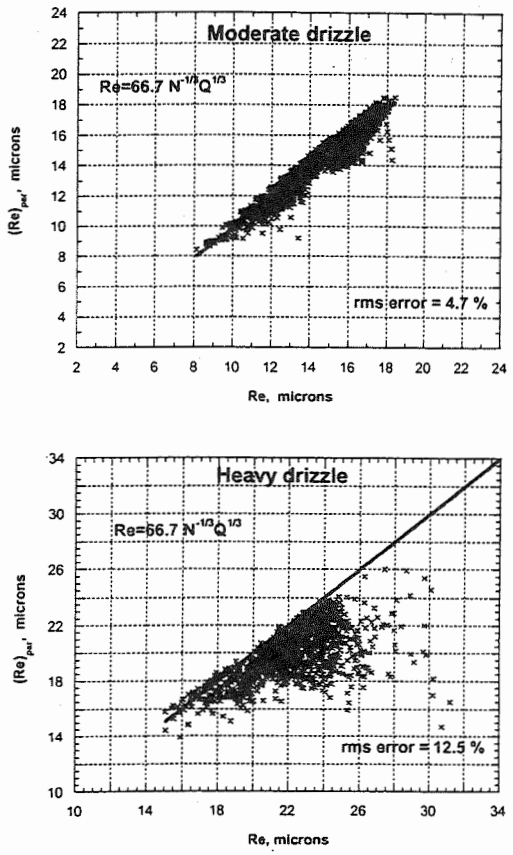

Fig. 1. The scatter plots of Martin et al 1994 $(R_e)_{par}$ versus the benchmark value of R_e from the explicit microphysical model.

Using regression analysis, it is possible to define R_e as a more general function of two variables, Q and N, which provides a more accurate parameterization for R_e (Fig. 2). In the new parameterization the constant $k=0.8$ is replaced with an expression $k=0.57(QN)^{0.15}$ for the M case and $k=0.95Q^{0.30}N^{0.03}$ for the H case. For values Q and N typical for our moderate drizzle case, $k\approx0.7$, while for heavy drizzle case $k\approx0.5$. Fig. 3 shows k as a function of R_e which can be considered as a measure of drizzle. Clearly, marine drizzling stratus with more drizzle (smaller N or larger R_e) will have a smaller k. Our expression for k is consistent with results observed during INDOEX field program. McFarquhar and Heymsfield (2000) report values of k =0.60 for clean drizzling clouds, while for non-drizzling clouds k=0.85. In some instances, they observed values of k as low as 0.4 (McFarquhar, personal communication, 2000).

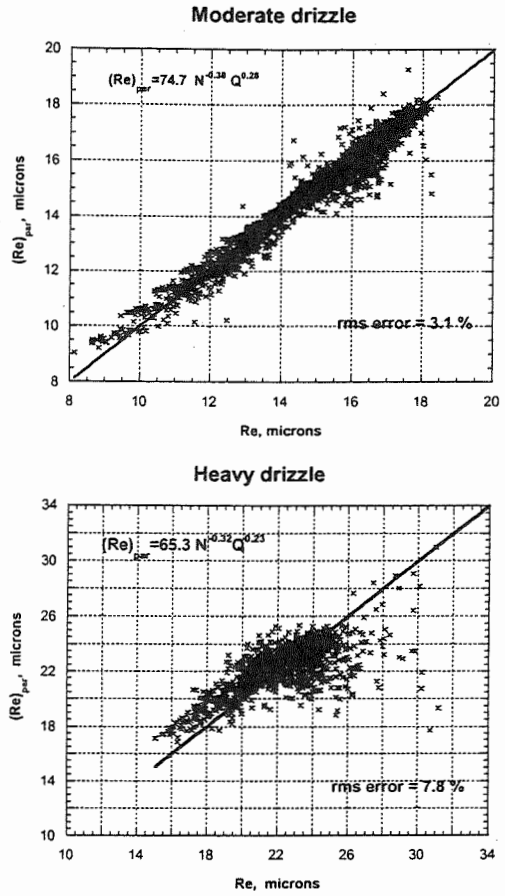

Fig. 2. The scatter plots of $(R_e)_{par}$ defined as a function of two variables versus the benchmark value of R_e from the explicit microphysical model.

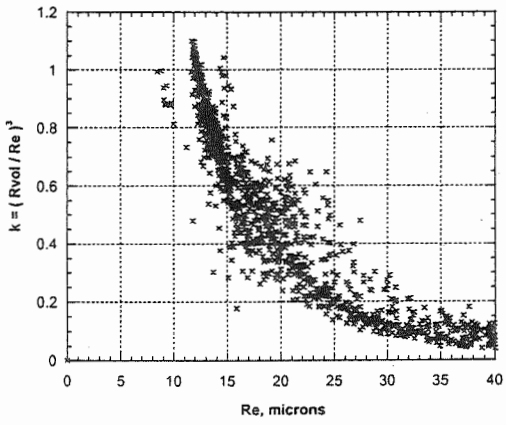

Fig. 3. The constant k as a function of effective radius (amount of drizzle).

Our results show that the two-variable parameterization performs rather accurately for the M case (rms error of 3.1%), but is still rather inaccurate for the heavy drizzle case (rms error of 7.8%). The accuracy of parameterization can be increased if radar reflectivity factor Z is added as a third variable. Fig. 4 shows that the rms error is reduced to 2.6% and 5.1% for the M and H case, respectively. Thus, the three-variable parameterization can be used for a wide range of ambient conditions characterizing marine drizzling stratocumulus.

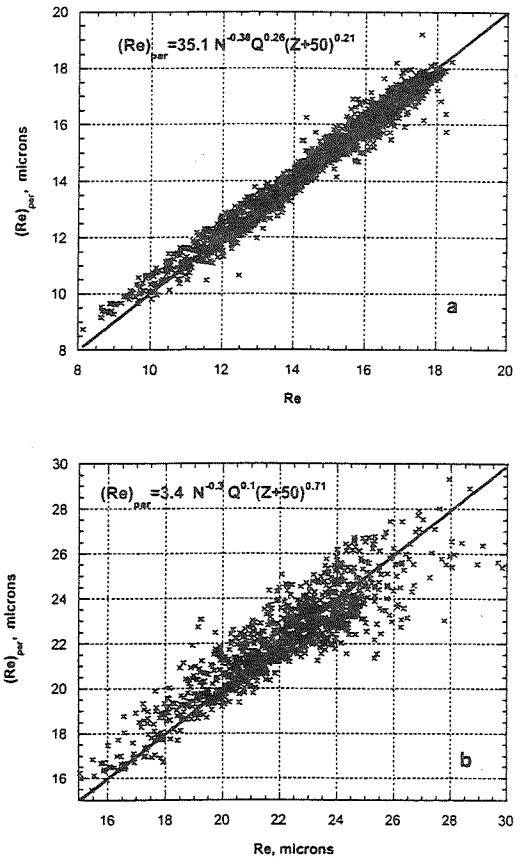

Fig. 4. The scatter plots of $(R_e)_{par}$ defined as a function of three variables versus the benchmark value of R_e from the explicit microphysical model.

The analysis of the pdf of R_{vol} for M and H cases shows that the condition $R_{vol}>16.5\mu$ is satisfied by 93% of the heavy drizzle data points and 7% of moderate drizzle points. Alternatively, $R_{vol}<16.5\mu$ defines equally well the moderate drizzle case. Thus, the parameterizations derived separately for M and H case can be used in a unified form:

$$(R_e)_{par}=35.1\,N^{0.38}\,Q^{0.26}\,(Z+50)^{0.2} \quad if\ R_{vol}<16.5\mu$$
$$(R_e)_{par}=3.4\,N^{0.3}\,Q^{0.1}\,(Z+50)^{0.71} \quad if\ R_{vol}>16.5\mu$$

The accuracy of unified parameterization is essentially the same as in the case of separate parameterizations shown in Fig. 4.

Finally, we derived a R_e parameterization based on partial moments using drizzle water content instead of the radar reflectivity. The error of this parameterization depends on how the threshold radius dividing the cloud and drizzle water is defined. The parameterization performs quite well for a particular threshold (32 μ), however, it performance becomes much worse if we use a different threshold, e.g., 25.4μ or 40.3μ. In the H case, the rms absolute error is 2 μ compared to 1.2 μ for the total moment parameterization. Thus, the uncertainty in the definition of the threshold radius leads to significantly larger errors in the case of partial moment parameterization.

CONCLUSIONS

The microphysical data obtained from LES model with explicit microphysics was used to derive parameterizations of the effective radius for drizzling marine stratus clouds. It was shown that the three-variable parameterization is the most accurate when it is based on total moments of the drop distribution function (total liquid water, drop concentration, and radar reflectivity) and can be confidently used for the whole range of R_e characterizing moderate to heavy drizzling clouds. The parameterization can be used in a unified form for all drizzle cases employing a separation criteria R_{vol}\16.5μ. The partial moment parameterization is less accurate due to uncertainty in the definition of the threshold radius dividing the cloud and drizzle water.

It was also shown that for marine drizzling clouds the parameter k relating R_e to R_{vol} (Martin et al. 1994) depends strongly on radar reflectivity, among other microphysical parameters. It can vary from 0.95 to as low as 0.4. On average, clouds with more drizzle (smaller N and larger Z) will have smaller value of k.

Acknowledgments. This research was supported by the NSF Grant ATM-9870492 and by the

Environmental Sciences Division of U.S. Department of Energy (through Battelle PNR Contract 144880-A-Q1 to the Cooperative Institute for Mesoscale Meteorological Studies) as part of the Atmospheric Radiation Measurement Program. Support for this research was also provided by the ONR Grants N00014-96-1-0687 and N00014-96-1-1112.

REFERENCES

Gultere, I., G.A. Isaac, W.R. Leaitch, and C.M. Banic, 1996: Parameterizations of marine stratus microphysics based on in situ observations: implications for GCMs. *Journal of climate*, 9, 2, 345-357.

Kessler, E., 1969: On the distribution and continuity of water substance in atmospheric circulation, *Meteor. Monogr.*, 10, No. 32, Amer. Meteor. Soc., 84 pp.

Khairoutdinov, M. F. and Y. L. Kogan, 1999: A Large Eddy Simulation Model with Explicit Microphysics: Validation Against Aircraft Observations of a Stratocumulus-Topped Boundary Layer. *J. Atmos. Sci.*, 56, 2115-2131.

Kogan, Y.L., and A. A. Belochitski, 2000: A new approach to parameterization of cloud physics processes. *Proceedings of the 13th International Conference on Clouds and Precipitation,* Reno, NE, 14 –18 August, 2000.

Martin, G. M., D. W. Johnson, and A. Spice, 1994: The measurement and parameterization of effective radius of droplets in warm stratocumulus clouds. *J. Atmos. Sci.,* 51,1823-1842.

McFarquhar G.M. and A.J. Heymsfield, 2000: Microphysics of clean and polluted clouds in the Indian ocean region: observations and parameterizations. *Proceedings of the 13th International Conference on Clouds and Precipitation,* Reno, NE, 14–18 August, 2000.

REALISTIC ESTIMATION OF CLOUD MICROPHYSICS IN CUMULUS/CLOUD PARAMETERIZATIONS: SENSITIVITY TO CLOUD OVERLAP ASSUMPTIONS

Chris J. Walcek
Atmospheric Sciences Research Center, State University of New York, Albany, New York, U. S. A.

1. INTRODUCTION

Cloud-scale dynamic and microphysical processes significantly impact larger-scale meteorological processes through several mechanisms. Unfortunately, regional or global-scale weather or climate models use horizontal grid sizes that are 10-100 times larger than most clouds, which have horizontal dimensions less than ~10 km. Therefore, only a fraction of any grid within a larger-scale atmospheric model is occupied by clouds, and rarely are model grids cloud-free. In larger-scale atmospheric models, processes influenced by clouds such as precipitation formation, radiation transfer, or convective mixing effects are usually highly parameterized using empirical approaches.

Here results of a "typical" cloud parameterization that includes a relatively comprehensive treatment of convective dynamics and numerous microphysical processes responsible for precipitation formation are presented. It is found that widely-varying precipitation formation rates can be calculated from the identical atmospheric column by reasonably adjusting numerous physical and microphysical assumptions over realistic ranges. Many factors such as cloud overlap assumptions are highly variable in the atmosphere, and virtually impossible to know accurately, and calculated effects of clouds are extremely sensitive to the precise layer-by-layer overlap relationship of clouds at various vertical levels in the atmosphere.

Author address: ASRC, 251 Fuller Rd., Albany, NY 12203-3649. (e-mail: walcek@asrc.cestm.albany.edu)

2. PARAMETERIZATION OVERVIEW

Fig. 1 summarizes schematically the microphysical and convective dynamical processes considered in this cloud model. Fractional cloud coverage is first specified based on satellite-derived relationships with observed relative humidity (Walcek, 1994). In conditionally unstable areas, air rises in convective updrafts which "shed" mass to layers above cloud base, inducing a convective-scale updraft/subsidence transilient mixing. Both convective and stratiform clouds generate precipitation using an autoconversion approach, and evaporation and accretional growth are calculated using Kessler's (1969) approach.

Unique features of this parameterization include its ability to realistically initiate precipitation when horizontally-averaged relative humidities are well below 100%, the interaction of convective and "stratiform" precipitation processes in a consistent manner, and a microphysically-reasonable description of precipitation evaporation which is important for simulating observed heating and moistening tendency profiles.

The model has been successfully evaluated using comprehensive tropical convection GATE and TOGA-COARE measurements. The treatment of precipitation evolution allows for the realistic description of whether precipitation falls through cloud-free portions of grid columns, thus evaporating quickly, or precipitation can fall through cloudy portions of grid calls, where rapid accretional growth of precipitation occurs. For both of these cloud effects, the degree to which clouds are overlapping between each layer strongly influences the calculated effects.

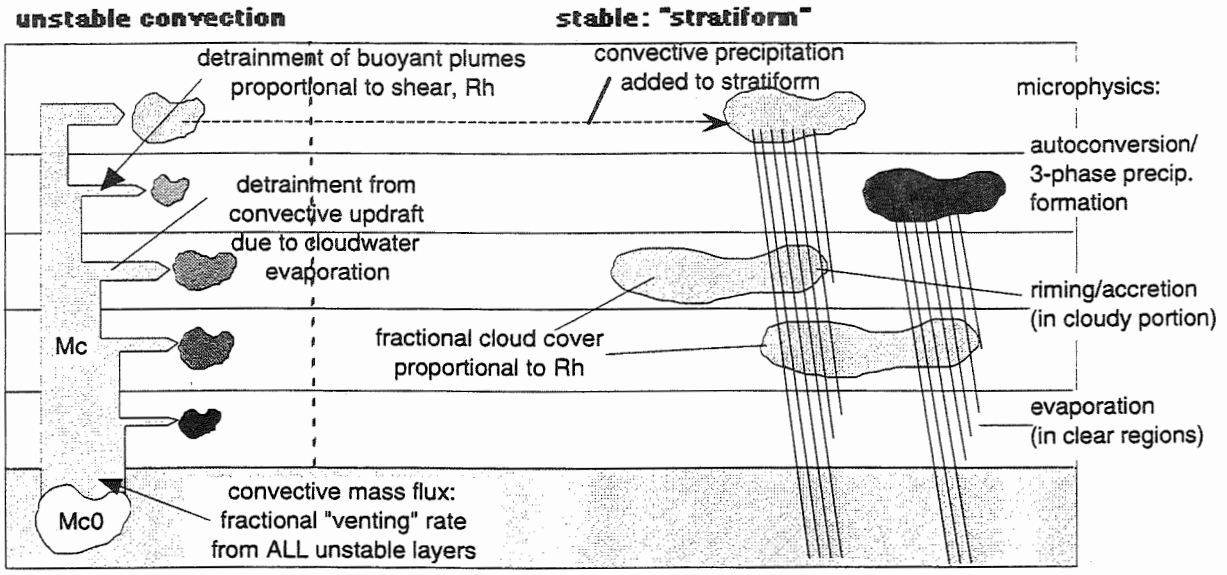

Fig 1. Schematic of subgrid-scale dynamical and microphysical processes considered in this cloud/convection parameterization

3. CASE STUDY

The following precipitation calculations were performed on a sounding taken from a conditionally unstable period in upstate NY on the evening of Sept. 7 1998 during the passage of an intense convective storm. Individual stations collected up to 25 mm of precipitation over the 1/2 - 1 h storm duration, and precipitation rates averaged over 1°x1° latitude/longitude areas averaged about 2-4 mm/h during the storm passage. Fig. 2 shows the observed Rh for this sounding, and the diagnosed cloud fraction and cloud condensed water content for this area, While uncertain techniques were used to infer water contents and fractional cloud coverage from this sounding, that is not the focus of this study. Here it is assumed that the cloudy field is well characterized, and it is shown that uncertainties in cloud overlap can introduce considerably uncertainty in resulting tendency calculations.

4. RESULTS

Figs. 3 shows the sensitivity of the calculated grid-averaged precipitation rate to the change in the assumed convective-scale updraft mass flux at 940 mb. As expected, precipitation rates are nearly linearly related to the updraft mass flux, and an "optimum" venting rate of about 10% of the mass of the lowest 60 mb (6 mb/h) approximately matches the observed precipitation rate, However, many additional factors strongly influence calculated precipitation intensity.

Fig. 4 shows how changes in the assumed cloud fraction affect calculated precipitation from these

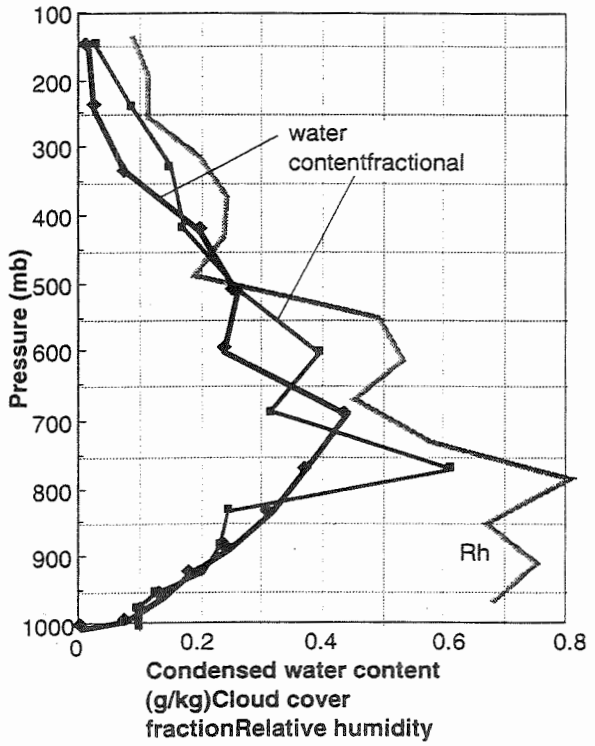

Fig 2. Observed Rh, and diagnosed cloud fraction and condensed water content in clouds during conditionally unstable period near Syracuse, NY, 2AM local time 7 Sept. 1998.

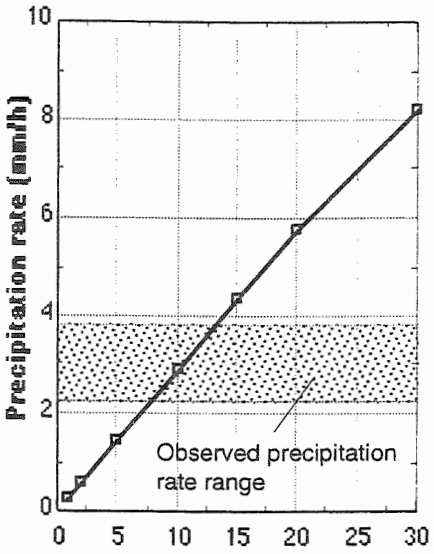

Fig 3. Precipitation rate vs. Convective mass flux for sounding conditions of Fig. 2.

convective cells. Here cloud fraction only affects the fate of precipitation already generated in the atmosphere. Cloud amount varies from the assumed cloud fraction shown in Fig. 2 ("1" on Fig. 4) to clear skies ("0" on Fig. 4) to totally cloud filled skies ("2" on Fig. 4).

Fig. 5 shows how adjustments in the assumed water content of clouds affects calculated surface precipitation. Cloud water contents are adjusted upward and downward from the amounts shown in Fig. 1. Higher water contents contribute to more efficient growth via the "seeder-feeder" mechanism for precipitation falling through clouds from above.

Lastly, Fig. 6 shows how the precipitation rates vary depending on the assumed overlap assumption. In

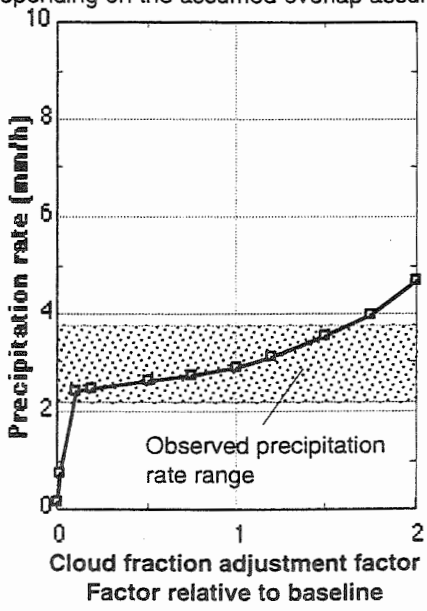

Fig 4. Precipitation rate vs. assumed cloud fraction for evaporation and accretion calculations. "0" means no cloud (all precipitation falls through cloud-free air). "1" means cloud fraction on Fig. 1 used, and "2" means 100% cloud fraction assumed (all precipitation grows via accretion).

this model, precipitation is produced only in a fraction of the cloudy portion at each level, which varies vertically. This model uses 15 layers between 1000-100 mb. As precipitation passes from one layer to the next lowest layer, it is necessary to decide whether the falling precipitation enters clear or cloudy areas in the lower layer, where either evaporation or accretion will occur. The parameterization uses a sliding scale allowing smooth adjustment between minimum overlap (where precipitation falling out of the cloud at one layer has an extremely high probability of entering cloud-free air below), to random, to maximum overlap (clouds stacked on top of one another vertically). Fig. 6 shows that calculated precipitation rises from almost nothing at minimum overlap to about 5 mm/h at maximum overlap. Here the storm precipitation area occupies only 1-10% of the grid area, so grid-averaged precipitation rates are considerably lower than instantaneous, single station measurements, as expected. The "optimal" overlap assumption for these storm conditions is found to be close to maximum overlap, suggesting an intense, vertically-developed storm. For more stratiform-like or slanted cloud alignments, calculated precipitation rates fall off appreciably.

By assuming that precipitation released into the atmosphere falls primarily through clouds (maximum overlap), significant precipitation growth (and removal of water substance) occurs. In contrast, if precipitation produced in clouds falls OUT of cloudy areas through clear areas below (minimum overlap), appreciable evaporation occurs, and surface precipitation and scavenging rates from the intervening clouds are significantly reduced.

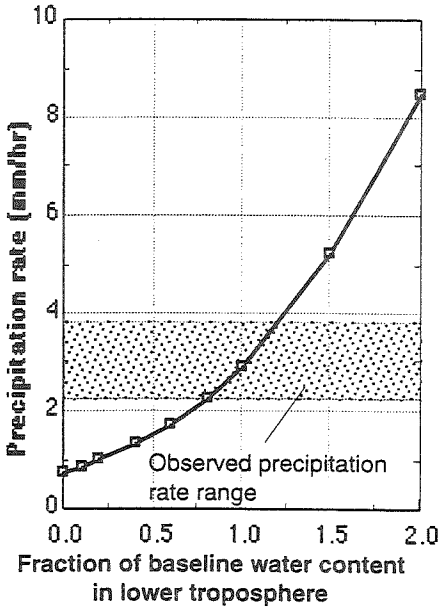

Fig 5. Precipitation rate vs. assumed condensed water content of intervening clouds intercepted by falling precipitation relative to water contents shown in Fig. 2.

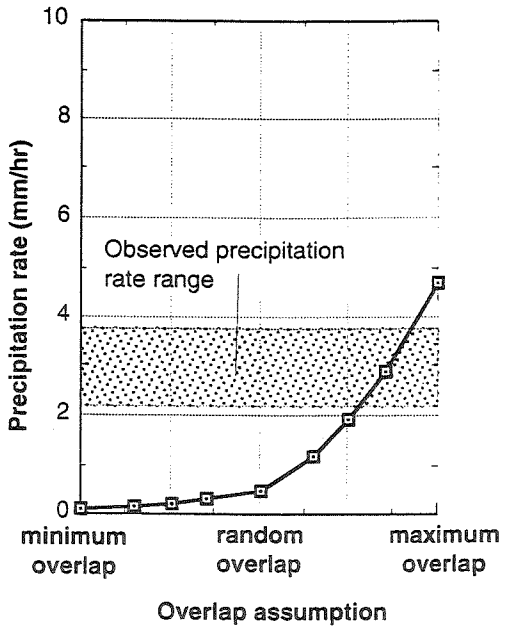

Fig 6. Precipitation rate vs. assumed cloud overlap assumption for the 15 atmospheric layers shown in Fig. 2.

5. CONCLUSIONS

Precipitation falling through cloudy regions rapidly grows by collision, coalescence, accretion and riming. Conversely, precipitation falling through clear regions rapidly evaporates. Therefore, the quantity of precipitation that eventually makes it to the surface, and the amount of water scavenged from intervening atmospheric clouds will be strongly influenced by the cloud overlap assumptions, as well as the assumed water content of clouds in the atmosphere. These factors can never be accurately specified in current larger-scale meteorology and climate models due to their poor horizontal resolution.

In partially cloud-covered areas, calculated precipitation rates and moistening and heating tendencies are also highly uncertain, varying by up to a factor of 3-10 depending on overlap assumptions. These results suggest that many tropospheric microphysical processes can only be crudely simulated within existing microphysical parameterizations, and even small changes in the assumed and often empirically-derived methods for estimating the mean water content, overlap, convective fluxes, or cloud fraction can have significant feedbacks on longer-term climate simulations.

REFERENCES

Kessler E. (1969) On the distribution and continuity of water substance in atmospheric calculations. *Meteorological Monographs, 10,* #32 American Meteorological Society.

Walcek C. (1994) Cloud cover and its relationship to relative humidity during a springtime midlatitude cyclone. *J. Atmos. Sci.* **122,** 1021-1035.

VAPOR PRESSURE MEASUREMENT OF DEEPLY SUPERCOOLED WATER

N. Fukuta and C. M. Gramada

Department of Meteorology, University of Utah, Salt Lake City, Utah 84112-0110, USA

1. INTRODUCTION

Vapor pressure of supercooled water is one of the most fundamental properties for microphysical processes in the atmosphere at subfreezing temperatures. The best data currently available for the pressure, such as in the Smithsonian Meteorological Table or the International Meteorological Table, are mostly due to Goff (1942 and 1949) and Goff and Gratch (1945 and 1946), which are valid from 0 to 100°C. There exists no completely satisfactory formula for the vapor pressure over liquid water at temperature below 0°C List (1966), and data in the tables are direct extrapolation from the above range. Studies of supercooled water in emulsion form (Angell et al. 1982) indicated a sharp increase in the specific heat when the temperature lowers toward –40°C. Therefore, a new, direct and accurate method was devised, and vapor pressure measurements were carried out with supercooled water (Gramada 1998). We report the results below.

2. METHOD OF MEASUREMENT

To measure the vapor pressure of deeply supercooled water, it is preferable to use a phenomenon where the vapor is directly involved, instead of relying on an indirect one that determines relevant thermodynamic properties, and assess the pressure from them. In the direct method, holding the supercooled condition for any length of time induces a problem of disruption in the measurement by ice nucleation. The dew point hygrometer method avoids this problem, for the measurement ends at the moment of condensation and requires no time for holding the condensed phase under supercooling.

The dew point hygrometer method requires a well defined reference vapor source with high reproducibility. To this end, saturated vapor over ice is selected since it is the equilibrium property of stable phase and the specific latent heat of deposition, L_d, is essentially constant. Thus, the tabulated values are reliable being based on measurement. It is a sole function of temperature, T, so that its slow change brings the necessary variation to the pressure. At the moment of dew forming nucleation, the effect of temperature difference at the source can be estimated by the flux balance as will be shown later.

Corresponding author's address: N. Fukuta, Department of Meteorology, University of Utah, 135 S 1460 E, Rm 819, Salt Lake City, UT 84112-0110; E-Mail: nfukuta@met.utah.edu

2.1 Design of Apparatus

The design of the dew point hygrometer used in the present study is shown in Fig. 1. It is made of

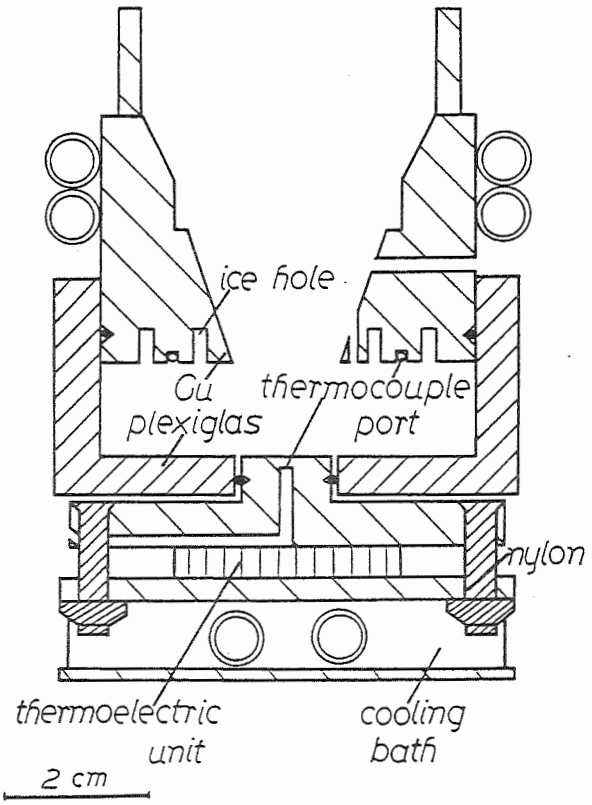

Fig. 1. Design of the dew point hygrometer.

two copper blocks. The top block has ice holes as well as grooves for thermocouple holding. A coil of copper tubing is attached to it for cooling liquid from a refrigerated, circulating bath. The bottom one, with a thermocouple hole leading to the polished

observation surface, is attached to a thermoelectric unit which is cooled by the same cooling liquid. Both are separated by a thermally insulating, Plexiglas cylinder, and all of them are o-ring sealed so that they can be separated for service. Copper-constantan thermocouples are embedded in grooves with thermal compound. A slide projector is used to illuminate the observation surface through the Plexiglas wall, and detection of condensation onset was carried out from above by a stereo-microscope with a rubber sleeve insulating the top of the upper copper block and the lens from the surrounding room air. The whole apparatus is thermally insulated by polypropylene foam.

2.2 Measurement

In preparation for measurement, ice holes at the bottom of the top copper block are filled with distilled water. Then, the whole system is cooled by cooling liquid from the refrigerated, circulating bath to a temperature slightly above that for measurement. When the temperature stabilizes and the water frozen, the electric current to the thermoelectric unit is slowly raised while the polished surface of bottom copper block is being observed by the microscope. At the moment the dew point condensation occurs, the surface appearance suddenly changes, and the temperature for top block and that for bottom block are recorded on a strip chart recorder. Then, polarity of the current is reversed to warm the bottom block surface to evaporate the condensed water. The temperature at which the condensed water has completely evaporated is also recorded. By recovering the original polarity of the current and after quickly coming to the condensation point previously assessed, under a new reduced cooling rate, the point of condensation is redetermined with higher accuracy.

Measurements were carried out with the whole system gradually cooling to, and slowly warming from a low T.

3. RESULT OF MEASUREMENT AND DISCUSSION

3.1 Balance of Vapor Fluxes

At the moment of condensation, the water vapor flux density from ice in the top copper block of higher temperature, T_i, balances with that of water drops just above the bottom copper block of lower temperature, T_w, or

$$n_i u_i = n_w u_w, \tag{1}$$

where n and u are the number density and velocity of water molecules in the normal direction, and subscripts i and w stand for ice and water, respectively,

$$T \propto u^2, \tag{2}$$

and the vapor pressure

$$e \propto nT \quad \text{(ideal gas)}. \tag{3}$$

From Relationships (1), (2), and (3), we have

$$\frac{e_w}{\sqrt{T_w}} = \frac{e'_i}{\sqrt{T_i}}, \tag{4}$$

where e_i is the saturation vapor pressure over ice at temperature $T_i \neq T_w$. By measuring T_w and T_i and using e'_i in the table, one can determine e_w.

3.2 Thermodynamic Properties

The Clausius-Clapeyron equation in the integral form gives

$$\ell n \frac{e}{e_1} = \frac{\bar{L}}{R_v}\left(\frac{1}{T_1} - \frac{1}{T}\right), \tag{5}$$

where e is the vapor pressure of the condensed phase at T, e_1 that at T_1, $\bar{L}$ the average specific latent heat of phase change over the temperature range between T_1 and T, R_v the specific gas constant for water vapor, and T_1 = 273.15K under 1 atm.

Applying Eq. (5) to water and ice in equilibrium with the vapor

$$\bar{L}_f = R_v \ell n(e_w/e_i) \Big/ \left(\frac{1}{T} - \frac{1}{T_1}\right), \tag{6}$$

where $\bar{L}_f$ is the average specific latent heat of fusion, e_w and e_i being saturation vapor pressure over water and that over ice under the same temperature, T, and

$$\bar{L}_f = \left[L_f + L_f(T_1)\right]/2. \tag{7}$$

In Eq. (7), L_f, the specific latent heat of fusion at T, may be calculated based on $L_f(T_1)$ from the table and $\bar{L}_f$ from Eq. (6) in which e_w is determined experimentally based on T_w and T_i measurements in Eq. (4).

Among the specific latent heats, we find

$$L_f = L_d - L_c, \quad (8)$$

and

$$\bar{L}_f = \bar{L}_d - \bar{L}_c. \quad (9)$$

In addition, the Kirchhoff equation gives

$$c_{p,w} - c_{p,i} = \frac{dL_f}{dT}, \quad (10)$$

where $c_{p,w}$ and $c_{p,i}$ are the specific heat at constant pressure for water and ice, respectively.

3.3 Measurements

Figure 2 shows the vapor pressure ratio between the observed and the table values for supercooled water. As can be seen in the figure, there is no appreciable difference for data between cooling and warming. On the other hand, data for evaporation of droplet are lower. By the time evaporation measurements were done, droplets already had achieved some size. To evaporate droplets of the size in a finite time, some vapor pressure difference was needed which made the measured vapor pressure of water smaller. For this reason, more weight was put on condensation data when the representing curve was drawn. At the moment of condensation, droplets start growing practically from zero size and the process is very sharp.

It is clear in the figure that deviation from the table value begins when the temperature lowers to about -20°C and becomes significant thereafter, while matching between the observed data and table values is excellent at temperatures above it. The measured values around -36°C or lower contain large amount of error due to the homogeneous freezing process which quickly follows the condensation.

An empirical equation of polynomial form for the curve drawn in the figure is obtained as

$$\begin{aligned} e_0/e_T = {} & 0.9991817 \\ & + 7.112591 \cdot 10^{-4}\, x \\ & - 1.846514 \cdot 10^{-4}\, x^2 \\ & + 1.188611 \cdot 10^{-5}\, x^3 \\ & + 1.130318 \cdot 10^{-7}\, x^4 \\ & - 1.743127 \cdot 10^{-8}\, x^5, \end{aligned} \quad (11)$$

where x = t+19, t the temperature in °C. The deviation of Eq. (11) from the plotted curve is within

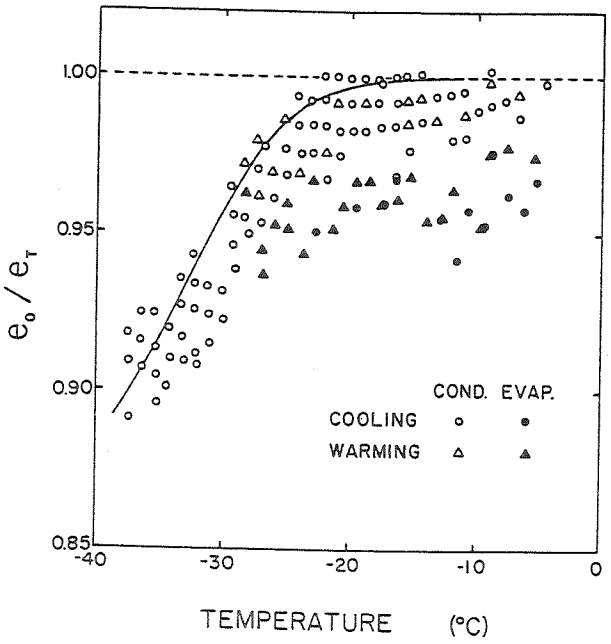

Fig. 2. The vapor pressure ratio between the observed and the table value, e_0/e_T, for supercooled water plotted as a function of temperature.

0.2%.

The thermodynamic properties of supercooled water thus determined are listed for the temperature range below -20°C in Table 1. In the table, subscripts 0 and T stand for observed and table

Table 1. List of measured vapor pressure, the specific latent heats of phase change, and their ratios with Smithsonian table values.

T (°C)	$e_{w,0}$ (hPa)	$e_{w,0}/e_{w,T}$	$L_{f,0}$ (cal/g)	$L_{f,0}/L_{f,T}$	$L_{c,0}/L_{c,T}$
-20	1.250	0.997	66.4	0.962	1.004
-25	0.796	0.987	58.0	0.879	1.013
-30	0.487	0.957	41.5	0.659	1.034
-35	0.288	0.917	24.1	0.404	1.065

values, respectively. The largest deviation from the table value is seen with L_f ratio in the 5th column. The ratio decreases from 0.96 to 0.4 as the temperature drops from -20 to -35°C. For the same temperature change, the ratio between the observed and table values shifts from 1.00 to 0.92 for the vapor pressure of supercooled water and from 1.00 to 1.07 for the specific latent heat of

condensation.

Figure 3 shows the ratio of specific latent heat of fusion between the measured and the table values. In the figure like the measured vapor pressure deviation from the table value seen in Fig. 2, the observed latent heat of fusion begins to come down as the temperature lowers and appears to asymptotically approach to zero at some temperature below -40°C.

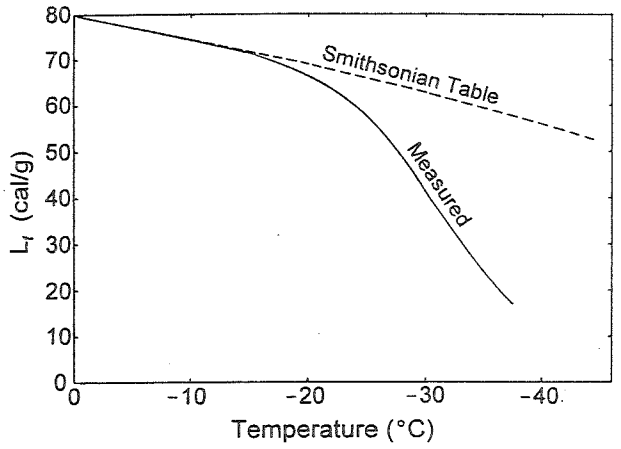

Fig. 3. Ratio of the specific latent heat of fusion between the measured and the table values plotted as a function of temperature.

$c_{p,w}$ was determined at -30°C from Eq. (10) with $c_{p,i}$ = 0.45 cal/g/°C, and found that it is 3.4 times larger than that measured in the emulsion cooling method (Angell et al. 1982). The latter method is under the influences of solubility of the carrier oil in water, the necessarily high cooling rate on the order of 10K/min for the system consisting of mostly oil with small thermal conductivity and freezing problem of emulsified water under prolonged condition of supercooling.

The discrepancy found at temperatures below -20°C between the measured data and table values is expected to affect the current view in the following atmospheric processes, especially below -20°C. The vapor pressure decrease with the supercooled water will lead to the cloud base altitude slightly lower than that assessed by the existing table values and higher liquid water content there. Cloud glaciation (Fukuta 1972) leads to considerably less amount of heating and the associated buoyancy development while cloud formation results in slightly more heating due to the increased L_c. The largest impact is anticipated with the mechanism of homogeneous freezing nucleation (Pruppacher 1995) where the surface free energy at water-ice interface and the relevant nucleation mechanism are expected to change drastically (Fukuta and Guo 2000)

4. ACKNOWLEDGMENT

This work was partially supported by NSF under Grant ATM-9626600.

5. REFERENCES

Angell, C. A., M. O. Guni, and W. J. Sichina, 1982: Heat capacities of water at extremes of supercooling and superheating. *J. Phys. Chem.*, **86**, 998-1002.

Fukuta, N., 1973: Thermodynamics of cloud glaciation. *J. Atmos. Sci.*, **30**, 1645-1649.

Fukuta, N., and G. Guo, 2000: Thermodynamic properties of molecular clusters in nucleation. Extended Abstract, 15th Internat. Conf. on Nucleation and Atmos. Aerosols, Rolla MO.

Goff, J. A., 1942: Vapor pressure of ice from 32° to -280°F. *Amer. Soc. Heat. Vent. Eng. Trans.*, **48**, 299.

Goff, J. A., 1949: Standardization of thermodynamic properties of moist air. *Trans. Am. Soc. Mech. Engs.*, **55**, 459-485.

Goff, J. A., and S. Gratch, 1945: Thermodynamic properties of moist air. *Amer. Soc. Heat. Vent. Eng. Trans.*, **51**, 125.

Goff, J. A., and S. Gratch, 1946: Low-pressure properties of water from -160° to 212°F. *Amer. Soc. Heat. Vent. Eng. Trans.*, **52**, 95-129.

Gramada, C. M., 1998: Vapor pressure measurement of supercooled water, M.S. Thesis, Department of Meteorology, University of Utah, 42 pp.

List, R. J., 1966: *Smithsonian Meteorological Tables*, Smithsonian Institution Press, Wash., DC, 527 pp.

Pruppacher, H. R., 1995: A new look at homogeneous ice nucleation in supercooled water drops. *J. Atmos. Sci.*, **52**, 1924-1933.

A LABORATORY STUDY OF THE EFFECT OF VELOCITY ON HALLETT-MOSSOP ICE CRYSTAL MULTIPLICATION

C P R Saunders[1] and A S Hosseini

Physics Department, UMIST, Manchester, UK

1. INTRODUCTION

There is evidence that ice particles in some clouds may originate by ice multiplication, the Hallett-Mossop process, involving the production of small ice fragments during the freezing of supercooled water droplets accreted on graupel pellets. Hallett et al. (1978) confirmed the effect in Florida cumuli while Harris-Hobbs et al. (1987) studied the initiation of the ice phase in cumulus in Montana, California and Florida in the United States and found that the data followed the trends indicated by laboratory studies which note active multiplication in the temperature band -3 to -8°C. Blyth and Latham (1997) modelled the development of cumulus glaciation in summer thunderstorms in New Mexico and noted agreement with the Hallett-Mossop (H-M) process. Bower et al. (1996) recorded high concentrations of small columnar ice crystals in stratiform clouds that straddle the -3/-8°C zone, the highest concentrations of $\approx$500 l^{-1} occurring at the -6°C level with another maximum at the -15°C level. Mason (1998), suggested that the high concentrations of small crystals with d<125 μm, reported at the -15°C level, originate as ice splinters produced in the H-M zone. The splinters grow slowly in the absence of a water cloud in ice supersaturated conditions between the -8°C and -12°C levels, and thereafter grow more rapidly in convective cells with liquid water and updraughts of $\approx$1ms^{-1}. Mason (1996) showed that the H-M process is also consistent with observations of ice particles in aged cumulus with weak updraughts.

Hallett and Mossop (1974) conducted laboratory experiments in which simulated graupel pellets were moved through a cloud of supercooled droplets to become covered in rime ice; ejected ice fragments were counted after they grew to visible sizes in the supersaturated cloud. The secondary ice particles were found at cloud temperatures between -3°C and -8°C with peak production at -5°C. The authors established that the production of splinters is dependent on the presence in the cloud of droplets ≥25 μm diameter and that splinter production is proportional to the rate at which these large droplets are collected. According to Mossop (1976), one splinter is produced for about every 250 droplets of diameter ≥25 μm accreted in the target velocity range 1.4 to 3 m s^{-1} at a temperature of -5°C. Goldsmith et al. (1976), and Mossop (1978, 1985) increased the ratio of small to large droplets captured by the rimer, and found that splinter production is increased by the presence of droplets ≤12 μm diameter in the cloud. Mossop (1976) and Wishart (1977) noted that increasing the centripetal acceleration of their target by 60% at a constant velocity of 1.4 m s^{-1} had no appreciable effect on splinter production at this low velocity. Foster and Hallett (1982) and Heymsfield and Mossop (1984) noted that the rimer surface is heated during the freezing of accreted droplets and they demonstrated that secondary ice production is a function of both the surface temperature of the rime and the cloud temperature, at least for surface temperature elevations ≤ 2°C.

The mechanism of multiplication is still under discussion. Choularton et al. (1978, 1980) and Mossop (1980) suggested that large droplets ≥ 25 μm diameter are sometimes accreted in such a way that they are attached to the ice substrate by only a narrow bridge made from the small droplets frozen on the rimer. Symmetrical heat loss to the air then leads to the formation of a complete ice shell around a droplet as it freezes. Pressure build up inside the droplet is relieved by the cracking of the shell and the formation of a protuberance and spike of ice leading to fracture of the end of the spike with ejection of one or more fragments. Mossop (1980) gave credence to this hypothesis when he noted that ice shells weakened by the presence of ammonia reduced the number of protuberances and splinters; furthermore Visagie (1969) and Mossop et al. (1974) found that the presence of carbon dioxide led to numerous protuberances that increased splinter production. The peak in splinter production at -5°C, according to the shell-fracture hypothesis, is thought to be due to limiting factors which are more important at higher and lower temperatures. At higher temperatures, particularly above -3°C, droplets tend to spread over the substrate instead of freezing as distinct spheres, according to Macklin and Payne (1967). Griggs and Choularton (1983) suggested that the cut-off at about -8°C is due to the more rapid growth of the ice shell at lower temperatures leading to a shell which is too strong to be disrupted by the internal pressure. Mason (1996) calculated that the shell would fracture when its thickness was less than the expansion of the freezing water droplet: his theory predicts a low temperature limit to multiplication around -7°C when the shell thickness is equal to the expansion.

An alternative multiplication mechanism was put forward by Dong and Hallett (1989) who reported that droplets freezing on an ice surface tend to spread at all temperatures above about -8°C. They pointed out that the kinetic energy of the droplets was too low to cause spreading upon impact and so they attributed the observed spreading to wetting of the substrate facilitated by a liquid like layer on the ice surface. They concluded that splinter production by pressure build-up inside individual frozen droplets is unlikely to be responsible for shatter and they

[1] Corresponding author: C P R Saunders, Physics Department, UMIST, Manchester, M60 1QD, UK. email: clive.saunders@umist.ac.uk

suggested that fragmentation is associated with the stresses built up in an accreted droplet when it experiences a temperature gradient between the colder substrate and the surface of the droplet freezing at 0°C. Above -3°C the accreted droplets form a thin layer which freezes upwards with little stress, while at lower temperatures the shear stress increases leading to a peak in ice production at -5°C. Lowering the temperature reduces further the probability of cracking because of the increase in solubility of air in supercooled water; at low temperatures, the higher freezing rates lead to smaller air bubbles which make the ice more plastic so that fracture is unlikely below -10°C. In this fracture mechanism, there is apparently no dependence of multiplication on the presence of small droplets. Furthermore, the absence of protuberances when the droplets fell at terminal velocity onto an ice surface above -10°C is in contrast to the observation of Choularton et al. (1980) who show a photograph of discrete frozen droplets together with a protuberance obtained at -3°C.

Early measurements of the effect of rimer velocity on multiplication by Hallett and Mossop (1974) indicated a low velocity cut-off in splinter production at 0.7 m s^{-1}; however, Mossop (1985) suggested that splintering may occur down to 0.2 m s^{-1}. By using suitable values of rimer target diameter, with velocities in the range 0.55 to 5 m s^{-1}, Mossop (1985) studied splinter production as a function of velocity with a constant collision efficiency, independent of droplet size. He noted a peak production rate in the velocity range 2 to 4 m s^{-1} and suggested that splinter production would continue above 5 m s^{-1} although he cautioned that the radial acceleration of the rimer in his experiments at high velocities may affect the rime structure and hence influence the multiplication. Mossop pointed out that the evidence for multiplication at high velocities could increase the cloud temperature range for splinter production; a graupel pellet falling at speed in a high liquid water content cloud at temperatures below -8°C may be heated by accretion sufficiently for the surface to be in the -3/-8°C splinter zone. This suggestion is consistent with the findings of Heymsfield and Mossop (1984) who found that splinter production depends on rime surface temperature rather than on cloud temperature. However, Mossop (1985) and Foster and Hallett (1982) noted that the low temperature cut-off for splinter production was not affected by the accretion rate, although Foster and Hallett showed that the temperature for peak splinter production does shift to lower cloud temperatures with increase in cloud liquid water content. Despite the lack of experimental evidence, all the theories outlined above are consistent with a lowering of the low temperature cut-off when the rime surface is heated by increased accretion. According to Griggs and Choularton the strength of the ice shell is temperature dependent so rimer heating should weaken the shell; in the case of the Dong and Hallett concept of temperature gradient induced stress, increased heating decreases the solubility of air in water; in Mason's concept, a higher rime surface temperature does not affect the amount of expansion on change of state, but the increased rime surface temperature reduces the shell thickness, making splintering more likely.

Foster and Hallett noted that the temperature band for multiplication could be pushed to lower cloud temperatures by increasing the velocity from 1 to 2 m s^{-1}; they obtained multiplication at -10.7°C, the lowest recorded temperature to date at a rimer speed of 2 m s^{-1} in a cloud of liquid water content 1.6 g m^{-3}. The observations discussed above show that increasing the rimer temperature by increasing the cloud liquid water content in order to increase the rime accretion rate, does not lower the cloud temperature for low temperature cut-off; yet an increase in velocity, which will also increase the accretion rate, does lower the low temperature cut-off.

Rimer velocities up to 12 m s^{-1} have been used in the present work in order to extend the measurements of the velocity dependence of multiplication into the domain of large graupel and to help identify the multiplication mechanism. The measurements were made with one diameter of riming target, one droplet spectrum, and a rime surface temperature in the range -4 to -5°C, which is the temperature range for maximum splinter production. Two values of rotational acceleration were studied in order to check whether a high g force can affect multiplication. The rime temperature was kept approximately constant at all velocities investigated by adjusting the cloud liquid water content appropriately.

2. EXPERIMENTAL PROCEDURE

Experiments were conducted in a cloud chamber located inside a cold room. The chamber, made of aluminium sheet, measured 0.95x1.5 m^2 by 2 m. A cloud of supercooled water droplets was formed by an open boiler inside the chamber. This arrangement ensured that the roof of the chamber was kept above 0°C, so there was no risk of a spurious crystal count by crystals falling from the chamber ceiling. The boiler was insulated to minimize the input of significant heat to the cloud.

The liquid water content and the droplet size distribution of the cloud were dependent on the power input to the steam boiler and the size of boiler orifice respectively, according to Mossop (1984). The orifice, of diameter 12 cm, was chosen in order to obtain a broad droplet size distribution extending beyond 24 μm diameter. The cloud reached a stable temperature and droplet size distribution after about 60 to 90 minutes, thereafter the droplet spectrum changed only slowly during the remainder of the experiment provided the chamber remained closed. The stability of the droplet concentration indicates that a balance was reached between activation of new condensation nuclei and the fall-out of droplets. In each set of experiments the droplet size spectrum was determined several times by microscopic analysis after drawing the cloud particles past formvar coated slides mounted in a tube connected to the chamber. Figure 1 shows a typical droplet size spectrum obtained with a boiler power input of 600 W providing a liquid water content, LWC, of 0.9 g m^{-3}.

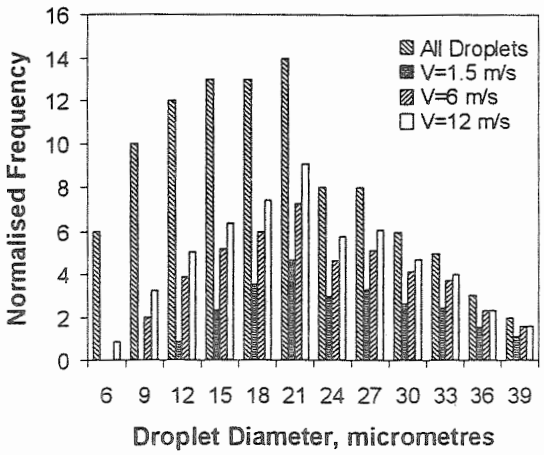

Figure 1. Droplet sizes in the cloud and on the target.

The riming targets were two vertical stainless steel rods of 4 mm diameter, 15 cm long, which could be moved through the cloud about a vertical axis at radii of either 15 or 25 cm in order to test the effect of acceleration. In the cloud, the moving rods simulated riming graupel pellets and gathered supercooled droplets which froze upon the front face as rime. Ice crystals growing upon any fragments ejected during the rime accretion could be observed within a light beam shining across the chamber from below the rotating rods and were counted visually over 1 minute periods. The average splinter count was corrected by subtracting the background count caused mainly by rime on the target supporting arms. An initial check was made before each run without target movement in order to ensure that the cloud was clear of ice crystals, then after each set of 12 successive experiments under the same conditions, the horizontal supporting arm was rotated at the same speed as in each set of experiments but without any vertical rods, in order to determine the background count. Both the main and background experiments took 12 minutes each and counts were fairly constant.

The number of crystals passing through the light beam per second was multiplied by nine in order to determine the total crystal production rate from the ratio of viewing volume to the total volume available for the growth of fragments into crystals. Since the experiments were consistently continued for long enough (12 minutes) for the rate of appearance of crystals in the beam to become fairly constant, it could be assumed that the rate of fallout equalled the rate of production (Mossop, 1976).

At the end of each set of experiments, in order to determine the LWC and the rime surface temperature, the rods were weighed. The rime width on the 4 mm rods was measured and averaged over the time of the experiment and the average diameter of the rods at each given velocity was used to calculate the Rime Accretion Rate (RAR g m^{-2} s^{-1}). The Effective Liquid Water Content, EW, is that portion of the cloud LWC captured by the rimer on account of its collision efficiency; EW is thus dependent on droplet and collector size and their relative velocity. Traditionally, numerical models of graupel growth have used values of LWC rather than EW with the assumption that EW = LWC, but this is certainly not true for small graupel falling at a few metres per second in a cloud of droplets. In these laboratory experiments EW is determined directly from the rime weight measurement and the relationship RAR=EWxV. The LWC in the cloud was determined from EW taking into account the droplet spectrum determined from the slide sample together with droplet collision efficiency values. Typical LWC values were around 1 g m^{-3}, which is representative of conditions inside the ice activation regions of cumulus clouds.

The cloud temperature (T_c) is taken as the average of the values from two thermocouples located in the cloud outside the diameter of the rotating system. T_c increased upwards in the chamber and the greatest temperature difference from the top to the bottom of the rods was 0.5°C. The surface temperature (T_s) of the accreted rime was raised above the cloud temperature by the release of the latent heat of fusion and (T_s) was calculated. Because accretion increases with velocity, rime heating also increases; in order to keep the rime surface temperature constant at about -4/-5°C, the cloud temperature (T_c) and the LWC were adjusted appropriately. This procedure was rather empirical and so the data used for the analysis exclude those cases for which T_s was not close to the desired range.

3. RESULTS

Figure 2 shows the number of splinters per mg of rime accreted and indicates a clear maximum splinter production rate at around 6 m s^{-1}. The figure shows a higher splinter production for the smaller rotation radius, which experiences a higher rotational acceleratio. An indication that a higher g force favours splinter production may be drawn from the fact that this result applies at every velocity, however, the error bars overlap sufficiently to make any conclusion uncertain. It is true that splinter production increases with velocity and acceleration, up to about 6 m s^{-1}, but the decrease in production at higher speeds and accelerations indicates that acceleration alone is not the primary cause of the observed results. Thus the effect of shear, due to the rotational acceleration, on accreted droplets freezing on the rimer is not influencing the results from this type of experimental set-up, as has been conjectured in the past. Because it is the accreted droplets that are important in influencing the microphysics of the rimer surface, the accreted droplet spectra have been determined for three velocities using collision efficiency data. The measured final widths of the droplet accretions were used to calculate average values of target diameter at each velocity. Figure 1 shows the cloud spectrum and the accreted droplet spectra at 1.5, 6 and 12 m s^{-1}. The small change with velocity of the droplet mean volume diameters is not likely to be the reason for the peak in splinter production at 6 m s^{-1}, however, it is clear from the spectra that the number of small droplets accreted (<12μm diameter) increases significantly with velocity, which

Figure 2. Velocity dependent splinter production.

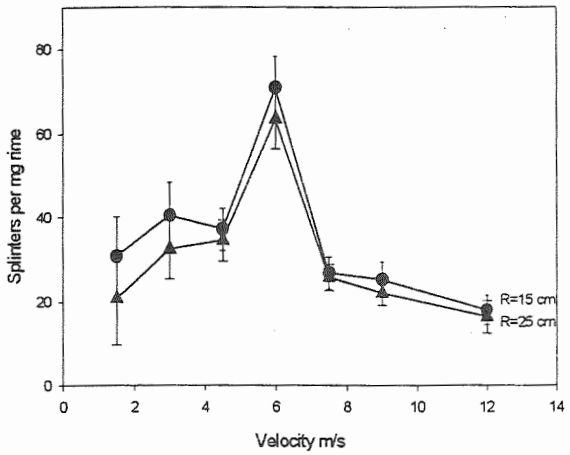

increases the number of suitable sites for larger droplets to accrete and produce splinters.

The reason for the decrease in splinter production at high velocity is not clear. There is a rapid increase in acceleration at high velocities, but at any particular velocity the higher count occurs at the higher value of acceleration, while the number of small droplets accreted continues to increase with velocity. Rime density increases non-linearly with velocity so that the accreted droplets become closer packed, which may restrict the number of suitable sites for multiplication to occur; however, the density values at 6 and 12 m s^{-1} are not appreciably different.

4. CONCLUSIONS

Ice multiplication has been studied as a function of rimer velocity. The measurements have extended the previously studied velocity range to 12 m s^{-1} and have found a maximum production rate at 6 m s^{-1}. The implication for clouds is continued splinter production in the later stages of storm development when larger graupel pellets, falling at several metres per second, will extend the ice spectrum by the initiation of new small ice particles. The results confirm that the mechanism of splinter production is favoured by an increase in the number of small droplets (<12 μm diameter) accreted on the riming graupel.

5. REFERENCES

Blyth A., and J. Latham, 1997: A multi-thermal model of cumulus glaciation via the Hallett-Mossop process. *Quart. J. Roy. Met. Soc.*, **122**, 1815-1844.

Bower, K. N., S. J. Moss, D. W. Johnson, T. W. Choularton, J. Latham, P. R. A. Brown, A. M. Blyth and J. Cardwell, 1996: A parametrization of the ice water content observed in frontal and convective clouds. *Quart. J. Roy. Met. Soc.*, **104**, 631-651.

Choularton, T.W., J. Latham, and B. J. Mason, 1978: A possible mechanism of ice splinter production during riming. *Nature*, **274**, 791-792.

Choularton, T.W., D. J. Griggs, B. Y. Humood and J. Latham, 1980: Laboratory studies of riming and its relation to ice splinter production. *Quart. J. R. Met. Soc.*, **106**, 367-373.

Dong Ya Yi., and J. Hallett, 1989: Droplet accretion during rime growth and the formation of secondary ice crystals. *Quart. J. Roy. Met. Soc.*, **115**,127-142.

Foster, T. and J. Hallett, 1982: A laboratory investigation of the influence of liquid water content on the temperature dependence of secondary ice crystal production during soft hail growth. Preprints, Cloud Phys. Conf., Chicago, 123-126. A.M.S., Boston.

Goldsmith, P., J. Gloster, and C. Hume,1976: The ice phase in clouds. Preprints. Int. Conf. Cloud Phys., Boulder, Colorado, 163-167. A.M.S., Boston.

Griggs, D.J., and T. W. Choularton, 1983: Freezing modes of riming droplets with application to ice splinter production. *Quart. J. R. Met. Soc.*, **109**, 243-253.

Hallett, J., and S. C. Mossop, 1974: Production of secondary ice particles during the riming process. *Nature*, **249**, 26-28.

Hallett, J., R. I. Sax, D. Lamb, and A. S. Ramachandra Murty, 1978: Aircraft measurements of ice in Florida cumuli. *Quart. J. Roy. Met. Soc.*, **104**, 631-651.

Harris-Hobbs, R. L., and W. A. Cooper, 1987: Field evidence supporting quantitative predictions of secondary ice production rates. *J. Atmos Sci.*, **44**, 1071-1082.

Heymsfield A. J. and S. C. Mossop, 1984: Temperature dependence of secondary ice crystal production during soft hail growth by riming. *Quart. J. Roy. Met. Soc.*, **110**, 765-770.

Macklin W. C and G. S. Payne, 1967: Some aspects of the accretion process. *Quart. J. Roy. Met. Soc.*, **94**, 167-175.

Mason, B. J., 1996: The rapid glaciation of slightly supercooled cumulus clouds. *Quart. J. Roy. Met. Soc.*, **122**, 357-365.

Mason, B. J., 1998: The production of high ice-crystal concentrations in stratiform clouds. *Quart. J. Roy. Met. Soc.*, **124**, 353-356.

Mossop S. C., J. L. Brownscombe, G. J. Collins, 1974: The production of . secondary ice particles during riming. *Quart. J. Roy. Met. Soc.*, **100**, 427-426.

Mossop, S.C., 1976: Production of secondary ice particles during the growth of graupel by riming. *Quart. J. R. Met. Soc.*, **102**, 45-57.

Mossop, S.C., 1978: The influence of drop size distribution on the production of secondary ice particles during graupel growth. *Quart. J. R. Met Soc.*, **104**, 323-330.

Mossop, S.C., 1980: The mechanism of ice splinter production during riming. *Geophys. Res. Lett.*, **7**, 167-169.

Mossop, S.C., 1984: Production of laboratory clouds. *Quart. J. R. Met. Soc.*, **110**, 275-279.

Mossop, S.C., 1985: Secondary ice particle production during rime growth: the effect of drop size distribution and rimer velocity. *Quart. J. R. Met. Soc.*, **111**, 1113-1124.

Wishart, E.R., 1977: An instrument for measuring liquid water content of laboratory supercooled clouds. *J. de Recherches Atmospheriques*, **11**, 191-196.

Visagie, P. J., 1969: Pressures inside freezing water drops. *J. Glaciol.*, **8**, 301-309.

NEW MODEL FOR THE VAPOR GROWTH OF HEXAGONAL ICE CRYSTALS

Stephen E. Wood[1], Marcia B. Baker[1], and Donna Calhoun[2]

[1]Geophysics Program, University of Washington, Seattle, WA, 98195-1650
[2]Department of Computer Science, Courant Institute of Mathematical Sciences, New York

1. INTRODUCTION

We present a new microphysical model for the vapor growth and shape evolution of faceted ice crystals in the atmosphere. Our model is based on a novel, efficient numerical method for solving Laplace[1]s equation on the surface of a three-dimensional hexagonal prism, and also takes into account the surface kinetic processes of crystal growth. We calculate a self-consistent solution for the distribution of the supersaturation and the kinetic coefficient on each crystal face, for several different assumptions regarding the crystal growth mechanism and ice surface properties.

We compare our predicted mass growth rates with those of the capacitance model for spheres and ellipsoids to look at the effects of crystal shape and surface kinetics. We also use this model to predict the steady-state aspect ratio for growing, faceted ice crystals over a range of temperatures and supersaturations, as well as to predict the supersaturation at which crystal faces become hollowed. Finally, we insert the single particle code into an adiabatic parcel cloud model to investigate the feedbacks between crystal surface kinetics, shape, and the thermodynamic properties of clouds.

2. CRYSTAL GROWTH MECHANISMS AND SURFACE PROPERTIES

Unlike the case of liquid droplets, vapor molecules which strike and adsorb on the surface of a growing ice crystal do not necessarily become incorporated into the condensed phase. They diffuse across the surface and may desorb before reaching a site where they are more strongly bound. Such sites are provided by the edges of new molecular layers, or ledges, as they move across the crystal face. Crystal growth then depends on having a mechanism for producing these ledges. Two mechanisms which have been observed on crystals of other substances are two-dimensional nucleation (2DN) and screw dislocations (SD), but which of these operate on the surfaces of ice crystals, and when, is not known. This is important because crystal faces with no dislocations can only grow by 2DN, and then only if the supersaturation at the crystal surface (σ_s) is greater than a critical value ($\sigma_{cr,2DN}$). Faces having dislocations can grow at any finite supersaturation.

Therefore we have considered 3 types of crystals to cover a range of possibilities. Let D_n indicate a crystal with emergent dislocations on n sets of faces; i.e.,

- D_0: No dislocations on any facet
- D_1: Dislocations are present only on one set of faces, prism (D_{1a}) or basal (D_{1c}).
- D_2: Dislocations are present on all faces.

When dislocations are present, growth occurs by either SD or 2DN, depending on which mechanism yields the highest flux. The ledge source location for SD is always assumed to be at the center of the face and that for 2DN is either at the center or corner depending on which has the higher σ_s.

3. MASS GROWTH RATES: COMPARISONS TO CAPACITANCE MODEL

The rate of mass growth of a crystal is usually approximated in atmospheric work by use of the so-called capacitance model in which the crystals are assumed to be ellipsoids of revolution. The two main differences between our model and the capacitance model lie in their treatments of crystal shape and the microphysics of crystal growth. We calculate the growth of regular hexagonal prisms and relate the evolution of particle shape to surface parameters that can in principle be measured. The capacitance model can be used to simulate crystals with different shapes and aspect ratios, but it cannot *predict* what those shapes will be. Secondly, the diffusive flux of vapor to a crystal is driven by the difference between the ambient supersaturation (σ_∞) and the supersaturation at the crystal surface, and in

[1]Corresponding author's address: Stephen E. Wood, Geophysics Program, University of Washington, Box 351650, Seattle WA 98195-1650, USA; Email: sewood@atmos.washington.edu.

the capacitance model σ_s is assumed to be zero. In reality, σ_s must be greater than zero in order to drive the surface kinetic processes of crystal growth [*Kuroda*, 1984].

In cases where the surface kinetic effects are low ($\sigma_\infty \gg \sigma_{cr,2DN}$), we found that the capacitance model predicts mass growth rates for ellipsoids $10-20\%$ higher than our model predicts for hexagonal crystals of the same aspect ratio and mass. The equivalent mass sphere model also produces mass growth rates more than 10% higher than our model predictions. Much larger errors are possible if surface kinetics are neglected in cases where dislocations are not present and the ambient supersaturation is less than a few times $\sigma_{cr,2DN}$. The values of $\sigma_{cr,2DN}$ are not well known, but measurements at temperatures above -15C indicate strongly temperature-dependent values ranging from 0.2%-2.5% [*Nelson and Knight*, 1998]. Because liquid droplets are likely to also be present in clouds at these temperatures (in vapor saturated with respect to liquid water at T°C, $\sigma_\infty \simeq |T|\%$), it is usually the case that $\sigma_\infty \gg \sigma_{cr,2DN}$, so that crystal surface kinetics will only affect shape and not growth rates. However at lower temperatures such as in cirrus clouds, there is evidence that $\sigma_{cr,2DN}$ is much higher ($\geq 10\%$) [*Wood et al.*, 2000], so that surface kinetics could limit growth rates over a much larger range of atmospheric conditions, and would therefore be a more important model process to take into account.

4. STABILITY LIMIT FOR FACETED GROWTH

From observations of vapor-grown ice crystals in the atmosphere and in the laboratory, it is well known that compact faceted shapes are usually found at low supersaturations while hollowed or dendritic shapes are found at high supersaturation. The empirical boundary between these two regimes seems to depend on temperature but is not well characterized. The shape of ice crystals plays an important role in determining their radiative properties, fall speeds, and collision/collection efficiencies, so it is valuable to have a way of predicting this shape transition in cloud models.

Growing crystals can maintain macroscopically flat faces only as long as the product $\alpha\sigma_s$, where α is the kinetic coefficient, remains constant across each face [*Wood et al.*, 2000]. Because the crystal corners stick our farther into the vapor diffusion field, σ_s is greater at the corners than the center of a growing face. Uniform growth is maintained by a compensating gradient in α. However, these gradients increase as σ_∞ increases, and when α reaches its maximum value of unity, the growth rate at center of the face can no longer keep up with the corners, and the crystal begins to hollow.

Because our model calculates the distribution of σ_s and α across the surfaces of three-dimensional hexagonal prism crystals, we can determine this point of instability (σ_∞^{hol}) for a given crystal shape and set of ambient conditions. Our results are given in terms of the values for the critical supersaturation for 2-D nucleation on each face, $\sigma^a_{cr,2DN}$ and $\sigma^c_{cr,2DN}$ As better measurements of $\sigma_{cr,2DN}$ become available, our model predictions can be more confidently translated into actual atmospheric supersaturation values.

We find that faceted growth becomes unstable when the ambient supersaturation reaches a value of 2-5 times that of $\sigma^{low}_{cr,2DN}$, the lower of the two values for the basal and prism faces. Therefore, using the values of $\sigma_{cr,2DN}$ measured by Nelson and Knight [1998], under conditions of water saturation in mixed phase clouds warmer than -15C, nonfaceted growth is predicted by our model, as observed. At temperatures below -20C, the observations of unhollowed crystals at supersaturations as high as 40% in the polar atmosphere [*Korolev et al*, 1999], combined with our model-derived stability limits, suggest that $\sigma_{cr,2DN}$ is 10%.

5. HABIT AND STABILITY DIAGRAM

From interpretations of observed crystal shapes [*Wood et al.*, 2000], we have constructed plausible functions $\sigma^c_{cr,2D}(T)$ and $\sigma^a_{cr,2D}(T)$ for $-30° < T < -15$°C which merge into the values measured by Nelson and Knight [1998] at higher temperatures. Based on these functions we can extend our calculations of the stability limits for D_2 and D_0 crystals to lower temperatures. The results are shown in Figure 1. While the calculations below -15°C are based on conjecture, they illustrate several important points. Faceted crystals are likely to be stable at much higher σ_∞ at low temperatures than they are at higher temperatures, even in the presence of supercooled liquid droplets. There is also a much wider range of supersaturations below $\sigma_{cr,2D}$, making it more likely that models that do not take into account crystal surface kinetics will be inaccurate. For example, D_0 crystals would not be expected to grow at all for $\sigma_\infty < 10\%$ at -30°C based on these results, and D_1 crystals would grow only

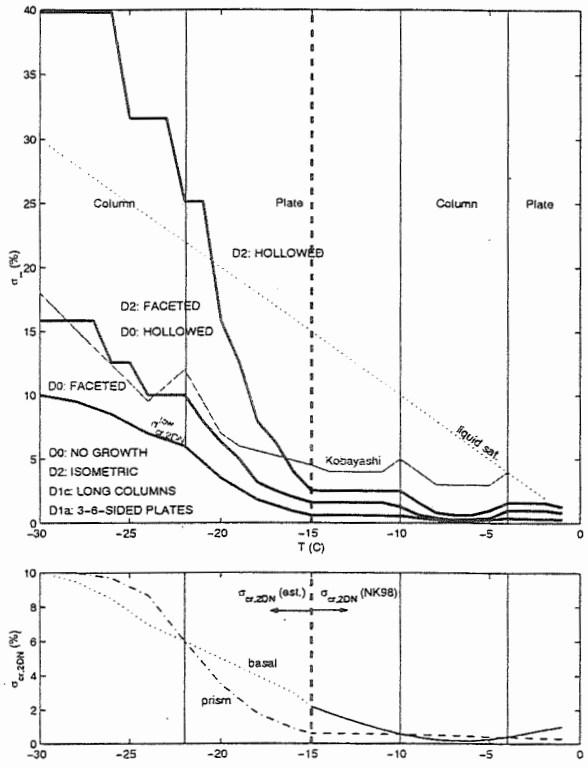

Figure 1: Conjectured habit and growth process diagram for ice crystals as a function of temperature and ambient supersaturation. The thin solid and dashed lines above -15 °C represent the values of $\sigma^c_{cr,2DN}$ and $\sigma^a_{cr,2DN}$, respectively, based on the Nelson and Knight [1998] measurements. The dotted and dot-dashed lines below -15°C represent our estimated extension of these values to lower temperatures based on field observations. The thick curved solid lines indicate our model-calculated stability limits for D_0 (lower) and D_2 (upper) crystals. The straight diagonal dotted line indicates the ice supersaturation in vapor saturated with respect to supercooled liquid water. The vertical dashed lines indicate the temperatures at which transitions between tabular and columnar habits have been typically observed [*Chen and Lamb*, 1994].

on the faces with dislocations. Note that this latter possibility could produce plates in the nominal "column" temperature range ($T < -22$°C), or columns in the "plate" range ($-22° < T < -10$°C), as is sometimes observed. Experimentally distinguishing between D_2, D_1, and D_0 crystals on the basis of shape should be much easier at low temperatures.

To compare our model predictions with observations of ice crystal stability limits, we have taken from Kobayashi's famous habit diagram the line separating the "solid" crystal regime from the hollow or "skeleton" regime, and replotted it in Figure 1. At temperatures above −15°C, Kobayashi's observed limit is closer to, but somewhat higher than, our predictions for D_2 crystals, and has a remarkably similar shape. Below −15°, Kobayashi's limit matches very closely our predicted stability limit for D_0 crystals. Although our model results can only be as accurate as the input values of $\sigma_{cr,2DN}$, this comparison suggests that ice crystals may contain fewer dislocations at lower temperatures.

6. CLOUD MODEL

Because of its speed, our single crystal growth code can be inserted in large-scale cloud models to more accurately represent the microphysics. As a first step, we have used a simple adiabatic updraft model to examine the effect of different surface kinetic mechanisms on crystal size and aspect ratio Γ as well as the ambient supersaturation σ_∞ as a cloud evolves.

For each run we assume all of the crystals have identical size, shape, and surface characteristics, as they evolve with time. We have not included nucleation of new particles so the number density of particles remains constant. We have also ignored radiative effects on growth, but these are small for the cases we examine.

In Figure 2, we show results for the case of an ice cloud at around -30°C with an updraft velocity of 35 cm/s, as representative of cirrus clouds, for 4 different assumptions regarding the presence of dislocations on the crystal faces (Types D_2, D_0, D_{1c}, and D_{1a} crystals). We assume the crystals are initially isometric, close to equilibrium, and determine the mass and aspect ratio evolution self-consistently from the calculated values of $\dot{a}$ and $\dot{c}$.

We find a variation in final mass of nearly a factor of two between the D_0 crystals and the other crystal types, and the peak supersaturation reached varies from almost 10% for D_2 crystals to nearly 15% for

the D_0 crystal model. The predicted shape evolution is also dramatically different for each crystal type. The aspect ratios attained after 10 minutes are 0.1 for D_{1a} crystals compared to 4.3 for D_0 crystals, and near 1.0 for D_2 crystals (Γ for D_{1c} crystals exceeded 7 after only 2 minutes). These results demonstrate that both plates and columns can form at the same temperature, depending on the distribution of dislocations on the crystals.

We have also found that the shape of growing ice crystals depends not just on temperature, as is often assumed, but also on its history due to the rapid variation of environmental conditions in clouds. Also, at low temperatures, the effect of surface kinetics can substantially increase supersaturations in fully glaciated clouds, which may have important effects on new particle nucleation rates.

ACKNOWLEDGEMENTS This work was supported by NSF ATM-9704156.

References

[*Chen and Lamb*, 1994] Chen, J. and D. Lamb, 1994: The theoretical basis for the parameterization of ice crystal habits: growth by vapor deposition. J. Atmos. Sci. 51, 1206-1221.

[*Korolev et al*, 1999] Korolev, A., G. Isaac and J. Hallett. 1999: Ice Particle Habits in Arctic Clouds. Geophys. Res. Lett. 26, 1299-1302.

[*Kuroda*, 1984] Kuroda, T., 1984: Rate determining processes of growth of ice crystals from the vapour phase. Part I: theoretical consideration. J. Met. Soc. Japan 62, 552-561.

[*Nelson and Knight*, 1998] Nelson, J. and C. A. Knight, 1998; Snow Crystal Habit Changes Explained by Layer Nucleation. J. Atmos. Sci. 55, 1452-1465,

[*Wood et al.*, 2000] Wood, S. E., M. B. Baker, and C. Calhoun, 2000: New model for the vapor growth of hexagonal ice crystals in the atmosphere, *submitted to* J. Geophys. Res.

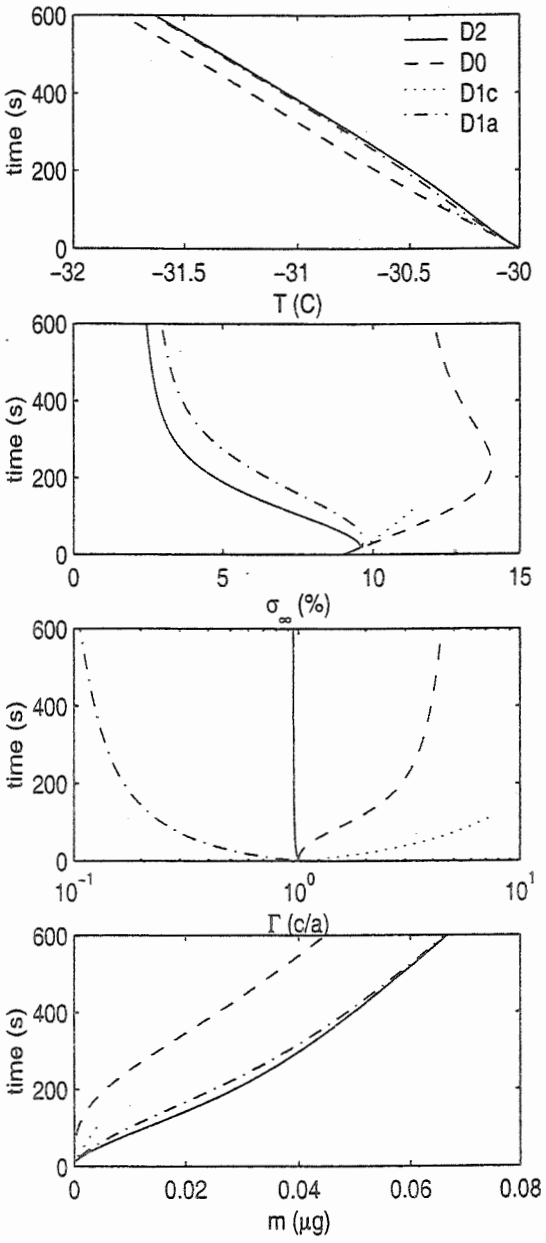

Figure 2: Evolution of ambient conditions and ice crystal characteristics for adiabatic parcel model of a fully glaciated cloud (w = 35cm/s, $N = 10^6 \mathrm{m}^{-3}$, p = 500 mbar) consisting of crystals with dislocations on all faces (*solid lines*), no faces (*dashed lines*), basal faces only (*dotted lines*), and prism faces only (*dot-dashed lines*). In each case we assumed $\sigma_{cr,2DN}$ = 10% on both prism and basal faces. In terms of vertical displacement the ordinate would range from 0 to 200 m.

LABORATORY STUDIES ON THE ICE NUCLEATION ABILITY OF BIOLOGICAL AEROSOL PARTICELS

K. Diehl*, C. Quick, S. Matthias-Maser, S.K. Mitra, and R. Jaenicke

Institut für Physik der Atmosphäre, Johannes Gutenberg–Universität Mainz, Germany

1. INTRODUCTION

Field measurements have shown that biological aerosol particles are an essential part of the total atmospheric aerosol with a fraction up to 25 % (Matthias–Maser and Jaenicke, 1995). In earlier studies the ice nucleating ability of some biological aerosol particles has already been proven. Bacteria with 0.2 to 1 μm diameter are able to act as contact and immersion freezing nuclei at temperatures up to -2° C (Vali et al, 1976; Levin and Yankofski, 1983), leaf litters with diameters between 45 nm and 24 μm are able to act as immersion freezing nuclei at temperatures as warm as -4° C (Schnell and Vali, 1976; Schnell and Tan–Schnell, 1982). However, it was also shown that the actual ice–initiating particles had been bacteria which were sitting on the leaf litters. The ice nucleating ability of the leaf litters were the higher the more decayed they were (Schnell and Vali, 1976, Yankofski et al., 1981). So there is the possibility that bacteria and plant litters which are colonised by bacteria are involved in the formation of clouds and precipitation. Plant litters are released world-wide from decaying vegetation and transferred into the atmosphere by wind erosion or by re-condensation of vapors with an estimated flux to the atmosphere of 10^1 to 10^3 nuclei cm^{-2} day^{-1} (Vali et al., 1976).

A natural conjecture is that larger biological particles — among them pollen with radii between 10 and 100 μm — might act as ice nuclei even more efficiently (Georgii and Kleinjung, 1967). Earlier studies have shown that pollen of anemophile plants are able to reach high altitudes up to 3000 m and even higher in the atmosphere (Scheppegrell, 1924; Rempe, 1937). Usually their concentration decreases continuously with altitude (Rempe, 1937) but during balloon ascent measurements in or above an inversion layer pollen concentrations higher than ground concentrations were found (Linskens and Jorge, 1986). That means pollen may temporarily be present in the atmosphere in concentrations comparable to those of ice nuclei (Pruppacher and Klett, 1997).

For the present study pollen with diameters around 30 μm and, thus, with low sink velocities were chosen because only these will have the chance to stay at high atmospheric altitudes for rather long times. Their ice nucleating ability was investigated at temperatures between 0 and -35° C in different freezing modes: the deposition mode, the immersion mode, and the contact mode. Furthermore, since in earlier studies, no explicit mention has been made regarding the ice nucleating ability of leaf litters in the deposition mode, the present study was extended to include this investigation of leaf litters and pollen partials colonised by bacteria and funges.

2. EXPERIMENTAL DETAILS

Four kinds of pollen were selected for the experiments: two deciduous tree pollen (birch, oak), one conifere pollen (pine), and one grass pollen. Birch, oak, and grass pollen were commercially available in a standardized dried form while pine pollen were sampled directly from the plants. For a comparison also naturally sampled birch pollen was used in the experiments. Preliminary studies of the hygroscopic characteristics of the pollen had shown that they are able to take up significant amounts of water from a humid environment not only at their surface but also into their interior (Wurzler et al., 1999). For the deposition freezing experiments in addition to the above mentioned pollen samples decayed leaf litters (oak) with diameters around 20 μm, pollen resuspended from decayed leaves containing bacteria and fungus, and crushed pollen grains were used.

In a first set of experiments the deposition freezing was studied by means of a deposition

*Corresponding author's adress: Karoline Diehl, Institut für Physik der Atmosphäre, Johannes–Gutenberg–Universität, Becherweg 21, 55099 Mainz, Germany; E–mail: kdiehl@mail.uni-mainz.de

growth chamber. During this freezing mode at temperatures lower than 0° C ice crystals are growing by depositing water vapor from an ice–supersaturated environment at the particles. The growth chamber was installed inside a walk–in cold chamber where temperatures down to -38° C can be reached. Particle–free air was led through an humidifier so that it became ice–saturated which was controlled by checking the dew–point of the air. Afterwards, the ice–saturated air was led into the growth chamber where single biological particles were placed on a ultra–pure silicon plate. At this location the air was further cooled down by means of a Peltier element so that ice–supersaturation of the air was reached. Through a microscope, installed above the growth chamber, the appearance of ice crystals on the biological particles growing by the deposition of water vapor from ice supersaturated environmental air was monitored. This study was carried out at different temperatures and ice supersaturations. Before starting with our actual experiments the system was tested with kaolinite particles which act as deposition freezing nuclei under known conditions (Schaller and Fukuta, 1979).

In a second set of experiments the ice nucleating ability of pollen in the immersion freezing mode was studied in the Mainz vertical wind tunnel which allows supercooled drops to be freely suspended (Diehl and Mitra, 1998). During this freezing mode particles are taken up by water drops — for example by scavenging — and act as immersion freezing nuclei inside the drop if it is supercooled below a critical temperature. At first, the freezing behavior of supercooled drops formed from highly purified distilled water was examined at temperatures down to -28° to establish the absence of ice nuclei amongst residual particles present in the distilled water sample. Afterwards, drops were injected into the tunnel which were generated from the same purified distilled water to which a defined amount of the pollen was added. Drops with radii of 250 and 375 μm were suspended for a short period of time and watched whether they froze. If a drop froze this was visible at once because it became opaque and its falling mode in the wind tunnel abruptly changed. For each drop size, temperature, and pollen kind around 50 drops were observed one by one and the fraction of frozen drops was determined. From this the median freezing temperature — the temperature at which 50 % of the observed drops freeze — for each pollen kind was estimated.

In a third set of experiments a study is underway in which the ice nucleating ability of pollen in the contact mode is investigated by freely suspending pure water drops of 375 μm radius in the Mainz vertical wind tunnel and letting pollen come in contact with it. In this freezing mode particles act as contact ice nuclei if on collision with supercooled drops they initiate freezing. At various temperatures the drops are suspended in the wind tunnel until they reach temperature equilibrium with the ambient air. Afterwards they are exposed to a short burst of different kinds of pollen, and it is observed how many drops freeze after collision with the pollen.

3. RESULTS AND CONCLUSIONS

1. The results of the deposition freezing experiments showed that pollen, including pollen which were resuspended from decayed leaves, and crushed pollen grains, as well as leaf litters are not able to act as deposition ice nuclei at temperatures down to -35° C and supersaturations, respective to ice, up to 35 %. As higher supersaturations are rarely present in the atmosphere one may conclude that biological aerosol particles like pollen and leaf litters do not play any role as ice nuclei in the deposition mode.

2. The results of the immersion freezing experiments showed that drops containing pollen started freezing at temperatures as warm as -10° C (birch), -13° C (oak), -14° C (grass), and -16° C (pine) while the pure water drops did not freeze at temperatures above -28° C. The mean freezing temperatures were found to be -13.8° C for birch pollen, -15.8° C for oak pollen, and -16.2° C for grass and pine pollen. No differences could be observed between the freezing characteristics of naturally sampled birch pollen and standardized dried birch pollen within the bounds of experimental scatter. As dried standardized and bottled pollen are not expected to contain any bacteria anyway one may conclude that the pollen itself are the ice–initiating particles. Furthermore it is to be noted that bacteria initiate freezing at substantially warmer temperatures (Vali et al, 1976; Levin and Yankofski, 1983).
The results are given as two examples in Figures 1 and 2 which represent the fraction of frozen drops at various temperatures for birch and grass pollen, respectively. As the two different drop sizes did not result in significant deviations in

drop freezing the data for both drop sizes were summarized in the figures.

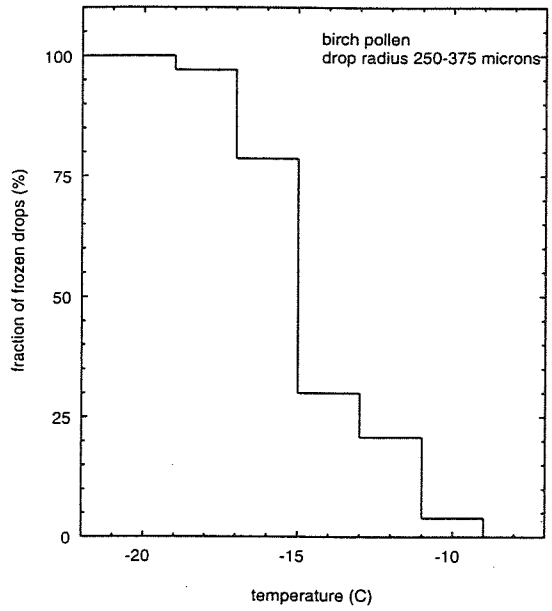

Fig.1 Variation of the fraction of drops frozen due to immersion freezing with temperature. Drops with radii 250 to 375 μm containing birch pollen.

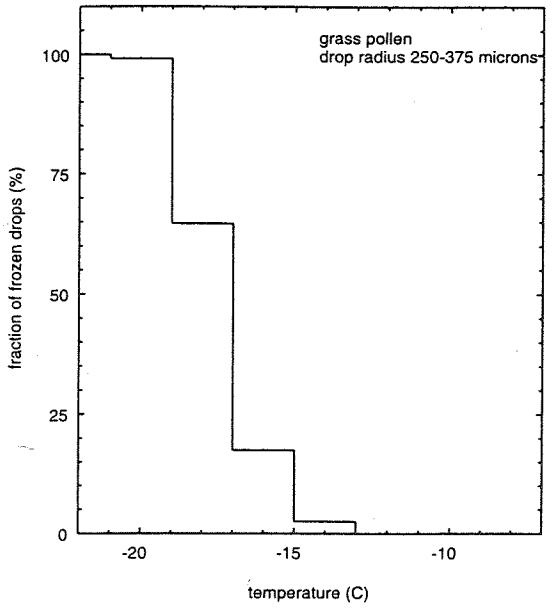

Fig.2 Variation of the fraction of drops frozen due to immersion freezing with temperature. Drops with radii 250 to 375 μm containing grass pollen.

3. Results of the contact freezing experiments will shortly be available and will be presented at the conference but preliminary tests have established a significant ice nucleation capability. Following earlier results one should expect that the contact mode works more efficiently than the immersion mode (Pruppacher and Klett, 1997).

These results confirm the importance of biological aerosol particles in cloud and precipitation processes in their ability to act as ice nuclei at relative warm temperatures.

4. ACKNOWLEDGEMENTS

These studies were supported by the Ministry for Research and Education of the Federal Republic of Germany under project 07AF219/3.

5. REFERENCES

Diehl, K., and S. K. Mitra, 1998: A laboratory study of the effects of a kerosene burner exhaust on ice nucleation and the evaporation rate of ice crystals. Atmos. Environ., **32**, No.18, 3145–3151

Georgii, H. W. und E. Kleinjung, 1967: Relations between the Chemical Composition of Atmospheric Aerosol Particles and the Concentration of natural ice nuclei. J. Rech. Atm., **3**, 145–156

Levin, Z., and S.A. Yankofsky, 1983: Contact versus immersion freezing of freely suspended droplets by bacterial ice nuclei. J. Clim. Appl. Met., **22**, 1964–1966

Linskens, H.F., and W. Jorge (1986) Pollentransport in großen Höhen. Beobachtungen während der Fahrt mit einem Gasballon. Allergologie, **9**, Nr.2, 55–58

Matthias–Maser, S., and R. Jaenicke (1995) Size distribution of primary biological aerosol particles with radii $\geq 0.2\mu$m. J. Atmos. Res., **39**, 279–286

Pruppacher, H.R., and J.D. Klett (1997) Microphysics of Clouds and Precipitation. 2nd ed., Kluwer Academic Publishers

Rempe, H. (1937) Untersuchungen über die Verbreitung des Blütenstaubes durch die Luftströmungen. Planta, **27**, 93–147

Schaller, R.C., and N. Fukuta, 1979: Ice nucleation by aerosol particles: Experimental studies using a wedge–shaped ice thermal diffusion chamber. J. Atm. Sci., **36**, 1788–1802

Scheppegrell, W. (1924) Airplane tests of hayfever pollen density in the upper air. Med. J. Rec., **119**, 185–189

Schnell, R.C., and G. Vali, 1976: Biogenic ice nuclei: Part I. Terrestrial and marine sources. J.

Atm. Sci., **33**, 1554–1564
Schnell, R.C. and S.N. Tan–Schnell, 1982: Kenyan tea litter: A source of ice nuclei. Tellus, **34**, 92–95
Vali, G., M. Christensen, R.W. Fresh, E.L. Galyan, L.R. Maki, and R.C. Schnell, 1976: Biogenic ice nuclei. Part II: Bacterial sources. J. Atm. Sci., **33**, 1565–1570
Wurzler, S., A. Bott, S. Gruber, K. Diehl, and S. Matthias–Maser, 1999: The influence of biological aerosol particles on cloud microphysics: Numerical case studies using new experimental data. J. Aerosol Sci., **30**, Suppl.1, S811–S812
Yankofski, S.A., Z. Levin, T. Berthold, and N. Sandlerman, 1981: Some basic characterstics of bacterial freezing nuclei. J. Appl. Met., **20**, 1013–1019

NUCLEATION, GROWTH AND HABIT DISTRIBUTION OF CIRRUS TYPE CRYSTALS UNDER CONTROLLED LABORATORY CONDITIONS

Matthew Bailey and John Hallett

The Desert Research Institute, Reno NV 89506

1. INTRODUCTION

Cirrus clouds at times are optically thin and consist almost exclusively of small crystals with dimensions less than a few tens of microns. At other times they are optically thick and consist of varying add mixtures of larger crystals ranging in size from 50 microns to a few millimeters in length, with the larger crystals dominating the mass distribution of ice in the cloud [Heymsfield and McFarquhar, 1998]. These differences are clearly evident from comparisons of non-convective cirrus with cirrus anvils (Poellot et al. 1999) While the variations are due in part to microphysical properties such as temperature, relative humidity, and the type of ice nuclei (IN) present, it also is likely to be due to the nucleation conditions under which the constituent ice crystals form. Ventilation also has an effect when comparing crystals falling at terminal speed in a quiescent environment versus those experiencing turbulent updrafts as in the convective case. The two examples of cirrus described have very different optical and radiative properties, and in order to characterize the role of cirrus in global circulation and radiative transfer models, it is necessary to understand the effects of each of these factors separately on crystal size, habit, and habit distribution.

We have recently completed a comprehensive study of some fundamental aspects of ice crystal growth at cirrus temperatures and pressures. This study has employed a static diffusion chamber operated between -30°C and -70°C, pressures ranging from 100-600 hPa, and ice supersaturations from 0-200%.

2. REVIEW OF LABORATORY STUDIES

Over the past few decades, the effects of temperature and humidity on ice crystal habit and growth rate have been considerably studied in the laboratory, a summary of which can be found in Pruppacher and Klett (1997). These experiments have employed a number of different methods for exploring crystal growth, each with advantages and limitations. While many of these experiments have provided important insight concerning the characteristics of ice crystal growth under specific conditions, the results from some have justifiably been met with scepticism as to their relevance to real crystals in the atmosphere when compared with in-situ observations. For example, cold temperature growth experiments conducted on a PbI substrate (Kobayashi 1965) indicated that the ice crystal habit for crystals grown between -40°C and -90°C at atmospheric pressure was exclusively columnar for all supersaturations. It is not surprising that such epitaxial results are at odds not only with in-situ data but with data from other experiments utilizing AgI smoke particles and non-oriented substrates which reveal plate and polycrystalline behavior in this region in addition to columnar growth [Hallett(2000), Bailey and Hallett (1998), Gonda (1983), Kikuchi(1973), Sato and Kikuchi, (1989)]. With the recent improvements in the resolution of cloud microphysics probes, it is clear that the habit of ice crystals in both cirrus and non-cirrus environments is generally dominated by irregular polycrystalline forms (Korolev et al. 1999).

Different methods of nucleation have also been extensively explored and present additional difficulties when trying to correlate the laboratory results with the in-situ observations. Schaefer (1949) and Yamashita (1984) demonstrated that extremely cold homogeneous nucleation of water droplets, using either dry ice or liquid nitrogen, bias habit distributions in favor of small (< 30 μm) single crystals (pristine plates and columns) and at times lead to the appearance of crystals with trigonal symmetry. Experiments utilizing AgI smoke have likewise yielded results not observed in the atmosphere, but this is not surprising since AgI has a crystallographic orientation similar to ice-I_h, and has been observed to nucleate ice-I_h even under conditions when other forms are expected (Evans, 1965). Low supersaturations (due to large particle concentrations) and short growth times also effected these results.

Non-oriented bulk substrates can provide a useful means of exploring crystal growth when the substrate or isolated structures on the substrate approach the size of typical CCN and IN in the atmosphere. In this case the term "bulk" is no longer appropriate. It is a fact the majority of ice nuclei encountered in the atmosphere are

* *Corresponding author address*: Matthew Bailey, The Desert Research Institute, 2215 Raggio Parkway, Reno NV 89512; e-mail: bailey@www.drI.edu

typically insoluble materials with crystallographic parameters quite different from ice, and while chemical composition certainly plays a significant role in terms of a particle being a good IN, it appears that surface structure also plays a role. It is well established that aerosol particles (AP) of the Aitken size range are considerably less efficient IN than larger sized AP. Topographic surface features on AP may also play a role in their nucleability. Experimental evidence for this comes from photographs taken during the course of several epitaxial growth studies which reveal that ice crystals appear preferentially at cleavage and growth steps, at cracks and in cavities, and at the edge of substrate surfaces (Pruppacher and Klett,1997).

3. RESULTS FROM THIS STUDY

A schematic of the thermal diffusion chamber used in this study is shown in figure 1. Ice crystals were nucleated and grown on drawn glass threads with typical diameters of 50μm to 70 μm. Crystal growth was observed and recorded with a time lapse camera and microscope system. One of the advantages of using this type of setup is that a spectrum of temperatures and ice supersaturations are obtained allowing the simultaneous growth of crystals of different habits under different conditions.

The glass from which the threads were drawn was a type of soda lime glass which contains approximately 70% silica and a 30% mixture of calcium and sodium oxides. Examination of a typical fiber with a microscope reveals pits and cracks of approximately 2 to 5 μm in size, the edges of which contain even smaller features. While pure silica has a poor ice nucleability, most crustal materials analyzed from cirrus particles are mixtures of silicates and other materials (Pruppacher and Klett, 1997). Hence glass threads of the proper size and topographic characteristics are reasonably appropriate material for simulating processes in the laboratory.

The experimental setup has produced habit results for crystals with sizes greater than approximately 30 μm over a broad range of temperatures, pressures, and ice supersaturations which show good correlation with in-situ data. Additionally, these results confirm that poly-crystalline ice dominates the habit at low temperatures and low to moderate ice supersaturations as observed in both in-situ observations (Korolev et al., 1999) and other cold temperature laboratory studies below -40°C (Gonda, 1983). While the optical system cannot be used to study crystals smaller than 30μm, it is the larger crystals in cirrus as studied in this experiment which at times contribute most to total cloud optical depth (Heymsfield and McFarquhar, 1998). Additionally, the authors have extensive experience with "cold box" ice nucleation and growth experiments which indicate that crystals with sizes less than 30 μm are rarely polycrystalline in form; however under some natural conditions, faceted polycrystals as small as 20 μm have been observed (Hallett et al., 2000).

One of the the motivations for performing this study was to see if crystal habit and growth rate characteristics could be used as an indicator of the temperature and ice supersaturation conditions under which crystal growth occurs. In-situ temperature measurements are quite reliable, but the accuracy of relative humidity measurements has at times been problematical due to the spatial variability within cirrus and due to uncertainties introduced by the placement of instruments on aircraft. For example, spatial variability of water vapor and particle distributions in a contrail plume can vary over a few tens of centimeters while aircraft mounted instruments can have separations of 10 to 20 meters. Coupled with the speed and instability of an aircraft flying through such a structure, the snapshot of conditions obtained in these studies together with time averaging techniques of data analysis can yield a distorted picture, plagued by erroneous or poorly correlated measurements.

Also, in-situ measurements at times relate more to the region where ice crystals are collected and not to the region in which they spent the majority of their growth phase. In a general sense, a correlation between habit, temperature, ice supersaturation and in-situ observations has been obtained from this study and is presented in Figure 2, confirming the basic working principle of a thermal diffusion chamber used for ice crystal growth. That is, a crystal grown in a static environment at a particular ice supersaturation is approximately equivalent

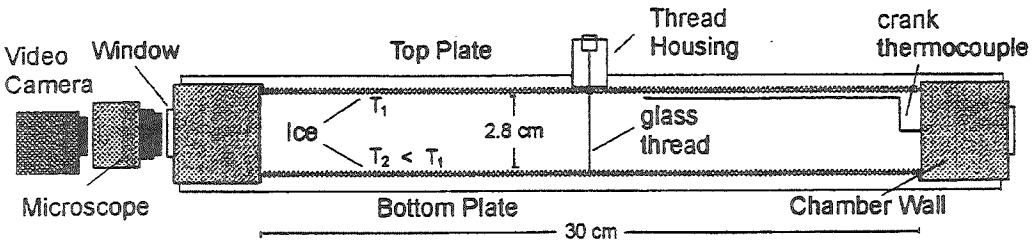

Figure 1. A schematic representation of the static diffusion chamber. The width to height ratio is 10:1.

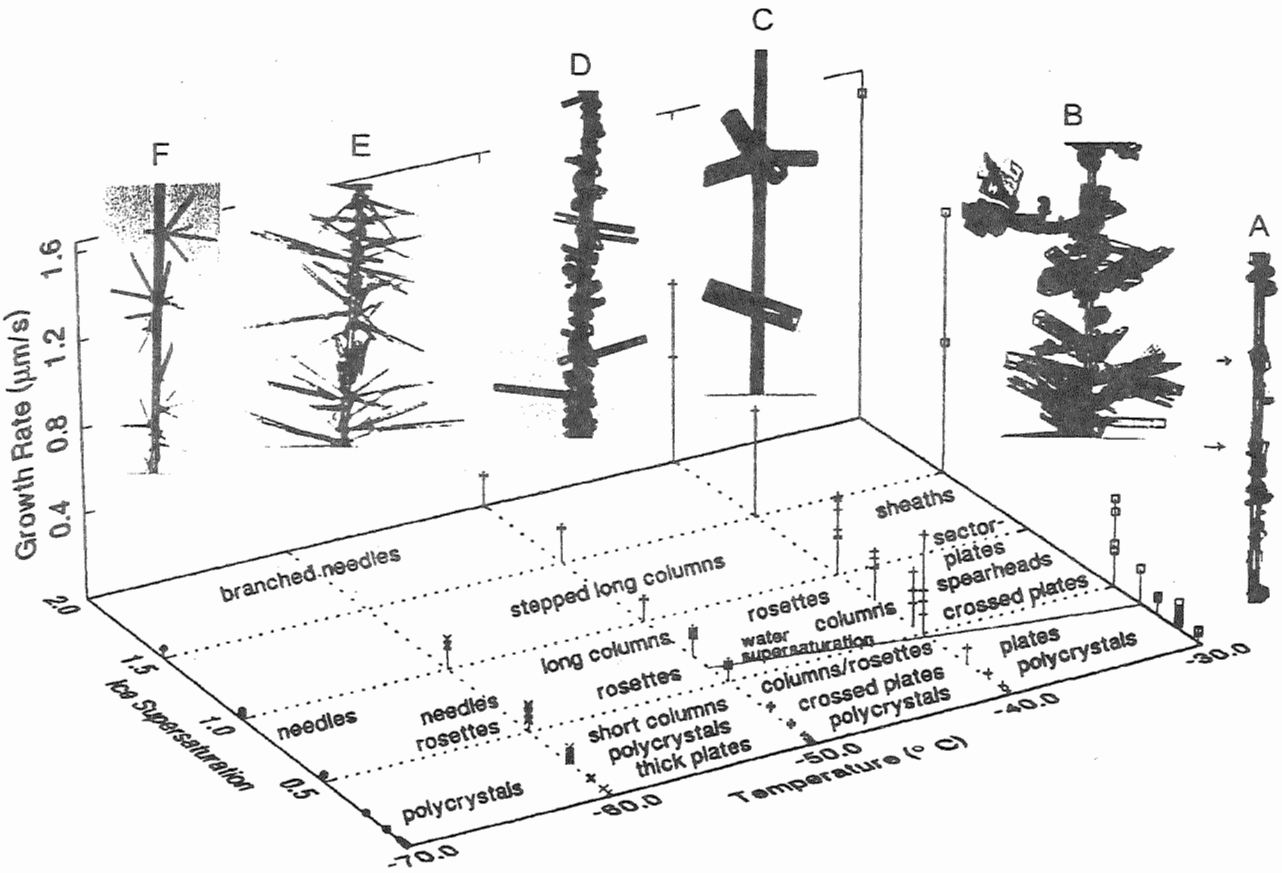

Figure 2. A summary of crystal habit and growth rate results as a function of temperature and ice supersaturation (IS). Standard atmosphere pressures appropriate to the temperatures indicated were used for all the data shown.

to a crystal growing at a lower supersaturation while falling at terminal velocity, the fall speed increasing the effective supersaturation (Keller and Hallett, 1982).

While performing this study, it was discovered that nucleation conditions had a significant effect on the habit distribution for crystals growing at low to moderate ice supersaturations, the conditions being determined by the rate of evacuation of the chamber. The rate of evacuation can be controlled to simulate the rapid change in pressure for crystals growing in the strong updrafts of convective cells with vertical speeds of 1 to 2 m/s to the more sedate change encountered in cirrus formed by orographic forcing with vertical speeds of approximately 10 cm/s. The variation of nucleation conditions was found to effect both the frequency of polycrystalline ice and certain unique types of polycrystals such as the crossed-plate type described by Furukawa (1978), in addition to affecting the frequency of pristine columns, needles and plates. The fact that habit distribution can be affected by nucleation conditions has important implications for the development of remote sensing methodologies for the detection and retrieval of cirrus cloud properties.

The photos in Figure 2 show a few of the notable features observed in this study, namely: **A)** T = -30 °C and IS = 0.02, small plates and polycrystals, including two "tabular columns" (arrowed), a term invented by Tape (1994) to describe a type of flattened short column observed in the antarctic; **B)** A readily observable transition from predominantly plate-like to columnar behavior which occurs at T = -38 °C near and above water saturation; **C)** thick column and bullet rosette at T = -40 °C and IS = 0.50; **D)** Transition from short, to moderate, to long length columns occurring for -40 °C < T < -50 °C near water saturation **E)** Transition from long columns to needles observed at T = -55 °C with IS = 1.0; and **F)** Needle rosettes growing at T = -60 °C and IS = 0.50.

Additional features indicated in the figure are as follows: (**T = -30°C, P = 400 hPa**) habit is dominated by plate-like polycrystals, including robust crossed plate

forms, with infrequent simple plates and short columns (c/a < 2) (the complexity of the polycrystals, if observed in-situ, might be assumed to be due to aggregation); **(T = -40°C, P = 300 hPa)** habit at low to modest ice supersaturation again dominated by plate-like polycrystals (including elongated crossed plates) with occasional short columns (c/a < 3), columnar behavior dominating the habit below T = -38 °C and IS > 0.4; **(T = -50 °C, P= 250 hPa)** plate and short column polycrystals dominate the habit for IS < 0.25, columns dominating for higher IS with increasing aspect ratio. Columns often have a flattened or long "tabular" appearance (this tabular behavior is apparent in both replicator data and columns gathered in-situ on glass slides); **(T = -60 °C, P =200 hPa)** polycrystals and occasional columns (c/a < 4) dominate the habit at IS < 0.25, needles, often flattened or tabular, dominate for IS > 0.3 with growth rates similar to long columns at T = -50 °C; **(T= -70°C, P=150 hPa)** sharply angled polycrystals at low to modest IS, exclusively needles at higher IS.

For IS > 0.4 and -70 °C < T < -40 °C, rosettes are frequently seen, with up to 8 individual bullets, though 3 or 4 is most common. Tabular needles and long tabular columns, alone or in rosettes, when warmed to T = -40 °C, regain their basal face ends and regular hexagonal cross section, demonstrating that their long axis is the c- axis.

Finally, Figure 3 shows linear regression fits of growth data as a function of ice supersaturation, including some data gathered at T = -20 °C and P = 500 hPa. The results indicate a nonlinear relation between

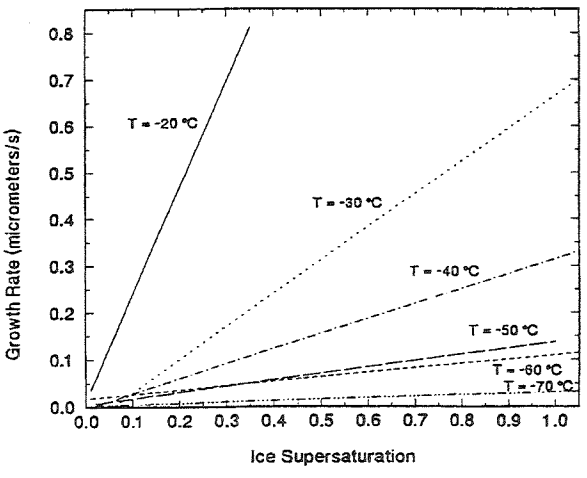

Figure 3. Regression fits of growth data.

temperature and growth rate. The similarity between T = -50 °C and T = -60 °C shows needle tip growth at T = -60 °C proceeds at only a slightly slower rate than basal face growth at T = -50 °C.

4. CONCLUSION

The results presented here show good correlation with in-situ data and can be used as a reliable guide for estimating habit and growth rate of cirrus crystals as a function of ice supersaturation and temperature for a variety of conditions. Analysis currently underway will address specifics such as the growth rate of pristine plates and columns as a function of axial ratio (c/a) and the associated growth mechanism, a comparison of mass growth rates for polycrystals versus single crystals, and an analysis of polycrystalline/single crystal frequency as a function of nucleation conditions.

This work is supported by NSF Grant ATM-9900560 and NASA Grant NAG-1-2046.

REFERENCES

Bailey, M. and J. Hallett 1998a: Laboratory Investigation of the Characteristics of Ice Grown From the Vapor Under Cirrus Conditions. In *Cirrus*, OSA Technical Digest (Optical Society of America, Washington D.C.), pp 69-71.

Evans, L.F., 1965: Requirements of an Ice Nucleus. *Nature*, **206**, 822.

Furukawa, Y. and Kobayashi, T. , 1978: On the Growth Mechanism of Polycrystalline Snow Crystals with a Specific Grain Boundary. *J. Crys. Gr.*, **45**, 57-65.

Gonda, T., 1983: Morphology of ice crystals grown in free fall at the temperatures between -40 and -140 °C. *Memoirs of National Institute of Polar Research; Special Issue, 29*, 110-120.

Hallett, J., W.P. Arnott and M.P. Bailey, 2000: Ice Crystals in Cirrus. in *Cirrus*, Oxford University Press (in press).

Heymsfield, A.J. and G.M. McFarquhar, 1998: Cirrus cloud microphysical properies from in-situ observations and their relation to shortwave radiative properties. In *Cirrus*, OSA Technical Digest (Optical Society of America, Washington D.C. 1998), pp 29-31.

Keller, V.W. and Hallett, 1982: Influence of air velocity on the habit of ice crystal growth from the vapor. *J. Crys. Gr., 60*, 91-106.

Kikuchi, K., 1970: Peculiar Shapes of Solid Precipitation Observed at Syowa Station, Antarctica. *J. Meteorol. Soc. Jpn., 48*, 243-249.

Kobayashi, T. , 1965: Vapour Growth of Ice Crystals between -40 and -90 C. *J. Meteor. Soc. Japan, 43*, 359-367.

Korolev, A.V., G.A. Isaac and J. Hallett, 1999: Ice particle habits in Arctic clouds. *Geophys. Res. Lett., 26*, 1299-1302. and this conference.

Poellot, M.R., K.A. Hilburn, W.P. Arnott and K. Sassen, 1999: In Situ Observations of Cirrus from the 1994 ARM RCS IOP. *Proceedings of the Ninth Atmospheric Radiation Measurement (ARM) Science Team Meeting*, March 22-26, 1999, San Antonio, Texas, pp 954.

Pruppacher, H.R. and J.D. Klett, *Microphysics of Clouds and Precipitation*, Kluwer Academic Publisher, 1997.

Sato, N. and K. Kikuchi, 1989: Crystal Structure of Typical Snow Crystals of Low Temperature Types. *J. Meteorol. Soc. Jpn., 48*, 521-528.

Schaefer, V.J. 1949; The formation of ice crystals in the laboratory and the atmosphere. *Chem. Rev., 44*, 291-320.

Tape, W., *Atmospheric Halos: Antarctic Research Series, 64*, American Geophysical Union, Washington, D.C., 1994.

Yamashita, A., A. Asaharu, T. Ohno and M. Wada, 1984: Ice crystals grown from the vapor at temperatures lower than -15°C. *Sixth Symposium on Polar Meteorology and Glaciology*, 99-104.

THE SCALE AND ROLE OF SPATIAL DISCONTINUITIES OF PARTICLES IN CLOUDS

J. Hallett[1] and J. T. Hallett[2]

[1]Desert Research Institute, Reno, NV, 89512, U.S.A.
[2]California State University, San Bernardino, CA, 92407, U.S.A.

1. INTRODUCTION

An understanding of the behavior of particulate clouds in a turbulent atmosphere depends on use of a successful conceptual approach in prescribing gradients of particle concentration at mixing interfaces - the cloud edge - and also at interior regions of the cloud as at interfaces between updraft and downdraft. Different circulatory motions may lead to particle size separation by centrifugal forces, adding to the effect of differential fall velocity under gravity, Baker et al 1984; Hill and Choularton, 1985; Telford et al 1993; Shaw et al 1998. Measurements of spatial distribution of particle spectra and concentration requires carrying instruments along selected tracks by aircraft or balloon, with resolution limited by sample volume and Poisson statistics of each class of particle. Alternatively, remote sensing by pulsed radiation as radar/lidar gives particle properties subject to pulse sample volume.

2. VISUAL OBSERVATION

Simple observation of cloud edges has long demonstrated that cloud bases are not only sharp within limits a few meters, but sometimes uniform within similar limits. Thus in a field of well mixed boundary layer air forming small convective clouds, as cumulus humilis, bases are visually at a uniform level (Warner 1965). Convective clouds and indeed convective elements at the tops of stratiform clouds, have sharp upshear edges (clouds look 'hard') but fuzzy downshear edges when viewed normal to the direction of vertical shear. Upwind and downwind edges of lenticular clouds often are more diffuse when viewed from below, but also on occasion appear sharp as are the tops and bases of such clouds, viewed from the side. In general visual observations inside clouds do not give useful observations of such variations although on occasion gradients of cloud can be seen - as in a wing tip vortex (Fig 1), a phenomenum which can be readily demonstrated in simulated laboratory tornadoes and waterspouts (Grotjahn, 2000).

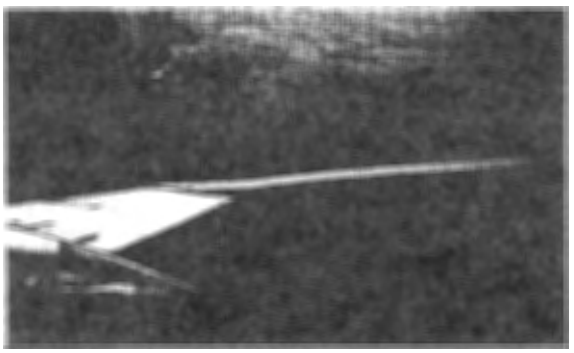

Figure 1. Discontinuity in droplet distribution related to rotation in a wing tip vortex from an aircraft wing.

2.1 Limits of Measurement

It is of interest to question the limits of measurement of the actual concentration/size distribution gradients demonstrated by visual observation and whether such gradients are significantly narrower in reality. Visual observations of clouds are evidently limited to distances of a few meters, although the sharpness shown in Figure 1 is clearly over a scale of a few cm. We can ask the question as to how our standard particle measurement instruments would respond to an idealized step distribution of particles, distributed randomly in space with a prescribed mean concentration to one side of a discontinuity and a different

Corresponding author address: John Hallett, Desert Research Institute, 2215 Raggio Parkway, Reno, NV 89512-1095; email: hallett@dri.edu.

concentration (which could be zero) on the other side. As an example, consider the ancient, but still useful, formvar continuous replicator, where a solution coated film is drawn past a slit exposed normal to the airflow, which collects and images particles impacted during its passage past the slit. A sharp discontinuity in air concentration is thus spread out into a linear gradient of concentration on the film over a time of b/R (b = slit width; R = film speed) equivalent to a distance along the flight path of U b/R, about 1m with typical values and spread out over 0.2 cm of film, a distance easily used to obtain a size distribution. Optical microscopy readily gives a droplet size resolution of near size resolution of near 1um. Fig 2a, 2b shows such a discontinuities taken during a flight in a developing convective cloud over Colorado and Texas. Other considerations apply to optical probes, depending on selection of bin width and sample time required to give a statistically meaningful concentration in each bin. Thus a monodisperse droplet spectrum may straddle one or two bins (Liu and Hallett, 1998), which may be selected as 3 μm in width with a sample time to give (say) 100 droplets in each bin with a variance of +/- 10, giving a sample time of a few tenths of a second and a spatial average over less than a few meters as discussed elsewhere (Bourrianne and Brenguier, 1998).

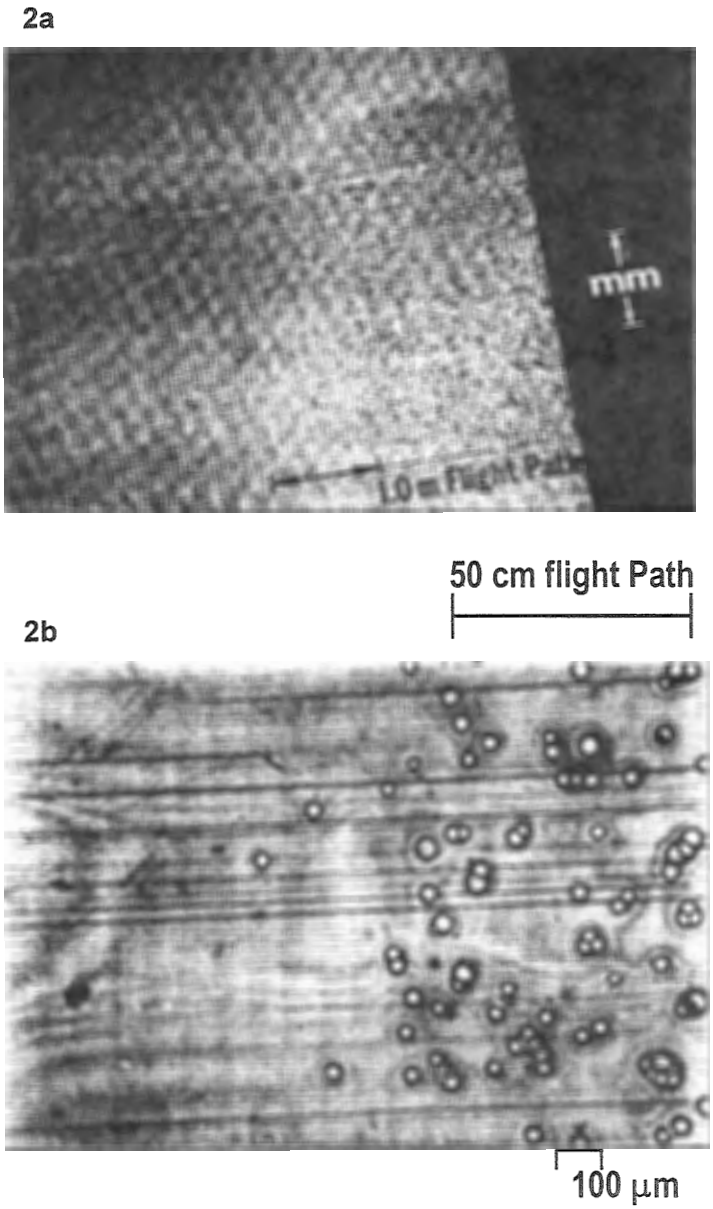

Figure 2a, 2b: Sharpness of a cloud edge revealed by cloud droplet replica in upshear edge of a growing cumulus cloud.

3. MIXED PHASE CLOUDS

Equivalent considerations apply to mixed clouds containing both ice and water particles. Conceptually, it is necessary to distinguish between a cloud with particles mixed in a random sense - as when ice particles from an ice cloud layer aloft fall into a supercooled water layer cloud below. Simultaneous measurements of ice and water in the same air volume are necessary to determine whether ice is distributed at random; a replica technique here provides a spatial average over all particles over a scale of 1 meter. If separate instruments are used, a significantly greater uncertainty exists arising from the spatial variability on the scale of the instrument separation and exposure, some tens of meters. This is of particular importance in convective cloud sheared in the vertical. Figure 3 shows schematically the variability across a deep convective cloud in Florida (related to a sea breeze front, left in Figure) with transition from all supercooled water in the updraft to all ice in the downdraft. A further complication here is relating particles to the interface between up and down draft with a time constant of instrument response of seconds. This is the interface region where a mix of graupel, actively growing from super-cooled cloud, and smaller ice particles, possibly originating from rime splintering, lead to rapid glaciation and is potentially the site for electrical charge separation. (Hallett, 1999). The physical reality appears to be an interface which is in a near steady state, water cloud eroding on the upshear edge; an interface between ice and water at the vertical velocity shear interface and a diffuse down shear ice interface. Observations point to an interface ice - supercooled cloud of some hundreds of meters (Willis et al 1994). This interface may be wiggly and convoluted, making its characterization by aircraft penetration difficult as the local direction may differ from the mean direction of the plane of the front. Yet the microphysical picture may be changing on a scale which we are unable to resolve. The observations further demonstrate the difficulties in use of a diffusion processes as providing a model for a cloud interface - the sharpness of the observations is not consistent with any such mechanism, although interface diffusion may lead to a local supersaturation (Figure 4).

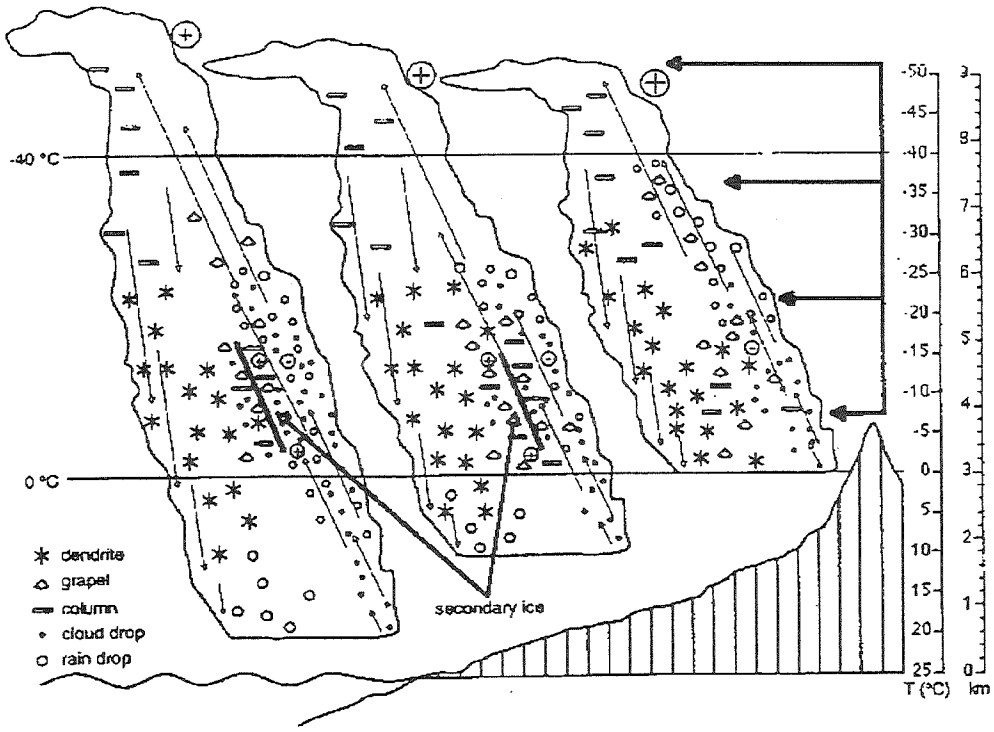

Figure 3. Schematic of discontinuities in particle type and concentration with all water cloud in updraft to right, all ice in descending on a left and a narrow interface in between over a distance of a few hundred meters. Different cloud base temperatures influence particles types in up and downdraft.

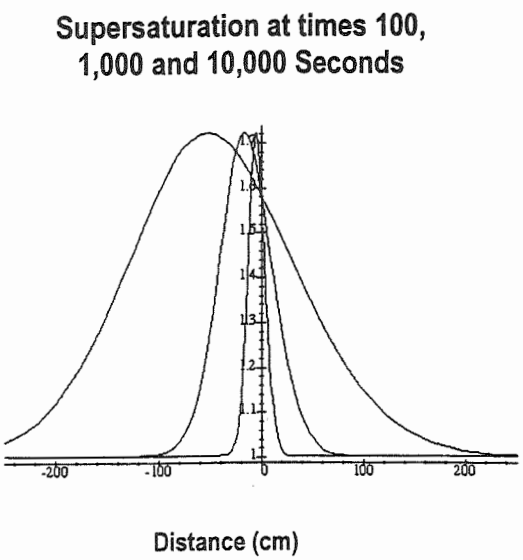

Figure 4: Calculations of a supersaturation wave from a sharp interface produced in the cold air by double diffusion of heat plus water vapor from warm saturated to cold saturated air at different times (time α x^2/D) for 0.5 atmosphere pressure. Long times are necessary to produce an effect on a scale of about 1 meter and we are left with interpreting the sharpness shown in Fig. 2 as an edge mixing process. The detailed mechanisms are largely unknown and pose a future problem for investigation.

4. CONCLUSION

The general theme of the above discussion may be extended downward on a variety of scales and ultimately on the scale differentiating homogeneous and heterogeneous mixing (Telford et al, 1993; Baker et al, 1984). Of particular import is the stabilization of an entity by rotation as in Fig. 1 for a linear system or in a 3D vortex ring type of motion (Hallett and Christensen, 1984) with separation of particles around the axes of rotation achieved through centrifugal forces. It follows that regions of shear induced by buoyancy effects may be responsible in decay for smaller scale motions which localize cloud microphysical processes. Particle distribution in sheared motion in clouds associated with a variety of scales is important in leading to a variety of phenomena related to ice and liquid phase microphysical processes with application to aircraft icing. Simultaneous measurement of cloud particle type and motion distributions on a small scale not currently available may be necessary to show the importance of these effects.

5. ACKNOWLEDGMENTS

The work and ideas developed herein were supported in part by grants: NSF ATM-9413437; 9900560, Arlington, VA; and US Air Force DEPSCOR Grant F49620-96-1-0470.

6. REFERENCES

Baker, M. B., Breidenthal, R. E., Choularton, T. W., and Latham, J., 1984: The effects of turbulent mixing in clouds. *J. Atmos. Sci., **41,*** 209-304.

Bourrianne, T., Brenguier, J-L., 1998: Improvements of Droplet Size Distribution Measurements with the Fast-FSSP (Forward Scattering Spectrometer Probe). *J. Atmos. & Ocean. Techn., **15,*** 1077-1090.

Grotjahn, R., 2000: Multiple Waterspouts at Lake Tahoe. *Bulletin, Amer. Meteor. Soc., **81,*** 695-702.

Hallett, J., 1999: Charge Generation with and without Secondary Ice Production. *11th International Conference on Atmospheric Electricity. Huntsville, Alabama, June 1999,* 355-358.

Hallett, J. and L. Christensen, 1984: The splashing and penetration of raindrops into water, *J. Rech. Atmos., **18,*** 226-242.

Hill, T. A. and Choularton, T.W., 1985: An airborne study of the microphysical structure of cumulus clouds. *Q. J. R. Meteorol. Soc., **111,*** 517-544.

Liu, Y. and J. Hallett, 1998: On Size Distributions of Cloud Droplets Growing by Condensation: A New Conceptual Model. *J. Atmos. Sci.. Soc., **55,*** 527-536.

Shaw, A. R., W. C. Reade, L. R. Collins and J. Verlinde, 1998: Preferential Concentration of Cloud Droplets by Turbulence: Effects on the Early Evolution of Cumulus Cloud Droplet Spectra. *J. Atmos. Sci., **55***, 1965-1976.

Telford, J. W., K.-E. Kim, T.S. Keck and J. Hallett, 1993: Entrainment in cumulus clouds. II. drop size variability, *Q. J. R. Meteorol. Soc., **119,*** 631-653.

Warner, J., 1965: The initial formation of cumulus cloud and the uniformity of base height. *International Conference on Cloud Physics,* May 24 – June 1, Sapporo and Tokyo, Japan. 16-19.

Willis, P.T., J. Hallett, R.A. Black and W. Hendricks, 1994: An aircraft study of rapid precipitation development and electrification in a growing convective cloud, *J. Atmos. Res., **33***, 1-24.

CLUMPY CIRRUS

Brad A Baker, R. Paul Lawson and Carl G. Schmitt
SPEC inc.

1. INTRODUCTION

This paper presents data from the Cloud Particle Imager (CPI), a relatively new airborne instrument for in situ cloud microphysics research (Lawson et al. 1998; Korolev et al. 1999). The CPI records high-definition images of small (0.2 cm^{-3}) volumes of cloud and only takes an image when it has been triggered by a particle, or group of particles, passing through the Particle Detection System (PDS). General characteristics of cirrus clouds, also based primarily on CPI data, are described by Schmitt et al. (2000), which is also found in this volume. Here we focus on the extreme spatial variability ("clumpiness") seen on small scales.

We first show an example of CPI measurements collected by the SPEC Learjet in a cirrus cloud studied over the Cloud And Radiation Testbed (CART) site in Oklahoma. The DOE Atmospheric Radiation Measurement (ARM) program operates the CART site. In this case, clumps with high concentrations of small particles are interspersed with the large (mostly bullet rosette) ice particles that exist at relatively low concentrations. Next, an example from an arctic cirrus cloud is shown that displays the same sort of clumpiness as found in the Oklahoma cirrus. Finally, a relatively homogeneous part of an arctic boundary layer cloud is examined to demonstrate that the CPI is not creating the clumpiness seen in the cirrus clouds.

2.0 MEASUREMENTS

2.1 Oklahoma Cirrus Cloud

Figure 1 shows a time series of average concentrations measured by a FSSP, a 2DC, and the CPI PDS as the aircraft flew through cirrus cloud from 8.5 to 8.8 Km MSL (–38 and –41 °C) over the CART site. The measurements show that there is considerable spatial structure to the cloud on scales greater than the 150 m resolution of the instruments. The concentrations measured by the FSSP are greater than those measured by the 2DC and the CPI PDS for two reasons: 1) The sample volume used in estimating the FSSP concentration is under estimated for the large ice particles, and 2) because there are high concentrations of small particles that are counted more efficiently by the FSSP than the other probes. The effectiveness of the 2DC at counting particles decreases with decreasing size (i.e., rolls off) starting at roughly 25μm versus roughly 5μm for the FSSP. The effectiveness of the CPI PDS at counting particles also roles off at around 25μm, but the higher concentration spikes indicate that it still detects some of the smaller particles.

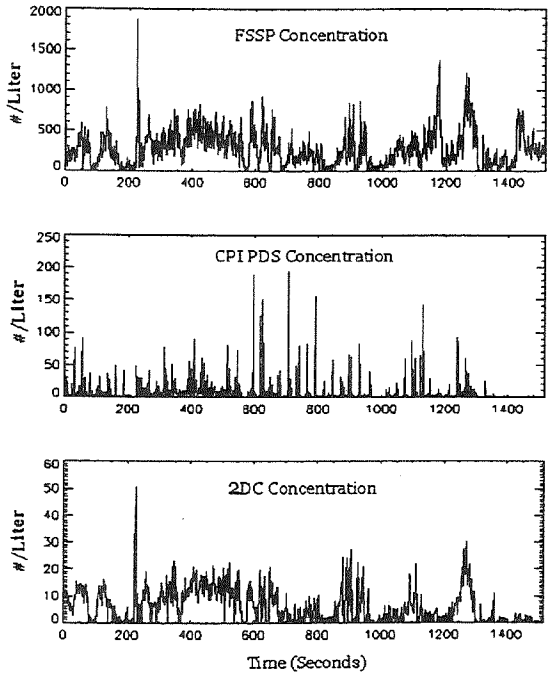

FIGURE 1: Time series of concentrations measured by various probes in a cirrus cloud over Oklahoma on 1 March 2000.

The particle size distribution compiled from the CPI image frames (**Figure 2**) confirms the existence of high concentrations of small particles. We now show that small particles are found in clumps with very high local concentrations that are interspersed with regions of larger particles in low concentrations. **Figure 3a** shows a distribution of the number of particles per image frame taken by the CPI. The Poisson distribution with the same mean is also shown in the figure. The Poisson distribution would be the result of random sampling in a homogeneous cloud. The comparison in **Figure 3a** shows that the CPI particle size distribution differs significantly from the Poisson distribution. To accentuate this point, conditional size distributions are shown in **Figure 3b**. One conditional distribution was made of the sizes of particles imaged in frames with only one particle, while the other was made

Corresponding author's address: Brad Baker C/O SPEC inc.
5401 Western avenue Suite B, Boulder CO 80301
email: brad@specinc.com

from the sizes of particles imaged in frames with 5 or more particles. If the cloud were homogeneous, the conditional size distributions would be identical. However, as seen in **Figure 3b**, the high concentration frames contain only small particles.

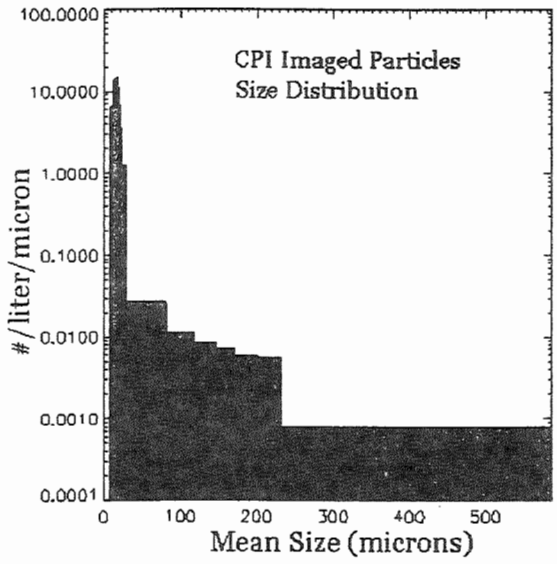

FIGURE 2: Size distribution of particles imaged by the CPI during the time period shown in Figure 1.

That is, the large particles are most often found in concentrations so low that to capture more than one particle in a frame is rare. The small particles can be found at low concentration and at extremely high concentration. Where there are several to tens of particles in a given image frame, the local to thousands per cm^{-3}. The conditional size distributions shown in **Figures 3a** and **3b** could result from the aircraft flying first through a single region of large particles in low concentration, followed by a single region of small particles in high concentrations. However inspection of the CPI image frames themselves, shown in **Figure 4**, reveals that the regions of high concentrations of concentrations in the small volumes imaged are on the order of hundreds small particles are interspersed with regions of low concentrations of large particles. It is important to note at this point that the high and low concentration regions are interspersed, and not superimposed.

2.2 Arctic Cirrus Cloud

Figures 5 and **6** are analogous to Figures 3 and 4 except for a cirrus cloud observed in the arctic during the NASA FIRE Arctic Cloud Experiment (FIRE.ACE). The FIRE.ACE project is described by Curry et al. (2000) and features of

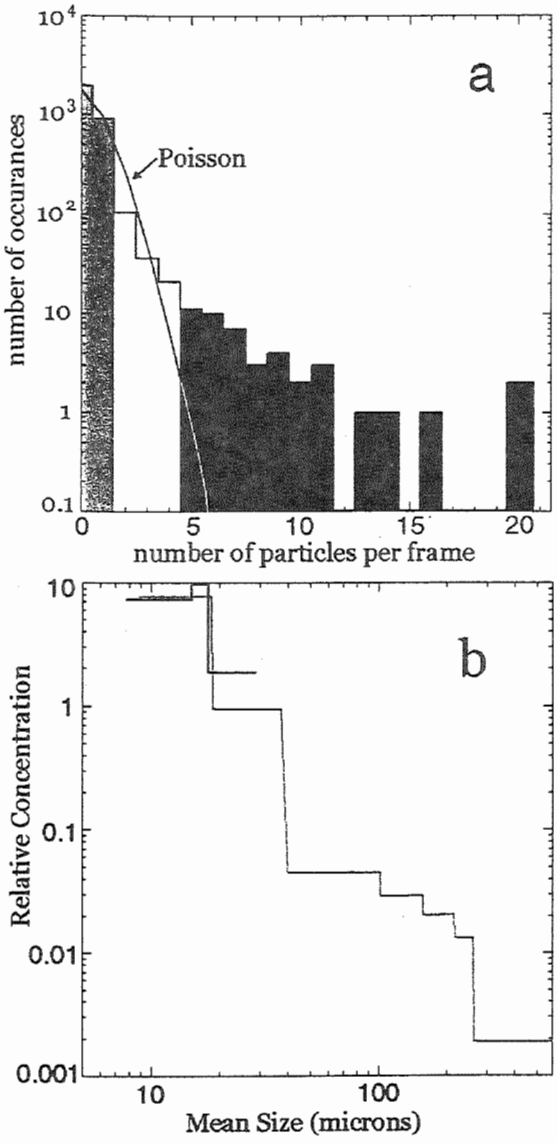

FIGURE 3: Histograms of (top) the number of particles per frame for all the CPI imaged frames during the time period shown in Figure 1 along with the Poisson distribution with the same mean, and (bottom) conditional particle size distributions produced by using only those particles in frames with 5 or more particles (black) and using only those particles that were imaged alone (gray).

boundary layer clouds observed during the project are described in this volume by Lawson et al. (2000). The data in **Figures 5** and **6** were collected over a period of 25 min as the NCAR C-130 flew at an altitude of about 5400 m (–25 °C). The implication from these figures is again that high concentration pockets of small particles are interspersed with the larger particles.

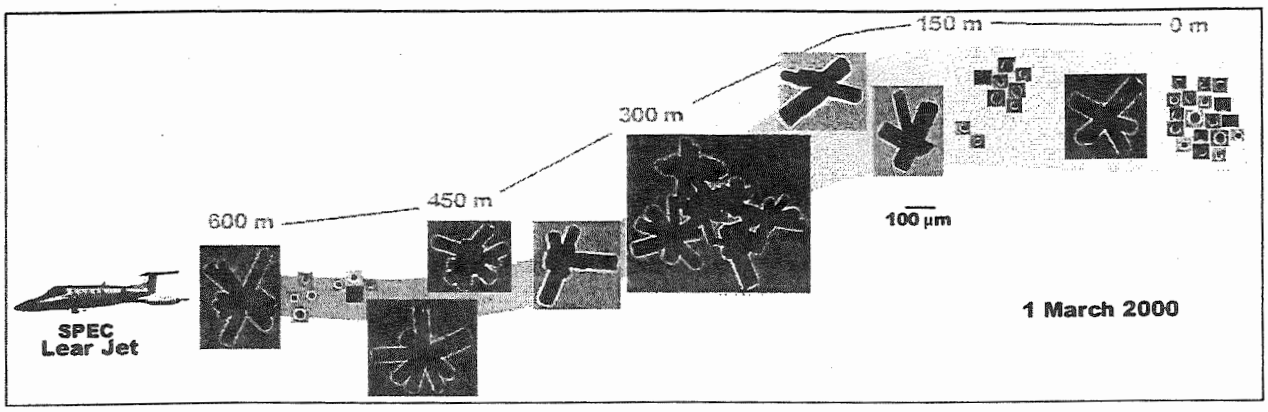

FIGURE 4: Images of the cirrus ice particles sampled over a 600 m region. Each box with a large crystal or aggregate represents one CPI image frame, as does each group of small boxes. The image frames reflect the relative positions of particles as they were actually observed.

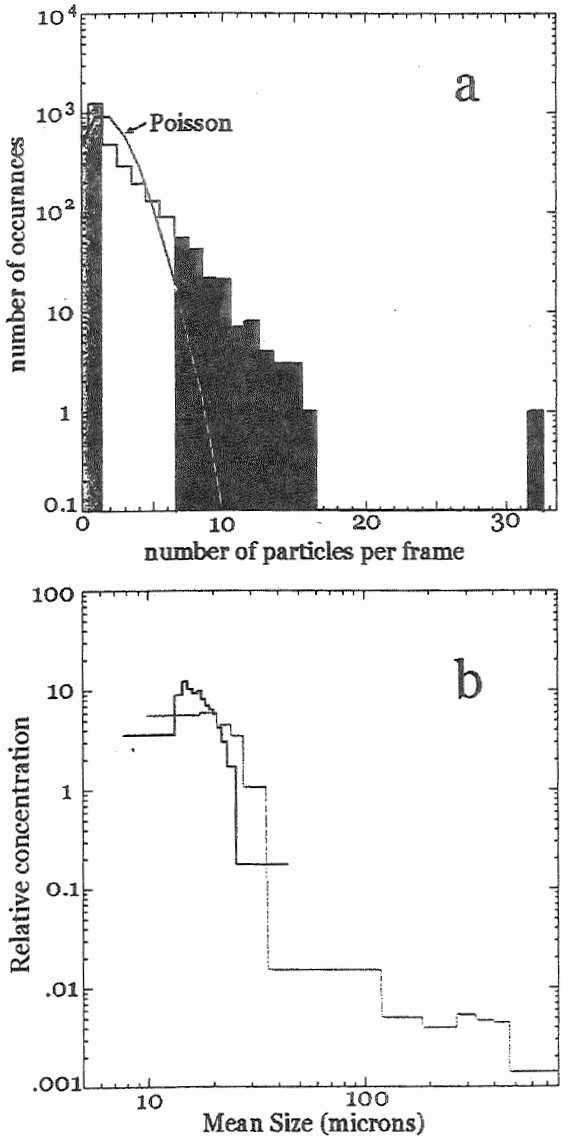

FIGURE 5. Histograms of (top) the number of particles per frame for all the CPI imaged frames during 25 min of flight through an arctic cirrus cloud along with the Poisson distribution with the same mean, and (bottom) conditional particle size distributions produced by using only those particles in frames with 7 or more particles (black) and using only those particles that were imaged alone (gray).

2.3 Arctic Boundary Layer Cloud

CPI measurements in a (mostly) homogeneous arctic boundary layer cloud are now examined to verify that triggering of the CPI does not cause the clumpiness observed in the cirrus clouds previously discussed. This is important, because asynchronous triggering could feasibly create such an effect. CPI data from wind tunnel tests (not shown here) indicate that, at very high PDS triggering thresholds in a very inhomogeneous cloud, clumpiness is amplified by triggering.

A short time before sampling the arctic cirrus cloud discussed in Section 2.2, the C-130 executed a stepped ascent through a stratiform, all-liquid boundary layer cloud. Cloud base was at about 100 m and cloud top was about 450 m MSL. The cloud was entraining environmental air at cloud top and mixing the entrained air downwards. The case is discussed in more detail in this volume by Lawson et al. (2000).

Here we discuss the distribution of particles in this boundary layer cloud in the same manner as used in **Figures 3** and **5**. At about 180 m MSL, the droplet size distribution was mono-modal, the particles-per-frame distribution was nearly Poisson and the conditional spectra were identical. All these, together with smooth liquid water and temperature measurements, imply that this region of cloud was quite uniform. At about 270 m MSL the droplet size distribution was bimodal, indicating that the effects of entrainment and mixing at cloud top had reached this level. As shown in **Figure 7**, the particles-per-frame distribution is still nearly Poisson and the conditional spectra are still identical, indicating the cloud was fairly well mixed, despite entrainment. The data in **Figure 7** do not indicate any clumpiness in the boundary layer cloud. The CPI was operated in the same manner as in the previous examples, so the point here is that the cloud is

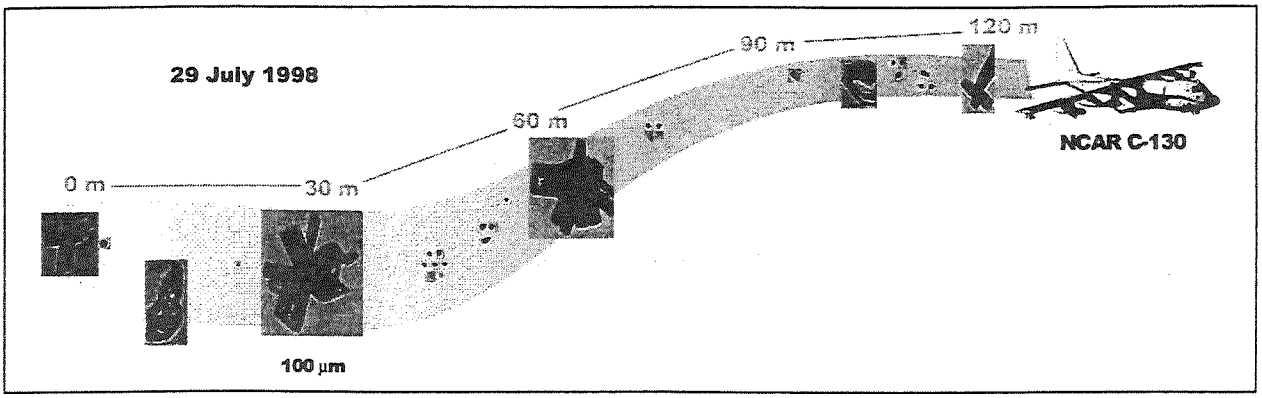

FIGURE 6. Images of arctic cirrus ice particles sampled on July 29 1998 during FIRE.ACE. Each box with a large crystal and each group of small boxes represents one CPI image frame. The image frames reflect the relative positions of particles as they were actually observed. A significant point here is that the spatial variation between low concentrations of large particles and high concentrations of small particles is on the order of ten meters or less.

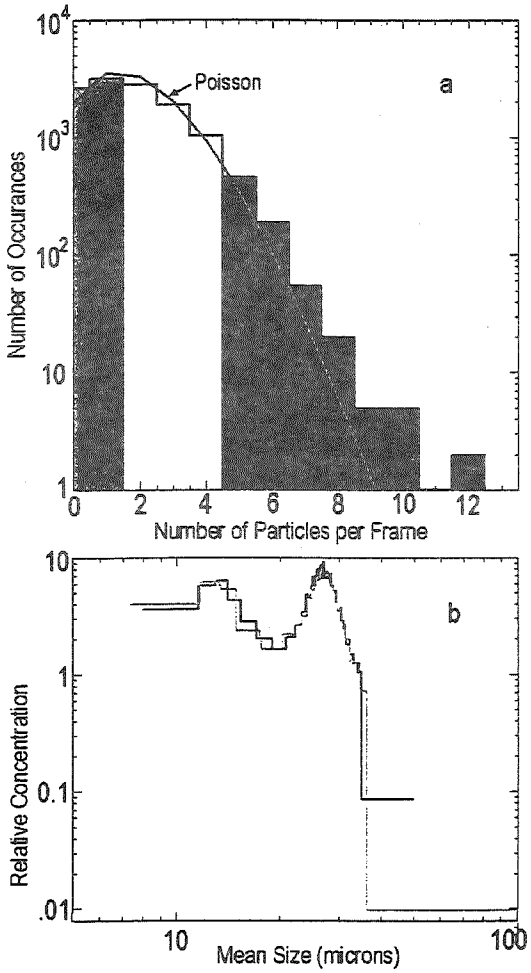

FIGURE 7. Histograms of (top) the number of particles per frame for all the CPI imaged frames during 7 min of flight at 270 m through an arctic boundary layer cloud on July 29 1998 along with the Poisson distribution with the same mean, and (bottom) conditional particle size distributions produced by using only those particles in frames with 5 or more particles (black), shown with particle size distribution using only those particles that were imaged alone (gray).

fairly homogeneous and the CPI asynchronous triggering is not causing any apparent clumpiness. At about 420 m, near cloud top, the conditional size distributions were not identical, implying that the cloud was inhomogeneous. Interestingly, near cloud top in this all-liquid boundary layer cloud, the trend for smaller droplets to be in higher concentration regions was similar to the trend seen for small ice particles observed in cirrus.

3.0 SUMMARY

Cirrus clouds observed over Oklahoma and in the arctic are shown to have regions of relatively low concentrations (on the order of tens L^{-1}) of large (bullet rosette) ice particles, and also regions of high concentrations (on the order of hundreds to thousands cm^{-3}) of small ice particles. The individual regions are interspersed on scales down to at least tens of meters and perhaps smaller.

Acknowledgements: This research has been supported by NSF Grant ATM-9904710, NASA FIRE contract NAS1-96015, NASA EOS contract (from Univ. Utah) 98-0-03 and DOE contract 354593-A-Q5. We would also like to thank pilot Bill Harris and Rainbow Chaser, LLC, the owner of the Learjet operated by SPEC.

REFERENCES

Curry, J.A., P. Hobbs, M. King, D. Randall, P. Minnis, et al., 2000: FIRE Arctic Clouds Experiment, *Bull. Amer. Meteorol. Soc.*, 81, 5-29.

Korolev, A.V., G.A. Isaac and J. Hallett, Ice particle habits in Arctic clouds, 1999: *Geophys. Res. Letters*, **26**, 1299-1302.

Lawson, R. P, A. V. Korolev, S. G. Cober, T. Huang, J. W. Strapp and G.A. Isaac, 1998: Improved Measurements of the Drop Size Distribution of a Freezing Drizzle Event, *Atmos. Res.*, ***47-48***, 181-191.

Lawson, R. P., B. A. Baker and C. G. Schmitt, 2000: Microphysical properties of arctic boundary layer clouds observed during FIRE.ACE. In this volume.

Schmitt, C. G., R. P. Lawson and B. A. Baker, In situ measurements of mid-latitude and tropical cirrus clouds. In this volume.

A Laboratory Investigation of the Orientation, Alignment, and Oscillation of Ice Crystals

T. C. Foster[1] and J. Hallett

Desert Research Institute, Reno, NV
[1]Permanent Address: California Polytechnic State University, San Luis Obispo, CA

1. INTRODUCTION

Ice crystals in the atmosphere tend to orient and to oscillate due to aerodynamic forces; Brownian motion tends to destroy this alignment, preferentially for smaller crystals. Electric fields exert torques on the crystals to change this orientation. Results of experiments on laboratory ice are compared to theoretical predictions of how these crystals behave. Theory centers on both Brownian motion, as is evidenced by the apparent twinkling of the crystals, and the response of the crystals to torques produced by electric fields applied in the cloud. Applications reach into diverse areas. Global warming depends on solar energy being reflected by cirrus clouds and trapping of outgoing infrared radiation; electric fields may reorient ice crystals to change the reflection or trapping. Radar propagation through clouds depends on the orientation of the crystals relative to the direction of propagation, which can be changed by electric fields. There is the worry that research aircraft, if they are charged, may change the orientation of the ice crystals they are measuring. Lightning striking a launched rocket may be influenced by the alignment of crystals in nearby clouds and it may be possible to assess the likelihood of such lightning by measurements of the crystal alignment. There is a report of a pilot briefly seeing through a cirrus cloud following lightning. Finally various atmospheric optical phenomena (sundogs, the subsun, the circumzenith arc, sun pillars, etc.) depend on orientation and oscillation of ice crystals and may be affected by local electric fields.

2. EXPERIMENTAL APPARATUS

Cloud was produced in a standard chest freezer in a temperature range from -15 C to -25 C by an ultrasonic nebulizer. A strong tungsten microscope lamp illuminated the cloud. An unloaded compressed air pellet gun was discharged into the cloud to nucleate ice using a "cooling by adiabatic expansion" technique. Electric fields were produced by steady D.C. voltages up to 5 kV applied to various pairs of conductors inside the freezer. Data were recorded by visual inspection of changes in the cloud, by standard photography, and by video recording. The crystals produced in the freezer were largely thin hexagonal plates, with some structure at the edges, and ranged up to roughly 30 μm in diameter. We estimated thickness to be approximately 1 μm from the thin film interference colors seen both in the free crystals and in captured crystals viewed under a microscope. This was done by calculating the CIE x-y chromaticity of the light reflected from the crystals as a function of their thickness, plotting this chromaticity on a conventional CIE graph, and comparing the color seen with the value predicted (Walker, 1978). Crystal diameters were measured by capturing the crystals on a cold surface and viewing them using a cold microscope. Theoretical fall speed for such crystals is less than 1 cm/s (Pruppacher and Klett, 1980). Reynolds numbers for these crystals were less than about 0.015.

Corresponding author's address: J. Hallett, Desert Research Institute, 2215 Raggio Parkway, Reno, NV 89512; E-Mail: hallett@dri.edu.

3. BROWNIAN MOTION

Conventional wisdom is that hexagonal plate crystals with Reynolds numbers between 1 and 100 lie horizontally in the atmosphere and fall vertically (Sassen, 1980). Theory suggests that smaller plates that happen to be at orientations other than horizontal remain at that angle and fall downward at a different, constant angle (Katz, 1998). However Cox has shown (see Fraser, 1979, Weinheimer and Few, 1987, and Katz, 1998) that there is a small torque on even the smallest particles trying to reorient them horizontally. Orientation is influenced by Brownian motion (Hallett, 1987) and small particles in a size range between 10 and 20 μm are observed to "twinkle" due to Brownian motion oscillations (Reist, 1993).

The "twinkling" rate can be estimated using standard theory. Fuchs (1964) gives theory for the Brownian rotation of spheres and flat disks and for the latter the angle turned through as a function of time is given by

$$\langle\theta^2\rangle = [3kT/16\,\eta]t/r^3,$$

where θ is in radians, k is Boltzmann's Constant, T is Kelvin temperature, η is the dynamic viscosity of air, and r the disk radius. Inserting a light cone angle appropriate to the microscope lamp which illuminates our cloud and taking r = 10 μm yields a "twinkling time" of about 0.1 s. Fig.1 is a short time exposure of some of our crystals, taken by sweeping the camera across the crystals. The "dashed" lines seen in several of the streaks are consistent with the time estimated above.

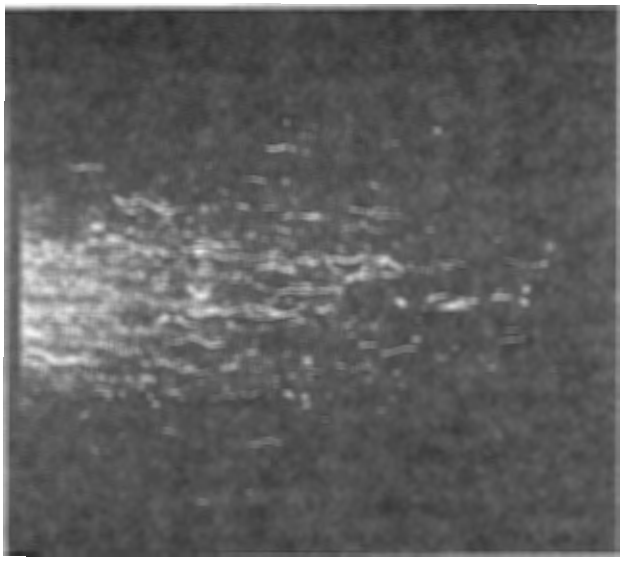

Fig 1. Close-up time exposure photograph of crystals taken with a moving camera. The length of an average streak corresponds to the 1 s exposure time. The width of the light beam, measured vertically, is about 3 cm. Some of the streaks appear as "dashed" lines and indicate ice crystals vibrating as a result of Brownian motion.

4. ELECTRICAL ALIGNMENT OF CRYSTALS

When uncharged crystals are in the presence of electric fields, charges are induced across the crystal and these charges experience an electrical torque. Electrical potential energy is produced if the crystal is rotated from its preferred orientation. Both Weinheimer & Few (1987) and Fuchs (1964) give the expression for the electrical potential energy, assuming the crystals can be represented by ellipsoids of revolution. In the notation used by Fuchs the potential energy is

$$1/2\ \varepsilon_o V E^2 [1/K_2 - 1/K_1] \cos^2\theta$$

where V is the ellipsoid volume, E is the electric field magnitude, the K's are shape factors that depend on the ellipsoid radii and the dielectric constant of ice, and θ is the angle between the symmetry axis and the E-field direction. Fuchs also has an expression for the statistical mechanical probability of the ellipsoid symmetry axis being oriented at an angle θ from the direction of the E-field:

$$P(\theta)d\theta = b \exp\{-0.5\ \varepsilon_o V E^2 [1/K_2 - 1/K_1] \cos^2\theta/kT\} \sin\theta\, d\theta$$

where b is a normalization constant which gives the integral of the probability to be equal to unity.

Fig. 2 gives a graph of the calculated probability vs. θ for several different E-field magnitudes (ellipsoid major diameter 20 μm and thickness 1 μm). Using the probability equation above, the average value of $\cos(\theta)$ can be determined. A completely random array corresponds to an average value of 0.5 while an average value of zero means all ellipsoids are aligned along the E-field (with the symmetry axis 90 degrees from it). For an E-field of 500 V/m the average values of $\cos\theta$ are 0.49 and 0.41 for 10 μm and 20 μm equatorial diameter ellipsoids respectively (both for a polar diameter of 1μm). For 1 kV/m fields the average values are 0.45 and 0.25. For 5 kV/m fields the average values are 0.14 and 0.05. For 10 kV/m fields the average values are 0.07 and 0.03. This indicates theoretically that crystals of the sizes used in our experiments become strongly aligned with an external E-field for field magnitudes greater than 5 kV/m and are substantially unaligned for field strengths less than 500 to 1000 V/m. Calculations done using the expressions for electrical torque and potential energy contained in Weinheimer and Few (1987) yield essentially the same results.

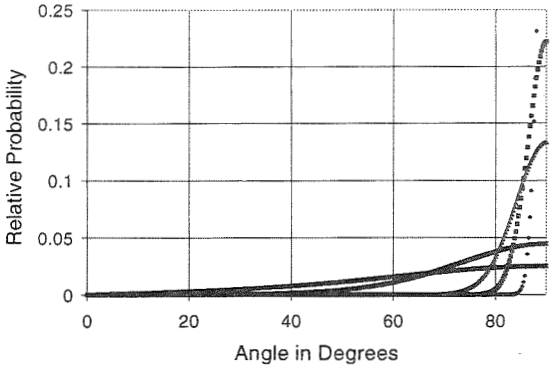

Fig. 2. Relative probability of finding crystals oriented at a given angle due to electrical torques. The angle is measured from the ellipsoid symmetry axis to the E-field and so a 90 degree angle indicates complete alignment of the ellipsoid equatorial plane with E. The graphs are for E-fields of 500, 1000, 3000, 5000, and 10,000 V/m with the large E-fields associated with graphs strongly localized near 90 degrees.

Measurements were made to determine the minimum magnitude of the electric field required to align the crystals in the cloud and the field magnitude required to produce essentially complete alignment. In these experiments two electrodes were placed in the freezer and a light beam was set to illuminate a relevant segment of the crystals present, at which point the magnitude and direction of the field can be calculated. The beam was set up so that there was little specular reflection toward the viewer without the field but a strong reflection with a strong field turned on (or sometimes vice versa). Then a number of qualitative optical measurements were made, at different voltages across the electrodes and so at different E-field strengths at the position of our crystals in the light beam. Videotapes of these experiments were taken and later checked against the direct optical observations. One set of typical results is summarized in Table 1. These measurements showed that significant alignment occurs with electric fields stronger

than about 10 kV/m and little if any occurs for fields below about 1000 V/m.

V	E	t1	t2	t3	E	t1	t2	t3
5000	21	A	A	A	18	A	A	A
3500	15	A	A	A	13	A	A	A
3000	13	A	A	A	11	A	A	A-
2500	11		A	B	9		A	A-
2000	8	B	B	B	7	B+	B+	B
1750	7	B	B	B	6	B+	B+	B+
1500	6	BC	BC	B-	5	B	B	B
1250	5	C	C	C	4	B	B	B
1000	4	C	C	C	3	BC	C+	C
600	3	O	O	O	2	C-	D+	D
300	1	O	O	O	1	O	O	O

Table 1. Degree of crystal alignment obtained by visual observation, as a function of electric field strength. Voltage is measured in volts, E in kV/m, and the t's are either 1, 2, or 3 minute delay times after the cloud was nucleated. The "letter grades" A, B, C, and D refer to maximum alignment, strong alignment, some alignment, and weak alignment respectively. The O grade indicates no or negligible alignment.

Figs. 3 and 4 show the behavior of the ice crystals in the cloud seen from outside when no electric field was present and then with a strong field produced by applying a high voltage to the metal rod seen in the pictures. A strong microscope light shone into the cloud and from the left of the rod and the view is symmetrically from the right of the rod. The cloud is seen as significantly brighter in the second picture due to the crystals being aligned by the E-field and reflecting light to the camera.

5. ELECTRICAL OSCILLATIONS

The behavior of the ice crystals after the switching on of an electric field mathematically is like the behavior of a classical damped harmonic oscillator. Following Weinheimer and Few (1987) the differential equation for the orientation angle of the crystal is

$$- 8\pi\eta a^3 g \, d\phi/dt - 4\pi\varepsilon_o a^3 f E^2 \phi = I d^2\phi/dt^2,$$

assuming small oscillations. ϕ is the angle between the plane of the crystal and the E-field. f & g are hydrodynamic factors for ellipsoids. Solutions of the equation show that for large E-fields (greater than about 200 kV/m) the crystal oscillates around its new equilibrium orientation but with a period longer than the exponential damping time. For fields greater than 2,000 kV/m distinct oscillations may be observable, with damping times and oscillation periods of the order of 40 μs. We were unable to photographically document these oscillations or see them on videotape. For smaller E-fields the system is overdamped and the crystal exponentially approaches its aligned orientation. For quite small E-fields this exponential time is long. We visually observed time delays of the

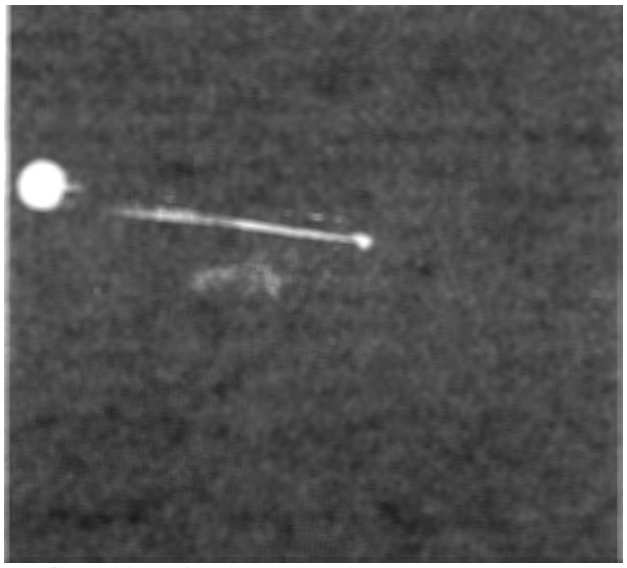

Fig. 3. View of an ice cloud before an electric field was present. The diameter of the rod, seen at the left of the picture, is about 1 cm. The light beam and viewing angle are appropriate so that the crystals reflect light to the camera if they are aligned along the electric field. The picture indicates little alignment in that orientation.

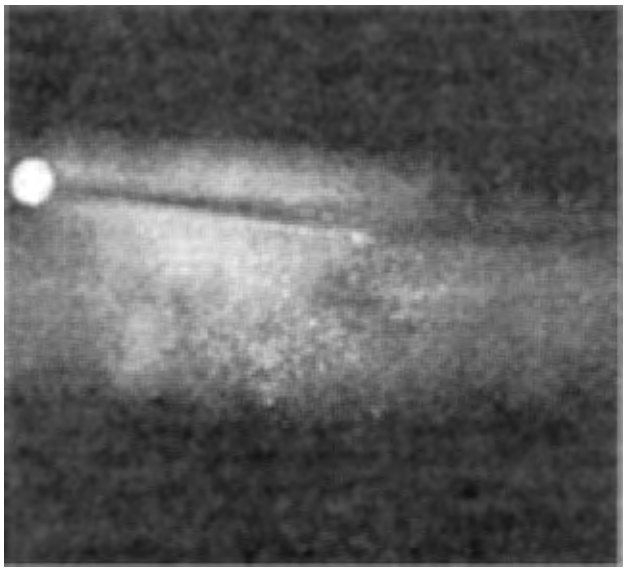

Fig. 4. The same cloud as in the previous picture but with a strong electric field near the rod. The bright reflection indicates significant alignment of the crystals along the electric field.

alignment process in our chamber when there were different magnitude E-fields present; this took the form of a "wave" of alignment progressing from the higher E-field region to the lower and we estimated the speed of this wave (about 0.2 m/s) from frame-by-frame inspection of the videotape. In one case crystals located where the E-field was between 6 and 3 kV/m clearly aligned faster where the E-field was larger. We calculated the E-field magnitude and alignment time at the positions of the advancing wave and got alignment

time differences of about 0.04 to 0.05 s (for 20 μm diameter ellipsoids 1 μm thick), consistent with the observed time differences of 0.03 s, within the uncertainty of the measurements.

The time dependence of the electrically produced alignment was also investigated with time varying fields. Our electrodes were a rod parallel to a plate, oriented at 45° in our freezer. A square wave voltage whose on-time and off-time could be separately controlled was applied across the electrodes. We looked for situations where the visual crystal alignment did or did not pulse in time with the E-field. Brownian motion tends to disorient our crystals in times like 0.1 s and Cox's low Reynolds number torque tends to align our crystals horizontally in times of the same order (Katz 1998), so our off-times were longer. With a field of 8 kV/m midway between the rod and the plate on for 0.2 s intervals and off for 0.3 s, we noticed that pulsating crystal alignment did result. But with the on-time reduced to 0.1 s and the off-time at 0.4 s, the alignment disappeared. This indicates that a time of from 0.1 and 0.2 s is required for an 8 kV/m field to align our crystals. Calculation using the overdamped solution to the harmonic oscillator equation gives an exponential alignment time of about 0.07 s for 20 μm diameter thin ellipsoids in an 8 kV/m field, again roughly consistent with the measurement.

6. CONCLUSIONS

Our experiments seem to be consistent with theoretical work predicting degree of alignment and its time dependence for plate crystals in electric fields.

They show that laboratory ice crystals respond well to electric fields of 10 kV/m and greater. Saunders and Rimmer (1999) cite values closer to 50 kV/m but they looked for electrical alignment from an enhancement of the 22° and 46° halo refraction by their crystals in strong electric fields. Alignment of our thin crystals would not have produced a sharp angle refraction due to a broad diffraction band in this direction. Since fair weather atmospheric fields are about 100 V/m but fields associated with lightning in thunderstorms are as large as 100 kV/m, it seems clear that electrical alignment must be considered in atmospheric situations where orientation of ice crystals is significant.

Strong electric fields align plate crystals in times of the order of tens of μs, essentially zero insofar as most atmospheric processes are concerned. Weak fields produce overdamped "oscillations" and our work indicates that alignment times are tenths of seconds for fields about 5 kV/m. Research aircraft can become electrically charged flying through clouds or can have charge induced due to local fields. These charged aircraft produce fields of the order of 50 kV/m (Black and Hallett, 1999). We calculate that ice crystals with a speed of 100 m/s relative to the plane are in fields of 35 kV/m for 5 ms. Calculations show that thin 20 μm crystals align in 3 to 4 ms in a 35 kV/m E-field, which indicates that the local electric field of the plane is sufficient to realign the crystals. Aerodynamic shear tends to orient ice crystals near the particle detectors on the aircraft and electrical torque could change this orientation. So measurements made by various 2-D probes on aircraft may have to take into account combined orientation changes caused both by the aircraft fields and by aerodynamics.

This work verifies that remote sensing by lidar of changes of planar crystal orientation must take into account changes in local electric fields due to distant lightning. Inverting this argument, it may be argued that the presence of local electric fields may be inferred from measurement of such changes in crystal orientation over times of a fraction of a second. The rate processes would provide information on the magnitude and direction of the local electric field, assuming that the averaging time for the lidar measurement is sufficiently short.

7. ACKNOWLEDGMENTS

We thank S. Keck of DRI for help in digitizing our images and D. Wermers of DRI for the design and construction of the MOSFET circuitry. This work was partially supported by National Science Foundation Grant ATM-9900560 and U.S. Air Force DEPSCOR Grant, April 2000.

8. REFERENCES

Black, R. A., and J. Hallett, 1999: Electrification of the Hurricane. *J. Atmos. Sci.*, **56**, 2004-2028.

Fraser, A. B., 1979: What size of ice crystals causes the halos? *J. Opt. Soc. Amer.*, **69**, 1112-1118.

Fuchs, N. A., 1964: *The Mechanics of Aerosols.* MacMillan, 408 pp.

Hallett, J., 1987: Faceted snow crystals. *J. Opt. Soc. Amer.*, **A4**, 581-588.

Katz, J. I., 1998: Subsuns and Low Reynolds Number Flow. *J. Atmos. Sci.*, **55**, 3358-3362.

Klett, J. D., 1995: Orientation Model for Particles in Turbulence. *J. Atmos. Sci.*, **52**, 2276-2285.

Pruppacher, H. R. and J. D. Klett, 1980: *Microphysics of Clouds and Precipitation.* D. Reidel, 714 pp.

Reist, P. C., 1993: *Aerosol Science and Technology.* McGraw-Hill, 379 pp.

Sassen, K., 1980: Remote Sensing of Planar Ice Crystal Fall Attitudes. *J. Meteor. Soc. Japan*, **58**, 422-429.

Saunders, C. P. R., and J. S. Rimmer, 1999: The electric field alignment of ice crystals in thunderstorms. *Atmos. Res.*, **51**, 337-343.

Walker, J., 1978: The Amateur Scientist, The bright colors in a soap film are a lesson in wave interference. *Sci. Am.*, **239**, 232-237.

Weinheimer, A. J., and A. A. Few, 1987: The Electric Field Alignment of Ice Particles in Thunderstorms. *J. Geophys. Res.*, **92**, 14833-14844.

ICE NUCLEATION IN OROGRAPHIC WAVE CLOUDS: A MODEL—OBSERVATION COMPARISON OF AN ISOLATED GRAVITY WAVE CLOUD

Richard J. Cotton[1], Paul R. Field[1] and Doug Johnson[1]

[1]Meteorological Research Flight, Met. Office, UK

1 INTRODUCTION

During the INTACC (INTeraction of Aerosol and Cold Clouds) campaign in october 1999 the Met. Office C-130 aircraft measured various orographic clouds over the Scandinavian mountains. One objective of this was to investigate how ice particles are formed. Presented here is a model-observation comparison of a single stationary isolated gravity wave cloud measured during flight A722. This cloud had significant liquid water and ice at all heights with the temperature varying from -18°C at cloud base to -32°C at cloud top (figure 1). To get a similar liquid water-ice cloud structure a heterogeneous freezing process such as contact-freezing is required.

2 MODEL DESCRIPTION

A model has been developed which simulates the microphysical and dynamical aspects of wave clouds. The cloud simulation consists of repeatedly running a parcel model, each starting at a different height and following a trajectory given by the measured horizontal and vertical winds. The parcel model is an extension of that described in Spice (1999) which considers an adiabatic parcel of air containing a conserved mass of water. An updraft profile describes rising and falling of the parcel. Each parcel is initialised with temperature and water relative humidity which defines its total water content.

At the start of the model run the dry CCN are deliquesced to the equilibrium haze droplet radii calculated using a Newton-Raphson iteration on the Kohler equation. It was assumed that the CCN species was sulphuric acid with a Van't Hoff factor of 3. During the model run, haze and activated cloud droplets share the same bins. The bin radii are explicitly varied in time using the droplet diffusional growth rate equation.

There are also a fixed number of ice particle radius bins, which are initially empty. Ice particles may develop in these bins as a result of primary nucleation processes, either by the homogeneous freezing of supercooled water droplets or by various heterogeneous freezing processes. The ice particle bin radii are explicitly varied in time using the ice particle diffusional growth rate equation.

The homogeneous freezing rate J is calculated by a fit to Jeffery's (1997) formulation, which matches with observed rates.

$$
\begin{aligned}
T_e < -65: &\quad \log(J) = 25.63 \\
-65 \geq T_e \geq -30: &\quad \log(J) = -243.4 - 14.75T_e - \\
&\qquad 0.3068T_e^2 - 0.002871T_e^3 - \\
&\qquad 0.00001021T_e^4 \\
T_e > -30: &\quad \log(J) = -7.63 - 2.996(T_e + 30)
\end{aligned}
$$

where T_e is in °C and J in cm^3 s^{-1}.

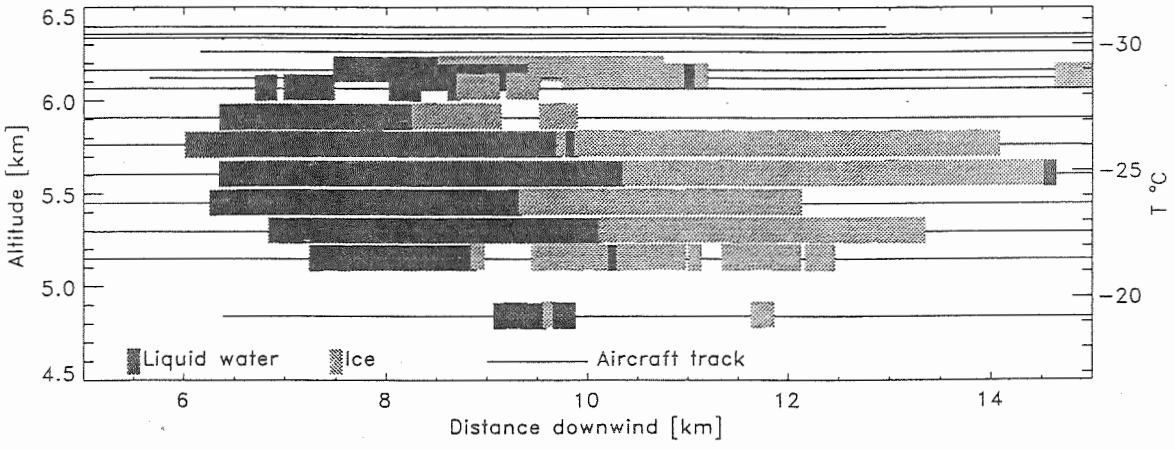

Figure 1: **A stack of aircraft runs through an isolated wave cloud. The water phase is determined by the SID (Small Ice Detector) probe which determines the asphericity of cloud particles**

[1]Corresponding authors address: Richard J. Cotton, Meteorological Research Flight, DERA, Y46, Farnborough, GU14 0LX email: rjcotton@meto.gov.uk

The solution effect is included by using an effective temperature T_e ($> T_C$), given by

$$T_e = T_C + \lambda \delta T$$

δT quantifies the melting temperature depression in less strongly bonded impure ice particles. δT for sulphuric acid aqueous solution droplets is calculated using the following fit to standard tabulated values (Paul Demott, personal communications)

$$\delta T = 3.514G + 0.4716G^2 + 0.03321G^3 + 0.02505G^4$$

where G is the droplet molality. λ quantifies additional non-ideal ionic interactions between the solute and liquid water during the reverse process, droplet freezing. $\lambda = 2.0$ is used for sulphuric acid particles. This parcel model is part of the GEWEX cloud systems study WG2 cirrus parcel model comparison project, in which the homogeneous freezing studies all agree closely, see Lin R-F. this issue.

One heterogeneous freezing process that can be used in the model is the combined deposition and condensation-freezing as described in Meyers (1992),

$$N_d = \exp(-0.639 + 12.96\sigma_i)$$

where N_d is the number of IN that act as either deposition or condensation-freezing nuclei [litre^{-1}] and σ_i is the ice supersaturation [fraction]. During the model run, any IN that are activated are immediately utilised, generating 0.1μm radius ice crystals.

Another heterogeneous freezing process that can be used is contact-freezing nucleation where the IN initiates freezing at the moment of its contact with a supercooled water drop. The ice crystal concentration observed over all the INTACC flights is used as the contact-freezing IN activation spectrum,

$$N_{cf} = 10^{-3} \exp(11.001 - 0.212T_C)$$

where N_{cf} is the number of IN that act as contact-freezing nuclei [litre^{-1}] and T_C is the parcel temperature [°C]. See Field P. this issue. Collection rates as described in Young (1974) which include Brownian motion, thermophoretic and diffusiophoretic effects determine at what time during the model run these events occur. This collection rate reduces the N_{cf} upper limit to the potential ice-crystal concentration. An aerosol radius of 0.05μm was used. 0.05μm is the heavily populated smallest bin radius in the PCASP (Passive Cavity Aerosol Spectrometer Probe) spectrum. Generally large activated cloud droplets and small IN in a water subsaturated environment give the highest collection rate.

3 CCN SPECTRUM

The dry CCN size spectrum is derived from upwind aerosol measurements using the PCASP, CNC (Condensation Nuclei Counter) and SID probes (figure 2). A log-normal was fitted to the PCASP accumulation mode aerosols with the constraint that the total number of aerosols was that measured by the CNC (325 cm^{-3}). The model input CCN spectrum was derived from the fitted log-normal (14 bins) combined with the clear air SID probe measurements of coarse mode aerosols (6 bins).

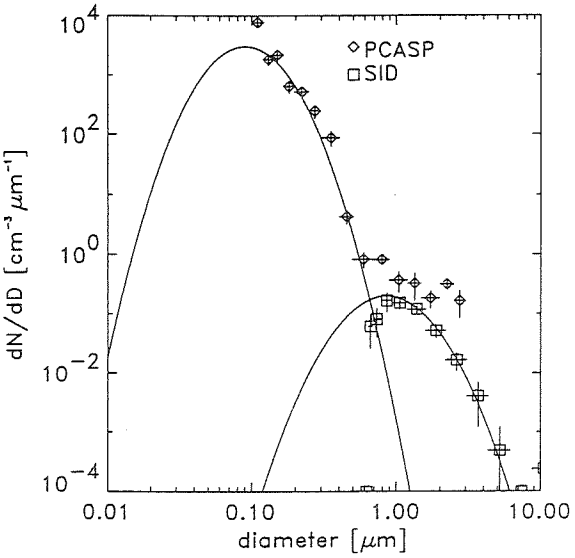

Figure 2: Model input CCN spectrum

4 WAVE CLOUD SIMULATION

Figures 3–5 show model simulations of the observed gravity wave cloud. The aircraft measured the cloud using a stack of straight and level runs parallel to the wind. Each model parcel must however, follow a separate trajectory. The measured vertical and horizontal winds are interpolated to produce a 2D wind field. A parcel trajectory is then defined by its starting altitude in this field. Alternatively using the environmental lapse rate (upwind measurements indicate -7.39°C km^{-1}) the parcel starting air temperature determines its trajectory. The dotted lines on the model simulation figures represent parcel trajectories which started 1°C apart. The temperature on the right axis is that of the undisturbed upwind region.

Figure 3 shows that even with a constant upwind relative humidity profile (here 70%) there is no possibility of getting ice by homogeneous freezing in the altitude range of the aircraft measurements (since 70% relative humidity at higher levels is too moist). A more realistic upwind relative humidity profile (70% between −18°C and −24°C, falling to 50% outside this region) gives the general height structure of the wave cloud. Figure 4 includes only homogeneous freezing and only generates the liquid water part of the cloud. Figure 5 includes the contact-freezing heterogeneous ice nucleation process and gives the observed liquid water-ice structure of the cloud—there is significant liquid water and ice at all heights with the ice becoming dominant in the downdraft region. Deposition ice nucleation is not the dominant freezing mode in this cloud. There is a large ice supersaturation well before any water saturation in the updraft region, and any deposition IN would quickly activate and grow to large ice crystals. No ice crystals were observed near the cloud leading edge.

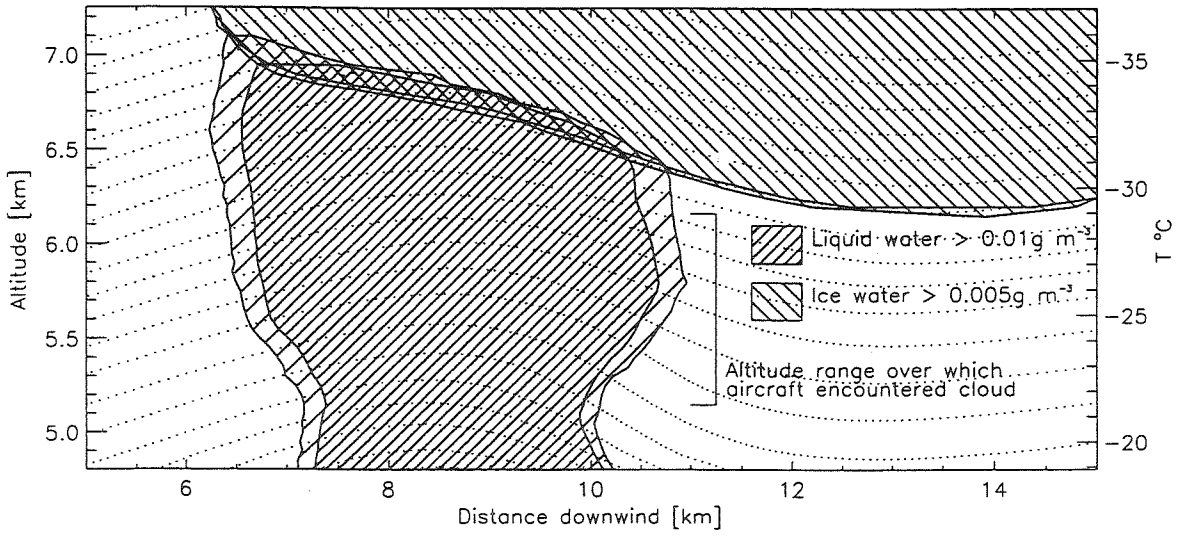

Figure 3: **Constant 70% upwind relative humidity, homogeneous freezing only**

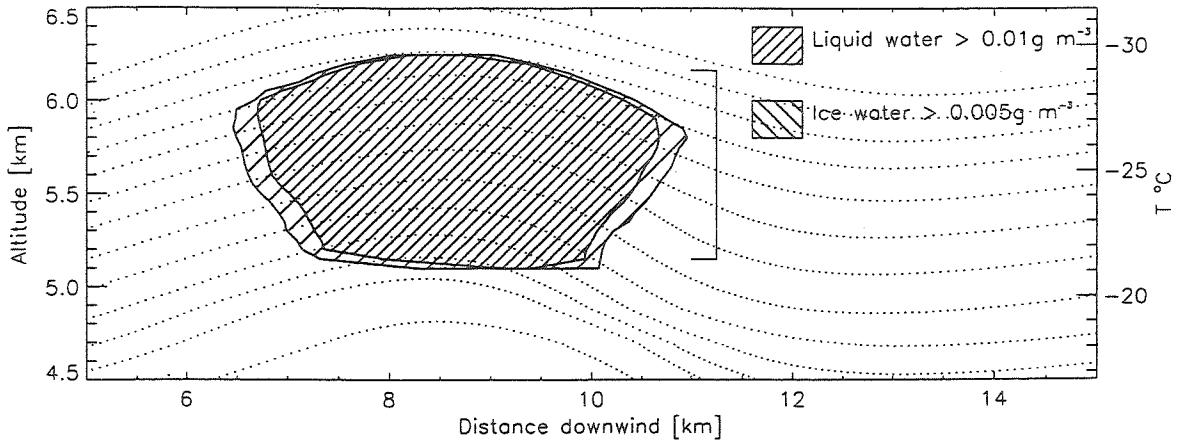

Figure 4: **Upwind relative humidity profile 50%—70%, homogeneous freezing only**

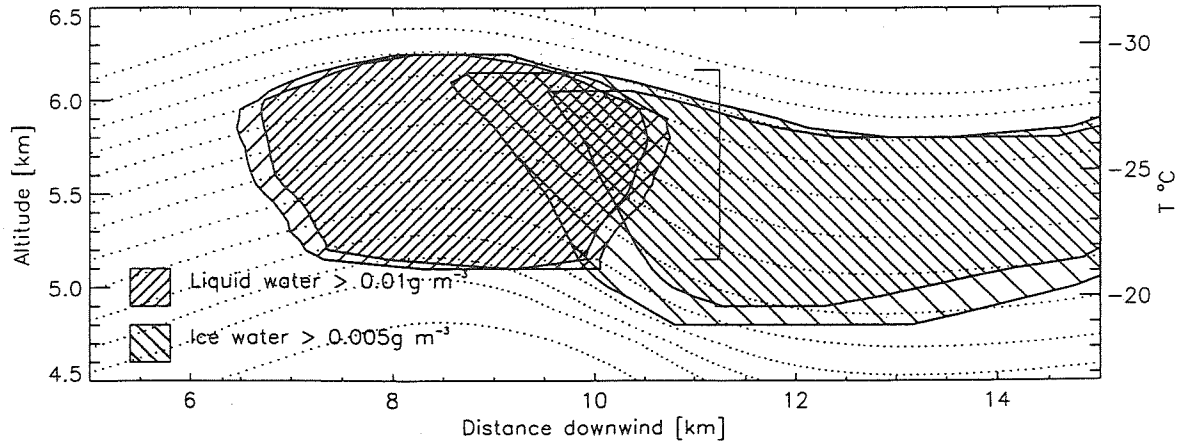

Figure 5: **Upwind relative humidity profile 50%—70%, homogeneous freezing + contact-freezing**

The cloud simulation can be compared more directly with the aircraft measurements by extracting data from a single altitude of the simulation, equal to one of the flight altitudes. An example is shown in figure 6.

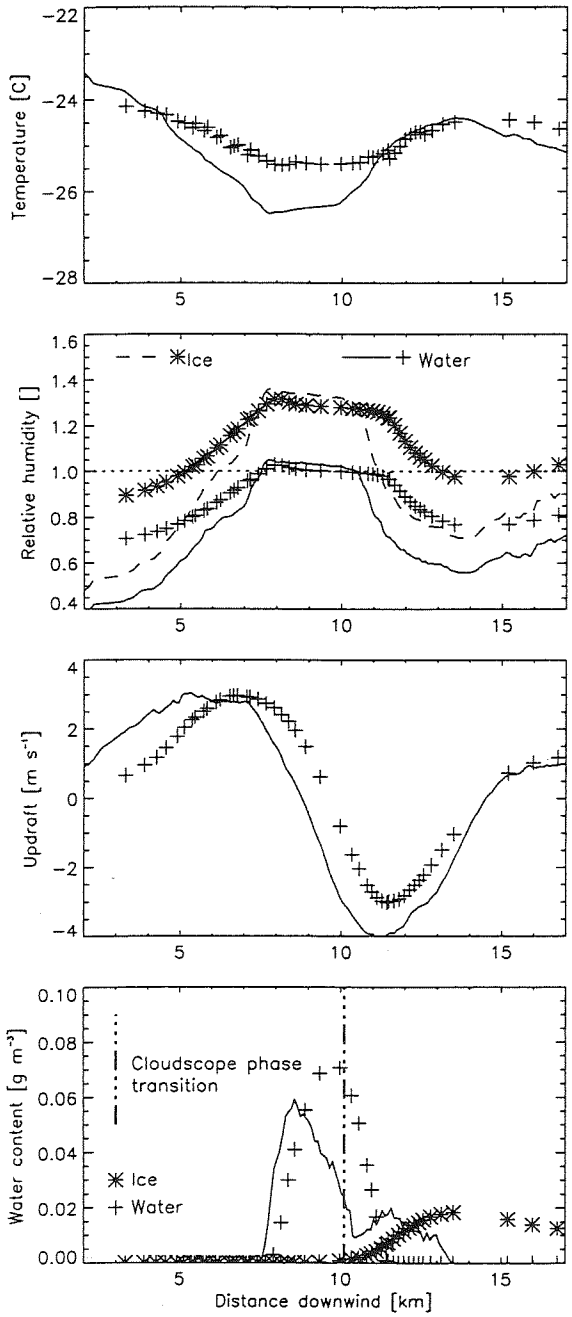

Figure 6: **Synthetic aircraft track for run R1-11, taken from the simulation of figure 5. In each figure, aircraft observations are shown by lines, and model values by symbols. (The cloudscope is a video camera which gives a visual indication of the phase of particles greater than 10 μm.)**

There are clearly some differences in the horizontal position and amplitude of features, which are likely to be due to temporal variations in the wind field during the period required to complete the stack of aircraft runs. There is also some disagreement in the relative humidity in the cloud free trough regions of the wave. This is thought to be due to calibration bias in the Lynman-α hygrometer used for the observations. The figure does, however, confirm that the simulation produces a good qualitative and quantitative agreement with the observed microphysical characteristics.

5 CONCLUSION

Ice formed in the gravity wave cloud measured during flight A722 was not caused by homogeneous freezing. The heterogeneous process of contact-freezing is the most likely source of the ice crystals.

6 ACKNOWLEDGEMENTS

The authors thank the staff of MRF and the RAF C-130 aircrew. INTACC was partly funded by an EU research grant ENV4-CT97-0549.

REFERENCES

Spice A. et. al, 1999: Primary ice nucleation in orographic cirrus clouds: A numerical simulation of the microphysics. Q. J. R. Meteorol. Soc., **125**, 1637–1667

Jeffery C. A. and Austin P. H., 1997: Homogeneous nucleation of supercooled water: Results from a new equation of state. J. GeoPhys. Res.,**102** 25,269–25,279.

Meyers M. P., DeMott P. J. and Cotton W. R., 1992: New primary ice-nucleation parametrizations in an explicit cloud model. J. Appl. Meteor., **31**,708–721.

Young K. C., 1974: The role of contact nucleation in ice phase initiation in clouds. J. Atmos. Sci.,**31** 768–776.

PARTICLE BREAKUP BY MELTING AND EVAPORATING ICE

R. G. Oraltay[1] and J. Hallett[2]

[1]Physics Department, Marmara University, Istanbul, Turkey
[2]Desert Research Institute, Reno, NV, 89512, U.S.A.

1. INTRODUCTION

As ice particles fall into regions with ice relative humidity below 100% or into regions where the wet bulb temperature is above 0°C, particle breakup may occur by evaporation or melting. Such processes lead to a shift in the ice particle spectrum towards smaller sizes and may be associated with separation of electric charge. Particles may disappear completely or evaporate to nuclei, ice nuclei and CCN, which may subsequently be reactivated should air be lofted to become supersaturated. Flights through regions where such processes happen display modest turbulence, suggesting that vertical motions may be locally lofting such particles. Further, because of differential fall velocity of different size and density particles, phase changes may be delayed in larger particles to give locally much stronger gradients of temperature and vapor than an assumption of uniform lifting or fall conditions would suggest. Interpretation of the vertical structure of the radar melting band depends critically on changes in particle size and shape and concentration, together with changes of dielectric constant on melting. We present an assessment of conditions likely to take place during such changes and means of confirming what is happening by laboratory simulation; specific evaporation/melt signatures in images from aircraft penetration should occur.

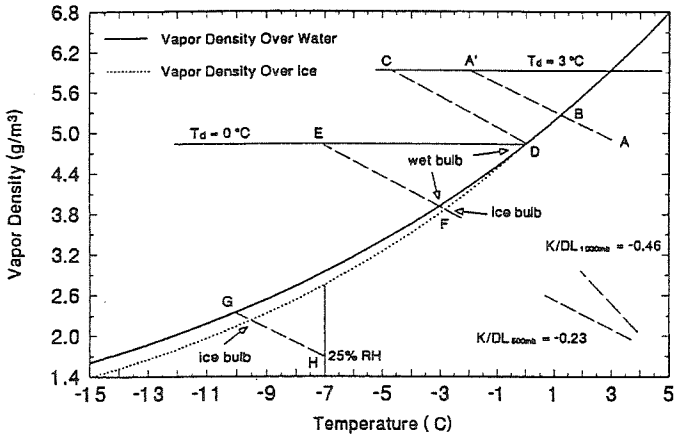

Figure 1: Equilibrium water saturation vapor density near 0°C and conditions resulting from particles under growth and evaporation and also particles under non equilibrium conditions resulting from mixed water/ice particles lofting to lower temperatures or lowering to higher temperatures. The growth/evaporation conditions are represented by points *off* the equilibrium curves and the particle surface conditions by the intersection of the lines **K/DL** with the curves. **A' B** represents wet bulb temperature of an evaporating drop; **AB** the wet bulb temperature of a growing drop. Thus the wet bulb temperature of a growing drop is *above* 0°C even through the ambient temperature is below 0°C. For the case **CD** the growing particle is at 0°C. **EF** represents the case for mixed ice/water particles in an environment at -7°C and 25% ice relative humidity. Conditions are for 500 hpa pressure; the slope of the lines for 1000 hpa is shown.

2. CONDITIONS FOR MELT AND EVAPORATION

It is evident that ice particles falling into a warmer environment will melt as the ice/wet bulb temperature rises above 0°C; particles falling into a low relative humidity environment will evaporate. The environmental conditions may be represented on a vapor pressure (density) - temperature plot as in Figure 1. Supersaturation gives points above the equilibrium lines; undersaturation gives points below the lines. The growth/evaporation conditions may be represented approximately by

Corresponding author address: Riza G. Oraltay, Physics Department, Marmara University, Istanbul, Turkey; email: hallett@dri.edu.

the mass - heat transfer equations, assuming a balance between sensible heat by conduction and latent heat by vapor-liquid-solid transition. We assume that the vapor/heat ventilation effects are identical, which gives sufficient accuracy for our purpose. Thus selecting a point at ambient temperature and vapor density, a line through the point slope K/DL intersects the equilibrium vapor curve at the wet bulb/ice bulb temperature. For evaporation there is a cooling; for growth there is a heating. A shape factor enters the equations for ice and may be taken as identical for heat and mass transfer to sufficient accuracy. Things are complicated near 0°C. Thus melting will require a temperature a few degrees above 0°C under conditions of lower relative humidity Figure 1; A B. Similarly a large ice particle falling to temperatures above 0°C (or carried in a downdraft) and maintained in an environment saturated at Td near, say, +3C in the presence of smaller ice particles, (already melted) at this temperature, will not be in equilibrium as long as it contains ice and will continue to melt because of both sensible heat transfer and also latent heat of condensation of water on the ice surface Figure 1; A' B. Conversely should such a mixed ice/water particle be lofted in an updraft, it will maintain a temperature near 0°C until almost completely frozen and provide vapor for neighboring ice crystals to grow with shape characteristic of a supersaturation much higher than ice in the presence of supercooled water at the ambient temperature (Figure 1; E F). At lower temperature and subsaturation particles evaporate and cool as shown in Figure 1; G H.

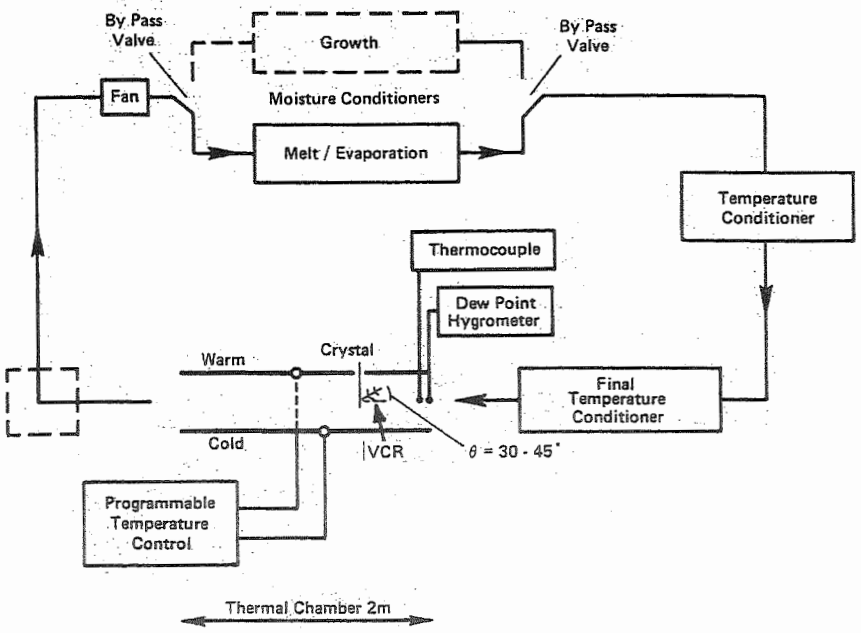

Figure 2: Wind tunnel arrangement for sequential growth/evaporation of ice particles.

These situations may provide conditions for particles to melt and evaporate; particles may bend and/or fragment under aerodynamic stress depending on local air flow as the particle falls and gyrates. We here discuss techniques for reproducing these phenomena under controlled laboratory conditions and more importantly cycling the particle through growth/melt/evaporation cycles as might occur under the turbulent conditions usually found near the 0°C level.

Earlier work (Oraltay and Hallett, 1989; Oraltay, Dong and Hallett 1994) has demonstrated the likelihood of ice particle break up under both evaporation and melting. Ice crystals were grown

in a dynamic diffusion chamber at shapes dependent on temperature and supersaturation and then evaporated and or melted in air in reverse flow under conditions of estimated terminal velocity (Fig. 2). Two distinct kinds of phenomena are observed:

i: particles become thin and deform at specific sites and may retain a different crystallographic orientation providing the particle does not completely melt or evaporate; regrowth of ice turns a single crystal into a polycrystal and may provide the basis for "irregular" particles which are observed to be common under many conditions (Korolev et al, 2000; (13th International Conference on Clouds and Precipitation, Reno, Nevada).

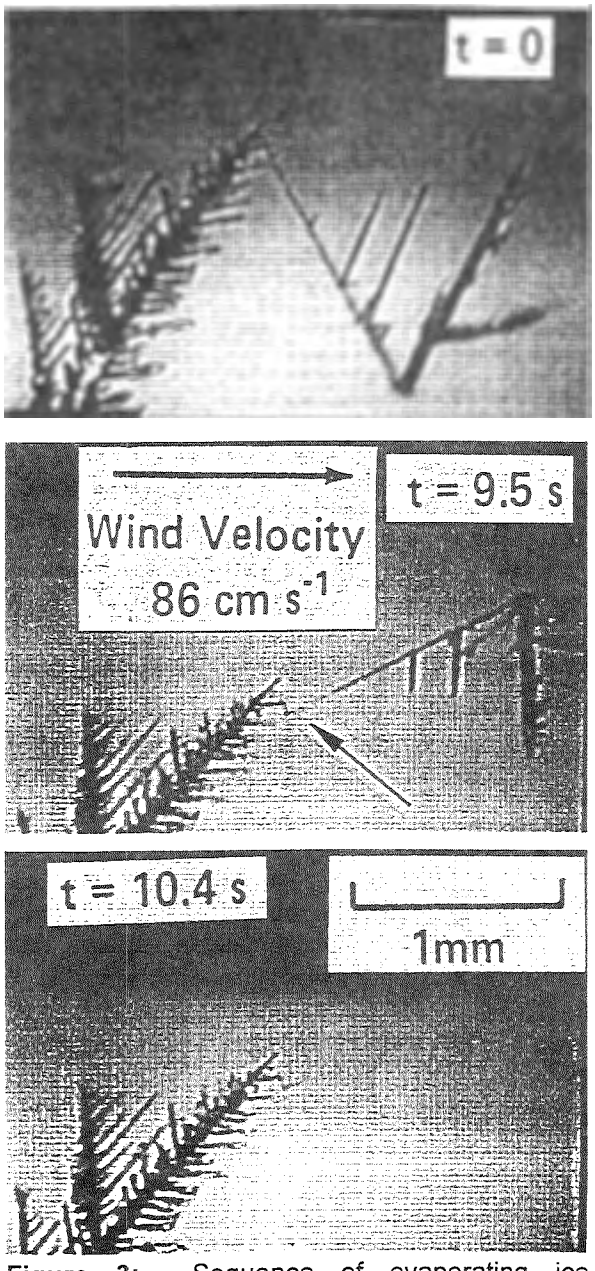

Figure 3: Sequence of evaporating ice dendrites grown at –15C, breaking, re-attaching and breaking again. The crystal in (c) has angles which depart significantly from the dendrite 60/120°C angles.

ii: sometimes particles separate from the larger crystal and are carried away in the airflow of the wake from the fall of the larger particle. It is noted that particles of mixed water and ice in the process of melting at ambient temperature above 0°C and freezing below 0°C have a temperature close to ice water equilibrium for approximately a fraction ratio of ice/water of greater than 0.1 or less than 0.9.

Strange behavior of satellite particles strongly suggests the presence of electrostatic effects during these processes, a phenomenum currently under investigation by measuring the current to ground of a particle during break-up, as already done for evaporation and growth by Dong & Hallett, 1992.

3. CONCLUSIONS

The detail of particle breakup during both melt and evaporation are complex and depend on the ambient relative humidity. It depends particularly on the occurrence of water condensation on existing ice at temperatures above 0°C. At temperatures below 0°C evaporation of ice under lower ice relative humidity, particularly below 70% is required for breakup. There is a further dependence on particle shape. Equiaxed and plate-like particles tend not to fragment at all, whereas needles and dendrites fragment and deform depending on the axial length ratio and the structure of the dendrites themselves. The size of the fragments tends to be a few times the arm/branch/needle width after ejection; these particles may further evaporate and then grow again depending on circumstances. It is noted that an inspection of the snow crystals in works such as Nakaya and Bentley and Humphries show symmetry of the earliest growth at the center down to small sizes of order at least 50 μm. This could be selection for the most perfect picture. Alternatively it suggests an even smaller beginning for a seed particle which grows out as a single crystal. Yet the statistical analysis of Korolev et al 2000 suggests that most crystals are irregular and the regions of well defined dendrites or columns/needles are the exception rather than the rule. It must also be remembered that drops may nucleate and freeze as single or polycrystal

depending on temperature of nucleation. Thus we are forced to the conclusion that most (> 80%) crystals result from sequences of growth, evaporation and possibly melting. It has long been realized that the typical dendrite snow crystal has

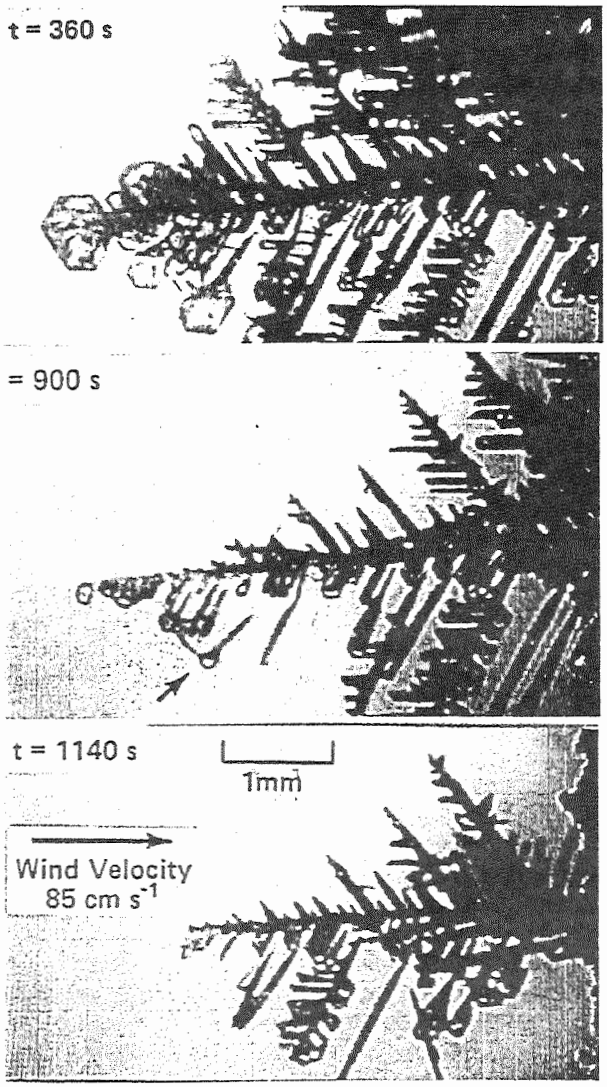

undergone changes in its environmental growth conditions - supersaturation, temperature and fall

Figure 4: Evaporation of plate crystals, grown by vapor diffusion near -12°C, at -1°C and 70% relative humidity over ice in ambient airflow of 85 cm s^{-1}. The crystals have changed orientation; the evaporating plate could be mistaken for a frozen droplet.

velocity, giving plate, sector plate, dendrite with symmetrical or asymmetrical arms or even six simple branches lacking arms entirely. The instantaneous periphery of the growing crystal represents growth under a particular set of conditions. The observed complexity thus relies on much more complex behavior in an atmospheric turbulent environment, only capable of investigation through the controlled laboratory simulation.

Such situations are common near 0°C but may occur at any level in the atmosphere, particularly when a layered structure is prevalent. From the viewpoint of cirrus crystals, density changes outward from the mass center may change significantly during evaporation and regrowth processes and lead to major uncertainty in particle mass, important for estimation of terminal velocity and radiative properties. Secondary ice particles may also occur at any level and may be responsible for the observation that ice concentration is on occasion invariant with height. It remains to determine the relative importance of polycrystalline nucleation of the beginning particle and deformation associated with melt/evaporation/ growth in the formation of the dominant irregular ice particles.

4. ACKNOWLEDGMENTS

The work and ideas developed herein were supported in part by grants: 9413437; 9900560, National Science Foundation, Arlington, Virginia.

5. REFERENCES

Dong, Y.Y. and J. Hallett, 1992: Charge separation by ice and water drops during growth and evaporation. *J. Geophys. Res.*, **97**, 20,361-20,371.

Dong, Y.Y., R. G. Oraltay and J. Hallett, 1994: Ice particle generation during evaporation, *J. Atmos Res.*, **32**, 45-53.

Hallett, J. and J. T. Hallett, 2000: The Scale And Role of Spatial Discontinuities Particles in Clouds. *AMS, 13th International Conference on Clouds and Precipitation,* 14-18 August, 2000, Reno, Nevada.

Korolev A., G. A. Isaac and J. Hallett; 2000: Ice particle habits in stratiform clouds. *AMS, 13th International Conference on Clouds and Precipitation,* 14-18 August, 2000, Reno, Nevada.

Korolev, A., G. A. Isaac and J. Hallett, 2000: Ice particle habits in stratiform clouds. Q. J. Roy. Meteor. Soc. Accepted for publication.

Oraltay, R.G. and J. Hallett, 1989: Evaporation and melting of ice crystals: a laboratory study, *Atmos. Res.*, **24**, 169-189.

CHANGES IN SNOW CRYSTAL SHAPES CAUSED BY ATMOSPHERIC RADIATION

Hisashi SHIO

Science Education Graduate Sapporo-Iwamizawa School
Hokkaido University of Education

1. INTRODUCTION

Nakaya [1] made a Ts-s diagram based on his experiments to show how the shapes of snow crystals depend on ambient temperatures and humidities. Later, Gold and Power [2] used a meteorological sonde during snowfalls to determine the ambient conditions of snow formation; the results closely matched Nakaya's. Magono [3] then revised Nakaya's diagram on the basis of may snow crystals collected at five observation point between 100-m and 1000-m elevations on Mt.Teine in Hokkaido. Also,he suggested that dendritic snow crystals can grow at humidities below water saturation. Shaw and Mason [4] studied sublimation of prismatic ice crystals on a substrate in ambient air and reported that the crystal edges rounded at undersaturations greater than about 10%. Sassen et al. [5] observed rounded edges on ice crystals collected in a cirrus cloud that was estimated to be undersaturated. Recently, Nelson [6] found that ice crystals have rounded shapes at ambient temperatures from -0.1°C to -18°C with undersaturations from 0.05 %. Nelson showed that the sulimation rates were accurately predicted by the diffusion equation with the surface vapor density at equilibrium for a uniform surface temperature, and slos showed that theory predicts that they evolve into spheroidal shapes as observed. Our results described below are similar to Nelson's.

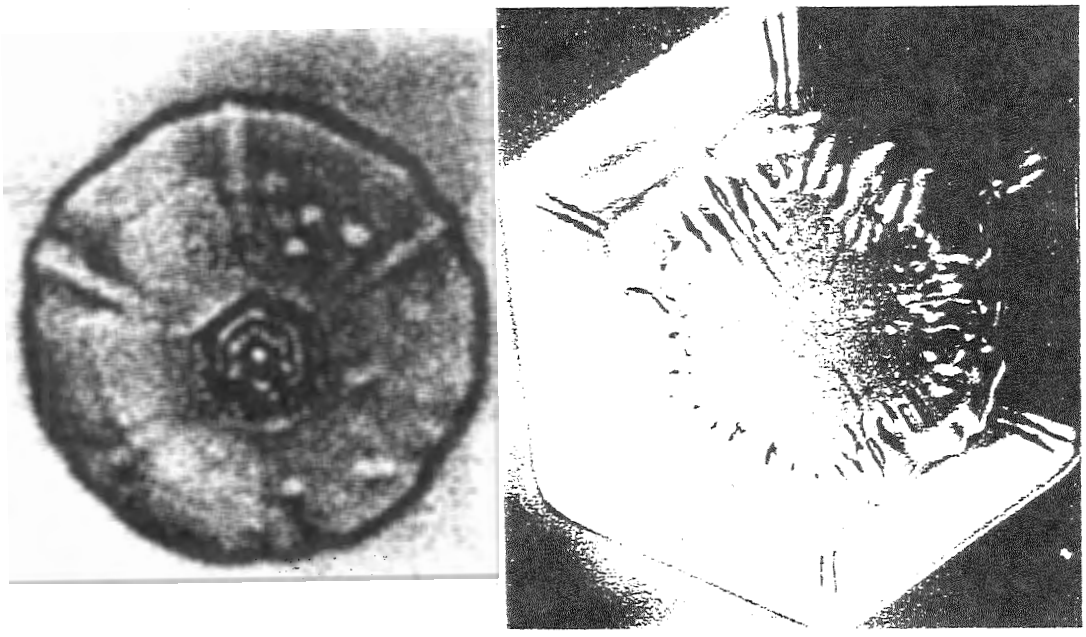

Fig.1. a) Disc-shaped snow crystal b) Hexagonal plate grown from disc-snow crystal included a lot of bubbles at cetner of crystal.

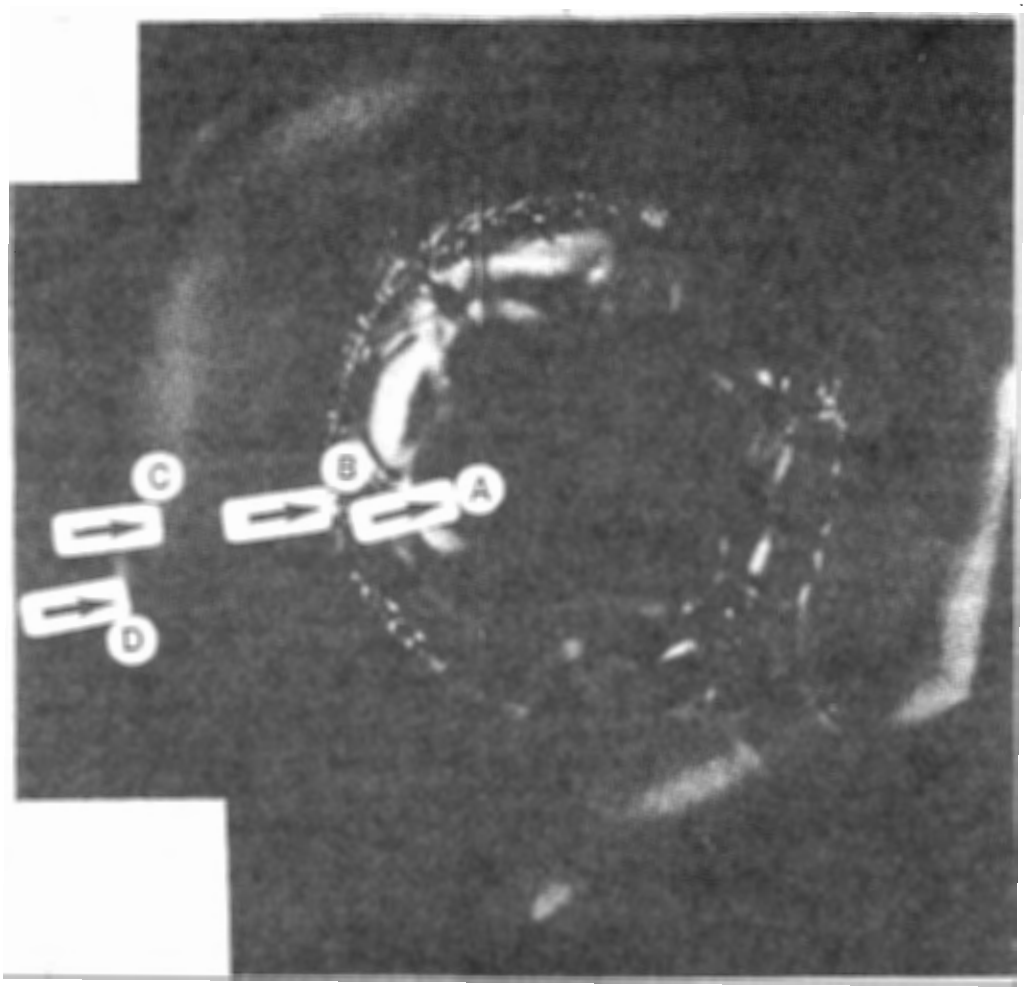

Fig.2. Disc-shaped snow crystal with four concentric patter n.

Fig.3. Metamorphosing of the snow crystal under near ice saturation.

2. THE METEOROLOGICAL ENVIRONMENT AT THE OBSERVATION SITE

The observation site is in a bowl-shaped region surrounded by four mountains: Mt. Tomamu (1240m), Mt.Ishiyama (1074m), Mt. Furikari (1323m), and Mt.Ochiai (1168m). On clear days, the temperature before sunset is about -15°C, but by midnight, the temperature reaches -36°C due to radiative cooling from the snowfield. On days and nights with clouds, the temperature ranges from-20 to -25°C.

The snow crystals were observed using a reflection-type, differential interference microscope.

3. RESULTS

The crystals in figure 1 were collected with ambient conditions of -33°C, near ice saturation, and exposure to a clear sky at midnight. Figure 1a shows a disc-shaped snow crystal with a frozen droplet and hexagonal plate at its center. In figure 1b has grown into a hexagonal plate and the interior droplet and plate are no longer visible.

Figure 2 shows a snow crystal with four concentric pattern from the center, they are (A) a rounded hexagonal star at center of crystal, (B) a circular pattern 400-um across, (C) a spherical shape of diameter 720 um, and (D) a hexagonal outer boundary,which was precipitated under near ice saturation, an ambient temperature -34°C at midnight with moon.

Figure 3 shows a crystal that grew and sublimated at temperatures between -25°C and -35 °C and with humidities close to ice saturation under a clear sky at midnight . As shown in figure 3-A At 0.05 am, a frozen droplet fell upon the cooled glass plate of our microscope leaving the small, spherical pattern marked (a) in figure 3-A. Because the vapor was supersaturated, a hexagonal star crystal grew (b), followed by a disc-shaped crystal (c). The photograph was taken at 1.06 am when the crystal was a hexagonal plate (d) and the temperature was -34°C. The photograph in figure 3-B was taken at 2:24 am. The vapor had been slightly supersasturated and the temperature was -35°C. The ice droplet is no longer visible in the star pattern (e), the disc crystal (c) has changed to a thick plate, and the outer boundary (d) remains a hexago-

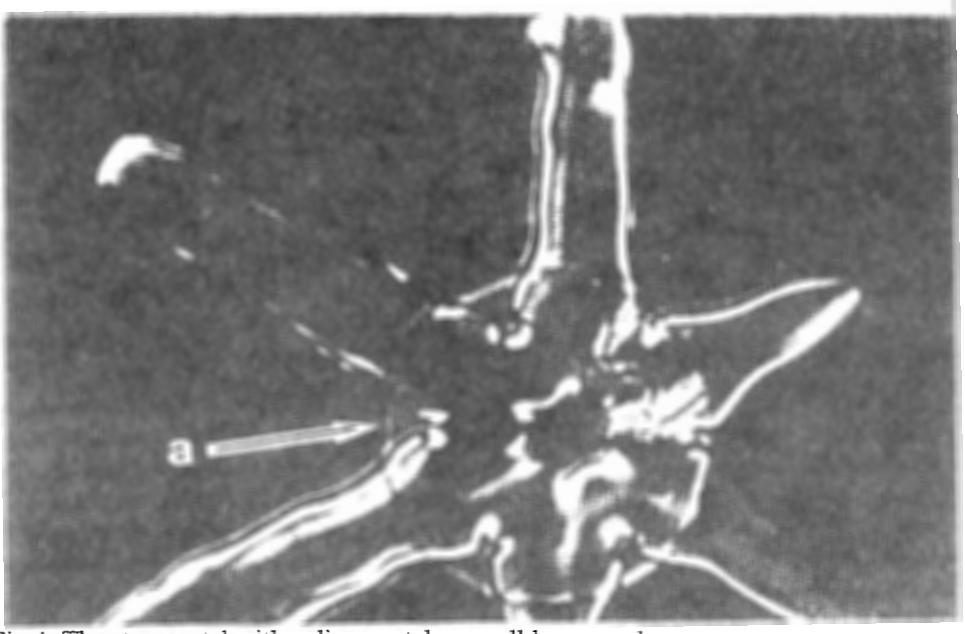

Fig.4. The star crystal with a disc crystal, a small hexagonal plate crystal.

nal plate, but is larger (g). After the photograph in Figure 3 B was taken, the vapor became undersaturated. As shown in figure 3-C the outer hexagonal plate (g) has become a disc at (i), whereas the star (e) and plate (f) have together become a hexagonal plate (h).

Figure 4 shows the star crystal with a disc crystal, a small hexagonal plate crystal under a few snow precipitation at ambient temperature -28°C. The disc crystal, the small hexagonal plate crystal are similar to these crystal (i,h) in Fig. 3-C.

CONCLUSIONS

It seems that under near ice saturation the disc snow crystal is generated. The hexagonal plate crystal is grown on the disc snow crystal under humidity of lower ice saturation, conversely, disc snow crystal is formed on sublimating of hexagonal plate crystal.

ACKNOWLEDGEMENTS

We would like to thank Jon Nelson for his assistance in processing the data presented in this report.

REFERENCES

Gold, L.W. and B.W.Power,.1954: Dependence of the forms of natural snow crystals on meteorological conditions.J. Met., 11, 33-42.

Magono, C., 1966: Meteorological Classification of Natural Snow Crystals, J. Fac. Sci. Hokkkido Univ. Japan 7., II., 321-335.

Nakaya, U., 1954: Snow Crystals, Harvard Univ. Press, 76.

Nelson, J., 1998: Sublimation of Ice Crystals, J. Atmos. Sci., 55, 910-918.

Sassen, k,N.C. Knight, Y. Takano, and A.J. Heymsfield,1994: Effects of ice crystal structure on halo formation: Cirrus cloud experimental and ray-tracing modeling studies. Appl. Optics,33, 4590-4601.

Shaw, D., and B.J. Mason, 1955: The growth of ice crystals from the vapor. Phils. Mag., 46, 249-262.

PHASE TRANSFORMATION IN CLOUDS

I.P. Mazin[1*], A.V. Korolev [2]., and G. A. Isaac[2]

[1]Center for Earth and Space Research George Mason University, Fairfax, VA, USA
[2]Meteorological Service of Canada, Toronto, Ontario, M3H 5T4, Canada

1. Introduction.

The processes related to phase transformation and the associated release of latent heat are among the most important processes in cloud thermodynamics. Phase transformation in clouds effects the processes on both the macro- and micro- scale. It changes the vertical profiles of temperature and humidity. The supersaturation S in clouds is governed by adiabatic cooling or heating in vertical motions and condensation/evaporation of the water vapor by cloud particles. As a result the supersaturation tends to some equilibrium value S_p. The characteristic time for changes of the supersaturation τ_p is called the "time of phase relaxation". The time of phase relaxation is one of fundamental parameters in cloud microphysics.

The phase transformation also affects in-cloud turbulence. Clouds may be stable for small scale turbulence ($\tau_t << \tau_p$) and unstable for large values ($\tau_t >> \tau_p$) (Kabanov and Mazin, 1970). Here τ_t is a characteristic time scale of turbulent fluctuations. At temperatures below freezing, droplets and ice particles quite often co-exist. The questions associated with this problem are considered in section 3.

2. Time of phase relaxation

The supersaturation S in a vertically moving cloud parcel may be described by the equation

$$\frac{1}{1+S}\frac{dS}{dt} = au_z + b\frac{dq}{dt}. \qquad (1)$$

Here

$$a = \frac{g}{R_a T}\left(\frac{LR_a}{c_p R_v T} - 1\right), \qquad (2)$$

$$b = \frac{1}{q} + \frac{L^2}{c_p R_v T^2}, \qquad (3)$$

$$q = \frac{E(1+S)}{\rho_a R_v T}, \qquad (4)$$

Corresponding author: Ilia Mazin, 7401 Eastmoreland Road, 214, Annandale, VA 22003 USA
e-mail: ilmaz@juno.com

T, the air temperature; u_z the vertical velocity of a cloud parcel; g, the acceleration of gravity; L, the specific heat of condensation; ρ_a the density of air; R_a, R_v the specific gas constant of air and water vapor, respectively; c_p, the specific heat capacity of the air at constant pressure; E, the saturation vapor pressure with respect to water.

The solution of the Eq. (1) shows that the supersaturation in a cloud volume with time approaches some equilibrium value (Squires, 1952),

$$S_p = \frac{au_z}{cN\bar{r}} \qquad (5)$$

Here

$$c = 4\pi Ab\rho_w / \rho_a, \qquad (6)$$

$$A = \frac{DE}{\rho_w R_v T\left(1 + \left(\frac{L}{R_v T} - 1\right)\frac{DLE}{R_v T^2 k_a}\right)}, \qquad (7)$$

N is the droplet number concentration; $\bar{r}$ is an average droplet radius; k_a is the thermal conductivity of air; ρ_w the density of liquid water.

Mazin (1966) and Kabanov et al. (1971) showed that the characteristic time for changing supersaturation is

$$\tau_p \cong \frac{1}{4\pi DN\bar{r}}. \qquad (8)$$

Here D is a coefficient of water vapor diffusion in air. The physical meaning of the time of phase relaxation is that during the time period τ_p the difference $|S - S_p|$ decreases ("relaxes") by $1/e$ times due to condensation or evaporation of water vapor by cloud particles.

Equation 8 was derived by Mazin, (1966) under certain assumptions and simplification. More rigorous consideration are given by Kabanov et al. (1971) and Korolev (1994)

$$\tau_p = \frac{1}{cN\bar{r} + au_z} = \frac{F}{4\pi DN\bar{r}}. \qquad (9)$$

Here

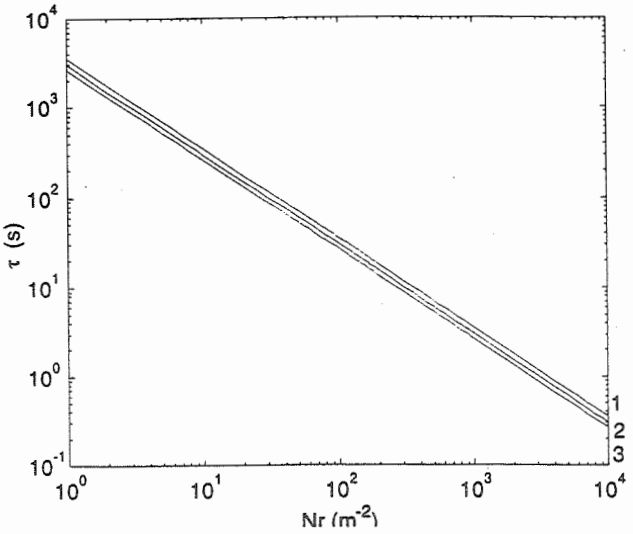

Figure 1. Time of phase relaxation versus $N\bar{r}$ for different temperatures (1) T=10°C, (2) T=-10°C, (3) T=-30°C.

$$F = \frac{4\pi D}{c + a\beta}, \tag{10}$$

$$\beta = \frac{u_z}{N\bar{r}}, \tag{11}$$

For ice particles (IP)

$$\beta = \beta_i = \frac{u_z}{\delta_1 N\bar{l}}. \tag{12}$$

Here $\bar{l}$ is an average ice particle size, δ_1 is the shape factor determined by the equation $f = \delta_1 l$. l is the accepted IP size and f is the electrostatic capacity of a conductor with the same shape as the ice particles (for spheres δ_1 =1).

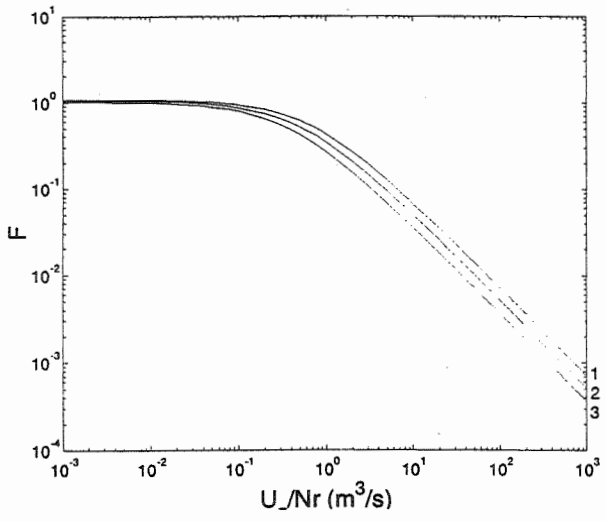

Figure 2. F versus $U_z/N\bar{r}$ for different temperatures (1) T=10°C, (2) T=-10°C, (3) T=-30°C.

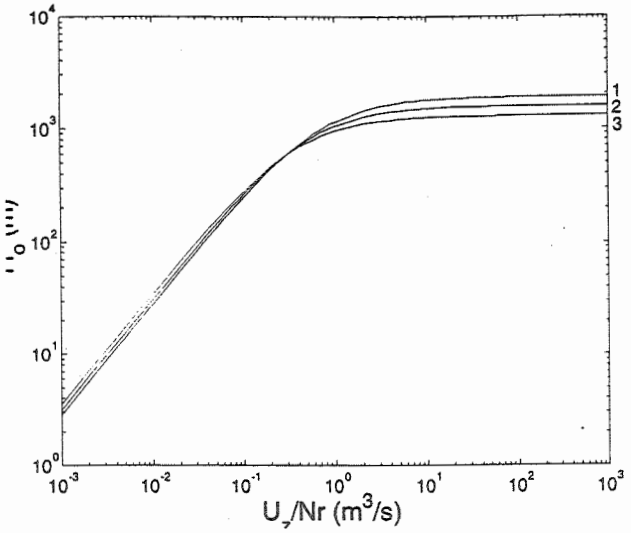

Figure 3. H_0 versus $U_z/N\bar{r}$ for different temperatures (1) T=-30°C, (2) T=-10°C, (3) T=10°C.

Fig. 1 shows time of phase relaxation versus $N\bar{r}$ for liquid clouds. It is seen from Fig. 1 that for typical $N\bar{r}$ ($10^3 m^{-2}$) in liquid clouds the time of phase relaxation is of the order of few seconds. Fig. 2 shows the dependence of the parameter F versus β. For liquid clouds usually β<0.1m^3/s. As it is seen from Fig. 1 for β<0.1m^3/s the value of F is rather close to unity and Eq. 8 can be used for calculation of τ_p with an accuracy of about a few percent. For β>0.1m^3/s F may be significantly different from unity and Eq. 9 should be used instead of Eq. 8. The situations with β>0.1m^3/s are typical for ice clouds, cloud boundaries and hazes.

To determine the phase transformation impact upon physical process in clouds, one must compare the characteristic time τ of the process with τ_p. For example, for high frequency turbulence when $\tau_t << \tau_p$, the latent heat of condensation/evaporation does not affect the dynamical processes in clouds and the turbulence could be considered the same as in clear air. This happens due to the condensational inertia of droplets, that is, the supersaturation changes are so fast that the cloud particles have no time to consume the excess water vapor (when S>0) or evaporate (when S<0) to keep the supersaturation close to S_p. For low frequency turbulence ($\tau_t >> \tau_p$) the temperature in a vertically moving parcel is close to wet-adiabatic conditions, since the cloud particles adapt to a supersaturation close to S_p.

The spatial scale of turbulence that divides these two type of processes (so called the phase

scale of turbulence) is $L_p = (\varepsilon \tau_p^3)^{1/2}$ (Kabanov and Mazin, 1970). Here ε is the rate of turbulent energy dissipation. For the turbulent fluctuations with the scales $L_r << L_p$ the role of phase transformation is negligibly small. The same approach may be used for assessing the role of condensational processes on the thermodynamics of a vertically moving cloud parcel with the velocity u_z. Consider a vertical displacement of a cloud parcel

$$H_0 = u_z \tau_p \qquad (13)$$

The physical meaning of H_0 is that for $H << H_0$ the condensation and associated heat processes in clouds may be neglected, whereas for $H >> H_0$ they should be taken into account. Substituting Eqs (9)-(10) into Eq. (13) yields

$$H_0 = \frac{F\beta}{4\pi D} = \frac{\beta}{c - a\beta} \qquad (14)$$

Fig. 3 shows the dependence of H_o versus β. It can be seen from Fig. 2 that for $\beta > 0.5 m^3/s$ $H_0 > 0.8$ km. In such a situation, if a vertical displacement of the cloud parcel is much less than about 0.8 km, the condensation of water vapor can be neglected. The value of H_o increases with increasing β up to about 2 km.

3. Glaciation of clouds

Assume that a cloud parcel in a mixed cloud contains ice particles with the concentration N_i and ice water content (IWC) W_i and liquid droplets with the liquid water content (LWC) W_w. The initial humidity at time $t=0$ is equal to the saturation over water and the vertical velocity of the parcel is $u_z=0$. The time of glaciation τ_g can be estimated as the time when

$$W_i(t) - W_i(0) = W_w(0) \qquad (15)$$

i.e. as a time when the changes in IWC would be equal to initial LWC. This time may be calculated using the equation of ice particle growth as (Mazin, 1983a)

$$\tau_g = C \frac{(\delta_2 \rho_i)^{1/3}}{\delta_1} \left(\frac{W_w(0)}{N_i} \right)^{2/3} \qquad (16)$$

$$C = \left(\frac{9\pi}{2} \right)^{1/3} \frac{E_i}{E_w - E_i} \left(\frac{R_v T}{4\pi D E_i} + \frac{L_i^2}{4\pi k_a R_v T^2} \right). \qquad (17)$$

$$\delta_2 = \frac{3 m_i}{4\pi l^3 \rho_i}. \qquad (18)$$

Here ρ_i is average ice particle density; E_w, E_i are the saturation water vapor pressure over liquid water and ice, respectively; m_i is the mass of a single ice particle.

In Eq. 16 it is assumed that ice particles have a monodisperse size distribution, and the supersaturation stays constant and close to the supersaturation over water during droplet evaporation.

Applying Eq. 16 to a mixed cloud at $T=-20°C$ with $W_w=0.1 g/m^3$ and spherical ice particles ($\delta_2=1$) having number concentration $N_I=10l^{-1}$ the time for glaciation is about τ_g ~5 min (Fig. 4). In natural clouds, ice concentrations larger than $10l^{-1}$ occur often in mixed phase conditions (Mazin et al.,1992). However, if the glaciation time were as short as 5-10 min, these zones would occur very infrequently. If the estimations of τ_g is correct, a possible explanation for the frequent occurrence of mixed phase is the existence of vertical (regular and turbulence) motions in clouds. For favorable conditions, the humidity in an updraft may be higher than the saturation value with respect to water and droplets will not evaporate even if ice particles do exist.

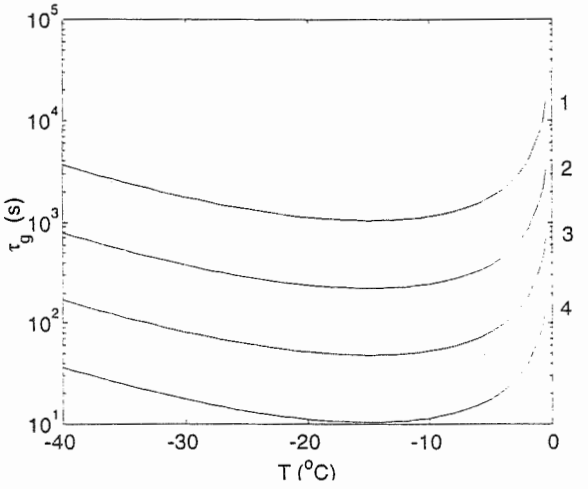

Figure 4. Glaciating time versus temperature. $W_w(0)=0.1 gm^{-3}$; (1) $N_I=1l^{-1}$, (2) $N_I=10l^{-1}$, (3) $N_I=100l^{-1}$; (4) $N_I=1000l^{-1}$.

In a rising ice cloud parcel, the equilibrium relative supersaturation with respect to ice (in this case $L=L_i$ in Eq.2) may be written as

$$S_{p,i} = \frac{a u_z \tau_p}{1 - a u_z \tau_p}. \qquad (19)$$

(15)

Using Eqs. 8-10 we can rewrite Eq.19 as

$$S_{p,i} = a\beta / c \qquad (20)$$

The value of a is of order 10^{-3}-10^{-4} m^{-1} and Eq.20 is valid when $u_z \tau_p$ is less than 1 km.

In liquid clouds usually (excluding the relatively thin boundary layers) τ_p is about ten seconds and u_z is about or less than 1 m, thus $u_z\tau_p$ is of order of 0.01km.

When a cloud parcel rises with some velocity from the level where supersaturation is equal to the equilibrium value for a motionless mixed cloud parcel (humidity is less than saturation with respect to water) the supersaturation rises. Thus, the rate of droplet evaporation slows down until saturation with respect to water is reached. At this point, droplets stop evaporating and start to grow. In such conditions even new droplets may appear. When the cloud becomes saturated with respect to water, the ice particles grow rather fast. They may become large enough and fall out from the cloud. The mixed cloud will transform in this case into a liquid one. This situation probably does not occur often, but in principle it is possible. If after that, the updraft velocity diminishes the relative humidity will decrease. The droplets begin to evaporate while new ice particles may originate. Thus the liquid cloud will transform once again into a mixed one. Such cycles were predicted by Bujkov, (1978). They can exist in layer clouds or in portions of these clouds and may lead to sharp horizontal inhomogeneity of the phase structure.

If the parameter β_i (and thus the parameter $u_z\tau_p$ as well) is small enough, than $S_{p,i}<S_{w,i}$, cloud droplets evaporate, and the mixed cloud glaciates. Here $S_{w,i}$ is the supersaturation with respect to ice when the air is saturated with respect to water. When $S_{p,i}>S_{w,i}$, mixed clouds keep their phase state or even transform into liquid clouds. The demarcation condition $S_{p,i}=S_{w,i}$, separate one possibility from the other (Mazin, 1986). Substituting in the equality $S_{p,i} = S_{w,i}$, the expression of $S_{p,i}$ from eq.(20) and using the Eqs. 8-10 we find that the direction of the process is determined by the parameter $\beta_i = u_z / \delta N \bar{l}$. Droplets evaporate when parameter G (we may call it the glaciating parameter) is negative, where

$$G = \beta_i - \frac{c}{a} S_{w,i}. \qquad (21)$$

Droplets can exist steadily in clouds when the glaciating parameter G is positive. Thus, for p= 800mb and T=-30°C, $\delta N_i \bar{l}$=10 m^{-2} ($N_i=10^2 l^{-1}$ and $\bar{l}$=100μm) droplets can appear if u_z>0.7ms^{-1}.

The time to glaciate the cloud depends mainly on the parameter β_i i.e. on the product of ice particle sizes and their concentration, and on an updraft velocity.

REFERENCES

Bujkov M.V., 1978: Numerical modeling of stratiform clouds (in Russian). *The review VNIIGMI-MCD, ser. "Meteorology"* Obninsk. 62 p.

Kabanov, A. S., and I. P. Mazin., 1970: The influence of phase transition processes on turbulence in clouds (In Russian). *Ttudy CAO.*, **98**, 113-121.

Kabanov A.S., Mazin I.P., and V.I. Smirnov, 1971: Water vapor supersaturation in clouds. (In Russian). *Trudy CAO.*, **95,** 50-61.

Korolev A.V., 1994: A study of bimodal droplet size distributions in stratiform clouds. *Atmos. Res.* 32, 143-170.

Mazin, I.P., 1966: On temperature and humidity stratification in clouds . (In Russian) *Trudy CAO*, **71**, 3-15.

Mazin, I.P., 1983: Phase changes in clouds. *Soviet Meteorology and Hydrology*, N7, 26-34

Mazin, I.P., 1986: Relationship between phase structure of clouds and vertical movements. *Meteorology and Hydrology*, N 11.

Mazin I.P., and S.M., Shmeter, 1983: *Clouds, their structure and formation.* (In Russian). Leningrad, Gidrometeoizdat, 279 p.

Mazin I.P., Nevzorov A.N., Shugaev V.F., and A.V Korolev.,1992: Phase structure of stratiform clouds. *Proc. 11th ICCP*, Montreal, 332-335.

Squiers, P., 1952:The growth of cloud drops by condensation. *Aust. J. Sci. Res.*, **5**, 66-86

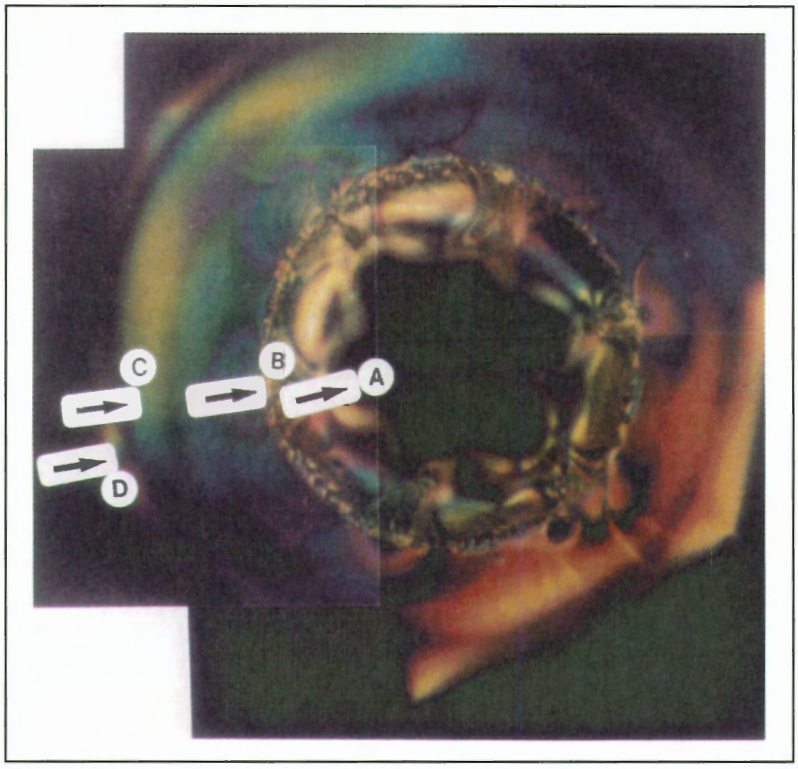

Disc-shaped snow crystal with four concentric patterns.

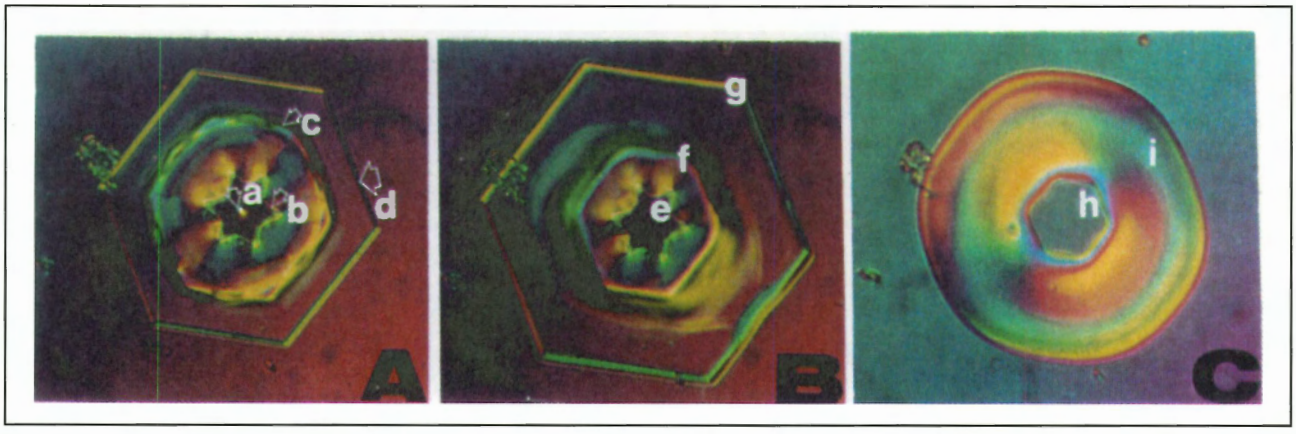

Metamorphosing of a snow crystal under near ice saturation.

See Volume 1, paper 9.11, p. 653.

Cloud edges and evolving wave; see Volume 1, paper 9.6, p. 633.